Numerical Simulation of Specific Absorption Rate and Induced Currents in a Rat's Pixel Brain due to Radiofrequency Fields

R. Rojas, S. E. Solis, and A. O. Rodríguez
Centro de Investigacion en Instrumentacion e Imagenologia Medica
Universidad Autonoma Metropolitana
Iztapalapa, Av. San Rafael Atlixco 186, Mexico DF 09340, Mexico

Abstract— The Specific Absorption Rate has been adopted as the reliable parameter for RF power safety for performing magnetic resonance imaging experiments. When the magnetic field is greater than 3 T, the RF coil performance is strongly dependent of the interaction with organic tissues. Additionally, the rat body size becomes comparable to the RF wavelength and the interactions between the tissue and the coil becomes important for safety reasons. Mathematical expressions based on Maxwell equations can be derived to study the interaction between matter and the RF coil for the simplest cases. However, when dealing with complex coil layouts the analytical solutions become extremely difficult to find. A numerical method based on the finite element method is presented here as an alternative method to study this problem. Specific Absorption Rate and induced currents were numerically computed with this methodology.

1. INTRODUCTION

The Specific Absorption Rate (SAR) has been adopted as the reliable parameter for RF power safety when performing Magnetic Resonance Imaging (MRI) procedures. When the magnetic field is greater than 3 T, the performance of the RF coil is a function of the interaction with organic tissues, because the Larmor frequency (MR imager operational frequency) increases proportionately with magnetic the field strength, then the human head/body size becomes comparable to the RF wavelength and, the interaction between the tissue and the coil becomes an important issue [1], because the eddy currents are greatly increased inside the biological sample. The temperature change of the tissue can produce changes in the rate of biochemical reactions and/or burns tissue [2]. Mathematical expressions based on Maxwell equations can be derived for the simplest cases [3], but is very difficult to derive analytical expressions for more complex geometries of RF coils. The numerical study of the electromagnetic interactions of MRI coils and biological tissues is a good alternative. A numerical method based on Finite Element Method (FEM) to compute the electric and magnetic fields, and the induced currents in a pixeled rat brain model is presented here. This approach was also used to numerically calculate SAR. With the intention to experimentally validate our computational results, we designed and built a circular-shaped coil and tested it on a 7 T/21 cm Varian animal scanner.

2. THEORETICAL BACKGROUND

The SAR is a measure of power dissipated in biological sample and is defined by:

$$\text{SAR} = \frac{\text{Total RF energy dissipated in sample}}{(\text{Exposition time})(\text{Sample weigh})} \tag{1}$$

Alternatively, it may regarded as:

$$\text{SAR} = \frac{P}{m} \tag{2}$$

where, P is the power losses, and m is the sample mass. An expression for the power losses in the form of Joule heating within the specimen can be derived from eddy currents induced by the alternating magnetic field [4]:

$$P = \sigma \left|\vec{E}\right|^2 V \tag{3}$$

where σ is the effective conductivity, $/E/$ is the amplitude of the electric field produced by the sample, and V is the sample volume. Considering that loss power is absorbed by tissue, and there mass density ρm, replacing Equation (3) in (2), the SAR is [5]:

$$\text{SAR} = \frac{\sigma \left|\vec{E}\right|^2}{\rho_m} \tag{4}$$

Rojas and Rodríguez [6] proposed a matrix numerical scheme based on a Finite Element Method (FEM) to compute the electric and magnetic fields using a commercial software tool.

3. NUMERICAL METHOD

An anatomical 3D pixel model of the rat brain head (brain and skull) was designed with the software AUTODESK 3DS MAX (V.9.0 Autodesk, San Rafael, CA, USA) then a single loop coil figure was also developed and placed over the head model as shown in Fig. 1.

The electric and magnetic fields were computed with FEM using the tissue properties reported in [7] at 10, 50, 100 and 300 MHz. The coil was operated in the transmission mode, and it produce a magnetic field over the pixeled rat brain, Fig. 2 shows a 3D coronal cut of the electric field over the sample at 50 MHz, then the electric current density induced in the head model by the coil was estimated. The electric field was used to assess the SAR with especially developed program was used MATLAB (MathWorks, USA).

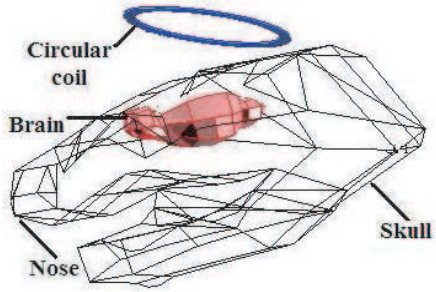

Figure 1: Brain and skull pixel head model, with RF single loop coil.

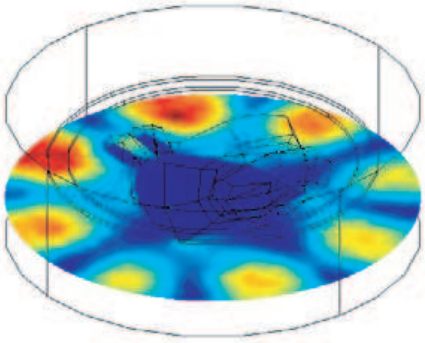

Figure 2: Electric field produced over the sample. Coronal cut of pixel head model at 50 MHz.

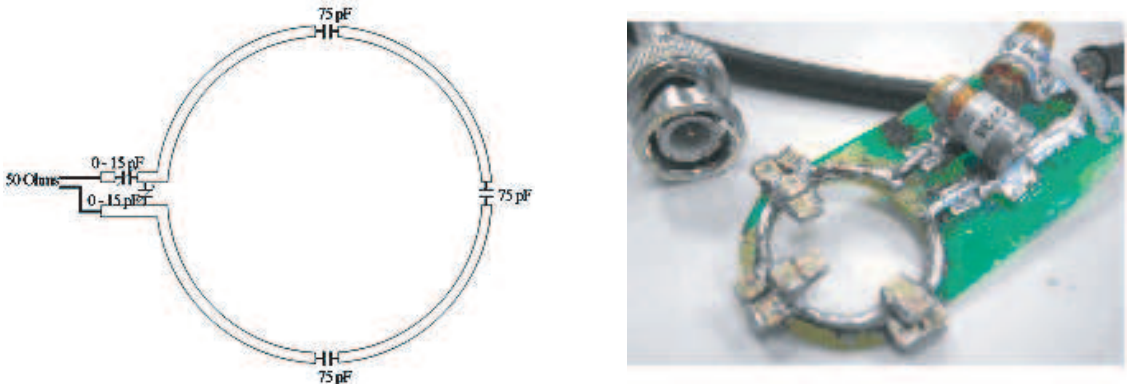

Figure 3: Single-loop surface coil prototype, with capacitors configuration and 50 Ω coaxial cable attached. Electronic components scheme (left), Photo (right).

4. EXPERIMENTAL METHOD

A single-loop circular coil, having the same diameter of the slotted surface coil, was also built to compare our theoretical results experimentally. This single-loop surface coil prototype, was developed for rats using a 0.2 mm thickness copper sheet. The coil dimensions were: outside diameter 2.1 cm, inside diameter 2.0 cm. The schematic distribution of the electronic components are shown in Fig. 3 (left), the Fig. 3 (right) shown a coil photo. A 50 Ω-coaxial cable was attached to the coil prototype to conduct the signal to the low-noise preamplifier. The coil prototype was matched and tuned to 50 Ω and 170.2 MHz, respectively. The resonant frequency was measured using a network analyzer (Model 4396A, Hewlett Packard, Agilent Technologies, CA), with the loss return (S_{11}). This coil prototype, was first proved with a cooking oil-filled phantom, once determined the coil safety and there excellent imaging quality, it was used over a real head rat.

5. RESULTS

Figure 4 shows images of the magnetic and electric fields calculated with Fem, this images taken in a 2D projection (coronal cut), was transformed in numerical matrices sets, and SAR of the coil operating in the transmission mode, was calculated using the electric matrix with MATLAB program, the result is a numerical matrix of the SAR, that was transformed in to image showed in Fig. 4 too.

Figure 5 shows another important and expected result, due to the electric properties of the brain, the induced currents are displaced from the middle to the surface of the brain, the intensity increments proportionally with the frequency, and the magnitude of this intensity is extremely low and consequently safety.

To experimentally validate our method, we acquired MR images of a rat brain using a single surface coil designed and developed in our laboratory. T1-weighted images were acquired with a standard gradient-echo sequence with TR = 900 ms, TE = 25 ms, FOV = 16 × 16 mm, thickness = 2 mm, NEX = 1, Matrix = 256 × 256. All imaging experiments were conducted on a 7 T/21 cm

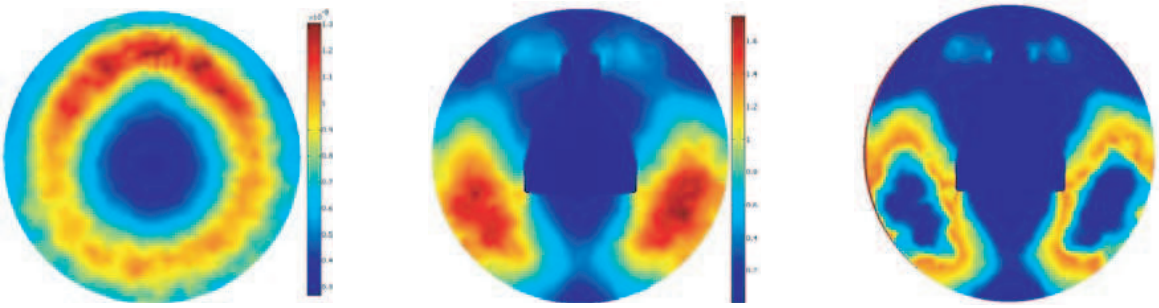

Figure 4: Magnetic field (left). Electric field (middle). SAR (right). All at 1 MHz.

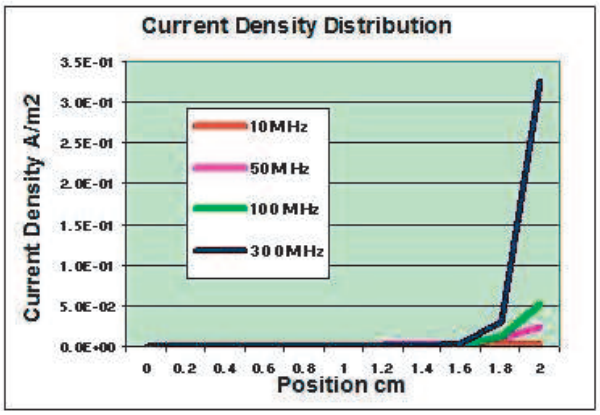

Figure 5: Graphic: Profiles were computed from middle to the surface of the pixel rat's brain and plotted vs. current density.

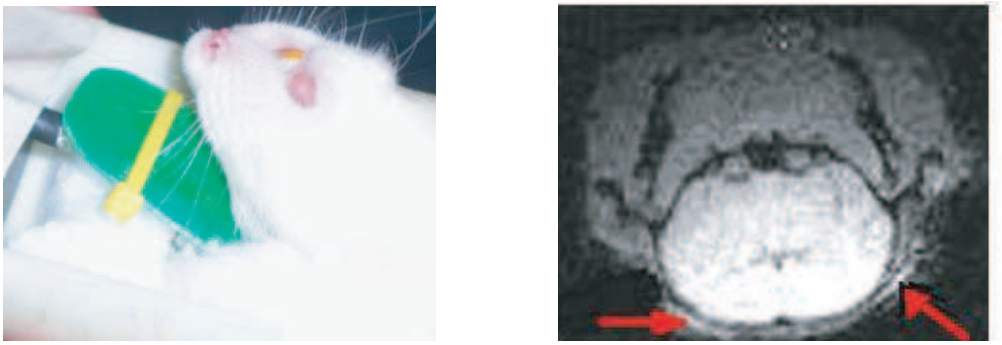

Figure 6: Single circular coil position on the animal model (left).

Varian system. Fig. 6 shows the single circular coil position on the animal model (left), and shows too MR brain image of a rat (right).

6. DISCUSSION

A single surface coil was chosen for simplicity, however it can also be extended to more complex coil configurations such as the birdcage or coil arrays. Other pixel anatomical models for human organs can be constructed and numerically simulated with this method. This numerical method can offer a graphical tool to illustrate the behaviour of the SAR and the eddy currents inside the organs and tissues. Fig. 5 shows an expected result, the induced currents intensity, depends of the frequency, and this currents transform into surface currents, similar to conductor materials. However, the current density generated had a very low intensity, so the energy dissipated in the form of heat is very poor. Experimental results of Fig. 6 (right), compare very well with those in Fig. 4. The maximum intensity is in the coil proximity. The Fig. 6 (right) image shows hyperintensities as predicted by the numerical simulations of Fig. 5.

ACKNOWLEDGMENT

National Council of Science and Technology of Mexico for a Ph.D. scholarship.

REFERENCES

1. Ibrahim, T. S., A. M. Abduljalil, B. A. Baertlein, R. Lee, and P. M. L. Robitaille, "Analysis of B1 field profiles and SAR values for multi-strut transverse electromagnetic RF coils in high field MRI applications," *Phys. Med. Bio.*, Vol. 46, 2545–2556, 2001.
2. Ocali, O. and E. Atalar, "Ultimate intrinsic signal-to-noise ratio in MRI," *Magn. Reson. Med.*, Vol. 39, 462–473, 1998.
3. Ocegueda, K. and A. O. Rodríguez, "A simple method to calculate the signal-to-noise ratio of a circular shaped coil for MRI," *Con. Magn. Reson.*, Vol. 28A, 422–429, Part A, 2006.
4. Bottomley, P. A. and E. R. Andrew, "RF magnetic field penetration, phase shift and power dissipation in biological tissue: Implications for NMR imaging," *Phys. Med. Bio.*, Vol. 23, 630–643, 1978.
5. Jin, J., *Electromagnetic Analysis and Design*, 24–25, CRP Press, Boca Raton Florida, 1999.
6. Rojas, R. and A. O. Rodríguez, "Numerical study of the optimal geometry of MRI surface coils," *20th IEEE EMBS Conf.*, 2007.
7. Gabriel, S., R. W. Lau, and C. Gabriel, "The dielectric properties of biological tissues: III. Parametric models for the dielectric spectrum of tissues," *Phys. Med. Bio.*, Vol. 41, 2271–93, 1996.

Computation of SNR and SAR Based on Simple Electromagnetic Simulations

R. Rojas and A. O. Rodriguez
Centro de Investigacion en Instrumentacion e Imagenologia Medica, Universidad Autonoma Metropolitana Iztapalapa, Av. San Rafael Atlixco 186, México DF 09340, México

Abstract— The signal-to-noise ratio is an accepted parameter to measure radiofrequency coil performance. The specific absorption rate is the only quantifiable safety measure for RF coils. Analytical expressions can be derived for the simplest cases of surface coils, but more complex coil configurations require a very complicated mathematical framework to be solved. The numerical study of the electromagnetic behavior of magnetic resonance imaging coils and interaction with biological tissues is a good alternative. A numerical method based on the finite element method to compute the electromagnetic fields of single surface coil is presented here. These numerical simulations are used to numerical calculate the signal-to-noise ratio and specific absorption rate for a circular-shaped coil and, the induced currents generated.

1. INTRODUCTION

The quality of the magnetic resonance image is greatly determined by the radiofrequency (RF) coil performance. The signal-to-noise ratio (SNR) is the widely accepted parameter to measure coil performance. The SNR depends mainly on the electric field generated by the sample and the coil magnetic field [1, 2]. The electric field may be regarded as the source of noise and the magnetic field generated by the coil as the source of stored energy. The specific absorption rate (SAR) is the safety measure and is a function of the electric field generated by the sample to be imaged. Both parameters depend on electromagnetic fields generated by both the sample and the RF coils. A simple numerical approach is proposed in this paper to compute these electromagnetic fields.

2. MATHEMATICAL BACKGROUND

The noise is proportional to the effective resistance R_{effec} including the interaction with organic tissue, system electronics, and coil induction [3]. Because, the SNR is proportional to the induced MR signal (v) and inversely proportional to the RMS of thermal noise voltage in coil, Edelstein proposed the following expressions for a single coil, along the coil axis [4]:

$$\text{SNR} = \frac{v}{\text{rms of thermal noise}} \tag{1}$$

and

$$v = \omega M V B_{1z} \tag{2}$$

$$\text{rms of thermal noise} = \sqrt{4kT\Delta f R_{effec}} \tag{3}$$

where ω is Larmor's frequency, M magnetization, V voxel volume, B_{1z} magnetic field produced by the coil in z direction, k Boltzmann's constant, Δf bandwidth, and R_{effec} effective resistance.

Using (2) and (3) in (1), the SNR is:

$$\text{SNR} = \frac{\omega M V B_{1z}}{\sqrt{4kT\Delta f R_{effec}}} \tag{4}$$

The effective resistance depends on the power losses P and of the induced current I, then

$$P = I^2 R_{effec} \tag{5}$$

and the power by volume unit is a function of conductivity σ and the electric field

$$\frac{dP}{dV} = \sigma \left|\vec{E}\right|^2 \tag{6}$$

Using the Equations (5) and (6) in (4), we have

$$\mathrm{SNR} = \frac{\omega M V B_{1z}}{\sqrt{4kT\Delta f \sigma V E_z}} \tag{7}$$

simplifying,

$$\mathrm{SNR} \propto \frac{\text{Magnetic field}}{\text{Electricf field}} = \frac{\left|\vec{B}_{1z}\right|}{\left|\vec{E}_z\right|} \tag{8}$$

(SAR) is the only quantifiable safety measure for RF coils. The interaction between the RF and organic tissue can increase the temperature and produce biochemical reaction changes or inclusive a possible burn of tissue [5]. The US FDA recommends that the energy absorption should not be greater than 0.4 W/kg in body and 3.2 W/kg in head [6]. It is very important the SAR determination to assure the patient safety. Since SAR is a measure of the energy dissipated in the biological sample, it can be defined as:

$$\mathrm{SAR} = \frac{\text{Total energy of RF dissipated in sample}}{(\text{Exposition time})(\text{Sample weight})} \tag{9}$$

The power losses can be expressed using the Joule effect absorbed by the tissue, which is inversely proportional to tissue mass density. Finally, SAR can be expressed using Jin's formulation [7] and the Equation (9):

$$\mathrm{SAR} = \frac{P}{\rho_m} \tag{10}$$

Replacing Equation (6) in (10), a good approximation can be obtained:

$$\mathrm{SAR} = \frac{\sigma V \left|\vec{E}\right|^2}{\rho_m} \tag{11}$$

then

$$\mathrm{SAR} \propto \left|\vec{E}\right|^2 \tag{12}$$

Analytical expressions for both the SNR and SAR based on Maxwell equations can be derived for the simplest cases of surface coils, but it is very difficult derive expressions for more complex geometries due to the complicated mathematical framework involved in it. The numerical study of the electromagnetic behavior for MRI coils and biological tissues is a good alternative. A numerical method based on the Finite Element Method (FEM) to compute the electromagnetic fields of single surface coils is presented here. These numerical simulations are the base to finally calculate the SNR and SAR for a circular-shaped coil and the induced currents generated by it.

3. METHODOLOGY

An anatomical pixel model of the human head (brain and skin) was developed using the software tool, AUTODESK 3DS MAX (V. 3.2 Autodesk, San Rafael, CA, USA). This pixel model was imported to the software tool, COMSOL MULTIPHYSICS (V. 3.2, COMSOL, Burlington, MA, USA). A single loop coil was also developed with the same tool and placed over the head model as shown in Fig. 1(a) the electric and magnetic fields were computed with COMSOL using the tissue properties reported in [8] for the resonant frequency of 128 MHz. In the first run, the coil was operated in transmission mode and the electric current density induced in the head model by the coil was estimated. In the second run, the induced currents were used to numerically compute the electric field produced by the head. With these data, matrices were formed to numerically compute the SNR and the SAR using specially-written programmes in MATLAB (Math Works, USA). Fig. 1(b) shows a three-dimensional illustration of the electric field in sagittal orientation.

Figure 2 shows a coronal cut of model (a) gives an image of the coil magnetic field in the transmission-mode operation, (b) shows the electric field generated by the sample after the excitation (reception coil operation).

Using the magnetic and electric fields data in Fig. 2, the SNR and the SAR were computed for this particular configuration.

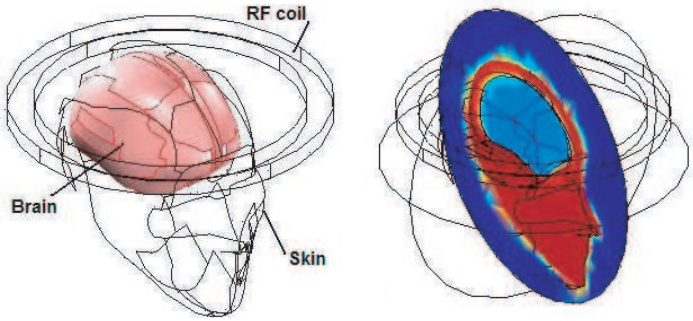

(a) (b)

Figure 1: (a) Anatomical pixel model of human head, (b) three-dimensional electric field of the sample in sagittal orientation with the coil in transmission mode only.

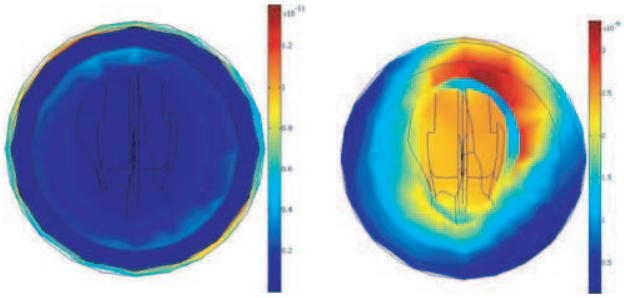

(a) (b)

Figure 2: (a) Magnetic field generated by the coil in transmission mode, (b) electric field generated by the sample after excitation by the RF coil.

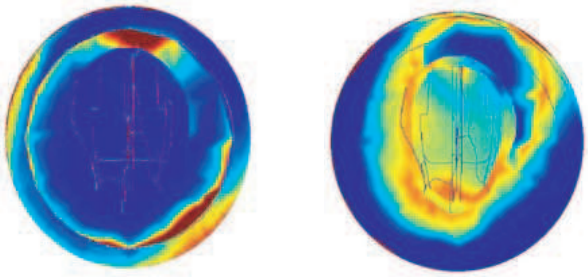

(a) (b)

Figure 3: (a) Surface coil SNR operating in transmission-mode, (b) SAR generated by the sample.

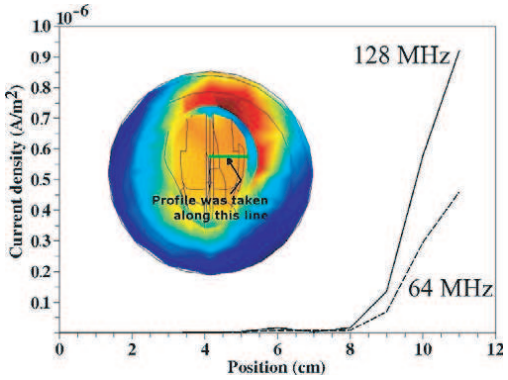

Figure 4: Current density induced over the brain measured from the centre towards the brain border.

Figure 4 shows profiles of current density as a function of position for two different frequencies. An increase in the induced currents is observed at the surface of the brain, this is due to the electric properties of the brain and that higher frequency leads to a higher current density. Additionally, induced currents were also computed and showed an expected pattern. Therefore, the induced current intensity increases as a function of the frequency.

4. CONCLUSION

It has been proved that it is possible to numerically compute the electromagnetic fields for a simple coil configuration together with a pixel model. A circular-shaped coil was chosen for simplicity, however this approach can also be extended to more complex coil configurations such as the birdcage or coil arrays. Other pixel anatomical models of human organs can be constructed and numerically simulated with this method for higher resonant frequencies applications too. This numerical method can offer a graphical tool to illustrate the behavior of the SNR and SAR. It can be particularly useful for those students and researches starting to familiarise with the development of RF coil for MRI, since the simulation method is easy to implement. The induced current intensity obtained, may serve as guidelines to study safety issues involving RF coils.

A simple numerical method to assess the SNR and SAR is presented using he FEM and this can be extended to other coil configurations and regions of interest. The numerical results showed the viability of this method to study the coil performance of simple coil configurations involving models simulating human organs.

ACKNOWLEDGMENT

- Centro de Investigacion en Instrumentación e Imagenologia Medica. Universidad Autonoma Metropolitana Iztapalapa.
- National Council of Science and Technology of Mexico for a Ph.D. scholarship.

REFERENCES

1. Schwartz, M., *Information Transmission, Modulation, and Noise*, Chapter 5, Mc Graw-Hill, 1959.
2. Ocali, O. and E. Atalar. "Ultimate intrinsic signal-to-noise ratio in MRI," *Magn. Reson. Med.*, Vol. 39, 462–473, 1998.
3. Hoult, D. I. and R. E. Richardsm, "The signal-to-noise ratio of the nuclear magnetic resonance experiment," *J. Magn. Reson.*, Vol. 24, 71–72, 1976.
4. Edelstein, W. A., G. H. Glover, C. J. Hardy, and R. W. Redington, "The intrinsic signal-to-noise ratio in MNR imaging," *Magn. Reson. Med.*, Vol. 3, 604–618, 1968.
5. Challis, J. L., "Mechanisms for interaction between RF fields and biological tissue," *Bioelectromagnetics Supp.*, Vol. 7, 98–106, 2005.
6. Beravs, K., R. Frangez, and F. Demsar, "Specific absorption rate study for radiofrequency current density imaging using a two-dimensional finite element model," *Magn. Reson. Med.*, Vol. 44, 610–615, 2000.
7. Jin, J., *Electromagnetic Analysis and Design*, CRP Press, Boca Raton Florida, 24–25, 1999.
8. Gabriel, S., R. W. Lau, and C. Gabriel. "The dielectric properties of biological tissues: III. Parametric models for the dielectric spectrum of tissues," *Phys. Med. Biol.*, Vol. 41, 2271–2293, 1996.

Biological Measurement in Healthcare Refrigerator

Bo-Rim Ryu[1] and Heung-Gyoon Ryu[2]

[1]Seoul Women's University, Korea
[2]Chungbuk National University, Korea

Abstract— In this paper, we like to investigate the biological measurement in the healthcare refrigerator, which can be implemented by body data measuring sensors and internet access. Some desired body data can be measured by the handle sensor and foot mat sensor in front of the refrigerator without extra health sensor on the body. Especially, the refrigerator can provide healthcare functions: 1) Basic body diagnosis and monitoring, 2) healthcare and report, 3) provision of well-being menu or healthy menu, and 4) search and recommendation of restaurant information, etc. The refrigerator furnished in all home could play important roles including both healthcare and personal nutritionist. Health or well-being meals after checking health state can be recommended to help improvement of dietary or health life. Also, we will show the function realization in the above proposed structure.

1. INTRODUCTION

We want to diagnose the basic body status before going to see medical doctor through devices of home network or portable equipment in any feasible convenient method. Connecting for the medical service, it is possible to take preventive measures, diagnosis, medical treatments and management all the time, everywhere. It is a new paradigm of medical service that is not restricted by time and space. But sometimes for the healthcare, people must intentionally attach the sensor on their body and have the devices related with sensor. Therefore, getting data is very uncomfortable. Internet has already been deeply settled in our life. Many researchers and companies try to apply Internet to many fields. So, we like to propose the concept of smart refrigerator practically by integrating internet with life appliances, refrigerator which is power on every time.

Some related studies were proposed. They proposed a way of managing wireless home network security which allowed appliances to determine whether other appliances belonged to the same network. They assumed that a way of protecting communication was already provided in the data link layer, and provided a way of distributing an encryption key [1]. Another work presented a smart medical refrigerator [2]. The method was suggested to monitor the elderly patient continual usage of medications on time. The smart medical refrigerator monitored the use of prescribed medicine by patients and could alert a physician, healthcare provider or family members if the patient did not access the medicine in a set time frame. The smart medical refrigerator was connected to a standard telephone line.

Therefore, in this paper, we propose and discuss the design and system performance of smart refrigerator for biological health care. Some wanted body data can be measured by the handle sensor and foot mat sensor in front of the refrigerator without extra health sensor on the body. Especially, the refrigerator can provide healthcare functions: 1) Basic body diagnosis and monitoring, 2) healthcare and report, 3) provision of well-being menu or healthy menu, and 4) search and recommendation of restaurant information, etc. The refrigerator furnished in all home could play important roles including both healthcare and personal nutritionist. Health or well-being meals after checking health state can be recommended to help improvement of dietary or health life. The design of the smart refrigerator structure and function can be implemented by body data measuring sensors and internet access. Also, we will show the function realization in the above proposed structure. Smart refrigerator can help to improve healthy life by providing the suitable diet menu after measuring the state of health. Additionally, the designed smart refrigerator shows the necessary menu materials for shopping and restaurants information.

2. CONCEPTS AND SYSTEM DESCRIPTION

From the system configuration point of view, smart refrigerator proposed is composed of 5 parts. First part is the measurement part which gathers the sensing signal from the living body. Second part is the processing part that is the heart of this system and finally provides the output of the 1) basic body diagnosis and monitoring, 2) healthcare and report, 3) provision of well-being menu or healthy menu, and 4) search and recommendation of restaurant information, etc. Third part is

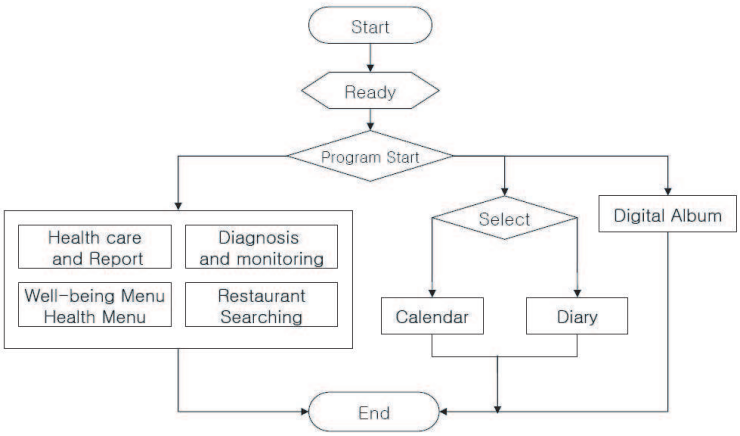

Figure 1: Flow chart of basic operation.

the data storage part which stores and manages the living body signals processed. Fourth part is the graphic generation part which generates the image signals to display the data as image. And last part is the display part which displays the data through the screen on the refrigerator. The data storage part is equipped with the user's interface part and the storage part which contains the user's physical data from the user interface part. The storage part has a menu database and program. The classified menu is stored in a menu database according to the living body signals. By using a menu database the program can automatically order the necessary foods through internet shopping mall. The menu is selected from personal health data. Personal health data is reported in accordance with the physical data, the living body signals and health state.

3. MEASUREMENT AND ANALYSIS OF BODY DATA

Until now, we have measured the state of the body by attaching the sensor on the body, which is very inconvenient. So we like to suggest the sensing can be possible when user stand and take the door handle in front of the smart refrigerator proposed. The devices which sense the living body signals are placed on the refrigerator door knob and bottom mat. This device will be turned on when the user stands on the mat. If we turn off the devices, the display part of refrigerator will be used as digital album to show the digital pictures. The obtained data are stored in individual folders of the storage part and are shown as graphs on the screen by comparing with standard weight, body mass index etc. The monitor has a built-in CPU and displays results from measurements.

There are two parts of sensors: Sensor of door handle and floor mat. Body data such as the quantity of body fat, muscle and body water could be measured by both handle sensor and floor mat sensor. Handle sensor can measure the body temperature. When the height and age value come, the smart health care program analyzes the input data and shows the result. The sensors can read the data while user is holding sensors and standing. First of all, body composition analysis result can show the present status of body composition. By comparing these results with the standard range, it is easy to understand the current body condition. Muscle-Fat analysis and obesity diagnosis are also a sort of body composition analysis. Bar graph can be used to display important features necessary to diagnose obesity. By comparing the lengths of bars, obesity can be identified. Body water checks segmental water distribution and the levels of muscles development in each segment. The amount of body water is closely related to muscle mass, allowing for segmental muscle development to be estimated.

There are some fitness score which reflects the health state. Those would be basal metabolism rate, obesity diagnosis, calorie recommendation, menu recommendation and checking body balance. Compared with standard weight and obesity rate, the final diagnosis results can be shown in the graph form through LCD screen. The results can be stored in processor memory embedded in the monitor. When electricity from both handles and bottom sensors flows through the body, depending on the amount of body water, electricity value is measured. A body composition checking system is based on the assumption that the body is a cylinder. Body water within the cylinder can be calculated using the length, volume value. The weight and height are inputted by a user. Fig. 3 shows the measurement of body data and analysis module. Smart refrigerator proposed can access

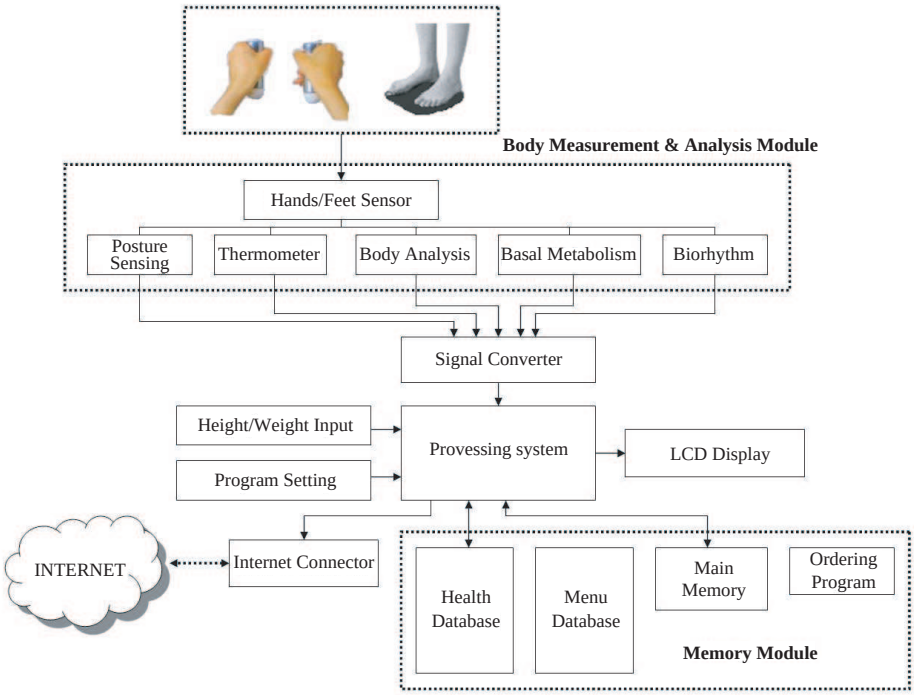

Figure 2: Block diagram of body measurement and analysis module.

Sensor items	Extra-Input data	Output by the health care program
Handle sensors - Body temperature - Body composition elements (Muscle-fat analysis, Visceral fat, Body water), etc Floor mat sensors - Body weight - Body composition, etc	Height, Age	- Basal Metabolic Rate - Obesity diagnosis - Calorie recommendation - Menu recommendation - Checking body balance

Figure 3: Body data measurement.

internet and has a LCD/Touch Screen. This feature is very powerful because we can always get information that we want through internet. For measuring the body signals and other data, user stands upright on the mat and holds the handle knob for 30 seconds. There should be many kinds of data for the health management for all diseases. However, several measurement items will be good barometers for the basic every day health care. Most probably living body data which can be obtained from human body are temperature, the quantity of body fat, quantity of muscle, biorhythm, basal metabolism and quantity to consume recommendation a day.

Body fat is the percentage of the fat weight in total weight. It can be measured by using the principle of analyzer of body substances. In case of males, if it is over 25% and in case of females, if it is over 30%, they can be judged as obesity. In recent years, body substances are measured and analyzed by using the method of BIA (Bioelectric Impedance Analysis). BIA is the method to measure resistance by sending weak electric current through human body. If weak electrical current is flown into human body, it runs following the body water. The amount of resistance of human body against the current depends on the body water. Processing system plays an important role of connecting refrigerator with external internet, analyzing and processing obtained data from sensing devices, interchanging internal data with memory module and outputting into the monitor. And its components are largely divided into body measurement module, memory module, LCD Screen

Measurement method	Impedance measurements by using 3 different frequencies
Frequency	5, 50, 150 kHz
Measurement points	Left arm, left leg, right arm, right leg, torso
A flow of electricity	180 μA
power source	AC100~220V, 50/60 Hz
Data input equipment	Touch screen type
Measure extent	100~950 Ω
Measurement duration	less than 30sec
Height range	80~200㎝
Weight range	10~200㎏
Age range	5~100
Operation environment	10~40℃, 30~75%RH

Figure 4: Measurement specification.

and external internet.

We like to propose the function to provide recommended health and wellbeing menu.

- The features to provide basic menu with housewives who are at the center of home life and order materials for food.
- To provide diet menu with those who are dieting.
- To provide for one-dish dinner for simple meal with tired housewives or those who are not accustomed to cook.
- To provide menu considering health and longevity for anti-aging and prevention of cancer for senior citizens.

It is possible to select 4 kinds of menu recommended as a result of user's choice. And if a user wants, it is possible to order materials of food by immediately connecting with internet shopping malls through the refrigerator LCD screen.

After selecting menu, if a user doesn't want to order the materials through the internet, it is possible that the user can transmit the list of materials to their cellular phone. Therefore, all users can go out to buy materials of food without additional memo. This action sending text message to user's cellular phone is controlled by the switch attached on the sensor. And when the switch is off, the monitor of refrigerator is used as digital frame instead.

As shown in Fig. 4, refrigerator provides information about delicious and dietary restaurants. Information is type of food and location of restaurants for user's convenience. And if necessary, ordering is possible for delivery. According to the data inputted from touch monitor, it is composed of the display part, the communication part, the memory part and the control part. The display part is on the front of refrigerator to show the information of menu, materials, restaurants' type or location. Information is downloaded according to the individual data about health in the memory. The memory part includes the program to interlock database of menu, individual health information and materials of food.

4. CONCLUSIONS

Smart refrigerator proposed has not almighty functions. There may be a lot of health management data for all diseases. However, several measurement items will be good barometers for the basic every day health care. Most probably living body data which can be obtained from human body are temperature, the quantity of body fat, quantity of muscle, biorhythm, basal metabolism and quantity to consume recommendation a day. In this paper, we discussed the design and system performance of smart refrigerator for health care. Some wanted body data can be measured by the handle sensor and foot mat sensor in front of the refrigerator without extra health sensor on the body. Especially, the refrigerator can provide healthcare functions: 1) Basic body diagnosis and monitoring, 2) healthcare and report, 3) provision of well-being menu or healthy menu, and 4) search and recommendation of restaurant information, etc. The design of the smart refrigerator structure and function can be implemented by body data measuring sensors and internet access.

The future growth possibilities of functions and features are endless. By using the proposed system, ordinary people can manage their health easily and effectively.

REFERENCES

1. Nakakita, H., K. Yamaguchi, M. Hashimoto, T. Saito, and M. Sakurai, "A study on secure wireless networks consisting of home appliances," *International Conference on Consumer Electronics, ICCE 2002*, Digest of Technical Papers, 178–179, 2002.
2. Kuwik, P., T. Largi, M. York, D. Crump, D. Livingston, and J. C. Squire, "The smart medical refrigerator," *IEEE Potentials*, Vol. 24, No. 1, 42–45, Feb.–Mar. 2005.
3. Loh, P. K. K. and D. Y. H. Let, "A cost-effective space sensing prototype for an intelligent refrigerator," *8th International Control, Automation, Robotics and Vision Conference, ICARCV 2004*, Vol. 2, 798–803, Dec. 6–9, 2004.
4. Lee, K.-S., K. C. Lee, S. Lee, K.-T. Oh, and S.-M. Baek, "Network configuration technique for home appliances based on LnCP," *IEEE Transactions on Consumer Electronics*, Vol. 49, No. 2, 367–374, May 2003.
5. Yu, F. and S.-Y. Park, "An implementation on remote control of embedded network system using a PDA," *International Conference on Hybrid Information Technology, ICHIT'06*, Vol. 1, 42–50, Nov. 9–11, 2006.

Computerized Calculation of Complex Object RCS Using Physical Theory of Diffraction

A. M. Lebedev, **A. I. Fedorenko**, **and V. N. Kisel**
Institute for Theoretical Applied Electromagnetics, Russian Academy of Sciences, Russia

Abstract— The conception of elementary edge waves (EEW) in physical theory of diffraction (PTD) is shown to be robust in computer-aided calculation of radar cross section (RCS) of complex objects with metal edges. The backscattered field of near-the-edge inhomogeneous current, which is the difference between actual current and its homogeneous part, given by physical optics (PO), is exhibited not to have magnitude singularities and phase jumps. The contribution to RCS from inhomogeneous current along a lengthy edge can be evaluated as a superposition of EEW. This contribution is shown to become negligible with increasing of deviation from the plane, perpendicular to the edge. Averaging of RCS, calculated with PTD, in angular and/or frequency range and some numerical correction of EEW for rounded edges and thin plate ends permit widening the scope of PTD application.

1. INTRODUCTION

The following approach to calculation of RCS of 3D object with metal edges is assumed. Firstly backscattering is calculated in PO approximation. It gives the correct estimation of contribution into RCS from surfaces with normal oriented in direction or close to direction of irradiation-observation. Secondly the backscattering, produced by near-the-edge inhomogeneous part of the current (further inhomogeneous current for short), is calculated with PTD [1–3] for the edges of special cross section form. PTD is only applicable to the edges, which vicinities are of close to the wedge form, and provide a profound widening of angular intervals of correct evaluation of contribution into RCS from every such edged surface. Inhomogeneous current is the difference between actual current and its homogeneous PO part.

In [1–3], it was suggested to approximate the inhomogeneous current contribution into the scattered field by superposition of elementary edge waves. EEW is the field generated by inhomogeneous currents on the pair of semi-infinite strips of small width. The strips are directed along the diffracted rays on the sides of the straight-line tangent wedge, which locally approximates the edge, as it is shown in Fig. 1.

The PTD applicability means that the backscattered fields produced by currents on two pairs of strips, cut by the diffracted ray cones from the real curvilinear wedge and from the tangent wedge surfaces (these two pairs of strips are shown in Fig. 1), are approximately equal. It can only be if: 1) currents in proximity to the edge are close in value, 2) the main contributors are currents in the vicinities of the edge, 3) the backscattered field integral, taken over the interval along the strip beginning from the edge, represents the function of the interval length, which oscillates somewhere near the value of integral along idealized half-infinite strip.

2. EEW BACKSCATTERING DISTRIBUTION

Two cases of wave incidence on the edge are distinguished: E_θ-wave and H_θ-wave, see Fig. 1. There is not enough space to repeat and comment any EEW fields formulae from [1–3] in this article. We

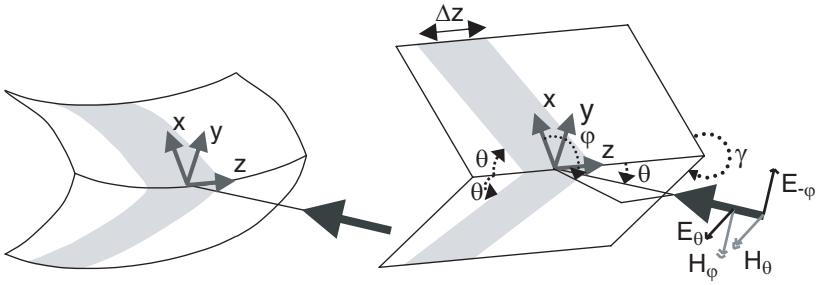

Figure 1: Curvilinear edge and its tangent wedge approximation.

only notice here, that EEW represents spherical wave emanating from a middle point of a common side of the strips. For example, the far zone field of EEW, related to the point with coordinate z along the straight edge, takes the following form in case of E_θ-wave incidence:

$$E_\theta(r,\theta,\varphi) = E_{o\theta}\cdot\Delta z\cdot F(\theta,\varphi)\cdot e^{2ik_o z\cdot\cos\theta}\cdot\frac{e^{-ik_o r}}{r}, \tag{1}$$

where r,θ,φ are spherical coordinates, related to the local piece of edge, see Fig. 1. So azimuthal angles $\varphi = 0^\circ$ and $\varphi = \gamma$ correspond to faces of tangent edge, and $\theta = 90^\circ$ for plane perpendicular to the edge.

In order to quantitivly estimate the backscattering from the pair of strips, we will reference to the equivalent RCS $\sigma_{3D}(\theta,\varphi)$ of inhomogeneous, full and PO current on the strips (equivalent, because the scattering object and/or current on it are artificial). Its normalized value $\sigma_{3D}(\theta,\varphi)/\left(2\cdot\Delta z^2\right)$ is equal to also normalized RCS of the wedge $\sigma_{2D}(\varphi)/\lambda$ in $\theta = 90^\circ$ plane, where λ is the wavelength.

Smooth variation of backscattered field in θ,φ coordinates, the absence of magnitude singularities and phase jumps are favorable features of EEW. By contrast, the fields, generated by the PO current and, consequently, the full current on the same strips, do have magnitude singularities and phase jumps, as it follows from Fig. 2. The ridges of distribution $\sigma_{3D}(\theta,\varphi)$ in Fig. 2(b)) are due to PO current on the strips and correspond to incidence-observation perpendicular to the strips. The inhomogeneous current adds to PO current backscattering in the close to on-nose incidence angular region, but its contribution subtracts from PO contribution on the other side of the ridge. So the ridge means simultaneous magnitude singularity and 180° jump of phase of PO current field.

Since EEW is calculated as the difference between the full and PO current fields, special precautions must be taken while calculating EEW in the vicinity of PO field singularity.

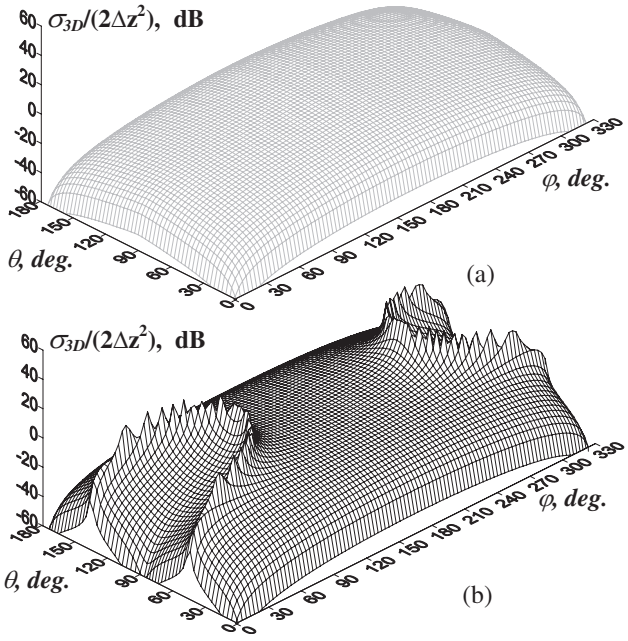

Figure 2: Spatial distribution of the equivalent RCS of pair of strips, forming EEW, E_θ wave incidence. The currents on the strips are (a) inhomogeneous, (b) full.

3. STRAIGHT EDGE CONTRIBUTION INTO BACKSCATTERING

EEW of (1) type, generated from the straight edge of length L, interfere

$$E_\theta = E_{o\theta}\cdot F(\theta,\varphi)\cdot\frac{e^{-ik_o r}}{r}\cdot\int\limits_{-L/2}^{L/2} e^{2ik_o z\cdot\cos\theta}dz = E_{o\theta}\cdot F(\theta,\varphi)\cdot L\cdot\frac{\sin(k_o L\cos\theta)}{k_o L\cos\theta}\cdot\frac{e^{-ik_o r}}{r}. \tag{2}$$

As the result, spatial RCS distribution of the edge becomes folded in direction of θ variation, as it is shown in Fig. 3 for the equivalent RCS of inhomogeneous current in case of edge length $L = 30\cdot\lambda$, $\lambda = 3.2\,\mathrm{cm}$ and E_θ wave incidence.

The envelope of the folding does not depend on the length of the edge L, as it follows from (2) and can also be seen from comparison of RCS distributions for $L = 30 \cdot \lambda$ and $L = 4 \cdot \lambda$ in Fig. 3. However, the central spike of RCS distribution, corresponding to the perpendicular to the edge plane, becomes narrower and its altitude grows as L^2 with L increasing. The maximum contribution of inhomogeneous current can be estimated in RCS terms as $\approx 0.2\,\text{sm}$ for this particular length$L = 30 \cdot \lambda = 96\,\text{cm}$, though the maximum itself depends only on the edge length L and does not depend on the wave length λ, as it follows from (2).

Fast decrease of folding envelope with growing deviation from the plane, perpendicular to the edge, permits to terminate calculation of EEW contributions to RCS starting from some big enough $|\theta - 90°|$. For example, the equivalent RCS of inhomogeneous current can not be higher than $10^{-4}\,\text{sm}$ for whatever lengthy edge at selected here wave length, if $|\theta - 90°| > 15°$.

4. 3D MODEL PREPARATION

In course of computer-aided simulation, complex object is fully depicted in geometrical CAD. Then the meshed model is created either in the same CAD, or with some attendant program. The appropriate location and configuration of Ufimtsev's tangent wedges is also specified within the 3D model via three polylines: first defines the edge, two others determine the desirable local orientation of wedge faces.

5. TESTS

Comparisons with the method of moments calculations for plates, cones and cylinders demonstrate applicability and high accuracy of PTD approximation.

The computed azimuthal RCS diagrams of 5-corner metal plate of infinitesimal thickness at 5° elevation are shown in Fig. 4 for two polarizations of incident wave, the coplanar and cross-polarized backward response was determined. The plate dimensions were $120 \times (300 + \text{nose}150)\,\text{mm}$, the wavelength $\lambda = 3.2\,\text{cm}$.

The existence of angular intervals, where the RCS calculation with PTD are quite accurate for both coplanar and cross-polarized responses, proves that 1) EEW field formulae in [1–3] are exact, and 2) they have been programmed accurately. Deviations from strict numerical solution are observed in the angular intervals where the plate's nose as such is a noticeable contributor to backscattering.

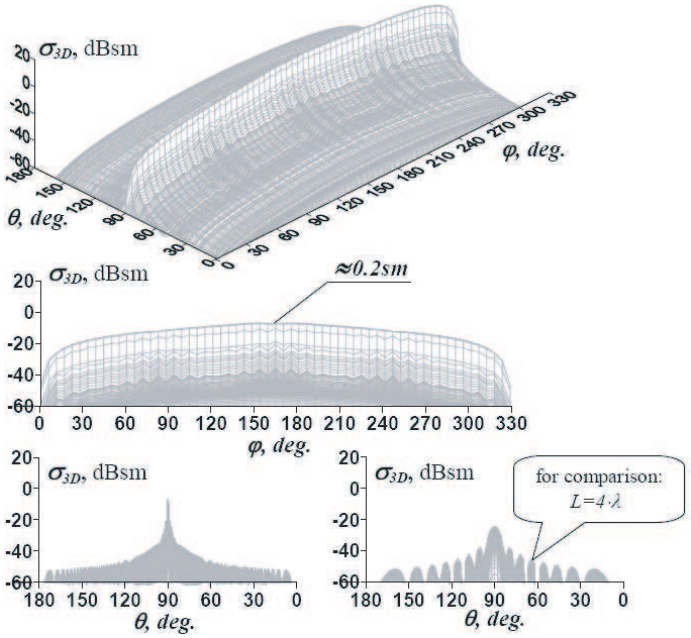

Figure 3: The result of interference of EEW, emanating from the straight edge. E_θ — wave incidence. The edge length is $L = 30 \cdot \lambda$, $\lambda = 3.2\,\text{cm}$.

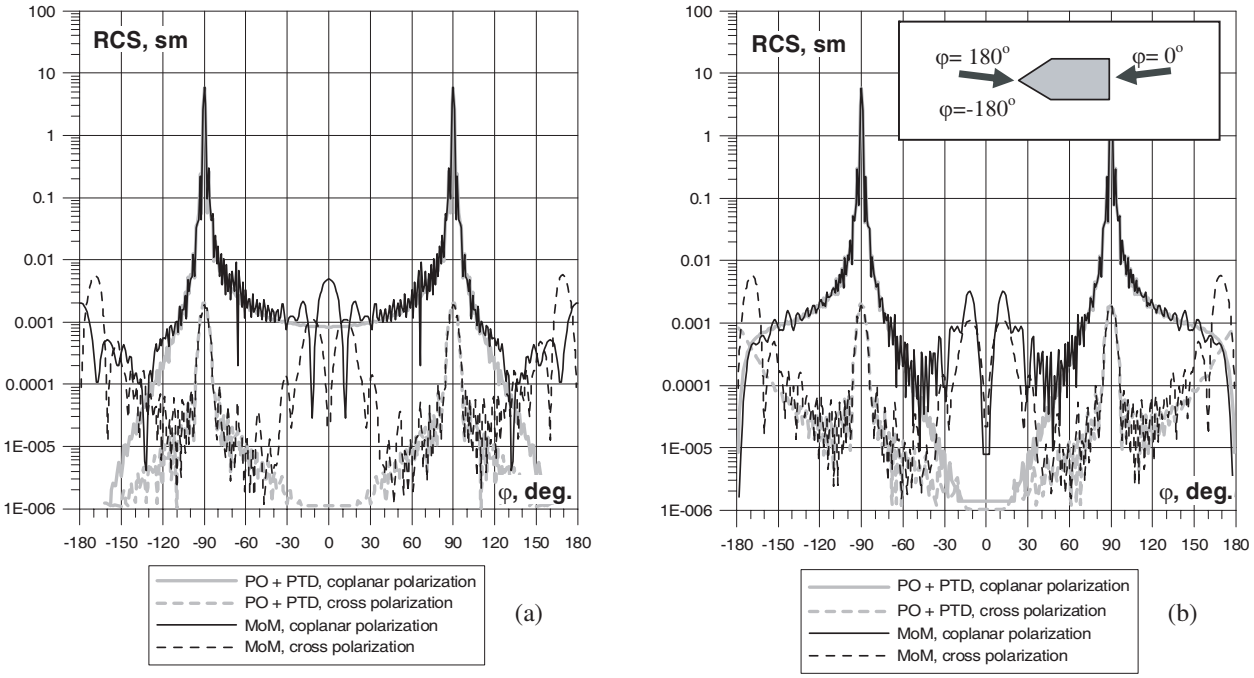

Figure 4: Azimuthal RCS diagram of 5-corner plate at elevation 5°, polarization (a) vertical, (b) horizontal.

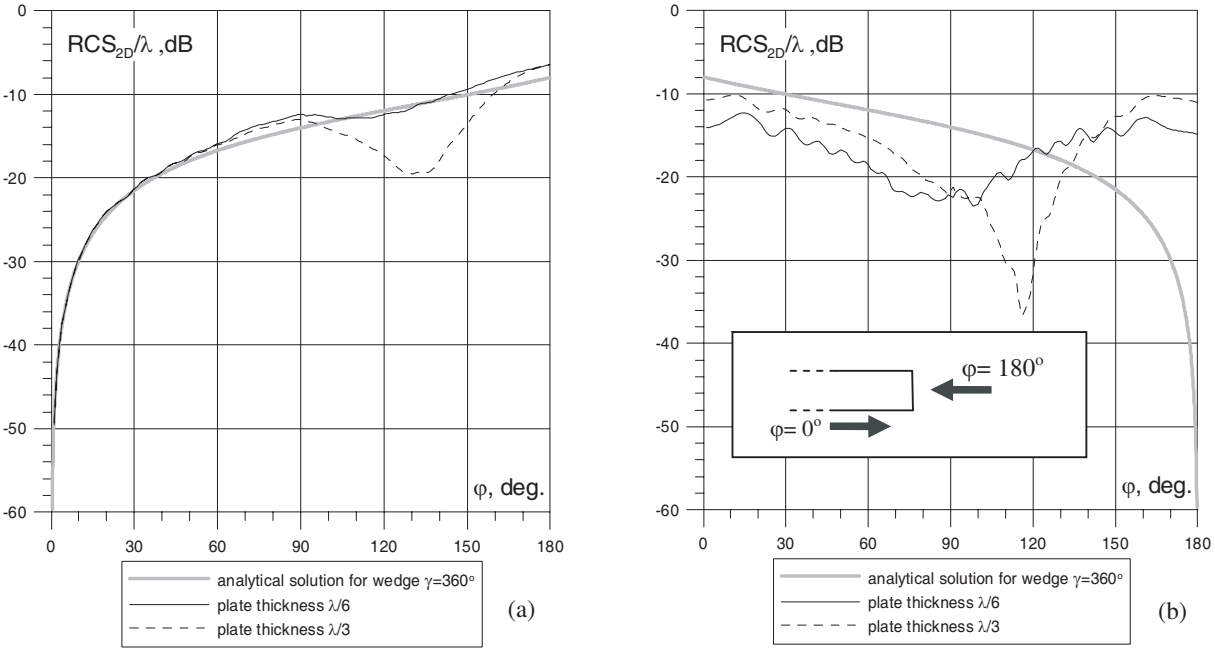

Figure 5: The equivalent RCS of inhomogeneous current near the edge of the 2D plate of various thickness. The inhomogeneous current is the difference between actual (MoM) and PO currents. Polarization (a) vertical, (b) horizontal.

6. LIMITS AND EXTENTION OF PTD

The following two points substantially widen the scope of PTD approximation application. First, if one or both forming the edge surfaces end abruptly in close proximity to the edge, then PTD approximation can not provide literally exact results of calculation. However, the integration of inhomogeneous current contributions to backscattering from the portions of surface, increasingly distant from the edge, gives the result, oscillating somewhere around the value for the half-infinite tangent wedge. Thus PTD-based calculation is worthwhile if RCS is averaged in angular and/or frequency range.

Secondly, some numerical correction of EEW is possible for certain deviations of edge cross section from canonical form, such as rounded edges and edges of thin plate end form. The results of numerical stimulation of backscattering from the 2D edge, representing the end of semi-infinite thin metal plate, are displayed in Fig. 5. Here the inhomogeneous current is defined as the difference between the actual current, calculated with MoM, and the PO current. Analytically found diagram of equivalent RCS of inhomogeneous current around the edge of metal half-plane, and numerically calculated equivalent RCS diagrams of inhomogeneous current in the vicinity of thin plate end for various plate thicknesses are shown, again for two polarizations of incident wave. The 2D diagrams can be reevaluated as equivalent EEW RCS diagrams in plane $\theta = 90^\circ$ via $\sigma_{3D} = \sigma_{2D} \cdot \frac{2 \cdot \Delta z^2}{\lambda}$. The comparison of diagrams show that EEW can easily be numerically corrected for increasing of plate thickness up to at least $\lambda/6$.

7. CONCLUSIONS

Tests for objects with metal edges showed high accuracy of RCS calculations in PO+PTD approximation.

Smooth variation of EEW backward field is the reason for convenient PTD usage.

As the contributions from EEW along the straight edge interfere, the equivalent RCS diagram of the edge gets folded along the angle of deviation from the plane, perpendicular to the edge. The integrated EEW contributions along the straight edge can conveniently be added to backscattering as a single entity.

The envelope of the near-the-edge inhomogeneous current backscattering diagram does not depend on the length of the wedge, but its maximum in the plane, perpendicular to the edge, is proportional to the squared edge length. The RCS contribution from inhomogeneous current in the vicinity of the edge becomes negligibly small for big enough deviation from the plane, perpendicular to the edge.

The scope of PTD application can be widened via 1) averaging of RCS, calculated with PTD, in angular and/or frequency range and 2) numerical correction of EEW for rounded edges and thin plate ends.

REFERENCES

1. Butorin, D. I., D. A. Martinov, and P. Y. Ufimtsev, "Asymptotic expressions of elementary edge wave," *Radiotechnics and Electronics*, 1818–1829, 1987 (in Russian).
2. Ufimtsev, P. Y. "Elementary edge waves and the physical theory of diffraction," *Electromagnetics*, Vol. 11, No. 2, 125–160, 1991.
3. Ufimtsev, P. Y., "Improved physical theory of diffraction: Removal of the grazing singularity," *IEEE TAP*, Vol. 54, No. 10, 2698–2702, 2006.

Variational Effective Index Method for 3D Vectorial Scattering Problems in Photonics: TE Polarization

O. V. Ivanova[1], **R. Stoffer**[2], **L. Kauppinen**[1], **and M. Hammer**[1]

[1]MESA+ Institute for Nanotechnology, University of Twente, Enschede, The Netherlands
[2]Phoenix Software, Enschede, The Netherlands

Abstract— In order to reduce the computational effort we develop a method for 3D-to-2D dimensionality reduction of scattering problems in photonics. Contrary to the 'standard' Effective Index Method the effective parameters of the reduced problem are always rigorously defined using the variational technique, based on the vectorial 3D Maxwell equations. Results for a photonic crystal slab waveguide show that this approach predicts the location of the bandgap and other spectral features much more precisely than any 'standard' EIM approximation.

1. INTRODUCTION

Fully vectorial 3D simulations of photonic components are often almost prohibitively CPU-time and memory intensive, so one would opt for reduced models that capture the essence of the full 3D structure, while being computationally much more efficient. Traditionally, integrated optics designers use a technique called the Effective Index Method (EIM) [1, 4, 7] to reduce simulations of 3D structures to two spatial dimensions. However, frequently, as is the case for photonic crystal slabs (Figure 1, left), the effective parameters for the 2D simulation are only rather ambiguously defined, i.e., rely more or less on guesswork. Here we have developed a mathematical formulation that allows to a priori derive these parameters when going from 3D to 2D based on a sound variational reasoning (Variational EIM, VEIM). This is achieved by approximating the total 3D vectorial electromagnetic field along one spatial dimension by a suitable 1D mode profile. Then, by means of a variational procedure, the field distribution in the other two dimensions is found, such that the product of these two fields represents as good as possible the true 3D vectorial solution. On the boundaries of the computational domain in 2D we use combined Transparent Influx Boundary Conditions with Perfectly Matched Layers in order to allow influx into the domain to be prescribed and radiation to freely pass through the computational window boundaries. Results for a photonic crystal slab waveguide show that this approach predicts the location of the bandgap and other spectral features much more precisely than any guesses using a 'standard' EIM.

2. FORMULATION OF SCATTERING PROBLEMS IN OPTICS

The time-harmonic propagation of a given optical influx with frequency ω through a medium, characterized by the refractive index distribution $n(x, y, z)$, is governed by the Maxwell curl equations

$$\nabla \times \mathbf{E} = -\mathrm{i}\,\omega\mu_0\mu\mathbf{H}, \quad \nabla \times \mathbf{H} = \mathrm{i}\,\omega\varepsilon_0\varepsilon\mathbf{E}, \tag{1}$$

for the electric and magnetic fields $\mathbf{E} = (E_x, E_y, E_z)$ and $\mathbf{H} = (H_x, H_y, H_z)$ respectively. ε_0 and μ_0 are the vacuum permittivity and permeability, $\varepsilon(x, y, z) = n^2(x, y, z)$ is the relative dielectric permittivity. The relative permeability μ is assumed to be one, as is appropriate for most materials at optical frequencies.

Solutions $(\mathbf{E}, \mathbf{H})$ of Equation (1) are stationary points of the functional [6]

$$\mathfrak{F}(\mathbf{E}, \mathbf{H}) = \int \Big(\mathbf{E} \cdot (\nabla \times \mathbf{H}) + \mathbf{H} \cdot (\nabla \times \mathbf{E}) - \mathrm{i}\,\omega\varepsilon_0\varepsilon\mathbf{E}^2 + \mathrm{i}\,\omega\mu_0\mu\mathbf{H}^2 \Big)\, \mathrm{d}x\, \mathrm{d}y\, \mathrm{d}z. \tag{2}$$

In the following, we will work with this variational formulation only.

3. VARIATIONAL EFFECTIVE INDEX METHOD

Let us consider only one TE slab mode propagating in the direction z with propagation constant β_r from a reference slice with permittivity distribution $\varepsilon_\mathrm{r}(x)$:

$$\begin{pmatrix} E_x, E_y, E_z \\ H_x, H_y, H_z \end{pmatrix}_{\text{slab}} (x, z) = \begin{pmatrix} 0, & X^{E_y}(x), & 0 \\ X^{H_x}(x), & 0, & X^{H_z}(x) \end{pmatrix} \cdot e^{-\mathrm{i}\,\beta_\mathrm{r} z}, \tag{3}$$

The principal electric component X^{E_y} satisfies the equation

$$\left(X^{E_y}(x)\right)'' + k^2\varepsilon_{\mathrm{r}}(x)X^{E_y}(x) = \beta_{\mathrm{r}}^2 X^{E_y}(x) \tag{4}$$

with vacuum wavenumber $k = 2\pi/\lambda$. The remaining two nonzero components of the mode profile can be derived directly from X^{E_y}.

We assume that this vertical shape constitutes an adequate approximation for the (polarized) optical field in the 3D structure

$$\begin{pmatrix} E_x, E_y, E_z \\ H_x, H_y, H_z \end{pmatrix}_{\text{complete}} (x,y,z) = \begin{pmatrix} 0, & X^{E_y}(x)P^{E_y}(y,z), & X^{E_y}(x)P^{E_z}(y,z) \\ X^{H_x}(x)P^{H_x}(y,z), & X^{H_z}(x)P^{H_y}(y,z), & X^{H_z}(x)P^{H_z}(y,z) \end{pmatrix}, \tag{5}$$

with some unknown functions P. Note that the y- and z-components of the electromagnetic field are approximated by the same functions X.

The governing equations for the functions P can be found by restricting the functional (2) to the template (5), i.e., by requiring, after insertion of (5) into (2), the variations of $\mathfrak{F}$ with respect to all P to vanish. Using the relations between the slab mode components, it turns out that P^{H_x} satisfies the following second order differential equation

$$\left(\partial_y \frac{1}{\varepsilon_{\text{eff}}(y,z)}\partial_y + \partial_z \frac{1}{\varepsilon_{\text{eff}}(y,z)}\partial_z + k^2\right) P^{H_x}(y,z) = 0 \tag{6}$$

with

$$\varepsilon_{\text{eff}}(y,z) = \frac{\beta_{\mathrm{r}}^2}{k^2} + \frac{\displaystyle\int \left(\varepsilon(x,y,z) - \varepsilon_{\mathrm{r}}(x)\right)\left(X^{E_y}(x)\right)^2\, dx}{\displaystyle\int \left(X^{E_y}(x)\right)^2\, dx}. \tag{7}$$

This looks exactly like a 2D TM Helmholtz equation with (effective) permittivity ε_{eff}, and similar to what is used in the standard Effective Index Method. In the reference slice, where $\varepsilon(x,y,z) = \varepsilon_{\mathrm{r}}(x)$, the effective permittivity is equal to the squared effective mode index β_{r}^2/k^2. Elsewhere, however, this squared effective index is modified by the difference between the local permittivity and that of the reference slice, weighted by the local intensity of the major component of the reference mode profile. Hence, contrary to the EIM, even in slices where no guided mode exists the effective indices are still rigorously defined.

Note that the original problem (2) deals with six unknown field components, each depending on three spatial coordinates. The present approximation reduced it to a single function of two spatial coordinates only.

All other field components are related to P^{H_x} in the following manner:

$$\begin{pmatrix} P^{E_x}, P^{E_y}, P^{E_z} \\ P^{H_x}, P^{H_y}, P^{H_z} \end{pmatrix}(y,z) = \frac{\mathrm{i}\,\beta_{\mathrm{r}}}{k^2\varepsilon_{\text{eff}}} \begin{pmatrix} 0, & \partial_z P^{H_x}, & -\partial_y P^{H_x} \\ (-\mathrm{i}\,k^2\varepsilon_{\text{eff}}/\beta_{\mathrm{r}})P^{H_x}, & \partial_y P^{H_x}, & \partial_z P^{H_x} \end{pmatrix}. \tag{8}$$

Equation (8) permits a quite intuitive interpretation. Inside each homogeneous region a partial solution of (6) is

$$P^{H_x}(y,z) = c\,\mathrm{e}^{-\mathrm{i}\,(k_y y + k_z z)}, \quad \text{with} \quad k_y^2 + k_z^2 = k^2\varepsilon_{\text{eff}}. \tag{9}$$

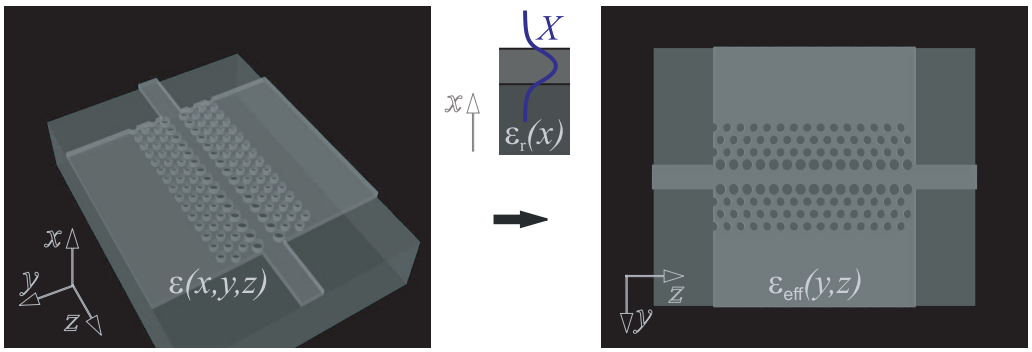

Figure 1: By using a TE slab mode of a reference slice with permittivity $\varepsilon_{\mathrm{r}}(x)$ as an approximation for the x-dependence of the field, the simulation of wave propagation in the structure is reduced from 3D to 2D.

If we define $\rho^2 = k^2\varepsilon_{\text{eff}}$, and an angle θ such that $\cos\theta = k_z/\rho$ and substitute it in (8), we obtain

$$\begin{pmatrix} P^{E_x}, P^{E_y}, P^{E_z} \\ P^{H_x}, P^{H_y}, P^{H_z} \end{pmatrix}(y,z) = c\frac{\beta_{\text{r}}}{\rho}\,\mathrm{e}^{-\mathrm{i}\,\rho(-\sin\theta y + \cos\theta z)} \begin{pmatrix} 0, & \cos\theta, & \sin\theta \\ \frac{\rho}{\beta_{\text{r}}}, & -\sin\theta, & \cos\theta \end{pmatrix}. \tag{10}$$

In the reference slice we have $\rho = \beta_{\text{r}}$, and hence the functions P act as a rotation of the slab mode around the x-axis. In all other regions, in addition to the rotation of the y- and z-components, the x-component is scaled by ρ/β_{r}.

Moreover, as (10) is only a partial solution and the fundamental solution of (6) is a superposition of partial solutions, the functions P (8) act as a superposition of the slab mode X rotated around the x-axis by different angles θ.

So far, the formulation has not been restricted to a computational domain, and Equation (6) holds in entire $\mathbb{R}^2$. In practice, however, solving (6) requires a finite computational window, with boundaries such that influx can be prescribed and radiation can freely flow out. We use a modified version of the Transparent Influx Boundary Conditions from [3, 5] which fulfill these requirements. In this scheme, a finite element calculation of the field in the interior of the domain is connected to a semi-analytical solution of the exterior.

4. NUMERICAL RESULTS

In this section, we compare the results of EIM, VEIM and 3D FDTD [2] -simulations of the photonic crystal waveguide of Figure 1, for the following specification: The structure is composed of a 225 nm thick Si ($n_{\text{Si}} = \sqrt{12.1}$) layer on top of a SiO_2 ($n_{\text{SiO}_2} = 1.445$) substrate with air ($n_{\text{air}} = 1.0$) around. The waveguide and holes are defined by etching fully through the Si layer. The triangular lattice photonic crystal with lattice constant $a = 440\,\text{nm}$ consists of circular holes with radius 135 nm; the input and output waveguides are $\sqrt{3}a \approx 762\,\text{nm}$ wide. A defect waveguide is created by removing a row of holes and enlarging the first row of holes on either side to a radius of 170 nm. In total, there are four rows of holes on either side of the defect waveguide.

This geometry is particularly interesting because no guided mode exists in the vertical slices, where holes are located. So to apply 'standard' EIM one has to guess the effective refractive index of those regions: should it be the refractive index of the Si substrate or air, or something in between? VEIM uniquely defines these numbers.

As shown in Figure 2, the VEIM predictions of the location of the stopband and the general spectral features are reasonably close to the 3D FDTD reference results, while the 'conventional' EIM data, using either the cladding (1.0) or substrate refractive indices (1.445) as effective values for the hole regions, are much further off. Via the template (5), the VEIM allows to assemble an approximation to the vectorial electromagnetic field in 3D. Figure 3 shows a series of corresponding field profiles. Note that the effective permittivity (7) can very well turn out to be negative, as it happens to be in the present example. Inside the hole regions the effective permittivity varies

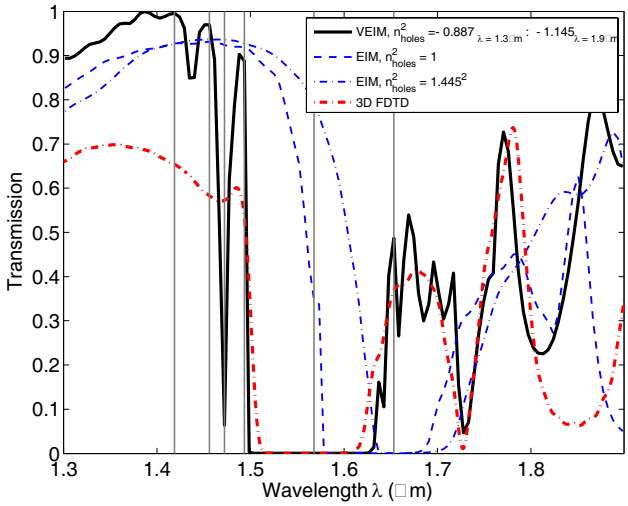

Figure 2: Transmission spectrum of the photonic crystal waveguide shown in Figure 1.

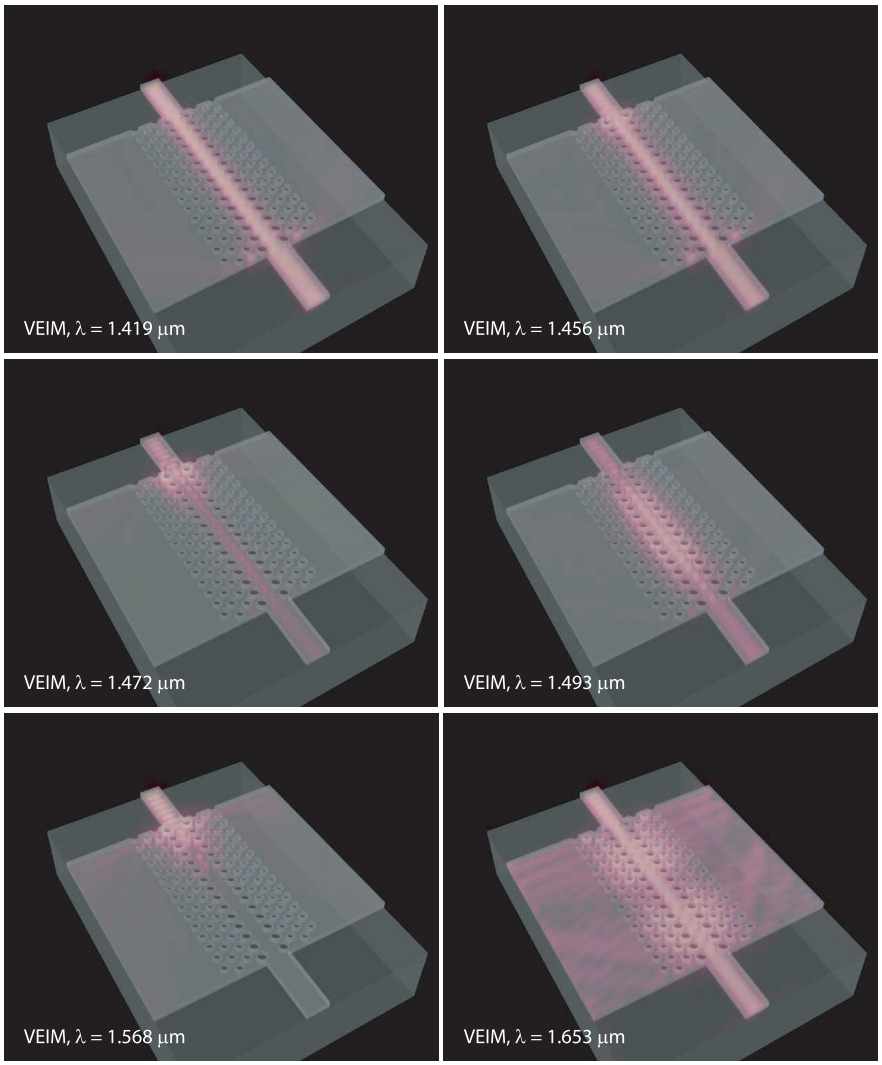

Figure 3: 3D light propagation through the photonic crystal slab waveguide of the Figure 1 at several vacuum wavelengths; absolute value of the major magnetic component of the optical field.

between $-0.887_{@\lambda=1.3\,\mu m}$ and $-1.145_{@\lambda=1.9\,\mu m}$. So in all air regions in Figure 3 the field H_x decays exponentially.

5. CONCLUDING REMARKS

The present technique allows in a straightforward and simple way reduce the dimensionality of the scattering problems from 3D to 2D for TE-like polarized light. A similar procedure has also been developed for TM polarization. Currently, work is in progress to extend the method to deal with the third dimension even more accurately, by means of superpositions of contributions of the form (5) related to multiple slab modes.

ACKNOWLEDGMENT

This work was supported by the Dutch Technology foundation (BSIK/NanoNed project TOE.7143). The authors would like to thank Lasse Kauppinen for performing 3D FDTD calculations for Figure 2.

REFERENCES

1. Dems, M. and W. Nakwaski, "The modelling of high-contrast photonic crystal slabs using the novel extension of the effective index method," *Optica Applicata*, Vol. 36, No. 1, 51–56, 2006.
2. MEEP, "Free finite-difference time-domain simulation software package developed at MIT," http://www.ab-initio.mit.edu/meep.

3. Nicolau, J. B. and E. van Groesen, "Hybrid analytic-numeric method for light through a bounded planar dielectric domain," *Journal of Nonlinear Optical Physics and Materials*, Vol. 14, No. 2, 161–176, 2005.
4. Qiu, M., "Effective index method for heterostructure-slab-waveguide-based two-dimnsional photonic crystals," *Applied Physics Letters*, Vol. 81, No. 7, 1163–1165, 2002.
5. Stoffer, R., A. Sopaheluwakan, M. Hammer, and E. van Groesen, "Helmholtz solver with transparent influx boundary conditions and nonuniform exterior," *Proc. of XVI International Workshop on Optical Waveguide Theory and Numerical Modelling*, Copenhagen, Denmark, 2007. book of abstracts 3.
6. Vassallo, C., *Optical Waveguide Concepts*, Elsevier, Amsterdam, 1991.
7. Yang, L., J. Motohisa, and T. Fukui, "Suggested procedure for the use of the effective-index method for high-index-contrast photonic crystal slabs," *Optical Engineering*, Vol. 44, No. 7, 078002-1–078002-7, 2005.

The A, B, C Numbers and Their Application in the Theory of Waveguides

Mariana Nikolova Georgieva-Grosse[1] **and Georgi Nikolov Georgiev**[2]

[1]Meterstrasse 4, D-70839 Gerlingen, Germany
[2]Faculty of Mathematics and Informatics, University of Veliko Tirnovo "St. St. Cyril and Methodius"
BG-5000 Veliko Tirnovo, Bulgaria

Abstract— A new definition of the A, B, C numbers is advanced by means of the roots of the equations, connecting the normalized phase constant resp. the off-diagonal element of ferrite permeability tensor with the radial wavenumber (with the eigenvalue spectrum) of normal TE_{0n} modes in the azimuthally magnetized circular and coaxial ferrite waveguides. The values of numbers A_{cr}, B_{cr}, C_{cr}, relevant to the cutoff state, are computed by a special iterative procedure and presented graphically as a function of the structures parameters. The possibility to figure the differential phase shift provided, using the quantities considered, is demonstrated.

1. INTRODUCTION

A, B, C numbers are called the quantities, yielding the relation between the normalized differential phase shift $\Delta\bar{\beta}$, produced by the circular waveguides with ferrite of azimuthal magnetization (configurations, apt for the design of nonreciprocal phase shifters for electronically scanned antenna arrays, working in the normal TE_{01} mode [1–5]), the magnitude of off-diagonal ferrite tensor element $|\alpha|$ and the normalized guide radius $\bar{r}_0$. They appeared in the developed in terms of complex Kummer confluent hypergeometric function [6] theory of the simplest of the transmission lines mentioned — of the one, wholly filled with anisotropic medium and have been defined through the expressions: $A = \Delta\bar{\beta}/|\alpha|$, $B = \Delta\bar{\beta}\bar{r}_0$ and $C = (\Delta\bar{\beta}/|\alpha|)\bar{r}_0$ [1]. Knowing them for a network of parameters $\{|\alpha|, \bar{r}_0\}$ allows to find $\Delta\bar{\beta}$ by elementary formulae [1]. The density of network determines the accuracy of results. The computation of the values of numbers, however is a laborious task, requiring the employment of complicated iterative techniques [1].

The core of this investigation form the novel definition of the quantities in question in case of circular and coaxial geometries of the type referred to and the numerical study of a partial case of the numbers — of the bound up with the cutoff frequencies of the structures ones A_{cr}, B_{cr}, C_{cr}. The application of the latter in the calculation of the differential phase shift provided, is illustrated.

2. *A*, *B*, *C* NUMBERS

Definition 1: *Let* $\zeta_{k,n}^{(c)}$ *and* $\chi_{k,n}^{(c)}(\rho)$ *are the* n*th positive purely imaginary zeros in* x *of the functions* $\Phi(a,c;x)$ *and* $F(a,c;x,\rho) = \Phi(a,c;x)\Psi(a,c;\rho x) - \Phi(a,c;\rho x)\Psi(a,c;x)$, *resp.* $(n = 1, 2, 3 \ldots)$ *in which* $\Phi(a,c;x)$ *and* $\Psi(a,c;x)$ *are the Kummer and Tricomi confluent hypergeometric functions with* $a = c/2 - jk$ *— complex,* $c = 3$, $x = jz$ *— positive purely imaginary,* z *— real, positive,* k *— real,* $-\infty < k < +\infty$, ρ *— real, positive,* $0 < \rho < 1$. *Let in addition*

$$\sigma_{1\pm,2\pm}^2 = 0.5\left[\left(1-\bar{\beta}_{2\pm}^2\right) \pm \sqrt{\left(1-\bar{\beta}_{2\pm}^2\right)^2 - 4\times 4\bar{\beta}_{2\pm}^2 k_\pm^2}\right] \tag{1}$$

in that $1 - \bar{\beta}_{2\pm}^2 \geq 4\bar{\beta}_{2\pm}|k_\pm|$, $(1 > \sigma_{1\pm} \geq \sigma_{2\pm} \geq 0)$ *are the real positive roots of the biquadratic equation*

$$\sigma_\pm^4 - \left(1-\bar{\beta}_{2\pm}^2\right)\sigma_\pm^2 + 4\bar{\beta}_{2\pm}^2 k_\pm^2 = 0 \tag{2}$$

with $\bar{\beta}_{2\pm} = \chi_{k_\pm,n}^{(c)}(\rho)/(2\bar{r}_0)$ ($\bar{r}_0$ *— real, positive,* $\bar{r}_0 > (\chi_{0,n}^{(c)}(\rho)/2)$). *Then, A, B, C numbers are named the real positive quantities:*

$$A = A_- - A_+, \tag{3}$$
$$B = B_- - B_+, \tag{4}$$
$$C = C_- - C_+ \tag{5}$$

where

i) on condition that $\sigma_{1-} > \sigma_{1+} > \sigma_{2-} = \sigma_{2+} > 0$, $A_- = \sigma_{1-}/\sigma_{2-}$, $A_+ = \sigma_{1+}/\sigma_{2+}$, $B_- = \sigma_{1-}\bar{r}_0$, $B_+ = \sigma_{1+}\bar{r}_0$, $C_- = (\sigma_{1-}/\sigma_{2-})\bar{r}_0$, $C_+ = (\sigma_{1+}/\sigma_{2+})\bar{r}_0$ *and in view of this it is correct* $+\infty > A_- > A_+ > 1$, $+\infty > C_- > C_+ > \bar{r}_0$;

ii) assuming that $\sigma_{1-} > \sigma_{1+} = \sigma_{2-} = \sigma_{2+} > 0$, $A_- = \sigma_{1-}/\sigma_{2-}$, $A_+ = \sigma_{1+,2+}/\sigma_{2+,1+}$, $B_- = \sigma_{1-}\bar{r}_0$, $B_+ = \sigma_{1+,2+}\bar{r}_0$, $C_- = (\sigma_{1-}/\sigma_{2-})\bar{r}_0$, $C_+ = (\sigma_{1+,2+}/\sigma_{2+,1+})\bar{r}_0$ *and on account of this it is true* $+\infty > A_- > A_+ = 1$, $+\infty > C_- > C_+ = \bar{r}_0$;

iii) when $\sigma_{1-} > \sigma_{1+} = \sigma_{2-} > \sigma_{2+} > 0$, $A_- = \sigma_{1-}/\sigma_{2-}$, $A_+ = \sigma_{2+}/\sigma_{1+}$, $B_- = \sigma_{1-}\bar{r}_0$, $B_+ = \sigma_{2+}\bar{r}_0$, $C_- = (\sigma_{1-}/\sigma_{2-})\bar{r}_0$, $C_+ = (\sigma_{2+}/\sigma_{1+})\bar{r}_0$ *and because of this it is implemented* $+\infty > A_- > 1 > A_+ > 0$, $+\infty > C_- > \bar{r}_0 > C_+ > 0$;

iv) provided $\sigma_{1-} = \sigma_{1+} = \sigma_{2-} > \sigma_{2+} > 0$, $A_- = \sigma_{1-,2-}/\sigma_{2-,1-}$, $A_+ = \sigma_{2+}/\sigma_{1+}$, $B_- = \sigma_{1-,2-}\bar{r}_0$, $B_+ = \sigma_{2+}\bar{r}_0$, $C_- = (\sigma_{1-,2-}/\sigma_{2-,1-})\bar{r}_0$, $C_+ = (\sigma_{2+}/\sigma_{1+})\bar{r}_0$ *and for this reason it is fulfilled* $1 = A_- > A_+ > 0$, $\bar{r}_0 = C_- > C_+ > 0$;

v) on the understanding that $\sigma_{1-} = \sigma_{1+} > \sigma_{2-} > \sigma_{2+} > 0$, $A_- = \sigma_{2-}/\sigma_{1-}$, $A_+ = \sigma_{2+}/\sigma_{1+}$, $B_- = \sigma_{2-}\bar{r}_0$, $B_+ = \sigma_{2+}\bar{r}_0$, $C_- = (\sigma_{2-}/\sigma_{1-})\bar{r}_0$, $C_+ = (\sigma_{2+}/\sigma_{1+})\bar{r}_0$ *and in consequence of this it is valid* $1 > A_- > A_+ > 0$, $\bar{r}_0 > C_- > C_+ > 0$;

vi) if $|\{1 - [\chi^{(c)}_{0,n}(\rho)/(2\bar{r}_0)]^2\}^{1/2}| = \sigma_{1-} = \sigma_{1+} > \sigma_{2-} > \sigma_{2+} = 0$, $A_- = \sigma_{2-}/\sigma_{1-}$, $A_+ = \sigma_{2+}/\sigma_{1+}$, $B_- = \sigma_{2-}\bar{r}_0$, $B_+ = \sigma_{2+}\bar{r}_0$, $C_- = (\sigma_{2-}/\sigma_{1-})\bar{r}_0$, $C_+ = (\sigma_{2+}/\sigma_{1+})\bar{r}_0$ *and to this end it is carried out* $1 > A_- > A_+ = 0$, $\bar{r}_0 > C_- > C_+ = 0$.

Since $\lim_{\rho\to 0} F(a,c;x,\rho) = \Phi(a,c;x)$, *resp.* $\lim_{\rho\to 0} \chi^{(c)}_{k,n}(\rho) = \zeta^{(c)}_{k,n}$, *the relations for* $\chi^{(c)}_{k,n}(\rho)$ *are truthful also for* $\zeta^{(c)}_{k,n}$. *In items ii) and iv) the quantities with the first or second subscript could be considered. In the cases i)–v)* $B_- > B_+ > 0$ *and in the one vi)* $B_- > B_+ = 0$. *(The subscripts "+" and "−" relate to* $k_+ > 0$ *and* $k_- < 0$ *resp.)*

Definition 2: *The quantities in the sense of Definition 1 vi) are termed critical numbers and are denoted by the subscript "cr". It holds:*

$$A_{cr} = A_{cr-}, \tag{6}$$

$$B_{cr} = B_{cr-}, \tag{7}$$

$$C_{cr} = C_{cr-} \tag{8}$$

in which $A_{cr-} = \sigma_{cr,\,2-}/\sigma_{cr,\,1-}$, $B_{cr-} = \sigma_{cr,\,2-}\bar{r}_{0cr}$ *and* $C_{cr-} = (\sigma_{cr,\,2-}/\sigma_{cr,\,1-})\bar{r}_{0cr}$ *with* $\bar{r}_{0cr} = (\chi^{(c)}_{0,\,n}(\rho)/2)/(1-\sigma^2_{cr,1-})^{1/2}$ *and*

$$A_{cr+} = B_{cr+} = C_{cr+} = 0 \tag{9}$$

where $|\{1 - [\chi^{(c)}_{0,n}(\rho)/(2\bar{r}_{0cr})]^2\}^{1/2}| = \sigma_{cr,1-} = \sigma_{cr,1+} > \sigma_{cr,2-} > \sigma_{cr,2+} = 0$. (For details, concerning the $\Phi(a,c;x)$ and $\Psi(a,c;x)$ functions consult the F. G. Tricomi's classical work *Funzioni Ipergeometriche Confluenti* [6].)

3. PHYSICAL INTERPRETATION

Let $\beta_\pm$ and $\beta_{2\pm} = \{\omega^2\varepsilon_0\mu_0\varepsilon_r(1-\alpha^2_\pm) - \beta^2_\pm\}^{1/2}$ are the phase constant and the radial wavenumber of normal TE_{0n} modes in a coaxial (circular) waveguide of outer and inner conductor radii r_0 and r_1, resp., entirely filled with azimuthally magnetized ferrite, described by a Polder permeability tensor of off-diagonal element $\alpha = \gamma M_r/\omega$, ($\gamma$ — gyromagnetic ratio, M_r — ferrite remanent magnetization, ω — angular frequency of the wave) and a scalar permittivity $\varepsilon = \varepsilon_0\varepsilon_r$. Let also $\bar{\beta} = \beta/(\beta_0\sqrt{\varepsilon_r})$, $\bar{\beta}_2 = \beta_2/(\beta_0\sqrt{\varepsilon_r})$, $\bar{r}_0 = \beta_0 r_0\sqrt{\varepsilon_r}$, $\bar{r}_1 = \beta_0 r_1\sqrt{\varepsilon_r}$, $\rho = \bar{r}_1/\bar{r}_0$ (ρ — central conductor to waveguide radius ratio) and $\beta_0 = \omega\sqrt{\varepsilon_0\mu_0}$. Further, provided $x = x_0$, $x_0 = jz_0$, $z_0 = 2\bar{\beta}_2\bar{r}_0$, $k_\pm = \alpha_\pm\bar{\beta}_\pm/(2\bar{\beta}_{2\pm})$, the zeros $\zeta^{(c)}_{k,n}$ and $\chi^{(c)}_{k,n}(\rho)$ acquire sense of roots of the characteristic equation of the second and first structures, resp. [1, 2]:

$$\Phi\,(a,c;x_0) = 0, \tag{10}$$

$$F\,(a,c;x_0,\rho) = 0. \tag{11}$$

Then, by means of the relations $\bar{\beta}^2_\pm + \bar{\beta}^2_{2\pm} = 1 - \alpha^2_\pm$ and $k_\pm = \alpha_\pm\bar{\beta}_\pm/(2\bar{\beta}_{2\pm})$ [1, 2], it easily could be shown that Equation (2) for $\sigma_\pm$ is equivalent to two identical ones for $\bar{\beta}_\pm$ and $|\alpha_\pm|$, resp. in which the expression for $\bar{\beta}_{2\pm}$ from Definition 1 determines the eigenvalue spectrum of the fields examined. For the roots of equations mentioned it is true:

$$\bar{\beta}_{(1)\pm,(2)\pm} = \sigma_{1\pm,2\pm}, \tag{12}$$

$$|\alpha_{1\pm,2\pm}| = \sigma_{2\pm,1\pm}, \tag{13}$$

$$|\alpha_{1\pm}| = \bar{\beta}_{(2)\pm}, \tag{14}$$

$$|\alpha_{2\pm}| = \bar{\beta}_{(1)\pm}. \tag{15}$$

(The subscripts "+" and "−" apply to positive ($\alpha_+ > 0$, $k_+ > 0$) and negative ($\alpha_- < 0$, $k_- < 0$) magnetization. In case of circular geometry ($r_1 = 0$, $\rho = 0$) in all expressions $\chi^{(c)}_{k,n}(\rho)$ should be replaced by $\zeta^{(c)}_{k,n}$ [1, 2].) Correspondingly, setting $\bar{\beta}_{(1)\pm} = \bar{\beta}_\pm$ and $|\alpha_{1-}| = |\alpha_{1+}| = |\alpha|$, for the items i) and ii) in Definition 1, it holds $\sigma_{1\pm} = \bar{\beta}_\pm$ and $\sigma_{2\pm} = |\alpha|$. Putting $\bar{\beta}_{(1)-} = \bar{\beta}_-$, $\bar{\beta}_{(2)+} = \bar{\beta}_+$ and $|\alpha_{1-}| = |\alpha_{2+}| = |\alpha|$ in cases iii) and iv), it is true: $\sigma_{1-} = \bar{\beta}_-$, $\sigma_{2+} = \bar{\beta}_+$ and $\sigma_{1+} = \sigma_{2-} = |\alpha|$. If $\bar{\beta}_{(2)\pm} = \bar{\beta}_\pm$, $|\alpha_{2-}| = |\alpha_{2+}| = |\alpha|$, in points v) and vi) of the same Definition, it is valid: $\sigma_{2\pm} = \bar{\beta}_\pm$ and $\sigma_{1+} = \sigma_{1-} = |\alpha|$. Due to their limiting character items ii) and iv) could be regarded jointly either with points i) and iii) (as done here) or with the ones iii) and v), resp. In the first (second) case the first (second) subscripts in the expressions for A_+, B_+ and C_+, resp. for A_-, B_- and C_- are taken into account. Moreover, it holds: $\bar{\beta}_- > \bar{\beta}_+ > |\alpha| > 0$, $\bar{\beta}_- > \bar{\beta}_+ = |\alpha| > 0$, $\bar{\beta}_- > |\alpha| > \bar{\beta}_+ > 0$, $\bar{\beta}_- = |\alpha| > \bar{\beta}_+ > 0$, $|\alpha| > \bar{\beta}_- > \bar{\beta}_+ > 0$ and $|\alpha| > \bar{\beta}_- > \bar{\beta}_+ = 0$ in items i) through vi), resp. In view of what has been said, it is fulfilled: $A_- = \bar{\beta}_-/|\alpha|$, $A_+ = \bar{\beta}_+/|\alpha|$, $B_- = \bar{\beta}_-\bar{r}_0$, $B_+ = \bar{\beta}_+\bar{r}_0$, $C_- = (\bar{\beta}_-/|\alpha|)\bar{r}_0$, $C_+ = (\bar{\beta}_+/|\alpha|)\bar{r}_0$. Thus, on the understanding that $\Delta\bar{\beta} = \bar{\beta}_- - \bar{\beta}_+$, definitions (3)–(5) harmonize with the ones of the numbers $A = \Delta\bar{\beta}/|\alpha|$, $B = \Delta\bar{\beta}\bar{r}_0$ and $C = (\Delta\bar{\beta}/|\alpha|)\bar{r}_0$, advanced earlier [1]. Since $\sigma_{cr,1-} = \sigma_{cr,1+} = |\alpha_{cr}|$, $\sigma_{cr,2-} = \bar{\beta}_{c-}$, $\sigma_{cr,2+} = \bar{\beta}_{cr+} = 0$ and $\bar{r}_{0cr} = (\chi^{(c)}_{0,n}(\rho)/2)/(1-\alpha^2_{cr})^{1/2}$, for the critical values it could be written: $A_{cr} = \bar{\beta}_{c-}/|\alpha_{cr}|$, $B_{cr} = \bar{\beta}_{c-}\bar{r}_{0cr}$ and $C_{cr} = (\bar{\beta}_{c-}/|\alpha_{cr}|)\bar{r}_{0cr}$, ($\bar{\beta}_{c-}$ — normalized phase constant of the propagating wave for $\alpha_- < 0$, squaring to the case $\alpha_- = -|\alpha_{cr}|$ and $\bar{r}_0 = \bar{r}_{0cr}$; $\bar{\beta}_{c-} > \bar{\beta}_{cr-}$, $\bar{\beta}_{cr-} = \bar{\beta}_{cr+} = 0$). The A, B, C numbers are functions of the set of parameters $\{c, |\alpha|, \bar{r}_0, \rho, n\}$, whereas the critical ones depend on $\{c, |\alpha_{cr}|, \rho, n\}$, (on $\{c, \bar{r}_{0cr}, \rho, n\}$). The values of the latter are figured through an iterative scheme. For a chosen pair $\{\rho, |\alpha_{cr}|\}$ the constant $\bar{\beta}_{c-}$ is reckoned from the formula $\bar{\beta}_- = \{(1-\alpha^2_-)/[1+(\alpha_-/(2k_-))^2]\}^{1/2}$ with $\alpha_- = |\alpha_{cr}|$ in which $k_- < 0$ is altered, until the numerical equivalent of $\bar{r}_0$, counted from the term $\bar{r}_0 = (k_-\chi^{(c)}_{k_-,n}(\rho)/\alpha_-)\{[1+(\alpha_-/(2k_-))^2]/(1-\alpha^2_-)\}^{1/2}$, coincides with $\bar{r}_{0cr}$ with a prescribed accuracy. The value of $\bar{\beta}_-$ obtained is accepted as one of $\bar{\beta}_{c-}$. In each iteration Equation (11), resp. (10) is solved numerically for the relevant k_- and its roots $\chi^{(c)}_{k_-,n}(\rho)$ ($\zeta^{(c)}_{k_-,n}$) are inserted in the

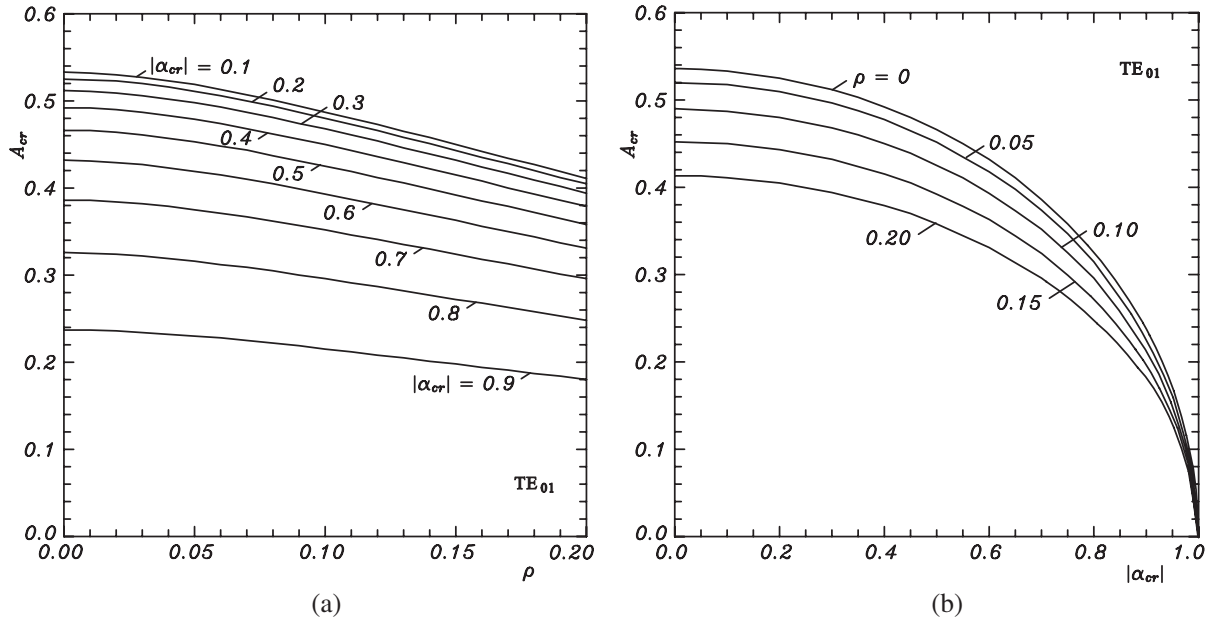

Figure 1: A_{cr} for normal TE_{01} mode vs.: (a) ρ with $|\alpha_{cr}|$ as parameter; (b) $|\alpha_{cr}|$ with ρ as parameter.

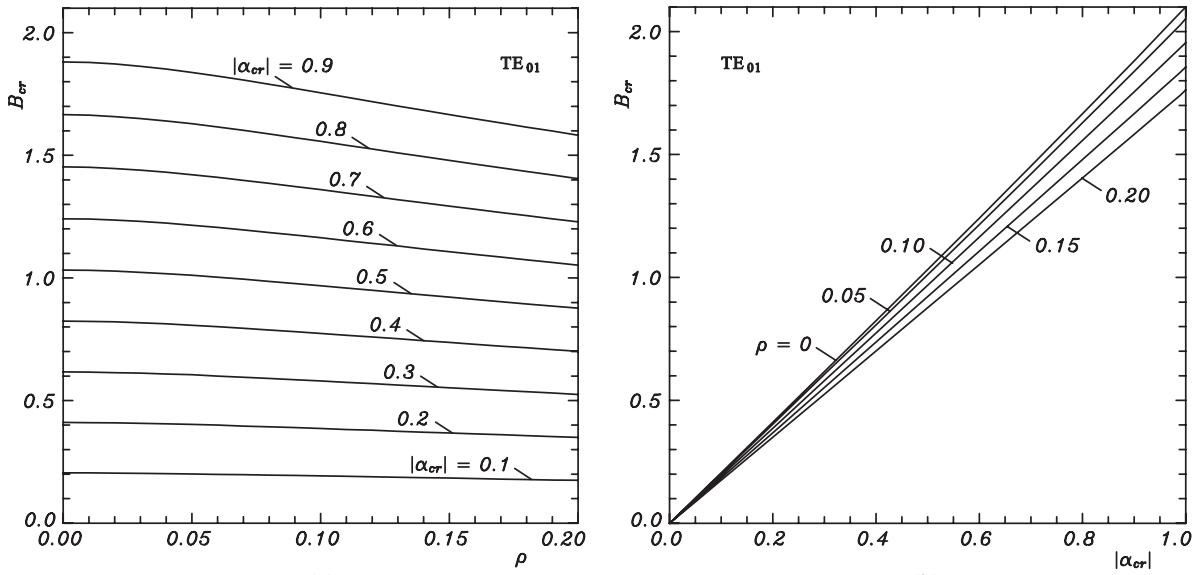

Figure 2: B_{cr} for normal TE_{01} mode vs.: (a) ρ with $|\alpha_{cr}|$ as parameter; (b) $|\alpha_{cr}|$ with ρ as parameter.

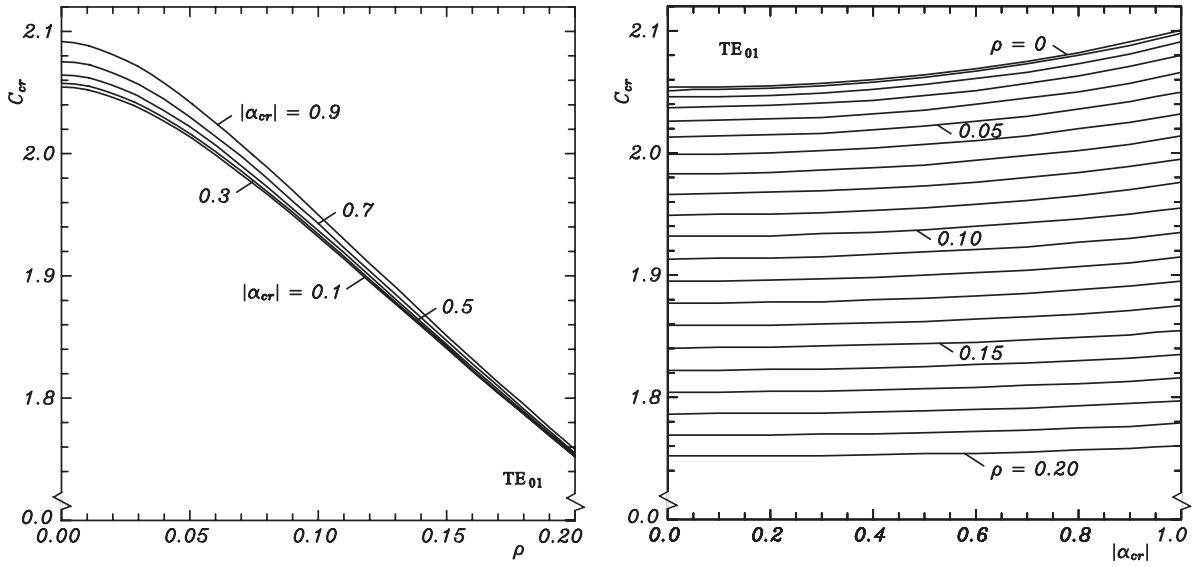

Figure 3: C_{cr} for normal TE_{01} mode vs.: (a) ρ with $|\alpha_{cr}|$ as parameter; (b) $|\alpha_{cr}|$ with ρ as parameter.

expression for $\bar{r}_0$ pointed out. The effect of ρ and $|\alpha_{cr}|$ on A_{cr}, B_{cr} and C_{cr} is shown in Figs. 1–3 and in Table 1, assuming $n = 1$ (normal TE_{01} mode).

4. APPLICATION

As seen from Fig. 3 and Table 1, C_{cr} nearly does not change with $|\alpha_{cr}|$, resp. with $\bar{r}_{0cr}$, especially if ρ is larger (e.g., $\rho = 0.2$). This is in agreement with the earlier results for the case $\rho = 0$, showing that C is a slightly varying function of both $|\alpha|$ and $\bar{r}_0$ [1]. Therefore, for each ρ the exact value of C_{cr} for any $|\alpha_{cr}|$ ($C_{exact,cr}$) could be accepted as an approximate one of C ($C_{approx,cr}$) for any set of parameters $\{|\alpha|, \bar{r}_0\}$ for which propagation may take place. It is assumed that $C_{approx,cr}$ is constant with respect to both $|\alpha|$ and $\bar{r}_0$ (ρ is fixed). The quantities $A_{approx,cr}$ and $B_{approx,cr}$ for any $|\alpha|$ and $\bar{r}_0$ are figured from the terms $A = C/\bar{r}_0$ and $B = C|\alpha|$ which follow directly from the Definition 1. In the same way it could be established effortless that the differential phase shift could be calculated in normalized form with the help of the formula

$$\Delta\bar{\beta} = AB/C. \tag{16}$$

Table 1: Values of the critical numbers A_{cr}, B_{cr} and C_{cr} for normal TE_{01} mode as a function of ρ and $|\alpha_{cr}|$.

ρ \ $\lvert\alpha_{cr}\rvert$		0.1	0.2	0.3	0.4	0.5	0.6	0.7	0.8	0.9
0.0	A_{cr}	0.533 482	0.525 665	0.512 325	0.492 952	0.466 691	0.432 140	0.386 871	0.326 141	0.237 874
	B_{cr}	0.205 444	0.411 146	0.617 360	0.824 361	1.032 431	1.241 874	1.453 020	1.666 237	1.881 935
	C_{cr}	2.054 444	2.055 728	2.057 867	2.060 902	2.064 861	2.069 790	2.075 743	2.082 796	2.091 038
0.1	A_{cr}	0.487 853	0.480 568	0.468 152	0.450 147	0.425 789	0.393 829	0.352 098	0.296 346	0.215 729
	B_{cr}	0.193 229	0.386 589	0.580 214	0.774 238	0.968 800	1.164 043	1.360 116	1.557 177	1.755 390
	C_{cr}	1.932 287	1.932 945	1.934 045	1.935 596	1.937 599	1.940 071	1.943 023	1.946 471	1.950 433
0.2	A_{cr}	0.411 574	0.405 347	0.394 740	0.379 376	0.358 626	0.331 453	0.296 059	0.248 913	0.180 975
	B_{cr}	0.175 211	0.350 470	0.525 826	0.701 326	0.877 022	1.052 963	1.229 197	1.405 778	1.582 759
	C_{cr}	1.752 107	1.752 350	1.752 752	1.753 316	1.754 045	1.754 938	1.755 996	1.757 223	1.758 621

(The subscript "*cr*" here indicates that the symbol in question relates to the cutoff state.) For example, picking from Table 1 $C_{approx,cr} = 1.752350$ for $\rho = 0.2$, $|\alpha| = 0.2$ yields for normal TE_{01} mode in case $\rho = 0.2$, $|\alpha| = 0.1$, $A_{approx,cr} = 0.350470$ and $B_{approx,cr} = 0.175235$, and $\Delta\bar{\beta}_{approx,cr} = 0.035047$. The exact values of the latter, obtained by the iterative method, suggested earlier [1], are $A_{exact} = 0.350422$, $B_{exact} = 0.175211$, $C_{exact} = 1.752111$ and $\Delta\bar{\beta}_{exact} = 0.035042$. The absolute error of computations $\delta\Delta\bar{\beta} = |\Delta\bar{\beta}_{exact} - \Delta\bar{\beta}_{approx,cr}| = 0.000005$ is insignificant.

5. CONCLUSION

Using the differences of the ratios of the taken in a specially chosen order roots of the equations, linking the normalized radial wavenumber $\bar{\beta}_2$ of the normal TE_{0n} modes in the ferrite-loaded circular and coaxial waveguides with azimuthal magnetization, with the normalized phase constant $\bar{\beta}$ of the waves and with the magnitude of the off-diagonal ferrite permeability tensor element $|\alpha|$, resp., a new definition of the positive real numbers A, B, C (the products of the normalized differential phase shift $\Delta\bar{\beta}$ produced by the structures by the factors $1/|\alpha|$, $\bar{r}_0$ and $\bar{r}_0/|\alpha|$, resp.), is formulated. An analysis of the numbers is made in the special case, corresponding to the cutoff state of the geometries. Based on their slight dependence on some of the parameters of the latter, illustrated graphically, an approximate approach is sketched for finding the differential phase shift.

ACKNOWLEDGMENT

We express our gratitude to our mother Trifonka Romanova Popnikolova for her self-denial, patience and for the tremendous efforts she exerts to support all our undertakings.

REFERENCES

1. Georgiev, G. N. and M. N. Georgieva-Grosse, "Formulae for differential phase shift computation in an azimuthally magnetized circular ferrite waveguide," in *Proc. Millenn. Conf. Antennas Propagat. AP-2000*, 1002, in CDROM, Davos, Switzerland, April 9–14, 2000.
2. Georgiev, G. N. and M. N. Georgieva-Grosse, "A property of the $L(c, \rho, n)$ numbers and its application to waveguide propagation," in *Proc. XXIX URSI General Assembly*, in CDROM, BK.6 (120), Chicago, IL, USA, August 7–16, 2008.
3. Georgiev, G. N. and M. N. Georgieva-Grosse, "Propagation in an azimuthally magnetized circular ferrite-dielectric waveguide," in *Proc. 3rd Europ. Conf. Antennas Propagat. EuCAP 2009*, 345–349, in CDROM, Berlin, Germany, March 23–27, 2009.
4. Georgiev, G. N. and M. N. Georgieva-Grosse, "Phase behaviour of a two-layered circular ferrite-dielectric waveguide with azimuthal magnetization," in *Proc. 26th Progr. In Electromagn. Res. Symp.*, Moscow, Russia, August 18–21, 2009 (in print).
5. Georgiev, G. N. and M. N. Georgieva-Grosse, "An application of the complex Tricomi function," in *Proc. Eleventh Int. Conf. Electromagn. Adv. Applicat. ICEAA'09*, Turin, Italy, September 14–18, 2009 (in print).
6. Tricomi, F. G., *Funzioni Ipergeometriche Confluenti*, Edizioni Cremonese, Rome, Italy, 1954.

Ray Tracing Scattering Simulations for Cavities Filled with Dielectric Material

F. Weinmann
Research Institute for High Frequency Physics and Radar Techniques
FGAN e.V., Neuenahrer Str. 20, Wachtberg 53343, Germany

Abstract— This contribution presents a very efficient Shooting-and-Bouncing-Rays (SBR) algorithm, which has been combined with Physical Optics (PO) and the Physical Theory of Diffraction (PTD). According to previous studies, this algorithm has been proved to provide very accurate results when calculating mono- or bistatic RCS of arbitrary large metallic objects. To enhance the accuracy of the simulations, diffracted rays according to the well-known Uniform Theory of Diffraction (UTD) have been implemented. Also dielectric objects, such as radomes, have been modeled. However, there is a lack of validation possibilities because numerically exact methods generally require much more computational resources for dielectric objects.

Recent advances of the presented ray tracing algorithm include the modeling of objects composed of metallic as well as dielectric parts. A special class of such objects are cavities with a dielectric filling, which can easily be studied in terms of RCS measurements in a standard anechoic chamber and thus serve as ideal objects for validation purposes. Furthermore, the simulations allow the fast generation of data over a certain frequency band, which can be used for calculating a two-dimensional image of the object. Such images can also be used for visualization of the main scattering phenomena. In the case of the empty cavity, virtual scattering centers can clearly be assigned to specific directions of incidence and multiple reflections inside the cavity. These directions also coincide with RCS maxima in the azimuth plane. If the cavity is filled with a PVC cube or slab, propagation mechanisms become much more complex due to multiple reflections inside the dielectric material and enclosed air space, respectively. This leads to a much more complex shape of scattering centers.

Overall, the ray tracing simulations show an excellent agreement with measurement results for both empty cavities and cavities filled with dielectric material. Thus, this ray tracing algorithm is well-suited not only for metallic objects but also for the modeling of objects composed of different materials, e.g., interiors of vehicles, antennas covered by radomes, etc.

1. INTRODUCTION

For the electromagnetic modeling of scattered fields from large and complex objects, a very efficient simulation tool based on the well-known Shooting-and-Bouncing-Rays (SBR) technique has been developed [1]. This algorithm uses field-based high-frequency approaches for finding the relevant propagation paths, i.e., rays are traced through the scenario according to the laws of Geometrical Optics (GO) and diffracted rays are generated according to the laws of the Uniform Theory of Diffraction (UTD). This GO/UTD part is combined with a source-based approach, where each ray generates an equivalent surface current at each interaction with the object. These currents are calculated using Physical Optics (PO) and Physical Theory of Diffraction (PTD), and the superposition of all these contributions leads to the total scattered field strengths. Further technical details about the ray tracing approach can be found in [1, 2]. With this simulation tool, large and complex objects can be modeled, which are still too costly for numerically exact methods. Generally, both metallic and dielectric objects [2], and also combined metallic-dielectric objects, can be modeled. This paper concentrates on simulations of generic metallic cavities, which are filled fully or partly with dielectric materials. Realistic environments would include the modeling of radomes on aircraft or the consideration of the interior of vehicles.

2. MODELING OF CAVITIES FILLED WITH DIELCTRIC OBJECTS

For the objects studied in this paper, the validation of the simulations by measurements is one of the most important tasks. Thus, only relatively simple objects can be analyzed. In the past, measurements were performed at a cube made of PVC. The edge length of this cube is 12 cm, and this object has also been used as a test object in the scope of the Workshop EM ISAE 2008 [3]. According to the dimensions of this cube, a metallic cavity with inner edge length 12 cm has been manufactured, which thus can be filled completely by inserting the PVC cube. Besides, a PVC

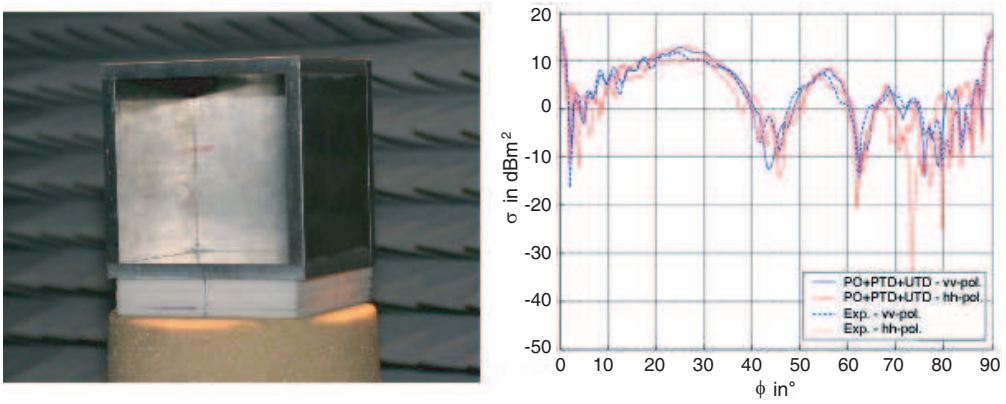

Figure 1: Metallic cavity inside the anechoic chamber and corresponding RCS at $f = 30\,\mathrm{GHz}$.

plate of size $12 \times 12 \times 2\,\mathrm{cm}$ has been manufactured, which can close the aperture of the metallic cavity. From these basic objects, various scenarios are generated, which are studied in the frequency range 20–40 GHz using the ray tracing code as well as measurements. Note that although these objects do not seem to be very complex, they are already very large for a numerically exact code and would require a large amount of computation time. For this reason, the validation of the ray tracing data is performed only by measurements in the scope of this paper.

As a first step towards estimating the influence of the dielectric objects, the scattered fields of the empty metallic cavity (Figure 1) is studied. Figure 1 also shows the monostatic RCS in the azimuth plane for vertical and horizontal polarisation and compares the simulated and measured data. Apart from the PO and PTD contributions according to [1], the UTD enhanced ray tracing simulation considers also rays, which are diffracted at the aperture and further propagate inside the cavity [4]. As can be seen from Figure 1, the measured and simulated data show good agreement over large angular intervals for both polarisations. According to the chosen angular convention, the direction of the incident wave is perpendicular to the aperture at $\phi = 0°$, whereas the incident wave hits the side surface of the cavity at $\phi = 90°$. The characteristic shape of the RCS curve can be explained by the geometry of the object, e.g., for angles up to approx. 40° the cavity behaves like a dihedral corner reflector.

If the cavity is filled with dielectric material (PVC, $\varepsilon_r = 2.7 - j^*0.01$), the propagation properties in the interior have changed radically. One the one hand, different field contributions are superposed at the point of observation, e.g., at normal incidence (with respect to the aperture) part of the incident wave is reflected at the air-PVC boundary and another part of the wave is transmitted and reflected inside the cavity. On the other hand, the dielectric medium causes refraction towards the normal vector of the aperture plane, which causes the effect of the dihedral corner reflector to appear over a larger range of angles. However, these phenomena interfere with each other, and thus the RCS curve shows a rather complex shape. Nevertheless, the simulation is in good accuracy with the measured results. The propagation phenomena become even more complex, if the cavity holds the PVC plate at the aperture instead of being filled completely. In the arrangement with the plate, multiple reflections will occur inside the plate as well as inside the enclosed air space. The results of both scenarios are depicted in Figure 2.

Concerning the simulations with the PVC material, it must be pointed out that both PTD and UTD are switched off because the formulations have been implemented only for perfectly conducting edges in an air environment. In both examples, however, three different materials (metal, PVC, air) meet at the aperture. Although neglecting the diffraction effect, the comparison of measured and simulated data shows good agreement over a large range of angles.

In the second part of this paper, the propagation mechanisms are studied using two-dimensional scattering analyses. For this purpose, simulation results are generated over the frequency range 20–40 GHz with a frequency step $\Delta f = 50\,\mathrm{MHz}$ and an angular resolution of 0.25°. The resulting data of scattered field strengths allows the calculation of an image of the object [5], which also exhibits the relevant scattering centres. Thus, further conclusions on the corresponding propagation mechanisms can be deduced. As an example, Figure 3 shows the scattering analysis of the empty cavity (open side points to the top of Figure 3) with the colour bar denoting the relative RCS in dB. The contour of the cavity is clearly visible, with the upper line being less distinct. At this

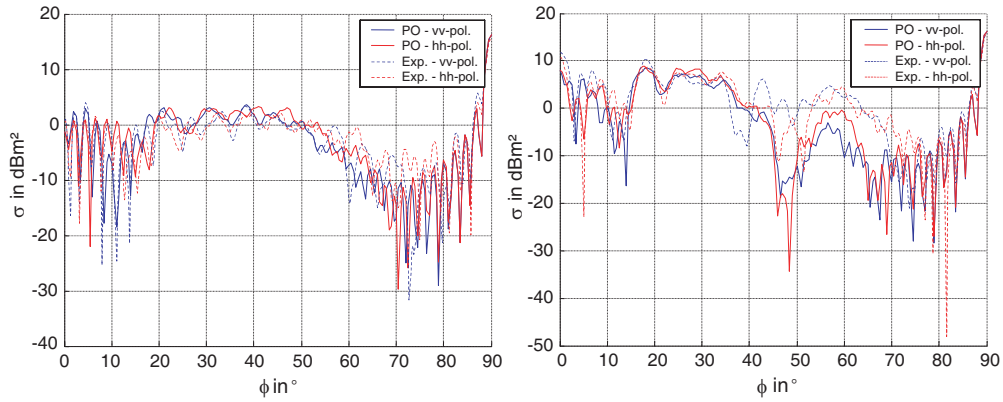

Figure 2: RCS of metallic cavity filled with PVC material at $f = 30\,\text{GHz}$. Left hand side: Cavity filled with PVC cube, right hand side: PVC plate at aperture.

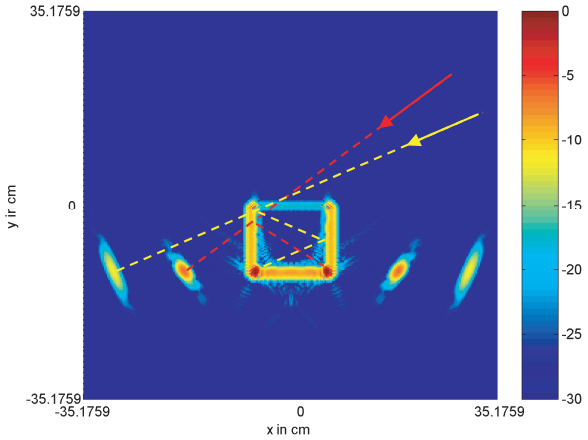

Figure 3: Scattering analysis of the empty metallic cavity ($f = 20$–$40\,\text{GHz}$, $\Delta f = 50\,\text{MHz}$).

position, the open aperture is surrounded by metallic plates with a thickness of 1 cm, leading to a lower intensity of scattering, as compared to the side surfaces. Special attention must be drawn towards the scattering centres on the lower left and right parts of the figure, which do not have an equivalent surface on the object. These virtual scattering centres are generated by rays which experience multiple reflections inside the cavity (see sketch of rays in Figure 3). Consider a wave impinging on the aperture from the top right and being reflected inside the cavity. Under certain angles of incidence, this wave is reflected back into the monostatic direction. From the point of observation, however, only the direction and path length can be deduced and thus the scattering centre is projected on a point outside of the object's real geometry. In comparison with Figure 1, the angles corresponding to the virtual scattering centres can be associated with the maxima at 55° and 65°, so these maxima can be explained graphically. Further scattering centres belonging to higher order reflections are also present, but these are outside of the depicted xy range of Figure 3.

When inserting dielectric material into the cavity, the relevant propagation phenomena are clearly different, which is visible from Figure 4. The left hand part of this figure shows the scattering analysis for the cavity being filled completely with PVC. As expected, the shape of the object is clearly to observe. The scattering effect of the aperture is slightly increased (as compared to Figure 3) because it is closed with dielectric material and thus also reflects part of the incident wave. However, additional scattering centres in the lower part of the figure are produced by fields being transmitted through the aperture plane. The associated "rays" propagate inside the cavity and seem to have an increased delay because of the dielectric filling of the cavity. Thus, the corresponding scattering centers are projected at points outside of the real geometry of the object. Furthermore, as stated above, the characteristics of a dihedral corner reflector are present over a large range of angles, which leads to the arch-like virtual scattering centres.

In the right hand part of Figure 4, the aperture of the cavity is closed by the PVC plate, which

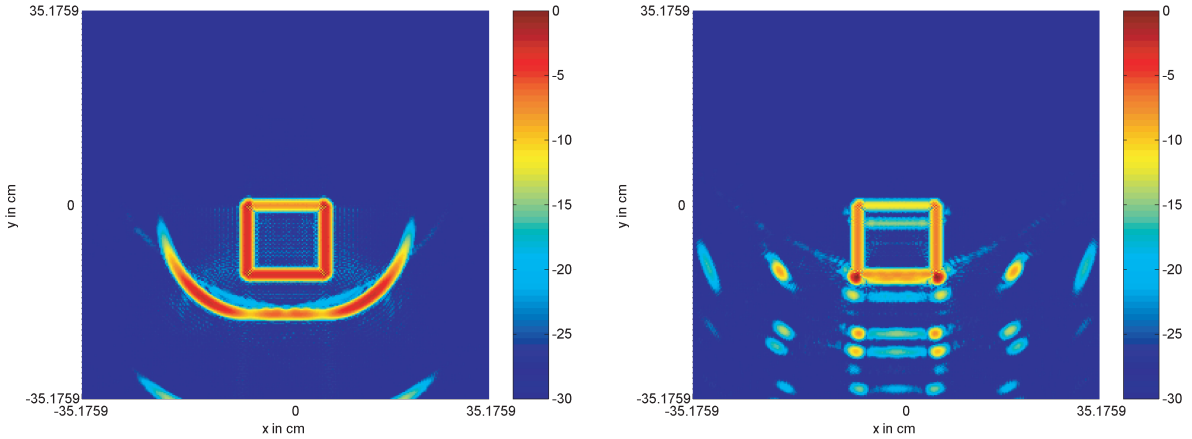

Figure 4: Scattering analysis of the metallic cavity filled with PVC material ($f = 20$–$40\,\mathrm{GHz}$, $\Delta f = 50\,\mathrm{MHz}$). Left hand side: Cavity filled with PVC cube, right hand side: PVC plate at aperture.

leads to a rather complex pattern of scattering centres. These are caused by multiple reflections inside the plate, inside the enclosed air space, or by various combinations of both phenomena. Thus, a direct assignment of scattering centres to the geometry of the scattering object is not trivial at all. However, the horizontal coloured bars at the bottom part of the figure give a feeling about the relevant multiple reflections at normal incidence on the aperture.

3. CONCLUSION

It has been shown that a ray tracing algorithm based on high-frequency methods is able to predict the scattered fields of cavities very well, even if the cavity holds some dielectric material. The simulated results have been compared with measurements and two-dimensional scattering analyses have been created from the simulated data. Both approaches of validation show a good accuracy of the results. Apart from validation, the scattering analysis is also well-suited to study the relevant propagation mechanisms, which are not obvious if the object is composed of different materials, e.g., a metallic cavity with a dielectric plate at the aperture.

REFERENCES

1. Weinmann, F., "Ray tracing with PO/PTD for RCS modeling of large complex objects," *IEEE Trans. Antennas Propagat.*, Vol. 54, 1797–1806, Jun. 2006.
2. Weinmann, F., "PO/PTD ray tracing for arbitrary metallic and dielectric objects," *Proceedings of the EuCAP 2006 — European Conference on Antennas & Propagation*, Nice, France, Nov. 6–10, 2006.
3. Workshop EM ISAE 2008, Toulouse, France, Nov. 14, 2008.
4. Weinmann, F., "UTD shooting-and-bouncing extension to a PO/PTD ray tracing algorithm," *ACES Journal*, Vol. 24, 281–293, Jun. 2009.
5. Vaupel, T. and T. F. Eibert, "Comparison and application of near-field ISAR imaging techniques for far-field radar cross section determination," *IEEE Trans. Antennas Propagat.*, Vol. 54, 144–151, Jan. 2006.

Ultra-wideband Co-planar Boat Microstrip Patch Antenna with Modified Ground Plane by Using Electromagnetic Band Gap Structure (EBG) for Wireless Communication

Dalia Nashaat[1], **Hala A. Elsadek**[2], **Esamt Abdallah**[2], **Hadia Elhenawy**[3], **and Magdy Iskander**[1]

[1]Hawaii Center for Advanced Communication, Hawaii, Honolulu, USA
[2]Electronics Research Institute, Giza, Egypt
[3]Faculty of Engineering, Ain Shams University, Cairo, Egypt

Abstract— A new antenna structure using triangular microstrip patch antenna alongside a small trapezoidal shape ground plane with proximity fed by a microstrip line is proposed in this paper. This printed antenna structure resembles a boat hence it is called boat microstrip patch antenna. The boat MPA is used for ultra-wide bandwidth intelligent antenna systems application. This antenna was numerically designed using HFSS simulation software package. The final proposed antenna design provides an impedance bandwidth ($S_{11} < -10$ dB) in the range from 2 GHz to up 35 GHz with a lot of bandwidth discontinuity. Etching 2D electromagnetic band-gap structure (2D-EBG), as dumb-bell shape in line feed increases the bandwidth to three times than the original bandwidth and reduces antenna size as well as enhancing the antenna gain. Simulations and measurements were carried out, and the comparison between them shows good agreement. The gain of antenna is also studied and the E and H-plane radiation pattern of the proposed antenna are presented.

1. INTRODUCTION

Microstrip patch antennas have been studied extensively over the past many years because of its low profile structure, light weight, and low cost in fabrication planar and nonplanar surfaces, compatibility with MMIC designs, and mechanically robust flexibility when mounted on rigid surfaces [1]. They are extremely compatible for embedded antennas in handheld wireless devices such as cellular phones, pagers, etc. These low profile antennas are also useful in aircraft, satellite and missile applications, where size, weight, cost, performance, ease of installation, and aerodynamic profile are strict constraints. Some of the principal advantages of this type of antennas are low profile nature, conformability to. However, a major drawback of these antennas is the narrow bandwidth. There have been various efforts from researchers toward increasing its bandwidth. Ultra-Wideband (UWB) is an emerging radio technology that has received much attention recently. Ultra wideband (UWB) communication systems can be broadly classified as any communication system whose instantaneous bandwidth is many times greater than the minimum required to deliver particular information. To include all the existing wireless communication systems such as AMPC800, GSM900, GSM1800, PCS1900, WCDMA/UMTS (3G), 2.45/5.2/5.8-GHz-ISM, UNII, DECT, WLAN, European Hiper LAN I, II [1], microstrip patch antennas on a thin dielectric substrate inherently have the disadvantage of narrow impedance bandwidth. To increase the bandwidth of a single layer microstrip patch antenna several configurations have been proposed such as design parasitic patches on the same layer with the main patch [1], E shaped patch [2] placing a U-slot on the patch [3], planer microstrip fed tap monopole antenna [4], etc. So we use co-planar feed to increase bandwidth of antenna. Unlike the usual method of placing the radiating patch of microstrip antenna on top of a ground plane, the patch is placed along side a small rectangular ground co-planar to it. They can be easily integrated with microwave integrated circuits (MIC) and monolithic microwave integrated circuits (MMIC). One simple but powerful technique is to replace the coaxial feeding or line feeding to coplanar feed. Another way to increase the impedance bandwidth of the microstrip patch antennas can be achieved by modifying the ground plane. Novel shape of modified ground plane as trapezoidal shape and using proximity feed are used to increase bandwidth and the geometry of the proposed antenna is shown in Figure 1. Recently, electromagnetic bandgap (EBG) structures have attracted much attention among researchers in the microwave and antennas communities due to their excellent pass and rejection frequency band characteristics [5].

In general, EBG structure is a periodic structure that forbids the propagation of all electromagnetic surface waves within a particular frequency band called the bandgap. It permits an additional

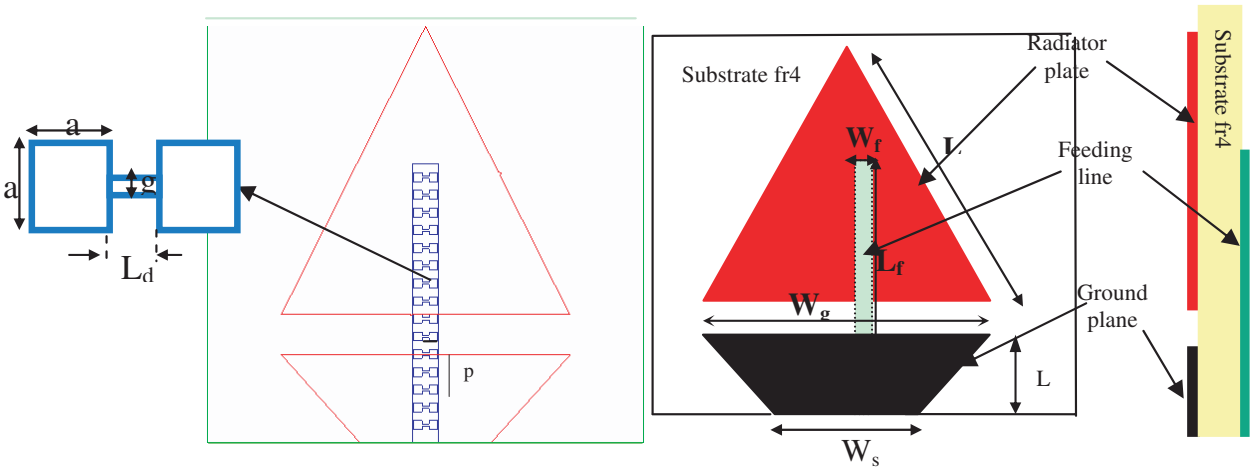

Figure 1: The prototype of the proposed antenna without and with EBG.

control of the behavior of electromagnetic waves other than conventional guiding and/or filtering structures. EBG has the potential to provide a simple and effective solution to the problems of surface and leaky waves. Various types of EBG structures have been studied. In one of the first applications a planar antenna mounted onto an EBG substrate was considered to increase the overall radiation efficiency of the device [6]. Increasing antenna directivity was studied using an EBG structure. A compact spiral EBG structure was studied for microstrip antenna arrays [7]. As the spiral EBG structure is very compact and useful in wireless communications, hence it was also studied to improve the performance of a triple band slot antenna [5].

The contribution of this paper is to further develop the idea in [6] by using electro magnetic structure as etching 2D-EBG as dumb-bell shape on the feed line to improve the bandwidth of the antenna and compare it with the bandwidth of the prototype antenna for same feed position, increase passband, reduce antenna size and remove the harmonic wave. The optimized antenna structure operates in the frequency range from 2 to 35 GHz which means it has an impedance bandwidth of almost %1000 from fundamental resonant frequency.

2. ANTENNA GEOMETRY

First part in this paper is investigating the novel shape of boat microstrip patch antenna. The geometry of the proposed antenna is shown in Figure 1, where an equal sides triangular patch with $L = 70\,\text{mm}$ is placed co-planar to a finite ground plane that has a trapezoidal shape with size of $W_s = 30\,\text{mm}$ and $W_g = 63\,\text{mm}$ and length $L_g = 21\,\text{mm}$. The dielectric substrate used is FR4 with dielectric constant $\varepsilon_r = 4.7$ and dimension $100 \times 100\,\text{mm}^2$ with thickness $h = 3.2\,\text{mm}$. The patch is proximity fed by a $50\,\Omega$ microstrip line with line length and width $L_f = 63\,\text{mm}$ and $W_f = 2.9\,\text{mm}$, respectively. The top and side views of the proposed antenna are shown in Figure 1.

To obtain a good impedance match the end of the feed line has to extend beyond the centre of the patch. Initially, several different simple shapes for the patch antenna was used but in order to minimize the size of the patch and at the same time maximize the bandwidth it was found that a triangular patch and an optimized geometry of the whole structure (the ground plane dimension, separation between the patch and the ground and feed line position) gives the best possible impedance bandwidth.

Second part of this paper is etching 2D electromagnetic bandgap structure as dumb-bell shape in the line feed to improve the impedance matching, the head square has dimension $a = 2\,\text{mm}$, slot length $L_d = 1.6\,\text{mm}$, width $0.5\,\text{mm}$ and periodicity $P = 4\,\text{mm}$.

3. SIMULATION AND MEASURED RESULTS

The antenna performance was investigated both by simulation via a commercially available finite element program, high frequency structure simulator (HFSS) version 11, and through measurement by using photolithographic techniques in fabrication. In order to provide design criteria for the proposed antenna, the effect of each geometrical parameter are analyzed. The effecting of co-planar length is studied as shown in Figure 2. There is an optimized value of the feed length which is 63 mm as shown in the figure. The simulated return loss with various ground plane width, W_g

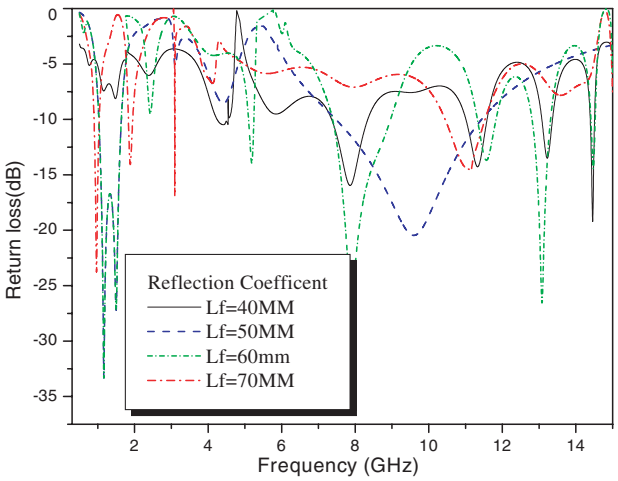

Figure 2: Studying the effect of changing L_f on antenna reflection coefficient.

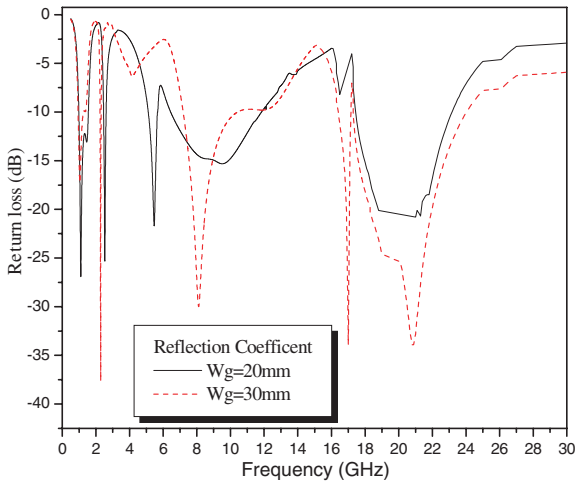

Figure 3: The variation of the ground width.

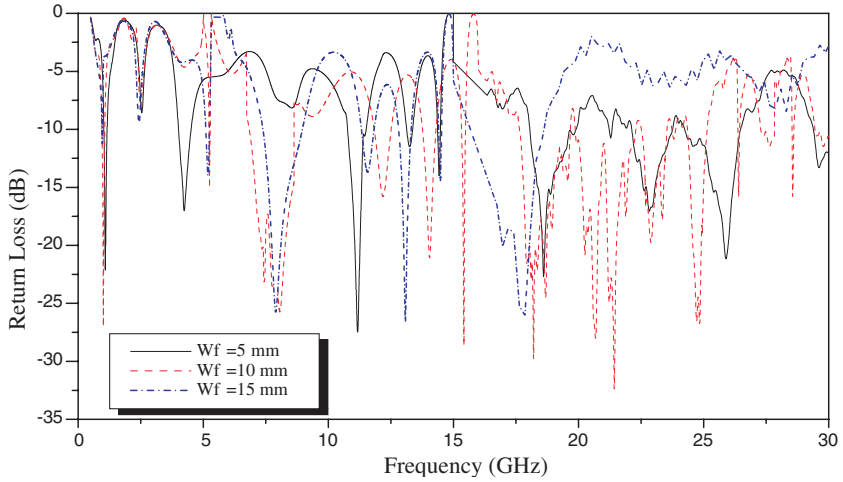

Figure 4: The variation of separation between the radiator and the ground plane.

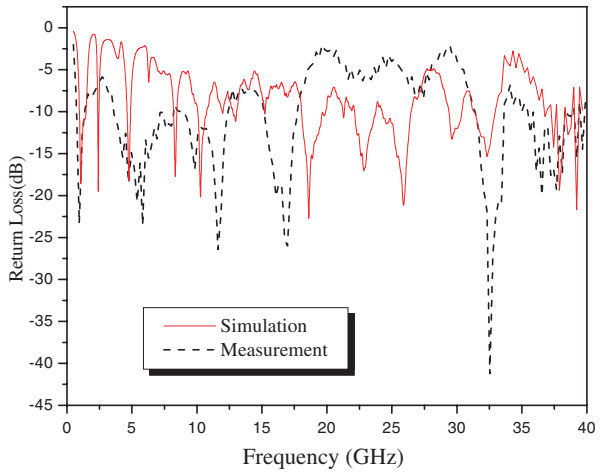

Figure 5: Comparison between simulated and measured return loss of the coplanar proposed antenna.

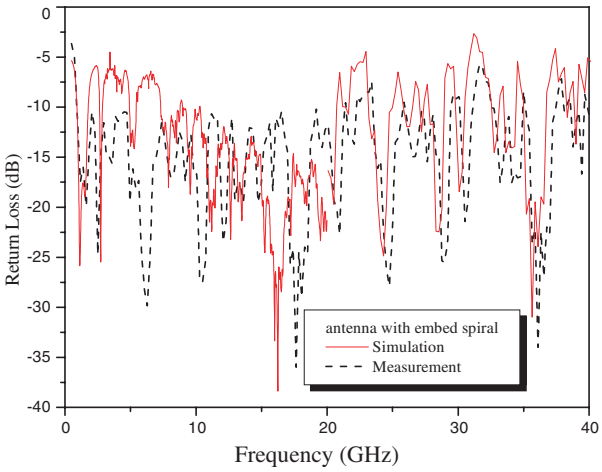

Figure 6: Comparison between simulated and measured return loss for coplanar antenna with dumbbell DGS.

are shown in Figure 3 where it can be seen that the higher width gives a broader bandwidth as well as a lower return loss magnitude.

The effect of the separation between radiating plate and ground plane was studied as shown in Figure 4. The proposed antenna is sensitive to L_g and in fact broadband performance is obtained for $L_g = 21$ mm. It is known that in proximity fed patch antennas the position of the feed line under patch is important. The reflection coefficient as obtained from simulation and measurement for optimum dimension of the proposed antenna is shown in Figure 5.

Finally, we use the EBG concept to improve the bandwidth of the microstrip patch antenna, and surface wave suppression; Figure 6 shows comparison between simulated and measured reflection coefficient of the proposed antenna with 2D-EBG. There is an improvement in bandwidth from 2 GHz to more than 35 with a lot of discontinuities. The average antenna gain is about 13 dBi. The photo of fabricated antenna is shown in Figure 7. Figure 8 shows the E-plane and H-plane radiation pattern of the proposed antenna with 2D-EBG etched on the line feed at different frequencies.

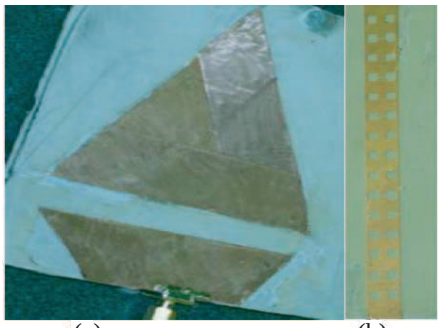

(a) (b)

Figure 7: Photo of (a) radiator antenna and (b) feed with 2D-dumble EBG.

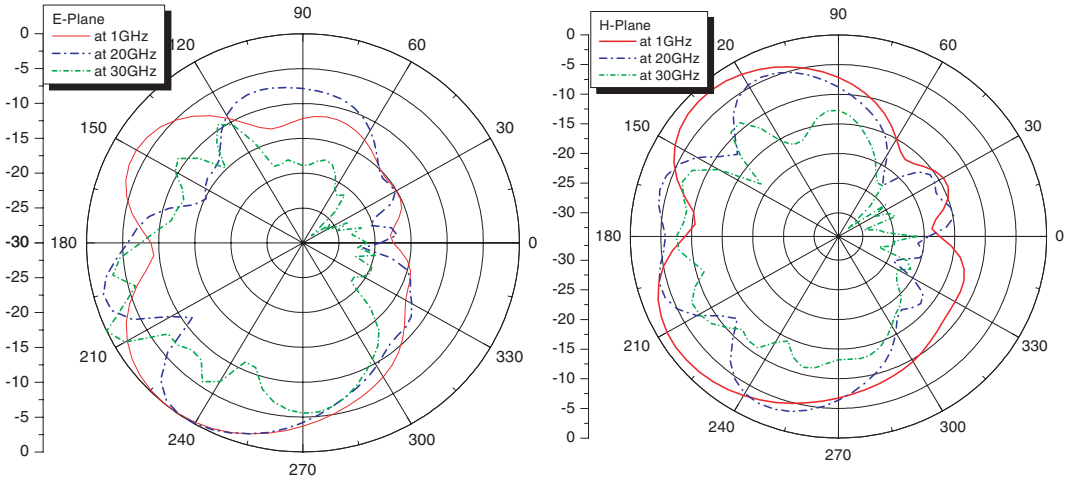

Figure 8: The measured E-plane and H-plane radiation pattern at 1, 20 and 30 GHz.

4. CONCLUSION

Rise in information capability, reduction in volume are very attractive to UWB applications. In this paper a co-planar triangular microstrip patch antenna as boat shape has been proposed. Ultra-wide bandwidth was obtained using trapezoidal ground plane on the same side of the radiating antenna. EBG concept is used to enhance the antenna bandwidth and gain. 2D-EBG is used to improve impedance matching and to broaden. There is very good agreement between simulated and measured results for proposed antennas. Further more acceptable E-plane and H-plane radiation pattern at different frequencies with average antenna gain 13 dBi are achieved.

REFERENCES

1. Kumar, G. and K. C. Gupta, "Directly coupled multiple resonator wide-band microstrip antenna," *IEEE Transactions on Antennas and Propagation*, Vol. 33, 588–593, June 1985.
2. Yang, F., X.-X. Zhang, X. Ye, and Y. Rahmat-Samii, "Wide-band E-shaped patch antennas for wireless communications," *IEEE Transactions on Antennas and Propagation*, Vol. 49, No. 7, 1094–1100, July 2001.
3. Weig, S., G. H. Huff, K. H. Pan, and J. T. Bernard, "Analysis and design of broadband single layer U-slot microstrip patch antennas," *IEEE Transactions on Antennas and Propagation*, Vol. 51, No. 3, 457–468, March 2003.
4. Cheng, S., P. Hall, Jr., and A. Ryberg, "Printed slot planar inverted cone antenna for ultra wideband applications," *IEEE Antennas and Wireless Propagation*, Vol. 7, 2008.
5. Cakir, G. and L. Sevgi, "Design of a novel microstrip electromagnetic band-gap (EBG) structure," *Microwave Opt. Technol Lett.*, Vol. 46, 399–401, 2005.
6. Gujral, M., T. Yuan, C.-W. Qiu, L.-W. Li, and K. Takei, "Bandwidth increment of microstrip patch antenna array with opposite double-E EBG structure for different feed positions," *International Symposium on Antennas and Propagation, ISAP*, 2006.
7. Artificial magnetic conductors, soft/hard surfaces and other complex surfaces (special issue), *IEEE Transactions on Antennas and Propagation*, Vol. 53, 2005.

Cell Bathing Medium as a Target for Non-thermal Effect of MMW on Heart Muscle Contractility

G. S. Ayrapetyan, E. H. Dadasyan, E. R. Mikayelyan, S. V. Barseghyan, and Sinerik Ayrapetyan
UNESCO Chair-Life Sciences International Postgraduate Educational Center, Armenia

Abstract— The comparative study of the effects of weak intensity specific absorption rate (SAR = 1.8 mW/g) of 4Hz modulated 160 GHz millimeter wave (MMW) and near Infrared (IR) irradiation on thermodynamic properties, specific electrical conductivity (SEC) of physiological solution (PS) and hydrogen peroxide (H_2O_2) formation in it as well as the effect of MMW-treated PS on heart muscle contractility, ^{45}Ca uptake was performed. The heat fusion capacity of MMW-pretreated PS after freezing by liquid nitrogen (N_2) is significantly less than the heat fusion capacity of sham and IR-treated PS. MMW unlike IR, has time-dependent elevation effect on water SEC and SAR, which is accompanied by the increase of H_2O_2 formation in it. The direct MMW radiation, MMW-pretreated PS and H_2O_2-containing PS have increasing effect on heart muscle contractility. The MMW-pretreated PS and the H_2O_2–containing PS have activation effect on ^{45}Ca uptake and dehydration effect on heart muscle contractility. Thus, the obtained data allow us to consider water dissociation as a main target through which the non-thermal effect of MMW on physicochemical properties of water is realized, while the MMW-induced formation of H_2O_2 in cell bathing medium serves as a messenger through which the modulation of intracellular metabolism takes place.

1. INTRODUCTION

The phenomenon of non-thermal biological effect of low intensity Millimeter Waves (MMW) has been known for several decades (Devyatkov 1973; Adey 1981; Lin 2004; Belyaev 2005). Although, it is more and more widely used in alternative treatments of a variety of diseases (Ziskin 2006; Markov 2007), the physicochemical mechanisms underlying the non-thermal biological effect of MMW still remain unclear.

As MMW penetration in body depths is only a few tenths of a millimeter, it is suggested that the therapeutic effect on organisms is initiated by water within the skin components ($\sim 70\%$), for which the absorption coefficient is the largest (Ziskin, 2006). However, the nature of low intensity MMW-induced changes of physicochemical properties of extracellular water, which could modulate cell metabolic activity, is not clear yet.

Although the higher sensitivity of hydrogen bonding makes water dissociation as one of the most variable properties of water, adequate attention has not been paid by investigators to water ionization as a universal and extra sensitive "primary" target for the biological effects of weak intensity environmental factors, including electromagnetic fields (EMF) (Szent-Gyorgyi 1968; Klassen 1982). It is known that even partial alignment of water molecules with the electric field may bend or break the hydrogen bonding (Chaplin 2008). Therefore, it is predicted that the MMW-induced water dipole vibration could increase water dissociation and in presence of oxygen (O_2) form reactive oxygen species (ROS), which are strong modulators for cell metabolism. The formation of hydrogen peroxide (H_2O_2) upon the high intensity MMW has been demonstrated (Gudkova et al. 2005). However, the possibility of ROS generation in water and water solutions upon the influence of extremely low intensity MMW is not clear yet.

For checking the above mentioned hypothesis whether the weak intensity MMW could modulate the water dissociation and generate H_2O_2, through which the effect of MMW on heart contractility is realized, the following two series of experiments were performed in present work:

1. A comparative study of the effects of MMW and near IR (1–100 THz) radiation on physicochemical properties of PS.
2. A comparative study of the effects of MMW-pretreated and H_2O_2-containing PS on heart muscle contractility, ^{45}Ca-uptake.

2. METHODS

As an experimental model serves PS (composition (in mM) NaCl-80, KCl-4, $CaCl_2$-7, Tris-HCl-5, pH-7.5) and isolated-intracordial perfused heart muscle of snail *Helix pomatia*. The MMW generator

"Artsakh-04M" (Russian production), designated for clinical applications, which generates 90–160 GHz MMW modulated by 4 Hz EMF was used. As IR source serves the "NOVAFLEX" Fibber Optic Illuminator (World Precision Instruments, USA) with near IR light filter. The determination of SAR (SAR $= C_{w(PS)}\Delta T/\Delta t$) of PS and heart for MW and IR radiation was used a high-precision differential calorimetric device "Biophys MWD-001" (Simonyan et al. 2006). For the determination of H_2O_2 content, the enhanced chemiluminescence method in a peroxidase-luminol-*p*-iodophenol system was used. The chemiluminescence and ^{45}Ca uptake by muscle were quantified by "Walac" liquid scintillation counter (Finland production).

2.1. The Comparative Study of MMW and IR Radiation on Physicochemical Properties of PS

As the SEC of water solutions is determined by ions, in order to find out whether MMW radiation leads to water ionization, the comparative study of the effects of MMW and IR radiation on SEC of PS was performed.

The data presented on Figure 1 show that at 18°C the SEC of 10-min-MMW-pretreated PS is significantly higher (4.1%) than in case of equivalent intensity IR-preheated and sham-treated PS. It is worth to note that the second 10 min of MMW exposure (a') has more pronounced elevation effect (50.2 %) on PS SEC than the first 10 min of exposure (a), while in case of IR irradiation both, the first (b) and the second (b') 10 min of exposures have the same effect on PS SEC (Figure 1(a)).

It is known that the SAR of water is related to electrical conductivity (σ) and density (ρ) expressed as SAR $= \sigma E^2/\rho$, where E is electric field intensity. Therefore, it is predicted that the MMW-induced possible changes of water dissociation could cause time-dependent changes of water SAR during MMW radiation. To check this hypothesis the thermal effects of double exposure of MMW and IR radiation on PS for 10 min (with 10 min intervals) were studied. During 10 min inter-exposure period the temperature of PS samples was returned to the initial temperature (18°C).

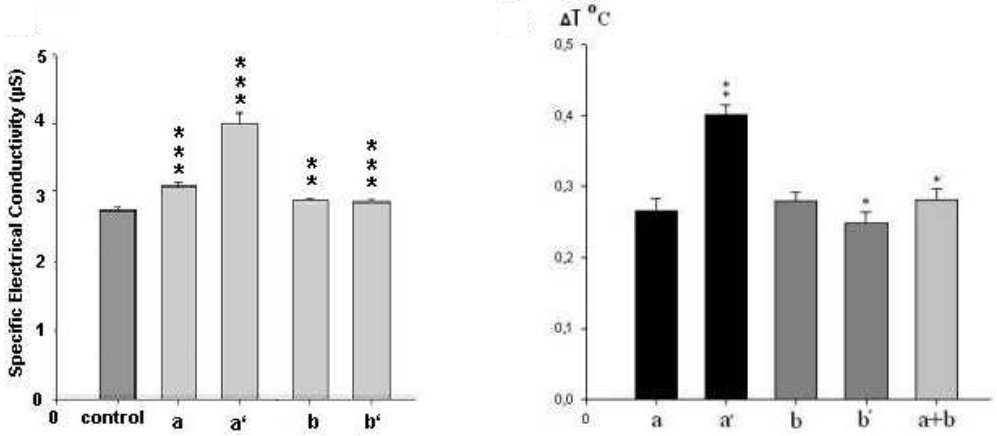

Figure 1: The effect of MMW and IR irradiation on specific electrical conductivity (a) and thermal capacity (b) of PS: (a) and (b) the first (a, b) and the second (a', b') 10 min of MMW and IR exposures, correspondingly and (b) (a+b) — 10 min MMW exposure followed by 10 min IR irradiation. ** $P < 0.0001$; *** $P < 0.000001$.

The data presented on Figure 1(b) show that 5.8 mW/sm^2 MMW-induced thermal effect on PS after the second 10 min of exposure (a') was higher than after the first 10 min of exposure (a) (0.22°C). While in case of IR radiation, its thermal effect was the same after the first (b) and the second (b') 10 min of exposures. The increase of MMW-induced heating after the second 10 min of exposure could be the result of either the decrease of the thermal capacity or the increase of SAR of PS. The absence of the elevation of the thermal effect after IR exposure (10 min) on MMW-pretreated (10 min) PS ($a + b$) could be explained by MMW-induced increase of PS SAR.

As water structure changes predict the adequate changes of its ice structure, in the next series of experiments the kinetics of melting process of sham-, MMW- and IR-treated PS frozen in liquid N_2 (−50°C) were studied.

As it can be seen from these data, the melting curve of MMW-pretreated PS (a) is significantly different from sham- and IR-pretreated PS. The heat fusion time of MMW-pretreated PS is twice shorter than in case of sham- and IR- pretreated PS. These data could serve as an evidence of non-thermal structural (poliarity) changes of PS upon MMW irradiation.

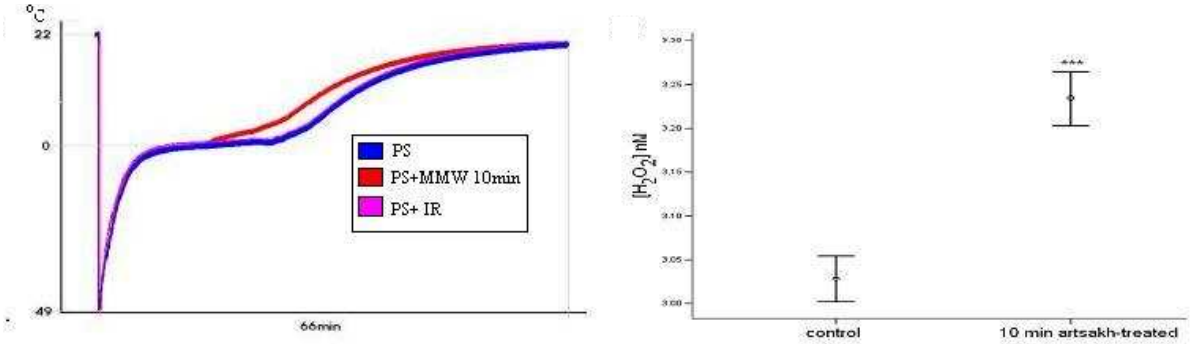

Figure 2: (a) The time-dependent melting curves of sham (PS), MMW- (PS+MMW) and IR- (PS+IR) pretreated PS frozen in liquid N_2. MMW and IR radiation was performed 3 times with 10min intervals. Typical curves of one of 20 experiments. (b) The amount of H_2O_2 in control and 10 min MMW-treated PS. ($n = 10$).

In order to find out whether MMW-induced elevation of water dissociation leads to the formation of ROS in DW and PS, in the next series of experiments the concentration of hydrogen peroxide (H_2O_2) in non-treated and MMW-treated PS was determined.

As it can be seen on Figure 2(b) the level of H_2O_2 in PS was increased by 10 min MMW irradiation (SAR = 1.8 mW/g) from 3.03 to 3.24 nM.

2.2. The Comparative Study of MMW-pretreated and H_2O_2 Containing PS on Heart Muscle Contractility

As it is presented on Figure 3 both, 10-min-direct-exposure of MMW (a) and MMW-treated PS (b) have contraction effect on heart muscle contractility brining to fully stop of heart beating. Previously it was shown that H_2O_2-containing PS has also inhibitory effect on heart muscle beating (Ayrapertyan et al. 2007). Such similar depressing effects of MMW-pretreated and H_2O_2-containing PS on heart muscle contractility could be considered as coincide data for the hypothesis that the MMW-induced formation of H_2O_2 in PS could serve as a pathway through which the biological effects of MMW are realized.

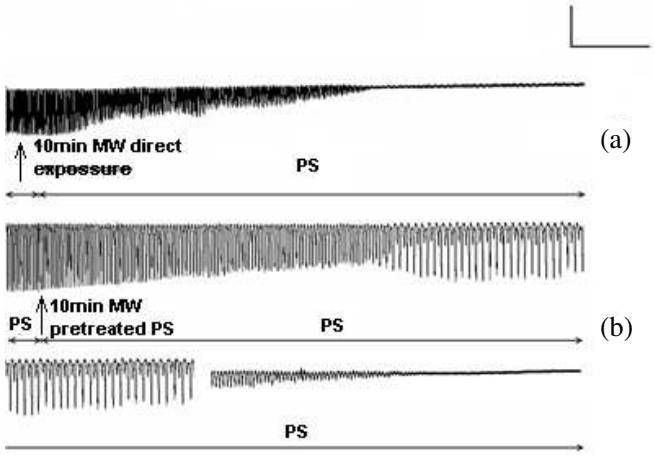

Figure 3: The effect of direct MMW 10 min-exposure (a) and MMW-pretreated PS (b) on heart muscle contractility. The interruption period of the recording was 15 min. Calibration: contraction amplitude-250 mg, time-5 min.

However, to finalize the above mentioned data we need to clarify if MMW-pretreated and H_2O_2-containing PS have a common metabolic pathway through which they modulate heart muscle contractility. As the intracellular Ca ion has a crucial role in the regulation of muscle contractility in the next series of experiments the study of the effects of MMW-treated and H_2O_2–containing PS on ^{45}Ca uptake was performed. The heart muscle 10min-exposure by H_2O_2 (5×10^{-9} M) containing PS and 5 min exposure by MMW has elevation effect on ^{45}Ca uptake in heart muscle by $20 \pm 1.9\%$ ($n = 10$), while H_2O_2 (10^{-7} M) and 1 min MMW direct exposure leads to the decrease of ^{45}Ca uptake

by 30%. This data indicate that MMW exposure could increase the local H_2O_2 concentration until 10^{-7} M. Thus, the obtained data allow us to conclude on common ^{45}Ca-dependent mechanisms through which their effects on muscle contractility are realized.

This conclusion is in close agreement with an early suggestion of Arber and Lin (Lin 2004) showing that the MMW effect on snail neuron was triggered by the increase of intracellular free Ca^{2+}, which was completely eliminated by intracellular injection of Ca^{2+} chelating agent-EDTA.

3. CONCLUSIONS

The obtained data show that the non-thermal biological effects of MMW could be explained by dissociation increase of cell bathing aqua solution bringing to generation of ROS through which the modulation of Ca-dependent metabolic mechanisms responsible for heart muscle contractility is realized.

ACKNOWLEDGMENT

Project was realized in framework of Armenian research foundation, Office of Naval Research Global (ONRG) program (No. A-1592P) and European Office of Aerospace Research and Development (No. A-1571P).

REFERENCES

1. Adey, W. R., "Tissue interactions with non-ionizing electromagnetic field," *Physiol. Rev.*, Vol. 61, 435–514, 1981.
2. Ayrapetyan, S. N., "Cell aqua medium as a preliminary target for the effect of electromagnetic fields," *Bioelectromagnetics: Current Concepts, NATO Science Series*, 31–64, S. Ayrapetyan and M. Markov, eds., Springer Press, The Netherlands, 2006.
3. Belyaev, I., "Non-thermal biological effects of microwaves," *Microwave Rev.*, Vol. 11, 13–29, 2005.
4. Binhi, V. N. and A. B. Rubin, "Magnetobiology: the kT paradox and possible solutions," *Electromag. Biol. and Med.*, Vol. 26, No. 1, 45–62, 2007.
5. Chaplin, M., "Water structure and science," 2009, http://www.lsbu.ac.uk/water/.
6. Devyatkov, N. D., "Effect of a SHF (mm-band) radiation on biological objects", *Uspekhi Fizicheskikh Nauk*, Vol. 110, 453–454, 1973.
7. Gudkova, O. Yu., S. V. Gudkov, A. B. Gapeev, V. I. Bruskov, A. V. Rubanik, and N. K. Chemeris, "The study of the mechanisms of formation of reactive oxygen species in aqueous solutions on exposure to high peak-power pulsed electromagnetic radiation of extremely high frequencies," *Biophysics*, Vol. 5, 773–779, 2005 (in Russian).
8. Klassen, V., *Magnetized Water Systems*, "Chemistry" Press, 296 (in Russian); English translation: *European Biology and Bioelectromagnetics*, 2006, Vol. 1, No. 2, 201–220, 1982.
9. Lin, J. C., "Studies of microwaves in medicine and biology: from snails to humans," *Bioelectromagnetics*, Vol. 25, No. 3, 146–159, 2004.
10. Markov, M., "Expanding use of pulsed electromagnetic field therapy," *Elec. Biol. And Med.*, Vol. 26, No. 3, 257–274, 2007.
11. Szent-Gyorgyi, A., *Bioelectronics: A Study in Cellular Regulations, Defense, and Cancer*, Academic Press, NY, 1968.
12. Simonyan, R. H., A. Ghulyan, and S. N. Ayrapetyan, "High-frequency device for the measurement of specific absorption rate of biotissues of high intensity," *Bioelectromagnetics: Current Concepts, NATO Science Series*, 291–296, S. Ayrapetyan and M. Markov, eds., Springer Press, The Netherlands, 2006.
13. Ziskin, M. C., "Physiological mechanisms underlying millimeter wave therapy," *Bioelectromagnetics: Current Concepts, NATO Science Series*, 241–251, S. Ayrapetyan and M. Markov, eds., Springer Press, The Netherlands, 2006.
14. Lin-Liu, S. and W. R. Adey, "Low frequency amplitude-modulated microwave fields change calcium efflux rates from synaptosomes," *Bioelectromagnetics*, Vol. 3, No. 309, 322, 1982.
15. Bawin, S. M., L. K. Kaczmarek, and W. R. Adey, "Effects of modulated VHF fields on the central nervous system," *Ann. N.Y. Acad. Sci.*, Vol. 247, 74–81, 1975.

Calculation of Optimal Volume Ratio at Parallel Using of Ray and FDTD Method

Robert Dady, **Andrea Farkasvolgyi**, **and Lajos Nagy**
Department of Broadband Infocommunications and Electromagnetic Theory
Budapest University of Technology and Economics (BME)
H-1111 Budapest, Goldmann György tér 3, Hungary

Abstract— In this paper, we would like to present our results of combining the ray methods and FDTD for official environment. For the optimal combination, we have determined several parameters accordingly by minimal calculation electrical field level can be calculated in a good resolution around the receiver. Our simulation environment has been developed for solving a new problem. By this problem, we encountered that the ratio of the size of the space around the receiver and the whole indoor size must be given. For describing the space around the receiver, the FDTD method has been used while for the other part of space the ray method was applied. In this article, we confirm that the combined use of ray and FDTD methods is more effective than the other calculation procedures.

1. INTRODUCTION

The increasing interest on wireless communication and services resulted the need for techniques proposed for propagation. The main point of this techniques is the distribution of power. This increasing demand on wireless communication causes large traffic density, which may be solved by optimal placement of transmitters. Ray Tracing and Ray Launching are common ray optical methods for solving such placement tasks [1].

2. RAY METHODS

Ray methods are derived from geometrical optics where the objects dimensions are much larger than the wave length. Electromagnetic waves are modeled as rays with flat wave-fronts. In case of ray launching, rays are followed until they hit an object where a reflected and/or transmitted ray is initiated in the next reflection and/or transmission depth. The direction of the new ray after reflection and/or transmission is determined by Snellius' law (aka. law of refraction). Detailed expanding is in [2].

2.1. Ray Tracing

Ray tracing can be distinguished in ray launching and ray imaging techniques. Applying the imaging method, where new image sources are constructed of all existing (image) sources in the current reflection and/or transmission depth for all planes, each ray (path) from the transmitter to the receiver is exactly determined. The main problem of this scheme is, that complex scenarios with large number of walls become difficult in an reasonable time because with an increasing number of interactions (reflection and/or transmission and diffraction) the computational effort exponentially increases [2, 3]. Fig. 1 shows several rays in a standard scenario with three walls inside the room. The black point in the transmitter while the gray one is the receiver surrounded by a FDTD grid. Fig. 2 shows the theoretical interactions of ray path's.

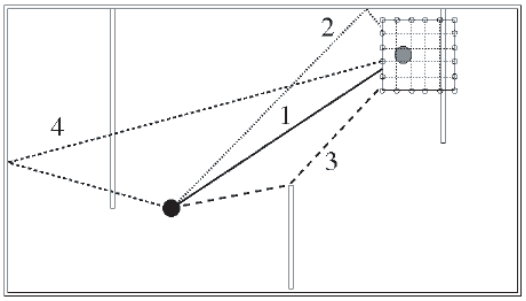

Figure 1: Ray paths (1 — direct, 2 — reflected, 3 — diffracted, 4 — transmitted, reflected, transmitted) in indoor environment and FDTD grid.

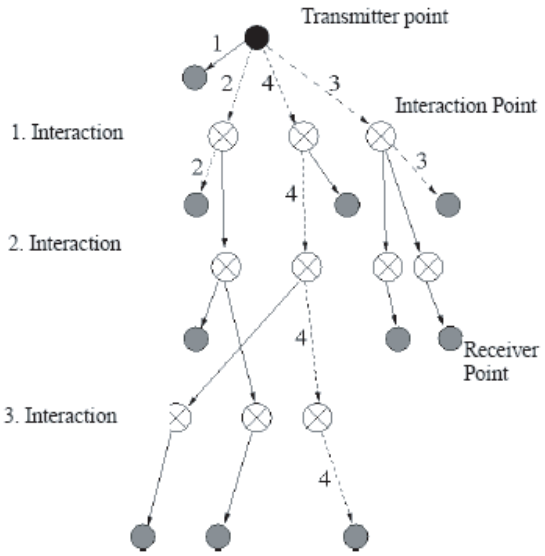

Figure 2: Ray paths on a tree structure (few paths from Fig. 1).

2.2. FDTD

The FDTD method is a time domain solution of the Maxwell's equations described in differential form and is widely used in circuit analysis because of its simplicity. The method divide the space investigated into finite grid elements and on the grid the time and space approximation of the electrical and magnetic field strength is performed [4, 5].

Starting from the generalized differential matrix operators, the Maxwell's curl equations can be express in the rectangular coordinate system, next the Yee algorithm [5] is than used for a discrete grid and consider a substitution of central differences for the time ($\partial/\partial t$) and space ($\partial/\partial x$, $\partial/\partial y$, $\partial/\partial z$) derivatives one get for the time marching solution of the coupled equations. The algorithm defines the discretized field components in the FDTD rectangular unit cell (the Yee cell). This cell in three dimension has volume of $\Delta x \Delta y \Delta z$ and the electric and magnetic field components locations are interleaved by half of the discretization length ($\Delta x/2$, $\Delta y/2$ and $\Delta z/2$).

The discretization on the simulation volume is made by cubic lattice so $\Delta x = \Delta y = \Delta z = \Delta$ which results in a significant simplification of the finite difference equations.

Stability of the FDTD solution requires that the electromagnetic wave must not pass through more than one cell in one time step, i.e., the time step and the unit cell dimension satisfy the Courant condition [1, 2, 4]. Fig. 3 shows a FDTD grid divided into optimal Yee cells.

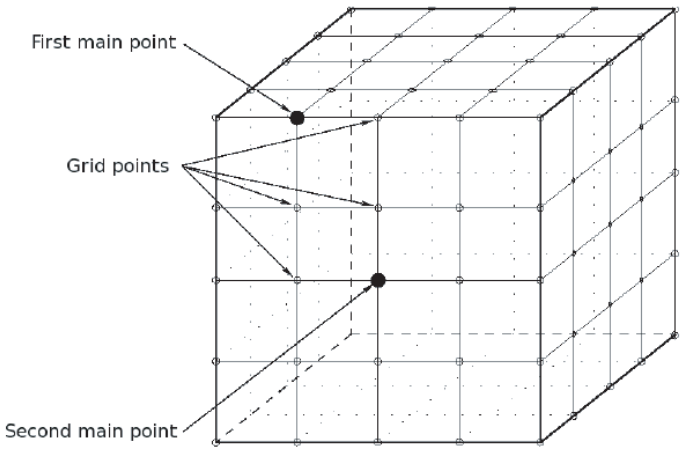

Figure 3: FDTD grid with main points.

3. COMBINATION OF RAY TRACING AND FDTD

By this combination method, we want to calculate the ideal place of the receiver antennas. We declare an initial position for the receiver antenna and the calculation can place the antenna to an optimal position. The resulted optimal position can be found in the initial positions' environment which is part of calculated space of FDTD. The outcome of calculation depends on that the transmitter or the receiver antennas place was fixed. The problem is symmetric in sense that receiver and transmitter can be swapped.

The optimality of the combination means that the simulation lengths is minimal when the calculated field strengths approaches the measured one.

The idea of the combination of both methods is really effective approach because Ray Tracing handles only rough scenarios that is the objects of the simulated area are presented mostly as plain surfaces. Contrarily FDTD consists of a grid resolution. The size of the grid is proportional with the real particularity of the surfaces of different objects e.g., buttons of a computers keyboard. FDTD allows a more precise calculation but it needs accordingly more computational memory capacity to store its results.

That is why Ray Tracing is used for whole scenario and FDTD is used only for the local environment of the observed antenna.

The interface of the both algorithms is the 3 dimensional grid of FDTD. Each grid point acts as a receiver point from point of view of the Ray Tracing and each grid point means a separate Ray Tracing simulation. There is no restriction on where to put the FDTD volume. Inside the volume, the grid size is defined by the Yee cell — As mentioned before. If the FDTD volume happens to contain some objects so the chosen grid size has to be adapted to the new circumstances. As the wavelength of the EM wave gets smaller inside of materials so has to be the grid size also be smaller. If an object inside the grid has an irregular form a more regular shape has to be choose e.g., cube to continue the calculation. The distance of the grid points of the inner object and the distance of the grid points outside of the inner object should a integer multiples of each other. Some literature refers to the volume enclosed by grid points as voxel (volume pixel).

4. OPTIMIZATION BY COMBINED SIMULATION

During the Ray Tracing, calculation on the FTDT initial grid points the path components of the resulted trace are recorded.

The receiver points of Ray Tracing at the FTDT initial grid are chosen not sequentially but in a distance dependent on the FTDT grid size and the smallest object in the simulation area. This distance means that these points are not adjacent grid points but between them there are one or more grid points. Fig. 3 shows an example where first grid point is at location (0, 1) and second receiver point of the Ray Tracing is located at (2, 2) assuming the upper left corner to be at location (0, 0). We call these points main points. Optimal choice of these main point is desirable, but as rule grid points located on the edges of the FDTD cube is a good choice. After calculating each main point with Ray Tracing the closest main points' ray path components (see Fig. 2.) have to be compared. If these ray paths are identical in components and there is a bijection between the paths components' interaction media i.e., same walls in the same sequence are present in both paths, then intermediate grid points can be calculated (as Ray Tracing receiver) as follows. There is no need to take every wall in RT calculation. Same ray paths have to calculated as by main grid points where the interacting walls and their sequence is given.

This method avoids large calculation for intermediate FDTD grid points lying between main grid points.

5. CONCLUSION

There are many optimizations for Ray Methods but the combination of Ray Methods and FDTD needs further investigation. In this article, we presented a method for reducing the number of Ray Tracing simulations e.g., the number of simulations for the FDTD grid points as receivers by obtaining the smallest objects size and the wavelength accordingly.

ACKNOWLEDGMENT

This work was carried out in Mobile Innovation Center, Hungary (MIK) and supported by the Hungarian National Office for Research and Technology in the framework of Oszkar Asboth program. This work was also supported by the EU. PF6 framework ACE2 project.

REFERENCES

1. Wang, Y., S. Safavi-Naeini, and S. K. Chaudhuri, "A hybrid technique based on combining ray tracing and FDTD methods for site-specific modeling of indoor radio wave propagation," *IEEE Transactions on Antennas and Propagation*, Vol. 48, No. 5, 743–754, May 2000.
2. Nagy, L., R. Dady, and A. Farkasvolgyi, "Algorithmic complexity of FDTD and ray tracing method for indoor propagation modelling," *The European Conference on Antennas and Propagation, EuCAP 2009*, Berlin, Germany, Mar. 23–27, 2009.
3. Wang, Y., S. Safavi-Nacini, and S. K. Chaudhuri, "A combined ray tracing and FDTD method for modeling indoor radiowave propagation," *IEEE Antennas and Propagation Society International Symposium*, Vol. 3, No. 21–26, 1668–1671, Jun. 1998.
4. Taflove, A. and S. C. Hagness, *Computational Electrodynamics: The Finite-difference Time-domain Method*, Artech House, Norwood, 2005.
5. Yee, K. S., "Numerical solution of initial boundary value problems involving Maxwell's equations in isotropic media," *IEEE Transactions on Antennas and Propagation*, Vol. 14, No. 3, 302, 1966.
6. Nagy, L., "MIMO cube in realistic indoor environment," *The European Conference on Antennas and Propagation, EuCAP 2006*, Nice, France, Nov. 6–10, 2006.
7. Gschwendtner, B. E. G. Wölfle, B. Burk, and F. M. Landstorfer, "Ray tracing vs. ray launching in 3D microcell modelling," *1st European Personal and Mobile Communications Conference (EPMCC)*, 74–79, Bologna, Nov. 1995.

Effect of Antenna Space on MIMO Channel Capacity in Practicable Antenna Structures

Andrea Farkasvolgyi, Robert Dady, and Lajos Nagy
Department of Broadband Infocommunications and Electromagnetic Theory
Budapest University of Technology and Economics
H-1111 Budapest, Goldmann Sq. 3, Hungary

Abstract— This article presents our simulation results of a MIMO (Multiple Input Multiple Output) antenna systems for channel capacity maximization by correlation coefficient between antennas. The primary purpose was confirmation that the maximal channel capacity parallel with minimal antenna correlation coefficient can be realized by selecting of perfect antenna space in a given MIMO antenna structure. The analytical proofs with simulation' results can be confirm the primly hypothetical assumptions.

1. INTRODUCTION

The element characteristic of the MIMO systems is that this system can be worked with higher mean channel capacity by the usage of several antennas on the receiver and the transmitter side, symmetrical ($n \times n$) or non symmetrical ($n \times m$) design. Frequently used systems are 2×2 or 3×3. Prevalent utilization is the Laptops antennas or whatever device which communicate with antennas. In these adaptations, there are not too much places for the antennas (the place is restricted by the metal part of the device). This is why the most important problem is the minimal place of the antennas, namely the antenna system have to be minimal size. Consequently the antennas would be placed minimal distance with that restriction that the channel capacity will be high.

In our early project, we investigated 3×3 MIMO antenna system we came into that in this case the usage of phase and distance diversity issues in the highest mean channel capacity. In this article, we analyzed a 2×2 antenna system. The based of the optimization were the correlation coefficient which can be perfectly characterized the system. The antennas were situated into a 3D DB (double bouncing) environment. We chose this model because this can be written down or managed most efficiently the specialty of official environment for example the disturbing object in the channel. The effect of these objects is that waves of arbitrary polarizations are incident on the antenna structure from all possible directions. In the 3D DB model, the scatterers are handled in a random scattering polarization matrix and they are situated with randomly and uniform distribution on a ball–shape surface around the transmitter and the receiver antennas [1, 2].

In this paper, there is writing down the calculation mechanism of correlation coefficient and mean channel capacity (Chapter 2), together with the results of simulation is shown (Chapter 3), which confirm our original supposal.

2. DISCIPLE FOR CALCULATION

2.1. Correlation Coefficient

In antenna systems, the correlation coefficient is a perfect parameter for quality of channel. When the correlation coefficient is lower at a special position of the system, the channel capacity will be higher. This is why we investigated the correlation coefficient between the antennas in a 2×2 antenna system. The transmitter and receiver antennas were situated in constant distance. In the simulation, the transmitter and receiver antennas were moved for distance 0 to 1.8. The correlation coefficient were calculated by the following method:

$$\rho\left(h_i, h_j\right) = \frac{C\left(h_i, h_j\right)}{\sqrt{C\left(h_i, h_i\right) \cdot C\left(h_j, h_j\right)}} \tag{1}$$

where,

$C(h_i, h_j)$ — covariance between the antennas
$C(h_i, h_i)$ — standard deviation
h_i — received power of antenna [5, 7]

Parallel with the calculation of correlation coefficient the channel capacity were determined versus distance between antenna-couples [3]. By the full channel matrix (H) can be calculated the Eigen values of the actual channel, the sign to noise ration and the number of effected active channels by the following method:

$$C = \sum_{i=1}^{r'} ld\,(1 + \lambda_i \mathrm{SNR}_i) \tag{2}$$

where,

λ — are the eigen-values of the channel by SVD
SNR_i — individual SNR of the eigenmodes after waterfilling
r' — denotes the number of useful eigenmodes with positive power allocation

2.2. Function of Mutual Coupling

According to our original assumption the mutual coupling has positive effect for the mean channel capacity. It means that the antennas are not totally separated, thus they interact.

We investigated the real effect of mutual coupling for the mean channel capacity. By the mutual coupling the several impedances can be influenced the channel. The channel matrix can be calculated by the following method with the effect of mutual coupling:

$$H_{\mathrm{mut}} = \frac{(C_{\mathrm{tr\_mut}} \cdot H \cdot C_{\mathrm{re\_mut}})}{C_{\mathrm{re}} \cdot C_{\mathrm{tr}}} \tag{3}$$

where

C_{re} — normalizing factors for $\mathrm{C_{tr\_mut}}$
C_{tr} — normalizing factors for $\mathrm{C_{re\_mut}}$.

The mutual coupling matrixes on the receiver and transmitter sides are given by the next functions:

$$C_{\mathrm{re\_mut}} = \frac{Z_{\mathrm{load}}}{(Z_{\mathrm{re}} + Z_{\mathrm{load}})} \tag{4}$$

$$C_{\mathrm{tr\_mut}} = \frac{Z_{\mathrm{tr}}}{(Z_{\mathrm{tr}} + Z_{\mathrm{source}})} \tag{5}$$

where Z_{tr} and Z_{re} are 2×2 mutual impedance and Z_{load} and Z_{source} contain the load and source impedances of the system. In the case of conjugate matching, the full channel matrix was calculated with $Z_{\mathrm{load}}(n,n) = Z^*_{\mathrm{re}(n,n)}$ and $Z_{\mathrm{source}}(n,n) = Z^*_{\mathrm{tr}(n,n)}$, where $()^*$ donates the conjugate of matrix [4, 6].

3. SIMULATION RESULTS

In this simulation we have investigated a $l/\lambda = 0.25$ antenna system. Both of the receiver and transmitter antenna side there were two antennas. Accordingly in this simulation we investigated a 2×2 antenna system. In the course of simulation the distance between the antennas were varied form zero to 0.8 in wavelengths.

First of all we simulated antenna correlation coefficient. The distance between the antennas both of the receiver and the transmitter were systematically changed. The Fig. 1 shows the results of simulation of antenna correlation coefficient.

If the correlation is about zero it means that the channel is none correlated and probably at this position the mean channel capacity will be maximal. The result of correlation shows periodical minimum which starts at about 0.15 and the period is 0.5.

The result of mean channel capacity is shown in Fig. 2. It is in evidence that the first maxima of the capacity is at 0.3 are the most relevant minimum of the correlation function. The mean capacity function is also cyclical and the period is 0.5, like by the correlation coefficient function.

We investigated the effect of conjugate matching or non conjugate matching (with mutual coupling). The usage of conjugate matching has not shown relevant difference in correlation, but in our earlier publication we presented, that conjugate matching effects a bit higher channel capacity. We have to take into account that the usage of conjugate matching is really complicated, and the increment is just some percentage.

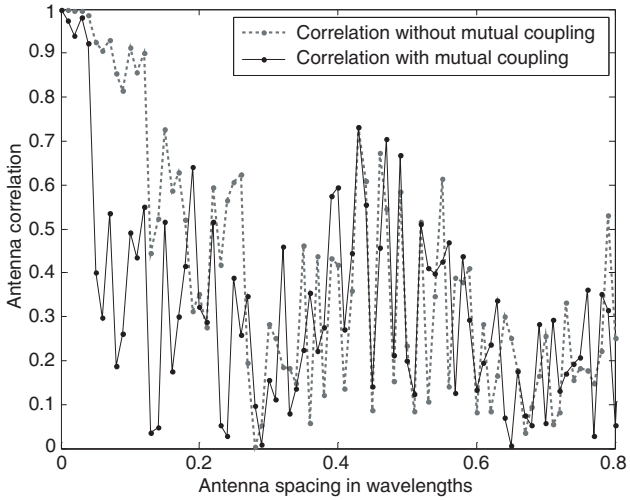

Figure 1: Correlation coefficient of 2×2 MIMO antenna system versus antenna spacing in wavelengths.

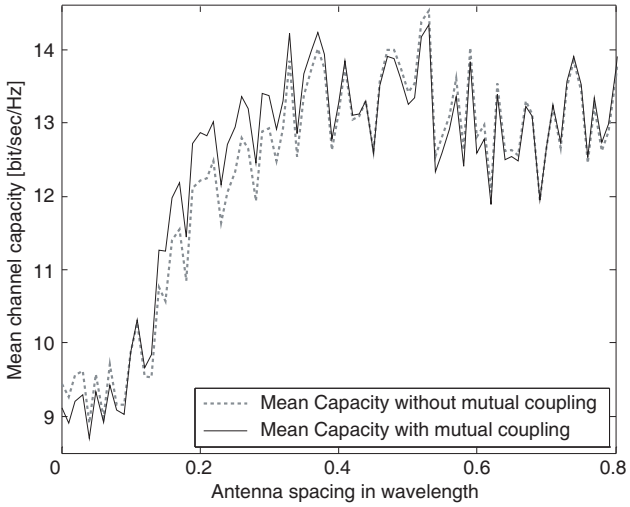

Figure 2: Mean channel capacity versus antenna spacing in wavelengths.

4. CONCLUSION

In this project, we investigated the minimal distance between in MIMO system, with that restriction that the mean channel capacity does not decline radically. We have came into that the antenna length is $l/\lambda = 0.25$ and with the effect of mutual coupling the minimal distance between the antennas is $\sim 0.15l/\lambda$. In case of separated antenna system, this distance is minimum ~ 0.3–$0.4l/\lambda$. By the simulations we could confirm that the distances between antennas would be minor because of the effect of mutual coupling. In the future, we would like to extend the simulation for frequency problem and we would like to present the results of measuring of this project.

ACKNOWLEDGMENT

This work was carried out in the framework of Mobile Innovation Center, Hungary (Mobil Innovációs Központ) and supported by the Hungarian National Office for Research and Technology in the framework of Oszkár Asbóth program.

REFERENCES

1. Collin, R. E., *Antennas and Radiowave Propagation*, McGRaw-Hill Book Company, New York, 1985.
2. Getu, B. N. and J. B. Andersen, "The MIMO cube — A compact MIMO antenna," *IEEE Trans. Wireless Commun.*, Vol. 4, No. 3, 1136–1141, May 2005.

3. Getu, B. N. and R. Janaswamy, "The effect of mutual coupling on the capacity of the MIMO cube," *IEEE Antennas Wireless Propagat. Lett.*, Vol. 4, 240–244, 2005.
4. Zombory, L. and M. Koltai, *Elektromagneses Terek Gepi Analizise*, Muszaki Konyvkiado, 1979 (in Hungarian).
5. Chiu, C. Y. and R. D. Murch, "Experimental results for a MIMO cube," *IEEE Transactions on Antennas and Propagation*, 2006.
6. Janaswamy, R., "Effect of element mutual coupling on the capacity of fixed length linear arrays," *IEEE Antennas Wireless Propagat. Lett.*, Vol. 1, 157–160, 2002.
7. Farkasvolgyi, A., and L. Nagy, "Optimization for MIMO antenna system," *Mobile and Wireless Communications Summit, 2007. 16th IST*, July 1–5, 2007.
8. Wallace, J. W. and M. A. Jensen, "Mutual coupling in MIMO wireless system: A rigorous network theory analysis," *IEEE Trans. Wireless Commun.*, Vol. 3, No. 4, 1317–1325, 2004.

Investigation for Maximal MIMO Channel Capacity by Genetic Algorithm

Andrea Farkasvolgyi, Robert Dady, and Lajos Nagy
Department of Broadband Infocommunications and Electromagnetic Theory
Budapest University of Technology and Economics
H-1111 Budapest, Goldmann Sqr. 3, Hungary

Abstract— In this article, we would like to present our results on channel capacity maximization by indoor environment. In this simulation, we investigated a 3×3 indoor MIMO (Multiple-Input Multiple-Output) antenna system. By the used indoor model, we could perfectly describe the office environment. The model statistically describes the material, surface and place of these objects which result in phase and amplitude error in the course of propagation. The structure of antennas is not fixed at present, but the antennas can take free position within a closed space. We looked for the perfect antenna structure and position for maximal channel capacity by applying genetic algorithm. In this paper, we would like to present the results of simulation. In our each simulation, we calculated with effect of mutual coupling because generally the antennas are not separated neither on transmitter nor on receiver side.

1. INTRODUCTION

Generally, in MIMO (Multiple Input-Multiple Output) systems, the most significant mission is the rise of the mean channel capacity. In this project, the main goal was to find the best antenna structure for highest channel capacity. We investigated several fixed structures but by this searching method, the structure we found resulted not the maximal theoretical value just a good approximation.

We present the searching methods and the best structures which result the maximal attainable channel capacity. Previously, we also dealt with immovable antenna structure types but it is a really interesting problem trying to find an absolutely free (non attainable) structure for maximal channel capacity. Fundamentally, the simulation methods parallel with our original methods. We make an effort to show the changing of channel capacity according to the variation of the middle points and orientations of antennas. The orientation is defined by ϑ and φ angles, where φ is referred as azimuth and ϑ is referred as zenith in spherical coordinate system.

When finding the best totally free structure for optimal channel capacity the simulations come too little if the analyzed structures are chosen randomly and because most of the structure would be analyzed. Therefore, we had to search a right method for the optimal selection of the structure.

The GA — Genetic Algorithm can not stick in a local extreme not like the other well-known optimization algorithms, but it can find the global minimum or maximum of the composite multivariable function. Alike the terrestrial evolution the GA handles the functional parameters as biological gene. The different input parameters are crossed among the population where the population is defined as a set of all-time actual available input parameters. Just like in biology the survival rate of the strongest candidates has a higher probability furthermore the reproduction of the next generation parameter-set is influenced by mutation of earlier analyzed-selected input-parameters. The variety of the first generation initial input parameter set is guaranteed by initialization of the GA with random values [1, 2].

The scattering environment model which we applied in the simulation was a three dimension (3-D) double bouncing (DB) stochastic scattering channel model with wide angular spread as a basis at both ends. By using this model we wrote down perfectly an unmitigated office-indoor environment [3].

2. CALCULATION METHOD

2.1. Channel Model and Calculation of Channel Capacity

The antenna system is situated in a 3-D scattering environment indoor scenario. The electromagnetic waves launch from the transmitter antennas and the waves in a short time reach scatterer objects which are on a surface of a ball. From here, the waves are reflected toward the second group of scatterers (around receiver antennas) and finally they are reflected to the receiving antennas.

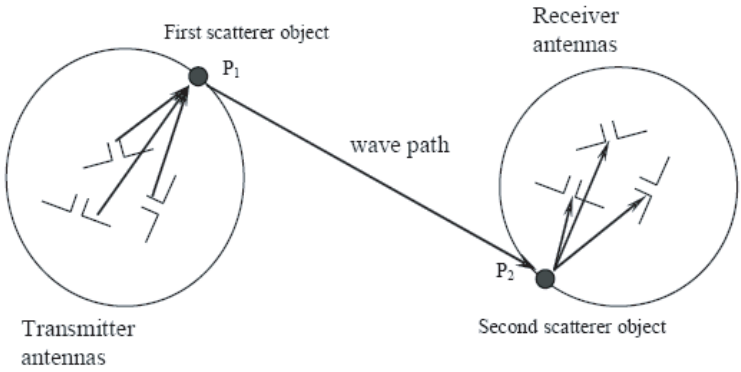

Figure 1: Signal wave path in a scattering environment. Transmitter and receive dipole antennas in a DB scattering environment [3].

The connection between the transmitter and receiver antenna structure is the channel. This MIMO channel is characterized by the transmission matrix (**H**).

The scatterers have a random scattering polarization matrix and they are situated with randomly and uniform distribution on a ball–shape surface around the transmitter and the receiver antennas.

Figure 1 shows the transmitter and the receiver antennas and some of the scatterers around the antennas, and furthermore presents a probable path from the transmitter through the two scatterers — Surfaces to the receiver antennas. Our multiple antenna system is composed of $M_t = 3$ and $N_r = 3$ electric dipoles at both the transmitter and the receiver units. In this way, the transmission channel matrix **H** consists of nine transmission links (3×3) which connect the antennas [3, 4].

2.2. Theoretical Channel Capacity and Normalization

For a MIMO radio channel with channel matrix **H**, the positive eigenvalues were calculated from SVD of HH^{H}. With the assumption of known channel at the transmitter, the theoretical capacity from water filling [6] is given as

$$C = \sum_{i=1}^{r'} \log_2 \left(1 + \lambda_i \mathrm{SNR}_i\right) \tag{1}$$

where λ are the eigen-values of the channel, $\mathrm{SNR}_i = P_t/\sigma^2$ is the individual SNR of the eigenmodes after waterfilling algorithm and r' denotes the number of useful eigenmodes with positive power allocation [6, 7].

In the course of calculation, the channel matrix is normalized with the average path gain Ψ.

$$\Psi^2 = \left\{ 1/m_{tr} \cdot m_{re} \cdot \sum_{i=1}^{m_{tr}} \sum_{j=1}^{m_{re}} \left|H(i,\, j)\right|^2 \right\} \tag{2}$$

where m_{tr} and m_{re} are the number of antennas on the both side. For computing the average path gain, it shall make the expectation value for all random channels [8].

2.3. Calculation of the Effect of Mutual Coupling

At the examination of the effect of mutual coupling, we have to use the modified channel matrix H_{mut}. It is given by

$$H_{mut} = \frac{(C_{tr\_mut} \cdot H \cdot C_{re\_mut})}{C_{re} \cdot C_{tr}} \tag{3}$$

where, C_{re} — Normalizing factors for C_{tr_mut}, C_{tr} — Normalizing factors for C_{re_mut}, C_{re_mut} and C_{tr_mut} — Mutual coupling matrixes on the receiver and transmitter sides [4, 6].

3. SIMULATION RESULTS

3.1. Capacity Maximization for Fix Structure of 3×3 MIMO Antenna System

In earlier publications [7], we presented our simulation just about special fixed antenna structure. In the constellation, the antennas start-points were in the origin all of them parallel with axis Z.

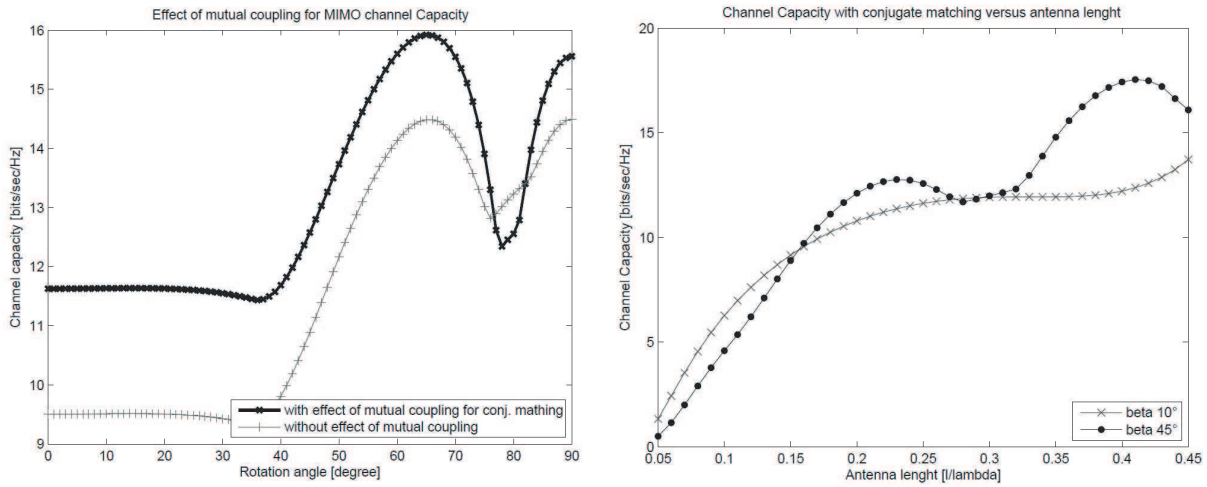

Figure 2: Effect of the mutual coupling for mean capacity versus rotation angle (left) and antenna length (right).

In the simulation, the structure was opened like an umbrella as far as plane X-Y. In the course of opening operation, we looked for the ideal position for the highest channel capacity. We found the optimal position for this antenna structure. We found that in this bound system in the best constellation the angles between antennas and axis-Z is about 60°. It is like the antennas are placed onto three edge of a cube (the angle between the edges of a cube and diagonal of cube is $\text{arctg}\sqrt{2} \cong 54.75°$). In this structure, the antennas are pairwise perpendicular. The Fig. 2 shows the results of the simulation for bound structure [8].

3.2. Full Optimal Antenna Structure Searching by Genetic Algorithm

Genetic algorithm (GA) found the optimal antenna structure in a definite separated place. In these simulation, the transmitter and receiver antennas were located interior of a sphere with $r = 0.5l/\lambda$, where r means the radius of the ball and l/λ is define as the ration of the antenna half-length (l) and wavelength (λ). In the course of simulation, GA changed the orientation and the position of antennas for localization the structure with highest channel capacity.

As a consequence of the simulation, the GA computed several constellations which have resulted the same channel capacity. On the face of it, the results of the simulation presented several different structures. However, after detailed analysis, we have found that these structures are much the same just they are rotated and reflected, however, these transformations do not modify the system and the channel capacity.

We have found that antenna structures which results the maximal channel capacity have two relevant characteristics. First of all, there were appeared the effect of polarisation and spatial diversity: Antennas are pair wise approximately perpendicular; the distance between the antennas

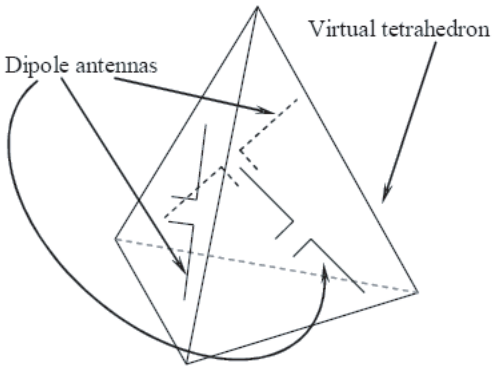

Figure 3: Dipole antenna structure with highest MIMO channel capacity, the antennas are on the faces of a tetrahedron and they are pairwise perpendicular.

middle point is about $\lambda/2$ proven. Secondly, by additional detailed analysis, we have found that the antennas are on the surfaces of a tetrahedron. The tetrahedron analysis method is the following: One of the antenna endpoints with the top vertices of tetrahedron appoint a plane, in this manner, the tree antennas with the top vertices arise three planes which can be written down parametrically. The angles in a tetrahedron between the faces are defined ($\mathrm{arctg}(2\sqrt{2})$). By the parametrical system of equations ,the top of tetrahedron can be calculated for ever two pairs of planes. If the calculated points are coincide with together the antennas on the surface of a tetrahedron. The picture Fig. 3 presents a conceivably tetrahedron-type antenna structure [1, 9, 10].

As compared the earlier and newest simulations, the results point to several speciality. Firstly, in both effects of simulations the antennas are pairwise perpendiculars, confirming the phase diversity theory. Secondly, the antennas are on the highest maximum distance accordingly to the criteria of space diversity.

4. CONCLUSION

In this project, we have been looking for a perfect antenna constellation for maximal channel capacity in a 3×3 MIMO antenna system by applying an optimization algorithm. In this article, we have presented the results of our simulations including GA results. Our GA simulation were effectives and we have found the antenna structure with maximal channel capacity which confirms with the capacity calculation. In this simulation, we have taken account the effect of mutual coupling because the simulated system is a real MIMO channel in which the antennas mutually effect together.

ACKNOWLEDGMENT

This work was carried out in the framework of Mobile Innovation Center, Hungary (Mobil Innovációs Központ) and supported by the Hungarian National Office for Research and Technology in the framework of Oszkár Asbóth program.

REFERENCES

1. Haupt, R. L. and S. E. Haupt, *Practical Genetic Algorithms*, John Wiley nad Sons, New Jersey, USA, 2004.
2. Collin, R. E., *Antennas and Radiowave Propagation*, McGRaw-Hill Book Company, New York, 1985.
3. Getu, B. N. and J. B. Andersen, "The MIMO cube — A compact MIMO antenna," *IEEE Trans. Wireless Commun.*, Vol. 4, No. 3, 1136–1141, May 2005.
4. Getu, B. N. and R. Janaswamy, "The effect of mutual coupling on the capacity of the MIMO cube," *IEEE Antennas and Wireless Propagation Letters*, Vol. 4, 240–244, 2005.
5. Zombory, L. and M. Koltai, *Elektromagneses Terek Gepi Analizise*, Muszaki Konyvkiado, Hungarian, 1979.
6. Chiu, C. Y. and R. D. Murch, "Experimental Results for a MIMO cube," *IEEE Transactions on Antennas and Propagation*, 2006.
7. Janaswamy, R., "Effect of element mutual coupling on the capacity of fixed length linear arrays," *IEEE Antennas and Wireless Propagation Letters*, Vol. 1, 157–160, 2002.
8. Farkasvolgyi, A. and L. Nagy, "Optimization for MIMO antenna system," *Mobile and Wireless Communications Summit, 16th IST*, Jul. 1–5, 2007.

Low Profile Circular Yagi-Uda Array and Planar Collinear Monopole Antenna Comparison

Lajos Nagy, **Andrea Farkasvölgyi**, **and Róbert Dady**
Department of Broadband Infocommunications and Electromagnetic Theory
Budapest University of Technology and Economics
H-1111 Budapest, Goldmann György tér 3, Hungary

Abstract— The paper presents an overview on the development of Circular Yagi-Uda and collinear type of antenna. The genetic algorithm is used to optimize the two antenna architecture. The main goal of the article is a comparison of directivity and bandwith of the two omnidirectional type of antennas. In our analysis, the method of moments (MoM) is used to compute the current distribution and directivity of the yagi antenna. Microstrip technology is used for planar collinear monopole antenna and simulation with ground plane has been performed using Ansoft HFSS 3D simulator. Prototypes have been realized and measured.

1. INTRODUCTION

Growing interest in 802.11b, 802.11g and 802.11a and other applications has precipitated the need for omnidirectional antennas at 2.4–2.5 GHz, 5.15–5.35 GHz and for special applications in the C band. A number of approaches for gained omnidirectional antennas researchers have taken in the past. One of these most promising designs are the collinear dipole arrays built up from half wavelength radiators. The radiators are connected to each others either using transmission lines or directly by insertion of 180 degree phase shift.

One of such solution uses half-wavelength sections of coaxial transmission line which have their inner and outer conductor connections reversed at each junction. This reversal causes the current on the outer conductor of each segment to be in phase and radiate an omnidirectional pattern. This type of antenna is often called coaxial collinear antenna (COCO).

A geometry for a planar microstrip omnidirectional antenna introduced by Bancroft and Bateman is presented [1]. The basic idea is to create alternating sets of 50 Ω microstrip transmission lines. Each section is approximately one-half wavelength long at the frequency of operation. Each groundplane section was initially set to be about 5 times the conductor width of the microstrip transmission line and later optimized for driving point impedance.

The circular Yagi-Uda antenna geometry is started from the linear element antenna and by rotating of the elements we have a low profile omnidirectional antenna. The antenna is optimized by varying the lengths and spacings of the circular elements.

As comparison the radiation pattern, gain, input reflection and bandwidth are compared for the two antennas.

2. DESIGN OF THE PLANAR COLLINEAR MONOPOLE ANTENNA

A geometry for a planar microstrip omnidirectional antenna introduced by Bancroft and Bateman [2] is used for the design.

We also followed the design of [2] and first the simple planar structure was analyzed without ground plane using Ansoft Designer. The planar collinear structure is made of one dielectric layer in form of thin/thick section microstrip line. The figure represents the geometry of the antenna.

The geometry of the structure analyzed is shown on Fig. 1. Dielectric material Rogers RO 4003 has been used with thickness of 1.5 mm.

On the Fig. 2, the simulated current distribution on each side of the planar structure is presented and the effect of shorts also illustrated. The antenna W_1, W_2 and L dimensions are optimized to the working frequency of 4.5 GHz operation.

The simulated results are showing a 14% impedance bandwith and a 4.5 dBi realized gain at the operational frequency. Using the previous results, the collinear antenna with the supplementing ground plane was constructed. At the bottom part of the Fig. 1, planar structure the short plane is placed as can be seen in Fig. 5. With this arrangement, the current distribution change not significant and therefore the modification of microstrip element size change to tune the antenna into the operational frequency will be not to much.

Next the monopole structure suggested will be analyzed using the Ansoft HFSS the 3D modeling software.

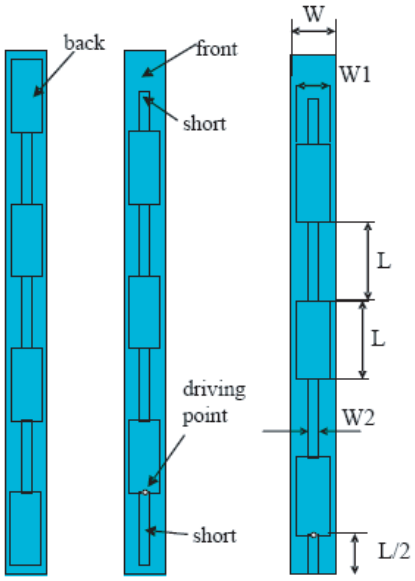

Figure 1: Omnidirectional planar microstrip antenna and main dimensions.

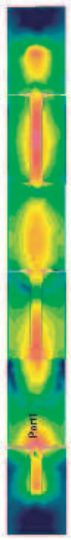

Figure 2: Simulated current distribution on the microstrip elements.

2.1. The Monopole Collinear Antenna

The main parameters and dimensions of the final structure are the following:

The thickness of the dielectric layer is $h = 1.5\,\text{mm}$, the dielectric material Rogers RO 4003, which has the dielectric characteristic: Relative permittivity: 3.38; dielectric loss tangent 0.0027.

The measurements are: $L = 17\,\text{mm}$ $W = 16.7\,\text{mm}$ $W_1 = 11\,\text{mm}$ $W_2 = 2.2\,\text{mm}$

Ground plane size $100 \times 100\,\text{mm}$ with 0.5 mm thickness. The pictures taken from the fabricated antenna are represented on the Fig. 5.

The simulation and optimization of the final structure has been performed using Ansoft HFSS. The vacuum box size for simulation is $x = 140\,\text{mm}$; $y = 140\,\text{mm}$; $z = 200\,\text{mm}$ and the radiation boundary condition was used on its surface. The simulation has been performed on an Intel Centrino Duo bi-processor 1.83 GHz with 1 GB RAM memory, and the simulation takes 30 min for 11 frequency points and 30000 tetrahedras are used.

3. DESIGN OF THE LOW PROFILE CIRCULAR YAGI-UDA ANTENNA

The circular Yagi-Uda antenna geometry is started from the conventional linear element Yagi-Uda antenna geometry and by rotating of the elements we form a low profile omnidirectional antenna. In the center of the rotational symmetric, geometry is placed the driven dipole. Antenna is optimized by varying the lengths and spacings of the circular elements.

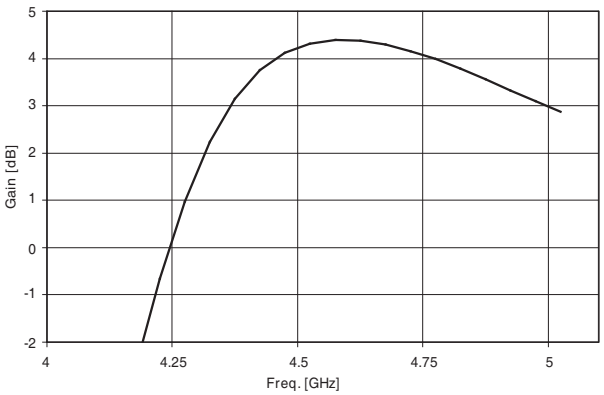

Figure 3: Gain of omnidirectional planar microstrip antenna.

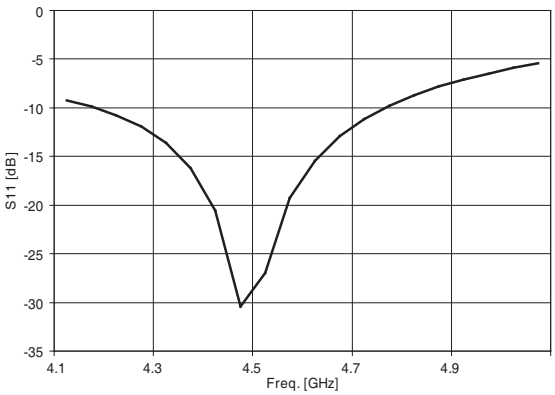

Figure 4: Gain of omnidirectional planar microstrip antenna.

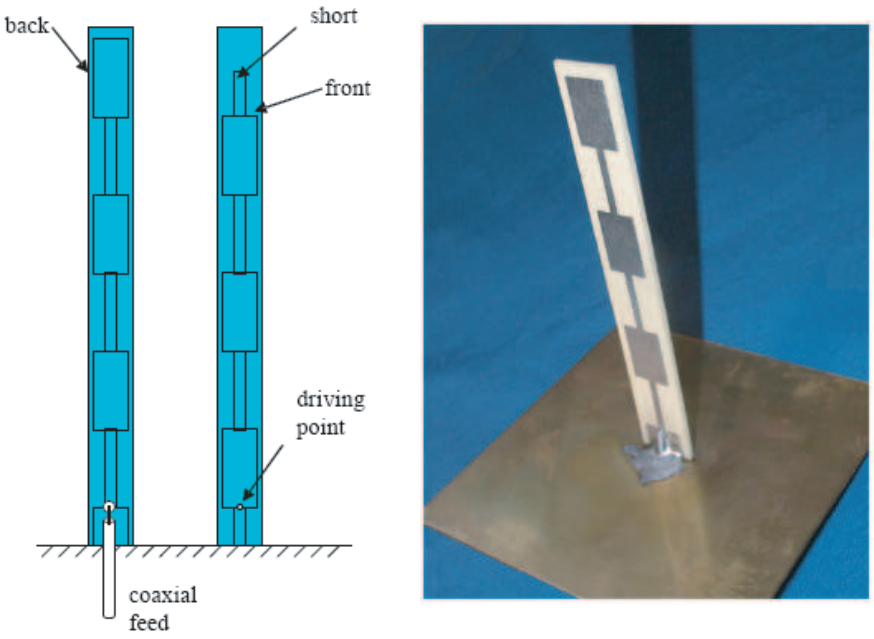

Figure 5: Definition and photo of the planar collinear monopole structure.

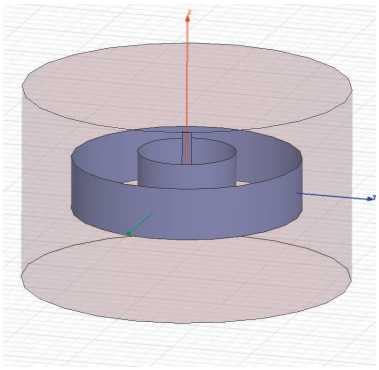

Figure 6: Low profile circular Yagi-Uda antenna (Ansoft HFSS).

Symmetrical geometry has been analyzed and optimized using in house developed Moment Method solver and Genetic Algorithm based optimizer. Finally, an analysis of the circular Yagi-Uda geometry was made using Ansoft HFSS solver.

The Figs. 7 and 8 are showing gain and input impedance bandwidths of the two designed antennas.

Each antenna were optimized to the same 4.5 GHz center frequency. The maximum gain is equal for the two antennas and the circular Yagi-Uda shows a slightly bigger gain bandwidth. Then again the impedance bandwidth of the circular Yagi-Uda antenna is significantly below the collinear one. The relative bandwidths are 6.5% and 13.5% respectively.

4. MEASUREMENT RESULTS

The measurement of the input reflection coefficients has been performed using an anechoic chamber of our department with the size of $4 \times 3 \times 3$ m.

The Fig. 9 presents the measured and simulated input reflection coefficients. The measurement result are showing a small bandwidth increase compared to the simulated one and a slight operational frequency shift which are not significant.

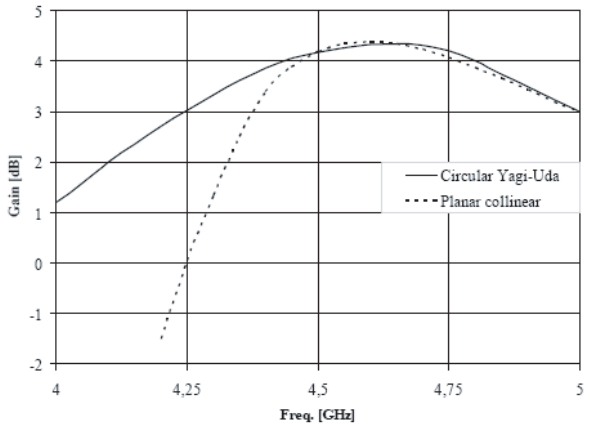

Figure 7: Gain comparison of circular Yagi-Uda vs. collinear antenna.

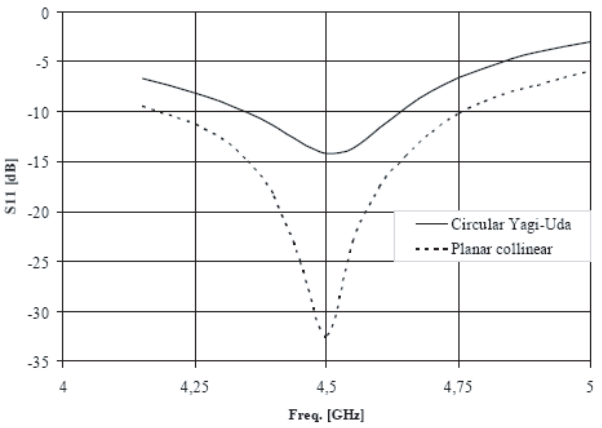

Figure 8: S_{11} comparison of circular Yagi-Uda vs. collinear antenna.

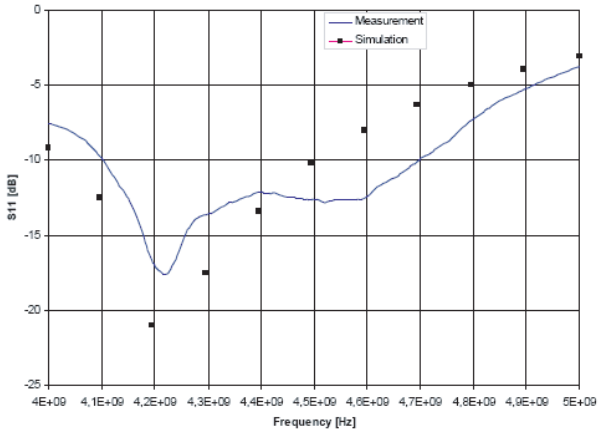

Figure 9: Input reflection of monopole planar collinear antenna.

5. CONCLUSION

Conventional omnidirectional designs are not well suited to operation at microwave frequencies which include the C band. This is due to their geometry or lack of performance. A microstrip omnidirectional antenna has been developed which is a cost effective solution for many applications. We presented simulated and also measured results to verify the behavior of the proposed antenna.

The comparisons on Figs. 7 and 8 are showing that the circular Yagi-Uda antenna consisting of 3 elements has similar antenna gain characteristic as the collinear monopole. Then again the impedance bandwidth of the circular Yagi-Uda antenna is significantly below the collinear one.

ACKNOWLEDGMENT

This work was carried out in the framework of Mobile Innovation Center, Hungary (Mobil Innovációs Központ) supported by the National Office for Research and Technology (NKTH) Asbóth Oszkár Programme.

REFERENCES

1. Judasz, T. J. and B. B. Balsley, "Improved theoretical and experimental models for the coaxial colinear antenna," *IEEE Transactions on Antennas and Propagation*, Vol. 37, No. 3, 289–296, Mar. 1989.
2. Bancroft, R. and B. Bateman, "An omnidirectional planar microstrip antenna," *IEEE Transactions on Antennas and Propagation*, Vol. 52, No. 11, 3151–3154, Nov. 2004.
3. Pozar, D., "Directivity of omnidirectional antennas," *IEEE Antennas and Propagation Magazine (Antenna Designer's Notebook)*, Vol. 35, No. 5, 50–51, Hal Shrank Ed., Oct. 1993.

Testing and Optimizing of 16-element Antenna Array

A. Jeziorski[1], **W. Kolosowski**[1], **P.Gajewski**[1], **E. Sedek**[2], **and Z. Bielecki**[1]

[1]Military University of Technology, Poland
[2]Telecomunication Research Institute, Poland

Abstract— The objective of this study is to test and optimize the design of a 16-element antenna array made up of radiating elements in the form of Tapered Slots Antenna (TSA). Optimization of array construction and results of measurement of radiating characteristic of antenna is presented in the paper. The results from the needs to develop broadband antenna elements suitable for a variety of application in the UWB systems.

1. INTRODUCTION

TSA elements represent now one of the antenna technology areas that develop at the highest rate. This results from the needs to develop broadband antenna elements suitable for a variety of applications on the one hand, and on the other hand from the TSA elements' capacity to meet numerous requirements that are specific to the needs. The aforementioned applications include dynamically developing UWB (Ultra Wide Band) systems and georadars, but also traditional radiolocation and telecommunication systems, a broadening of the antenna bandwidth of which may result in increased data throughput rate and significant improvement of radar system performance. A TSA antenna design should feature a low wave standing coefficient over as wide frequency band as possible, with a symmetrical radiation characteristic retained at minimum side-lobes. A significant requirement was also suitability to transmission operation, i.e., with a high microwave power. Also important were antennas design simplicity and low manufacturing cost.

A traditional tapered slot antenna (initially called the Vivaldi antenna) was developed on a laminate with appropriately etched fields and power supply paths. Authors of this study have developed a number of such antenna's varieties. It was maintained in the published at that time literature that an antenna developed on a dielectric base (a laminate) may not be used as a transmitting antenna meant to radiate large powers. Therefore a concept was devised of a "metal" antenna made up of two slots cut in two parallel metal walls and an activation loop set perpendicular to the slots.

2. APPLICATION OF WIPL-D SOFTWARE IN TSA ELEMENT DESIGNING

Analysis of measurement results has shown that the TSA elements presented on Fig. 1. are the most promising, so it was decided to choose it for multi-element aerial arrays.

The computer model of analysed TSA antenna is presented in Fig. 2. The slot activation loop (a half-loop in fact), supplied from a coaxial line, is opened at its end. Attempts were made at development of a solution with a line closed at its end. This would contribute to the loop's rigidity.

The main factors of antenna performance include the slot's shape, as well as the supply loop's design, size, and position. Therefore the designers focused on solving just this problem. For this purpose a computer analysis was completed using WIPL-D software [4].

For full accomplishment of the adopted objective it was necessary to familiarise with WIPL-D software that would enable computer simulation and selection of the ultimate solution. With the slot shape already determined, development was attempted of a transmitting array that would

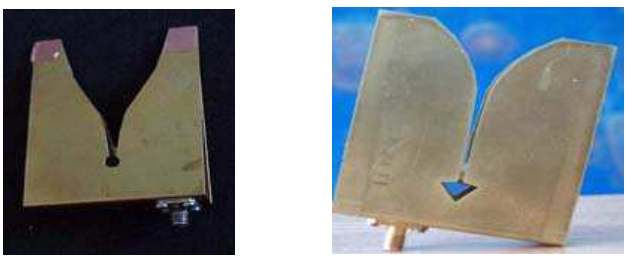

Figure 1: Examples of TSA elements.

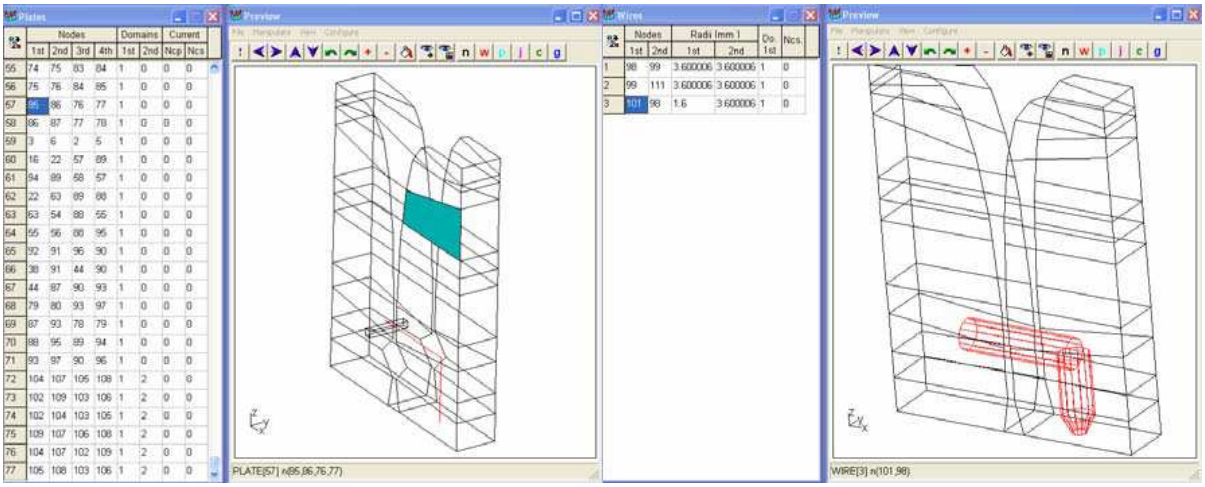

Figure 2: TSA antenna model in WIPL-D.

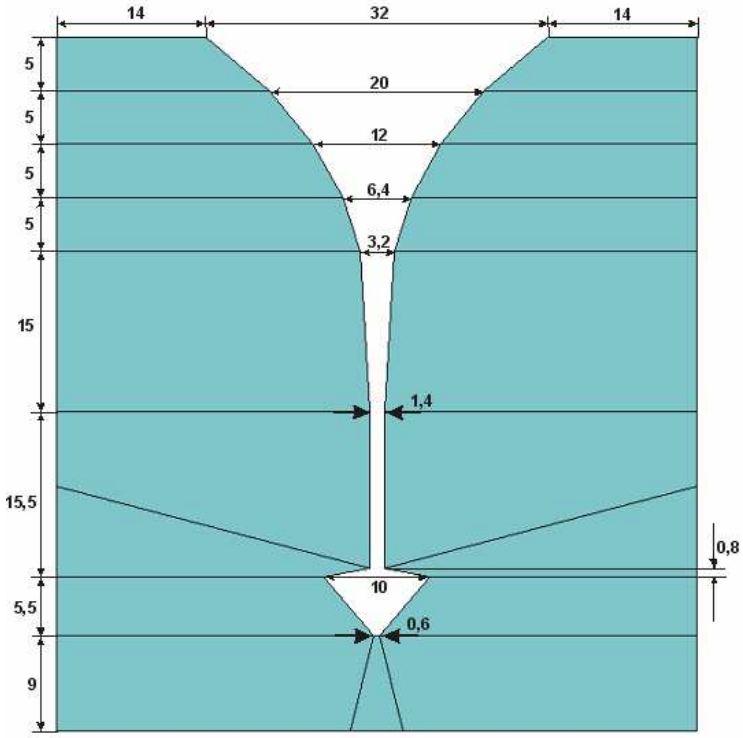

Figure 3: Designed TSA antenna geometry.

by far outperform the earlier designed antenna model with a broad bandwidth at the same time retained. The slot shape and supply line dimensions were calculated using WIPL-D software.

The TSA element was developed in a few stages. First the shape presented on Fig. 3 was cut of 1 mm brass sheet. The applied cutting technology enabled cutting a shape in a dozen or so packs of the sheet stacked one on another. Then openings were drilled for (SMA-type) supply seat, and plates were bent according to the dotted lines shown on the drawing. The last stage involved fixing the seat and loop.

With the slot shape already determined, development was attempted of a transmitting array that would by far outperform the earlier designed antenna model with a broad bandwidth at the same time retained.

The best matching course achieved is presented on Fig. 4. The loop-shape and size have become the designed antenna's geometric specifications.

Figure 4: WFS of TSA antenna supplied from half-wave loop.

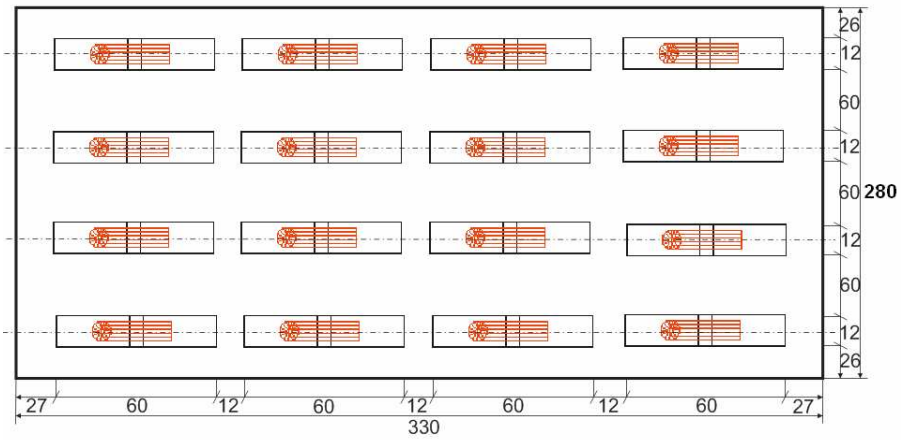

Figure 5: The 4×4 antenna element's layout.

Figure 6: The 4×4 antenna matrix view.

3. MULTI-ELEMENT ANTENNA SYSTEM

The model of antenna with TSA elements so developed is designed for operation in the S-band. The elements' layout is presented on Fig. 5, whereas the view of a ready antenna is presented on Fig. 5. It was decided that at this stage of R&D works the distances between elements would be selected according to traditional criteria, i.e., ca. 0.5λ. Combined with cophasal and equal activation of

individual elements it produced an antenna of performance far away from that required of operable items. The point was to check suitability of the idea of multi-element antenna with TSA radiators.

4. RESULTS OF MULTI-ELEMENT ANTENNA MEASUREMENT

The multi-element antenna's radiation characteristics were measured in the planes of both vectors — E and H, and the results are presented on Fig. 7 and Fig. 8.

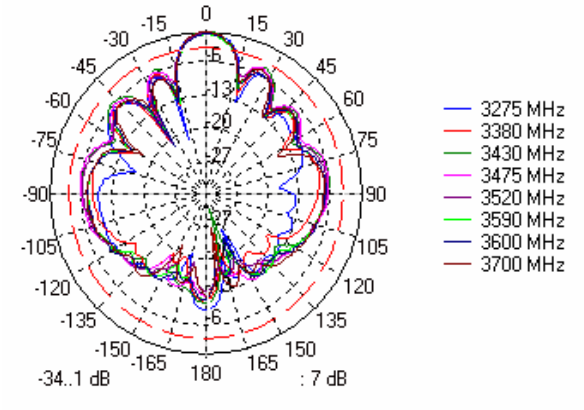

Figure 7: The radiation characteristics measured in E-plane vector.

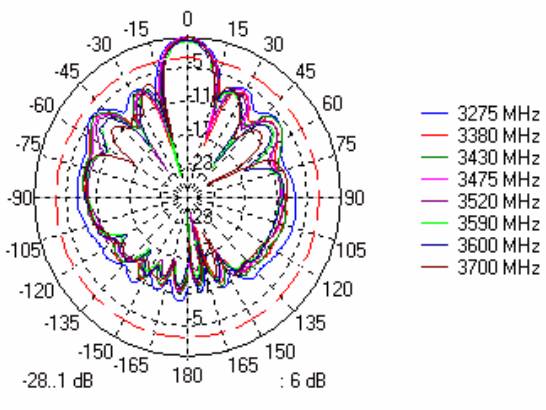

Figure 8: The radiation characteristics measured in H-plane vector.

5. SUMMARY AND CONCLUSIONS

The objective of this study was to design a multi-element antenna using radiating elements in the form of tapered slot elements. Both the individual element and the entire array are innovative solutions that may provide alternatives to the solutions so far applied in the radiolocation engineering.

The basis for simulation and design of the TSA aerial array was analysis of the existing solutions and properties of both narrow slot as well as multi-element antennas. In the next stage following familiarisation with WIPL-D software the TSA antenna design methodology was presented that enabled relatively quick development of even quite complex antenna structures by the software future users. The WIPL-D software was used in the study to present the characteristics of simple arrays made up of TSA antennas. With the aid of the software the designed array's parameters were selected to be subsequently used for building its physical model. The objective of the study, i.e., development and testing of an aerial array suitable for operation in a broad frequency band with symmetrical radiation characteristics and a narrow main lobe, has been fully accomplished, and the study results have justified the claim that the aerial arrays may provide in the future an alternative to the antenna systems used so far in the S-band of frequencies.

Features of the examined elements include the following:

antenna bandwidth at SWR $< 230.45\%$,
antenna bandwidth at SWC $< 1.318.53\%$,
symmetrical radiation characteristic, see Figs. 7 and 8,
fixed radiation characteristic shape throughout bandwidth,
stable input impedance throughout bandwidth,
simple design,
small antenna size,
low manufacturing cost,
damage-proof design.

Subsequent R&D efforts should focus on further performance improvements of both the individual element and arrays made up thereof. Subsequent solutions that would feature even broader bandwidth than those of existing solutions should be sought after with the use of WIPL-D software and modelling the element's slot. Whereas modelling the elements' positioning on-screen and the

screen itself even more directional characteristics should be sought after of the side lobes' lower level. However, the studies so far completed fully confirm growing interest in TSA antennas and their operation in phased aerial arrays and encourage continued works so aimed. These may also provide some interesting material to be used in laboratory exercises as familiarisation with TSA antennas and their advantages compared to the hitherto recognised solutions.

This work may be continued by designing a TSA antenna model of even better performance, a broader bandwidth in particular. Such a new model will have a changed slot shape and size, as well as a better way of slot activation. Based on the performance of the already developed TSA antenna and the algorithm of programming in the WIPL-D environment a design, development, and computer simulation should be possible of a new TSA antenna and an aerial array made up of eight radiating elements. This should result in better radiation characteristics and broader bandwidth than those of the TSA antenna model hereby presented.

REFERENCES

1. Prasad, S. N. and S. Mahapatra, "A new MIC slot-line aerial," *IEEE AP*, Vol. 31, No. 3, May 1983.
2. Janaswamy, R. and D. H. Schaubert, 'Analysis of the tapered slot antenna," *IEEE AP*, Vol. 35, No. 9, September 1987.
3. Kołosowski, W., H. Gruchała, M. Wnuk, and A. Jeziorski, "Antena z rozszerzająca się szczeliną zasilana z linii komplanarnej," *KKRRiT 2003*, Wrocław, 2003.
4. Kołosowski, W., M. Wnuk, and A. Jeziorski, "New construction of tapered slot antennas," *ICAP'2003*, Exeter, 2003.
5. Kołosowski, W., P. Gajewski, A. Jeziorski, and A. Sedek, "The dielectric-free tapered slot antennas array," *EuMW*, Manchester, 2006.
6. Kolundzija, B. M., J. S. Ognjanovic, and T. K. Sakar, "WIPL-D: Electromagnetic modeling of composite metallic and dielectric structures," *Software User's Manual*, Artech House, Boston, London, 2000.

Miniaturized and Multiband Operations of Inset Feed Microstrip Patch Antenna by Using Novel Shape of Defect Ground Structure (DGS) in Wireless Applications

Dalia Nashaat[1], **Hala A. Elsadek**[2], **Esamt Abdallah**[2], **Hadia Elhenawy**[3], **and Magdy Iskander**[1]

[1]Hawaii Center for Advanced Communication, Hawaii, Honolulu, USA
[2]Electronics Research Institute, Giza, Egypt
[3]Faculty of Engineering, Ain Shams University, Cairo, Egypt

Abstract— Microstrip patch antenna (MPA) with inset feed has been studied extensively over the past two decades because of its advantages. However, length of MPA is comparable to half wavelength with single resonant frequency with bandwidth around 2%. Electromagnetic bandgap (EBG) structure as defected ground structure (DGS) is proposed in this paper, so that significant improvement in antenna size reduction and multi-band resonant frequencies operation are achieved. Two novel shapes of DGS are investigated. First, DGS is comparable to the first iteration of a fractal carpet concept. Second one is composed of four arms of a spiral shape. More than 45% reduction in size is achieved in the first shape. While second shape is two cells of spiral-shaped with four arms are used in the design. Simulation results show that more than 50% reduction in size was achieved as well as fives resonant frequencies resulted from the new design. One resonance resulted from the fundamental patch antenna while the other four resulted from each spiral arms. Acceptable E-plane and H-plane radiation patterns and an antenna gain of about 4 dB are achieved. The band-gap characteristics of the DGS are explained by using high frequency structure simulator HFSS®.

1. INTRODUCTION

Microstrip patch antennas have been studied extensively over the past many years because of its low profile, light weight, low cost and easy fabrication. They are extremely compatible for embedded antennas in handheld wireless devices such as cellular phones, pagers etc. These low profile antennas are also useful in aircraft, satellites and missile applications, where size, weight, cost, ease of installation, and aerodynamic profile are strict constraints. Some of the principal advantages of this type of antennas are conformability to planar and non planar surfaces, compatibility with MMIC designs, and mechanically robust flexibility when mounted on rigid surfaces [1]. However, the microstrip patch antennas suffer from a number of disadvantages as patch length is around half wavelength. Many methods are used to reduce size of MPA like using planar inverted F antenna structure (PIFA) [2] or using substrate with high dielectric constant. DGS Method is used for size reduction [3] as well as multi-band operation. DGS for the inset line fed microtrip is one hotspot of microwave circuit design recently [4]. Compared to photonic band-gap (PBG) [5], DGS have gained significant interests as it has flexibility of accepting/rejecting certain frequency bands, and hence it is called electromagnetic band-gap (EBG) structures [6, 7]. DGS is simple and has potentially great applicability in microwave circuit design such as filters, amplifiers and oscillators [8, 9].

In this paper, two novel shapes of DGS cell are investigated, designed and analyzed. The first shape is composed of a first iteration of fractal gasket carpet antenna. It is proposed for antenna size reduction. Second shape is composed of four spiral arms to introduce four resonant frequencies. The validity of the proposed DGS is verified by simulation and measurement. HFSS simulation is used for analyzing these structures. More than 100 simulations were carried out to study the best shape and location of the DGS and achieve optimum coupling between defect and the radiator so as to maximize size reduction.

2. MINIATURIZED DESIGN CONSIDERATION

The miniaturization of microwave planar antenna is an essential issue for integrated transceiver front-ends. In this viewpoint, a novel design method using first iteration of fractal carpet gasket is utilized as DGS cell to study the size miniaturization unit. Figure 1(a) shows schematics of the one cell proposed DGS. The DGS is etched on the back side of the metallic ground plane as shown in Figure 1(b). The substrate is RT/Duroid with 0.813 mm thickness and dielectric constant $\varepsilon_r = 3.38$. The feed line width $w = 1.85$ is chosen for the characteristics impendence of 50 Ω

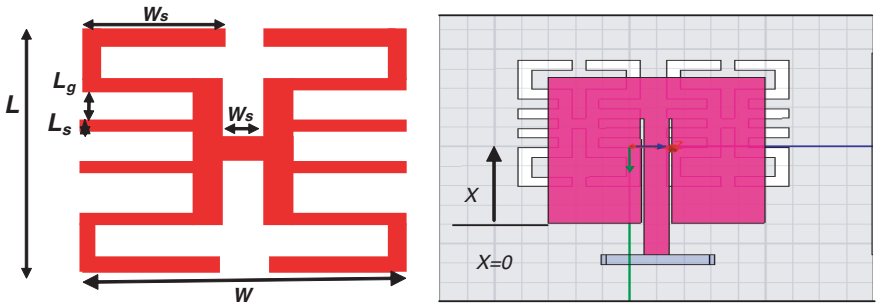

(a) (b)

Figure 1: (a) The geometry of one unit cell of defected ground structure and (b) the proposed antenna prototype.

Table 1: Antenna parameters with changing the displacement X from antenna edge of one unit cell and two unit cells.

X mm	Resonance frequency GHz		Reflection coefficient dB		Bandwidth % MHz		Antenna efficiency		Antenna gain dB	
	One cell	Two cell	One cell	Two cell	One cell	Two cell	One cell	Two cell	One cell	Two cell
0	5.25	5.25	−20	−20	0.12	0.12	0.9427	0.9427	10	8
4	4.2	4.4	−25	−25	0.14	0.14	0.7658	0.8658	8	5
8	3.8	4.25	−33	−33	0.11	0.11	0.42	0.5	2	1
10	2.45	3.25	−20	−20	0.09	0.09	0.411	0.4771	4	3
14	3.6	4.5	−25	−25	0.09	0.09	0.54	0.64	6	5
20	5.2	5.2	−20	−20	0.11	0.11	0.96	0.96	10	7.5

microstrip line at frequency 5.25 GHz. The defect unit is with length 12 mm and width 9 mm, $L_g = 1$ mm, $L_s = 1$ mm, $W_g = 1$ mm and $W_s = 3$ mm. The effect of one as well as two unit cells of DGS on inset feed microstrip patch antenna performance is studied by etching the defect from certain reference point as start at distance $X = 0$ mm as shown in Figure 1(b) and gradually increase X to change the position of DGS with step 2 mm until DGS is faraway from the image projection under the radiating surface. For further reduction two unit cells of proposed DGS are used, which are etched in face to face with separation 3 mm. Table 1 summarizes the variation effect of position of one unit and two unit cell of DGS on the MPA performance. From Table 1 get that the maximum size reduction is 35% in case of one unit cell at defect displacement $X = 10$ mm from antenna edge. While in case of two unit cells the maximum reduction ratio reached 53% at same defect position.

3. MULTIBAND DESIGN CONSIDERATION

Miniaturization of planar microwave antenna is an essential design consideration for integrated and compact transceiver front-ends. In many applications it is also important to design single feed antenna for multiband resonant frequencies. Spiral defect ground structure DGS is used to provide both multi resonant frequencies and compact size. Figure 1(a) shows schematic of the proposed one cell spiral DGS. Spiral structures, however, are known to produce large cross polarization. Therefore to completely eliminate the cross polarization, a four-arm spiral is explored, as shown in Figure 2(a). Four spiral branches, each with a 0.01 $\lambda_{5.2\,\mathrm{GHz}}$ width, split from the center and rotate outwards are used in the design. As it may be seen, this geometry is symmetric not only in $+/-x$ or $+/-y$ directions, but also in x and y directions. As a result, the cross-polarized components are canceled. Moreover each arms of spiral DGS produced resonant frequency according to spiral arm length. A design using one unit cell of the spiral DGS is simulated and as it may be seen in Table 2 the effect of increasing distance X on antenna performance of one cell as well as two unit cell. As distance X increases the resonant frequencies were reduced until certain distance and after that the trend was reversed. Maximum reduction in the fundamental resonant frequency was achieved at distance $X = 9$ mm ($0.16\lambda_{5.2\,\mathrm{GHz}}$) and DGS shifted from width center W_d equal to 3 mm

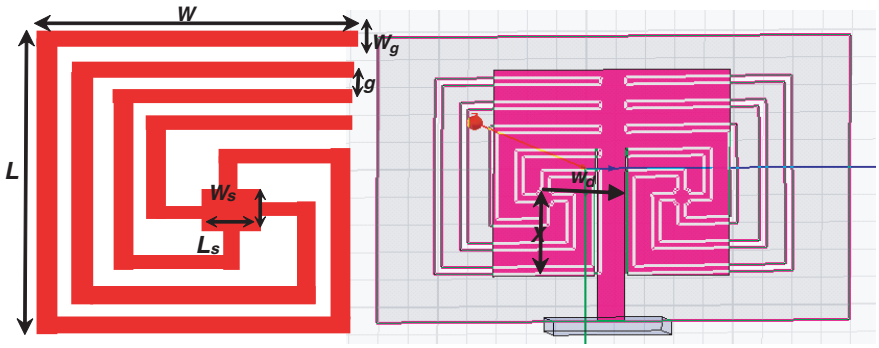

(a) (b)

Figure 2: (a) The geometry of one unit cell of defect ground structure slot, (b) the proposed antenna prototype.

Table 2: Antenna parameters with changing the displacement X from antenna edge of one DGS spiral unit cell and two unit cell.

X mm	Resonance frequency GHz	Bandwidth % MHz		Antenna efficiency		Antenna gain dB	
		One cell	Two cell	One cell	Two cell	One cell	Two cell
0	5.2, 6.5	0.12, 0.11, not matched	0.12, 0.11, not matched	0.93	0.93	10	8.5
2	4.6, 5, 6.5, 7.5	0.14, 0.12, 0.16, 0.13	0.14, 0.12, 0.16, 0.13	0.85	0.80	8	7
4	3.5, 4.5, 6, 7	0.11, 0.12, 0.15, 0.12	0.11, 0.12, 0.15, 0.12	0.55	0.50	0.6	1
8	3.2, 3.8, 4.5, 4.9	0.09, 0.12, 0.15, 0.12	0.09, 0.12, 0.15, 0.12	0.43	0.40	4	3.5
10	3, 4, 4.8, 5	0.09, 0.12, 0.16, 0.13	0.09, 0.12, 0.16, 0.13	0.64	0.55	3	6
20	5.2, 6.4	0.11, 0.14, not matched	0.11, 0.14, not matched	0.95	0.9	9	8

($0.083\lambda_{5.2\,\mathrm{GHz}}$). More reduction in resonant frequency was achieved by using two unit cells of spiral DGS which are placed face to face and at a separation distance from center to center is $2W_d$ equal to 10 mm ($0.18\lambda_0$) with separation W_g equal to 3 mm ($0.054\lambda_{5.2\,\mathrm{GHz}}$). We use same previous substrate and antenna dimensions are $15 \times 16\,\mathrm{mm}^2$ and DGS is etched in the bottom of the metallic ground plane as in Figure 2(b). DGS is etched in the bottom of the metallic ground plane and indicated by dashed line. The dimension of the defect is the largest arms length $L = 13.25$ mm and largest width $W = 11.25$ mm, air-gap $g = 0.5$ mm and $L_g = 2$ mm with spacing patch $L_s = W_s = 1$ mm with 0.5 mm inner square is used in the design. The line width $w = 1.85$ is chosen for the characteristics impendence of 50 Ω microstrip line at frequency 5.25 GHz. From Table 2, it is noted each spiral arm produces resonance frequency according to arm length. The fundamental MPA resonance frequency is reduced by using one unit cell DGS which shifted from length center by $0.011\lambda_0$. In case of using two unit cells, maximum reduction in resonant frequency occurred when the cells are face to face and centered under radiating plate but far from width center by $0.05\lambda_0$.

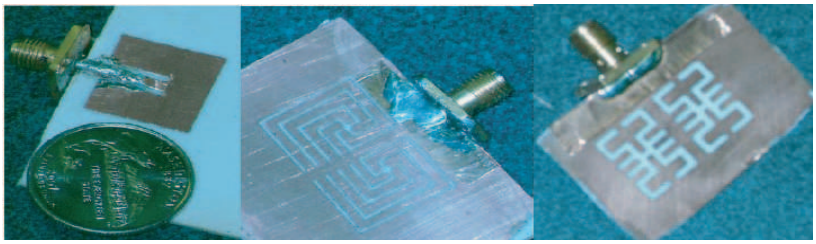

Figure 3: Photo of the fabricated two proposed antennas.

4. MINIATURIZED AND MULTI-BAND SIMULATION AND MEASUREMENT

As discussed in Sections 2 and 3, we used two unit cells of fractal carpet shaped and spiral shaped face to face to obtain optimum reduction and multi-band performance, respectively. The final two proposed antenna configurations were fabricated as shown in Figure 3 by using the photolithographic techniques at Electrical Physical Lab in Hawaii center for advanced communication (HCAC). The measurement of reflection coefficient and radiation pattern is done by using E8364A vector network analyzer and antenna echoic chamber for radiation pattern measurements The reduction in antenna resonant frequency is due to increase in both electrical and magnetic coupling from ground to radiating antenna plate. First proposed antenna was fabricated then the comparison between measured and simulated results is shown in Figure 4. second proposed antenna was fabricated also and the multi-band and reduced antenna size antenna was achieved and the comparison between simulation and measurement of reflection coefficient is shown in Figure 5. Figure 6 is the comparison between simulated and measured radiation pattern (E-plane and H-plane) for the first shape antenna at lowest frequency 2.5 GHz. Figure 7 shows the comparison between simulated and measured radiation pattern (E-pane and H-plane) for second antenna at three different frequencies; 2.5 GHz, 3.8 GHz, and 5.25 GHz.

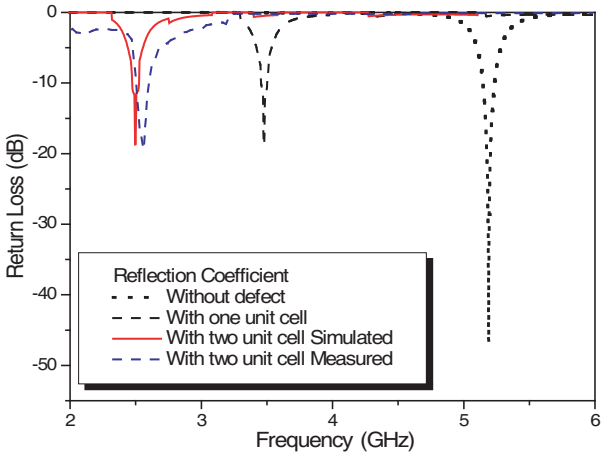

Figure 4: The reflection coefficient comparison between antenna without and with one and two gasket carpet like unit cells simulated and measured.

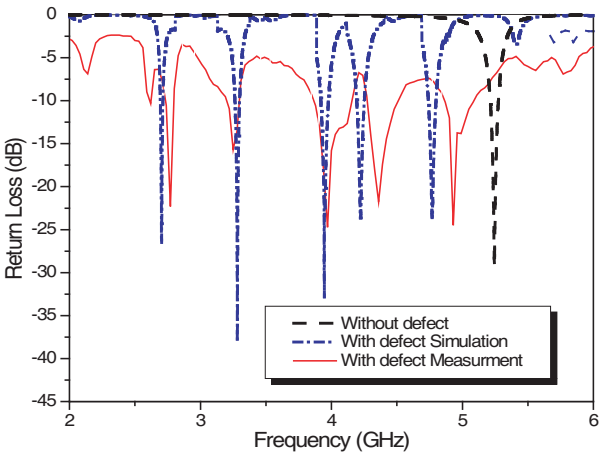

Figure 5: The reflection coefficient comparison between without and with two unit cell of spiral DGS simulated and measured.

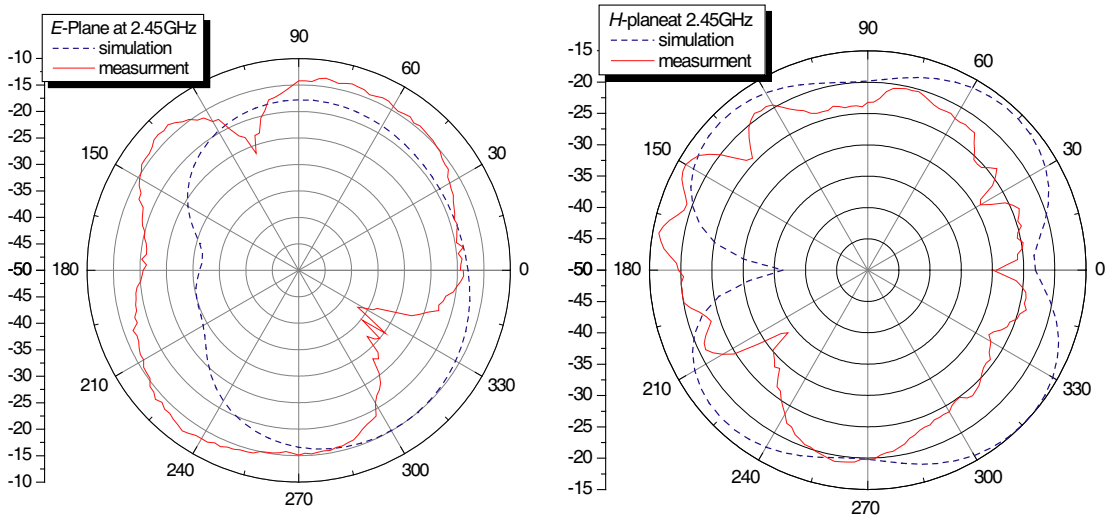

Figure 6: Comparison between measurement and simulation of the radiation pattern E-plane and H-plane at 2.45 GHz.

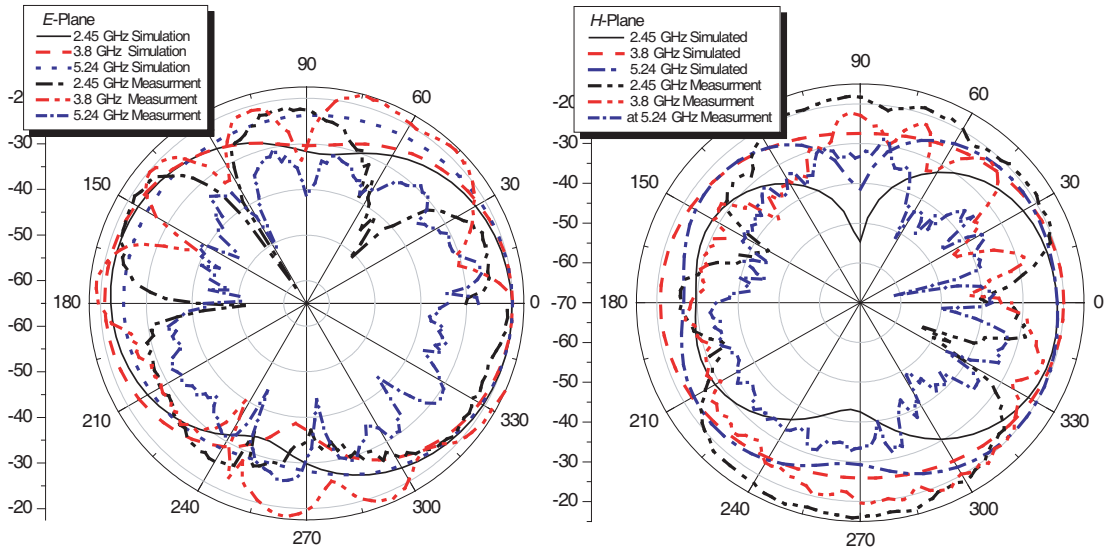

Figure 7: Comparison between measurement and simulation of the radiation pattern E-plane and H-plane at 2.45, 3.8, and 5.24 GHz.

5. CONCLUSION

A novel DGS shapes for inset feed microstrip patch antenna are designed, analyzed and fabricated on ground plane of microstrip patch antenna. Simulation by using HFSS and measurements confirm the validity of designs. The effect of DGS on antenna performance is reduced resonance frequency from wireless band 5.25 GHz to Bluetooth band 2.45 GHz at the first proposed antenna. Generating multi resonant frequencies and reducing in fundamental resonant frequency is achieved by using spiral DGS with four arms. The fundamental resonance reduced from 5.25 GHz to Bluetooth band 2.45 GHz with average bandwidth of around 3%. The optimum position of DGS is at displacement $X = 0.011\lambda_o$ from antenna center length and 0.05 λ_o from antenna center width in both cases. There is a very good agreement between the simulation and the measurement results. The proposed antennas have acceptable radiation pattern and antenna gain around 4.5 dBi.

REFERENCES

1. Balanis, C. A., *Antenna Theory: Analysis and Design*, 3rd Edition, John Wiley & Sons, 1997.
2. Nashaat, D., H. Elsadek, and H. Ghali, "Multiband miniaturized PIFA for compact wireless communication applications," *Microwave and Optical Technology Letters*, Vol. 42, No. 3, 230–235, August 2004.
3. Lim, J. S., C. S. Kim, Y. T. Lee, D. Ahn, and S. Nam, "Design of lowpass filters using defected ground structure and compensated microstrip line," *Electronics Letters*, Vol. 38, 1357–1358, 2002.
4. KIM, C. S., J. S. Park, A. Ahn, et al., "A novel 1-D periodic defected ground structure for planar circuits," *IEEE Microwave and Guided Wave Letters*, Vol. 10, 131–133, 2000.
5. Fu, Y. Q., N. C. Yuan, and G. H. Zhang, "A novel fractal microstrip PBG structure," *Microwave and Optical Technology Letters*, Vol. 32, 316–318, 2002.
6. Mandal, M. K. and S. Sanyal, "A novel defected ground structure for planar circuits," *IEEE Microwave and Wireless Components Letters*, Vol. 16, No. 2, 93–95, February 2006.
7. Liu, H., Z. Li, and X. Sun, "Compact defected ground structure in microstrip technology," *Electronics Letters*, Vol. 41, No. 3, February 2005.
8. Chung, Y., S.-S. Jeon, S. Kim, D. Ahn, and J.-I. Choi, "Multifunctional microstrip transmission lines integrated with defected ground structure for RF front-end application," *IEEE Transactions on Microwave Theory and Techniques*, Vol. 52, No. 5, 1425–1432, May 2004.
9. Isik, O., Y. Ge, and K. P. Esselle, "Novel spiral EBG structures," *Proc. 12th Int. Symposium on Antenna Technology and Applied Electromagnetics (ANTEM)*, Montreal, Canada, 561–564, July 2006.

Annular Ring Microstrip Patch Antenna on a Double Dielectric Anisotropic Substrate

C. F. L. Vasconcelos[1], **S. G. Silva**[1], **M. R. M. L. Albuquerque**[1], **J. R. S. Oliveira**[2], **and A. G. d'Assunção**[1]

[1]Universidade Federal do Rio Grande do Norte (UFRN), 59078-970 Natal, RN, Brazil
[2]Centro Federal de Educação Tecnológica do Rio Grande do Norte (CEFET-RN) 59015-000 Natal, RN, Brazil

Abstract— This paper presents a full-wave analysis of microstrip antennas with annular ring patches printed on double dielectric anisotropic substrates. The problem is formulated in Hankel transform domain. Green's functions are determined by application of Hertz vector potentials formulation. Galerkin's method and Parseval's theorem are used to obtain the resonant frequencies. Numerical results are presented and discussed for the resonant frequencies and radiation patterns.

1. INTRODUCTION

There are many commercial applications such as mobile radio and wireless communications that use patch antennas. The interest in designing of such microstrip antenna has increased because of light weight, easy production, conformability, and so forth. In this class of antennas, the annular-ring microstrip antennas exhibit interesting features associated with the annular ring patch. For a given frequency, these antennas, when operating in the fundamental mode, have smaller size as compared to the rectangular or circular patch antennas [1–4]. This characteristic allows the antenna elements in array designs to be more compacted, favoring the flexibility and the miniaturization of the antenna arrays. The small size is an important requirement for portable communication equipment, such as global positioning satellite (GPS) receivers. Moreover, when compared to the circular patch antenna, the annular ring microstrip antenna has less stored energy and larger bandwidth [5–9].

Much of the previous work on annular-ring microstrip antenna has been devoted to antennas on isotropic substrates. However, many materials used in microstrip structures have some degree of natural anisotropy, or unintended anisotropy due to material processing. These materials provide flexibility and accurate in integrated circuit design and can be used to overcome patch antennas limitations imposed by the dielectric substrates [1, 4].

It is the aim of this work to perform an accurate and efficient analysis of annular-ring microstrip antennas on double uniaxial anisotropic substrates, as well as to perform the analyses for annular ring microstrip antennas on a single layer substrate and on a suspended substrate, as particular cases. The analysis uses the full-wave formulation by means of the Hertz vector potentials method in the Hankel transform domain. The dyadic Green function and Galerkin's method are used to determine the resonant frequencies and radiation patterns [3].

The analysis for suspended annular ring microstrip antenna shows that various parameters of the annular ring patch antenna depend on the thickness of the air gap between the anisotropic substrate and the ground plane. Instead of controlling the resonance frequency by changing the radii of annular ring patch, it is also possible to adjust the antenna resonant frequency by varying the height of the air layer thickness.

2. THEORY

The geometry under consideration is shown in Figure 1. The antenna substrate consists of two anisotropic dielectric layers (regions 2 and 3) having permittivity $\vec{\vec{\varepsilon}}_i (i = 2, 3)$ and permeability μ_0 with optical axis normal to the patch. Region 1 is air-filled with permittivity ε_0 and permeability μ_0. The annular ring patch has inner radius r_1 and outer radius r_2.

Starting from the Maxwell's equations in source-free region characterized by $\mu = \mu_0$ and uniaxial anisotropic substrate with the optical axis along the z-direction, the electric permittivity tensor is given as [3]:

$$\vec{\vec{\varepsilon}} = \varepsilon_0 \begin{bmatrix} \varepsilon_{\rho\rho i} & 0 & 0 \\ 0 & \varepsilon_{\phi\phi i} & 0 \\ 0 & 0 & \varepsilon_{zzi} \end{bmatrix} \tag{1}$$

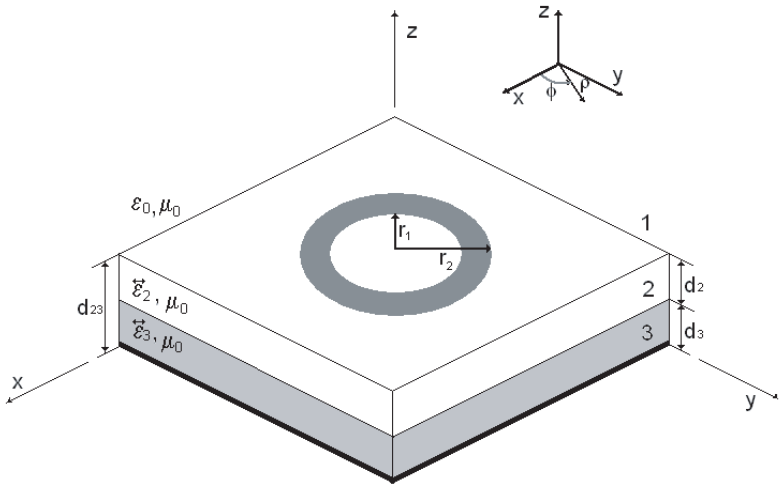

Figure 1: Annular ring microstrip patch antenna on double dielectric anisotropic substrate.

where ε_{zzi} is the permittivity component along the optical axis, and $\varepsilon_{\rho\rho i} = \varepsilon_{\phi\phi i}$ are perpendicular to it $(i = 2, 3)$.

The Hertz vector potentials are expressed as follows [2, 3]:

$$\vec{\pi}_e = \pi_{ei}\vec{a}_z, \quad \vec{\pi}_h = \pi_{hi}\vec{a}_z. \tag{2}$$

The fields are assumed to have harmonic time dependence of the type $\exp(j\omega t)$ and are derived from Maxwell's equations, in terms of the electric $(\vec{\pi}_e)$ and magnetic $(\vec{\pi}_h)$ Hertz vector potentials oriented in the z-direction [5]. The electric and magnetic fields are given as:

$$\vec{E} = -j\omega\mu_0 \nabla \times \vec{\pi}_{hi} + \omega^2 \mu_0 \varepsilon_0 \vec{\pi}_{ei} + \frac{\varepsilon_0}{\varepsilon_{\rho\rho i}} \nabla \left(\nabla \cdot \vec{\pi}_{ei} \right) \tag{3}$$

$$\vec{H} = j\omega\varepsilon_0 \nabla \times \vec{\pi}_{ei} + \nabla \left(\nabla \cdot \vec{\pi}_{hi} \right) - \nabla^2 \vec{\pi}_{hi} \tag{4}$$

The Hertz vector potentials should satisfy the following wave equations for TE and TM modes:

$$\nabla^2 \pi_{ei} + k_{ei}^2 \pi_{ei} + \left(\frac{\varepsilon_{zzi} - \varepsilon_{\rho\rho i}}{\varepsilon_{\rho\rho i}} \right) \frac{\partial^2 \pi_{ei}}{\partial z^2} = 0 \tag{5}$$

$$\nabla^2 \pi_{hi} + k_{hi}^2 \pi_{hi} = 0 \tag{6}$$

$$\text{with} \qquad k_{ei} = \omega\sqrt{\mu_0 \varepsilon_0 \varepsilon_{zzi}}, \quad k_{hi} = \omega\sqrt{\mu_0 \varepsilon_0 \varepsilon_{\rho\rho i}}. \tag{7}$$

It is useful to point out that if $\varepsilon_{\rho\rho i} = \varepsilon_{\phi\phi i} = \varepsilon_{zzi} = 1$, the wave equations in the air region can be easily obtained under the condition that the field components vanish at infinity.

Considering the antenna structure symmetry, Hertz potentials π_{ei} and π_{hi} can be written as [3, 6]:

$$\pi_{e,hi}(\rho, \phi, z) = e^{jn\phi} \int_0^\infty \tilde{\pi}_{e,hi}(\alpha, z)\ J_n(\alpha\rho)\, \alpha d\alpha, \tag{8}$$

where $\tilde{\pi}_{e,hi}(\alpha, z)$ are the Hankel transform of $\pi_{e,hi}$ and $J_n(\alpha\rho)$ is the Bessel function of first kind and order n.

On the conducting patch plane, $z = d_{23}$ (Figure 1), by imposing the boundary conditions, the transformed electric field components are written as functions of the transformed current density components allowing the determination of the impedance matrix, in the Hankel domain. The matrix equation is taken in the form [4, 6]:

$$\begin{bmatrix} \tilde{E}_x \\ \tilde{E}_z \end{bmatrix} = \begin{bmatrix} \tilde{Z}_{11} & \tilde{Z}_{12} \\ \tilde{Z}_{21} & \tilde{Z}_{22} \end{bmatrix} \begin{bmatrix} \tilde{J}_x \\ \tilde{J}_z \end{bmatrix}, \tag{9}$$

Following, Parseval's theorem and Galerkin's method are used to obtain the determinantal equation that enables the numerical calculation of the resonant frequencies.

3. RESULTS

Results for suspended annular ring microstrip antenna on sapphire substrate are shown in Figures 2 and 3. The anisotropic substrate is separated from the ground plane by an air-filled layer ($\varepsilon_{r3} = 1$). Figure 2 shows the resonant frequency against the air gap thickness for various inner and outer radii of the annular ring patch. It is seen that the operating frequency increases with the air layer thickness for a given value of patch size, however, it depends inversely on the patch size for a given air gap width d_3. Radiation pattern for E_θ field component is shown in Figure 3 for different values of the air gap thickness. It is verified that an increase in the air gap thickness improves the directivity of the antenna.

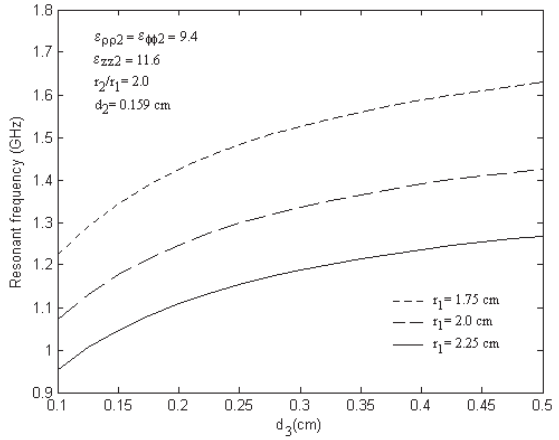

Figure 2: Resonant frequency versus air gap thickness for different values of patch radius.

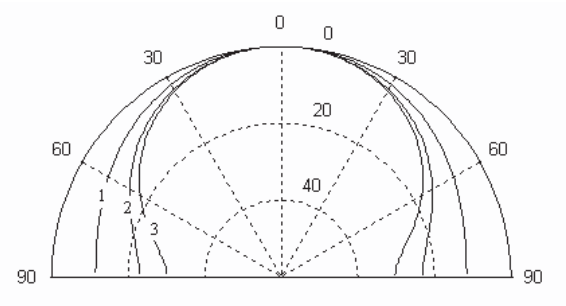

Figure 3: Radiation pattern (E_θ) versus air gap thickness: (1) $d_3 = 0.1$ cm, (2) $d_3 = 0.3$ cm, and (3) $d_3 = 0.5$ cm.

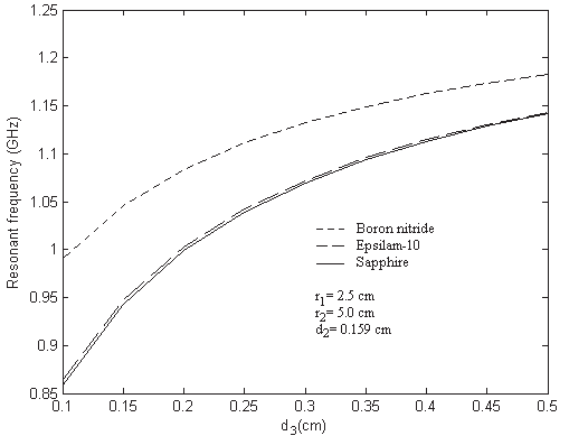

Figure 4: Resonant frequency versus air gap thickness for different anisotropic dielectric substrates.

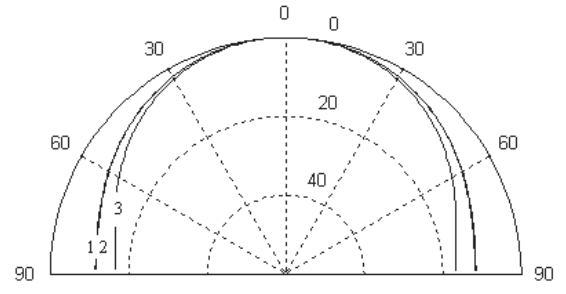

Figure 5: Radiation pattern (E_θ) for different anisotropic dielectric substrates.

Figure 4 depicts the influence of the air gap thickness on the resonant frequency of an annular ring microstrip patch for three anisotropic dielectric substrates: boron nitride ($\varepsilon_{zz2} = 3.4$, $\varepsilon_{\rho\rho 2} = \varepsilon_{\phi\phi 2} = 5.12$), epsilam-10 ($\varepsilon_{zz2} = 10.3$, $\varepsilon_{\rho\rho 2} = \varepsilon_{\phi\phi 2} = 13$), and sapphire ($\varepsilon_{zz2} = 11.6$, $\varepsilon_{\rho\rho 2} = \varepsilon_{\phi\phi 2} = 9.4$). The substrate has thickness $d_2 = 0.159$ cm and the air gap width is varied from 0.1 cm to 0.5 cm. As it can be seen, the resonant frequency reduces considerably when the dielectric substrate changes from boron nitride to epsilam-10, and this is in contrast to what happens when the medium changes from epsilam-10 to sapphire. Also it is observed that the resonant frequency increases with the air gap thickness. The corresponding radiation pattern for E_θ field is shown in Figure 5. It is observed

that when the annular ring patch is supported by boron nitride substrate, the antenna exhibits an increase in its directivity.

Figure 6 shows results of the resonant frequency against the anisotropy ratio $\left(n_\rho/n_z = (\varepsilon_{\rho\rho 2}/\varepsilon_{zz2})^{1/2}\right)$ for an annular ring microstrip patch printed on single anisotropic layer. The results are obtained for a fixed value of $\varepsilon_{\rho\rho 2}$, while the parameter ε_{zz2} varies. Results for an isotropic substrate are chosen by setting $n_\rho/n_z = 1$. It can be noted that the resonant frequency increases with the anisotropy ratio. Also, it is also seen that the resonant frequency shifts to a higher frequency as the $\varepsilon_{\rho\rho 2}$ parameter value decreases.

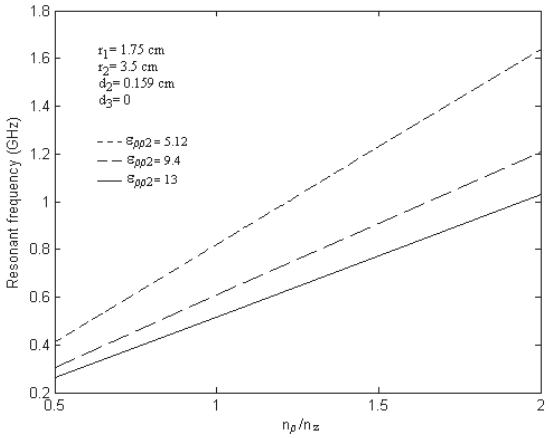

Figure 6: Resonant frequency versus anisotropy ratio n_ρ/n_z for different $\varepsilon_{\rho\rho 2}$.

4. CONCLUSIONS

This paper has described an analysis of the behavior of the annular ring microstrip antenna supported by anisotropic dielectric material. Results have been presented for resonant frequencies and radiation patterns. Our simulations agree well with those presented in [6] and [7]. It is shown that anisotropy plays an important role in the designing of microstrip antennas and cannot be neglected. It is also found that the resonant frequency of the suspended annular ring microstrip patch antenna can be tuned by controlling the air gap thickness variation.

ACKNOWLEDGMENT

We thank the Brazilian Research Agencies CNPq and CAPES for partial financial support.

REFERENCES

1. Garg, R., P. Bhartia, I. Bahl, and A. Ittipiboon, *Microstrip Antenna Design Handbook*, Artech House, Boston, 2001.
2. Nelson, R. M., D. A. Rogers, and A. G. d'Assunção, "Resonant frequency of a rectangular microstrip patch on several uniaxial layers," *IEEE Trans. on Antennas and Propagation*, Vol. 38, 973–981, 1990.
3. Vasconcelos, C. F. L., S. G. Silva, M. R. M. L. Albuquerque, J. R. S. Oliveira, and A. G. d'Assunção, "Annular ring microstrip antennas for millimeter wave applications," *International Journal of Infrared Millimeter Waves*, Vol. 28, 821–829, 2007.
4. Araki, K. and T. Itoh, "Hankel transform domain analysis of open circular microstrip radiating structures," *IEEE Trans. on Antennas and Propagation*, Vol. 29, 84–89, 1981.
5. Sabri, H. and Z. Atlasbaf, "Two novel compact triple-band microstrip annular-ring slot antenna for PCS-1900 and WLAN applications," *Progress In Electromagnetics Research Letters*, Vol. 5, 87–98, 2008.
6. Fan, Z. and J. Huang, "Hankel transform domain analysis of an annular ring microstrip antennas with air gap," *Proceedings International Conference on Computation in Electromagnetics*, 312–314, London, UK, November 1991.

7. Ribeiro, J. M., J. P. Damiano, and R. Staraj, "Accurate analysis and synthesis of annular ring microstrip antennas," *IEE Proceedings: Microwaves, Antennas and Propagation*, Vol. 144, 341–346, 1997.
8. Slim, C. S., J.-S. Row, and K.-W. Lin, "Design of an annular-ring microstrip antenna for circular polarization," *Microwave Optical Technology Letters*, Vol. 42, 156–157, 2004.
9. Bao, X. L., and M. J. Ammann, "Compact concentric annular-ring patch antenna for triple-frequency operation," *Electronics Letters*, Vol. 42, 1129–1130, 2006.

Effect of Exposure to Static, High Voltage Electric Field Generated Nearby HVDC Transmission Lines on Antioxidant Activity of Hepatocytes in Rats

G. Cieslar[1], J. Fiolka[2], J. Mrowiec[1], P. Sowa[3], S. Kasperczyk[2], E. Birkner[2], and A. Sieron[1]

[1]Department and Clinic of Internal Diseases, Angiology and Physical Medicine
Silesian Medical University, Poland
[2]Department of Biochemistry, Silesian Medical University, Poland
[3]Institute of Power System and Control, Silesian University of Technology, Poland

Abstract— The effect of long-term, whole-body exposure to strong, static electric field generated usually nearby high voltage direct current (HVDC) transmission lines on activity of some antioxidant enzymes in homogenats of liver tissue of rats was investigated in this study. Experimental material consisted of 64 male Wistar albino rats aged 8 weeks, weighting 180–200 g. During the whole experiment all animals were placed in identical environmental conditions under a 12 h light-dark cycle with free access to standard laboratory pellet food and tap water. All animals were randomly divided into 2 groups (32 animals each). The rats from experimental group were exposed for 56 consecutive days (8 hours daily) to static electric field with electric field intensity values of 25 kV/m (usually measured nearby actually existing HVDC transmission lines), in a specially designed experimental system. The control animals were subjected to a sham-exposure in the same experimental system, during which no electric field was generated between electrodes. At 14th, 28th and 56th day of exposure cycle and then in 28th day after the end of exposure cycle a part of animals from all groups (8 rats at a same time) was exsanguinated in Morbital narcosis. Then in homogenats prepared from obtained liver samples the activity of some antioxidant enzymes as catalase, glutathione S transferase, glutathione peroxidase, glutathione reductase and superoxide dismutase was determined with use of spectrophotometric methods as well as the concentration of malone dialdehyde (marker of intensity of oxidative processes in tissues) was estimated. As a result of repeated exposures in experimental electric field-exposed group of rats a significant increase in activity of glutathione peroxidase and glutathione reductase at 56th day of exposure cycle, a significant decrease in superoxide dysmutase activity at 14th day of exposure cycle as well as no statistically significant changes in activity of catalase and glutathione S-transferase both during and after the end of exposure cycle were observed. Moreover in experimental group of rats a significant decrease in malone dialdehyde concentration in homogenats of liver tissue at 28th day after the end of exposure cycle as compared to control rats was observed. On the basis of obtained results it was concluded that strong static electric fields with parameters generated usually nearby high voltage direct current transmission lines does not cause any persistent unfavorable effect on antioxidant reactions in the liver of rodents. These data indicate that proper construction of high voltage direct current transmission lines enables to avoid serious health hazards for human population related to disturbances of antioxidant processes in living organisms.

1. INTRODUCTION

Some experimental data indicate that strong electromagnetic fields generated nearby electric field transmission lines can produce an increased amount of reactive oxygen species in tissues, resulting in stimulation of peroxidation of membrane lipids leading to apoptosis and death of cells [1, 2]. As in our previous experiment [3] we found that strong, static electric field with parameters higher than these allowed by actual legislative regulations in construction of high voltage direct current transmission lines causes transcient inhibition of antioxidant enzymes activity in erythrocytes with subsequent adaptative stimulation of this activity after the end of exposure cycle, the aim of the present study was to estimate the influence of long-term, whole-body exposure to static electric field with parameters usually generated by actually existing transmission lines on activity of some antioxidant enzymes and concentration of malondialdehyde (a marker of intensity of pathological oxidative processes in living organism) in liver homogenats of rats.

2. MATERIAL AND METHODS

Experimental material consisted of 96 male Wistar albino rats aged 8 weeks, weighting 180–200 g. During the whole experiment all animals were placed in identical environmental conditions (constant

temperature $22 \pm 1°C$ and humidity of air) under a 12 h light-dark cycle with free access to standard laboratory pellet food and tap water. All animals were randomly divided into 3 groups (32 animals each) with no significant differences in body weight.

The animals from 2 experimental groups were exposed for 56 consecutive days (8 hours daily) to static electric field with different electric field intensity values in a specially designed experimental system consisting of autotransformer, high voltage transformer 220 V/60000 V, cascade rectifier, water rheostat, 2 electrodes with round shape and specially profiled edges placed in a distance of 50 cm from each other, plastic cage placed between both electrodes containing 8 animals at a same time and magnetostatic kilo-voltmeter C196 type.

Rats from experimental group were exposed to static electric field with intensity of 25 kV/m usually measured nearby high voltage direct current (HVDC) transmission lines. The control animals were subjected to sham-exposure in the same experimental system, during which no electric field was generated between electrodes.

At 14th, 28th and 56th day of exposure cycle and then at 28th day after the end of exposure cycle a part of animals from both groups (8 rats at a same time) was exsanguinated in Morbital narcosis. Then in liver homogenats prepared from obtained liver samples the activity of some antioxidant enzymes as glutathione peroxidase, glutathione reductase, superoxide dismutase, glutathione S transferase and catalase was determined with use of spectrophotometric methods [4–6], as well as the concentration of malondialdehyde was estimated according to Ohkawa et al. [7].

3. RESULTS

The results of measurements of activity of particular antioxidant enzymes as well as concentration of malone dialdehyde in homogenats of liver tissue in both groups of rats are presented in Figures 1–6.

As a result of repeated exposures in electric field-exposed group of rats a significant increase in activity of glutathione peroxidase, Figure 1, and glutathione reductase, Figure 2, at 56th day of exposure cycle, as well as significant decrease in activity of glutathione reductase at 28th day after the end of exposure cycle, Figure 2, and superoxide dysmutase at 14th day of exposure cycle, Figure 3, as compared to control group of shame-exposed rats were observed.

No statistically significant changes in activity of glutathione S-transferase, Figure 4, and catalase, Figure 5, both during and after the end of exposure cycle were noticed.

Moreover in experimental group of electric field-exposed rats a significant decrease in malone dialdehyde concentration in homogenats of liver tissue at 28th day after the end of exposure cycle as compared to control rats was observed, Figure 6.

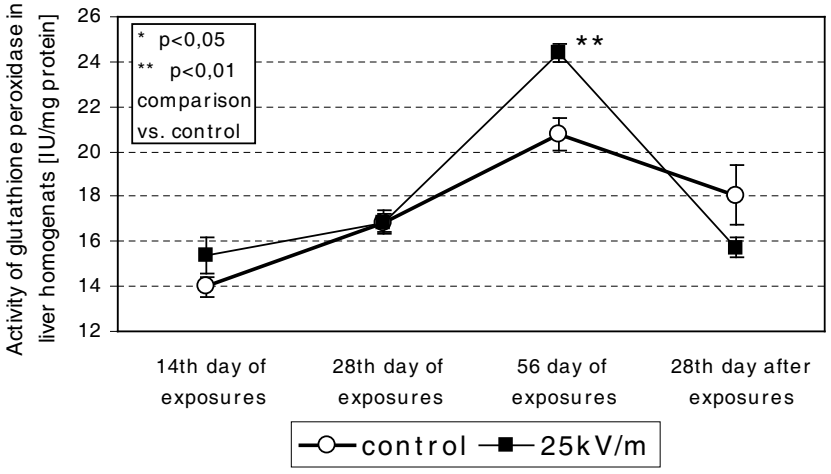

Figure 1: Activity of glutathione peroxidase in homogenats of liver tissue in group of electric field-exposed rats and in control group of shame-exposed rats in particular days of exposure cycle and in 28th day after the end of exposure cycle.

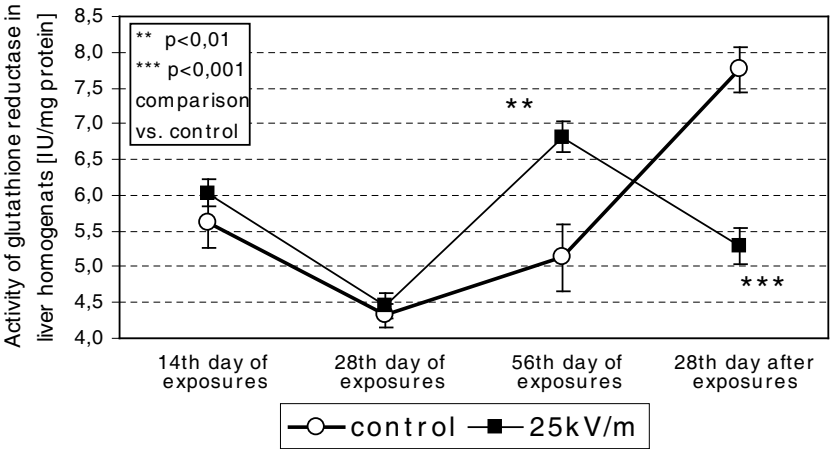

Figure 2: Activity of glutathione reductase in homogenats of liver tissue in group of electric field-exposed rats and in control group of shame-exposed rats in particular days of exposure cycle and in 28th day after the end of exposure cycle.

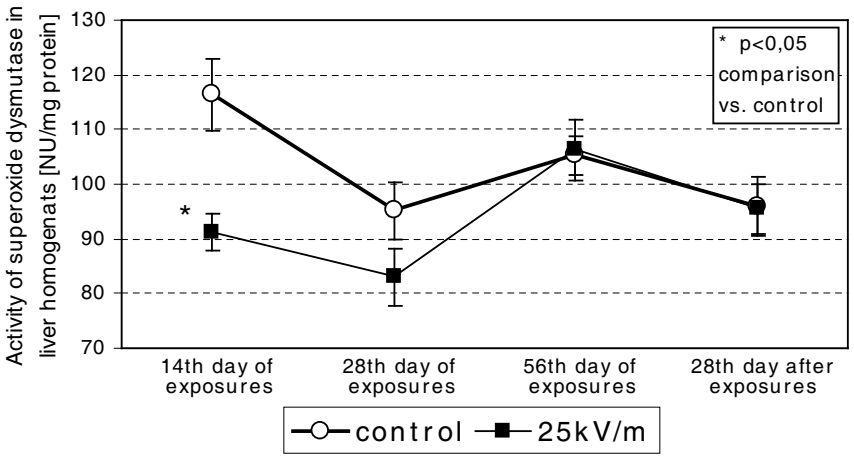

Figure 3: Activity of superoxide dysmutase in homogenats of liver tissue in group of electric field-exposed rats and in control group of shame-exposed rats in particular days of exposure cycle and in 28th day after the end of exposure cycle.

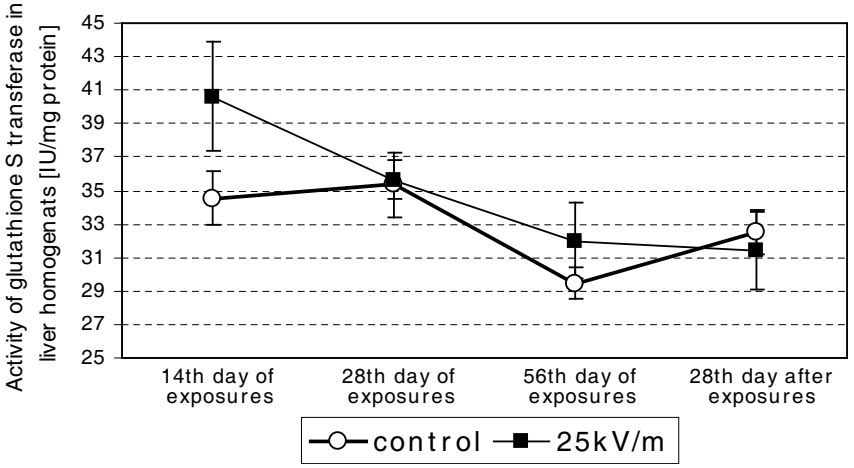

Figure 4: Activity of glutathione S transferase in homogenats of liver tissue in group of electric field-exposed rats and in control group of shame-exposed rats in particular days of exposure cycle and in 28th day after the end of exposure cycle.

4. DISCUSSION

The most important antioxidant enzymes are catalase, glutathione peroxidase, and superoxide dismutase, which collaborating with each other protect the organism against toxic action of reactive oxygen species [8–10]. Lower activity of superoxide dysmutase in early phase of exposure cycle with further increase in activity of glutathione peroxidase and glutathione reductase at last day of exposure cycle, without significant changes in concentration of malone dialdehyde during exposure cycle suggest the adaptative modification of oxidant/antioxidant status resulting in protection of hepatocytes against unfavorable intensification of oxidative processes under the influence of static electric field.

Moreover decrease in glutathione reductase activity and concentration of malone dialdehyde and lack of significant changes in activity of other antioxidant enzymes at 28th day after the end of exposure cycle confirm that long-term exposure to static electric field with parameters usually existing nearby HVDC transmission lines does not have any persistent, pathological effect on oxidant/antioxidant balance, which could result in intensification of peroxidation of lipids in biological membranes in liver tissue.

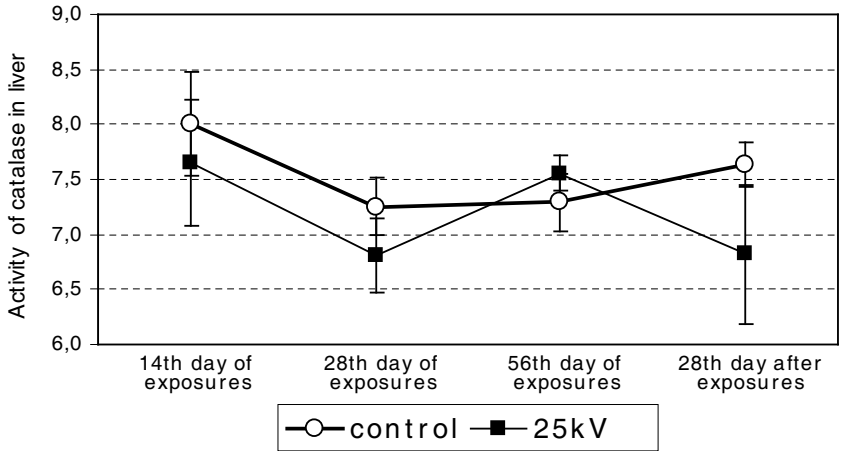

Figure 5: Activity of catalase in homogenats of liver tissue in group of electric field-exposed rats and in control group of shame-exposed rats in particular days of exposure cycle and in 28th day after the end of exposure cycle.

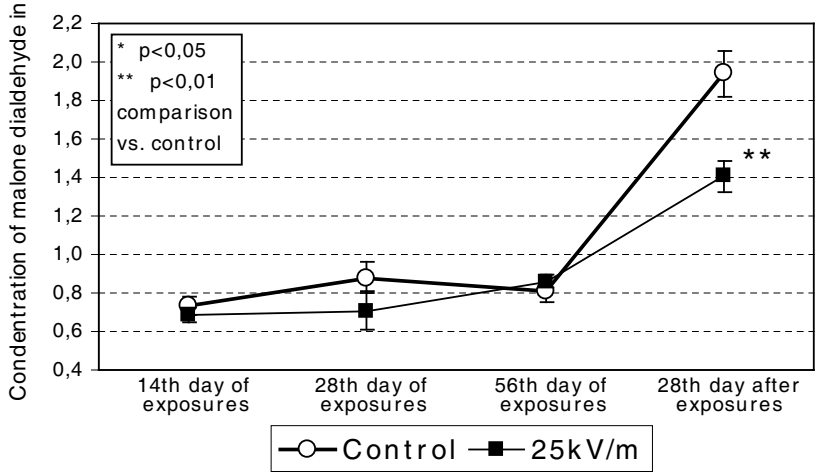

Figure 6: Concentration of malone dialdehyde in homogenats of liver tissue in group of electric field-exposed rats and in control group of shame-exposed rats in particular days of exposure cycle and in 28^{th} day after the end of exposure cycle.

5. CONCLUSIONS

Exposure to static electric field with physical parameters generated usually nearby HVDC transmission lines does not cause any persistent, harmful effect on antioxidant reactions in liver of experimental animals. These experimental data indicate that proper construction of high voltage direct current transmission lines enables to avoid serious health hazards for human population related to disturbances of antioxidant processes in living organisms.

REFERENCES

1. Hisamitsu, T., K. Narita, and T. Kasahara, "Induction of apoptosis in human leucemic cells by magnetic fields," *Japan Journal of Physiology*, Vol. 47, No. 3, 307–310, 1997.
2. Wolf, F. I., A. Torsello, B. Tedesco, S. Fasanella, A. Boninsegna, M. D'Ascenzo, C. Grassi, G. B. Azzena, and A. Cittadini, "50-Hz extremely low frequency electromagnetic fields enhance cell proliferation and DNA damage: Possible involvement of a redox mechanism," *Biochimica et Biophysica Acta,* Vol. 1743, No. 1–2, 120–129, 2005.
3. Cieslar, G., A. Sieron, and P. Sowa, "Influence of high voltage static electric field on activity of antioxidant enzymes in rats," *Proceedings of 25th Annual International Conference of the IEEE Engineering in Medicine and Biology Society '2003*, Vol. 4, 3257–3260, 2003.
4. Aebi, H., "Catalase in vitro," *Methods in Enzymology*, Vol. 105, 121–126, 1984.
5. Paglia, D. and W. Valentine, "Studies on the quantities and qualitative characterization of erythrocyte glutathione peroxidase," *Journal of Laboratory and Clinical Medicine*, Vol. 70, No. 1, 158–169, 1967.
6. Oyanagui, Y., "Evaluation of assay methods and establishment of kit for superoxide dismutase activity," *Analytical Biochemistry*, Vol. 142, No. 2, 290–296, 1984.
7. Ohkawa, H., N. Ohishi, and K. Yagi, "Assay for peroxides in animal tissues by thiobarbituric acid reaction," *Analytical Biochemistry*, Vol. 95, No. 2, 351–358, 1979.
8. Fridovich, I., "Superoxide radical and superoxide dismutases," *Annual Review of Biochemistry*, Vol. 64, 97–112, 1995.
9. Suzuki, Y. J., H. J. Forman, and A. Sevanian, "Oxidants as stimulators of signal transduction," *Free Radicals in Biology and Medicine*, Vol. 22, No. 1–2, 269–285, 1997.
10. Dröge, W., "Free radicals in the physiological control of cell function," *Physiological Reviews*, Vol. 82, No. 1, 47–95, 2002.

Effect of Exposure to Static, High Voltage Electric Field Generated Nearby HVDC Transmission Lines on Behavior of Rats

G. Cieslar[1], J. Mrowiec[1], P. Sowa[2], S. Kasperczyk[3], and A. Sieron[1]

[1]Department and Clinic of Internal Diseases, Angiology and Physical Medicine
Silesian Medical University, Poland
[2]Institute of Power System and Control, Silesian University of Technology, Poland
[3]Department of Biochemistry, Silesian Medical University, Poland

Abstract— The effect of long-term, whole-body exposure to strong static electric field generated usually nearby high voltage direct current (HVDC) transmission lines on behavior of rats, basing on estimation of locomotor activity, exploratory activity, space memory and irritability was analyzed in this study. Experimental material consisted of 16 male Wistar albino rats aged 8 weeks, weighting 180–200 g. During the whole experiment all animals were placed in identical environmental conditions, under a 12 h light-dark cycle with free access to standard laboratory pellet food and tap water. All animals were randomly divided into 2 groups (8 animals each). The rats from experimental group were exposed for 56 consecutive days (8 hours daily) to static electric field with electric field intensity values of 25 kV/m (usually measured nearby actually existing HVDC transmission lines), in a specially designed experimental system. Rats from control group were sham-exposed in the same experimental system, with no electric field generated between electrodes during exposure. The evaluation of behavior was made at 24 hours before first exposure, at 24 hours after first exposure, at 7th, 14th, 21st, 28th, 42nd and 56th day of exposure cycle and at 28th day after the end of a cycle of exposures. A locomotor activity was determined in the "open field" test, an exploratory activity was examined in the "hole" test, space memory was determined by means of water maze test and an irritability was investigated by means of Nakamura and Thoenen's score test. As a result of repeated exposures in experimental group of electric field-exposed rats a significant decrease in the number of episodes of crossings (at 7th day of exposure cycle), peepings (at 7th and 14th day of exposure cycle) and defecations (at 28th day of exposure cycle) in the "open field" test was observed as compared to control animals. On the other hand in experimental group of electric field-exposed rats no significant changes in the water maze crossing time, in the number of episodes of rearings and washing in the "open field" test as well as in the number of head dips in the "hole" test and in irritability score were observed comparing with control animals. On the basis of obtained results one can conclude that long-term, whole-body exposure of rats to strong, static electric field with parameters generated nearby actually existing HVDC transmission lines causes only a transient, significant reduction of locomotor activity in the initial phase of exposure cycle, without any other persistent changes in the behavior.

1. INTRODUCTION

In available literature there are only few data on the influence of 50–60 Hz electric fields generated nearby electric field transmission lines on the function of brain resulting in behavioral alterations in occupationally exposed humans [1, 2]. In experimental studies it was found that low frequency high voltage electric fields can change the behavior of mice, rats, and nonhuman primates; however, these transitory changes were probably secondary to detection of a novel stimulus, and did not suggest acute adverse effects [3–7]. The aim of this study was to estimate in an experimental model the effect of long-term, whole-body exposure to strong static electric field with physical parameters, which frequently occur nearby actually existing high voltage direct current transmission lines on such behavioral reactions as locomotor activity, exploratory activity, space memory and irritability in rats.

2. MATERIAL AND METHODS

Experimental material consisted of 16 male Wistar albino rats aged 8 weeks, weighting 180–200 g. During the whole experiment all animals were placed in identical environmental conditions (constant temperature $22 \pm 1^{\circ}$C and humidity of air) under a 12 h light-dark cycle with free access to standard laboratory pellet food and tap water. All animals were randomly divided into 2 groups: experimental and control (8 animals each) with no significant differences in body weight.

The animals from experimental group were exposed for 56 consecutive days (8 hours daily) to static electric field in a specially designed experimental system consisting of autotransformer, high voltage transformer 220 V/60000 V, cascade rectifier, water rheostat, 2 electrodes with round shape and specially profiled edges placed in a distance of 50 cm from each other, plastic cage placed between both electrodes containing 8 animals at a same time and magnetostatic kilo-voltmeter C196 type. Rats from experimental group were exposed to static electric field with intensity of 25 kV/m — usually measured nearby actually existing HVDC transmission lines. The control animals were subjected to sham-exposure in the same experimental system, during which no electric field was generated between electrodes.

The evaluation of behavior was made at 24 hours before first exposure, at 24 hours after first exposure, at 7th, 14th, 21st, 28th, 42nd and 56th day of exposure cycle and at 28th day after the end of a cycle of exposures. A locomotor activity was determined in the open field test by recording

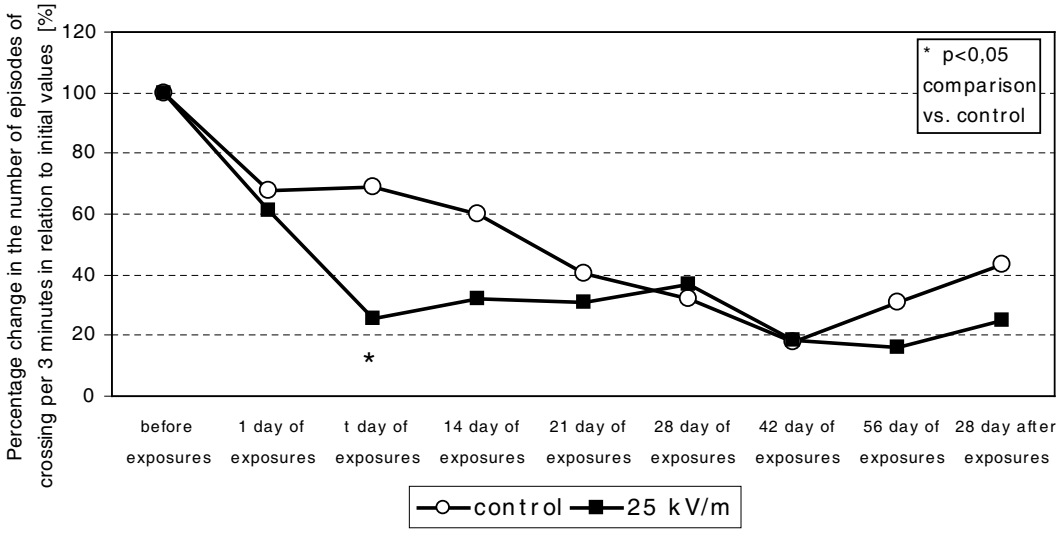

Figure 1: Percentage change in the number of episodes of crossings in "open field" test in relation to initial values before the beginning of exposure cycle in particular days of exposure cycle and in 28 day after the end of exposure cycle in group of electric field-exposed rats and in control group of sham-exposed rats.

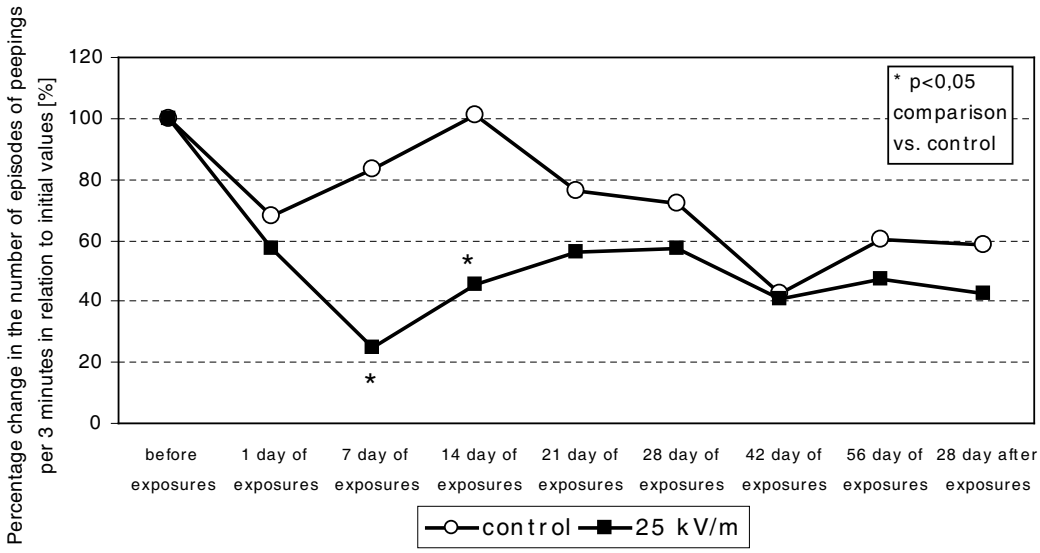

Figure 2: Percentage change in the number of episodes of peepings in "open field" test in relation to initial values before the beginning of exposure cycle in particular days of exposure cycle and in 28 day after the end of exposure cycle in group of electric field-exposed rats and in control group of sham-exposed rats.

a number of episodes of crossings, peepings, rearings, washing and defecation per 3 minutes of observation [8]. An exploratory activity was examined in the hole test by recording a number of head dips into a board hole per 3 minutes [9]. Space memory was determined by means of water maze test on the basis of measurement of time required for crossing of a specially constructed water maze [10, 11]. An irritability was investigated by means of Nakamura and Thoenen's score test [12]. The results of particular tests were presented as percentage change in relation to initial values before a beginning of exposure cycle. Statistical analysis was performed by means of ANOVA and post-hoc Mann-Whitney's U test.

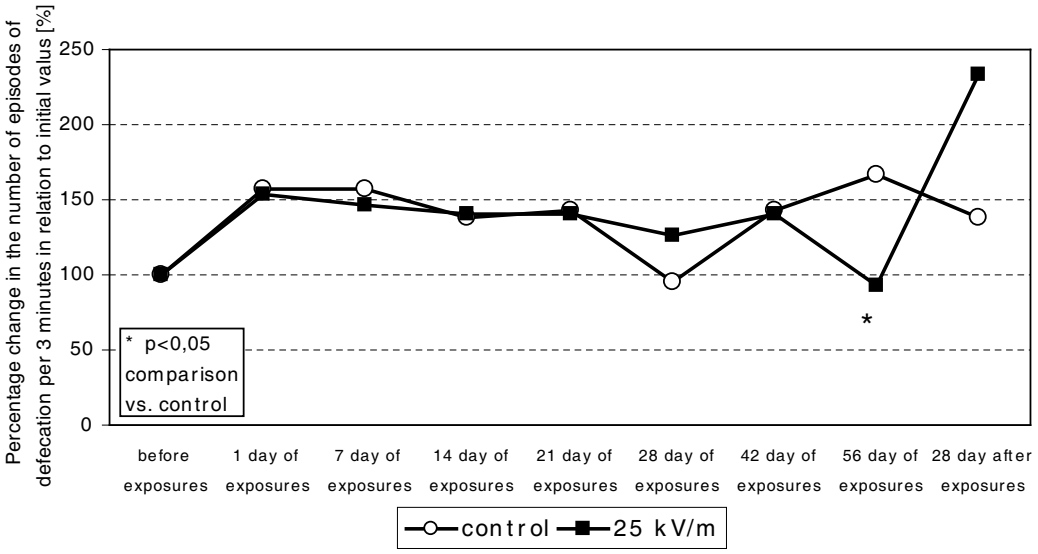

Figure 3: Percentage change in the number of episodes of defecation in "open field" test in relation to initial values before the beginning of exposure cycle in particular days of exposure cycle and in 28 day after the end of exposure cycle in group of electric field-exposed rats and in control group of sham-exposed rats.

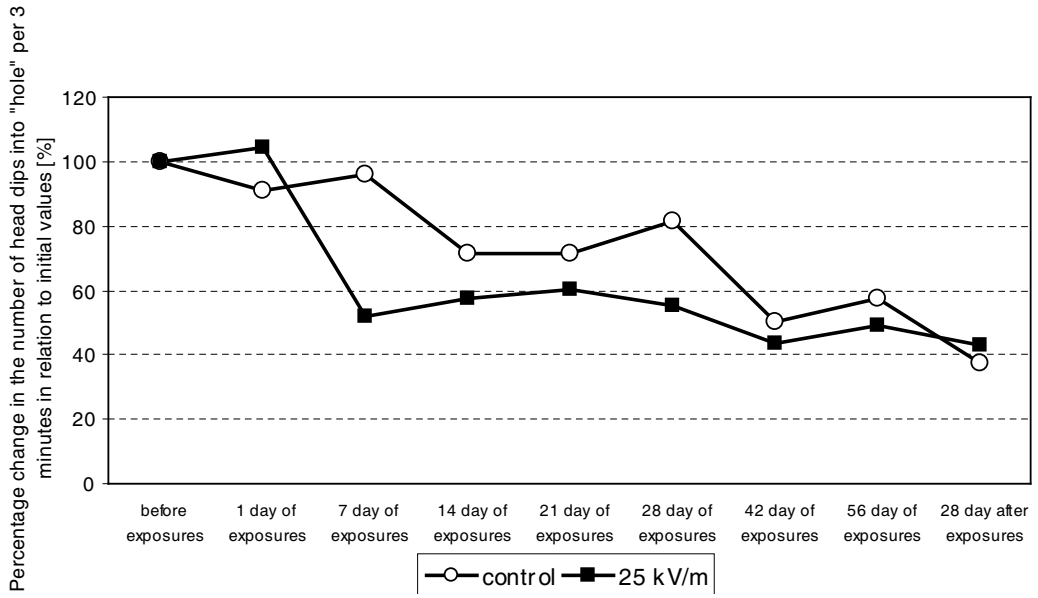

Figure 4: Percentage change in the number of head dips in "hole" test in relation to initial values before the beginning of exposure cycle in particular days of exposure cycle and in 28 day after the end of exposure cycle in group of electric field-exposed rats and in control group of sham-exposed rats.

3. RESULTS

The results of particular behavioral test in both groups of rats in succeeding days of exposure cycle or sham-exposure cycle respectively) as well as in 28th day after the end of exposure cycle are presented in Figures 1–6.

As a result of repeated exposures in experimental group of electric field-exposed rats a significant decrease in the number of episodes of crossings at 7th day of exposure cycle, Figure 1, episodes of peepings at 7th and 14th day of exposure cycle, Figure 2, and episodes of defecations at 28th day of exposure cycle, Figure 3, in the "open field" test were observed as compared to control group of sham-exposed rats.

On the other hand in experimental group of electric field-exposed rats no significant changes in the number of episodes of rearings and washing in the "open field" test as well as in the number of head dips in the "hole" test, Figure 4, in irritability score, Figure 5, and in the water maze crossing time, Figure 6, were observed, as compared to control sham-exposed animals.

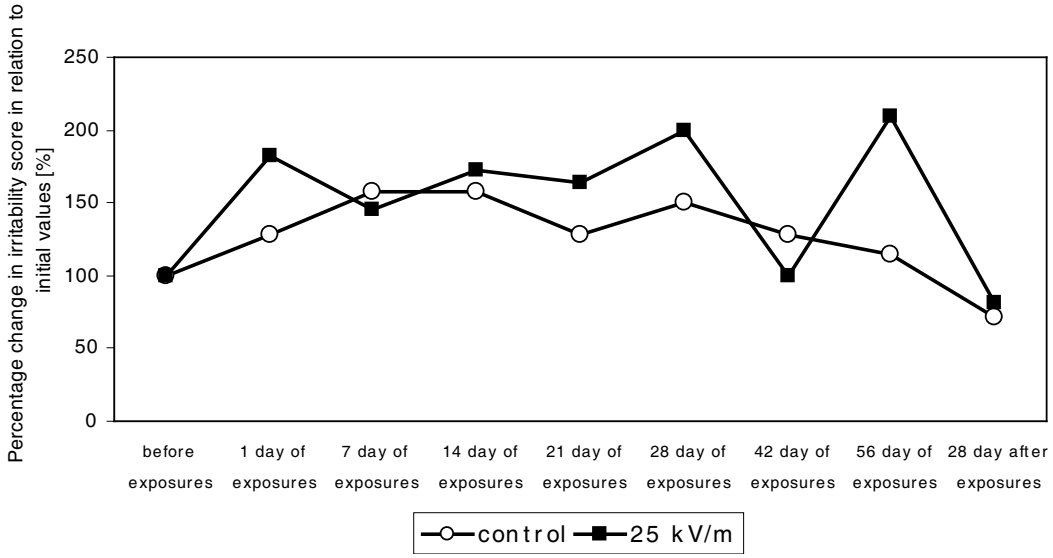

Figure 5: Percentage change in irritability score in Nakamura and Thoenen's test in relation to initial values before the beginning of exposure cycle in particular days of exposure cycle and in 28 day after the end of exposure cycle in group of electric field-exposed rats and in control group of sham-exposed rats.

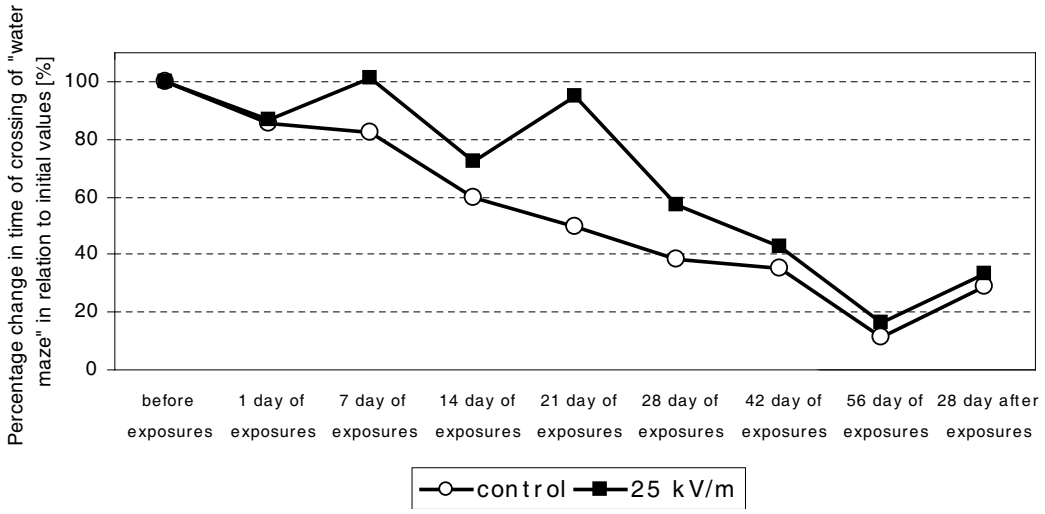

Figure 6: Percentage change in time of crossing of "water maze" in relation to initial values before the beginning of exposure cycle in particular days of exposure cycle and in 28 day after the end of exposure cycle in group of electric field-exposed rats and in control group of shame-exposed rats.

4. CONCLUSION

Long-lasting, whole-body exposure of rats to strong, static electric field generated usually nearby high voltage direct current transmission lines causes only a transient, significant reduction of locomotor activity in the initial phase of exposure cycle, without any pathological disturbances of exploratory activity, space memory or irritability.

REFERENCES

1. Fole, F. F., "The HVS effect in electric power substations," *Medicina y Seguridad del Trabajo*, Vol. 23, 15–18, 1973.
2. Hauf, R. and J. Wiesinger, "Biological effects of technical, electric, and electromagnetic VLF fields," *International Journal of Biometeorology*, Vol. 17, No. 3, 213–215, 1973.
3. Coelho, Jr., A. M., S. P. Easley, and W. R. Rogers, "Effects of exposure to 30 kV/m, 60 Hz electric fields on the social behavior of baboons," *Bioelectromagnetics*, Vol. 12, No. 2, 117–135, 1991.
4. Easley, S. P., A. M. Coelho, Jr., and W. R. Rogers, "Effects of a 30 kV/m, 60 Hz electric field on the social behavior of baboons: A crossover experiment," *Bioelectromagnetics*, Vol. 13, No. 5, 395–400, 1992.
5. Hjeresen, D. L., W. T. Kaune, J. R. Decker, and R. D. Phillips, "Effects of 60 Hz electric fields on avoidance behavior and activity of rats," *Bioelectromagnetics*, Vol. 1, No. 3, 299–312, 1980.
6. Hjeresen, D. L., M. C. Miller, W. T. Kaune, and R. D. Phillips, "A behavioral response of swine to a 60 Hz electric field," *Bioelectromagnetics*, Vol. 3, No. 4, 443–452, 1982.
7. Rosenberg, R. S., P. H. Duffy, and G. A. Sacher, "Effects of intermittent 60 Hz high voltage electric fields on metabolism, activity, and temperature in mice," *Bioelectromagnetics*, Vol. 2, No. 4, 291–303, 1981.
8. Janssen, P. A., A. H. Jageneau, and K. H. Schellekens, "Chemistry and pharmacology of compounds related to 4-(4-hydroxy-4-phenyl-piperidino)-butyrophenone. IV. Influence of haloperidol (R 1625) and of chlorpromazine on the behaviour of rats in an unfamiliar 'open field' situation," *Psychopharmacologia*, Vol. 1, 389–392, 1960.
9. File, S. E., "Effects of chlorpromazine on exploration and habituation in the rat," *British Journal of Pharmacology*, Vol. 49, No. 2, 303–310, 1973.
10. Morris, R., "Development of a water maze procedure for studying spatial learning in the rat," *Journal of Neuroscience Methods*, Vol. 11, No. 1, 47–60, 1984.
11. Plech, A., T. Klimkiewicz, and H. Jakrzewska, "Neurotoxic effect of copper salts in rats," *Polish Journal of Environmental Studies*, Vol. 9, 301–304, 2000.
12. Nakamura, K. and H. Thoenen, "Increased irritability: A permanent behaviour change induced in the rat by intraventricular administration of 6-hydroxydopamine," *Psychopharmacologia*, Vol. 24, No. 3, 359–372, 1972.

Gradient Decay Measurement in NMR Tomography

R. Kubásek[1], **E. Gescheidtová**[1], **and K. Bartušek**[2]

[1]Department of Theoretical and Experimental Electrical Engineering
Brno University of Technology, Kolejní 2906/4, Brno 612 00, Czech Republic
[2]Institute of Scientific Instruments, Academy of Sciences of the Czech Republic
Královopolská 147, Brno 612 64, Czech Republic

Abstract— The article describe simple and novel method for gradient time course measurement in NMR tomography. The pulse sequence with two time symmetrical vessel position flux density measurement is present. The experimental measurement of gradient decay and pre-emphasis compensation of that gradient decay are shown.

1. INTRODUCTION

The magnetic resonance (MR) imaging techniques of tomography and spectroscopy are exploited in many applications [1]. For the MR instruments to function properly it is necessary to maintain a high quality of homogeneity of the fundamental and gradient magnetic field [2]. The method described leads us to measure gradient decay [3] and determine the quality of generated gradient field [4]. Also, pre-emphasis compensation of the generated gradient can be set correctly and precisely [5].

2. METHOD

The principle of measuring the waveform of gradient pulse consists in determining the changes in instantaneous frequency of MR signal produced by the resonance of nuclei excited in two thin layers positioned symmetrically about the gradient field centre, as shown on Fig. 1. The average inductions of magnetic field $B(x_{n,t})$ are measured in the excited layer in the $+x_n$ and $B(-x_{n,t})$ positions in the $-x_n$ layer. The symmetrical position is chosen for simple arrangement of holder, generally, position can be anyone and the gradient field can be measure in any position or in many positions for whole space gradient mapping.

From the differences of the two inductions measured the magnitude of gradient can be calculated according to the relation:

$$G_x(t) = \frac{1}{2x_n}\left[B(x_n,t) - B(-x_n,t)\right]. \tag{1}$$

The sum of the $B(x_{n,t})$ and $B(-x_{n,t})$ inductions measured determines the change in basic homogeneous magnetic field according to the relation:

$$B_{0x}(t) = \frac{1}{2}\left[B(x_n,t) + B(-x_n,t)\right]. \tag{2}$$

The measured layer is determinate by cuboid bowl vessel ($30 \times 30 \times 0.6\,\mathrm{mm}$) and is mechanical set in holder as shown on Fig. 2. Mechanical delimitation of measured layer leads to higher MR signal,

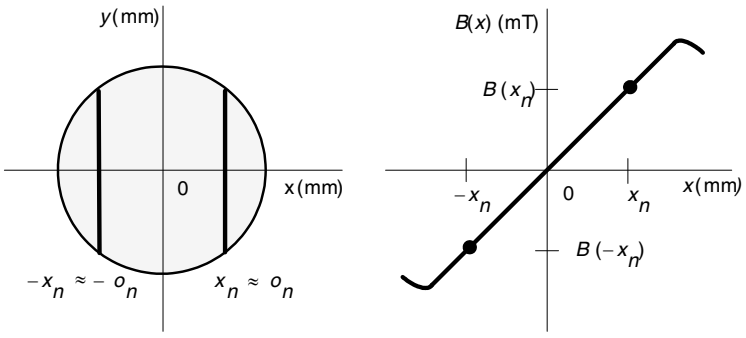

Figure 1: Position of layers in working space of MR device.

unfortunately also decrease repeatability of measurement. The angle errors in speciment arrange was verified by image in axial cut and is less than 1°.

The pulse sequence for gradient decay measurement is shown on Fig. 3. This sequence outputs a gradient pulse followed by an RF pulse and then acquires data. Series of events can be repeated up to 10 times. The delay between the end of the gradient pulses and the excitation RF pulse can not be less then 0.1 ms. Varying delay between the RF pulse with flip angle α and acquisition and above all acquisition length determine total time length of measured gradient decay. The pulse sequence can be set for various experiments made-to-measure. The gradient present position can be set anywhere in pulse sequence, but then the sequence must be adjust. Gradient present directly in excitation and acquisition leads to shorter FID signal, gradient cause de-phasing of nucleus and total vector sum of nucleus contribution decrease rapidly.

3. EXPERIMENTAL RESULTS

The experiments were carried out on an MR tomograph system 4.7 T/120 mm (i.e., 200 MHz for ^{1}H nuclei). Actively shielded gradient coils yield a maximum gradient field magnitude of 180 mT/m. The data measured were processed in the MAREVISI and MATLAB programs. Experimental results are shown on Fig. 4. Fig. 4(a) shows gradient decay without any compensation, its natural gradient decay reached by obtained quality shielding coil design. On Fig. 4(b) is shown its basic flux density filed B_0, B_0 doesn't change for any experiment with pre-emphasis, crossover between direct pre-emphasis and B_0 is zero. Second experiment on Fig. 4(c) with purposely very high pre-emphasis, demonstrate pre-emphasis functionality. The gradient decay matches with das-dotted

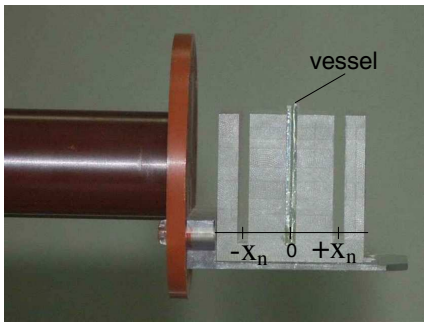

Figure 2: Holder for water bowl, vessel in zero position.

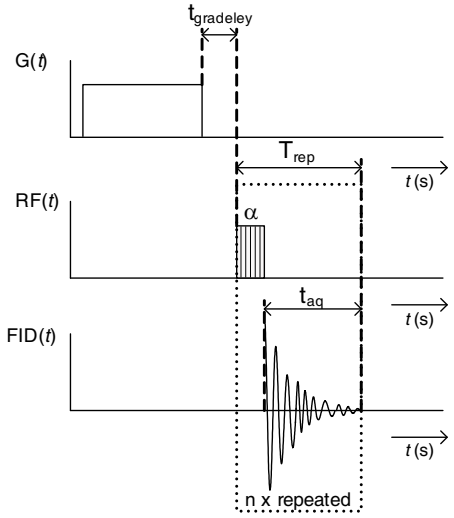

Figure 3: The pulse sequence for gradient decay measurement.

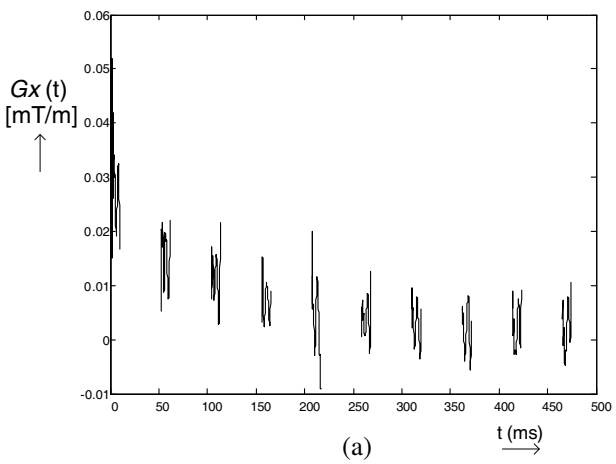

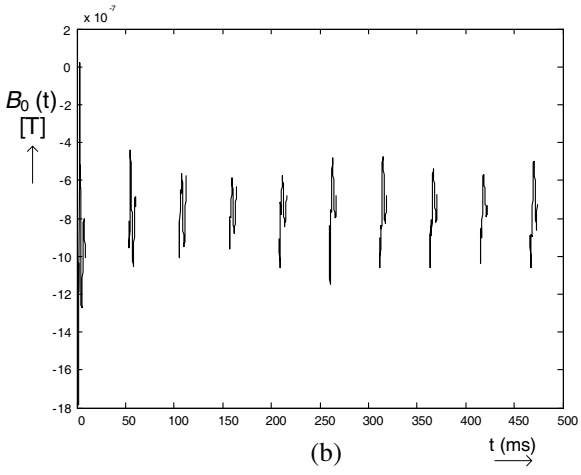

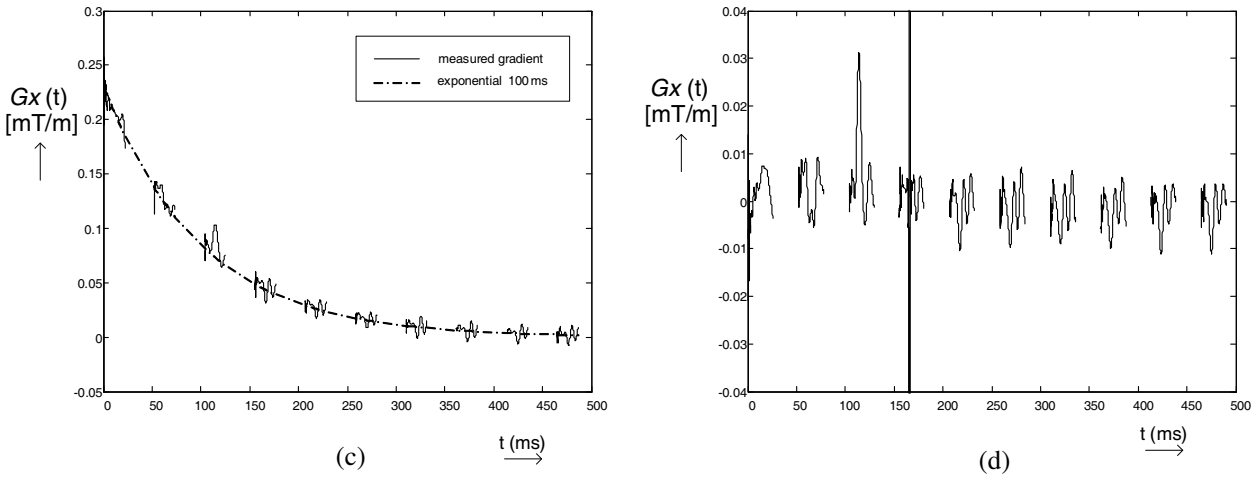

Figure 4: (a) Gradient decay without any correction and (b) its B_0 (c) gradient decay with experimental pre-emphasis 100 ms, (d) gradient decay with "optimal" pre-emphasis set.

ideal exponential course perfectly. Also can be said, that gradient measurement method work correctly. The last gradient decay on Fig. 4(d) was measured for pre-emphasis set by approximation of course from Fig. 4(a). The shorter and lower gradient transition in amplitude was obtained, pre-emphasis demonstrate its usefulness.

4. CONCLUSIONS

The method for gradient time course measurement described in article is simple and work properly. The exact homogeneity know lead as to determine or enlarge possible errors in many MR techniques where gradients are used. The imaging techniques, diffusion and relaxation measurement are typical of them.

ACKNOWLEDGMENT

This work was supported within the framework of research plan MSM 0021630513 and project of the Grant Agency of the Czech Republic No. 102/07/0389.

REFERENCES

1. Vlaardingerbroek, M., *Magnetic Resonance Imaging*, Springer-Verlag, 2000.
2. Mansfield, P. and B. Chapman, "Active magnetic screening of gradient coils in NMR imaging," *Journal of Magnetic Resonance*, Vol. 66, 573–576, 1986.
3. Kubásek, R., E. Gescheidtová, and K. Bartušek, "Measurements of time characteristics of the gradient magnetic field," *27th Annual International Conference Medicine and Biology Society*, 1–4, Shanghai, 2005.
4. Bartusek, K. and E. Gescheidtova, "Testing the quality of magnetic gradient fields for studying self-diffusion processes by magnetic resonance methods," *Measurement Science and Technology*, Vol. 17, 2256–2262, 2006.
5. Bartusek, K. and E. Gescheidtova, "MR measurement technique of rapidly switched gradient magnetic fields in MR tomography," *Applied Magnetic Resonance*, Vol. 29, No. 12, 675–686, 2006.

Fiber Optic Current Sensing in Pulsed Power Application

Radek Kubasek, Pavel Fiala, and Petr Drexler
FEEC, BUT, UTEE, Kolejni 2906/4, Brno 612 00, Czech Republic

Abstract— In order to optical fiber linear birefringence compensation a promising method was chosen for pulsed current sensor design. The method employs orthogonal polarization conjugation by the back direction propagation of the light wave in the fiber. The Jones calculus analysis presents its propriety. Presented result is a new approach to the Jones calculus treatment in birefringent media. This approach simplifies the analysis. An experimental fiber optic current sensor has been designed and realized. The advantage of the proposed method was proved considering to the sensitivity improvement. The sensitivity has improved by a factor $A_S = 174$ in compare to the basic sensor setup. The detailed description of the experimental setup is described. For measurement of the sensor bandwidth a pulsed current source with very fast rise time is required. The description of the fast rise time current source design is presented also.

1. INTRODUCTION

It is possible to utilize the concept of integral fiber-optic sensor for the current sensor realization. Single mode optical fiber serves as a magneto-optic element [1], which is called Faraday rotator. The basic setup shows Fig. 1.

The sensor principle is based on the Ampere's law

$$\oint_l \mathbf{B} \cdot dl = \mu I, \tag{1}$$

where μ is the permeability of Faraday rotator material. Magnetic flux density vector $\mathbf{B}$ circulates round the conductor with the current. Faraday rotator in the form of loop of optical fiber encircles the conductor and implements the integration loop in (1). Considering the $i(t)$ current measurement we can derive the relation for the waveform of polarization rotation angle $\theta(t)$ in fiber-optic sensor with number of loops N

$$\theta(t) = \mu V \oint_l \mathbf{B}(t) \cdot dl = \mu_0 V N i(t). \tag{2}$$

For a given rotator with Verdet constant V the polarization rotation in time $\theta(t)$ depends only on the measured current waveform $i(t)$. The rate of the polarization rotation and the measured current value can be evaluated by means of polarimetry.

2. LINEAR BIREFRINGENCE SUPPRESSION

Considering the need for preservation of single polarization state during the propagation the application of single mode fiber is demanded [2]. Winding the sensor fiber in loops leads to mechanical stress and consecutively to linear birefringence formation in fiber core [3]. The linear polarization of coupled light wave transforms into elliptical polarization and sensor sensitivity is decreased [4].

The sensors with back light propagation can be constructed for the birefringence compensation. This approach exploits the non-reciprocity of Faraday effect and the reciprocity of linear birefringence. The light wave is reflected on the far end and its polarization state is rotated with an angle

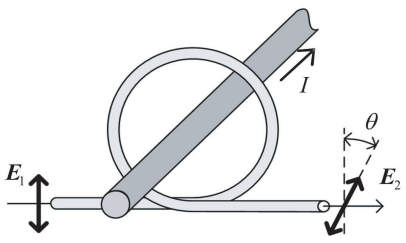

Figure 1: The principle of integral fiber-optic current sensor.

$\theta = 90°$. Then, it is coupled back into the fiber. The light wave which travels the same path in the opposite direction experiences a double polarization rotation imposed by the Faraday effect, due to its non-reciprocity. The orthogonal wave components are swapped in relation to the fast and slow fiber axis (as described in the Introduction). The phase shift is equalized and the influence of linear birefringence disappears in the ideal case. The orthoconjugate retroreflector (OCR, Faraday mirror) is exploited for the light reflection and polarization rotation.

3. ANALYSIS OF OCR

The Jones calculus can be exploited for theoretical analysis of fiber-optic sensor with OCR. The analyzed setup is shown in Fig. 2. For the simplification the analysis does not take into account a power losses in fiber and on the optical components. The next simplification is the assumption that the single mode fiber which is being analyzed is free from intrinsic linear birefringence. This can be fulfilled for available fibers.

The analysis of the fiber optic sensor has been presented in [5]. The result for the presence of linear birefringence δ only ($\phi = 0$) is

$$\mathbf{J}_4' = \mathbf{T}_{\mathrm{OF}} \cdot \mathbf{T}_{\mathrm{OCR}} \cdot \mathbf{T}_{\mathrm{OF}} \cdot \mathbf{J}_1 = \frac{1}{\sqrt{2}} \begin{bmatrix} \cos^2 \frac{\delta}{2} + \sin^2 \frac{\delta}{2} \\ -\left(\cos^2 \frac{\delta}{2} + \sin^2 \frac{\delta}{2}\right) \end{bmatrix} = \frac{1}{\sqrt{2}} \begin{bmatrix} 1 \\ -1 \end{bmatrix}, \tag{3}$$

We have obtained a linearly polarized wave at the close end of the fiber. The polarization state is rotated with an angle $\theta = 90°$ in compare to the original one. The influence of linear birefringence has disappeared.

In the second instance, consider the presence of circular birefringence ϕ only ($\delta = 0$) which is induce by the measured magnetic field. After the back propagation in the fiber the light wave is described by the resultant vector

$$\mathbf{J}_4'' = \mathbf{T}_{\mathrm{OF}} \cdot \mathbf{T}_{OCR} \cdot \mathbf{T}_{\mathrm{OF}} \cdot \mathbf{J}_1 = \frac{1}{\sqrt{2}} \begin{bmatrix} \cos^2 \phi - \sin^2 \phi + \sin 2\phi \\ -\left(\cos^2 \phi - \sin^2 \phi - \sin 2\phi\right) \end{bmatrix}. \tag{4}$$

The term $\sin 2\phi$ in (4) represents phase shift due to the circular birefringence induced by the magnetic field. The light wave travels the fiber twice experiencing a double rotation 2ϕ. On the output of the fiber the polarization state can be evaluated by means of dual quadrature polarimetry.

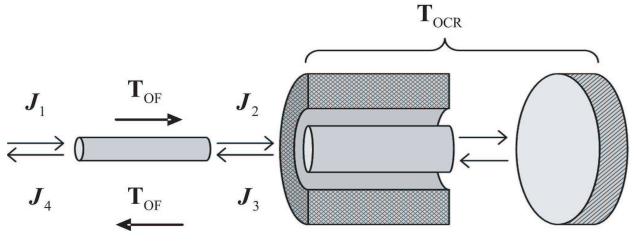

Figure 2: The Jones calculus description of fiber optic sensor setup.

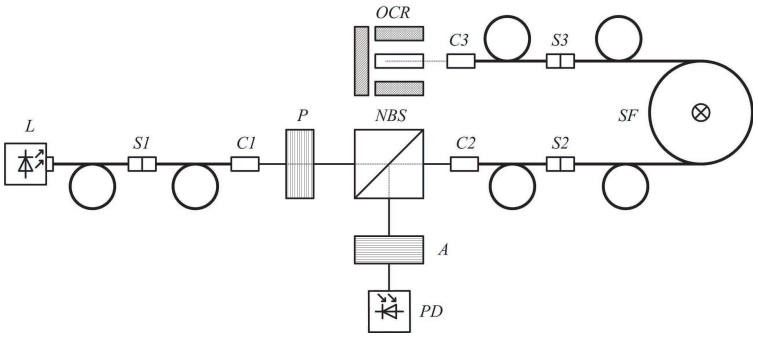

Figure 3: The experimental sensor setup with OCR.

4. EXPERIMENTAL REALIZATION OF FIBER OPTIC SENSOR

On the base of obtained results in previous chapter a current sensor has been designed. The sensor setup utilizing OCR is depicted in the Fig. 3. The source of the carrier optical signal is laser diode ($\lambda = 633\,\mathrm{nm}$) L with single mode fiber pigtail. The polarizer P ensures initial linear polarization. After passing the non-polarizing beam splitter *NBS* the beam is coupled into the sensing fiber SM600 via the collimator $C2$. $C3$ collimates the beam for OCR and couples it back into the fiber. After the back propagation the beam is deflected by *NBS*, analyzed by the means of analyzer A a sensed by the photodetector *PD*. Sleeves S are utilized in the setup.

Proposed sensor was experimentally realized for the measurement of pulsed current with oscillating frequency $f = 59\,\mathrm{kHz}$ and first peak's value in the range $I_p = 1300 \div 1600\,\mathrm{A}$. Two sensing fiber loops encircled two wire loops of the inductive load. A double current value was indicated then. The waveform of the current pulse was measured by the Rogowski coil sensor also. For sensitivity comparison, the current pulse measurement without and with the presence of OCR were performed, as shown in the Fig. 4. On Fig. 4(a), the first waveform (from the top) is the Rogowski coil voltage and the second its integral, which indicates the real current waveform in the load with the top value $I_p = 1550\,\mathrm{A}$. The third and fourth waveforms are the voltages on the photodetector's quadrature outputs. Waveforms which were captured by measurement with OCR are shown in the Fig. 4(b). The first waveform from the top is the Rogowski coil voltage and the second its integral. The third waveform is the photodetector's output voltage.

When we compare the photodetector's output voltages in Fig. 4(a) and Fig. 4(b) it is obvious that only very low sensitivity was achieved with the sensor without OCR. In the Fig. 4(a), the voltage value does not exceed 5 mV in the moment of the current top $I_p = 1550\,\mathrm{A}$.

The estimated voltage top value is $U_p = 1,4\,\mathrm{mV}$. A strong photodiode's shoot noise and thermal noise of the transimpedance amplifier dominates in the output signal. When the sensor with OCR was used for the current pulse measurement a much larger sensitivity was achieved, Fig. 4(b). The sensors output voltage $U_p = 214\,\mathrm{mV}$ corresponds with the current top $I_p = 1365\,\mathrm{A}$. The sensitivity has improved by a factor $A_S = 174$. Interference is observable in the waveforms in Fig. 4(b). It is probably caused by the steep current rise by the thyristor switching.

5. FAST RISE TIME CURRENT PULSE GENERATOR

For the magneto-optical sensing part the theoretical maximum bandwidth for a one fiber loop with the radius $R_l = 5\,\mathrm{cm}$ and the fiber refractive index $n_f = 1,5$ is

$$BW = \frac{0,44c}{2\pi R_1 n_f N} = \frac{0,44 \cdot 3 \cdot 10^8}{2\pi \cdot 5 \cdot 10^{-2} \cdot 1,5 \cdot 1} = 280\,\mathrm{MHz}. \tag{5}$$

This bandwidth sets the pulse edge prolongation to the value $\Delta t = 0,35/289 \cdot 10^6 = 1,25\,\mathrm{ns}$. However, the maximum bandwidth of the complete sensor setup will be influenced by the propagation delay of the light wave in the fiber stage between the sensing part and the Faraday mirror also. Next limitation will be determined by the optical receiver bandwidth. In order to find out the real maximum sensor bandwidth a fast rise time current pulse generator is required. The generator which has been used in Section 5 is insufficient due to the large inductance in the sensor setup [6].

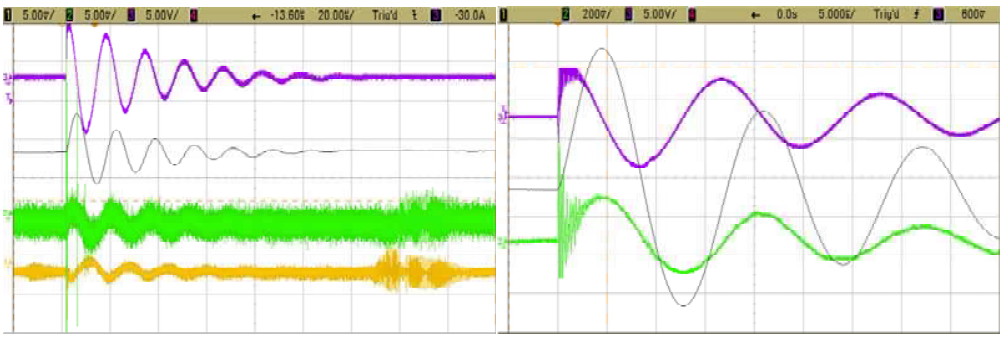

(a) without OCR (b) with OCR

Figure 4: The waveforms captured by the current pulse measurement.

The significant part of the whole circuit inductance has been represented by the high voltage capacitor parasitic inductance $L_p = 300\,\mathrm{nH}$. This inductance together with the other circuit inductance contributions in combination with the capacitance $C = 8\,\mu\mathrm{F}$ has determined the current rise time $t_r = 300\,\mathrm{ns}$. The rise time will be not significantly shorter even in the case of low inductance generator load.

A suitable way to generate fast rise time current pulses is to exploit coaxial transmission line as a capacitive storage system. The line inductance is included in the characteristic line impedance Z_0 which can be of real character. Simultaneously, the matched load $Z_L = Z_0$ can be used to avoid reflections and pulse shape distortion.

The transmission line generator depicted on the Fig. 5(a) has been experimentally realized with coaxial cable RG-58. A sparkgap has been used as a switch S and the load Z_L has been matched to the line impedance $Z_0 = 50\,\Omega$. The transmission line was charged at the voltage level $U = 8\,\mathrm{kV}$. By the discharge to the matched load the current pulse with the level $I_p = 83\,\mathrm{A}$ and the rise time $t_r = 5{,}4\,\mathrm{ns}$ has been generated, Fig. 6. The current pulse was measured by the wideband current transformer. The maximum current level is determined by the ratio of the impedances Z_0 and Z_L and by the electric strength of the coaxial cable. To achieve larger current levels a multiple line generators has been designed as shown in Fig. 5(b). The designed generator comprises of 10 parallel connected URM-67 coaxial cable sections with the common total characteristic impedance $Z_0 = 5\,\Omega$ and the electrical strength $U_{br} = 40\,\mathrm{kV}$. The load $Z_L = 5\,\Omega$ has to withstand the voltage pulse with peak value $U_p = 20\,\mathrm{kV}$ and the pulsed power $P_P = 80\,\mathrm{MW}$. For this purposes a coaxial water load has been designed. The load uses cooper electrodes and cooper sulfate solution as an electrolyte, Fig. 7. The final generator setup is in development.

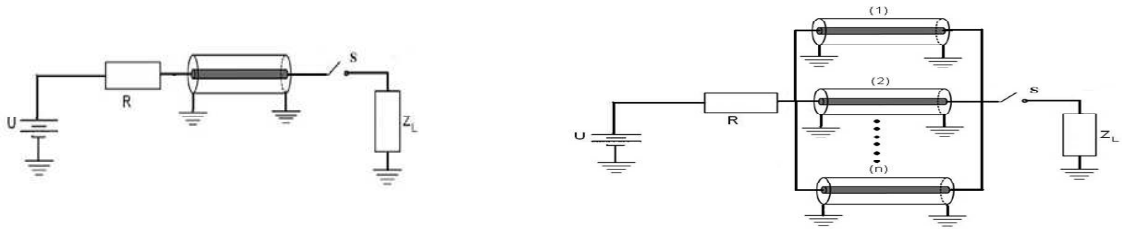

(a) single line generator (b) multiple line generator

Figure 5: The setup of pulsed current generators exploiting coaxial transmission lines and matched load.

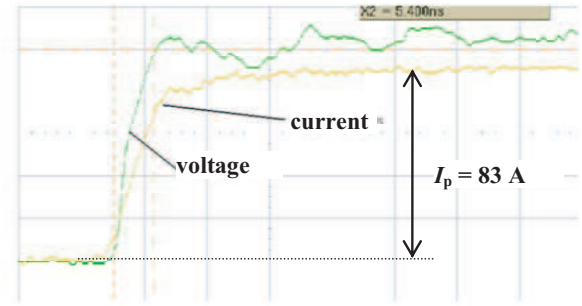

Figure 6: Waveforms captured by the discharge of RG-58 line generator.

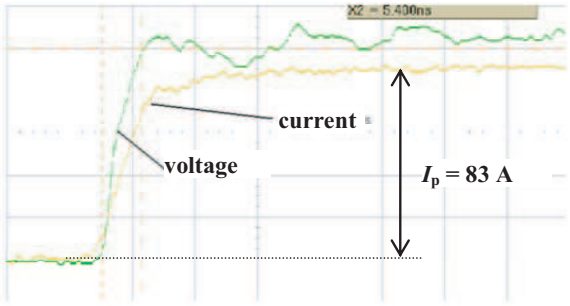

Figure 7: The realization of low inductance high power water load.

6. CONCLUSIONS

This paper describes the linear birefringence compensation method in pulsed current sensor design. This method utilizes orthogonal polarization conjugation. It has been theoretically analyzed by means of Jones calculus. The ability of linear birefringence compensation has been proved together with. The results of the analysis have been experimentally demonstrated by the measurement of the pulse current waveform with the rise time $t_r = 300\,\mathrm{ns}$. For the determination of maximum sensor bandwidth the fast rise time coaxial line generator has been designed and there are presented

preliminary results of the current pulse generation with the rise time $t_r = 5,4\,\mathrm{ns}$. The multiple line pulsed power generator is in development. The results of the fast current pulse measurement by means fiber optic sensor will be presented soon.

ACKNOWLEDGMENT

The paper was prepared within the framework of the research plan No. MSM 0021630513 of the Ministry of Education, Youth and Sports of the Czech Republic.

REFERENCES

1. Ripka, P., *Magnetic Sensors and Magnetometers*, IEEE, Artech House, London, 2001.
2. Craig, A. E. and K. Chang, *Handbook of Optical Components and Engineering*, John Willey & Sons, Inc., New Jersey, 2003.
3. Rose, A., Z. F. Ren, and G. W. Day, "Twisting and annealing optical fiber for current sensors," *Journal of Lightwave Technology*, Vol. 14, No. 11, 2492–2498, 1996.
4. Tang, D., A. Rose, G. W. Day, and S. M. Etzel, "Annealing of linear birefringence in single-mode fiber coils: Applications to optical fiber current sensors," *Journal of Lightwave Technology*, Vol. 8, No. 11, 1031–1037, 1991.
5. Drexler, P., P. Fiala, and R. Kadlec, "Utilization of faraday mirror in fiber optic current sensors and experiments," *PIERS Proceedings*, 137–141, Beijing, China, March 23–27, 2009.
6. Drexler, P. and P. Fiala, "Utilization of faraday mirror in fiber optic current sensors," *Radioengineering*, Vol. 17, No. 4, 101–107, 2008.

Air Ions Concentration Influence on Bacterial Colony Count in the Dwelling Spaces

Z. Szabó[1] and K. Bartušek[2]

[1]Department of Theoretical and Experimental Engineering
Faculty of Electrical Engineering and Communication, Brno University of Technology
Kolejní 2906/4, Brno 612 00, Czech Republic
[2]Institute of Scientific Instruments, Academy of Sciences of the Czech Republic, v.v.i.
Královopolská 147, Brno 612 64, Czech Republic

Abstract— The influence of air ion concentration on the bacterial colony count in the living spaces was examined by means of guardian condenser and aeroscopic method. Experiment was realized at the Department of Theoretical and Experimental Electrical Engineering (DTEEE) in the Faraday cage room and in the common laboratory. The methodology and the technique of our measurement are described in this article. Some of our measurement results are presented. The relation between the measured bacterial colony count and the air ion concentration was evaluated. The conclusion is made on the basis of the relations which were found out.

1. INTRODUCTION

Air ions are extremely important for human health. Air ions affect the metabolic functions of cells in the lungs, the blood supply in the organism, and also the psychic functions of man. Through their electric charge the air ions also affect the earth's atmosphere and the environment we live in. The metrology of air ions has been known for a long time. One of its methods is based on measurement using the aspiration capacitor. This method is applied in the measurement described in this paper. The aim of the study described is to verify the hypothesis of reducing the number of bacteria and fungi in the air of living spaces.

2. MEASURING METHOD

An aspiration capacitor with variable electric field and an electrometer for measuring small currents were used to measure the concentration of various kinds of ions (light-weight, light heavy-weight, heavy-weight) and ions of different polarities. The principle of the measuring method is obvious from Fig. 1; it has been taken over from [1, 2]. A known amount of air under examination $M = 1.021 \cdot 10^{-3}\,\mathrm{m/s}$ (volume rate of flow) flows through a cylindrical capacitor, which has polarization voltage U ($U = 0$–$100\,\mathrm{V}$).

Electrostatic forces attract the air ions to the electrodes. The number of ions captured by the electrode create a small electric current I. The concentration of ions of one polarity is proportional to the magnitude of this current according to the relation

$$n = \frac{I}{M \cdot e} \tag{1}$$

where $e = 1.6.\ 10$–$19\ C$ is the electron charge.

The capacitor collector captures all ions whose mobility is lower than the minimum mobility given by the relation

$$k_m = \frac{M}{4 \cdot \pi \cdot C \cdot U} = \frac{M \cdot \ln \dfrac{d_2}{d_1}}{2 \cdot \pi \cdot l \cdot U}, \tag{2}$$

where M is the volume rate of flow of air through the capacitor, C is the capacitor capacitance, U is the voltage across the electrodes, and d_1, d_2 and l are the dimensions of the aspiration capacitor. The methodology of measuring and the calculations are described in more detail in [1–3].

Aeroscopic measurement of air was carried out in cooperation with the Department of Preventive Medicine of Masaryk University in Brno. Samples of air were taken using the BIOTEST HYCON RCS Plus measuring instrument. Used as the culture medium was the strip for total capture of bacteria. The volume of air taken was 2001 and the results were converted to values per $1\,\mathrm{m}^3$.

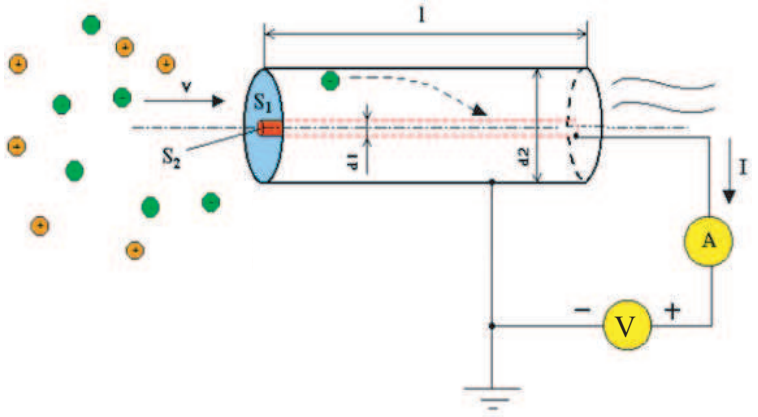

Figure 1: Principle of measuring air ions, using aspiration capacitor.

3. EXPERIMENTAL RESULTS

Two different spaces were chosen for the measurement. The first was a Faraday cage with a minimum magnitude of electric field. We assumed that the negative air ions would be concentrated in the centre of the cage and that the number of bacteria and fungi would be comparable with the laboratory space. In the course of measuring the quality of air by the aeroscopic method the density of ions in the space being measured was recorded during and after ionization. The space was ionized by a BIV-06 ionizer.

The other space was an infrequently used laboratory. This space approaches working and living spaces in which people will usually stay for quite some time. The measurement proceeded in the same way as in the case of Faraday cage.

3.1. Measurement in the Faraday Cage

The BIV-06 ionizer was axially positioned 2.5 m from the aspiration capacitor opening. In the course of the measurement of ions, samples of air were taken simultaneously. The first two measurements were performed without ionization and the results were averaged. Another two measurements took place after 10 minutes' ionization and the results were again averaged. The results of measuring the ion fields are given in Fig. 2. On this figure, the ion concentration increases after 60 and then it decays. This effect could have been caused by air turbulences what was started up after closing the Faraday cage door. With a natural ion concentration in the Faraday cage of ca. 700 ions/cm^3 (Fig. 2, left) an average of 198 bacterial colonies per 10001 of the air being measured and 2 colonies of fungi were measured. The results show the evident effect of ionization on the number of bacteria in the space. After 10 minutes' ionization, the number of bacterial colonies dropped by 7.5%.

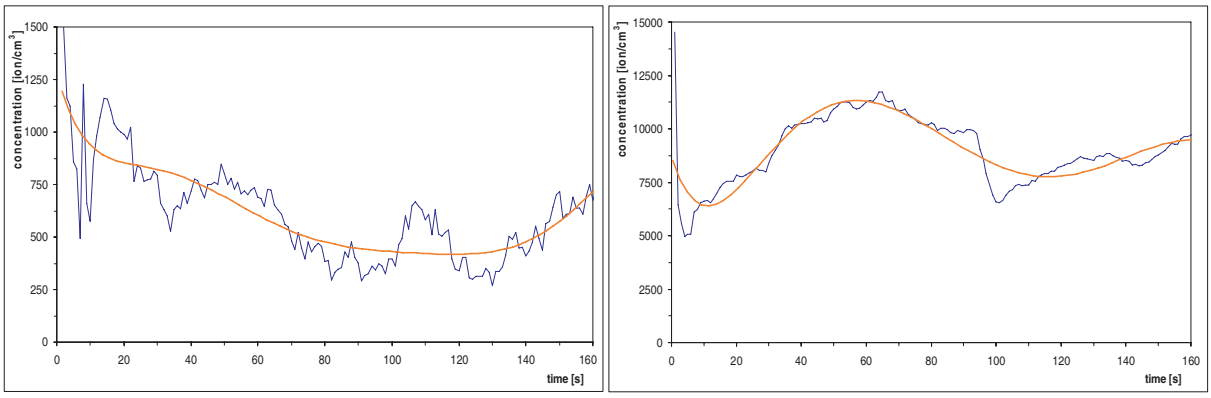

Figure 2: Natural concentration of air ions in Faraday cage, left — Before ionization, right — After ionization.

3.2. Measurement in the Living Space

The BIV-06 ionizer was used for the measurement in the living space. The ionizer was positioned in the axis of aspiration capacitor at a distance of 2.3 m from its opening. Prior to the ionization,

125 ions/cm^3 (Fig. 3), 300 bacterial colonies and 1 colony of fungi were measured in the space.

After 25 minutes' ionization in the laboratory an average of 10,500 ions/cm^3 (Fig. 3), 125 bacterial colonies and no fungi were measured. The drop in the number of bacterial colonies was 58%.

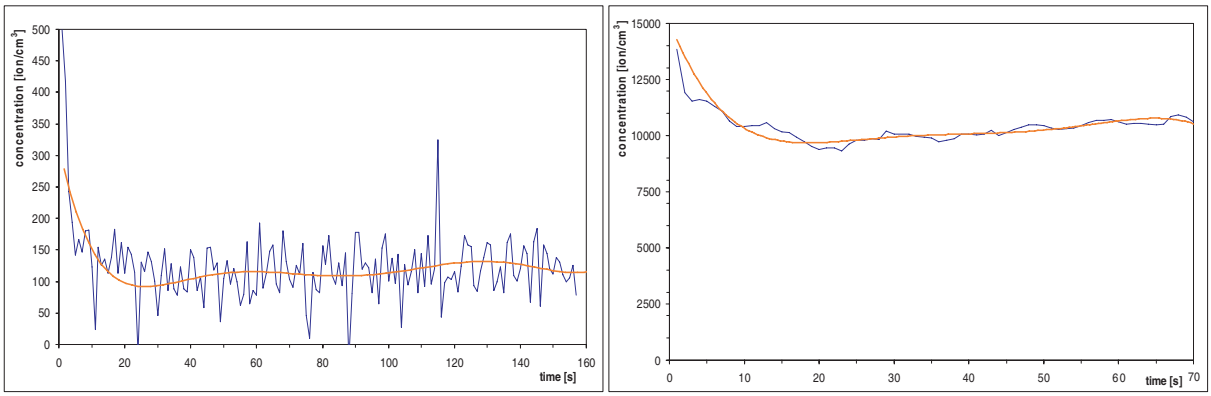

Figure 3: Natural concentration of air ion in the laboratory, left — Before ionization, right — After ionization.

4. CONCLUSION

In cooperation with the Department of Preventive Medicine of Masaryk University in Brno the effect of the concentration of air ions on the number of bacteria was measured in two spaces. An electromagnetically shielded Faraday cage and the space of a DTEEE laboratory were chosen as spaces for the experiment. In the two spaces the natural concentration of air ions was measured using an aspiration capacitor while natural microflora was measured by the aeroscopic method. In the Faraday cage an average air ion density of 900 ions/cm^3 was measured while the value for the living space was 150 ions/cm^3. The high number of air ions in the Faraday cage corresponds with the reduced recombination of ions in a space with markedly reduced electric field. For the above density of air ions and average of 200 bacterial colonies per 10001 of air were measured in the Faraday cage and an average of 275 bacterial colonies per 10001 of air in the living space. After the measurement of natural concentration of air ions, the air in the Faraday cage was ionized by a BIV-06 ionizer for a period of 10 minutes. After the 10-minute ionization the average ion density measured for the cage was 9000 ions/cm^3 and the average number of bacterial colonies was 180 per 10001 of air. The same measurement was carried out in the living space. After 25 minutes of ionization by the BIV-06 ionizer, 10,500 ions/cm^3 were measured while the number of bacterial colonies dropped to an average of 110 per 10001. It follows from the results measured that the density of air ions and the time of ionization affect the number of bacterial colonies in ionized spaces. With an initial ion density of 10,500 ions/cm^3 and an ionization duration of 25 minutes, a 60% drop in bacterial colonies was established in the living space. In the Faraday cage after 10 minutes of ionization, 9000 ions/cm^3 and a 7.5% drop in bacterial colonies were established. The higher drop in the number of bacterial colonies in the living space could have been caused by a longer time of ionization. The measurement results show that ionization reduces the number of bacterial colonies and fungi, which is very favourable to the health of people staying in such an environment.

ACKNOWLEDGMENT

The paper was prepared within the framework of BUT Brno of the Czech Republic and with the support of the research plan MSM 0021630516 and grant GACR 102/09/0314.

REFERENCES

1. Bartusek, K., "Merení spektrálních charakteristik iontových polí," http://www.elektrorevue.cz/clanky/01038/index.html, 2001.
2. Bartusek, K., P. Fiala, T. Jirků, and E. Kroutilova, "Experiments of accuracy air ion field measurement," *PIERS Online*, Vol. 3, No. 8, 1330–1333, 2007.
3. Bartusek, K., "Merení s aspiracním kondenzátorem," http://www.elektrorevue.cz/.
4. Alpin, K. L., "Instrumentation for atmospheric ion measurements," Ph.D. Thesis, University of Reading, August 2000.

A Simple Economical Building FDNR Blocks with Modern Operational Amplifiers

Jiří Sedláček and Zoltán Szabó
BUT Brno, UTEE, Kolejní 2906/4, Brno 612 00, Czech Republic

Abstract— Active RC filters designed using non-cascade filter synthesis method exhibit some advantages — namely low sensitivities. However these parameters are paid on the other hand due to the necessity to use more complicated building blocks which should be able to realize a circuit simulation of required ideal RLC ladder prototype elements (e.g., ideal inductors). That fact unfortunately brings higher filter sensitivities to real parasitic properties of active function blocks.

Usage of new modern active elements (operational amplifiers with high GBW) and possibilities of goal-directed lossy RLC ladder prototypes enables to design optimized ARC filter realizations with simple and economic active building blocks. These simple grounded active selective blocks working only with one active element enable in present time to design active filters with optimized parameters and minimized influence of real active elements for frequency range up 1 MHz. In paper here are some parameters of simple and economic building selective blocks with modern active elements at higher frequencies discussed and briefly new possibilities of ARC lowpass filter optimization in some practical examples presented.

1. INTRODUCTION

In the active filter design based on RLC ladder prototypes many different active selective building blocks are used. By the lowpass (LP) filter design there is used very often the Bruton's transformation, where RLC filter structure is transformed to RCD filter structure. Here are used as basic building blocks active elements named as FDNR (frequency depended negative resistor).

In the present time a new modern active elements working successfully at higher frequency range (voltage OAs with GBW about 1 GHz or CFA amplifiers with high frequency performance) and using the synthesis method based on goal-lossy RLC ladder prototypes [2, 4] enable to design ARC filters for frequency range up 1 MHz with simple and economic selective building blocks (FDNR) working successfully only with one active element (OA).

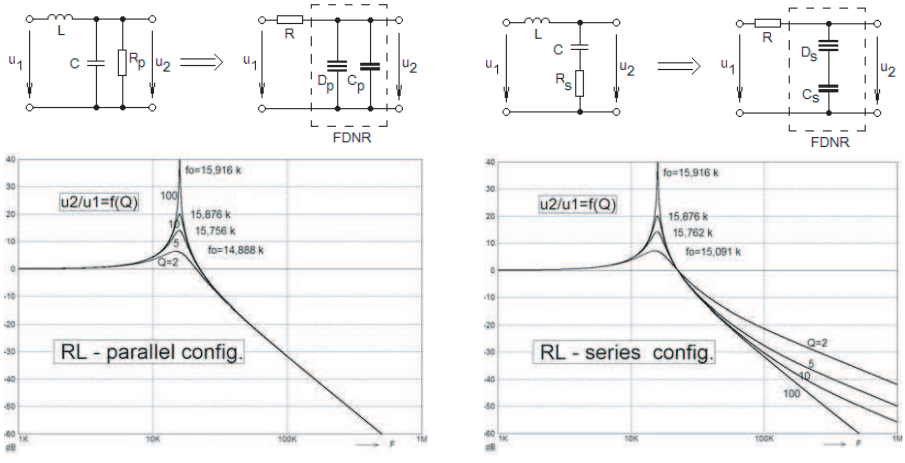

(a) (b)

Figure 1: Real FDNR building blocks and their transfer voltage ratio, (a) circuit with parallel lossy element, (b) circuit with serial lossy element.

2. A SIMPLE ECONOMIC GROUNDED FDNR BUILDING BLOCKS

By LP filter design using Bruton's transformation method there are used a real active building blocks FDNR, which simulate impedance $Z(j\omega)$, or admittance $Y(j\omega)$:

$$\mathbf{Z}(j\omega) = \frac{1}{j\omega C_S} - \frac{1}{\omega^2 D_S} \tag{1}$$

$$\mathbf{Y}(j\omega) = j\omega C_P - \omega^2 D_P \tag{2}$$

It means that the real active block of FDNR can be modelled as serial or parallel connection of ideal FDNR (with parameter D) and lossy kapacitor (with parameter C) how it is seen from Fig. 1.

From figure are also seen the transfer ratios of equivalent lowpass RLC and RDC circuits. The comparison between both types of connections declare advantages of parallel circuits, the serial circuits exhibit some decreasing of transfer slope in stop band which is depending on equivalent Q factor value of circuit. The second effect common for both connections, which is seen from curves,

Table 1: Some practical FDNR circuit connections.

FDNR		
Type	Connection	Remark
I	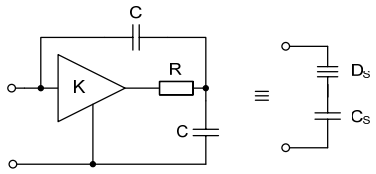 K=1 $D_S = RC^2$ $C_S = C/2$	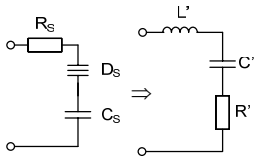 $\omega_0 = \frac{1}{C\sqrt{R_S R}}$ $Q = \frac{1}{2\omega_0 RC} = \frac{1}{2}\sqrt{\frac{R_S}{R}}$
II	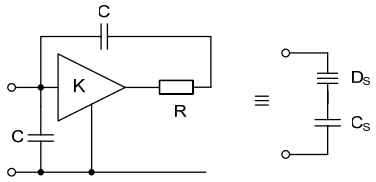 $K = 2$ $D_S = RC^2$ $C_S = C$	$\omega_0 = \frac{1}{C\sqrt{R_S R}}$ $Q = \frac{1}{\omega_0 RC} = \sqrt{\frac{R_S}{R}}$
III	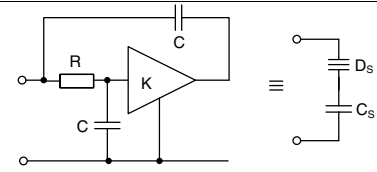 $K = 2$ $D_S = RC^2$ $C_S = C$	$\omega_0 = \frac{1}{C\sqrt{R_S R}}$ $Q = \frac{1}{\omega_0 RC} = \sqrt{\frac{R_S}{R}}$
IV	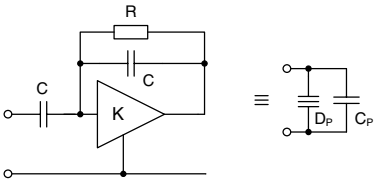 $K = 2$ $D_P = RC^2$ $C_P = C$	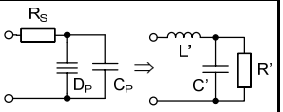 $\omega_0 = \frac{1}{C\sqrt{R_S R}}$ $Q = \omega_0 RC = \sqrt{\frac{R}{R_S}}$
V	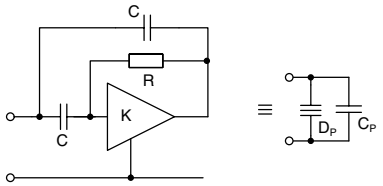 $K \to \infty$ $D_P = RC^2$ $C_P = 2C$	$\omega_0 = \frac{1}{C\sqrt{R_S R}}$ $Q = \frac{\omega_0 RC}{2} = \frac{1}{2}\sqrt{\frac{R}{R_S}}$

is some shift of resonant frequency of transfer function by small value of Q to smaller frequency. This fact must be kept to filter design account in case of small value of Q factor (To the $Q = 10$ the resonant frequency shift is negligible, by $Q = 2$ is about 6%).

Some practical connections of single grounded FDNR blocks working with minimum number of passive elements and only with one active element (e.g., OA) witch are useful by non-cascade active filter design method were analyzed. Using circuit analysis were derived basic parameters of all FDNR building blocks (C, D, ω_w, Q) and these were ordered into Table 1 too.

Presented types of FDNR building blocks can be divided to two groups. How it is seen from Table 1, the circuit connections labelled as FDNR I–III types exhibit equivalent serial lossy elements (C_s), while the types labelled as FDNR IV, V exhibit equivalent parallel lossy elements (C_p).

3. ARC LOWPASS FILTERS DESIGNED USING ECONOMIC FDNR BUILDING BLOCKS

By classical RLC ladder filter design there are usually single or double-sided termination RLC filter prototypes used. In many catalogues are these standard LC ladder prototypes which are using ideal lossless reactive L and C elements wide tabled.

Table 2: The prototypes of Tschebyschev and Butterworth single terminated RLC ladder filter (Fig. 5(b)), normalized to $\omega = 1$ with terminal resistor $r = 1\Omega$ — serial losses R_s.

Type	**o**	$\mathbf{R}_s$	$\mathbf{l}_1$	$\mathbf{c}_1$	$\mathbf{l}_2$	$\mathbf{c}_2$	$\mathbf{l}_3$	$\mathbf{c}_3$	$\mathbf{l}_4$
Butterworth	**5**	-	**1,5443**	**1,6936**	**1,3813**	**0,8940**	**0,3089**	-	-
		0,05	1.3487	1,7132	1.4194	0,9068	0.3355	-	-
		0,10	1,1284	1,7808	1.4705	0,9247	0.3651	-	-
	7	-	**1,5571**	**1,7982**	**1,6583**	**1,3967**	**1,0546**	**0,6557**	**0,2224**
		0,05	1,2676	1,8322	1,6896	1,4187	1,0953	0,6709	0,2439
		0,10	0,8987	2,0297	1,7600	1,4588	1,1472	0,6915	0,2685
Tschebyshev	**5**	-	**2,1489**	**1,3016**	**2,6224**	**1,2502**	**1,7406**	-	-
		0,025	1,8980	1,2964	2,6500	1,2908	1,8893	-	-
		0,050	1,5203	1,3316	2,7802	1,3656	2,0765	-	-
	7	-	**2,1828**	**1,3281**	**2,7143**	**1,3613**	**2,6752**	**1,2665**	**1,7593**
		0,025	1,7158	1,3066	2,7485	1,4008	2,7863	1,3409	1,9799
		0,035	1,1636	1,4291	2,9934	1,4907	2,9220	1,4003	2,1028

Table 3: The prototypes of Tschebyschev and Butterworth single terminated RLC ladder filter (Fig. 5(a)), normalized to $\omega = 1$ with terminal resistor $r = 1\Omega$ — parallel losses R_p.

Type	**o**	$\mathbf{R}_p$	$\mathbf{l}_1$	$\mathbf{c}_1$	$\mathbf{l}_2$	$\mathbf{c}_2$	$\mathbf{l}_3$	$\mathbf{c}_3$	$\mathbf{l}_4$
Butterworth	**5**	-	**1,5443**	**1,6936**	**1,3813**	**0,8940**	**0,3089**	-	-
		6	1.1040	2.1440	1.2400	1.0290	0.3336	-	-
		4	0.9630	2.3700	1.1590	1.0980	0.3450	-	-
		2	0.6928	3.0570	0.9805	1.2820	0.3726	-	-
	7	-	**1,5571**	**1,7982**	**1,6583**	**1,3967**	**1,0546**	**0,6557**	**0,2224**
		6	0.9751	2.5700	1.2700	1.1800	0.9382	0.7628	0.2422
		4	0.8167	2.9500	1.1400	2.0100	0.8876	0.8132	0.2507
		2	0.5438	4.1200	0.8605	2.6100	0.7593	0.9585	0.2725
Tschebyshev	**5**	-	**2,1489**	**1,3016**	**2,6224**	**1,2502**	**1,7406**	-	-
		6	0.8225	2.0080	2.3880	1.5428	2.6329	-	-
		4	0.5053	2.8621	2.2035	1.6660	3.0700	-	-
	7	-	**2,1828**	**1,3281**	**2,7143**	**1,3613**	**2,6752**	**1,2665**	**1,7593**
		6	0.3768	3.5100	2.0600	2.0600	2.5300	1.4700	3.0600
		4	0.2207	5.7500	1.5700	2.3800	2.2200	1.5900	3.8100

In [2] was described a new method how to optimize resulting active filter structures based on classical ladder prototypes using goal-lossy filter prototype design, where the losses are dispersed to the required place of RLC ladder structure.

As an example here are presented resulting normalized parameters of Tchebyshev and Butterworth types LP filters of 5th and 9th filter order with serial (Table 2) and parallel (Table 3) lossy resistors which have been calculated using developed programs based on iterative numerical methods.

Using this goal-directed lossy prototypes can be ARC filters (after Burton's transformation to RCD filter structure) above presented (parallel or serial lossy) FDNR building blocks with very small required resulting Q factor value designed. This method of filter synthesis enables to design ARC filters, which exhibit transfer responses very near to ideal.

4. SOME EXAMPLE OF ARC LOWPASS FILTERS DESIGNED USING ECONOMIC FDNR BUILDING BLOCKS

As the example a lowpass Butterworth filter of 5th order with active building block FDNR V type with parallel lossy (with cutoff frequency $f_c = 1\,\mathrm{MHz}$, terminal resistor $R_L = 1000\,\Omega$, and operational amplifier of AD 8045 (GBW $= 1\,\mathrm{GHz}$) and OPA 656 (GBW $= 400\,\mathrm{MHz}$) has been designed. In Fig. 2(a) is shown the basic lossy RLC prototype, in Fig. 2(b) resulting ARC structure is seen. In Fig. 3, the calculated and measured magnitude responses of resulting filter from Fig. 2(b) are presented. From figure is seen, that in case of higher GBW calculated and measured magnitude responses are very closely to ideal. In case of smaller GBW the bigger slope of filter can be obtained.

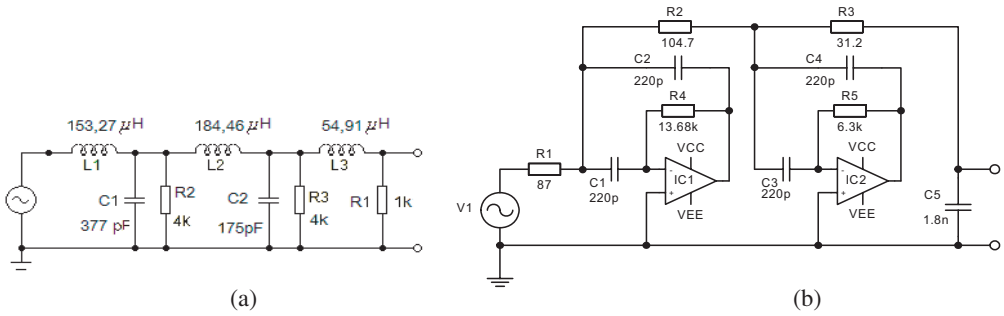

(a) (b)

Figure 2: LP filter of Butterworth type with FDNR V blocks (paralell losses), (a) RLC prototype structure, (b) ARC filter structure.

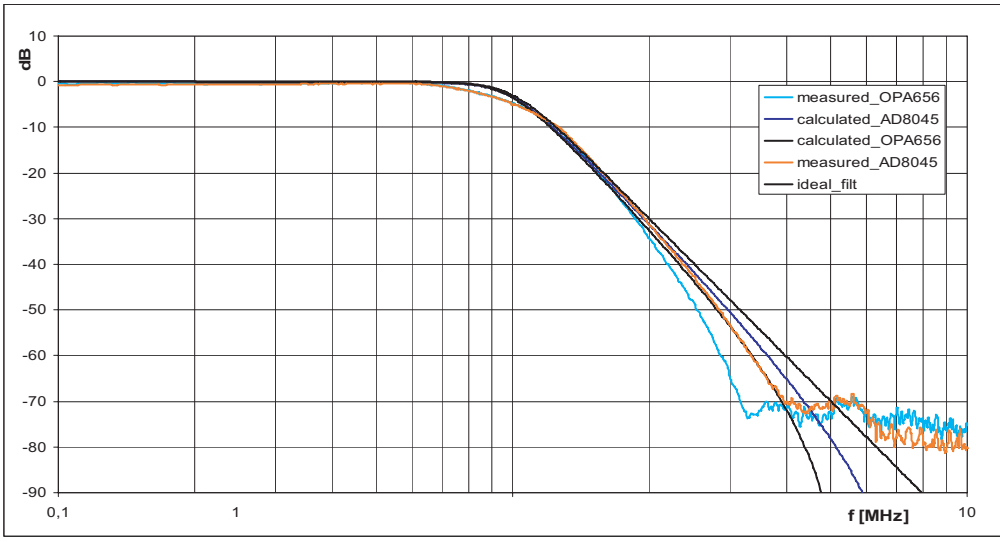

Figure 3: Calculated and measured tranfer responses of LP Butterworth filter type of 5th order designed using (parallel losses) FDNR V type building blocks.

5. CONCLUSION

In this contribution are presented the simple grounded connections of selective building FDNR blocks which enable to realize simple economic active lowpass filters. Performance of presented FDNR blocks at higher frequencies and their parameters required to filter design is widely discussed. One example of LP Butterworth filter type for cutoff frequency $f_0 = 1\,\mathrm{MHz}$ with parallel lossy FDNR blocks and its performance and resulting responses with modern operational amplifiers is here presented. Here described method of filter design based on goal-directed lossy filter RLC prototypes enable to construct economic lowpass filters with minimum number of passive as well of active elements. Thus the described simple economic FDNR blocks can be successfully used in area of filter design and optimization.

ACKNOWLEDGMENT

This work has been supported by the Research Project: MSM 0021630513 and Grant Agency of the Czech Republic under Grant 102/03/1181, 102/04/0442.

REFERENCES

1. Hájek, K. and J. Sedláček, "Kmitočtové filtry," *Vydavatelství BEN Praha*, 2002.
2. Hájek, K. and J. Sedláček, "Lossy LC ladder prototypes and their use for arc filter optimization," *Wseas Transactions on Electronics*, Vol. 2, No. 3, 94–99, July 2005.
3. Martinek, P. and T. Daša, "Evolutionary algoritmes by ARC filter synthesis," *ECCTD 05*, 155–159, Cork, 2005.
4. Hájek, K., V. Michal, J. Sedláček, and M. Steinbauer, "A simple method of goal-directed lossy synthesis and network optimization," *Advances in Electrical and Electronic Engineering*, 249–253, Žilina, 2006.
5. Hájek, K., V. Michal, and J. Sedláček, "Modern operational amplifiers and their degeneracy effects on active filter performance," *IC-SPETO 2006*, 505–507, Gliwice-Ustroň, 2006.

Noise Spectroscopy in Micro-wave Material Structute Examination

R. Kubásek[1], **P. Drexler**[1], **P. Fiala**[1], **and K. Bartušek**[2]

[1]Dept. of Theoretical and Experimental Electrical Engineering
Brno University of Technology, Kolejní 2906/4, Brno 612 00, Czech Republic
[2]Institute of Scientific Instruments, Academy of Sciences of the Czech Republic
Královopolská 147, Brno 612 64, Czech Republic

Abstract— The article describes the basic study of broadband noise signal application in the investigation of materials. The aim is find a metrology method utilizable for the research on metamaterials in the frequency range of about 100 MHz to 10 GHz. The instrumental equipment and other requirements are presented. This research report provides an overview of the current potentialities in the described field and summarizes the aspects necessary for noise spectroscopy.

1. INTRODUCTION

In the complex investigation of material structures for the micro-wave application (tensor and composite character), the properties of materials are studied by means of the classic single-frequency methods, which bring about certain difficulties in the process [1]. In boundary changes with a size close to the wave-length there can occur wrong information concerning the examined objects [2, 3]. One of the possible ways of suppressing the negative sources of signals consists in the use of wide-band signals like white noise, and in researching into the problem of absorption in the examined material [4]. These methods require a source of noise, a receiving and a transmitting antenna, and A/D conversion featuring a large bandwidth; for our puproses, the bandwidth ranged between 0 Hz and 10 GHz. Until recently it had not been possible to realize an A/D converter of the described speed, or devices with the above-mentioned bandwidth. Currently, high-end oscilloscopes are available with a sampling frequency of tens of GSa/s.

2. NOISE SOURCE

For UWB systems, several methods of the generation of short pulses with large bandwidth have been developed to date [5]. However, these singly-iterative processes are not applicable for noise spectroscopy; in this respect, there is a need of a continuous source of noise signal (ideally of white noise) with the given bandwidth. The type of source referred to is currently being produced by certain manufacturers specialized in this field. Importantly, for the noise spectroscopy application we require a comparatively large output power of up to 0 dB/mW; the assumed bandwidth characteristics range up to 10 GHz. Nevertheless, at this point it is appropriate to mention the fact that there occurs the fundamental problem of finding active devices capable of performing signal amplification at this kind of high frequencies. As a matter of fact, our requirements are thus limited by the current status of technology used in the production of commercially available devices; the highest-ranking solution for the bandwidth of up to 10 GHz can be found only up to the maximum of 0 dB/mW.

Our response to the above-discussed problem consisted in an attempt to produce a noise generator in laboratory conditions as, in principle, this type of generator can be considered as sufficient for testing and basic measurement. In view of the price and availability of noise diodes we decided to apply thermal noise on electrical resistance as the basic source of noise. The specific connection is shown in Fig. 1. The first transistor is in the CC configuration, where we require mainly a high input impedance of the amplifier. The thermal noise at the input is given by its input parameters. The generator could operate even without a resistor at the transistor input, yet the unconnected input would cause a substantial deterioration of the stability. The second and the third transistors form a cascade voltage amplifier in the CE configuration. The output impedance of the third amplifier is 50 Ω for its matching to coaxial line.

Figure 2 shows the realization of the tested noise generator; the BFP620 vf transistors were applied. This type of transistor features the characteristic of $f_t = 65$ GHz and the maximum stable amplification of 11 dB at the frequency of 6 GHz. The overall amplification of the two CE amplifiers in cascade for the output power of 0 dB/mW would have to approximate the value of 10000, and there is no hf transistor available for this kind of stable amplification. Therefore, for the stable noise generator we have to accept a lower output power.

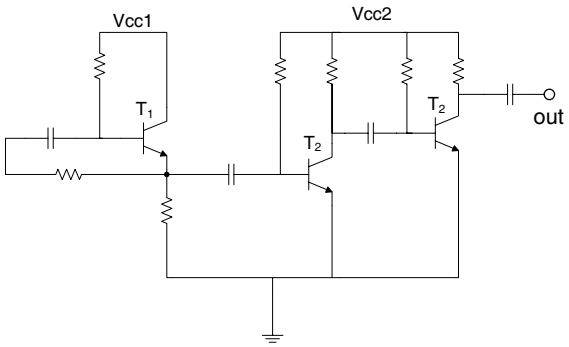

Figure 1: The noise generator configuration diagram.

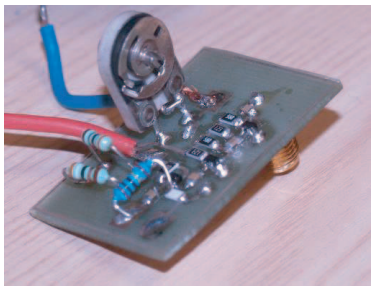

Figure 2: The noise generator realization.

Figure 3 shows the waveforms and the output voltage spectrum of the noise generator for three different working points. Figs. 3(a) and 3(b) display the generator output voltage waveform and spectrum for the situation when no large oscillations are yet measurable that normally cause the transistor closing and the subsequent transient process. There occur moderate oscillations, which are visible in the spectrum; their amplitude and frequency are subject to chaotic shifitng and the output voltage can be considered as stochastic. However, we can not label this as white noise. Figs. 3(c) and 3(d) show a situation when, owing to large amplification, there already occur oscillations causing the transistor closing that is well noticeable in the waveform in the time of 2 µs. This type of pulses are randomly repeated within the time range of 10 to 30 µs. In the spectrum, they will upgrade the frequency range in the field of 20 MHz. In applying the low-pass filter we would obtain a signal that could be regarded as stochastic.

The last one of the described situations is given in Figs. 3(e) and 3(f), this situation is related to the operating field with the maximum amplification adjustable for the transistor safe operation region. The third transistor already randomly passes between the conditions of "closed" and "open" and the linear operating region. The closing interval ranges from units of ns to several tens of ns. No matter how stochastic this type of signal may be, still it rather models extreme shot noise combined with coloured noise. Its spectrum is the densest and importantly, the most stable of all the situations. For all measurement, spectrum analyzers noise background was −60 dB/mW.

3. ANTENNA

The purpose of the transmitting antenna connected to the noise generator output is to form an electromagnetic wave. As a matter of fact, in the field of noise we indeed have to consider a whole spectrum of electromagnetic waves, and it is not possible to define the antenna proximity area. In addition to this, most principles or rules related to the configuration of antennas have to be regarded as void here. The electromagnetic wave is let to impinge on the investigated material and the reflected or partially absorbed wave is then received through the receiving antenna, to the output of which an oscilloscope has been connected. This type of measurement configuration can be seen in Fig. 4.

Both antennas ought to feature a large bandwidth with, if possible, constant amplitude and defined radiaton pattern. In this respect, let us mention the fact that there exist approaches to the design of antennas that come close to the broadband requirements of noise spectroscopy. Suitable solutions include, for example, the spiral fractal antenna or the planar log-periodic antenna. The designed planar log-periodic antenna is applicable for transmission within the frequency range of between 100 MHz and 10 GHz; its real characteristics or qualities depend heavily on the quality of the design practical implementation. Fig. 5(a) shows the realization of a planar log-periodic antenna. The numerical design was performed for currently available materials and its evaluation exhibited the undulating module frequency characteristics. The antenna realization experiments using the PCB showed, above all, troubled transmission at higher frequencies from 2 GHz and problematic modification of the feeder. Other antenna designs are directed towards applying the fractal spiral version.

The experiments and spectroscopy tests will be performed in an anechoic laboratory. We have selected a system of compelementing the Faraday cage shielding with absorbers of electromagnetic waves. The absorbers were designed for the range of 100 MHz–10 GHz with dampening below 35 dB. Thanks to the shielded and separated chamber, the external environment should not affect

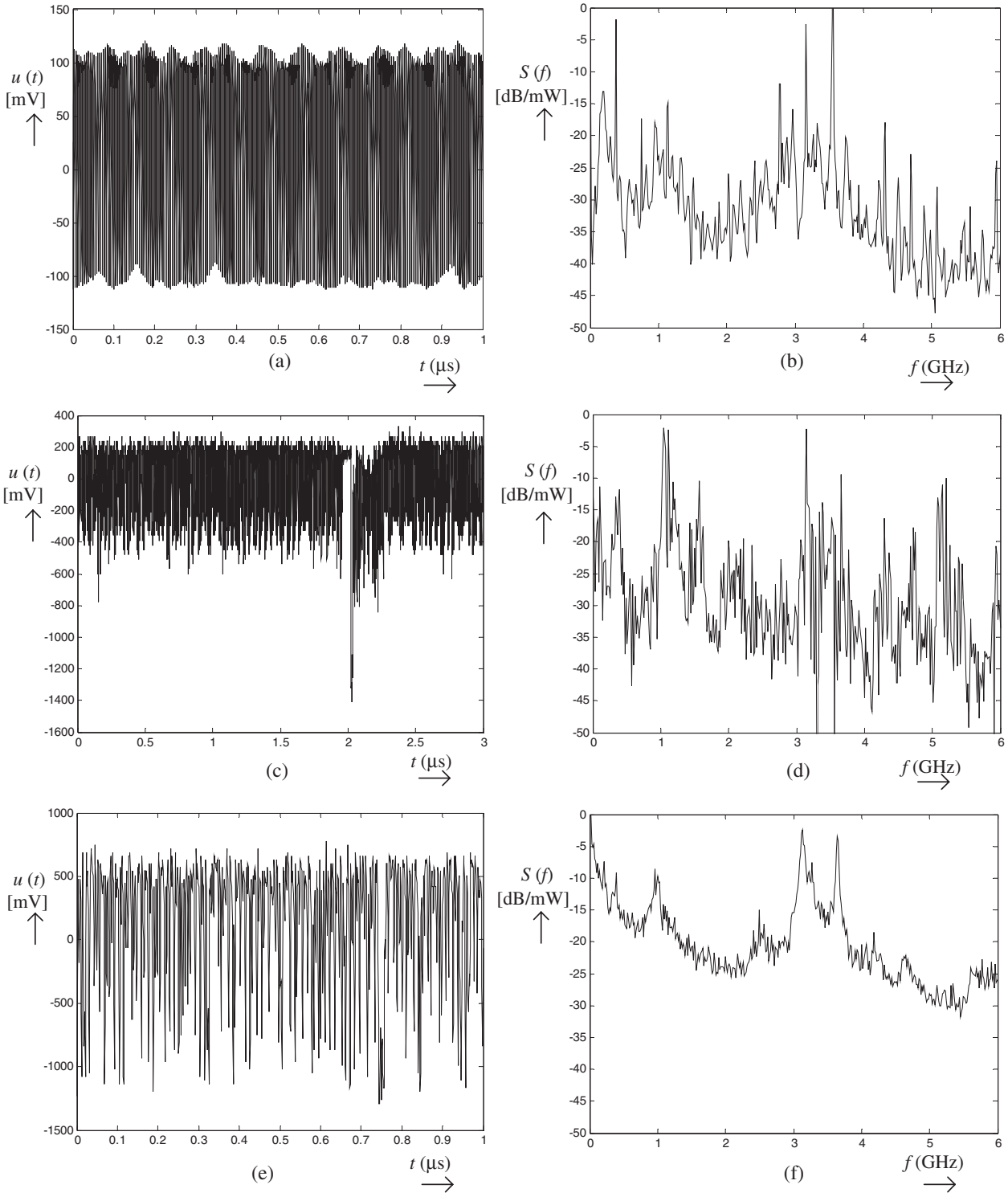

Figure 3: The waveform and spectrum of the noise generator output for three different working points.

the internal part of measurement, and the complemented absorbers will enable us to lower foreign signals to a level of below −60 dB/mW. Thus, the measurement will not be affected by the outside environment of external electromagnetic sources like mobile phone and WiFi network signals or stationary waves and reflection within the Faraday cage.

4. DIGITAL RECIVER

The process of sensing (scanning) has to be necessarily supported by a costly high-end digital oscilloscope featuring a bandwidth of about 10 GHz. Here, the limiting factor is clearly represented

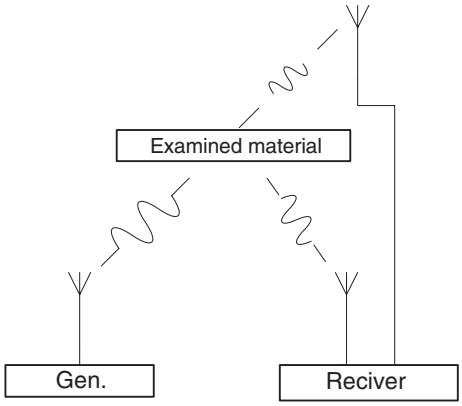

Figure 4: The experiment configuration.

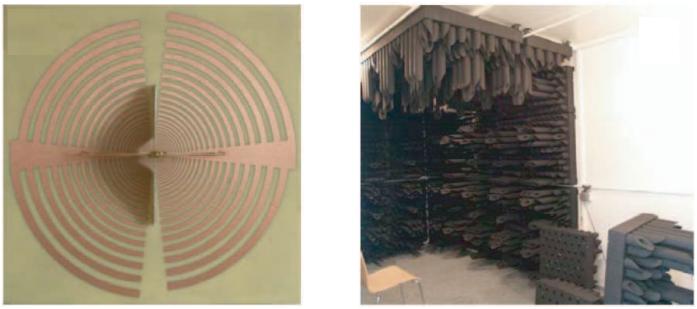

(a) (b)

Figure 5: (a) Planar log-periodic antenna, (b) Faraday cage.

by the final price, unfortunately, it is not possible to realize this type of fast A/D converter using the researchers' own means and facilities. In the assessment of spectral properties of materials, the use of a spectral analyzer is normally a fully sufficient and financially effective method. This method, however, can not be utilized for the assessment of a system via the input-output technique, for the correlation analysis, or for other techniques utilizing the measured signal waveform.

5. CONCLUSION

The research paper provides an elementary overview and description of laboratory equipment for the realization of noise spectroscopy measurement. In the text, it is generally noted that the search of an applicable source of noise will be markedly problematic in terms of the output power, which is normally low for broadband applications. Yet it is also noted that, for the laboratory tasks, considerably lower values of transmission power are sufficient for broadband systems in comparison with their "narrowband" counterparts. The designing of a broadband antenna is, to a great extent, an uneasy-to-solve problem, and the requirements placed on the width of the antenna transmitted band are very intensive. Another parameter to be mentioned in this respect is the linear transmission characteristics depending on the frequency. Noise spectroscopy for the frequency band of between 100 MHz and 10 GHz is realizable using the current means of technology.

ACKNOWLEDGMENT

This work was supported within the framework of research plan MSM 0021630516 and project of the Grant Agency of the Czech Republic No. 102/09/0314.

REFERENCES

1. Maslovski, S., S. Tretyakov, and P. Alitalo, "Near-field enhancement and imaging in double planar polariton-resonant structures," *J. Appl. Phys.*, Vol. 96, 1293, 2004.
2. Freire, M. and R. Marques, "Near-field imaging in the megahertz range by strongly coupled magnetoinductive surfaces: Experiment and ab initio analysis," *J. Appl. Phys.*, Vol. 100, 063105, 2006.
3. Machac, J., P. Protiva, and J. Zehentner, "Isotropic epsilon-negative particles," *2007 IEEE MTT-S Int. Microwave Symp. Dig.*, Honolulu, USA TH4D-03, June 2007.
4. Fiala, P., E. Gescheidtova, and T. Jirku, "Tuned structures for special THz applications," *PIERS Proceedings*, 151–155, Beijing, China, March 23–27, 2009.
5. Protiva, P., J. Mrkvica, and J. Machác, "Universal generator of ultra-wideband pulses," *Radioengineering*, Vol. 17, No. 4, 74–79, 2008.
6. Maslovski, S., S. Tretyakov, and P. Alitalo, "Near-field enhancement and imaging in double planar polariton-resonant structures," *J. Appl. Phys.*, Vol. 96, 1293, 2004.

Integral Equation Method in the Theory of Dielectric Waveguides

E. M. Karchevskiy
Kazan State University, Russia

Abstract— The eigenvalue problems for generalized natural modes of an inhomogeneous dielectric waveguide without a sharp boundary and a step-index dielectric waveguide with smooth boundary of cross-section are formulated as problems for the set of time-harmonic Maxwell equations with partial radiation conditions (Sveshnikov radiation conditions) at infinity in the cross-sectional plane. The original problems by integral equations method are reduced to nonlinear spectral problems with Fredholm integral operators. Theorems on spectrum localization are proved, and then it is proved that the sets of all eigenvalues of the original problems can only be some sets of isolated points on the Reimann surface, ant it also proved that each eigenvalue depends continuously on the frequency and dielectric permittivity and can appear and disappear only at the boundary of the Reimann surface. The Galerkin method for numerical calculations of the generalized natural modes are proposed, and the convergence of the method is proved. Some results of numerical experiments are discussed.

1. INTRODUCTION

Optical fibers are dielectric waveguides (DWs), i.e., regular dielectric rods, having various cross sectional shapes, and where generally the dielectric permittivity may vary in the waveguide's cross section [1]. Although existing technologies often result in a dielectric permittivity that is anisotropic, frequently it is possible to assume that the fiber is isotropic [2], which is the case investigated in this work. The study of the source-free electromagnetic fields, called natural modes, that can propagate on DWs necessitates that longitudinally the rod extend to infinity. Since often DWs are not shielded, the medium surrounding the waveguide transversely forms an unbounded domain, typically taken to be free space. This fact plays an extremely important role in the mathematical analysis of natural waveguide modes, and brings into consideration a variety of possible formulations. Each different formulation can be cast as an eigenvalue problem for the set of time-harmonic Maxwell equations, but they differ in the form of the condition imposed at infinity in the cross-sectional plane, and hence in the functional class of the natural-mode field. This also restricts the localization of the eigenvalues in the complex plane of the eigenparameter [3]. All of the known natural-mode solutions (i.e., surface guided modes, leaky modes, and complex modes) satisfy the partial radiation conditions at infinity (see, for example, [4]), which firstly were originally introduced by A. G. Sveshnikov [5] for a scattering problem. The partial radiation conditions in waveguiding problems are connected with the fact that propagation constants β may be complex and may be generally considered on the appropriate logarithmic Reimann surface [6, 7]. For real propagation constants on the principal ("proper") sheet of this Reimann surface, one can reduce the partial radiation conditions to either the Sommerfeld radiation condition or to the condition of exponential decay. The partial radiation conditions may be considered as a generalization of the Sommerfeld radiation condition and can be applied for complex propagation constants. This conditions may also be considered as the continuation of the Sommerfeld radiation condition from a part of the real axis of the complex parameter β to the appropriate logarithmic Reimann surface [8].

2. GENERALIZED NATURAL MODES OF A STEP-INDEX DIELECTRIC WAVEGUIDE

Let the three-dimensional space be occupied by an isotropic source-free medium, and let the dielectric permittivity be prescribed as a positive real-valued function $\varepsilon = \varepsilon(x)$ independent of the longitudinal coordinate and equal to a constant $\varepsilon_\infty > 0$ outside a cylinder. In this section we consider the generalized natural modes of an step-index optical fiber and suppose that the dielectric permittivity is equal to a constant $\varepsilon_+ > \varepsilon_\infty$ inside the cylinder. The axis of the cylinder is parallel to the longitudinal coordinate, and its cross section is a bounded domain Ω_i with a twice continuously differentiable boundary γ (see Fig. 1). The domain Ω_i is a subset of a circle with radius R_0. Denote by Ω_e the unbounded domain $\Omega_e = \mathbb{R}^2 \setminus \overline{\Omega}_i$. Denote by U the space of complex-valued continuous and continuously differentiable in $\overline{\Omega}_i$ and $\overline{\Omega}_e$, twice continuously differentiable in Ω_i and Ω_e functions. Denote by Λ the Riemann surface of the function $\ln \chi_\infty(\beta)$, where $\chi_\infty = \sqrt{k^2\varepsilon_\infty - \beta^2}$. Here $k^2 = \omega^2\varepsilon_0\mu_0$, ω is a given radian frequency; ε_0, μ_0 are the free-space dielectric and magnetic

constants, respectively. Denote by Λ_0 the principal ("proper") sheet of this Riemann surface, which is specified by the condition $\mathrm{Im}\chi_\infty(\beta) \geq 0$.

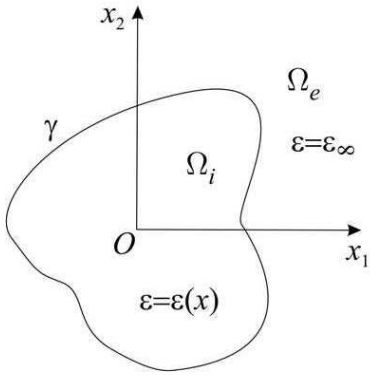

Figure 1: A schematic waveguide's cross-section.

A nonzero vector $\{\mathrm{E}, \mathrm{H}\} \in U^6$ is referred to as generalized eigenvector (or eigenmode) of the problem corresponding to an eigenvalue $\beta \in \Lambda$ if the following relations are valid [9]:

$$\mathrm{rot}_\beta \mathrm{E} = i\omega\mu_0 \mathrm{H}, \quad \mathrm{rot}_\beta \mathrm{H} = -i\omega\varepsilon_0\varepsilon \mathrm{E}, \quad x \in \mathbb{R}^2 \setminus \gamma, \tag{1}$$

$$\nu \times \mathrm{E}^+ = \nu \times \mathrm{E}^-, \quad x \in \gamma, \tag{2}$$

$$\nu \times \mathrm{H}^+ = \nu \times \mathrm{H}^-, \quad x \in \gamma, \tag{3}$$

$$\begin{bmatrix} \mathrm{E} \\ \mathrm{H} \end{bmatrix} = \sum_{l=-\infty}^{\infty} \begin{bmatrix} \mathrm{A}_l \\ \mathrm{B}_l \end{bmatrix} H_l^{(1)}(\chi_\infty r) \exp(il\varphi), \quad r \geq R_0. \tag{4}$$

Here differential operator rot_β is obtained from usual operator by replacing generating waveguide line derivative with $i\beta$ multiplication; and $H_l^{(1)}(z)$ is the Hankel function of the first kind and index l. The conditions (4) are the the partial radiation conditions.

Theorem 1 (see [9]). *The imaginary axis $\mathbb{I}$ and the real axis $\mathbb{R}$ of the sheet Λ_0 except the set $G = \left\{\beta \in \mathbb{R} : k^2\varepsilon_\infty < \beta^2 < k^2\varepsilon_+\right\}$ are free of the eigenvalues of the problem (1)–(4). Surface and complex eigenmodes correspond to real eigenvalues $\beta \in G$ and complex eigenvalues $\beta \in \Lambda_0$, respectively. Leaky eigenmodes correspond to complex eigenvalues β belonging to an "improper" sheet of Λ for which $\mathrm{Im}\chi_\infty(\beta) < 0$.*

The results of the theorem 1 generalize the well known results on the spectrum localization of the step-index circular dielectric waveguide, which were obtained by separation of variables method (see, for example, [10]).

We use the representation of the eigenvectors of problem (1)–(4) in the form of the single-layer potentials u and v:

$$\mathrm{E}_1 = \frac{i}{k^2\varepsilon - \beta^2}\left(\mu_0\omega\frac{\partial v}{\partial x_2} + \beta\frac{\partial u}{\partial x_1}\right), \quad \mathrm{E}_2 = \frac{-i}{k^2\varepsilon - \beta^2}\left(\mu_0\omega\frac{\partial v}{\partial x_1} - \beta\frac{\partial u}{\partial x_2}\right), \quad \mathrm{E}_3 = u, \tag{5}$$

$$\mathrm{H}_1 = \frac{i}{k^2\varepsilon - \beta^2}\left(\beta\frac{\partial v}{\partial x_1} - \varepsilon_0\varepsilon\omega\frac{\partial u}{\partial x_2}\right), \quad \mathrm{H}_2 = \frac{i}{k^2\varepsilon - \beta^2}\left(\beta\frac{\partial v}{\partial x_2} + \varepsilon_0\varepsilon\omega\frac{\partial u}{\partial x_1}\right), \quad \mathrm{H}_3 = v, \tag{6}$$

$$\begin{bmatrix} u(x) \\ v(x) \end{bmatrix} = \frac{i}{4}\int_\gamma H_0^{(1)}\left(\sqrt{k^2\varepsilon_{+/\infty} - \beta^2}\,|x-y|\right)\begin{bmatrix} f_{+/\infty}(y) \\ g_{+/\infty}(y) \end{bmatrix} dl(y), \quad x \in \Omega_{i/e}, \tag{7}$$

where unknown densities $f_{+/\infty}$ and $g_{+/\infty}$ belong to the space of Hölder continuous functions $C^{0,\alpha}$. The original problem (1)–(4) by single-layer potential representation (5)–(7) is reduced [9] to a nonlinear eigenvalue problem for a set of singular integral equations at the boundary γ. This problem has the operator form

$$A(\beta)w \equiv (I + B(\beta))w = 0, \tag{8}$$

where I is the identical operator in the Banach space $W = (C^{0,\alpha})^4$ and $B(\beta) : W \to W$ is a compact operator consists particularly of the following boundary singular integral operators:

$$Lp = -\frac{1}{2\pi}\int_0^{2\pi} \ln|\sin\frac{t-\tau}{2}|p(\tau)d\tau, \quad t \in [0,2\pi], \quad L : C^{0,\alpha} \to C^{1,\alpha}, \tag{9}$$

$$Sp = \frac{1}{2\pi}\int_0^{2\pi} \mathrm{ctg}\frac{\tau-t}{2}p(\tau)d\tau + \frac{i}{2\pi}\int_0^{2\pi} p(\tau)d\tau, \quad t \in [0,2\pi], \quad S : C^{0,\alpha} \to C^{0,\alpha}. \tag{10}$$

The original problem (1)–(4) is spectrally equivalent [9] to the problem (8). Namely, suppose that $w \in W$ is an eigenvector of the operator-valued function $A(\beta)$ corresponding to an eigenvalue $\beta \in \Lambda_0 \setminus D$, $D = \{\beta \in \mathbb{I}\} \bigcup \{\beta \in \mathbb{R} : \beta^2 < k^2\varepsilon_\infty\}$. Then using this vector we can construct the densities of the single-layer potential representation (5)–(7) of an eigenmode $\{\mathrm{E},\mathrm{H}\} \in U^6$ of the problem (1)–(4), corresponding to the same eigenvalue β. For other side, any eigenmode of the problem (1)–(4), corresponding to an eigenvalue $\beta \in \Lambda_0 \setminus D$ can be represented in the form of single-layer potentials. The densities of this potentials construct an eigenvector $w \in W$ of the operator-valued function $A(\beta)$ corresponding to the same eigenvalue β.

Theorem 2 (see [9]). *For each $\beta \in \{\beta \in \mathbb{R} : \beta^2 \geq k^2\varepsilon_+\}$ the operator $A(\beta)$ has the bounded inverse operator. The set of all eigenvalues β of the operator-valued function $A(\beta)$ can be only a set of isolated points on Λ. Each eigenvalue β depends continuously on $\omega > 0$, $\varepsilon_+ > 0$, and $\varepsilon_\infty > 0$ and can appear and disappear only at the boundary of Λ, i.e., at $\beta = \pm k\sqrt{\varepsilon_\infty}$ and at infinity.*

The results of the theorem 2 generalize the well known results on the dependence of the propagation constants β of the step-index circular dielectric waveguide on the wave number k and dielectric permittivity ε (see, for example, [10]).

3. GENERALIZED NATURAL MODES OF AN INHOMOGENEOUS WAVEGUIDE

In this section we consider the generalized natural modes of an inhomogeneous optical fiber without a sharp boundary. Let the dielectric permittivity ε belongs to the space $C^2(\mathbb{R}^2)$ of twice continuously differentiable in $\mathbb{R}^2$ functions. Denote by ε_+ the maximum of the function ε in the domain Ω_i, let $\varepsilon_+ > \varepsilon_\infty > 0$. A nonzero complex vector $\{\mathrm{E},\mathrm{H}\} \in (C^2(\mathbb{R}^2))^6$ is referred to as generalized eigenvector (or eigenmode) of the problem corresponding to an eigenvalue $\beta \in \Lambda$ if the following relations are valid [3]:

$$\mathrm{rot}_\beta \mathrm{E} = i\omega\mu_0\mathrm{H}, \quad \mathrm{rot}_\beta \mathrm{H} = -i\omega\varepsilon_0\varepsilon\mathrm{E}, \quad x \in \mathbb{R}^2, \tag{11}$$

$$\begin{bmatrix}\mathrm{E}\\ \mathrm{H}\end{bmatrix} = \sum_{l=-\infty}^{\infty} \begin{bmatrix}\mathrm{A}_l\\ \mathrm{B}_l\end{bmatrix} H_l^{(1)}(\chi_\infty r)\exp(il\varphi), \quad r \geq R_0. \tag{12}$$

Theorem 3 (see [3]). *The imaginary axis $\mathbb{I}$ and the real axis $\mathbb{R}$ of the sheet Λ_0 except the set $G = \left\{\beta \in \mathbb{R} : k^2\varepsilon_\infty < \beta^2 < k^2\varepsilon_+\right\}$ are free of the eigenvalues of the problem (11), (12). Surface and complex eigenmodes correspond to real eigenvalues $\beta \in G$ and complex eigenvalues $\beta \in \Lambda_0$, respectively. Leaky eigenmodes correspond to complex eigenvalues β belonging to an "improper" sheet of Λ for which $\mathrm{Im}\chi_\infty(\beta) < 0$.*

If vector $\{\mathrm{E},\mathrm{H}\} \in (C^2(\mathbb{R}^2))^6$ is an eigenvector of problem (11), (12) corresponding to an eigenvalue $\beta \in \Lambda$, then (see [3])

$$\mathrm{E}(x) = k^2\int_{\Omega_i}(\varepsilon(y)-\varepsilon_\infty)\,\Phi(\beta;x,y)\mathrm{E}(y)dy + \mathrm{grad}_\beta\int_{\Omega_i}\left(\mathrm{E},\varepsilon^{-1}\mathrm{grad}\varepsilon\right)(y)\Phi(\beta;x,y)dy, \quad x \in \mathbb{R}^2, \tag{13}$$

$$\mathrm{H}(x) = -i\omega\varepsilon_0\mathrm{rot}_\beta\int_{\Omega_i}(\varepsilon(y)-\varepsilon_\infty)\,\Phi(\beta;x,y)\mathrm{E}(y)dy, \quad x \in \mathbb{R}^2. \tag{14}$$

Using the integral representation (13) for $x \in \Omega_i$ we obtain a nonlinear eigenvalue problem for integral equation on the domain Ω_i. This problem has the operator form

$$A(\beta)\mathrm{F} \equiv (I - B(\beta))\mathrm{F} = 0, \tag{15}$$

where the operator $B(\beta) : (L_2(\Omega_i))^3 \to (L_2(\Omega_i))^3$ satisfies the right side of the integral representation (13) for $x \in \Omega_i$. For any $\beta \in \Lambda$ the operator $B(\beta)$ is compact [3].

It was proved in the paper [3] that the original problem (11), (12) is spectrally equivalent to problem (15). Namely, suppose that $\{\mathrm{E}, \mathrm{H}\} \in (C^2(\mathbb{R}^2))^6$ is an eigenmode of problem (11), (12) corresponding to an eigenvalue $\beta \in \Lambda$. Then $\mathrm{F} = \mathrm{E} \in [L_2(\Omega_i)]^3$ is an eigenvector of the operator-valued function $A(\beta)$ corresponding to the same eigenvalue β. Suppose that $\mathrm{F} \in [L_2(\Omega_i)]^3$ is an eigenvector of the operator-valued function $A(\beta)$ corresponding to an eigenvalue $\beta \in \Lambda$, and also suppose that the same number β is not an eigenvalue of the following problem:

$$\left[\Delta + \left(k^2\varepsilon - \beta^2\right)\right] u = 0, \quad x \in \mathbb{R}^2, \quad u \in C^2(\mathbb{R}^2), \tag{16}$$

$$u = \sum_{l=-\infty}^{\infty} a_l H_l^{(1)}\left(\chi_\infty r\right) \exp\left(il\varphi\right), \quad r \geq R_0. \tag{17}$$

Let $\mathrm{E} = B(\beta)\mathrm{F}$ and $\mathrm{H} = (i\omega\mu_0)^{-1}\mathrm{rot}_\beta \mathrm{E}$ for $x \in \mathbb{R}^2$. Then $\{\mathrm{E}, \mathrm{H}\} \in (C^2(\mathbb{R}^2))^6$, and $\{\mathrm{E}, \mathrm{H}\}$ is an eigenvector of the original problem (11), (12) corresponding to the same eigenvalue β.

Theorem 4 (see [3]). *For each $\beta \in \{\beta \in \mathbb{R} : \beta^2 \geq k^2\varepsilon_+\}$ the operator $A(\beta)$ has the bounded inverse operator. The set of all eigenvalues β of the operator-valued function $A(\beta)$ can be only a set of isolated points on Λ. Each eigenvalue β depends continuously on $\omega > 0$, $\varepsilon_+ > 0$, and $\varepsilon_\infty > 0$ and can appear and disappear only at the boundary of Λ, i.e., at $\beta = \pm k\sqrt{\varepsilon_\infty}$ and at infinity.*

4. NUMERICAL METHOD

Describe a projection method for numerical solution of the problem (8). Denote by N the set of integers. We use the representation of the approximate eigenvector of the operator-valued function $A(\beta)$ in the form

$$w_n = (w_n^{(j)})_{j=1}^4, \quad w_n^{(j)}(t) = \sum_{k=-n}^{n} \alpha_k^{(j)} \exp(ikt), \ n \in N, \ j = 1, 2, 3, 4.$$

We look for unknown coefficients $\alpha_k^{(j)}$ by Galerkin method

$$\int_0^{2\pi} (Aw_n)^{(j)}(t) \exp\left(-ikt\right) dt = 0, \ k = -n, \ldots, n, \ j = 1, 2, 3, 4.$$

The trigonometric functions $\exp(ikt)$ are the orthogonal eigenfunctions of the singular integral operators $L : C^{0,\alpha} \to C^{1,\alpha}$ and $S : C^{0,\alpha} \to C^{0,\alpha}$, corresponding to the following eigenvalues:

$$\lambda_m^{(L)} = \{\ln 2 \text{ if } m = 0, \ (2|m|)^{-1} \text{ if } m \neq 0\},$$
$$\lambda_m^{(S)} = \{i \text{ if } m = 0, \ i\,\mathrm{sign}(m) \text{ if } m \neq 0\}$$

for the operators L and S respectively. Hence, the action of the main (singular) parts of the integral operators in (8) on the basis functions is expressed in the explicit form.

Denote by W_n^T the set of all trigonometric polynomials of the orders up to n. Denote by $W_n \subset W$ the space of the elements $w_n = (w_n^{(j)})_{j=1}^4$, where $w_n^{(j)} \in W_n^T$. Using the Galerkin method for numerical solution of the problem (8), we get finite-dimensional nonlinear spectral problem

$$A_n(\beta) w_n = 0, \quad A_n : W_n \to W_n. \tag{18}$$

Theorem 5 (see [11]). *If β_0 belongs to the spectrum $\sigma(A)$ of the operator-valued function $A(\beta)$, then there exists some sequence $\{\beta_n\}_{n\in N}$ with $\beta_n \in \sigma(A_n)$, that $\beta_n \to \beta_0$, $n \in N$. If $\{\beta_n\}_{n\in N}$ is a sequence such that $\beta_n \in \sigma(A_n)$ and $\beta_n \to \beta_0 \in \Lambda$, then $\beta_0 \in \sigma(A)$. If $\beta_n \in \sigma(A_n)$, $A_n(\beta_n)w_n = 0$, and $\beta_n \to \beta_0 \in \Lambda$, $w_n \to w_0$, $n \in N$, $\|w_n\| = 1$ then $\beta_0 \in \sigma(A)$ and $A(\beta_0)w_0 = 0$, $\|w_0\| = 1$.*

Figure 2 shows the dispersion curves for the complex modes (on the left) and for the surface guided modes (on the right) of the step-index waveguides of circular and square cross-section. The numerical results obtained by Galerkin method marked by circles and by squares on the left of the Fig. 2. The dispersion curves for circular waveguide are plotted here by solid line, $\widetilde{\beta} = \beta/(k\sqrt{\varepsilon_\infty})$ and $V = kR\sqrt{\varepsilon_+ - \varepsilon_\infty}$. The right side of the Fig. 2 compares the experimental data [12] for surface waves of square waveguide (marked by squares) with our numerical results (solid lines). Here a is a half of the square's side.

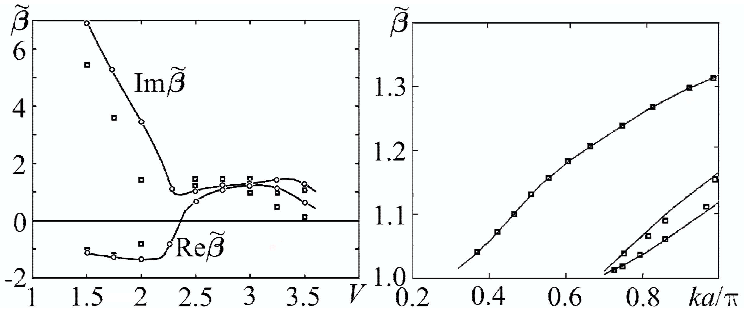

Figure 2: The dispersion curves for the complex modes (on the left) and surface guided modes (on the right) of the step-index waveguides of circular and square cross-section.

ACKNOWLEDGMENT

The work was supported by the Russian Foundation for Basic Research, grant 09-01-97009.

REFERENCES

1. Marcuse, D., *Theory of Dielectric Optical Waveguides*, Academic Press, New York, 1974.
2. Snyder, A. W. and D. Love, *Optical Waveguide Theory*, Chapman and Hall, London, 1983.
3. Kartchevski, E. M., A. I. Nosich, and G. W. Hanson, "Mathematical analysis of the generalized natural modes of an inhomogeneous optical fiber," *SIAM J. Appl. Math.*, Vol. 65, No. 6, 2033–2048, 2005.
4. Dautov, R. Z. and E. M. Karchevskii, *Integral Equations Method and Exact Nonlocal Boundary Conditions in the Theory of Dielectric Waveguides*, Kazan State University, Kazan, 2009 [in Russian].
5. Sveshnikov, A. G. "The principle of limit absorption for a waveguide," *Dokl. AN SSSR*, Vol. 80, No. 3, 345–347, 1951 [in Russian].
6. Il'inskii, A. S. and Yu. V. Shestopalov, *Application of the Methods of Spectral Theory in the Problems of Wave Propagation*, Moscow State University Press, Moscow, 1989 [in Russian].
7. Nosich, A. I. "Radiation conditions, limiting absorption principle, and general relations in open waveguide scattering," *Journal of Electromagnetic Waves and Applications*, Vol. 8, No. 3, 329–353, 1994.
8. Shestopalov, Yu. V., Yu. G. Smirnov, and E. V. Chernokozhin, *Logarithmic Integral Equations in Electromagnetics*, VSP, Leiden, The Netherlands, 2000.
9. Karchevskii, E. M. "The fundamental wave problem for cylindrical dielectric waveuides," *Differential Equations*, Vol. 36, 1109–1111, 2000.
10. Veselov, G. N. and S. B. Raevskiy, "Layered metal-dielectric waveguides," *Radio i Sviaz'*, Moscow, 1988 [in Russian].
11. Karchevskii, E. M. "Mathematical analysis and numerical modeling of the guided modes of the step-index optical fibers," *SIAM Proc. in Applied Mathematics*, Vol. 102, 414–419, 2000.
12. Goncharenko, A. M. and V. A. Karpenko, "The foundations of the theory of optical waveguides," *Nauka i Tekhnika*, Minsk, 1983 [in Russian].

Exact Nonlocal Boundary Conditions in the Theory of Dielectric Waveguides

R. Z. Dautov and E. M. Karchevskiy
Kazan State University, Russia

Abstract— The original problem in an unbounded domain is reduced to a linear parametric eigenvalue problem in a circle, which is convenient for numerical solution. The examination of the solvability of this problem is based on the spectral theory of compact self-adjoint operators. The existence of surface guided waves is proved, and properties of the dispersion curves are investigated. An algorithm for the numerical solution of the problem based on the finite element method is proposed. The convergence of the numerical method is proved. Numerical results are discussed.

1. INTRODUCTION

Optical waveguides are dielectric cylindrical structures that can conduct electromagnetic energy in the visible and infrared parts of the spectrum. The waveguides used in optical communication are flexible fibers made of transparent dielectrics. The cross section of a waveguide usually consists of three regions: the central region (core) is surrounded by a cladding which, in turn, is surrounded by a protective coating. The dielectric permittivity ε of the core can be constant or can vary over the cross section; the dielectric permittivity of the cladding is usually positive constant (denote it by ε_∞). The coating is optically isolated from the core; for this reason, it is usually neglected in mathematical models, and it is assumed that the cladding is unbounded from the outside.

We use the classical model (see [1]), in which the waveguide is assumed to be unbounded and linearly isotropic. A mathematical analysis of surface waves based on the theory of unbounded self-adjoint operators can be found in [2]. In that paper, the original problem is considered as a problem of the form $A(\beta)\mathrm{H} = k^2\mathrm{H}$ with respect to the spectral parameter k^2, and the dependence $k = k(\beta)$ is studied (H is the magnetic vector amplitude, k is the wavenumber, β is the propagation constant). In [3], a similar technique is used to extend the results obtained in [2] to the case of waveguides with a variable magnetic permeability.

The results obtained in [2, 3] give a complete understanding of the qualitative properties of the spectrum of surface guided waves; however, in order to calculate the spectral characteristics of waveguides, numerical methods are needed (see survey [4]). The formulations of the problems used in [2, 3] are not quite convenient for obtaining numerical solutions. This is due to two specific features of those statements.

1. The problems are formulated for the entire plane $\mathbb{R}^2$. For a numerical solution, special measures must be taken to restrict the integration domain and to formulate additional boundary conditions.

2. Spectral problems (except for a point spectrum) have a continuous part of the spectrum. Although the location of this part is known exactly, a numerical solution requires that false approximate solutions be detected and discarded.

Statements of problems suggested in [5, 6] are free of those drawbacks. In those papers, exact nonlocal boundary conditions (see [7, 8]) are used to reduce the problems that were originally formulated for the entire plane $\mathbb{R}^2$ to equivalent problems in a circle. In [5, 6] the spectral problems are formulated in a circle Ω which includes waveguide's cross-section domain Ω_i (see Fig. 1); these problems have no continuous spectrum. Moreover, their spectrum is identical to the point part of the spectrum of the original problem. These statements are convenient for the finite element method. The cost of this advantage is that the spectral parameter appears in the equation in a nonlinear fashion; more precisely, the problems have the form $\mathrm{A}(\beta, \lambda)\mathrm{H} = \lambda\mathrm{H}$, where A is a compact self-adjoint operator. The solution of such problems requires the use of special iterative methods.

In this paper, we use a new formulation of the problem proposed in [9]. The original problem by exact nonlocal boundary conditions method is reduced to an equivalent linear self-adjoint eigenvalue problem $A(p)\mathcal{H} = \beta^2 B(p)\mathcal{H}$ in the circle Ω. Here, the parameter p is the transverse wave number $p = \sqrt{\beta^2 - k^2\varepsilon_\infty}$; for each $p \geq 0$ the operators $A(p)$ and $B(p)$ are bounded and $B(p)$ is compact; vector $\mathcal{H} = (\mathrm{H}_1, \mathrm{H}_2)$ represents the first two components of the intensity vector H. We examine the solvability of the problem and investigate some properties of the dispersion curves. Then we

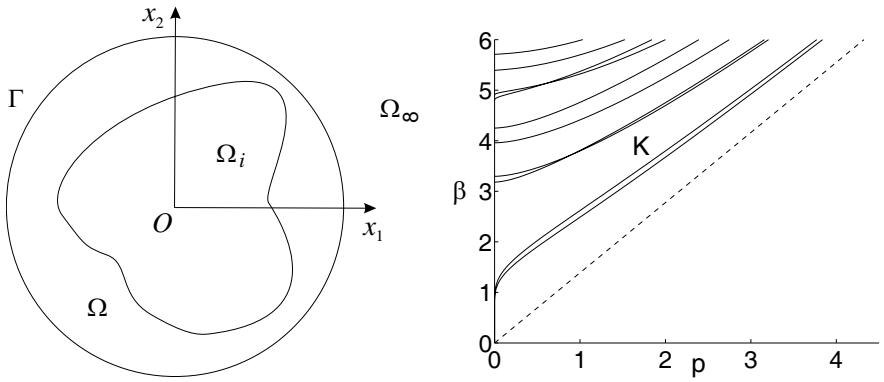

Figure 1: A schematic waveguide's cross-section (on the left) and the dispersion curves for 1.5×1 rectangular waveguide, $\varepsilon(x) = 2.08$, $x \in \Omega_i$, $\varepsilon_\infty = 1$ (on the right).

propose an algorithm for the numerical solution of the problem based on the finite element method. We prove the convergence of the numerical method and discuss some numerical results.

2. SOLVABILITY OF THE PROBLEM

First, we recall the statement of the problem given in [2]. Let $\overline{\mathrm{H}}$ be the complex conjugate of H. For the complex-valued vector fields $\mathrm{H} = (\mathrm{H}_1, \ldots, \mathrm{H}_l)$ and $\mathrm{H}' = (\mathrm{H}'_1, \ldots, \mathrm{H}'_l)$ $(l \geq 1)$, we define

$$\begin{aligned} \mathrm{H} \cdot \mathrm{H}' &= \mathrm{H}_1\mathrm{H}'_1 + \ldots + \mathrm{H}_l\mathrm{H}'_l, \quad |\mathrm{H}|^2 = \mathrm{H} \cdot \overline{\mathrm{H}}, \quad \nabla\mathrm{H} = (\nabla\mathrm{H}_1, \ldots, \nabla\mathrm{H}_l), \\ \nabla\mathrm{H} \cdot \nabla\mathrm{H}' &= \nabla\mathrm{H}_1 \cdot \nabla\mathrm{H}'_1 + \ldots + \nabla\mathrm{H}_l \cdot \nabla\mathrm{H}'_l, \quad |\nabla\mathrm{H}|^2 = \nabla\mathrm{H} \cdot \nabla\overline{\mathrm{H}}. \end{aligned}$$

Let $V(D) = H^1(D)$ be the Sobolev space of complex-valued scalar functions defined on the domain $D \subseteq \mathbb{R}^2$, and $V^l(D) = [H^1(D)]^l$ be the corresponding space of l-dimensional vector-functions. The scalar product and norm in Hilbert space $V^l(D)$ are defined in the conventional way:

$$(\mathrm{H}, \mathrm{H}') = \int\limits_D \left(\nabla\mathrm{H} \cdot \nabla\overline{\mathrm{H}'} + \mathrm{H} \cdot \overline{\mathrm{H}'}\right) dx, \quad \|\mathrm{H}\|_{1,D} = (\mathrm{H}, \mathrm{H})^{1/2}.$$

Consider a weak formulation of the original problem [2]: Find nonzero vectors $\mathrm{H} \in V^3(\mathbb{R}^2)$ and all pairs $(\beta, k) \in \Lambda = \{(\beta, k) : \beta/\sqrt{\varepsilon_+} < k < \beta/\sqrt{\varepsilon_\infty}, \beta > 0\}$ such that

$$\int\limits_{\mathbb{R}^2} \left(\frac{1}{\varepsilon}\mathrm{rot}_\beta\mathrm{H} \cdot \overline{\mathrm{rot}_\beta\mathrm{H}'} + \frac{1}{\varepsilon_\infty}\mathrm{div}_\beta\mathrm{H}\,\overline{\mathrm{div}_\beta\mathrm{H}'}\right) dx = k^2 \int\limits_{\mathbb{R}^2} \mathrm{H} \cdot \overline{\mathrm{H}'}\, dx, \tag{1}$$

for any $\mathrm{H}' \in V^3(\mathbb{R}^2)$. Here differential operators div_β and rot_β are obtained from usual operators by replacing generating waveguide line derivative with $i\beta$ multiplication; ε_+ is the maximum of the function ε. We suppose that $\varepsilon \geq \varepsilon_\infty$, $x \in \mathbb{R}^2$.

Definition 1. The vector-function $\mathrm{H} \in V^l(\mathbb{R}^2)$ is called metaharmonic in $D \subset \mathbb{R}^2$ if

$$-\triangle\mathrm{H} + p^2\mathrm{H} = 0, \; x \in D, \quad p \neq 0.$$

The vector-function $\mathrm{H}_p \in V^l(\mathbb{R}^2)$ is called metaharmonic extension of $\mathrm{H} \in V^l(\Omega)$ to $\Omega_\infty = \mathbb{R}^2 \setminus \overline{\Omega}$ if H_p is metaharmonic in Ω_∞ and $\mathrm{H}_p\big|_\Omega = \mathrm{H}$.

The dielectric permittivity ε is equal to ε_∞ in the domain Ω_∞. Therefore, if a vector-function H satisfies (1) then it is metaharmonic [2]. This fact let us to obtain (see [9] for technical details) a new formulation of the original problem: For each $p > 0$ find all parameters $\beta > 0$ and nonzero vectors $\mathrm{H} = (\mathcal{H}, i\mathrm{H}_3) \in V^3(\Omega)$, where H_l, $l = 1, 2, 3$, are real-valued functions, such that the following relations are valid:

$$A(p)\mathcal{H} = \beta^2 B(p)\mathcal{H}, \quad \mathrm{H}_3 = \beta T(p)\mathcal{H}. \tag{2}$$

Here $B(p) = D + C^* L^{-1}(p) C$ and $T(p) = L^{-1}(p) C$; by C^* denote the adjoint operator. The linear operators $C : V^2(\Omega) \to V(\Omega)$, $D : V^2(\Omega) \to V^2(\Omega)$, and $L : V(\Omega) \to V(\Omega)$ are defined by the following relations:

$$
\begin{aligned}
(A(p)\mathcal{H}, \mathcal{H}') &= \int\limits_{\Omega} \Big(\frac{1}{\varepsilon} \mathrm{rot}\mathcal{H}\, \mathrm{rot}\mathcal{H}' + \frac{1}{\varepsilon_\infty} \mathrm{div}\mathcal{H}\, \mathrm{div}\mathcal{H}' + \frac{p^2}{\varepsilon_\infty} \mathcal{H} \cdot \mathcal{H}' \Big)\, dx \\
&\quad + \frac{2\pi}{\varepsilon_\infty} \sum_{n=-\infty}^{\infty} \mathbb{K}_n(Rp)\, a_n(\mathcal{H}) \cdot \overline{a_n(\mathcal{H}')} + \frac{1}{\varepsilon_\infty} \int\limits_0^{2\pi} \Big(\frac{\partial \mathrm{H}_1}{\partial \varphi}\, \mathrm{H}_2' - \frac{\partial \mathrm{H}_2}{\partial \varphi}\, \mathrm{H}_1' \Big)\Big|_{r=R} d\varphi, \\
(D\mathcal{H}, \mathcal{H}') &= \int\limits_{\Omega} \sigma \mathcal{H} \cdot \mathcal{H}'\, dx, \quad (C\mathcal{H}, H') = \int\limits_{\Omega} \sigma \mathcal{H} \cdot \nabla H'\, dx, \quad \sigma = \varepsilon_\infty^{-1} - \varepsilon^{-1}, \\
(L(p)H, H') &= \int\limits_{\Omega} \Big(\frac{1}{\varepsilon} \nabla H \cdot \nabla H' + \frac{p^2}{\varepsilon_\infty} H H' \Big) dx + \frac{2\pi}{\varepsilon_\infty} \sum_{n=-\infty}^{\infty} \mathbb{K}_n(Rp)\, a_n(H)\, \overline{a_n(H')}. \\
\mathbb{K}_n(z) &= -z K_n'(z)/K_n(z), \quad a_n(H) = \frac{1}{2\pi} \int\limits_0^{2\pi} H|_{r=R}\, e^{-in\varphi}\, d\varphi.
\end{aligned}
$$

Here $\mathrm{rot}\mathcal{H} = \partial \mathrm{H}_2/\partial x_1 - \partial \mathrm{H}_1/\partial x_2$, $\mathrm{div}\mathcal{H} = \partial \mathrm{H}_1/\partial x_1 + \partial \mathrm{H}_2/\partial x_2$, R is the radius of the circle Ω, and $K_n(z)$ is the modified Bessel function of order n. The following theorem states some important properties of the operators of the problem (2).

Theorem 1 (see (9)). *For each $p > 0$ the operator $A(p)$ is self-adjoint and positive definite; for $p = 0$ this operator is self-adjoint and nonnegative. The operator-function $A(p)$ is continuously differentiable and increasing for $p > 0$. For each $p \geq 0$ the operator $B(p)$ is self-adjoint, nonnegative and compact. The operator-function $B(p)$ is continuously differentiable and nonincreasing for $p > 0$. For each $p > 0$ the operator $T(p)$ is compact. For each $p > 0$ the operator $L(p)$ is continuously invertible. All operators mentioned above are real.*

The original problem (1) and problem (2) are equivalent in the sense of the following theorem.

Theorem 2 (see [9]). *Suppose that (β, p, H) is a solution of the problem (2). Then $(\beta, p) \in K$, where $K = \{(\beta, p) : p > 0,\ \beta > p\sqrt{\varepsilon_+/(\varepsilon_+ - \varepsilon_\infty)}\}$. Let H_p be the metaharmonic extension of H to Ω_∞, and let $k = \sqrt{(\beta^2 - p^2)/\varepsilon_\infty}$. Then (β, k, H_p) is the solution of the problem (1). Conversely. Suppose that (β, k, H) is a solution of the problem (1). Let $p = \sqrt{\beta^2 - k^2\varepsilon_\infty}$. Then $(\beta, p, \mathrm{H}|_\Omega)$ is the solution of the problem (2) with $(\beta, p) \in K$.*

The existence and qualitative properties of the spectrum of surface guided waves were investigated in the book [10] using new formulation (2) of the problem.

Theorem 3 (see [10]). *For each $p > 0$ the set of all existing solutions of the problem (2) can be represented as $\{\beta_l(p), \mathrm{H}_l(p),\ l = 1, 2, \ldots\}$. Moreover, the following assertions hold:*

(a) *$\beta_1(p) \leq \ldots \leq \beta_l(p) \leq \ldots$, $\beta_l(p) \to \infty$ as $l \to \infty$; any $\beta_l(p)$ has a finite multiplicity (i.e., $\beta_l(p)$ can coincide only with a finite number of $\beta_j(p)$, $j \geq 1$).*

(b) *$(A(p)\mathcal{H}_l, \mathcal{H}_j) = \delta_{l,j}$.*

(c) *The functions $p \to \beta_l(p)$, $l = 1, 2, \ldots$, are increasing and have the local Lipschitz property.*

(d) *$\beta_l(p)/p \to k_0 = \sqrt{\varepsilon_+/(\varepsilon_+ - \varepsilon_\infty)}$ as $p \to \infty$, $l \geq 1$.*

(e) *$\beta_1(p) \to +0$, $\beta_2(p) \to +0$ as $p \to +0$; $\beta_l(0) > 0$, $l \geq 3$.*

The dispersion curves $\beta = \beta_l(p)$ for a homogeneous waveguide with a rectangular cross section are shown in Fig. 1 on the right. Setting $p = 0$ in the first Equation (2), we obtain the cut-off equation for finding the squares of the cut-off points $\beta_l(0)$.

3. APPROXIMATE SOLUTION OF THE PROBLEM

For discretization of the problem (2) we use finite element method with numerical integration. Approximation V_h of the real Sobolev space $H^1(\Omega)$ is based on usual conformal Lagrange finite elements of the order m. Thus we obtain the real matrices $A_h^N(p)$, D_h, C_h, and $L_h^N(p)$ which are discrete analogs of the operators $A(p)$, D, C, and $L(p)$, respectively [10]. These approximations

depend on two parameters: the real parameter h (the characteristic size of finite elements, $h \to 0$) and the integer parameter N, which specifies the number of the Fourier harmonics taken into account ($N \to \infty$). Since we assume that the circle Ω of radius R is fixed, we do not explicitly indicate the dependence on the third parameter R of the problem here.

The finite-dimensional approximation of the first equation in (2) is naturally described as the generalized algebraic linear eigenvalue problem regarding spectral parameter $(\beta_h^N)^2$:

$$A_h^N(p)\mathcal{H}_h^N = (\beta_h^N)^2 B_h^N(p)\mathcal{H}_h^N, \quad B_h^N(p) = D_h + (C_h)^T (L_h^N(p))^{-1} C_h. \tag{3}$$

Here, $A_h^N(p)$, $L_h^N(p)$, and $B_h^N(p)$ are large symmetric and positive definite matrices for each $p > 0$; matrices $A_h^N(p)$, $L_h^N(p))$, and C_h are sparse; $B_h^N(p)$ is full and such that there is an efficient method for multiplying this matrix by a vector (after an LL^T factorization of the matrix $L_h^N(p)$). For each fixed $p \geq 0$, we have to find all eigenvalues $(\beta_h^N)^2 = (\beta_h^N)^2(p)$ of the problem (3) from the given interval $(p^2/(1-\varepsilon_\infty/\varepsilon_+), \beta_{\max}^2)$ and the corresponding eigenvectors $\mathcal{H}_h^N = \mathcal{H}_h^N(p)$. There are many methods that solve problem (3) subject to the constraints specified above. We used the Lanczos method.

After solution of the problem (3) we can find $\mathrm{H}_{3,h}^N = \beta_h^N (L_h^N(p))^{-1} C_h \mathcal{H}_h^N$. The pair $(\beta_h^N, \mathrm{H}_h^N)$, where $\mathrm{H}_h^N = (\mathcal{H}_h^N, \mathrm{H}_{3,h}^N)$, is the discrete solution of the problem (2). A theorem analogous to the theorem 3 on the existence of the discrete solutions for h small enough was proved in [10]. The convergence of the numerical method is justified by the following theorem.

Theorem 4 (see [10]). *Let for $p \geq 0$ a pair $(\beta(p), \mathrm{H}(p))$ be a solution of the problem (2) and $\beta(p)$ has the multiplicity is equal to one. Let $(\beta_h^N(p), \mathrm{H}_h^N(p))$ be a corresponding solution of discrete problem. Then for h small enough and $N \geq c_0 \ln(1/h)$, $c_0 = m/\ln(R/R_0)$, the following assertions hold:*

$$\|\mathrm{H}(p) - \mathrm{H}_h^N(p)\|_{1,\Omega} \leq c(p)h^m, \quad |\beta(p) - \beta_h^N(p)| \leq c(p)h^{2m}.$$

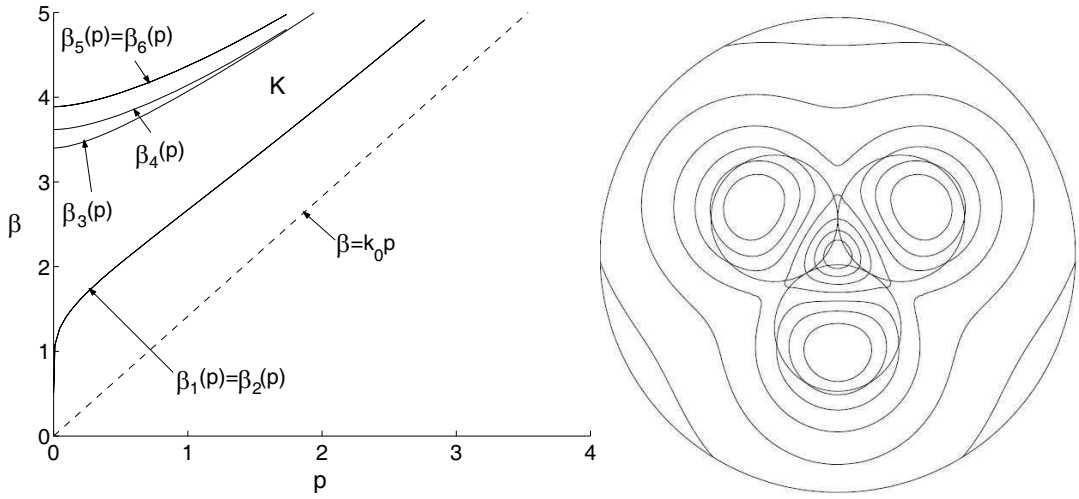

Figure 2: The dispersion curves for the three-circle waveguide (on the left) and the level curves of the function $|\mathrm{H}| = (\mathrm{H} \cdot \mathrm{H})^{1/2}$ corresponding to $\beta_4 = 3.6532$ and $p = 0.2$ (on the right).

Table 1: Calculation error $e = h^{-2}|\beta_4 - \beta_{4,h}^N|/|\beta_4|$ against N and N_h, where β_4 is the approximate value of the propagation constant obtained with 6006 grid nodes.

$N \vert N_h$	78	335	1093
1	0.5	23.3	92.5
3	0.619	1.67	1.56
5	0.62	1.67	1.57
7	0.62	1.67	1.57
15	0.62	1.67	1.57

Here R_0 is the minimal radius of the circumscribed circle Γ (see Fig. 1 on the left).

An analogous result holds for β which has a finite multiplicity [10].

To demonstrate the universality of the proposed method, we numerically solved the problem for the domain Ω_i consisting of three circles of radius 0.4 tangent to each other. The center of the domain Ω_i coincided with the center of the circle Ω of radius 1.5. The dielectric permittivity within Ω_i was $\varepsilon = 2$, and $\varepsilon_\infty = 1$. For each fixed p in the interval from 0 to 3, the first six (with account for the multiplicity) eigenvalues β^2 of problem (3) and the corresponding eigenvectors were found. The calculations were based on the linear triangular finite elements ($m = 1$) and were performed for the number N_h of the grid nodes in Ω in the range from 78 to 6006. Table 1 presents the results for the forth eigenvalue β_4 for $p = 1$. From this table we can conclude that it is enough to use only five of the Fourier harmonics, $N = 5$, at that $|\beta_4 - \beta_{4,h}^N|/|\beta_4| \approx 1.6h^2$.

The dispersion curves for the three-circle waveguide are shown in Fig. 2 on the left. There are only four dispersion curves because the upper and the lower curves are multiple due to the symmetry of the problem: $\beta_1 = \beta_2$ and $\beta_5 = \beta_6$. Fig. 2 on the right shows, for $p = 0.2$, the level curves of the function $|\mathrm{H}| = (\mathrm{H} \cdot \mathrm{H})^{1/2}$ corresponding to $\beta_4 = 3.6532$. The calculations were performed with 3150 grid nodes within Ω.

ACKNOWLEDGMENT

The work was partly supported by the Russian Foundation for Basic Research (E. M. Karchevskiy, grant 09-01-97009).

REFERENCES

1. Snyder, A. W. and D. Love, *Optical Waveguide Theory*, Chapman and Hall, London, 1983.
2. Bamberger, A. and A. S. Bonnet, "Mathematical analysis of the guided modes of in optical fiber," *SIAM J. Math. Anal.*, Vol. 21, 1487–1510, 1990.
3. Joly, P. and C. Poirier, "Mathematical analysis of electromagnetic open waveguides," *Math. Modell. Numer. Anal.*, Vol. 29, 505–575, 1995.
4. Bonnet-Ben Dhia, A. S. and P. Joly, "Mathematical analysis and numerical approximation of optical waveguides," *Mathematical Modelling in Optical Science, SIAM Frontiers Book Series in Applied Mathematics*, Ed. by G. Bao, L. Cowsar, and W. Masters, Vol. 22, 273–329, SIAM, Philadelphia, 2001.
5. Joly, P. and C. Poirier, "A numerical method for the computation of electromagnetic modes in optical fibres," *Math. Meth. Appl. Sci.*, Vol. 22, 389–447, 1999.
6. Dautov, R. Z. and E. M. Karchevskii, "Solution of the vector eigenmode problem for cylindrical dielectric waveguides based on a nonlocal boundary condition," *Comput. Math. Math. Phys.*, Vol. 42, 1012–1027, 2002.
7. Il'inskii, A. S., V. V. Kravtsov, and A. G. Sveshnikov, *Mathematical Models in Electrodynamics*, Vysshaya Shkola, Moscow, 1991 [in Russian].
8. Givoli, D. "Nonreflecting boundary conditions (review article)," *J. Comput. Phys.*, Vol. 94, 1–29, 1991.
9. Dautov, R. Z., E. M. Karchevskii, and G. P. Kornilov, "A numerical method for finding dispersion curves and guided waves of optical waveguides," *Comput. Math. Math. Phys.*, Vol. 45, 2119–2134, 2005.
10. Dautov, R. Z. and E. M. Karchevskii, *Integral Equations Method and Exact Nonlocal Boundary Conditions in the Theory of Dielectric Waveguides*, Kazan State University, Kazan, 2009 [in Russian].

The Over-determined Boundary Value Problem Method in the Electromagnetic Waves Propagation and Diffraction Theory

N. B. Pleshchinskii[1], **I. E. Pleshchinskaya**[2], **and E. M. Karchevskiy**[1]

[1]Kazan State University, Russia
[2]Kazan State Technological University, Russia

Abstract— The over-determined boundary value problems in the partial domains are proposed to be used as the auxiliary problems to investigate the wave processes in the complex structures. The necessary and sufficient conditions of solvability of the over-determined problem are the dependencies between the boundary functions. These dependencies can be obtained in terms of the Fourier transforms or Fourier coefficients of the boundary functions. The diffraction problems for the electromagnetic waves on the conducting screens in the space and in the waveguides with metallic walls are considered as the examples.

1. INTRODUCTION

The method of partial domains is widely used in the electromagnetic wave propagation and diffraction theory to solve the conjugation problems and boundary value problems with mixed boundary conditions. In the case when the integral or summatorial representations of the field to be found are obtained in some parts of the waveguide structure it is possible to get the integral or summatorial equations equivalent to the initial problem.

It is convenient to consider the over-determined boundary value problems in the partial domains as the auxiliary problems. By this we are to consider more boundary conditions on some pieces of the domains boundaries than it is necessary to choose the unique solution. The review of articles devoted to over-determined boundary value problem method for the partial differential equations is given in the paper [1].

The necessary and sufficient conditions of solvability of the over-determined problems have the form of the supplementary connections between the auxiliary boundary functions. These connections together with the initial boundary conditions and the conjunction conditions form the complete set of equations to determine the electromagnetic field. In many cases the conditions at the infinity for the unbounded domains (the radiation conditions) can be formulated also as the auxiliary conditions for the boundary functions in the over-determined problem.

2. TWO-DIMENSIONAL PROBLEMS IN THE PLANE WAVEGUIDE

Consider the diffraction problem for two-dimensional TE-wave in the plane waveguide on the infinitely thin ideally conducting screen (see Fig. 1).

The eigen TE-wave of the waveguide with potential function $u^0(x,z)$ is falling down on the screen M. It is necessary to find the potential functions $u^{\mp}(x,z)$ of the field being generated by the diffraction of this wave.

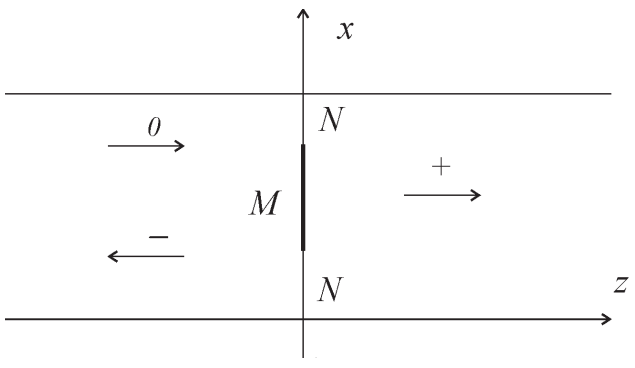

Figure 1: Lateral screen in the plane waveguide.

It is well known that the potential function $u(x,z)$ of any of two possible polarizations of two-dimensional electromagnetic field in the plane waveguide is to satisfy the Helmholtz equation

$$\frac{\partial^2 u}{\partial x^2}+\frac{\partial^2 u}{\partial z^2}+k^2u=0, \tag{1}$$

here and further k being the real number. The function $u(x,z)$ is to vanish on the walls of the waveguide $x=0$ and $h=h$ for TE-waves.

Consider the auxiliary over-determined boundary value problem in the right-hand part $z>0$ of the waveguide structure. It is necessary to find the solution of the Equation (1) in the half-strip $0<x<h,\ z>0$, satisfying the boundary conditions on the walls of the waveguide $u(0,z)=0,\ u(h,z)=0$ and the conditions $u(x,0+0)=u_0(x),\ \frac{\partial u}{\partial z}(x,0+0)=u_1(x)$ on its cross-section. Besides, the solution to be found is not to contain the elementary harmonics transferring energy from infinity or infinitely increasing by $z\to+\infty$.

It is easy to show that solution of such over-determined boundary value problem for the Helmholtz equation exists and is unique if and only if the Fourier coefficients of the functions $u_0(x)$ and $u_1(x)$ satisfy the conditions

$$u_{1n}+i\gamma_n u_{0n}=0,\quad n=1,2,\dots, \tag{2}$$

where

$$\gamma_n=\sqrt{k^2-\left(\frac{\pi n}{h}\right)^2},\quad n=1,2,\dots$$

Let us determine these numbers in such way that either $\operatorname{Re}\gamma_n\geq 0$, or $\operatorname{Im}\gamma_n<0$. By this

$$u^-(x,z)=\sum_{n=1}^{+\infty}A_n\varphi_n(x)\,e^{i\gamma_n z},\quad u^+(x,z)=\sum_{n=1}^{+\infty}B_n\varphi_n(x)\,e^{-i\gamma_n z},$$

where

$$\varphi_m(x)=\sqrt{\frac{2}{h}}\sin\frac{\pi m x}{h},\quad m=1,2,\dots$$

In the same time functions $u_0(x)$ and $u_1(x)$ then and only then are traces on the cross $z=0$ of the solution of the Helmholtz equation in the half-strip satisfying the boundary conditions and the condition at the infinity when

$$u_0(x)=\int_0^h u_1(t)\,K_1(t,x)\,dt,\quad x\in(0,h),\quad K_1(t,x)=\sum_{m=1}^{+\infty}\frac{1}{\gamma_m}\varphi_m(t)\varphi_m(x). \tag{3}$$

The same statements are valid for the left-hand half of the waveguide structure.

As it is shown in [2], by $\varepsilon^{\pm}=\varepsilon$ the diffraction problem for the electromagnetic wave on the lateral screen in the plane waveguide is equivalent to the infinite set of linear algebraic equations

$$A_k-\sum_{n=1}^{+\infty}A_n\gamma_n\sum_{m=1}^{+\infty}\frac{1}{\gamma_m}I_{nm}J_{mk}=-C_l\,I_{lk},\quad k=1,2,\dots \tag{4}$$

or to integral equation

$$u_1^-(x)-\int_M u_1^-(t)\,L(t,x)\,dt=-iC_l\,\psi_l(x),\quad x\in M,$$

where $I_{nm},\ J_{mk}$ are some constants, $L(t,x),\ \psi_l(x)$ are some functions.

3. THE CAUCHY PROBLEM FOR A HALF-SPACE

Consider the Maxwell equations set for complex amplitudes E and H of the electric and magnetic vectors of the electromagnetic field harmonically dependent on time

$$\operatorname{rot} H = i\omega\varepsilon_0\varepsilon\, E, \quad \operatorname{rot} E = -i\omega\mu_0\mu\, H \tag{5}$$

in the upper half-space R^3_+ and in the lower half-space R^3_-, here $\varepsilon = \varepsilon(z) = \{z > 0 : \varepsilon_+;\ z < 0 : \varepsilon_-\}$ and μ are real numbers. Let the traces of tangent components E and H be given on the plane $z = 0$ and

$$[z_0, E](x, y, 0) = e(x, y), \quad [z_0, H](x, y, 0) = h(x, y). \tag{6}$$

We call the solution E, H of Maxwell equations set in the domain R^3_+ outgoing into a half-space if each of its components is the distribution of slow growth not containing harmonics which transfer the energy on infinity and the traces (6) are defined correctly.

Let k be a wave number, $k^2 = \omega^2\mu_0\mu\varepsilon_0\varepsilon$. Denote by

$$\gamma(\xi, \eta) = \left\{\xi^2 + \eta^2 \geq k^2\ :\ i\sqrt{\xi^2 + \eta^2 - k^2};\ \ \xi^2 + \eta^2 \leq k^2\ :\ \sqrt{k^2 - \xi^2 - \eta^2}.\right\}$$

Vector-functions E, H are the solution of the Cauchy problem (5), (6) in the class of solutions outgoing into the half-space if and only if, when [3] the equality for the Fourier transforms of traces of their components on the plane $z = 0$

$$\omega\varepsilon_0\varepsilon\gamma(\xi, \eta)e(\xi, \eta) + P(\xi, \eta)h(\xi, \eta) = 0 \quad \text{or} \quad P(\xi, \eta)e(\xi, \eta) - \omega\mu_0\mu\gamma(\xi, \eta)h(\xi, \eta) = 0 \tag{7}$$

is fulfilled, where

$$P(\xi, \eta) = \begin{pmatrix} \xi\eta & k^2 - \xi^2 \\ \eta^2 - k^2 & -\xi\eta \end{pmatrix}, \quad A = \begin{pmatrix} 1 & 0 \\ 0 & 1 \\ 0 & 0 \end{pmatrix}, \quad B(\xi, \eta) = \begin{pmatrix} 0 & 0 \\ 0 & 0 \\ \eta & -\xi \end{pmatrix}.$$

Formulas (7) follow one from another; they determine the dependence between the traces of the tangent components of the field given on the boundary of the domain in terms of their Fourier transforms. It follows from (7) that

$$\begin{aligned} e(x, y) &= -\frac{1}{\omega\varepsilon_0\varepsilon} \iint K(x_1, y_1; x, y)\ h(x_1, y_1)\ dx_1\ dy_1, \\ h(x, y) &= \frac{1}{\omega\mu_0\mu} \iint K(x_1, y_1; x, y)\ e(x_1, y_1)\ dx_1\ dy_1, \end{aligned} \tag{8}$$

where

$$K(x_1, y_1; x, y) = \frac{1}{(2\pi)^2} \iint \frac{1}{\gamma(\xi, \eta)}\ P(\xi, \eta)\ e^{i(x_1 - x)\xi + i(y_1 - y)\eta}\ d\xi\ d\eta.$$

In the case of analogues statements for the solutions of the Cauchy problem outgoing into the lower half-space in R^3_- one should change a sign of the function $\gamma(\xi, \eta)$ in above given formulas.

4. THE DIFFRACTION PROBLEM ON A PLANE SCREEN

Let M be a metallic screen placed in the plane $z = 0$ and N be its supplement up to the whole plane. Let $\varepsilon_\pm = \varepsilon,\ \mu_\pm = \mu$ and $E_0(x, y, z)$ be the electric field of a wave falling down on the screen. It is necessary to seek the solutions of the Maxwell equations set outgoing from the plane $z = 0$ into half-spaces satisfying the boundary conditions

$$[z_0, E_\pm + E_0](x, y) = 0, \ \ (x, y) \in M,$$

$$[z_0, E_+ - E_-](x, y) = 0, \ \ [z_0, H_+ - H_-](x, y) = 0, \ \ (x, y) \in N.$$

Let us write down the equalities of the form (8) for the traces of tangent components of the vectors $E_\pm,\ H_\pm$. It follows from the boundary conditions that $e_+ = e_- = -e_0$ on M and $e_+ = e_-$ on N. Denote by $e = e_+ = e_-$. Then $h_+ + h_- = 0$ everywhere on the plane $z = 0$, by this $h_+ = h_-$ on N. Thus

$$e(x, y) = \mp\frac{1}{\omega\varepsilon_0\varepsilon} \iint\limits_M K(x_1, y_1; x, y)\ h_\pm(x_1, y_1)\ dx_1\ dy_1,$$

$$h_{\pm}(x,y) = \mp\frac{1}{\omega\mu_0\mu}\iint\limits_M K(x_1,y_1;x,y)\,e_0(x_1,y_1)\,dx_1\,dy_1 \pm \frac{1}{\omega\mu_0\mu}\iint\limits_N K(x_1,y_1;x,y)\,e(x_1,y_1)\,dx_1\,dy_1.$$

It is proved in [3] that the diffraction problem on a plane screen is equivalent to the vector integral equations

$$\begin{aligned}
&\mp\frac{1}{\omega\varepsilon_0\varepsilon}\iint\limits_M K(x_1,y_1;x,y)\;h_{\pm}(x_1,y_1)\;dx_1\;dy_1 = -e_0(x,y);\\
&e(x,y) + \iint\limits_N e(x_1,y_1)L_M(x_1,y_1;x,y)\,dx_1\,dy_1 = \iint\limits_M e_0(x_1,y_1)L_M(x_1,y_1;x,y)\,dx_1\,dy_1,\\
&L_M(x_1,y_1;x,y) = \frac{1}{k^2}\iint\limits_M K(x_1,y_1;x_2,y_2)K(x_2,y_2;x,y)\,dx_2\,dy_2;\\
&h_{\pm}(x,y) + \iint\limits_M h_{\pm}(x_1,y_1)L_N(x_1,y_1;x,y)\,dx_1\,dy_1 = \mp\frac{1}{\omega\mu_0\mu}\iint\limits_M K(x_1,y_1;x,y)e_0(x_1,y_1)dx_1dy_1,\\
&L_N(x_1,y_1;x,y) = \frac{1}{k^2}\iint\limits_N K(x_1,y_1;x_2,y_2)\,K(x_2,y_2;x,y)\,dx_2\,dy_2.
\end{aligned} \tag{9}$$

5. THE CLOSED WAVEGUIDE OF ARBITRARY SECTION

Let C be media interface in the waveguide with metallic walls placed along axis z, and S be a lateral section on the waveguide (see Fig. 2). Let the function $z = f(x,y),\ (x,y) \in S$ determine the media interface C. We are to obtain the integral identities connecting on C the traces $[n,E] = e(x,y),\ [n,H] = h(x,y),\ (x,y) \in S$ of tangent components of the vectors E and H of the field from the right-side on C.

As it is known, any solution of the Maxwell equations set for complex amplitudes in the case of harmonic dependence on time can be represented as a superposition of fields of normal TE- and TM-waves. For TE-waves we have

$$E = i\omega\mu_0\mu\,\mathrm{rot}\,\Pi^m, \quad H = \mathrm{grad}\,\mathrm{div}\,\Pi^m + k^2\Pi^m,$$

for TM-waves we have

$$E = \mathrm{grad}\,\mathrm{div}\,\Pi^e + k^2\Pi^e, \quad H = -i\omega\varepsilon_0\varepsilon\,\mathrm{rot}\,\Pi^e,$$

where

$$\Pi^m = \left(0,0,\sum_{n=1}^{+\infty} B_n^m e^{i\gamma_n^m z}\varphi_n^m(x,y)\right), \quad \Pi^e = \left(0,0,\sum_{n=1}^{+\infty} B_n^e e^{i\gamma_n^e z}\varphi_n^e(x,y)\right),$$

γ^m and $\varphi^m(x,y)$ are the eigen values and eigen functions of the Laplace operator with homogeneous Neumann conditions on the boundary S, γ^e and $\varphi^e(x,y)$ are the eigen values and eigen functions of the Laplace operator with homogeneous Dirichlet conditions. For the waves going in the direction of the axis z the sign of γ is chosen so that $\mathrm{Re}\,\gamma \geq 0$ or $\mathrm{Im}\,\gamma > 0$ by $\mathrm{Re}\,\gamma = 0$. For the waves going in the opposite direction in is suitable to assume that numbers γ have another sign and, more over, the vector E for TE-waves and the vector H for TM-waves have the another direction.

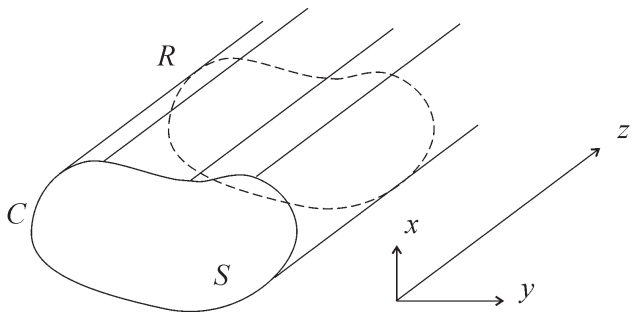

Figure 2: Cross-section of the closed waveguide.

Let us construct 2×2-matrix $K(\xi, \eta, x, y)$ of the elements of the form

$$\sum_{r=0}^{+\infty} \sum_{s=0}^{+\infty} k_{rs} \varphi_r(\xi, \eta) \varphi_s(x, y)$$

so that

$$e(x, y) = \iint_S K(\xi, \eta, x, y) h(\xi, \eta)\, d\xi_S\, d\eta_S, \quad (x, y) \in S. \tag{10}$$

By this the coefficients of all elements of the matrix $K(\xi, \eta, x, y)$ are determined from the infinite set of the linear algebraic equations in the form of the linear equation for the infinite matrices. Formula (10) is the initial integral identity.

Let us transform the conditions of conjugation of fields on C in the diffraction problem

$$[n, E^0] + [n, E^-] = [n, E^+], \quad [n, H^0] + [n, H^-] = [n, H^+]$$

by the following way: we apply the integral operator with the kernel $K(\xi, \eta, x, y)$ to the left-hand side of the second kind equation [4]. Having projected the new vector equation onto the set of functions $\varphi_m^m(x, y)$, $\varphi_m^e(x, y)$, we obtain regular (i.e., with the properties of the operator equation of the first kind) infinite set of linear algebraic equations for propagation constants of the field in the left half of the waveguide. The reduction method can be applied to this set of equation.

ACKNOWLEDGMENT

Supported by RFBR 09-01-97009-r-povolzh'e-a.

REFERENCES

1. Pleshchinskaya, I. E. and N. B. Pleshchinskii, "Over-determined boundary value problems for elliptic partial differential equations and their application to waves diffraction theory," *Uchenye Zapiski Kazanskogo Gosudarstvennogo Universiteta*, Vol. 147, No. 3, 41–32, 2005 (in Russian).
2. Pleshchinskii, N. B., *Models and Methods of Waveguided Electrodynamics*, Kazan State Unuversity, Kazan, 2008 (in Russian).
3. Pleshchinskaya, I. E. and N. B. Pleshchinskii, "The over-determined Cauchy problems for the Maxwell equations set and electromagnetic waves diffraction on the metallic screens," *Conf. Proc. 11th Int. Conf. Mathematical Methods in Electromagnetic Theory MMET*06*, 255–257, Kharkov, Ukraine, June 2006.
4. Pleshchinskii, I. N. and N. B. Pleshchinskii, "The over-determined boundary value problem method for the problems of electromagnetic waves diffraction in the waveguides with metallic bounds," *Conf. Proc. 11th Int. Conf. Mathematical Methods in Electromagnetic Theory MMET*06*, 288–290, Kharkov, Ukraine, June 2006.

Eigenmodes of a Screened Slot Line

A. S. Il'inskiy and E. V. Chernokozhin
Moscow State University, Faculty of Computational Mathematics and Cybernetics, Russia

Abstract— The problem of eigenmodes of a screened slot line is considered. The line consists of two rectangular waveguides coupled through a slot in the common horizontal wall and is characterized by the total width c, heights of the waveguides b_1 and b_2, and permittivities of the waveguide fillings ε_1 and ε_2. The aim is to find solutions to the system of the homogeneous Maxwell equations that correspond to traveling waves.

1. FORMULATION OF THE BOUNDARY VALUE PROBLEM

Consider the problem of eigenmodes of a screened slot line with a rectangular cross section. The line consists of two rectangular waveguides coupled through a slot of width $2l$ in the common horizontal wall (Fig. 1) and is characterized by the total width c, heights of the waveguides b_1 and b_2, and permittivities of the waveguide fillings ε_1 and ε_2. The aim is to find solutions to the system of the homogeneous Maxwell equations that correspond to traveling waves. It is assumed that the waveguides have infinitely thin perfectly conducting boundaries and that the media are nonmagnetic. The problem is to find solutions $(\vec{E},\, \vec{H})^T$ to the system of the homogeneous Maxwell equations that correspond to traveling waves, i.e., can be represented in the form

$$\begin{pmatrix}\vec{E}\\ \vec{H}\end{pmatrix} = \begin{pmatrix}\vec{E}(x,\, y)\\ \vec{H}(x,\, y)\end{pmatrix} e^{i(\gamma z-\omega t)}.$$

Let us denote the fields in the upper and lower waveguides by $(\vec{E}^1,\, \vec{H}^1)^T$ and $(\vec{E}^2,\, \vec{H}^2)^T$, respectively. All the components of the fields can be uniquely expressed in terms of the longitudinal components E_z^i and H_z^i.

Functions E_z^i and H_z^i must satisfy the Helmholtz equations

$$\begin{aligned}\Delta E_z^i + \tilde{k}_i^2 E_z^i = 0\\ \Delta H_z^i + \tilde{k}_i^2 H_z^i = 0\end{aligned} \tag{1}$$

with the coefficients $\tilde{k}_i^2 = k_i^2 - \gamma^2$, boundary conditions on metal

$$E_z|_M = 0, \quad \left.\frac{\partial H_z}{\partial n}\right|_M = 0, \tag{2}$$

matching conditions on the slot

$$[E_z]|_S = 0, \quad [H_z]|_S = 0, \tag{3}$$

$$\omega \left[\frac{\varepsilon}{\tilde{k}^2}\frac{\partial E_z}{\partial y}\right]\Bigg|_S - \gamma \left[\frac{1}{\tilde{k}^2}\frac{\partial H_z}{\partial x}\right]\Bigg|_S = 0, \quad \gamma \left[\frac{1}{\tilde{k}^2}\frac{\partial E_z}{\partial x}\right]\Bigg|_S + \omega\mu \left[\frac{1}{\tilde{k}^2}\frac{\partial H_z}{\partial y}\right]\Bigg|_S = 0. \tag{4}$$

and conditions of finiteness of energy [1].

It is necessary to determine complex numbers γ such that the boundary value problem (1)–(4) has nontrivial solution and find this solution.

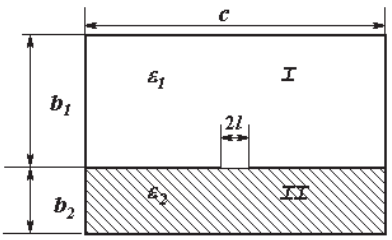

Figure 1.

2. THE SYSTEM OF INTEGRAL EQUATIONS

Using the Green's functions G_j^i of the first and second boundary value problems, we represent fields E_z^i and H_z^i by the formulas

$$H_z^1(x,y) = -\int\limits_{p-l}^{p+l} G_1^2(x,y,x_0,0)\left.\frac{\partial H_z^1}{\partial y_0}\right|_{y_0=+0}(x_0)dx_0, \qquad 0<x<c,\ 0<y<b_1,$$
$$H_z^2(x,y) = \int\limits_{p-l}^{p+l} G_2^2(x,y,x_0,0)\left.\frac{\partial H_z^2}{\partial y_0}\right|_{y_0=-0}(x_0)dx_0, \qquad 0<x<c,\ -b_2<y<0, \tag{5}$$

$$E_z^1(x,y) = \int\limits_{p-l}^{p+l} \left.\frac{\partial G_1^1}{\partial y_0}\right|_{y_0=+0}(x,y,x_0)E_z^1(x_0,0)dx_0, \qquad 0<x<c,\ 0<y<b_1, \tag{6}$$

$$E_z^2(x,y) = -\int\limits_{p-l}^{p+l} \left.\frac{\partial G_2^1}{\partial y_0}\right|_{y_0=-0}(x,y,x_0)E_z^2(x_0,0)dx_0, \qquad 0<x<c,\ -b_2<y<0. \tag{7}$$

Satisfying the matching conditions on the slot, we reduce the boundary value problem to the homogeneous system of integral equations [2]

$$\begin{pmatrix} K_{11}(\gamma) & K_{12}(\gamma) \\ K_{21}(\gamma) & K_{22}(\gamma) \end{pmatrix}\begin{pmatrix} \varphi \\ \psi \end{pmatrix} = \begin{pmatrix} 0 \\ 0 \end{pmatrix} \tag{8}$$

with respect to unknowns $\varphi = \frac{1}{k_2^2}\left.\frac{\partial H_z^2}{\partial y}\right|_{y=0}$ and $\psi = \omega\left.\frac{\partial E_z^2}{\partial x_0}\right|_{y=0}$, with the additional condition

$$(\psi,\,1) \equiv \int\limits_{p-l}^{p+l}\psi(x)dx = 0.$$

Thus, it is necessary to determine complex numbers γ such that system (8) has nontrivial solution and find this solution.

3. ANALYSIS OF THE SYSTEM OF INTEGRAL EQUATIONS

Operator $K(\gamma)$ of system (8) can be represented in the form

$$K(\gamma) = X(\gamma) + M(\gamma),$$

where $X(\gamma)$ is the characteristic part and $M(\gamma)$ is the completely continuous part of the operator. Here,

$$X(\gamma) = \begin{pmatrix} a_{11}L & a_{12}L \\ a_{21}S & a_{22}S \end{pmatrix}, \tag{9}$$

where a_{ij} are number coefficients and L and S are integral operators with the kernels $\frac{1}{\pi}\ln\frac{1}{|x-x_0|}$ and $\frac{1}{\pi}\frac{1}{x_0-x}$, respectively.

Operator $X(\gamma)$ can be explicitly inverted by the formulas

$$(X^{-1})_{11}f = \frac{a_{22}}{\Delta}S^{-1}f' + \frac{1}{a_{11}\ln\frac{2}{l}}\left(f(p) - (LS^{-1}f')(p)\right)\frac{1}{R(x)} - \frac{a_{12}a_{21}}{a_{11}\Delta\pi}\left(S^{-1}f',1\right)\frac{1}{R(x)},$$
$$(X^{-1})_{12}g = -\frac{a_{12}}{\Delta}S^{-1}g + \frac{a_{12}}{\pi\Delta}\left(S^{-1}g,1\right)\frac{1}{R(x)},$$
$$(X^{-1})_{21}f = -\frac{a_{21}}{\Delta}S^{-1}f' + \frac{a_{21}}{\pi\Delta}\left(S^{-1}f',1\right)\frac{1}{R(x)}, \quad (X^{-1})_{22}g = \frac{a_{11}}{\Delta}S^{-1}g - \frac{a_{11}}{\pi\Delta}\left(S^{-1}g,1\right)\frac{1}{R(x)},$$

where $R(x) = \sqrt{(p+l-x)(x-p+l)}$ and $\Delta = a_{11}a_{22} - a_{12}a_{21}$.

4. THE SPECTRUM OF OPERATOR FUNCTION $K(\gamma)$

Henceforward, quantity l is considered as a small parameter. The study of the spectrum of operator function $K(\gamma)$ is based on the possibility of representing it in the form

$$K(\gamma) = X(\gamma) + C(\gamma) + s(\gamma), \tag{10}$$

where operator $X(\gamma)$ is explicitly invertible, $C(\gamma)$ is a one-dimensional operator, and operator $s(\gamma)$ is small in the sense that $\|s(\gamma)\| \to 0$ as $l \to 0$. Representation (10) follows from the analysis of the kernels of the integral operators and takes place at any γ different from the poles of Green's functions G_1^2, G_2^2, G_1^1, and G_2^1 and the roots of equation

$$k_1^2 + k_2^2 - 2\gamma^2 = 0. \tag{11}$$

Theorem 1. For any point, γ different from the poles of Green's functions G_1^2, G_2^2, G_1^1, and G_2^1 and the roots of Equation (11), there exists l_0 such that, for any $l < l_0$, the continuous inverse operator $K^{-1}(\gamma)$ exists.

In particular, Theorem 1 implies [2] that, for sufficiently small l, the points of the spectrum can be located only near the roots of Equation (11) and poles of Green's functions G_1^2, G_2^2, G_1^1, and G_2^1. Taking into account the dependence on frequency, one can assign to each singular point a curve on the plane $(k_1 c, \gamma/k_1)$.

Equation (11) can be written as

$$(\gamma/k_1)^2 = (1+\varepsilon)/2. \tag{12}$$

It specifies a horizontal straight line.

The poles of functions G_1^2, G_2^2, G_1^1, and G_2^1 correspond to two families of curves

$$\frac{\gamma}{k_j} = \sqrt{1 - \lambda_{nm}^{(j)}}, \quad j = 1,\, 2\,; \quad n,\, m = 0,\, 1,\, 2, \ldots \tag{13}$$

where $\lambda_{nm}^{(j)} = \pi^2 \left(\frac{n^2}{c^2} + \frac{m^2}{b_j^2} \right)$.

A possible location of limit curves (12)–(13) is shown in Fig. 2. For sufficiently small values of l, the dispersion curves (propagation constants versus frequency) should pass in the vicinity of specific limit curves. For example, pole curves (13) correspond to TE- and TM-modes of the upper or lower rectangular waveguide and are limit curves for dispersion curves of quasi-TE- and quasi-TM-modes. The curve specified by Equation (12) is a limit curve for the slot mode. Since some of the limit curves intersect with each other, mutual transformation of modes takes place under frequency variation.

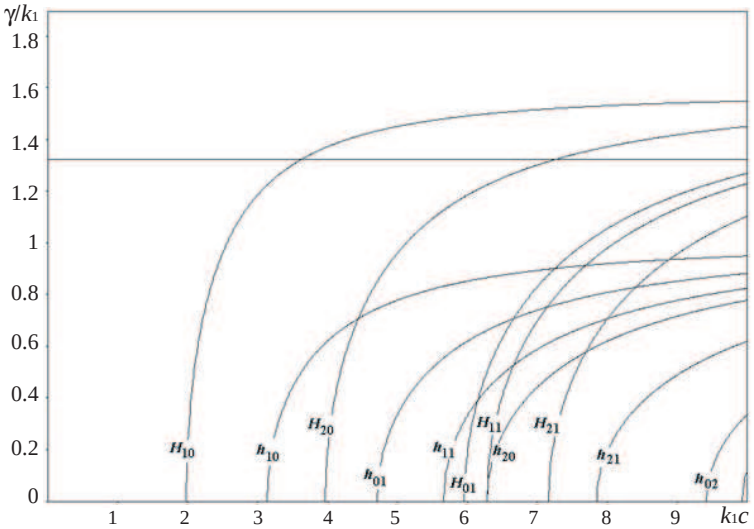

Figure 2.

Representation (10) allows one to approximately invert operator function $K(\gamma)$ and obtain dispersion equations that can be also approximately solved. Depending on the choice of a limit curve, the following modes are obtained.

5. QUASI-TE-MODES

In a vicinity of curves (13) for $j = 1$ and even N, we obtain the following approximate solution to the dispersion equation corresponding to the quasi-TE-modes:

$$\frac{\gamma}{k_1} = \sqrt{\varepsilon - \frac{\lambda_{NM}^{(2)}}{k_1^2}} + \beta \frac{\lambda_{NM}^{(2)}}{k_1^2} \frac{\pi}{2b_2 c k_1^2} \frac{1}{\sqrt{\varepsilon - \dfrac{\lambda_{NM}^{(2)}}{k_1^2}}} \frac{1}{\dfrac{\varepsilon - 1}{2} - \dfrac{\lambda_{NM}^{(2)}}{k_1^2}} + O(\beta^2), \tag{14}$$

where $\beta = \left(\ln \frac{2}{l}\right)^{-1}$.

The qualitative behavior of the dispersion curves is shown in Fig. 3(a). For $\gamma/k_1 < \sqrt{(\varepsilon+1)/2}$, the dispersion curve lies below the limit pole curve, and, for $\gamma/k_1 > \sqrt{(\varepsilon+1)/2}$, it lies above the limit pole curve.

Under the same conditions but odd N, we obtain the following solution to the dispersion equation:

$$\frac{\gamma}{k_1} = \sqrt{\varepsilon - \lambda_{NM}^{(2)}/k_1^2} - \frac{l^2}{\sqrt{\varepsilon - \lambda_{NM}^{(2)}/k_1^2}} \frac{\pi^3 N^2}{4\lambda_{NM}^{(2)} b_2 c^3} \left(\frac{2\varepsilon}{\varepsilon+1} \frac{\lambda_{NM}^{(2)}}{k_1^2} + \frac{\varepsilon-1}{\varepsilon+1} \left(\varepsilon - \frac{\lambda_{NM}^{(2)}}{k_1^2} \right) \right) + O(l^4 \ln l). \tag{15}$$

The qualitative behavior of the real dispersion curves is shown in Fig. 3(b). For any $\gamma > 0$, the dispersion curve lies below the limit pole curve.

6. SLOT MODE

In a vicinity of straight line (11), we obtain the following approximate solution to the dispersion equation corresponding to the slot mode:

$$\gamma^2 = \frac{k_1^2 + k_2^2}{2} + \beta\pi \frac{k_2^2 - k_1^2}{2} \left(C_2 \left(\sqrt{\frac{k_1^2 + k_2^2}{2}} \right) - C_1 \left(\sqrt{\frac{k_1^2 + k_2^2}{2}} \right) \right) + O(\beta^2),$$

where C_1 and C_2 are known analytic functions.

For the slot line type under consideration, a slot mode always has a cutoff frequency, because the solution to the dispersion equation does not exist in a certain vicinity of zero frequency.

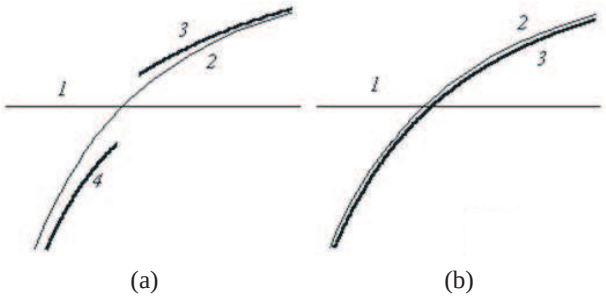

Figure 3.

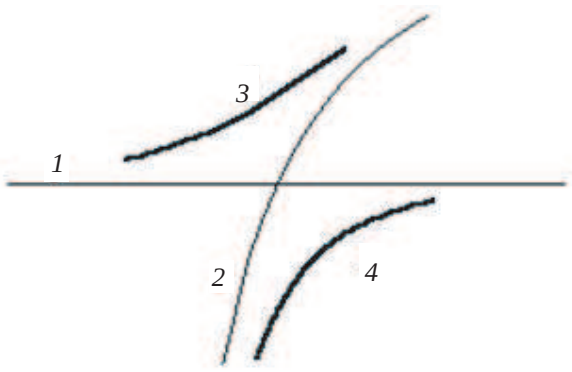

Figure 4.

7. MUTUAL TRANSFORMATION OF SLOT AND QUASI-TE-MODES UNDER VARIATION OF FREQUENCY

The behavior of dispersion curves in the vicinity of the intersection point of lines $\gamma = \sqrt{\left(k_1^2 + k_2^2\right)/2}$ and $\gamma = \sqrt{k_2^2 - \lambda_{NM}^{(2)}}$ is approximately described by the equation

$$\frac{\gamma}{k_1} = \sqrt{\frac{\varepsilon+1}{2}} \pm \frac{\sqrt{\beta}}{4} \frac{\varepsilon - 1}{\sqrt{\varepsilon+1}} \sqrt{\frac{2}{b_2 c}} + O(\beta), \quad \beta \to 0,$$

which gives the following qualitative pattern (Fig. 4): As the distance from the intersection point increases, the dispersion curves approach either curve (12) or curve (13). Thus, it is seen that, as frequency varies, a slot mode is transformed into a quasi-*TE*-mode and vice versa.

8. QUASI-TM-MODES

For the slot line type under consideration, pole curves (13) that correspond to *TM*-modes of closed rectangular waveguides simultaneously correspond to the *TE*-modes of these waveguides. Hence, pole curves (13) with $N > 0$ and $M > 0$ are limit curves for the quasi-*TE*- and quasi-*TM*-mode simultaneously.

In the vicinity of curves (13), for $j = 1$, odd N, and $M > 0$, two dispersion curves are located: One of them lies below the limit curve and may be associated with a quasi-*TE*-mode and the other one lies above the limit curve and may be associated with a quasi-*TM*-mode. Both the curves lie apart from the pole curve at a distance of $O(l^2)$.

Under the same condition but even N, we obtain two curves. The curve corresponding to a quasi-*TE*-mode is described by formula (14) and lies apart from the pole curve at a distance of $O(\beta)$; the curve corresponding to a quasi-*TM*-mode lies apart from the pole curve at a distance of $O(l^4)$. The qualitative behavior of this curve is shown in Fig. 5.

9. QUASI-*TE*- AND QUASI-*TM*-MODES CORRESPONDING TO *TE*- AND *TM*-MODES OF THE UPPER WAVEGUIDE

For even N, the dispersion curves of the quasi-*TE*-mode are described by the formula

$$\frac{\gamma}{k_1} = \sqrt{1 - \frac{\lambda_{NM}^{(1)}}{k_1^2}} - \beta \frac{\lambda_{NM}^{(1)}}{k_1^2} \frac{\pi \delta_N \delta_M}{b_1 c k_1^2} \frac{1}{\sqrt{1 - \dfrac{\lambda_{NM}^{(1)}}{k_1^2}}} \frac{1}{\dfrac{\varepsilon - 1}{2} + \dfrac{\lambda_{NM}^{(1)}}{k_1^2}} + O(\beta^2) \tag{16}$$

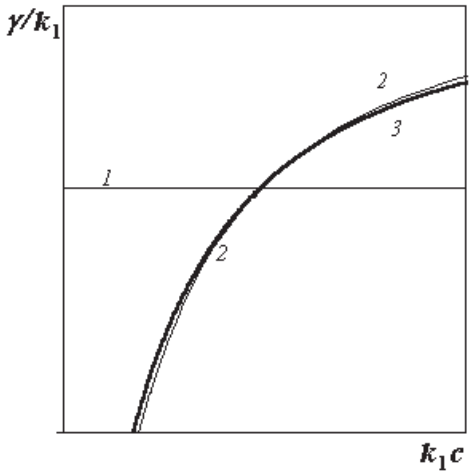

Figure 5.

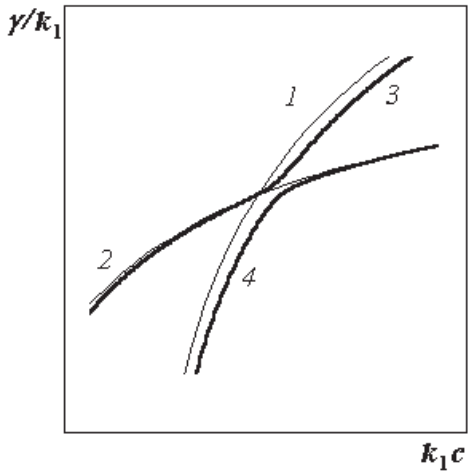

Figure 6.

and, for odd N, by the formula

$$\frac{\gamma}{k_1} = \sqrt{1-\lambda_{NM}^{(1)}/k_1^2} - \frac{1}{b_1 c}\frac{l^2\pi^2 N^2}{\sqrt{1-\lambda_{NM}^{(1)}/k_1^2}\lambda_{NM}^{(1)} c^2}\frac{\pi}{(1+\varepsilon)}\left(\frac{\lambda_{NM}^{(1)}}{k_1^2}\frac{(\varepsilon+1)}{4} + \frac{(1-\varepsilon)}{4}\right) + O(l^4 \ln l). \quad (17)$$

In this case, dispersion curves of quasi-TE-mode lie below their limit curves.

Pole curves (13) corresponding to TE- and TM-modes of the upper waveguide do not intersect line (12) and, therefore, the corresponding quasi-TE- and quasi-TM-modes of the slot line are never transformed into a slot mode. However, pole curves corresponding to TE- and TM-modes of the upper and lower waveguides intersect.

Intersection of two limit curves (13) does not result in intersection of the corresponding dispersion curves. Their qualitative behavior in this case is shown in Fig. 6.

REFERENCES

1. Il'inskii, A. S. and E. G. Smirnov, "Diffraction of electromagnetic waves from thin screens," *IPRZh Radiotekhnika*, Moscow, 1996 [In Russian].
2. Il'inskii, A. S. and E. V. Chernokozhin, "Eigenmodes of a screened slot line," *Comm. Electron. Tech.*, Vol. 49, No. 7, 773–789, 2004.

The Radiotransparent Windows Formed of Waveguides with Complex Cross Sections

A. S. Ilinskiy[1] **and Yu. Ya. Kharlanov**[2]

[1]Moscow State University, Russia
[2]16th Central Research Institute, Russia

Abstract— Radiotransparent windows with plane surfaces that are periodic structures are considered. The periodic structures are based on dual-polarization and wideband waveguides of a complex section with minimal intercenter distances between waveguides. The aperture efficiency for such windows is simulated.

1. INTRODUCTION

The use of radiotransparent waveguide windows (frequency-selective surfaces) is a promising line in the development of highly durable and vibrostable centimeter- and millimeter-wave antennas. One of the main requirements of radiotransparent waveguide windows is good matching of their aperture surfaces with free space. Reflections from a window are determined to a considerable extent by reflections from the apertures of its waveguide elements. Available structures of waveguide windows contain square, circular, and rectangular waveguides whose open ends are poorly matched with free space. In addition, windows based on square and circular waveguides cannot be applied in a wide frequency band when frequency-coverage coefficient K_f equal to the ratio of the upper and lower frequencies of a waveguide window exceeds $\sim 1.2 \ldots 1.3$. The use of waveguides with a complex shape of the cross section can improve the characteristics of radiotransparent windows [1–4]. A change in the parameters of sections can govern the internal and external characteristics of radiators and radiotransparent windows based on such waveguides.

In our investigations, we used the mathematical model of an infinite array antenna (AA) formed of waveguides with an arbitrary section. The model involves solution of the exterior problem by means of the field-joining projection method and solution of the interior problem by means of the finite element method [5]. Propagation of electromagnetic waves through both surfaces of a window is taken into account. The walls of waveguides are assumed infinitely thin.

2. APERTURE EFFICIENCY OF ARRAYS

When the operating frequency band is relatively narrow ($K_f < 1.3 \ldots 1.4$), square, hexahedral, cross-shaped, and square four-ridge waveguides are of the most practical interest for designing waveguide windows ensuring operation with the rotating field polarization (Fig. 1). Such waveguides form dense cellular packages without parasitic zones in the aperture that are not related with the waveguide channels of the window.

Simulation and optimization of the characteristics of AAs based on the aforementioned dual-polarization waveguides with the minimal intercenter distances between elements have shown that the minimal reflection coefficient is attained when the waveguides in the AA aperture are arranged on a triangular grid and when their dimensions are chosen such that the upper frequency of a waveguide's single-mode regime coincides with the upper frequency of the AA operating band [3]. For AAs formed of cross-shaped and four-ridge waveguides, there are optimal parameters of waveguides' sections. The best matching within scanning sector 2θ extending to $\pm 28^\circ$ is ensured by

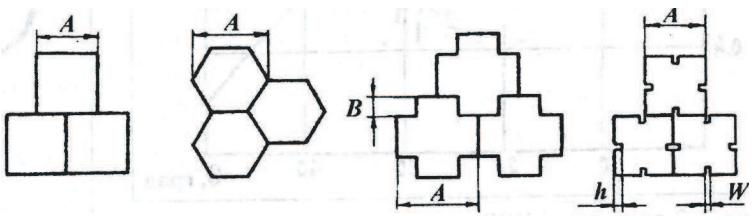

Figure 1: Radiating aperture.

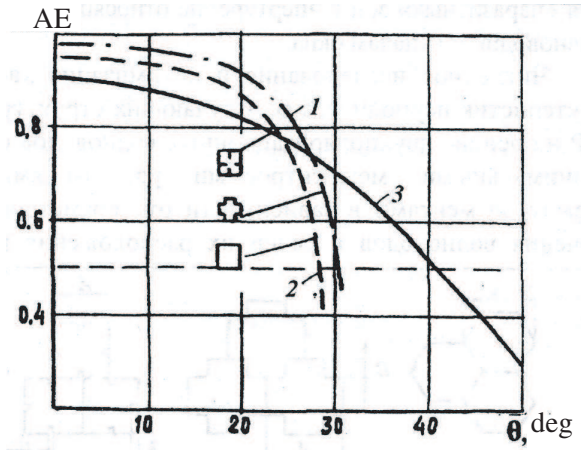

Figure 2: Aperture efficiency.

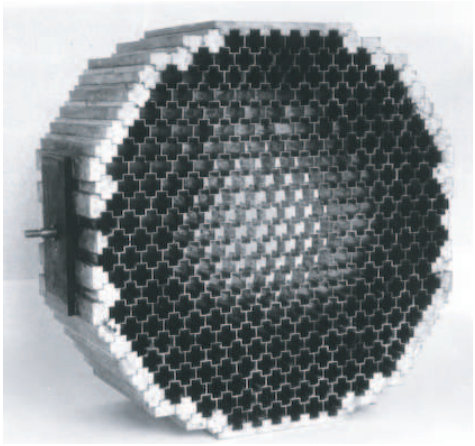

Figure 3: Aperture of cross-shaped waveguides.

AAs formed of cross-shaped waveguides with the section parameter $B/A = 0.25$. When square four-ridge waveguides are used, the minimal reflection coefficient is attained at the relative height of a ridge $h/A \approx 0.14$ ($W/A = 0.1$).

The comparison of the AEs of various types of waveguide windows has shown that the maximal AE is attained with the use of cross-shaped waveguides (Figs. 2 and 3). In this situation, the AE is no less than 0.5 within the angular sector $2\theta = 63°$, while $2\theta = 54°$ for square waveguides. The application of square four-ridge waveguides ensures a substantially wider effective scanning sector, $2\theta = 86°$, the AE being no worse than 0.5.

3. DOUBLE-BAND ARRAYS

Certain prospective radar and radio communications systems and systems that are being developed use several frequency bands simultaneously. In this case, wideband waveguides with a complex shape of the cross section (Fig. 4) that cover the necessary frequency band in the single-mode regime or combined structures based on single- or dual-polarization waveguides can be applied as radiators in waveguide windows or AAs.

The AEs of radiotransparent windows based on H-shaped and modified cocoon-shaped waveguides operating in the same frequency band (Fig. 5) are estimated and compared. When H-shaped waveguides are used, the acceptable AE values are attained within several frequency bands (AE $\approx 0.32 \ldots 0.59$ within a band of $3.4 \ldots 8.4$ GHz). In this situation, the AE is substantially larger than that for cocoon-shaped waveguides (AE $\approx 0.14 \ldots 0.46$). The AE of radiotransparent windows can still be increased through using dielectric coatings of the aperture or introducing dielectric insertions into waveguide channels.

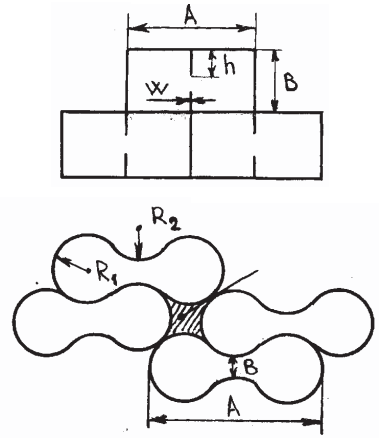

Figure 4: Cross sections of waveguides.

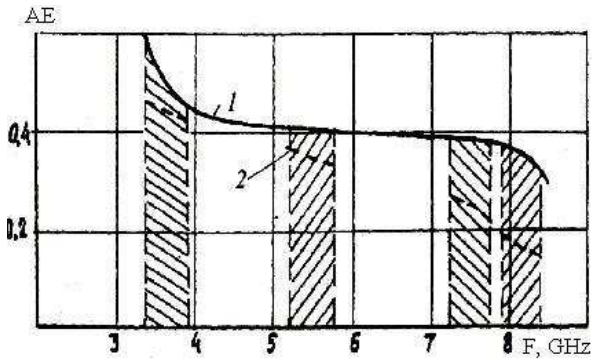

Figure 5: Comparison of AEs.

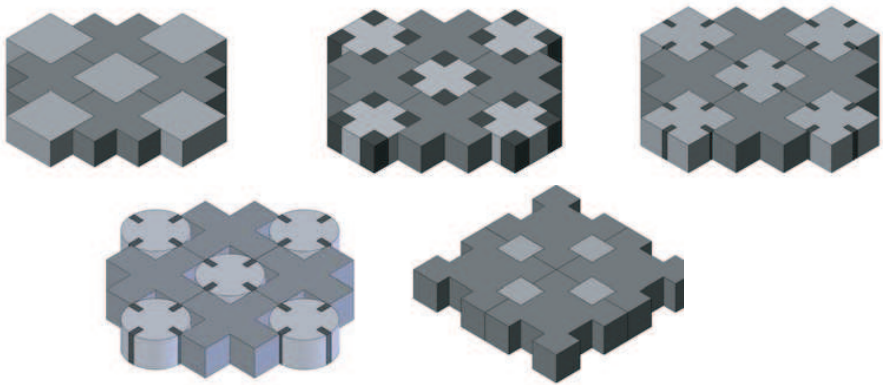

Figure 6: Double-band radiating aperture.

4. CHARACTERISTICS OF RADIATORS

The design of radiotransparent windows that are based on wideband radiating elements and operate within a sufficiently wide frequency band is impeded by the necessity to provide for the required patterns and matching quality within a frequency band and within a preassigned scanning angular sector.

When neighboring frequency bands are considerably spaced, a more effective method involves the use of combined structures, each operating in one of the frequency bands [6, 7]. However, when rectangular and circular waveguides are applied for this purpose, one may encounter problems in providing for required distances between the centers of radiators operating in one band. Therefore, it is necessary to use waveguides with a dielectric filling so as to decrease the dimensions of the structure or to use more complex configurations of radiators. The application of waveguides with a complex shape of the cross section makes it possible to considerably reduce these difficulties, because the appropriate choice of the shape of the cross section can ensure an acceptable trade-off between the requirements on the electric characteristics of radiators and their arrangement in the aperture.

Some variants of double-band combined radiating apertures are considered. These apertures are based on cross-shaped and four-ridge (circular and square) waveguides whose dimensions are smaller than those of standard (circular and square) waveguides operating in the same frequency band (Fig. 6).

In the upper frequency band, the maximum dimension of the waveguide's section is determined in these cases by the shape and dimensions of the lower frequency (base) waveguide. It is also possible to realize a combined radiator configuration such that closely spaced bands are covered by wideband radiators and more distant frequency bands are covered by separate radiating structures located together with the wideband radiators in one aperture.

When a cross-shaped waveguide is employed as a base one, rather closely spaced bands can be combined. When a four-ridge waveguide is employed as a base one, bands spaced by several octaves can be combined. The frequency band of the embedded waveguide with a square section is unambiguously determined by the dimensions of the base waveguide. When embedded waveguides with a cross-shaped and four-ridge sections are used, a change in the parameters of the sections provides for an additional degree of freedom in choosing frequency bands. In particular, the use of a four-ridge waveguide makes it possible to combine even frequency bands adjoining each other.

The internal and external characteristics of radiators that are open ends of waveguides are studied numerically and experimentally, and the mutual influence of closely located waveguides operating in different bands is experimentally assessed [1, 2]. It is shown that, when waveguides with optimal or close to optimal parameters of the sections are employed, necessary frequency bands can be combined through choosing the type of waveguides and using operating frequency bands located in the single-mode regions of these waveguides.

5. ARRAY WITH COMBINED RADIATORS

When elements radiating in different frequency bands are combined within one aperture, the radiators may noticeably interact because of diffraction effects on their surfaces and leakage of the electromagnetic energy of one band into the elements of another band.

In this situation, the influence of the high-frequency subarray on the low-frequency one is more substantial, because the field produced by the high-frequency radiator is transmitted into the channel of the low-frequency radiator and leads to excitation and propagation of the fundamental and higher order modes, while the high-frequency radiator is evanescent for the low-frequency band. This influence can be reduced through polarization decoupling. When it is necessary to provide for independent dual-polarization operation in each frequency band, the mutual influence of elements should be minimized and the effect of this influence on the amplitude–phase field distribution over the aperture should be taken into account.

An effective method for elimination of the mutual influence of the subarrays of a combined double-band structutre without deterioration of the Q factor of the antenna system is the use of open ends of diaphradmic waveguides as radiators of the low-frequency subarray. In the high-frequency band, such waveguides have stopbands for all modes propagating in them [8]. The dimensions of the section, the depth of grooves, and the period of the structure are chosen such that the single- or multimode regime is realized in the low-frequency band and stopbands are provided for all modes propagating in the high-frequency band. Diaphragms may have different shapes-rectangular, sinusoidal, etc. — That are determined from the design philosophy.

The schematic of a structure containing cross-shaped and circular diaphragmic waveguides is displayed in Fig. 7. The results of the experimental investigation of the dispersion characteristics of a circular diaphragmic waveguide used for the low-frequency subarray are presented in Fig. 8. The shaded strips in the figure are the operating bands of the combined structure. It is seen

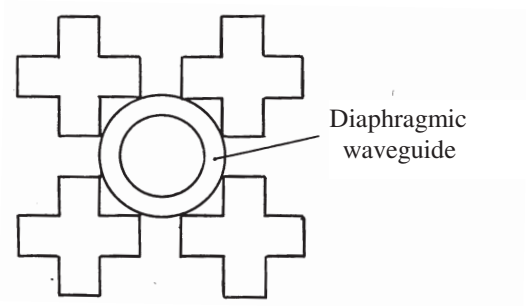

Figure 7: Schematic of a double-band aperture.

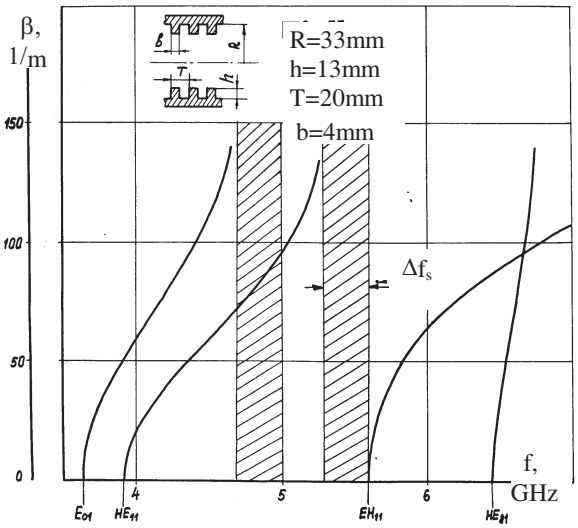

Figure 8: Dispersion characteristics.

that stopband Δf_s (which is common to all propagating modes) of the low-frequency radiator corresponds to the upper operating frequency band. Hence, when the high-frequency subarray is excited in this band, no modes propagate in the low-frequency radiators and, practically, there is no influence of subarrays.

Note that the method proposed for aperture decoupling is most efficient when the operating frequency bands are closely spaced, i.e., in the case most important for practice. As an example, a frequency band of 7/8 GHz is considered. In the frequency band 7.25...7.75 GHz, the dimensions of the diaphragmic radiator are $R = 23.8$ mm, $h = 10.9$ mm, $T = 15.5$ mm, and $b = 4.6$ mm. In the frequency band 7.9...8.4 GHz, the dimensions of the cross-shaped radiator are $A = 21.6$ mm and $B = 4.9$ mm. Diaphragmic waveguides with various (in particular, cross-shaped) sections can be used in the structures considered above.

6. CONCLUSION

The obtained results show that waveguides with complex sections should be preferred for constructing radiotransparent waveguide windows (frequency-selective structures) and can be used for designing antennas with radiotransparent windows and AAs.

REFERENCES

1. Il'inskii, A. S., Y. Y. Kharlanov, and Y .N. Vasilenko, "Properties of the dual-polarization waveguide-horn radiators of complex cross-section," *Radiotekh. Elektron.*, Vol. 41, No. 10, 1183, Moscow, 1996 (in Russian).
2. Il'inskii, A. S., Y. Y. Kharlanov, and Y. N. Vasilenko, "Cross-shaped and four-ridge wavegide-horn radiators: Internal and external characteristics," *Radiotekh. Elektron.*, Vol. 51, No. 1, 6, Moscow, 2006 (in Russian).
3. Il'inskii, A. S., Y. Y. Kharlanov, and Y. N. Vasilenko, "Investigation and optimization of the characteristics of a periodic structure based on the dual-polarization complex section waveguides," *Antenny*, No. 1(38), 76, 1997 (in Russian).
4. Il'inskii, A. S., Y. Y. Kharlanov, and Y. N. Vasilenko, "Modeling of lens antennas on the basis of waveguide with a complex cross section," *Radiotekh. Elektron.*, Vol. 42, No. 3, 295, Moscow, 1997 (in Russian).
5. Grinev, A. Y., A. S. Il'inskii, Y. V. Kotov, and I. P. Chepurnykh, *Radiotekh. Elektron.*, Vol. 24, No. 7, 1291, Moscow, 1979 (in Russian).
6. Vasilenko, Y. N., V. M. Golub, A. S. Il'inskii, and Y. Y. Kharlanov, "Double-band radiators based on waveguides with complex cross sections," *Phased Array Antennas and Their Elements: Computer-Aided Design and Automatic Measurements (PAA-90) (Proc. All-Union Scientific and Engineering Conf.*, 56, Kazan Aviation Institute, Kazan, Russia, June 11–15, 1990.
7. Voskresenskii, D. I., Y. V. Kotov, Y. Y. Kharlanov, and E. V. Ovchinnikova, "Multifunctional array antenna curtains," *Antenny*, No. 9(112), 5–23, 2006 (in Russian).
8. Il'inskii, A. S., Y. V. Medvedev, Y. Y. Kharlanov, and K. N. Tsibizov, "Double-band combined waveguide array antenna with frequency-selective decoupling of apertures", RF Patent No. 2 258 284, Int. Cl. H 01 Q 21/00, Priority 24.11.2003, Published 10.08.2005, Byull. Isobret. No. 22.

The Investigation of Properties of Periodic System of X-ray Waveguides

A. M. Lerer, **M. I. Mazuritsky**, **P. V. Makhno**,
V. V. Makhno, **and G. P. Synavsky**
Southern Federal University, Rostov-on-Don, Russia

Abstract— The approximate decision of the scalar Helmholtz equation for periodic structure of dielectric has been performed. This decision is applied for research of electromagnetic waves propagation in the x-ray waveguides and 2-D photonic crystals.

It's well-known, that development of X-ray optics faces difficulties, significantly different from infrared and visible range optics. This is due to very low reflectance at big angles of incidence of X-ray from surfaces of all known substances. One of the ways to overcome this difficulty is the use of grazing incidence optics, which is based on the phenomenon of total X-ray reflection (TXR) which occurs at the condition of total external reflection holds when incident photons impinge on a surface at a glancing angle. For x-rays, a solid medium is optically less dense than a vacuum, and thus total external reflection occurs. This phenomenon is due to the dielectric constant of almost all materials for X-ray is less than one ($n \approx 1 - \delta$). Because $0 < \delta \ll 1$, the vacuum in this frequency range is optically more dense media than the material.

It's well-known, that at high angles of incidence of electromagnetic waves on the boundary between mediums of quite close values of refractive coefficients, coefficients of refraction of waves of two orthogonal polarizations are close. This allows to calculate dielectric waveguides (DW), which have close refractive coefficients of waveguiding region and surrounding media. The examples of such DWs are optical fibers, especially single-mode, and X-ray waveguides.

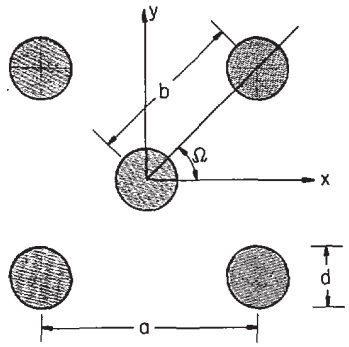

Let's consider in scalar approximation the propagation of eigenwaves in bi-dimensionally periodic system of dielectric waveguides. DWs are infinite in z-direction. Refractive indices of DW and surrounding space are equal to, correspondingly, n_1, n_2, periods of grating in x, y-axis are $d_{x,y}$. Let's write down the Helmholtz equation for y-th component of electric field strength:

$$\left[\frac{\partial^2}{\partial x^2} + \frac{\partial^2}{\partial y^2} - \gamma^2 + (kn_2)^2 + k^2\delta(x,y)\right] E(x,y) = 0, \tag{1}$$

where γ — propagation constant of the wave in z-direction, k — wavenumber in a vacuum,

$$\delta(x,y) = n_1^2(x,y) - n_2^2.$$

Let's disintegrate the solution of Equation (1) and the function $\delta(x,y)$ in double Fourier series

$$E(x,y) = \frac{1}{a\,d}\sum_{m=-\infty}^{\infty}\sum_{n=-\infty}^{\infty} E_{m,n}\exp\left[i\left(\alpha_m x + \beta_{mn} y\right)\right], \tag{2}$$

$$\delta(x,y) = \frac{1}{a\,d}\sum_{m=-\infty}^{\infty}\sum_{n=-\infty}^{\infty} \delta_{m,n}\exp\left[-i\left(\alpha_m x + \beta_{mn} y\right)\right], \tag{3}$$

where $\alpha_m = \frac{2m\pi}{d}$, $\beta_{mn} = \frac{2n\pi}{d} - \alpha_m \mathrm{ctg}\Omega$, $d = b\sin\Omega$. (???????????) (?????????????)

Substituting (2), (3) into (1) and setting equal the members with identical numbers of spatial harmonics. As a result we obtain the system of linear algebraic equations (SLAE) in unknowns $E_{m,n}$

$$\left[-\alpha_m^2 - \beta_{mn}^2 - \gamma^2 + (kn_2)^2\right] E_{m,n} + k^2 \frac{1}{d_x\, d_y} \sum_{p=-\infty}^{\infty} \sum_{q=-\infty}^{\infty} E_{p,q}\delta_{p-m,q-n} = 0, \tag{4}$$

$$m = 0, \pm1, \pm2\ldots,\ n = 0, \pm1, \pm2\ldots$$

The equality to zero of determinant of SLAE (4) is the dispersion equation in γ.

The performed transformations are accurate only for the case of continuity of refractive index n_1 and its normal (to the DW's boundary) derivative. For the case:

$$\frac{n_1 - n_2}{n_1} \ll 1 \tag{5}$$

both conditions are satisfied approximately.

SLAE (5) is solved by reduction method — discarding unknowns and equations with the numbers $|m| > M_x$, $|n| > M_y$. The number of unknowns is decreasing, if DW's have planes of symmetry. If DWs are symmetric with respect to plane $x = 0$, then $E_{-m,n} = \pm E_{m,n}$. The sign is determined by parity of field with respect of symmetry plane. Analogous for the case of symmetry of DW with the respect of plane $y = 0$.

Let's transform SLAE (5) for circular DWs, using normalized frequency $F = kR\sqrt{n_1^2 - n_2^2}$ and normalized moderating ratio $B = \sqrt{\frac{(\gamma/k)^2 - n_2^2}{n_1^2 - n_2^2}}$:

$$-\left[\left(\rho^R_{m,\,n}\right)^2 + (F\,B)^2\right] E_{m,n} + F^2 \frac{1}{d_x\, d_y} \sum_{p=-\infty}^{\infty} \sum_{q=-\infty}^{\infty} E_{p,q}\bar{\delta}_{p-m,q-n} = 0 \tag{6}$$

$$m = 0, \pm1, \pm2\ldots,\ n = 0, \pm1, \pm2\ldots$$

$$\rho_{m,n} = \sqrt{\alpha_m^2 + \beta_{mn}^2}$$

Further transformation of SLAE (6), which consider the field's symmetry, are elementary and not listed here.

For the case of propagation of electromagnetic waves in two-celled photonic crystal (bi-dimensionally periodic system of dielectric cylinders) listed above solution of Helmholz equation will be accurate at any $n_{1,\,2}$, if:

- magnetic permeabilities of cylinders and surrounding media are equal to one;
- the wave propagates perpendicularly to the cylinders;
- electric field is polarized along cylinders.

In this case in (4) we have to set $\gamma = 0$, besides, in (2), (4) a substitution has to be made:

$$\alpha_m \to \bar{\alpha}_m = \frac{2m\pi}{d_x} + k_x,\ \beta_{mn} \to \bar{\beta}_{mn} = \frac{2n\pi}{d_y} + k_y,$$

where $k_x = k\cos\varphi$, $k_y = k\sin\varphi$, φ — angle between wave vector and x-axis. Expression (3) and expressions for $\bar{\delta}_{m,n}$ will not change. In dispersion equation the unknown will be wavenumber k.

To validate obtained solution and estimate the limits of its possible application the comparison of obtain results with the results of calculation by accurate method [1] was performed. It is shown, that relative inaccuracy of the solution is not higher than $\frac{n_1 - n_2}{2n_2}$.

On the Fig. 1 dispersion curves for the fundamental mode of waveguide at different values of ratio $d_x/2R$ at $d_x = d_y$, $\Omega = 0$ are presented.

If the normalized moderating ratio $B > 0.8$, B is almost independent on d_x, otherwise, propagation constants of periodic and single DW are close. Moderating ratio weakly depends on Ω (Fig. 2, $d_x = d_y$, $R/d_x = 0.4$, the ordinate-axis is the relative variation of normalized moderating ration δB).

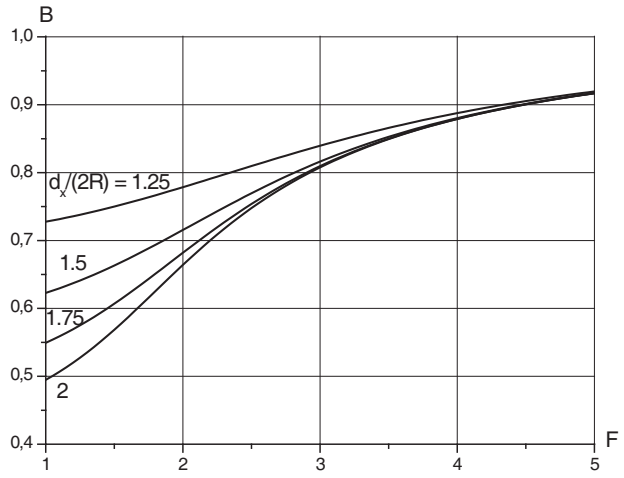

Figure 1.

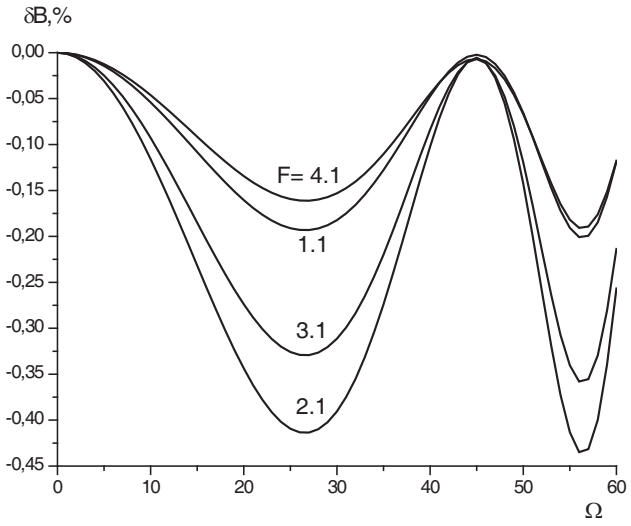

Figure 2.

Thereby, obtained approximate solution of scalar Helmholz equation allows to solve quite wide range of boundary problems of applied electrodynamics, including problems of propagation of X-ray waves in waveguides. It's shown, that in practically used microcapillary structures (in bi-dimensional periodic X-ray waveguides) propagation constants of periodic and single DWs are close. The problem of wave's propagation in photonic crystals (bi-dimensionally periodic system of dielectric cylinders) have been solved, the influence of cylinders' parameters on location and sizes of opacity window have been investigated.

REFERENCES

1. Lerer, A. M., P. V. Makhno, and M. I. Mazuritsky, "The investigation of eigenwaves in periodic system of round shaped metallic nanowires," *Electromagnetic Waves and Electronic Systems*, Vol. 11, No. 5, 43–45, 2006.

Mathematical Modeling of Waveguiding Systems Based on Photonic Crystals

A. N. Bogolyubov, **I. A. Butkarev**, **and Yu. S. Dementieva**
Faculty of Physics, M. V. Lomonosov Moscow State University, Russia

Abstract— In this paper we present mathematical model and numerical algorithm allowing to investigate two-dimensional and three-dimensional photonic crystals and waveguiding systems based on photonic crystals. We demonstrate spectral characteristic of photonic crystals and systems based on them.

1. INTRODUCTION

Photonic crystals have been considered as composite structures made up of two lossless isotropic media with different refractive indices n_1 and n_2. In photonic crystals the propagation of electromagnetic waves is forbidden for a certain frequency range. This property provides a promising tool to control the flow of light in integrated optical devices. In the last several years, there is a great deal of interest in developing photonic crystal based components such as waveguides, lasers, splitters, fibers, optical circuits, and ultrafast optical switches.

2. NUMERICAL ALGORITHM

We construct numerical algorithm allowing to calculate propagation of electromagnetic waves across systems based on photonic crystals. Using this algorithm we calculated spectral characteristics of photonic crystals and waveguiding systems based on them. The algorithm consists of finite-difference time-domain method (FDTD), perfectly matched layer technique (PML) and total-field/scattered-field formulation (TF/SF).

The FDTD method gives the easy way to construct numerical algorithms for calculation of electromagnetic wave propagation in different waveguiding systems. Main disadvantage of this method is high computational cost, it can be overcome by using computer clusters.

Maxwell's equations can be written as

$$\varepsilon_0\varepsilon\frac{\partial E_y}{\partial t} = \frac{\partial H_x}{\partial z} - \frac{\partial H_z}{\partial x} \tag{1}$$

$$\mu_0\mu\frac{\partial H_x}{\partial t} = \frac{\partial E_y}{\partial z} \tag{2}$$

$$\mu_0\mu\frac{\partial H_z}{\partial t} = -\frac{\partial E_y}{\partial x} \tag{3}$$

We define the grid as $\omega_h = \{x_i = ih_x,\, z_j = jh_z,\, i = 0, 1, \ldots, N_x,\, j = 0, 1, \ldots, N_z\}$. Any function of space and time is written as $F^s_{i,j} = F(ih_x, jh_z, s\tau)$. The spatial and temporal derivatives of F are written using central finite difference approximations as

$$\frac{\partial F^s_{i,j}}{\partial x} \approx \frac{F^s_{i+\frac{1}{2},j} - F^s_{i-\frac{1}{2},j}}{h_x} \tag{4}$$

$$\frac{\partial F^s_{i,j}}{\partial t} \approx \frac{F^{s+\frac{1}{2}}_{i,j} - F^{s-\frac{1}{2}}_{i,j}}{\tau} \tag{5}$$

These equations are applied to the Maxwell's equations resulting in finite difference equations

$$\varepsilon_0\varepsilon_{i,j}\frac{(E_y)^{s+1}_{i,j} - (E_y)^s_{i,j}}{\tau} = \frac{(H_x)^{s+1/2}_{i,j+1/2} - (H_x)^{s+1/2}_{i,j-1/2}}{h_z} - \frac{(H_z)^{s+1/2}_{i+1/2,j} - (H_z)^{s+1/2}_{i-1/2,j}}{h_x} \tag{6}$$

$$\mu_0\mu_{i,j}\frac{(H_x)^{s+1/2}_{i,j+1/2} - (H_x)^{s-1/2}_{i,j+1/2}}{\tau} = \frac{(E_y)^s_{i,j+1} - (E_y)^s_{i,j}}{h_z} \tag{7}$$

$$\mu_0\mu_{i,j}\frac{(H_z)^{s+1/2}_{i+1/2,j} - (H_z)^{s-1/2}_{i+1/2,j}}{\tau} = -\frac{(E_y)^s_{i+1,j} - (E_y)^s_{i,j}}{h_x} \tag{8}$$

In all of the finite difference equations the components of $\vec{E}$ and $\vec{H}$ are located within a single unit cell in the three-dimensional lattice depicted in Fig. 1. $\vec{E}$ and $\vec{H}$are evaluated at alternate half time steps using Equations (6)–(8), such that all field component are calculated in each time step.

$$(E_y)_{i,j}^{s+1} = (E_y)_{i,j}^{s} + \frac{\tau}{\varepsilon_0 \varepsilon_{i,j} h_z}\left[(H_x)_{i,j+1/2}^{s+1/2} - (H_x)_{i,j-1/2}^{s+1/2}\right] - \frac{\tau}{\varepsilon_0 \varepsilon_{i,j} h_x}\left[(H_z)_{i+1/2,j}^{s+1/2} - (H_z)_{i-1/2,j}^{s+1/2}\right] \quad (9)$$

$$(H_x)_{i,j+1/2}^{s+1/2} = (H_x)_{i,j+1/2}^{s-1/2} + \frac{\tau}{\mu_0 \mu_{i,j} h_z}\left[(E_y)_{i,j+1}^{s} - (E_y)_{i,j}^{s}\right] \quad (10)$$

$$(H_z)_{i+1/2,j}^{s+1/2} = (H_z)_{i+1/2,j}^{s-1/2} - \frac{\tau}{\mu_0 \mu_{i,j} h_x}\left[(E_y)_{i+1,j}^{s} - (E_y)_{i,j}^{s}\right] \quad (11)$$

The total-field/scattered-field (TF/SF) formulation has been used to model infinite plane wave excitation in two-dimensional (2-D) and three-dimensional (3-D) finite-difference time-domain (FDTD) grids.

The computational grid is divided into two regions. The scattered field region where only the scattered field components are stored, lies outside of the scattering object, and the total field region fills the remainder of the grid. At the border between the two regions, special connecting condition are required where the incident field is either added or subtracted from the total field quantities. Since the incident field can be specified analytically and is only required on the connecting surface, computer storage is minimized.

The perfectly matched layer is a technique of free-space simulation developed for solving unbounded electromagnetic problems with the finite-difference time-domain method. Referred to as PML, this technique is based on the use of a layer especially designed to absorb the electromagnetic waves without reflection from the vacuum-layer interfaces.

In the PML medium, each component of the electromagnetic field is split into two parts. For example, in two-dimensional case Maxwell equations are replaced by equations:

$$\varepsilon_0 \varepsilon \frac{\partial E_{yz}}{\partial t} + \sigma_z E_{yz} = \frac{\partial H_x}{\partial z} \quad (12)$$

$$\varepsilon_0 \varepsilon \frac{\partial E_{yx}}{\partial t} + \sigma_x E_{yx} = -\frac{\partial H_z}{\partial x} \quad (13)$$

$$\mu_0 \mu \frac{\partial H_x}{\partial t} + \sigma_z^* H_x = \frac{\partial (E_{yz} + E_{yx})}{\partial z} \quad (14)$$

$$\mu_0 \mu \frac{\partial H_z}{\partial t} + \sigma_x^* H_z = -\frac{\partial (E_{yz} + E_{yx})}{\partial x} \quad (15)$$

3. RESULTS

Using this algorithm we calculated spectral characteristics of two-dimensional and three-dimensional photonic crystals and waveguiding systems based on them. We obtain spectral characteristic of

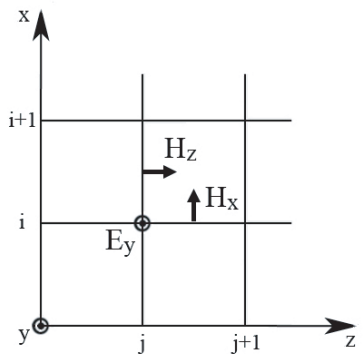

Figure 1.

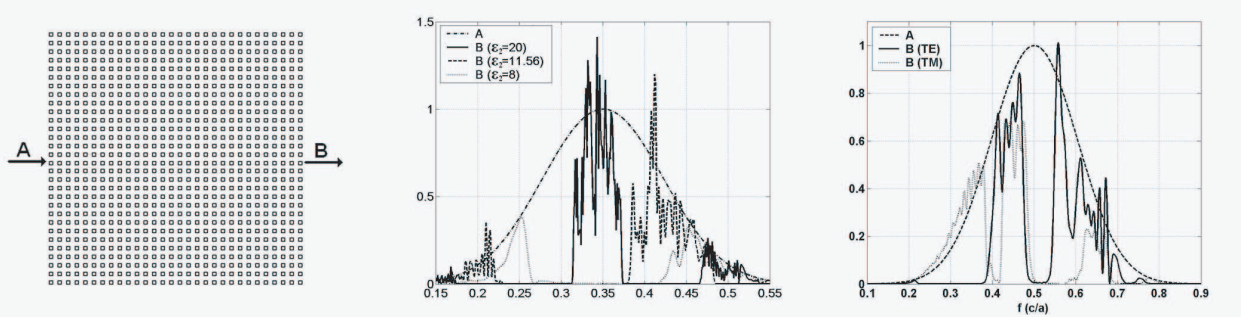

Figure 2.

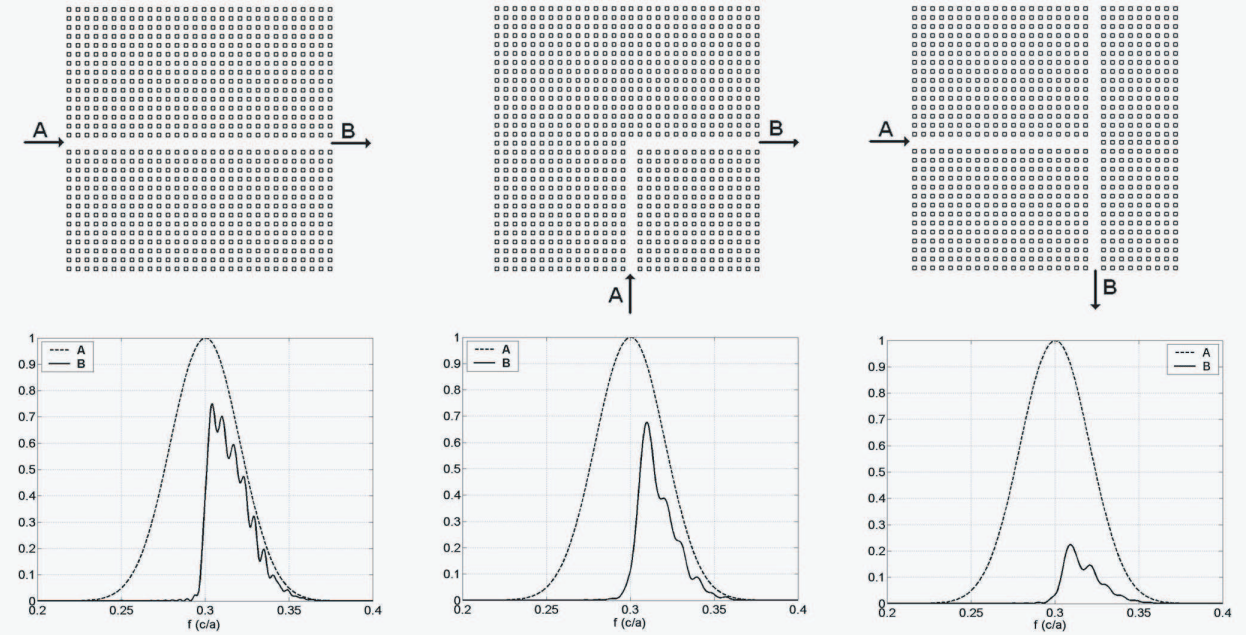

Figure 3.

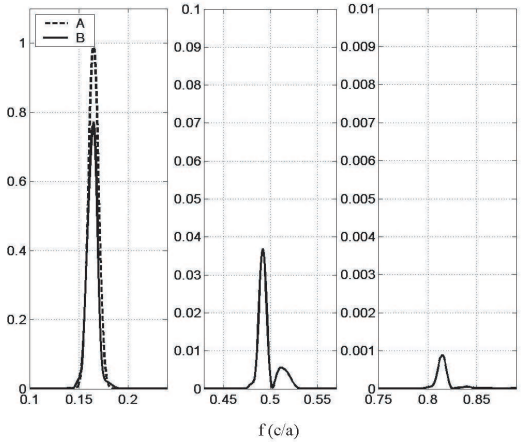

Figure 4.

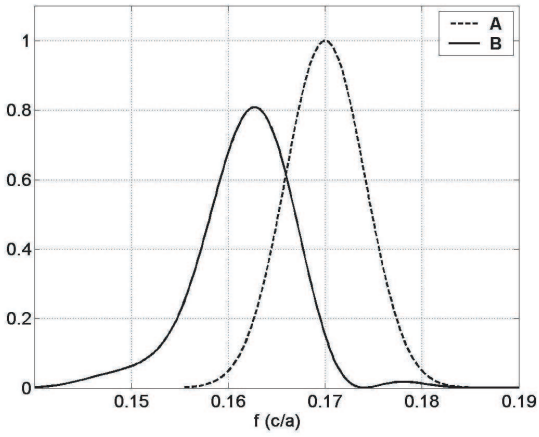

Figure 5.

various configurations of photonic crystals, for example, straight waveguides, bends, T-waveguides (see Fig. 2). Also we obtain spectral characteristic of photonic crystals with various refractive indices (see Fig. 3).

Using the finite difference time domain method, we calculated light propagation characteristics in a two dimensional photonic crystal, which is composed of lattice airholes in a third-order nonlinear medium. In this medium $\vec{D} = \varepsilon_0 \varepsilon \vec{E} + \varepsilon_0 \chi |\vec{E}|^2 \vec{E}$. The results showed the characteristic change of the transmission.

It is obvious from the above equation that odd higher order nonlinear waves, i.e., $3f$, $5f$ etc., are excited by the nonlinearity. Figs. 4 and 5 show examples of simulated field profiles and spectrum of light.

We considered bistable photonic crystal configuration consisting of a waveguide sided coupled to a single-mode cavity with Kerr nonlinearity. The results showed the characteristic change of the transmission spectrum resulting in the strong saturation of the response, and the sufficiently low transmission loss with the help of projection-type airholes at input and output interfaces.

4. CONCLUSIONS

Calculation results show that photonic crystals allow to decrease size of optical devices and they are a promising tool to control the flow of light in integrated optical devices. Our recent investigations concern modeling various waveguiding systems using three-dimensional algorithm.

REFERENCES

1. Yablonovitch, E., "Inhibited spontaneous emission in solid-state physics and electronics," *Phys. Rev. Lett.*, Vol. 58, 2059–2062, 1987.
2. LIGHTWAVE Russian edition, No. 3, 47–53, 2004.
3. Yee, K. S., "Numerical solution of initial boundary value problems involving Maxwell's equations in isotropic media," *IEEE Trans. Antennas Propagat.*, Vol. 14, 302–307, May 1966.
4. Taflove, A. and S. C. Hagness, *Computational Electrodynamics*, Artech House, Norwood, MA, 2000.
5. 1983.
6. 2003.
7. Berenger, J.-P., "Three-dimensional perfectly matched layer for the absorption of electromagnetic waves," *Journal of Computational Physics*, Vol. 127, 363–379, 1996.
8. Anantha, V. and A. Taflove, "Efficient modeling of infinite scatterers using a generalized total-field/scattered-field FDTD boundary partially embedded within PML," *IEEE Transactions on Antennas and Propagation*, Vol. 50, No. 10, 1337–1349, October 2002.
9. 1978.

A Simple Method to Find the Number of Branch Points of Propagation Constants of a Lossless Closed Guide without Constructing the Dispersion Curve

K. Karayahsi[1] and N. Yener[2]

[1]Kırac Namık Kemal Mah, 510 Sk. Bankkent Sit. A5 Blok D:2
Esenyurt, Istanbul, Turkey
[2]Technical Education Faculty, Umuttepe Campus, Kocaeli University
Izmit 41380, Kocaeli, Turkey

Abstract— Making use of the fact that the characteristic equation that results from application of the moment method, is an algebraic equation for closed and lossless guides filled with inhomogeneous and/or gyrotropic media, we attempt to determine the degree of the discriminant of this equation, assuming we have no explicit expression for the coefficients of this equation in terms of frequency. This is achieved by successive numeric differentiation of the discriminant which we know is a polynomial, and the number of such differentiations to yield a constant value will be the degree of this polynomial. This information gives the number of branch points in the dispersion curve of a lossless closed waveguide, without having to draw the dispersion curve over the full frequency axis. Maxwell's partial differential equations can be transformed into a linear algebraic equation system whose coefficient matrix has squares of the propagation constant functions as eigenvalues. It is also discussed that the discriminant of the algebraic equation is a polynomial in the complex frequency $p = \sigma + j\omega$ and that the zeroes of this polynomial correspond to singular points (branch points) of the square of the propagation constant function and this function attains multiple values at these zeroes. In our problem, we assume that the coefficients of the characteristic equation are not known analytically. Considering for instance a 20TE + 20TM truncation of the coefficient matrix which has entries that are functions of p, it is pointed out in the literature also that, it is cumbersome to compute these coefficients analytically as functions of p. In our approach, we have chosen to use the numeric evaluation of these coefficients. Hence the aim of this work is to determine the degree of the discriminant polynomial of the characteristic equation when the coefficients of this equation are not known analytically. This degree will give us the total number of multiple roots of the characteristic equation without having to draw the dispersion curve along the full frequency axis. As an example, for a structure consisting in a lossless closed circular guide loaded with a coaxial dielectric rod, we compute derivatives of the discriminant with respect to p in the complex frequency plane numerically with a view to reach a constant value after successive differentiations. The number of such differentiations will give the sought after degree. This procedure is effected through obtaining contour-plots of the various differentiations over a region of the complex frequency plane in the neighborhood of the origin. Then the same procedure is repeated yet for another region of the complex frequency plane. The set of results in both regions confirm each other by yielding the same degree for the discriminant.

1. INTRODUCTION

It has been established in [1, 2] and [3] that after applying Galerkin's version of moment method on Maxwell's equations, the characteristic equation of the resulting coefficient matrix of the linear algebraic system is an algebraic equation, for closed, lossless guides filled with inhomogeneous and/or gyrotropic media. Consequently in [2, 3] elementary algebraic function concepts were applied to this resulting algebraic equation whose roots are the squares of the approximate propagation constant functions when the above matrix is truncated, and the exact propagation constant functions when it is not truncated. In [4–6], this approach has been advanced to exact analysis in infinite dimensions. It is also discussed in [2, 3] that as stated in [7], the discriminant of the algebraic equation is a polynomial in the complex frequency $p = \sigma + j\omega$ and that the zeroes of this polynomial correspond to singular points (branch points) of the propagation constant function and this function attains multiple values at these zeroes. Similar problems have been addressed in the literature [8]. In our problem, we assume that the coefficients of the characteristic equation are not known analytically. Considering for instance a 20TE + 20TM truncation of the coefficient matrix which has entries that are functions of p, it is cumbersome to compute these coefficients analytically as functions of p [9]. In our approach, we have chosen to use the numeric evaluation of these coefficients.

The aim of this work is to determine the degree of the discriminant polynomial of the characteristic equation when the coefficients of this equation are not known analytically. This degree will give us the total number of multiple roots of the characteristic equation without having to draw the dispersion curve along the full frequency axis. This is achieved using for the discriminant, the definition,

$$D = \prod_{i<j}^{N} (r_i - r_j)^2 \tag{1}$$

where D is the discriminant, r_i, r_j are the roots of the algebraic function for which D is the discriminant, N is the order of truncation of the coefficient matrix. Next we compute derivatives of D with respect to p in the complex plane numerically with a view to reach a constant value after successive differentiations. The number of such differentiations will give the degree of D in p. This procedure can be carried out in any region of the complex plane since D is a polynomial.

We chose examination of a closed guide with a lossless coaxial rod as the guiding structure (inset of Figure 1(a)). Exact solution of this problem is known vis-à-vis the dispersion relation [10].

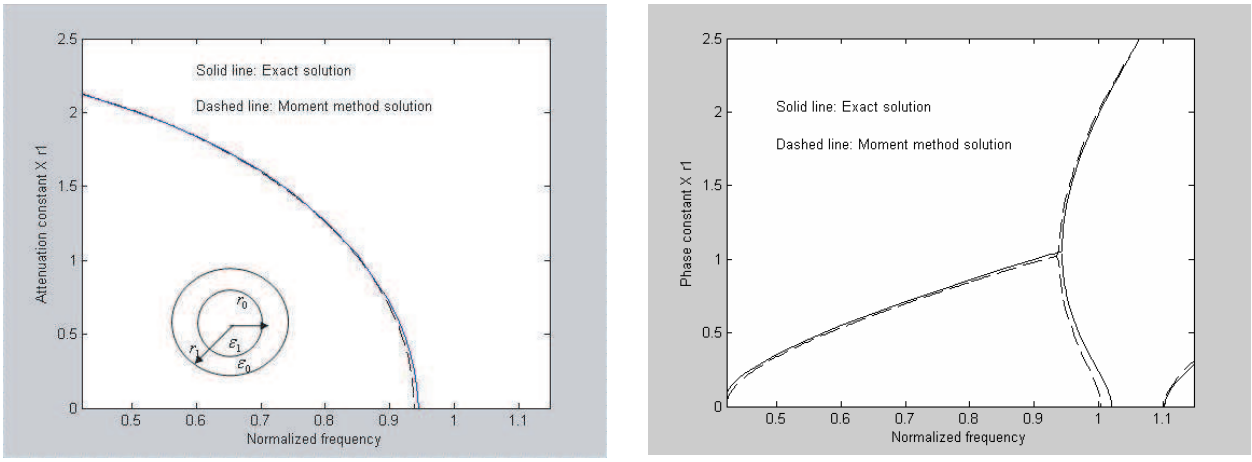

(a) (b)

Figure 1: (a) Exact and moment method attenuation constant variation with frequency. Inset: Investigated guiding structure cross-section. (b) Exact and moment method phase constant variation with frequency.

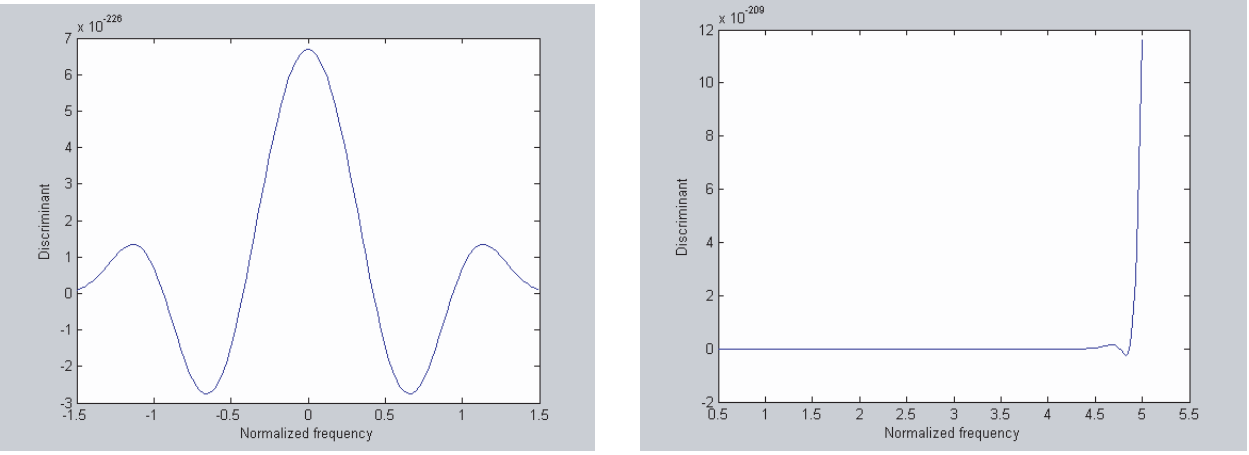

(a) (b)

Figure 2: (a) Discriminant variation with frequency. (b) Discriminant variation with frequency at higher frequencies.

Parameter values are $\varepsilon_1 = 15\varepsilon_0$, $r_1 = 0.25''$, $r_0 = 0.67r_1$. We defined a normalized complex frequency as $\bar{p} = (\sigma + j\omega)\sqrt{\varepsilon_0\mu_0}r_1 = \bar{\sigma} + j\bar{\omega}$. We have used 20TE and 20TM modes as expansion

functions in applying the moment method. Comparison of this method with exact dispersion curve is depicted in Figures 1(a) (real part) and 1(b) (imaginary part). The interval between the normalized frequencies $\bar{\omega} = 0.4146$ and $\bar{\omega} = 0.9425$ on the exact curve corresponds to a complex wave mode.

Using (1) and using only the imaginary part $\bar{\omega}$, of the complex frequency $\bar{p} = \bar{\sigma} + j\bar{\omega}$, we end up with Figure 2(a) as the variation of the discriminant with frequency. Notice that D is an even function in $\bar{\omega}$ because for the structure considered $ZY = Ap^2 + B$ form is valid for the coefficient matrix derived by moment method from Maxwell's equations [1], where A and B are constant matrices making the propagation constant function, a function of $\bar{\omega}^2$ when $\bar{\sigma} = 0$. This plot is obtained again by 20TE + 20TM modes in the moment method. The zeroes of the curve clearly correspond to the above critical frequencies (0.4141 and 0.942) which are the onset and ending points of the complex wave mode interval. These are the branch points of the propagation constant function. Figure 2(b) on the other is an extended plot of the discriminant vs. frequency over a wider band.

While implementing the Matlab program for all of the runs in the paper, ZY was divided by $10^{7.517}$ and the contour-plotted functions were multiplied by 10^{230}. These operations have no effect on the results, since division of ZY does not change the location of the multiple roots on the complex plane, because all of the eigenvalues of ZY will have been multiplied by the same constant and this will not affect the zeroes of the discriminant (see definition in (1)). On the other hand, multiplication of the contour-plotted functions by a constant is a matter of scaling, which does not affect contour plots.

2. DETERMINATION OF THE DEGREE OF THE DISCRIMINANT IN A NEIGHBORHOOD OF THE ORIGIN OF THE COMPLEX PLANE

The idea of this section is that the discriminant is a polynomial in p, and its successive differentiation with respect to p ought to yield the degree of the discriminant. Indeed such differentiations will terminate at a number equal to the degree, when one has a constant over the entire complex plane. One could plot D over a limited region of the complex plane and try to find the number of zeroes. But this could be misleading as zeroes might exist in another region of the complex plane and these would not appear in the plot. To circumvent this problem we propose to take successive derivatives in any region and find when one ends up with a constant value over the region.

If there ever is a singular point corresponding to a multiple root, it must be one of a pair, since such points represent the onset and terminal points of a complex wave mode interval [2, 3]. Because of the mentioned p^2 dependence, we must have at least four critical points, taking into account negative frequencies as well (Figure 3(a)). The poles in the figure are located at $(0 \pm j0.94)$ and $(0 \pm j0.415)$ in terms of normalized frequency. These are also the positions of the branch points mentioned above. Figure 3(b) is the contour plot of reciprocal of the absolute value of the first derivative of the discriminant. In successive differentiations we have used the forward

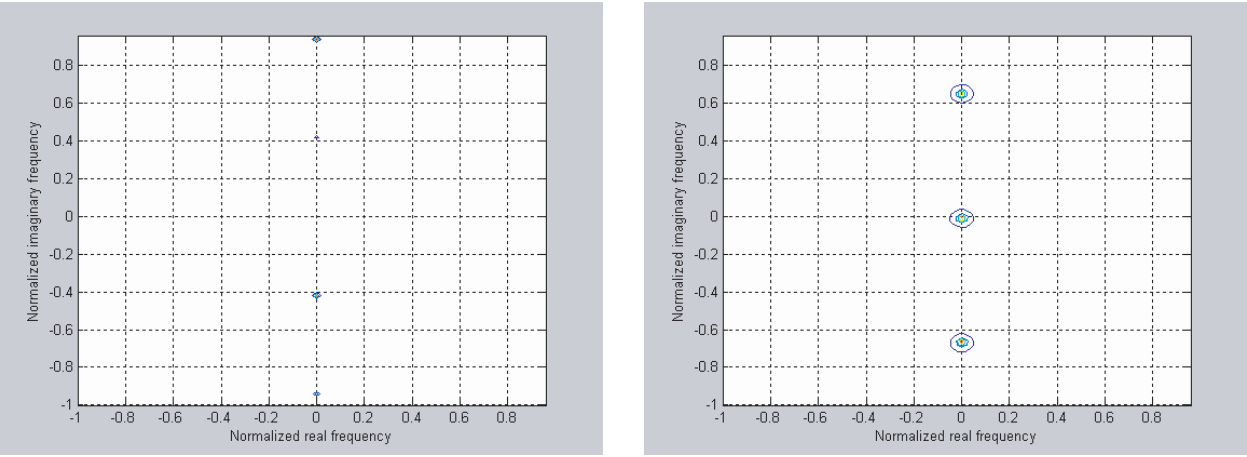

(a) (b)

Figure 3: Contour-plots (a) for reciprocal of the absolute value of the discriminant, (b) for reciprocal of the absolute value of the derivative of the discriminant.

difference formulas $\frac{df}{d\bar{p}} = \frac{f(\bar{\sigma}+\Delta_{\bar{\sigma}},j\bar{\omega})-f(\bar{\sigma},j\bar{\omega})}{\Delta_{\bar{\sigma}}}$ and $\frac{df}{d\bar{p}} = \frac{f(\bar{\sigma},j[\bar{\omega}+\Delta_{\bar{\omega}}])-f(\bar{\sigma},j\bar{\omega})}{j\Delta_{\bar{\omega}}}$. In the limits $\Delta_{\bar{\sigma}} \to 0$ and $\Delta_{\bar{\omega}} \to 0$, the two formulas are equivalent because f is a polynomial, hence analytic and therefore Cauchy-Riemann equations hold for it [7]. We have used an increment of $\Delta_{\bar{\sigma}} = \Delta_{\bar{\omega}} = 0.02$ in the computations of Figure 3(a) through 5(e). Figure 3(b) points out the poles at $(0 \pm j0.66)$ and $(0 + j0)$. Figure 4(a) is the absolute value of the second derivative of the discriminant. The zeroes are at $(0 \pm j0.34)$. Figure 4(b) is the absolute value of the third derivative of the discriminant. The zero is at the origin. Figure 4(c) is the absolute value of the fourth derivative of the discriminant and practically no variations are visible indicating that this result corresponds to a constant value over the complex plane, i.e., the discriminant has a degree four.

3. DETERMINATION OF THE DEGREE OF THE DISCRIMINANT IN A REGION WHERE THE DISCRIMINANT APPROACHES INFINITY

Since the discriminant is a polynomial, its absolute value will approach infinity as $\bar{p} \to \infty$. Such a region is common to all polynomials that are not a constant and hence to any such discriminant as well. Consider Figure 2(b) and notice that around a normalized frequency of 5, the discriminant rises sharply, approaching infinity. In the neighborhood of this point, we will test the procedure of Section 2. In Figure 5, reciprocals of the absolute values of the discriminant, its first, second, third and fourth derivatives are plotted, using the same difference formulas as in Section 2 for the derivatives. It is seen that in the first four plots, we have maxima at the point $j3$, whereas in the fifth plot almost no curves are visible indicating a constant value achieved over the region of interest in the complex plane. Hence in this region, our test has yielded the same result; a fourth degree

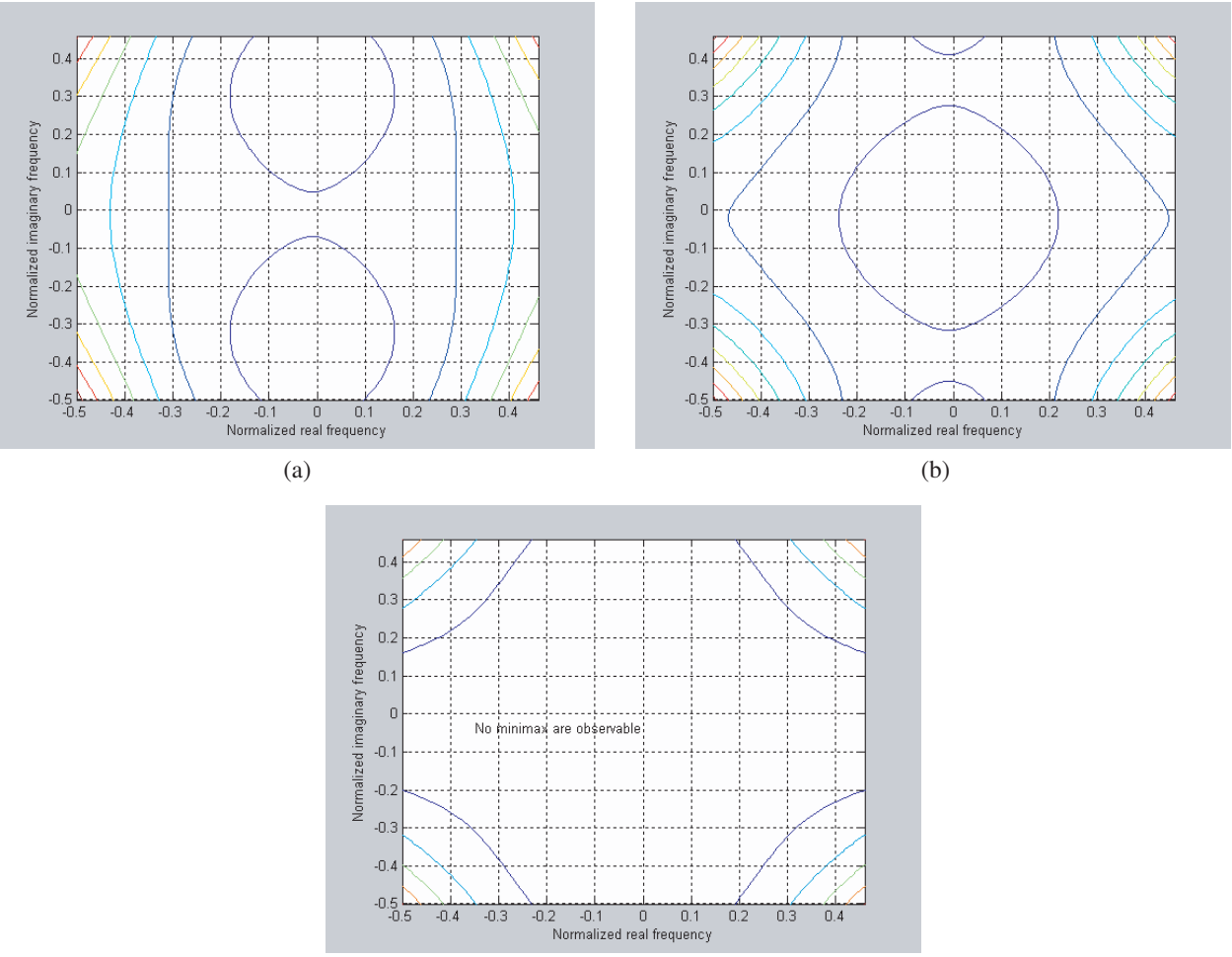

Figure 4: Contour-plots (a) for the absolute value of the second derivative of the discriminant, (b) for the absolute value of the third derivative of the discriminant, (c) for the absolute value of the fourth derivative of the discriminant.

discriminant. It must be remarked that in Figure 5(e), the very small area of non-constant values, compared with the size of maxima in the preceding four figures can be neglected as a constant value area.

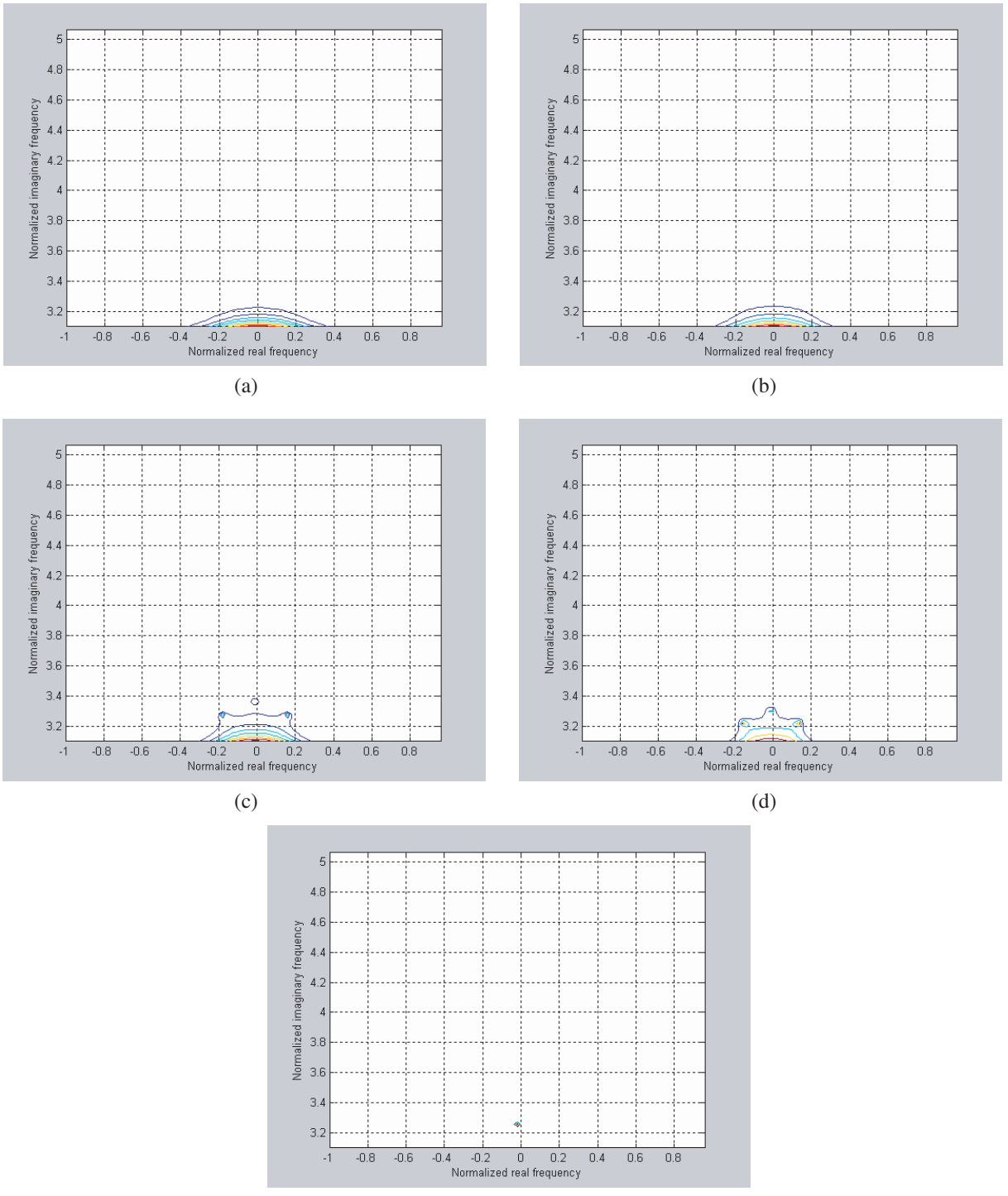

(a) (b)

(c) (d)

(e)

Figure 5: Contour-plots in the high frequency range for various quantities regarding the discriminant, (a) for the reciprocal of the absolute value, (b) for the absolute value of the first derivative, (c) for the reciprocal of the absolute value of the second derivative, (d) for the reciprocal of the absolute value of the third derivative, (e) for the reciprocal of the absolute value of the fourth derivative.

REFERENCES

1. Noble, D. F., "Circuit properties of dispersive coupled transmission lines and waveguides," Ph.D. dissertation, School of Electrical Engineering, Cornell University, Ithaca, N.Y., 1971.
2. Yener, N., "Algebraic function approximation in eigenvalue problems of lossless metallic waveguides (revisited)," *Progress in Electromagnetics Research*, PIER 55, 147–174, 2005.
3. Yener, N., "Algebraic function approximation in eigenvalue problems of lossless metallic waveguides: Examples," *Journal of Electromagnetic Waves and Applications*, Vol. 20, No. 6, 731–745, 2006.
4. Yener, N., "Advancement of algebraic function approximation in eigemnvalue problem of lossless metallic waveguides to infinite dimensions, Part I: Properties of the operator in infinite dimensions," *Journal of Electromagnetic Waves and Applications*, Vol. 20, No. 12, 1621–1628, 2006.
5. Yener, N., "Advancement of algebraic function approximation in eigemnvalue problem of lossless metallic waveguides to infinite dimensions, Part II: Transfer of results in finite dimensions to infinite dimensions," *Progress in Electromagnetics Research*, PIER 65, 41–58, 2006.
6. Yener, N., "Advancement of algebraic function approximation in eigemnvalue problem of lossless metallic waveguides to infinite dimensions, Part III: Examples verifying the theory," *Journal of Electromagnetic Waves and Applications*, Vol. 20, No. 13, 1861–1874, 2006.
7. Knopp, K., *Theory of Functions*, Part II, Dover Publications, New York, 1996.
8. Tian, Y. B. and J. Qian, "Ultraconveniently finding multiple solutions of complex transcental equations based on genetic algorithm," *Journal of Electromagnetic Waves and Applications*, Vol. 20, No. 4, 475–488, 2006.
9. Samuelson, P. A., "A method of determining explicitly the coefficients of the characteristic equation," *The Annals of Mathematical Statistics*, Vol. 13, No. 4, 424–429, 1942.
10. Clarricoats, P. J. B., "Circular-waveguide backward wave structures," *Proc. Inst. Elec. Eng.*, Vol. 110, 261–270, 1963.

Peculiarities of Intelligence Optimization of a Microstrip Filter on Folded Dual-mode Resonators

I. A. Dovbysh and V. V. Tyurnev
Kirensky Institute of Physics of SB RAS, Krasnoyarsk, Russia

Abstract— This paper presents a generalization of the intelligence optimization method of a microwave filter in case of dual-mode resonators. A priori knowledge about the resonators' couplings and resonant frequencies effects on filter frequency response in the passband is used. The correction operations, eliminating distortions of filter frequency response, are built in terms of structural parameter variations for the two-resonator four-pole microwave filter on folded stepped-impedance microstrip resonators. The intelligence optimization method successfully passed an examination in a computer program for a filter design.

1. INTRODUCTION

An intelligence optimization method is successfully used in microstrip filter design in more ten years [1–3]. This method is based on application a priori knowledge about bandpass filters composed of microwave resonators [4, 5].

Heretofore application of the method was constrained the case of single-mode resonators. The most difficulty arises when two modes of dual-mode resonator are not degenerated and their fields have the same polarization and similar space distribution.

In this paper, the regulations of intelligence optimization method are generalized for the case of dual-mode resonators. Their application for the case of two-resonator four-pole microstrip filter on folded stepped-impedance dual-mode resonators is demonstrated.

2. GENERAL REGULATIONS OF OPTIMIZATION

The aim of intelligence optimization is to form a specified frequency response in a passband, using minimum number of structural parameters for adjustment. The other parameters are constants during the optimization. They may be used, for example, for a possible subsequent optimization of the frequency response in a stopband.

Usually a current frequency response in a passband for n-pole filter is described with $n + 1$ parameters. They are passband center frequency F, bandwidth ΔF, and return loss maximums L_{ri} $(i = 1 \dots n - 1)$, located in the passband between n attenuation poles. In an adjusted filter, the frequency response parameters must satisfy the conditions

$$F = F_0,\ \Delta F = \Delta F_0,\ L_{r\,i} = L_{r\,\max}\ (i = 1 \dots n - 1), \tag{1}$$

where F_0, ΔF_0, and $L_{r\,\max}$ are specified parameters.

In intelligence optimization, it is convenient to use a deflection vector $\mathbf{D}$, characterizing distortions of frequency response in the passband. This vector has $n + 1$ components. When all the components turn into zero, all Equations (1) are valid. Therefore, deflection vector $\mathbf{D}$ may be considered as vector goal function.

The first distortion is characterized by the component

$$D_1 = (F - F_0)/F_0. \tag{2}$$

The correction operation, eliminating the first distortion, is obvious. It is a synchronous tuning all resonant frequencies.

The second distortion is characterized by the component

$$D_2 = (\Delta F - \Delta F_0)/\Delta F_0. \tag{3}$$

This distortion, according to Cohn-Matthaei approximate direct synthesis formulas [6, 7], is eliminated by means of proportional changing all the couplings in the filter.

The third distortion is characterized by the component

$$D_3 = \frac{1}{n-1}\sum_{i=1}^{n-1} L_{ri} - L_{r\,\max}. \tag{4}$$

The correction operation, eliminating the third distortion, includes the synchronous adjustment of the input and output couplings above other couplings [4, 5].

The definition of other deflection vector components varies depending on the pole number n. Hereinafter we suppose $n = 4$. Then the deflection vector has five components. Two last components are

$$D_4 = L_{r1} - L_{r3}, \tag{5}$$

$$D_5 = L_{r2} - \frac{1}{2}(L_{r1} + L_{r3}). \tag{6}$$

In a single-mode case, the forth distortion is eliminated by means of adjustment of the resonant frequency difference for external and internal resonators. Whereas the fifth distortion is eliminated by means of adjustment of the coupling difference for central and side pairs of adjacent resonators [4, 5].

These regulations may be applied to a dual-mode case, if every resonator of the dual-mode filter were compared with a proper imagine pair of coupled single-mode resonators. For such imagine pair, the resonant frequencies of coupled oscillations must coincide with resonant frequencies of dual-mode resonator.

The intelligence optimization process is successive executing of the correction operations, eliminating the distortion with maximum $|D_i|$. This process converges due to all the correction operations, conjugated to the normal distortions, are quasi-orthogonal. That means the absolute value of the eliminated old distortion much greater than absolute values of all new arisen distortions. The only exception is the operation, eliminating the third distortion characterized by D_3. However, this defect is easy overcome with other operations.

3. CORRECTION OPERATIONS FOR 2-RESONATOR 4-MODE FILTER

Figure 1 shows the metallization pattern of the microstrip filter [8, 9]. As adjustable structural parameters, we use the resonator length l_r, the tapping length l_c, the strip widths w_1, w_2, and the strip spacings S_1, S_2.

Two correction operations are obvious. The first distortion is eliminated by adjustment l_r. When $D_1 > 0$ the resonator length l_r is to be increased.

The third distortion elimination needs in increasing l_c, when $D_3 > 0$.

The stating of the other correction operations needs in considering resonant frequency dependencies of structural parameters in the folded dual-mode resonator. Fig. 2 shows the ratio of two first resonant frequencies versus the strip width ratio ($w_1 + w_2 = \text{const}$) for three spacing values.

It is seen that the frequency ratio F_2/F_1 depends on both the ratio w_1/w_2 and the spacing S_1. Since the ratio F_2/F_1 is also a property of imagine coupled resonators, the coupling between imagine resonators may be varied with variation of w_1/w_2 or S_1. A test of the whole filter shows that the coupling is an increasing function of S_1. Whereas the coupling between real dual-mode

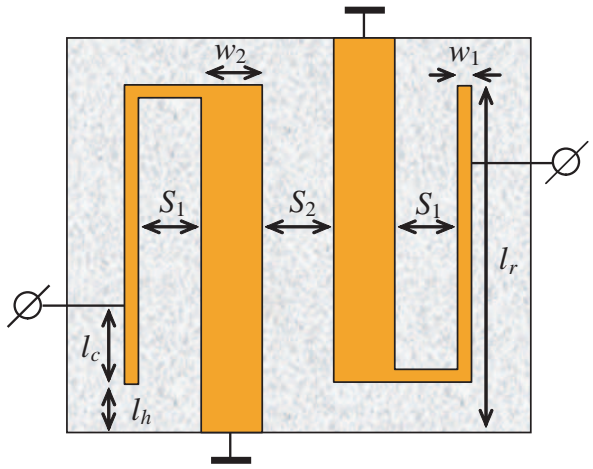

Figure 1: Two-resonator four-pole microstrip filter.

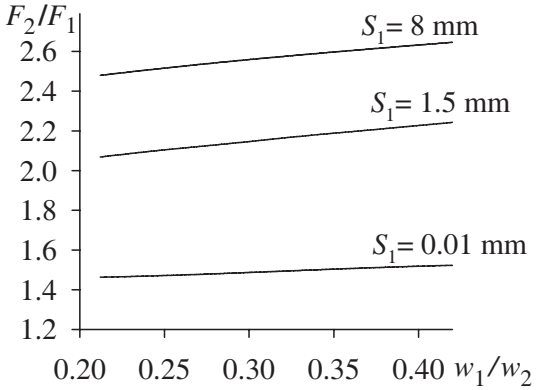

Figure 2: Resonant frequency ratio versus the strip width ratio.

resonators is a decreasing function of S_2. These two behaviors allow stating two next correction operations.

The fifth distortion is eliminated by simultaneous synphase variation of S_1 and S_2. When $D_5 > 0$, the product S_2S_1 is to be increased.

The second distortion is eliminated by simultaneous antiphase variation of S_1 and S_2. When $D_2 > 0$, the ratio S_2/S_1 is to be increased. An alternative operation, eliminating the second distortion, is a simultaneous antiphase variation of w_1 and w_2. When $D_2 > 0$, the ratio w_1/w_2 is to be increased. These alternative operations allow avoiding extremely narrow spacing or width.

The forth distortion is eliminated by simultaneous synthase variation of w_1 and w_2. When $D_4 > 0$, the product w_1w_2 is to be increased.

4. CONCLUSIONS

The intelligence optimization method, using a priori knowledge, is applied for the first time for dual-mode resonator filters. Handling of an imagine pair of coupled single-mode resonators allows the known general regulations of optimization to be applied for dual-mode case optimization.

The optimization operations, stated in structural parameter changes, are built for the two-resonator four-pole microstrip filter on folded stepped-impedance dual-mode resonators. This intelligence optimization method, realized in the form of computer program, successfully passed an examination.

ACKNOWLEDGMENT

This work was sponsored by the Council for Grants of the President of the Russian Federation for Support of Leading Scientific Schools, grant No. NSh-3818.2008.3.

REFERENCES

1. Belyaev, B. A., M. I. Nikitina, V. V. Tyurnev, et al., "Intelligent system for the designing of microstrip filters," *J. of Computer and Systems Sciences Int.*, Vol. 39, No. 2, 255–261, 2000.
2. Aleksandrov, K. S., B. A. Belyaev, A. A. Leksikov, and V. V. Tyurnev, "System for automated design and manufacture of microstrip filters," *Nauka-Proizvodstvu*, No. 5, 2–5, 2003.
3. Belyaev, B. A., S. V. Butakov, V. V. Tyurnev, et al., "Expert System filtex32 for computer-aided design of bandpass microstrip filters," *15th Int. Crimean Conf. "Microwave & Telecommunication Technology" (CriMiCo'2005)*, Vol. 2, 504–505, Sevastopol, Crimea, Ukraine, Sept. 12–16, 2005.
4. Belyaev, B. A., M. I. Nikitina, and V. V. Tyurnev, "Effective method of microstrip filter optimization," *1997 IEEE-Russia Conf. "High Power Microwave Electronics: Measurements, Identification, Applications" (MIA-ME'97)*, 104–109, Novosibirsk, Russia, Sept. 23–25, 1997.
5. Belyaev, B. A. and V. V. Tyurnev, "The Method for Microstrip Filters Parametric Synthesis," *16th Int. Crimean Conf. "Microwave & Telecommunication Technology" (CriMiCo'2006)*, Vol. 2, 517–519, Sevastopol, Crimea, Ukraine, Sept. 11–15, 2006.
6. Cohn, S. B., "Direct-coupled-resonator filters," *Proc. IRE*, Vol. 45, No. 2, 187–196, 1957.
7. Matthaei, G., L. Young, and E. M. T. Jones, *Microwave Filters, Impedance-matching Networks and Coupling Structures*, McGraw-Hill Book Co., New York, NY, 1964.
8. Belyaev, B. A., L. T. Rachko, and A. M. Serzhantov, "Broad-band microstrip bandpass filter," Patent RU, No. 2182738, Bulleten' Izobretenii, No. 14, 2002.
9. Belyaev, B. A., A. A. Leksikov, and A. M. Serzhantov, "Wide-band microstrip filter" *11th Int. Conf. "Microwave & Telecommunication Technology" (CriMiCo'2001)*, Sept. 10–14, 2001, Sevastopol, Crimea, Ukraine, 2nd ed., 501–502, Weber, Sevastopol, 2005.

Numerical Investigation of Rectangular Dielectric Resonator Antennas (DRAs) Fed by Dielectric Image Line (DIL)

Hamide Dashti[1], **M. H. Neshati**[2], **and F. Mohanna**[1]

[1]Electrical Department, Sistan and Baluchestan University, Iran
[2]Electrical Department, Ferdowsi University of Mashhad, Iran

Abstract— In this paper Rectangular Dielectric Resonator Antennas (RDRA) fed by Dielectric Image Line (DIL) which is excited through a narrow slot on the ground plane is numerically investigated. The antenna structure is studied based on the Finite Element Method (FEM) using High Frequency Structure Simulation (HFSS) package. The effects of the slot size are considered on the radiation performance of the antenna. Results show that the optimum length and width of the slot, for 7 dB gain at 10 GHz, are 3.7 mm and 0.144 mm respectively. The return loss and radiation patterns of the antenna are also provided for a specific DRA.

1. INTRODUCTION

Dielectric Resonators (DRs) made of high dielectric constant and low loss material have been used as a tuning elements in microwave filters and oscillators. DRs are small in size, low in cost and light in weight offering high temperature stability [1, 2]. Due to these specific performances, they have been replaced metal waveguide cavities especially in MICs and MMICs. In recent years, the subject of open DRs as an electromagnetic radiator has been increased in literature because of no inherent conductor loss leading to high radiation efficiency. It has been reported that cylindrical, hemispherical, cylindrical rings and rectangular shaped DRs could operate as an efficient antennas. Another advantage of DRAs is compatibility with all types of transmission line such as coaxial probe, microstrip line, microstrip-slot coupled and coplanar waveguide [1–3].

The radiation efficiency of the communication system is reduced at high frequencies due to skin effect and high conductive loss of microstrip lines. Dielectric transmission lines such as Dielectric Image Line (DIL) have lower losses at microwave frequencies compare to conventional transmission line [1, 3]. Rectangular DRAs fed by DIL can be excited at their resonant frequency through a narrow slot on the ground plane.

In this paper a RDRA fed by DIL which is excited through a narrow slot on the ground plane is numerically investigated. The antenna structure is studied based on the Finite Element Method (FEM) using High Frequency Structure Simulation (HFSS) package. The effects of the slot size on the radiation performance of the antenna are studied. The optimum length and width of the narrow slot, for 7 dB gain at 10 GHz is obtained. Return loss, radiation patterns and the variation of the RDRA gain versus frequency are presented.

2. ANTENNA STRUCTURE

The geometry of the antenna structure is shown in Fig. 1. A rectangular DRA of length a, width b, height c with the relative permittivity of ε_d is placed on the ground plane. A slot of length L and width W is etched at the center of the metal plane to excite the resonator at the dominant mode. DIL, as the transmission media, comprise a rectangular dielectric slab of relative permittivity ε_r with a length of 3λ at 10 GHz placed under the ground plane. The dimensions of the DIL transverse plane are $2a_d$ and b_d shown in Fig. 1 and all dimensions are summarized in Table 1. The most important feature of this structure is placing the feed network of the RDRA at the backside of the ground plane, isolating the radiating parts from spurious radiation provides by the DIL especially at high frequencies [6, 7]. The slot width is chosen smaller than the wavelength of guided wave by the DIL. For a strong coupling between DIL and the RDRA, the slot should be placed in a region of strong magnetic fields [4, 5].

3. ANTENNA SIMULATION

The RDRA structure is numerically investigated using HFSS [8]. To excite the DIL, a standard metal waveguide is used at the input and output of the transmission media. Three sections of waveguide using a proper tapering provide transition from TE_{10} mode of the metal rectangular waveguide to dominant mode of the DIL. Rectangular dielectric waveguides support TM^y_{mn}, TM^z_{mn}

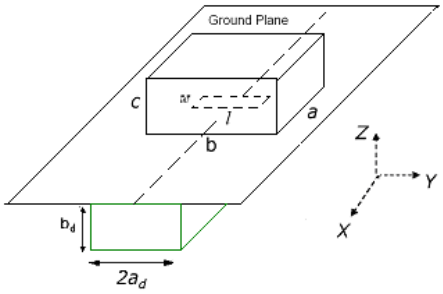

Figure 1: The geometry of the DRA fed by DIL through a narrow slot.

a	6.2 mm
b	6 mm
c	6.1 mm
a_d	4.25 mm
b_d	4.03 mm
ε_d	10.2
ε_r	10.2
DIL Length $= 3\lambda$	66.67mm

Table 1: Dimensions of the antenna structure.

modes. The presence of ground plane lead to propagating only TM^z_{mn} mode [5]. The dimension of the DIL is chosen in such a way that only the principal mode of operation, TM^z_{11} is excited over a considerable range of frequency around 10 GHz. This structure has two ports as show in Fig. 2. Port one is defined as the input to excite the TE_{10} mode of metal waveguide. The second port at the output is terminated to a matched load so; a travelling wave is propagated in DIL which efficiently excites the RDRA at the resonance frequency. For simplicity, all simulations are carried out for infinite ground. The slot on the ground plane upon which the RDRA is located determines the amount of power coupled from the DIL to the resonator. The slot operates as a magnetic current in parallel to the resonator length exciting the RDRA at the principal TE_{111} mode of the operation [4, 7].

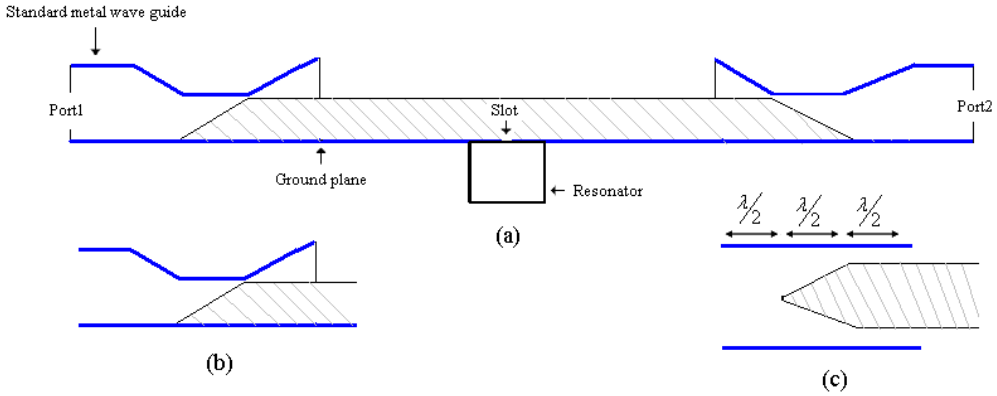

Figure 2: (a) Feed structure of the RDRA, (b) side view of the feed port, (c) top view of the feed port.

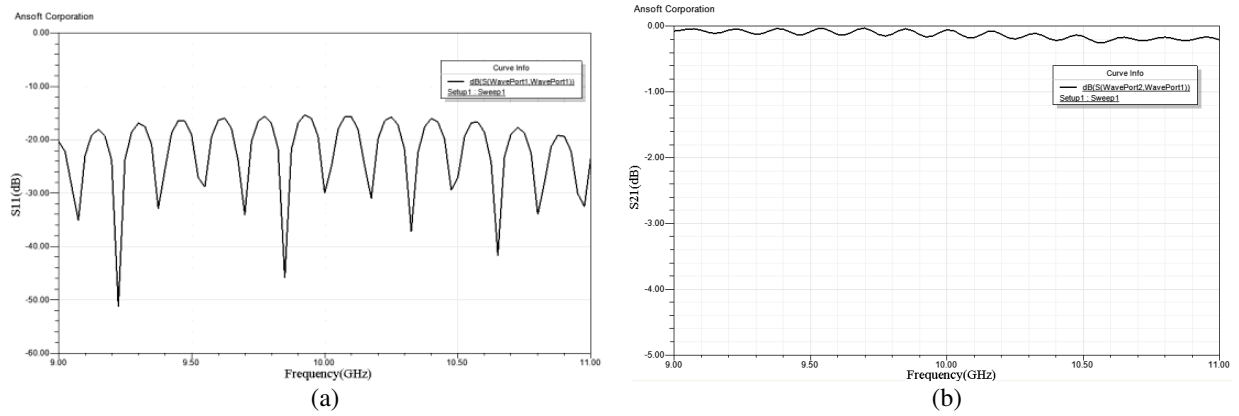

Figure 3: (a) Return loss and (b) transmission coefficient of the antenna structure for only DIL without slot and RDRA.

4. RESULTS

Return loss of the simulated DIL is shown in Fig. 3(a). it can be seen a good matching condition is obtained at input port. Fig. 3(b) shows the transmission coefficient of the DIL, while port 2 is also considered as an exciting port. It can be seen that over the frequency range of 9 GHz to 11 GHz, insertion loss of less than 0.3 dB is obtained that providing well propagation at the operation mode.

The simulated return loss and transmission coefficient of the whole structure, including DIL, slot and RDRA, is shown in Figs. 4(a) and 4(b). It can be seen that a good matching at input port, while about at 10.1 GHz most of the input power is radiated by RDRA and a part of power is delivered to the matched load.

Figure 5(a) shows the effect of the slot on the antenna gain. Fig. 5(b) shows the antenna gain versus frequency for different slot length and constant slot width of $W = 0.144$ mm. From both figures can be seen that maximum gain of 7 dB is obtained for the optimum slot length and width of $L = 3.7$ mm and $W = 0.144$ mm respectively. In Fig. 6 the return loss is shown for the optimum slot size which is similar to Fig. 3(a). Co polarization and cross polarization radiation patterns of the RDRA for the optimum slot size and infinite ground plane are shown in Fig. 7(a) and Fig. 7(b) respectively. Radiation patterns of the structure are broadside perpendicular to the ground plane. It can be seen that the RDRA radiates a linear polarized wave where the cross polarized level is at least 30 dB lower than the co-polarized in E- and H-Plane patterns.

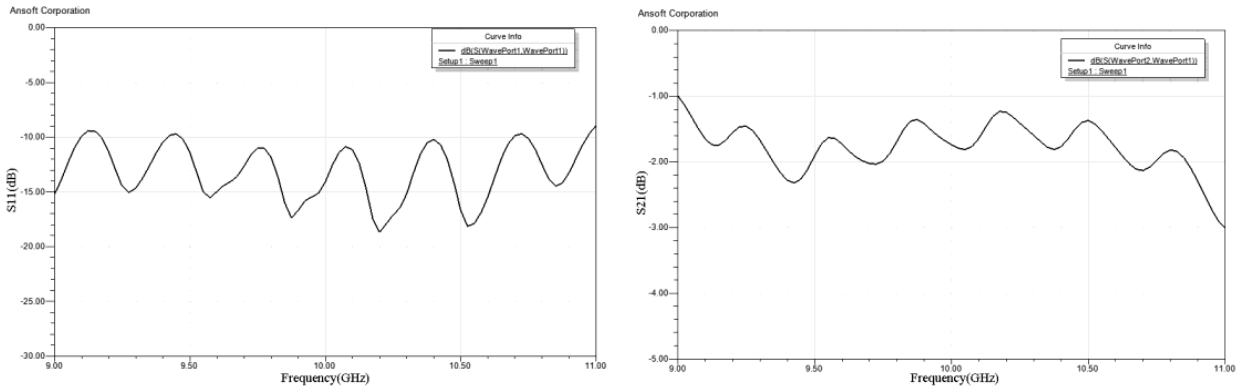

(a) (b)

Figure 4: (a) Return loss and (b) transmission coefficient of the antenna structure including DIL, slot and RDRA.

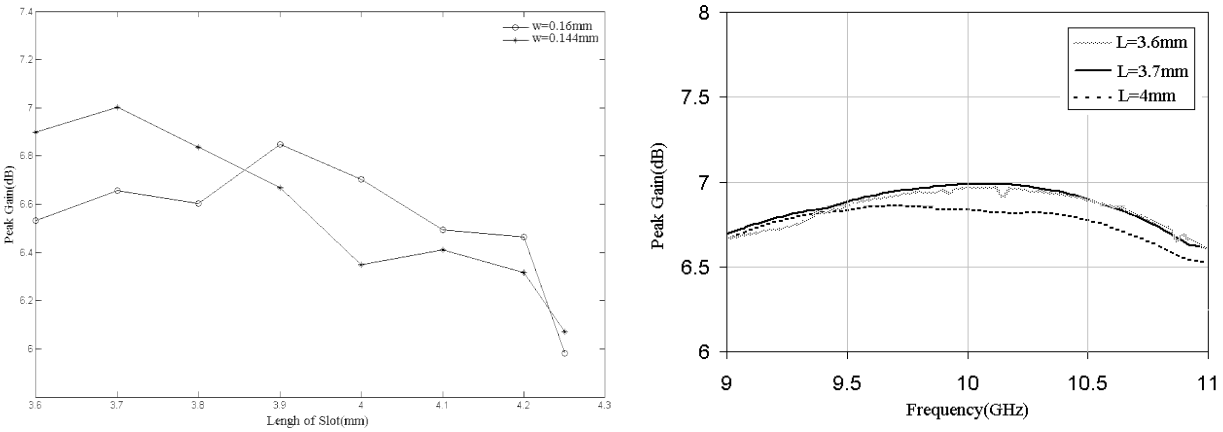

(a) (b)

Figure 5: (a) Peak gain of RDRA versus slot length for two values of width, (b) RDRA gain versus frequency for different slot length and constant width of $W = 0.144$ mm.

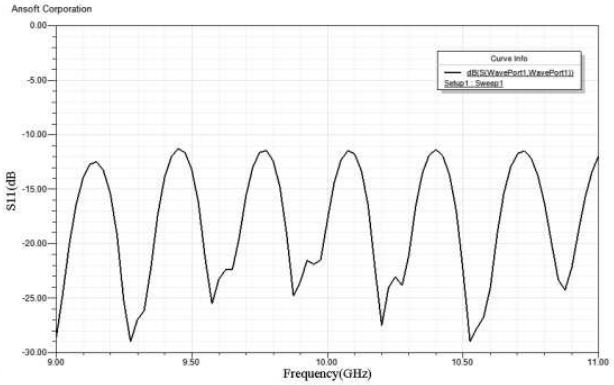

Figure 6: Return loss for optimum slot.

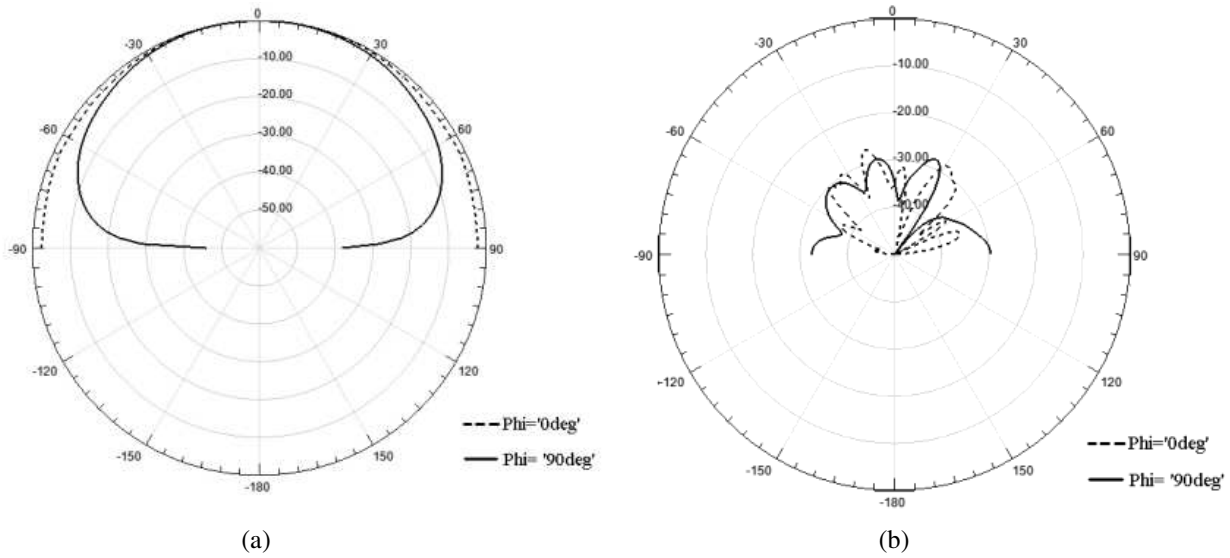

Figure 7: Radiation pattern at optimum dimension of slot for (a) co polarization, (b) cross polarization.

5. CONCLUSION

In this paper the slot coupled RDRA fed by a Dielectric Image Line (DIL) was investigated numerically using HFSS package for an infinite ground plane. For a specific dielectric resonator a parametric study for the slot size was carried out and optimum slot was obtained at the resonance frequency of 10 GHz. A good return loss and a linear polarized broadside radiation patterns was obtained. Results show 7 dB gain at the resonance frequency of the resonator while the cross polarization level is at least 30 dB lower than the co polarization patterns. However, further investigation is needed to consider the effect of finite ground plane on the radiation performance of the antenna structure.

ACKNOWLEDGMENT

The authors would like to thank Iran Telecommunication Research Center (ITRC) for its financial supports under the contract No. 500/11180.

REFERENCES

1. Luk, K. M. and K. W. Leung, *Dielectric Resonator Antennas*, Research Studies Press Ltd., Baldock, Hertfordshire, England, 2003.
2. Petosa, A., *Dielectric Resonator Antennas Handbook*, Artech House Inc., 2007.
3. Baghaee, R. M., M. H. Neshati, and J. R. Mohassel, "Rigorous analysis of rectangular dielectric resonator antenna with a finite ground plane," *IEEE Transaction on Antenna and Propagation*, Vol. 56, No. 9, 2801–2809, September 2008.

4. Al-Zoubi, A. S., A. A. Kishk, and A. W. Glisson, "Analysis and design of a rectangular dielectric resonator antenna FED by dielectric image line through narrow slots," *Progress In Electromagnetic Research*, PIER 77, 379–390, 2007.
5. Antar, Y. M. M. and Z. Fan, "Theoretical investigation of aperture-coupled rectangular dielectric resonator antenna," *IEE Proc. — Antennas Propag.*, Vol. 143, No. 2, 113–118, April 1996.
6. Kanamaluru, S., M.-Y. Li, and K. Chang "Analysis and design of aperture coupled microstrip patch antennas and arrays fed by dielectric image line," *IEEE Transaction on Antenna and Propagation*, Vol. 44, No. 7, 964–974, July 1996.
7. Bhartia, P. and I. J. Bahl, *Millimeter Wave Engineering and Applications*, John Wiley, New York, 1984.
8. HFSS, High Frequency Structure Simulator Based on Finite Element Method, v.11, Ansoft Corporation.

UWB Antenna with Band-stop Filter

Seokjin Hong, **Dongho Kim**, **and Jaehoon Choi**
Department of Electronics Computer Engineering, Hanyang University
17 Haengdang-Dong, Seongdong-Gu, Seoul 133-791, Korea

Abstract— We propose a new band-stop antenna for ultra-wideband application. The proposed antenna consists of two spiral radiating elements, a microstrip fed line, and ground plane with two circular slots for wideband performance. To achieve band-stop filtering characteristic, two open stubs are attached to the microstrip feed line. The developed antenna features wideband performance, omni-directional radiation patterns and flat gain variation.

1. INTRODUCTION

Ultra-wideband (UWB) communication systems give engineers difficult tasks of designing an antenna covering wide bandwidth 3.1 GHz to 10.6 GHz released by the Federal Communications Commission [1]. Recently, many types of UWB antennas have been investigated in literatures [2, 3]. These antennas have good impedance performances, radiation patterns and flat gain variations. However, due to the possible interference between UWB system and existing wireless local area network (WLAN; 5.15 GHz to 5.825 GHz), UWB antenna is required to have band-stop characteristic. To realize the band-stop function, planar monopole antennas with various techniques have been used [4, 5].

In this paper, we propose novel UWB antenna with band-stop characteristic. The antenna is formed by a spiral radiating element for wideband performance. The L-shaped stubs attached to the microstrip line act as a band-stop filter at the stop-band. The measured return loss characteristics, radiation patterns, and gain performance of the constructed prototype are presented.

2. ANTENNA DESIGN AND RESULTS

The proposed antenna is composed of two spiral elements, 50 Ω microstrip feed line, ground plane with two circular slots, and two open stubs as shown in Figure 1. The antenna was fabricated on a 1.6 mm FR4 epoxy substrate with dielectric constant of 4.4. The antenna has total dimension of 30 mm × 40 mm × 1.6 mm. HFSS [6] was used to optimize the antenna performance and the design parameters are shown in Figure 1.

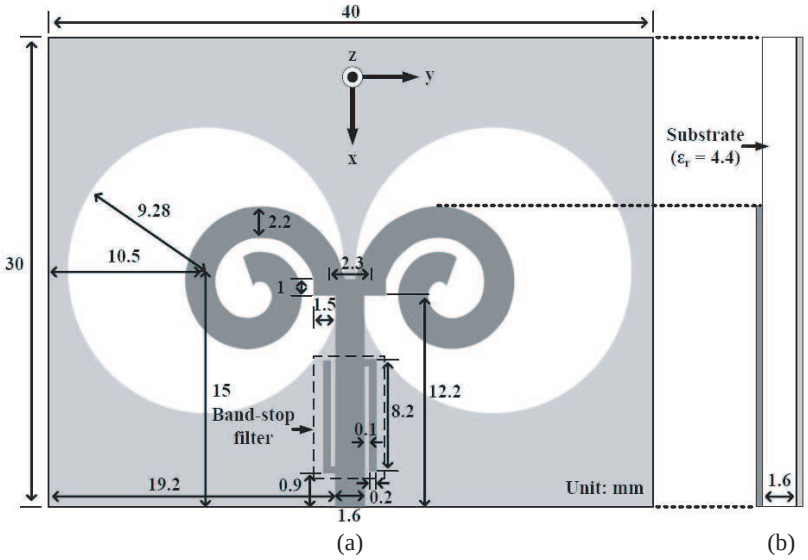

Figure 1: Geometry of the proposed antenna (a) top view, (b) side view.

To widen the antenna impedance bandwidth, two spiral elements are used. One can enhance the operating bandwidth by adjusting the parameters of spiral structure. To achieve the band-stop filtering property at the WLAN band, two L-shaped stubs are attached to both sides of a microstrip

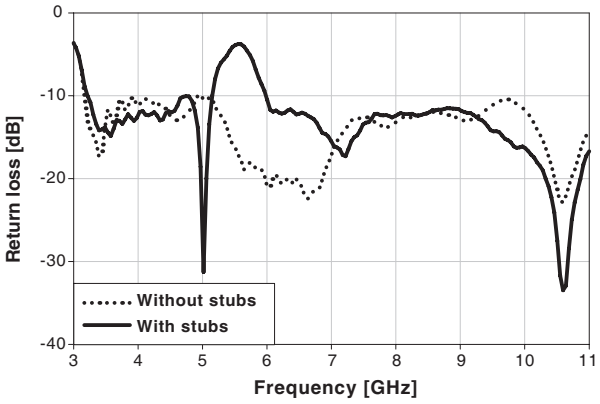

Figure 2: Measured return loss characteristics with and without L-shaped stubs.

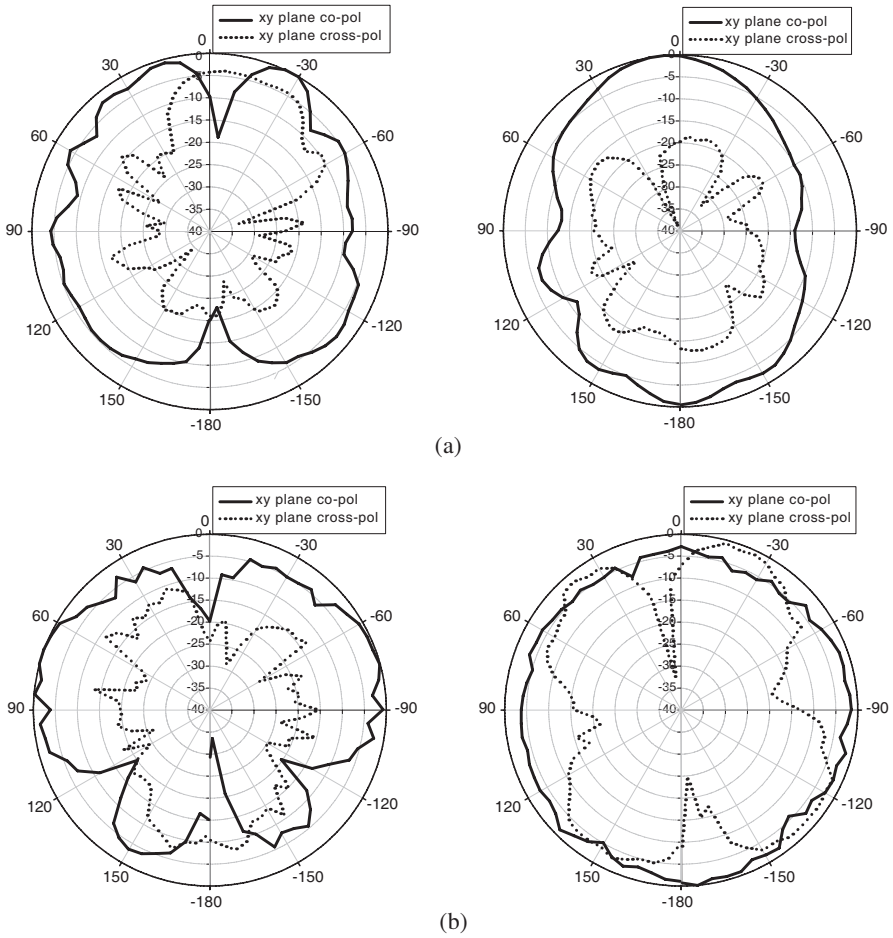

Figure 3: Measured radiation patterns: (a) 4 GHz, (b) 8 GHz.

line. Figure 2 shows the measured return loss characteristics with and without L-shaped stubs. The fabricated antenna has stop-band from 5.14 GHz to 5.96 GHz while satisfying the 10 dB return loss requirement from 3.17 GHz to more than 11 GHz. The measured radiation patterns of the antenna are shown in Figure 3 for different frequencies. The radiation patterns are near omni-directional in yz plane and bidirectional patterns in the xy plane, respectively. As shown in Figure 4, the gain of designed antenna is greater than 2 dBi with the gain variation of less than 3 dB over the whole UWB band except for the stop band.

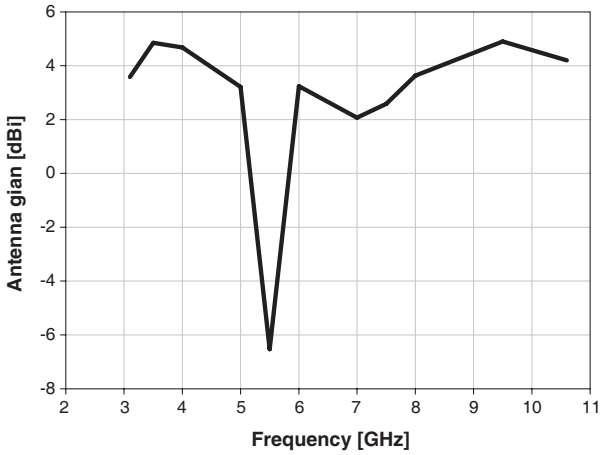

Figure 4: Measured antenna gain.

3. CONCLUSION

A simple microstrip fed antenna with band-stop characteristic at 5 GHz WLAN band is presented. The spiral structure is used to achieve the wide impedance bandwidth over the UWB frequency band. To provide the band-stop performance, two L-shaped stubs are attached to a microstrip line. Measured resutls show that the proposed antenna not only has good impedance bandwidth but also has good radiation patterns with flat gain variation. The proposed antenna can be a good candidate for UWB system.

ACKNOWLEDGMENT

This research was supported by the MKE (Ministry of Knowledge Economy), Korea, under the ITRC (Information Technology Research Center) support program supervised by the IITA (Institute of Information Technology Assessment) (IITA-2008-C1090-0801-0019).

REFERENCES

1. "First report and order, revision of part 15 of the commission's rules regarding ultra-wideband transmission systems," *Federal Communications Commission*, Vol. 02-48, Apr. 2002.
2. Chen, Z. N. and Y. W. Nichael, *Broadband Planar Antennas Design and Applications*, Wiley-Interscience, England, 2005.
3. Li, P., J. Liand, and X. Chen, "Study of printed elliptical/circular slot antennas for ultrawideband applications," *IEEE Trans. Antennas Propag.*, Vol. 54, No. 6, 1670–1675, 2006.
4. Jung, J., H. Lee, and Y. Lim, "Compact band-notched ultra-wideband antenna," *Electron. Lett.*, Vol. 44, No. 6, 391–392, 2008.
5. Zhang, J.-P., Y.-S. Xu, and W.-D. Wang, "Microstrip-fed semi-elliptical dipole antennas for ultrawideband communications," *IEEE Trans. Antennas Propag.*, Vol. 56, No. 1, 241–244, 2008.
6. Ansoft High-Frequency Structure Simulator (HFSS), Ver. 11.0, Ansoft Corporation.

Design of an Orthomode Transducer for Use in Multi-band Antenna Feeds

Soon-Mi Hwang, **Sung-Soon Choi**, **Jea-Min Kim**, **and Bierng-Seok Song**
Korea Electronics Technology Institute (KETI), Republic of Korea

Abstract— In this paper, we present the design of an Orthomode Transducer (OMT) to be used in multi-band antenna feeds. The OMT is realized in the form of a tapered square waveguide, where two side ports of 18–20 GHz are placed in the taper region, while 30–45 GHz ports are placed in line with the waveguide axis. Each port is designed that the return coefficient is less than −20 dB and the isolation between ports is lower than 15 dB. Thin septum are inserted in side ports to reduce the effect of side ports on the return loss of the in-line port. The commercial software HFSS® is used to design the whole structure.

1. INTRODUCTION

An Orthomode Transducer (OMT) is important for implementing antenna feeds in satellite communication as a system separating two electromagnetic wave components polarized orthogonally [1–5]. Recently, a several kinds of transducer have used in earnest. Especially, the use of Orthomode Transducer has increased according to the growth of artificial satellite. In addition to, it is necessary to share the same frequency by changing polarization due to the rapid growth of radio communication. As a satellite broadcast is generalized, Orthomode Transducer is used as antenna feeds where one reflector is used to receive several satellite broadcasts [6–8].

In this paper, Orthomode Transducer for feeds in multi-band (K, Ka, Q-band) is designed by using commercial software HFSS® and the result of the design is represented.

2. SUBJECT

Figure 1 shows OMT designed in this paper. This OMT operates in four band (18.1–19.1 GHz, 20.2–21.2 GHz, 30.0–31.0 GHz, 43.5–45.5 GHz). If a suitable wideband polarizer is connected to transceiver port of OMT, linear polarized signal can be converted to circular polarized signal.

The OMT is consisted of, as shown in Fig. 1, a) square waveguide of port 1 (sector size $C \times C$), b) square waveguide of port 2 (sector size $R \times R$), c) transition of port 1 and port 2 (length G_2), d) coupling slot of ports 3 and 4 (long × wide = $a \times b$), e) waveguide of ports 3 and 4 (long × wide = $A \times B$), and f) septum of ports 3 and 4 (thickness = t, length L_1, L_2). The design method of each components is followed.

2.1. Design of Square Waveguide of Ports 1 and 2

A square waveguide is designed cut-off frequency to be $0.7 \sim 0.9$ times of operating frequency and its size is decided by considering the one of other waveguides connected ports 1 and 2. In case port 1, $C = 10$ mm and cut-off frequency is 15 GHz which is 0.83 times of 18.1 GHz. In case port 2, $R = 6$ mm and cut-off frequency is 22.73 GHz which is 0.76 times of 30.0 GHz.

2.2. Transition Design of Ports 1 and 2

Transition which is a device to connect between 10×10 mm and 6×6 mm waveguide is designed to lower return loss in 30.0–45.5 GHz. In this paper, simple linear figure is used as a shape of transition, instead of exponential, Klopfenstein, step, etc [1]. The length of transition is minimum value in which return loss is under given value. Because, bandwidth of side ports (ports 3 and 4) is narrower, as the length of transition is longer. In this paper, the length of transition part, G_2 is 13 mm.

2.3. Design of Coupling Slot of Side Ports (Ports 3 and 4)

The size of wave-guide of side port is usually the same as standard waveguide (in this paper, WR-42, $A = 10.67$ mm, $B = 4.32$ mm). If other size is needed inevitably for impedance matching, it is transformed to desirable size by using taper. After design of side port waveguide, coupling slot is designed as next step. The design is the most difficult work. Usually, the appropriate value to implement is selected for a thickness, size ($a \times b$) and position G_4.

In this paper, the thickness of coupling slot is 1.3 mm, $G_4 = 0$, and appropriate **a** and **b** are selected by exchanging them alternately in 18.1–21.2 GHz. In general, it is optimum when

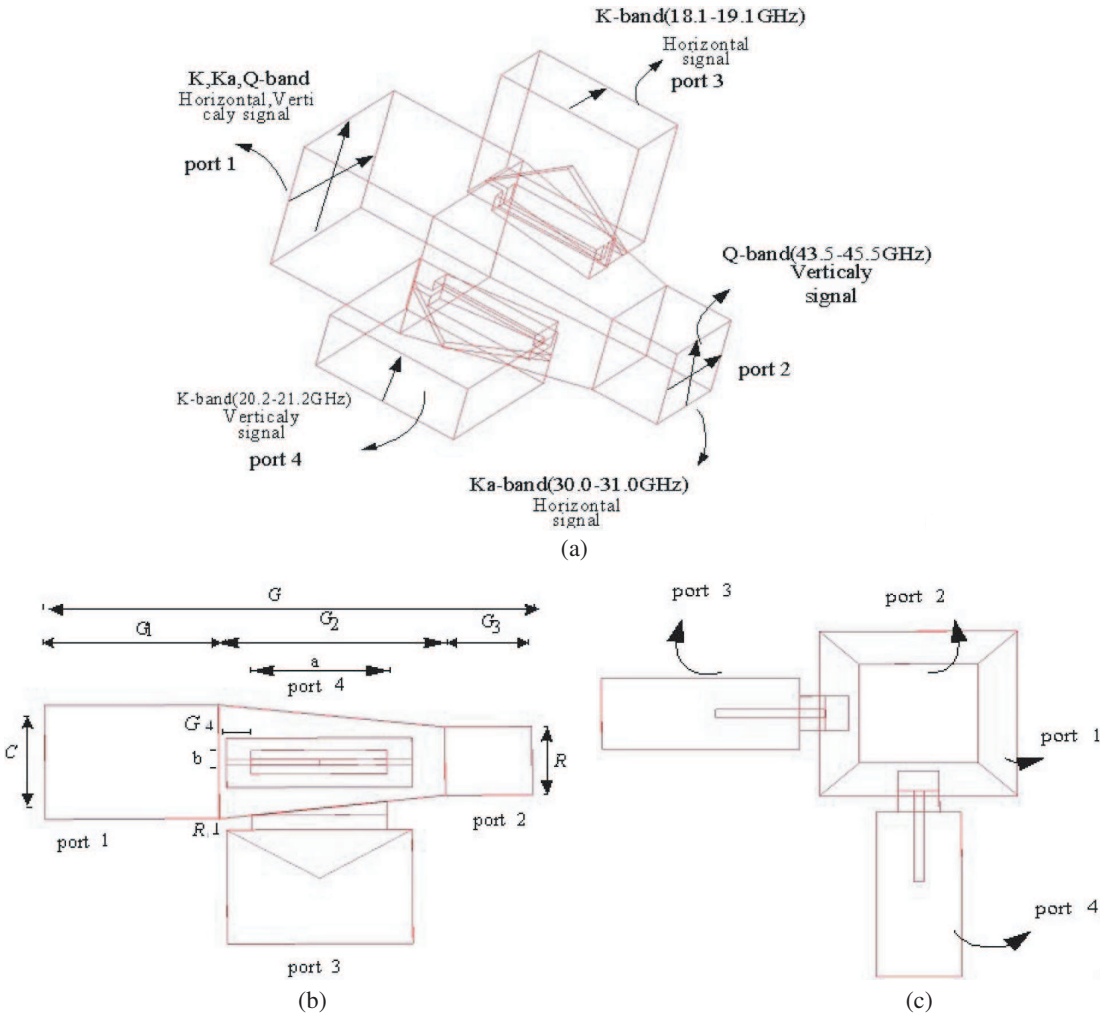

Figure 1: Orthomode Transducer for multi-band antenna feeds. (a) Structure, (b) a side view, (c) a front view.

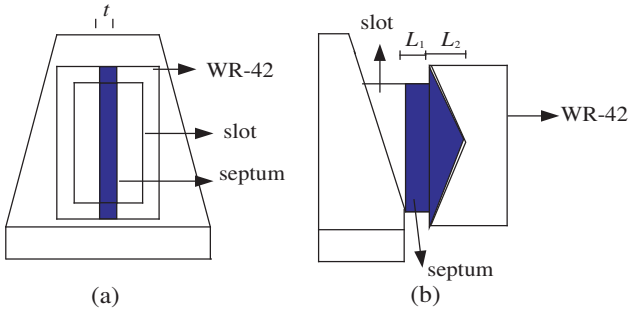

Figure 2: The shape inserted of septum in side port. (a) A front view, (b) a side view.

a is around $0.8A$, and an init value of **a** is $0.78A$ in this paper. Since **b** doesn't change return characteristic sensitively, the value is given in range of 0.3–0.6 times of **a** properly. However, since the mutual combination between ports decreases as the value of **b** is small, the minimum value which satisfies return loss should be chosen. In this paper, **b** is chosen to 2.3 mm from tuning test of several times.

After deciding a size of the slot, as next step, we find the best case of return loss while changing the position of slot, G_4. The values of a and b are controlled in detail with change of G_4 to be optimum return loss. By simulation of several times, $a = 7.8$ mm, $b = 2.3$ mm, and $G_4 = 1.4$ mm is obtained. Fig. 4 shows return loss of side port to position of slot.

2.4. Design of Septum of Side Port

The coupling slot of side port increases return loss of 30.0–31.0 GHz and 43.5–45.5 GHz signal in port 2. To solve this problem, the diaphragm is organized in the coupling slot of side port. Consequently, the interference on signal of port 2 can be minimum without effecting to return loss

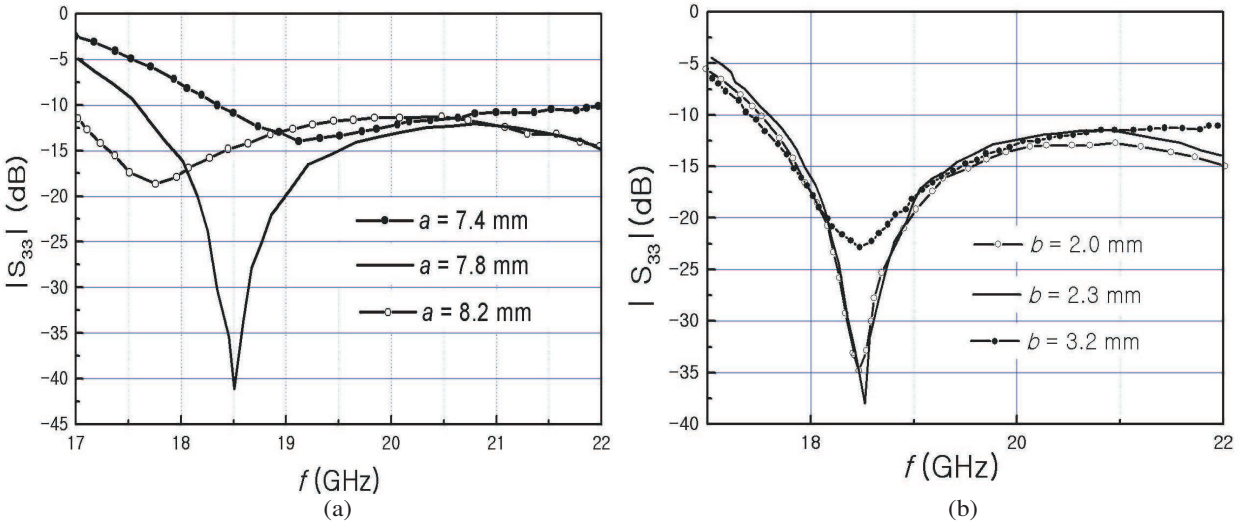

Figure 3: Coupling slot of a side port. (a) Return loss to length, (b) return loss to width.

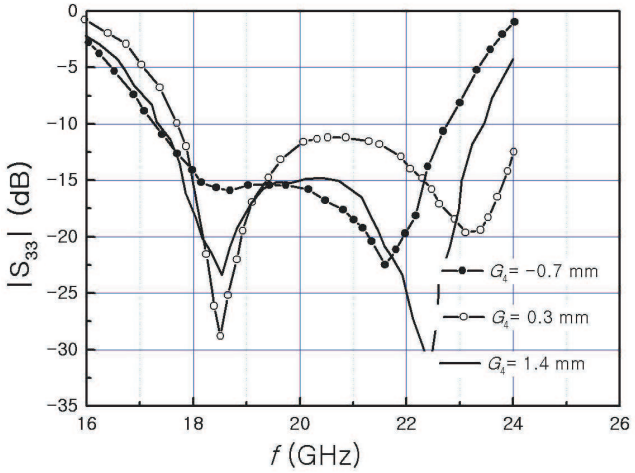

Figure 4: Return loss of side port to position of slot.

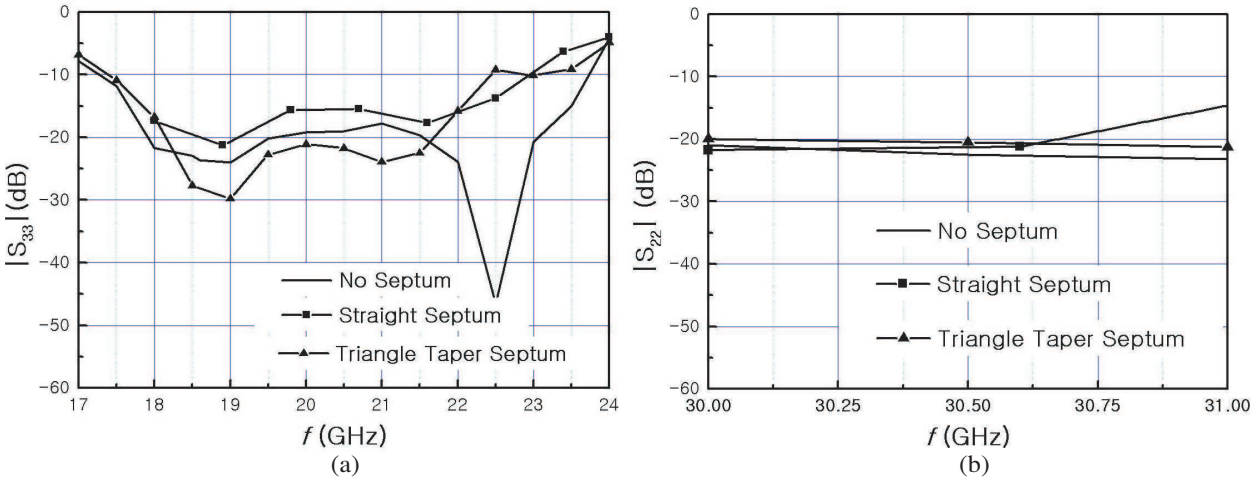

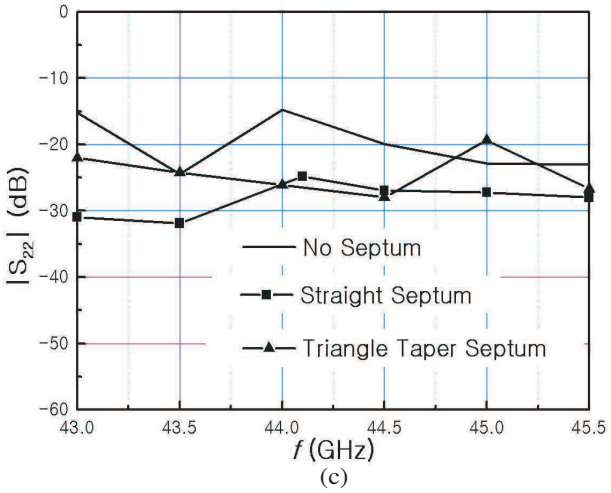

Figure 5: Return loss characteristic to septum.

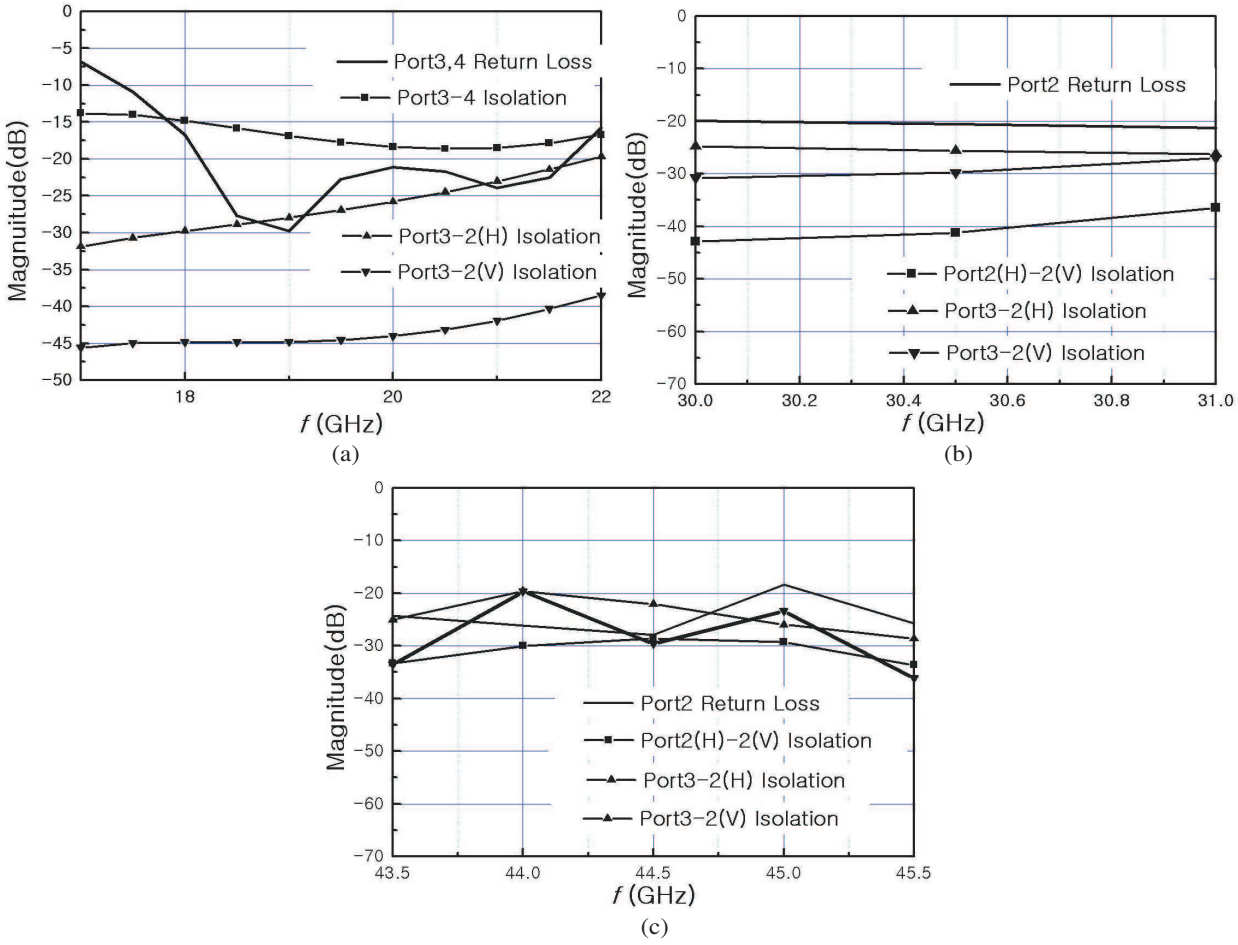

Figure 6: Return loss and coupling coefficient characteristic in each bands. (a) K-band, (b) Ka-band, (c) Q-band.

of side port. Though the shape of diaphragm maximizing return loss of port 2 is straight septum, the return loss of side port gets worse relatively. In this case, it is possible to improve return loss characteristic of side port as well as port 2 when the tapered diaphragm is organized to side port as Fig. 2. In this paper, we insert a septum to side port by using a method implemented to Fig. 2. A several of simulations gives the best results when $t = 0.5\,\text{mm}$, $L_1 = 1.3\,\text{mm}$, and $L_2 = 5\,\text{mm}$. Fig. 5 is to compare return loss in case of use and no use of the diaphragm. As seen in Fig. 7, the

use of the diaphragm improves return loss of port 2 to be less than −18 dB. Waveguide length (G_1, G_3, R_2) of each ports is decided the value which degrades high order mode sufficiently. Usually it is the maximum value between long and wide of waveguide section. In this paper, they are given by that $G_1 = 20\,\text{mm}$, $G_3 = 5\,\text{mm}$, and $R_2 = 10\,\text{mm}$.

3. ORTHOMODE TRANSDUCER DESIGN RESULT

Applying the above process, we finally analyze designed OMT by using HFSS®. The simulation result is represented in Fig. 6.

From the Fig. 6, it is observed to pass horizontal polarization in 18.1–19.1 GHz in case of port 3, vertical polarization in 20.2–21.2 GHz in case of port 4, and horizontal polarization in 30.0–31.0 GHz and vertical polarization in 43.5–45.5 GHz in case of port 2.

4. CONCLUSION

In this paper, we designed Orthomode Transducer for multi-band antenna feeds. Square waveguide was used as common port (pass bands of 18.1–19.1 GHz, 20.2–21.2 GHz, 30.0–31.0 GHz and 43.5–45.5 GHz). It was designed to pass vertical polarization of 20.2–21.2 GHz in the other side (port 4) and horizontal polarization of 18.1–19.1 GHz in one side (port 3) of two side ports concatenated. And it was designed to pass horizontal polarization of 30.0–31.0 GHz and vertical polarization of 43.5–45.5 GHz in port 2. Especially, a triangular tapered diaphragm was organized to a slot of side port to improve return loss characteristic. As a result, the return loss of port 2 was less than −18 dB.

By computer simulation, we obtained return loss less than −18 dB in all ports and isolation less than −15 dB.

REFERENCES

1. Joglekar, H. P. and M. Singh, "A rectangular waveguide orthomode transducer," *International Journal of Electronics*, Vol. 47, No. 5, 515–517, 1979.
2. Dang, N. D., S. Kapartis, and D. J. Brain, "A wideband compact end-entry septum polariser OMT," *ICAP87*, Vol. 1, No. 274, 419–423, 1987.
3. Shahan, O., "Orthomode transducer fits tight quarters," *Microwave Systems News*, Vol. 19, No. 8, 60–62, 1989.
4. Boifot, A. M., "Simple and broadband orthomode transducer," *IEE Proceedings H*, Vol. 137, No. 6, 396–400, 1990.
5. Skinner, S. J. and G. L. James, "Wideband orthomode transducers," *IEEE Trans. on Microwave Theory and Techniques*, Vol. 39, No. 2, 294–300, Feb. 1991.
6. Baylin, F. and B. Gale, *Ku-band Satellite TV: Theory, Installation and Repair*, Baylin Publications, 1991.
7. Ishida, O., Y. Isota, M. Miyazaki, and F. Takeda, "A wideband orthomode transducer for a Ku-band earth station," *Trans. Inst. Electronics Comm. Eng.*, Vol. J68, No. 11, 1408–1414, Japan, Nov. 1986.
8. Uher, J., J. Bornemann, and U. Rosenerg, *Waveguide Components for Antenna Feed Systems: Theory and CAD*, Artech House, 1993.

Wideband Microstrip Array Antenna Using Aperture Coupled Elements

N. Ghassemi and Sh. Mohanna
Electrical Engineering Department, University of Sistan & Baluchestan, Zahedan, Iran

Abstract— A 1×4 microstrip array antenna by using aperture coupled feed elements is presented in this paper for wideband applications in S and C bands. The antenna array has more than 60% impedance bandwidth and the gain of the structure is more than 12 dB from 2.8 GHz to 4.6 GHz (48%).

1. INTRODUCTION

Microstrip antennas have been used in many various categories; specially in mobile communication because of their benefits like low cost, small size and easy of application; but they have some disadvantages like low gain and narrow bandwidth. There is some technique to overcome these drawbacks such as: Using multilayer structure, material with low dielectric constant, and air-gap between layers [1, 2].

Array structure can be used to obtain high gain; but to yield to a wideband microstrip array antenna, a wideband antenna, and a wideband microstrip feed network should have been used [3–6]. An aperture coupled microstrip antenna with a rectangular patch, non-symmetric U-shaped feed line, and two slots on the ground plane has been reported recently [7, 8]. This paper presents a new wideband feed network, to obtain a 1×2 and a 1×4 high gain microstrip array antenna. Both structures have more than 60% impedance bandwidth. The 1×2 array antenna has more than 10 dB gain from 2.8 GHz to 4.5 GHz, and gain of the 1×4 array antenna is more than 12 dB from 2.8 to 4.6 GHz (46%).

2. ARRAY STRUCTURE

The array structure has three dielectric layers, the bottom and top layers are made from a material with the relative permittivity of 2.2 and the thickness of 1.6 mm; these two layers are separated with an air gap with the thickness of 6 mm. Under the air gap there is a ground plane and patches are placed upper the top dielectric layer (Fig. 1).

Each antenna element consist of a 50 Ω feed line which has been divided to, two 100 Ω feed lines; and a rectangular patch which has been fed throw two slots on the ground plane [7].

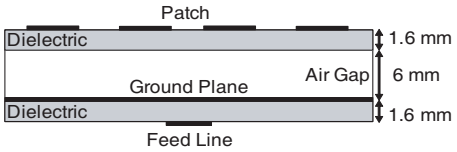

Figure 1: Side view of the structure.

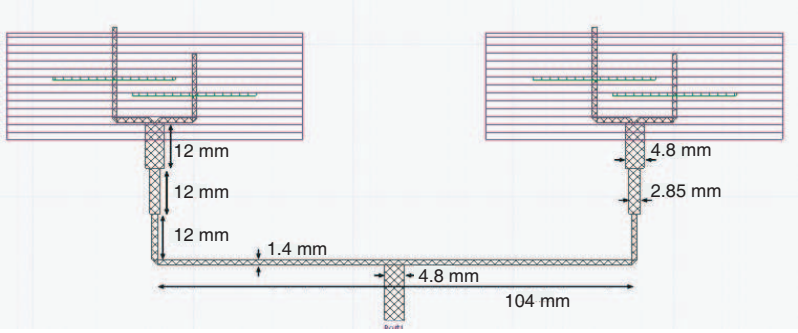

Figure 2: Top view of the 1×2 antenna array and its dimensions.

The feed network is under the first dielectric layer, that have a single 50 Ω main feed line which has been divided into two 100 Ω line. Top view of the 1×2 and 1×4 array structures, and all dimensions of their feed networks are shown in Fig. 2 and Fig. 3 respectively.

VSWR and gain of the one element [7], 1×2 and 1×4 array antenna are shown in Fig. 4 and Fig. 5. Both structures have more than 60% impedance bandwidth. The 1×2 array antenna has more than 10 dB gain from 2.8 GHz to 4.5 GHz, and gain of the 1×4 array antenna is more than 12 dB from 2.8 to 4.6 GHz (46%). The 1×2 and 1×4 array antennas have maximum gain of

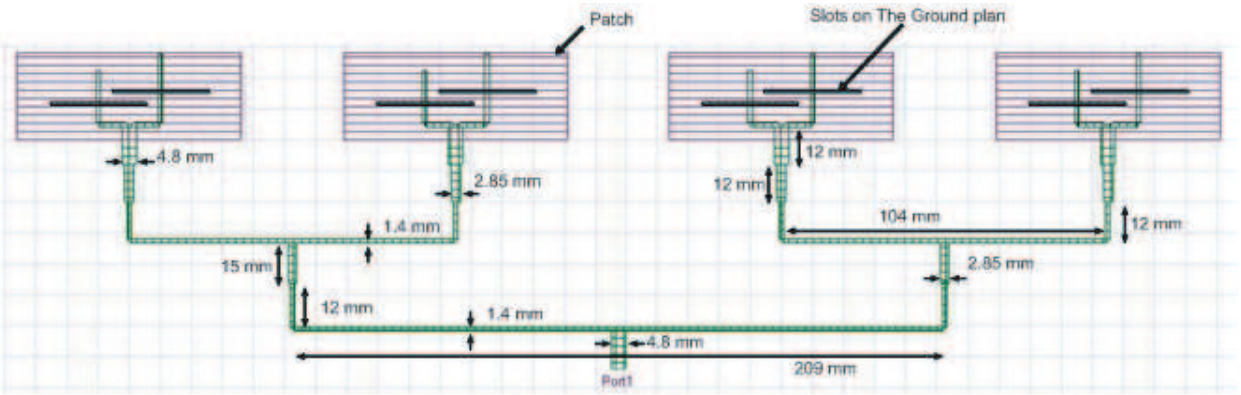

Figure 3: Top view of the 1×4 antenna array and its dimensions.

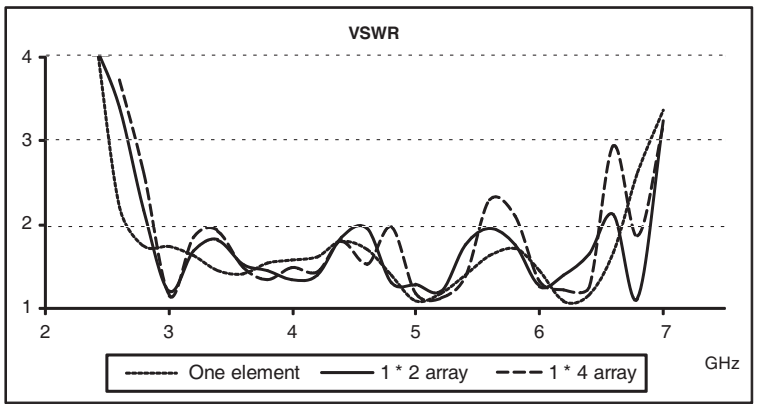

Figure 4: VSWR of one element [7], 1×2 and 1×4 antenna array.

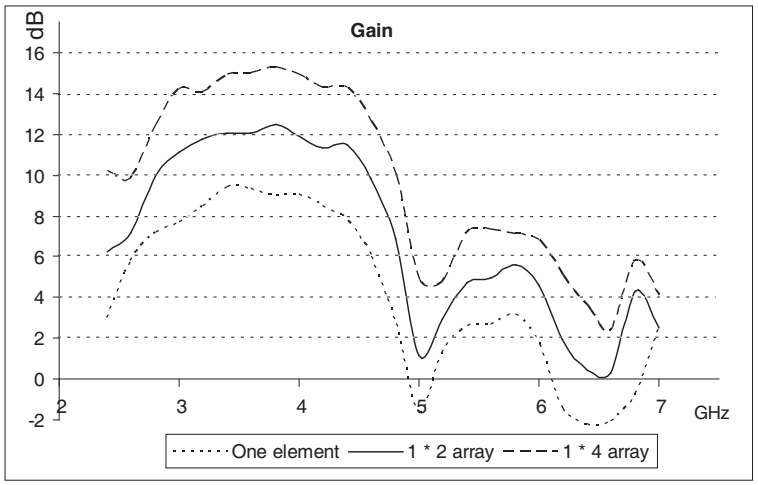

Figure 5: Gain of one element [7], 1×2 and 1×4 antenna array.

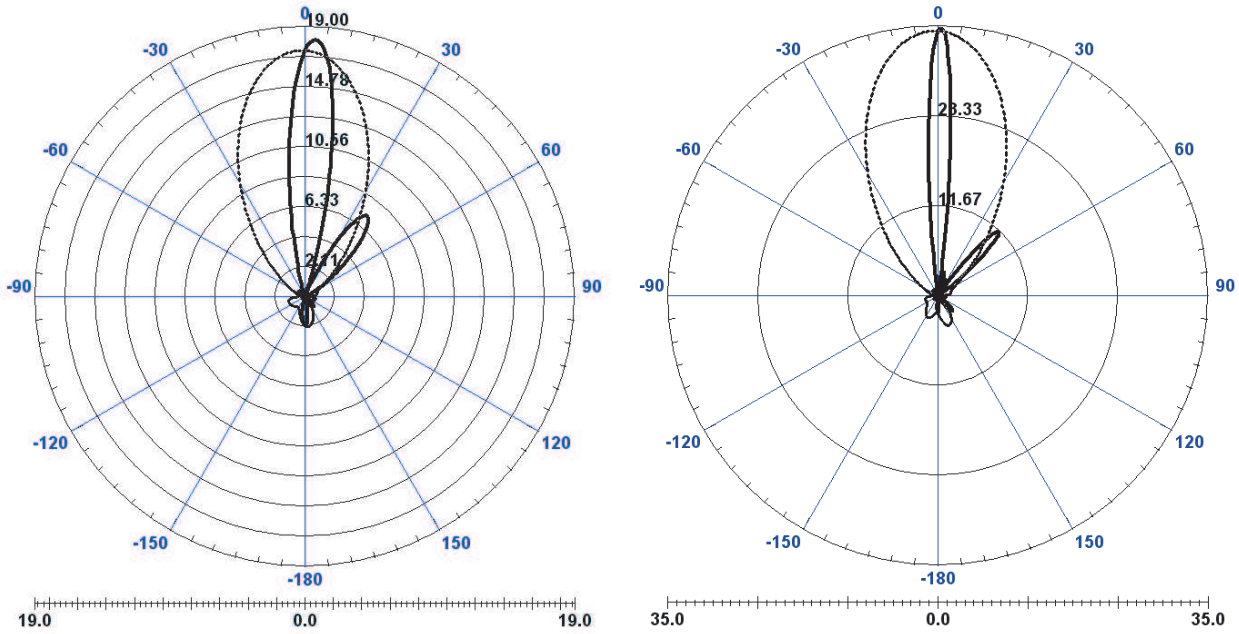

Figure 6: Radiation patterns of the (a) 1×2 and (b) 1×4 antenna array at 14 GHz.

12.5 dB and 15.2 dB respectively at 3.8 GHz. Fig. 6 shows the radiation pattern of the 1×2 and 1×4 array antennas at 14 GHz.

3. CONCLUSION

This paper presents a wideband feed network for aperture coupled microstrip array antenna. By using this feed network a 1×2 and a 1×4 array antenna have been presented to obtain high gain for wideband applications in S and C bands. The 1×2 and 1×4 array antennas has more than 10 dB and 12 dB gain respectively in 47% of their bandwidth.

REFERENCES

1. Ghassemi, N., M. H. Neshati, and J. Rashed-Mohassel "A high gain probe-feed microstrip antenna for wideband applications," *Microwave and Optical Technology Letters*, Vol. 50, No. 12, 3027–3029, Sep. 2008.
2. Ghassemi, N., J. Rashed-Mohassel, M. H. Neshati, S. Tavakoli, and M. Ghassemi "A high gain dual stacked aperture coupled microstrip antenna for wideband applications," *Progress In Electromagnetics Research B*, Vol. 9, 127–135, 2008.
3. Yun, W. and Y.-J. Yoon, "A wide-band aperture coupled microstrip array antenna using inverted feeding structures," *IEEE Transactions on Antennas and Propagation*, Vol. 53, No. 2, 861–862, Feb. 2005.
4. Kim, T., J. Choi, and J. S. Jeon, "Design of a wideband microstrip array antenna for PCs and IMT-2000 service," *Microwave and Optical Technology Letters*, Vol. 30, No. 4, 261–255, Aug. 20, 2001.
5. Angelopoulos, E. S., A. Z. Anastopoulos, D. I. Kaklamani, A. A. Alexandridis, F. Lazarakis, and K. Dangakis, "A novel wideband microstrip-fed elliptical slot array antenna for Ku-band applications," *Microwave and Optical Technology Letters*, Vol. 48, No. 9, 1824–1828, Sep. 2006.
6. Denidni, T. A. and N. Hassaine, "Broadband and high-gain E-shaped microstrip antennas for high-speed wireless networks," *Progress In Electromagnetics Research C*, Vol. 1, 105–111, 2005.
7. Ghassemi, N., J. Rashed-Mohassel, S. Mohanna, and G. Moradi, "A wideband aperture coupled microstrip antenna for S and C bands," *Microwave and Optical Technology Letters*, Vol. 51, No. 8, 1807–1809, Aug. 2009.
8. Ghassemi, N., S. Mohannam, J. Rashed-Mohassel, and M. H. Neshati, "A UWB aperture coupled microstrip antenna for S and C bands," *4th IEEE International Conference on Wireless Communication, Networking and Mobile Computing*, Dalian, China, Oct. 12–14, 2008.

Design of a Miniaturized Broadband Tag Antenna for UHF RFID System

Xingyu Zhang and Anping Zhao
Advanced Systems Engineering, Nokia Research Center, Beijing 100176, China

Abstract— In order to achieve the characteristics of miniature, low cost and broad bandwidth for RFID tag antennas, a novel passive UHF planar tag antenna is proposed in this paper. The proposed antenna is designed in the form of inductively coupled and comprised of a long folded dipole and a modified double T-matching network. It was constructed with a thin copper layer printed on a 0.24 mm-thick PET substrate for low cost production. The presented antenna provides a fairly wide bandwidth, which is much larger than those of the existing antennas with similar structures and satisfies the bandwidth requirements of the worldwide UHF RFID systems. Besides, the main radiation pattern of the reported antenna tends to the orientation that is perpendicular to the antenna surface which helps to identify the target objects. Furthermore, the gain of the antenna meets the demands of UHF RFID systems. All the features above make the proposed antenna applicable in use for UHF RFID systems.

1. INTRODUCTION

Radio frequency identification (RFID) that just began its explosive development in the last decade is actually with a long history of more than half a century [1]. It has lately attracted more and more attention for use in efficiently tracking and identifying objects in various supply chains from security and control point of view. An RFID system basically consists of a transponder (a tag), a reader antenna and a computer connected to the reader. Data is transferred between the tag and the read/write device by means of electromagnetic waves at the allocated frequency bands of 125 kHz, 13.56 MHz, 840–845 MHz, 869 MHz, 902–928 MHz, 955 MHz, 2.45 GHz and 5.8 GHz [2]. Antennas are fundamental elements in RFID communication systems. Also, the design of RFID tag antenna becomes more complicated and critical when the operating frequency rises to the microwave band region. A tag antenna should be small size, low profile and simple structure for low cost in production and convenient in use. Various kinds of RFID tag antennas have been reported in the open literatures. A compact slotted PIFA-type RFID tag antenna was studied in [3]. A tag antenna using the cavity for long reading range was presented in [4]. Two inductively coupled RFID antennas in two different structures, namely arc-shape and dual-body configurations, were designed in [5]. A dipole-type printed RFID antenna operating at UHF band (from 868 to 965 MHz) was reported in [6, 7]. However, these tag antennas are neither small in size and low in profile nor broad in bandwidth for practical applications.

In this paper, a compact planar RFID tag antenna with low profile and fairly wide bandwidth is proposed. The antenna is inductively coupled in order to easily implement the impedance conjugate-matching between the tag antenna and the microchip, for the reactance of the microchip is rather large because of the production process. The presented antenna is comprised of a folded dipole and a modified double T-matching network. It was fabricated by printing a thin copper layer on a PET substrate the profile of which is 0.24 mm. The designed antenna with a volume of $40 \times 50 \times 0.28\,\text{mm}^3$ is smaller than those antennas mentioned above. Besides, the operational bandwidth of the designed antenna when conjugate-matched to the microchip satisfies the bandwidth requirements of the RFID systems in all UHF bands, which helps to the world-wide circulation of the RFID merchandise.

2. ANTENNA DESIGN AND RESULTS ANALYSIS

The configuration of the proposed RFID tag antenna is shown in Fig. 1. The antenna has a simple and symmetrical structure by printing it on one side of a PET (dielectric constant $\varepsilon_r = 3.6$ and loss $\tan\delta = 0.003$) substrate with size of $40 \times 50\,\text{mm}^2$ and thickness of 0.24 mm. The antenna consists of a long folded dipole that is used to reduce the size of the antenna. A double T-matching network is used to adjust the power transmission coefficient between the tag antenna and the microchip (i.e., to implement the impedance conjugate-matching between the tag antenna and the microchip). The uniform width of the meandered stripline is 2 mm and a 2 mm length slot in the center is reserved for the feeding position (i.e., the place for attaching the microchip).

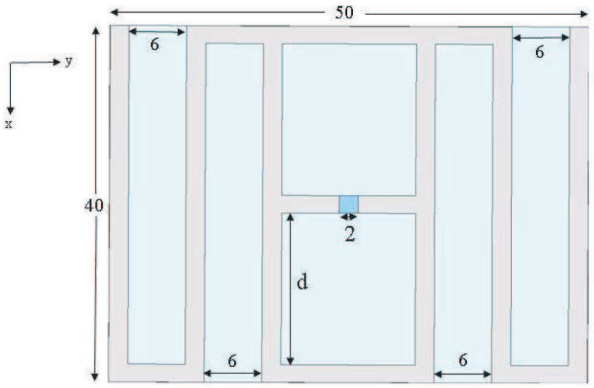

Figure 1: Geometry of the proposed RFID tag antenna.

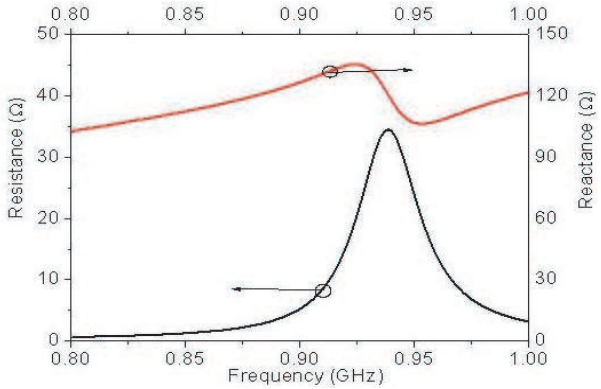

Figure 2: Impedance characteristics of the proposed antenna.

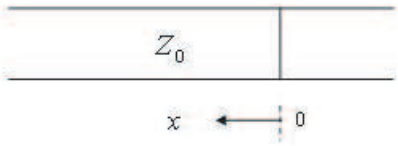

Figure 3: Equivalent model of the feeding structure of the tag antenna.

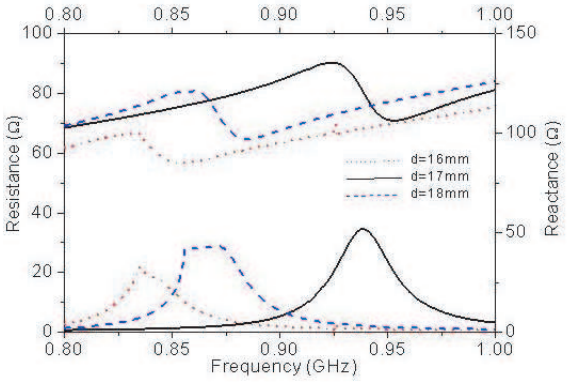

Figure 4: Impedance variations of the studied RFID tag antenna.

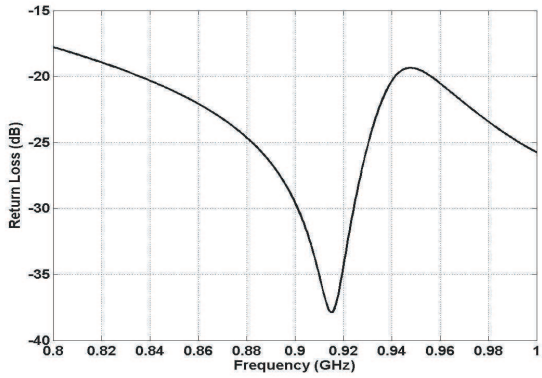

Figure 5: Return loss of the presented antenna when conjugate-matched to the microchip impedance.

Figure 2 depicts the simulated impedance characteristics of the proposed antenna. It can be clearly seen from Fig. 2 that the impedance of the designed antenna is $11.2+j132$ at 915 MHz. The input impedance of the microchip (ALN-9338-R) specified in this study is $6.2-j127\,\Omega$ at 915 MHz which indicates that this antenna design meets the requirement of the impedance conjugate-matching between the tag antenna and the microchip. Besides, the feeding structure of the tag antenna in the center can be clearly explained by the transmission line theory. Fig. 3 shows the equivalent model of the feeding structure. The input impedance of the transmission line in ideal situation can be described as formula (1):

$$Z(x) = jZ_0 \tan\left(\frac{2\pi x}{\lambda}\right) \tag{1}$$

when x satisfies the condition of $0 < x < \lambda/4$, $\tan(2\pi x/\lambda) > 0$ can be achieved. In this case, $Z(x)$ acts as an inductor and the reactance becomes larger with the increase of x. While x satisfies the condition of $x > \lambda/4$, $\tan(2\pi x/\lambda) < 0$ can be observed. $Z(x)$ then acts as a capacitor and the reactance becomes smaller with the increase of x. Hence, the impedance of the tag antenna can be simply adjusted by changing the distance (described by d in Fig. 1) between the feeding and the shorting striplines. Meanwhile, the impedance of the tag antenna can also be changed by adjusting the stripline width of the dipole and double T-matching network, and the separation

between the meandered strplines of the dipole (which is fixed at 6 mm in this study). Fig. 4 portrays the impedance characteristics of the studied RFID tag antenna with variation of the parameter d. It can be seen from Fig. 4 that the impedance conjugate-matching is optimized while d is 17 mm.

Figure 5 denotes the computed return loss of the presented antenna when conjugate-matched to the impedance of the microchip. One can see from Fig. 5 that the return loss of the antenna is lower than −10 dB when the frequency ranges from 0.8 to 1 GHz, which satisfies the bandwidth need of the worldwide RFID system in UHF bands. In particular, compared to the existing antennas with the same structures, much bigger operational bandwidth is achieved for the proposed antenna. This also helps to the circulation and practical applications of the RFID merchandise in the world.

The far-field radiation patterns of the designed tag antenna at 915 MHz are plotted in Fig. 6. It can be noted that, due to the symmetrical structure, the main radiation direction of the presented antenna tends to the orientation that is perpendicular to the antenna surface, which helps to the identification of the target objects for the RFID tag antenna.

The calculated gain of the proposed RFID tag antenna at the operational frequency band is exhibited in Fig. 7. One can conclude from Fig. 7 that the gain is between −0.5 and 2.11 dBi when the operating frequency ranges from 0.8 to 1 GHz. It can also be illustrated that the gain of the antenna doesn't decrease much although fold and coupling of the long dipole exist in the antenna design.

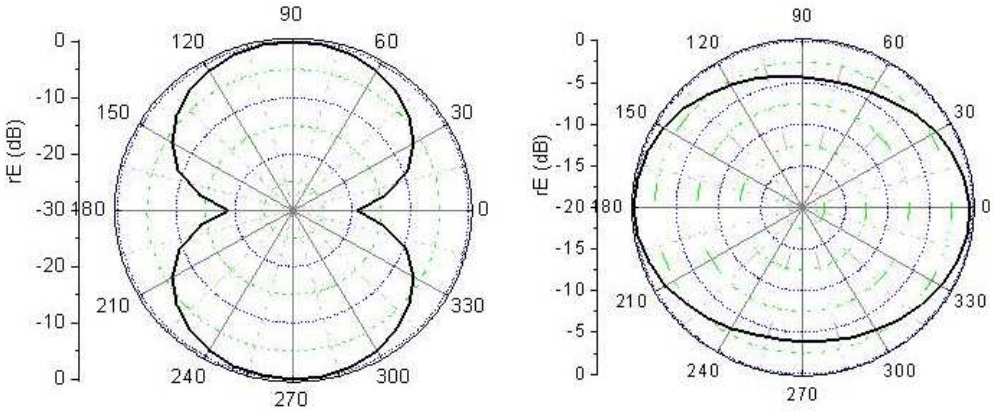

(a) E-plane (b) H-plane

Figure 6: Radiation patterns of the proposed tag antenna at 915 MHz.

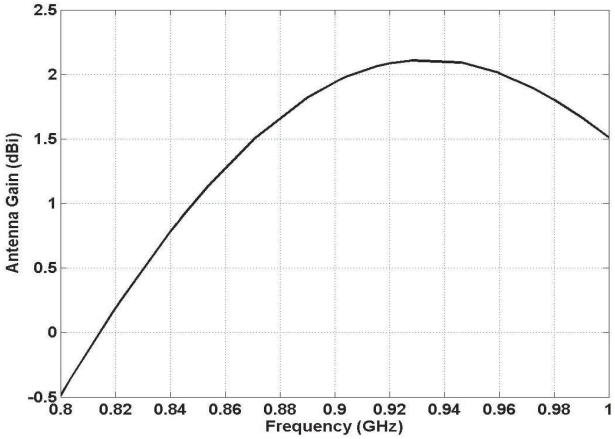

Figure 7: Gain of the proposed RFID tag antenna at the operational frequency band.

3. CONCLUSIONS

A compact and low profile passive RFID tag antenna with broadband characteristics has been designed in this paper. It realizes a fairly broad bandwidth ($S_{11} < -10\,\mathrm{dB}$ between 0.8 GHz and 1 GHz) and achievable gain (from -0.5 to 2.11 dBi) with acceptable radiation patterns, although its volume is only $40 \times 50 \times 0.28\,\mathrm{mm}^3$ based on a long folded dipole. The antenna can be fabricated by simply printing a copper layer on one side of the PET substrate. The impedance of the tag antenna can be simply adjusted by changing the width and distance of the copper stripline that helps to the impedance conjugate matching between the tag antenna and the microchip. Moreover, this antenna can be easily mounted and has good compatibility with other microwave circuit components.

REFERENCES

1. Landt, J., "The history of RFID," *IEEE Potentials*, Vol. 24, No. 4, 8–11, Oct.–Nov. 2005.
2. Keskiammi, M. and M. Kivikoski, "Using text as a meander line for RFID transponder antennas," *IEEE Antennas and Wireless Propagation Letters*, Vol. 3, 372–374, 2004.
3. Kwon, H. and B. Lee, "Compact slotted planar inverted-F RFID tag mountable on metallic objects," *Electronics Letters*, Vol. 41, No. 24, 1308–1310, 2005.
4. Kyoung, H. L., L. Jin-Seong, K. Goojo, and H. M. Byung, "Design of UHF RFID metal tag with long reading range using cavity," *Asia-Pacific Microwave Conference (Invited Paper)*, Dec. 16–20, 2008.
5. Yang, L., B. S. Serkan, and M. M. Tentzeris, "Design and development of novel inductively coupled RFID antennas," *IEEE International Symposium on Antennas and Propagation*, 1035–1038, Jul. 2006.
6. Ahmed, I., T. Vuong, G. Anthony, and T. Smail, "New design antenna for RFID UHF tags," *IEEE International Symposium on Antennas and Propagation*, 1355–1358, Jul. 2006.
7. Cho, C., H. Choo, and I. Park, "Broadband RFID tag antenna with quasi-isotropic radiation pattern," *Electronics Letters*, Vol. 41, No. 20, 1091–1092, 2005.

Design and Demonstration of 1-bit and 2-bit Transmit-arrays at X-band Frequencies

H. Kaouach[1], **L. Dussopt**[1], **R. Sauleau**[2], **and Th. Koleck**[3]

[1]CEA, LETI, MINATEC, F38054 Grenoble, France
[2]IETR, UMR CNRS 6164, Université de Rennes 1, 35042 Rennes, France
[3]CNES, 18 avenue Edouard Belin, 31401 Toulouse, France

Abstract— This article describes the design of new planar transmit-arrays at 10 GHz with 1-bit and 2-bit phase quantization and specific unit-cell designs in each case. The influence of the main design parameters are investigated numerically. The simulated directivity/gain values equal 26/23 dBi for the 1-bit design, and 31/28 dBi for the 2-bit design, respectively. In particular, the influence of the phase quantization is highlighted. Both designs are built on a two-layer printed circuit board assembly and operate in linear polarization in source focal side. In free space side, the 1-bit design operates in linear polarization and 2-bit design operates in circular polarization. Beam-steering characteristics up to ±30° are investigated and compared by tilting the feed source and by changing the phase distribution across the array.

1. INTRODUCTION

At millimeter-wave frequencies, antenna arrays are generally implemented as lens-arrays or reflect-arrays with free-space feeding schemes to minimize the inherent loss and parasitic radiation of the feed network. Transmit-arrays (double-array discrete lenses) are low-profile and low-cost planar alternatives to dielectric lens antennas [1, 2] for millimeter-wave applications like automotive radars, high data rate wireless communication systems, imaging systems, and quasi-optical power combiners [3–7].

They typically consist of two planar arrays of printed antennas, whose elements are interconnected or coupled with a specific transmission phase in order to generate a uniform or linear phase distribution across the array (Fig. 1).

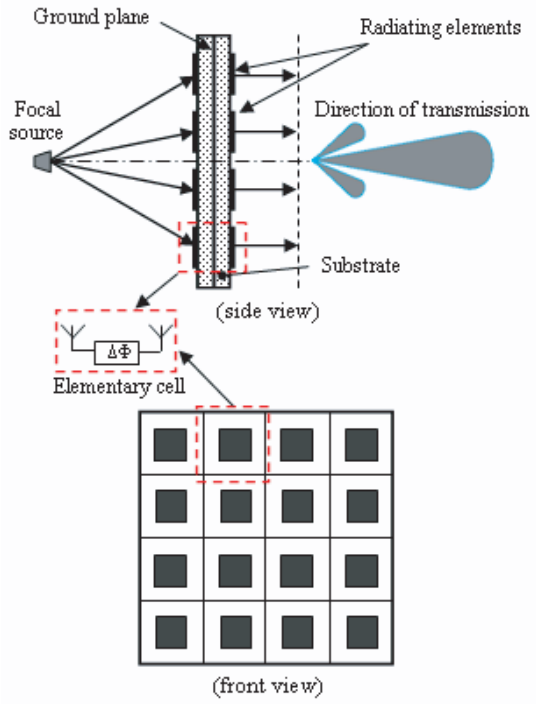

Figure 1: General description of a transmit-array.

Transmit-arrays are based on similar concepts as for reflect-arrays except that they operate in a transmission mode rather than in reflection [8]. In contrast to reflect-arrays, such configurations

offer several advantages, such as reduction of blockage effects due to the focal array, and easier integration and mounting onto various platforms. On the other hand, transmit-arrays are more complex to design and optimize.

This paper is organized as follows. Section 2 presents several numerical results on the general performance of transmit-arrays as a function of element spacing, phase quantization and feed position. Then two different designs with 1-bit and 2-bit phase quantization are proposed and compared in Sections 3 and 4. The capabilities of both solutions for beam steering are investigated in Section 5. Conclusions are drawn in Section 6.

These prototypes are designed after a first 2-bit design [9] in order to improve his directivity, gain and efficiency. The elementary cell of the first 2-bit design consists of two patch antennas connected by a coplanar (CPW) transmission line. Both patches are coupled to the CPW line through a rectangular slot loop etched in the ground plane. The phase delay induced by each cell is proportional to the t-line length.

2. TRANSMIT-ARRAY DESIGN

An in-house CAD tool has been developed to design and compute the performance of transmit-arrays, starting from the electromagnetic characteristics of the elementary cell and the focal source. The radiation pattern of the feed is first used to determine the electric field distribution illuminating the first antenna array. The radiation patterns and S-parameters of each elementary cell are then used to compute the radiation pattern, gain and directivity of the transmit-array.

A preliminary study has been performed to investigate the influence of the main design parameters on the antenna performance. This study is done at 10 GHz and is based on a generic elementary cell with a gain of 5 dBi, which is a typical value for patch antennas. The total array area is fixed at $300 \times 300\,\text{mm}^2$, corresponding to a maximum directivity of 31 dBi. The feed is a 10-dBi horn antenna with 3-dB beamwidths of 52° and 49° in E- and H-planes, respectively. This feed is placed at 260 mm away from the array, which results in 1.8-dB spill-over loss.

The influence of the element spacing on the array directivity and gain is represented in Fig. 2 when varying the element spacing in the E-plane direction and keeping it fixed at $\lambda_0/2$ in the other one. As expected, minimizing the element spacing is desirable so as to collect the radiation from the feed source with maximum efficiency. Since we are limited by the patch antenna size, a typical element spacing of $\lambda_0/2$ will be considered in the following.

The main challenge in designing transmit-arrays is the ability to generate the appropriate phase-shift for each cell in order to transform the incoming spherical wave radiated by the focal source into a plane wave on the free-space side, i.e., to produce a nearly-flat phase distribution with a given phase gradient depending on the main beam direction. Since this phase compensation cannot be ideal, we have investigated the effect of phase quantization on the directivity and gain of the array (Table 1). A constant difference of 3.1 dB between directivity and gain is due to spill-over and reflection loss on the transmit-array. Insertion losses are very low. It is seen that a 1-bit (180° phase steps) or 2-bit (90° phase steps) design result in 4.3 dB and 0.8 dB loss, respectively, as compared to the ideal case (Table 1).

Finally, the best location of the feed horn for maximum gain was found to be at $7.6 \times \lambda_0$ (228 mm) from the array (Fig. 3). While the gain decreases slowly for longer focal lengths, the directivity

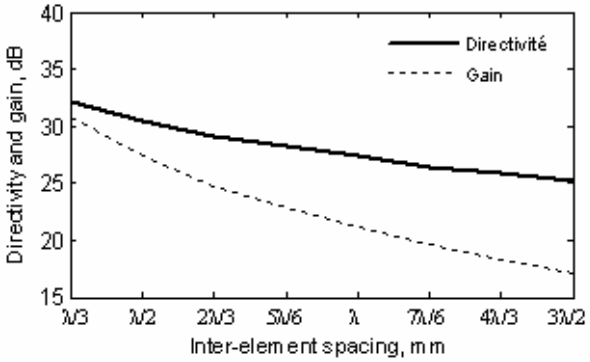

Figure 2: Impact of the element spacing in the gain and directivity with ideal phase compensation.

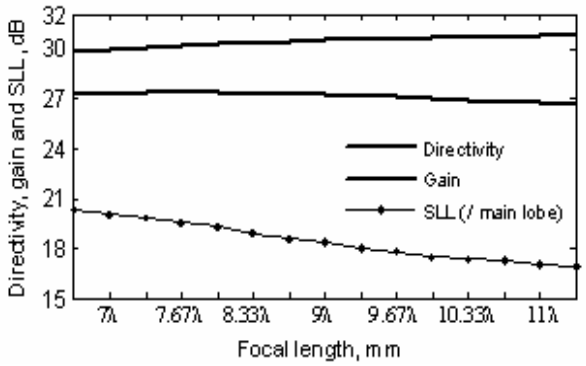

Figure 3: Impact of the feed position with ideal phase compensation.

Table 1: Impact of the phase quantization.

Bit resolution	0-bit	1-bit	2-bit	3-bit	ideal
Directivity (dB)	15.4	26.1	29.6	30.2	30.4
Gain (dB)	12.5	23.3	26.8	27.3	27.5

increases and the side-lobe level decreases because of the 'more uniform illumination' of the array.

Based on these results, two designs of transmit-arrays are proposed and compared in the following, with 1-bit (Section 3.1) and 2-bit (Section 3.2) phase quantization.

3. ELEMENTARY CELL DESIGN

3.1. 1-bit Design

The elementary cell is represented in Fig. 4. It consists of a single ground plane, two substrate layers (Rogers RO4003, $\varepsilon_r = 3.38$, $h = 1.524\,\text{mm}$) and two patch antennas connected by a via hole. The two transmission phase values with a 180° phase difference (1-bit) are obtained by flipping one of the patches with respect to the via connection. The patch and cell sizes equal $7.4 \times 7.6\,\text{mm}^2$ and $15 \times 15\,\text{mm}^2$ ($\lambda_0/2 \times \lambda_0/2$), respectively.

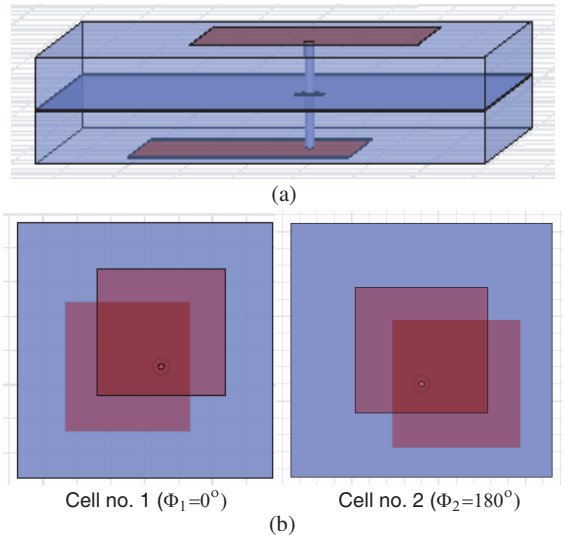

Figure 4: Elementary cell for the 1-bit design, (a) side view, (b) front view.

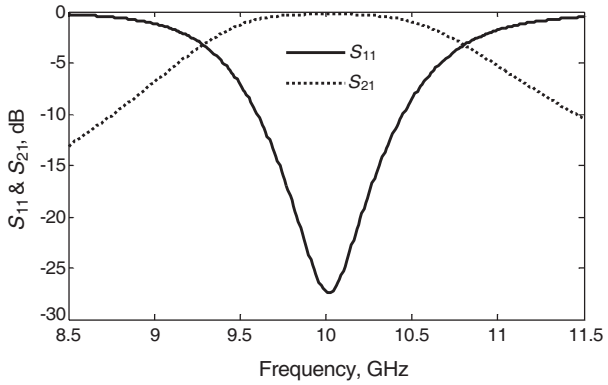

Figure 5: S-parameters of the elementary cell (1-bit design).

This unit-cell was simulated with Ansoft-HFSS using periodic boundary conditions and Floquet port excitations [10, 11]. The $-10\,\text{dB}$ return loss bandwidth is 850 MHz (8.8%) (Fig. 5). The

maximum directivity and gain are 5 dBi and 4.8 dBi in the broadside direction, respectively. The patches on both sides of the array are rotated by 90°, providing a natural polarization decoupling between the feed radiation and the array radiation.

3.2. 2-bit Design

The elementary cell of the 2-bit design is almost the same as the elementary cell of 1-bit design, in terms of dimensions and materials. For against in this case, we have 4 different elementary cells (Fig. 6), instead of 2 elementary cells, for achieve 2-bit phase quantization.

The 4 elementary cells have designed to reach 0°, 90°, 180° and 270° of transmission phase between the input and output signal of the array antennas.

The different transmission phase values are obtained by turning the patch in the free space side at 90° against the other patch with respect to the via connection.

3.3. Discussion

An important advantage of these two designs is their simplicity with only two dielectric substrates and three metal layers. The two designs benefit from a small size, thus allowing a cell spacing of $\lambda_0/2$ in both directions. The 2-bit design, in contrast to the 1-bit design, permits an improved phase quantization.

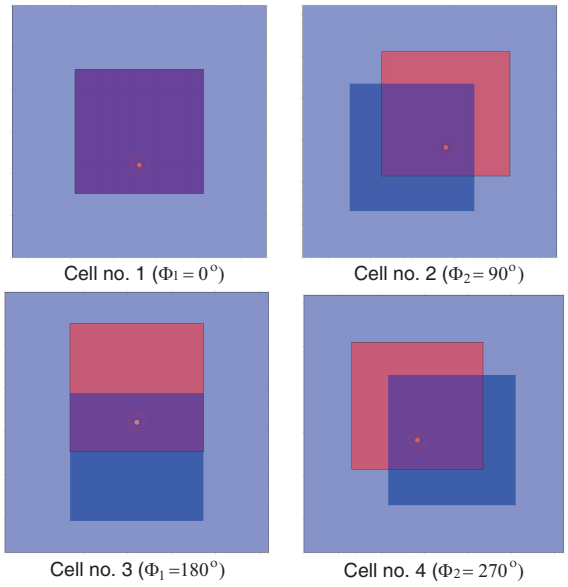

Figure 6: Elementary cell for the 2-bit design, front view.

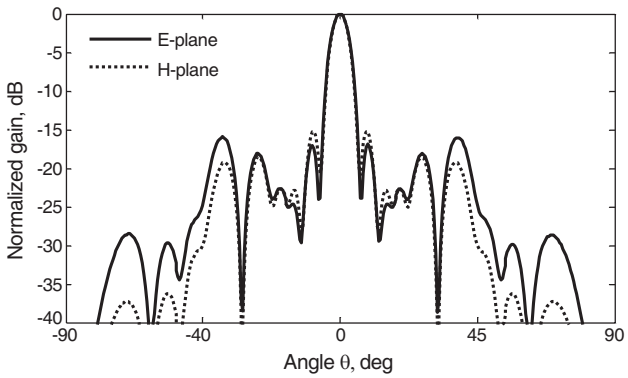

Figure 7: Radiation pattern simulated at 10 GHz for the 1-bit design.

4. PERFORMANCE OF THE TRANSMIT-ARRAYS

4.1. 1-bit Design

The 1-bit design transmit-array comprises 20×20 cells. The feed horn is placed at 260 mm ($8.7 \times \lambda_0$), which corresponds to an acceptable trade-off between the taper efficiency (7.5 dB) and spill-over efficiency (1.8 dB).

The simulated radiation patterns at 10 GHz show a directivity and gain of 26 dBi and 23 dBi, respectively, with side-lobe levels lower than −15 dB (Fig. 7).

4.2. 2-bit Design

The 2-bit design is designed like the 1-bit design; the only difference is that the quantization phase is more important.

The simulated radiation patterns at 10 GHz show a directivity and gain of 31.2 dBi and 28 dBi, respectively, with side-lobe levels lower than −15 dB (Fig. 8).

5. BEAM-STEERING

Beam-steering or beam-switching can be achieved via two methods. The first one relies on the feed horn that can be tilted at a specific angle from the main axis of the array. The second method consists in changing the phase-shift distribution across the array to produce a desired phase gradient to steer the beam, as done classically for antenna arrays. This second method is investigated here only for fixed-beam passive arrays. It is expected that tunable phase-shifter may be used in the future to achieve fully reconfigurable transmit-arrays [12].

5.1. Beam-steering by Tilting the Feed Horn

This method has been studied experimentally for the first 2-bit prototype with steering angles up to ±30° [9]. A gain reduction of 2.8 dB was obtained experimentally for the maximum scan angle, which is due both to the increase of the spill-over loss and to the limited beamwidth of elementary cells.

The simulated radiation patterns for the 1-bit design are represented in Fig. 9 for 10°- and 30°-scan angles. The corresponding gain values equal to 22.6 dBi and 18.7 dBi, respectively.

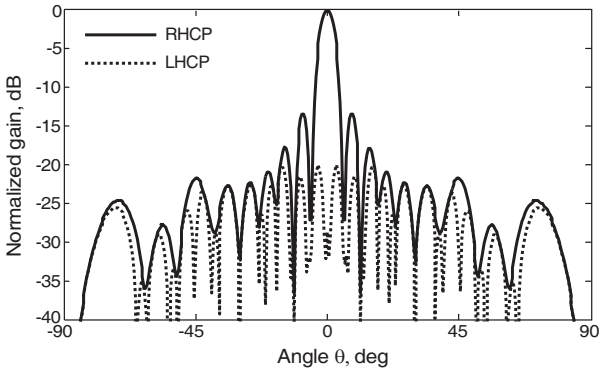

Figure 8: Radiation pattern measured at 10 GHz for the 2-bit design.

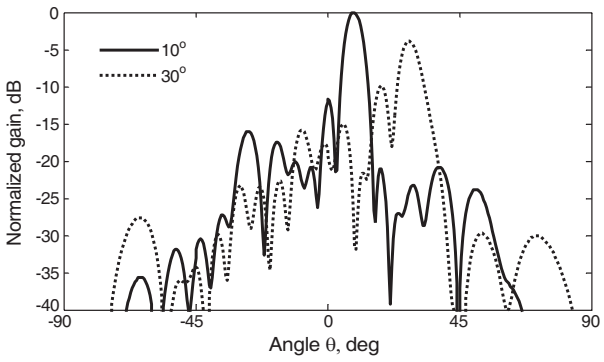

Figure 9: 1-bit design with tilted feed horn. Simulated radiation patterns at 10 GHz for two scan angles (10° and 30°).

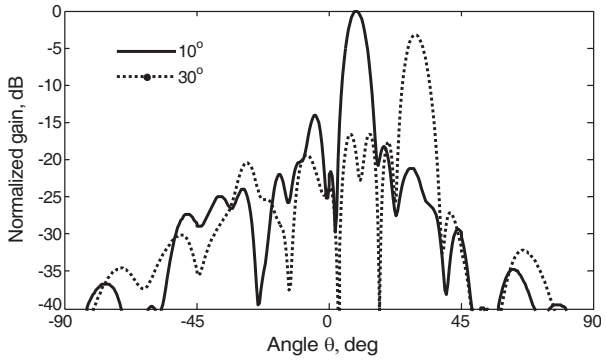

Figure 10: 1-bit design with optimized phase gradient. Simulated radiation patterns at 10 GHz for two scan angles (10° and 30°).

5.2. Beam-steering by Modifying the Phase-shift Distribution

Here the feed horn is placed along the main axis, and the phase gradient is tuned to steer the main beam at 30° (Fig. 10). Compared to the previous method, this strategy provides better performance in terms of gain reduction and side-lobe level (−14 dB). The gain values are 23.5 dBi and 20.3 dBi at 10° and 30°, respectively.

6. CONCLUSION

Passive transmit-arrays operating at X-band have been investigated numerically and experimentally. The numerical study has highlighted the impact of cell spacing, phase quantization and focal length upon the gain and directivity of the array. Two designs have been proposed, with 1-bit and 2-bit phase quantization. The first design provides a 23 dBi-gain, and the gain of the second one is equal to 28 dBi due to the phase quantization. The beam-steering capabilities of the 1-bit design have been studied for scan angles up to 30°.

REFERENCES

1. Godi, G., R. Sauleau, L. Le Coq, and D. Thouroude, "Design and optimization of three dimensional integrated lens antennas with genetic algorithm," *IEEE Trans. Antennas Propag.*, Vol. 55, No. 3, 770–775, Mar. 2007.
2. Costa, J. R., C. A. Fernandes, G. Godi, R. Sauleau, L. Le Coq, and H. Legay, "Compact Ka-band lens antennas for LEO satellites," *IEEE Trans. Antennas Propag.*, Vol. 56, No. 5, 1251–1258, May 2008.
3. McGrath, D. T., "Planar three-dimensional constrained lenses," *IEEE Trans. Antennas Propag.*, Vol. 34, No. 1, 46–50, Jun. 1986.
4. Pozar, D. M., "Flat lens antenna concept using aperture coupled microstrip patches," *Electronics Letters*, Vol. 32, No. 23, 2109–2111, Nov. 1996.
5. Popovic, D. and Z. Popovic, "Multibeam antennas with polarization and angle diversity," *IEEE Trans. Antennas Propag.*, Vol. 50, No. 5, 651–657, May 2002.
6. Padilla de la Torre, P. and M. Sierra-Castañer, "Transmitarray for Ku band," *Second European Conference on Antennas and Propagation, EuCAP 2007*, Edinburgh, UK, Nov. 11–16, 2007.
7. Barba, M., E. Carrasco, and J. A. Encinar, "An X-band planar transmitarray," *30th ESA Workshop on Antennas for Earth observation, Science, Telecommunication and Navigation Space Missions*, 236–239, Noordwijk, The Netherlands, May 27–30, 2008.
8. Pozar, D. M. and S. D. Targonski, "Design of millimeter wave microstrip reflectarrays," *IEEE Trans. Antennas Propag.*, Vol. 45, No. 2, 287–295, Feb. 1997.
9. Kaouach, H., L. Dussopt, R. Sauleau, and Th. Koleck, "Design and demonstration of an X-band transmit-array," *European Conference on Antennas and Propagation, EuCAP 2009*, Berlin, Germany, Mar. 23–27, 2009.
10. Turner, G. and C. Christodoulou, "Broadband periodic boundary condition for FDTD analysis of phased array antennas," *IEEE Antennas Propag. Soc. Int. Symp.*, Vol. 2, No. 12, 1020–1023, Jun. 1998.
11. Ansoft HFSS, http://www.ansoft.com/products/hf/hfss/.
12. Cheng, C., A. Abbaspour-Tamijani, and B. Lakshminarayanan, "Reconfigurable lens-array with monolithically integrated MEMS switches," *European Microwave Conference, EuMC 2008*, Amsterdam, The Netherlands, Oct. 27–31, 2008.

Amplification of Space Charge Waves of Millimeter Wave Range in Transversely Nonuniform n-GaN Films

V. Grimalsky, S. Koshevaya, M. Tecpoyotl-T., and J. Escobedo-A.
CIICAp, Autonomous University of Morelos (UAEM), Cuernavaca ZP 62209, Mor., Mexico

Abstract— Amplification of space charge waves (SCW) due to the negative differential conductivity in n-GaN films placed onto a semi-infinite substrate is investigated theoretically. A case of transverse nonuniform film is considered. The diffusion-drift equations for volume electron concentration were used jointly with the Poisson equation for the electric field. The transverse nonuniformity results in a decrease of the electron mobility near the surfaces of the film and, correspondingly, to some decrease of spatial increments. It is demonstrated that the nonuniform doping can compensate an influence of the surfaces on the spatial increment of amplification. It is possible to observe an amplification of SCW in n-GaN films of submicron thicknesses at essentially higher frequencies $f \geq 100\,\mathrm{GHz}$, when compared with n-GaAs. High ($\sim 10\,\mathrm{kV/cm}$) output electric fields of the short wave part of the millimeter wave range can be obtained.

1. INTRODUCTION

Amplification of traveling space charge waves (SCW) of the microwave range in n-GaAs films has been under investigations for many years [1]. When bias electric fields are higher than the critical value for observing negative differential conductivity (NDC), SCW are subject to amplification. But the critical value of bias electric field in GaAs is $E_c = 3.5\,\mathrm{kV/cm}$ that limits the maximum values of the microwave electric field of SCW. Also, the frequency range of amplification of SCW in GaAs films is $f < 50\,\mathrm{GHz}$. At frequencies $f > 50\,\mathrm{GHz}$, it is better to use new materials possessing NDC at higher frequencies $f = 100 \ldots 500\,\mathrm{GHz}$, like gallium nitride GaN [2–5]. The properties of GaN are: a high critical bias field $E_c \sim 100\,\mathrm{kV/cm}$; extended frequency range for observing NDC $f \leq 500\,\mathrm{GHz}$; high temperature stability, and NDC at higher values of doping $\leq 10^{18}\,\mathrm{cm}^{-3}$.

In thin films of submicron thicknesses, an influence of film surfaces of electron mobility can be essential. Namely, the mobility near the surfaces is lower than in the center of the film. Therefore, the transverse nonuniformity of the film should be taken into account properly. In the present paper the spatial increments of amplification of SCW due to NDC in nonuniform n-GaN films have been calculated. An amplification of SCW is possible up to the frequencies $f \sim 200 \ldots 300\,\mathrm{GHz}$. An influence of the nonuniformity can be compensated by inhomogeneous doping. The output electric field of SCW in a linear regime of amplification can achieve the values $\geq 10\,\mathrm{kV/cm}$.

2. BASIC EQUATIONS

Consider n-GaN film of a sub-micron thickness placed onto a semi-infinite dielectric substrate, see Fig. 1. The GaN of cubic symmetry (zinc blende structure) is considered. The bias electric field is directed along z-axis, the SCW are excited by an input antenna I and propagate in z-direction.

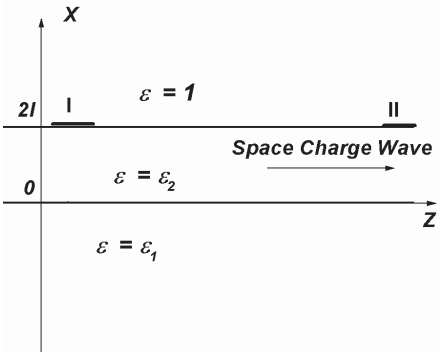

Figure 1: Geometry of the problem. The n-GaN film occupies the region $0 < x < 2l$, $x > 2l$ is vacuum, $x < 0$ is a semi-infinite substrate. I is an input antenna, II is output one.

The dynamics of SCW is described by the equations of motion of electrons jointly with the Poisson equation. At frequencies $f \leq 200\,\mathrm{GHz}$, the simplest hydrodynamic diffusion-drift equation

for the electron fluid is used:

$$\begin{aligned} &\frac{\partial n}{\partial t} + \mathrm{div}(\vec{v}(E)n - D(x)\nabla n) = 0, \quad \vec{v} = \mu(|E|, x)\vec{E}; \\ &\mathrm{div}(\varepsilon_0\varepsilon(x)\nabla\tilde{\varphi}) = -e(n - n_0(x)), \quad \vec{E} = -\nabla\tilde{\varphi} + \vec{e}_z E_0 + \vec{e}_x E_{x0} \end{aligned} \tag{1}$$

Here n is the electron concentration, $\tilde{\varphi}$ is the electric potential of the alternative field, $\boldsymbol{v}$ is the electron velocity, n_0 is the equilibrium electron concentration, D is the diffusion coefficient, $\mu(E)$ is the electron mobility, E_0 is the bias electric field. The data for GaN are taken from [5, 6]. The coordinate frame is aligned along the crystalline axes. The lower indices 1, 2 relate to the substrate and the film, correspondingly. The dielectric permittivities of the substrate and the film are ε_1 and ε_2. The dependence of the electron velocity on the electric field **for bulk** GaN is given in Fig. 2 [6].

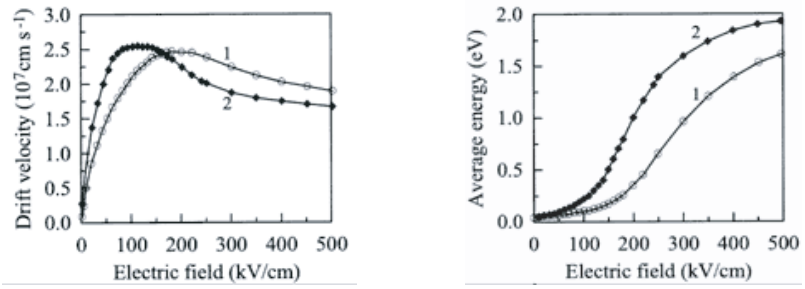

(a) (b)

Figure 2: Dependencies of the drift velocity on the electric field for wurtzite (curve 1) and zinc blende (curve 2) n-GaN (part a); dependencies of the average energy on the electric field for wurtzite (curve 1) and zinc blende (curve 2) n-GaN (part b) [6].

Linear amplification of SCW is investigated below. The following boundary conditions for the density of electric current $\boldsymbol{j}$ at the boundaries of the film are used:

$$j_x(x = 0) = 0, \quad j_x(x = 2l) = 0; \quad \text{where} \quad \vec{j} = e(\vec{v}(E)n - D_n\nabla n) \tag{2}$$

These boundary conditions are equivalent to an absence of surface density of charge at the boundaries of the film [1]. The linearized set of Eq. (1) takes the form:

$$\begin{aligned} &\frac{\partial\tilde{n}}{\partial t} + \frac{\partial}{\partial x}(v_{0x}\tilde{n}) - \frac{\partial}{\partial x}\left(n_0\mu\frac{\partial\tilde{\varphi}}{\partial x}\right) + v_0\frac{\partial\tilde{n}}{\partial z} - \mu_d n_0\frac{\partial^2\tilde{\varphi}}{\partial z^2} - \frac{\partial}{\partial x}\left(D\frac{\partial\tilde{n}}{\partial x}\right) - D\frac{\partial^2\tilde{n}}{\partial z^2} = 0, \quad 0 < x < 2l; \\ &\mathrm{div}\,(\varepsilon_0\varepsilon(x)\nabla\tilde{\varphi}) = -e\tilde{n}, \quad \tilde{\vec{E}} = -\nabla\tilde{\varphi}, \tilde{v}_x = \mu\tilde{E}_x; \quad \mu_d \equiv \frac{dv_z}{dE}; \\ &\tilde{v}_x n_0 - D\frac{\partial\tilde{n}}{\partial x}|_{x=0} = \tilde{v}_x n_0 - D\frac{\partial\tilde{n}}{\partial x}|_{x=2l} = 0 \end{aligned} \tag{3}$$

Here $n = n_0 + \tilde{n}$ ($|\tilde{n}| << n_0$); $\tilde{n}$, $\tilde{\varphi}$ are alternative parts of electron concentration and electric potential; E_0 is a bias electric field within the film, $v_0(x) = \mu(x, E_0)E_0$ is the steady state part of the electron drift velocity; $\mu = \mu(x, E_0) = v_0/E_0$. For a sake of simplicity, we consider the motion of positive charge, so $\mu > 0$.

The following simple model of transverse nonuniformity of the film is considered:

$$\begin{aligned} \mu(x) &= \mu_0 - (\mu_0 - \mu_f)F(x), \quad \mu_d(x) = \mu_{d0} - (\mu_{d0} - \mu_{df})F(x); \\ F(x) &= \exp\left(-x^2/x_0^2\right) + \exp\left(-(2l - x)^2/x_0^2\right) \end{aligned} \tag{4}$$

Namely, it is assumed that in the center of the film $x = l$ the value of electron mobility is maximal: $\mu = \mu_0$ and the differential mobility μ_d is negative. At the surfaces the electron mobility takes a smaller value $\mu_f < \mu_0$ whereas the differential mobility is negative or positive there: $\mu_d = \mu_{df}$. The scale of the inhomogeneity is $x_0 < l$. The diffusion coefficient is proportional to the electron mobility: $4D(x) = \mu(x)(k_B T_e/e)$, where T_e is the electron temperature. The electron

temperature has been calculated from the relation: $k_B T_e \approx (2/3) w(E_0)$, where w is the average electron energy [4, 5]. In the case of NDC, $T_e \sim 5 \times 10^3$ K.

Also the inhomogeneous doping of the film by donors is taken into account:

$$N_d(x) = N_{d0} \exp\left(-(x-l)^2/x_d^2\right) \tag{5}$$

Here N_{d0} is the donor concentration in the center of the film, x_d is the scale of the inhomogeneous doping. The steady distribution of the electric potential of the transverse electric field $\varphi_0(x)$ and the steady electron concentration $n_0 \equiv n_0(x)$ should be calculated from the following Poisson equation:

$$\frac{d^2\varphi_0(x)}{dx^2} = -\frac{e}{\varepsilon_0\varepsilon_2}(n_0(x) - N_d(x)),\ n_0(x) = C \times \exp\left(-\frac{e\varphi_0(x)}{k_B T_e}\right),\ C = \frac{\int\limits_0^{2l} N_d(x)dx}{\int\limits_0^{2l} \exp\left(-\frac{e\varphi_0(x)}{k_B T_e}\right) dx} \tag{6}$$

From the symmetry, the transverse electric potential has the same values at the surfaces of the film: $\varphi_0(0) = \varphi_0(2l) = 0$. The steady state component of the transverse electric field and electron velocity at the surfaces are also equal to zero. The constant C is determined from the condition of the steady electric neutrality.

The solution for alternative parts $\tilde{n}$, $\tilde{\varphi}$ is searched as a traveling wave: $\sim \exp(i(\omega t - kz))$. The equations for $\tilde{n}$ within the film $0 < x < 2l$ and for the electric potential are:

$$\begin{gathered}\frac{\partial}{\partial x}\left(D\frac{\partial \tilde{n}}{\partial x}\right) - \frac{\partial}{\partial x}(v_{0x}\tilde{n}) - \left(i(\omega - kv_0) + \omega_M + Dk^2\right)\tilde{n} + \frac{\partial}{\partial x}(\mu n_0)\frac{\partial \tilde{\varphi}}{\partial x} + n_0 k^2(\mu - \mu_d)\tilde{\varphi} = 0, \\ \frac{d^2\varphi}{dx^2} - k^2\varphi = -\frac{e\tilde{n}}{\varepsilon_0\varepsilon_2}, \quad 0 < x < 2l; \quad \frac{d^2\varphi}{dx^2} - k^2\varphi = 0, \quad \tilde{n} \equiv 0 \quad \text{for} \quad x < 0 \quad \text{and for} \quad x > 2l\end{gathered} \tag{7}$$

Here $\omega_M = en_0\mu/\varepsilon_0\varepsilon_2$ is the Maxwellian relaxation frequency.

The problem of propagation of SCW in n-GaN films has been reduced to solving Eq. (7) for $\tilde{n}$, $\tilde{\varphi}$ at $0 < x < 2l$ added by boundary conditions (2) and electrodynamic ones. The circular frequency ω is assumed as real. Therefore, a problem of amplification (damping) of traveling SCW is considered. Nontrivial solutions exist only for specific values of $k = k(\omega)$. Generally, the values of the wave numbers k are complex: $k = k' + ik''$, $k' > 0$. We are interested in the positive values of $k'' > 0$ that correspond to amplification of SCW in the case of NDC: $\mu_{d0} \equiv dv/dE < 0$ at $x = l$. The Eq. (7) has been approximated by finite differences.

3. RESULTS OF SIMULATIONS

The following parameters of the bulk n-GaN are used: the electron concentration is $n_0 \approx 10^{17}\,\mathrm{cm}^{-3}$, the bias electric field is $E_0 \approx 150\,\mathrm{kV/cm}$, the drift velocity is $v_0 \approx 2 \times 10^7\,\mathrm{cm/s}$; the dielectric permittivity is $\varepsilon_2 = 5.8$. The thickness of the film is $2l = 0.05 \ldots 0.2\,\mu\mathrm{m}$. The dielectric permittivity of a dielectric substrate is $\varepsilon_1 = 10$.

The dependencies of the spatial increment of SCW k'' on frequency $f = \omega/2\pi$ for transversely homogeneous n-GaN films are given in Fig. 3. An amplification of SCW in GaN film of a thickness $2l = 0.1\,\mu\mathrm{m}$ occurs in a wide frequency range, and the maximum spatial increment is $k'' \sim 10^3\,\mathrm{cm}^{-1}$ at the frequency $f \approx 150\,\mathrm{GHz}$. When compared with a case of the n-GaAs film, it is possible to observe an amplification of SCW in n-GaN films at essentially higher frequencies $f \geq 100\,\mathrm{GHz}$. To obtain an amplification of SCW $\approx 20\,\mathrm{dB}$, it is necessary to use the distance between the input and output antennas of about $50\,\mu\mathrm{m}$. An amplification of SCW in GaN films should be realized in a pulse regime (of a duration $< 1\,\mu\mathrm{s}$), because of heating the GaN film. We do not consider here the frequency range $f > 300\,\mathrm{GHz}$, because an applicability of hydrodynamic equations for the electron fluid is doubtful there [4]. Note that for n-GaN the hydrodynamic approximation is valid within the wider frequency range, compared with n-GaAs [4].

An influence of transverse nonuniformity of electron mobility on amplification of SCW is presented in Fig. 4. It is seen that the surface scattering decreases essentially the frequency range of amplification of SCW, compare the curve 1 (uniform film) and curves 2, 3 (decreased values of electron mobility at the surfaces). Therefore, it is necessary to compensate this influence by nonuniform doping.

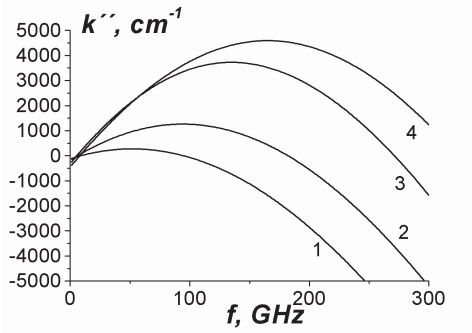

Figure 3: Spatial increments of instability $k''(f)$ of SCW in a homogeneous zinc blende GaN film with uniform doping. The curve 1 is for the bias field $E_0 = 150\,\mathrm{kV/cm}$, electron concentration is $n_0 = 10^{17}\,\mathrm{cm}^{-3}$, the film thickness is $2l = 0.05\,\mu\mathrm{m}$; the curve 2 is for $E_0 = 150\,\mathrm{kV/cm}$, $n_0 = 10^{17}\,\mathrm{cm}^{-3}$, $2l = 0.1\,\mu\mathrm{m}$; the curve 3 is for $E_0 = 150\,\mathrm{kV/cm}$, $n_0 = 2 \times 10^{17}\,\mathrm{cm}^{-3}$, $2l = 0.1\,\mu\mathrm{m}$; the curve 4 is for $E_0 = 150\,\mathrm{kV/cm}$, $n_0 = 2 \times 10^{17}\,\mathrm{cm}^{-3}$, $2l = 0.2\,\mu\mathrm{m}$.

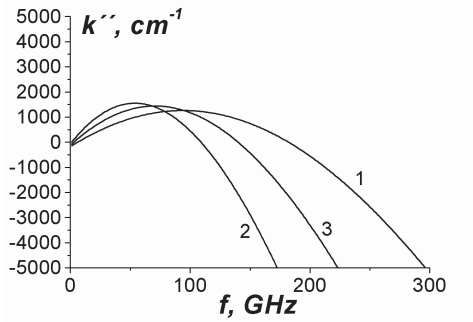

Figure 4: Spatial increments of instability $k''(f)$ of SCW in a zinc blende GaN film with uniform doping. The bias field is $E_0 = 150\,\mathrm{kV/cm}$, the electron concentration is $n_0 = 10^{17}\,\mathrm{cm}^{-3}$, the thickness is $2l = 0.1\,\mu\mathrm{m}$. The curve 1 is for the uniform film, the curve 2 is for the transversely nonuniform film where the scale is $x_0 = 0.025\,\mu\mathrm{m}$, $\mu_f = 0.2\mu_0$, $\mu_{df} = 0.2\mu_{d0}$; the curve 3 is for nonuniform film where the scale is $x_0 = 0.025\,\mu\mathrm{m}$, $\mu_f = 0.5\mu_0$, $\mu_{df} = 0.5\mu_{d0}$.

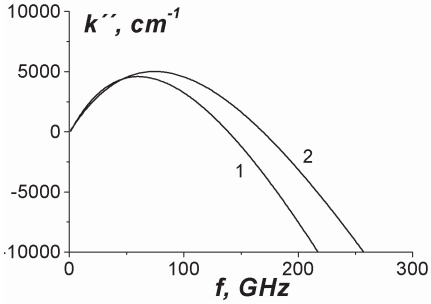

(a)

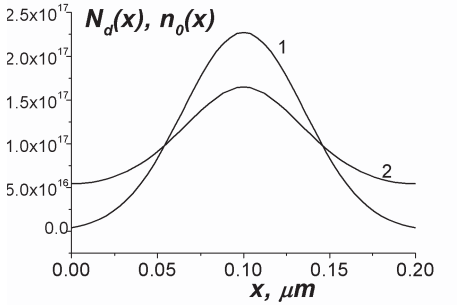

(b)

Figure 5: Part (a): Spatial increments $k''(f)$ for the film with uniform doping (curve 1) and with nonuniform doping (curve 2). Part (b): nonuniform doping profile $N_d(x)$ (curve 1) and steady state distribution of electron concentration $n_0(x)$ (2). The thickness of the film is $2l = 0.2\,\mu\mathrm{m}$, $E_0 = 150\,\mathrm{kV/cm}$, $\frac{1}{2l}\int_0^{2l} N_d(x)dx = 10^{17}\,\mathrm{cm}^{-3}$.

In Fig. 5, the results of simulations of instability of SCW in the films with nonuniform doping are given. The cases when the total integral doping charge is the same is considered: $\frac{1}{2l}\int_0^{2l} N_d(x)dx = \mathrm{const}$. One can see that in the films with nonuniform doping the surface scattering can be partially compensated, and the frequency interval of amplification of SCW can be extended. This effect is more expressed in the films of thicknesses $2l > 0.1\,\mu\mathrm{m}$. The built-in transverse electric field $E_{x0} < 50\,\mathrm{kV/cm}$ is smaller than the longitudinal bias one $E_0 = 150\,\mathrm{kV/cm}$.

Direct numerical simulations of Eq. (1) have confirmed pointed above results on linear increments of SCW amplification. Also a possibility of nonlinear frequency doubling and mixing has been demonstrated. To get the effective frequency doubling in the millimeter wave range, it is better to use the films with uniform doping, as our simulations have been shown.

4. CONCLUSIONS

The calculations of spatial increments of instability of space charge waves in n-GaN films, possessing negative differential conductivity, of submicron thicknesses have demonstrated a possibility of

amplification of space charge waves up to the frequencies $f \leq 300\,\mathrm{GHz}$. To obtain an amplification of about 20 dB, it is necessary to use the films of the lengths $\approx 50\,\mu\mathrm{m}$. Because the values of the bias electric fields, which are necessary for observations of negative differential conductivity in n-GaN films, are one order higher than for n-GaAs ones, it is possible to obtain the values of electric fields in the millimeter wave range of about $10^4\,\mathrm{V/cm}$.

ACKNOWLEDGMENT

This work was supported by CONACyT, Mexico (Project 48955).

REFERENCES

1. Royer, D. and E. Dieulessaint, *Elastic Waves in Solids*, Vol. 2, Springer, New York, 2000.
2. Pearton, S. J., J. C. Zolper, R. J. Shul, and F. Ren, "GaN: processing, defects, and devices," *Journ. Appl. Phys.*, Vol. 86, No. 1, 1–79, 1999.
3. Jain, S. C., M. Willander, J. Narayan, and R. Van Overstraeten, "III-nitrides: Growth, characterization, and properties," *Journ. Appl. Phys.*, Vol. 87, No. 3, 965–1006, 2000.
4. Gruzhinskis, V., P. Shiktorov, E. Starikov, and J. H. Zhao, "Comparative study of 200–300 GHz microwave power generation in GaN TEDs by the Monte Carlo technique," *Semicond. Sci. Techn.*, Vol. 16, No. 8, 798–805, 2001.
5. Levinshtein, M. E., S. L. Rumyantsev, and M. S. Shur, *Properties of Advanced Semiconductor Materials: GaN, AlN, InN*, Wiley-Interscience, New York, 2001.
6. Internet site: http://www.ioffe.ru/SVA/NSM/Semicond/GaN/.

A Novel Microwave Absorbing Structure Using FSS Metamaterial

H. Y. Chen, X. Y. Hou, and L. J. Deng
State Key Laboratory of Electronic Thin Film Integrated Device
University of Electronic Science and Technology of China, Chengdu, China

Abstract— Artificially constructed electromagnetic metamaterials have attracted much interest recently. A novel absorbing structure in microwave range with metamaterial frequency selective surface (FSS) is presented in this paper. The absorber is a simple unit cell layer planar structure based upon two metamaterial resonators that couple separately electric and magnetic fields so as to absorb almost all incident fields. The resulting structure which consists of metallic elements has superior absorbance characteristics compared to conventional passive absorbers of corresponding thickness. Experimental results are presented and compared to obtained from a finite difference time domain (FDTD) approach, demonstrates a peak absorbance greater than 87% at 12.8 GHz.

1. INTRODUCTION

Artificially constructed electromagnetic metamaterials have attracted much interest recently due to the potential to produce exotic electromagnetic phenomena such as negative index of refraction [1, 2] or the possibility to fabricate an invisible device such as an electromagnetic cloak [3]. The realization of such properties lies in these materials which response to incident radiation have the opposite direction between the group velocity, which characterizes the flow of energy, and the phase velocity, which characterizes the movement of the wave fronts. The electromagnetic metamaterial structures which are very freedom in geometrically have been widely used in every technologically relevant frequency distribution range from radio to optical [4–8], due to their low loss, low cost and flexibility in adjusting the frequency. Recently these exotic characteristics which the electromagnetic metamaterial constructions have behaved demonstrate great presage for future application.

After the early work of Veselago [9], research enthusiasm about negative index materials has been in a recession, because no naturally occurring material meet simultaneously with $\mu < 0$ and $\varepsilon < 0$ in a frequency band [10]. The situation changed in 2000, however, when a composite structure based on split ring resonators (SSRs) was presented and demonstrated existing a frequency band over which μ and ε were both negative. As such, the primary focus has been on the characteristic impedance of the media for propagating electromagnetic wave defined as, where a metamaterial can be impedance-matched to free space by matching μ and ε, minimizing reflectivity. As we know, metamaterials can be regarded as effective media and characterized by a complex electric permittivity and complex magnetic permeability. The electric loss and magnetic loss of metamaterial can be respectively characterized by the ratio of the imaginary and real part of electric permittivity $\mathrm{tg}\delta_\varepsilon = \varepsilon_2/\varepsilon_1$, and the ratio of the imaginary and real part of magnetic permeability $\mathrm{tg}\delta_\mu = \mu_2/\mu_1$, the more its value, the higher the rate of absorption of the metamaterial. The loss componements of the media constant (ε_2 and μ_2) have much potential for the creation of exotic and useful materials as well. In this paper, a novel absorbing structure which shows a high absorbance and can be used in some devices such as bolometric wave detector.

2. DESIGN

In order to know the characteristics of an infinite periodic structure, the unit cell can be studied by using Periodic Boundary Condition (PBC). A single unit cell of absorber consists of two distinct metallic elements: An electric four-legged loaded resonator (EFLL) and a split wire, as shown in Figs. 1(a) and 1(b). Electric coupling was supplied by the electric four-legged loaded resonator (EFLL) [11]. The element consisted of two standard split square loop staggered from one another can be placed such that the metamaterial shapes are in the plane of the k-vector of the incident wave or the shapes are perpendicular to the k-vector, shown in Fig. 1(c). Considering that the magnetic coupling required a more complicated arrangement, and in order to couple to the incident H-field, we prompt the response with a cut wire in a parallel plane separated by a substrate, shown in Fig. 1(c). The magnetic component of spectral couples to both the electrical ring resonator and the split wire, and its response can be tuned independently of the electrical resonator by changing the geometry of the cut wire, the distance of the gap of the four-legged loaded resonator and the

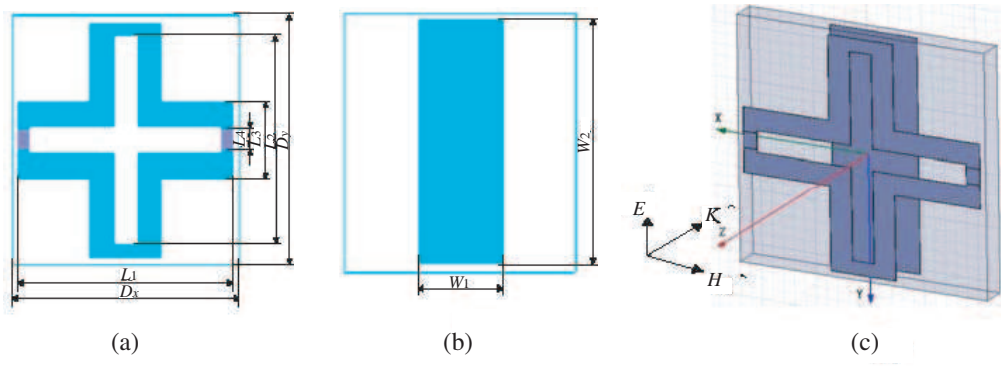

Figure 1: (a) Electric four-legged loaded resonator and (b) cut wire. Dimension notations are listed in (a) and (b). The unit cell is shown in (c) with axes indicating the propagation direction.

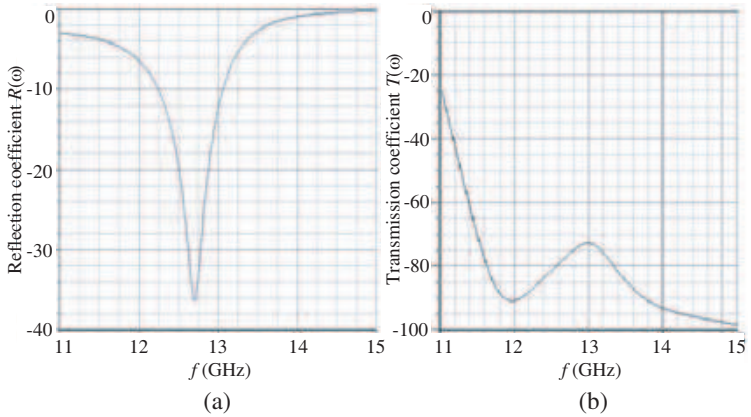

Figure 2: Simulated results of the absorbing structure. The reflection coefficient ($R(\omega)$) and transmission coefficient ($T(\omega)$) are plotted on (a) and (b) respectively.

distance between the electrical four-legged loaded resonator and the split wire. Therefore it is possible to match the impedance of the element to free space by tuning each of the resonators at s specific frequency. When the element is impedance matched, the reflectivity will reach minimum, at the same time, the high absorption can reach.

We performed computer simulations using the commercial finite-difference time domain (FDTD) solver CST Microwave Studio TM 2008. The metamaterial depicted in Fig. 1 were modeled as loss copper with a conductivity of $\sigma = 5.80 \times 107\,\mathrm{s/m}$. The substrate was modeled as FR-4 with a dielectric constant of 4.4. After determining the approximate size of the unit by theoretically calculation, we will investigate the S-parameters of transmission (S_{21}) and reflection (S_{11}) of the unit with perfect electric (yz-plane) and perfect magnetic (xz-plane) boundary conditions. The absorbtivity was calculated using the equation $A = 1 - |S_{21}|^2 - |S_{11}|^2$, noted S_{11} and S_{21} were converted from DB. Therefore, from the S parameter data, we can obtain the absorptivity. By tuning the electric permittivity and magnetic permeability at resonant frequency, we may achieve $\varepsilon = \mu$, that is to say, 100% absorbance is theoretically possible. After repeatedly adjusting the parameters of the unit by the simulative results, we finally decided that the absorbing structure unit has the dimensions, in millimeters, of: $Dx = Dy = 4.56$, $L_1 = 4.36$, $L_2 = 3.86$, $L_3 = 1.2$, $L_4 = 0.4$, $W_1 = 1.6$, $W_2 = 4.36$, the loaded Inductance is given 6 nH, and the metamaterials structure elements were separated by 0.45 in the z direction. While performing the simulation, we must simultaneously consider the minimum line widths available to us and other various fabrication tolerances. We show the simulation results for the reflection coefficient ($R(\omega)$) curves and transmission coefficient ($T(\omega)$) curves of the absorbing structure, as shown Fig. 2(a) and Fig. 2(b). $R(\omega)$ is large 0.4 dB near the bounds of the plot, 11 GHz and 15 GHz, but there is a minimum of a minimum of -36 dB at $\omega_0 = 12.6$ GHz. $T(\omega)$ will reach a minimum near ω_0 and yields a value of -80 dB. Having the results of the above, we attained the absorbance $A(\omega) = 99\%$ with a FWHM of 3% compared to ω_0.

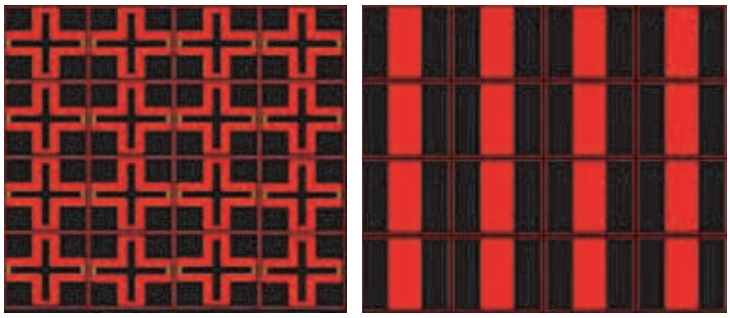

(a) (b)

Figure 3: Photographs of the both sides of the absorbing structure. (a) Top and (b) bottom.

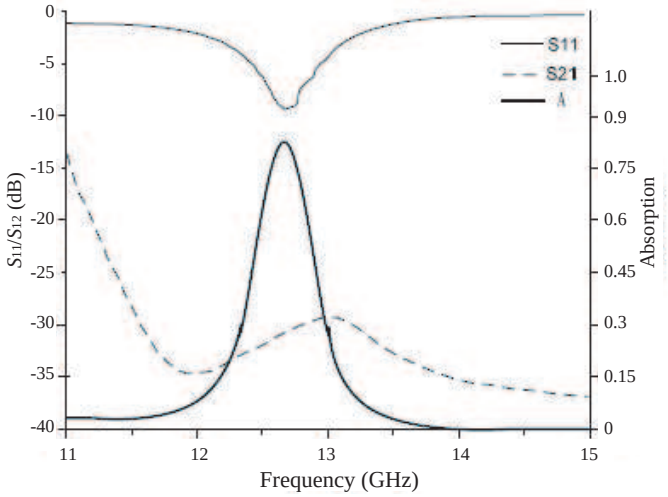

Figure 4: Measured results of the absorbing structure.

3. EXPERIMENTAL RESULTS

The absorbing structure shown Fig. 1 was fabricated using a standard optical lithography process, and the period planar array structure (outer dimensions of 19 cm × 19 cm) of the as-fabricated samples are showed Fig. 3. Each metallization was fabricated on a FR-4 substrate with a thickness of 0.2 mm. The substrate consisted of a photosensitized FR-4 board with a 17 µm copper thickness. After fabricated, two boards were assembled together by an adhesive with 0.05 mm thickness. The final results were that the metamaterial elements were separated by 0.45 mm in z direction.

The absorbing structure was measured using an HP 8510C network analyzer. The experimental performances of the absorbing structure are presented in Fig. 4. The absorbing structure revealed a minimum reflection of −9 dB and transmission of about −30 dB at $\omega_0 = 12.8$ GHz. A small shift in the resonant frequency is observed due to contributions from adhesive which have not been taken into account in the simulation procedure. Then we can calculate that the absorbance is equally with 87% at $\omega_0 = 12.8$ GHz. The experimental results compared well with the results of the simulation.

4. CONCLUSION

In summary, a novel absorbing structure with metamaterial FSS has been simulated and measured. We have demonstrated that the absorbing structure can be highly absorptive over a narrow frequency range. The metallic element plays a major role in achieving high absorbance. Moreover, the material of the substrate is very important for attaining high absorbance and achieving an appropriate resonant frequency. By merging a substrate with a highly consistent dielectric constant, we will be able to optimize the design at the correct resonant frequency.

Certainly, because the polarization of the electromagnetic field in the designed structure is sensitive and there exists manufacturing tolerance, it is necessary to further improve the currently design method for many absorbers based on metamaterial FSS.

REFERENCES

1. Markley, L. and G. V. Eleftheriades, "A polarization independent negative refractive index metamaterial for incident plane waves," *Antennas and Propagation Society International Symposium 2006*, 1923–1926, IEEE, Jul. 9–14, 2006.
2. Grzegorczyk, T. M., C. D. Moss, et al., "Properties of left-handed metamaterials: Transmission, backward phase, negative refraction, and focusing," *IEEE Transactions Microwave Theory and Techniques*, Vol. 53, No. 9, 2956–2967, Sep. 2005.
3. Kidal, P.-S., A. Kishk, and Z. Sipus, "RF invisibility using metamaterials: Harry Potter's cloak or the Emperor's new clothes?," *IEEE AP-S Symposium*, Hawaii, Jun. 2007.
4. Kiani, G. I., A. R. Weily, et al., "A novel absorb/transmit FSS for secure indoor wireless networks with reduced multi-path fading," *IEEE Microwaves and Wireless Components Letters*, Vol. 16, No. 6, 378–380, Jun. 2006.
5. Tennant, A. and B. Chambers, "Adaptive radar absorbing structures with active FSS," *Proceedings of SPIE — The International Society for Optical Engineering*, Vol. 4934, 190–199, 2002.
6. Landy, N. I., S. Sajuyigbe, et al., "Perfect metamaterial absorber," *Physical Review Letters*, Vol. 100, 207402, May 23, 2008.
7. Tao, H., N. I. Landy, et al., "A metamaterial absorber for the terahertz region: Design, fabrication and characterization," *Optics Express*, Vol. 16, No. 10, 7181–7188, May 2008.
8. Lopatin, A. V., Yu. N. Kazantsev, et al., "Radio absorbers based on magnetic polymer composites and frequency-selective surfaces," *Journal of Communications Technology and Electronics*, Vol. 53, No. 9, 1114–1122, ISSN 1064–2269, 2008.
9. Veselago, V. G., "The electrodynamics of substances with simultaneously negative values of ε and μ," *Usp. Fiz. Nauk.*, Vol. 92, 517—526, 1967.
10. Smith, D. R., J. B. Pendry, et al., "Metamaterials and negative refractive index," *Science*, Vol. 305, 788–792, Aug. 6, 2004.
11. Munk, B. A., *Frequency Selective Surfaces: Theory and Design*, Wiley, NY, 2000.

Measurement of Dielectric Anisotropy of Microwave Substrates by Two-resonator Method with Different Pairs of Resonators

Plamen I. Dankov, **Boyan N. Hadjistamov**, **Iliyana P. Arestova**, **and Valda P. Levcheva**
Faculty of Physics, University of Sofia, Sofia, Bulgaria

Abstract— The measurement of the dielectric constant and loss tangent anisotropy of the planar RF substrates by the two-resonator method is considered in this paper. The principles of the separate determination of these parameters parallel and perpendicular to the substrate surface is discussed by three pairs of cavity measurement resonators, based on cylinder, reentrant, split cylinder and split post dielectric resonators. Examples of the measured anisotropy of known materials are presented.

1. INTRODUCTION

The measurement of the dielectric substrate parameters becomes one of the most important things connected with the modern RF electronics, computer and communication hardware. The main reason is the new modern manner of the electronic devices' design, based on electromagnetic or schematic simulators, where the knowledge of the accurate values of the substrate dielectric constant and loss tangent has a decisive importance.

There are a variety of measurement methods for characterization of the dielectric parameters of PWB (Printed Wire Board) substrates [1]. The most spread of them is the standardized IPC TM-650 2.5.5.5 stripline-resonator method [2], widely used by the substrate producers. This method gives only the near-to-perpendicular values of the dielectric constant ε_r and loss tangent $\tan\delta_\varepsilon$. This increasing problem for the modern RF design can be overcame, if the anisotropy of the dielectric parameters has been determined (i.e., the different values of the parallel and normal dielectric parameters; $\varepsilon_\parallel \neq \varepsilon_\perp$; $\tan\delta_{\varepsilon\parallel} \neq \tan\delta_{\varepsilon\perp}$ — Fig. 1). A modified IPC TM-650 method (by Bereskin [3]) gives an opportunity to separate determine these parameters by "staking" of several thin substrates into a thick bulk sample and measurements in the both directions, but this method is rather inconvenient.

The main principle to determine of the substrate dielectric anisotropy is not new — to use a dual or triple modes resonator with dominant electric-field distribution parallel or perpendicular to the sample surface. The planar resonators are not very suitable for this purpose, because their modes have both parallel and normal E-fields in an arbitrary mixture (for example — the microstrip linear resonators). The cavity (bulk) resonators are more suitable for anisotropy measurements. Several years ago we introduced the two-resonator method [4–6], which is based on two different ordinary measurement cylinder resonators, marked as R1 and R2, supporting two suitable for anisotropy measurement modes — TE_{011}-mode in R1 (for determination of pure $\varepsilon_\parallel$, $\tan\delta_{\varepsilon\parallel}$) and TM_{010}-mode in R2 (for determination of pure $\varepsilon_\perp$, $\tan\delta_{\varepsilon\perp}$). The successes of this method depends on the accuracy of the analytical relations between the measured resonance parameters, resonance frequency f_{0meas} and the unloaded quality factor Q_{0meas}, and the substrate dielectric parameters [4]. In order to increase the measurement accuracy, we developed the two-resonator method with application of the 3D electromagnetic simulators as an assistance tools for the anisotropy measurements [7].

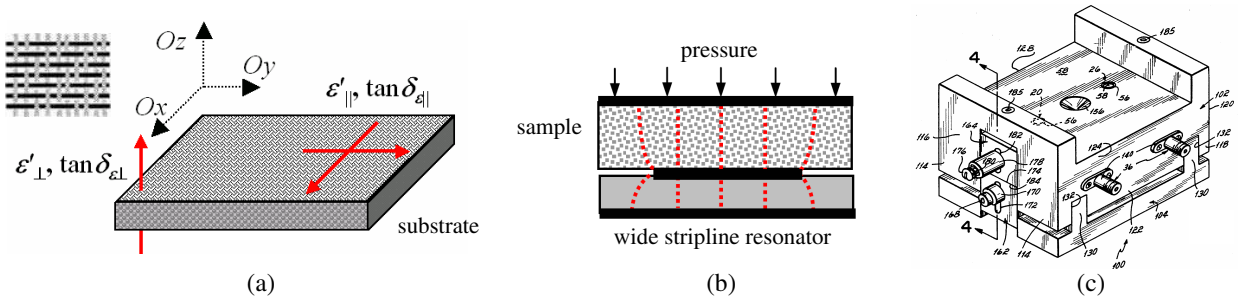

Figure 1: (a) Planar substrate with uniaxial anisotropy; (b) IPC TM-650 2.5.5.5 test method [2]; (c) Bereskin measurement fixture [3].

This allows us to use measurement resonators with more complicated shape [8, 9]. In this paper we systematize our experience to measure the dielectric anisotropy of planar substrates by the two-resonator method, extended with new pairs of measurement resonators.

2. TWO-RESONATOR METHOD WITH PAIR OF ORDINARY CYLINDER RESONATORS

Figures 2(a) and (b) presents two simplest cylindrical resonators with diameter $D_{1,2}$ and height $H_{1,2}$. They are designed to support different modes in order to evaluate the sample anisotropy by analytical method [4, 5]: TE_{011}-mode resonator **R1**, which is suitable for measurement of the longitudinal parameters $\varepsilon_{\|}$ and $\tan\delta_{\varepsilon\|}$, and TM_{010}-mode resonator **R2** — for measurement of the normal parameters $\varepsilon_{\perp}$ and $\tan\delta_{\varepsilon\perp}$. The resonators need of disk samples with diameters, equal to the resonator diameters. Similar ability as R1 resonator, but for samples with arbitrary shape, has the split-cylinder resonator **SC** (Fig. 2(c)) [9]. A set of pairs of R1 and R2 resonators with different diameters allows characterization of the dielectric anisotropy, ΔA_{ε} and $\Delta A_{\tan\delta\varepsilon}$, in wide frequency range — $\Delta A_{\varepsilon} = 2(\varepsilon'_{\|} - \varepsilon'_{\perp})/(\varepsilon'_{\|} + \varepsilon'_{\perp})$ and $\Delta A_{\tan\delta\varepsilon} = 2(\tan\delta_{\varepsilon\|} - \tan\delta_{\varepsilon\perp})/(\tan\delta_{\varepsilon\|} + \tan\delta_{\varepsilon\perp})$. The measuring errors by this method are evaluated as small enough: $< 1.5\%$ for $\varepsilon'_{\|}$, $< 5\%$ for $\varepsilon_{\perp}$, $< 7\%$ for $\tan\delta_{\varepsilon\|}$ and $< 15\%$ for $\tan\delta_{\varepsilon\perp}$ in the case of typical substrates with thickness 0.15–2.0 mm. This relatively good accuracy is achieved mainly due to the use of equivalent parameters — equivalent resonator diameters and equivalent wall conductivity [4].

The measurement errors (especially for thin substrates) can be decreased additionally by utilization of 3D simulators for extraction of the dielectric parameters of the samples. The suitable 3D models of R1, R2 and SC resonators are drawn in Fig. 3. We use 3 main rules to construct these models for accurate and time-effective processing of the measured resonance parameters — stylized drawing of the resonator body with equivalent diameters D_{1e} or D_{2e}, optimal number of line segments (N = 72–180) for construction of the cylindrical surfaces and suitable for the operating mode splitting (1/4 or 1/8), accompanying with the necessary boundary conditions.

The measurement procedure is as follows. First of all, we measure the resonance parameters of the empty cavity and by simulation of its 3D model we determine the effective diameter $D_{1,2e}$ and effective wall conductivity $\sigma_{1,2e}$, for which the measured and calculated parameters coincides, $f_{0sim} \sim f_{0meas}$; $Q_{0sim} \sim Q_{0meas}$. Then we measure the cavity with sample and after similar simulations we determine the corresponding dielectric parameters (longitudinal for R1 or perpendicular

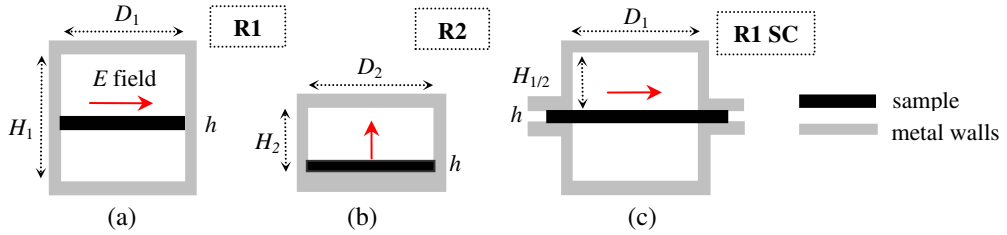

Figure 2: (a) TE_{011}-mode cavity R1; (b) TM_{010}-mode cavity R2; (c) TE_{011} split-cylinder cavity SC as R1 resonator.

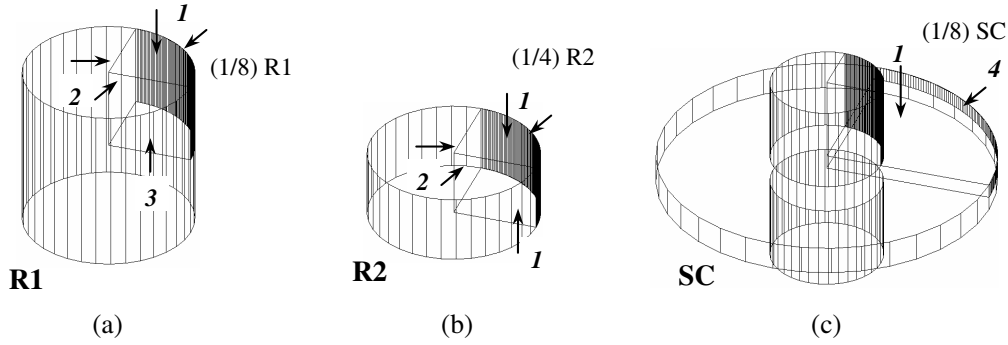

Figure 3: Equivalent 3D models of the considered cavities and the boundary conditions BC (BC legend: 1 — finite conductivity; 2 — E-field symmetry; 3 — H-field symmetry; 4 — perfect H-wall (natural BC between two dielectrics); the BC over the metal bodies are 1.)

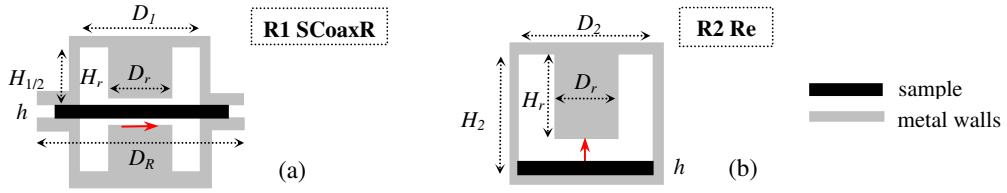

Figure 4: Pair of tunable resonators: (a) split-coaxial cylinder cavity **SCoaxR** as R1; (b) Reentrant cavity **Re** as R2.

for R2 — Figs. 5(a), (b), (c)). The accurate determination of the both effective parameters is very important for the measurement error reduction and we always use this procedure for "daily" actualization of their values. The problem of the considered pair of simple cylinder resonators is the fixed frequencies of measurements, which depends mainly on the resonator diameter and the dielectric constant of the sample. This can be particularly avoided, using another pair of tunable resonators.

3. TWO-RESONATOR METHOD WITH DIFFERENT PAIRS OF RESONATORS

As a pair of tunable resonators for realization of the two-resonator method in wide frequency range we utilize the split-coaxial resonator (**SCoaxR**), proposed in [9], as R1, and the reentrant resonator **Re** [8] as R2 — see Figs. 4(a), (b). The SCoaxR is a variant of the split-cylinder resonator with a pair of top and bottom cylindrical posts of height H_r and diameter D_r into the resonator body. The tuning of the resonance frequency is possible by the height H_r of metal posts with more than one octave below the resonance frequency of the hollow split-cylinder resonator. The reentrant resonator is known low-frequency measurement structure. It has also an inner tuning cylinder of height H_r and diameter D_r. The analytical solutions for the resonance parameters of these resonators do not ensure the needed accuracy for measurement purposes. Therefore, we use only 3D simulators as assistant tools during the anisotropy measurements. We follow the same principles to construct the 3D models of these complicated resonance structures — see Figs. 5(d), (f). The only problem is the determination of a new equivalent parameter — the height of the post cylinder H_{re}. The measurement procedure is similar, but have an additional step: 1) measurement of the resonator without inner post (to determine the outer equivalent diameter D_e); 2) measurement of resonator without sample (to determine the equivalent height H_{re} and the effective wall conductivity σ_e); and 3) measurement of the resonator with sample (final extraction of the dielectric parameters). The last two steps should be repeated at each fixed height H_r.

A problem of the measurement reentrant and split-coaxial resonators is the lower unloaded Q factors (200–1500) compared with these of the original cylinder resonators (3000–15000). In order to overcome this problem for measurements at low frequency, we propose a new pair of measurement resonators: split-post dielectric resonators **SPDR** of electric or magnetic type of splitting [1] — Figs. 6, 7. The main novelty of this pair is the inserted high-Q dielectric resonator DR, which set the operating frequency. We use DR's from high-quality materials (sapphire, alumina, quartz, etc.) and this allows achieving of unloaded Q factors about 5000–20000. The modeling and measurement principles of this pair of resonators are very similar. Here the knowledge of the actual parameters of the used DR's is very important for the successful utilization of the method. The measurement procedure consists of 4 steps: 1) measurement of the empty resonator (to determine the equivalent

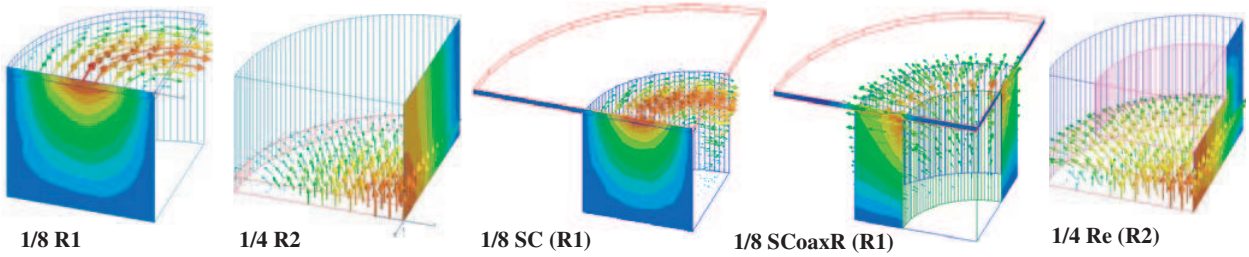

Figure 5: Calculated electric field distribution (scalar and vector) in the considered pairs of measurement resonators (as R1 or R2).

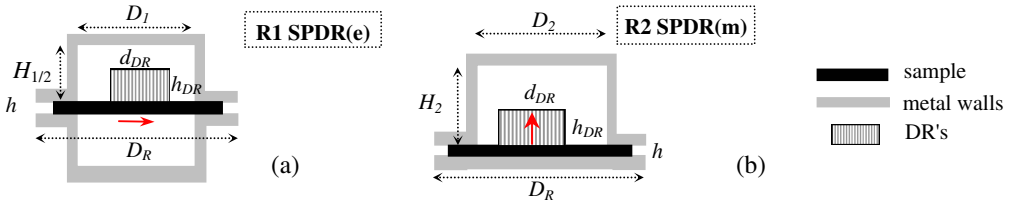

Figure 6: Pair of split-post dielectric resonator SPDR: (a) TE_{010}-mode cavity **SPDR(e)**; (b) magnetically-splitted **SPDR(m)**.

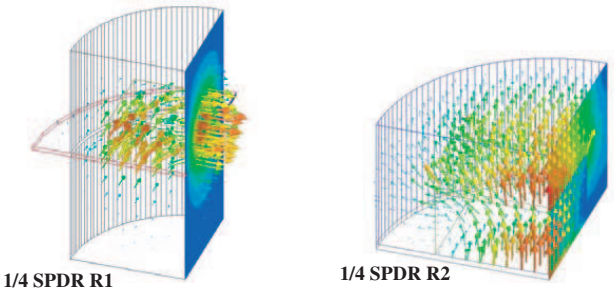

Figure 7: Calculated electric field distribution (scalar and vector) in the considered SPDR (as R1 or R2) (in fact, a unsplitted version for R2 is presented here).

diameter D_e and effective wall conductivity σ_e); 2) measurement of resonator with foam support for the DR (if exists) (to determine the its parameters); 3) measurement of the resonator with DR and foam support (to extract the actual DR parameters) and 4) measurement of the resonator with DR and sample (extraction of the sample parameters). The variation of the frequency is achieved by DR replacement. We use DR's with different shapes: cylinder, rectangular and ring. The DR's dielectric constant should be not very high to ensure good accuracy.

4. TEST RESULTS FOR THE MEASURED ANISOTROPY OF TWO SAMPLES

It is very important to know the ability of the considered pair of resonators to measure "pure" longitudinal or "pure" transversal parameters of the samples and therefore, to evaluate the dielectric anisotropy ΔA_ε and $\Delta A_{\tan\delta\varepsilon}$, Fig. 8 presents the numerical results for the ratios $(f, Q)_{anisotropic}/(f, Q)_{isotropic}$ versus the anisotropy ΔA_ε, $\Delta A_{\tan\delta\varepsilon}$ at a fixed sample height (~ 1.53 mm). If this ratio is small, the corresponding resonator has ability to measure the "pure" dielectric parameters. The cylindrical resonators (R1, R2), the reentrant resonator Re and the split-coaxial resonator SCoaxR meet these requirements (error less than $\pm 0.2\%$ for the dielectric constant ε_r and less than $\pm 1\%$ for the loss tangent $\tan\delta_\varepsilon$, when the anisotropy is changed with $\pm 10\%$). Only the pure split-cylinder resonator SC has bigger error: $\pm 2.5\%$ for ε_r and $\pm 10\%$ for $\tan\delta_\varepsilon$.

Finally, the measured dielectric anisotropy for two known materials are given as illustration in Fig. 9. The first material is pure isotropic — 0.51-mm thick transparent polycarbonate. The measured "anisotropy" of this material is less than 3% for ΔA_ε and less than 11% for $\Delta A_{\tan\delta\varepsilon}$ in wide frequency range 2–18 GHz. These data should be considered as a limit for ability of the

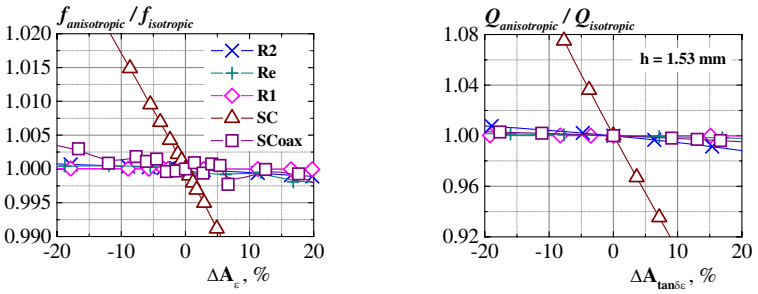

Figure 8: Dependencies of the normalized resonance frequency and Q-factors of the resonance modes for isotropic and anisotropic samples versus the dielectric anisotropy ΔA_ε and $\Delta A_{\tan\delta\varepsilon}$.

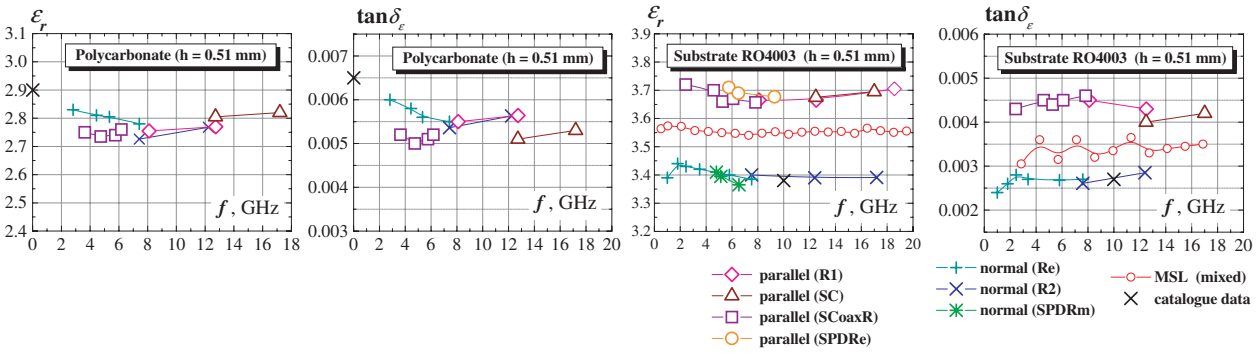

Figure 9: Measured dielectric parameters ($\varepsilon_{\|}$, $\varepsilon_{\perp}$, $\tan\delta_{\varepsilon\|}$, $\tan\delta_{\varepsilon\perp}$) of two materials with equal thickness: isotropic polycarbonate and anisotropic RO4003 substrate by different pairs of resonators.

two-resonator method to evaluate the practical isotropy. The second example is for the popular microwave non-PTFE reinforced substrate RO4003 ($h = 0.51$ mm). The mean measured anisotropy of the substrate in wide frequency range 2–18 GHz is ∼8.7% for ΔA_{ε} and ∼48% for $\Delta A_{\tan\delta\varepsilon}$ (or ∼8.4% for ΔA_{ε} and ∼35% for $\Delta A_{\tan\delta\varepsilon}$ at 12 GHz). These data are fully acceptable, nevertheless the catalogue data are $\varepsilon_r = 3.38$ and $\tan\delta_{\varepsilon} = 0.0027$ at 10 GHz.

5. CONCLUSIONS

The investigations show that the two-resonator method is fully acceptable for determination of the substrate dielectric anisotropy by the help of 3D simulators with error less than 3% for the dielectric constant and less than 10% for the dielectric loss tangent in wide frequency range by different pairs of measurement resonators.

ACKNOWLEDGMENT

The authors thank to the Scientific Research Found of the University of Sofia for the financial support.

REFERENCES

1. Baker-Jarvis, J., B. Ridldle, and M. D. Janezic, "Dielectric and magnetic properties of printed wiring boards and other substrate materials," *National Institute of Standards and Technology, Technical Note 1512*, Boulder, CO, USA, Mar. 1999.
2. IPC TM-650 2.5.5.5, Test Methods Manual, "Stripline test for permittivity and loss tangent at X-band," Mar. 1998.
3. Bereskin, A. B., "Microwave test fixture for determining the dielectric properties of the material," US Patent 50083088, Jan. 1992.
4. Dankov, P. I., "Two-resonator method for measurement of dielectric anisotropy in multi-layer samples," *IEEE Transaction on Microwave Theory and Technique*, Vol. 54, No. 4, 1534–1544, Apr. 2006,
5. Levcheva, V. N., B. N. Hadjistamov, and P. I. Dankov, "Two-resonator method for characterization of dielectric substrate anisotropy," *Bulg. J. Phys.*, Vol. 35, 33–52, 2008.
6. Dankov, P. I., V. P. Levcheva, and I. I. Arestova, "Two-resonator method for characterization of high-permittivity dielectric and ferrite substrate," *Proc. ICMF'2007*, 27–30, Budapest, Hungary, May 20–21, 2007.
7. Dankov, P. I., V. P. Levcheva, and V. N. Peshlov, "Utilization of 3D simulators for characterization of dielectric properties of anisotropic materials," *Proc. 35th European Microwave Conference EuMW'2005*, 515–519, Paris, France, Oct. 2005.
8. Hadjistamov, B. N., V. P. Levcheva, and P. I. Dankov, "Dielectric substrate characterization with Re-entrant resonators," *Proc. Vth Mediterranean Microwave Symposium (MMS'2007)*, 183–186, Budapest, Hungary, May 14–16, 2007.
9. Dankov, P. I. and B. N. Hadjistamov, "Characterization of microwave substrates with split-cylinder and split-coaxial-cylinder resonators," *Proc. 37th European Microwave Conference*, 933–936, Munich, Germany, Oct. 2007.

A Study on the Coupled Image Guide Structures

I. I. Arestova, P. I. Dankov, and V. P. Levcheva
Department of Radio Physics and Electronics, Faculty of Physics
University of Sofia "St. Kliment Ohridski", Bulgaria

Abstract— This work includes both experimental and numerical analysis of coupled image guide structures (CIGSs) at millimeter wavelengths. The experimental measurement of the electric field components has been performed using electric probes. The experimental research has been complemented by a numerical simulation of the CIGSs using a finite element method (FEM). The results can be used for a computer aided design (CAD) of components on the base of the image guide (IG). In addition some conclusions are made about the features of the electric probes.

1. INTRODUCTION

The IG structures have been traditionally considered as a perspective for millimeter wavelengths [1], in particular for design of nonreciprocal components — isolators and circulators [2–4]. There have been proposed various configurations of nonreciprocal CIGSs containing ferrite IG sections with different magnetization — longitudinal, transverse or mixed one. There have been investigated two-port [2, 4] and four-port [3] configurations, the former representing a prototype of an isolator and the lather — of a circulator.

The difficulties in the design and optimization of nonreciprocal devices on the base of CIGSs arise not only from the complexity of the wave propagation in a magnetized ferrite IG and its coupling to the dielectric IG, but also from the processes emerging because of the finite length of the ferrite sample. Its open ends represent strong irregularities that may produce undesirable and hardly controlled radiation, reflection etc. In an earlier investigation of a nonreciprocal CIGS with non-homogeneously magnetized ferrite [4] we had measured with the help of the electric probes the distributions of both transverse components of the electric field — E_y and E_x. That investigation had shown the usefulness of the electric probes and also the complexity of the processes taking place.

In an attempt to clear up the operating mechanism of such complex CIGSs, we have examined in this work two CIGS that contain only isotropic dielectric materials. The first one represents two identical alumina IGs and the second — primary alumina IG coupled to the secondary IG fabricated from magnesium titanate. This time we have measured using electric probes not only the transverse components of the electric field, but also the longitudinal component E_z. Next, in order to improve the understanding of the processes taking place at these CIGSs, we have included the CAD approach and have simulated numerically both of the CIGSs by the FEM.

The top view of the CIGS under investigation is shown in Figure 1. The primary IG 1 is coupled to the secondary IG 2 by a separation distance d and a coupling length l. There are two transitions 3 on both ends of the primary IG that perform a conversion of the dominant mode H_{10} in the rectangular waveguide (RWG) to the mode E_{11}^y in the rectangular IG. The transitions

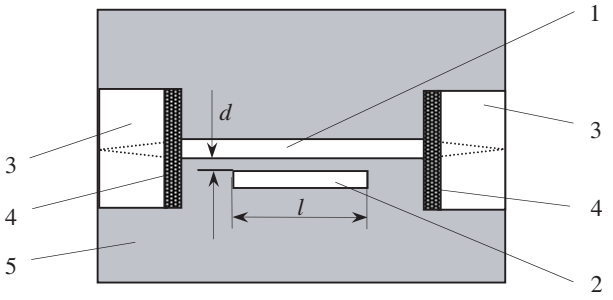

Figure 1: Top view of the CIGS. 1 — primary IG; 2 — secondary IG; 3 — RWG-IG transition; 4 — absorbing plates; 5 — metal plate.

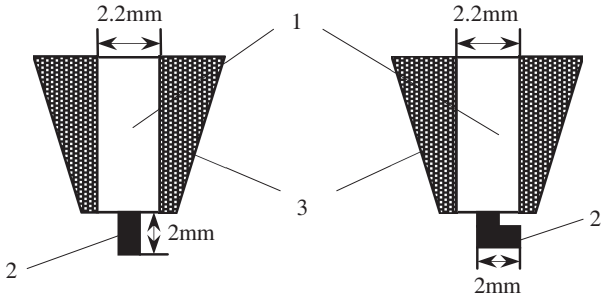

Figure 2: Electric probes for E_y component (left) and E_x and E_z components (right). 1 — semi-rigid coaxial cable; 2 — inner conductor; 3 — absorbing coating.

are performed by a symmetrical H-plane tapering of the dielectric core and thereafter putting the tapers into RWG sections of the same length. The whole length of the test CIGS was 80 mm including the two 15 mm transitions. The transverse surfaces of the transitions were coated with absorbing plates 4 to minimize undesirable reflections.

2. EXSPERIMENTAL INVESTIGATION

The electric probe represents a section of a 50 Ohm semi-rigid coaxial cable, which has its outer conductor removed at both ends on the length of about a quarter of a wavelength. One of the ends of the coaxial cable was inserted into a hole in the broad wall of a RWG section with one of its ports shorted at about a quarter of a wavelength. The second port of the RWG section was connected with a waveguide detector.

The geometry of the second end of the coaxial section is shown in Figure 2. The electric probe for E_y component (Figure 2(a)) contains a straight vertical section of the inner conductor, while the electric probe for E_x and E_z — a 90° bend section (Figure 2(b)). The probe for the E_x and E_z components inevitably contains a small vertical section that arises in some extent a registration of the E_y component as well.

The diagram of the experimental setup is shown in Figure 3. The scalar network analyzer 1 contains the generator 2 (26–38 GHz) and the indicator 3. It includes RWG components with a cross section $7.2 \times 3.4\,\text{mm}^2$. The directional couplers 4 with the build-in detectors 5 permit a separation of the incident and the transmitted wave to and out of the CIGS 6. The electric probe 7 was mounted on a vernier 3-axis mechanism.

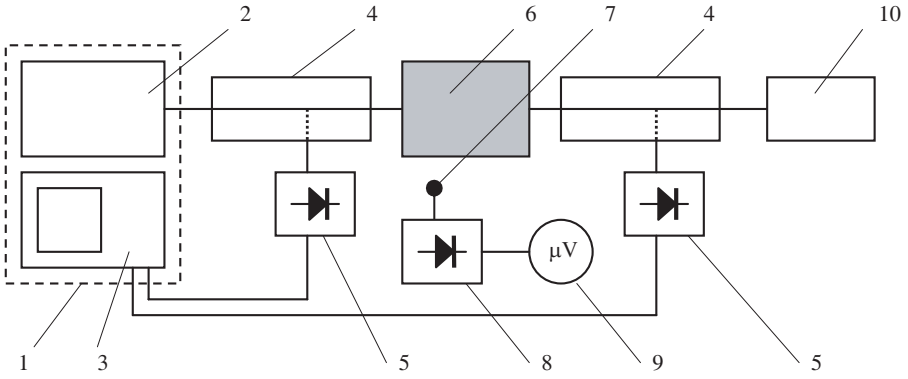

Figure 3: Experimental setup. 1 — Scalar network analyzer; 2 — generator; 3 — indicator; 4 — directional couplers; 5 — detectors; 6 — CIGS; 7 — electric probe; 8 — detector; 9 — microvoltmeter; 10 — matched load.

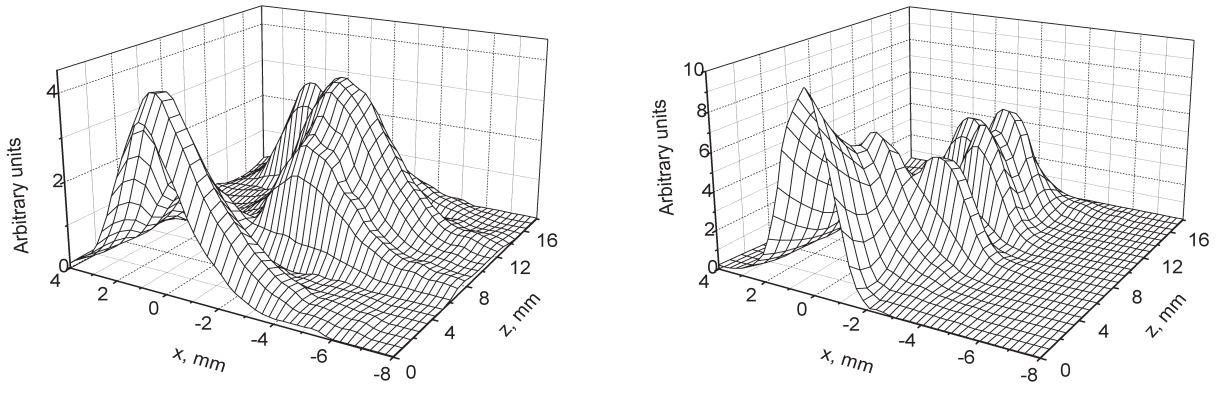

Figure 4: Measured distributions of the E_x (a) and E_z (b) components in the Al_20_3 CIGS.

The primary IG in both CIGSs and the secondary IG of the second CIGS have been made from alumina ($\varepsilon_r = 9.6$, $\text{tg}\delta_\varepsilon = 10^{-4}$) with a cross section $2 \times 0.97\,\text{mm}^2$. The secondary IG of the

second CIGS was made from magnesium titanate ($\varepsilon_r = 15.5$, $\mathrm{tg}\delta_\varepsilon = 7.10^{-4}$) with a cross section $2 \times 0.92\,\mathrm{mm}^2$. The first CIGS had parameters $d = 0.4\,\mathrm{mm}$ and $l = 14.65\,\mathrm{mm}$ and the second — $d = 0.3\,\mathrm{mm}$ and $l = 17\,\mathrm{mm}$ (Figure 1). The electric probes were kept at a height of 0.5 mm above the dielectric cores at all measurements.

The distributions of the E_x and E_z components in the first CIGS are shown in Figure 4. The origin of the x-axis is at the middle of the primary IG. The distribution of the E_y component is not shown here because it is almost identical to that of the E_x component, but at a much greater level. The reason for this is that the E_x component is much smaller than the E_y component and because of the aforementioned imperfections of the electric probe for E_x and E_z components, it also registers the E_y component. In other words, the electric probe for the E_x and E_z components works appropriately when these components are comparable to the E_y component. The distribution of the E_z component, shown in Figure 4(b), differs from the distributions of the E_x and E_y components due to its large value in the CIGS. The maximum of the E_y component along the secondary IG was at $z = 9.85\,\mathrm{mm}$, which is equal to the period of the power transfer L [5]. In Table 1 are shown the measured periods of the power transfer at different frequencies and for two different separation distances d. The values of the coupling coefficient C, where $CL = \pi$ [5], have been also calculated and presented in Table 1. As it could be seen, the coupling length L increases with the increment of the frequency and the separation distance while the coupling coefficient C — decreases. The distribution of the E_y component in the second CIGS is shown in Figure 5. Because of the greater permittivity of the secondary IG made from magnesium titanate, the field decays quicker out of the dielectric core. That is why the maximum of the E_y component in the secondary IG at $z = 7.45\,\mathrm{mm}$ is hardly remarkable in Figure 5. The period of the power transfer in this case is smaller than in the case with two identical IGs, which is in agreement with the theory [5].

Table 1: Measured period of the power transfer L and the coupling coefficient C in the Al_20_3 CIGS.

Frequency	$d = 0.4\,\mathrm{mm}$		$d = 0.6\,\mathrm{mm}$	
[GHz]	L [mm]	C [mm^{-1}]	L [mm]	C [mm^{-1}]
31	7.80	0.40	8.50	0.37
32	8.65	0.36	10.00	0.31
33	9.85	0.32	11.00	0.29
34	10.15	0.31	12.20	0.26
35	12.75	0.25	12.95	0.24
36	13.20	0.24	15.45	0.20

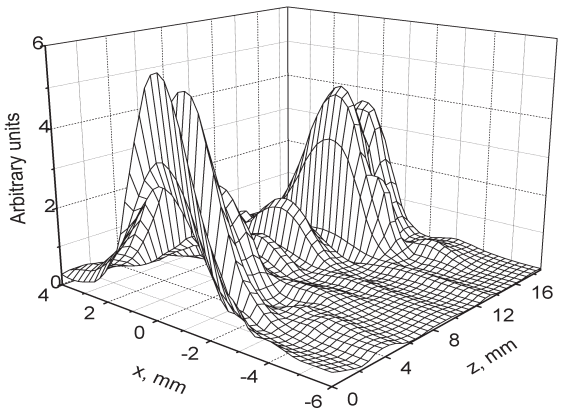

Figure 5: Measured distribution of the E_y component in the Al_20_3-$MgTiO_3$ CIGS.

3. NUMERICAL ANALYSIS

The numerical simulation has been done using the software product Ansoft HFSS (High Frequency Structure Simulator) that performs the FEM analysis of the structures. The structures with the same parameters as in the experimental investigation have been simulated. The simulated fields at both CIGSs are shown in Figures 6 and 7. The magnitude of the electric field intensity is shown only in the volumes of the dielectric cores. The distribution of the field out of the dielectric cores has been omitted in these figures in order to have more evident images. It would be appropriate to note that the simulation has shown that the fields are strongly bound to the dielectric cores and decrease rapidly out of the cores. The sizes of the airbox have been picked large enough not to disturb the fields. All faces of the airbox except the bottom one have been defined as radiating surfaces while the bottom one — as a perfect conducting (ground) plane.

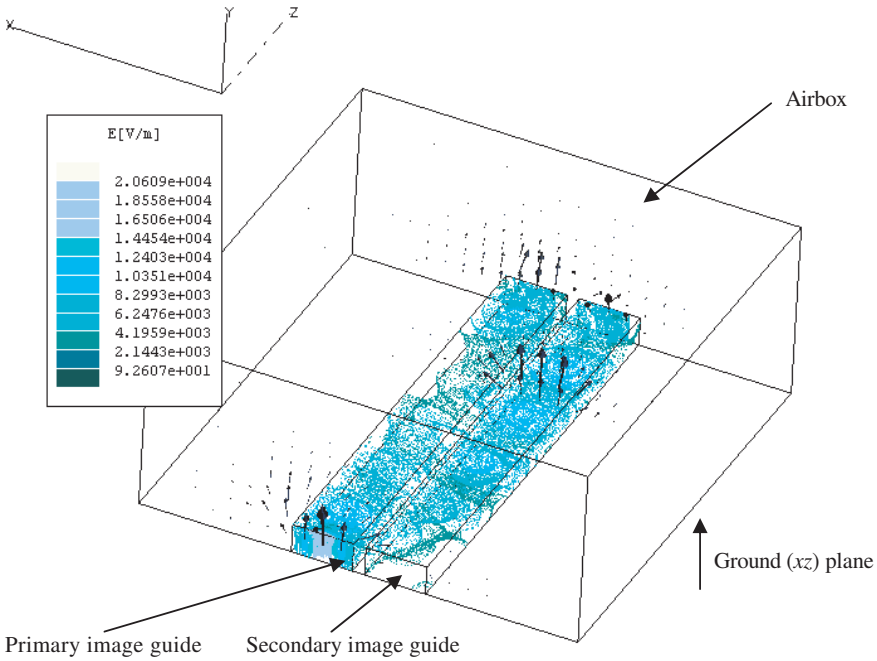

Figure 6: Numerical simulation of the electromagnetic field in the Al_20_3 CIGS.

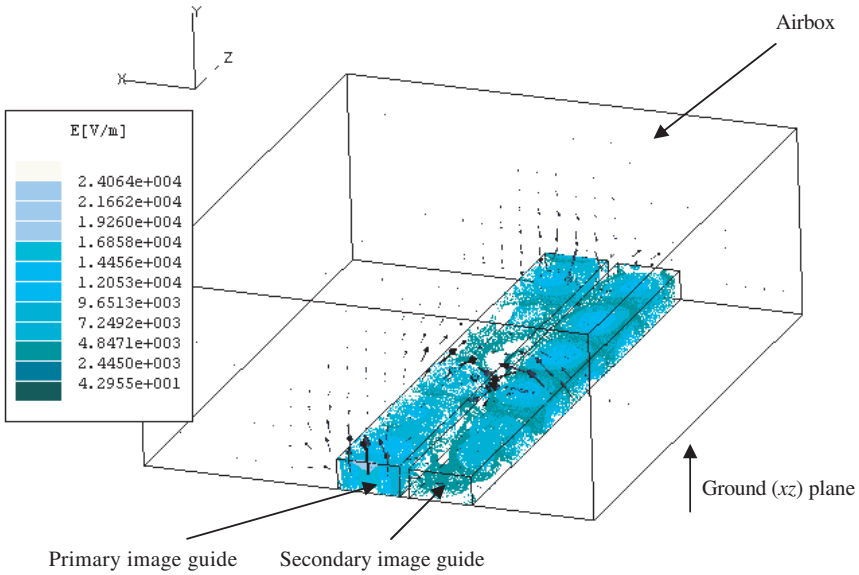

Figure 7: Numerical simulation of the electromagnetic field in the Al_20_3-$MgTiO_3$ CIGS.

In Figure 6 is shown the magnitude of the electric field intensity together with three vector diagrams that present the vector **E** at three cutplanes — $z = 0$, $z = L = 9.85\,\text{mm}$ and $z = l = 14.65\,\text{mm}$. The middle cutplane is situated where the maximum power transfer had been observed during the electric probe measurements. Similarly, in Figure 7 are shown the vector diagrams at the following cutplanes — $z = 0$, $z = L = 7.45\,\text{mm}$ and $z = l = 17\,\text{mm}$. The main difference observed between both CIGSs is in the significant value of the E_x component at the middle cutplane in the second CIGS compared with the first CIGS. This could be treated as a coupling between modes with a principal component E_y in the first case and a coupling between modes with principal components E_x and E_y in the second case. Apparently, a good agreement between the measured and the simulated results takes place.

4. CONCLUSION

The performed investigation has shown that the electric probes no matter all their imperfections can be used as a testing instrument in the design procedure of open structure devices. The results of both approaches — the electric probe measurements and the CAD are believed to ease the design of nonreciprocal components for millimeter wavelengths in the future.

ACKNOWLEDGMENT

The authors thank the Scientific Research Fund of Sofia University for supporting the investigations. They also thank the Ray Sat Bg Ltd. for the possibility to use the software product Ansoft HFSS.

REFERENCES

1. Fiedziuszko, S. J., et al., "Dielectric materials, devices and circuits," *IEEE Trans. Microwave Theory Tech.*, Vol. 50, No. 3, 706–720, 2002.
2. Ahumyan, A. A., S. S. Gigoyan, B. A. Murmughev, and R. M. Martirosyan, "Ferrite isolators for millimeter wavelengths based on the alumina image guide," *Radiotechnics*, No. 2, 41–43, 1990.
3. Kwan, P. and C. Vittoria, "Scattering parameters measurements of a nonreciprocal coupling structure," *IEEE Trans. Microwave Theory Tech.*, Vol. 41, No. 4, 652–657, 1993.
4. Arestova, I. I. and S. A. Ivanov, "Nonreciprocal effects in coupled ferrite-dielectric image guide structures," *Proceedings of XII International Conference on Microwave Ferrites*, 188–192, Gyulechica, Bulgaria, September 1994.
5. Miller, S. E., "Coupled wave theory and waveguide applications," *The Bell System Technical Journal*, No. 5, 661–719, 1954.

Performance Investigation of Microstrip Exponential Tapered Line Impedance Transformer Using MathCAD

Mazlina Esa, **Nik Noordini Nik Abd Malik**,
Nadiyatulakmar Abdul Latif, **and Jayaseelan Marimuthu**
Faculty of Electrical Engineering, Universiti Teknologi Malaysia
81310 UTM Skudai, Johor, Malaysia

Abstract— Impedance transformer is an essential part of a system which allows two different loads to be perfectly connected without any loss due to reflections. This paper presents investigations performed on a microstrip exponential taper impedance, ETLI, transformer. Mathematical computations were performed using MathCAD software. The reflection coefficient and return loss responses are in good agreement with theory. Broadband characteristics have been observed. To further investigate the performance of the taper, the ETLI transformer is simulated. Four different load impedances have been considered and various lengths of ETLI were investigated. It was found that as the frequency increases, the number of optimum lengths has also increased with a smaller difference between the optimum lengths. The same pattern occurs with any load impedance, from 70 to 100 Ohm. In addition, the behaviour of ETLI transformer with variation of loads at a particular frequency showed that 80 Ohm load appeared to be the most matched. As the frequency increases, higher loads are matched with longer ETLI. Different loads are well-matched with longer ETLI transformers at higher frequencies from 6 GHz.

1. INTRODUCTION

Several studies have been reported on the design and use of impedance transformers [1–7]. Impedance transformer is an essential part of a system which allows two different loads to be perfectly connected without any loss due to reflections of incident signals back to the input. Hence, there will be lost of power that can be delivered from the input or source to the load or other parts of the system. Consequently, this could damage and overheat the transmitter which dissipates the reflected power. Thus, an impedance matching network is needed between a source and load as shown in Fig. 1. A simple impedance transformer is the quarter wavelength transformer which is suitable for matching two real impedances. However, the transformer is suitable for single frequency application, unless several cascades of such transformers are designed. This is undesirable since the overall size of the circuit or system will increase. Impedance transformers in the form of tapers allow for impedance matching of such loads, however it is for broadband application. Hence, the study of the behaviour of such transformers is important from the engineering education point of view, as well as using it for any microwave application due to its broadband feature.

This paper presents investigations of an impedance matching technique that has broadband feature. The chosen configuration is the exponential taper designed on microstrip technology. The top view is shown in Fig. 2. Other taper configurations are triangular and Klopfenstein. Mathematical computations were performed using MathCAD software [8]. The reflection coefficient and return loss, RL, responses of the exponential taper line impedance, ETLI, transformer are analysed and compared with theory. Further investigations have been carried out with four different load impedances and various lengths of ETLI transformer, using numerical simulation [9].

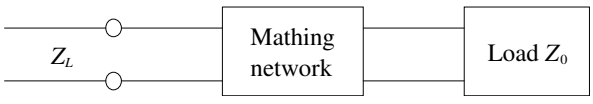

Figure 1: Concept of impedance matching network [1].

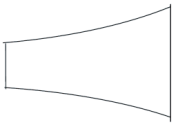

Figure 2: Exponential taper configuration [1].

2. DESIGN CONSIDERATIONS

The design is focused on mathematical approach, whereby the performances of the circuit are investigated with plottings of relevant characteristics. The impedance and reflection coefficient

variations over length and with varying lengths, respectively, are depicted in Figs. 3 and 4. The important parameter is the reflection coefficient which can be presented as power quantity of return loss in dB. The design specifications are return loss of less than −10 dB, variable values of load impedances to be matched, 50 Ohm input impedance and broad bandwidth. MathCAD is used for further simulation of varying impedance values and ETLI lengths.

3. MATH COMPUTATIONS USING MATHCAD

The math formulae are available in the literature [1]. The characteristic impedance variation for the ETLI transformer over the range $0 \le z \le L$ is given as $Z(z) = Z_0 e^{az}$. As indicated in Fig. 3, at $z = 0$, $Z(0) = Z_0$ as desired. At $z = L$, it is important to have $Z(L) = ZL = Z_0 e^{aL}$, which determines the constant a as:

$$a = \frac{1}{L} \ln\left(\frac{ZL}{Z_0}\right) \tag{1}$$

$\Gamma(\theta)$ is found by using the equation:

$$\Gamma = \frac{1}{2} \int_0^L e^{-j2\beta z} \frac{d}{dz} \ln\left(e^{az}\right) dz = \frac{\ln\left(\frac{ZL}{Z_0}\right)}{2e^{-j\beta L}} \frac{\sin \beta L}{\beta L} \tag{2}$$

The derivation assumes that β, the propagation constant of the tapered line, is not a function of z. The assumption is generally valid for TEM lines. In Fig. 4, peaks of $|\Gamma|$ decrease with increasing length, while the length should be greater than $\lambda/2$ (or $\beta L > \pi$) to minimise the mismatch at low frequencies.

The simulation work starts with the MathCAD computation of the impedance curve for each ETLI transformer. The loads are varied from 70 Ohm to 100 Ohm with 10 Ohm intervals, with fixed input impedance of 50 Ohm. An exponential impedance curve computed using MathCAD is shown in Fig. 5 for 80 Ohm load. The corresponding impedance plot is given in Fig. 6. Each ETLI transformer has similar shape to the corresponding layout drawn for numerical simulations, which are in agreement with the literature.

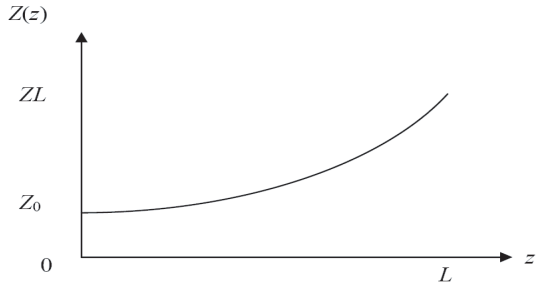

Figure 3: Variation of impedance over length of ETLI [1].

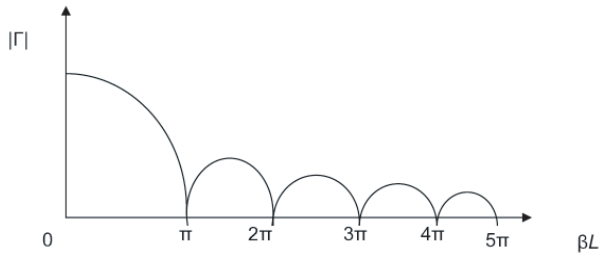

Figure 4: Variation of reflection coefficient for ETLI with varying length [1].

$Z1 := 80 \qquad Zo := 50 \qquad n := 0.00001, 0.00002 .. 1$

$$a := \frac{1}{75 \cdot 10^{-3}} \cdot \ln\left(\frac{Z1}{Zo}\right) \qquad a = 6.267$$

$$X(n) := 50 \cdot e^{a \cdot n}$$

Figure 5: MathCAD computation for an impedance variation.

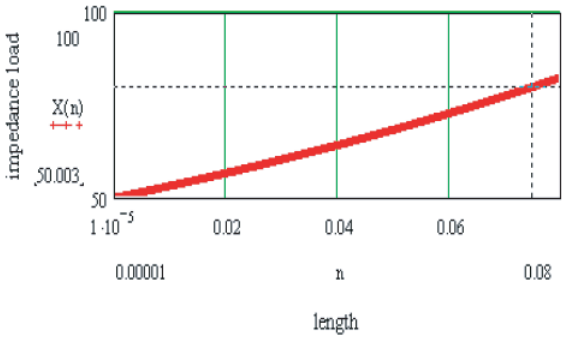

Figure 6: Exponential impedance curve when load is 80 Ohm.

Next, the reflection coefficients were computed in magnitude and decibel or RL forms. These can then be compared with numerical simulations. MathCAD computations are depicted in Figs. 7 and 8, for a chosen combination of 50 Ohm input and 80 Ohm load impedances.

4. NUMERICAL INVESTIGATIONS AND DISCUSSION

The ETLI transformers were then numerically simulated. Variations of lengths were implemented to study the performance of each taper with length. For each load impedance, there were nine different lengths. Hence, there were a total of 36 configurations being considered. The simulated RL of the ETLI transformer of varying lengths with 80 Ohm load are shown in Fig. 9. It depicted the broadband nature of the ETLI transformer. However, when $L = 15$ mm, ripples appeared while the broadband characteristic is maintained with good RL values below -10 dB. Within the length from 25 mm to 45 mm, poor RLs were observed. The first frequency where the poor RL occurred depends on the length. When L increases, RL worsens at lower frequencies and number of ripples increases. It can be concluded that as the impedance difference increases, the earlier is the occurrences of the frequency where the first poor RL occurred.

From the simulations performed, there are important characteristics observed on the ETLI transformer. The behaviour of RL against L can be further investigated at each frequency within the simulated frequency range for ETLI configuration with different load impedance. The relationships are plotted in MathCAD as four responses; RL versus L, RL versus load impedance, $|S_{11}|$ versus L and $|S_{11}|$ versus load impedance, at a certain frequency from 1 GHz to 9 GHz. The overall performance is then tabulated for comparison. An example at 7 GHz is shown in Fig. 10. It can be seen how the ETLI transformer works with variation of lengths at a particular frequency. It can be inferred that as the frequency increases, the number of optimum lengths has also increased with a smaller difference between the optimum lengths. The same pattern occurs with each considered load. The reflection coefficient behaviours show similar patterns since both parameters are interrelated.

The relationships of RL against ZL at a particular frequency, for each transformer length were

$Zl := 80 \quad Zo := 50 \quad n := 0.1\cdot\pi, 0.2\cdot\pi .. 65\pi$

$$X(n) := \frac{\ln\left(\frac{Zl}{Zo}\right)}{2}\cdot e^{-jn\cdot\left(\frac{\sin(n)}{n}\right)}$$

$20\cdot\log(|X(n)|) =$

-12.722
-13.158
-13.905
-14.999
-16.501

Figure 7: MathCAD computation for a reflection coefficient variation.

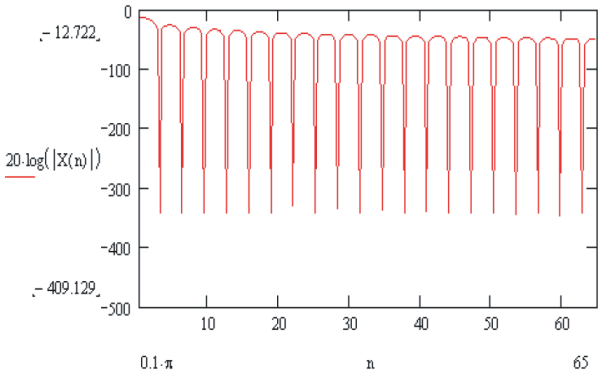

Figure 8: RL response in MathCAD for 80 Ohm load.

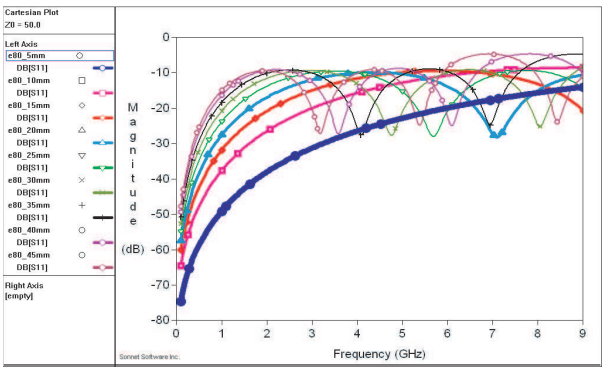

Figure 9: Simulated RL of ETLI transformer with varying lengths. Load = 80 Ω.

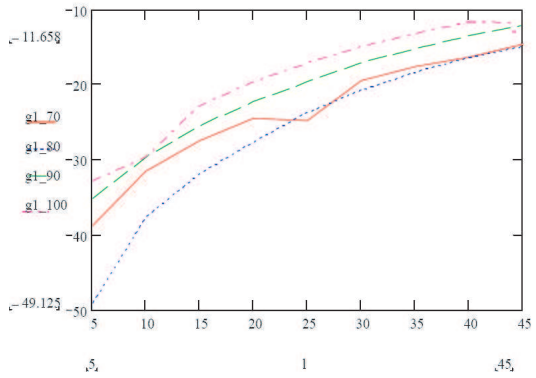

Figure 10: RL of different loads vs ETLI lengths, at 1 GHz.

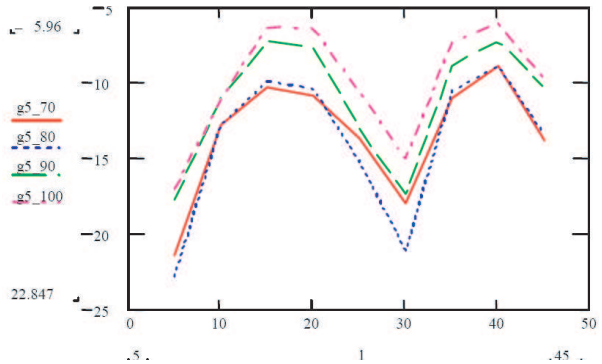

Figure 11: RL of different loads vs ETLI lengths, at 5 GHz.

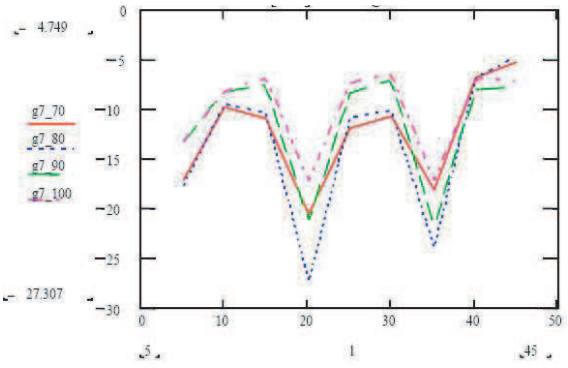

Figure 12: RL of different loads vs ETLI lengths, at 7 GHz.

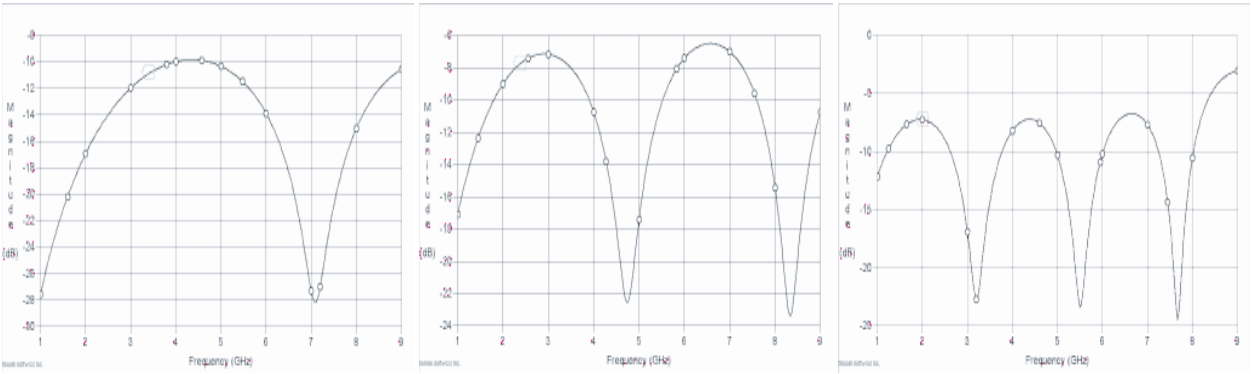

(a) (b) (c)

Figure 13: Numerical simulation showing RL variations for 80 Ohm load for ETLI lengths of (a) $L = 20$ mm, (b) $L = 30$ mm, (c) $L = 45$ mm.

plotted in MathCAD. Examples are given for 1 GHz and 7 GHz in Figs. 11 and 12. Theoretically, ETLI transformer should be well matched over all lengths and over the whole range of frequencies. However, 80 Ohm load appeared to be the most matched. It can be observed that as the frequency increases, higher loads are matched with longer ETLI. Different loads are matched with longer ETLI transformers at higher frequencies from 6 GHz. Similar behaviours were observed for the reflection coefficient responses due to their interrelated properties. Fig. 13 showed RL variation of 80 Ohm optimum load for three selected lengths.

5. CONCLUSION

The mathematical modelling of the broadband exponential taper line impedance transformer has been successfully developed in MathCAD. It was found to be in good agreement with the theory presented in the literature. The results are then further analysed. Numerical simulations were also performed. ETLI transformer is observed to be able to match with the shortest matching section compared to other taper configurations.

ACKNOWLEDGMENT

The work is supported by Universiti Teknologi Malaysia.

REFERENCES

1. Pozar, D. M., *Microwave Enginnering*, 3rd Edition, John Wiley & Sons Inc., New York, 2007.
2. Chang, K., *Encyclopedia of RF and Microwave Engineer*, Vol. 3, John Wiley & Sons Inc., New York, 2005.
3. Vendelin, G. D., A. M. Pavio, and U. L. Rohde, *Microwave Circuit Design Using Linear and Non Linear Techniques*, 2nd Edition, John Wiley & Sons Inc., NJ, 2005.

4. Shirasaki, H., "Design charts by waveguide model and modematching techniques of microstrip line taper shapes for satellite broadcast planar antenna," *Proc. of Int. Symp. on Antennas and Propagation*, Vol. 4, 2000–2003, 2000.
5. El Kamchouchi, H. and G. Abouelseoud, "MAMA: A new methodically designed broadband microstrip antenna using offtheshelf components," *IEEE Antenna and Propagation Magazine*, Vol. 48, No. 2, 72–81, 2006.
6. Fooks, E. H. and R. A. Zakarevicius, *Microwave Engineering Using Microstrip Circuits*, Prentice Hall, Sydney, New York, 1990.
7. Balanis, C. A., *Antenna Theory*, 3rd Edition, John Wiley & Sons Inc., New York, 2005.
8. http://www.mathsoft.com.
9. http://www.sonnetusa.com.

A Novel Bandpass Defected Microstrip Structure (DMS) Filter for Planar Circuits

M. Kazerooni[1], **A. Cheldavi**[1], **and M. Kamarei**[2]

[1]College of Electrical Engineering, Iran University of Science and Technology, Tehran, Iran
[2]Faculty of Electrical and Computer, University of Tehran, Tehran, Iran

Abstract— A new defected microstrip structure (DMS) unit lattice is proposed in order to perform a bandpass filter (BPF). The proposed DMS provides the good cutoff and passband characteristics. Also in this paper we extract the model of BPF. In order to show the improved the parameters, several circuits were designed and simulated. The BPF has a bandwidth more than 39%.

1. INTRODUCTION

Recently, the defected ground plane structures (DGS) and defected microstrip structures (DMS) have been proposed for suppression of spurious response in the microstrip filters [1–4]. However, the existing DGS and DMS configurations provide only the bandstop characteristic. In this paper, we report a new DMS bandpass filter in a defected microstrip line. We also report its circuit model. The desired and tuned frequency resonance can be obtained by changing the T-cell dimensions and by the gap space at the beginning and end of structure.

2. BANDPASS DMS CIRCUIT AND EQUAIVALENT CIRCUIT EXTRACTION

The bandstop DMS with its parallel resonance equivalent circuit is reported in [1]. It behaves as a lumped inductor at frequency below the parallel resonance frequency. The proposed bandpass DMS configuration, shown in Fig. 1 is created by a coupling gap (g_1) on a microstrip line. The proposed structures are designed on a substrate with relative permittivity $\varepsilon_r = 2.33$ and thickness $h = 0.787\,\text{mm}$.

The parallel and series-parallel combined circuit models for bandstop and bandpass DMS configuration are shown in Figs. 2–3.

At frequency below the series resonance, the bandpass DMS configuration behaves as a capacitor. The bandpass configuration shows both the series and parallel resonance. According to [4] we can obtain the capacitance C_p in pF, the inductance L_p in nH and the resistance R_P in ohm of the equivalent circuit of a bandstop DMS shown in Fig. 2:

$$C = \frac{f_c}{200\pi(f_0^2 - f_c^2)} \tag{1}$$

Once the capacitance value of the equivalent circuit is extracted, the series equivalent inductance

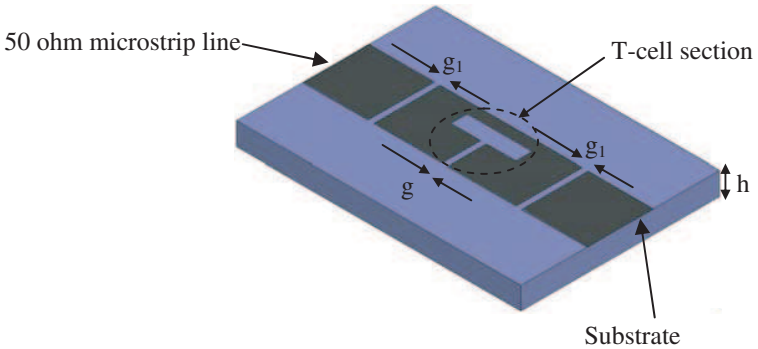

Figure 1: Bandpass DMS configuration.

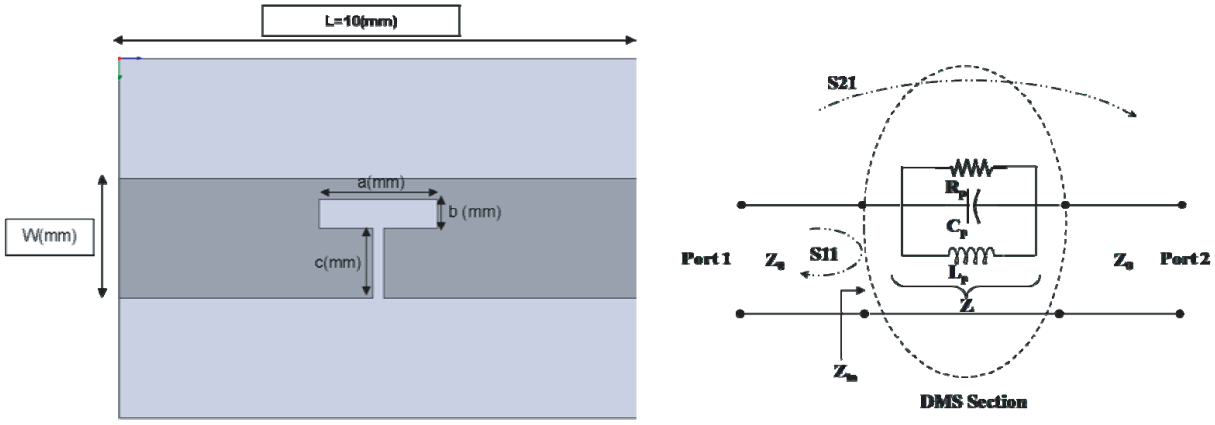

Figure 2: Bandstop DMS configuration and related equivalent circuit.

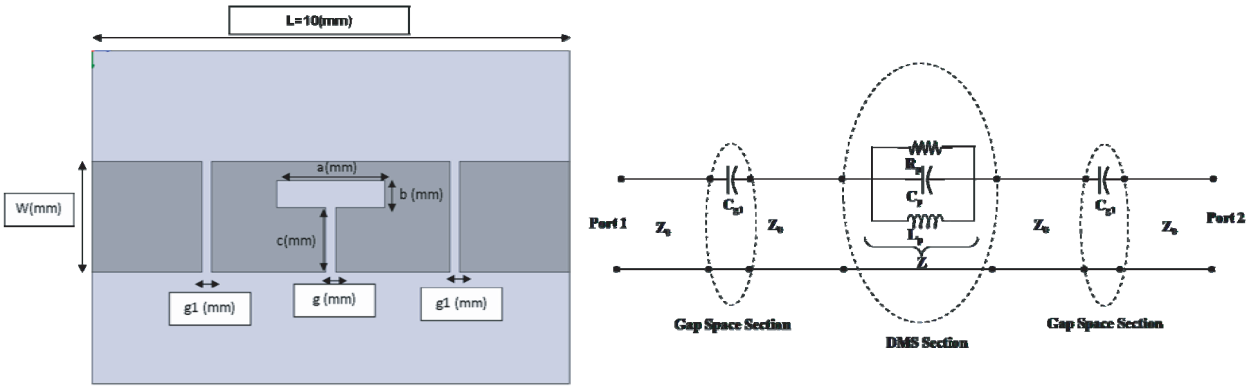

Figure 3: Bandpass DMS configuration and related Equivalent circuit.

and resistance for the given DMS bandstop unit section can be calculated as:

$$L = \frac{1}{4\pi^2 f_0^2 C} \tag{2}$$

$$Y = \frac{1}{Z} = \frac{1}{R(\omega)} + j\left(\omega C - \frac{1}{\omega L}\right) \tag{3}$$

$$z_{in} = z + z_0 \tag{4}$$

$$S_{11} = \frac{z_{in} - z_0}{z_{in} + z_0} = \frac{1}{1 + 2z_0 y} \tag{5}$$

$$R(\omega) = \frac{1}{\frac{1}{2z_0}\sqrt{\frac{1}{(s_{11}(\omega))^2} + (2z_0(\frac{1}{\omega L} - \omega C))^2} - 1} \tag{6}$$

where f_0 and f_C are the resonant frequency and 3-dB cutoff frequency, respectively. However in resonance phenomena role of R_P is important but in the lower and upper of this phenomena roles of inductor and capacitor are important. For simplicity we ignore the frequency dependence of R_P and use a constant value for R_P obtained for $\omega = \omega_0$. Using

$$S_{21} = \frac{2z_0}{2z_0 + z}, \tag{7}$$

for $\omega = \omega_0$, $z = R_P$ and then R_P is given as

$$R_P = 2z_0 \frac{1 - S_{21}(\omega_0)}{S_{21}(\omega_0)} \tag{8}$$

To validate the circuit model, this model has been simulated using Ansoft Designer v_3 (a circuit simulator). The extracted R_P, L_P, and C_P values from aforementioned equations are 3.0949 kΩ, 0.81297 nH, and 0.10471 pF, where f_C and f_0 from Fig. 4 are 11.25 and 17.25 GHz, respectively, and $S_{21}(\omega_0) = 0.0313$. However these models are very simple but the error is acceptable. Fig. 4 shows good agreement of results of the circuit model with results of the Ansoft HFSS simulator.

In case of a bandpass DMS configuration, the equivalent inductance and coupling capacitance form a series resonance circuit. However, when the gap spaces are used in the bandpass structure, its pole f_P frequency is changed by a small amount. We assume that its 3-dB cutoff frequency, f_C for the bandstopt DMS is also 11.25 GHz.

The bandpass structure has series resonance $f_S = 7.4$ GHz and parallel resonance $f_P = 18.1$ GHz. They provided $C_P = 0.089$ pF, $L_P = 0.868$ nH and $C_{g1} = 0.532$ pF for the circuit model. We have assumed that the 3-dB cutoff frequency, for the bandpass case is also 6.12 GHz. Fig. 4 shows

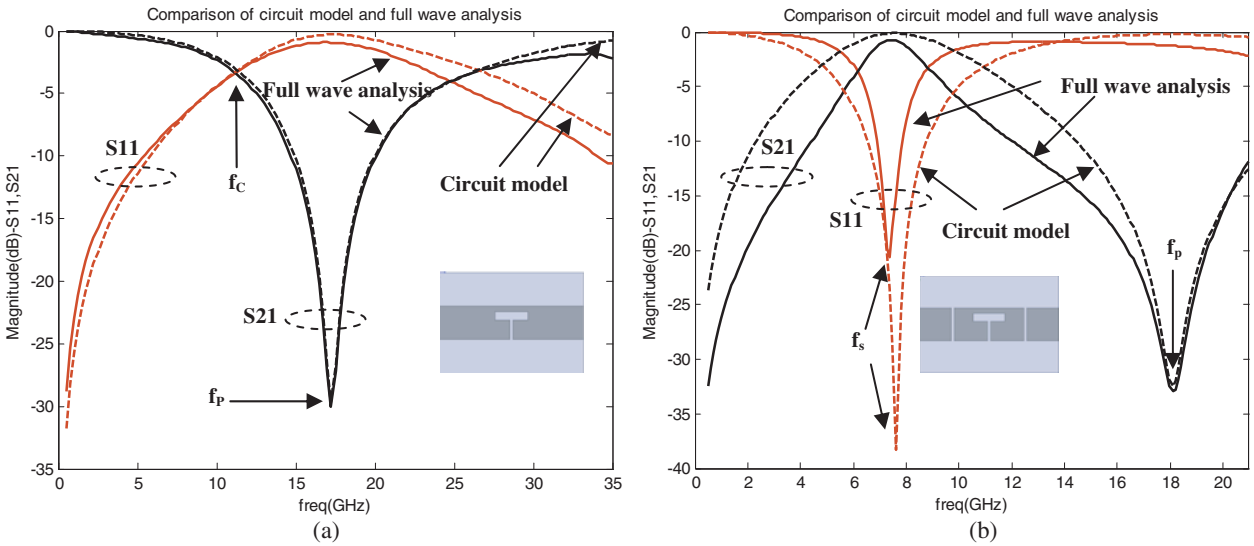

Figure 4: Magnitude frequency response due to circuit modeling and full wave analysis with $a = 2.2756$ mm, $b = 0.5728$ mm, $c = 1.3572$ mm, $g = 0.2$ mm, $g_1 = 0.01$ mm and $W = 2.33$ mm. (a) Bandstop DMS frequency response. (b) Bandpass DMS frequency response.

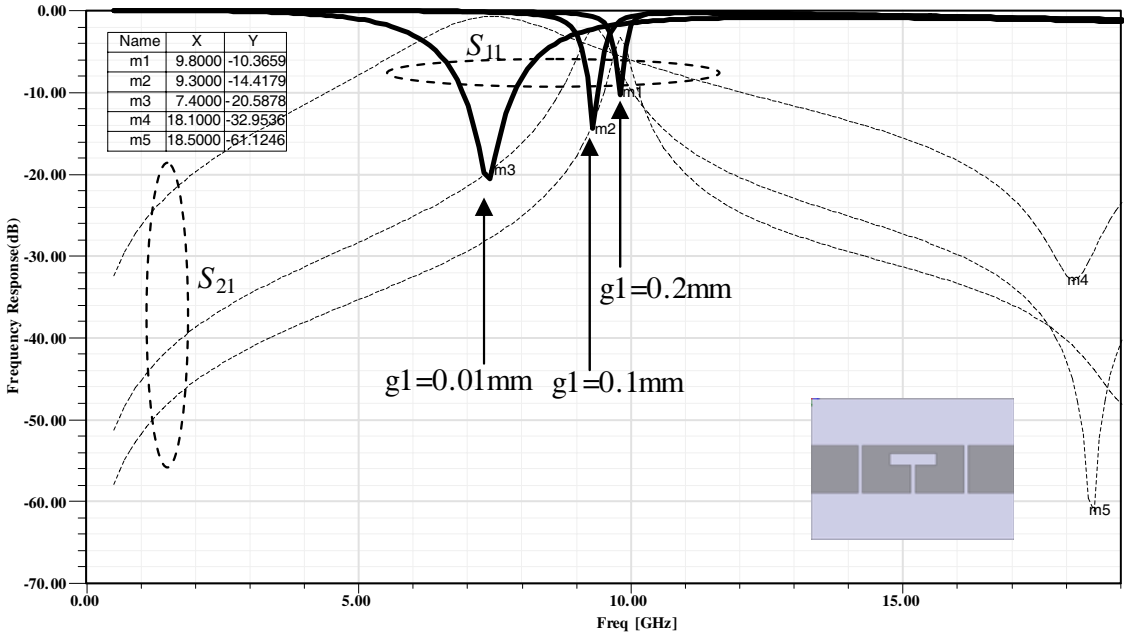

Figure 5: S_{11} and S_{12} of bandpass DMS element response with $a = 2.2756$ mm, $b = 0.5728$ mm, $c = 1.3572$ mm, $g = 0.2$ mm and $W = 2.33$ mm.

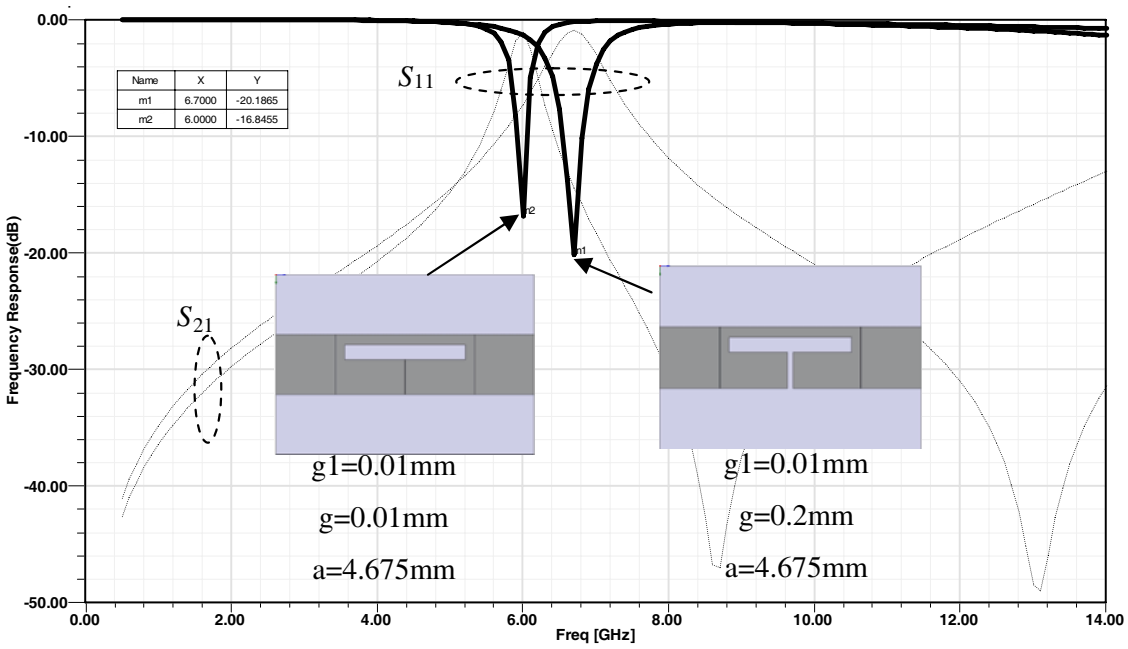

Figure 6: More tuning of resonance frequency using change dimensions of T-cell.

satisfactory agreement of results. Also this figure shows that the bandwidth of BPF is more than 39%.

3. TUNING OF BANDPASS DMS FILTER

The responses for several values of g_1 are shown in Fig. 5. As can be seen in this figure, by decreasing the gap spaces, the resonance response goes to the lower frequencies, insertion loss is improved and pass band become wider.

Addition to change of gap spaces for more tuning of resonance frequency of bandpass DMS filter, we can displacement this frequency by changing the T-cell dimensions. As can be seen in Fig. 6, by increasing a and decreasing g the resonance frequency tend to be lower frequency and then this frequency can be tuned.

4. CONCLUSION

We have introduced a new DMS bandpass component. By using the bandpass DMS components, we have developed a compact BPF of superior performance.

REFERENCES

1. Ahn, D., J. S. Park, C. S. Kim, J. Kim, Y. Qian, and T. Itoh, "A design of the low-pass filter using the novel microstrip defected ground structure," *IEEE Trans. Microwave Theory and Tech.*, Vol. 49, 86–93, Jan. 2001.
2. Yang, F. R., Y. Qian, and T. Itoh, "A novel uniplanar compact PBG structures for filter and mixer applications," *IEEE Microwave Theory and Tech. Symp.*, 919–922, 1999.
3. Park, J. S., J. Kim, J. Lee, and S. Myung, "A novel equivalent circuit and modeling method for defected ground structure and its application to optimization of a DGS lowpass filter," *IEEE Microwave Theory and Tech. Symp. Dig.*, 417–420, 2002.
4. Kazerooni, M., G. Rezai Rad, and A. Cheldavi, "Behavior study of simultaneously defected microstrip and ground structure (DMGS) in planar circuits," *PIERS Proceedings*, 895–900, Beijing, China, March 2009.

Investigation of Static Phasing Distribution Characteristics of Passive Reflectarray Antenna Elements

M. Y. Ismail, **M. F. M. Shukri**, **Z. Zakaria**, **A. F. M. Zain**,
M. F. L. Abdullah, **and M. A. Ubin**
Wireless and Radio Science Center (WARAS), Faculty of Electrical & Electronics Engineering
University Tun Hussein Onn Malaysia, Malaysia

Abstract— There has been much interest recently in developing reflectarray antennas due to the combination of some of the best features between the parabolic reflector and phased array antennas. This paper presents the study of the relationship between phasing distribution characteristics and the bandwidth of different resonant reflectarray elements. The gradient characteristics of different elements of patch, dipole and ring, printed on a grounded dielectric substrate have been investigated at X-band frequency range using the commercial CST computer model. The preliminary simulated results generated from the computer model demonstrate that ring elements contribute the highest reflection loss performance of about 1.74 dB compared to the other two elements of dipoles and patches. The attainable static linear phase range of 177° for ring elements is shown to offer a trade-off between the static phase range and the bandwidth of the reflectarray elements. Results of CST simulations made show that the ring element also contribute the highest reflection loss performance of 2.95 dB compared to the other two elements.

1. INTRODUCTION

A microstrip reflectarray antenna consists of a flat array of microstrip patches or dipoles printed on a thin dielectric substrate [1]. Simillarly as its conventional counter part, it uses a primary feed and a reflecting surface. However, in microstrip antenna, the latter component is planar and forms by many microstrip antenna element. When the incident signals illuminating from a feed antenna to the array elements and scatter the incident field with the proper phase required forming a planar phase. Many types of resonant elements can be used in printed reflectarray antennas depending on the required applications such as dual frequency [7] and solar panel reflectarray [5]. Examples of reflectarray antenna elements are the variable size patch elements [2, 3], spiral patch elements [4], cross dipole elements [5, 6], and ring elements [7, 8]. The focus in this paper is on the range and slope of phase characteristics of a unit cell of a reflectarray formed by different types of elements: Patch, dipole and ring. In the reflectarray design, the obtained phase characteristics are used to work out the sizes of the individual elements in the reflectarray to compensate for the phase differences. There are two main parameters that are important in the phase compensation process, the range and the slope. The phasing range needs to be 360° at a given frequency of operation, in the way to provide suitable compensation. Meanwhile, the phase slope oversees the manufacturing tolerances and the operational bandwidth of the element. As the slope are slower, its offers smaller manufacturing errors and provide larger operational bandwidth. In this paper, the phasing distribution characteristics was analyzed using different resonant elements. The operating frequency of operation is in the X-band frequency range (8–12 GHz).

2. BACKGROUND

2.1. Reflectarray Antennas

A reflectarray combines the feature of both a reflector and an array. As the introduction of the printable microstrip antennas, the technologies of combining the reflectarray and microstrip radiators were investigated [9]. A feed antenna illuminates the array whose individual elements are designed to scatter the incident field with the proper phase required to form a planar phase surface in front of the aperture, The bandwidth performance of a reflectarrray is shown to be narrower compared to a parabolic reflector. For a printed microstrip reflectarray, its bandwidth is primarily limited by two factors that are narrow bandwidth of the microstrip patch elements on the reflectarray surface and the differential spatial phase delay [10]. The path length from the feed to all patch elements is all different. This leads to different phase delays. In order to compensate for the different path lengths, the elements must have corresponding method to overcome the problem. The reflection loss, S_{11} of a reflectarray antenna should be 0 dB at resonance in order to get a maximum reflected energy. Minimum reflection loss can be achieved when the signal energy reflection is the same as when signal energy is illuminated.

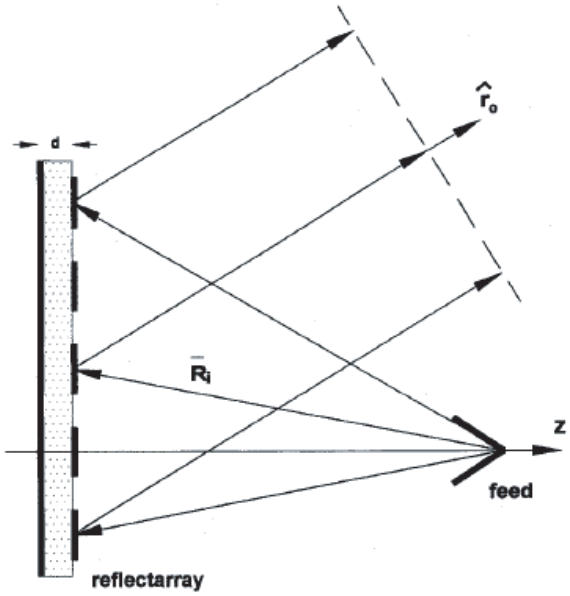

Figure 1: Geometry of the microstrip reflectarray.

2.2. S-shaped Phase Curve Plots

The slope of the phase versus frequency is a measure of the bandwidth of reflectarray as a curve with a smaller phase slope will lead to less phase error [1]. It has been reported by Pozar that there is a trade-off between phase range and the bandwidth [1]. This is indicated by the gradient of the S-shaped phase curve. To provide a suitable compensation for all the elements in array, the phasing range needs to be close to 360° at a given frequency [11]. Resonance occurs at 180° phase difference, where the maximum reflection of the signal occurs.

3. METHODOLOGY

The considerations start with a microstrip reflectarray operating in the X-band with the center frequency of 10 GHz. The reflectarray is assumed to be formed by elements printed on a substrate of dielectric constant and thickness and arranged in a square lattice. In the built model simulator, the elements are assumed to have symmetry with respect to the X and Y axis. In order to work out the phase characteristics, only the case of a vertically polarized (in Y-axis) TEM plane wave that is normally incident on an infinite periodic array is considered. These considerations based on the

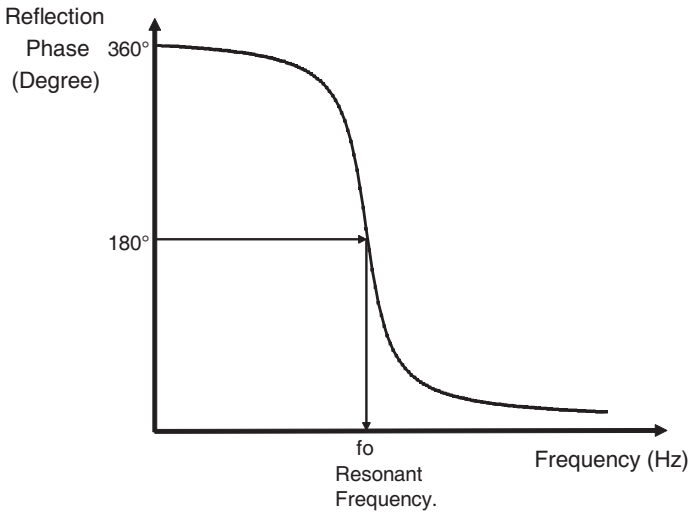

Figure 2: Reflection phase versus frequency.

fact that TEM provides a good approximation to the phase range and slope. In order to identify phase distribution characteristics, different types of elements are used. By using the equivalent waveguide approach, the phase of the reflected wave at each element is determined as the phase of the scattering parameter for the waveguide one-port containing these elements. The structure was modeled using the commercial full-wave electromagnetic software CST Microwave Studio. The reflection loss performance and the phase characteristic of unit cells with different type of resonant element were generated. The parameters such as S_{11} and S-shaped phase curves obtained from commercially available CST computer model have been investigated. Current distributions of resonant elements of dipole, patch and ring have been studied to observe the effect on the reflection loss and static linear phase range performance.

4. RESULTS AND DISCUSSIONS

This section reports on simulated results for the phase characteristic of different type of resonant reflectarray element as obtained with CST Microwave Studio. The relationship between the static linear phase range and the bandwidth is investigated in order to find the best element which suits the criteria for greater phase range and low loss performance of reflectarray elements.

Resonant patch elements of dipole, patch and ring have been analyzed using the commercially available CST computer model. The simulated results shown in Figure 3 show that ring element has higher loss compared to dipole element and rectangular patch element, -1.7 dB, -1.4 dB, and -1 dB respectively. This is significantly due to the surface area of ring element as shown in surface color contour distribution in Figure 3(c) which has smaller area compared to dipole element and rectangular patch element that allows more current distribution to be concentrated in that particular region. Because of the area of the resonant elements, ring element has a higher loss due to the reflection properties from the elements and hence less bandwidth compared to dipole element and rectangular patch element [1]. This is clearly shown by the surface current distribution generated from the CST computer model. The red color represents the areas which have the highest concentration of current ddistributions. Figure 4 below shows static phase range generated from the CST computer models for three different types of resonant elements of ring, dipole and patch.

As shown in Figure 4, the ring element shows a greater static linear phase range compared to the other two elements. However the increase in the static phase range has to be traded off with the bandwidth and the reflection loss performance of the reflectarray. Although the bandwidth of the reflectarray elements is shown to be very narrow, it can be increased by suitable choosing suitable ratios of the outer and inner radius ratio [7].

Figure of Merit (FoM) as defined in (1) can be used as an indicator to describe phasing distribution of the static linear phase range. It is defined as the phase range where the static phase

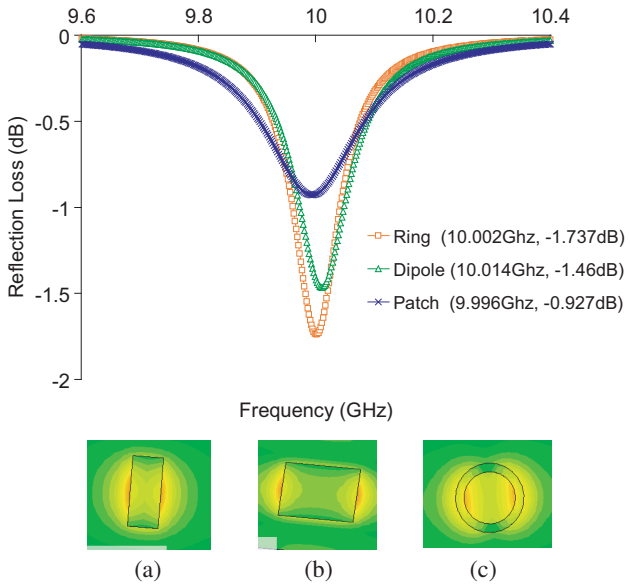

Figure 3: Combination of ring, dipole and rectangular patch element in S_{11} (dB) parameter. (a) Dipole, (b) patch, (c) ring.

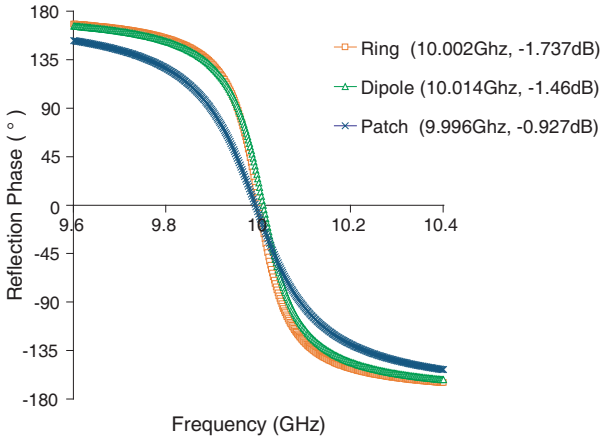

Figure 4: Comparison between S-shaped phase curves of ring, dipole and rectangular patch element.

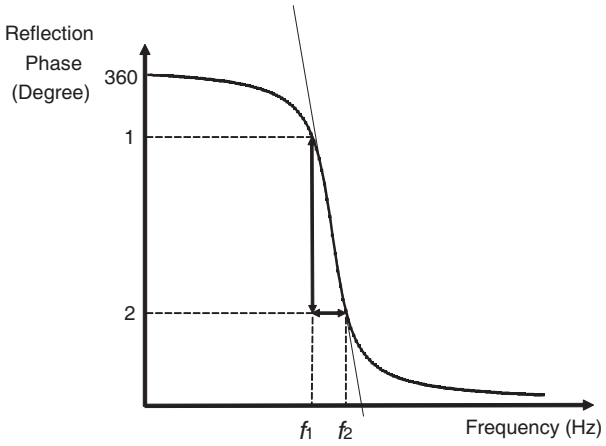

Figure 5: Phasing distribution of the static linear phase range.

Table 1: Figure of merit (FoM).

Case	Elements	Linear Phase Range (°)	Figure of Merit (FoM) (°/GHz)
1	Ring	177	1967
2	Dipole	171	1710
3	Rectangular Patch	150	1250

range occurs at a certain frequency range.

$$\text{Figure of Merit} = \text{Static Linear Phase Range / Frequency Range}$$

$$\text{FoM} = \frac{\Delta\Phi}{\Delta f} = \frac{(\Phi_1 - \Phi_2)}{(f_1 - f_2)} \tag{1}$$

Table 1 summarizes the static linear phase range and figure of Merit for three resonant elements of dipole, ring and patch. It is clearly shown that both the linear phase range and larger figure of Merit are contributed by ring element but however it has to be traded off between narrow bandwidth and greater linear phase range.

5. CONCLUSION

In conclusion, the trend of the S-shaped phase curves of the reflectarray antenna has been investigated using different resonant elements. Analysis of the phase distribution of resonant elements were carried out using CST computer model demonstrate that there is a trade off between the static phase range and the reflection loss of the elements. Predicted results generated from commercially available CST computer model demonstrate that ring elements offer a greater static phase range compared to the elements of dipole and patch. The figure of Merit has been defined in order to give an indicator of the performance between the static phase range and the reflection loss of different resonant elements of reflectarray. Waveguide simulator measurements will be performed in order to see the reliability of the predicted results obtained from the commercially available CST computer model.

ACKNOWLEDGMENT

The authors would like to thank to RF & Microwave Laboratory and Wireless and Radio Science Centre (WARAS) for providing simulation and measurement facilities. Thanks are also due to the Ministry of Higher Education of Malaysia for providing the FRGS (VOT 0558) fund for this project.

REFERENCES

1. Pozar, D. M., S. D. Targonski, and H. D. Syrigos, "Design of milimeter wave microstrip reflectarrays," *IEEE Transactions on Antennas and Propagation*, Vol. 45, No. 2, 1997.

2. Pozar, D. M. and T. A. Metzler "Analysis of a reflectarray antenna using microstrip patches of variable size," *Electronics Letters*, Vol. 29, No. 8, 657–658, April 15, 1993.
3. Pozar, D. M. and S. D. Targonski, "Analysis and design of a microstrip reflectarray using patches of variable size," *IEEE AP-S Symposium Digest*, 1820–1823, 1994.
4. Datthabasombat, S., A. Prata, J. P. Brown, and O. Quientero, "Spiral microstrip patch element for reflecarray," *IEEE Antennas and Propagation Society International Symposium*, Vol. 3, 721–724, 2001.
5. Bialkowski, M. E., A. M. Abbosh, and K. H. Sayidmarie, "Investigations into phasing characteristics of printed single and double cross elements for use in a single layer microstrip reflectarray," *Microwave and Optical Technology Letters*, April 2008.
6. Pozar, D. M. and S. D. Targonski, "A microstrip reflectarray using crossed dipoles," *IEEE Antennas and Propagation Society International Symposium*, Vol. 2, 1008–1011, 1998.
7. Misran, N., R. Cahill, and V. F. Fusco "Reflection phase response of microstrip stacked ring elements," *Electronics Letters*, Vol. 38, No. 8, 2002.
8. Sayidmarie, K. H. and M. E. Bialkowski "Multi-ring unit cells for increased phasing range in single layer microstrip reflectarrays," *Proceedings of iWAT*, 2008.
9. Gupta, V. R. and N. Gupta, "Gain and bandwidth enhancement in compact microstrip antenna".
10. Encinar, J. A. and J. A. Zornoza, "Broadband design of three layer printed reflectarrays," *IEEE Transactions on Antennas and Propagation*, Vol. 51, No. 7, 2003.
11. Kraus, J. D. and R. J. Marhefka, *Antennas for All Applications*, McGraw-Hill Higher Eduction, 2002.
12. Huang, J., J. A. Encinar, "Reflectarray antennas," Institute of Electrical and Electronic Engineers, 2008.
13. Balanis, C. A., *Antenna Theory Analysis and Design*, John Wiley & Sons, Inc., 1997.
14. Sze, K. Y. and L. Shafal, "Analysis of phase variation due to varying patch length in a microstrip reflectarray," *IEEE Antennas and Propagation Society International Symposium*, Vol. 2, 1134–1137, 1998.

Investigation of Broadbanding Techniques on a Novel Folded Meander Line Antenna (FMLA)

A. A. M. Ezanuddin, P. J. Soh, M. F. Malek, and M. Z. A. Abdul Aziz
School of Computer and Communication Engineering, University Malaysia Perlis (UniMAP)
No. 12 & 14, Jalan Satu, Tmn Seberang Ramai, Fasa 3, 02000 Kuala Perlis, Perlis, Malaysia

Abstract— In this work, Folded Meander Line Antennas (MLAs) have been designed to operate in WLAN b/g band. Two prototypes were tested: The first antenna is shaped like a fish-bone (Fish Bone MLA), while the second design has a structure of a folded meander line looped back to its starting position (Folded MLA). Both design are either fabricated on FR-4 or RO3010 boards. Two broadbanding techniques are investigated in this work, by adding vias and implementing the proximity coupling technique, using CST software. Investigation is aimed to determine and compare the effectiveness between the two techniques on these new antenna structures. Investigation have found that prototype 2 fed using the proximity coupling technique has produced the widest bandwidth with a value of 939.5 MHz.

1. INTRODUCTION

Wireless local area network (WLAN) technology, is extensively used to connect the internet had been widely, applied in modern electronic communication and communication devices such as personal computer, notebook, and access point (AP), etc. Factors such as wide bandwidth and small in size are most reason why such characteristics of antennas have always been favored in many indoor wireless communication systems, particularly when limited space is available for the installation of the antenna [1].

Meander line formations allow smaller volume and provide wideband expansion [2]. As a meaning on increasing number of meander turn, these models provide reasonable approximation of the relative changes in resonant frequency [3]. This antenna is an interesting class of resonant antennas and is extensively studied in order to reduce the size of the radiating element similarly to the wired antennas such as monopole, dipole and also folded dipole type antennas [4]. The desired resonant frequency is harder to be tuned if more turns are added in folded meander line antenna. Therefore, in order to prevent this, the whole antenna composition must always be optimized. A good S_{11} when simulating any type of antenna will have a response dip at the desired frequency with at least -10 dB lines [5].

2. ANTENNA DESIGN AND PARAMETRIC STUDY

The antenna has been designed using CST software which will then be fabricated on FR-4 and RO3010 boards based on wet etching technique. Such reign is a norm in comparing between measured and simulated results by seeking the change of resonant frequency, return loss and also bandwidth [6]. The folded meander itself would be able to employ multi-band function owing the three or four turns it was experimented on a single FR-4 board ($\varepsilon = 5.4$). Fig. 1 below presents 10 samples concluded from various heights (v) performed onto the whole meander line. The narrow bandwidth is still a problem, but the first broadbanding technique, which is the proximity coupled design started with $v = 19.44$ mm at 2.419 GHz. Length of feeding and width-to-line ratio patch used at the second layer (same substrate) can be used to control matching and this leads to a broader bandwidth obtained [7], as illustrated in Fig. 2. As many as 18 samples manipulated width (cond2_w) was prepared, with 11.1053 mm fitting the purpose of making available bandwidth greater than 100 MHz. As the patch width plays a major role in attaining targeted bandwidth proved previously, a thinner substrate with an epsilon of 10.2 and thickness of 0.635 mm was exploited acting as first layer above the FR-4 patch which leads to an uneven thickness and epsilon value used [8]. Fig. 3 was an initial discovery maneuvering dissimilar distance of both left and right meander line. As observed, each sample swept gave an expression that the closer the gap is, a worse return loss is produced. Fortunately, all samples did present an appropriate starting point in between 2.4 GHz and 2.48 GHz in executing proximity coupling marked as (A).

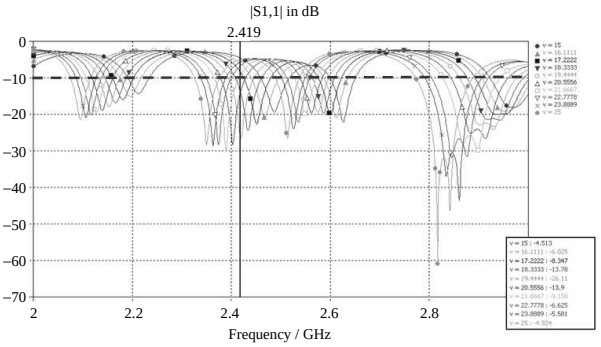

Figure 1: Height (v) here is swept around 10 samples to observe return loss and its corresponding bandwidth.

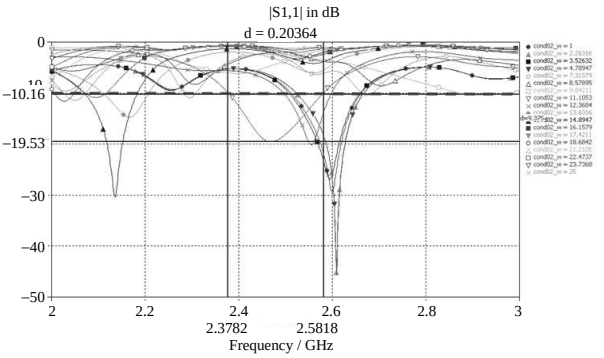

Figure 2: Proximity coupling method (cond2_w) sampling permitted bandwidth expansion.

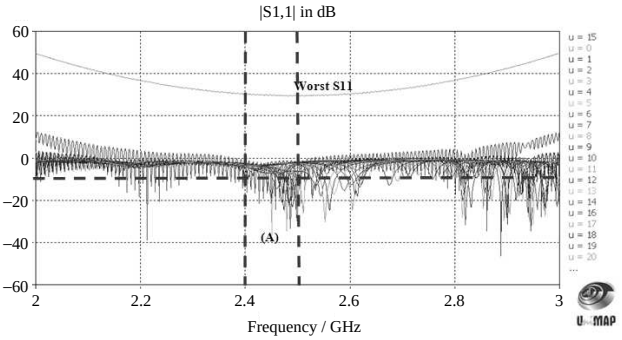

Figure 3: Distance between two folded meander line (u) was studied gave multiple return loss.

3. RESULT AND DISCUSSION

Figure 4 displays a top view of the folded meander line design. This larger new design is anticipated to have a higher directivity and gain due to the larger conductor surface made available. Continuing with FR-4 ($\varepsilon = 5.4$) thickness of 1.6 mm, the folds were reduced to three turns whereas the waveguide port is situated on the lower right. Trailing from this simulation, Fig. 5 provided narrow band return loss -26.47 dB at 2.419 GHz. From the observation, the folded meander formation can produce multiple band in which can be configured to a single band operation. FMLA frequencies are reallocated by changing the copper width by formula (1).

$$w_{eff} = w + t\frac{1+\dfrac{1}{\varepsilon_r}}{2\pi}\ln\left(\frac{4e}{\sqrt{\left(\dfrac{t}{h}\right)^2+\left(\dfrac{1}{\pi}\dfrac{1}{\dfrac{w}{t}+\dfrac{11}{10}}\right)^2}}\right) \tag{1}$$

ε_r = dielectric constant of substrate, w = width of strip, h = thickness ('height') of substrate, t = thickness of strip metallization. The proximity coupling technique is applied into practice by adding the second layer ($\varepsilon = 5.4$) below the folded meander, structure as shown in Fig. 7. Upon modification, broadening of bandwidth occurred to a nearly 200 MHz starting at 2.39 GHz ending at 2.59 GHz. The second layer etched copper is shaped as a regular radiator, centered on top of the folded meander. A balanced dimension must be ensured to enable current flow in TM mode, resulting in radiation perpendicular to the formation surface [8]. Comparison of these two techniques is found in Table 1.

Next, the prototype in Fig. 9 was enhanced to four turns. Unlike before, the first upper layer retain the same formation except using RO3010 ($\varepsilon = 10.2$) with different thickness of 0.635 mm. The higher dielectric value used the produced a narrow return loss as seen in Fig. 10 in contrast

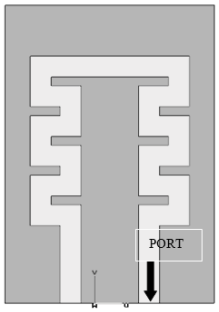

Figure 4: General view of folded meander line antenna.

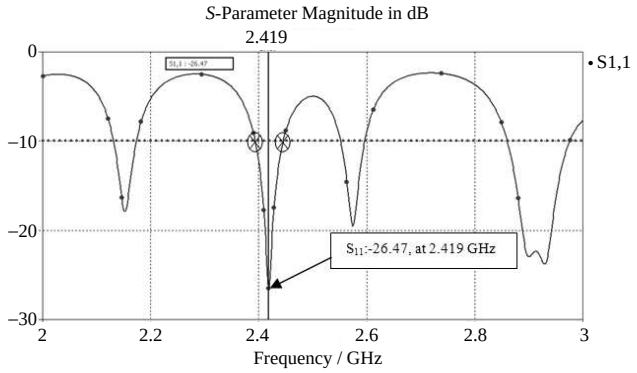

Figure 5: Return loss obtained at 2.419 GHz, −26.47 dB.

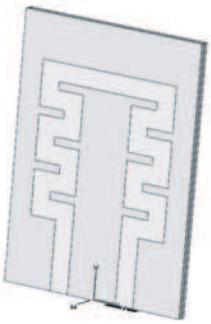

Figure 6: First upper layer of the FMLA.

Figure 7: Same substrate used as proximity coupling.

Table 1: Bandwidth improvement through application of proximity coupling technique.

Antenna	Proximity Coupling	Bandwidth (MHz)
FMLA-00	NO	20.0
FMLA-01	YES	200.0

Table 2: Bandwidth improvement through proximity coupling and EBG method.

Antenna	Proximity Coupling	Bandwidth (MHz)
FMLA-03	NO	5.0
FMLA-04	YES	80.0
FMLA-05	YES — Including rectangular EBG and high impedance surface (HIS) at the ground plane	939.5

to Fig. 8. Figure 9 was then repeated to Fig. 11 with an FR-4 board placed underneath. This board also brought about the similar idea — a lengthened rectangular etched copper, in order to widen the bandwidth. This modification did boost up bandwidth initiated from 2.40 GHz onwards to 2.48 GHz generating a 80 MHz bandwidth showed in Fig. 12. From here and beyond, another technique was attempted and proven its capability in broading up bandwidth significantly. This prototype was designed using RO3010 as the first layer (1), followed by FR-4 (2) and finally an ohmic sheet valued at 400 Ω above the ground plane (3) as demonstrated in Fig. 13 and Fig. 14. Interestingly, modification was also done to the ground plane where rectangular dual loops are cut out to utilize Electromagnetic Band Gap (EBG) concept. EBG occupy only the lower half segment of the ground plane as shown in Fig. 15. While it is valid that the proximity coupling technique greatly provided bandwidth enhancement, an even greater improvement is provided by adding a EBG structure to the design. The EBG structure has provided a good amount of electromagnetic coupling between the two layers, by producing up to 940 MHz of bandwidth, whereas without it, a relatively small bandwidth of about 80 MHz is produced.

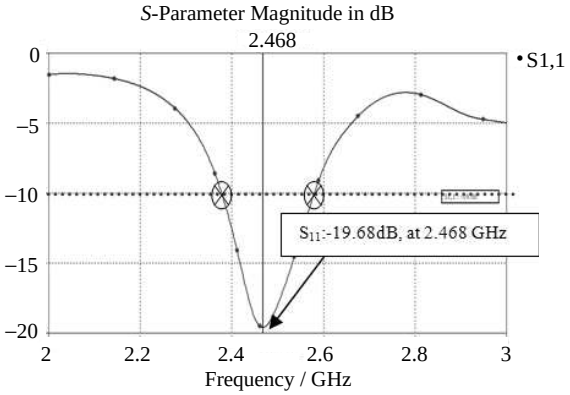

Figure 8: Simulated return loss at 2.468 GHz, −19.68 dB.

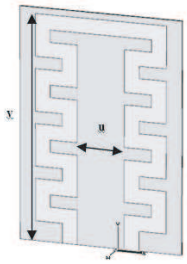

Figure 9: FMLA experimented with 4 turns.

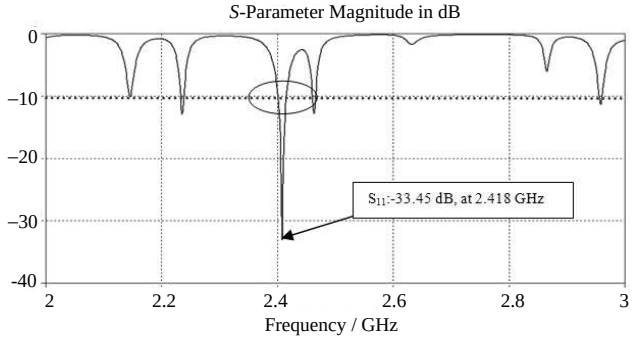

Figure 10: Return loss obtained at 2.418 GHz, −33.45 dB.

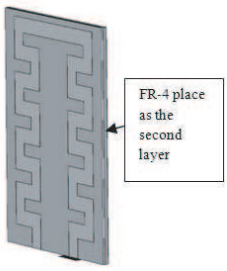

Figure 11: FR-4 board placed as the second layer applying proximity coupling method.

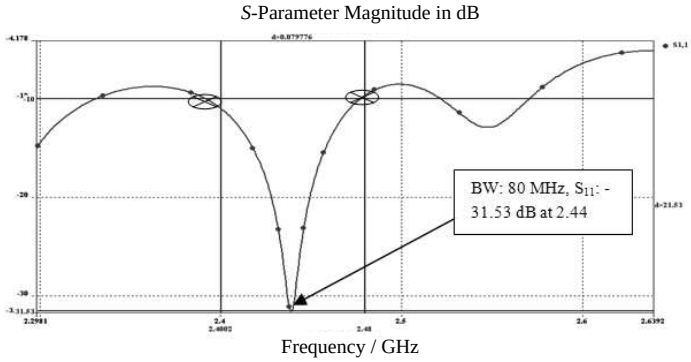

Figure 12: Significant changes to the return loss.

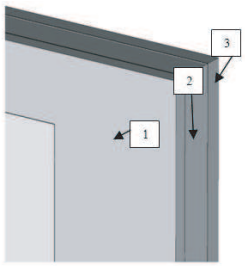

Figure 13: Using prior design, two more material was added whereas ground plane was altered.

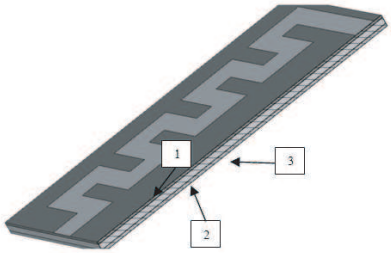

Figure 14: RO3010 as the first layer followed by FR-4 then ohmic sheet.

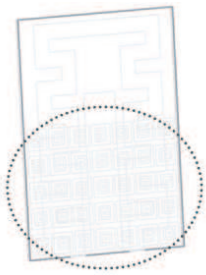

Figure 15: Half portion of the ground plane had been altered with rectangular EBG.

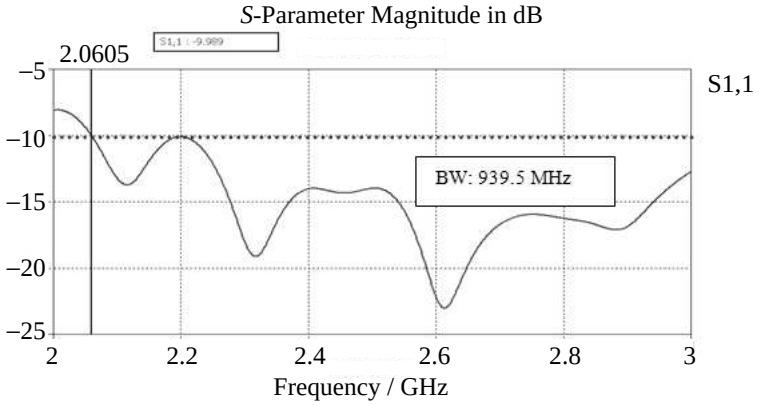

Figure 16: Bandwidth increase to nearly 940 MHz.

4. CONCLUSION

To widen a bandwidth, proximity coupling feed method can be applied onto the FML. From the investigation also, we found out that using same substrates may provide larger bandwidth than a design where different substrates are placed together to form a multiple-layered antenna.

REFERENCES

1. Wong, K. L., *Planar Antennas for Wireless Communication*, Wiley, Hoboken, NJ, 2003.
2. Khaleghi, A., A. Azooulay, and J. C. Bolomey, "A dual band back couple meandering antenna for wireless LAN applications," *Vehicular Technology Conference*, Gof sur Yvette, France, 2005.
3. Best, S. R. and J. D. Morrow, "Limitation of inductive circuit model representations of meander line antenna," *IEEE Antennas and Propagation Soc. Int. Symp.*, 852–855, 2003.
4. Nakono, H., H. Tagami, A. Yoshizawa, and J. Yamauchi, "Shortening ratios of modified dipole antennas," *IEEE Trans. Antennas Propagat.*, Vol. 32, 385–386, Apr. 1984.
5. Huang, C.-W. P., A. Z. Elsherbeni, J. J. Chen, and C. E. Smith, "FDTD characterization of meander line antennas for RF and wireless communications," *Progress In Electromagnetics Research*, PIER 24, 185–199, 1999.
6. Ezanuddin, A. A. M., P. J. Soh, A. A. H. Azremi, and S. L. Ooi, "Miniaturization and broadbanding techniques for folded meander line microstrip antennas," *2009 International Workshop on Antenna Technology (IWAT 09)*, in Press, Santa Monica, California, Mar. 2–4, 2009.
7. Ezanuddin, A. A. M., P. J. Soh, A. A. H. Azremi, and S. L. Ooi, "Design and analysis of a novel dielectric loaded helical antenna for wlan applications," *International Symposium on Antenna and Propagation (ISAP'08)*, 210–215, Taipei, Taiwan, Oct. 27–30, 2008.
8. Soh, P. J., M. K. A. Rahim, A. Asrokin, and M. Z. A. Abdul Aziz, "Design, modeling and performance comparison of feeding techniques for a microstrip patch antenna," *Jurnal Teknologi*, 47(D), 103–120, 2007.
9. Maeda, S., T. Kashiwa, and I. Fukai, "Full-wave analysis and propagation characterisctics of a throuth hole using the finite difference time-domain method," *IEEE Trans. Microwave Theory Tech.*, Vol. 3/39, No. 12, 2154–2159, 1991.
10. Balanis, C. A., *Antenna Theory Analysis and Design*, Wiley-Interscience, John Wiley & Sons, Hoboken, New Jersey.

Microwave Corona Breakdown in rf Devices

J. Rasch[1], **D. Anderson**[1], **M. Lisak**[1],
V. E. Semenov[2], **and J. Puech**[3]

[1]Chalmers University of Technology, Göteborg, Sweden
[2]Institute of Applied Physics, Nizhny Novgorod, Russia
[3]Centre National d'Études Spatiales, Toulouse, France

Abstract— The main physical properties of microwave corona breakdown in gases in the presence of inhomogeneous electric fields are investigated using numerical calculations of the continuity equation for the density of free electrons. In particular, the interplay between diffusion and attachment in redistributing electrons from high field regions to low field regions and the concomitant effect on the breakdown threshold is studied for different examples of the variation of the electric field strength. The results give a clear physical picture of the dependence of breakdown electric field on pressure with two complementary limits; a high pressure limit with a localized breakdown plasma confined to the high field region and a low pressure limit determined by the properties of the low field region only and a breakdown plasma extending over the entire volume of the rf device. A comparison between results for the critical microwave breakdown field as obtained by numerical calculations and experimental results in a microwave cavity show very good agreement.

1. INTRODUCTION

Corona breakdown is a potentially serious failure mechanism in many gas-filled microwave devices like antennas, wave guides etc. since the technological development tends to constantly increase the power in the system and there are natural limitations to the electrical field intensity a system can withstand before failing. The basic physics involved in the corona breakdown process — the avalanche-like growth of the free electron density which creates a conducting (plasma) region in or around the rf system under the ionizing action of high energy electrons created by the microwave field — is rather well understood for homogeneous microwave fields, [1]. However, many rf components involve inhomogeneous fields due to mode structure and/or to the presence of e.g., tuning screws or other details introduced for constructive purposes (e.g., impedance matching) or simply defects in the device. When the electric field in a gas-filled microwave device is inhomogeneous in space, the interplay between the concomitant inhomogeneous ionization, which tends to create free electrons, and the diffusion and attachment mechanisms, which tend to decrease the free electron density, becomes complicated and depends significantly on the geometry of the device and on the gas pressure. In cases with locally enhanced ionization, the breakdown threshold is determined as an interplay between diffusion and attachment where diffusion transfers free electrons out of the localized region with high field into regions with weaker fields where attachment operates as a sink for the free electrons. For small pressures, diffusion is a strong electron redistributing effect and the influence of the high field region is small, but for large pressures, diffusion is weak and the breakdown threshold is set by attachment balancing the locally high ionization, which may significantly lower the breakdown threshold as compared to the corresponding homogeneous situation. Thus, in the case of inhomogeneous field profiles, the pressure becomes an important factor in determining the size and location of the conducting region.

Corona breakdown in gas filled rf devices has been analyzed for a number of different designs and microwave mode structures, including situations involving field singularities e.g., sharp corners or edges where the electric field strength (and the ionization) becomes locally very high. For inhomogeneous electric fields, the corresponding breakdown threshold can be calculated analytically only in a few special cases and usually resort must be taken to approximate and numerical methods, c.f. [2, 3]. However, many different and technically important situations still lack a complete understanding of the breakdown conditions.

In the present work we will illustrate the coupling between diffusion, attachment, and the inhomogeneous ionization by considering two specific situations where the inhomogeneity of the field plays an important role in determining the breakdown threshold; a rectangular resonant cavity excited in the TE_{110} mode, and a small high field region adjacent to a conducting surface surrounded by a low field region.

2. THE GENERAL PROCEDURE

The determination of the microwave breakdown threshold involves two steps: (i) determination of the electric field strength in the device (while neglecting plasma effects) and (ii) solving the equation for the plasma dynamics in this electric field, i.e., solving the continuity equation for the electron density, viz.

$$\frac{\partial n(\bar{r},t)}{\partial t} = D\nabla^2 n(\bar{r},t) + \nu_i n(\bar{r},t) - \nu_a n(\bar{r},t) \tag{1}$$

where $n(\bar{r},t)$ is the plasma (electron) density, D is the diffusion coefficient, ν_i is the ionization frequency, and ν_a is the attachment frequency. These parameters depend on the type of gas, gas pressure (p), and electric field strength. Whereas D and ν_a depends primarily on pressure (scaling as $D \propto 1/p$, $\nu_a \propto p$), the ionization frequency in addition also depends strongly on the electric field strength and an often used empirical approximation is $\nu_i \propto pE_{\text{eff}}^{\beta}$ where e.g., $\beta = 5.33$ for air. Here the effective electric field, E_{eff}, is defined by $E_{\text{eff}}^2 = E_{\text{rms}}^2/(1+\omega^2/\nu_c^2)$ where E_{rms} denotes the rms electric field, ω is the microwave angular frequency, and ν_c is the collision frequency between electrons and gas particles. The breakdown threshold is determined by the condition that the losses of electrons through diffusion and attachment is balanced by ionization, i.e., $\partial n(\bar{r},t)/\partial t = 0$. Eq. (1) can then be formulated as the eigenvalue problem

$$\nabla^2 n(\bar{r},t) + (\lambda s(\bar{r}) - q)n(\bar{r}) = 0 \tag{2}$$

where $n(\bar{r})$ must vanish on the boundary of the considered volume, $\lambda = \max \nu_i/D$, $q = \nu_a/D$, and $s(\bar{r}) = (E(\bar{r})/\max E(\bar{r}))^{\beta}$. The eigenvalue, λ, determines the breakdown electric field as a function of the physical parameters of the gas and the geometry of the device.

3. BREAKDOWN IN A RESONANT CAVITY

Resonant cavities play an important role in many microwave applications. One relevant configuration is the rectangular resonant cavity in which the field (excited in its E_{110} mode) is given by

$$\vec{E} = E_0 \sin\left(\frac{\pi x}{a}\right) \sin\left(\frac{\pi y}{b}\right)\hat{z} \tag{3}$$

where a and b are the dimensions in the x and y directions. When this field is inserted into the eigenvalue equation, the z-dependence of the plasma density can be separated out by writing $n(\bar{r}) = Z(z)n(x,y)$, where $Z(z) = \sin(\pi z/L)$, and L is the height of the cavity. The remaining equation for the function $n(x,y)$ then becomes

$$\nabla_{\perp}^2 n(x,y) + (\lambda s(x,y) - \tilde{q})n = 0 \tag{4}$$

where $\tilde{q} = q + \pi^2/L^2$ accounts for the losses due to attachment and diffusion in the $\hat{z}$ direction and $s(x,y) = \sin^{\beta}(x/a)\sin^{\beta}(y/b)$. Eq. (4) is not tractable for exact analytical analysis, but a powerful and convenient approximate approach is to use direct variational methods based on the Ritz optimization procedure as demonstrated in [4].

An interesting aspect of breakdown plasma behavior, characteristic of situations involving inhomogeneous electric fields, is the interplay between attachment and diffusion in determining the electron losses and its dependence on pressure. As noted above, diffusion decreases with increasing pressure whereas attachment increases. Thus, the length an electron diffuses before it is lost by attachment is significantly smaller than the cavity dimensions at high pressures, and the breakdown plasma tends to become localized in the region where the ionization is larger than the attachment frequency. This means that as the pressure inside the cavity increases, the region occupied by the plasma becomes successively smaller. This is illustrated in a succinct way in Fig. 1 below. The plasma profile to the left in Fig. 1 is dominated by diffusion to the walls, it varies almost sinusoidally, extends over the entire cavity area, and smoothly approaches zero at the edges. This situation corresponds to low pressure and a breakdown plasma extending over the entire volume. On the other hand, the plasma density profile to the right in Fig. 1 has contracted into a needle-like profile due to the high pressure which decreases the diffusion out of the over-critical region in the center where ionization is larger than the attachment losses.

The breakdown plasma density will also have an extension in the z-direction according to the sinusoidal variation determined by the function $Z(z)$, but in the x,y-plane the curves of constant

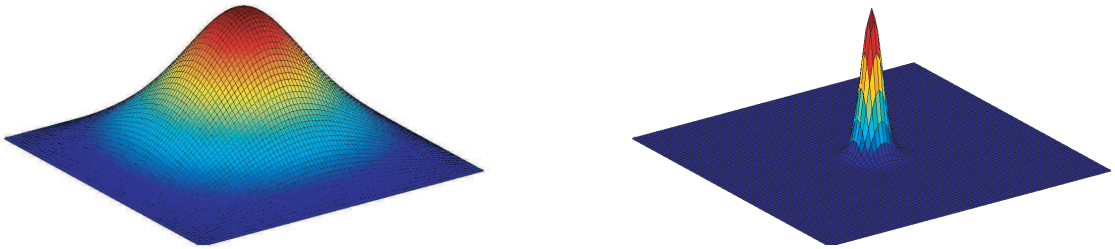

Figure 1: Illustration of the effect of pressure on the extension of the breakdown plasma. Left, low pressure. Right, high pressure.

density describes concentric circles. In the figures shown above, a and b has been chosen equal. If the relative size of the cavity sides is changed, the density curves will describe concentric ellipses in the x, y-plane.

4. BREAKDOWN AROUND A HEMISPHERICAL BOSS

Another important situation is the one where there is a small region of local field enhancement in an otherwise homogeneous field. We have investigated several different models for the ionization profile; a step-like profile, an exponential profile, and a profile corresponding to the field around a small hemispherical boss on an infinite conducting plane. The variation of the field profile was seen to play an important role for the size of the plasma region in the high pressure regime.

In the case of the hemispherical boss, the electric field around the boss is known in explicit form, and is given by

$$E(r,\theta) = E_0\sqrt{\left(1+\frac{2a^3}{r^3}\right)^2\cos^2\theta + \left(1+\frac{a^3}{r^3}\right)^2\sin^2\theta}. \tag{5}$$

where r and θ are spherical coordinates and the profile is rotationally symmetric. The main features of this field are that $E \to E_0$ as $r \to \infty$, and $E \to 3E_0$ as $r \to a$.

We have performed simulations of this problem in a cylindrical coordinate system. The boundary conditions were $n(r = R) = 0$ and $n(z = 0)(z = H) = 0$, where R and H were taken as different multiples of a. For very low pressures, the effect of the field enhancement around the boss was found to be negligible, and the continuity equation, Eq. (2), can be solved using $n(x, y, z) = N(r)Z(z)$, where $Z(z) = \sin(z\pi/H)$ and $N(r) = J_0(r)$ with $J_0(r)$ being the zero order Bessel function. The eigenvalue can then be evaluated exactly as $\lambda = q + \pi^2/H^2 + j_0^2/R^2$, where $j_0 \approx 2.4$ is the first zero of $J_0(r)$. In the pressure regime where this formula is valid, the breakdown plasma will fill the entire volume. However, when the pressure increases, the influence of the boss becomes stronger and eventually the electric field strength necessary to initiate breakdown becomes smaller than that without the field enhancement. The plasma also starts to contract and to become localized around the boss. For even higher pressures, the breakdown threshold will become determined by the balance of attachment and ionization in the very close vicinity of the boss surface. In the purely mathematical limit when the pressure becomes infinite, the plasma region will become infinitely small, and the breakdown threshold is given by the equality $\nu_i(r = a) = \nu_a$. These qualitative considerations are illustrated in Fig. 2 below, which shows the shrinking of the plasma region as the pressure increases. The left figure shows the plasma filling the entire chamber, and the influence of the boss is relatively small, a situation corresponding to low pressures. Only half the plasma section is shown, corresponding to $r \in [0, R]$ and $z \in [0, H]$, the system being symmetric round the z-axis. The right figure shows the breakdown plasma for a higher pressure. Now the situation is completely dominated by the field around the boss, and the plasma region is very small and localized to the vicinity of the boss surface. The numerically obtained predictions for the breakdown thresholds in the rectangular cavity and for the hemispherical boss have been compared with experiments reported in [5] and show excellent agreement, see Fig. 3.

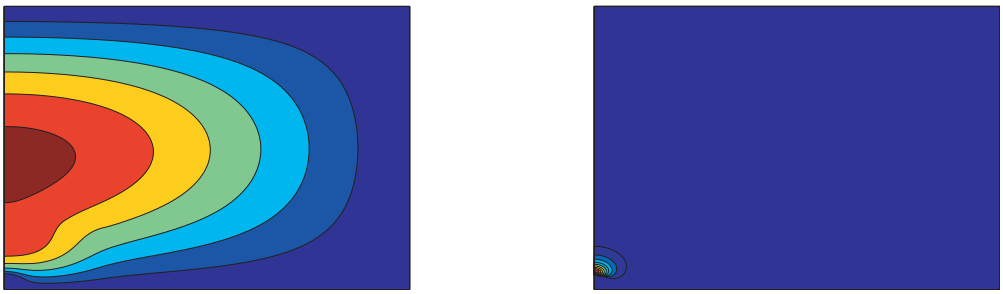

Figure 2: Illustration of the influence of pressure on the extension of the breakdown plasma around a hemispherical boss. Left, low pressure. Right, high pressure.

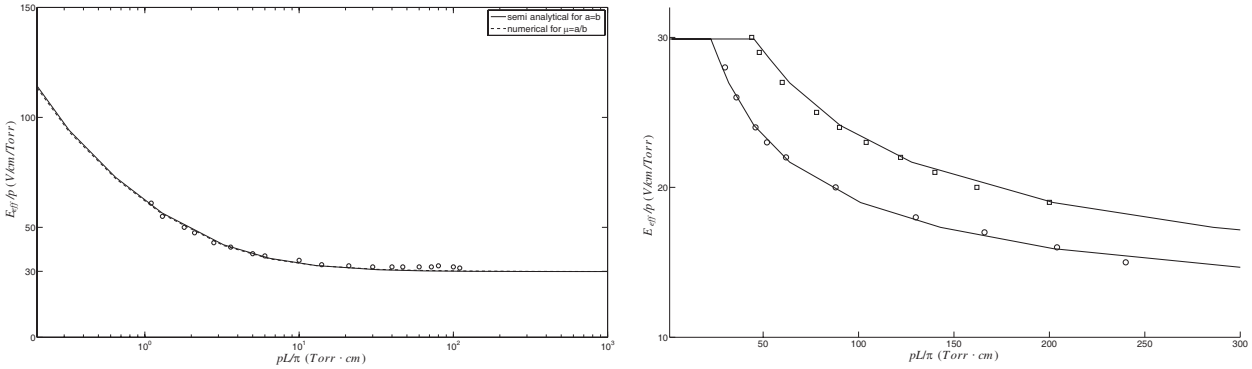

Figure 3: Comparison between experimental results (taken from [5]) and theoretical predictions for the rectangular cavity (left figure — taken from [4]) and for the hemispherical boss for two different boss radii (right figure).

5. CONCLUSION

The two systems analyzed above are very different, but have the common feature of involving inhomogeneous profiles of the electric field strength. In both cases, this makes the quasi-steady plasma region, described by the solution of the continuity equation, change size with changing pressure. With increasing pressure the plasma generally tend to contract around the region with highest electric field. An important implication of this behaviour for rf systems in general should be emphasized: At high pressures in combination with strongly inhomogeneous electric fields, the concomitant small plasma region does not necessarily have an important deleterious effect on the operation characteristics of the rf device. On the other hand, the creation of such a local quasi-steady plasma may lead to significant local absorption of rf power, which heats the surrounding gas and on a longer time scale may lead to important effects on the device, either by causing local melting of surrounding material or by lowering the global threshold so that full scale breakdown occurs. Thus, the stability and power absorbtion of the quasi-steady plasma should also be investigated before any general prediction about the breakdown threshold can be made.

REFERENCES

1. MacDonald, A. D., *Microwave Breakdown in Gases*, John Wiley and Sons, New York, 1966.
2. Jordan, U., D. Anderson, L. Lapierre, M. Lisak, T. Olsson, J. Puech, and V. E. Semenov, "On the effective diffusion length for microwave breakdown," *IEEE Trans. Plasma Science*, Vol. 34, 421, 2006.
3. Taylor, W. C., W. E. Scharfman, and T. Morita, *Advances in Microwaves*, L. Young, editor, Academic Press, New York, 1971.
4. Rasch, J., D. Anderson, M. Lisak, V. E. Semenov, and J. Puech, "Microwave corona breakdown in a gas-filled rectangular resonator cavity," *J. Phys. D: Appl. Phys.*, Vol. 42, 2009.
5. Platzman, P. M. and E. H. Solt, "Microwave breakdown of air in nonuniform electric fields," *Phys. Rev.*, Vol. 119, 1143, 1960.

Measurement of Differential Radar Cross Section of UHF RFID Tags

A. Pouzin[1,2], **T. P. Vuong**[3], **S. Tedjini**[1], **M. Pouyet**[2], **and J. Perdereau**[2]

[1]Laboratoire de Conception et d'Intégration des Systµemes (LCIS), Grenoble INP, France
[2]Laboratoire National de Métrologie et d'Essais (LNE), France
[3]IMEP-LAHC, Grenoble INP, France

Abstract— This paper presents an analysis and a methodology for Differential Radar Cross Section (ΔRCS) measurement.

1. INTRODUCTION

To modulate the backscattered signal, the RFID chip switches its input impedance between two states, which can be seen as an amplitude modulation. In order to improve the reading range, the tag's antenna is generally matched to the impedance of the chip. The matching is performed in special conditions, i.e., at a given frequency and usually for tag placed in free space. However, we know that the impedance of the chip is a function of frequency and received power and the impedance of the antenna is highly dependent on the support on which the tag is placed [1]. There are numerous papers on the RCS [2–5] but only few works are related to the analysis of the ΔRCS and its importance on the determination of the tag performances [6, 7]. The ΔRCS is an important parameter in the tag performance determination when the distance of communication is dependent on the quality of backscattered signal by the tag. This is the case of semipassive tags and in some conditions when a passive tag is no longer in the expected configuration of use, for example when it is mounted on a disruptive, or it is physically deformed, or the reader operates at a frequency other than the tag's resonance.

2. PROTOCOL

For the ΔRCS measurement, we reform the "transmitter-tag-receiver" link (Fig. 1).

The Agilent MXG-N5182A vector signal generator sends a query command. The tag response is received on the Tektronix RSA3408A real-time spectrum analyzer in the form of I/Q baseband signals as shown on the Fig. 2.

Calibration of the measurement system is necessary in order to remove systematic errors due to the input port mismatch and internal reflections inside the anechoic chamber. To calculate backscattered signal by the tag, we subtract the reference measurement for empty anechoic chamber without tag from the measured value in the presence of the tag.

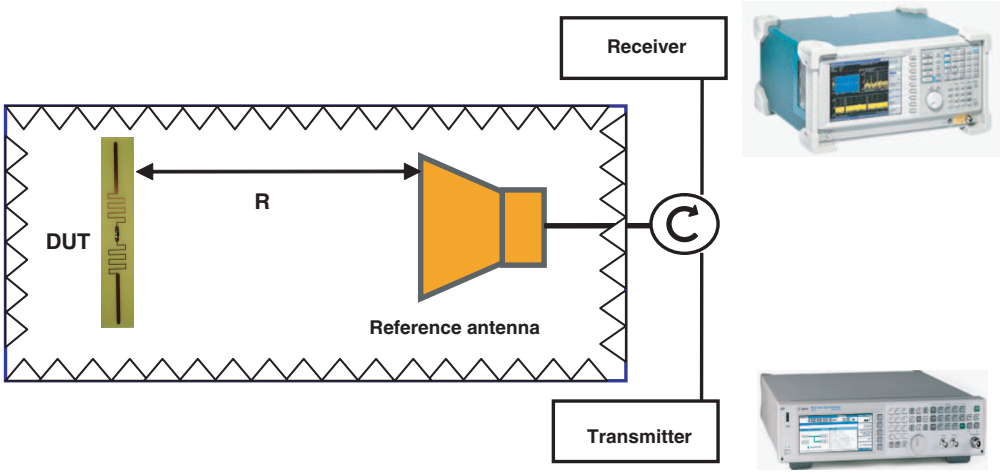

Figure 1: Experimental setup to measure the ΔRCS of the tag in the mono-static configuration.

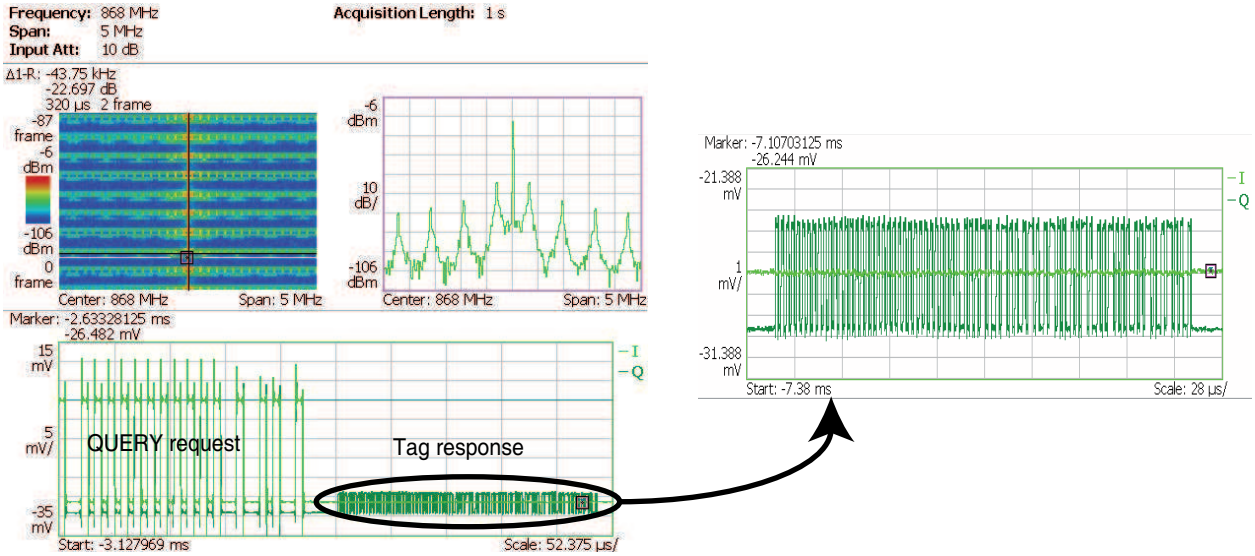

Figure 2: Query request and tag response received on the RSA3408A in the form of I/Q baseband signals.

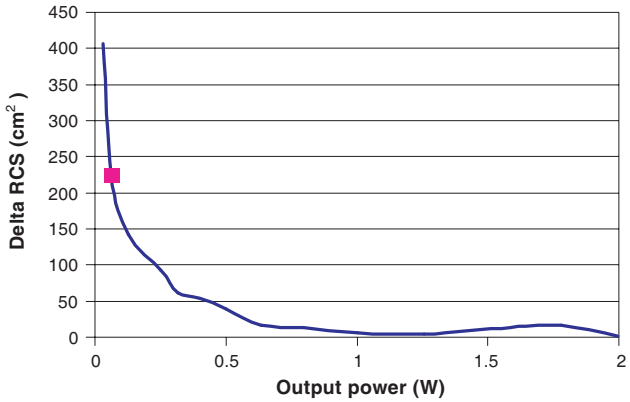

Figure 3: Measurement result of the ΔRCS of a tag as a function of the transmitter output power at a frequency of 868 MHz.

Finally, the ΔRCS can be determined from the difference between the low and high levels of the backscattered power as

$$\Delta RCS = \frac{\Delta P_R}{P_T} \frac{(4\pi)^3 R^4}{G_{ref}^2 \lambda^2} \tag{1}$$

where P_T is the transmitted power at the antenna port, G_{ref} is the reference antenna gain and R is the distance between the reference antenna and the tag.

3. RESULTS

The Fig. 3 shows the ΔRCS of a commercialized tag as a function of the reader output power for a frequency set at 868 MHz.

As specified in the ISO 18000-6 standard, the ΔRCS is greater than 50 cm^2 when output power is equal to 1.2 times the threshold power. Furthermore, it decreases when the power increases, in this manner the depth of modulation seen by the reader remains constant.

4. CONCLUSION

In this paper, we have developed a useful methodology for Differential Radar Cross Section (ΔRCS) measurement. The ΔRCS is expressed as a function of the ratio of power sent by the transmitter and the power reflected from the tag. Measurement results are those we expected. In the near future, we will carry out other measurement, explore the ways of measuring the ΔRCS as a function of frequency.

We expect these research results to enable the characterization of UHF RFID tags.

REFERENCES

1. Pillai, V., "Impedance matching in RFID tags: To which impedance to match?," *IEEE Antennas and Propagation International Symposium*, 3505–3508, June 2006.
2. Kim, G., Y. Park, and Y. C. Chung, "Circular UHF RFID tag antenna and relashionship between reading range and RCS of the tag antenna," *IEEE Antennas and Propagation International Symposium*, 1757–1760, June 2007.
3. Rao, K. V. S., P. V. Nikitin, and S. F. Lam, "Antenna design for UHF RFID tags: A review and a practical application," *IEEE Transaction on Antennas and Propagation*, Vol. 53, No. 12, December 2005.
4. Nikitin, P. V. and K. V. S. Rao, "Theory and measurement of backscattering from RFID tags," *IEEE Antennas and Propagation Magazine*, Vol. 48, No. 6, 212–218, December 2006.
5. Penttilä, K., M. Keskilammi, L. Sydanheimo, and M. Kivikoski, "Radar cross-section analysis for passive RFID systems," *IEE Proceeding — Microwaves Antennas and Propagation*, Vol. 153, No. 1, 103–109, February 2006.
6. Yen, C. C., A. E. Gutierrez, D. Veeramani, and D. van der Weide, "Radar cross-section analysis of backscattering RFID tags," *Antennas and Wireless Propagation Letters*, Vol. 6, 279–281, 2007.
7. Nikitin, P. V., K. V. S. Rao, and R. D. Martinez, "Differential RCS of RFID tag," *Electronics Letters*, Vol. 43, No. 8, 2007.

Optimising of Node Coordination in Wireless Sensor Network

Nik Noordini Nik Abd Malik, **Mazlina Esa**,
Sharifah Kamilah Syed Yusof, **and Jayaseelan Marimuthu**
Faculty of Electrical Engineering, Universiti Teknologi Malaysia
81310 UTM Skudai, Johor, Malaysia

Abstract— Beamforming has been introduced in Wireless Sensor Networks (WSNs) in order to increase the transmission range of individual sensor nodes. One approach of optimizing node coordination is by implementing the theory of linear array for beamforming method. The approach is presented in this paper. The linear sensor node array (LSNA) is constructed within random sensor node deployment. The LSNA is optimized as a conventional uniform linear array (ULA) to minimize the position errors which will improve the beamforming performance in terms of gain, transmission range and characteristics. A simulation model is implemented to study the adaptive LSNA. Several scenarios were evaluated by comparing with the theoretical results of conventional ULA. The performance of the constructed adaptive LSNA demonstrated an excellent agreement compared to the conventional ULA.

1. INTRODUCTION

Wireless sensor networks (WSNs) have been extensively researched and analyzed in the communication research community. One significant issue that exists in WSN applications is the requirement to transmit data over long distance using individual power-constrained sensor node. By using a limited power source, these sensor nodes in WSNs have very limited lifetime thus contribute to the issues of restricted communication and computing capabilities [2]. Nevertheless, the transmission range of sensor nodes can be improved based on the beamforming theoretical [3, 4]. In WSN environment, the sensor nodes can be deployed in the form of clusters within the random deployment. In these clusters, the sensor nodes act collaboratively as a set of small non-directional antennas to simulate a large directional antenna. Each sensor node will share the data with other sensor nodes in the cluster before synchronously transmitting it to the receiver. The nodes can cooperate to coordinate their radiated transmission into a narrow beam that increases the transmission range. Thus, it can concentrate the radiation power in the desired direction whilst decrease the power loss in other directions.

Recently, there has been increased attention in using advanced beamforming technologies in WSNs. Implementation of beamforming algorithms in WSNs environment made use of signal processing techniques [5, 6]. Most of the reported work analyzes the performance of beamforming using the theory of random arrays. The random topology condition will generate phase errors thus affecting the performance of the antenna array. Hence, resulting in degraded beamformer performance, compared to that of an array of equally spaced fixed elements. Works on the linear array have been proposed [7, 8] to overcome such random deployment issues. In this paper, the work of [9, 10] are referred. Earlier work reported in [11] is extended which includes the sensor nodes coordination that utilizes an adaptive linear sensor node array (LSNA). Each sensor node is assumed with identified location and equipped with isotropic antennas which in random deployment. The normalized power gain characteristics derived in the case of the adaptive LSNA are compared with the conventional uniform linear array (ULA).

2. SYSTEM MODEL AND RADIATION PATTERN OF THE ANTENNA ARRAY

The geometrical configuration of the randomly distributed sensor nodes and the target point are illustrated in Fig. 1. All the sensor nodes are assumed to be located on the x-y plane. Each sensor node is denoted in Cartesian coordinate (x_k, y_k) while the location of the target point is given in spherical coordinates, $R_x(R, \phi_0, \theta_{\alpha 0})$. The angle $\phi \in [-\pi, \pi]$ represents the azimuth direction and $\theta \in [0, \pi]$ represents the elevation angle. In the system modeling, the following assumptions are made:

(i) Sensor nodes are plotted in random distribution inside the region of interest of $100\,\mathrm{m}^2$.
(ii) Each sensor node is modeled as isotropic antenna element and mutualcoupling between nodes is excluded.
(iii) There is no multipath fading or shadowing.

After deployment, the sensor nodes intelligently organize themselves into clusters. Each cluster has a centre node (CN) designated as the head which manages and organizes a subset of its sensor nodes into a LSNA. A linear array of q_k isotropic elements as shown in Fig. 2 is constructed as a ULA. The CN also acts as the centre of the ULA. If d_k is the distance between the kth node and the reference node at the origin, then the signal $s(t)$ arrives t_k seconds earlier at the kth element, with respect to the reference sensor node [9] as given by:

$$t_k = \frac{d_k \cos\theta_{\alpha 0}}{c} \tag{1}$$

where c is the speed of light and d_k is the distance of the kth element.

Each array element is weighted by a complex weight w_k

$$w_k = I_k e^{j\omega t_m \theta_{\alpha 0}} \tag{2}$$

for $k = 0, 1, 2, \ldots, K-1, K$ which multiplies the incoming signal.

The amplitude of each element response, I_k, is assumed to be unity. The summation of all the elements' weighted inputs equals the radiation pattern (the spatial response) of the array or the array factor [9], $F(\theta_\alpha)$. By using Eq. (1) and the wave number $\beta = 2\pi/\lambda$, this is written as:

$$F(\theta_\alpha) = \sum_{k=1}^{K} w_k^* e^{j\beta d_k \cos\theta_\alpha} \tag{3}$$

The maximum value of $F(\theta_\alpha)$ at $\theta_\alpha = \theta_{\alpha o}$ is the main lobe of the radiation pattern pointing towards $\theta_{\alpha o}$. The normalized power gain G is given by

$$G(\theta_\alpha) = \frac{|F(\theta_\alpha)|^2}{\max|F_{\theta\alpha}(\theta_\alpha)|^2} \tag{4}$$

3. NODE COORDINATION

Initially, 150 sensor nodes are randomly plotted. Each sensor node will communicate with nearby neighbor nodes which are located within the communication radius. The algorithm starts by selecting the CN which has the most neighbor nodes within its communication radius. Then, the active cluster is determined by referring to the CN as the centre of a cluster. A linear array of nodes is then constructed in the randomly deployed sensor nodes with internode spacing of $\lambda/2$. For case-study, a linear array of 9-nodes was constructed.

The development of the algorithm is aimed at determining the optimum sensor nodes coordination for beamforming. The radiation beampattern from the optimum LSNA has to be comparable to that of the ULA. Instead of exploiting all the sensor nodes in the active cluster, the algorithm is designed to choose only one set of sensor nodes in the linear node coordination that approximates the ULA. ULA is assumed with internode spacing of $\lambda/2$, isotropic antenna elements, and the CN represents the centre element as shown in Fig. 2.

A virtual line that passes through the CN is first constructed using the line equation

$$f(x) = m_2 x + m_1 \tag{5}$$

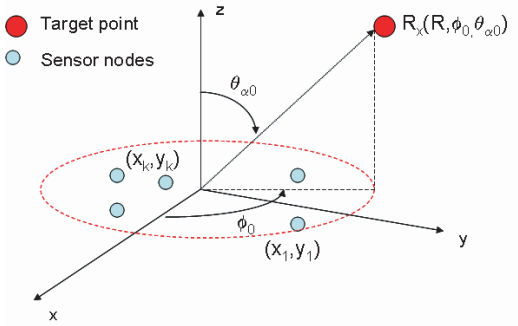

Figure 1: Definition of notations.

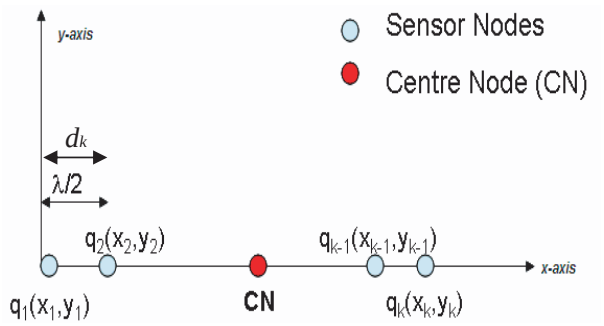

Figure 2: LSNA of equally spaced isotropic elements.

where m_2 is a virtual line slope and m_1 represents the offset of the origin. The CN is located at the centre point of the virtual line. By constructing the virtual line, selection of the sensor nodes is realizable. The ideal coordinate for the node's location is then identified by referring to the virtual line to demonstrate the ULA.

$$q(x_{k+1}, y_{k+1}) - q(x_k, y_k) = \lambda/2 \tag{6}$$

where $k = 1, 2, \ldots, 9 \cong$ number of elements, and $q(x_k, y_k)$ is the coordinate of the kth element. Fig. 3 shows the virtual line being constructed in MATLAB environment that passes through the CN.

Consequently, the algorithm intelligently optimizes the sensor node coordination in order to form an optimum LSNA. Two simulation scenarios in MATLAB environment are shown in Figs. 3 and 4. It is observed that from the random deployment of sensor nodes, the active cluster has been selected with reference to the chosen CN. The optimization of the LSNA has been successfully accomplished for 20 iterations. The process was repeated in different angles for optimum LSNA.

4. COMPARISON OF NODE COORDINATIONS

Performance comparisons of the optimized 9-element LSNA with 9-element conventional ULA are possible with the incorporation of beampattern analysis feature in the simulation environment. Figs. 3 and 4 show the first and second iterations of node coordination with different angles, while Figs. 5 and 6 illustrate the beampattern analysis of the node coordination, respectively.

From Figs. 5 and 6, it can be observed that the normalized array factor or normalized gain demonstrates maximum gain at the desired angle of 45°. It can be inferred that by using adaptive LSNA, the radiation power can be concentrated only to the desired angle or direction while suppressing the radiation powers at other angles. The optimized LSNA causes severe impact on the

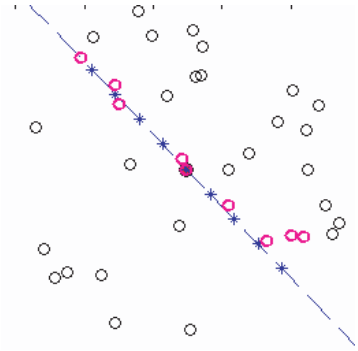

Figure 3: 1st iteration of sensor node coordination. Blue star and magenta circle denotes ULA and LSNA, respectively.

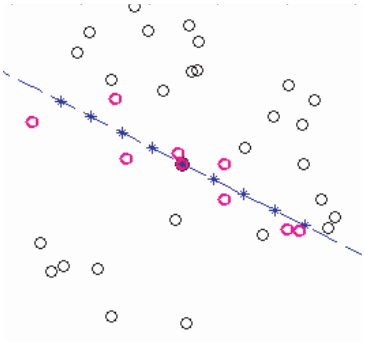

Figure 4: 2nd iteration of sensor node coordination. Blue star and magenta circle denotes ULA and LSNA, respectively.

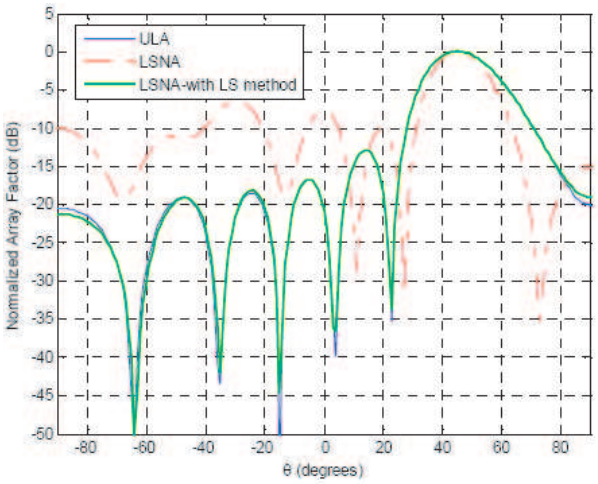

Figure 5: Normalized array factors of 1st iteration.

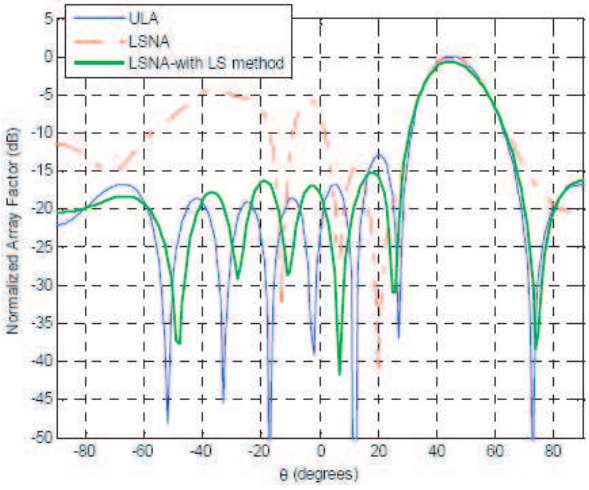

Figure 6: Normalized array factors of 2nd iteration.

increment of the sidelobe levels but only minimal reduction for the main lobe gain. However, by using Least Square (LS) method, the beampattern analysis of LSNA demonstrates excellent agreement with the performance of ULA. The maximum normalized power gain remains unchanged although in the presence of position errors in the LSNA coordination. In addition, the gain of the first sidelobe level also shows a promising performance and also only a slight decrements of the other lobes.

The simulated results also demonstrate the different effect on the beampattern performance with the alteration of the node coordination. Fig. 5 illustrates a wider 3-dB beamwidth compared to the 3-dB beamwidth of Fig. 6. The desired beampattern performance can be selected by using the beampattern analysis in order to meet the desired transmission signal.

5. CONCLUSION

The combination of the transmission of multiple sensor nodes is proven to provide greater transmission distances. The array geometry that has been considered is LSNA. The node coordination is optimized to identify the most excellent node coordination to participate in the LSNA. Simulation results illustrate that the construction of the adaptive-LSNA from random deployment offer superior performance to closely approximate conventional ULA.

ACKNOWLEDGMENT

The work is supported by Universiti Teknologi Malaysia and Ministry of Higher Education, Malaysia.

REFERENCES

1. Akyildiz, I. F., W. Su, Y. Sankarasubramaniam, and E. Cayirci, "Wireless sensor networks: A survey," *IEEE Communications Magazine*, 102–114, August 2002.
2. Chen, J. C., K. Yao, and R. E. Hudson, "Source localization and beamforming," *IEEE Signal Processing Magazine*, March 2002.
3. Ochiai, H., P. Mitran, H. V. Poor, and V. Tarokh, "Collaborative beamforming for distributed wireless ad hoc sensor networks," *IEEE Trans. Signal Processing*, Vol. 53, No. 11, 4110–4124, November 2005.
4. Mudumbai, R., G. Barriac, and U. Madhow, "On the feasibility of distributed beamforming in wireless networks," *IEEE Trans. Wireless Communications*, Vol. 6, No. 5, 1754–1763, May 2007.
5. Yao, K., R. E. Hudson, C. W. Reed, D. Chen, and F. Lorenzelli, "Blind beamforming on a randomly distributed sensor array system," *IEEE Journal on Selected Areas in Communications*, Vol. 16, No. 8, 1555–1567, October 1998.
6. Xu, F., G. Zhong, D. D. Richard III, and A. N. Willson, Jr., "A ringprocessor based blind beamformer design for use in wireless sensor networks," *Proc. of Int. Sym. on Circuits and Systems (ISCAS 2002)*, Vol. 4, IV205–IV208, 2002.
7. Vincent, P., M. Tummala, and J. McEachen, "A beamforming approach for distributed wireless sensor networks," *Proc. of IEEE Int. Conf. on System of Systems Engineering*, 1–6, April 2007.
8. Papalexidis, N., T. O. Walker, C. Gkionis, M. Tummala, and J. McEachen, "A distributed approach to beamforming in a wireless sensor network," *Proc. of IEEE Forty-first Asilomar Conference on Signals, Systems and Computers*, 4–7, November 2007.
9. Litva, J. and T. Kwok-Yeung Lo, *Digital Beamforming in Wireless Communications*, Artech House, Boston, 1996.
10. Mouhamadou, M., P. Vaudon, and M. Rammal, "Smart antenna array patterns synthesis: Null steering and multi-user beamforming by phase control," *Progress In Electromagnetics Research*, PIER 60, 95–106, 2006.
11. Malik, N. N. N. A., M. Esa, and S. K. S. Yusof, "Intelligent optimization of node coordination in wireless sensor network," *Conference on Innovative Technologies in Intelligent Systems & Industrial Applications (CITISIA 2009)*, 25–26, July 2009.

The Influence of Fog on the Propagation of the Electromagnetic Waves under Lithuanian Climate Conditions

S. Tamosiunas[1, 2], **M. Tamosiunaite**[1, 2], **M. Zilinskas**[1, 3], **and M. Tamosiuniene**[4]

[1]Faculty of Physics, Vilnius University, Sauletekio 9, LT-10222 Vilnius, Lithuania
[2]Institute of Materials Science and Applied Research, Vilnius University
Sauletekio 9, LT-10222 Vilnius, Lithuania
[3]Department of Radio Communication
Communications Regulatory Authority of the Republic of Lithuania
Algirdo 27, LT-03219 Vilnius, Lithuania
[4]Semiconductor Physics Institute, A. Gostauto 11, LT-01108 Vilnius, Lithuania

Abstract— The types of fog and the existing methods of calculation of the electromagnetic waves attenuation due to fog are reviewed. The meteorological data, which was measured in the localities of Lithuania, has been analyzed. According to this data, the specific attenuation due to fog has been computed under the Lithuanian climatic conditions. The models that have been used in calculations of fog attenuation are based on the liquid water content and optical visibility.

1. INTRODUCTION

Moist fog frequently appears over the localities of Lithuania. The influence of fog on the attenuation of the electromagnetic waves can lead to the perturbation of the wireless communication. In [1], it was mentioned that fog may be one of dominant factors in determining the reliability of millimeter wave systems, especially in coastal areas where dense moist fog with high liquid water content happen frequently. Fog results from the condensation of atmospheric water vapor into water droplets that remain suspended in air [2]. Fog can be characterized by water content, optical visibility, drop size distribution and temperature [1, 3]. Several meteorological mechanisms will determine whether fog will form and degree of its intensity. There were observed a strong influence of wind, turbulence, radiation, surface configuration and wetness on the fog formation. The physical mechanism of the formation of the fog can be reduced to three processes: cooling, moistening, and vertical mixing of air parcels with different temperatures and humidity; all three processes can occur, although one meteorological mechanism may dominate [4]. This circumstance leads to the different types of the fog. There are several types of fog. The main types of fog are the advection fog and the radiation one [3, 5]. Both types of fog differ in the location and in the methods of formation. In [6], the fog is classified in four types: strong advection fog, light advection fog, strong radiation fog, and light radiation fog. Radiation fog forms when the ground becomes cold at night and cools the adjacent air mass until it becomes supersaturated. Advection fog forms when warm moist air moves across a cooler surface [5, 7]. The influence of the local factors in the formation of radiation fog was studied in [3, 5]. In [7], it was mentioned that average drop size of an advection fog is usually larger than that of a radiation fog. The advection fog is coastal fog, and the radiation fog is inland fog. The advection fog may cover the hundred thousands of kilometers. The advection fog has no cleared away even by day. The water vapor content of fog varies from less than 0.4 up to as much as $1\,\mathrm{g/m^3}$; typical liquid water content values for the fog vary from 0.1 to $0.2\,\mathrm{g/m^3}$ [2].

There are many foggy days in a year in Lithuania. In the year 1958, there were 100–122 foggy days in the North and in the East Lithuania, and there were 130–141 foggy days in Samogitian Hill. There were 107–113 foggy days in Samogitian Hill in the year 1964. There were 20 foggy days in July of 1977 year in Vilnius. This month was the foggiest month from the year 1875 in Vilnius. The visibility was only 100 meters on 15–17 October 1991. Even on 18 hours the moist fog covers Varena in 2–3 November 1984. On 15 hours the moist fog covers the Airport of Vilnius in 9–10 March 1994. In light of these facts, it is necessary to analyze the influence of the fog on the attenuation of electromagnetic waves when the telecommunication systems are planning in Lithuania.

In [8], the values of the electromagnetic waves attenuation due to the rain and clouds have been determined by using the meteorological data measured at the ground level in the localities of Lithuania. However, the influence of fog on the propagation properties of the electromagnetic waves at the Lithuanian climatic conditions as far, as we know, has been no examined yet.

The main goals of the paper were to analyze the fog events in Lithuania, to review the methods for determining fog attenuation, and to apply them for the calculation of the fog attenuation under the Lithuanian climatic conditions.

2. CALCULATION METHODS FOR DETERMINING OF FOG ATTENUATION

The calculation methods for determining of fog attenuation are frequently used. In [9], a one-dimensional radiation fog model, which includes a detail description of the interaction between atmospheric radiative transfer and the microphysical structure of the fog was presented. In [10] model, attenuation due to clouds and fog was expressed in terms of the water content, and was mentioned that microstructure of the fog can be ignored for fog consisting entirely of small droplets at frequencies below 200 GHz. The parameters of gamma drop size distribution model of fog and clouds are derived based on the liquid water content and optical visibility in [6] and [10]. The propagation properties for microwave and millimeter-wave frequencies at the foggy air conditions were examined in [11]. The values of the specific attenuation were derived from a complex refractivity based on the Rayleigh absorption approximation of Mie's scattering theory. In [11], the particle mass content and permittivity, which depends on the frequency and the temperature, were key variables.

Attenuation due to fog is a complex function of the density, extent, index of refraction, and wavelength. Normalized fog attenuation directly, given only the wavelength and fog temperature is presented in [7]:

$$A = -1.347 + 0.0372\lambda + 18.0/\lambda - 0.022t \tag{1}$$

where A is attenuation in (dB/km)/(g/m^3), λ is wavelength in mm, t is temperature in °C. The relation (1) is valid only if 3 mm $< \lambda <$ 3 cm and -8°C $< T <$ 25°C.

It was mentioned in [7], that the total fog attenuation could be obtained by multiplying the normalized attenuation by the fog density in g/m^3 and the fog extent in km.

Fog is often characterized by the visibility. The visibility is defined as the greatest distance at which it is just possible for an observer to see a prominent dark object against the sky at the horizon in [7]. In [3], the visibility is defined as that distance from an observer at which a minimum contract ratio C between a black target and a bright background is equal to $C = 0.02$. It was noted in [12], that within each fog classification the liquid water content decreases as the visibility increases. The relation of visibility V (km) and optical attenuation α (dB/km) was presented in [3]:

$$V = 4.343/\alpha \ln|1/C| = 16.99/\alpha \tag{2}$$

In [7], the empirical formula for fog visibility as a function of fog density was derived:

$$V = 0.024M^{-0.65} \tag{3}$$

where V is the visibility in km and M is the liquid water content in g/m^3.

It was mentioned in [7], that the empirical formula (3) is valid for drop diameter between 0.3 µ and 10 µ. For the case of dense haze or other special type fogs, the coefficient 0.024 recommends be replaced by 0.017 in [11]. If the visibility data are available, but the fog density data are not available, the following expression may be used for fog [7, 12]:

$$M = (0.024/V)^{1.54} \tag{4}$$

In [1, 6], and [10] based on the Rayleigh approximation, the specific attenuation due to the fog α_{fog} has been written as:

$$\alpha_{\text{fog}} = KM \text{ (dB/km)} \tag{5}$$

where K is specific attenuation coefficient expressed in dB/km/g/m^3:

$$K = 6.0826 \cdot 10^{-4} f^{-1.8963} \theta^{\gamma} \tag{6}$$

where $\gamma = (7.8087 - 0.01565 \cdot f - 3.0730 \cdot 10^{-4} f^2)$, $\theta = 300/T$, f is frequency (GHz), and T is temperature (K).

3. RESULTS AND DISCUSSION

Analysis of meteorological data measured in Lithuanian weather stations show, that the climate of Lithuania is variable and contrasting. Depending on the relief of locality, there are differences in the distribution of the foggy days. In average, there are 90–105 foggy days a year in the west slant of Samogitian Hill and there are 60–80 ones in the west slant of Baltic Hill [5]. Only 38–51 foggy days a year were registered in Lowland of Lithuania Mid. In Lithuania, November–March are the foggiest months in a year. March–May are the foggiest months in a year in Seacoast of Lithuania. However, there are least of all foggy days in May–July in the other part of territory. In average, there are 350–650 foggy hours a year in Lithuania (most of them were observed in Samogitian Hill and in East of Lithuania) [5].

According to the data measured in Lithuanian weather stations, in average, there are 41–105 foggy days a year in Lithuania. 4–6 hours is the average duration of a fog event. However, the maximum duration of the fog event is several days. In Lithuania, according to the data of Lithuanian Hydrometeorological Service, the advection fog events consist 50–60% of all the fog events and the radiation ones consist 20–30% of all the fog events.

By using (4) we determined M values in the cases when the values of visibility V (the data of visibility was taken from the website http://www.rp5.ru) were starting from 0.1 km up to 1 km (see Table 1). It is seen, that the M values various from $0.003\,\mathrm{g/m^3}$ up to $0.111\,\mathrm{g/m^3}$ in the localities of Lithuania.

In March 2008 and February 2009, the Values of Visibility V Varied from 0.5 km up to 10 km in Klaipeda.

Table 1: The values of fog water content M.

V, km	M (g/m^3)
0.1	0.111
0.2	0.038
0.3	0.020
0.5	0.010
1.0	0.003

Table 2: The duration τ of the periods with the different V in February 2009 in Klaipeda.

V, km	τ, hr	%
0.5	27	4.0
2.0	3	0.5
4.0	222	33.0
10.0	351	52.3

Table 3: The duration τ of the periods with different V in March 2008 in Klaipeda.

V, km	τ, hr	%
0.5	24	3.5
2.0	30	4.5
4.0	87	12.0
10.0	593	80.0

It is worth to mention, that the fog events with the visibility $V \leq 1$ km were observed in afternoon and night in most cases in the localities of Lithuania.

The values of visibility V on the 8th of October 2008 in Kaunas, Klaipeda, and Laukuva (Laukuva is the dampest locality of Lithuania; the average annual amount of precipitation is 820 mm) are presented in Table 4. It is clearly seen the difference in these values. The data of visibility observed in Lithuanian weather stations in that day show, that the strong fog (with the visibility of $V = 0.1$ km) was in Kaunas, Lazdijai, and in the vicinities of Vilnius. Almost all the territory of Lithuania swims in fog in most part of the night on 8th of October 2008. The visibility of 1 km or above was only over the Seacoasts and over the pinewood of Dzukija. The ideal conditions for formation of fog (high pressure, anticyclone (Indian summer) the bright sky at days, and high humidity) there were at days. When the sun was down, the water vapour condensed into the water drops. Such type of fog is a radiation one.

The fog event with $V = 0.5$ km was observed in Laukuva on the 16th–18th of November 2006. The duration of this fog event was 45 hours (6.25% of the month time). Almost all the time the humidity was about 100% in this period. The average temperature of the period mentioned above was 6.2°C.

There is the Geographical Centre of Europe near the city of Lithuania Vilnius and it was interesting to analyse the conditions of radio wave propagation in this locality. Analysis of meteorological data measured in Vilnius shows, that there were 267 foggy hours in the year 2008 (approximately 3% of the year time) when the visibilities V were of 0.3–1 km. The middle fog (the values of visibility were of 0.3–0.5 km) hovers over Vilnius 147 hours in the year 2008 (approximately 1.7% of the year time). February was the foggiest month in 2008 in Vilnius (63 hours). There were no foggy days in June of 2008 in Vilnius. Only 3 foggy hours were in March and August. The foggiest months were October–February. It corresponds to the general tendency of weather in Lithuania.

Table 4: The values of visibility V on 8th October 2008 in Kaunas, Klaipeda, and Laukuva.

Locality / Time	Kaunas V, km	Klaipeda V, km	Laukuva V, km
21.00	0.2	10.0	10.0
18.00	20.0	10.0	10.0
15.00	10.0	10.0	10.0
12.00	0.2	10.0	10.0
09.00	0.2	4.0	10.0
06.00	0.1	4.0	0.5
03.00	0.5	4.0	0.5
00.00	0.5	4.0	4.0

Even 60–63 foggy hours there were in January, February, and November in Vilnius. There were often the foggy days a year with visibilities of 1–10 km in Vilnius (7173 hours); even 735 hours with visibilities from the range mentioned above were in December.

In the morning of the 7th of November 2006, the moist fog covers Kaunas. The visibility V was only 0.2 km. The value of $M = 0.038\,\mathrm{g/m^3}$ was determined by using Eq. (4).

As already was mentioned above, the data of visibility V varies in location. In Laukuva, there were 99 foggy hours in December 2008 when $V = 0.5$ km (13.3% of month time) and 3 hours when $V = 1.0$ km (in the other time, the visibility was above the value of $V = 1.0$ km).

As already was mentioned above, the visibility varies in time. The data of visibility measured in December of 2008 in Siauliai confirms this proposition. The duration of the events with $V = 20$ km was 426 hours in this month. However, there were 15 hours with $V = 0.5$ km and even 27 hours with $V = 0.2$ km.

On the 6th of December 2008, there was fog event with visibility of $V = 0.2$ km in Siauliai. The duration of this event was 18 hours except 3 hours within this period when the visibility value was of $V = 0.5$ km.

Table 5: The number of hours with visibilities of $V = 0.5$ km in Laukuva.

Year	**Jan**	**Feb**	**Mar**	**April**	**May**	**Jun**	**Jul**	**Aug**	**Sep**	**Oct**	**Nov**	**Dec**
2006	42	30	27	39	12	18	6	24	18	33	105	36
2007	6	9	132	12	9	9	12	–	24	24	147	60
2008	33	66	30	27	6	12	12	3	18	30	27	99

The visibility data shows that the visibility of $V \leq 0.5$ km was on 366 hours a year (4.2% of time) in Laukuva and on 150 hours per year (1.7% of time) hours in Vilnius in 2008. The duration of fog events with visibilities $V \leq 1$ km was of 273 hours (3.1% of year time) and total duration fog and mist events with $V \leq 10$ km was of 507 hours (5.8% of year time) in the year 2008 in Vilnius.

As far as we have been collected and analysed the visibility data in different localities of Lithuania, the least value of the visibility $V = 0.1$ km has been observed. The value $M = 0.111$,g/m^3 was obtained by using the relationship (4). By using relationship (1) and the meteorological data measured on 8th of October 2008 in Kaunas, we determined normalized fog attenuation A. The value of $A = 5.31\,\mathrm{dB/km/g/m^3}$ was obtained when $f = 90$ GHz and $t = -0.5°$C. Since the visibility $V = 0.1$ km was in that night, we by using the value of $A = 5.31\,\mathrm{dB/km/g/m^3}$ and the value of $M = 0.111\,(\mathrm{g/m^3})$ determined the specific fog attenuation A_s. The value of $A_s = 0.589\,\mathrm{dB/km}$ was obtained and it is the highest A_s-value determined by using the visibility — data analysed here. The least value of water content within fog is $M = 0.003\,\mathrm{g/m^3}$ and the minimum value $A_s = 0.0159\,\mathrm{dB/km}$ has been determined.

Fog is a cloudbank that is in contact with the ground [13]. Therefore, we determined the water content M at the height $h = 5$ m by using the semi–empirical cloud attenuation model presented in [14, 15] and relationships proposed in [2]. We consider the fog event on 8th October 2008 in Kaunas ($t = -0.5°$C, $H = 100\%$, $V = 0.1$ km). The value of $M = 0.051\,\mathrm{g/m^3}$ has been determined and it is lower than one determined using relationship (4). However, it is more near the value of $0.065\,\mathrm{g/m^3}$ determined when the coefficient 0.024 in (4) was replaced by coefficient 0.017. It

is worth to mention, that value of $M = 0.051\,\mathrm{g/m^3}$ was determined in that case when the height above the ground was 5 m and this value may be lower than one at the ground surface.

4. CONCLUSIONS

The meteorological data measured in the localities of Lithuania have been analyzed. It was obtained, that the values of visibility varied starting from 0.1 km up to 1 km when fog has been formed under the localities of Lithuania. The differences in the values of visibility have been observed both in the locations and time. The total duration of strong and middle fog events with visibilities of $V \leq 0.5\,\mathrm{km}$ was 366 hours a year (4.2% of time) in 2008 in Laukuva and 150 hours a year (1.7% of time) in Vilnius. In Vilnius, the total duration of fog events with visibilities $V \leq 1\,\mathrm{km}$ was of 507 hours (5.8% of time). The least value of water content is $M = 0.003\,\mathrm{g/m^3}$ and the maximum one is $0.111\,\mathrm{g/m^3}$. The highest A_s-value determined by using the visibility — data analysed here is $A_s = 0.589\,\mathrm{dB/km}$. The least value of water content is $M = 0.003\,\mathrm{g/m^3}$ and the minimum value $A_s = 0.0159\,\mathrm{dB/km}$ has been determined. The value of the coefficient in relationship (4) will be specifying according the Lithuanian climate conditions when more meteorological data would be collected.

REFERENCES

1. Chen, H., J. Dai and Y. Liu, "Effect of fog and clouds on the image quality in millimeter communications," *Int. J. of Infrared and Millimeter Waves*, Vol. 25, No. 5, 749–757, 2004.
2. Freeman, R. L., *Radio System Design for Telecommunications*, John Wiley & Sons, Inc., New York, 2009.
3. Zhao, Z. and Z. Wu, "Millimeter-wave attenuation due to fog and clouds," *Int. J. of Infrared and Millimeter Waves*, Vol. 21, No. 10, 1607–1615, 2000.
4. Duynkerke, P. G., "Radiation fog: A comparison of model simulation with detailed observations," *Monthly Weather Review*, Vol. 119, 324–341, 1991.
5. Bukantis, A., *The Unusual Natural Phenomena in the Territory of Lithuania in the 11th–20th centuries*, Geography Institute, Vilnius, 1998 (in Lithuanian).
6. Galati, G., I. Dalmasso, G. Pavan, and G. Brogi, "Fog detection using airport radar," *Proceedings of International Radar Symposium IRS 2006*, 209–212, Krakow, Poland, May 24–26, 2006.
7. Altshuler, E. E., "A simple expression for estimating attenuation by fog at millimeter wavelengths," *IEEE Trans. on Antennas and Propagation*, Vol. 32, No. 7, 757–758, 1984.
8. Zilinskas, M., M. Tamosiunaite, S. Tamosiunas, and M. Tamosiuniene, "The influence of the climatic peculiarities on the electromagnetic waves attenuation in the Baltic Sea region," *PIERS ONLINE*, Vol. 4, No. 3, 321–325, 2008.
9. Bott, A., U. Sievers, and W. Zdunkowski, "A radiation fog model with a detailed treatment of the interaction between radiative transfer and fog microphysic," *J. Atmospheric Sciences*, Vol. 47, No. 18, 2153–2166, 1990.
10. Attenuation due to clouds and fog, *ITU-R Recommendation PN 840–3*, 1–7, 1999.
11. Liebe, H. J., T. Manabe, G. A. Liebe, and G. A. Hufford, "Millimeter-wave attenuation and delay rates due to fog/cloud conditions," *IEEE Trans. on Antennas and Propagation*, Vol. 37, No. 12, 1617–1623 1989.
12. Eldridge, R. G., "Haze and fog aerosol distributions," *J. Atmospheric Sciences*, Vol. 23, No. 5, 605–613, 1996.
13. http://en.wikipedia.org/wiki/Fog.
14. Dintelmann, F. and G. Ortgies, "Semiempirical model for cloud attenuation prediction," *Electronics Letters*, Vol. 25, No. 22, 1487–1488, 1989.
15. Tamosiunaite, M., S. Tamosiunas, M. Tamosiuniene, and M. Zilinskas, "Influence of clouds on attenuation of electromagnetic waves," *Lithuanian Journal of Physics*, Vol. 48, No. 1, 65–72, 2008.

Bandwidth Efficient Inter-carrier Interference Cancellation Technique for OFDM Digital Communication Systems

Akhil Kamboj[1], **Abhinav Keshari**[1], **Vivek K. Dwivedi**[1], **and G. Singh**[2]

[1]Department of Electronics and Communication Engineering
Jaypee Institute of Information Technology University, Noida-201 307, India
[2]Department of Electronics and Communication Engineering
Jaypee University of Information Technology, Solan-173 215, India

Abstract— Orthogonal Frequency Division Multiplexing (OFDM) is a promising technique for the broadband wireless multimedia communication systems. This system is very sensitive to the carrier frequency offset that destroys the orthogonal properties of OFDM sub-carriers and introduces inter-carrier interference (ICI) which degrades the bit error rate (BER) performance. In this paper, we have proposed a novel bandwidth efficient technique which have bit error rate comparable to that of conjugate cancellation method. We also discussed carrier-tointerference ratio (CIR) and compared with the other reported literature.

1. INTRODUCTION

Future wireless communication systems are expected to offer extremely high data rates with appropriate link quality over poor transmission environments. One efficient way to achieve this is by using OFDM technique because of its sufficient handling of radio channel impairments. Its bandwidth efficiency is due to overlapping of the orthogonal sub-carriers. Despite its benefits, its major problem is its sensitivity to frequency offset. The frequency offset can result from a Doppler shift due to a mobile environment, as well as from carrier frequency synchronization error. Such frequency offset causes the loss of carrier's orthogonality and hence ICI will occur. Various schemes have been proposed in literature [1–4] for mitigating the ICI. The scheme proposed in [1] requires to modulate one data symbol on to the next sub-carrier with predefined inversed weighting coefficients "−1". This concept of predefined weighting coefficients makes the ICI component in the received signal to cancel among themselves. The scheme proposed in [2] requires data to be sent on two paths. The first path employs a regular OFDM algorithm and the second path uses the conjugate transmission of the first path. However, the above schemes in [1–4] have bandwidth efficiency equal to half that of standard OFDM.

In this paper, we have proposed a new bandwidth efficient technique and compared its performance against existing techniques [1–4] for different values of frequency offsets. The model of transmitter and receiver of regular OFDM system is explained in Section 2. Section 3 presents the proposed scheme and the corresponding sequential and parallel architectures. The simulation results are discussed in Section 4 and finally, Section 5 concludes the works.

2. OFDM SYSTEM MODEL

In an OFDM system, the input bit stream is multiplexed into N symbol streams, each with symbol period T, and each symbol stream is used to modulate parallel, synchronous sub-carriers. The sub-carriers are spaced by $1/NTs$ in frequency, thus they are orthogonal over the interval $(0, Ts)$. A typical discrete-time baseband OFDM transceiver system is shown in Fig. 1. First, a serial-to-parallel (S/P) converter groups the stream of input bits from the source encoder into groups of $\log_2 M$ bits, where M is the alphabet of size of the digital modulation scheme employed on each sub-carrier A total of N such symbols, X_l, are created. Then, the N symbols are mapped to bins of an inverse fast Fourier transform (IFFT). These IFFT bins correspond to the orthogonal sub-carriers in the OFDM symbol.

Therefore, the OFDM symbol can be written as:

$$x(n) = \frac{1}{N} \sum_{l=0}^{N-1} X_l e^{j\frac{2\pi nl}{N}} \tag{1}$$

where the X_l's are the baseband symbols on each sub-carrier. The digital-to-analog (D/A) converter then creates an analog time-domain signal which is transmitted through the channel. At the

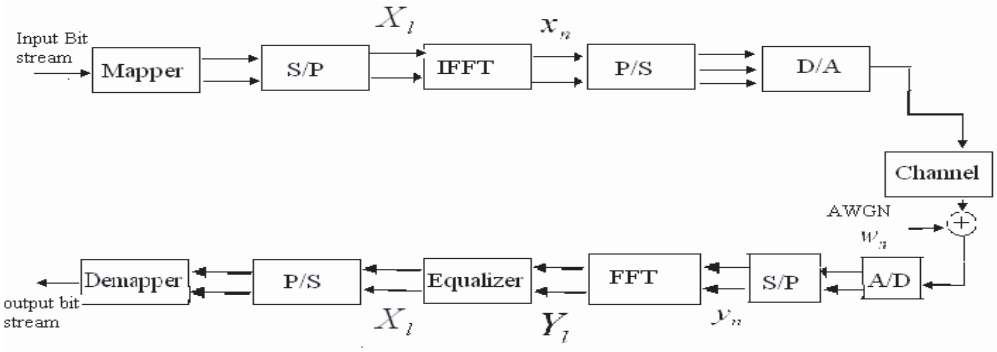

Figure 1: Block diagram of standard OFDM system.

receiver, the signal is converted back to a discrete N point sequence $y(l)$, corresponding to each sub-carrier. This discrete signal is demodulated using an N-point fast Fourier transform (FFT) operation at the receiver. The demodulated symbol stream is given by:

$$Y(l) = \sum_{l=0}^{N-1} y(n) e^{\frac{-2\pi nl}{N}} + W_l \tag{2}$$

where, $W(m)$ corresponds to the FFT of the samples of $w(n)$, which is the Additive White Gaussian Noise (AWGN) introduced in the channel.

3. PROPOSED SCHEME

In this scheme a two path algorithm is used to send the data as shown in Fig. 2. The first path sends a specially modulated data symbols which results from weighted subtraction of an even numbered BPSK symbol and its consecutive symbol. The second path uses the conjugate of a similar type of specially modulated data symbols which results from weighted addition of an even numbered BPSK symbol and its consecutive symbol.

3.1. Modulation

Assume $a_0, a_1, \ldots, a_{2N-1}$ be the first $2N$ BPSK symbols as in [5]. On the first path the transmitted symbols X_l are constrained so that $X_0 = a_0 - a_1$, $X_1 = a_2 - a_3, \ldots, X_{N-1} = a_{2N-2} - a_{2N-1}$. Similarly, on the second path the transmitted symbols X_l' are constrained so that $X_0 = a_0 + a_1$, $X_1 = a_2 + a_3, \ldots, X_{N-1} = a_{2N-2} + a_{2N-1}$. Here the predefined weighting coefficients for BPSK symbols is "1". N-point IFFT of the modulated data symbols from first and second path is

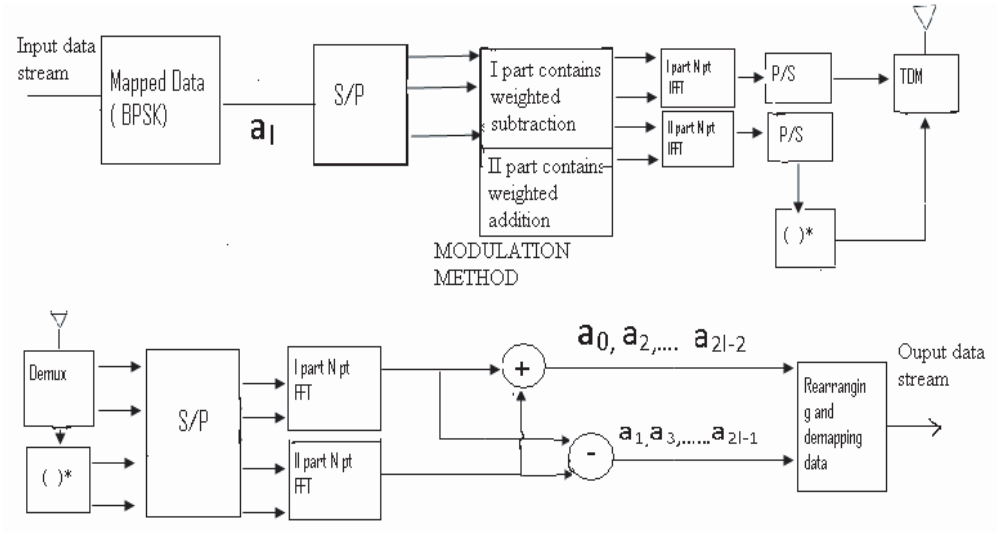

Figure 2: Simulation block diagram of proposed system model.

performed separately. Data symbols from the first path is as it is converted from digital to analog and transmitted whereas data symbols from the second path is conjugated, converted to analog and then transmitted on successive Time Division Multiplexing (TDM) frame. Data signal sent on first path is:

$$x(n) = \frac{1}{N}\sum_{l=0}^{N-1} X_l e^{j\frac{2\pi nl}{N}} \text{ where } X_l = a_{2l} - a_{2l+1} \tag{3}$$

Similarly, data signal sent on second path is:

$$x'(n) = \frac{1}{N}\sum_{l=0}^{N-1} (X'_l) * e^{-j\frac{2\pi nl}{N}} \text{ where } X'_l = a_{2l} + a_{2l+1} \tag{4}$$

3.2. Demodulation

On being received and converted into digital form these signals look like

$$y(n) = \frac{1}{N}\sum_{l=0}^{N-1} X_l e^{j\frac{2\pi n(l+\varepsilon)}{N}} + w_n \tag{5}$$

$$y'(n) = \frac{1}{N}\sum_{l=0}^{N-1} (X'_l) * e^{-j\frac{2\pi n(l-\varepsilon)}{N}} + w'_n \tag{6}$$

After conjugating the signal from the second path, leaving the signal from first path as it is, and thereafter performing N-point FFT of these signals separately, they look like

$$Y(k) = \sum_{l=0}^{N-1} X_l S(l-k) + w_l \tag{7}$$

$$Y'(k) = \sum_{l=0}^{N-1} X_l T(l-k) + w'_l \tag{8}$$

where $k = 0, 1, 2, \ldots, N-1$. The $S(l-k)$ and $T(l-k)$ is defined as ICI coefficient between lth and kth sub carriers which can be expressed as:

$$S(l-k) = \frac{\sin(\pi(l+\varepsilon-k))}{N\sin\left(\frac{\pi}{N}(l+\varepsilon-k)\right)} \cdot \exp\left(j\pi\left(1-\frac{1}{N}\right)(l+\varepsilon-k)\right) \tag{9}$$

$$T(l-k) = \frac{\sin(\pi(l-\varepsilon-k))}{N\sin\left(\frac{\pi}{N}(l-\varepsilon-k)\right)} \cdot \exp\left(j\pi\left(1-\frac{1}{N}\right)(l-\varepsilon-k)\right) \tag{10}$$

For receiving the even numbered BPSK symbols (i.e., $a_0, a_1, \ldots, a_{2l-2}$) $Y(k)$ is added to $Y'(k)$ and further divided by 2. Similarly, for receiving the odd numbered BPSK symbols (i.e., $a_1, a_3, \ldots, a_{2l-1}$) $Y(k)$ is subtracted from $Y'(k)$ and further divided by 2.

4. SIMULATION RESULTS AND DISCUSSION

For simulation, modulation is BPSK with $N = 64$ and guard interval 7. In Fig. 3, CIR of proposed scheme is compared to the conjugate cancellation scheme and it is observed that for frequency offset, $\varepsilon = 0.25$ to 0.5 proposed scheme is better than conjugate cancellation. Figs. 4, 5, and 6 show the comparison of BER amongst self cancellation method, conjugate cancellation and proposed scheme for normalized frequency offset 0.05, 0.1 and 0.15, respectively. For frequency offset 0.05, by using self cancellation scheme, at SNR = 10 dB, BER is just greater than 10^{-1} and by using proposed scheme, at SNR = 10 dB, BER is just less than 10^{-1} For frequency offset 0.15, by using self cancellation scheme, at SNR = 10 dB, BER is greater than 10^{-1} and by using proposed scheme, at SNR = 10 dB, BER is just greater than 10^{-1}. Also the bandwidth efficiency of proposed scheme is double that of self cancellation. So, the proposed scheme is better than the self cancellation scheme.

The BER for both, the conjugate cancellation scheme as well as proposed scheme is comparable at SNR = 10 dB, for offset values 0.05 and 0.15. Here also the bandwidth efficiency of proposed scheme is double that of conjugate cancellation scheme. So the proposed scheme is better than the conjugate cancellation scheme.

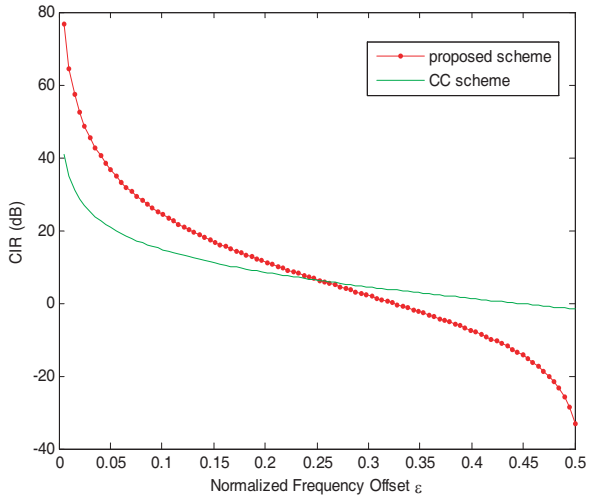

Figure 3: (CIR) vs normalized frequency offset.

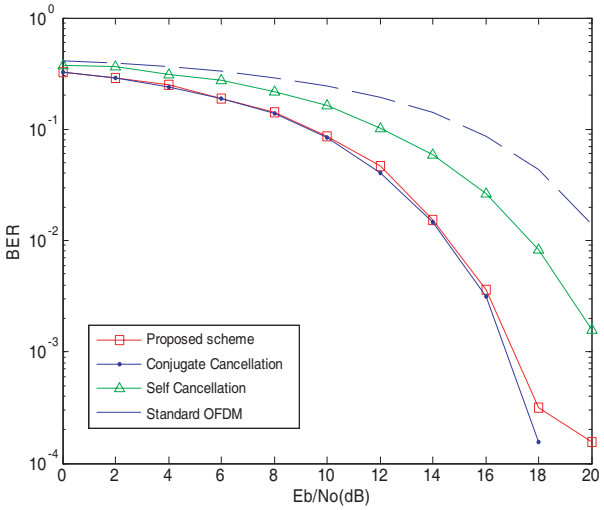

Figure 4: BER comparison in AWGN channel (BPSK) $N = 64$, $\varepsilon = 0.05$.

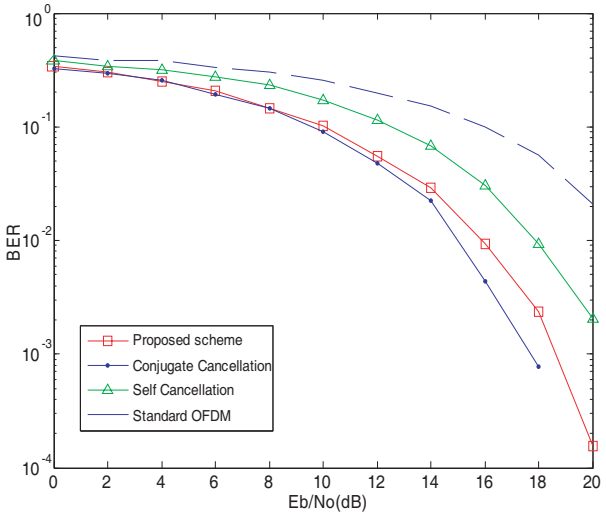

Figure 5: BER comparison in AWGN channel (BPSK) $N = 64$, $\varepsilon = 0.1$.

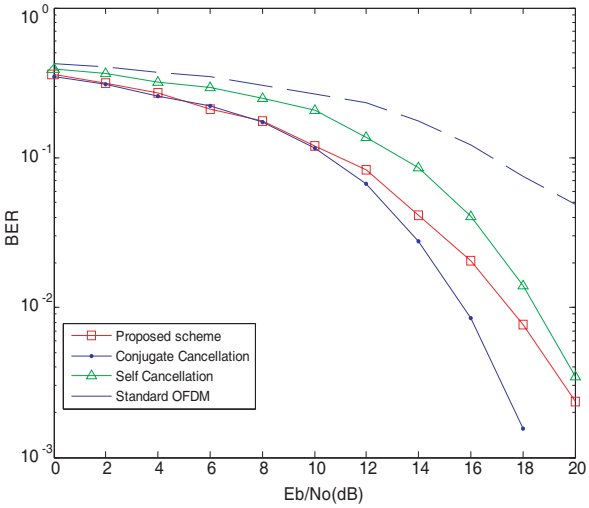

Figure 6: BER comparison in AWGN channel (BPSK) $N = 64$, $\varepsilon = 0.15$.

5. CONCLUSION

In this paper, we proposed a novel technique for OFDM systems which has double bandwidth efficiency than existing schemes as discussed in [1–4, 6]. The proposed scheme has better BER than self-cancellation for frequency offsets 0.05, 0.1, and 0.15. The BER of proposed scheme is comparable to conjugate cancellation for frequency offsets 0.05 and 0.1. For frequency offset greater than 0.15 conjugate cancellation performs better. Moreover, for frequency offsets 0.25–0.5 CIR of proposed scheme is better than that of conjugate cancellation.

REFERENCES

1. Zhao, Y. and S.-G. Haggman, "Inter-carrier interference self-cancellation scheme for OFDM mobile communication systems," *IEEE Trans. Commun.*, Vol. 49, No. 7, 1185–1191, Jul. 2001.
2. Dwivedi, V. K. and G. Singh, "An efficient BER analysis of OFDM systems with ICI conjugate cancellation method," *PIERS Proceedings*, 166–171, Cambridge, USA, July 2–6, 2008.
3. Yeh, H.-G., Y. K. Chang, and B. Hassibi, "A scheme for canceling inter-carrier interference using conjugate transmission in multicarrier communication systems," *IEEE Trans. Wireless Commun.,* Vol. 6, 3–7, Jan. 2007.
4. Armstrong, J., "Analysis of new and existing methods of reducing inter-carrier interference due to carrier frequency offset in OFDM," *IEEE Trans. Commun.*, Vol. 47, 365–369, Mar. 1999.

5. Proakis, J. G., *Digital Communications*, 4th Edition, McGraw-Hill Series, 2001.
6. Sathananantan, K. and R. M. A. P. Rajatheva, "Analysis of OFDM in presence of frequency offset and method to reduce performance degradation," *Proc. IEEE Globecom.*, Vol. 172–176, San Fransisco, CA, Nov. 2000.
7. Dwivedi, V. K. and G. Singh, "Inter-carrier interference cancellation scheme for OFDM systems," *Proc. National Conference on Wireless and Optical Communication (WOC-2007)*, 245–248, India, 2007.

Performance Analysis of Coded OFDM System Using Various Coding Schemes

Vivek K. Dwivedi[1], **Abhinav Gupta**[1], **Richansh Kumar**[1], **and G. Singh**[2]

[1]Department of Electronics and Communication Engineering
Jaypee Institute of Information Technology University, Noida, India
[2]Department of Electronics and Communication Engineering
Jaypee University of Information Technology, Solan-173 215, India

Abstract— In this paper, we have presented the bit error rate (BER) analysis of the orthogonal frequency division multiplexing (OFDM) communication systems for space-time trellis code and space-time turbo codes. In the first part of our work, an effort has been made to illustrate the mathematical derivation for BER of the OFDM system for various space-time coding techniques. Later simulation results for various forward error-correction coding techniques are shown. The space-time turbo coding with OFDM system is seen to provide maximum coding and diversity gain.

1. INTRODUCTION

Recently, orthogonal frequency-division multiplexing (OFDM) is becoming more popular in broadband wireless communication areas [1]. In an OFDM scheme, a large number of orthogonal, over lapping sub-carriers are transmitted in parallel which divide the available transmission bandwidth and data can be recovered at the receiver by exploiting the orthogonality among the sub-carriers. The result of OFDM using a large number of narrowband sub-carriers is that each sub-carrier suffers from flat fading because the sub-carriers are subject to flat fading [1]. The attraction of OFDM is mainly due to how the system handles the multi-path interference at the receiver [2]. The orthogonal properties among sub-carriers of OFDM lead to high spectral efficiency, strong robustness to frequency-selective fading, and simple equalizer implementation. Due to these advantages, OFDM has become the physical layer of choice for many wireless and mobile communication standards, such as digital audio and video broadcasting (DAB/DVB), wireless local access networks (WLANs) and wireless metropolitan area networks (WMANs) [2]. Multi-path generates two effects such as frequency selective fading and inter-symbol interference (ISI). Using powerful error correcting codes together with time and frequency interleaving yields robustness against frequency selective fading [2]. Recently, various space time trellis coding (STTC) in OFDM systems, referred to as STTC-OFDMs, have been investigated [3, 4].

It is shown that space-time coding can be used to achieve high data rates at low signal-to-noise ratios (SNRs) over different channels with different multi-path delay profiles. Space-time coded OFDM system provide both coding gain and diversity gain. Space-time turbo coding (STTuC) technique for OFDM system has been proposed to achieve maximum diversity and coding gains in multi-input multi-output (MIMO) fading channels. STTC technique can also be used to achieve both the diversity and coding gains in MIMO fading channels in an OFDM system [5, 6]. Also various codes like turbo codes [7] and trellis codes which provide only coding gain are compared.

2. THE SYSTEM MODEL

Figure 1 shows a typical discrete-time base-band equivalent model of a coded OFDM system.

2.1. Space Time Trellis Coded OFDM System

We consider a multiple antenna wireless communication system which is equipped with n_T transmit and n_R receive antennas. In practice, the number of transmit and receive antennas is constrained by the cost.

$$\text{Input} = (C_0, C_1, \ldots C_t, \ldots) \quad \text{where } C_t = \left(C_t^1, C_t^2, \ldots C_t^m\right) \tag{1}$$

$$x = (X_0, X_1, \ldots, X_t, \ldots) \quad \text{where } x_t = \left(X_t^1, X_t^2, \ldots, X_t^{nT}\right) \tag{2}$$

where nT = number of transmitting antennas and m = number of shift registers as given by [5]

$$x_t^i = \sum_{k=1}^{m} \sum_{j=0}^{v_k} g_{j,i}^k c_{t-j}^k, \quad v = \sum_{k=1}^{m} v_k, \quad v_k = \left[\frac{v+k-1}{\log_2 M}\right] \tag{3}$$

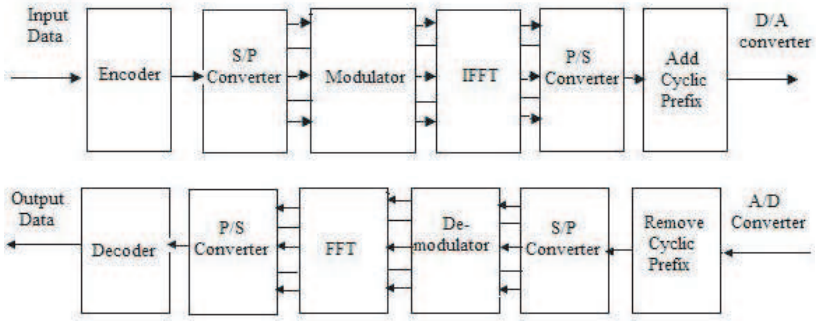

Figure 1: System model for OFDM communication systems.

where x_t^i is the output of encoder at time t for ith antenna, g is the generator sequence, v is total memory order of encoder and v_k is memory order of kth branch of encoder. Now these bits are modulated using QPSK scheme and output of this block is $X_i(k)$ for ith antenna at kth carrier. Taking FFT [2]

$$x_n^i = \frac{1}{N}\sum_{k=0}^{N} x_i(k)\exp(2\pi jnk/N) \quad \text{where } N = \text{number of subcarriers} \tag{4}$$

After FFT signal $Y_n(k)$ for nth receive antenna for kth OFDM subcarrier becomes

$$Y_n(k) = \frac{1}{\sqrt{N_t}}\sum_{m=0}^{N_t-1} s_0 h_{mn}(k)x_m(k) + \frac{1}{N_t}\sum_{m=0}^{N_t-1}\left(\sum_{l=0,l\neq k}^{N-1} s_{l-k}h_{mn}(l)x_m(l)\right) + w_n(k) \text{ as given in [8]} \tag{5}$$

for $0 \le n \le N_r - 1$ and $0 \le k \le N-1$, $x_m(k)$ is the transmitted data symbol from mth transmit antenna on kth subcarrier

$$Y_n(k) = \frac{1}{N_t}\sum_{m=0}^{N_t-1} s_0 h_{mn}(k)x_m(k) + z_n(k) \tag{6}$$

where

$$z_n(k) = \frac{1}{\sqrt{N_t}}\sum_{m=0}^{N_t-1}\sum_{l=0,l\neq k}^{N-1} s_{l-k}h_{mn}(l)x_m(l) + w_n(k) \text{ and } s_k = \frac{\sin\pi(k+\varepsilon)}{N\sin\frac{\pi}{N}(k+\varepsilon)}\exp\left[j\pi\left(1-\frac{1}{N}\right)(k+\varepsilon)\right] \tag{7}$$

2.2. Space Time Turbo Codes

In this section, we present turbo code design and decoding algorithm [9].

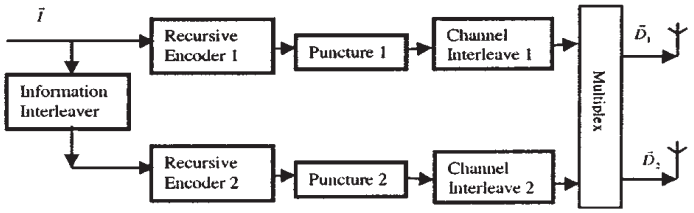

Figure 2: Space time turbo code encoder for two transmit antenna system.

Encoder Design: The encoder has k parallel branches of register where $k = \log_2 M$. At each time slot t, k bit information is applied to each branch in parallel. Let ith branch contain v_i register. Then the memory of encoder is the sum of the number of register of each branch

$$v = \sum_{i=1}^{k} v_i \tag{8}$$

The parity symbol output and polynomial coefficients are related by following equation

$$c_i(t) = \sum_{j=1}^{k} \sum_{k=0}^{v_j} x^j(t-k) g_{k,i}^j \bmod M \tag{9}$$

where $2 \leq i \leq n_t$ and $c_i(t)$ is the parity symbol, and $g_{k,i}^j$ is feed forward polynomial coefficient. The value of $g_{k,i}^j$ is the integer from 0 to $M-1$ as given by [9].

$$x^j(t) = I_j(t) + \sum_{k=1}^{v_j} x^j(t-k) q_k^j \bmod 2 \tag{10}$$

where q_k^j is binary feedback polynomial coefficient.

3. PERFORMANCE ANALYSIS OF SPACE TIME TRELLIS CODED OFDM SYSTEM

Now using maximum likelihood decoding algorithm (MLD) [3],

$$c^{\wedge} = \arg\min \sum_{j=1}^{m} \sum_{k=0}^{N-1} \left| Y_n(k) - \sum_{i=1}^{n} h_{mn}(k) c_i(k) \right|^2 \tag{11}$$

$$B\left(c - c^{\wedge}\right) = c - c^{\wedge} = \begin{bmatrix} c_1^1 - c_1^{\wedge 1} & \cdots & c_N^1 - c_N^{\wedge 1} \\ \vdots & & \vdots \\ c_1^{nT} - c_1^{\wedge nT} & \cdots & c_N^{nT} - c_N^{\wedge nT} \end{bmatrix} \tag{12}$$

$$A\left(c, c^{\wedge}\right) = B\left(c, c^{\wedge}\right) B^H\left(c, c^{\wedge}\right) \tag{13}$$

Assuming ideal channel state information, the probability of transmitting c and deciding in favour of $c^{\wedge}$ at the decoder is as following given by [6]:

$$P\left(c, c^{\wedge} / h_{i,j} i = 1, 2, \ldots n_T, j = 1, 2, \ldots n_R\right) = Q\left(\sqrt{\tfrac{E_s}{2N_0}} d^2\left(c, c^{\wedge}\right)\right) \tag{14}$$

$$P\left(c \to c^{\wedge} / h_{i,j} i = 1, 2, \ldots n_T, j = 1, 2, \ldots n_R\right) \leq \exp\left(-d^2\left(c, c^{\wedge}\right) E_s / 4N_0\right) \tag{15}$$

where $N_0/2$ is the noise variance per dimension and

$$d^2\left(c, c^{\wedge}\right) = \sum_{j=1}^{n_R} \sum_{t=1}^{l} \left| \sum_{i=1}^{n_T} h_{i,j} \left(c_t^i - c_t^{\wedge l}\right) \right|^2 \quad \text{is the Euclidian distance.} \tag{16}$$

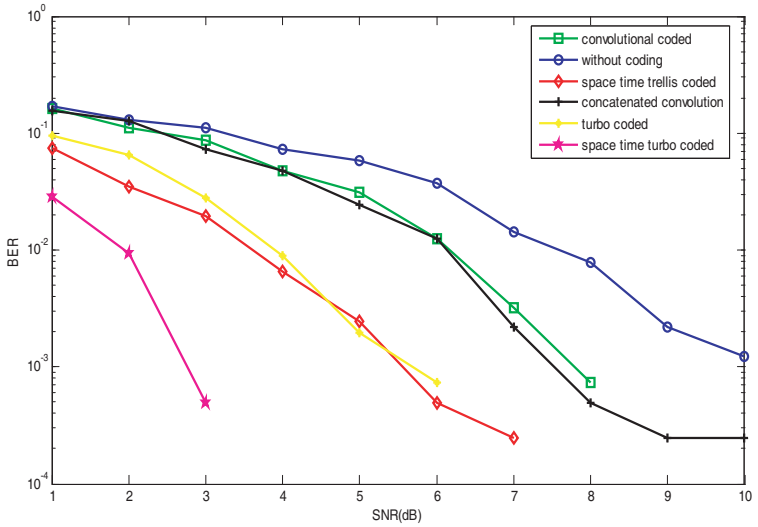

Figure 3: BER versus SNR (dB) (Transmitting antenna = 3, Receiving antenna = 1).

4. RESULTS AND DISCUSSIONS

For simulation modulation used is QPSK and $N = 128$, Fig. 3 shows comparison of BER for various coding schemes like space time turbo coding, space time trellis coding, turbo coding and trellis coding using OFDM modulation technique for frequency offset 0.1.

In this frequency offset of 0.1 by using space time trellis coding (Transmitting antenna = 3, Receiving antenna = 1) method BER is found to be greater than 10^{-1} at SNR = 0 dB and BER less than 10^{-5} at SNR = 10 dB and for space time turbo coding using OFDM system (Transmitting antenna = 3, Receiving antenna = 1) BER is greater than 10^{-2} for 0 dB SNR and BER is less than 10^{-5} for SNR as low as 4 dB. Fig. 4 shows various forward error correction coding techniques with OFDM modulation at normalized frequency offset of 0.1 where transmitting antenna = 3 and receiving antenna = 2. Clearly response is better than for 1 receiving antenna.

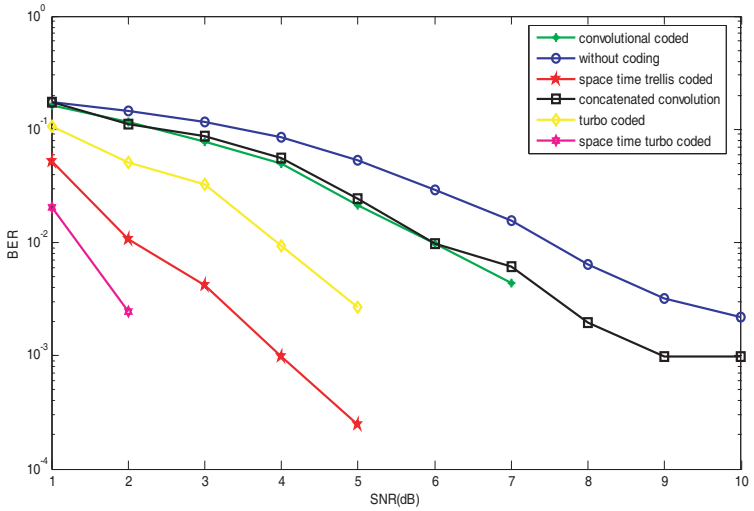

Figure 4: BER versus SNR (dB) (Transmitting antenna = 3, Receiving antenna = 2).

5. CONCLUSION

We have shown that for three transmitting antenna and one or two receiving antenna the bit error rate (BER) is clearly low for space time turbo coded (STTuC) OFDM system [9] than space time trellis coded (STTC) OFDM system [5]. As the number of receiving antenna increases from one to two, BER decreases for both STTC and STTuC. Also BER for space time coded OFDM system is found to be better than BER for coded OFDM system as space time codes provide diversity gain as well as coding gain.

REFERENCES

1. Bingham, J., "Multicarrier modulation for data transmission: An idea whose time has come," *IEEE Comm. Mag.*, Vol. 28, 5–14, 1990.
2. Nee, R. V. and R. Prasad, *OFDM Wireless Multimedia Communications*, Artech House, Norwood, MA, 2000.
3. Agrawal, D., V. Tarokh, A. Naguib, and N. Seshadri, "Space-time coded OFDM for high data-rate wireless communication over wideband channels," *IEEE Vehicular Technology Conference*, Vol. 3, 2232–2236, 1998.
4. Bolcskei H. and A. Paulraj, "Space-frequency coded broadband OFDM systems," *IEEE WCNC*, Vol. 1, 1–6, 2000.
5. Hong, Y. and Z. Y. Dong, "Performance analysis of space-time trellis coded OFDM system," *Int. J. Applied Mathematics and Computer Sciences*, Vol. 2, 59–65, 2006.
6. Tarokh V., N. Seshadri, and A. R. Calderbank, "Space-time codes for high data rate wireless communications: Performance criterion and code construction," *IEEE Trans. Inform. Theory*, Vol. 44, No. 2, 744–765, 1998.

7. Burr, A., "Turbo-codes: The ultimate error control codes?," *Electronics and Communication Engineering Journal*, Vol. 13, 155–165, 2001.
8. Athaudage C. R. N. and K. Sathananthan, "Probability of error of space time coded OFDM systems with frequency offset in frequency selective Rayleigh fading channels," *IEEE International Conference on Comm.*, Vol. 4, 2593–2599, 2005.
9. Liu, Y., M. P. Fitz, and O. Y. Takeshita, "Full rate space-time turbo codes," *IEEE Journal on Selected Areas in Communications*, Vol. 19, No. 5, 969–979, 2001.

Electromagnetic Field Analysis of Axial Flux High Temperature Superconducting Synchronous Motor

L. Y. Li, B. Q. Kou, and J. W. Cao
School of Electrical Engineering, Harbin Institute of Technology, China

Abstract— we are developing a 15 kW-250 rpm synchronous motor with a superconducting winding as the armature winding. The excitation superconducting winding is located in the cover in cake-type, and rotor doesn't have any excitation winding. The stator has iron metrical and the HTS (High Temperature Superconducting) coils locate in the stator slot. This structure can ensure the HTS coils can afford larger current because the magnetic field around the HTS coil is smaller in the same temperature. So we plan to use the liquid nitrogen to cool the HTS coils. In this paper, we analyze the electromagnetic field characteristic of the novel structure HTS motor and the magnetic field around the HTS coils in the stator slot and uses simulation result to prove this structure is effective.

1. INTRODUCTION

HTS motors have great advantages in weigh, power density and efficiency in comparison to conventional motors [1–3]. Recently, we are developing the large power HTS motor system. The novel HTS motor's structure is different from the conventional synchronous motor and superconducting motor. Compared with the conventional synchronous motor, the novel HTS motor's rotor doesn't have any excitation winding and the rotor's structure only has attract and allot the flux which is produced by the cover's HTS coils. Compared with conventional HTS motor and LTS motor, the HTS motor's excitation magnetic field is produced by cover's HTS coils, and the excitation magnetic field through the rotor into the air gap; the armature winding are also used by HTS coils, and located in the stator iron slot. We analyze the novel HTS motor's electromagnetic field characteristics and design a 15 kW-250 rpm HTS motor with copper coils.

2. ELECTROMAGNETIC FIELD ANALYSIS

The HTS motor the paper presents is composed of the covers, HTS excitation coils, the magnetic out claws, the magnetic inner claws, rotor, shaft, stator, the armature HTS coils, as shown in the Fig. 1.

Because we cancel structure that the excitation coils in the rotor, using the cover's HTS coils and the permanent magnet produce the magnetic field. In the Fig. 2, we showed the HTS motor's sectional view. As the figure shown, the rotor has permanent magnets to increase the direct axis reactance, because the superconducting armature reaction is larger.

The HTS motor's parameter is as shown in the Table 1.

In the HTS motor, we use the hyper dispersion air gap to improve the motor performance. Using the Ansoft 2D software to simulate the motor model, the result is as shown:

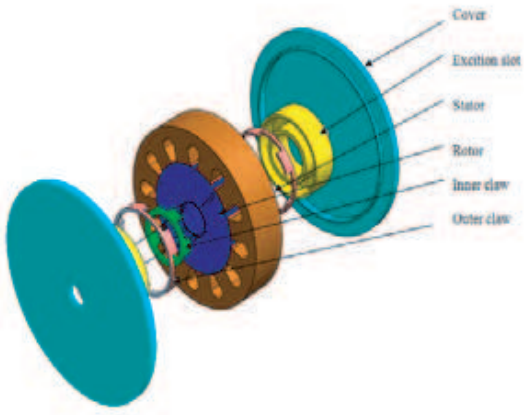

Figure 1: HTS synchronous motor structure.

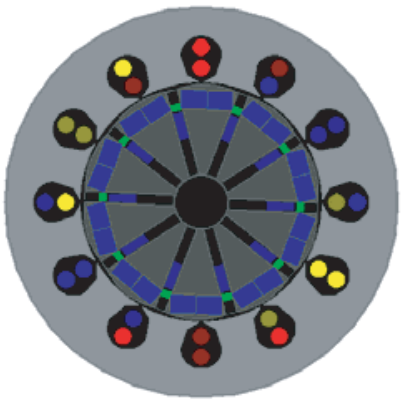

Figure 2: HTS motor sectional view.

Table 1: Main design result of the motor.

Voltage [V]	380	Wingding style	Y style
Speed [r/min]	250	Shaft diameter [mm]	30
Air gap [mm]	0.5	Frequency [Hz]	50
Rotor diameter [mm]	139	Current [A]	30
Max air gap [mm]	2	Density [T]	0.7

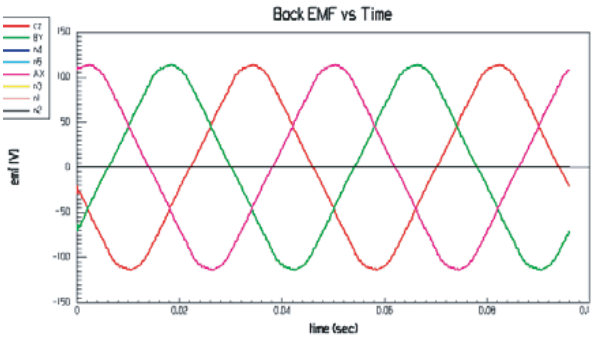

Figure 3: The back EMF with no-load.

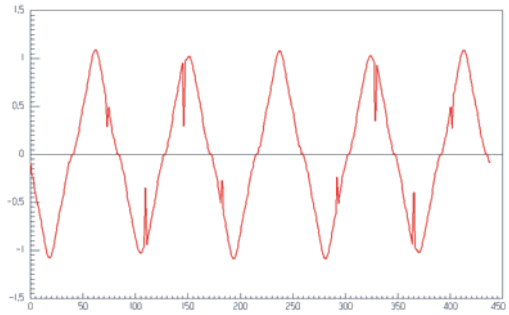

Figure 4: The air gap flux density with no-load.

Because the motor has two magnetic source, one is the permanent magnet, and the other is the superconducting coil in the cover. So the motor has two working style. Firstly, The performance without electrical excitation is shown as shown:

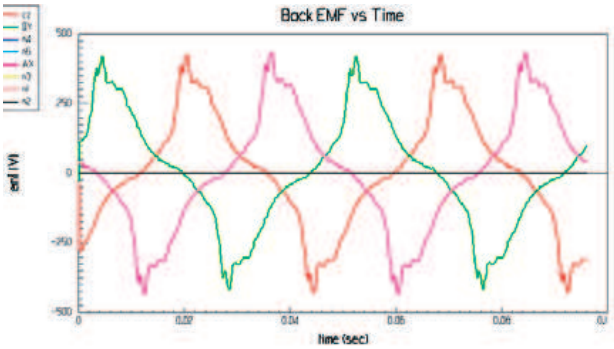

Figure 5: The back EMF with load.

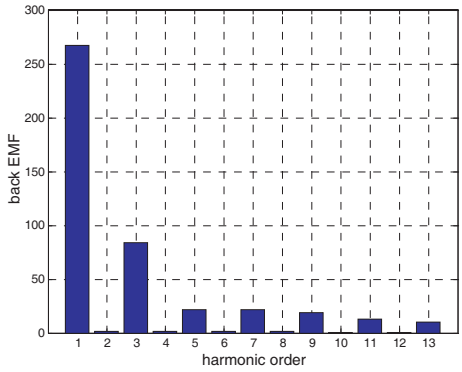

Figure 6: Back EMF FFT transformation result.

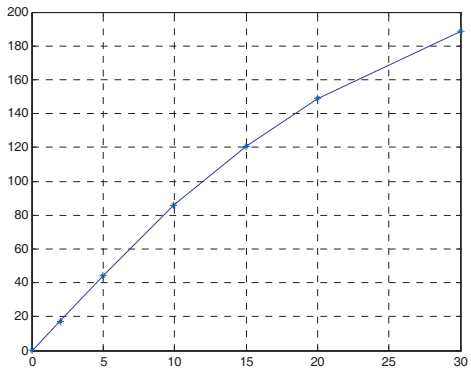

Figure 7: The torque vs. current.

When the armature current is 30 A, the electrical excitation coil is flowed DC current. The result is as shown:

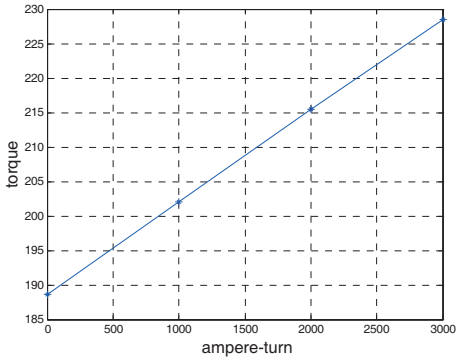

Figure 8: The torque vs. ampere-turn.

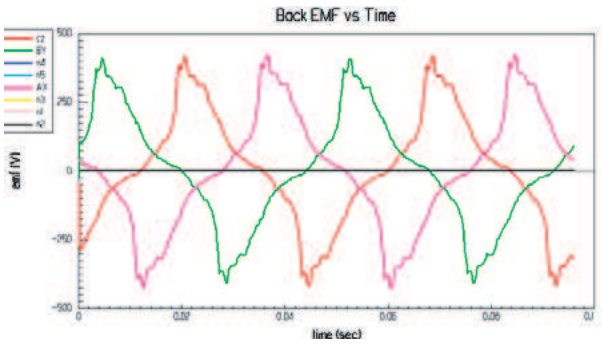

Figure 9: Back EMF with 3000 ampere-turn.

Form Fig. 8 and Fig. 9, we can see that the electrical excitation can decrease the motor's *d*-axis reactance and decrease the motor armature reaction. So the electrical excitation is the most important part because it can decrease the armature reaction which is product by the stator iron. This effect will make this structure HTS motor easily be implemented.

3. ELECTROMAGNETIC FIELD AROUND HTS COILS

The value of electromagnetic field around the HTS coils can decide the critical current of the HTS coils, so the electromagnetic field in the stator slot and the terminal of the coils is needed to analyze. This structure makes the stator iron around the HTS coils. The stator iron will attract flux until it is saturation that will ensure the HTS coils has better electromagnetic performance. Fig. 10 shows the stator slot magnetic field distribution with load.

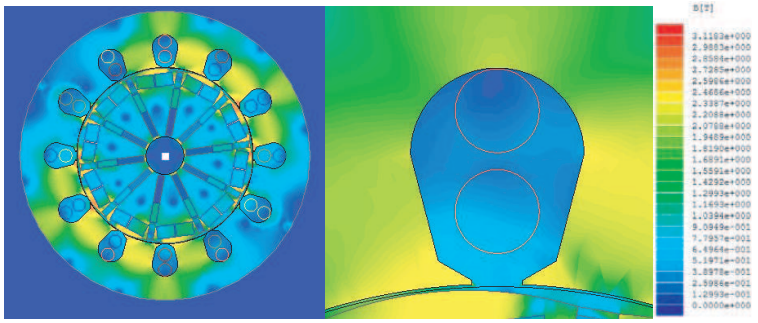

Figure 10: The stator slot magnetic field distribution with 30 A armature current.

Form the Fig. 10, the stator slot magnetic field max flux density position is slot edge. The magnetic field in the center of the slot is 0.2 T–0.3 T. So the less magnetic distribution let the HTS coils get better performance.

4. CONCLUSION

This paper presents a novel HTS motor with axial flux, and analyze the motor's electromagnetic characteristic, and point the weak point of this structure and the solve method. The simulation result proves this method is effective and let this HTS motor get better performance. Finally, the paper analyzes the magnetic field distribution around the HTS coils. The simulation shows the magnetic field around is less and this can ensure the HTS coils get better performance. Those results will help us study HTS motor performance and supply basic research data.

REFERENCES

1. Masson, P. J., M. Breschi, and C. A. Luongo, "Design of HTS axial flux motor for aircraft propulsion," *IEEE Transactions on Applied Superconductivity*, Vol. 17, No. 2, 1533–1536, 2007.
2. Lopez, J., J. Lloberas, R. Maynou, et al., "AC three-phase axial flux motor with magnetized superconductors," *IEEE Transactions on Applied Superconductivity*, Vol. 17, No. 2, 1633–1636, 2007.

3. Masson, J. P., D. S. Soban, E. Upton, et al., "HTS motors in aircraft propulsion: Design considerations," *IEEE Transactions on Applied Superconductivity*, Vol. 15, No. 2, 2218–2221, 2005.

A New Perspective and Applications of Amorphous Microwires on Electromagnetic Shielding

O. Baltag
Faculty of Medical Bioengineering
"Gr. T. Popa" University of Medicine and Pharmacy, Iasi, Romania

Abstract— The paper presents the results of a research regarding new applications of amorphous microwires in the realisation of some new composite textile material and the possibility to use it in electromagnetic shielding and protection equipment manufacturing. The textile material and the technical problems raised by its manufacturing technology are described, and its shielding, reflection and polarization properties are evaluated. A biocompatibility study was carried out to highlight certain of its possible allergic effects. The material was subjected to sanitation action by washing with liquid solution of water and domestic detergents. After this, it apparently preserved its mechanical characteristics, suffered no distortion through manual squeezing, and registered no shrinking. The measurement of the attenuation coefficient before and after washing was carried out with the same installation within the frequency range of (900–1800) MHz. No modifications were found out after washing A protective equipment was experimented, made of a coupon of material, lined with a neuter material from the electromagnetic point of view. The equipment was previously evaluated from the standpoint of its electromagnetic shielding capacities, and it was found out that the values measured under laboratory conditions had not changed. The equipment was used daily, two hours a day, for two weeks, under various conditions of temperature and humidity, both indoor and outdoor, and in environments with different degrees of electromagnetic pollution. The equipment was used such that to ensure mechanical protection, to perform the shielding function in electromagnetically polluted environments.

1. INTRODUCTION

The composite textile materials represent a group of multi-functional materials with special properties conferred by imbedding structures with electromagnetic properties within the textile material. These structures can be of various types and compositions: metallic or metal coated wires, metallic particles, but the properties of these materials also depend of the manner in which the metallic particles and wires were incorporated, namely by weaving or thin layer deposition. The composite textile materials with antistatic action and electromagnetic shielding properties are used in different industrial and military applications, in the protection against electromagnetic environment, etc. Taking into account the ever increasing market demand for these materials due to the intensification of the concern with respect to the health conditions of the people working in environments with high electromagnetic pollution and not only, they became the object of intense studies meant to improve their qualities. The biological effects of the electromagnetic radiations have been detected from the very beginning of the production and utilization of these forms of energy. The effects of the electromagnetic field on the living organisms are well known [1]. There are various sources of electromagnetic field, both in our inhabited spaces (domestic appliances, microwave ovens, mobile phones, etc), and in the spaces where various activities are performed (industrial equipment and installations, high voltage cables, computers, etc). Yet, recently these effects have been more intensely and deeply studied, so that one can know and quantify exactly the affections produced by them. Given the alarming increase of the number of affections, some of them very severe, produced by the exposure to electromagnetic fields, especially within the microwave range, the appearance of these materials on the market was more than welcome. On the other hand, the static electricity represents a real hazard, the highest risk being in the environments where the electrostatic fields and electric discharges can cause explosions or fires. In this connection, the materials mostly used in shielding have a high conductivity and magnetic permeability. With this purpose in view, the manufacturing companies have used composite structures shaped as absorbing or reflecting panels consisting of: materials which contain metallic wires or non-ferromagnetic metallic alloys (Cu, Ag, Ni, Au) which show certain shortcomings: they are heavy, easy to break, get oxidized in atmosphere and can not be used in corrosive environments [2]; graphite plated plastic materials, with a low screening coefficient and ferrite type ferromagnetic nano-particle powders [3].

In order to increase the coefficient of electromagnetic shielding, one can also use amorphous magnetic materials which show the following advantages: stability of the electric and magnetic

parameters to mechanic strength and resistance to the action of oxidizing chemical agents. From these, one can produce textile and nontextile materials with a wide utilization in electromagnetic screening: wall coating (total screening), door and window coating, manufacturing of protection clothes or suits for the personnel who works in highly electromagnetic environments. The electromagnetic screening can also be executed by means of composite textile materials (amorphous ferromagnetic wire coated with a glass sheath and twisted with cotton yarn).

2. DESCRIPTION OF THE MATERIAL

The studied material has a composite structure, being made of amorphous ferromagnetic wires coated with glass and twisted with cotton or synthetic yarns. The cloth has special electromagnetic properties since the amorphous wire has a high magnetic permeability within a wide frequency range. The amorphous wire was obtained by drawing and water jet cooling. The composition of the amorphous wire is as follows: $Co_{68}Mn_7B_{15}Si_{10}$ [4]. The amorphous wire with the diameter of 10 µm is coated with a glass sheath and twisted together with cotton yarns [5].

The utilized microwires have the inner diameter ranging between 10 µm and 13 µm, while the outer diameter of the glass insulation is between 15 µm and 20 µm. The values of the anisotropy field range between 18 A/m and 150 A/m, while the coercive force ranges between 18 A/m and 70 A/m, and the ratio B_r/B_s is about 0.9. The amorphous magnetic microwires were obtained by a well known technology, namely water jet fast cooling of the ferromagnetic alloy which is introduced into a glass tube; the material heating and melting is carried out by high frequency induction currents. The microwire and the glass sheath are rapidly drawn through a water jet and then wound on metallic bobbin, the length of a wire sample being of about 1500 m. The research team has tried more technological solutions on classical weaving machines, adjusted such that the wire is not broken and one can realize a textile material structure. The material was woven according to a conventional technology using classical machines, but with the precautions with respect to the weaving rate, given the presence of the amorphous wire. In order to avoid the breaking of the amorphous wire, this was first twisted with cotton yarn and then introduced in the weaving machine. Several types of textile materials were tested, the best results being obtained with kapron and cotton yarns. The textile material was woven in several versions: ACAC. . . , ACCA. . . , (A — amorphous wire; C — cotton yarn); the image of the textile is presented in Figure 1.

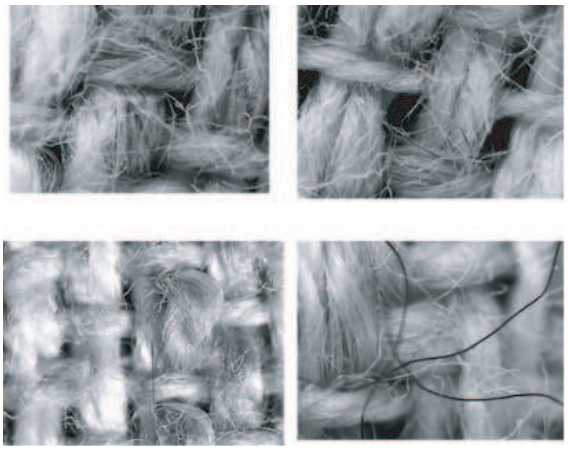

Figure 1: Microscopic image of different texture types.

The measured parameters were both of physical and chemical nature, those of physical nature being mechanical, thermal and electromagnetic parameters. In order to be used as absorbing or reflecting material, or to refract the electromagnetic radiation to other absorbing materials, it is necessary for the dielectric materials used as additions to the textile fibres to satisfy certain mechanical conditions. These physical parameters are:

- mechanical stability: important for some materials used in composite structures;
- shape preservation: minimum distortions during utilization;
- high thermal conductivity: the possibility of heat energy leaking toward the heat energy dissipative elements.

- long term stability to the environmental parameters: temperature variations, various storing temperatures, humidity, noxious industrial gases;
- thermal expansion similar to that of the associated elements in the composite structures, in order to avoid the generation of mechanical strengths which could modify the properties;
- small variations of the geometric dimensions:

The obtained textile prototype was subjected to various conditions and it preserved its mechanical properties, remaining undistorted during the utilization, and was not degraded due to the storing or wearing conditions.

3. PARAMETERS OF ELECTROMAGNETIC SHIELDING

The measurements have been carried out at the laboratory; a square sample of $(1,000\,\text{mm} \times 1,000)\,\text{mm}$ was cut from each assortment. The installation for testing the shielding coefficients consists of a receiver coupled to a guide that has the lighting aperture with the diameter of 150 mm for the frequency of 1800 MHz and 250 mm for 1200 MHz, as well as a microwave transmitter. The polarization plane E is vertical. The cloth stretched on a wooden frame was placed equidistantly between the aerial lighting apertures. The cloth is oriented according to two directions (with the yarn parallel and respectively perpendicular to the polarization plane). The attenuation coefficients varied between 7 dB and 32 dB, within the frequency range (900–1300) MHz, Figure 2.

The polarizing properties, Malus law at higher frequencies of (8–10) GHz, are presented in Figure 3.

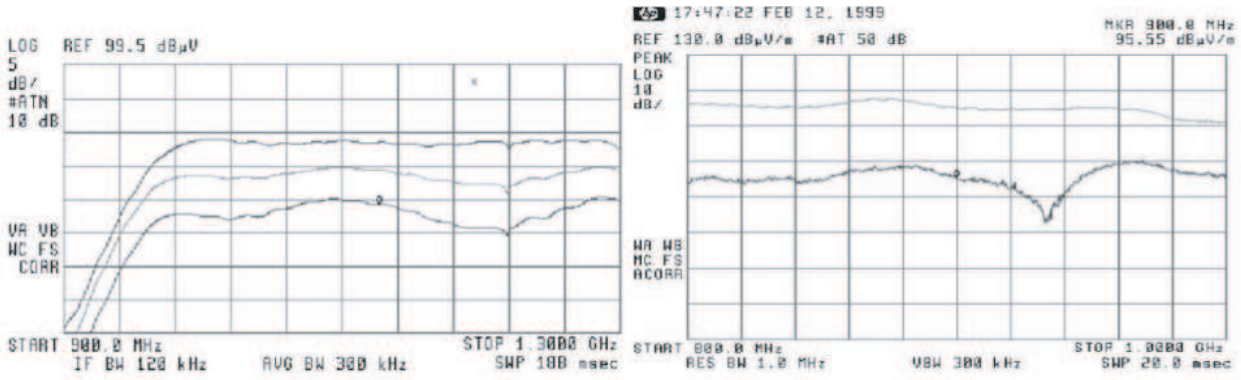

Figure 2: Attenuation in (900–1300) MHz range.

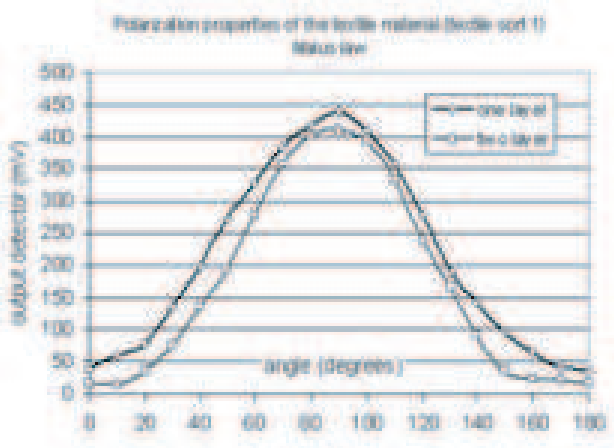

Figure 3: Polarization Malus law.

4. BIOCOMPATIBILITY

The equipment was subjected to a sanitation action by washing with a liquid solution of water and domestic detergents. After this, it apparently preserved its mechanical characteristics, suffered no

distortion by manual squeezing, and registered no shrinking (no size diminution). The measurement of the attenuation coefficient before and after washing was carried out with the same installation within the frequency range of (900–1800) MHz. No modifications were found after washing. The results of the measurements are presented in Figure 4.

A protective equipment was experimented, consisting of a sample of material sized (500 × 500) mm and lined with a neuter material from the electromagnetic point of view. The equipment was previously evaluated from the standpoint of its electromagnetic shield ing capacities, and it was found out that the values measured under laboratory conditions had not changed. The equipment was used daily, two hours a day, for two weeks, under various conditions of temperature and humidity, both indoor and outdoor, and in environments with different degrees of electromagnetic pollution.

The study had in view the occurrence of some allergic reactions or other objective signs indicating the appearance of a disease. The synthesis of the manifestations is presented in the table.

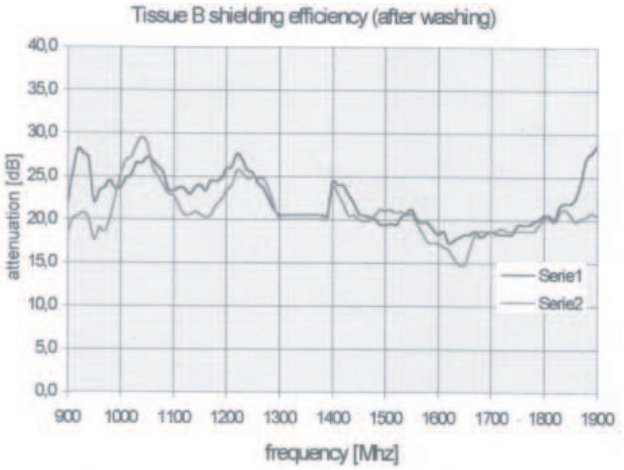

Figure 4: Variation of the attenuation coefficient after washing.

Type of manifestation	%
Cutaneous	12
Respiratory	12
Cardio-vascular	8
Nervous	8

5. CONCLUSIONS

The textile materials with composite structure (amorphous ferromagnetic wire covered with glass and wound with cotton wires) can be used with good results for electromagnetic shielding in a relatively large frequency range. The clinical manifestations were cutaneous, respiratory and cardio-vascular. The subjects who had previously a cutaneous pathology determined by the contact with allergens from the hospital environment complained of the recrudescence of these manifestations when wearing the protection equipment, and another patient presented a slight irritation which disappeared after removing the protection equipment. The subjects with cardio-vascular pathology complained of an increased fatigue at stress and sudden increases of arterial pressure values. At 3 subjects the respiratory effort was higher and a slight, dry coughing accompanied by clogged nose was reported. Part of the subjects suffered from a slightly nervous condition and cephalalgia, with increased sensitivity to odors and tobacco. No manifestations of ocular or auditory pathology were recorded.

REFERENCES

1. Vander Vorst, A., A. Rosen, and Y. Kotsuka, *RF & Microwaves Interaction with Biological Tissues*, John Willey & Sons Inc, New-York, 2004.

2. Bogush, V., *Journ. of Opt. and Adv. Mat.*, Vol. 7, 1635–1642, 2005.
3. Rubacha, M. and J. Zieba, *Fibres & Tex. in East. Europe*, Vol. 14, 49–53, 2006.
4. Zhukov, A., M. Vasquez, J. Velasquez, A. Hernando, and A. Larin, *J. M. M. M.*, Vol. 170, 1997.
5. Baltag, O., D. Costandache, C. Cantore, A. Torcunov, and V. Larin, "Study of a texture of an amorphous magnetic material able to screen non-ionogenic radiations," *Proceedings. of Int. Symposium on Nonlinear Electromagnetic Systems*, 717–720, Pavia, Italia, 1999.

Novel Principle of Transformer Protection Based on Variable Window Parameter Estimation

Heng-Xu Ha[1], **Zhi-Qiang Zhang**[1], **Yu-Zhen Tan**[1], **Bo Chen**[2], **and Z. Q. Bo**[3]

[1]Shandong University of Technology, Zibo 255049, China
[2]Dispatching Center, Shaanxi Electric Power Company, 710045, China
[3]AREVA T&D UK Limited, UK

Abstract— A novel principle of transformer protection, which is radically immune to the nonlinear core saturation, also to the self-induction and the mutual-induction exists at both sides of transformer, is proposed in this paper. Based on the transformer flux linkage banlance equation, the system parameters will be estimated precisely online utilizing variable window parameter estimating method. Then, by means of Gaussian elimination method, the corresponding protection criterion will be constructed. Through selecting suitable window width, variable window least square parameter estimation method will be adopted, which realizes reasonable electrical datum collection, including transient information and steady information. The ATP simulations showed that the principle is correct and efficient, it can reflect interior faults and exterior faults accurately.

1. INTRODUCTION

The power transformers, which are applied widely in different voltage grades of network, play an important role in distribution system. Due to the inrush current, the protection will maloperate which causes the power system unstable [1, 2]. At present, the action time is still not perfect for both the inrush current is attenuate and the process is terdious, several methods [3, 4] have been proposed to deal with these drawbacks. Papers [5–7] present a principle to distinguish fault types through both excitation characteristic curves and the magnetic flow-difference current curves, which is easier to realize by computer and overcome the limitation of the second harmonics principle. While, the criterion is only suitable to the single-phase transformer for the complexity of flux linkage balance equation. Literature [8] brings forward a transformer protection scheme based on sequence impedance, which is not affected by CT saturation and change disagreement. That is to say, the positive sequence impedance and the negative sequence impedance of transformer are not in the same quadrant when the fault happens. Literature [9] explains the identification criterion of excitation inrush current by improving the quadrant area division. But the sequence impedance principle is sensitive to current rush, which decreases action dependability. Article [10] expatiates that the active power of transformer is low under the healthy situation, whilst, the active power will greatly increase due to the arc discharging radiation when the insulation of transformer is broken. Hence, the transformer can judge the inner fault through checking the quantity of consuming active power. The principle based on the law of conservation of energy can reflect the real circulation status of transformer and it is also immune to the current rush. While this method has some disadvantages, such as the copper loss is difficult to calculate and the criterion must avoid the first period of charge process. The copper loss cannot obtain for the inner current of Δ side winding to the Y/Δ connecting transformer is uncertain.

2. THE DEDUCTION OF TRANSFORMER MAGNETIC LINKAGE ACTION EQUATION

2.1. The Magnetic Action Equation of Single-phase Transformer

Figure 1 is single phase transformer with two windings. The foundation of the transformer protection principle based on magnetic linkage balance equation is magnetic linkage balance equation. Then,

$$\begin{cases} u_1 = i_1 R_1 + L_{\sigma 1}\dfrac{di_1}{dt} + N_1\dfrac{d\Phi_m}{dt} \\ u_2 = i_2 R_2 + L_{\sigma 2}\dfrac{di_2}{dt} + N_2\dfrac{d\Phi_m}{dt} \end{cases} \tag{1}$$

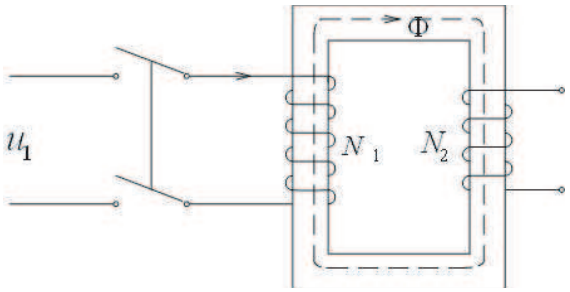

Figure 1: The model of single-phase transformer.

In the Equation (1), $d\Phi_m/dt$ contain the nonlinear relation of B-H curved, which was difficult to obtain. By means of Gaussian Elimination, $d\Phi_m/dt$ will be counteract. Suppose $k = N_1/N_2$, then Equation (1) will be reorganized:

$$u_1 - ku_2 - (i_1R_1 - ki_2R_2) - \left(L_{\sigma 1}\frac{di_1}{dt} - kL_{\sigma 2}\frac{di_2}{dt}\right) = 0 \tag{2}$$

Owing to the changing circuit structure, K_{zd} varied when the transformer inner fault happened.

2.2. The Magnetic Action Equation of Three-phase Transformer

Through the deduction of the magnetic action equation of single-phase transformer, the magnetic action equation of three-phase Y/Y connection transformer with two windings will be got. (Fig. 2)

$$\begin{cases} K_{dz1} = \left(u_A - r_A i_A - L_{\sigma A}\dfrac{di_A}{dt}\right) - n_B\left(u_a - r_a i_a - L_{\sigma a}\dfrac{di_a}{dt}\right) \\ K_{dz2} = \left(u_B - r_B i_B - L_{\sigma B}\dfrac{di_B}{dt}\right) - n_B\left(u_b - r_b i_b - L_{\sigma b}\dfrac{di_b}{dt}\right) \\ K_{dz3} = \left(u_C - r_C i_C - L_{\sigma C}\dfrac{di_C}{dt}\right) - n_B\left(u_c - r_c i_c - L_{\sigma c}\dfrac{di_c}{dt}\right) \end{cases} \tag{3}$$

And for the transformer with Y_0/Δ connection (Fig. 3),
And suppose that

$$\begin{cases} L_{\sigma A} = L_{\sigma B} = L_{\sigma C} = L_{1\sigma} \\ L_{\sigma a} = L_{\sigma b} = L_{\sigma c} = L_{2\sigma} \end{cases} \tag{4}$$

The equation of transformer magnetic linkage balance is built up at the voltage and current of winding. The principle utilizes the line current to realize the protection criterion for the current of Δ-side winding is unknown. The current of Δ-side winding is calculated by the "Angle to Star" method. As to the winding of Δ-side, for the winding current donot contain zero sequence current, the current of Y_0-side winding will be employed to work out the zero sequence current.

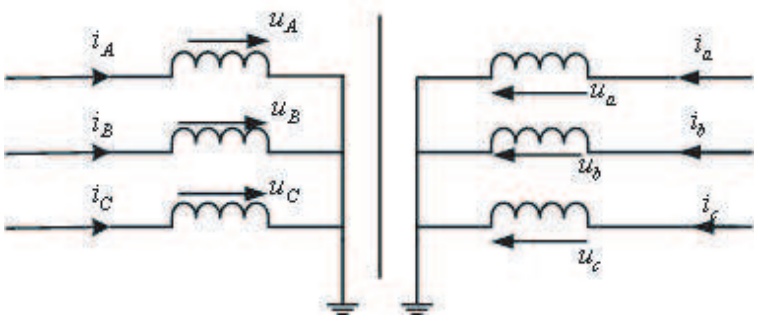

Figure 2: Three-phase transformer model with Y/Y connection.

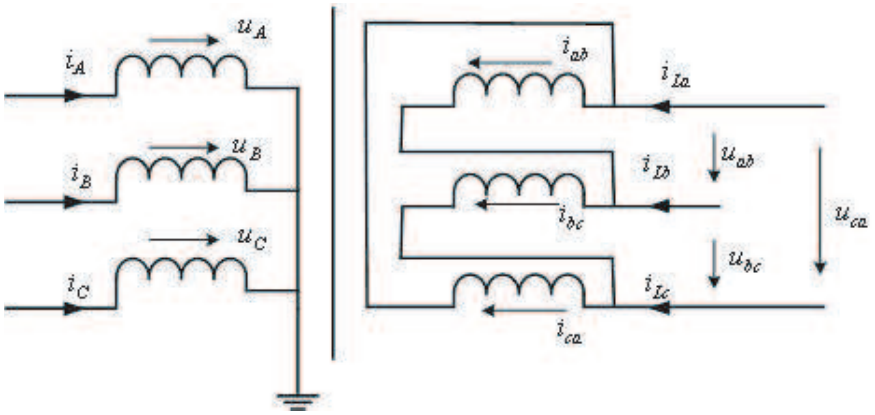

Figure 3: Three-phase transformer model with Y_0/Δ connection.

The action equation of transformer with Y_0/connection is shown as followed.

$$\begin{cases} K_{zd1} = (u_A - u_B) - n_B (u_{ab} - u_{bc}) - \left[r_1 (i_A - i_B) - n_B r_2 \left(\dfrac{i_{La}}{3} - \dfrac{2i_{Lb}}{3} + \dfrac{i_{Lc}}{3} \right) \right] \\ \qquad - \left[L_{1\sigma} \dfrac{d(i_A - i_B)}{dt} - n_B L_{2\sigma} \left(\dfrac{di_{La}}{3dt} - \dfrac{2di_{Lb}}{3dt} + \dfrac{di_{Lc}}{3dt} \right) \right] \\ K_{zd2} = (u_B - u_C) - n_B (u_{bc} - u_{ca}) - \left[r_1 (i_B - i_C) - n_B r_2 \left(\dfrac{i_{Lb}}{3} - \dfrac{2i_{Lc}}{3} + \dfrac{i_{La}}{3} \right) \right] \\ \qquad - \left[L_{1\sigma} \dfrac{d(i_B - i_C)}{dt} - n_B L_{2\sigma} \left(\dfrac{di_{Lb}}{3dt} - \dfrac{2di_{Lc}}{3dt} + \dfrac{di_{La}}{3dt} \right) \right] \\ K_{zd3} = (u_C - u_A) - n_B (u_{ca} - u_{bc}) - \left[r_1 (i_C - i_A) - n_B r_2 \left(\dfrac{i_{Lc}}{3} - \dfrac{2i_{La}}{3} + \dfrac{i_{Lb}}{3} \right) \right] \\ \qquad - \left[L_{1\sigma} \dfrac{d(i_C - i_A)}{dt} - n_B L_{2\sigma} \left(\dfrac{di_{Lc}}{3dt} - \dfrac{2di_{La}}{3dt} + \dfrac{di_{Lb}}{3dt} \right) \right] \end{cases} \tag{5}$$

3. TRANSFORMER PROTECTION PRINCIPLE BASED ON VARIABLE WINDOWS PARAMETER ESTIMATE

Through transformer magnetic linkage action equation, we can judge the circulate state of transformer by the size of K_{zd}. The crucial technique of this principle lies in the parameter (R and L_σ) of transformer winding. But the calculated parameter by nameplate unable to reflect the change of winding parameter, such as working state, working environment, etc.

System identification is an effective tool for power system analysis, which contains the Least Square, the Kallman Filtering and so on. The Least Square is widely used in the parameter estimation for power system.

3.1. Parameter Estimate Based on Least Square

For the nonlinear model,

$$Y(t) = \phi(t)\theta + \sum E(t) \tag{6}$$

The Least Square principle is utilize to search the estimated value θ' for the unknown parameter vector θ. Then, the performance index J will be:

$$J = [Y(t) - \phi(t)\theta]^T [Y(t) - \phi(t)\theta] \tag{7}$$

Supposed that $\partial J/\partial\theta = 0$, then,

$$-2\phi^T(t)[Y(t) - \phi(t)\theta] = 0 \tag{8}$$

Through deduction,

$$\phi^T(t)\phi(t)\theta = \phi^T(t)Y(t) \tag{9}$$

The Least Square estimation value of θ will be calculated:

$$\overline{\theta}(t) = \left[\phi^T(t)\phi(t)\right]^{-1}\phi^T(t)Y(t) \tag{10}$$

3.2. Variable Windows Parameter Estimate

The Least Square parameters estimation assure that the mean square deviation of estimating is least. The estimation process of matrix θ' requires to calculate the inverse of a matrix of $\theta^T(t)\theta(t)(n \times n)$. The quantity of calculation becomes complex with the increase of coefficient matrix dimension.

The process, which varied from steady state to another steady state, is continuous when the state of power system changed. And the initial transient state of this process makes no difference to steady state. The improvement that maintain the quantity of dimension calculation satisfies the real-time window estimation. The parameter estimation of the least squares, which based on variable time window, is able to avoid the problem of large calculation quantities and long-time computation exists in the least square. Therefore, the parameter estimation is widely used in real-time online parameter estimation for the electrical equipment. The steps of the parameter estimation base on variable time window is listed as followed:

(1) Determine the parameter n, which is to be estimated. The parameter estimation of least squares is employed to solve equations. While the relationship between the number m of the equations and the number n of the unknown parameters will determine the existence of the solution.

(2) According to the voltage and current signals, the coefficient matrix Φ of the parameter estimation will be real-time calculated. When the dimension m of the coefficient matrix Φ is equal to the number n of the parameters, the transformer winding parameters will be estimated, until the matrix dimension m beyond the fixed time window W.

(3) When $m > W$, m will be restricted within W in order to guarantee the speed of calculation. Therefore, m will increase with the time change.

4. SIMULATIN VALIDATION

The simulation model of transformer shown in Fig. 4 is built up by ATPDraw. Transformer T is a three phase transformer with Y/Y connection. The parameter of transformer is shown as following: Rating capacitance (*2*kVA); Rating Voltage ($U_1/U_2 = 1000\,\mathrm{V}/220\,\mathrm{V}$); No-load current (*1.2%*); Open circuit losses (*0.9%*); Short-circuit voltage (*13.6%*); Short-circuit losses (*1%*). $T_s = 2E - 6$. Set $K_{zd} = 4$ as the threshold value of protection action.

4.1. The Simulation Validate of Transformer with Various Degrees Turn-to-turn Faults

Table 1 shows the action value K_{zd} curve when turn-to-turn fault happened. From the table, the action value of turn-to-turn fault is bigger than normal and external fault.

4.2. The Influence of Fault Types to Protection Principle

Figures 5 and 6 and Table 2 show the action values curve when three-phase fault happened. When the interior fault happened, the principle can identify fault types in 10 ms.

Figure 4: Drawing of system simulation.

Table 1: The curve of action value K_{zd} with turn-to turn fault.

Degree of Turn-to-turn Fault	Action Value	Action Time (ms)	Protection Acting
5%	7.877	2	Trip
20%	6.536	6	Trip
50%	14.91	5	Trip
95%	7.139	7	Trip

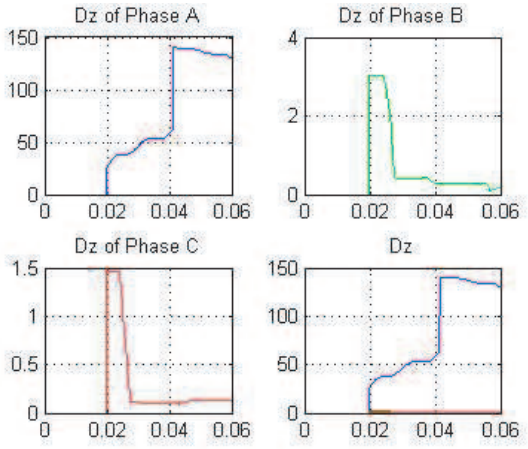

Figure 5: The curve of acting value when phase a short to earth.

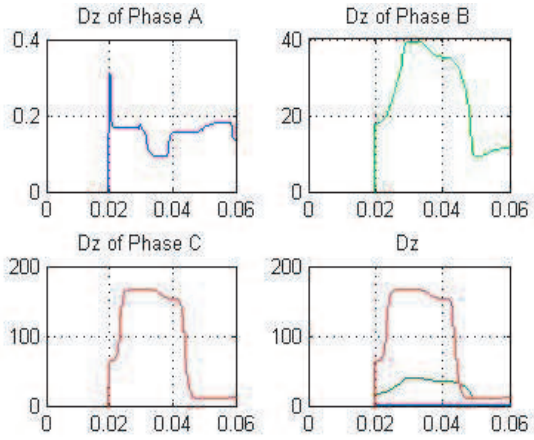

Figure 6: The curve of acting value when interphase fault happened.

Table 2: The influence of varied fault types to the protection.

Fault Type	Action Value A/B/C	Acting Time (ms)	Protection Acting
Phase A Short	25.34/3.035/1.48	10	Trip
Interphase Short	0.3088/17.89/63.58	10	Trip
Triphase Short	25.34/17.89/63.58	10	Trip

4.3. The Influence of the System Close Angle to the Principle

The transformer protection is effected by system closing angle for its electromagnetism characteristic. Table 3 shows the action value curve with various angles. From the table, when the system close at 0°, when the current rush happened, the action value curve is larger than other situation. At that time, the protection principle would not trip. Hence, the principle will not be affected by system close angle.

4.4. The Influence of Transition Resistance

The influence of transition resistance is the norm of protection dependability because that the principle is building at the voltage and current of transformer. Table 4 shows the action value when single phase fault happened with 0.05 Ω–500 Ω transition resistance.

Table 3: The act value under varied close angle of system.

System Angle	Action Value	Protection Acting
0	3.385	No Trip
10	0.1427	No Trip
30	0.1254	No Trip
60	0.1175	No Trip
90	0.08281	No Trip

Table 4: The act value of short fault with transition resistance.

Transition Resistance (Ω)	Action Value	Protection Acting
0.05	3.007	No Trip
5	2.647	No Trip
50	2.641	No Trip
200	2.641	No Trip
500	2.639	No Trip

5. CONCLUSIONS

Through the transformer model study, A novel protection principle based on variable window parameter estimate is proposed in this paper. And the characteristic of protection are shown as following:

(1) The protection principle is not affected by current rush for the criterion clears away the influence of mutual inductance magnetic flux. Hence, it will improve the right action rate of transformer protection.

(2) The Least Square principle assures the accuracy of parameter estimate. Due to the large computation quantity and long time calculation, it difficult to realize real-time algorithm. Parameter Estimating with variable windows reduces the quantity and time which suitable to real-time calculation.

(3) By means of the simulation validation, this principle can identify various fault types accurately (contains 5% turn-to-turn fault). And the protection principle is not sensitive to exterior transition resistance fault and system close angle.

ACKNOWLEDGMENT

The project is supported by National Natural Science Foudation of China (No. 50707002) and Shandong Educational Department Foudation (No. J06B06).

REFERENCES

1. Wang, G., C. Zhang, and Y. Huang, "The present state and development of the method for identifying transformer inrush current," *China Electric Power*, Vol. 31, No. 10, 19–22, 1998.
2. Zhang, F., "Discriminating method analysis of transformer magnetizing in-rush current and fault current," *Guangdong Electric Power*, Vol. 19, No. 6, 5–9, 2006.
3. Wang, W., "Novel technique of transformer protection: Novel protection technique considered excitation character [J]," *[Jap.] Electric Calculate*, Vol. 49, No. 6.
4. Phadke, A. G. and J. S. Trop, "A new computer-based flux restrained current differential relay for power transformer protection [J]," *IEEE Trans. on Power Apparatus and System*, Vol. 102, No. 11, 3624–3629, 1983.
5. Xu, Y., Z. Wang, Q. Yang, and D. Zhao, "Study on the improved transformer protection method based on magnetic flux characteristics [J]," *Relay*, Vol. 31, No. 9, 9–14, 2003.
6. Sidhu, T. S., "A power transformer protection technique with stability during current transformer saturation and ratio-mismatch conditions [C]," *IEEE Trans. on Power Delivery*, Vol. 14, No. 3, 798–804, 1999.
7. Zheng, T., W. Liu, H. Zhuang, et al., "Study of a transformer protective schems based on the improved sequence impedance algorithm [J]," *Automation of Electric Power Systems*, Vol. 28, No. 14, 67–71, 2004.
8. Sidhu, T. S., "A power transformer protection technique with stability during current transformer saturation and ratiomismatch conditions," *IEEE Trans. on Power Delivery*, Vol. 14, No. 3, 798–804, 1999.
9. Xiong, X., X.-L. Deng, and B. You, "Transformer protection using parameter identif ication-method," *Automation of Electric Power Systems*, Vol. 23, No. 11, 18–21, June 1999.
10. Wang, Z., Y. Xu, X. Wang, and Q. Yang, "Study on the novel transformer protection principle based on the transformer model [J]," *Proceedings of the CSEE*, Vol. 23, No. 12, 54–58, 2003.

The Susceptibility of Microcontroller Device with Coupling Caused by UWB-HPEM

Sun-Mook Hwang[1], **Joo-Il Hong**[1], **Seung-Moon Han**[1], **Chang-Su Huh**[1], **Uk-Youl Huh**[1], **and Jin-Soo Choi**[2]

[1]Department of Electrical Engineering, INHA University, Incheon, Korea
[2]Agency for Defense Development, Daejeon, Korea

Abstract— Modern electronic circuits are of importance for the function of communication, traffic systems and security systems. An intentional threat to these systems could be of big casualties and economic disasters. This paper examined damage effect of microcontroller device with coupling caused by UWB-HPEM (Ultra Wideband-High Power Electromagnetic). The UWB measurements were done at an Anechoic Chamber using a RADAN UWB voltage source, which can generate a transient impulse of about 180 kV. The susceptibility level for microcontroller has been assessed by field strength. The failure modes were observed in microcontroller. The A type of malfunction is returned to original functions by external rest at lower field strengths (9.1 kV/m). The B type of malfunction is recovered to original functions by power supply on/off when the amplitude of the electromagnetic pulse increases by about 4 times. Further increase of the amplitude leads to destruction. Based on the results, susceptibility of microcontroller can be applied to database to elucidate the effects of microwaves on electronic equipment.

1. INTRODUCTION

The interest in HPEM (High Power Electromagnetic) technology has been widely increased in recent decades [1]. Today's HPEM generators (HPEM: High Power Microwaves (HPM), Ultra Wideband (UWB)) can generate the electromagnetic waves of gigawatts level at short pulse. Then the main frequencies are 1–10 GHz and other frequencies can be made up to the maximum 30 GHz. The HPEM generators being developed in the United States, Britain, Russia and several other countries have studied mainly for the purposes of military. Its electromagnetic pulse is not the purpose of killing people and inflicts permanent damage to semiconductor because the internal circuit of the semiconductor is molten by strong IEMI (Intentional Electromagnetic Interference) around weapon and electronic equipment. Also, the motion of semiconductor is paralyzed by electromagnetic pulse for a certain time because of bringing logical error. Main targets of electromagnetic pulse are power plant, aircraft, high-speed railroad, fighter, main electronic equipment, etc, and its pulse brings not only power production but also the electrical ignition of cars and aircraft to stand. But modern societies are sued for the purposes of military as well as for the threat of terrorism. Therefore massive damage to attack major industrial facilities (medical, communications, traffic control, financial, security, etc.) to social, economic could happen. Also, because it can not be freedom from electromagnetic pulse, the IEMI countermeasure study for major industrial facilities and military equipment is necessary. Actually, semiconductor devices have been studied to experience serious failures and malfunction because of thermal secondary breakdown caused by high power electromagnetic, as devices are mostly comprised of integrated circuits and electronic component, which are sensitive to electromagnetic pulse. This is caused by over current when the reverse voltage is biased to the PN junction region [2]. Consequently, study of the effects of electromagnetic pulse on information instruments is needed. This research examines the destruction and malfunction of microcontroller caused by ultra wideband-high power electromagnetic.

2. SECTION 1

2.1. Experimental Details

Figure 1 shows the experimental equipment set up to analyzer date on destruction and malfunction of microcontroller device by the impact UWB-HPEM and the UWB measurement were done at an anechoic chamber using RADAN UWB voltage source, which can generate a transient impulse of about 180 kV (Peak to Peak). The waveform for the UWB-HPEM pulse is a bipolar transient with a pulse width of approximately 1ns and a rise time of about 200 ps (Fig. 2). D-dot probe (model AD-80 from Prodyn Technologies) has measured the electric field derivative at DUT. An oscilloscope (Tektronix TDS 7404 digital) was used to sample the pulse signals. The D-dot sensor was placed at the DUT and was connected to the oscilloscope by way of a shielded cable.

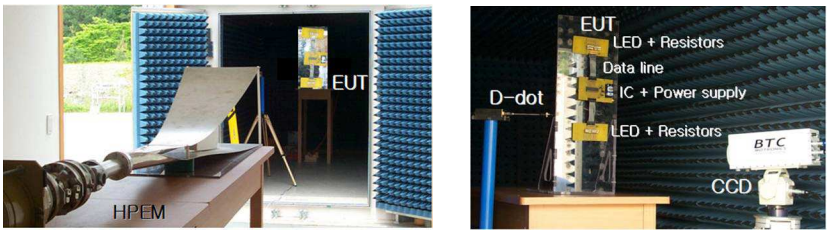

(a) UWB-HPEM experimental setup (b) EUT test setup

Figure 1: The schematic of experimental setup.

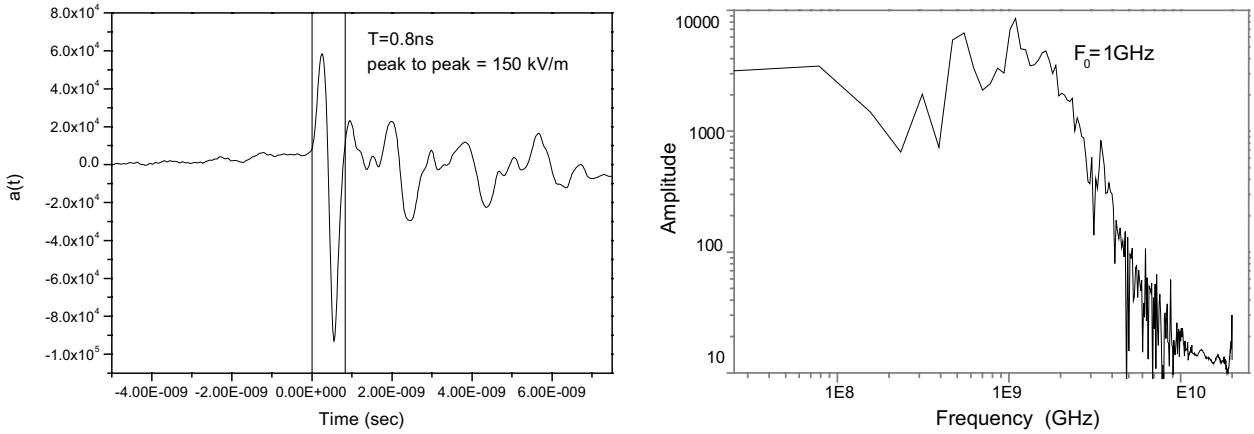

(a) Time domain (b) Frequency domain

Figure 2: The time domain and frequency domain of UWB-HPEM.

Figure 3 defines the malfunction and destruction to microcontroller by wideband-high power electromagnetic [3]. In this case, malfunction does not mean physical damage. After resetting (self-, external- or power reset), the original functions of the system can be recovered. The Malfunction Failure Rate (MFR) is defined as the number of malfunctions of the system divided by the total number of tested devices to the system. Destruction refers to physical damage of the system. Here, the system can not be restored to function again. The Destruction Failure Rate (DFR) is defined as the number of destructions divided by the total number of tested devices. Four quantities (MT; Malfunction Threshold, MR; Malfunction Range, DT; Destruction Threshold, DR; Destruction Range) were defined parameters for the description of the susceptibility of a system [3]. The features of the microcontroller (AT89C51) are:

- High-speed CMOS technology
- Fully Static Operation: 0 Hz to 24 MHz
- Flash Programmable and Erasable Read Only, Memory (PEROM)
- 128 × 8-Bit Internal RAM
- 32 Programmable I/O Lines

2.2. Results and Discussion

Figure 2 shows the malfunction characteristic of microcontroller system by impact of UWB-HPEM. The malfunction may be classified into two types. The A type of malfunction is returned original level of functioning by external rest at lower field strengths (9.1 kV/m). The B type of malfunction is recovered to original functions by power supply on/off when the amplitude of the electromagnetic pulse increases by about 4 times. Further increase of the amplitude leads to destruction. This effect can be explained by the parasitic thyrister near the N and P type channel transistors inside the microcontroller. Such damage to microcontroller was corresponded with previous experiment results [4]. Also the output voltage/current of IC component because of coupling current can be maintained to normal state from noise margin and static power dissipation fluctuation [5]. Therefore microcontroller system has considered that malfunction has occurred by bit error.

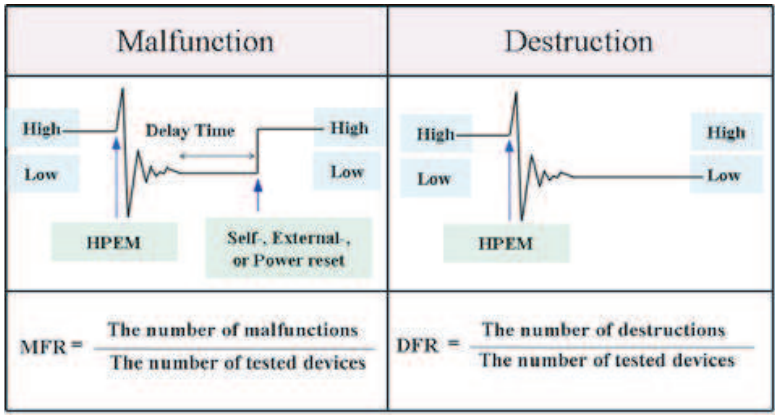

Figure 3: The definition of malfunction and destruction.

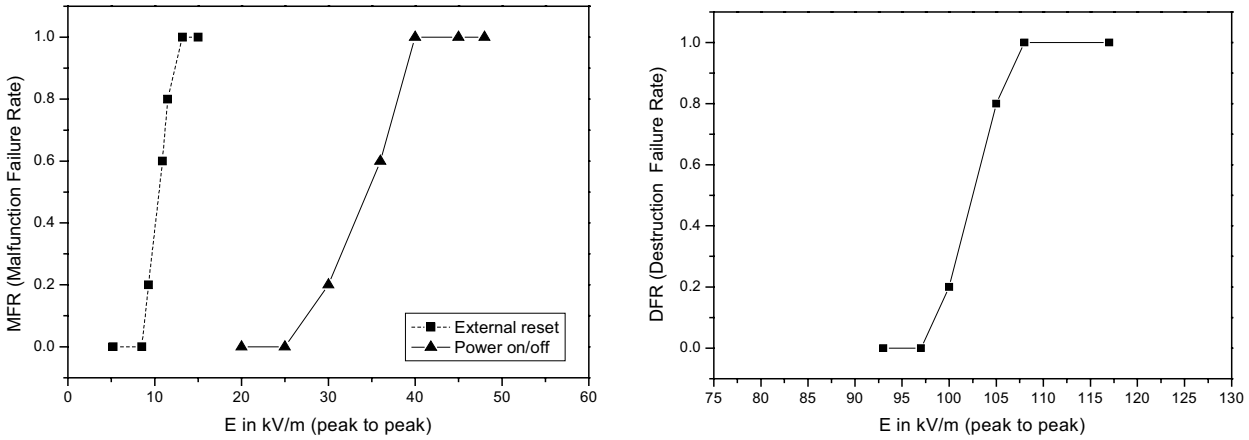

Figure 4: The malfunction and destruction failure rate of microcontroller by impact of UWB-HPEM.

The DT of the microcontroller is 97.5 kV/m and the DR of microcontroller is in a range of 97.5 kV/m to 107 kV/m. Also, the MT of the microcontroller is about 6.5 kV/m and 26.5 kV/m respectively, and the MR of the microcontroller is in a range of 6.5 kV/m to 9.1 kV/m and 26.5 kV/m to 37 kV/m respectively. Based on results of the experiment, breakdown of microcontroller was occurred as follows. If the MFR is smaller than 1, it is impossible to predict whether malfunction will be produced by high power microwave. In this case, malfunction affecting the microcontroller is irregular. Malfunction of microcontroller occurs when certain critical field strength is exceeded. The critical value of the field strength has depended on many factors. First, there are constant influencing factors such as chip fabrication technology and chip layout of the IC. Also, there are variable factors such as switching states of the transistor. Because of these uncertain outcomes, the critical value of field strength varies randomly [6]. Therefore, the effects on semiconductors in terms of malfunction and destruction could be more concretely identified by defining the failure rate in accordance with the field strength.

Figure 5 shows the change in power supply current and coupling current of the microcontroller upon malfunction of the semiconductor as a result of an ultra wideband-high power electromagnetic. As shown in the figure, the power supply current of malfunction A type has been charged irregularly and the power supply current of malfunction B type rapidly has increased from 47.5 mA to 86.1 mA rapidly when the field strength reaches approximately 31 kV/m and leveled off. The power supply current has been increased about 2 times in the case of the microcontroller relative to a normal current. The result was considered to be caused by a latch-up phenomenon due to parasitic bipolar components near the N and P type channel transistors in the CMOS device [7].

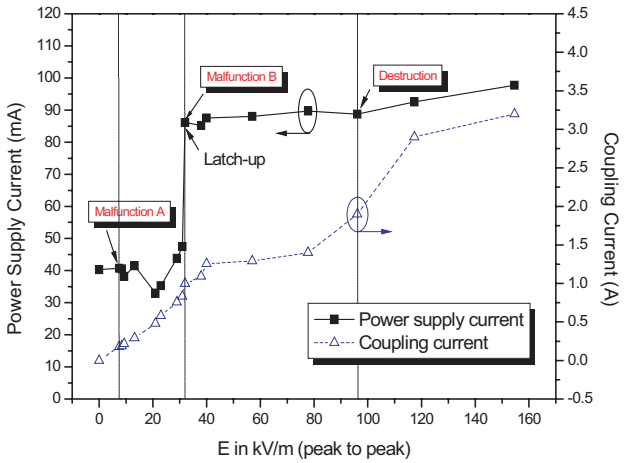

Figure 5: The coupling current and the power supply current of microcontroller by impact of UWB-HPEM.

3. CONCLUSIONS

The investigation of the susceptibility of microcontroller to ultra wideband-high power electromagnetic pulse has shown, that the malfunction and destruction range are influenced by the field strength. The A type of malfunction is returned original level of functioning by external rest at lower field strengths (9.1 kV/m). The B type of malfunction is recovered to original functions by power supply on/off when the amplitude of the electromagnetic pulse increases by about 4 times. Further increase of the amplitude leads to destruction. The result was considered to be caused by a latch-up phenomenon due to parasitic bipolar components near the N and P type channel transistors in the CMOS device. Also, the output voltage/current of IC component because of coupling current can be maintained to normal state from noise margins and static power dissipation fluctuation. This investigation can be applied to database to elucidate microwave effects of electronic equipment.

ACKNOWLEDGMENT

Authors are gratefully acknowledging financial support by the Agency for Defense Development.

REFERENCES

1. David Yang, H. Y. and R. Kollman, "Analysis of high-power RF interference on digital circuits," *Electromagnetics*, Vol. 26, 87–102, 2006.
2. Bäckström, M. G., "Susceptibility of electronic systems to high power microwaves: Summary of test experience," *IEEE Transactions on Electromagnetic Compatibility*, Vol. 46, No. 3, 2004.
3. Hwang, S. M., J. I. Hong, and C. S. Huh, "Characterization of the susceptibility of integrated circuits with induction caused by high power microwaves," *Progress In Electromagnetics Research*, PIER 81, 61–72, 2008.
4. Camp, M., H. Garbe, and D. Nitsch, "Influence of the technology on the destruction effects of semiconductors by impact of EMP and UWB pulses," *IEEE Trans. on EMC*, Vol. 1, 87–92, 2002.
5. Kim, K., "Critical upsets of CMOS inverters in static operation due to high-power microwave interference" *IEEE Trans. on EMC*, Vol. 49, No. 4, 2007.
6. Camp, M., H. Gerth, H. Garbe, and H. Haase, "Predicting the breakdown behavior of microcontrollers under EMP/UWB impact using a statistical analysis," *IEEE Trans. on Electromagnetic Compatibility*, Vol. 46, 368–79, 2004
7. "JESD78 latch-up testing standard," Electronic Industry Association JEDEC standards, Arlington, VA.

Characterisation and Testing Shielding Fabrics

Zoltán Szabó and Pavel Fiala
BUT Brno, UTEE, Kolejní 2906/4, Brno 612 00, Czech Republic

Abstract— In connection with rapidly increasing progress in the radio communication services and other technical branches, which influence electromagnetic environment, the problems connected with electromagnetic compatibility occur. Because of the electromagnetic interference minimization it is necessary to ensure the shielding of sensitive devices, buildings and also persons. The suitable alternative to the classical shielding materials can be special shielding-fabrics. The main advantages of these fabrics are their low weight, flexibility and their easy processability. Shielding is a very popular method of ensuring electromagnetic compatibility and of protecting electronic and electrical equipment and human beings against radiated electromagnetic energy. The knowledge of shielding effects of different types of material represents a basic prerequisite for further development and implementation of shielding devices. This paper presents an analysis of the measuring methods and a comparison of different materials in terms of their specific shielding effects. The absorption properties of the various submitted samples were measured using both a Crawford chamber and the Insertion loss method. In the samples, the capacity to absorb electromagnetic waves was determined with the help of a spectral analyzer.

1. INTRODUCTION

Shielding is a very popular method to ensure the electromagnetic compatibility, protection of electronic equipments and human beings against radiated electromagnetic energy. Decrease of radiation disturbances and increase of immunity to electromagnetic fields is obtained with grounded shielding eventually in combination with other suppression components. The shielding is also used to isolate some places from the external source of electromagnetic interference or to prevent radiation electromagnetic disturbance from the internal shielded source. There were used metallic materials with well known electromagnetic qualities for the shielding.

There are more and more used plastic materials for shielding with a conductive coating or with embedded conductors which ensure the shielding flexibility. Recently the researchers' attention is focused on even lighter and more flexible materials which are fabrics coated with absorptive film. These materials due to their flexibility and low cost price are promising candidates for instruments and human protection against unwanted electromagnetic radiation effect.

Measuring shielding and absorption qualities of fabrics and plastic materials is relatively difficult. There were developed many measuring methods that are used in various laboratories to solve these problems. A lot of producers who develop this type of fabrics are searching for relatively simple, not time-consuming and reliable measuring methods to measure shielding and absorption qualities which operate in a wide frequency range.

2. ELECTROMAGNETIC WAVE ABSORBTION

Electromagnetic wave attenuation is caused by absorption or reflection on particular material which is inserted between the source and the electromagnetic wave receiver. Depending on the applied attenuation measurement method the material properties can be defined variously, for example by the shielding effectiveness or by the insertion loss.

2.1. The Insertion Loss Method

The insertion loss is evaluated as the loss (attenuation) of the emitted signal facilitated by the material under testing

$$A = \frac{U_0}{U_1} \tag{1}$$

expressed in dB,

$$A_{\mathrm{dB}} = 20 \cdot \log \frac{U_0}{U_1} \tag{2}$$

where U_0 is the output voltage without the tested sample, U_1 is the same signal with the tested material.

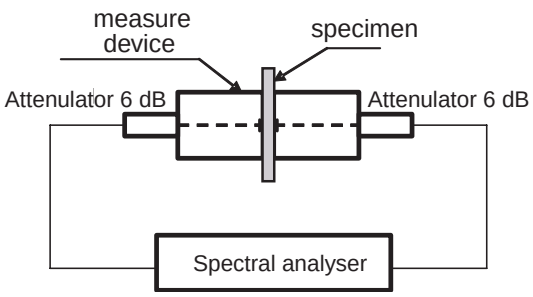

Figure 1: The device used for measuring the insertion loss.

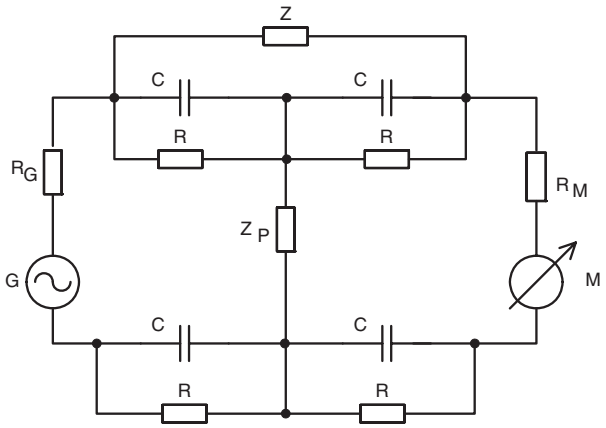

Figure 2: The equivalent model for insertion loss measuring [1].

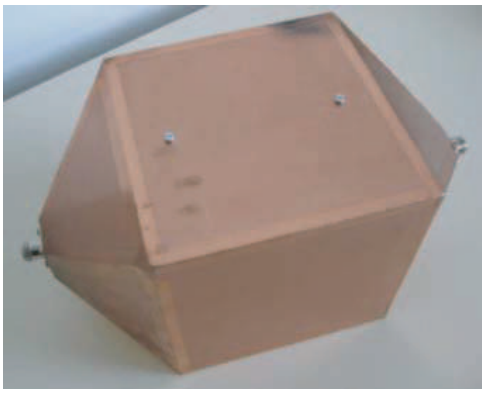

Figure 3: Miniature TEM cell (Crawford chamber).

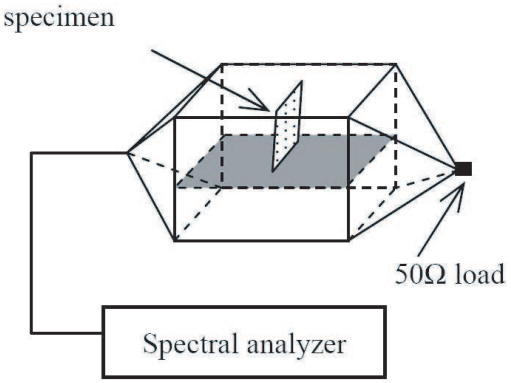

Figure 4: Block diagram of measuring device with Crawford chamber.

The measured task (Figure 1) implemented with the help of a symmetrical line can be presented diagrammatically using an equivalent diagram with concentrated parameters. The equivalent diagram with concentrated parameters is shown in Figure 2. The obtained results can be interpreted on the basis of this equivalent model of loss measuring. The parameters Z, C, R are eliminated during the task calibrating, and the insertion loss is represented by the Z_P element.

2.2. Shielding Effectiveness

The shielding effectiveness (SE) is defined as a ratio of electromagnetic field measured without (H_0) and with (H_1) tested material which separates the source from the receiver.

$$SE = \frac{H_0}{H_1} \tag{3}$$

expressed in dB,

$$SE_{\text{dB}} = 20 \cdot \log \frac{H_0}{H_1} \text{ [dB]} \tag{4}$$

There are used TEM cell (Crawford chamber) for this type of measurement — Figure 3.

3. PROJECT AND REALIZATION

The measuring place set consisted of an Agilent spectral analyzer and a Crawford chamber. This chamber had been designed for measuring with a 50 Ω line and for measuring samples with maximum dimensions of 80 × 100 × 30 mm. For generating electromagnetic field and analyzing the resulting signal we used a spectral analyser Agilent CSA Spectrum Analyzer N1996A-506 (from 100 kHz to 6 GHz). The apparatus incorporates both the signal generator and the spectrum analyzer.

The second realized method for measuring shielding fabrics quality is based on the measuring insertion loss. In this method we used the above mentioned theoretical descriptions. In the laboratory of DTEEE was made insertion loss measure device. This device consists of two cylindrical electrodes which are matched to 50 Ω transmission line. To generate and measure the insertion loss the spectral analyzer N1996A-506 from Agilent was used. Before the measuring the device was calibrated to eliminate the device insertion loss and unwanted signals. The calibration set the device insertion loss to zero. After the sample was inserted between the measuring electrodes on spectral analyzer, the level of insertion loss changed. This change was interpreted as a measured sample insertion loss.

4. EXPERIMENT RESULTS

The following figures (Figures 5–8) show the measurement results of the shielding effectiveness and the insertion loss measurement of various shielding fabrics which were measured by the above described methods. The Figure 5 illustrates shielding effectiveness for the woven fabric — FlecTron with the surface conductance 0.1 Ω/m^2. This fabric reaches its highest attenuation level in range from 1 to 1.5 GHz which is at average 20 dB. There was also measured the insertion loss for this fabric material. Its measured characteristic is illustrated in Figure 7. The maximum of insertion loss is about 50 dB in range from 0.5 to 2.5 GHz. If we compare these measurement results with a non-woven fabric made from carbon fibers with a surface conductance of 10 Ω/m^2 then the FlecTron type fabric has slightly worse shielding qualities. The shielding effectiveness of fabric made from carbon fibers is in average 20 dB in range from 0.5 to 2 GHz. The insertion loss reaches its maximum in interval to 0.5 GHz, approximately 40 dB, from 0.5–1.5 GHz it is about 35 dB and above 1.5 GHz the insertion loss decreases to the 30 dB (Figure 8).

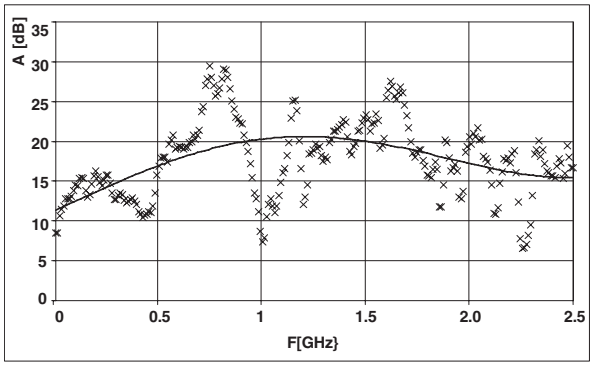

Figure 5: Shielding effectiveness for FlecTron fabric.

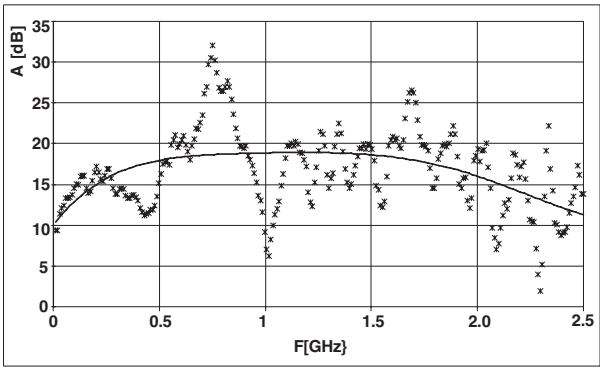

Figure 6: Shielding effectiveness for non-woven fabric from carbon fibers.

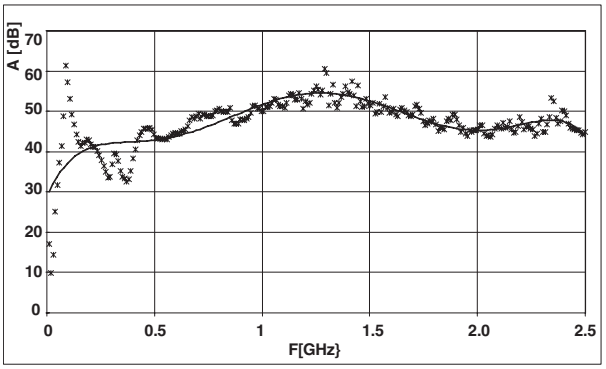

Figure 7: Insertion loss for FlecTron fabric type.

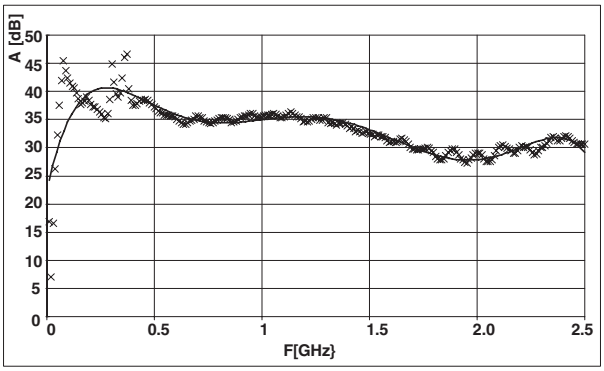

Figure 8: Insertion loss for non-woven fabric from carbon fibers.

5. CONCLUSION

This article analyzed problems with measurement shielding qualities of modern absorption fabrics. There were proposed two different methods to describe and measure the absorption fabrics quality. To verify the functionality of these methods there was made an experimental measurement on two different types of samples. The results of these experiments were demonstrated on graphic diagrams and described.

REFERENCES

1. Koprowska, J., M. Pietranik, W. Stawski, "New type of textiles with shielding properties," *Fibres & Textiles in Easten Europe*, July/October 2004.
2. Pocai, M. R. and E. Bottari, "Electromagnetic characterization of protective clothing," *1999 International Symposium on Electromagnetic Compatibility*, Tokyo, May 17–21, 1999.
3. Wilson, P. F. and M. T. Ma, "Techniques for measuring the electromagnetic shielding effectiveness of materials: Part II — Near-field source simulation," *IEEE Transactions on Electromagnetic Compatibility*, Vol. 30, No. 3, Part 2, 251–259, August 1988.
4. Wilson, P. F. and M. T. Ma, "Techniques for measuring the electromagnetic shielding effectiveness of materials. I. Far-field source simulation," *IEEE Transactions on Electromagnetic Compatibility*, Vol. 30, No. 3, Part 2, 239–250, August 1988.

Susceptibility of TTL Logic Devices to Narrow-band High Power Electromagnetic Threats

Joo-Il Hong[1], **Sun-Mook Hwang**[1], **Kwang-Yong Kim**[1], **Chang-Su Huh**[1], **Uk-Youl Huh**[1], **and Jin-Soo Choi**[2]

[1]Department of Electrical Engineering, INHA University, Incheon, Korea
[2]Agency for Defense Development, Daejeon, Korea

Abstract— The aim of this paper is to investigate the damage effects of TTL AND and NAND logic devices manufactured using five different technologies under narrow-band high power electromagnetic (NB-HPEM) waves by magnetron. The output of the magnetron was controlled from 0 to 1 kW and the operating frequency was narrow-band at 2460 ± 50 MHz. NB-HPEM waves were propagated into a closed-ended standard rectangular waveguide (WR-340) for 1 s. NB-HPEM waves were coupled with a directional coupler probe and the device under tests (DUTs) were placed under the probe. DUTs for the malfunction and destruction test setup were used for a light-emitting diode (LED) circuit and LEDs were used as loads to observe the operating states of the device. The TTL logic devices showed two types of damage i) malfunction, which means that no physical damage occurred in the device and after a self-reset or power-reset, the device returned to normal function, and ii) destruction, which means that the device incurred physical damage, and operation could not be recovered without replace by a new device. When the devices were damaged, the logic output of the TTL gate was connected to ground voltage (pulled down). The surfaces of the destroyed TTL logic devices were removed and the chip conditions were investigated with a microscope. The microscopic analysis of the damaged devices showed component, onchipwire and bondwire destruction such as breakthroughs and melting due to thermal effects.

1. INTRODUCTON

The rapid development of digital and semiconductor technology made it possible to produce the miniaturized electronic apparatus and equipment with composite, high speed, and low voltage features based on the advanced and complicated circuit technology [1–3]. Modern electronic devices have come into family, industry, and military use widely However, malfunction of such electronic devices in one of these areas could lead to casualties and economic disasters. The electromagnetic environment can disturb electronic devices to object operate rightly. As such, the susceptibility of electronic devices to electromagnetic environment such as electromagnetic pulse (EMP), ultra wideband (UWB) high power microwave (HPM) and high power electromagnetic waves (HPEM) is a topic that has warranted much attention [1–7].

The damage of electronic devices is determined by the amount of energy that is transferred while the electronic devices are coupled by electromagnetic environment. Coupling is a kind of mechanism whereby electromagnetic energy is delivered to device under test (DUT) through a circuit line or lead frame on the devices directly. Coupled voltage and current can cause a malfunction or destruction of electronic devices. For such cases, the analysis of electromagnetic environment is therefore necessary. The goal of this investigation is to analyze the influence of digital IC devices on the damage effects by high power electromagnetic waves.

2. EXPERIMENTAL

It is very difficult and dangerous to investigate the damage effects of electronic devices by high power and high frequency. The magnetron was the high power and high frequency electromagnetic waves oscillator which was used initially in early radar systems. We used a magnetron as an intentional high power electromagnetic waves source, because it is easy to control the output and it can generate high frequency and high output power [2–5]. The output of the magnetron was controlled from 0 to 1 kW and the operating frequency was narrow-band at 2460 ± 50 MHz. Narrow-band high power electromagnetic (NB-HPEM) waves were propagated into a closed-ended standard rectangular waveguide (WR-340) for 1 s as shown in Fig. 1(a). NB-HPEM waves were coupled with a directional coupler probe and the devices under tests (DUTs) were placed under the probe During the investigations five different TTL technologies (schottky, low power schottky, advanced schottky, advanced low power schottky, and Fairchild advanced schottky) were tested as shown in Table 1.

DUTs for the malfunction and destruction test setup were used for the LED circuit. LEDs were used as loads to observe the operating states of the device as shown in Fig. 1(b). The DUTs contain quadruple 2-input AND or NAND gates, as shown in Fig. 1(c).

To describe peak electric field in the WR-340 waveguide and the different failure effects two quantities have been defined [2, 3, 6, 7]. The malfunction failure rate (MFR) and destruction failure rate (DFR) behaves in principle as shown in Fig. 2. The electrical characteristics before and after NB-HPEM waves expose such as input and output voltage of the gates respectively, and supply current were measured. Destructed digital IC devices were removed these surface (decapsulation) and a chip conditions were analyzed by an optical microscope.

3. TEST RESULTS

The TTL logic devices showed two types of damage by NB-HPEM waves. One is malfunction, which means that no physical damage occurred in the device and after a self-reset or power-reset, the device returned to normal function, and the other is destruction, which means that the device incurred physical damage, and operation could not be recovered without replace by a new device. When the devices were damaged, the logic output of the TTL gate was connected to ground voltage (pulled down). Fig. 3 shows the MFRs and DFRs of TTL IC devices built using

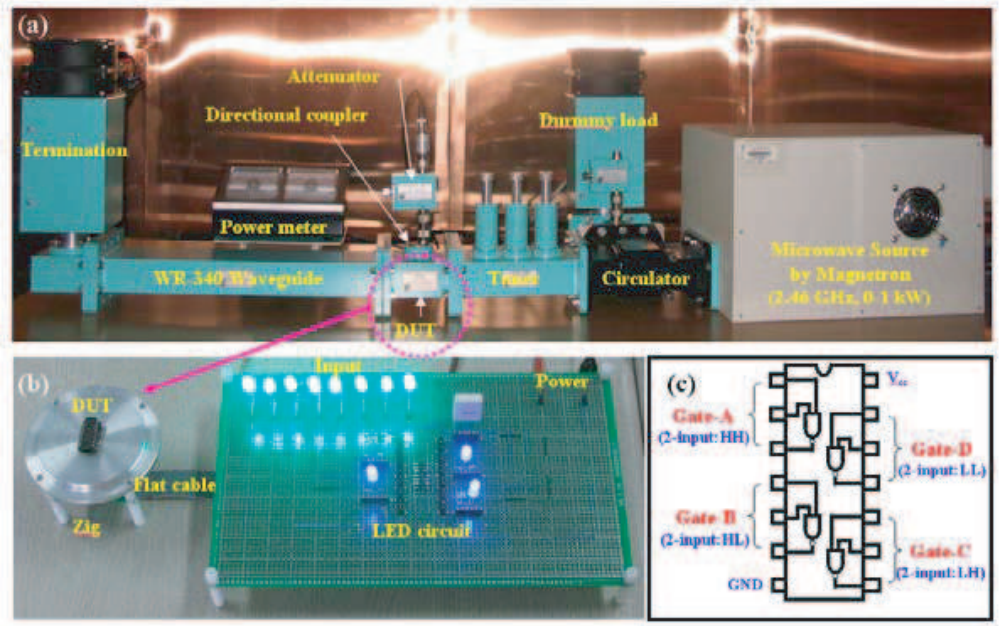

Figure 1: Damage effects of digital IC devices by NB-HPEM waves test setup: (a) NB-HPEM system setup; (b) LED circuit; and (c) logic diagram.

Table 1: Tested TTL logic devices built using three different technologies.

IC Processing Technology	TTL	Technology	Manufacturer	Package	Logic Type	Part code
		Schottky (S)	Texas Instruments	DIP	AND	SN74S08N
		Low Power Schottky (LS)				SN74LS08N
		Advanced Schottky (AS)				SN74AS08N
		Advanced Low Power Schottky (ALS)				SN74ALS08N
		Fairchild Advanced Schottky (F)				SN74F08N
		Schottky (S)			NAND	SN74S00N
		Low Power Schottky (LS)				SN74LS00N
		Advanced Schottky (AS)				SN74AS00N
		Advanced Low Power Schottky (ALS)				SN74ALS00N
		Fairchild Advanced Schottky (F)				SN74F00N

five different technologies. Each point is an average value for 10 times tested at the electric field strength respectively. By increasing the electric fields, the F, S, and ALS series of TTL AND and S, LS, and ALS series of TTL NAND devices underwent reversible malfunctions, which could be reversed by switching the power off and on or by self reset. However, only the AS and LS series of TTL AND and F, S, and AS series of TTL NAND devices underwent reversible malfunctions and experienced permanent destruction at much higher fields.

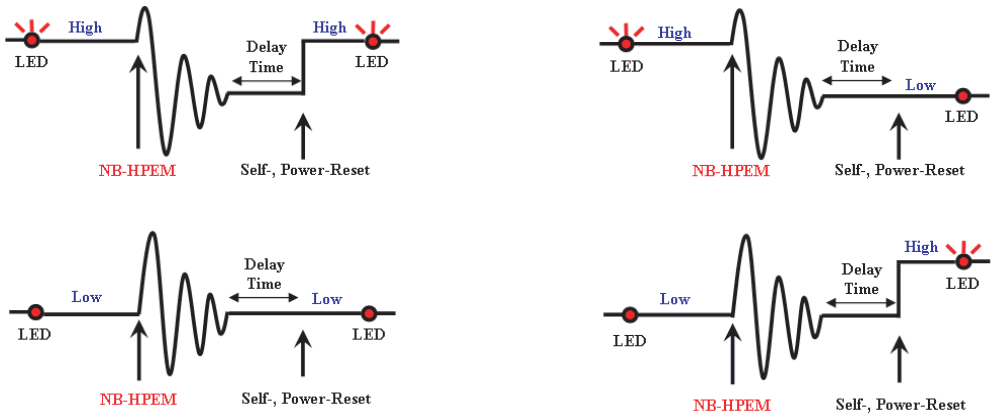

(a) (b)

Figure 2: Principle behavior of malfunction failure rate and destruction failure rate: (a) Malfunction failure rate; (b) Destruction failure rate.

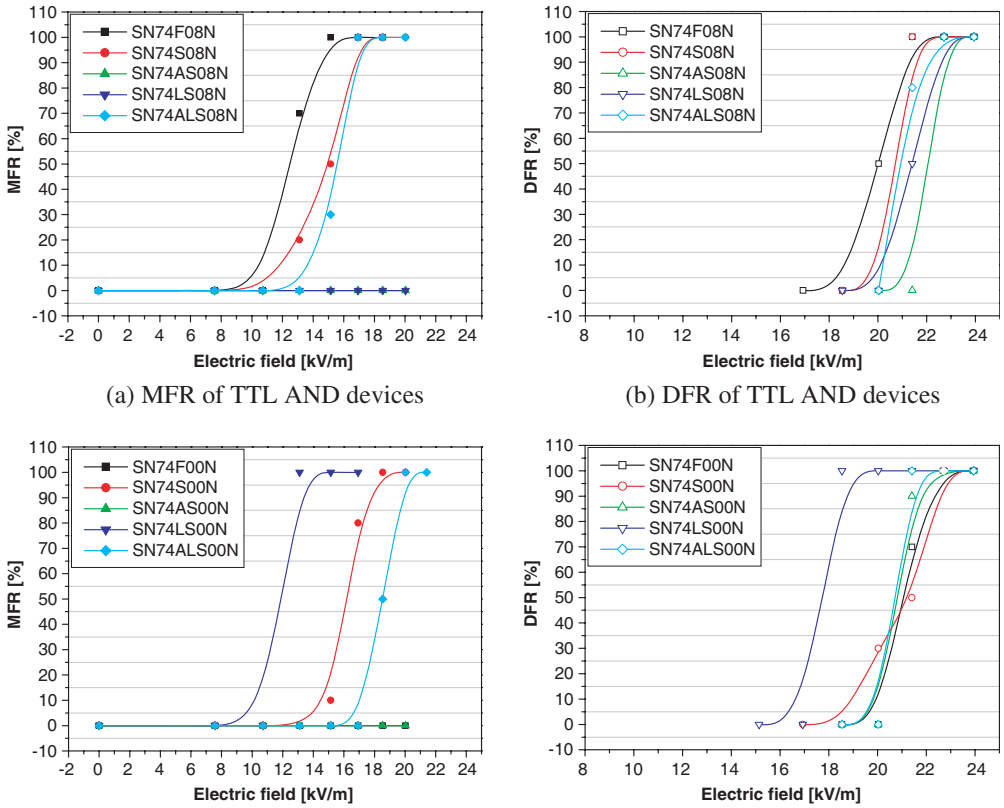

(a) MFR of TTL AND devices (b) DFR of TTL AND devices

(c) MFR of TTL NAND devices (d) DFR of TTL NAND devices

Figure 3: Malfunction and destruction failure rate of TTL logic devices under NB-HPEM waves by magnetron.

Destructed TTL logic devices were removed their surface and a chip conditions were analyzed by a microscope as shown in Fig. 4. Destructed devices generally show three different damaging

effects [2, 3, 6, 7]. At lower field strengths only electronic components like diodes or transistors on the chip, mostly as a result of flashover effects. If the amplitude of field strengths increases, additional onchipwire destructions and multiple component destructions occurred. Further increase of the amplitude leads to additional bondwire destructions and multiple component and onchipwire destruction. The coupling NB-HPEM waves are converted into a current, which rapidly flows into the chip. Consequently, the current causes thermal damages, such as onchipwire and bondwire melting, and as a result the devices undergo immediate destruction.

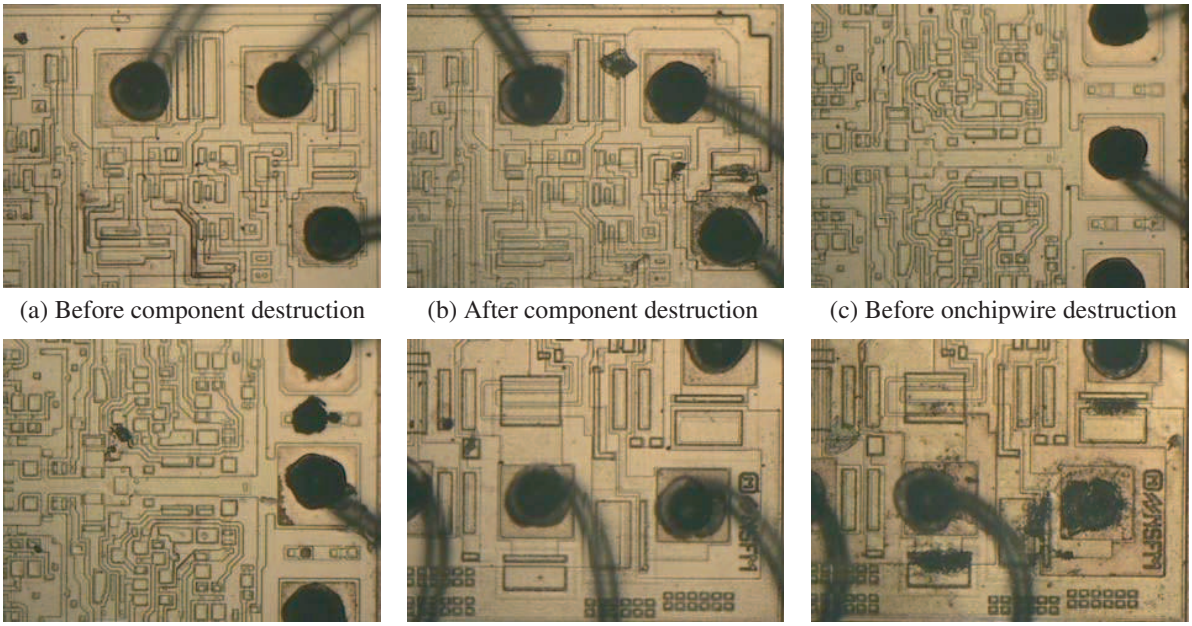

(a) Before component destruction (b) After component destruction (c) Before onchipwire destruction

(d) After onchipwire destruction (e) Before bondwire destruction (f) After bondwire destruction

Figure 4: Destructive effects of before and after NB-HPEM waves exposure on chip level: (a) and (b) SN74S08N; (c) and (d) SN74ALS08N; (e) and (f) SN74F00N.

4. CONCLUSION

The main goal of this study was to examine the susceptibility levels of digital IC devices, the process of malfunction, and the effects of damage. Investigation of the susceptibility of TTL IC AND and NAND devices to NB-HPEM waves by magnetron showed that the susceptibility of TTL IC devices varies between different technologies (S-TTL, LS-TTL, AS-TTL, ALS-TTL, and F-TTL). The microscopic analysis of the destroyed devices generally shows three different damaging effects (multiple electronic component, onchipwire, bondwire and bond-pad destructions) due to an increase in the current flow at a particular point in the junction in order to accommodate additional stress on the device. The tested results will be applied to the fundamental data which interprets the combination mechanism of digital IC devices from electromagnetic environment and are expected to the data which understand electromagnetic wave effects of electronic devices.

ACKNOWLEDGMENT

Author(s) are gratefully acknowledging the financial support by Agency for Defense Development.

REFERENCES

1. Kim, S. H., J. Y. Nam, K. I. Ouh, S. J. Hong, and C. B. Rim, "Analysis of coupling mechanism and solution for EFT noise on semiconductor device level," *Proceedings of the International Conference on Electromagnetic Interference and Compatibility*, New Delhi, India, 1999.
2. Hwang, S. M., J. I. Hong, and C. S. Huh, "Characterization of the susceptibility of integrated circuits with induction caused by high power microwaves," *Progress In Electromagnetics Reserarch*, PIER 81, 61–72, 2008.
3. Hong, J. I., S. M. Hwang, and C. S. Huh, "Susceptibility of microcontroller devices due to coupling effects under narrow-band high power electromagnetic waves by magnetron," *Journal of Electromagnetic Waves and Applications*, Vol. 22, 2451–2462, 2008.

4. Giri, D. V., *High-power Electromagnetic Radiators Nonlethal Weapons and Other Applications*, Harvard University Press, Cambridge, Massachusetts, and London, England, 2004.
5. Taylor, C. D. and D. V. Giri, *High-power Microwave Systems and Effects*, Tayloer & Francis, Washington D.C., 1994.
6. Giri, D. V. and F. M. Tesche, "Classification of intentional electromagnetic environments (IEME)," *IEEE Transaction on Electromagnetic Compatibility*, Vol. 46, No. 3, 322–328, 2004.
7. Camp, M., H. Garbe, and D. Nitsch, "UWB and EMP susceptibility of modern electronics," *2001 IEEE International Symposium on Electromagnetic Compatibility*, Vol. 2, 1015–1020, 2001.

Evaluation of Interference between Microwave Oven Noise and IEEE802.11b Using a GTEM Cell

Sangbong Jeon[1], **Yeon-Choon Chung**[2], **Chang-Han Jun**[1], **Suk-Tai Kwun**[1], **Jae Hoon Yun**[3], **and Sangho Choi**[1]

[1]Korea Radio Promotion Association, Korea
[2]Seokyeong University, Korea
[3]Electronics and Telecommunications Research Institute, Korea

Abstract— In this paper, we proposed the evaluation method of the interference between the microwave oven noise and the signal of the IEEE802.11b by using the GTEM Cell. We used microwave oven noise, unintentional noise in time domain realized by combining signals from an AM(Amplitude Modulation) modulator and a FM (Frequency Modulation) modulator to evaluate the interference effects on IEEE802.11b. Finally we analyzed the effect of microwave oven noise to the throughput of IEEE802.11b by using APD (Amplitude Probability Distribution) of the interfering noise.

1. INTRODUCTION

Recently the enlargement and convergence of various radio communication services require the large usage of the spectrum in small area and then yield the large spectrum density. Especially radio communication services such as Bluetooth and IEEE 802.11b, Wireless LAN are being widely used in the industry fields. The frequency bands of the systems are assigned within ISM (Industrial, Scientific and Medical) bands such as 2.4 GHz. The communication performance of radio communication services is critically decreased because the equipment such as microwave oven generates the electromagnetic noise within 2.4 GHz bands. Therefore, it is important to study on the modeling for the interference noise generated by microwave oven to evaluate the interference effects on the communication performance, and these studies are being actively progressed in the various fields [1, 2]. Especially Middleton has suggested the test method that evaluate the communication performance with BER (Bit Error Rate) for the radio link by modeling the microwave oven noises as the impulse noise with the statistical methods using the APD (Amplitude Probability Distribution) [3]. The statistical modeling has been expressed as the statistical parameter of APD. There is no information for the noise wave in time domain, so it is difficult to evaluate the BER performance with the small amount of sampled data. In addition, this modeling method has a problem that the statistical parameter for the hopping frequency channel has to be obtained to evaluate the performance for the interference of the FHSS (Frequency Hopped Spread Spectrum) system because the noise signal of microwave oven has experienced the frequency changes in time domain. In Japan, according to the recent paper, the microwave oven noise has been measured in time domain and this has been embodied as the modeled noise in time domain by combining the amplitude modulation and the frequency modulation [4]. In this paper, the modeled noise of microwave oven in time domain is embodied for the purpose of using the unintentional noise, the interference signal in 2.4 GHz.

Also the evaluation environment is required to evaluate the communication performance, and it is generally achieved by embodying the radio communication system such as wireless LAN in the non-echo chamber [5]. This kind of method is embodied by putting both EUT (Equipment Under Test) and the antenna in the non-echo chamber extended by cable from communication AP (Access Point) outside of the non-echo chamber. But, this is difficult for the realization as well as the expensive cost. According to the recent research, it is introduced the measurement environment using PW cell (Parallel Wired cell) to possibly communicate with each other between EUT and AP [6]. Although this is basically the same theory as TEM cell, this is different in structure by eliminating the side of TEM cell. Additionally, the effect for the noise from many other sources can't be totally excluded in yielding the measurement results because the side of PW cell is opened. The GTEM cell with the totally closed structure is used in this research in other to improve the problem in the case PW cell and increase the reliability for the performance evaluation of radio communication from many other noise sources.

This paper is intended to evaluate the interference effect of unintentional noise on the performance of the wireless communication service. For this, the modeled noise of the microwave oven is

used as the unintentional noise in time domain. The reliability is ensured by using GTEM cell as the interference effect assessment environment, and the objective and general assessment analysis method is suggested for the interference effect.

2. THE SIMULATION AND REALIZATION OF MICROWAVE OVEN NOISE

Microwave oven is the equipment radiating RF energy in 2.45 GHz frequency band and largely used in each house and office. According to the difference of high voltage power used to drive the magnetron, the general RF energy generator, the microwave oven is divided into two kinds of types, transformer and switching. The frequency of AC power line uses $50 \sim 60$ Hz and $30 \sim 50$ kHz for two types each other [7]. The transformer type is used in this paper. The basic presumption for the model of microwave oven noise is as follows [4]:

1) The width of noise pulse in time domain is the same as width of the time gap of driving power ($V(t)$) exceeding the threshold power (V_0).
2) The instantaneous amplitude of the pulse envelop curve is linearly changed for the driving power (AM).
3) Also the instantaneous frequency is linearly changed for the driving power (FM).

It is expressed as the Eq. (1).

$$I(t) = I_0 U(V(t)) \exp\left[2\pi i \left(f_0 t + f_{\max} \int_{-\infty}^{t} V(\zeta) d\zeta\right)\right] \tag{1}$$

where f_0 is carrier frequency ($\cong 2.45$ GHz), $f_{\max}$ is the maximum shift frequency of FM, $V(t)$ is the normalized driving voltage and I_0 is the maximum amplitude and phase of the noise as the complex parameter. It is presumed that the phase has the uniform distribution in $[0, 2\pi]$. $U(V)$ is driven by the threshold voltage of the amplitude modulation, V_0 given in the Eq. (2).

$$U(V) = \begin{cases} V & \text{for } V \geq V_0 \\ 0 & \text{for } V < V_0 \end{cases} \tag{2}$$

Also, $V(t)$ driven in magnetron can be represented as the Eq. (3), in case of the transformer type.

$$V(t) = \cos(2\pi f_v t) \tag{3}$$

where f_v is the frequency of the A.C. power.

Table 1: Noise parameter of the microwave oven.

AC mains frequency: f_v	50 Hz
Threshold voltage: V_0	0.3
Carrier frequency: f_0	2.42 GHz
Frequency deviation: $f_{\max}$	43 MHz
Amplitude: I_0	28.7 mV

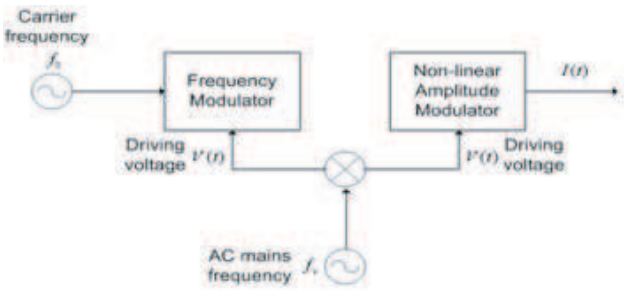

Figure 1: Model of the microwave oven noise.

The Fig. 1 shows modeling of the noise generated by combining both FM modulation signal and AM modulation signal in order to consider the operation of microwave oven as above mentioned. This can be simply realized using the signal generator. Generally, in case of microwave oven of the transformer type, the above mentioned parameter is presented as the Table 1 [4]. Fig. 2(a) shows the signal in the time domain when span equals 0 at 2.45 GHz and Fig. 2(b) shows the envelope amplitude in the frequency domain when spectrum analyzer is set with maximum hold mode.

3. INTERFERENCE EFFECT ANALYSIS

The Fig. 3 is the test outline diagram for the mutual effect analysis between the microwave oven noise and IEEE 802.11b. The signal generator is used as the input signal of GTEM cell generating the modeled microwave oven noise and is connected by the wireless putting the wireless notebook and AP inside GTEM cell to minimize the outside interference. Also, the AP in GTEM cell is connected to the outside notebook using LAN cable. We transmits data using 802.11b wireless link, measures the throughput transmitted from EUT inside GTEM cell and seeks the APD curve from this. The APD curve means the probability distribution that will be bigger than the specific thresholds.

The Fig. 4 shows both the frequency bands of IEEE 802.11b and the occupied frequency distribution of microwave oven noise [8]. Channel 1, 2 and 3 of wireless LAN are not shared by oven noise bandwidth from 2.434 GHz to 2.466 GHz, but channel 8 and 9 are totally co-shared by oven noise spectrum. The rest of channels are partially overlapped.

The Fig. 5 is the results that measure the envelope amplitude of microwave oven noise in time domain on each center frequencies of IEEE802.11b channels partially or totally shared by microwave oven noise. It shows that the time occupied rate and amplitude size of microwave oven noise is different according to the center frequency of the channel. Table 2 shows the occupied bandwidth in the frequency domain, time-occupied rate in time domain and maximum value of the interference noise of microwave oven based on each IEEE 802.11b channels.

The Fig. 6 shows the result presenting the interference effect on each channels of 802.11b as the probability distribution when microwave oven noise is inputted into the GTEM cell.

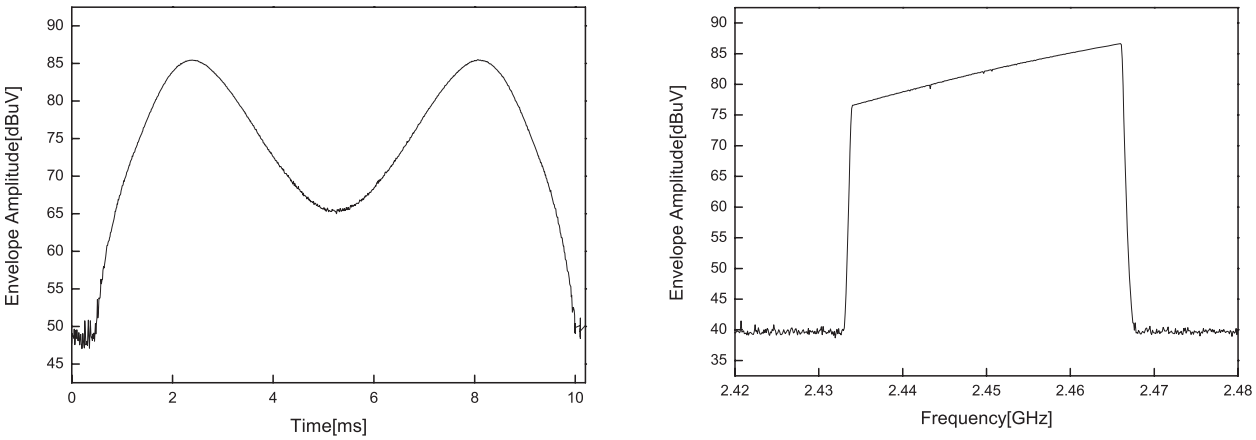

(a) (b)

Figure 2: Measured values of microwave oven noise modeled. (a) Time domain (at 2.45 GHz), (b) Frequency domain.

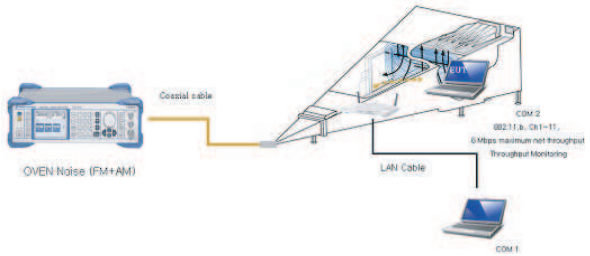

Figure 3: The setup for interference measurement of microwave oven noise and IEEE802.11b.

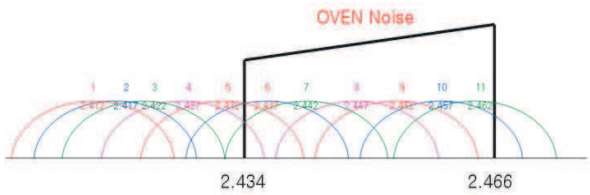

Figure 4: The frequency bands of the microwave oven noise and IEEE802.11b.

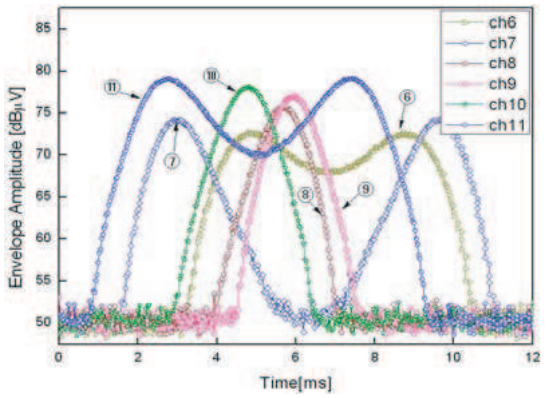

Figure 5: The waveform of microwave oven noise in time domain.

Table 2: Parameter of microwave oven noise interference to wireless LAN channels.

Channel	Occupied bandwidth(%)	Time occupied (ms)	Max (dBμV)
Ch 6	64	7.11	72.72
Ch 7	86	7.06	74.24
Ch 8	100	2.9	75.71
Ch 9	100	2.9	77.13
Ch 10	86	3.38	78.11
Ch 11	64	8.37	79.13

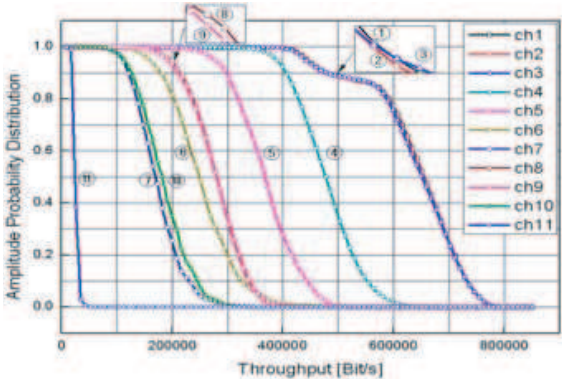

Figure 6: APD of the measured interference between microwave oven noise and IEEE802.b.

According to the analysis of the result, the probability for channel 1, 2 and 3 that throughput will be over 5.5 Mbps recommended in IEEE standards is 90%. That means the bandwidth doesn't have the shared bandwidth at all, so it presents there is no mutual interference between two systems. Also, the wider frequency bandwidth of LAN channel means the larger shared bandwidth and the lower throughput generally, except for channel 8 and 9. The reason is that the above cases for channel 8 and 9 are resulted from the relatively short occupied time, about 2.9 ms when compared with the other IEEE802.11b channels.

In this paper, the result shows that the microwave oven noise is generated according to the change of the amplitude and the frequency with time. Therefore when analyzing the mutual interference effect with wireless LAN, the performance of communication is assessed by the amplitude and time occupied rate in time domain as well as the mutually shared bandwidth in frequency domain.

4. CONCLUSION

This paper modeled the noise by combining both the amplitude modulation and the frequency modulation as the theory of microwave oven noise to analyze the mutual effect between microwave oven noise and IEEE802.11b. Also, GTEM cell was used to realize the environment for the eval-

uation of interference between two systems. The analysis for the effect of microwave oven noise on each channels of IEEE 802.11b has been done by monitoring the transmission throughput on Wireless LAN channels using the amplitude probability distribution.

As a result of the measurement, all of channel 1, 2 and 3 doesn't have the sharing bandwidth with microwave oven noise in frequency domain at all, and the probability that throughput will be represented over 5.5 Mbps is over 90% in this case. But for the other channel, the more the bandwidth of the microwave oven noise and LAN channels is overlapped, the higher the probability is, and the lower throughput is. Although the sharing bandwidth of channel 8 and 9 is wider than channel 7, 10 and 11, throughput of channel 8 and 9 is higher than over 1 Mbps when compared with channel 7, 10 and 11. The reason is due to the relatively short occupied rate in the time domain of microwave oven noise. It means that interference effect for the throughput is more critical in time domain from the viewpoint of occupied time rate than in the frequency domain from the viewpoint of the shared bandwidth.

ACKNOWLEDGMENT

"This work was supported by IT R&D program of MKE/IITA. [2008-F-014-01, Study on Electromagnetic Compatibility for Protecting Electromagnetic Environment in Ubiquitous Society]".

REFERENCES

1. Yamanaka, Y. and T. Shinozuka, "Statistical parameter measurement of unwanted emission from microwave ovens," IEICE Technical Report, EMCJ94-29, Sep. 1994.
2. Mingxin, N. and L. Ling, "Simulation of microwave oven interference on digital radio communication systemsk," *Proc. 3rd Int. Symp. on EMC*, 513–516, May 2002.
3. Kanemoto, H., S. Miyamoto, and N. Morinaga, "Modeling of microwave oven interference using class-A impulsive noise and optimum reception," *IEICE Trans. Commun.*, Vol. E80-B, No. 5, 670–677, May 1997.
4. Matsumoto, Y., M. Takeuchi, K. Fujii, A. Sugiura, and Y. Yamanaka, "A time domain microwave oven noise model for the 2.4 GHz band," *IEEE Trans. EMC*, Vol. 45, No. 3, 561–566, Aug. 2003.
5. IEC 61000-4-3, "Electromagnetic Compatibility, Part 4: Testing and measurement techniques, Section 3: Radiated radio frequency, electromagnetic field immunity test," Edition 2.1, 2002.
6. Tokuda, M., K. Ichikawa, Y. Honma, and M. Kitora, "Radio wave interference test method for wireless communication system by opened parallel wired cell," *IEICE Trans. Commun.*, Vol. E88-B, No. 8, 3242–3248, Aug. 2005.
7. Gewartowski, J. W. and H. A. Watson, *Principles of Electron Tubes*, Van Nostrand, New York, 1965.
8. IEEE, "IEEE Std.802. 11b-1999 Wireless LAN medium access control and physical layer specifications: Higher-speed physical layer extension in the 2.4 GHz band," IEEE Std. 802.11b-1999, 1999.

Investigation of an Agricultural Waste as an Alternative Material for Microwave Absorbers

H. Nornikman, P. J. Soh, A. A. H. Azremi, F. H. Wee, and M. F. Malek
School of Computer and Communication, University Malaysia Perlis, Perlis, Malaysia

Abstract— Agricultural waste bears huge potential to be applied as an alternative and beneficial invention for various applications. One of the identified is as an effective microwave signal absorbers for anechoic chamber. In this work, a type of agricultural waste, which is the rice husk, a by-product of paddy, is used in the design of a pyramidal microwave absorber which will be able to operate effectively in the microwave frequencies, from 1 GHz to 20 GHz. In order to test its feasibility, the best type of bonding resin must first be identified. Two types of resin, Urea Formaldehyde (UF) and Phenol Formaldehyde (PF) are mixed with the rice husk in order to investigate the dielectric property resulting from this blending process. Both materials are compared using three different percentage of binder content, which are 10%, 20% and 30%. Free Space Measurement Method is chosen to measure the dielectric constant of the different blends of rice husk. These microwave absorber are also simulated in CST Microwave Studio using the values that are obtained from the Free Space Measurement Method, in order to determine and compare the reflectivity performance in terms of S_{11} result. Observation of the results showed that different blends will give the different dielectric constant, and as a result, a different microwave absorber reflectivity. It also proved that with increasing binder percentage, reflectivity of the pyramidal microwave absorber is also improved. Thus, an alternative material, which is also used to be a less useful agricultural waste, is also proven potentially suitable for application as a microwave absorber.

1. INTRODUCTION

Agricultural waste or residue is made up of organic compounds from organic sources such as rice straw, oil palm empty fruit bunch, sugar cane bagasse, coconut shell, and others. Rice husk from paddy *(Oryza sativa)* is one example of alternative material that can be potentially applied for microwave absorber fabrication. Microwave absorbers are one of the main components in an anechoic chamber used to eliminate reflected signals. In recent years, there is a growing demand of anechoic chambers, due to its importance in qualifying the performance of many RF and microwave products such as antennas and front end devices. The readily available microwave absorbers are typically made of plastic foamed-based materials like polystyrene or polyurethane. Among the shapes that are commonly employed as microwave absorbers are pyramidal, wedge, walkway, convoluted, oblique incident, and etc. However, pyramidal-shaped absorbers are the most popular among them. Parameters of this absorber type that must be taken into careful consideration during design includes the material dielectric constant, angle of incidence, dimension of absorber, and carbon coating thickness. This work will focus on investigating the material aspects of the absorbers, which include method in determining the material's dielectric constant through simulation and the experimental method. The free space method is deployed in order to get an estimate of the relative dielectric constant of a processed waste board. The reflectivity, R can express the absorbing performance of the material and is a function of the complex permittivity and permeability of the material, and the frequency of the wave [1]. Equation (1) shows the formula of reflectivity for normal incident. The requirement of the best microwave absorber is must have the average reflectivity below than -10 dB.

$$R = 10 \log_{10} \left(\frac{P_r}{P_i} \right) \tag{1}$$

where P_r is plane wave reflected power density, P_i is plane incident power density.

There are two common absorber types in the electromagnetic wave range, which is in the microwave range (100 MHz to 300 GHz) and the lower frequency range (30 MHz to 1000 MHz) [2]. For the lower frequency, ferrite absorbers and hybrid absorbers are used to absorb reflected signal effectively. Dielectric constant is defined as the relative permittivity (ε_r) or the absolute permittivity (ε) relative to the permittivity of free space (ε_0) [3]. The dielectric constant of a material affects the velocity of microwave signals when it moves through the material. A high value of dielectric constant causes the decrease of wave velocity, due to the density of the material [4, 5]. Varying

the dielectric constants of the designed absorber will vary the absorber dimensions and reflectivity. Equation (2) shows the formula for dielectric constant.

Table 1: Element percentage in rice husk.

Element	% Element
Silicon dioxide	22.24
Carbon	35.77
Hydrogen	5.06
Oxygen	36.59
Nitrogen	0.32
Sulphur	0.02

Rice husk is unusually high in ash, which is 92 to 95% silica, highly porous and lightweight, with a very high external surface area. Its absorbent and insulating properties are useful to many industrial applications, such as acting as a strengthening agent in building materials [6]. This by-product of rice cultivation had been traditionally burnt in the field or trucked out and dumped [7]. Table 1 shows the typical chemical contents of rice husks. Carbon is the main element that helps to absorb the microwave signal, which is focal in ensuring satisfactory reflectivity of the microwave absorber, aside from being light in nature.

2. INVESTIGATION METHODOLOGY

Figure 1 shows the rice husk's feasibility study and dielectric constant measurement of the flow chart rice husk. The collected rice husks are processed into rectangular shaped particle boards. This is to ensure that the particle boards are able to be measured in terms of S_{11} using the free space method.

To fabricate the particle board, two bonding agents — Urea Formaldehyde (UF) and Phenol Formaldehyde (PF) with different part percentage were also investigated, in order to determine whether this factor is negligible in influencing the relative dielectric constant. UF is a non-transparent thermosetting resin or plastic, made from urea and formaldehyde heated in the presence of a mild base such as ammonia or pyridine. Density is a quantitative expression of the amount of mass contained per unit volume. The density of Urea is $1.07\,\mathrm{g/cm^3}$ while Phenol is $1.32\,\mathrm{g/cm^3}$ [8].

The material was then shaped into rectangular form by transferring it into a rigid frame over the hot press machine. After pressing, the product was cooled off to at the lower section of the machine. Figure 2 shows the hot press machine in UniMAP's Material Lab. Figure 3 shows the rice husk particle board with a dimension of 30.3 cm width × 30.3 cm length × 1.4 cm thickness. The size of the fabricated particle board will be determined by the horn antennas size that is used in the free space measurement method. i.e., Smaller horns are used with smaller particle boards. Literatures have stated that different density of particle boards will affect the value of the dielectric constant, since the dielectric constant describes a material's density relative to air. With denser particle board, the value of its dielectric property is higher [9]. To confirm if this phenomenon is valid in porous materials such as rice husks, different percentage of UF and PF are investigated and compared. The percentage values tested are shown in Table 2. Repetitive and averaging of the results are done during measurement to reduce systematic errors. Using the dielectric constant

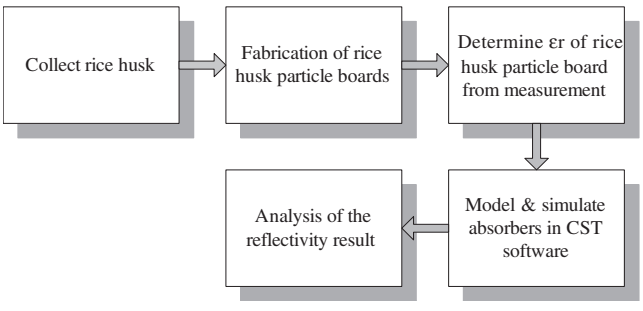

Figure 1: Feasibility investigation of rice-husk microwave absorbers.

Figure 2: Hot press machine in UniMAP's Material Lab.

Figure 3: Rice husk particle board.

Resin	Resin percentage in mixed material
Urea Formaldehyde (UF)	10%
	20%
	30%
Phenol Formaldehyde (PF)	10%
	20%
	30%

Table 2: Resin percentages in mixed materia.

value that was gathered from the measurement, the absorbers are then remodeled and simulated in the CST software to determine the best dimensions and performance for final fabrication.

3. MICROWAVE ABSORBER DESIGN

In this work, the microwave absorbers were designed using CST simulation software. The Rice Husk absorber *(RHA)* design is pyramidal shaped, based on dimensions similar to Eccosorb *VHP-8-NRL* Pyramidal Microwave Absorber [10], *TDK ICT-030* Pyramidal Microwave Absorber [11] and literatures [12–16]. Eccosorb absorber is designed using urethane foam, with carbon loaded at the top of the pyramid while *TDK ICT-030* absorber used carbon plus nonflammable material. The dimension of pyramidal RHA in this work is 5 cm length × 5 cm width × 15 cm height. Figure 4 shows the dimension of pyramidal rice husk microwave absorber while Table 3 shows dimension comparison of commercial microwave absorbers and the designed RHA, which have been miniaturized in size. This is done to potentially reduce the cost of mold fabrication, other than reducing the possibility of fabricating RHAs that are too bulky and heavy. The pyramidal absorber set contain 4 tips per piece, and a base which is 5 cm length × 5 cm width and 2 cm thickness. Six values of dielectric constant for different bonding agent and percentage are gathered during measurement using the Free Space Method. In the simulation, several instances were investigated, which is at normal incident (0°) with distance of 30 cm from the origin of the pyramidal RHAs, as to compare how they would perform when exited by a signal that is in the near-field region and far-field region.

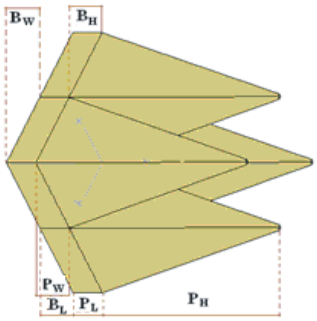

Figure 4: The designed dimension of rice husk pyramidal microwave absorber.

Part	Symbol	Absorber dimension (cm)		
		TDK	VHP	RHA
Pyramidal Width	P_W	10	6.8	5
Pyramidal Length	P_L	10	6.8	5
Pyramidal Height	P_H	25	17.8	13
Base Width	B_W	10	6.8	5
Base Length	B_L	10	6.8	5
Base Height	B_H	5	2.5	2

Table 3: Dimension of TDK, VHP and RHA pyramidal microwave absorber.

4. RESULT AND DISCUSSION

Table 4 presents the dielectric constant with different percentage of resin and rice husk particle board using the Free Space Measurement Method. From the observation, it shows that different content can affect the value of the dielectric constant of the material. The highest value of dielectric constant was shown by 30% PF content with $\varepsilon_r = 3.6808$, while the lowest value of dielectric constant was shown by 10% PF content. The dielectric constant increases when the resin percentage content was increased. This statement is true referring to both resin types — UF and PF. For example, the value difference for both 10% and 20% of UF content is 0.039. Best S_{11} point result is insufficient to sum up the overall performance of the pyramidal microwave absorber as it is only narrowly interpreted at one frequency point. The formula of average reflectivity or

Table 4: Dielectric constant of the different percentage of resin and rice husk particle board.

Resin	**Resin %**	ε_r
Urea Formaldehyde (UF)	10%	3.2355
	20%	3.2745
	30%	3.5813
Phenol Formaldehyde (PF)	10%	2.8907
	20%	3.4054
	30%	3.6808

S_{11} for all frequency range, R_{AR} used in Equation (3) was used to show the best performance in the whole of frequency range between 0.01 GHz to 20 GHz. The result produced was highly accurate as 1000 points was picked from the graph. Another formula in Equation (4) shows the average reflectivity or S_{11} for microwave range, $R_{\mu R}$ between 1 GHz to 20 GHz. The result also has high accuracy but it only have 950 points. Table 5 and Figure 5 show the S_{11} performance of pyramidal microwave absorber using Urea Formaldehyde and rice husk mixture. From the table, 10% content of UF produced the best S_{11} point with −71.597 dB at frequency point of 12.06 GHz followed by 30% UF with −69.911 dB at 6.92 GHz. The worst average S_{11} performance shown by 20% UF mixture with −63.110 dB at 7.02 GHz. The best reflectivity, R_{AR} for UF was shown by −40.922 dB while the worst was 10% UF with −39.620 dB. The best reflectivity in the microwave range for UF was shown by the 30% content with −42.312 dB while the worst was also shown by 10% with only −40.873 dB. From the data collection, we can conclude that the reflectivity, S_{11} will increase when the percentage of resin content is increased. This is because the bonding resin can increase the density of the mixed material. Without it, the rice husks will not be able to bond well allowing hollow spaces between the rice husk's particles, thus validating the statement in [9] that the density can cause an increase in the dielectric properties. Table 6 and Figure 6 show the result of S_{11} performance of pyramidal microwave absorber using mixed Phenol Formaldehyde and rice husk. From the table, 20% content of PF showed the best S_{11} point with −85.947 dB at frequency point of 7.98 GHz followed by 10% PF with −69.115 dB at 7.98 GHz, while the worst performing prototype is the board fabricated using 30% PF with −68.993 dB at 6.94 GHz. The finding in [9] can also be applied to this PF percentage content in the rice husk particle board. The best reflectivity for PF was shown by −40.914 dB while the worst was 10% PF blend with −40.463 dB

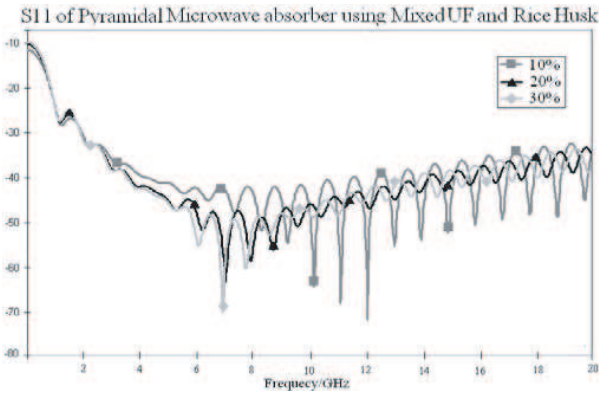

Figure 5: S_{11} result of Pyramidal microwave absorber using mixed UF and rice husk.

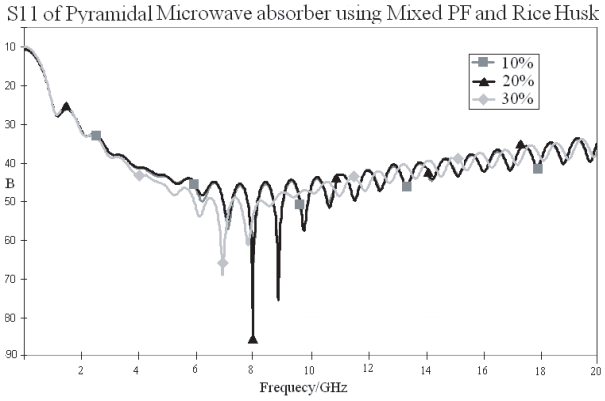

Figure 6: S_{11} result of Pyramidal microwave absorber using mixed PF and rice husk.

Table 5: S_{11} performance of pyramidal microwave absorber using mixed UF and rice husk.

% UF	**Best S_{11} point (dB)**	**Average S_{11} (dB)**	
		All range, R_{AR}	**Microwave range, $R_{\mu R}$**
10	−71.597	−39.620	−40.873
20	−63.110	−40.757	−42.121
30	−69.911	−40.922	−42.312

Table 6: S_{11} performance of pyramidal microwave absorber using mixed PF and rice husk.

% PF	Best S_{11} point (dB)	Average S_{11} (dB)	
		All range, R_{AR}	Microwave range, $R_{\mu R}$
10	−69.115	−40.463	−41.903
20	−85.947	−40.442	−41.779
30	−68.993	−40.914	−42.309

of reflectivity. The best reflectivity for PF was shown by 30% content with −42.309 dB while the worst also shown by 10% with only −41.903 dB. If both 20% or both 30% of UF and PF content is compared, we can see that UF have the best result for all frequency range, especially in the microwave range. This is because, UF has a higher density compared to PF. The density of Urea is 1.07 g/cm^3 while density of Phenol is 1.32 g/cm^3 [8].

5. CONCLUSION

The investigation showed that different resin mix will give different dielectric constant and reflectivity of a microwave absorber. It also shows that if we increase the percentage of resin, it can increase the reflectivity or S_{11} result of the pyramidal microwave absorber. Lastly, it also proofs that the agriculture waste such as rice husk have a huge potential in serving as an alternative material in fabricating microwave absorbers.

REFERENCES

1. Anzai, H., M. Saikawa, Y. Naito, and T. Mizumoto, "The equivalent representation of pyramidal absorbers at its application to the analysis of electromagnetic wave absorber's characteristic," IEEE, 2005.
2. Pozar, D. M., *Microwave Engineering*, 3rd Edition, John Wiley & Sons Inc, 2005.
3. Weisstein, E. W., "Eric weisstein's world of science," http://scienceworld.wolfram.com/physics/, 2008.
4. Lesurf, J., "Warp factor ε!," University of St. Andrews, http://www.st-andrews.ac.uk/∼www-_pa/Scots_Guide/info/comp/passive/capacit/dielec/di_const/dicon.html, 2006.
5. Rahman, N. A., P. J. Soh, A. A. M. Ezannuddin, and H. Nornikman, "A planar elliptical UWB antenna applied on different substrates," *4th International Conference on Electromagnetic Near Field Characterization and Imaging (ICONIC'09)*, Taipei, Taiwan, 2009.
6. Bronzeoak Ltd., United Kingdom, "Rice husk ash market study," 2003.
7. Padiberas Nasional Berhad, Annual Report 2007, Petaling Jaya, Selangor, 2007.
8. Walker, R., "Density of liquid," http://www.simetric.co.uk/si_c.htm, 2007.
9. Laverghetta, T. S., *Microwave Material and Fabrication Techniques*, Artech House Inc, 2000.
10. Emerson and Cumming, "Eccosorb VHP-NRL," http://www.eccosorb.com/file/444/eb100light.pdf, 2007/05-V02/1.
11. TDK RF Solution Inc, "Absorber for microwave and millimeter wave test chamber," 2008.
12. Nornikman, H., P. J. Soh, and A. A. H. Azremi, "Potential types of biomaterial absorber for microwave signal absorption," *4th International Conference on X-rays and Related Techniques in Research and Industry (IXCRI 2008)*, Universiti Malaysia Sabah (UMS), Malaysia, 2008.
13. Nornikman, H., P. J. Soh, A. A. H. Azremi, M. R. N. Husna, and O. S. Liam, "Parametric study of pyramidal microwave absorber design," *International Symposium on Antennas and Propagation (ISAP 2008)*, Taipei, Taiwan, 2008.
14. Nornikman, H., P. J. Soh, and A. A. H. Azremi, "Performance simulation of pyramidal and wedge microwave absorbers," *3rd Asian Modelling Symposium (AMS 2009)*, Bandung, Indonesia, 2009.
15. Nornikman, H., P. J. Soh, and A. A. H. Azremi, "Performance simulation on different shapes of microwave absorbers," Prince Songkhla University, UniMAP Postgraduate Seminar 2009, Hatyai, Songkhla, Thailand, 2009.
16. Nornikman, H., P. J. Soh, and A. A. H. Azremi, "Modelling simulation stage of pyramidal and wede microwave absorber design," *4th International Conference on Electromagnetic Near Field Characterization and Imaging (ICONIC'09)*, Taipei, Taiwan, 2009.

Gradient Magnetostriction and Field Induced Deformation of a Magnetostrictive Cantilever

B. Narsu[1] and Guohong Yun[1, 2]

[1]Key Laboratory of Physics and Chemistry of Functional Materials
College of Physics and Electronic Information, Inner Mongolia Normal University
Hohhot 010022, China
[2]Institute of Science and Technology, Inner Mongolia University
Hohhot 010021, Inner Mongolia, China

Abstract— A self consistent theory has been developed for the cantilever actuated by multilayered films with initial magnetostriction strain gradient based on the four-parameter bending regime. The magnetostriction strain with gradient was modeled as an n order polynomial. The exact solution of the bending state was obtained, and furthermore, an effective experimental method for measuring the magnetostriction strain and its gradient on the basis of curvature measuring technique of the bent cantilever is proposed. By modulating the thickness of the substrate in the cantilever system (for instance, etching), one can measure the magnetostrictive biaxial strain (stress) and its gradient definitely. In order to avoid the unexpected surface effect on the bending of the cantilever, thick substrate should be used.

1. INTRODUCTION

The electromagnetic solid state mechanics is one of the most popular, but still open issue in the study on material science due to the multifield coupling. The magnetostrictive thin film or the composite is one of the most popular candidates for electro-magneto-elastic coupling [1], in which, the magnetic field strongly couples with the mechanical deformations, in turn, the mechanical deformation modulates the magnetic properties, and vice versa. Multilayered thin film structures usually exhibit unbalanced residual stress due to surface and interface effects in both the fabrication process and post fabrication process [2], which affects the magnetostriction of the films and may induce a magnetostriction gradient.

Recently, a new type of bulk giant magnetostrictive composite (GMSC), Terfenol-D/epoxy composite, was fabricated by Clark et al. [3–7] to optimize the mechanical and high frequency property of the magnetostrictive materials. In order to micro-minimize such materials and apply to the micro-electromechanical systems (MEMS), some author has prepared giant magnetostrictive thin film composites [8–10]. The thickness of such composite system was so small that the GMSC films are usually inhomogeneous, namely, the magnetostriction of the film is not a constant through its thickness directions [11]. On the other hand, there always exists unbalanced internal stress around the interface of the heterogeneous multilayer films. These stress can also modulates the effective magnetostriction of the GMSC films [12, 13]. Furthermore, the thickness dependent magnetostriction or electrostriction may be very helpful to the optimization of the electromagnetic elasticity of the thin film composites [14]. Therefore, the inhomogeneous magnetostriction induced spontaneous deformation is a very important issue in the study on heterogeneous multilayer films. But corresponding theoretical description has not been addressed yet.

In this work, we address the biaxial bending problem of magnetostrictive multilayer films with internal stress gradient. Section 2 gives the general theory in the four parameter bending regime, and then analyzes the bending characteristic of the cantilever system. Then an experimentally practicable method for measuring stress gradient was proposed. The whole article is concluded in Section 3.

2. MODEL AND FORMULATION

2.1. General Theory

We consider a cantilever system consists of a non magnetic substrate and a multilayered magnetostrictive film. Here we assume that the multilayered system can be seen as a mechanically isotropic and totally demagnetized initially. And we further assume that there exists residual stress in the heterogeneous film and it cannot be neglected. When the quasibilayer system is exposed to the external field along one of the axial direction, the system bent and shows an anticlastic

surface. In order to solve the bending deformation of such a system, we introduce four geometrical parameters, respectively, uniform strains ε_x^0, ε_y^0 and curvatures α_x, α_y in two axial directions. Then the geometrical film strain of a bent cantilever composed of thin film and a substrate can be written as

$$\varepsilon_x = \varepsilon_x^{ben} - \lambda(z), \qquad \varepsilon_y = \varepsilon_y^{ben} - \eta(z). \tag{1}$$

where $\varepsilon_x^{ben} = \varepsilon_x^0 - \alpha_x z$ and $\varepsilon_y^{ben} = \varepsilon_y^0 - \alpha_y z$ are the bending strain of the film and the substrate, and the $\lambda(z)$ and $\eta(z)$ are the biaxial response function (magnetostrictive, piezoelectric etc.) of the thin film, which are defined as [15–17]

$$\lambda(z) = \sum_{n=0}^{K} \lambda_n \left(\frac{z}{t_f}\right)^n, \quad \eta(z) = \sum_{n=0}^{K} \eta_n \left(\frac{z}{t_f}\right)^n \quad z \geq 0$$

By applying film strain, the biaxial film stress can be written as [18],

$$\sigma_{x,f} = \frac{Y_f}{1-\nu_f^2}(\varepsilon_x + \nu_f \varepsilon_y), \quad \sigma_{y,f} = \frac{Y_f}{1-\nu_f^2}(\varepsilon_y + \nu_f \varepsilon_x). \tag{2}$$

We assume that the substrate is without any active strain, thus the stress of the substrate is also depicted by the Eq. (2) where the strain should be substituted with the bending strain ε_x^{ben}, ε_y^{ben}. The film-substrate system bends under the action of the external field, and there is any external stress and moment, therefore the bent state of the film-substrate system is determined by following equilibrium equation,

$$\sum_i \int_{S_i} \sigma_i(1,\, z) dS = 0 \quad i = s, f \tag{3}$$

where S_i demotes cross section of cantilever. In order to resolve the equilibrium equation, following simple transformation is performed on Eq. (3),

$$\varepsilon_\pm = \varepsilon_x^0 \pm \varepsilon_y^0, \quad \alpha_\pm = \alpha_x \pm \alpha_y. \tag{4}$$

After the transformation, the equilibrium equation yields,

$$\begin{pmatrix} A_\pm & -B_\pm \\ B_\pm & -C_\pm \end{pmatrix} \begin{pmatrix} \varepsilon_\pm \\ \alpha_\pm \end{pmatrix} = \begin{pmatrix} N_\pm \\ M_\pm \end{pmatrix}, \tag{5}$$

Where the coefficients are defined as,

$$\begin{aligned} (A_\pm,\ B_\pm,\ C_\pm) &= \int_{-t_s}^{t_f} Y'(z)\,(1 \pm \nu(z))\,\left(1,\ z,\ z^2\right) dz, \\ (N_\pm,\ M_\pm) &= \int_{-t_s}^{t_f} Y'(z)\,(1 \pm \nu(z))\,[\lambda(z) \pm \eta(z)](1,\ z) dz. \end{aligned} \tag{6}$$

where A, B and C are the extensional, extensional-flexural coupling and pure flexural rigidity of the cantilever system. And N and M are the equivalent force and the moment acting on the cantilever. In order to simplify the above expressions, here we used following two parameters

$$Y'(z) = \begin{cases} Y_f \big/ (1-\nu_f^2)\ , & z \geq 0 \\ Y_s \big/ (1-\nu_s^2)\ , & z < 0 \end{cases} \qquad \nu(z) = \begin{cases} \nu_f, & z \geq 0 \\ \nu_s. & z < 0 \end{cases}$$

The exact solution of the Eq. (5) can be given by,

$$\begin{pmatrix} \varepsilon_\pm \\ \alpha_\pm \end{pmatrix} = \frac{1}{B_\pm^2 - A_\pm C_\pm} \begin{pmatrix} M_\pm B_\pm - N_\pm C_\pm \\ M_\pm A_\pm - N_\pm B_\pm \end{pmatrix}. \tag{7}$$

With the aid of Eq. (6), the analytical expression of the $\varepsilon_\pm$, $\alpha_\pm$ can be obtained readily,

$$\varepsilon_\pm = 2\chi k(1 \pm \nu_f) K_1^\pm \sum_{n=0}^{K} \frac{\lambda_n(1 \pm \gamma_n)}{(n+1)(n+2)} \left\{[3k(n+1)+2(n+2)](1 \pm \nu_s) - \chi k^3 (n-1)(1 \pm \nu_f)\right\}, \tag{8a}$$

$$\alpha_\pm = -6\chi k(1 \pm \nu_f) K_1^\pm \sum_{n=0}^{K} \frac{\lambda_n(1 \pm \gamma_n)}{(n+1)(n+2)} \left\{[n(2k+1)+2(k+1)](1 \pm \nu_s) + \chi k^2 n(1 \pm \nu_f)\right\}, \tag{8b}$$

where $\gamma_n = \eta_n/\lambda_n$ is the local correlation coefficient, and $K_1^{\pm}$ are defined as

$$K_1^{\pm} = \left[(1 \pm \nu_s)^2 + 2\chi(1 \pm \nu_f)(1 \pm \nu_s)\left(2k + 3k^2 + 2k^3\right) + \chi^2 k^4 (1 \pm \nu_f)^2\right]^{-1}.$$

2.2. Bending Characteristics

According to the above analytical results, under the small deflection assumption, the free-end bending deflection along the x-axis is given by,

$$\Delta_x = -\frac{L^2}{4t_s}(\alpha_+ + \alpha_-), \tag{9}$$

and

$$\Delta = \Delta_x - \Delta_y = -\frac{9L^2\chi\lambda_d k(k+1)}{2t_s}(1-\nu_f)(1-\nu_s)K_1^-, \tag{10}$$

where λ_d is defined as the Equivalent Uniform Magneto Striction (short for EUMS),

$$\lambda_d = \frac{2}{3}\sum_{n=0}^{K}\frac{\lambda_n(1-\gamma_n)}{(n+1)(n+2)}\left[\frac{\chi k^2 n}{1+k}\frac{1-\nu_f}{1-\nu_s} + n\frac{1+2k}{1+k} + 2\right]. \tag{11}$$

Here λ_d is a function of the film-to-substrate thickness ratio k, considering a special condition of $\gamma_0 = \gamma_1 = \ldots = \gamma_n = -1/2$ and $\nu_s = \nu_f$, the EUMS can be expanded to be,

$$\lambda_d = \lambda_0 + \frac{1}{6}\frac{\chi k^2 + 4k + 3}{1+k}\lambda_1 + \frac{1}{12}\frac{2\chi k^2 + 6k + 4}{1+k}\lambda_2 + \ldots. \tag{12}$$

Following the above formulations, the EUMS is calculated as a function of the film-to-substrate thickness ratio for three different types of cantilevers, GMS/Silicon, GMS/Glass, GMS/Polymide, respectively. It is readily seen from the figure that, EUMS is an increasing function of the film thickness, and it may reach several thousands of ppm for thick films. This fact suggests that the strain gradient is favorable for increasing the cantilever deflection in relatively thick films, and further one can design a stress gradient in multilayered films to optimize the bending characteristics of the cantilever system.

In order to characterize the bending capability of the cantilever system, the free-end deflection of the single layered GMSC cantilever was plotted as a function of order of the strain gradient and film thickness. The film thickness taken into account in the Fig. 2 is $t_f = 10, 20, 30$ µm, and without lose of generality a linearly increasing gradient coefficient was taken into the calculation. As can be seen in Fig. 2, the greater the orders of gradients, the larger the bending deflection. Contrarily, the thick film degreases the bending deflection in the same conditions. It is agrees with the general assumptions that the relatively thin film is easy to be bent under the same bending torque.

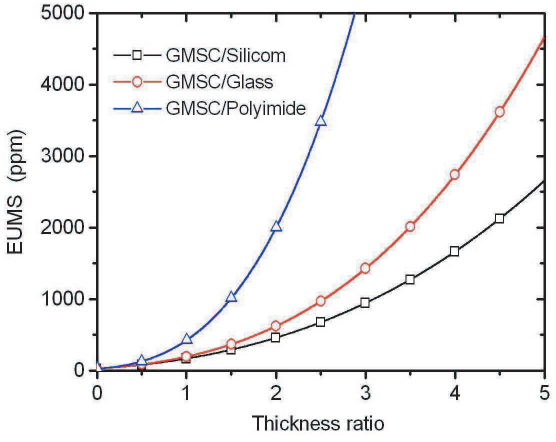

Figure 1: The EUMS vs film-to-substrate thickness ratio for three types of cantilever.

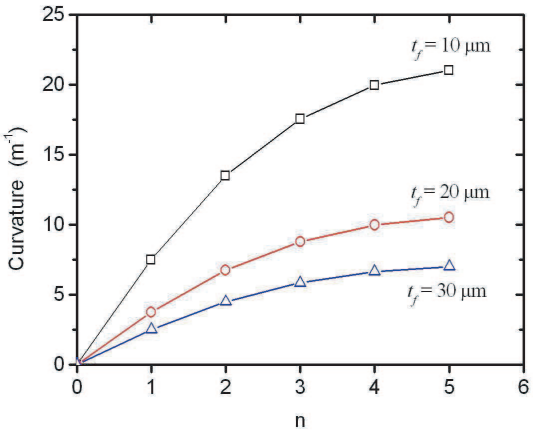

Figure 2: The n dependence of the bending curvature of a single film cantilever, the lines are guide for the eyes.

2.3. Measurement of the Magnetostriction Gradient

The well known cantilever bending technique is a possible way to determine the magnetoelastic behavior of the thin films [19–21]. In the following discussions, we show that this cantilever technique is also applicable to the determination of the magnetostriction gradients. Here Eq. (8b) is rewritten as,

$$\alpha_{\pm}(k) = \sum_{n=0}^{K} D_n^{\pm}(k)\lambda_n(1 \pm \gamma_n), \tag{13}$$

where the coefficient $D_n^{\pm}(k)$ is defined as

$$D_n^{\pm}(k) = -\frac{6\chi k(1 \pm \nu_f)\{[n(2k+1)+2(k+1)](1 \pm \nu_s) + \chi k^2 n(1 \pm \nu_f)\}}{(n+1)(n+2)[(1 \pm \nu_s)^2 + 2\chi k(1 \pm \nu_f)(1 \pm \nu_s)(2+3k+2k^2) + \chi^2 k^4(1 \pm \nu_f)^2]}, \tag{14}$$

As can be seen from Eq. (13), if we try to change (for instance, etching) the film-to-substrate thickness ratio and obtains a group of thickness ratio, k_1, k_2, ..., k_n, then Eq. (13) can be rewritten as

$$\begin{pmatrix} \alpha_{\pm}(k_1) \\ \alpha_{\pm}(k_2) \\ \vdots \\ \alpha_{\pm}(k_n) \end{pmatrix} = \begin{pmatrix} D_1^{\pm}(k_1) & D_2^{\pm}(k_1) & \dots & D_n^{\pm}(k_1) \\ D_1^{\pm}(k_2) & D_2^{\pm}(k_2) & \dots & D_n^{\pm}(k_2) \\ \vdots & \dots & \dots & \vdots \\ D_1^{\pm}(k_n) & D_2^{\pm}(k_n) & \dots & D_n^{\pm}(k_n) \end{pmatrix} \begin{pmatrix} \lambda_1(1 \pm \gamma_1) \\ \lambda_2(1 \pm \gamma_2) \\ \vdots \\ \lambda_n(1 \pm \gamma_n) \end{pmatrix}. \tag{15}$$

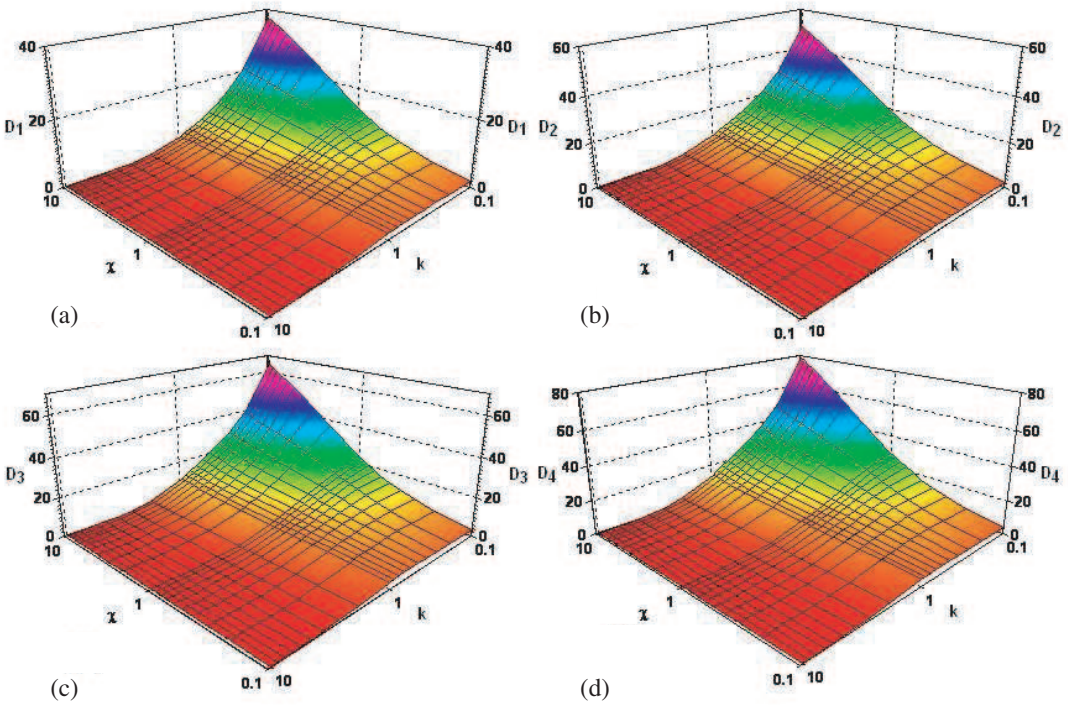

Figure 3: The bending factor D_n vs the film-to-substrate stiffness ratio χ and thickness ratio k.

Therefore, the series of biaxial curvature ($\alpha_{\pm}(k_1)$, $\alpha_{\pm}(k_2)$, ..., $\alpha_{\pm}(k_n)$) can be measured for different substrate thickness, and then one obtains,

$$\begin{pmatrix} \lambda_1(1 \pm \gamma_1) \\ \lambda_2(1 \pm \gamma_2) \\ \vdots \\ \lambda_n(1 \pm \gamma_n) \end{pmatrix} = \begin{pmatrix} D_1^{\pm}(k_1) & D_2^{\pm}(k_1) & \dots & D_n^{\pm}(k_1) \\ D_1^{\pm}(k_2) & D_2^{\pm}(k_2) & \dots & D_n^{\pm}(k_2) \\ \vdots & \dots & \dots & \vdots \\ D_1^{\pm}(k_n) & D_2^{\pm}(k_n) & \dots & D_n^{\pm}(k_n) \end{pmatrix}^{-1} \begin{pmatrix} \alpha_{\pm}(k_1) \\ \alpha_{\pm}(k_2) \\ \vdots \\ \alpha_{\pm}(k_n) \end{pmatrix}, \tag{16}$$

thus the biaxial magnetostriction gradients coefficients λ_n as well as the local correlation coefficient γ_n can be determined definitely. In this method, such technique as etching is proposed to be used, hence the substrates adopted must be thick enough to avoid the unexpected error stems from the surface effect in the etching process.

The film-to-substrate thickness ratio and stiffness ratio dependence of the bending coefficient D_n was calculated in Fig. 3. As can be seen from the figure, the role of the thickness ratio and stiffness ratio on the bending coefficient D_n is identical and the increasing n increases the absolute value of bending coefficient D. In addition, the Fig. 3 also suggests that the bending coefficient D is much sensitive to the variation of the thickness ratio when the substrate is relatively thick and soft, thus this condition is favorable for the magnetostriction gradient measurement. Therefore, one should select a relatively soft substrate such as Polyimide [22], and the substrate thickness should be several tens greater than the film, when the bent substrate technique is used to determine the magnetostriction gradients.

3. CONCLUDING REMARKS

In conclusion, based on the four-parameter model, an effective bending theory for the cantilever actuated by magnetostrictive films with initial strain gradient is presented for the first time. The polynomial expansion methods that have been developed to depict the residual strain and corresponding gradient in the epitaxial films is employed to describe the magnetostriction strain gradients. We furthermore proposed an effective experimental method for measuring the magnetostriction strain and its gradient on the basis of curvature measuring technique of the bent cantilever. By modulating the thickness of the substrate in the cantilever system (for instance, etching), one can measure the magnetostrictive biaxial strain (stress) and its gradient definitely. In order to avoid the unexpected surface effect on the bending of the cantilever, thick substrate should be used. The numerical work shows that relatively thick and soft substrate is favorable for this method. In addition, the advantage of the proposed method over the in situ measurement of the film stress in the growing process is that the inhomogenety and the surface effect can be avoided.

ACKNOWLEDGMENT

This work was supported by the National Natural Science Foundation of China (Grant No. 10762001), Program for New Century Excellent Talents in University (Grant No. NCET-05-0272), and the Key Project of the Chinese Ministry of Education (Grant No. 206024).

REFERENCES

1. Zhou, Y. H. and X. J. Zheng, *Electromagnetic Solid State Structural Mechanics*, Science Press, 2004.
2. Gancedo, L. G., et al., "Magnetomechanical properties of terfenol-d 2-2 composites with internal field biasing," *IEEE Trans. Magn.*, Vol. 41, 2781–2783, 2005.
3. Clark, A. E. and H. S. Belson, United State Patent, No. 4378258, 1983.
4. Sandlund, L., M. Fahlander, T. Cedell, et al., "Magnetostriction, elastic moduli, and coupling factors of composite Terfenol-D," *J. Appl. Phys.*, Vol. 75, 5656–5658, 1994.
5. Pinkerton, F. E., T. W. Capehart, J. F. Herbst, E. G. Brewer, and C. B.Murphy, "Magnetostrictive $SmFe_2$/metal composites," *Appl. Phys. Lett.*, Vol. 70, 2601–2603, 1997.
6. Guo, Z. J., S. C. Busbridge, Z. D. Zhang, et al., "Dynamic magnetic and magnetoelastic properties of epoxy-$TbFe_2$ composites," *J. Magn. Magn. Mater.*, Vol. 239, 554–556, 2002.
7. Or, S. W., T. Li, and H. L. W. Chan, "Dynamic magnetomechanical properties of Terfenol-D/epoxy pseudo 1-3 composites," *J. Appl. Phys.*, Vol. 97, 10M308-1-3, 2005.
8. Grabham, N. J., S. P. Beeby, and N. M. White, "Thick-film magnetostrictive material for MEMS," *Electron. Lett.*, Vol. 36, 332–334, 2000.
9. Grabham, N. J., S. P. Beeby, and N. M. White, "The formulation and processing of a thick-film magnetostrictive material," *Meas. Sci. Technol.*, Vol. 13, 59–64, 2002.
10. Grabham, N. J., S. P. Beeby, and N. M. White, "Effects of the binder material on the mechanical properties of thick-film magnetostrictive materials," *Sens. Actuators A*, Vol. 110, 365–370, 2004.
11. Pulliam, W. J., D. Lee, G. P. Carman, and G. P. McKnight, "Thin-layer magnetostrictive composite films for turbomachinery fan blade damping," *Proc. SPIE*, Vol. 5054, 360–371, 2003.

12. Zang, J. and F. Liu, "Modified Timoshenko formula for bending of ultrthin strained bilayer films," *Appl. Phys. Lett.*, Vol. 92, 021905-1-3, 2008.
13. Cooke, M. D., H. J. Hatton, L. C. Wang, et al. "Influence of interfaces on magnetostrictive granular films," *Phys. Rev. B*, Vol. 65, 174418-1-7, 2002.
14. Scheerschmidt, G., K. J. Kirk, and G. McRobbie, "Investigation of magnetostrictive microdevices," *IEEE Trans. Magn.*, Vol. 43, 2722–2724, 2007.
15. Yang, E. H., S. S. Yang, and S. H. Yoo, "A technique for quantitative determination of the profile of the residual stress along the depth of p^+ silicon films," *Appl. Phys. Lett.*, Vol. 67, 912–914, 1995.
16. Fang, W. and A. Wickert, "Comment on measuring thin film stress using bilayer micromachined cantilevers, " *J. Micromech. Microeng.*, Vol. 5, 276–281, 1995.
17. Fang, W. and J. A. Wickert, "Determining mean and gradient stresses in thin films using micromachined cantilevers," *J. Micromech. Microeng.*, Vol. 6, 301–309, 1996.
18. Landau, L. D. and E. M. Lifsitz, *Theory of Elasticity*, 38–42, 3rd Edition, World scientific, Butterworth-Heinemann, Beijing, 1999.
19. Huang, S. and X. Zhang, "Extension of the Stoney formula for film–substrate systems with gradient stress for MEMS applications," *J. Micromech. Microeng.*, Vol. 16, 382–389, 2006.
20. Huang, S. S. and X. Zhang, "Gradient residual stress induced elastic deformation of multilayer MEMS structures," *Sens. Actuators A*, Vol. 134, 177–185, 2007.
21. Huang, S. and X. Zhang, "Study of gradient stress in bimaterial cantilever structures for infrared applications," *J. Micromech. Microeng.*, Vol. 17, 1211–1219, 2007.
22. Honda, T., K. I. Arai, and M. Yamaguchi, "Fabrication of magnetostrictive actuators using rare earth (Tb, Sm)-Fe thin films," *J. Appl. Phys.*, Vol. 76, 6994–6999, 1994.

Analysis and Improvement for Thrust Fluctuation of Flat Type Voice Coil Motor

Liyi Li, **Donghua Pan**, **and Baoquan Kou**
School of Electrical Engineering, Harbin Institute of Technology, Harbin, China

Abstract— In the some special situation, the thrust of motor is required harshly for locating precisely, for instance, the linear motors hardly have thrust fluctuation in the lithography system. Voice coil motor has small thrust fluctuation, but it is necessary to improve thrust fluctuation of the voice coil motor for more precisely locating. In this paper, the thrust fluctuation of the voice coil motor is improved by optimizing pole-arc coefficient, Halbach array magnet. The function of elimination is proved by finite element method.

1. INTRODUCTION

The more precise location is pursued, so the performance of linear motor needs to be improved. The designs of servo linear motor and driver are constantly improved for fulfilling further requirement of ultra-precision location in the special servo system, for instant, the workpieces stage of lithograph. The voice coil motor is used in the lithograph system, and there are three voice coil motors to drive fine stage of the workpieces stage.

The structure of voice coil motor is simple, so the difficulty of precise manufacture is deceased. Than the coils of voice coil motor are operated under DC, so it is controlled easily and has little thrust fluctuation. To sum up, voice coil motor is used to accurately locating servo system compatibly. Voice coil motor has moving magnet steel and moving coil structures. The advantage of moving coil structure is immobility magnetic system has larger volume, so there is higher air-gap magnetic field density for enhancing thrust; but there are some disadvantages: Coils break off easily and the moving load gets quantity of heat from the coil. The advantage of moving magnet steel is ability of cooling is improved, the rated current is raised; but the air-gap magnetic field density is reduced. In the servo system, because the temperature could be unchanged, the moving magnet steel structure is used to this voice coil motor.

2. PRINCIPLE AND STRUCTURE OF FLAT TYPE VOICE COIL MOTOR

The principle of voice coil motor is simple: There is direct current in the coils of voice coil motor, then the force direction of all of the wires are same; the current direction is controlled to implement accelerate, decelerate and reverse motion.

The force **F** of voice coil motor is expressed as:

$$\mathbf{F} = n\mathbf{Bli} \tag{1}$$

where

n: Number of coil turns,
B: Mean value of air-gap magnetic density,
l: Stake length,
i: DC value.

For increasing thrust of flat type voice coil motor, the serial magnet structure which can add the area of the flux is used by the voice coil motor. The serial magnet structure could restrain magnetic flux adding when the force of voice coil motor is increasing, so thrust density of voice coil motor is advanced. Figure 1 shows the serial magnet structure of flat type voice coil motor.

3. ANALYSIS AND IMPROVEMENT FOR THRUST FLUCTUATION

But the serial magnet structure would bring a disadvantage which is increasing number of motor ending, the thrust fluctuation is increasing. The Halbach array magnet is used for solving this question. Figure 2 shows this halbach array and magnetizing direction.

This halbach array magnet structure can improve the wave of air-gap magnetic flux density to square wave for minishing the thrust fluctuation, and increases the air-gap flux density to increase

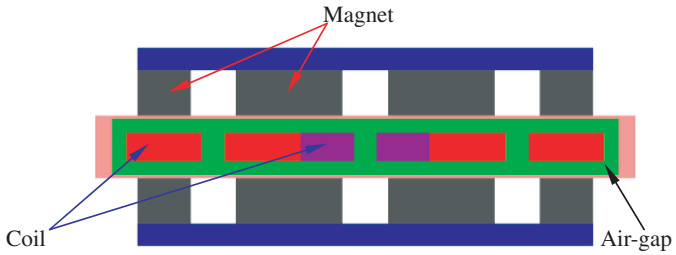

Figure 1: Serial magnet structure of flat type voice coil motor.

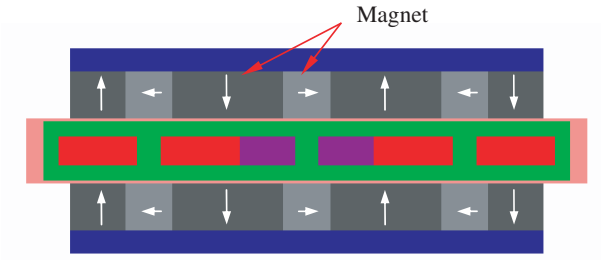

Figure 2: Halbach array magnet and magnetizing direction.

the thrust density of the voice coil motor. The Figure 3 shows the wave contrast of air-gap magnetic flux density between having array and no having halbach array. The results are obtained by Ansoft software.

The halbach array's other advantage is forming closed magnetic circuit by itself, so the mass and volume of mover yoke is decreased. Though the mass of magnet is added, the mass of mover is decreased because the mass of move yoke is decreased by the halbach array structure. The Figure 4 shows the contrast of magnetic flux density between having halbach array and no having halbach array. The maximum of magnetic flux density is 1.4 T in the having halbach array structure is less than maximum is 2.0 T in the no having halbach array structure. The Figure 5 shows the contrast of thrust between having halbach array and no having halbach array. The halbach array structure makes the thrust of voice coil motor to be larger and less fluctuation.

The rational pole-arc coefficient can improve the thrust, so the best pole-arc coefficient is calculated out by finite element optimized method. Table 1 shows different pole-arc coefficients correspond to thrust of flat type voice coil motor. When the pole-arc coefficient is 0.704, the voice coil motor has the maximum thrust is 67.19. The Figure 6 shows the meanings of d_1 and d_2 ($d_1 = 2d_3$).

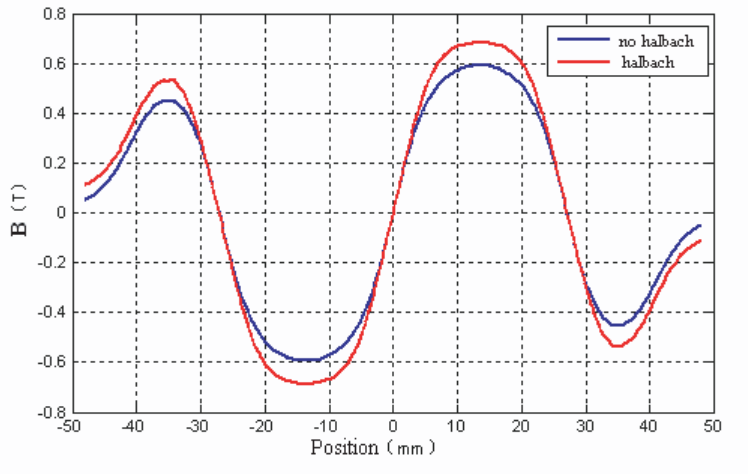

Figure 3: Wave contrast of air-gap magnetic flux density between having array and no having halbach array.

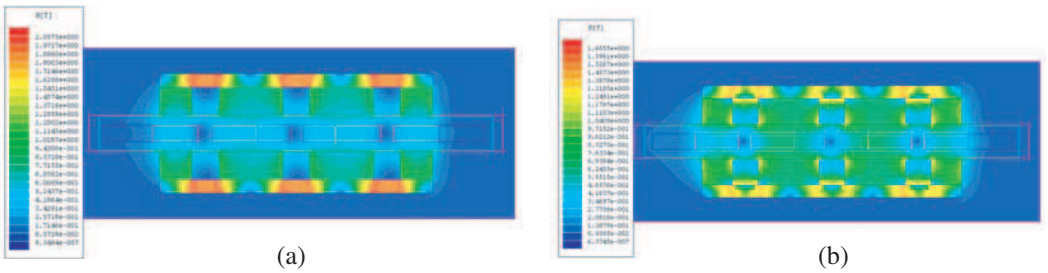

Figure 4: Contrast of magnetic flux density between having halbach array and no having halbach array. (a) Having halbach array, (b) no having halbach array.

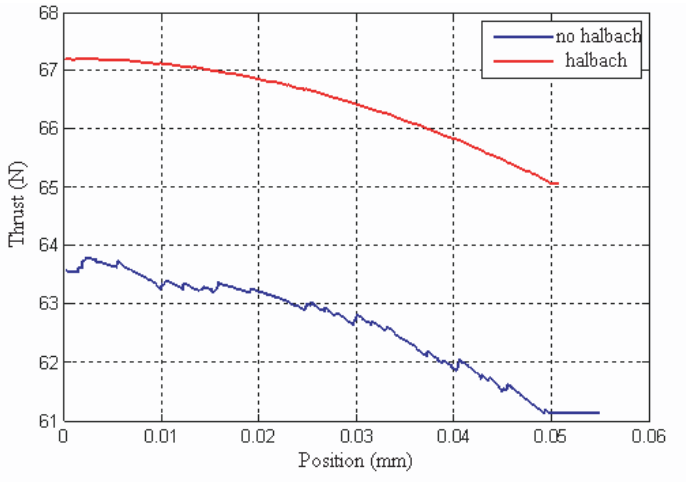

Figure 5: Contrast of thrust between having halbach array and no having halbach array.

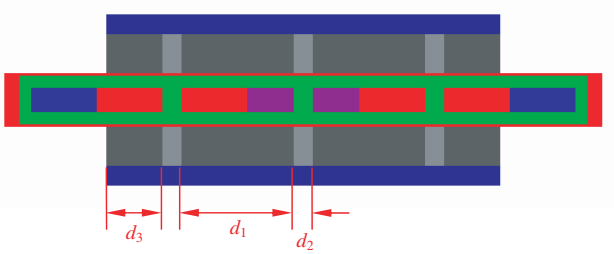

Figure 6: Meaning of d_1 and d_2.

Table 1: Different pole-arc coefficients correspond to thrust of flat type voice coil motor.

pole-arc coefficient α_i	d_1 (mm)	d_2 (mm)	F_{st} (N)
1.000	27	0	57.15
0.852	23	4	62.80
0.778	21	6	63.83
0.741	20	7	63.77
0.722	19.5	7.5	63.63
0.704	19	8	67.19
0.685	18.5	8.5	66.91
0.667	18	9	66.57

4. CONCLUSION

Optimizing pole-arc coefficient, Halbach array magnet, and adding two end coils could improve the thrust fluctuation of the flat type voice coil motor. When the pole-arc coefficient is 0.704, the flat type voice coil motor has the maximum thrust is 67.19 N. The thrust fluctuation is restrained could be proved by finite element method.

REFERENCES

1. Lee, D. J., K. N. Lee, N. C. Park, and Y. P. Park. "Development of 3-axis nano stage for precision positioning in lithography," *International Conference on Mechatronks and Automation Niagara Falls*, 1598–1603, Canada, Jul. 2005.
2. Cui, J. and C. Wang, "Design characteristic and force analysis of PM linear motor for fast response servo system," *Power Electronics and Motion Control Conference*, Vol. 2, 14–16, 1001–1004, Aug. 2004.
3. Luo, H., J. Wu, and W. Chang, "Minimizing thrust fluctuation in moving-magnet permanent-magnet brushless linear DC motors," *IEEE Transactions on Magnetics*, Vol. 43, No. 5, 1968–1972, May 2007.

Angular Dependence of the Exchange Bias with the Uniaxial Anisotropy Perpendicular to the Unidirectional Anisotropy

Yuhao Bai[1], **Guohong Yun**[1, 2], **and B. Narsu**[2]

[1]College of Physical Science and Technology, Inner Mongolia University, Hohhot 010021, China
[2]Inner Mongolia Key Laboratory of Physics and Chemistry of Functional Materials
College of Physics and Electronic Information, Inner Mongolia Normal University, Hohhot 010022, China

Abstract— Based on the principle of minimal energy, the angular dependence of exchange bias has been investigated with the uniaxial anisotropy perpendicular to the unidirectional anisotropy in ferromagnetic/antiferromagnetic bilayers. The competition between unidirectional and uniaxial anisotropies divides the initial magnetization state of the bilayer into monostable state and bistable state, which determine the angular dependence directly. By analyzing the magnetization reversal processes, one of the coercive fields of the hysteresis loop shows a discontinuity while the other is kept continuous at the orientation angles of the intrinsic easy axes, which induces a jump phenomenon in the curves of the angular dependence of the exchange bias. It is found that this jump phenomenon is an intrinsic property of the bilayers.

1. INTRODUCTION

Exchange bias [1, 2] in ferromagnetic (FM)/antiferromagnetic (AFM) bilayers has attracted a great deal of attention in the last five decades because of its technological importance in magnetoresistive sensors and read heads [3]. The effect manifests itself by several characteristics, among with the most well known is the shift of the hysteresis loop and an accompanying enhancement in the coercivity. For reviews, concerning both theories and experiments about the exchange bias see References [4, 5].

The angular dependence of exchange bias (ADEB) is very informative to understand the nature of exchange bias effect [6]. Recently, it has been confirmed by experiments that the exchange bias field H_{EB} and the coercivity H_C, defined as the shift and half-width of the hysteresis loop, respectively, can display a jump phenomenon in the curves of the ADEB [7–9]. This new feature of the ADEB is of technologic importance for optimizing the designs of the involved devices. However, the mechanism of this jump phenomenon was not interpreted in these works. On the other hand, in most studies, the cooling field H_{FC} used to induce a unidirectional anisotropy is always along the uniaxial anisotropy axis [7–10]. In this paper, the angular dependence of exchange bias with the uniaxial anisotropy perpendicular to the unidirectional anisotropy in the bilayers has been investigated, and the jump phenomenon has been explained by analyzing the magnetization reversal processes.

2. MODEL AND FORMULATION

We assume that the interface between the FM and AFM layers is uncompensated. The bilayer is taken to lie in the x-y plane, and the z axis is normal to the film plane. The FM layer with the thickness t_F is considered to have a uniaxial anisotropy with the axis along the x axis. The cooling field H_{FC} is applied in the film plane along the positive y semiaxis, which is perpendicular to the uniaxial anisotropy axis. The AFM layer is supposed to be thick enough to sustain the exchange bias [11]. The external field H is applied in the film plane. All the angles are counted clockwise starting from the positive x semiaxis, and these angles are θ_H for applied field H and θ_F for the ferromagnetic magnetization M_F. The free energy per unit area of the bilayer can be written as [7–10]

$$E = K_F t_F \sin^2\theta_F - J_E \cos\left(90^\circ - \theta_F\right) - HM_F t_F \cos\left(\theta_H - \theta_F\right), \tag{1}$$

where the first term represents the uniaxial anisotropy energy of FM layer with the anisotropy constant K_F. The second term is the unidirectional anisotropy energy characterized by the exchange coupling constant J_E. Finally, the last term stands for the Zeeman energy. We first study the state of the bilayer when the applied field is absent. The magnetization equilibrium orientations can be

obtained by the equilibrium conditions: $\partial E(H=0)/\partial\theta_F = 0$, $\partial^2 E(H=0)/\partial\theta_F^2 \geq 0$, which can be written as

$$\frac{1}{2}\sin 2\theta_F - J\cos\theta_F = 0, \quad \cos 2\theta_F + J\sin\theta_F \geq 0 \tag{2}$$

Here, $J = J_E/2K_F t_F$ is defined as the reduced interfacial exchange coupling constant. The solutions of the first equation in Eq. (2) are given as follows:

$$\theta_{F1} = \arcsin(J), \quad \theta_{F2} = 90^\circ, \quad \theta_{F3} = 180^\circ - \arcsin(J), \quad \theta_{F4} = 270^\circ. \tag{3}$$

Some interesting and important conclusions can be drawn by analyzing these solutions. For $0 \leq J < 1$, the bilayer presents two energy-minimum at θ_{F1} and θ_{F3}, meanwhile two energy-maximum appear at θ_{F2} and θ_{F4}. We define this state as "bistable state" because two stable magnetization equilibrium orientations exist. But for $J \geq 1$, the bilayer exhibits only one energy-minimum at $\theta_F = 90^\circ$ together with one energy-maximum at $\theta_F = 270^\circ$. This state is referred to as "monostable state" compared to the bistable state. These results can be seen clearly in Figure 1.

Furthermore, the orientations of M_F for the energy minimum and maximum are defined as the intrinsic easy and hard axes, respectively. When the bilayer is in the bistable state for $0 \leq J < 1$, two intrinsic easy axes θ_{F1} and θ_{F3} are symmetric about the y axis, i.e., $\theta_F = 90^\circ$. Two intrinsic hard axes θ_{F2} and θ_{F4} are collinear with the y axis. Once passing through any intrinsic hard axis θ_{F2} or θ_{F4}, M_F will jump irreversibly between the intrinsic easy axes θ_{F1} and θ_{F3}. For $J \geq 1$, the bilayer is in the monostable state, the intrinsic easy axis θ_{F1} and the intrinsic hard axis θ_{F2} are collinear with the y axis by the reason of $\theta_{F1} = 90^\circ$ and $\theta_{F2} = 270^\circ$.

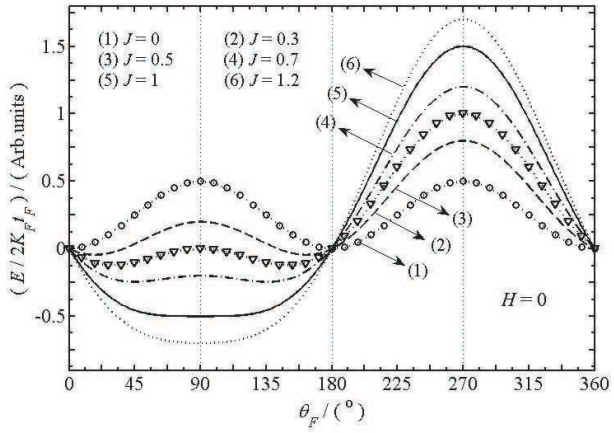

Figure 1: The normalized energy $E/2K_F t_F$ vs the ferromagnetic magnetization orientations θ_F, when the applied field H is absent.

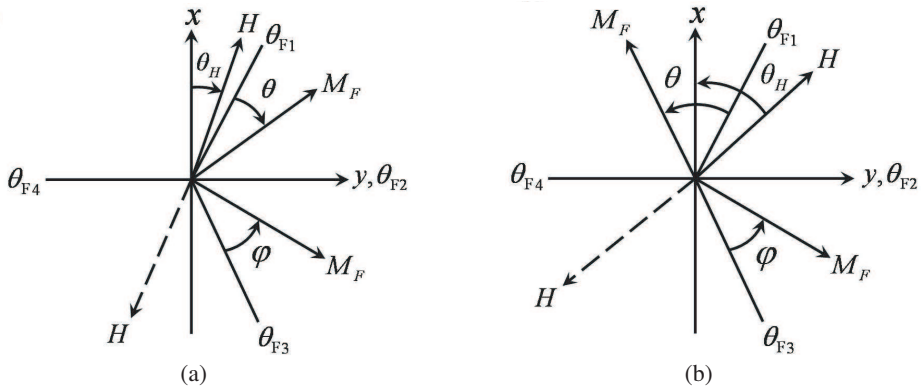

Figure 2: The rotation of M_F in the magnetization reversal processes for the bistable state over the angular ranges of $0^\circ \leq \theta_H < \theta_{F1}$ (a) and $\theta_{F1} \leq \theta_H < 90^\circ$ (b). The dashed lines with arrows represent the opposite orientation of the applied field H. θ and φ are the angles that M_F makes with θ_{F1} and θ_{F3}, respectively.

Obviously, there is a critical value $J = 1$: when J exceeds this critical value, the bilayer makes a transition from bistable state to monostable state. It is found that the parameter J plays a determined role on evaluating monostable state or bistable state of the bilayer at the initial magnetization stage. As the magnitude of J denotes the extent of the competition between unidirectional and uniaxial anisotropies in the bilayer, in essence, monostable state or the bistable state is controlled by this competition, leading to the bistable state when the uniaxial anisotropy is dominant for $0 \leq J < 1$, and the monostable state when the unidirectional anisotropy is dominant for $J \geq 1$, respectively.

Based on the coherent rotation model [12], H_{EB} and H_C can be obtained by

$$H_{EB} = (H_{SR} + H_{SL})/2, \quad H_C = (H_{SR} - H_{SL})/2, \tag{4}$$

where H_{SL} and H_{SR} are the coercive fields at descending and ascending branches of the hysteresis loop, respectively. We suppose that M_F stays at θ_{F1} when the applied field is absent at the initial magnetization stage. The magnetization reversal processes for the bilayer being in the bistable state are analyzed in order to explain the jump phenomenon.

Figure 2 shows the rotation of M_F during the magnetization reversal processes. For $0^\circ \leq \theta_H < \theta_{F1}$, as can be seen from Figure 2(a), with increasing H from zero to the positive saturation, M_F rotates away from θ_{F1} and towards the orientation of H because of the torque exerted on M_F by H. As H releases from the positive saturation to zero, M_F rotates back to θ_{F1} reversibly. In above magnetization procedure, it is not possible for M_F to be perpendicular to H so that neither the coercive field H_{SL} or H_{SR} occurs. However, when H reverses its direction and increases from zero to the negative saturation, M_F rotates away from θ_{F1} and rotates towards the opposite orientation of H in a clockwise sense to diminish the Zeeman energy. H_{SL} occurs at this magnetization stage, and the determined formula of H_{SL} is given by

$$\begin{aligned} &E/2K_F t_F = \frac{1}{2}\sin^2(\theta_{F1}+\theta) - J\cos(90^\circ - \theta_{F1} - \theta) - h\cos(180^\circ + \theta_H - \theta_{F1} - \theta), \\ &\begin{cases} \frac{1}{2}\sin 2(\theta_{F1}+\theta) - J\sin(90^\circ - \theta_{F1} - \theta) - h\sin(180^\circ + \theta_H - \theta_{F1} - \theta) = 0 \\ \cos 2(\theta_{F1}+\theta) + J\cos(90^\circ - \theta_{F1} - \theta) + h\cos(180^\circ + \theta_H - \theta_{F1} - \theta) \geq 0 \end{cases}. \end{aligned} \tag{5}$$

Here, $h = HM_F/2K_F$ is defined as the normalized field, and θ is the angle between M_F and θ_{F1}. At this magnetization stage, M_F passes through the intrinsic hard axis θ_{F2}, hence M_F will rotate towards another intrinsic easy axis θ_{F3} instead of rotating back to θ_{F1} as H releases from the negative saturation to zero. When H increases from zero to the positive saturation again, M_F rotates away from θ_{F3} and towards the positive orientation of H in a counterclockwise sense. H_{SR} appears at this magnetization stage, and the determined formula of H_{SR} is given by

$$\begin{aligned} &E/2K_F t_F = \frac{1}{2}\sin^2(\theta_{F3}-\varphi) - J\cos(\theta_{F3} - 90^\circ - \varphi) - h\cos(\theta_{F3} - \theta_H - \varphi), \\ &\begin{cases} -\frac{1}{2}\sin 2(\theta_{F3}-\varphi) - J\sin(\theta_{F3} - 90^\circ - \varphi) - h\sin(\theta_{F3} - \theta_H - \varphi) = 0 \\ \cos 2(\theta_{F3}-\varphi) + J\cos(\theta_{F3} - 90^\circ - \varphi) + h\cos(\theta_{F3} - \theta_H - \varphi) \geq 0 \end{cases}, \end{aligned} \tag{6}$$

where φ is the angle between M_F and θ_{F3}.

The magnetization reversal processes for $\theta_{F1} \leq \theta_H < 90^\circ$ is shown in Figure 2(b), H_{SL} also arises at the magnetization stage of increasing H from zero to the negative saturation, but it is in an anticlockwise sense that M_F rotates away from θ_{F1} and towards the opposite direction of H, which is different from the case of $0^\circ \leq \theta_H < \theta_{F1}$. The corresponding determined formula of H_{SL} is given by

$$\begin{aligned} &E/2K_F t_F = \frac{1}{2}\sin^2(\theta_{F1}-\theta) - J\cos(90^\circ - \theta_{F1} + \theta) - h\cos(180^\circ - \theta_H + \theta_{F1} - \theta), \\ &\begin{cases} -\frac{1}{2}\sin 2(\theta_{F1}-\theta) + J\sin(90^\circ - \theta_{F1} + \theta) - h\sin(180^\circ - \theta_H + \theta_{F1} - \theta) = 0 \\ \cos 2(\theta_{F1}-\theta) + J\cos(90^\circ - \theta_{F1} + \theta) + h\cos(180^\circ - \theta_H + \theta_{F1} - \theta) \geq 0 \end{cases}. \end{aligned} \tag{7}$$

At this magnetization stage, M_F crosses the intrinsic hard axis θ_{F4}, thus M_F will rotate towards θ_{F3} when reducing H from the negative saturation to zero. The coercive field H_{SR} occurs at

the magnetization stage of increasing H from zero to the positive saturation once more, and the determined formula is the same as Eq. (6).

Considering M_F rotates whether in clockwise or anticlockwise sense at the magnetization stage of increasing H from zero to the negative saturation, one can see that the determined formulas of H_{SL} are different in angular ranges of $0° \leq \theta_H < \theta_{F1}$ and $\theta_{F1} \leq \theta_H < 90°$, which are given by Eq. (5) and Eq. (7), respectively. Consequently, at the boundary of two angular ranges, i.e., $\theta_H = \theta_{F1}$, H_{SL} will be discontinuous, which means that H_{SL} shows an abrupt change at this angle, whereas H_{SR} is continuous at θ_{F1} because of the same determined formula given by Eq. (6) in both angular ranges mentioned above. According to Eq. (4), H_{EB} and H_C can also make an abrupt change, which results in the occurrence of the jump phenomenon.

3. RESULTS AND DISCUSSIONS

We can deduce the similar conclusions from the analyses of the magnetization reversal processes that at θ_{F3}, H_{SR} keeps continuous but H_{SL} shows a discontinuity. With the symmetry in hand, at $\theta_{F1} + 180°$ and $\theta_{F3} + 180°$, H_{SL} keeps continuous, while H_{SR} shows an abrupt change. At these angles, H_{EB} and H_C can also display the jump phenomenon. Therefore, four jumps will be presented in the curves of $H_{EB}(\theta_H)$ and $H_C(\theta_H)$ when the bilayer is in the bistable state. On the contrary, if the bilayer is in the monostable state, the intrinsic easy axis $\theta_{F1} = 90°$ and the intrinsic hard axis $\theta_{F2} = 270°$ are collinear with the y axis. By analyzing the magnetization reversal processes, both H_{SL} and H_{SR} are continuous in the whole angular range of $0° \leq \theta_H < 360°$, therefore no jump emerges in the ADEB. The corresponding calculation results for the angular dependence of H_{EB} and H_C are shown in Figure 3.

It can be observed that the shapes of the curves show a significant change as J varies from 0.3 to 2. Increasing the values of J, the curves of $H_{EB}(\theta_H)$ are enlarged, while the the curves of $H_C(\theta_H)$ are reduced, which demonstrates that the uniaxial anisotropy is gradually "weakened" with increasing J. Especially, it shows no hysteresis completely when the bilayer enters into the monostable state. The shapes of the curves for the monostable state are obviously different from that of the bistable state, which inidicates that the ADEB is determined directly by monostable and bistable states of the bilayers. Consequently, this jump phenomenon is an intrinsic property of the bilayers relied on the interfacial exchange coupling constant, the thickness and the uniaxial anisotropy of the FM layer. On the other hand, both H_{EB} and H_C are larger in the magnitude at

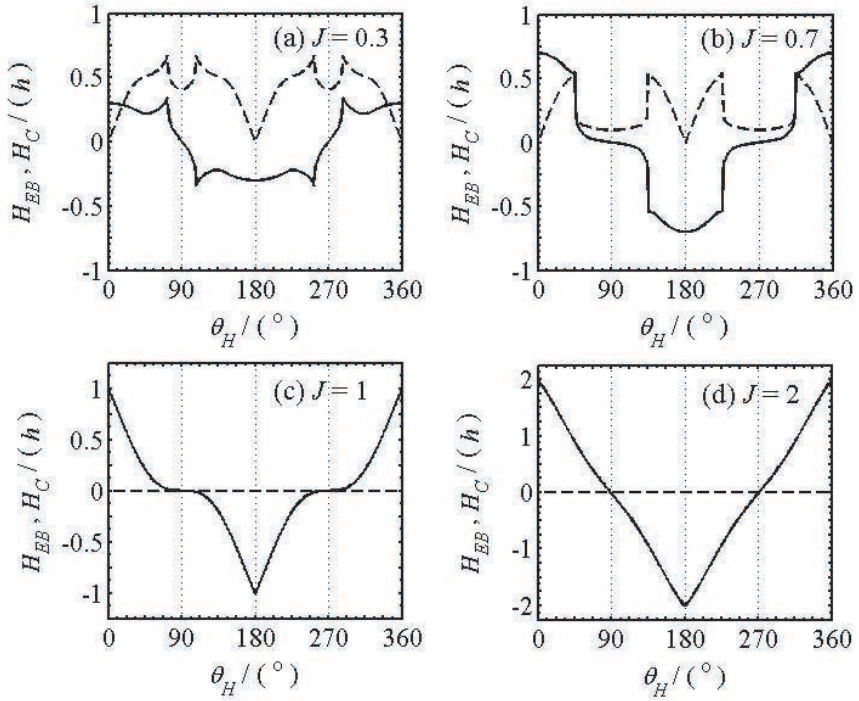

Figure 3: The angular dependence of exchange bias field H_{EB} (solid lines) and the coercivity H_C (dashed lines). The applied field H is normalized by h.

the points of the jumps, H_C reaches the maximum and sometimes H_{EB} can also reach the maximum as shown in Figure 3(a). However, no matter monostable state or bistable state the bilayer is in, H_{EB} and H_C exhibit the unidirectional and uniaxial symmetries, respectively, which is consistent with the experiments [6, 10].

4. SUMMARY

In conclusion, the angular dependence of the exchange bias with the uniaxial anisotropy perpendicular to unidirectional anisotropy in FM/AFM bilayers has been studied. The competition between unidirectional and uniaxial anisotropies divides the initial magnetization state of the bilayers into monostable and bistable states, which determine the ADEB directly. When the external field is applied along the intrinsic easy axes of the bistable state, by analyzing the magnetization reversal processes, one of the coercive fields of the hysteresis loop shows a discontinuity, while the other is kept continuous, which induces the jump phenomenon in the ADEB. The numerical calculations indicate that the exchange bias field and the coercivity are larger in the magnitude at the points of jumps. We hope that our method is helpful to gain larger values of the exchange bias field for optimizing the designs of the involved magnetoresistance devices.

ACKNOWLEDGMENT

This work was supported by National Natural Science Foundation of China under Grant No. 10762001, NCET under Grant No. 05-0272, and Specialized Research Found for the Doctoral Program of Higher Education of China under Grant No. 20080126003.

REFERENCES

1. Meiklejohn, W. H. and C. P. Bean, "New magnetic anisotropy," *Phys. Rev.*, Vol. 102, No. 5, 1413–1414, 1956.
2. Meiklejohn, W. H. and C. P. Bean, "New magnetic anisotropy," *Phys. Rev.*, Vol. 105, No. 3, 904–913, 1957.
3. Dieny, B., V. S. Speriosu, S. S. P. Parkin, B. A. Gurney, D. R. Wilhoit, and D. Mauri, "Giant magnetoresistive in soft ferromagnetic multilayers," *Phys. Rev. B*, Vol. 43, No. 1, 1297–1300, 1991.
4. Nogués, J. and I. K. Schuller, "Exchange bias," *J. Magn. Magn. Mater.*, Vol. 192, No. 2, 203–232, 1999.
5. Stamps, R., "Mechanisms for exchange bias," *J. Phys. D*, Vol. 33, No. 23, R2047–R268, 2000.
6. Ambrose, T., R. L. Sommer, and C. L. Chien, "Angular dependence of exchange Coupling in ferromag-net/antiferromagnet bilayers," *Phys. Rev. B*, Vol. 56, No. 1, 83–86, 1997.
7. Chung, S., A. Hoffmann, and M. Grimsditch, "Interplay between exchange bias and uniaxial anisotropy in a ferromagnetic/antiferromagnetic exchange-coupled system," *Phys. Rev. B*, Vol. 71, No. 21, 214430-1–10, 2005.
8. Kim, D. Y., C. Kim, C. O. Kim, M. Tsunoda, and M. Takahashi, "Angular dependence of exchange bias and coercivity in polycrystalline CoFe/MnIr bilayers," *J. Magn. Magn. Mater.*, Vol. 304, No. 1, e56–e58, 2006.
9. Spenato, D., V. Castel, S. P. Pogossian, D. T. Dekadjevi, and J. Ben Youssef, "Asymmetric magnetization reversal behavior in exchange-biased NiFe/MnPt bilayers in two different anisotropy regimes: Close and far from critical thickness," *Appl. Phys. Lett.*, Vol. 91, No. 6, 062515-1–3, 2007.
10. Xi, H. and R. M. White, "Angular dependence of exchange anisotropy in $Ni_{81}Fe_{19}/CrMnPt_x$ bilayers," *J. Appl. Phys.*, Vol. 86, No. 9, 5169–5174, 1999.
11. Mauri, D., E. Kay, D. Scholl, and J. Kent Howard, "Novel method for determining the anisotropy constant of MnFe in a NiFe/MnFe sandwich," *J. Appl. Phys.*, Vol. 62, No. 7, 2929–2932, 1987.
12. Stoner, E. C. and E. P. Wohlfarth, "A mechanism of magnetic hysteresis in heterogeneous alloys," *IEEE Trans. Magn.*, Vol. 27, No. 4, 3475–3518, 1991.

The Diagnostics of Ionosphere and Earth Ground Surface by Backscatter Sounding Data

S. N. Ponomarchuk, **V. I. Kurkin**, **and A. V. Oinats**
Institute of Solar-Terrestrial Physics SB RAS, Irkutsk, Russia

Abstract— We present modeling results of chirpsounder signals characteristics under backscatter sounding of the ionosphere in the framework of waveguide approach. We use an approximation in which scattered field is expressed through incidence field characteristics (incidence angle, amplitude) and local scattering pattern or scatter coefficient. Modeling results are used for analysis and interpretation of backscatter ionograms which were obtained on the base of ISTP SB RAS chirpsounder.

1. INTRODUCTION

In spite of intensive development of satellite systems for diagnostics of upper atmosphere and ground surface, the overland monitoring techniques remain actual. One of such techniques that give the most potential possibilities in decameter wavelength range is the technique of backscatter sounding (BS). Using this technique we can diagnose medium in large spatial regions within several thousands kilometers. The registration of backscatter ionograms allows us to control ionosphere conditions and investigate scattering properties of ground surface.

Our work deals with modeling results of chirp signals characteristics under ionosphere backscatter sounding in the framework of waveguide approach. We use approximation in which the scattered field is expressed by characteristics of incidence field (incidence angle, amplitude) and local scatter diagram or scatter coefficient. The modeling results are used for analysis and interpretation of backscatter ionograms that were obtained under sounding in various directions by chirp ionosonde of Institute of Solar-Terrestrial Physics SB RAS. The accumulated data array allows us to investigate the regularity of ionosphere conditions changes in various gelio and geophysical conditions. We also develop the techniques of radio channel current diagnostics in sounding sector for real-time ionosphere parameters correction and backscatter ionogram reconstruction under conditions of strong absorption. On the base of operative algorithms for BS signals characteristics calculation by upper front and secondary processing of experimental ionograms we carry out the identification of registered signals and tracks. The interpretation results are input data for maximal usable frequencies determination for backscatter propagation modes under given distance in sounding direction.

2. MODELING TECNIQUES

The modeling of chirp signals characteristics under backscatter ionosphere sounding in the framework of waveguide approach [1] is carried out on the base of incoherent scatter approximation in which scattered field characteristics are expressed through incidence field characteristics (incidence angle and amplitude) and local scatter diagram $\sigma(\alpha_i, \alpha_s)$ or scatter coefficient $\sigma_0(\alpha_i, \alpha_s)$ [2]. The introduction of specified notions is possible by means of relationship for normal wave excitement coefficients with scatter diagram of unit platform of terrestrial surface and incidence field amplitude. Under action of field $E(\vec{r}_\varsigma)$ falling on Earth surface $\vec{r}_\varsigma$ we have induced current which is a source of secondary emission, i.e., the reflecting surfaces define the scattered field sources. The estimation of reflecting platform sizes shows that for Earth surface incoherent scatter approximation can be sufficiently good. If we assume that within platform area the amplitude of incidence field, incidence angle and scatter coefficient are weakly changed in time then we can write the expression for scattered field $E_j^p(\vec{r}, t)$ in the form:

$$E_j^p(\vec{r}, t) = \mathrm{Re} \sum\nolimits_{n=n_1}^{n_m} a_n(\vec{r}, \tau_n) I_n(\varphi) \exp\left\{ i \int\limits_0^\theta \nu_n(\theta_1) d\theta_1 - i\omega t \right\}. \quad (1)$$

Here normal wave excitement coefficients has the form

$$I_n(\varphi) = A_i(r_\varsigma) \sqrt{\frac{\sigma_0(\alpha_i, \alpha_s) S \cos \alpha_i}{4\pi}} \ ,$$

where $A_i(r_\varsigma)$ — incidence field amplitude. Using approximate analytical (for sea surface [2]) and experimental (for land surface [3]) expressions for scatter coefficient $\sigma_0(\alpha_i, \alpha_s)$ as a function of incidence and scatter angles we can calculate backscatter signals characteristics on the base of technique for oblique ionosphere sounding. For given number of normal wave n_i the equation

$$L_n(\vec{r}, f) = \frac{1}{2\pi}[\Phi_n - \Phi_{n+1}] = l, \tag{2}$$

where $\Phi_n = ka\int\limits_0^\theta \gamma_n(\theta_1, f)d\theta_1$ — normal wave phase determines the propagation path of phased normal waves package with central number n_i (l — hop number). The solving of this equation for angular range θ for given values of n_i allows to construct the analogue of range-angle characteristic — the dependence of hop range on central number $n_i(\theta(n_i))$. Calculating of group delay of central wave n_i using $\theta(n_i)$ we get the analogue of range-angle characteristic $P(n_i)$, where P is group path. The minimum of $\theta(n_i)$ dependence corresponds to boundary of illuminated zone θ_m. The minimum of $P(n_i)$ dependence determines minimal group path. The dependences $P(n_i)$ and $\theta(n_i)$ are "asymmetrical", so the angle range of illuminated zone boundary is not equal to angle range on which we have the minimum of group path.

For constructing the amplitude relief $A(\vec{r}, t)$ for backscatter signal within incoherent approximation we need to carry out "gathering" of all rays in illuminated area and calculate the amplitude of summary signal in each given time moment. Using $P_l(n_i)$ and $\theta_l(n_i)$ dependences we can determine the local platforms of Earth surface from which the scattering is occurred in given time moment. By knowing of scattering area coordinates and central number n_i of waves groups that forming the incidence field we can calculate $A_i(\vec{r}_\varsigma)$ and α_i, restore excitement coefficients and calculate amplitude characteristics of scattered field in receiving point. It is assumed that backscatter signal field is formed by scattered signals which come to receiving point by same possible paths in which sounding signals propagates. The amplitudes of separate signals which come to receiving point in given time moment are added incoherently. The using of functions approximation technique by local B-splines of the second degree allows to realize the effective scheme for backscatter signals calculation. The modeling of envelope curve for registered spectrum of backscatter signal is carried out taking into account the processing signal technique in receiving device [4].

On the base of model calculation for chirp signal amplitude relief under backscatter ionosphere sounding we can motivate the choice of operative calculation technique for range-frequency backscatter signals characteristics by leading edge. Since the maximum of amplitude relief of backscatter signal is close to group path of leading edge, the calculation of backscatter ionogram can be carried out on the base of frequency dependence calculation for minimal group path P_m of oblique sounding signals which can be determined as minimums of function $P_l(f, n)$.

3. CURRENT DIAGNOSTICS OF RADIO CHANNEL

By modeling of backscatter sounding signal characteristics and experimental data analysis we have revealed weakly changed ratio (under ionosphere parameters variations) of group path P_m, which corresponds to leading edge of backscatter signal and distance to illuminated zone border D_m (P_m/D_m) [5]. Given adiabatic relation allows to determine maximal usable frequency (MUF) of propagation mode on given radio path with a help of backscatter data. For prognosis ionosphere parameters we can calculate range-frequency characteristics $P_m(f)$ and $D_m(f)$. Also, for given range D we calculate ratio $\eta = P_m/D$ and after that on real range-frequency characteristic of backscatter sounding by leading edge we can determine the frequency for which group path is equal to value $P = \eta D$. The calculated frequency will be real f_m for given range D.

In some cases on backscatter ionograms there is no signals scattered from ranges for which we need to determine radio communication characteristics. For reconstruction and interpretation of full range-frequency characteristic of backscatter signal from dependence of group path $P_m(f)$, obtained in limited frequency range we can use an algorithm based on adiabatic dependence of minimal group path of the scattered signal on relative frequency grid $\nu = f/f_m$. The frequency f_m can be chosen as MUF for maximal range of signal propagation. For ionosphere prognosis parameters on frequency grid we can carry out the calculation of range-frequency characteristic of backscatter signal by leading edge and after that these data transfer to grid ν. Then for experimental set of group path values we can determine the possible region of true frequency which corresponds to maximal hop range. The bottom boundary of this region is maximal frequency from sounding

frequencies set but upper is the frequency which is undoubtedly greater than true frequency f_m (for example, triple maximal sounding frequency). Then with a help predefined algorithm (for example, by dichotomy technique) in this frequency interval we can obtain true value of f_m, for which under transfer to relative frequency grid ν prognosis and experimental values of group path will be the closest to each other. By multiplying ν by calculated value of real f_m the prognosis value of range-frequency characteristic are transferred to frequency scale. Thereby we can restore range-frequency characteristic for lacking sounding frequencies.

4. SIMULATION RESULTS

The approbation of proposed technique for backscatter signals characteristics calculation is carried out by means of experimental data obtained by chirp ionosounder (Irkutsk, Russia, 52° N, 104° E). As an example on Fig. 1 we present backscatter ionogram obtained on 29 February 1996 4 : 49h UT under sounding in Asia-pacific ocean region direction (sounding azimuth 121°) with modeling results of range-frequency characteristics of backscatter signal by leading edge, processing by amplitude relief (1(a)) and interpretation by chosen fragment of ionogram (1(b)). The results of ionogram processing by amplitude relief are shown in white color. For backscatter signals interpretation we use reconstruction technique for range-frequency characteristics of backscatter signal by current backscatter data on the base of invariant P_m/D_m. The results of one-hop mode 1F2 reconstruction are presented on Fig. 1(b).

The processing of amplitude relief has shown the presence of horizontal tracks with nearly constant delay. For interpretation of these signals we used reconstruction technique for range-frequency characteristics of backscatter signal by current backscatter data. Using the results of backscatter signals modeling by leading edge and marked tracks of one-hop signals we can calculate MUF for oblique sounding (f_m^r) on fixed ranges grid. On the base of calculation results we can obtain ranges for which group path P_m approximately complies with horizontal track delay. Using the long-term forecast of range-frequency characteristics for oblique sounding on chosen ranges in relative frequency grid $\beta = f/f_m^p$, where f_m^p-prognosis value of MUF propagation mode, we can carry out the interpretation of horizontal "tracks" by means of recalculation of model oblique sounding range-frequency characteristics on real frequency grid βf_m^r. The calculation results of range-frequency oblique sounding characteristics for propagation mode 1F2 on ranges 1800 km and 2500 km are shown on Fig. 1(b) by lines with numbers 1 and 2 accordingly. The determination of scattering objects positions by receiving points coordinates of oblique sounding signals on chosen distances from transmitter shows that appearance of horizontal bands on backscatter ionograms in our experiment can be connected with scattering on transition border between sea and land (coast line of Yellow and Japanese seas).

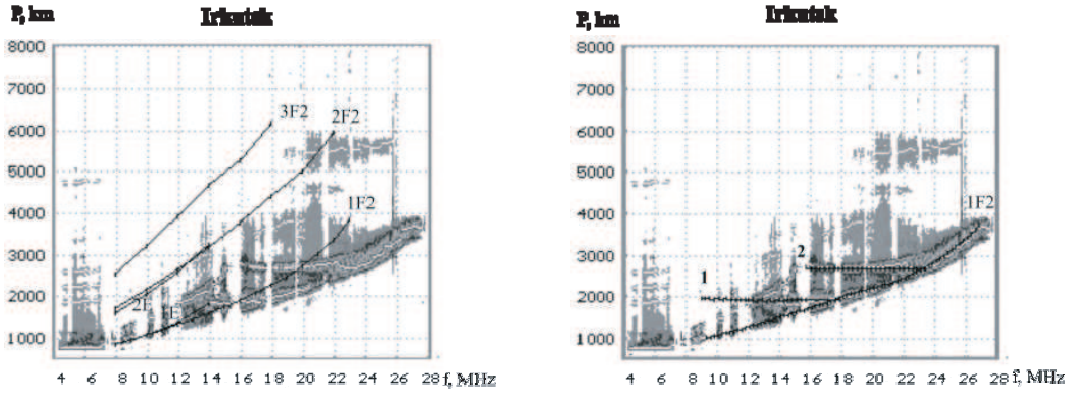

Figure 1: The ionograms of backscatter sounding, modeling results (a) and interpretations (b). 29 February 1996, 4 : 49h UT.

5. CONCLUSIONS

Our investigation has shown that proposed in the waveguide approach calculations techniques of registered chirp signal spectrum envelope and range-frequency characteristics of backscatter signals by leading edge under backscatter ionosphere sounding allows to carry out operative interpretation

of propagation modes, take into account the influence of ionosphere multi-layers, separate signals which are reflecting from various ionosphere layers and coming from different azimuths. The using of backscatter running data allows to carry out operative forecast of oblique propagation mode in real time scale.

ACKNOWLEDGMENT

The work is done under support of Russian fund of basic research (grant No. 08-05-00658).

REFERENCES

1. Kurkin, V. I., I. I. Orlov, and V. N. Popov, *Normal Wave Technique in HF Radio Communication Problem*, Nauka, Moscow, 1981.
2. Isimaru, A., *Wave Propagation and Scattering in Random Media*, Mir, Moscow, 1981.
3. Chernov, Y. A., *Backscatter Ionosphere Sounding*, Svyas, Moscow, 1971.
4. Ilyin, N. V., V. V. Khakhinov, V. I. Kurkin, et al., "The theory of chirp-signal ionospheric sounding," *Proceedings of ISAP'96*, 689–692, Chiba, Japan, 1996.
5. Kurkin, V. I., V. E. Nosov, S. N. Ponomarchuk, et al., "A technique for current diagnostics of the high-frequency radio channel," *Proceedings of ISAP'96*, 1189–1192, Sapporo, Japan, 1992.

The SAR Ocean Image Correlation Model and Its Validation by MultiBand SAR Ocean Images

Xiaoqing Wang[1], **Yongqiang Chen**[1], **Minhui Zhu**[1], **Yunxiang You**[2], **and Tianqun Hu**[2]

[1]National Key Lab of Microwave Imaging Technology, Institute of Electronics
Chinese Academy of Sciences, China
[2]School of Naval Architecture and Ocean Engineering, Shanghai Jiaotong University, China

Abstract— The correlation characteristic plays an important role in the SAR ocean image mechanism. The radiometric resolution of high correlation SAR images is lower than that of the SAR images with lower correlation. The correlation length of SAR ocean images is usually assumed simply to be the same as the size of the resolution cell in the previous studies. However, in this paper, a new correlation function model of SAR ocean images is present, which shows that the correlation length in range direction is depend only on the range resolution, but the azimuth correlation length is rather complex, it depends on azimuth resolution, ocean scattering coherent time and platform velocity. According to this model, the azimuth correlation length can be shorter than SAR azimuth resolution if the coherent time is short enough and the platform velocity is sufficiently low. In the ocean image of airborne high frequency band (such as X or Ku band) SAR, the azimuth correlation length is significant shorter than range resolution because that the scattering coherent time of high band is shorter and the velocity of airborne platform is relatively low. However, the azimuth correlation length of spaceborne SAR images are very close to the range correlation length because of its high velocity. Some airborne multiband (L, X, and Ku band) and spaceborne SAR ocean images are used to validate and support this model.

1. INTRODUCTION

Most ocean distributed targets such as ship wakes, oil spill and swells display large scale and low contrast information in the SAR ocean images. So the radiometric resolution is more important than geometric resolution in many SAR ocean applications. The radiometric resolution is quite low in the single look SAR images because of the speckle noise. To get high radiometric resolution, the multilook technique is often applied in which the image pixels in a $N \times N$ windows are summed incoherently. The radiometric resolution of multilook images depends on the correlation characteristic of the single look images. The radiometric resolution of high correlation SAR images is lower than that of the SAR images with lower correlation under the same multilook number. The correlation length of SAR ocean images is usually assumed simply to be the same as the size of the resolution cell in the previous studies [1]. However, the SAR ocean images of different bands and platforms show quite different speckle size, which means different correlation length. So the correlation length of SAR images cannot be assumed simply to be the same as the resolution size.

In this paper, a new correlation function model of SAR ocean images is present. The model shows that the correlation length in range direction depends only on range resolution, but the azimuth correlation length is rather complex, it depends on azimuth resolution, ocean scattering coherent time and platform velocity. Some airborne multiband (L, X, and Ku band) and spaceborne SAR ocean images are used to support this model. According to this model, the azimuth correlation length can be shorter than SAR azimuth resolution if the coherent time is short enough and the platform velocity is low. So the speckle noise in airborne high frequency band (such as X or Ku band) SAR ocean images looks very small because that the scattering coherent time of high band is shorter and the velocity of airborne platform is relatively low. So the airborne high band SAR system can obtain higher radiometric resolution ocean images than lower band or spaceborne SAR systems with the same multilook number.

2. THE CORRELATION MODEL OF SAR OCEAN IMAGE

After range match processing, the SAR signal can be expressed as

$$\mathbf{I_r}(t,t') = \int \rho(x,y,t) \exp\left[-2\left(\frac{x-vt}{L_x}\right)^2\right] \exp\left[-\frac{\pi^2}{4}\left(\frac{y\sin\theta - \frac{c}{2}t'}{\delta_y}\right)^2\right] \exp\left[-j\frac{1}{2}f_r\left(\frac{x}{v}-t\right)^2\right] dxdy \quad (1)$$

where t is the "slow" time between pulses, and t' is the "fast" time within the pulse, v is the platform velocity, $\rho(x,y,t)$ is the complex reflectivity of the surface, θ is the incident angle of radar, L_x is the azimuth length of the antenna footprint, δ_y is the range resolution

$$L_x = \frac{\lambda}{2\delta_x}R, \quad \delta_y = c/2B, \quad f_r = 2k_0v^2/R \tag{2}$$

where λ is the radar wavelength, δ_x is the azimuth resolution of antenna, k_0 is the radar wavenumber, R is the range distance to the surface.

The complex image is obtained, in turn, by convolving $\mathbf{I_r}(t,t')$ with the azimuth reference function

$$\begin{aligned}\mathbf{I_a}\left(t,t'\right) &= \int \mathbf{I_r}\left(t_1,t'\right)\exp\left\{j\frac{1}{2}f_r(t-t_1)^2\right\}dt_1 = \int \rho(x,y,t_1)\exp\left[-2\left(\frac{x-vt_1}{L_x}\right)^2\right] \\ &\exp\left[-\frac{\pi^2}{4}\left(\frac{y\sin\theta-\frac{c}{2}t'}{\delta_y}\right)^2\right]\exp\left[-j\frac{f_r}{2}\left(\frac{x}{v}\right)^2\right]\exp\left[jf_r\left(\frac{x}{v}-t\right)t_1\right]dxdydt_1\end{aligned} \tag{3}$$

The complex images can be expressed in terms of image position $[x_0\, y_0]$ by setting $x_0 = vt$, $y_0 = \frac{ct'}{2\sin\theta}$

$$\begin{aligned}\mathbf{I_a}(x_0,y_0) &= \int \rho(x,y,t_1)\exp\left[-2\left(\frac{x-vt_1}{L_x}\right)^2\right]\exp\left[-\frac{\pi^2}{4}\left(\frac{y-y_0}{\alpha_y}\right)^2\right]\exp\left[-j\frac{f_r}{2}\left(\frac{x}{v}\right)^2\right] \\ &\exp\left[j\frac{f_r}{v}\left(x-x_0\right)t_1\right]dxdydt_1\end{aligned} \tag{4}$$

where $\alpha_y = \delta_y/\sin\theta$. The autocorrelation function of the image is

$$\begin{aligned}R(\varepsilon,\eta) &= \langle \mathbf{I_a}(x_0,y_0)\mathbf{I_a}^*(x_0-\varepsilon,y_0-\eta)\rangle = \int \exp\left[-2\left(\frac{x_1-vt_1}{L_x}\right)^2\right]\exp\left[-2\left(\frac{x_2-vt_2}{L_x}\right)^2\right] \\ &\langle\rho(x_1,y_1,t_1)\rho(x_2,y_2,t_2)\rangle\exp\left[-\frac{\pi^2}{4}\left(\frac{y_1-y_0}{\alpha_y}\right)^2\right]\exp\left[-\frac{\pi^2}{4}\left(\frac{y_2-y_0+\eta}{\alpha_y}\right)^2\right] \\ &\exp\left[-j\frac{f_r}{2}\left(\frac{x_1}{v}\right)^2\right]\exp\left[j\frac{f_r}{v}\left(x_1-x_0\right)t_1\right]\exp\left[j\frac{f_r}{2}\left(\frac{x_2}{v}\right)^2\right] \\ &\exp\left[-j\frac{f_r}{v}(x_2-x_0-\varepsilon)t_2\right]dx_1dy_1dx_2dy_2dt_1dt_2\end{aligned} \tag{5}$$

The complex reflectivity can be assumed to have second-order statistic as described by [2]

$$\langle\rho(x_1,y_1,t_1)\rho(x_2,y_2,t_2)\rangle \approx \delta(x_1-x_2)\delta(y_1-y_2)\sigma_0\exp\left(-\frac{\tau^2}{\tau_c^2}\right) \tag{6}$$

where σ_0 is the NRCS of the ocean surface, τ_c is the coherent time of the ocean surface.

The following new variables are defined as:

$$X = \frac{x_1+x_2}{2},\ x = x_1-x_2,\ Y = \frac{y_1+y_2}{2},\ y = y_1-y_2,\ T = \frac{t_1+t_2}{2},\ \tau = t_1-t_2 \tag{7}$$

Substituting (7) into (5) and integrating in X, Y, T and τ, the normalized autocorrelation function is obtained as

$$R_0(\varepsilon,\eta) = \frac{R(\varepsilon,\eta)}{R(0,0)} = \exp\left[-\frac{\pi^2}{8}\left(\frac{\eta}{\alpha_y}\right)^2\right]\exp\left\{-\left[\left(\frac{L_xf_r}{4v^2}\right)+\left(\frac{2}{\tau_cv}\right)+\left(\frac{2}{L_x}\right)^2\right]\varepsilon^2\right\} \tag{8}$$

Inserting (2) into (8), $R_0(\varepsilon,\eta)$ may be rewritten as

$$R_0(\varepsilon,\eta) = \exp\left[-\frac{\pi^2}{4}\left(\frac{\eta}{\sqrt{2}\alpha_y}\right)^2\right]\exp\left\{-\frac{\pi^2}{4}\left[\left(\frac{1}{\delta_x}\right)^2+\left(\frac{4}{\pi\tau_cv}\right)^2+\left(\frac{4}{\pi L_x}\right)^2\right]\varepsilon^2\right\} \tag{9}$$

In most cases, $L_x \gg \delta_x$, therefore, the correlation length along x and y direction can be expressed as

$$\xi_x \approx 1/\sqrt{\left(\frac{1}{\delta_x}\right)^2 + \left(\frac{1}{\delta_\tau}\right)^2}, \quad \delta_r = \frac{\pi \tau_c v}{4}, \quad \xi_y = \sqrt{2}\delta_y / \sin\theta \tag{10}$$

The formula (9), (10) show that the correlation length along y direction depends only on the range resolution, whereas the correlation length of x direction depends on not only azimuth resolution, but also ocean coherent time and platform velocity. If $\delta_x \ll \delta_\tau$, ξ_x will be dominated by the azimuth resolution, otherwise, the correlation length will be less than δ_x.

3. MODEL ANALYSIS AND VALIDATION

Given a surface displacement spectrum, the coherence time can be estimated from the radial component of the RMS orbital velocity [3]. Fig. 1 shows estimated coherence times versus wind speed for six different frequencies given a spatial resolution of 30 m and a P-M type wave spectrum.

In Fig. 1, the ocean surface coherent time of X or Ku band (10 and 14 GHz) is the order of 10–30 ms under most wind speed. For the typical airborne platform velocity of 100 m/s, the second term in (10) is about $\delta_\tau \approx 0.78 \sim 2.34$ m. In most cases, the radar azimuth resolution is not much smaller than 2.34 m, so the azimuth correlation length of airborne high band SAR is significant less than azimuth resolution. However, for the typical spaceborne platform velocity of about 7500 m/s, $\delta_\tau \approx 75 \sim 225$ m. the radar resolution is, In general, much less than 75 m, so the azimuth correlation azimuth correlation length of spaceborne SAR is independent on surface coherent time.

The following 3 single look ocean SAR images (see Fig. 2) are obtained at the same time by 3-band airborne SAR (L, X and Ku band), the velocity of the platform is about 100 m/s, range and azimuth resolution are 3.6 m and 3.8 m respectively.

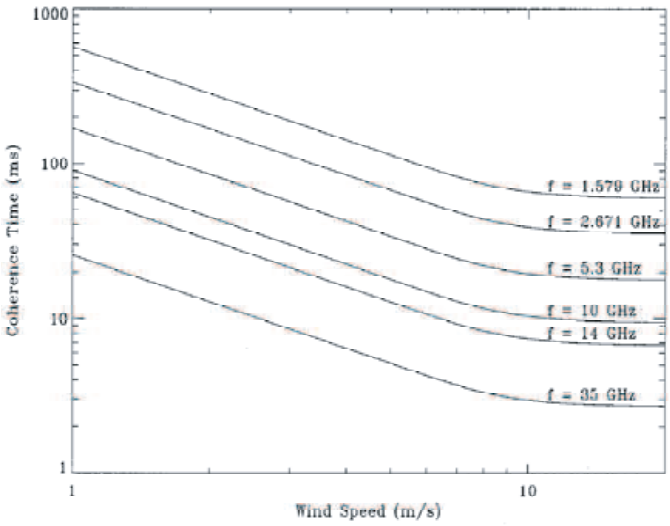

Figure 1: Estimated coherence time.

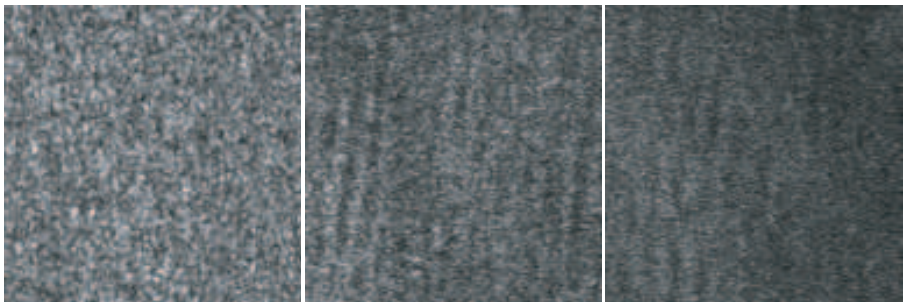

Figure 2: 3 Band single look ocean SAR images.

The size of speckle in the L band image looks quite larger than that of X and Ku band images. It means that the correlation length of L band is longer than that of X and Ku band.

Figure 3 shows the range and azimuth normalized autocorrelation function of these 3 images.

From Fig. 3, the range autocorrelation functions of the 3 images are very close to each other, the correlation length are all about 7 m. However, the azimuth autocorrelation functions are quite different from each other, the correction length of L, X and Ku band images are 7.5 m, 5.2 m and 3.4 m respectively. This result shows that the azimuth correlation length is dependent on coherent time.

Figure 4 gives an ocean single look image of X band TerraSAR with resolution of 3.6 m.

The range and azimuth autocorrelation functions are show in Fig. 5.

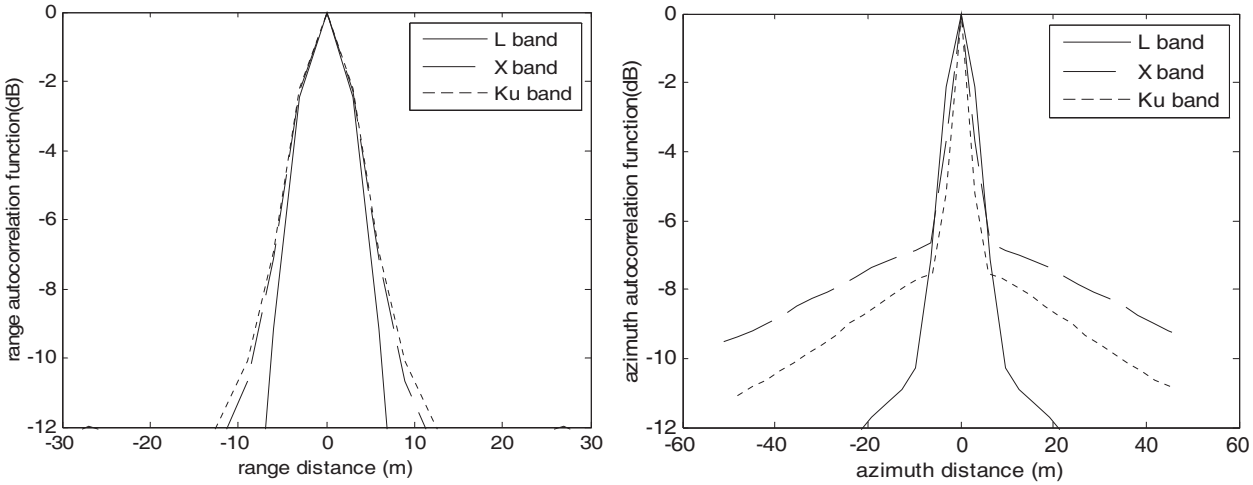

Figure 3: Range and azimuth normalized autocorrelation function.

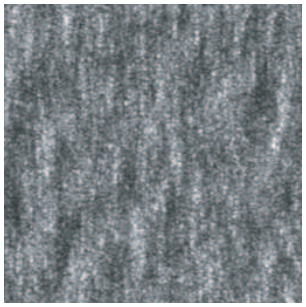

Figure 4: Ocean single look image of TerraSAR.

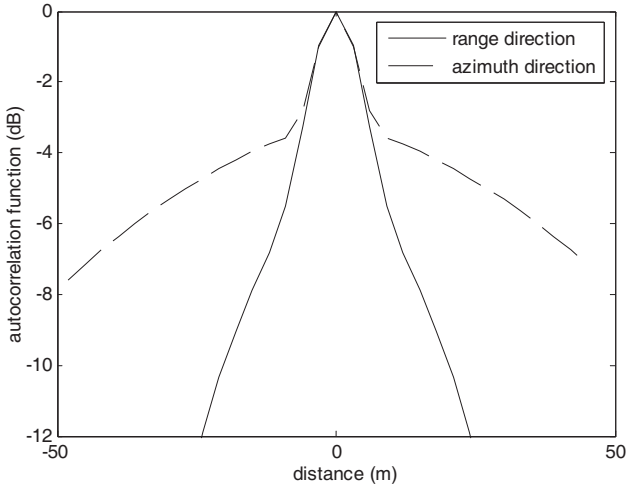

Figure 5: The range and azimuth autocorrelation function of TerraSAR image.

In Fig. 5, the range and azimuth correlation length are all about 6 m. This result means that the azimuth correlation length of spaceborne SAR is independent on the ocean surface coherent time because of its high velocity.

4. CONCLUSION

In this paper, a new SAR ocean image correlation model is given. The model shows that the range correlation length depends on range resolution only, whereas the azimuth correlation length depends on not only azimuth resolution but also coherent time and platform velocity. If the coherent time is short enough and the platform velocity is sufficiently low, the azimuth correlation length can be less than resolution size. We use 3-band (L, X, Ku band) airborne SAR images and the spaceborne X band TerraSAR images to support this model. The results show that the range correlation length of the 3 airborne SAR images are very close, whereas the azimuth correlation length of Ku and X band are shorter than that of L band significantly because of the short coherent time of Ku and X band SAR. A TerraSAR ocean image is also processed to validate the correlation function model, the processing result show that the correlation length of azimuth and range direction are very close. This result show that the azimuth correlation length of spaceborne SAR is independent on ocean surface coherent time because of its high velocity. The validation results are consistent with the correlation function model on the whole.

ACKNOWLEDGMENT

This work was funded by National Natural Science Foundation of China (NO. 40706063).

REFERENCES

1. Johannes, S. S. and L. Susanne, "A noise model for estimated synthetic aperture radar look cross spectra acquired over the ocean," *IEEE Trans. G. R. S.*, Vol. 43, No.7 , 1443–1452, 2005.
2. Plant, W. J., "Reconciliation of theories of synthetic aperture radar imagery of ocean waves," *J. G. R.*, Vol. 97, No. C5, 7493–7501, 1992.
3. Stephen, J. F. and J. C. Adriano, "Dual-beam interferometry for ocean surface current vector mapping," *IEEE Trans. G. R. S.*, Vol. 39, No. 2, 401–414, 2001.

Ground Penetrating Radar Exploration for Ground Water and Contamination

Ziaqiang Zhu, **Xianqi He**, **Guangyin Lu**, **Qunyi Liu**, **and Jianhui Li**
Geomatics and Info-physics School, Central South University, Changsha, China

Abstract— Ground-penetrating radar (GPR) is well known as one of the best tools to detect groundwater surface and water contamination. However, very few people take into account the effect of a capillary fringe over water table with groundwater survey and hydraulic properties estimation. Water contents vary from 100 percent to several percent in this capillary fringe. In this study, we took a stepwise approach to examine the influence of the capillary fringe. First, the principles of GPR are introduced and estimation of water content is studied, then the response of electromagnetic waves reflected from water table was examined in our test in changde hunan province.

1. INTRODUCTION

Ground-penetrating radar (GPR) is well known as one of the best tools to detect groundwater surface [1, 2]. GPR has been successfully applied for large-scale groundwater prospecting (Blindow et al., 1987). GPR, which offers high spatial resolution, can provide additional hydrogeologically relevant information about the nearsurface underground strata (Davis and Annan, 1989). Particularly in electrically low conductive sediments GPR has proved to be a powerful geophysical tool in hydrogeologic studies (Beres and Haeni, 1991; Jol and Smith, 1991; Smith and Jol, 1992). Summaries and descriptions of methodologies and applicabilities of GPR in engineering and environmental research are given by Daniels (1989) and Ulriksen (1982). Four-dimensional_4D.or time-lapse three- dimensional_3D.ground penetrating radar surveys can be used to monitor and image subsurface fluid flow [3]. This information can be used to create a model of hydrogeological properties.

2. PRINCIPLES OF GPR

GPR is a non-destructive technique that uses electromagnetic (EM) waves to "look" into a material. GPR systems operate in a similar manner to sonar — i.e., by emitting a series of brief pulses and estimating distance to objects from the time it takes to detect reflections. The strength of the reflection depends on the electrical contrast between materials [4, 5].

The GPR records the strength of reflections detected for a set duration after each pulse. A plot of this data is called a 'trace'.

As the EM waves travel very quickly, the time duration the GPR 'listens' for after each pulse is very brief. The trace signal is usually plotted against a time scale measured in nanoseconds [6].

GPR systems generate a rapid succession of traces, which are displayed as a "radargram". A radargram is simply a display of one trace after another with the intensity of the reflected signal represented by different colours or shades of grey [7].

Figure 1 shows an unprocessed radargram of the end of a girder shown with a grey scale palette.

3. WATER CONTENT ESTIMATION

The portion of the profile between the ground surface and the ground water table,the vadose zone, can be divided into a number of regions. In the upper part of the vadose zone, the water is held at a minimum, residual saturation. In the lower part of the vadose zone, known as the transition (funicular) zone, the water saturation rises above residual levels, increasing with depth until the groundwater surface is reached. The capillary fringe is located below the funicular zone where saturation (Figure 2) [9] approaches 100%. The capillary fringe above the water table is almost saturated with water, but the pressure head in this region is still slightly less than atmospheric. The water table is simply known as an interface between the unsaturated and saturated zones. It is best described as the depth where the pore water pressure is equal to the atmospheric pressure. The thickness of the capillary fringe and transition zone depends largely on the grain size distribution. The distinguishable reflections of main concern occurred at the top of the water saturated zone which is located at the top of the capillary fringe above the water table. The GPR response from the top of the capillary fringe was assumed to be the location of the water table [10]. Annan et al. show

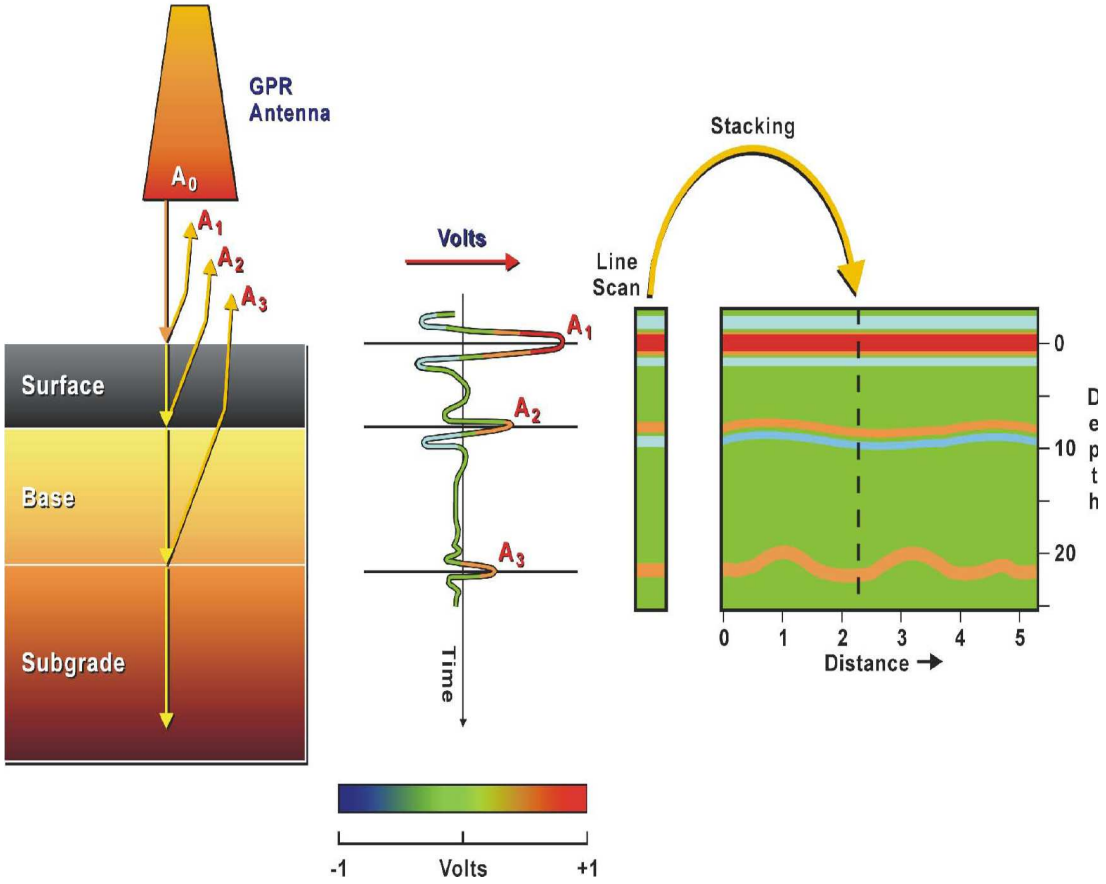

Figure 1: Unprocessed radargram.

that the radar reflection from the water saturated zone becomes more dispersed as the thickness of the transition zone above capillary fringe increases.

The difference between the relative dielectric constant of liquid water ($\varepsilon_{r,w} \cong 81$) and that of most rock matrix materials ($\varepsilon_{r,g} = 3 - 5$) is large [11]. Accordingly, it is known that the dielectric constant of most geological materials is governed by their water content. When the relative dielectric constant of the soil is ε_r, EM wave velocity in the soil is given by

$$v = c/\sqrt{\varepsilon_r} \tag{1}$$

where c is the velocity of light in air. Therefore, the two-way travel time for a boundary at the depth d is given by

$$\tau = \frac{2d}{v} = \frac{2d\sqrt{\varepsilon_r}}{c} \tag{2}$$

where c the dielectric permittivity is constant from the surface to depth d.

The velocity obtained from the velocity spectrum is the normal moveout (NMO) velocity, approximately the same as the RMS velocity assuming the medium is homogeneous from the surface to the boundary, when the subsurface consists of multiple horizontal layers. Therefore, in order to estimate the relative dielectric constant of each layer, the RMS velocities have to be corrected to interval velocities[12]. The average interval velocity of the n-th layer can be calculated using the Dix formula

$$V_n^2 = \frac{V_{RMS_n}^2 t(0)_n - V_{RMS_{n-1}}^2 t(0)_{n-1}}{} \tag{3}$$

where V_{RMS_n} and $t(0)_n$ denote the RMS velocity and vertical reflection travel time to the n-th layer. The relative dielectric constant can be obtained by Eq. (1) using the interval velocities, and the depth of each layer can be obtained by Eq. (2). Generally, the water content θ, porosity ψ and water saturation S_w are related as $\theta = \psi \cdot S_w$. Several cases showing the relationship between the dielectric constant and properties of θ, ψ and S_w have been reviewed by Sen et al. and Shen et al..

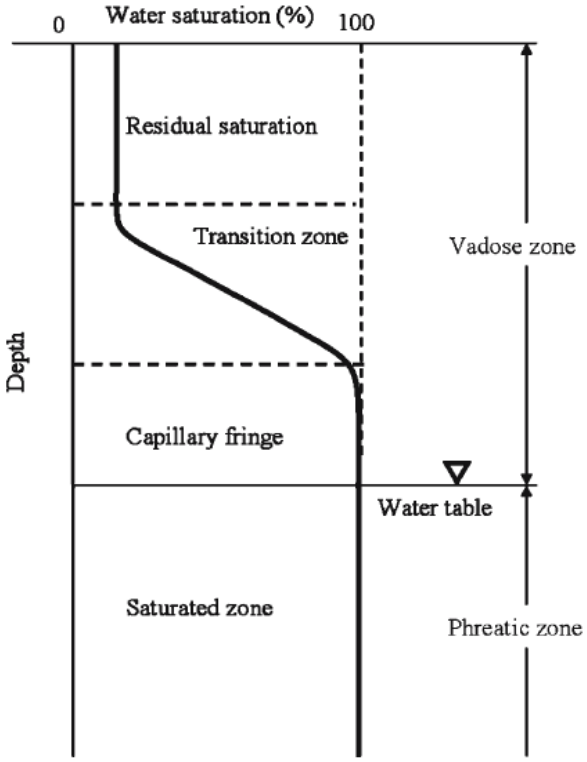

Figure 2: A conceptual model of the water saturation profile in the subsurface.

However, it is impossible in practice to derive both porosity ψ and water content θ independently from the dielectric constant [13, 14]. An empirical equation derived by Topp et al. using various soil samples with different degrees of saturation gives the relation between the dielectric constant and water content as

$$\theta = -0.0503 + 0.0292\varepsilon_r - 5.5 \times 10^{-4}\varepsilon_r^2 + 4.3 \times 10^{-6}\varepsilon_r^3 \tag{4}$$

4. ESTIMATION OF HYDRAULIC CONDUCTIVITY

For most medium the total dielectric:

$$\sqrt{\varepsilon_{total}} = \psi(1 - S_w)\sqrt{\varepsilon_{air}} + (1 - \psi)\sqrt{\varepsilon_{grain}} + S_w \cdot \psi\sqrt{\varepsilon_{water}} \qquad \theta = \psi \cdot S_w \tag{5}$$

From (4) (5) (6) can get that

$$\psi = \frac{\sqrt{\varepsilon_{total}} - \sqrt{\varepsilon_{grain}} + \theta\left(\sqrt{\varepsilon_{air}} - \sqrt{\varepsilon_{water}}\right)}{\sqrt{\varepsilon_{air}} - \sqrt{\varepsilon_{grain}}} \tag{6}$$

For most grain medium $\sqrt{\varepsilon_{grain}} = \approx 4.8$ and in saturation area $S_w = 1$.
When we get the proposity we can get the permeability as Kozeny-Carman

$$K = \frac{C_g\psi^3}{\mu_{water}\rho_{water}S_p^2D_R^2(1 - \psi)^2} \tag{7}$$

K — permeability, C — particle shape factor, g — acceleration of gravity, μ_{water} — The viscosity of water-gravity, S_p — Surface area of particle, D_R — The density of particle.

5. EXAMPLE

Controlled water productions were performed at a water source area of changde city, hunan province to evaluate the effectiveness of ground penetrating radar (GPR) for detecting and monitoring dynamic groundwater movements in the subsurface and for estimating the hydraulic properties of the aquifer. Field experiments in chnagde were carried out in 2007 and 2008. GPR data were

acquired using 400 MHz antennas. The GPR data sets were acquired very carefully by locating the antenna position accurately.

The radargrams show (Figure 3) a feature that is the water table reflections acquired at two different places. It helped to determine travel time and its effective reflection point from the top of the water saturated zone. The distinguishable reflections of main concern occurred at the top of the water saturated zone which is located at the top of the capillary fringe above the water table. It is clearly that the GPR response from the top of the capillary fringe was assumed to be the location of the water table. It was concluded that GPR can be successfully employed to monitor groundwater migration and to estimate hydraulic properties of the aquifer.

Recent studies have shown that the spatial/temporal variation in GPR signal attenuation can provide important information on the electrical properties of the sub-surface materials that, in turn, can be used to assess the physical and hydrological nature of the pore fluids and associated contaminants. By comparing laboratory-based,dielectric measurements of LNAPL contaminated materials with the GPR signal attenuation observed in both contaminated and 'clean' areas of an LNAPL contaminated site, new insights have been gained into the nature of contaminant distribution/saturation and the likely signal attenuation mechanisms. A generalized attenuation/saturation model has been developed that describes the physical and attenuation enhancement characteristics of the contaminated areas and reveals that the most significant attenuation is related to smeared zone surrounding the seasonally changing water table interface (Figure 4).

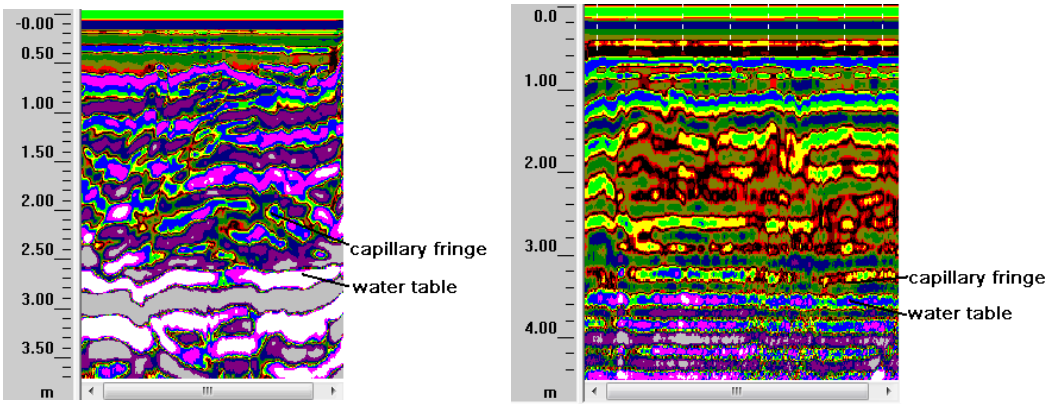

Figure 3: GPR sections at profile show changes in the electromagnetic signal during the exploration. Antenna frequency is centered in 400 MHz.

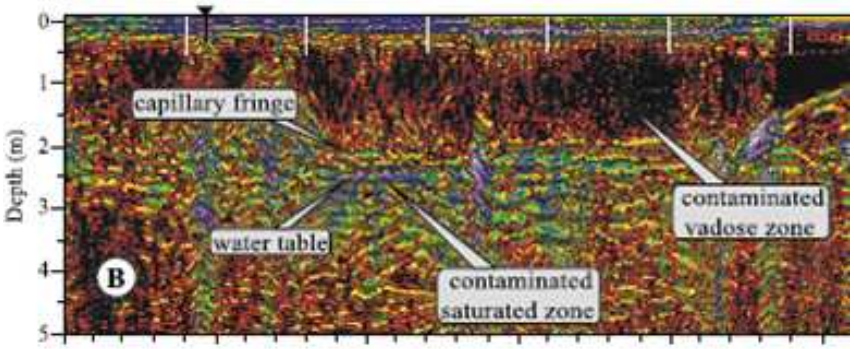

Figure 4: GPR sections at profile show changes in the electromagnetic signal during the exploration. Antenna frequency is centered in 400 MHz.

6. CONCLUSION

The GPR technique successfully yielded quantitative information about water table change, and the hydraulic properties could be estimated by combining GPR data and hydrogeologic data.

GPR profiles show consistency by locating the antenna position accurately. The groundwater table change could be quantitatively estimated by comparing the two sets of GPR data acquired

under different conditions. Quantitative information extracted from the GPR data indicates that GPR is a good tool for estimating the hydraulic properties of the aquifer. Quantitative information extracted from the GPR data with hydrogeological data, the estimation of hydraulic properties showed encouraging results. The study show that the physical and attenuation enhances characteristics of the contaminated areas and reveals that the most significant attenuation is related to smeared zone surrounding the seasonally changing water table interface

REFERENCES

1. Hopmans, J. W. and M. T. V. Genuchten, *Vadose Zone: Hydrological Processes*, Elsevier Ltd., 2005.
2. Huisman, J. A., S. S. Hubbard, J. D. Redman, and A. P. Annan, "Measuring soil water content with ground-penetrating radar: A review," *Vadose Zone Journal*, Vol. 2, 476–491, 2003.
3. Birken, R. and R. Versteeg, "Use of four-dimensional ground penetrating radar and advanced visualization methods to determine subsurface fluid migration," *Journal of Applied Geophysics*, Vol. 43, 215–226, 2000.
4. Kowalsky, M. B., S. Finsterle, J. Peterson, S. Hubbard, Y. Rubin, E. Majer, A. Ward, and G. Gee, "Estimation of field-scale soil hydraulic and dielectric parameters through joint inversion of gpr and hydrological data," *Water Resources Research*, Vol. 41, 2005.
5. Gribb, M. M., "Parameter estimation for determining hydraulic properties of a fine sand from transient flow measurements," *Water Ressources Research*, Vol. 32, 1965–1974, 1996.
6. Genuchten, M. T. V., "A closed form equation for predicting the hydraulic conductivity of unsaturated soils," *Soil Sci. Soc. Am. J.*, Vol. 44, 892–898, 1980.
7. Annan, A. P., S. W. Cosway, and J. D. Redman, "Water table detection with ground penetrating radar," *61st Annual International Meeting, Expanded Abstracts*, 494–496, Society of Exploration Geophysicists, E/G1.4, 1991; Bear, J., *Hydraulics of Groundwater*, McGraw-Hill Inc, 1979.
8. Bevan, M. J., A. L. Endres, D. L. Rudolph, and G. Parkin, "The non-invasive characterization of pumping-induced dewatering using ground penetrating radar," *Journal of Hydrology*, Vol. 281, 55–69, 2003.
9. Garambois, S., P. Sénéchal, and H. Perroud, "On the use of combined geophysical methods to assess water content and water conductivity of near-surface formations," *Journal of Hydrology*, Vol. 259, 32–48, 2002.
10. Al Hagrey, S. A. and C. Müller, "GPR study of pore water content and salinity in sand," *Geophysical Prospecting*, Vol. 48, 63–85, 2000.
11. Sen, P. N., C. Scala, and M. H. Cohen, "A self-similar model for s edimentary rocks with application to the dielectric constant of fused glass beads," *Geophysics*, Vol. 46, 781–795, 1981.
12. Trinks, I., "Processing and visualisation of 4D georadar data," Diploma thesis, Christian Albrechts University, Kiel, 1999.
13. Tsoflias, G. P., T. Halihan, and J. M. Sharp, "Monitoring pumping test response in a fractured aquifer using ground-penetrating radar," *Water Resources Research*, Vol. 37, 1221–1230, 2001.
14. Endres, A. L., W. P. Clement, and D. L. Rudolph, "Ground penetrating radar imaging of an aquifer during a pumping test," *Ground Water*, Vol. 38, 566–576, 2000.

Spatial Polarization Signal Processing in Circular Polarization Antenna

D. D. Gabriel'yan, **M. Yu. Zvezdina**, **E. D. Bezuglov**,
Yu. A. Zvezdina, **and S. A. Sil'nitsky**
Rostov Academy of Service of South Russian State University of Economy and Service, Russia

Abstract— The problem of guaranteeing the electromagnetic compatibility of radio electronics when using the spatial selection of the correlated signals is considered. The method is based on using adaptive antenna arrays and classical methods of spatial selection, i.e., signal-noise ratio criteria. The method provides signal processing close to optimal when excluding the signal out of the covariance noise matrix forming device. The results of numerical modeling are given.

1. INTRODUCTION

The usage of adaptive antenna systems is determined by the need to provide stable radio communications under the conditions of wide usage of communications electronics. The main device that allows forming the "null" of directivity pattern in the noise direction is noise covariance matrix forming module [1]. With the occurrence of the components resulting from both signal and its correlation to the noise signals in the elements of the noise covariance matrix leads to a sudden (by an order) decrease of a signal noise ratio that is considered to be the main efficiency measure of adaptive array functioning. To increase the signal noise ratio we propose to insert an additional device of prior signal processing that allows excluding signal components when forming the noise covariance matrix as it is show in [2] and taking into an account the differences of signal polarization properties by separate management of cross-shaped dipole arms. In terms of practical realization it leads to redoubling the antenna array dimensions, but it allows forming the "null" of directivity pattern not in the both components of vector directivity pattern but only in those corresponding to the noise signal polarization.

The device of prior signal processing is constructed by combining antenna radiating elements into subarrays. In such a case selection of the weighting coefficients in subarray elements is carried out in a way that would form "null" of directivity pattern in the signal direction in the combined radiating element pattern. Then, the modified signals enter the noise covariance matrix forming module. The insertion of device of prior signal processing leads to a case where signal noise ratio would guarantee quasioptimal processing of the received signals, because the control vector would deliver not a global, but local extremum after linear transformations.

2. SECTION 1

Let us consider the solution of the task of increasing the signal noise ratio by the example of an antenna array consisting of N elements and providing the reception of $L+1$ signals $S^{(\ell)}(\ell = 0, \ldots, L)$ of arbitrary polarization. Let's suppose that the radiating aperture parameters as well as signal parameters (direction of arrival, polarization and time structure) are known.

We shall increase the signal noise ratio by excluding the signal from the noise covariance matrix forming module. As an auxiliary condition let us suppose that the classic methods of optimal spatial signal processing, i.e. signal noise ratio maximum criteria. As it is known from [1, 3] these methods are more resistant to the weigh vector realization errors compared to the "superresolution" methods.

We shall exclude the signal basing on the fact that the antenna array can be considered as a spatial filter. To do so we combine N elements of the array into K subarrays, each one consisting of M elements.

The manifold of the signals at the subarrays output that are used to form the noise covariance matrix is the weighted sum with the weight coefficients $\tilde{W}_m^{(k)}$, $(k = 1, \ldots, K;\ m = 1, \ldots, M)$.

The operation is defined ambiguously and can be realized using an infinite number of weigh coefficients sets. An individual optimal weigh coefficients vector and, thus, an optimal signal noise ratio correspond to each one of these sets. Thus, the optimization problem is solved by choosing such a $\tilde{W}$ manifold that provides the highest signal noise ratio. The mathematical formula of the

optimization criteria is given by

$$\max_{\{\tilde{W}\}}\left\{\max_{\{W\}}\left(\frac{\nu_0\left(W\left(\tilde{W}\right)\right)^T(DS_0)^*(DS_0)^T\left(W\left(\tilde{W}\right)\right)^*}{\left(W\left(\tilde{W}\right)\right)^T\left(E+\sum_{l=1}^{L}\nu_l(DS_l)^*(DS_l)^T\right)\left(W\left(\tilde{W}\right)\right)^*}\right)\right\}. \tag{1}$$

Here ν_l is the ℓ-th signal power, normalized to the thermal noise power in the adaptive antenna array channels; E — identity matrix; S_ℓ — $2N \times 1$ dimension vector of complex amplitude of the currents excited by the ℓ-th signal at the radiators output; D — the $K \times N$ dimension matrix that defined the signals transformation during the processing.

To exclude the signal ($\ell = 0$) at the output of each subarray:

$$\tilde{S}_k^{(0)} = \sum_{m=1}^{M}\tilde{W}_m^{(k)}S_{m,\,k}^{(0)} = 0 \tag{2}$$

a weight coefficients vector is formed

$$\tilde{W}_m^{(k)} = \delta\left(m, \left[\frac{M+1}{2}\right]\right) - AF(k,\, m,\, \theta_f,\, \varphi_f). \tag{3}$$

A factor is defined by the correlation

$$A = \frac{F\left(k,\, 0.5\left(M+1\right),\, \theta_0,\, \varphi_0\right)}{\sum\limits_{m=1}^{M}\left(F\left(k,\, m,\, \theta_0,\, \varphi_0\right) - F\left(k,\, m,\, \theta_f,\, \varphi_f\right)\right)} \tag{4}$$

out of the known amplitude phase distribution that is formed by the subarray in the signal direction and of the amplitude phase distribution in the subarray given by the condition of forming the isotropic directivity pattern.

The following designations are used in formulae (2)–(4):

$$F\left(k,\, m,\, \theta,\, \phi\right) = \exp\left(-i2\pi\lambda_i^{-1}\varphi\left(P(k,\, m)\right,\, \theta,\, \phi\right), \tag{5}$$

Function $\varphi(\cdot)$ defines the phase progression for m-th radiator in k-th subarray centered at the point with the coordinates $P(\cdot)$ when the signal arrives from the direction θ, ϕ; λ_i — i-th signal wavelength; δ-Dirac delta-function; θ_f, φ_f — parameters that define the prior processing coefficients set, $\tilde{W}_m^{(k)}$. After the signal exclusion at the input of noise covariance matrix forming device we have the signals where the information on the noise direction of arrival would be described by the correlations

$$\tilde{S}^{(\ell)} = \tilde{D}S^{(\ell)}, \tag{6}$$

where $\tilde{D}$ is block diagonal matrix:

$$\tilde{D} = \oplus\sum_{k=1}^{2K}\tilde{D}_{kk}, \tag{7}$$

where the elements' dimension is $1 \times M$ and they are given by

$$\tilde{D}_{kk} = \begin{bmatrix}\tilde{W}_1^{(k)} & \ldots & \tilde{W}_M^{(k)}\end{bmatrix}. \tag{8}$$

$\tilde{S}_k^{(\ell)}$ signals are used to form the noise covariance matrix A_{ns} and to define optimal weight coefficients set, K, with the help of control vector J with the dimension of $K \times 1$. So, the prior signal processing makes the value of signal noise ratio quasi optimal, because the noise covariance matrix is formed basing on the signals containing corrupted information when excluding the signal.

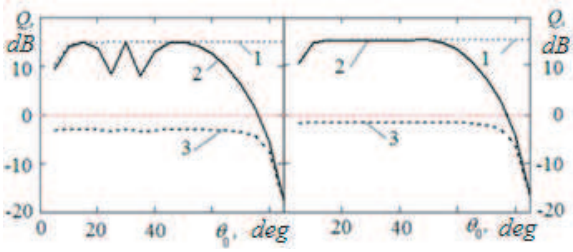

Figure 1.

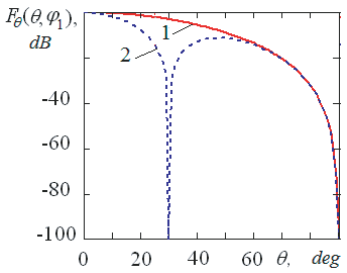

Figure 2.

3. SECTION 2

The research of the signal noise value when scanning the main lobe of the directive pattern depending on the subarrays parameters was carried out for the proposed way of antenna construction. The results are shown at the Figure 1. The left field of the figure corresponds to the case of combining the elements of antenna array of 8×8 cross-shaped half wave dipoles placed in increments of 0.5 wavelength in the grid nodes into subarrays of 4×4 elements, and the right field — to the case of subarrays of 2×2 elements.

Curves 1–3 on the figure describe the following cases: 1 — the signal is not presented in the noise covariance matrix forming device, 2 — the signal is presented but excluded, 3 — the signal is presented and not excluded. Figure 2 shows the cross-sections of the directive pattern of the subarrays of 2×2 elements (curve 1) and 4×4 elements (curve 2).

The analysis of the results on Figures 1 and 2 shows that the parameters of the subarrays into which the initial radiating aperture is divided essentially influence the efficiency of the signal exclusion out of the noise covariance matrix forming device. Herewith, isotropic character of the directive pattern of the subarray of 2×2 elements leads to uniform dependence of the signal noise ratio. The presence of the natural "null" in the directive pattern of the array of 4×4 elements determines the errors when forming the noise covariance matrix and weight coefficients vector respectively when the signal arrives from this direction. As a result, the sudden decrease of the signal noise ratio for the case of noise signal arrival from this direction takes place.

4. CONCLUSION

The obtained results allows making the following conclusions. The efficiency of the adaptive antenna arrays application to solving the electromagnetic compatibility problem for radioelectronic systems essentially reduces when the signal is presented in the noise covariance matrix forming device. The signal exclusion from the noise covariance matrix forming device can be realized basing on the fact that the antenna array can be considered as a spatial filter. The antenna array elements are combined into subarrays and the selection of the weighting coefficients is carried out to provide the formation of the "zero" of the directivity pattern of the subarrays in the direction of the signal. Prior signal processing leads to the quasi optimal signal noise ratio value for the noise covariance matrix is formed from the corrupted data after the exclusion of the signal. The directivity pattern shape of the subarrays into which the initial antenna aperture is divided has the great influence on the value of the signal noise ratio when excluding the signal. Isotropic directivity pattern makes it possible to obtain a signal noise ratio dependence close to uniform when scanning the beam. The presence of the natural "zero" in the directivity pattern determines the errors when forming the noise covariance matrix and the sudden decrease of the signal noise ratio value in the given direction correspondingly.

ACKNOWLEDGMENT

The authors are grateful to Prof. Boris D. Manuilov for his useful suggestions regarding the improvement of material of this paper.

REFERENCES

1. Monzingo, R. A. and T. W. Miller, *Introduction to Adaptive Arrays*, Wiley-Interscience, New York, 1980.
2. Gabriel'yan, D. D. and Yu. A. Zvezdina, "Quasi optimal method of spatial selection of signal in adaptive antenna arrays," *Proceeding of 3 International Radio Electronic Forum*, Vol. 1, Pt. 2, 45–48, Kharkov, Ukraine, October 2008.
3. Ratinsky, M. B., *The Adaptation and Supersolution in Antenna Arrays*, Radio and Svyaz, 2003.

Fractal Analysis of Chaff and Sea Mixed Clutter on Ka Band

Guangfu Tang, **Jianxiong Zhou**, **Hongzhong Zhao**, **and Qiang Fu**
ATR Lab., National University of Defense Technology, Changsha 410073, China

Abstract— When chaff cloud above the sea surface is measured by a radar system, its echo will be mixed with the sea clutter. The traditional fractal Brown model (FBM) is no longer valid to describe the mixed clutter's fractal characteristics. A combined fractal Brown model (CFBM) is proposed to describe the chaff cloud echo in sea clutter. An iterative estimation procedure is designed to extract the fractal parameters of the CFBM. Experiments using outfield measured data verify the validity of the CFBM. Results show that, when the wind speed of the sea surface is 5 m/s, chaff and sea clutter on Ka band are two fractal processes, the fractal dimension of sea clutter is 1.54, the fractal dimension of chaff clutter is 1.66, and the correlation coefficient of the two fractal processes is 0.01, which can be considered uncorrelated.

1. INTRODUCTION

Chaff is a typical passive interference. It is low cost, easy to produce and equip; moreover, it can interfere different radar systems from all directions at the same time. The researches on chaff clutter's characteristics are important for countering the chaff-jamming. The outfield measured data of chaff cloud are necessary to analyze its statistical features. But there is a difficulty in obtaining the pure chaff cloud data above the sea surface. As we know, when the beam of a radar system covers the chaff cloud which is launched above the sea surface, it will cover a part of the sea surface at the same time, and the chaff clutter will be mixed by the sea clutter inevitably (as shown in Figure 1).

Literatures [1–5] studied the fractal characteristics of sea clutter, and came to a conclusion that sea clutter is a fractal process. Although there are no literatures studying the fractal characteristics of chaff clouds, we can make an analysis on principle as follows: cloud is made up of numerous small water droplets and ice crystals, while chaff cloud is made up of numerous dipoles, cloud and chaff cloud are formed exactly in the same way, although the elements are different. Since cloud is fractal [6], so there are reasons to assume that chaff cloud is also fractal.

For the mixed clutter concerned in this paper, a combined fractal Brown model (CFBM) is proposed. For those range bins consist of pure sea clutter, the traditional FBM can be used to extract the sea clutter's fractal parameters, while for those range bins consist of both chaff and sea clutter, the CFBM can be used to extract the mixed clutter's fractal parameters. Experiments using the outfield measured data on Ka band not only verify the validity of the CFBM, but also achieve the chaff clutter's fractal parameters for the first time.

2. MATHEMATICAL MODEL FOR CFBM

The model of traditional FBM, which is not introduced in this paper for the sake of clarity, can be referred in literature [6]. The mathematical model of CFBM is given below.

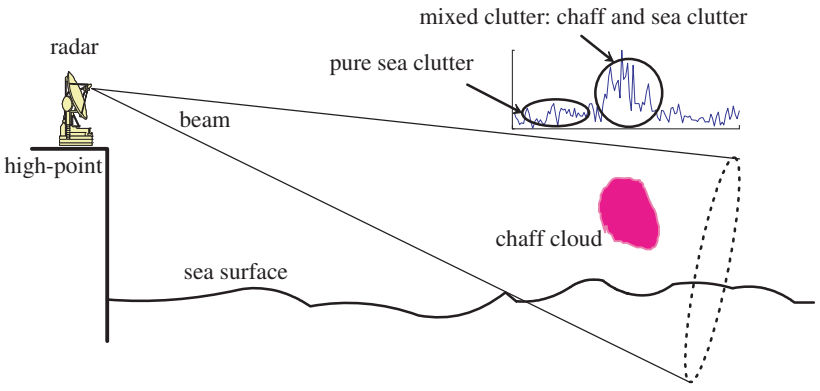

Figure 1: The sketch of experimental scene.

Assuming that a random process $x(t)$ is made up of two fractal processes $B_{H_1}(t)$ and $B_{H_2}(t)$, where $0 < H_1,\ H_2 < 1$, then $x(t)$ can be expressed as

$$x(t) = \alpha B_{H_1}(t) + \beta B_{H_2}(t) \tag{1}$$

where α and β are weighting coefficients, and $\alpha + \beta = 1$. The characteristic of Brown model shows that [6]

$$\begin{cases} B_{H_1}(t+1) - B_{H_1}(t) \sim N(0, \sigma_1^2) \\ B_{H_2}(t+1) - B_{H_2}(t) \sim N(0, \sigma_2^2) \end{cases} \tag{2}$$

The variance of $x(t)$ is

$$\begin{aligned} \sigma_x^2(\tau) &= E\left\{[x(t+\tau) - x(t)]^2\right\} = E\left\{[\alpha B_{H_1}(t+\tau) - \alpha B_{H_1}(t) + \beta B_{H_2}(t+\tau) - \beta B_{H_2}(t)]^2\right\} \\ &= \alpha^2\tau^{2H_1}\sigma_1^2 + \beta^2\tau^{2H_2}\sigma_2^2 + 2\alpha\beta\tau^{H_1+H_2}\sigma_1\sigma_2\rho \end{aligned} \tag{3}$$

where $\sigma_1\sigma_2\rho = \mathrm{cov}\{[B_{H_1}(t+1) - B_{H_1}(t)][B_{H_2}(t+1) - B_{H_2}(t)]\}$, and ρ is named the correlation coefficient of the two fractal processes under unit-scale. After taking logarithm, Formula (3) can be rewritten as

$$\log \sigma_x^{(\tau)} = 0.5 \log\left(\alpha^2\tau^{2H_1}\sigma_1^2 + \beta^2\tau^{2H_2}\sigma_2^2 + 2\alpha\beta\tau^{H_1+H_2}\sigma_1\sigma_2\rho\right) \tag{4}$$

Formula (4) can be rewritten by differential asassuming $H_1 \geq H_2$

$$\frac{d\log\sigma_x(\tau)}{d\log(\tau)} = H_1 - \frac{(H_1 - H_2)\left(\sigma_2^2 + \gamma\tau^{H_1-H_2}\sigma_1\sigma_2\rho\right)}{\left(\gamma^2\tau^{2(H_1-H_2)}\sigma_1^2 + \sigma_2^2 + 2\gamma\tau^{H_1-H_2}\sigma_1\sigma_2\rho\right)} \tag{5}$$

where $\gamma = \alpha/\beta$.

Fractal parameters are estimated according to Formula (3). Let the fractal parameters to be estimated be $\theta = (\alpha, \beta, H_1, H_2, \sigma_1, \sigma_2, \rho)^T$, the observed value be $\mathbf{Y}$, then the regression model is

$$\mathbf{Y} = \mathbf{F}(\theta) + \boldsymbol{\varepsilon} \tag{6}$$

where $\mathbf{Y} = [\,\sigma_x^2(1), \sigma_x^2(2), \ldots, \sigma_x^2(\tau_{\max})\,]^T$, $\mathbf{F}(\theta) = \alpha^2\tau^{2H_1}\sigma_1^2 + \beta^2\tau^{2H_2}\sigma_2^2 + 2\alpha\beta\tau^{H_1+H_2}\sigma_1\sigma_2\rho|_{\tau=1,2,\ldots,\tau_{\max}}$, and $\boldsymbol{\varepsilon}$ is the observed noise.

This is a nonlinear least squares problem in Formula (6), and the Gauss-Newton method is usually used to estimate its parameters. Let $\mathbf{V}(\theta) = [\partial\mathbf{F}/\partial\theta_m]_{N*7}$, where N is the row number of $\mathbf{Y}$, $m = 1, 2, \ldots, 7$, and the iterative equation is [7]

$$\theta^{i+1} = \theta^i + [\mathbf{V}^T(\theta^i)\mathbf{V}(\boldsymbol{\theta}^i)]^{-1}\mathbf{V}^T(\theta^i)[\mathbf{Y} - \mathbf{F}(\theta^i)] \tag{7}$$

According to the iteration in Formula (7), θ can be obtained by setting the initial value θ°. Further discussions on the convergency of the algorithm can be referred to section 2.2 in [7].

3. EXPERIMENTS

The outfield measured data of chaff and sea clutter were collected by a radar system working on Ka band. The weather of the experimental day was cloudy, the visibility was about 5 kilometers, and the wind speed above the sea surface was about 5 m/s. The radar was set up on a high-point of the seashore, and a chaff bomb was launched about 10 kilometers from the seashore, as shown in Figure 1. Figure 2 shows the range profiles of the measured data, from which we can see that: the mixed clutter appears at the sampling points from about 50 to 70, and the other sampling points are pure sea clutter. Figure 3 shows the amplitude sequence of the pure sea clutter, and Figure 4 shows that of the mixed clutter.

Figure 5 shows the $\{(\log\tau, \log\sigma(\tau))\}$ curve of pure sea clutter estimated by FBM, the slope of the curve is about 0.4603, which means the Hurst index of sea clutter is $H_{sea} = 0.4603$, so the fractal dimension of pure sea clutter can be achieved $D_{sea} = 2 - H_{sea} = 1.5379$. Abandoning the mixed clutter where the range bin is from 50 to 70, we carry out a Monte-Carlo experiment by FBM at an interval of 10 range bins, and the fractal parameters of pure sea clutter are shown in Table 1. The average Hurst index $\bar{H}_{sea} = 0.4596$, and the average fractal dimension $\bar{D}_{sea} = 1.5404$. The result coincides with that given in [8] (where D_{sea} is about $1.4 \sim 1.6$).

Figure 6 shows the $\{(\log\tau, \log\sigma(\tau))\}$ curve of mixed clutter estimated by FBM. From the figure we can see that the curve is no longer a straight line, but a concave curve. According to Formula (5), when $\tau \to 0^+$, $d\log\sigma_x(\tau)/d\log(\tau) \to H_2$, when $\tau \to +\infty$, $d\log\sigma_x(\tau)/d\log(\tau) \to H_1$, and we have assumed $H_1 \geq H_2$ previously, so the concave curve in Figure 6 have been well explained theoretically. At the same time, the concave curve in Figure 6 also reveals: FBM is no longer applicable for the mixed clutter, which is made up of two different fractal processes, and CFBM is needed to estimate the mixed clutter's fractal parameters.

Table 1: Fractal parameters of pure sea clutter.

Range Bin	10	20	30	40	80	90	100	110
Hurst Index	0.4613	0.4603	0.4559	0.4604	0.4584	0.4601	0.4540	0.4665
Fractal Dimension	1.5387	1.5397	1.5441	1.5396	1.5416	1.5399	1.5460	1.5335

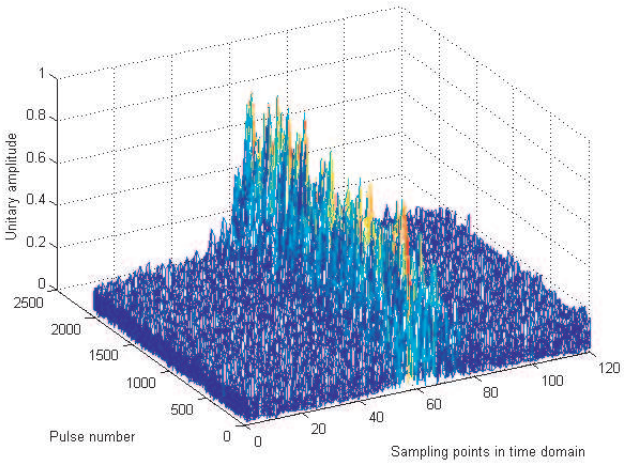

Figure 2: 2048 range profiles.

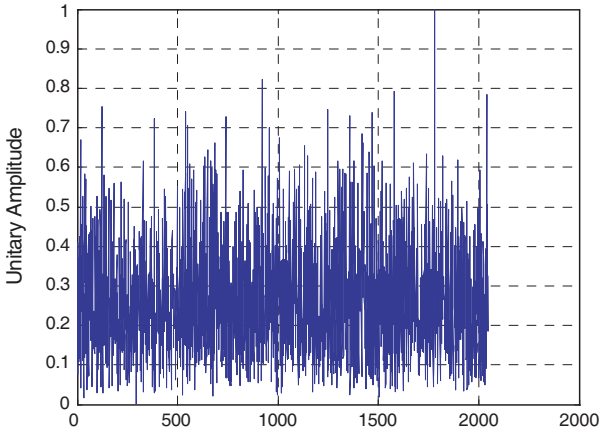

Figure 3: Pure sea clutter's amplitude sequence (the 20th sampling point).

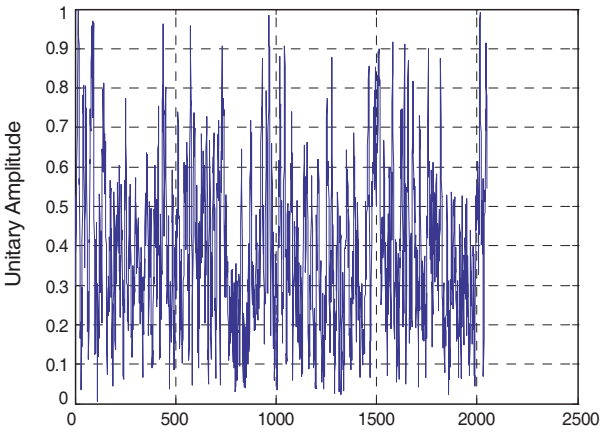

Figure 4: Mixed clutter's amplitude sequence (the 60th sampling point).

We estimate the parameters for the mixed clutter by CFBM (the range bins are 55, 60, 65 and 70), and the initial value of iteration is set as $\theta^\circ = [0.1, 0.9, 1.54, 1.8, 0.5, 1, 0]^T$, the mixed clutter's fractal parameters estimated by CFBM are shown in Table 2. The two averages of Hurst index are

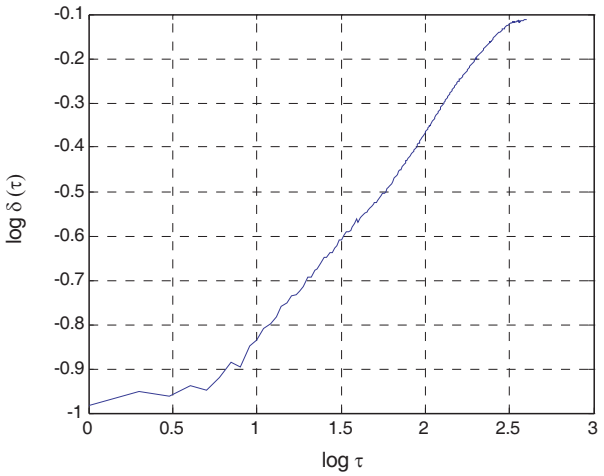

Figure 5: The $\{(\log\tau, \log\sigma(\tau))\}$ curve of pure sea clutter (the 20th range bin).

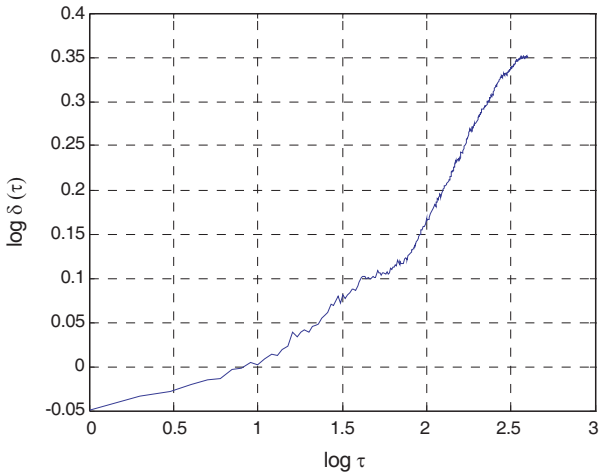

Figure 6: The $\{(\log\tau, \log\sigma(\tau))\}$ curve of mixed clutter (the 55th range bin).

$\bar{H}_1 = 0.4564$, $\bar{H}_2 = 0.3450$, and the results compared with $\bar{H}_{sea}$ is $\Delta_1 = |\bar{H}_1 - \bar{H}_{sea}|/\bar{H}_{sea} = 0.007$ and $\Delta_2 = |\bar{H}_2 - \bar{H}_{sea}|/\bar{H}_{sea} = 0.249$, therefore we can make a judgment: $\bar{H}_1$ is the sea clutter's Hurst index, α is the weighting coefficient of sea clutter, and σ_1 is the standard variance of Gaussian increment of sea clutter; while H_2, β and σ_2 are the corresponding fractal parameters of chaff clutter. The fractal dimension $\bar{D}_1$ of sea clutter which is estimated by CFBM from the mixed clutter is 1.5436 ($\bar{D}_1 = 2 - \bar{H}_1 = 1.5436$), and $\bar{D}_1$ is very close to $\bar{D}_{sea}$ (1.5404) which is estimated by FBM from the pure sea clutter. The chaff clutter's fractal dimension $\bar{D}_2$ estimated by CFBM from the mixed clutter is 1.6550. The correlation coefficient ρ of sea clutter and chaff clutter under unit-scale is 0.01, which can be considered uncorrelated.

Table 2: Fractal parameters of mixed clutter.

Range Bin	Fractal Parameters						
	α	β	H_1	H_2	σ_1	σ_2	ρ
55	0.2213	0.7787	0.4629	0.3525	0.2931	0.5238	0.0106
60	0.2012	0.7988	0.4562	0.3393	0.3086	0.4760	0.0073
65	0.1981	0.8019	0.4608	0.3419	0.3125	0.4996	0.0114
70	0.1834	0.8166	0.4455	0.3461	0.2841	0.4969	0.0132
Average	0.2010	0.7990	0.4564	0.3450	0.2996	0.4991	0.0106

4. CONCLUSION

The CFBM and its parameter estimation procedure proposed in the paper can be used to analyze the fractal characteristics of stochastic process consisting of two different fractal processes. This principle can be also applied to stochastic processes consisting of more than two processes with small modifications. The mixed fractal process widely exists in many applications, such as radar echoes contaminated by different clutters, etc, so the CFBM will be widely used.

The experiments using the outfield measured data of chaff and sea clutter not only verify the validity of the CFBM, but also achieve the chaff clutter's fractal parameters for the first time. The fractal characteristics of chaff clutter may help us to build a more accurate mathematical model to describe it, and also enlighten novel approaches to counter the chaff jamming.

REFERENCES

1. Hu, J., W.-W. Tung, and J. Gao, "Detection of low observable targets within sea clutter by structure function based multifractal analysis," *IEEE Transactions on Antennas and Propagation*, Vol. 54, No. 1, 136–143, 2006.

2. Gan, D. and Z. Shouhong, "Detection of sea-surface radar targets based on multifractal analysis," *Electronics Letters*, Vol. 36, No. 13, 1144–1145, 2000.
3. Berizzi, F., M. Greco, and L. Verrazzani, "Fractal approach for sea clutter generation," *IEE Proc. Radar Sonar Navig.*, Vol. 147, No. 4, 189–198, 2000.
4. Gan, D. and Z. Shouhong, "High-order fractal characterisation of sea-scattered signals and detection of sea-surface targets," *Electronics Letters*, Vol. 35, No. 5, 424–425, 1999.
5. Martorella, M., F. Berizzi, and E. D. Mese, "On the fractal dimension of sea surface backscattered signal at low grazing angle," *IEEE Transactions on Antennas and Propagation*, Vol. 52, No. 5, 1193–1204, 2004.
6. Falconer, K., *Fractal Geometry: Mathematical Foundations and Applications*, John Wiley & Sons, Ltd., 2003.
7. Douglas, M. B. and G. W. Donald, *Nonlinear Regression Analysis and Its Applications*, John Wiley & Sons, Ltd., 1988.
8. Gan, D. and Z. Shouhong, "Detection of sea-surface radar targets based on multifractal analysis," *Electronics Letters*, Vol. 36, No. 13, 1144–1145, 2000.

Electromagnetic Orbital Angular Momentum in Remote Sensing

Y. S. Jiang, **Y. T. He**, **and F. Li**
School of Electronic and Information Engineering
Beijing University of Aeronautics and Astronautics
37# Xueyuan Rd., Haidian District, Beijing 100191, China

Abstract— The orbital angular of electromagnetic wave beam and radiation fields has been discussed. The representation of multipole radiation fields is deduced. Besides, measuring methods of OAM and a few phenomena and results obtained are cited to elucidate firstly the feasibility of applying of remote sensing. It is shown that remote sensing applications of the orbital angular momentum of electromagnetic waves has come to fore in recent years, but have apparently never been attempted.

1. INTRODUCTION

Phenomena of electromagnetic wave carrying orbital angular momentum (OAM) was first proposed by J. H. Poynting theoretically in 1909 [1], and was proved experimentally by R. A. Beth and A. H. S. Holbourn in optical waveband (wavelength = 1.2 μm) during 1935–1936 [2–4]. Electromagnetic waves with angular momentum in centimeter wavelength was confirmed by N. Carrara in 1949 [5]. It was not until 1992, that generations and torque effects of orbital angular momentum carried by a laser beam had been studied detailed by L. Allen et al. [6]. Great attentions has been concentrated on the studies of orbital angular momentum of electromagnetic waves. The researchers have studied not only the common themes, such as orbital angular momentum of the continuous and pulse electromagnetic wave, law of the angular momentum conservation, the generation, propagation, transformation and measurement of the angular momentum [7–14], but also the specific themes, such as the scattering and absorption of the specific object, the torque of orbital angular momentum of application and so on [6, 15]. For example, G. F. Brand studied the generation, transformation and measurement of the orbital angular momentum of millimeter-wave [16]. J. Wu applied parametric encoding on the orbital angular momentum of the electromagnetic wave (optical wave) beam to free-space communication [17]. Recently, B. Thide performs further research on the generation and measurement of the orbital angular momentum of the electromagnetic wave whose wavelength is shorter than decimeter waveband by using of soft simulation and numerical computation [18]. In summary, the generation, propagation and interaction with object for orbital angular momentum of electromagnetic wave in various wave-band are more and more subject to attentions by scientific workers in different fields, for instance, material scientists applying orbital angular momentum of the electromagnetic wave to research characters and constructions of molecule and atom, biologists and medical scientists manipulating atom, molecule or cell by the torque effect of the orbital angular momentum, communication technicians studying quantum encoding on the orbital angular momentum of the electromagnetic wave in free-space security communication, and so on. But, the researches on applying orbital angular momentum to remote sensing has little been proceeded. In this paper, we propose a novel concept to remotely acquire information of objects based on the orbital angular momentum of electromagnetic waves.

Here we show how measurements of orbital angular momentum of photons and feasibility of a number of remote sensing applications. In Section 2 of this paper, we provided a short introduction to OAM of electromagnetic waves and multipole radiation fields which could be used in active and passive remote sensing respectively, followed in Section 3, by a description of the remote sensing instrumentation required to detect OAM of millimeter-wave and photon. Section 4 a number of phenomena and results are cited to elucidate feasibility of applying to remote sensing. Section 5 briefly summarizes the findings.

2. ORBITAL ANGULAR MOMENTUM BEAM OF ELECTROMAGNETIC WAVES AND MULTIPOLE RADIATION FIELDS

Remote sensing can be divided into two types: active remote sensing and passive remote sensing [19]. Active remote sensing is based radar (or laser radar) system consisting of a transmitter and a receiver. The transmitter sends out a electromagnetic (or sound) signal to the target and the scattering signal in a specified direction is measured by the receiver. Passive remote sensing is

based radiometry system which based that all substances at a finite absolute temperature radiate electromagnetic energy measured by receiver (or detector). Here we elucidate the electromagnetic theoretical basis for active and passive remote sensing with OAM, respectively.

2.1. Generation of OAM for Electromagnetic Waves Beam

It is important for active remote sensing with OAM of electromagnetic waves is the generation of beams carrying OAM. One classical example of a beam with a OAM is the higher order Laguerre-Gaussian (LG) mode described by

$$E_{p,m}(r,\varphi,z) = \frac{C}{\left(1+z^2/z_R^2\right)^{1/2}}\left(\frac{r\sqrt{2}}{w(z)}\right)^m L_{p,m}\left(\frac{2r^2}{w^2(z)}\right)\times\exp\left\{\frac{-r^2}{w^2(z)}\right\}$$
$$\exp\left\{i(2p+m+1)\tan^{-1}\frac{z}{z_R}\right\}\times\exp\left\{\frac{-ikr^2z}{2\left(z^2+z_R^2\right)}\right\}\exp\{-im\varphi\} \quad (1)$$

where z_R is the Rayleigh range, $w(z)$ is the radius of the beam, $L_{p,m}$ is the associated Lagguerre polynomial, C is a constant, and the beam waist is at $z = 0$. The Lorentz gauge has the advantage of been readily amenable in all coordinate systems and leads in this case to considerable symmetry in the x and y directions although the results are best expressed in cylindrical coordinates. The azimuthal phase term $\exp(-im\phi)$ in (1) creates helical wavefronts for the LG modes which posses an orbital angular momentum of $m\hbar$ per photon [6], quite distinct from the spin angular momentum associated with the polarization state. This orbital angular momentum has been demonstrated through an optical interaction with microscopic particles [20]. Curtis, Koss and Grier have produced beams of photons each with OAM as high as $200\hbar$ [21].

There are a number of methods for generating the beam of LG modes. To date, four different classes of generating methods have been demonstrated in various wave-band. Two of these which are used in optical wave, millimeter-wave and microwave (10 GHz) band, phase-plates and computer generated holographic (blazed grating) converters shown in Fig. 1 [22–25], induce the azimuthal phase term to a Hermite-Gaussian (HG_{00}) modes. In all these devices a screw phase-dislocation, produced on-axis, causes destructive interference leading to the characteristic ring intensity pattern in the far field. The third class of converter is the cylindrical-lens mode converter used in optical and millimeter-wave band [22, 26], which converts higher order HG modes to the corresponding LG mode. Unlike the spiral phase plate and the holographic converter, this method can produce pure LG modes. The fourth method of generating orbital angular momentum of electromagnetic waves is vector antenna arrays used in microwave band [18]. In this method, each antenna composed antenna array is located equidistantly along the perimeters of circles. The antennas are fed the same signal, but successively delayed relative to each other such that after a full turn around the antenna array axis, the phase has been incremented by $m^2\pi$ (m is a integer).

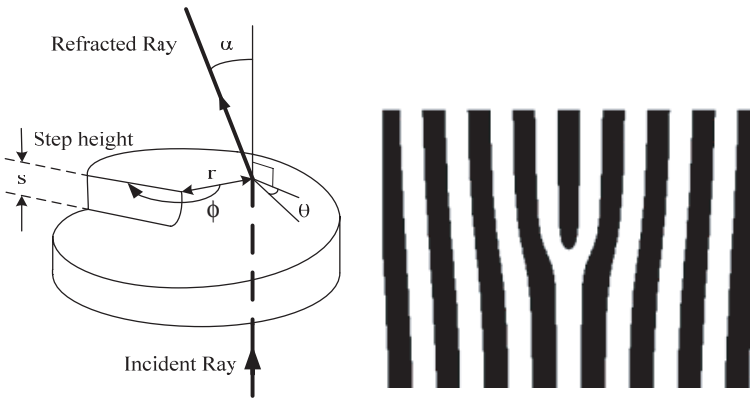

Figure 1: Orbital angular momentum produced by phase plate (a), and an example of a holographic phase plate (b). (For details to see the text in reference [22]).

For an active remote sensing system with OAM of electromagnetic wave, it can be visualized as a source of OAM of electromagnetic wave that illuminate the object being studied. An incident OAM

of electromagnetic wave interact with object and the scattering OAM is modulated by a number of interaction processes that contain the "fingerprints" of the object. But, for a passive remote sensing system with OAM of electromagnetic wave, the natural object being studied usually can be visualized as a gray-body which defined as a product of ideal radiation source (called a blackbody) and a specific emissivity. Since the surfaces of natural object are usually random and rough, so the radiation fields of object being studied can be regarded as multipole radiation fields.

2.2. Multipole Radiation Fields

The radiation fields of natural object can be described by superposition of electric and magnetic multipole [9]

$$\begin{cases} \vec{E} = Z_0 \sum\limits_{l,m} \left[\frac{i}{k} a_E(l,m) \nabla \times h_l(kr) \vec{X}_{l,m}(\theta,\varphi) + a_M(l,m) h_l(kr) \vec{X}_{l,m}(\theta,\varphi) \right] \\ \vec{H} = \sum\limits_{l,m} \left[a_E(l,m) h_l(kr) \vec{X}_{l,m}(\theta,\varphi) - \frac{i}{k} a_M(l,m) \nabla \times h_l(kr) \vec{X}_{l,m}(\theta,\varphi) \right] \end{cases} \tag{2}$$

where the coefficients $a_E(l,m)$ and $a_M(l,m)$, which are determined by the source and boundary conditions, specify the amounts of electric (l,m) multipole and magnetic (l,m) multipole fields, and for only electric multipole $a_M(l,m) = 0$, as well as for only magnetic multipole $a_E(l,m) = 0$. Z_0 is the impedance of free space. k in (2) is wave number, i is imaginary unit, ∇ is nabla operator. The radial function $h_l(kr)$ and normalized form of vector spherical harmonic function $\vec{X}_{l,m}(\theta,\varphi)$ are described by

$$h_l(kr) = (-i)^{l+1} \frac{e^{ikr}}{kr} \tag{3}$$

and

$$\vec{X}_{l,m}(\theta,\varphi) = \frac{1}{\sqrt{l(l+1)}} \vec{L} Y_{l,m}(\theta,\varphi) \quad \left(\vec{X}_{0,m}(\theta,\varphi) = 0 \right) \tag{4}$$

where index l and m are integers with $|m| \le l$, and $\vec{L}$ is $\hbar^{-1}$ ($\hbar$ = Plank's constant/2π) times the orbital angular momentum operator of wave mechanics given by

$$\vec{L} = -i(r \times \nabla) \tag{5}$$

and

$$Y_{l,m}(\theta,\varphi) = \sqrt{\frac{2l+1}{4\pi} \frac{(l-m)!}{(l+m)!}} P_l^m(\cos\theta) e^{im\varphi} \tag{6}$$

where $P_l^m(\cos\theta)$ is the associated Legendre polynomial given by [27]

$$P_l^m(\cos\theta) = (\sin\theta)^m \sum_{2j \le l-m} a_j (\cos\theta)^{l-m-2j} \tag{7}$$

where a_j is coefficient.

Substitute (5) into (4) and then substitute (3) and (4) into (2), and finally complete the operation of $\nabla\times$, we can obtain

$$\vec{E} = (-i)^{l+1} \frac{Z_0}{kr} \sum_{l,m} \frac{A}{\sqrt{l(l+1)}} \left[\hat{r} R_r + \hat{\theta}(R_\theta + iI_\theta) + \hat{\varphi}(R_\varphi + iI_\varphi) \right] \times e^{-i(\omega t - kr)} P_l^m(\cos\theta) e^{im\varphi}, \quad (m = \pm 1, \ldots, \pm l) \tag{8}$$

where ω is circular frequency of oscillation of electric and magnetic multipole. $\hat{r}$, $\hat{\theta}$ and $\hat{\varphi}$ is unit vector of spherical coordinate system. Magnetic fields $\vec{H}$ has similar form of (8) related through the transforms

$$\vec{E}^{(E)} \to -\vec{H}^{(M)}, \quad \vec{H}^{(E)} \to \vec{E}^{(M)} \tag{9}$$

where the superscripts (E) and (M), respectively, indicate electric multipole mode and magnetic multipole mode. The other variables in (8) is given by

$$\begin{cases} R_r = \dfrac{1}{kr} a_E(l,m)\, D(\theta) \\ R_\theta = \dfrac{r-1}{kr} a_E(l,m)\, C(\theta) + \dfrac{m}{\sin\theta} a_M(l,m) \\ I_\theta = -r a_E(l,m)\, C(\theta) \\ R_\varphi = -mr a_E(l,m) \\ I_\varphi = -\dfrac{1-\sin\theta}{k\sin\theta} m a_E(l,m) - C(\theta)\, a_M(l,m) \end{cases} \tag{10}$$

and

$$\begin{cases} A = \sqrt{\dfrac{2l+1}{4\pi}\dfrac{(l-m)!}{(l+m)!}} \\ D(\theta) = C(\theta)\cdot c\tan(\theta) + C'(\theta) \\ C(\theta) = m\cdot c\tan(\theta) - B\cdot\tan(\theta) \\ C'(\theta) = -\left[m\cdot\csc^2(\theta) + B\cdot\sec^2(\theta)\right] \\ B = l-m-2j \end{cases} \tag{11}$$

From the (8), we can see that radiation fields of electric and magnetic multipole, which propagates along radial direction, have radial component of $\vec{E}(E_r)$ or $\vec{H}(H_r)$. The propagating electromagnetic wave is not a plane wave, but consists of m intertwined helical wave fronts, and m is called the winding number or topological charge. Classically, the angular momentum of an electromagnetic wave is given by the volume integral of the cross product of position $\vec{r}$ measured from the center of the multipole and the Poynting vector $\vec{S}$ at $\vec{r}$ [9]

$$\vec{L} = \frac{1}{c^2}\int \vec{r}\times\vec{S}dV = \frac{1}{4\pi c}\int \vec{r}\times\left(\vec{E}\times\vec{H}\right)dV \tag{12}$$

where c is speed of light.

For applications to remote sensing, various objects of remote sensing (source of multipole field) have different weighting of radiation (different coefficients of $a_E(l,m)$ and $a_M(l,m)$). For the same multipole order l, the intensity of the magnetic radiation is smaller than the intensity of electric radiation by a considerable factor. For a pure electric multipole of order (l,m), the radial component of the reduces to a single term [28]

$$\begin{cases} H_r = 0 \\ E_r = i(ik)^l \dfrac{Z_0}{r^2}\dfrac{D(\theta)}{l^{3/2}}\dfrac{Q(l,m)}{(2l-1)!!}\sqrt{\dfrac{4\pi}{2l+1}\dfrac{(l-m)!}{(l+m)!}} \times e^{-i(\omega t-kr)} P_l^m(\cos\theta)\, e^{im\varphi} \end{cases} \tag{13}$$

where k is wave number, $D(\theta)$ is angular distribution of multipole radiation. $Q(l,m)$ is the electric multipole moment of order l, m, and is given by the following approximate expression

$$Q(l,m) = \int r^l Y_{l,m}^*(\theta,\varphi)\,\rho\left(\vec{r}\right)dV \tag{14}$$

The integration in (14) extends over the entire volume occupied by the charge distribution $\rho\left(\vec{r}\right)$.

Usually the multipole axis lies along some direction z-axis, to which the vector $\vec{r}$ is inclined at an angle θ, and φ is the azimuthal angle about the z-axis. Classically, a vibration motion along the multiple axis radiates perpendicular to axis, while a rotation about the z-axis produces radiation with angular momentum directed along the multipole axis. Quantum mechanically, the z-component of (5) can be written as [9, 29]

$$L_z = -i\hbar\frac{\partial}{\partial\varphi} \tag{15}$$

where $\hbar$ is Planck's constant divided by 2π. (15) shows that the term $e^{im\varphi}$ gives rise to an angular momentum component m about z-axis. From the (13), we can see that the probability of a radiation decreases rapidly as l increases. Hence in practice only the one or two lowest values of l consistent with conservation of angular momentum.

3. REMOTE SENSING INSTRUMENTATION TO MEASURE THE OAM

Theoretically, an azimuthal term $e^{im\varphi}$ in (13), describing the helical wavefront, can define an infinite-dimensional Hilbert space. Since the complexities and varieties of the remote-sensing object and environment, the multi-dimension of properties of the orbital angular momentum will play important roles in the mechanisms of remote-sensing information. The spiral electromagnetic wave with different value of l can be generated by different element antenna pattern, and can be detected by different method. But angular momentum along the direction of propagation for electromagnetic radiation is composed of the spin angular momentum associated with the circular polarization and the orbital angular momentum representing the helical phase-front of the electromagnetic wave. A single photon carries a spin angular momentum with a value of $\pm\hbar$ (where $\pm$ represent right and left circular polarization, respectively), and an orbital angular momentum, having a value of $m\hbar$. In generally, the spin angular momentum of electromagnetic wave (planar polarized electromagnetic wave) can construct two-dimensional (right and left) information basis. While the orbital angular momentum of electromagnetic wave (spiral electromagnetic wave), in principle, can construct infinite-dimensional information basis. The general relationship between energy E and angular momentum along the direction of propagation for electromagnetic radiation (L_z) is given by [30]

$$\frac{L_z}{E} = \frac{(m+\sigma)}{\omega} + \frac{\sigma}{\omega}\left[g\left(k\right)\right] \tag{16}$$

where σ is ± 1 for circularly polarized light and 0 for linear polarized light, and $g\left(k\right) \ll 1$ reflects the spectral and spatial distribution of the radiation and tends to be negligibly small. From (16) we see that although the spin and orbital angular momenta cannot be cleanly separated, it is always possible to measure the orbital angular momentum by passing a beam through a linear polarizer, which sets $\sigma = 0$, and leaves the orbital angular momentum intact. The ratio L_z/E then is m/ω. This shows that we can measure the OAM independently.

3.1. Dove-prism Mach-Zehnder Interferometers

This method has been described by Leach et al. [31]. Their apparatus was designed to deal with laser-generated modes, but the procedure is general, though instrumental details will differ for different wavelength ranges and applications. The method does not directly measure OAM. Instead, it identifies the symmetry properties of a beam of electromagnetic radiation subject to a sequence of rotations about its axis of propagation. This is achieved by sending light through a cascade of Mach-Zehnder interferometers with Dove prisms in each arm (Fig. 2). At each stage the beams in the two interferometer arms are rotated with respect to one another through an angle α, where $\alpha/2$ is the relative rotation of the Dove prisms about the optical axis in each beam. The first interferometer stage has $\alpha/2 = \pi/2$ and sorts photons with even values of orbital angular momentum m into one exit port and those with odd values of m into the other port. The photons with odd values of m are then sent through a hologram (Fig. 1(b)) that increases the OAM m carried by each photon to a value $m+1$, thus endowing all the photons with even values of m.

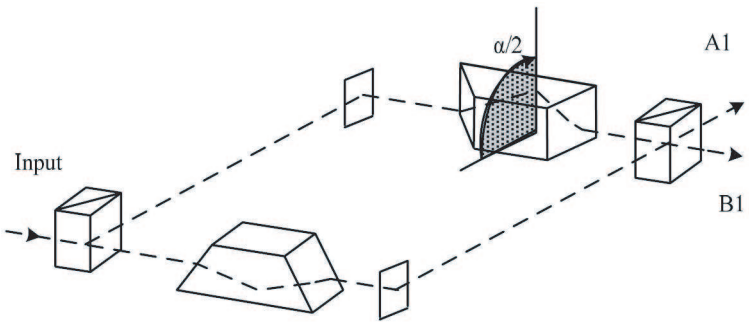

Figure 2: First stage of a Dove-prism Mach-Zehnder interferometer cascade for sorting photons carrying different amounts of orbital angular momentum.

Each of the beams emerging from the two ports of this first stage is then sent through a second Mach-Zehnder stage of its own, in which the two Dove prisms are rotated by an angle $\alpha/2 = \pi/4$ relative to each other. These two stages, respectively dedicated to what originally were odd n is an integer, from those with $m = 4n + 2$. This process is continued in successive Mach-Zehnder stages until photons with all desired values of m have benn sieved out. In principle, the Dove prisms could be replaced by equivalent all-reflected elements for use over wide wavelength ranges. The winding number m is invariant under a Lorentz transformation. This makes it a robust indicator of orbital angular momentum.

3.2. Digital Spiral Imaging

This method, which is also termed *spiral spectrally-resoled imaging*, comprises illuminating a target with a beam defined spiral spectral decomposition. This input beam $u_0(\rho, \phi, z)$, which can be a pure LG mode, or a combination of modes, is reflected or transmitted by the target. The reflected or transmitted beam with a certain transfer function which depends on the transverse coordinates $R(\rho, \phi)$ of target causes the output field. The output field, which is given by $u_{out}(\rho, \phi, z) = R(\rho, \phi)\, u_0(\rho, \phi, z)$, can be expanded into the spiral eigenstates of orbital angular momentum and vary depending on the physical properties of the target. Such variation directly translates to into changes into spiral spectrum. Thus, the difference between the input and output spiral content contains information about the transfer function of the target. By analyzing the weights of prescribed eigenstates in the detected signal we can acquire information of the target. The signal can be detected by using a fork-like holographic mask followed by CCD or a single mode fiber [32, 33].

4. FEASIBILITY OF REMOTE SENSING APPLICATIONS WITH OAM

The fact that the photon OAM of electromagnetic waves can be generated and detected from radio frequency to optical frequency opens a new field of applications of remote sensing. Furthermore, Since information can be encoded as OAM states that span a much larger state space than the two state spin angular momentum (SAM) [31], radio OAM techniques hold promise for the development of novel information-rich radar of remote sensing and methodologies.

4.1. Atmospheric Remote Sensing

Atmosphere above the earth surface can usually be divided into troposphere, stratosphere, mesosphere, thermosphere and ionosphere etc. [19]. Since there exist turbulence and temperature near the earth surface decreases as a function of altitude up to an altitude of 11 km, so atmospheric permittivity is inhomogeneous and random. To reach the remote sensor, the radiation traverse regions that may well have discontinuities impressing OAM on transmitted electromagnetic waves.

To visualize the production of OAM by a beam of electromagnetic wave passing through an inhomogeneous medium, one can envision the beam illuminating a spiral phase plate (Fig. 1(a)). The top surface of the plate is displaced by a height s after a full azimuthal rotation $\phi = 2\pi$. At a radial distance r from the axis, the local azimuthal slope of this surface is $\theta = s/2\pi r$. On emerging from the phase plate, a ray passing through r is deflected by an angle ψ, where Snell's law for small angles gives $(\psi + \theta) \sim n\theta$, and n is the refractive index of the plate. It is easy to see that $\psi \sim (n-1)\,\theta = (n-1)\,s/2\pi r$. Before entering spiral phase plate, a photon's linear momentum is h/λ. On exiting the phase plate, azimuthal direction is $p_\phi \sim h\psi/\lambda$, and its angular momentum about the optical axis is $L_z = rp_\phi \sim rh\psi/\lambda \sim (n-1)\,\hbar/s\lambda = m\hbar$. Here the step height s is chosen an integer multiple m of $\lambda/(n-1)$, so that $s = m\lambda/(n-1)$. The angular momentum component L_z is independent of the radial distance r at which radiation passes through the phase plate.

A turbulent medium with discontinuities can be envisaged as a screen of such spiral phase plates. The analysis of spatial discontinuities may then entail tracking changes in the observed winding number of the beam as the turbulent outflow.

Besides, for a laser beam carrying OAM propagating in turbulent atmosphere, it has been shown that, upon the transition from the case of week turbulence to the case of strong turbulence during the propagation of the laser beam, the rate of growth of OAM fluctuations changes [34]. In ionosphere, The group velocity of the wave is $c/n = c\left[1 + \omega_p^2/\omega^2\right]^{-1/2}$, where ω is the angular frequency of the wave and $\omega_p \sim 5.6 \times 10^4 n_e^{1/2}$ rad. S^{-1} is the plasma frequency. In particular, in the absorption of such a wave in a plasma, angular momentum is partly transferred to the electrons, and closed quausi-stationary electric currents arise and induced generation of magnetic

fields in plasma [35]. These phenomena show that one can determine atmospheric characteristics by measuring the changes of OAM of wave beam propagating through atmosphere.

4.2. The Earth-surface Remote Sensing

Inhomogeneous anisotropic median and various shape of object are usually classical models in remote sensing [19, 36]. Since conservation of angular momentum, so when interact with media spin angular momentum and orbital angular momentum take place conversion each other. L. Marrucci et al. have demonstrate that orbital angular momentum of a wave beam can be generated by controlling the input spin angular momentum (polarization) when the beam interact with inhomogeneous anisotropic media [37]. This phenomenon proves particularly valuable in the foreseen applications of these modes to acquisition of multi-parameters information for remote sensing object.

It has been proved that absorption and radiation of angular momentum of microwave depends solely on the specific geometry of the conductor [38]. Axisymmetric perfect conductor can not absorb or radiate angular momentum of electromagnetic wave when illuminated. However, any asymmetry allows absorption. Electromagnetic waves convey angular momentum at the edges of asymmetries. Conductors can also radiate angular angular momentum. The geometric absorption coefficient can be as high as 0.8, and the coefficient for radiation can be -0.4, larger than typical material absorption coefficients. These results can be applying to remote sensing target identifying and classification et al..

5. CONCLUSION

In summary, the orbital angular of electromagnetic wave beam and radiation fields has been studied deeply. The representation of multipole radiation fields is deduced. Besides, we have cited a few phenomena and results obtained by some researchers to elucidate firstly the feasibility of applying of remote sensing. Further researches about the specific problems, such as radiation transfer of orbital angular momentum and scattering etc., of applying orbital angular momentum to remote sensing are proceedings.

ACKNOWLEDGMENT

This work was supported in part by the Natural Science Foundation of P. R. China under Contract 40571097.

REFERENCES

1. Poynting, J. H., "The wave motion of a revolving shaft, and a suggestion as to the angular momentum in a beam of circularly polarized light," *Proc. Roy. Soc., London Ser. A*, Vol. 82, 560–567, 1909.
2. Beth, R. A., "Mechanical detection and measurement of the angular momentum of light," *Phys. Rev.*, Vol. 48, 471, 1935.
3. Beth, R. A., "Mechanical detection and measurement of the angular momentum of light," *Phys. Rev.*, Vol. 50, 115–125, 1936.
4. Holbourn, A. H. S., "Angular momentum of circularly polarized light," *Nature*, Vol. 137, 31, 1936.
5. Carrara, N., "Torque and angular momentum of centimeter electromagnetic waves," *Nature*, Vol. 164, 882–884, 1949.
6. Allen, L., M. W. Beijerbergen, R. J. C. Spreeuw, and J. P. Woerdan, "Orbital angular momentum of light and the transformation of Lagurre-Gaussian laser modes," *Phys. Rev.*, Vol. A45, 8185–8189, 1992.
7. Moe, G., et al., "Conservation of angular momentum for light propagation in a transparent anisotropic medium," *J. Phys. B: Atom. Molec. Phys.*, Vol. 10, No. 7, 1191–1208, 1997.
8. Schwartz, C., et al., "Conservation of angular momentum of light in single scattering," *Optical Express*, Vol. 14, No. 18, 8425–8433, 2006.
9. Jackson, J. D., *Classical Electrodynamics*, 3rd Edition, John Wiley & Sons, 1999.
10. Lekner, J., "Angular momentum of electromagnetic pulses," *J. Opt. A: Pure Appl. Opt.*, Vol. 6, S128–S133, 2004.
11. Konz, C., et al., "Geometric absorption of electromagnetic angular momentum," *Opt. Commun.*, Vol. 235, 227–229, 2004.
12. He, H., et al., "Direct observation of transfer of angular momentum to absorptive particles from a laser beam with a phase singularity," *Phys. Rev.*, Vol. 75, 826–829, 1995.

13. Terriza, G. M., et al., "Probing canonical geometrical objects by digital spiral imaging," *J. Eur, Opt. Soc.*, Vol. 2, 07014-1-6, 2007.
14. Jassemnejad, B., A. Bohannan, J. Lekki, and K. Weiland, "Mode sorter and detector based on photon orbital angular momentum," *Opt. Eng.*, Vol. 47, No. 5, 053001-1-5, 2008.
15. Cohen-Tannoudji, C. N., "Manipulating atoms with photons," *Rev. Mod. Phys.*, Vol. 70, 707–719, 1998.
16. Brand, G. F., "Millimeter-wave beams with phase singularities," *IEEE Transactions on Microwave Theory and Techniques*, Vol. 46, 948–951, 1998.
17. Wu, J., "Encoding information as orbital angular momentum states of light for wireless optical communications," *Opt. Eng.*, Vol. 46, 019701-1-5, 2007.
18. Thide, B., "Utilization of photon orbital angular momentum in the low-frequency radio domain," *Phys. Rev. Lett.*, Vol. 99, 087701-1-4, 2007.
19. Elachi, C. and J. V. Zyl, *Introduction to the Physics and Techniques of Remote Sensing*, 2nd Edition, John Wiley & Sons, Inc., Publication, 2006.
20. He, H., M. E. J. Friese, N. R. heckenberg, and H. R. Dunlop, "Direct observation of transfer of angular momentum to absorptive particles from a laser beam with a phase singularity," *Phys. Rev. Lett.*, Vol. 75, 826–829, 1995.
21. Curtis, J. E., B. A. Koss, and D. G. Grier, "Dynamic holographic optical tweezers," *Opt. Commun.*, Vol. 207, 169, 2002.
22. Allen, L., M. J. Padgett, and M. Babiker, "The orbital angular momentum of light," *Progress in Optics XXXIX*, edited by E. Wolf, 291–372, 1999.
23. Turnbull, G. A., D. A. Robertson, G. M. Smith, L. Allen, and M. J. Padgett, "The generation of free-space Laguerre-Gaussian modes at millimeter-wave frequencies by use of a spiral phaseplate," *Opt. Commun.*, Vol. 127, 183–188, 1996.
24. Brand, G. F., "Millimeter-wave beams with Phase singularities," *IEEE Transactions on Microwave Theory and Techniques*, Vol. 46, 948–951, 1998.
25. Kristensen, M., M. W. Beijersbergen, and J. P. Woerdman, "Angular momentum and spin-orbital coupling for microwave photons," *Opt. Commun.*, Vol. 104, 229–233, 1994.
26. Brand, G. F., "A new millimeter wave geometric phase demonstration," *International Journal of Infrared and Millimeter Waves*, Vol. 21, 505–518, 2000.
27. Folland, G. B., *Fourier Analysis and Its Applications*, Thomson Learning Pte Ltd., 1992.
28. Blatt, J. M. and V. F. Weisskopf, *Theoretical Nuclear Physics*, John Wiley and Sons, Inc., 1952.
29. Heitler, W., *The Quantum Theory of Radiation*, 3rd Edition, Oxford University Press, 1953.
30. Barnet, S. M. and L. Allen, "Orbital angular momentum and nonparaxial light beams," *Opt. Commun.*, Vol. 110, 670–679, 1994.
31. Leach, J., M. J. Padgett, S. M Barnett, S. F. Arnold, and J. Courtial, "Measuring the orbital angular momentum of a single photon," *Phys. Rev. Lett.*, Vol. 88, 257902-1-4, 2002.
32. Torner, L. and J. P. Torres, "Digital spiral imaging," *Optics Express*, Vol. 13, 873–881, 2005.
33. Terriza, G. M., L. Rebane, J. P. Torres, L. Torner, and S. Carrasco, "Probing canonical geometrical objects by digital spiral imaging," *J. Eur. Opt. Soc., Rapid Publications*, Vol. 2, 07014, 1007.
34. Aksenov, V. P., "Fluctuations of orbital angular momentum of vortex laser-beam in turbulent atmosphere," *Proc. SPIE*, Vol. 5892, 58921Y-1-8, 2005.
35. Sokolov, I. V., "The angular momentum of an electromagnetic wave, the Sadocskii effect, and the generation of magnetic fileds in a plasma," *Sov. Phys. Usp.*, Vol. 34, 925–932, 1992.
36. Tsang, L., J. A. Kong, and R. T. Shin, *Theory of Microwave Remote Sensing*, John-Wiley & Sons, Inc, 1985.
37. Marrucci, L., C. Manzo, and D. Paparo, "Optical spin-to-orbital angular momentum conversion in homogenous anisotropic media," *Phys. Rev. Lett.*, Vol. 96, 163905-1-4, 2006.
38. Konz, C. and G. Benford, "Geometric absorption of electromagnetic angular momentum," *Opt. Commun.*, Vol. 226, 249–254, 2003.

Accuracy Evaluation of the Huygens Subgridding Method

G. Gradoni, V. Mariani Primiani, and F. Moglie
Dipartimento di Ingegneria Biomedica, Elettronica e Telecomunicazioni
Università Politecnica delle Marche, Via Brecce Bianche 12, Ancona 60131, Italy

Abstract— In this work, an application of the recent Huygens Subgridding (HSG) method to study lossy materials with the finite-difference time-domain (FDTD) scheme is presented and a related error analysis discussed. Achieved HSG results showed a good agreement with a full higher-resolution reference guide for different electrical parameter values, indicating a negligible numerical dispersion on the transverse section. Moreover, the increasing decimation factor effect has been investigated to evaluate the subgridding accuracy. Findings are of interest in the numerical prediction of planar screens effectiveness, material parameters retrieval and microwave spectroscopy.

1. INTRODUCTION

In the last decades, Subgridding techniques have been widely investigated as an extension of the Finite-Difference Time-Domain (FDTD) lattice. They become particularly useful to simulate real structures which exhibit complex geometries and heterogeneous media or grids [1]. In those electromagnetic (EM) problems, a spatial step contraction (of the whole grid) is generally required to better model the physical presence of a material, which could be either electrically small and lossy [2]. The basic idea in realizing that, has been to include the material in the main grid and to follow the field propagation inside it. This can be done placing virtual nodes and modifying the classical FDTD equations through the integral form of Faraday's law, applied among the slab interfaces. There, the electrical parameters to be used in the algorithm have been established averaging those of medium and air, causing a non negligible inaccuracy of predicted fields [3]. A different way to realize the subgridding is grounded to the concept of *domain decomposition*: the EM problem is modeled by multiple FDTD grids coupled through physical principles. Basically, the (lossy) medium is removed from the principal lower-resolution (LR) domain and inserted into a separate higher-resolution (HR) domain. The most rigorous way to perform the separation of contiguous EM structures is the Huygens principle, which also gives the coupling relations in terms of tangential fields [4, 5]. The key feature of this method is that no approximations for electrical parameters of the material (ϵ_r, μ_r, σ) are used and the field inside heterogeneous media can be depicted in great detail. HSG has been already applied with success in [6–8].

In this work, we present the application of the HSG to the analysis of planar, thin and lossy materials inside a rectangular waveguide. The numerical domain has been decomposed into three structures, coupled by two Huygens/anti-Huygens pairs: the slab is embedded into an HR structure. An error analysis has been carried out making use of the comparison with classical (no subgridding) FDTD lattice.

2. PROBLEM FORMULATION AND MODELING

The electromagnetic problem to be simulated is rather canonical in numerical analysis: a rectangular TE_{10} waveguide with an electrically thin lossy slab in between, as shown in Fig. 1(a). Implemented dimensions are those of a classical $WR-340$ guide $86.45\,\mathrm{mm} \times 43.9\,\mathrm{mm}$, thus of transverse section; while the material sample has $w = 2.2\,\mathrm{mm}$ thickness and fills completely the cross section. The numerical domain is made of multiple separate structures: the first waveguide generates the proper incident field, a Gaussian pulse modulated sinusoid [9, 10], to excite the guide with the lossy thin slab.

2.1. Domain Discretization

The dissipative nature of the material causes the wave slowing down because of a propagation delay along the longitudinal direction

$$\tau_w = \mu_r \sigma w, \tag{1}$$

where τ_w is the material diffusion constant and w the sample thickness.

In a numerical context, hence subject to discretization, this implies the only spatial step Δz contraction, leaving Δx and Δy unchanged, and that the subgridding should be applied to the

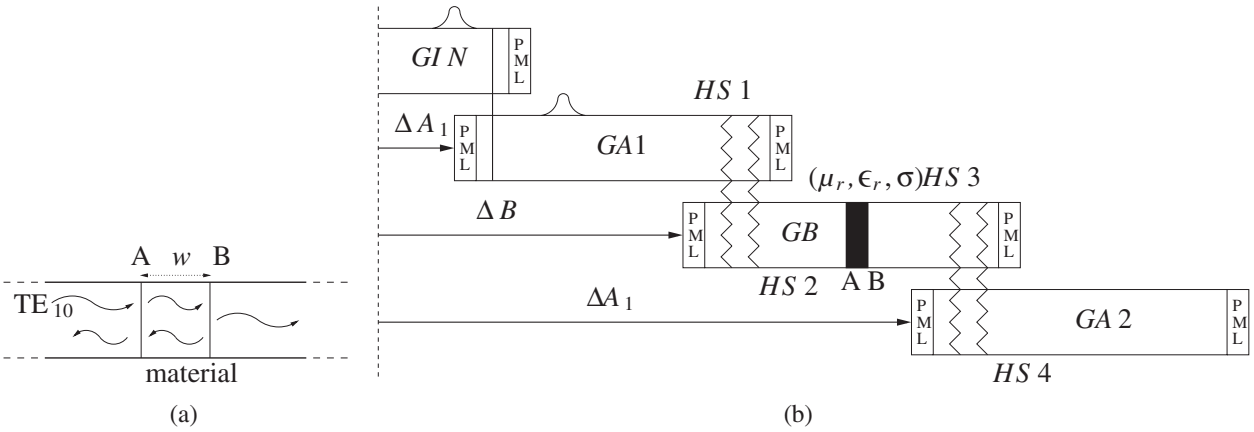

Figure 1: The EM problem is a rectangular waveguide with a lossy slab (AB) filling the transverse section. (a) Longitudinal view of the waveguide filled by a lossy thin slab. (b) The physical waveguide $WR-340$ has been represented by three independent FDTD lattices, coupled through the HSG method.

only E_x and E_y components, treating the computation as an array of mono-dimensional FDTD schemes [5]. Numerical code has been developed relying on this argument, allowing for a simplified application of the HSG method in our three-dimensional structure. Both the intrinsic HSG and the longitudinal approximation inaccuracies have been quantified through the relative error analysis. It is crucial to verify HSG efficiency, as its application leads to a strong reduction of the computation time. This makes use of the reference "fullgridding" scenarios: the first one is made of the classical FDTD lattice with a very coarse spatial discretization, while the second one is characterized by a very fine discretization. HSG model of the investigated problem is shown in Fig. 1(b). Tab. 1(b) reports the space and time steps for every implemented grid, and the number of total cells used to implement each guide. As shown in Fig. 1(b), each grid of the structure is independent from each other thanks to the spatial offset $\Delta A1$ introduced in $GA1$, ΔB in GB and $\Delta A2$ in $GA2$ referred the incident waveguide GIN. This allows for a grid length reduction and a comfortable lattice numbering w.r.t the reference waveguides GL and GH, provided a proper parametrization. As a matter of fact, the material slab has been placed between the node $A = 54$ and the node $B = 56$ with the conversion formulas

$$Z_{in} = (A - \Delta B) * N_s \tag{2}$$

$$Z_{fi} = (A - \Delta B + 1) * (N_s - 1) \tag{3}$$

taking account of the decimation from grids A. In virtue of the parametrization, it is possible to retrieve the higher-resolution reference guide case just setting $\Delta B = 0$. In our Huygens implementation we took the following offset values: $\Delta A1 = 0$, $\Delta B = 35$ and $\Delta A2 = 60$. Each domain is terminated by the PEC condition along $\hat{x}$ and $\hat{y}$, while PMLs [11] have been used to simulate the matching between domains, as noticeable in Fig. 1(b). Electric and magnetic field have been forced upon grids $GA1$ and GB plus GB and $GA2$ and *vice versa* to realize the coupling through the Equivalence Theorem. In our contest, the working region of $GA1$ and $GA2$ are placed at the left of $HS1$ and at the right of $HS4$ respectively, while that of GB is placed between $HS2$ and $HS3$. Complementary regions of each domain are, naturally, the non-working areas, which could be terminated to whatever condition. PMLs have been chosen as we found them naturally representative of the three structures matching: this is required as the physical waveguide has been modeled by separate structures.

2.2. FDTD Structure Details

The HSG structure is decomposed into three waveguides, coupled through the Huygens surfaces as shown in Fig. 1(b). The incident field propagates inside the coarse guide $GA1$ reaching the first Huygens/anti-Huygens pair, that excites the higher-resolution domain, containing the material slab. The field penetrated through the lossy material gets coupled to the coarse guide $GA2$ by the second Huygens/anti-Huygens pair. Waveguide GB needs for a spatial step reduction because of the presence of a lossy medium [12]. A way to quantify that reduction is to use the Courant-

Friedrich-Lewy condition, calculated with the complex propagation constant [5], as follows

$$\Delta z^b = \frac{c\Delta t^b \Delta x \Delta y}{\sqrt{\mathcal{C}\left(\sigma,\epsilon,\mu,\omega\right)\Delta x^2\Delta y^2 - c^2\Delta t^2\Delta y^2 - c^2\Delta t^2\Delta x^2}}\ , \tag{4}$$

where

$$\mathcal{C}\left(\sigma,\epsilon,\mu,\omega\right) = \frac{\epsilon_r\mu_r}{2}\left(1+\sqrt{1+\left(\frac{\sigma}{\omega\epsilon}\right)^2}\right)\ , \tag{5}$$

and which relates the material parameter to the spatial step Δz, since the propagation takes place along $\hat{z}$. It is worth remarking that the contraction does not affect Δx and Δy, which have been kept to the values adopted for $GA1/2$. Thus, the ratio

$$N_s = \left\lfloor \frac{\Delta t^a}{\Delta t^b} \right\rfloor = \left\lfloor \frac{\Delta z^a}{\Delta z^b} \right\rfloor, \tag{6}$$

gives the decimation factor N_s for the space and time step, which must be odd as pointed out by Berénger in his seminal paper [4]. There, a late time instability in HSG has been found, perhaps due to some spurious components generated by the subgridding operation, caused by the *imperfect* compensation between the re-radiating Huygens and anti-Huygens surfaces in working regions. As we will appreciate in the next Section, in our simulation we did not observe any late instability, even for very long simulation epochs (more than 10^5 iterations) compared with the pulse width. It is guessed that this effect could be ascribed to the presence of both PEC conditions and the dissipative material, which reduces the propagation time in guide GB and attenuates the spurious signals from the equivalent surfaces. If so, the instability has not been removed at all, but just delayed, either because of the use of a time limited excitation and the presence of a lossy medium. This aspect still needs for a clear and rigorous explanation. An important parameter, of interest in the evaluation of the FDTD accuracy in presence of a lossy medium, are the cell densities

$$\delta_x = \frac{\lambda_0}{\Delta x},\ \ \delta_y = \frac{\lambda_0}{\Delta y},\ \ \delta_z = \frac{\lambda_0}{\Delta z}. \tag{7}$$

It has been shown that the numerical dispersion (in this case along $\hat{z}$) is negligible if this density is greater than 20, as showed in Tab. 1(a). In other words, it is well known that simulating the propagation inside a lossy material requires a computation time proportional to the dissipative effect. This is the key aspect for deriving the grid sampling parameters. For example, Eq. (4) gives the time step contraction with an increasingly conductivity: a smaller Δt means a greater number of iterations for the same simulation epoch — i.e., a longer computation time.

Table 1: FDTD parameter values for the HSG model of simulated structures.

(a) Cell densities w.r.t. N_s.

WG	N_s	δx	δy	δz
GL	3	27.86	27.95	27.74
GH	3	83.59	83.26	83.23
$GA1/2$	3	27.86	27.95	27.74
GB	3	83.59	27.95	27.74
GL	5	27.86	27.95	27.74
GH	5	139.3	139.8	139.7
$GA1/2$	5	27.86	27.95	27.74
GB	5	139.3	27.95	27.74
GL	7	27.86	27.95	27.74
GH	7	195	195.7	194.2
$GA1/2$	7	27.86	27.95	27.74
GB	7	195	27.95	27.74

(b) Space and time steps for every implemented structure.

WG	Δx (mm)	Δy (mm)	Δz (mm)
$GINH$	$5.403125/N_s$	$5.3625/N_s$	$5.38/N_s$
GH	$5.403125/N_s$	$5.3625/N_s$	$5.38/N_s$
GIN	5.403125	5.3625	5.38
GL	5.403125	5.3625	5.38
$GA1$	5.403125	5.3625	5.38
$GA2$	5.403125	5.3625	5.38
GB	5.403125	5.3625	$5.38/N_s$

3. RESULTS

The main goal of our investigation was to compare the results of the HSG guide with those of the reference guides, in order to evaluate the HSG method accuracy. Figs. 2(a) and 2(b) report the frequency behavior of S_{11} and S_{21} for selected values of σ and ϵ_r. Fig. 2(b) reports the only S_{21} as in presence of a good conductor the reflection is high. From those plots it is possible to notice a very good agreement between HSG and the reference guides, whence the global discrepancy is less than 2–3 dB over the investigated frequency range and for different values of electrical parameters. Therefore, the HSG method has found to be appropriate in this class of EM problems. Besides, the validity of adopted numerical approximations has been demonstrated, especially for high conductivity, as shown in Fig. 2(b), where the HSG and HR results are almost superimposed, indicating that no spatial contraction is required on the transverse section to compensate the numerical dis-

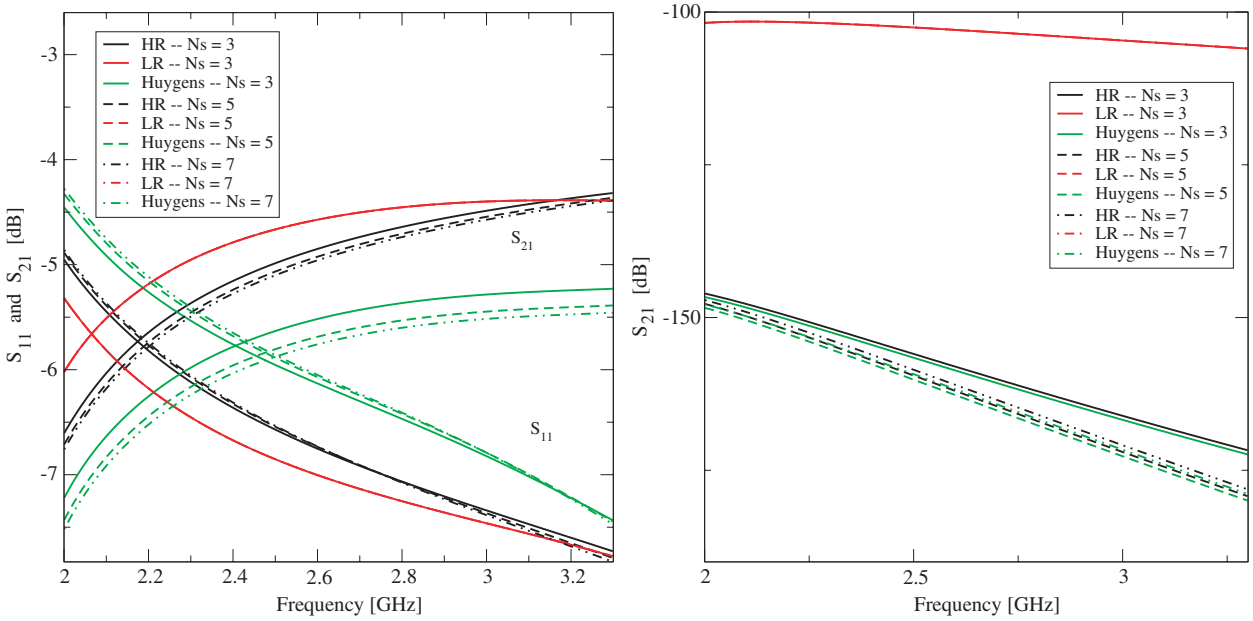

(a) S_{11} and S_{21} for σ= 0.2 S/m, ϵ_r = 2. (b) S_{21} for σ = 100 S/m, ϵ_r = 1.

Figure 2: Frequency behavior of S_{11} and S_{21} w.r.t. the reference guides and N_s.

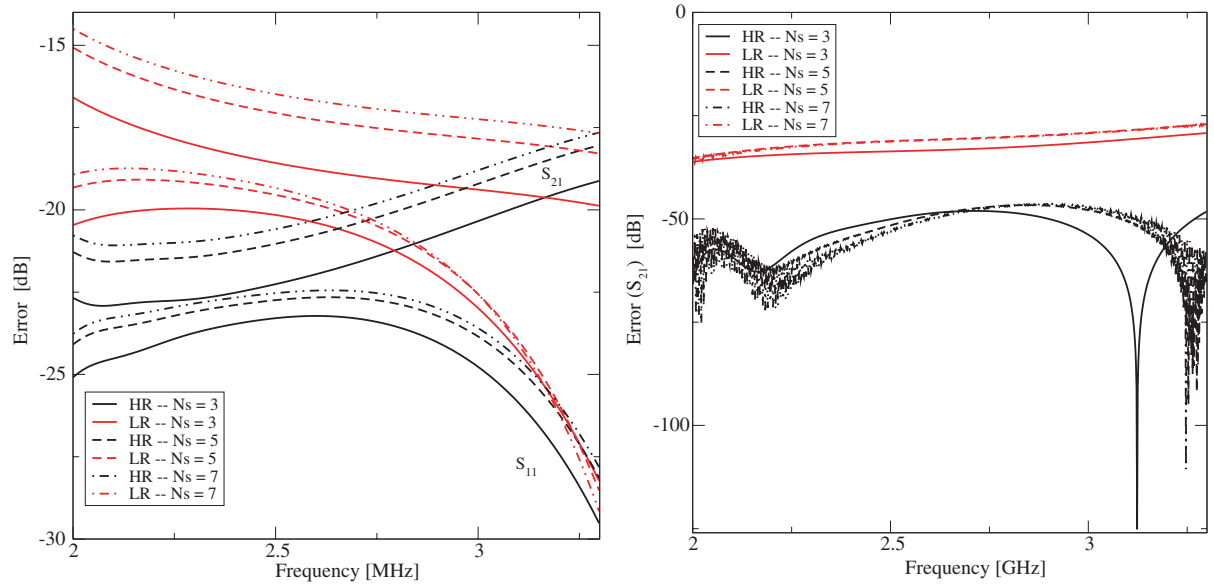

(a) S_{11} and S_{21} *relative error* for σ = 0.2 S/m, ϵ_r = 2. (b) S_{21} *relative error* for σ = 100 S/m, ϵ_r = 1.

Figure 3: Frequency behavior of S_{21} *relative error* w.r.t. the reference guides and N_s.

persion. On the contrary, the greater departure from LR results indicates the necessity of applying a longitudinal spatial contraction: this increases the computation time. On the other side, the possibility of taking out the material in a separate HR grid dramatically reduces the global domain resolution — i.e., less required time for the entire simulation epoch. We quantified the error introduced by our HSG application. In particular, relative errors are evaluated between the reference (higher-resolution HR and lower-resolution LR) and the HSG guides as

$$\epsilon = 20 \log \left[\frac{\left| S_{i1}^{HR,LR} - S_{i1}^{HSG} \right|}{\left| S_{i1}^{HR,LR} \right|} \right]. \tag{8}$$

where $i = 1, 2$. Results are reported in Figs. 3(a) and 3(b). As expected, the relative error is smaller for HR comparison when σ is greater than zero. Moreover, *epsilon* slightly increases with the decimation factor N_s, even with apparent convergent behavior, as well noticeable in S_{21} of Fig. 3(b). Oblique directions — i.e., $\hat{x}$ and $\hat{y}$ — becomes a key point when the sample is excited by the field of a resonant cavity, for example the chaotic field of an RC, simulated with multiple plane waves coming from random directions [5]. Last but not least, the HSG allows for reducing the computation time of a factor 2.

4. CONCLUSION

An application of the HSG method has been presented and validated. The implemented structure is a rectangular waveguide $WR-340$ with a planar sample in between, which fills completely the transverse section. The physical structure has been modeled by three numerical domains coupled by two Huygens/anti-Huygens surfaces: the first one (LR) hosts the incident/reflected signals, the second one (HR) embodies the lossy material while the third one (again LR) collects the transmitted signal. Results for S_{11} and S_{22} have been compared with two single domain reference guides, one (LR) without spatial contraction along the longitudinal section and one (HR) with the spatial reduction along the all Cartesian directions, in order to validate the goodness of the HSG application. Moreover, a relative error analysis has been presented to quantify the method inaccuracy, even w.r.t. the increasing decimation factor. Minimum errors have been obtained with the HR guide, demonstrating HSG is a reliable, accurate and less time consuming method.

REFERENCES

1. Chevalier, M., R. Luebbers, and V. Cable, "FDTD local grid with material traverse," *IEEE Transactions on Antennas and Propagation*, Vol. 45, No. 3, 411–421, March 1997.
2. Maloney, J. G. and G. S. Smith, "The efficient modeling of thin material sheets in the finite-difference time-domain (FDTD) method," *IEEE Transactions on Antennas and Propagation*, Vol. 40, No. 3, 323–330, March 1992.
3. Maloney, J. G. and G. S. Smith, "A comparison of methods for modeling electrically thin dielectric and conducting sheets in the finite-difference time-domain (FDTD) method," *IEEE Transactions on Antennas and Propagation*, Vol. 41, No. 5, 690–694, May 1993.
4. Bérenger, J.-P., "A Huygens subgridding for the FDTD method," *IEEE Transactions on Antennas and Propagation*, Vol. 54, No. 12, 3797–3804, December 2006.
5. Gradoni, G., F. Moglie, A. P. Pastore, and V. M. Primiani, "FDTD analysis of the field penetration through lossy materials in a reverberation chamber," *18th International Zurich Symposium on Electromagnetic Compatibility*, Munich, Germany, September 2007.
6. Costa, J., F. Costen, J.-P. Berenger, and A. Brown, "Inclusion of frequency dependency in the Huygens subgridding FDTD for uwb systems," *IEEE Antennas and Propagat. Soc. Int. Symp.*, Vol. 1, 3077–3080, Honolulu, Hawaii, June 2007.
7. Abalenkovs, M., F. Costen, J.-P. Berenger, and A. Brown, "Application of Huygens subgridding tech- nique to human body modelling," *IEEE Antennas and Propagat. Soc. Int. Symp.*, Vol. 1, 1–4, San Diego, California, July 2008.
8. Bérenger, J.-P., "On the huygens absorbing boundary conditions for electromagnetics," *Journal of Computational Physics*, Vol. 226, No. 1, 354–378, January 2007.
9. Moglie, F. and A. P. Pastore, "FDTD analysis of plane waves superposition to simulate susceptibility tests in reverberation chambers," *IEEE Transactions on Electromagnetic Compatibility*, Vol. 48, No. 1, 195–202, February 2006.

10. Gradoni, G., F. Moglie, A. P. Pastore, and V. Mariani Primiani, "Numerical and experimental analysis of the field to enclosure coupling in reverberation chamber and comparison with anechoic chamber," *IEEE Transactions on Electromagnetic Compatibility*, Vol. 48, No. 1, 203–211, February 2006.
11. Bérenger, J.-P., "Three-dimensional perfectly matched layer for the absorption of electromagnetic waves," *Journal of Computational Physics*, Vol. 127, No. 181, 363–379, 1996.
12. Taflove, A. and S. C. Hagness, *Computational Electrodynamics: The Finite-difference Time-domain Method*, 2nd Edition, Artech House, Boston, 2000.

Electromagnetic Exploration Based on System Identification for Seafloor Hydrocarbon Reservoir and Gas Hydrate

Weibin Luo and Qingchun Li
Department of Geology Engineering and Geomatics, Chang'an University, China

Abstract— A novel marine controlled-source electromagnetic method based on system identification using invert-repeated M Sequence as source signal is introduced. The M sequence signal has the similar auto-correlation with white noise and the spectrum distributed. Derived from Wiener-Hopf equation, the earth impulse response and frequency transfer function correlation identification using M sequence signal are analyzed. So the seafloor thin resistor can be detected both in time domain and frequency domain. In frequency domain we define the percent frequency effect (PFE) and relative phase with multi frequency electric field response. The IP effect influence on PFE and relative phase were studied by 1D modeling. If a high resistor with induced polarization (IP) formation is present, the differentiation of percent frequency effect with offset or the differentiation of relative phase with offset will have a peak value at appropriate offset, this offset can be used to estimate the buried depth of the resistor IP formation, it is empirically about 2.2 to 3.5 times of the buried depth.

1. INTRODUCTION

In recent years, a promising technology of marine controlled-source electromagnetic (MCSEM, seabed logging: SBL and multi-transient electromagnetic: MTEM) for hydrocarbon exploration have been established (Eidesmo et al., 2002; Ellingsrud et al., 2002; Srnka et al., 2006, Edwards, N., 2005; Constable S., 2006, 2007; Ziolkowski, et al., 2007). MCSEM methods use a horizontal electric dipole (HED) to probe the subsurface. Because HED is a galvanic source and charge buildups at the reservoir boundaries, so MCSEM has the sensitive ability to distinguish the resistive abnormal formation, especially the gas hydrate reservoir. The MCSEM method can be conducted both in frequency domain (FCSEM) and in time domain (TCSEM) surveys. The time-domain configurations have developed for it has less influence by the "air wave" in shallow water area than in frequency domain measurements (Yuguo Li, 2008; Ziolkowski, et al., 2007). But larger signal-to-noise ratios can be achieved at larger source receiver offsets in the frequency domain measurements in area of sea water depth is more than 500 meters.

In the frequency domain observation, the HED source is towed along survey line sinking in the sea water above the seabed about 50 meters, and continuous transmitting a square-wave current. A set of receivers (typically from 10 to 50) are deployed from a survey vessel along the survey profile line(s), and autonomously record the steady-state electromagnetic field response of the fundamental harmonic or the triple frequency harmonic. In order to improve efficiency, the pseudo-random signal was adopted as the source signal which contains a number of the main frequency (Rune Mittet, 2008). Many numerical results (Um 2007, Ueda 2008) show that survey with multi-frequency can improve the detection of deep buried thin resistor.

In shallow water areas survey in time domain have some advantages. Ziolkowski et al. (2008) reported they have obtained excellent marine multi-transient EM data in shallow water. The essence of the multi-transient electromagnetic (MTEM) method is that both the received voltage and the input current are measured simultaneously and the earth impulse response is recovered from these two measurements by deconvolution. The source signal is a coded finite-length signal such as a pseudo-random binary sequence (PRBS).

In this paper, we developed a method similar to MTEM, using invert-repeated PRBS sequence (put the bits of PRBS negative every two bits) as source signal. We call the invert-repeated PRBS sequence as M sequence. Its auto-correlation function is invert-repeated and has a wide frequency band. We use M sequence as source signal to recover the earth impulse response similar to MTEM. We also derived some parameter in frequency domain. These parameters can indicate deep buried thin resistor sensitively, but easily influenced by the strong induced polarization effect. We studied the IP effect influence on PFE and relative phase by 1D modeling.

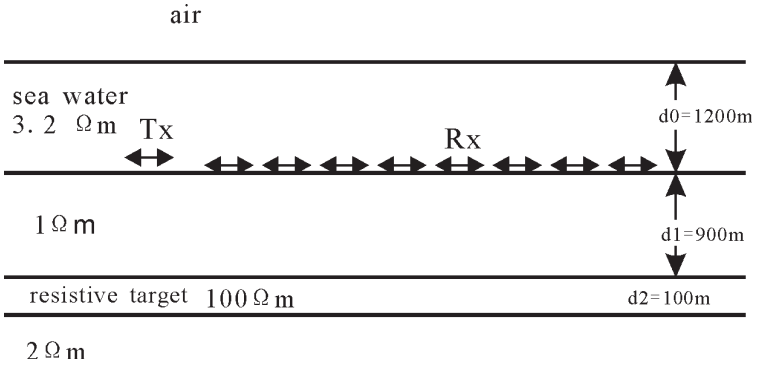

Figure 1: Multi-offsets inline dipole-dipole survey configuration.

2. PSEUDO-RANDOM MARINE CONTROLLED SOURCE ELECTROMAGNETIC BASED ON CORRELATION

Like seabed logging (SBL) and multi-transient electromagnetic (MTEM), pseudo-random marine controlled source electromagnetic use a HED to inject multi-transient current (M sequence) into the geo-electrical system, and using multiple receivers inline configuration with HED source measuring the electromagnetic field response simultaneously (see Fig. 1). So we can obtain multi-offset electromagnetic response with multi-frequency. And the earth impulse response is recovered by deconvolution of the source current signal and electromagnetic field response measured simultaneously.

A PRBS is a sequence that switches between two levels, say $+1$ and -1, at a pseudo-random integer multiple of a chosen time interval Δt. Conventionally the sequence consists of continuous series of identical cycles each of length $N = 2n-1$ samples where n is an integer known as the order of the PRBS. The autocorrelation function of the sequence consists of a series of peaks separated by the cycle period $N\Delta t$. We can get the M sequence by put the bits of PRBS negative every two bits, so one cycle M sequence is two times long than the PRBS.

For a linear system, if the input signal is $f(t)$, the output is $y(t)$, the system output is the convolution of input and impulse response

$$y(t) = \int_0^{T_s} h(\tau) f(t-\tau) d\tau \tag{1}$$

where T_s is the adjust time of the linear system. In the particular case $\tau > T_s$, $h(\tau) = 0$, so the cross correlation function $R_{fz}(\tau)$ of input $f(t)$ and output $y(t)$ is

$$R_{fz}(\tau) = \int_0^{T_s} h(s) R_{ff}(\tau - s) ds \tag{2}$$

This is Wiener-Hopf equation. Compare with (1), if the input signal is a δ function, the system output is impulse response $y(t) = \int_{-\infty}^{\infty} h(s)\delta(t-s)ds = h(t)$, in a similar way, if the auto correlation of input $f(t)$ is a δ function, we can obtain

$$R_{fz}(\tau) = \int_0^{T_s} h(s) R_{ff}(\tau - s) ds + R_{fn}(\tau) = \mathrm{K} \int_0^{T_s} h(s)\delta(\tau - s) ds = \mathrm{K}h(\tau) \tag{3}$$

where K is magnification factor. $R_{fn}(\tau)$ is the cross correlation of input $f(t)$ and noise $n(t)$.

Because the controlled source electromagnetic measurement is the earth system and recording system response to excite signal $f(t)$

$$y(t) = h_e(\tau) * h_s(\tau) * f(t) \tag{4}$$

where $h_e(\tau)$ is impulse response of earth system, $h_s(\tau)$ is impulse response of recording system. In Laplace domain, let $s = j\omega$, the Fourier transformation of $R_{fz}(\tau)$ the there is

$$S_{zf}(s) = H_s(s) H_e(s) S_f(s) \tag{5}$$

where $S_{zf}(s)$ is Laplace transformation of $R_{zf}(\tau)$, and $S_f(s)$ is Laplace transformation of $R_f(\tau)$. So the transfer function of the earth system in frequency domain can be obtained

$$H_e(j\omega) = \left(\frac{S_{zf}(j\omega)}{S_f(j\omega)}\right) / H_s(j\omega) \tag{6}$$

When exciting signal is M sequence, the solution of (6) can be easily achieved. And its invert Laplace transformation will be impulse response of seafloor geo-electrical system. So not only we can use the time information of recovered impulse response to estimate the distribution of electrical formation by multi-offset survey configuration (Edwards, 2005; Wright, et al., 2002, 2007), but also we can use multi-frequency electromagnetic response measured simultaneously to indicate the presence of deeply buried thin resistor.

3. SOME PARAMETERS IN FREQUENCY DOMAIN

Induced polarization (IP) is also an effective method for oil and gas exploration. Because the leaking hydrocarbon moves upward, the pyrite halo will be formed at the top of the reservoir. The reservoir traps also have significant differences in physical and chemical properties contrast to host rock. So a detectable difference of geophysical and geochemical fields is formed (for example, resistivity, IP, SP, et al.). This provides physical properties premise for directly oil-gas reservoir exploration using the electromagnetic and SIP method. The electric field response with multi-frequency can be recorded simultaneously with inline multi-offset dipole-dipole configuration, Based on pseudo-random invert-repeated M sequence as the source. We have put forward the PFE and differentiation of PFE with offset and differentiation of relative phase with offset in the frequency domain and these parameters have fine resolution ability for seabed resistive thin layer. So we can identify the oil and natural gas hydrate reservoir with Multi-parameters.

We have modified the layered 1D numerical modeling code to study the IP effect. The induced polarization effect is added by using Cole-Cole model. The complex resistivity formula of Cole-Cole model is

$$\rho^* = \rho_0\left(1 - m\left(1 - \frac{1}{1 + (i\omega\tau)^c}\right)\right) \tag{7}$$

where ρ^* is the complex resistivity; ρ_0 is the DC resistivity $(\Omega \cdot m)$; ω is the angular frequency; m is the intrinsic chargeability; τ is the time constant (s), c is the relaxation parameter depend on frequency.

Excited by galvanic current the electromagnetic field response observed in geophysical surveys, in general case, reflect two phenomena: (1) electromagnetic induction (EMI) in the earth, and (2) IP effects related to the relaxation of polarized charges in rock formations. It is the function of frequency and transmitter-receiver distance, with amplitude and phase in that

$$H_e(j\omega, r) = A(\omega, r)e^{j\phi(\omega,r)} \tag{8}$$

where ω is the angular frequency; r is the transmitter-receiver distance.

The electromagnetic response is measured simultaneously excited by multi-frequency pseudo-random signal, so three parameters are deduced

a. Percent frequency effect (PFE)

$$\mathrm{PFE}(r) = \frac{A(\omega_D, r) - A(\omega_G, r)}{A(\omega_G, r)} \times 100\%, (\omega_G > \omega_D) \tag{9}$$

b. Differentiation of PFE with offset

$$\mathrm{DPFE}\left(\frac{r_{i+1} + r_i}{2}\right) = \mathrm{PFE}(r_{i+1}) - \mathrm{PFE}(r_i) \tag{10}$$

c. Relative phase and differentiation of Relative phase with offset

$$pha(r) = \frac{k\varphi(\omega, r) - \varphi(k\omega, r)}{k - 1} \tag{11}$$

$$Dpha(r) = 100 \times (pha\,(r_{i+1}) - pha\,(r_i)) \tag{12}$$

In our numerical code of layered model of the seafloor electromagnetic response, the recursive algorithm released by Edwards (1997) is adopted. In the formula we use complex conductivity parameters. Layered seabed model is shown in Fig. 1. Multi-frequency electrical field response with multi-offset are calculated according to different depth of the sea water, different thickness of resistor, different layer resistivity of resistor, different buried depth of resistor, as well as different Cole-Cole model parameters m, τ and c of the resistor layer. We also compared the electromagnetic response with IP effects and without IP effects. In the model shown in Fig. 1, we select seven main frequencies response of 1/16 Hz, 1/8 Hz, 1/4 Hz, 1/2 Hz, 1 Hz, 2 Hz and 4 Hz. The transmitter-receive distance change from 800 meters to 8,000 meters, receiver interval is 50 meters.

Change Cole-Cole model parameters of the intrinsic chargeability m, time constant τ, frequency coefficient c, can cause distinctive change both in differentiation of relative phase with offset and differentiation of PFE with offset. We calculate the EM response with change the chargeability m as 0.1, 0.5, 0.8 respectively. The differentiation of relative phase with offset versus offset according to chargeability m was shown in Fig. 3. The EM response of high frequency 2 Hz and low frequency 1 Hz are used in calculation. As well as the EM response of high-frequency 2 Hz and low-frequency 1/16 Hz were used in calculation of PFE. The location of negative minimum of differentiation of relative phase with offset and the positive maximum of PFE in offsets would move to larger offset with the chargeability m increasing. The curves were shown in Fig. 3 and Fig. 4 separately. Change the frequency coefficient c and time constant τ cause a similar change trend.

The location of the negative minimum of differentiation of relative phase with offset and the maximum of differentiation of PFE with offset in offsets are related to the buried depth of resistor layer. And therefore these feature point can be used to find out the buried depth of resistive and high polarization thin layer qualitatively.

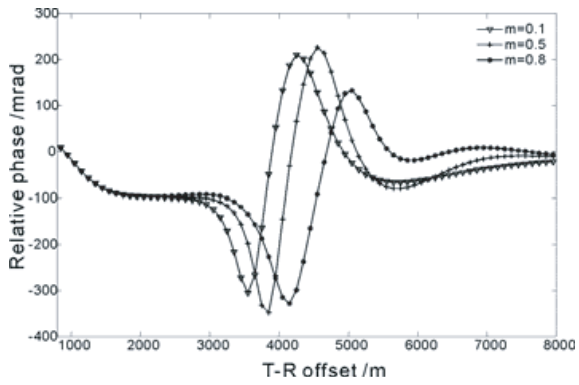

Figure 2: Differentiation of relative phase with offset versus offset according to chargeability m

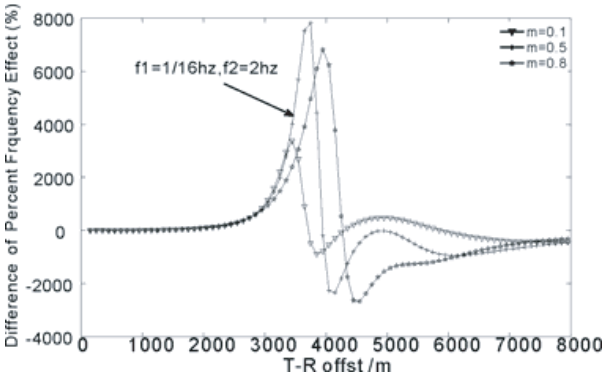

Figure 3: Differentiation of PFE with offset versus offset according to chargeability m

4. CONCLUSION

The impulse response and transfer function of the earth can be correlation identified using M sequence. The multi-frequency seafloor electromagnetic response can be measured simultaneously with inline multi-offset dipole-dipole configuration using M sequence as source signal. So we can detect the subsurface both in time domain and in frequency domain. In time domain the transient impulse peak time can be a good indicator for seafloor resistivity distribution. In frequency domain, Multi-frequency observation of the mCSEM is conducive to distinguish oil-gas resistor thin layer from seabed. Differentiation of relative phase and PFE with offset are derived from the multi-frequency electromagnetic response, these two definitions can be sensitive indicators for economic resistor thin layer. And the buried depth of the resistor thin layer can be estimated by the anomalous feature point location versus offset. Weak IP effect can induce the magnitude change of electrical field response versus offsets. Differentiation of relative phase (or PFE) with offset is more sensitive to reflect the resistor thin reservoir. Consider the effect of IP can make a practical explanation for marine controlled source electromagnetic surveying.

REFERENCES

1. Constable, S. and L. J. Srnka, "An introduction to marine controlled-source electromagnetic methods for hydrocarbon exploration," *Geophysics*, Vol. 72, WA3–WA12, doi:

10.1190/1.2432483, 2007.

2. Edwards, N., "Marine controlled source electromagnetics: Principles, methodologies, future commercial applications," *Surveys in Geophysics*, Vol. 26, 675–700, doi: 10.1007/s10712-005-1830-3, 2005.
3. Eidesmo, T., S. Ellingsrud, L. M. MacGregor, S. Constable, M. C. Sinha, S. Johansen, F. N. Kong, and H. Westerdahl, "Sea bed logging (SBL), a new method for remote and direct identification of hydrocarbon filled layers in deepwater areas," *First Break*, Vol. 20, 144–152, 2002.
4. Ziolkowski, A., B. A. Hobbs, and D. Wright, "Multitransient electromagnetic demonstration survey in France," *Geophysics*, Vol. 72, No. 4, F197–F209, 2007.

High-frequency Magneto-impedance in Ultra-thin Magnetically Soft Glass-coated Amorphous Microwires

M. Ipatov[1], **A. Zhukov**[1,2], **J. Gonzalez**[1], **and V. Zhukova**[1]

[1]Dpto. de Física de Materiales, Fac. Químicas
Universidad del Pais Vasco, San Sebastián 20009, Spain
[2]TAMAG, San Sebastin 20009, Spain

1. INTRODUCTION

Thin amorphous magnetically soft microwires attract recently growing attention because of their excellent soft magnetic properties and giant magneto-impedance (GMI) effect, extremely thin dimensions and possibility for applications in magnetic micro-sensors and tuneable composite materials. Magnetically soft properties and consequently GMI effect can be optimized in according to concrete applications by using appropriate heat treatments and manipulating fabrication parameters and/or chemical composition of metallic nucleus [1, 2]. GMI attracted great attention in then field of applied magnetism owing to the large sensitivity (up to 600%) to the DC magnetic field, H, when the high-frequency current flows along the magnetic conductor [3]. Additionally recently new class of tuneable composite materials based on thin ferromagnetic wires with the effective microwave permittivity depending on an external stimuli, such as DC magnetic field, tensile stress and/or temperature have been introduced [4].

Since the discovery of the magneto-impedance effect twenty years ago, a number of researches and developments in this direction have been widely performed. It has been found that high magneto-impedance effect is related with magnetic softness of magnetic wires and it is particularly high in wires with vanishing magnetostriction constant (CoFe-based microwire) [5]. Later the tensor nature of magneto-impedance in ferromagnetic amorphous microwire has been found and that only its off-diagonal components possess the asymmetrical dependence on magnetic field, the necessary condition for determination the magnetic field direction [6]. The real off-diagonal impedance sensor design for incorporation into integrated circuits was proposed in a number of papers [3, 7, 8]. Sensors based on off-diagonal impedance successfully applied in commercial products as high sensitivity magnetic field devices [1, 9].

Here we report novel results on high frequency GMI effect (between 10 MHz and 7 GHz) and its correlation with soft magnetic behaviour in thin amorphous microwires (Co-Fe-rich with nearly-zero magnetostriction constant) with metallic diameter between 6 and 16 μm choosing adequate samples composition and geometry we able to tailor their magnetoelastic anisotropy and respectively magnetic softness and GMI. Frequency dependence of GMI effect (microwire impedance Z) has been measured and analyzed. Hysteresis on $Z(H)$ curves has been observed at low H.

2. EXPERIMENTAL

Hysteresis loops have been measured by the induction method, as described elsewhere [1, 2].

Nearly-zero magnetrostrictive $Co_{67.1}Fe_{3.8}Ni_{1.4}Si_{14.5}B_{11.5}Mo_{1.7}$ microwires with metallic nucleus diameter between 6 and 16 μm have been fabricated by the Taylor-Ulitovski method, as described elsewhere [1].

Previously we already reported on excellent magnetic softness and high GMI effect of $Co_{67.1}Fe_{3.8}Ni_{1.4}Si_{14.5}B_{11.5}Mo_{1.7}$ microwires with metallic nucleus diameter, d about 20 μm [2].

The impedance was evaluated using impedance analyzer HP4192A at frequencies 10–500 MHz, as described elsewhere [2]. Real, imaginary components and absolute value of impedance have been measured.

The circular magnetic fields h_φ is produced by the currents i_w running through the wire. At the wire surface $h_z = i/2\pi a$, where a is the wire radius. The longitudinal magnetic fields h_z is produced by the currents i_c running through the exciting coil, $h_z = N_1 i_c$, where N_1 is the exciting coil number of turns.

In sensor application, pulse excitation is preferred over sinusoidal because of simple electronic design and low power consumption. The practical circuit design [3, 7–9] consists of pulse generator, sensor element and output stage.

3. RESULTS AND DISCUSSION

Both hysteresis loops and magneto-impedance, $Z(H)$ of nearly-zero magnetostrictive $Co_{67.1}Fe_{3.8}Ni_{1.4}$ $Si_{14.5}B_{11.5}Mo_{1.7}$ microwires exhibit strong sensitivity to the ratio, ρ, the metallic nucleus diameter, d, to the total microwire diameter, D. The hysteresis loops of microwires with different metallic nucleus diameters, d are presented in Fig. 1.

All studied microwires exhibit low coercivity (generally below 15 A/m) with well defined magnetic anisotropy field, H_k (see Fig. 1).

It worth mentioning that samples with different d but with similar ρ-ratio exhibit very similar hysteresis loops (see loops for the samples with 11.8 and 16.6 μm in Fig. 1), but the magnetic anisotropy field significantly depends on ρ-ratio. Therefore we can assume, that the ρ-ratio is the main parameter for comparison hysteretic magnetic properties between the samples.

Magnetic field dependence of real part of the longitudinal wire impedance, $Z(H)$ is also strongly affected by the ρ-ratio (see Fig. 2).

Field dependence of the off-diagonal ($\varsigma_{\varphi z} = v_c$) voltage response of nearly zero magnetostriction

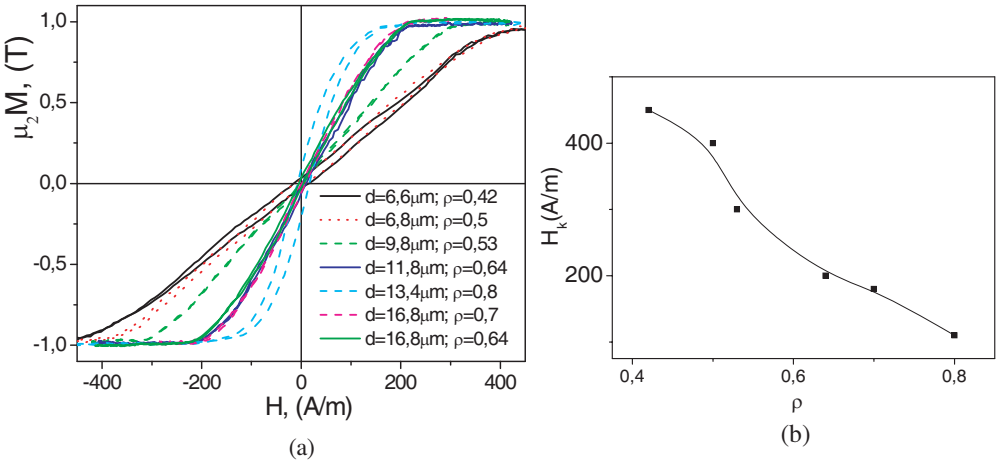

Figure 1: Hysteresis loops of $Co_{67.1}Fe_{3.8}Ni_{1.4}Si_{14.5}B_{11.5}Mo_{1.7}$ microwires with different ρ-ratio (a) and effect of sample geometry (ρ-ratio) on magnetic anisotropy field, H_k (b).

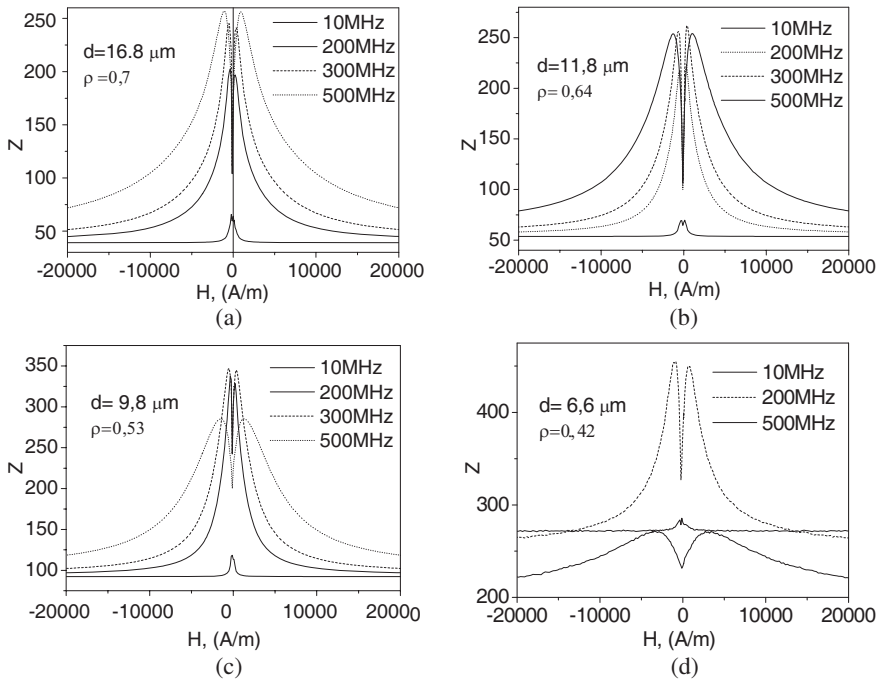

Figure 2: $Z(H)$ dependences of $Co_{67}Fe_{3.85}Ni_{1.45}B_{11.5}Si_{14.5}Mo_{1.7}$ microwires with different ρ-ratio.

($\lambda_s \approx -3 \times 10^{-7}$) $Co_{67.1}Fe_{3.8}Ni_{1.4}Si_{14.5}B_{11.5}Mo_{1.7}$ with metallic nucleus diameters, d ranging from 6.6 to 16.8 μm (ρ-ratios ranging between 0.42 and 0.8) exhibits anti-symmetrical and un-hysteretic shape (Fig. 3). At certain magnetic field, H_m, the off-diagonal voltage reaches the maximum value. Usually magnetic field corresponding to the maxima, H_m, is associated with the magnetic anisotropy field [9–11]. Between $-H_m$ and H_m at certain field range there is an almost linear dependence of the off-diagonal voltage on magnetic field. This linear region of the curve depends on microwires geometry but in any case is smaller than whole $-H_m$ to H_m range.

Absolute value, real and imaginary components of impedance have been measured at frequencies till 3 GHz. Results for absolute values of $Co_{67.1}Fe_{3.8}Ni_{1.4}Si_{14.5}B_{11.5}Mo_{1.7}$ microwires are shown in Fig. 4.

It is worth mentioning that although magnetic field corresponding to the maximum increases with frequency, f, there is a small hysteresis on $Z(H)$ dependence at low fields when we measuring Z first increasing and then decreasing magnetic field from negative maximum value of magnetic field, $-H_{\max}$ to $H_{\max}$. The field corresponding to the minimum, $H_{\min}$, does not change with f (Fig. 5).

Observed dependences can be attributed to ferromagnetic resonance (FMR)-like behaviour of GMI effect (increasing of H_m with frequency), while low field hysteresis should be related with low frequency magnetic properties and magnetic anisotropy.

Figure 6 shows $Z(f)$ dependences (real, imaginary and absolute value) measured for $Co_{67.ge1}Fe_{3.8}Ni_{1.4}Si_{14.5}B_{11.5}Mo_{1.7}$ microwires ($d = 21.4$ μm, $D = 26.2$ μm, $\rho = 0.82$) with applied magnetic field, H as a parameter. Observed dependences exhibit resonance-like behaviour. We plotted $f_{res}^2(H)$ dependence where f_{res} — frequency corresponding to such resonance (Fig. 7).

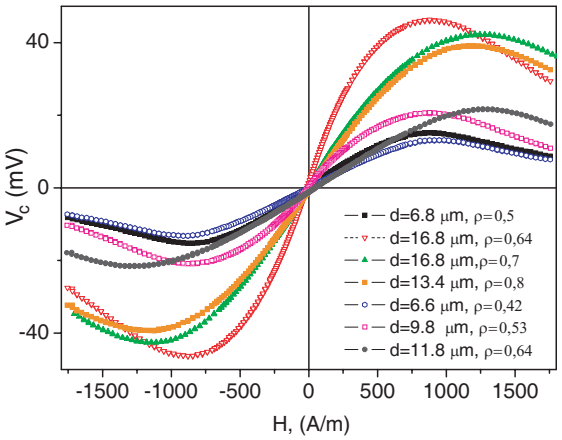

Figure 3: Field dependence of the off-diagonal voltage response for nearly zero magnetostriction $Co_{67.1}Fe_{3.8}Ni_{1.4}Si_{14.5}B_{11.5}Mo_{1.7}$ microwires with different d.

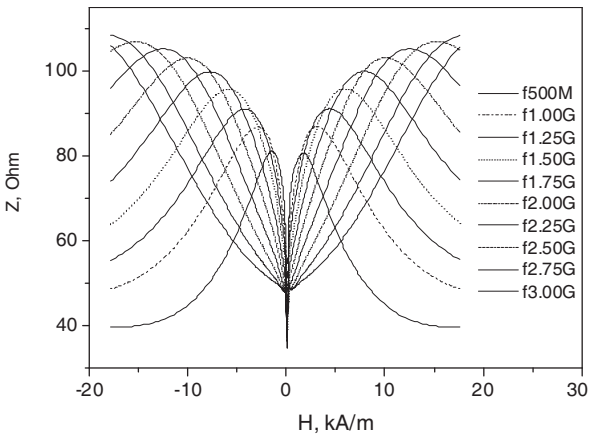

Figure 4: Frequency dependence of absolute values of $Co_{67.ge1}Fe_{3.8}Ni_{1.4}Si_{14.5}B_{11.5}Mo_{1.7}$ microwires ($d = 21.4$ μm, $D = 26.2$ μm, $\rho = 0.82$).

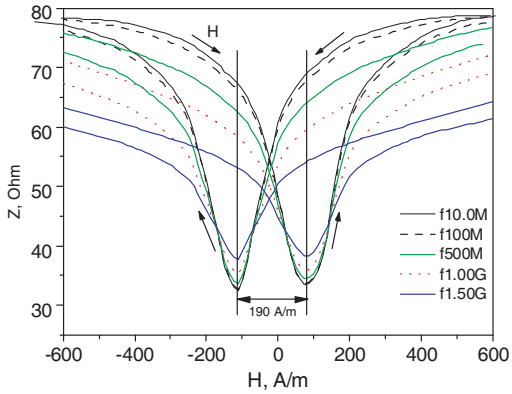

Figure 5: Frequency dependence of absolute values of $Co_{67.ge1}Fe_{3.8}Ni_{1.4}Si_{14.5}B_{11.5}Mo_{1.7}$ microwires at low frequencies ($d = 21.4$ μm, $D = 26.2$ μm, $\rho = 0.82$).

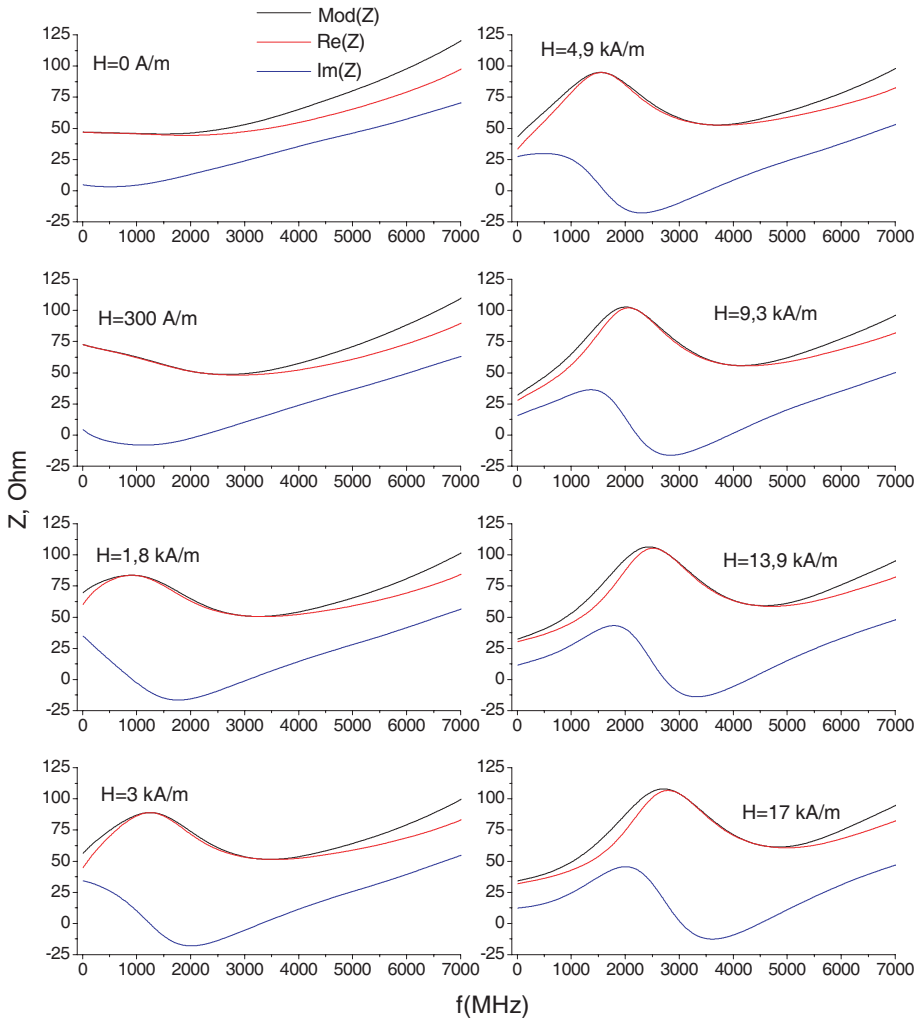

Figure 6: Dependences of real, imaginary and absolute value of impedance on frequency with applied field, H, as a parameter.

Indeed, $f_{res}^2(H)$ fits very well with linear dependence, like in the case of ferromagnetic resonance (Fig. 7).

Generally, most convenient way to tailor GMI properties of already fabricated microwires is thermal treatment. Joule heating gives simplest possibility to anneal the samples.

Under DC current annealing the H_m decreases from 480 A/m in as-cast state to 230 A/m after 5 min annealing with 50 mA current (see Fig. 6).

Observed dependences of the hysteresis loops and $Z(H)$ on ρ-ratio (Fig. 1) should be attributed to the magnetoelastic anisotropy related with the internal stresses induced by simultaneous quenching of metallic nucleus and glass coating [12]. The strength of such stresses increases with increasing of the glass coating thickness, i.e., decreasing ρ. Consequently, magnetic anisotropy field, H_k, decreases with ρ [12–14].

The Joule heating of nearly zero magnetostriction microwire results in decreasing of magnetoelastic energy and therefore improvement of the magnetic softness [1]. Therefore, observed change of $V_c(H)$ curves induced by Joule heating resulted in sharper $V_c(H)$, lower maximum field, H_m and higher magnetic field sensitivity (Fig. 8). These changes should be related with the stress relaxation.

Joule heating reduces internal stresses and enhances the V_c. It is important to note that even short current pulses affect $V_c(H)$ curves, indicating quite high sensitivity of $V_c(H)$ curves to internal stresses.

Understanding of the obtained results allows us to tailor the microwire magnetic properties for its application in magnetic sensors through the selection of their composition and/or thermal treatment conditions.

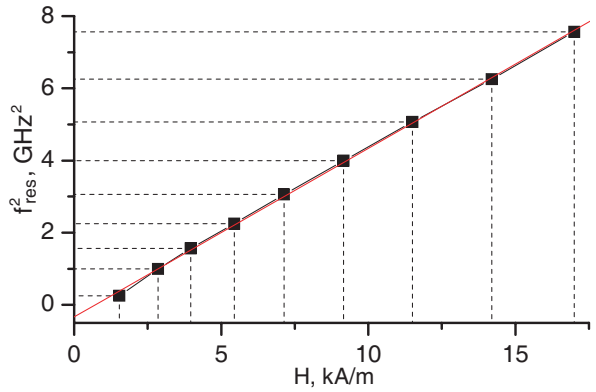

Figure 7: Resonance frequencies of $Co_{67.ge1}Fe_{3.8}Ni_{1.4}Si_{14.5}B_{11.5}Mo_{1.7}$ microwires ($d = 21.4\,\mu m$, $D = 26.2\,\mu m$, $\rho = 0.82$) as a functions of the applied field.

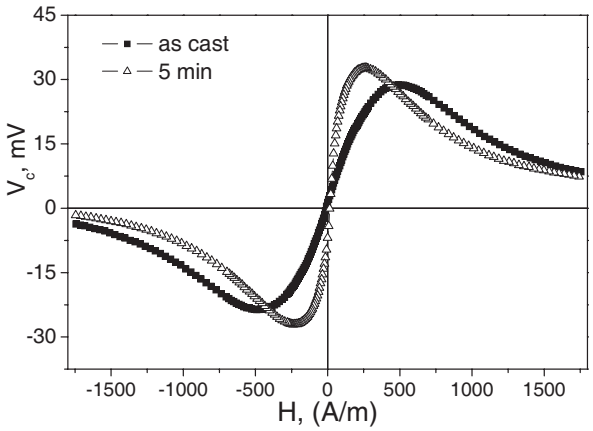

Figure 8: $V_c(H)$ dependences of as-prepared and annealed with 50 mA for 5 min $Co_{67}Fe_{3.85}Ni_{1.45}B_{11.5}Si_{14.5}Mo_{1.7}$ ($d = 9.4\,\mu m$, $D = 17\,\mu m$).

4. CONCLUSIONS

Magnetically soft $Co_{67.1}Fe_{3.8}Ni_{1.4}Si_{14.5}B_{11.5}Mo_{1.7}$ thin ($d = 6$–$16\,\mu m$) microwires with low coercivity values have been fabricated. Considerable dependence of magnetic anisotropy field, hysteresis loops, $\varsigma_{\varphi z}(H)$ and $Z(H)$ dependences on ρ-ratio is observed. Magnetic anisotropy field is determined by ρ-ratio. Microwires with nearly zero magnetostriction possess anti-symmetrical shape with almost linear magnetic field dependence within certain magnetic field range.

Frequency dependence of GMI effect (microwire impedance Z) has been measured and analyzed.

Joule heating significantly affects the off- diagonal MI curves of $Co_{67.1}Fe_{3.8}Ni_{1.4}Si_{14.5}B_{11.5}Mo_{1.7}$ microwires: after DC current annealing the H_m decreases and maximum value of V_c increases.

Thermal treating is additional effective factor in tuning of MI dependence along with alloy composition and geometric parameters.

ACKNOWLEDGMENT

Authors would like to acknowledge Mr. A. V. Torcunov for providing the microwire samples for current investigation. This work was supported by EU ERA-NET programme under project DEVMAGMIWIRTEC (MANUNET-2007-Basque-3) and the Basque Government under Saiotek 08 METAMAT Project.

REFERENCES

1. Zhukov, A. and J. González, *Advanced Magnetic Materials*, Vol. 3, Ch. 26, David J. Sellmyer, Yi Liu, and Daisuke Shindo, eds., Kluwer Academic Publishers, Norwell, 2005.
2. Zhukova, V., A. Chizhik, A. Zhukov, A. Torcunov, V. Larin, and J. Gonzalez, *IEEE Trans. Magn.*, Vol. 38, 3090–3092, 2002.
3. Panina, L. V. and K. Mohri, *Appl. Phys. Lett.*, Vol. 65, 1189–1191, 1994.
4. Panina, L. V., S. I. Sandacci, and D. P. Makhnovskiy, *J. Appl. Phys.*, Vol. 97, 13701, 2005.
5. Panina, L. V., K. Mohri, T. Uchiyama, M. Noda, and K. Bushida, *IEEE Trans. Magn.*, Vol. 31, 1249–1260, 1995.
6. Makhnovskiy, D. P., L. V. Panina, and D. Mapps, *Phys. Rev. B*, Vol. 63, 144424-1–144424-17, 2001.
7. Kanno, T., K. Mohri, T. Yagi, T. Uchiyama, and L. P. Shen, *IEEE Trans. Magn.*, Vol. 254–255, 399–403, 1997.
8. Kawajiri, N., M. Nakabayashi, C. M. Cai, K. Mohri, and T. Uchiyama, *IEEE Trans. Magn.*, Vol. 35, 3667–3669, 1999.
9. Honkura, Y., *J. Magn. Magn. Mat.*, Vol. 249, 375–381, 2002.

A Way of Modeling Radiation-Matter Interaction

S. L. Vesely[1] and A. A. Vesely[2]

[1]I.T.B.-C.N.R., Italy
[2]Via L. Anelli 13, Milano 20122, Italy

Abstract— In this paper we review the celebrated experiments of Einstein-de Haas and Zeeman for the charge/mass ratio determination, which are usually explained in the framework of quantum mechanics in terms of conservation of the total angular momentum of radiation and matter by means of the selection rules. We essay to show that both experiments are amenable to alternative explanations that dissent from quantum mechanics, as long as we are willing to distinguish between a "signal" and its "transduction". We also recall that the transduction effect for the Einstein-de Haas experiment has been reproduced under controlled conditions in autopilots. We propose that, whenever a generic transduction phenomenon, which in general is non linear, can be reproduced in a controlled fashion, such controlled reproduction is considered an "explanation" of the radiation-matter interaction that results in the given phenomenon.

1. INTRODUCTION

When probing for the "radiation-matter interaction" consists of illuminating the objects, receiving, processing and interpreting images from them, the result of the interaction is a photograph. An image may resolve the material *structure* as much as possible through magnification, and allow recognition of the subjects, without requiring nor permitting any tighter relationship with the matter. Advancements in teledetection let the misconception pass off that images faithfully reproduce material structures. Pseudo-coloring may replace the usual physiologic encoding with a different one, chosen on the basis of, say, geographical properties, so as to graphically render *functional* facets. The possibility to modulate light by pulse compression techniques supports investigating the sensibility of specific materials to different radiations. Quantum mechanics already tried to specify a connection between radiation and matter that involves more than photographic aspects. It consists of interpreting gas spectral lines as energy distributions, and assigning the corresponding dynamical behaviors to the atomic systems that have those energy eigenvalues. That approach, originally based upon an atomic model customary to chemists, eventually promoted communication technology as a tool in *analytical chemistry*.

Anyhow, some interactions with light are known that go beyond photographic aspects, as they *alter* the matter. Some vitally important processes, such as photosynthesis, explicitly include light among their "reactants" [1]; photography itself used photoreaction to create latent images on emulsion glass plates. Among such examples, we may also count transducers, including piezo- and thermoelectric ones, as well as coherers and diodes. The latter ones are considered detectors rather than "photo-reactants", because telecommunications traditionally deal with electromagnetic waves reception, without taking care all that much about the reactions that they might cause in the matter. In *preparative chemistry*, instead, light plays a role similar to that of electricity in galvanization processes and batteries. However, that has contributed to elude comprehension by quantum mechanics: On the one hand, in its attempt to explain the *chemical valence* as a consequence of its energetic interpretation of the spectra, quantum mechanics "photographs" the atomic-energetic state of each element in the periodic table. On the other hand, the wave-particle dualism lets it attribute to photons the same kind of reaction "by contact" that characterizes chemistry from J. Dalton onward. As chemical reactions are interpreted thermodynamically, that dualism has the practical effect to reduce the "thermal" or "non thermal" role that light may play in the interpretation of chemical mechanisms, to a definition question [2, 3][1]. The Cole brothers have proposed, as an alternative, to strengthen the analysis of permittivity of substances in bulk, presenting them schematically as linear electrical circuits [4]. To date, their alternative has suffered the lack of logical connections between electrical states and material states [5]. One way to obviate that deficiency is to completely drop connections between states, and associate reactions with the corresponding *variations* of electrical parameters. Obviously, those electrical variations cannot be interpreted as encoded signals; rather, their explanation relies upon the possibility to control the

[1]The temperature measured during an exothermic reaction does not necessarily correspond to a thermodynamic state parameter.

course of reactions. That point of view might establish a bridge toward radiochemistry. In the rest of this paper, we try and interpret the electromagnetic response of the matter so as to make the suggested alternative credible.

2. ABOUT THE RADIATION-MATTER INTERACTIONS

In chemistry, the main inorganic reversible reactions are explained by means of the law of mass action; that is, the law determining that, at equilibrium, the formation of products depends on the chemical formula and the stoichiometry of the reactants. Spectra for various concentration ratios can be recorded to plot binding isotherms. However, several reactions turn aside from that law, either because they require an activation energy to be overcome, or because they are chain reactions, catalytic, or autocatalytic. Such somewhat more complicated reactions are studied kinetically. Their reaction rates can be followed by monitoring spectral changes over time. Taking care of the electromagnetic response, various interesting modeling options for complex systems have been proposed [6, 7]. Reductionists tend to express interactions in terms of binding forces among elementary material components. Holistic stances try and represent the *functional information* exchanged [8]. One concept that allows holistic reasoning to detach from the mechanical layer is to regard the radiation-matter interaction as an exchange of information. However, until transmitting information implies an amount of energy[2], and conservation principles are applied to that exchange, the attribution to radiation of a nature different from that of bodies is only apparent, because the trade currency, energy, characterizes both of them in the same way. Instead, we propose to concentrate on reaction *rates*, so as to consider radiation a *property* of interaction among reactants. That way, electromagnetic waves don't play the role of reactants, but are attributes of the relevant chemical processes, and can be used to control them.

In this paper, we limit ourselves to examining the difference between reception and transduction, by illustrating it on two emblematic experiments: those of Einstein-de Haas, and Zeeman. Their interpretation in quantum mechanics requires to complicate both the atomic model and the conservation principles. That complication is associated with the spin hypothesis, a quantity that has no classic counterpart. R. W. Pohl used to exhibit a working mechanical model of a gyroscope during his lectures. He used it to show the interconnections between angular momentum and magnetic moment, in relation to spin. His gyroscope rotates around a vertical axis whose superior part is a permanent magnet, while the inferior part, the pivot, has an air vent that feeds a flywheel, conveniently pierced so that it works as a sprinkler. Two vertically layered Helmholtz coils cause it to precede, while the axis' slope can be varied through a horizontal couple of Helmholtz coils, by feeding current at the *precession frequency*. The Planck constant, typical of microscopic phenomena, does not show up in the equations of motion that rule the experiments of Einstein-de Haas and Zeeman; therefore, the energy related with the radiation-matter interaction can be given the classical interpretation of precession frequency. For the first experiment, the precession frequency is linked to the expectation value of the macroscopic angular momentum exchanged between radiation and matter. For the Zeeman experiment, the selection rules for the transition probability between known energy levels are in relation with the conservation, and spin quantization produces the spectral multiplets. Pohl's model serves to see that the energy transmitted to the gyroscope is maximal at the precession frequency, and possibly allows to grasp how quantum leaps happen between rotational states that are "in resonance" with each other. Both experiments, either making a mechanical determination of the torsion, or recording the spectral lines, result in the same measure of the ratio between two quantities, e and m. In order to highlight a concept of resonance more similar to the one found in acoustics, we observe that in the Einstein-de Haas experiment the electrical excitation is transduced by a soft iron pendulum bob, and the *induced* torsional oscillation is selectively amplified *at resonance*. Einstein and de Haas measure no bare electric response. Zeeman takes rather radical steps to obtain light emission from gaseous samples, and then only considers the optical response, which he interprets as "information" pertaining to a reorganization of the matter at the microscopic level. Today, the dynamical effect can be safely attributed to spins, as there is no bulk electromechanical transduction.

[2]For simple systems, the "information" is assumed to consist of supplying the energy required for the effect to take place. For complex systems, information is what allows them to self-organize, thereby lowering their entropy.

3. SIGNAL RECEPTION BY RESONANCE METHODS AND MECHANICAL TRANSDUCTION

Rather than stemming from the conservation of the angular momentum principle, like Pohl, we propose to consider *in the same way as signals* even radiations that, according to the current acceptation of "signal" in telecommunications, don't have the required qualifications. We don't mean that observed signals have some sort of natural encoding that we should be able to understand when we'll get the correct model, but we inquire whether signals accompanying transductions admit an explanation based on control. Let's recall the acoustic meaning of "resonance", to start with[3]. At ordinary temperatures, it is difficult to get ready of all mechanical vibrations, most of whose sounds remain unnoticed as they miss a resonant cavity. However, loud sounds sometimes result in *weak* mechanical phenomena. At the chime of a bell, one may observe segmentations in a nearby jet of water, or fluttering of pollen or similar light bodies. We can regard such phenomena as cases of acousto-mechanical transduction. Technical applications include, for example, deploying mechanical conversion of ultrasounds to detach small swarfs from glasswork (sonication). Conversely, it is possible to generate a steady sound by rubbing a mallet round a da-qing, or a wet finger round the brim of some glasses. Likewise, wind causes mechanical actions [9] that may result in sounds. Differently, sound can be obtained by "sympathetic vibrations" in calm air by Helmholtz resonators. In acoustics, the term *resonance* is used for both cases: acousto-mechanical transduction and selective amplification.

Much like sound, *low frequency* electrical waves also can be converted to and from sustained mechanical oscillations. In piezoelectric quartz crystals, elastic vibration modes can be elicited by filtering with electrical LC circuits. However, quartz, as a circuital element, works at higher frequencies than those convertible into audible sounds, and its Q[4] as an electric filter is much higher than that of common acoustics resonators. In addition, the higher the frequency, the more difficult its mechanical conversion, and the higher the Q, at the same time. Thus, besides frequency, at least the Q value is also important for conversion yields.

In modern medical applications of the Zeeman effect, samples are transiently excited at frequencies where no "macroscopic" conversion is believed to occur. However, since electrical effects don't need a transmission medium, one may still question whether conversions could be obtained by feedback controlling the excitation of the sample in resonant conditions. As a matter of facts, in air all luminous bodies burn, or somehow transform, at efficiency rates that can be sustained by keeping supplies steady. That's the case with carbon arc lamps, and oxy- or air-acetylene torches. But it's also the case with glowworms. By contrast, the effect of flash powder damps down. Besides those light producing substances, others are known in the literature, whose reaction yield is enhanced when they are polarized by means of electromagnetic impulses, in suitable conditions. As it happens for sounds, the reverse effects also occur. Light sparks chlorine-methane reactions, and even more swiftly hydrogen-chlorine reactions. On organic matter, the effects of light result in generally slower and modulated reactions. Today, they are explained with the production of unpaired electrons in the reactants' orbitals, with no reference whatsoever to electromagnetic parameters. Incidentally, it is known that also transformations of different kind than chemical reactions, such as changes in aggregation state or isotopic enrichment, are related with permittivity variations. Thus far, while it seems reasonable to expect to be able to electronically trigger and control a number of effects in matter, it seems appropriate to try and determine what opposes their spontaneous appearance whenever impedance variations are produced. Our analysis of Zeeman experiments highlights three kinds of problems. 1) If a substance happens to have a very narrow resonance bandwidth at some electromagnetic frequency, matching becomes essential to excite the sample as well as to detect its electrical response. Then, at the monitored spectral frequency the detector is in resonance with the sample, so that the observed resonance band characterizes the resonating system as a whole. If power is fed at that frequency, then most of it is conveyed to the resonator, because the sample's bandwidth saturates. As the detector is the most delicate part of the system, the power may fire it, which is not the wished transduction effect indeed. 2) If, by contrast, the natural Q of a resonance band is too low, discerning the band becomes difficult for the opposite problem. Nevertheless, assuming that the intensity of the response is proportional to the area of the plotted spectral band, quite a lot of power could be conveyed by coupling through that channel. Then, the transferred power may turn out to be insufficient to boost/sustain a transduction effect. Indeed, conversion

[3] Actually, the Latin term *resonare* (re + sonare = to sound again) recalls its acoustic origin.

[4] Q is the merit factor of a quartz working as a filter in a circuit. It may be tied to the gain of an amplifier. The relationship between Q and the efficiency of electromagnetic conversions, our current subject, is less studied.

cannot be sustained if it would take place too slowly or too rapidly in comparison to the power transfer rate[5]. To obviate such inconveniencies, one can deploy dopant, catalysing, or moderating substances, capable of changing the conversion rate. 3) Finally, an audio-frequency band that is excited at room temperature because of the environment, can superimpose on an excited high frequency. In this case, the superposition principle is valid for the signal received. However, if there is no cross talk among resonating bands, the modulation is a "ghost" and cannot be pumped at high frequencies.

4. THE CONSERVATION LAW FOR THE TOTAL ANGULAR MOMENTUM

In the past, the energy conservation principle used to be considered universal, and, most noticeably, experimental[6]. It is an additive principle, in the sense that the conserved quantity results from adding each single term that participates in the balance. Even without partaking in much of the energetic hype of his times, J. Clerk Maxwell did calculate expressions for the electric energy required for charging a capacitor, and the magnetic energy stored in a coil. By contrast, J. H. Poynting shared with M. Faraday the philosophy according to which the creation, including dielectrics, is imbued with a unique energy, that can be transformed into different forms, depending on its final usage, and is conserved even by *radiation*, if its flux across the system's boundary is taken into account. He derived from geometrical considerations the vector $\mathbf{S} = \mathbf{E} \times \mathbf{H}$ that today bears his name[7] and tied it to the expression of the energy that the electromagnetic field transports. In facts, it is $\nabla\mathbf{S}$, obtained using Gauss theorem[8], which is equated to the time derivative of electrical and magnetic energy densities $\frac{1}{2}\partial/\partial t[\epsilon_0 E^2 + \mu_0 H^2]$ in every volume element dV[9]. In special relativity notation, where x_j are spatial coordinates, and $x_4 = ict$ is the fourth coordinate, the energy density is just one component $T_{44} = -\frac{1}{2}[\epsilon_0 E^2 + \mu_0 H^2]$ of the energy-momentum tensor, which becomes the relativistic invariant. In this case, the "mixed" component: $T_{4j} = iS_j$, whose flux density is $\mathbf{S}/c$, is taken as an energy component. The spatial components of $T_{\mu\nu}$ are those of Maxwell stress tensor[10], that is $T_{jk} = \epsilon_0[E_j E_k - \frac{1}{2}\delta_{jk}E^2] + \mu_0[H_j H_k - \frac{1}{2}\delta_{jk}H^2]$. In four-dimensional notation, hence, the principle of energy conservation is put side by side with the momentum conservation law, derived from the expression $\partial_j T_{jk} + d/dt(p_{emk} + p_k) = 0$. As detailed above, one can formally split the time derivative in a term $\mathbf{p}$ for the density of the mechanical momentum, and a term $\mathbf{p}_{em} = \mathbf{S}/c^2$ for that of the electromagnetic field [10]. In four-dimensional notation the linear momentum density is described by the components T_{j4} of the energy-momentum tensor.

Following the mechanical rules, the conservation of the total angular momentum is point-wise tied to the sum of the mechanical and the radiation momentum, which is $\mathbf{M}_{em} = \mathbf{r} \times (\mathbf{E} \times \mathbf{H})/c^2$, where $\mathbf{r}$ is the position vector relative to the fixed point. Poynting [11] associated to *circularly polarized* light a stream of angular momentum that conditions the surfaces orthogonal to the direction of propagation: According to him, to an angular frequency ω corresponds a momentum per unit area in the propagation direction $|\mathbf{M}_{em}| = S/\omega$, given that $\mathbf{\Pi} = \mathbf{S}/c$ is the radiation pressure. Today, relativity considers the angular momentum conservation principle satisfied whenever $T_{4j} = T_{j4}$. In quantum physics, the principle is complicated because of the spin-radiation interactions, which neither Einstein-de Haas nor Zeeman considered. At any rate, the principle utilized by them allows to infer one or the other of the *two* momenta by just applying the formula: $\mathbf{M}_{tot} = \mathbf{\Theta} + \mathbf{M}_{em}$, where $\mathbf{\Theta}$ is the mechanical part.

---

[5] L. Boltzmann mentions he never could get a sound by "pressing" a grand piano key.

[6] J. P. Joule's experiments were among the most favorably accepted. The validity of the first law for single quanta $\hbar\omega$ has been a more controversial concept. For example, J. C. Slater unsuccessfully proposed that energy conservation may hold in a *statistical* sense. To unify microscopic and macroscopic conservation principles one needs to explain why nuclear energy, that pertains to a part of an atom, is so much higher than the total amount of energy that the whole atom can display in chemical reactions.

[7] This representation should not be confused with H. R. Hertz' one. Hertz avail himself of the concept of linked fields in order to geometrically model aether waves. On the opposite, Poynting geometrically represents the energy of the electro*static* and magneto*static* fields, for which he defines $\mathbf{E} \times \mathbf{H}$. Hence, in his representation the energy related to locally varying fields arrives "with delay" to the positions characterized by the static fields.

[8] Although Poynting's representation is geometrical, the surface on which Gauss theorem applies does not describe a geometric shape. Therefore, while geometrically the *shape enclosed within a boundary* should remain unchanged after a change of coordinates, in theory of relativity the *energy-momentum tensor density expression* is invariant thanks to Gauss theorem.

[9] In rationalized MKS units. Even without taking gauge transformations into account, $\forall \mathbf{R}\ \mathbf{S}' = \mathbf{S} + \nabla \times \mathbf{R}$ satisfies the same conservation principle.

[10] Maxwell called D and B stresses, E and H strains. Furthermore, he considered constitutive relations linear.

5. THE EXPERIMENT OF EINSTEIN AND DE HAAS

The Einstein-de Haas experiment originated from a patent lawsuit filed by Anschütz against Sperry on a gyrocompass oscillation-damping device, where Einstein participated as a consultant. Mechanics teaches that, when a rapidly spinning gyroscope, supported at a distance from the center, is hit orthogonally to its figure axis, rather than lapse in the direction of the hit, it develops a cyclic motion by deviating in a perpendicular direction. When the gyroscope is gimbal mounted on a watercraft where it serves as a compass, roll and pitch motions are the main sources of *impulsive* perturbation. Any precession thus originated has to be damped, which Anschütz provided for by means of an hydraulic brake. Anschütz's legal argument against Sperry was the feedback principle: Signals for corrections were gathered from the misalignment between the principal axis of inertia and the spin axis when the gyroscope's center of mass, which was normally located right below the center of suspension, began to wobble. As the dispute was about the principle, and since the device did *not* correct *slow* perturbations due to coming about, Einstein inquired whether an electromagnetic brake, based upon a conservation principle, would have allowed to keep boats on course. Corrections based upon a universal principle would have been independent of the kind of perturbation.

Einstein assumes that the mechanical impulse can be compensated by the variation of magnetization $d\mathbf{M}/dt$ by virtue of the total angular momentum conservation principle. If magnetization only depends on the magnetic moment $\mathbf{M}_{em} = A\mathbf{I}$[11] due to the electrons circulating in a loop of area A carrying a current I, the mechanical impulse $\mathbf{L}$ and the equivalent magnetic quantity are tied by the relation $d\mathbf{L}/dt = -m/ed\mathbf{M}_{em}/dt = \mathbf{M}_{em} \times \mathbf{H}$. In magnetic saturation conditions, for magnetization $\mathbf{M}$ we have $dL/dt \cong M_{em}B\vartheta$[12]. To evaluate the intensity of the magnetic moment, Einstein and de Haas measure the torsional oscillations of soft-iron cylinders under different experimental settings. In one of them the iron bob is of 7 cm length and 0.17 cm width, and it is sealed to one end of a glass fiber of approx. 8 cm length, that is clamped to a stationary frame on the other end. The bob hangs freely between two Helmholtz coils at a distance of 1 cm connected in series, that can generate an axially symmetric alternating field. They assume $dL/dt = Sd^2\vartheta/dt^2 + R\vartheta$, where ϑ is the angle of rotation of the cylinder, that they read projecting a light beam through the gap between the coils on a mirror fixed on the cylinder itself. S is the moment of inertia of the cylinder, R is the shear modulus of the glass fiber, supposedly independent of the frequency of induced oscillations. From the associated homogeneous equation they get $T = 2\pi\sqrt{(S/R)}$ for the period of free torsion oscillations[13]. Determining S and R, it is possible to find the conversion factor e/m. Modern quantum theory teaches that such factor is not a universal constant, but for the specific case of "free" metal electrons, it is to be fully ascribed to their spin[14]. There is also a more "classical" reason to hold that measure to not yield a universal constant: Until the cylinder oscillations are free, it is correct to hypothesize that R is independent of the frequency. However, since the free torsions of period T correspond to *one* natural frequency of the mechanical system, independence ceases as soon as they are forced at approximately that frequency. Indeed, Einstein and de Haas drive the coils exactly at that frequency, in order to *selectively amplify* torsional oscillations. Furthermore, they obtain steadiness by manually *controlling* the rise of the iron bob oscillations. Without feedback control, one motion would arise seemingly at random, because resonant systems are very sensible to initial and boundary conditions. Leaving aside "resonance amplification", the transient tremble of the pendulum obtained by imparting a single current impulse, is evidence of

[11] The assumption is that the electron is an electromechanical transducer whose efficiency is independent of power and velocity. The current I due to an electron circulating round a coil is $I = -ev/(2\pi r)$. If the enclosed surface measures $A = \pi r^2$, the magnetic moment can be written as: $\mathbf{M}_{em} = IA\mathbf{n} = -\frac{1}{2}e\mathbf{r} \times \mathbf{v}$, where n is the normal to the surface, and $\mathbf{v} = \omega \times \mathbf{r}$. On the other hand, in mechanics, when $d\mathbf{L}/dt = 0$ one has $\mathbf{L} = m\mathbf{r} \times (\omega \times \mathbf{r}) = m[r^2\omega - (\mathbf{r}\omega)\mathbf{r}] = mr^2\omega = S\omega$, where S is the moment of inertia of a mass m at a distance r from the rotation axis. Thus, for low speeds $\mathbf{M}_{em}/\mathbf{L} = -\frac{1}{2}e/m$ is the gyromagnetic ratio of the electron. Assuming, with Bohr, $L = h/(2\pi)$, the Bohr magneton is $\mathbf{M}_B = \frac{1}{2}eh/(2\pi m)$. However, there are two thorny issues. First, the ratio $\mathbf{M}_{em}/\mathbf{L}$ which is assumed to be constant in those measurements. That is correct if the masses don't depend on velocity. The second issue is that conservation principles hold for linear and additive quantities. According to Einstein's and de Haas' analysis, the conservation of the angular momentum $\mathbf{L}$ is related to the areal velocity: $L = m[x(dy/dt) - y(dx/dt)] = mr^2(d\varphi/dt)$. The latter expression results after we put $x = rcos\varphi$, $y = rsin\varphi$, which is not a linear transformation $(x, y) \to (r, \varphi)$ like the ones involving the same energy conservation rule on either coordinate plane. It can be easily seen that kinetic energy depends on geometric coordinates, and it is additive w.r.t. rotations and translations in polar coordinates only: $K = m/2[(dx/dt)^2 + (dy/dt)^2] = m/2[(dr/dt)^2 + r^2(d\varphi/dt)^2] = \frac{1}{2}mv^2 + \frac{1}{2}S\omega^2$.

[12] Einstein & de Haas compensated for the earth's magnetic field. Furthermore, they believed that the soft iron nucleus would magnetize as far as saturation by repeatedly imparting short current impulses to the coils.

[13] We neglected the damping term $Pd\vartheta/dt$, according to their analysis.

[14] The proportionality constant g in $\mathbf{L} = -g(m/e)\mathbf{M}$ is called *Landé g-factor*. Here $g = 2$.

electromagnetic transduction, which is due to the mobile iron core of the coils. Thus, we conclude that the effect that Einstein and de Haas observe is the feedback controlled resonance amplification of an electromagnetically induced torsional oscillation of the iron bob. The latter electromechanical coupling is associated with transduction. It cannot be explained with a universal principle, such as the conservation of angular momentum, because neither the electro-mechanical coupling nor its resonant amplification are linear[15].

6. THE ZEEMAN EXPERIMENT

In order to explain the Zeeman effect, we stem from the magnetic rotatory power discovered by M. Faraday. This vectorial effect of light is observed after completely extinguishing a white light beam passing through a transparent gyroelectric substance between two Nicol prisms, generally called polarizer the first and analyzer the second. When no light is transmitted, the polarizers are said to be crossed. Starting from the crossed condition, the effect consist in this: When applying a magnetic field parallel to the beam, the light resumes transmission, and, in order to extinguish it again, it is necessary to further rotate one of the prisms by an amount that depends on the gyrotropic medium. The effect is ascribed to the rotation of the light polarization plane due to the magnetic field. Much importance used to be given to that interpretation at the time, as it endorsed the representation of magnetism by means of curls. In practice, the only object that effectively rotates is one of the prisms, with respect to the other, and the effect can be described by specifying the angle of displacement from the crossed position. That displacement is approximately *proportional to the applied field* and to the amount of substance. However, it is not essential to apply a magnetic field for the effect to appear; actually, it is at least one order of magnitude greater using birefringent substances, said to be left- or right-handed according to the displacement of the prisms from the crossing position. Apparently, thus, magnets can induce optical birefringence in some substances that don't otherwise show it up.

To be able to observe magnetic rotation, Faraday already "amplified" it by silvering the optically polished surfaces on the beam's path. P. Zeeman pioneered the extension of those observations to gases, sodium vapors, at the beginning. The improvements he introduced concern fields of about 2 tesla generated by circular magnets having a small gap, and replacing silvered surfaces with a Michelson's echelon[16]; both of them contribute to amplification. In an attempt to get a uniform view of Faraday's and Zeeman's effects, let's suppose that, due to the magnet, light beams within a given passband are received with a frequency shift[17] proportional to the field applied. Let's then examine the magnifying effect of the field. Until the field is low, the shift between the spectral maxima is unnoticeable. The band can be visualized as broadening and blandly flickering, if some rhythm is perceived at all. Thus, phase shift could give an alternative explanation for polarization. As the field increases, the band maxima depart from each other because of the persistence of images (spatial echoes), and they appear spatially distinct in the spectrum. Let's now pass on to examine the echelon's contribution to amplification. It consists of the fact that the sodium yellow line, to exemplify that one, gets its frequency characterization from the grating, whose resolving power becomes sharper as the plates' number grows. Even in moderate observation conditions, when no strong non-linear contributions arise from sodium, as sharpness betters the apparent brightness increases, and upper orders and modulations appear from the echelon grating. Thence, some of the multiple lines are to be ascribed solely to the amplification. As today the Zeeman effect is ascribed to rotational levels, according to whether one whishes to observe the electronic multiplet structure or the nuclear hyperfine structure, one elicits and selectively amplifies a purely electromagnetic response at micro or radio waves, respectively [12s]. But in the original experiments, frequencies in the optical range took the role of those that Einstein and de Haas applied to their coils, while the grating allowed to resonantly amplify the optical response, and transduction took place too. To increase light intensity, he put samples to the flames (direct Zeeman effect), or electrically heated and excited them using arc light (inverse Zeeman effect). Indeed, he believed that the smallness of gas responses to light depended not much on their high

[15] According to the above principle, when a balanced flywheel spins uniformly, no forces are applied to its shaft. Geometry accounts for that, telling that centrifugal forces cancel out for symmetry reasons. From the point of view of the linear description, if a rotor is not well balanced, the forces applied to its shaft are apparent forces of the rotating reference frame. As we are suggesting that transduction is non-linearly tied to "structural" resonance effects, we note that they can unbalance the system.

[16] With prisms, that analyze light deploying angular dispersion, the effect wasn't noticed. Diffraction gratings allow to observe dispersion at higher diffraction orders. F. Paschen used Rowland gratings. Zeeman used an auxiliary spectrometer, when possible, besides echelon diffraction grating.

[17] A modulation of the strongest of the received radiations.

intrinsic Q factors, but rather on the low concentration of gas matter. Such processing did not better the matching conditions with the echelon; however, if vapors didn't settle on the optical surfaces of the tube, it purveyed a conspicuous *emission*. Burning and electrical heating have the shortcoming that samples end up being simultaneously excited for an enormous spectral range. In addition, burning was left unspecified from a chemical standpoint. Spectra were interpreted according to Lorentz's theory of the electron instead; that is, the dynamic of a microscopic cyclic system supplied the basis for the interpretation of spectral measurements. Accordingly, the large amount of observed lines was appreciated for its indication of that many degrees of freedom of the relevant oscillation/rotation. The value of e/m[18] could then be derived from the separation of optical multiplets, getting the possibility to compare it with the value obtained from determinations like those of Einstein-de Haas [13]. However, if the statistical analysis of non-interacting atoms agreed with both the interpretation of optical spectra and the functioning of electric engines, then there would be no need to distinguish microcosm from macrocosm[19]. Rather, by accepting that *emissions* bear different characteristics according to the way they have been generated, it makes sense to think that when the *received electromagnetic radiation* comes with a markedly different frequency, the accompanying events have indeed a different origin. For attempting to drive specific material processes at high frequencies, as far as we understand, it is necessary to monitor a band to start with, and successively reduce the artifacts while trying to steadily transfer power to the resonating system using *the same band as a channel*.

7. CONCLUSIONS

We have compared the Einstein-de Haas effect with the Zeeman one, and pointed out that in the former experiment the suspended iron cylinder is a transducer of the electric impulse rhythmically given to the coils into torsional oscillations, while the mechanical interpretation of the latter effect is based on electromagnetic responses at frequencies where mechanical transduction can't happen anymore, or at optical ranges.

As for observing responses, the visual perception of the trembling bob can be considered similar to a Zeeman's transient. However, neither transient can currently be explained in the framework of a theory of signals, if the explanation is meant to be independent of the reception method and derived by decoding the signal. It may well be that natural radiations can only be interpreted by extending the concept of signal.

As for the transduction, Einstein deployed the visual response for controlling an electromechanical conversion process, and, since controlling a phenomenon opens the way for linear analysis, explained it. However, following that approach it is necessary to keep in mind that while Fourier representations of whatever electrical response, even *unrepeatable*, are linear, the same is not true for its accompanying events. Unlike the Einstein-de Haas one, the Zeeman effect is not related to any transduction process. However, since photochemical reactions such as polymerization, hydration, redox, or involving chromophore groups are known, one may hypothesize that they can also be controlled by deploying feedback on the relevant signals.

As for this paper, we can summarize the difference between a mechanical effect, like that observed by Einstein and de Haas, and current instances of the Zeeman effect like so: When carrying out non-invasive cuttings in vivo for medical purposes, on the one hand one understands that the images obtained are *like* the corresponding anatomical sections, most of the latter being obviously obtainable postmortem. On the other hand, patients undergoing "tomographic" sections don't suffer mechanical treatments (dissections), nor are observed using sunlight. All in all, sectional images have a *very different* origin from their anatomical counterparts, even if the interpretation of the signals presented in tomographs today is largely based on the knowledge that has been gathered studying anatomical sections.

[18] If an electron is subject to an elastic force $kr = m\omega^2 r$ and the magnetic force eHv, both expressed in polar coordinates, the equation holds: $kr \pm eHv = m\omega'^2 r$, with $\omega' \approx \omega$. Hence $\pm eHv = \pm eH\omega r = m(\omega'^2 - \omega^2)r$, that is approx. $2\omega/\omega(\omega' - \omega) = \pm e/mH$.

[19] An antenna designer who conceives of an atom as a micro resonant antenna may wonder whether the proportionality that characterizes the linear working of antennas can also be applied to transduction. That is to say, whether electromechanical transduction linearly decreases as the wavelength of light decreases. In facts, there is no great evidence that light can be transduced as-is into mechanical effects. In any case, quantum theory, rather than conceive of the atom as a resonator, assigns to spectral lines an energy proportional to the frequency by means of relations $\lambda\nu = c$ and $W = h\nu$. For the interpretation of nuclear effects with statistical thermodynamics, see also note 6.

REFERENCES

1. Assion, A., T. Baumert, M. Bergt, T. Brixner, B. Kiefer, V. Seyfried, M. Strehle, and G. Gerber, "Control of chemical reactions by feedback-optimized phase-shaped femtosecond laser pulses," *Science*, Vol. 282, 919–922, 1998.
2. Herrero, M. A., J. M. Kremsner, and C. O. Kappe, "Nonthermal microwave effects revisited: on the importance of internal temperature monitoring and agitation in microwave chemistry," *J. Org. Chem.*, Vol. 73, No. 1, 36–47, 2008.
3. Yang, X. Q. and K. Huang, "Study on the key problems of interaction between microwave and chemical reaction," *Front. Electr. Electron. Eng. China*, Vol. 2, No. 4, 473–480, 2007.
4. Cole, K. S. and R. H. Cole, "Dispersion and absorption in dielectrics. I. Alternating current characteristics," *J. Chem. Phys.*, Vol. 9, No. 4, 341–351, 1941.
5. Detwiler, P. B., S. Ramanathan, A. Sengupta, and B. I. Shraiman, "Engineering aspects of enzymatic signal transduction: Photoreceptors in the retinar," *Biophys. J.*, Vol. 79, No. 6, 2801–2817, 2000.
6. Mulligan, Jr., J. H., "The role of network theory in solid-state electronics — Accomplishments and future challenges," *International Solid-State Circuits Conference*, 323–332, Philadelphia, USA, February 1963.
7. Amaral, L. A. N. and J. M. Ottino, "Complex networks. Augmenting the framework for the study of complex systems," *Eur. Phys. J. B*, Vol. 38, 147–162, 2003.
8. Mikulecky, D. C., "The application of electrical network theory to the analysis and simulation of dynamic physiological systems," *IEEE Proceedings of SoutheastCon*, 145–148, Williamsburg, USA, April 1991.
9. Billah, K. Y. and R. H. Scanlan, "Resonance, Tacoma narrows bridge failure, and undergraduate physics textbooks," *Am. J. Phys.*, Vol. 59, No. 2, 118–124, 1991.
10. Mikura, Z., "Variational formulation of the electrodynamics of fluids and its application to the radiation pressure problem," *Phys. Rev. A*, Vol. 13, No. 6, 2265–2275, 1976.
11. Poynting, J. H., "The wave-motion of a revolving shaft, and a suggestion as to the angular momentum in a beam of circularly polarised light," *Roy. Soc. Proc. A*, Vol. 82, 560–567, 1909.
12. Jen, C. K., "The Zeeman effect in microwave molecular spectra," *Phys. Rev.*, Vol. 74, No. 10, 1396–1406, 1948.
13. Scott, G. C., "Review of gyromagnetic ratio experiments," *Rev. Mod. Phys.*, Vol. 34, No. 1, 102–109, 1962.

Scattering Characteristics and Star-shaped Cylinder Parameters Correlation

D. D. Gabriel'yan, **M. Yu. Zvezdina**, **E. D. Bezuglov**,
S. N. Zabelkin, **and M. M. Mednaya**
Rostov Academy of Service of South Russian State University of Economy and Service, Russia

Abstract— The correlation defining geometrical parameters and spectral components of azimuthal harmonics of a surface impedance are received. Results of numerical researches are obtained.

1. INTRODUCTION

An evident progress observed in the all provinces of radioelectronics leads to the necessity of developing the analysis methods for electromagnetic fields of various radiating structures. It relates to the new types of radiating structures in the first place, in particular, to star-shaped cylinder antenna that allows implementing additional degrees of freedom of character change of excited fields distribution in space and managing electromagnetic waves scattering characteristics accordingly. Thus, changing geometric parameters of star-shaped contour allows changing the surface impedance value, surface currents distribution and accordingly changing the scattering characteristics accordingly [1–4].

The paper topic is researching the correlation of contour geometry parameters and vector of the intensity of the electromagnetic field scattered by the surface.

2. SECTION 1

Let us consider an infinite along the element ideally conducting cylinder with a star-shaped cross-section. The cylinder is excited by an electric dipole with moment $\vec{z}I_0 l$. Cross-section contour is described by

$$R(\varphi) = R_0 + \Delta R \cos(N\varphi), \tag{1}$$

where R_0, ΔR, N — the contour geometric parameters. Problem geometry is given by Figure 1.

The surface electric field distribution in the transverse plane is defined by

$$J_m^h(\varphi') = \sum_{m=-\infty}^{\infty} A_m^h \exp(im\varphi'). \tag{2}$$

Herewith according to the boundary problem solution structure given in [5], we use the concept of spectral component of surface count density and decomposition coefficients A_m^h accordingly.

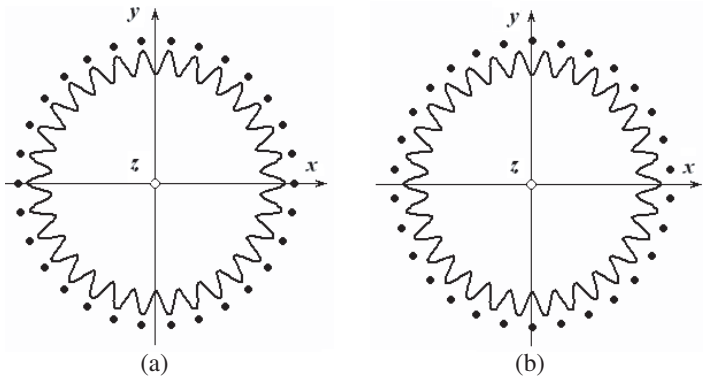

(a) (b)

Figure 1.

Spectral components of tangential components of electric and magnetic field intensities are defined by the following correlations basing on [5]:

$$E^h_{zm} = -\frac{i\beta^2 W_0}{k}\int\limits_0^{2\pi} A_m \exp\left(im\varphi'\right) H_0^{(2)}\left(\beta R\left(\varphi,\varphi'\right)\right) d\varphi' + I_0 l H_0^{(2)}\left(\beta R\left(\varphi,\varphi_0\right)\right), \tag{3}$$

$$H^h_{\varphi m} = \mathrm{rot}\Big(\int\limits_0^{2\pi} A_m \exp\left(im\varphi'\right) H_0^{(2)}\left(\beta R\left(\varphi,\varphi'\right)\right) d\varphi' + I_0 l H_0^{(2)}\left(\beta R\left(\varphi,\varphi_0\right)\right)\Big), \tag{4}$$

where $H_0^{(2)}(\cdot)$ — the zero-order Hankel function of the 2d kind; $W_0 = 120\pi$ Ohm — wave impedance of the free space; $\beta^2 = k^2 - h^2$ — transverse wave number.

Setting the boundary conditions for the tangential components of the electric field intensity on the cylinder surface allows defining the expansion coefficients and thus defining the current distribution on the surface.

Correlations (3) and (4) are the most general representation of the electric field intensity in the free space. To describe and define the far zone fields (directivity patterns) let us use the Hankel function asymptotes [5]

$$H_0^{(2)}(\beta r) \approx (2/\pi\beta r)^{0.5} e^{-i\beta r + i\pi/4}.$$

It allows representing the spectral components of the electric field density as

$$E^h_{zm} = -i\sqrt{\frac{2\beta^3}{\pi r}}\frac{W_0}{k}\int\limits_0^{2\pi} A_m e^{im\varphi' - i\beta r + i\pi/4} d\varphi' + I_0 l\sqrt{(2/\pi\beta R)} e^{-i\beta R + i\pi/4}, \tag{5}$$

$$H^h_{\varphi m} = \mathrm{rot}\Big(\int\limits_0^{2\pi} A_m e^{im\varphi' - i\beta r + i\pi/4} d\varphi' + I_0 l\left(2/\pi\beta R\right)^{0.5} e^{-i\beta R + i\pi/4}\Big), \tag{6}$$

The full electric and magnetic field intensities excited by longitudinal dipole can be defined by the following dependency

$$E_z = (8\pi i)^{-1}\sum_{m=-\infty}^{\infty}\int\limits_{-\infty}^{+\infty} E^h_{zm} e^{-ih|z-z'|} dh, \tag{7}$$

$$H_z = (8\pi i)^{-1}\sum_{m=-\infty}^{\infty}\int\limits_{-\infty}^{+\infty} H^h_{zm} e^{-ih|z-z'|} dh. \tag{8}$$

We can calculate the integrals (7) and (8) using the saddle-point method [5].

Herewith, the correlations (7) and (8) define the value of both the z-component of the electric field intensity and accordingly transverse components of the magnetic field in the far zone.

As it was mentioned earlier, using the suggested construction gives us additional degrees of freedom to manage the scattering fields and, hence, to manage the directivity pattern of the radiating element.

Another opportunity to manage the side and back lobes level is the height of the radiator placing towards the equivalent cylinder border. Herewith, a possible placing of the radiator lower than the equivalent cylinder border guarantees narrowing the directivity pattern and lowering the side and back lobes level.

3. SECTION 2

The research results of the cylinder construction parameters on scattering characteristics allowed educing some interesting regularities. Herewith, placing longitudinal dipoles above the construction crests leads to the widening of the main lobe and increasing the side lobes level. In the meantime

placing the dipoles above the contour gutters makes it possible to narrow the directive pattern main lobe and to lower the side lobes level. Moreover, it is possible to obtain an additional reduction of the side lobes level when placing the dipoles lower than the border of an equivalent cylinder.

The results are shown by patterns on Figures 2 and 3. The directivity patterns of the antenna array of radius equal to 3λ and consisting of 7 and 9 longitudinal electrical dipoles correspondingly with homogeneous amplitude-phase current distribution are shown by the dashed line. As a comparison the directivity patterns of the ideally conducting circular cylinder excited by the corresponding number of longitudinal electric dipoles are given (solid line). All the patterns are normalized to the maximum value of the directive pattern ideally conducting circular cylinder with the corresponding number of dipoles in the array. Parameter $\Delta R = 0.4\lambda$.

The analysis of the given results shows that the main regularities of the contour parameters influence ob the electromagnetic field scattering characteristics defining the antenna array directivity pattern change slightly depending on the dipoles number. So in particular, the lowest value of the directivity pattern level in the area of back and side lobes for the antenna array of 7 and 9 elements is obtained when the distance between the dipole and the gutter bottom is equal to $0.25\lambda \ldots 0.4\lambda$. It is necessary to mention that this kind of reducing the side and back lobes level of the directivity pattern is obtained when the dipoles are placed lower than the equivalent cylinder contour by the value of 0.1λ. The value of reducing the side and back lobes level obtained when using the gutters is equal to 5 ... 8 dB.

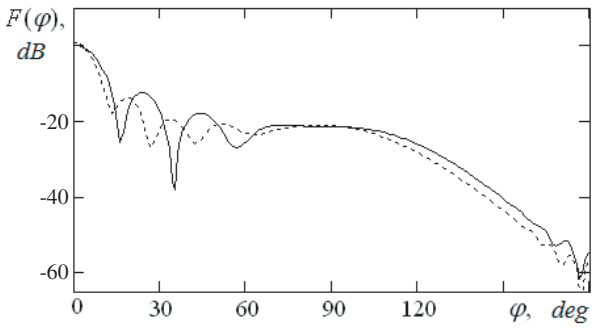

Figure 2.

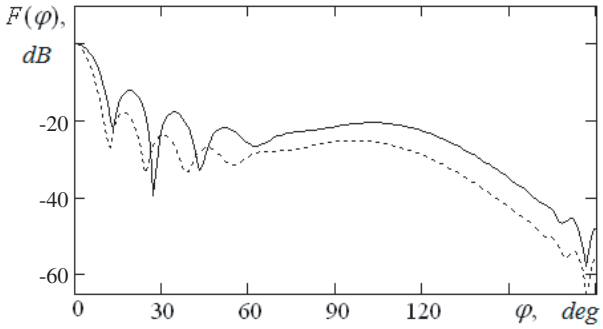

Figure 3.

4. CONCLUSION

The obtained results allow us to make some conclusions. Using cylinder antenna with star-shaped cross-section allows implementing additional degrees of freedom of character change of both excited and scattered fields. The possible places of situating the dipoles are either above the crests or above the gutters of the carrying structure. Placing the longitudinal dipoles above the crests leads to the widening of the main lobe and increasing the side lobes level. In the meantime placing the dipoles above the contour gutters makes it possible to lower the side and back lobes level without widening the directive pattern main lobe. In the paper, it is shown that for the array of 7 elements with the carrying structure radius is 3λ the lowest level of the directive pattern in the area of side and back lobes can be achieved when the distance between the dipole and the gutter bottom is equal to $0.25\lambda \ldots 0.4\lambda$. It is necessary to mention that this kind of reducing the side and back lobes level of the directivity pattern is obtained when the dipoles are placed lower than the equivalent cylinder contour by the value of 0.1λ. The value of reducing the side and back lobes level obtained when using the gutters is equal to 5 ... 8 dB. The gain in reducing the side and back radiation levels remains in case of using the tapered distribution. Similar regularities remain in case of 9 elements antenna array as well as in cases of arrays of alternate number of dipoles.

ACKNOWLEDGMENT

The author is grateful to prof. Boris D. Manuilov for his useful suggestions regarding the improvement of material of this paper.

REFERENCES

1. Mitchell, A., D. M. Kokotoff, and M. W. Austin, "Closed-form expressions for the numerical dispersion and refection in FEM simulations involving," *IEEE Trans. Antennas and Propag.*, Vol. 49, No. 2, 158–164, 2001.
2. Kishk, A. A., "Analysis of hard surfaces of cylindrical structures of arbitrary shaped cross section using asymptotic boundary conditions," *IEEE Trans. Antennas and Propag.*, Vol. 51, No. 6, 1150–1156, 2003.
3. Kishk, A. A., "Electromagnetic scattering from transversely corrugated cylindrical structures using the asymptotic corrugated boundary conditions," *IEEE Trans. Antennas and Propag.*, Vol. 52, No. 11, 3104–3108, 2004.
4. Zvezdina, M. Y., O. S. Labunko, and P. E. Syshoparov, "Impedance characteristics realization by contour parameters changing," *Electromagnetic Waves and Electronic Systems*, Vol. 12, No. 5, 13–15, 2007.
5. Felsen, L. B., N. Marcuvitz, *Radiation and Scattering of Waves*, Part 1, Prentice-hall, Inc., Englwood Cliffs, New Jersey, 1973.

Analytic Conversions in Diffraction Problems on Metal Cylinders with Multilayer Magnetodielectric Coating

D. D. Gabriel'yan, **M. Yu. Zvezdina**, **E. D. Bezuglov**,
S. N. Zabelkin, **and M. M. Mednaya**
Rostov Academy of Service of South Russian State University of Economy and Service, Russia

Abstract— In the paper, basing on the explicit form of the multilayer magnetodielectric cover transmission matrix the evaluation algorithm for the spectral expansion coefficients for tangential components of the electromagnetic field on the external cover border and corresponding surface impedance tensor elements is offered.

1. INTRODUCTION

The solution of electromagnetic wave diffraction problem on multilayer magnetodielectic coating is used in many practical applications, for example, in geomagnetic exploration of the Earth [1] or radio communication antenna creation [2] in particular. The knowledge of the field structure both inside and outside the coating is required in these practical application areas. Usually the problem is solved by joining the fields on layer boundaries using the numerical methods. But this kind of solution has a number of disadvantages. In particular, computational costs related to the obtaining the system residue waves as well as to the defining the structure fields are rather huge. Using the known numerical methods either makes it impossible to obtain the residue wave frequencies or are ineffective when modeling the coating with the large number of layers.

We suggest using a convolution algorithm to get rid of the disadvantages listed above. The algorithm was proposed by L. M. Brehovskih [3] for the case of plane layered media. In the work of J. R. Wait [1] it was proposed to use the algorithm for the case of excitation of multilayer magnetodielectric coatings on metal cylinder by slot radiators. The convolution algorithm makes it possible to reduce the analysis of the given multilayer coating field to the analysis of the equivalent coating of the same thickness but consisting of less layers. Decreasing the layers quantity makes it possible to hold the computational costs down while preserving the field structure within the layers provided by transmission matrix in the first place. Secondly, it allows obtaining the dispersion equation solution in a closed form by not complicated analytic transformations. Thirdly, it allows obtaining in a closed form the correlations that describe tangential components of electromagnetic field on the outer border of the coating. The last one allows linking the surface impedance tensor element values to the multilayer coating parameters and, thus, widening the research area of the coating design variations.

In the paper, the extension of the convolution algorithm to the case of an arbitrary source type and its arbitrary position towards the layers of the multilayer coating is given. As an example the expressions obtained by the usage of the algorithm when describing the multilayer magnetodielectric coating situated on a circular metal cylinder are given.

2. SECTION 1

Let us consider the infinite along the element ideally conducting circular cylinder of radius a with the coating consisting of $M+1$ concentric layers defined by the coordinates $\Omega_j = \{(\rho, \varphi, z) : \rho \in (\rho_j, \rho_{j+1}), a < \rho, z < \infty\}$ and made of magnetodielectric materials with relative electric and magnetic permittivity ε_j, μ_j $(j = 1, 2, \ldots, M+1)$ correspondingly. The layer count starts from the surface of the metal cylinder and the outer border of the $M+1$-th layer, with the parameters $\varepsilon_{M+1} = \mu_{M+1} = 1$, goes to $+\infty$ for describing the semi-infinite area. The structure is regular along the cylinder element. Arbitrary directed elementary source centered at $Q(\rho^0, \varphi^0, z^0)$ in the cylinder coordinate system $0\rho\varphi z$, 0z axis is parallel to the cylinder element, is situated in the p-th coating layer ($p = 1, 2, \ldots, M+1$), as it is shown in the Figure 1. It is necessary to obtain the field excited by the harmonic signal source in the arbitrary point with the coordinates $P(\rho, \varphi, z)$, satisfying the Maxwell equations and the radiation conditions at the infinity. Time factor $\exp(i\omega t)$ is omitted.

Let us find the solution of the formulated problem using the partial area method [4] by separating $M+1$ areas with the borders coinciding to the ones of the concentric layer coatings. Let us represent the field as the composition of incident and scattered (secondary) waves in the area that includes

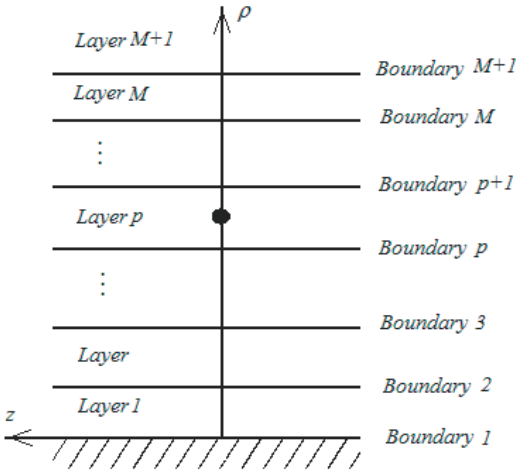

Figure 1: Problem geometry.

the source and as the secondary waves only — in other areas. Scattered field excluding the M+1-th area is the total of the waves radially propagating into two opposite directions. In $M+1$-th area under the Sommerfeld conditions the field is the composition of the waves going to the infinity only.

Using the spectral field representation for LM and LE waves as well as the continuity conditions for the tangential components of the electric and magnetic field at the interface of the layers and using the boundary conditions on the ideally conducting surface [4] in case of metal cylinder the linear algebraic equation system can be easily obtained regarding the azimuth field modes (index m):

$$[P_m(\rho)]K_m = F_m(\rho), \tag{1}$$

where $F_m(\rho) = (F_m^\rho(\rho)\ \ F_m^\varphi(\rho)\ \ F_m^z(\rho))^T$ — is the block column-vector describing the tangential components of the electric and magnetic fields on the layer boundaries for the ξ-components of the vector source ($\xi = \rho, \varphi, z$). From now on "T" designates operation of transposition. Vector elements look like:

$$F_m^{\xi(j)}(\rho) = \left(E^{(j)}_{z\xi\,m}(\rho) \quad E^{(j)}_{\varphi\xi\,m}(\rho) \quad H^{(j)}_{z\xi\,m}(\rho) \quad H^{(j)}_{\varphi\xi\,m}(\rho)\right)^T \tag{2}$$

and they are the dielectric and magnetic field intensities excited by the given source in the infinite media with the parameters ε_j, μ_j in the points corresponding to the interface. Column-vector K_m defines the unknown spectral expansion coefficients:

$$K_m(\rho) = \left(K_m^\rho(\rho) \quad K_m^\varphi(\rho) \quad K_m^z(\rho)\right)^T, \tag{3}$$

where the ξ-component for the j-th layer describes the expansion coefficients:

$$K_m^{\xi(j)}(\rho) = \left(c^{(j)}_{\xi\,m} \quad d^{(j)}_{\xi\,m} \quad a^{(j)}_{\xi\,m} \quad b^{(j)}_{\xi\,m}\right)^T. \tag{4}$$

Block matrix $|[P_m(\rho)]$ defines the influence of the layer parameters on the electromagnetic field components:

$$[P_m^(\rho)] = \mathrm{diag}(\ [P_m^\rho] \quad [P_m^\varphi] \quad [P_m^z]\ ). \tag{5}$$

Block matrix elements $[P_m^\xi]$ describe the correlation of the fields of the ξ-th components of the vector source with the electrodynamical layer parameters. The dimension of the elements depends on the number of the coating layers. For j-th layer ($j = 1, 2, \ldots, M$) of ξ-th block the matrix element is defined by

$$\underline{P}_m^{\xi(j)}(\rho) = \begin{pmatrix} p_{11}^{\xi(j)} & p_{13}^{\xi(j)} & p_{11}^{\xi(j)*} & p_{13}^{\xi(j)*} \\ p_{12}^{\xi(j)} & p_{14}^{\xi(j)} & p_{12}^{\xi(j)*} & p_{14}^{\xi(j)*} \\ -p_{13}^{\xi(j)} & p_{11}^{\xi(j)} W_j^{-2} & -p_{13}^{\xi(j)*} & p_{11}^{\xi(j)*} W_j^{-2} \\ -p_{14}^{\xi(j)} & p_{12}^{\xi(j)} W_j^{-2} & -p_{14}^{\xi(j)*} & p_{12}^{\xi(j)*} W_j^{-2} \end{pmatrix}. \tag{6}$$

Here "*" denotes complex conjugation operation, executed on the cylinder function only; W_j is the natural impedance of the j-th layer. The values of the $p_{11}^{\xi(j)}$, $p_{12}^{\xi(j)}$ and $p_{13}^{\xi(j)}$, $p_{14}^{\xi(j)}$ elements describe the diffraction field. In the M+1th layer the dimension of the vectors described by the correlations (4) and (6) is twice as little because of the radiation conditions execution in the free space.

3. SECTION 2

The analysis of the coefficients $[\underline{P}_m^{\xi}]$ matrix structure described in (6) shows that the matrices are block bidiagonal banded matrix with the exception of the first layer [5]. When using the direct approach to matrix inversion the order of the system under consideration depends on the number of coating layers M and in case of vector source is equal to $4M-1$. If it's not necessary to obtain fields inside homogeneous layers containing no extraneous sources then the algorithm suggested in [1, 3] can be used. The algorithm is based upon the recurrence relations binding the fields on the neighboring layer borders and allows replacing the field influence in the layer sequence by the transmission matrix. The algorithm application limitations are requirement of the layer homogeneity and the absence of the extraneous sources in the layers.

The convolution algorithm is formulated in the following manner:

1. Only the layers free of the extraneous sources can be subjected to the convolution.
2. The convolution starts at the most remote layers from the one containing the extraneous source and is carried out towards the source.
3. Depending on the mutual disposition of the convoluted layers with the radius described by variables ρ_j and the extraneous source placed on the distance of ρ^0 from the cylinder center the transmission matrix can be calculated as:

$$\overline{P}_m = (-1)^{ns} \begin{cases} P_m^{+(is)}(\rho_{is+1}) \prod\limits_{i=is+1}^{ns+is} \left\{ [P_m^{-(i)}(\rho_i)]^{-1} P_m^{+(i)}(\rho_{i+1}) \right\}, & \rho^0 < \rho_j \\ P_m^{-(ns+is)}(\rho_{ns+is+1}) \prod\limits_{i=is+1}^{ns+is} \left\{ [P_m^{+(i)}(\rho_{i+1})]^{-1} P_m^{-(i)}(\rho_i) \right\}, & \rho^0 > \rho_j \end{cases} \tag{7}$$

   Indexes "is" and "ns" define the numbers of the borders of the layer where the convolution begins and the quantity of the layers subjected to the operation; "+" and "−" signs show from which border (the upper one "+" or the lower one "−") the coefficients are calculated.
4. In the right part of the equation system, the elements $F_m^{\xi(j)}$ of the layers that are immediately adjacent to the source layer remain unchanged even when the layer is excluded.

As the result of the convolution instead of the real coating, we obtain equivalent in width but containing less layers. The quantity of the equivalent coating layers can be equal to one, two or three depending on the sourse position. So, when the extraneous source is placed in the free space (M+1-th layer) the equivalent coating consists of one layer. If the source is placed in the layer adjacent to metal or free space, then the layers number in the equivalent coating is equal to two. In all other cases the equivalent coating consists of three layers.

4. SECTION 3

The reduction of the layer quantity where it is necessary to define the field structure allows not only decreasing computational costs significantly but obtaining analytic correlations for tangential components of the fields on the coating outer border. These correlations make it possible to bind the surface impedance tensor elements to the electrodynamic parameters of the coating. So, for the initial coating with the number of layers equal to $M = 2$ for an elemental electric dipole oriented in parallel to the coated cylinder body element matrix (6) is given by:

$$\begin{bmatrix} P1_m^{+(1)}(\rho_1) & P2_m^{+(1)}(\rho_1) & 0 \\ \tilde{P}211_m^{-(2)}(\rho_2) & \tilde{P}212_m^{-(2)}(\rho_2) & \tilde{P}31_m^{+(3)}(\rho_3) \\ \tilde{P}221_m^{-(2)}(\rho_2) & \tilde{P}222_m^{-(2)}(\rho_2) & \tilde{P}32_m^{+(3)}(\rho_3) \end{bmatrix}. \tag{8}$$

"$\sim$" symbol denotes that the matrices are to be multiplied by the transmission matrix as a result of (7) depending on the source position. The convolution algorithm application makes it possible

to write down the correlations for spectral expansion coefficients for the fields on the coating outer border as matrix equation

$$K_m^{z(M+1)} = -N\left(A2 \cdot A1^{-1}C1 - C2\right), \tag{9}$$

$$N = \left(\tilde{P}32_m^{+(3)}(\rho_3) - A2 \cdot A1^{-1}\tilde{P}31_m^{+(3)}(\rho_3)\right)^{-1}, \tag{10}$$

$$A1 = \tilde{P}212_m^{-(2)}(\rho_2) - \tilde{P}211_m^{-(2)}(\rho_2)\left(P1_m^{+(1)}\right)^{-1} P2_m^{+(1)}(\rho_1), \tag{11}$$

$$A2 = \tilde{P}222_m^{-(2)}(\rho_2) - \tilde{P}221_m^{-(2)}(\rho_2)\left(P1_m^{+(1)}(\rho_1)\right)^{-1} P2_m^{+(1)}(\rho_1), \tag{12}$$

$$C1 = F2_m^z - \tilde{P}211_m^{-(2)}(\rho_2)\left(P1_m^{+(1)}(\rho_1)\right)^{-1} F1_m^z, \tag{13}$$

$$C2 = F3_m^z - \tilde{P}221_m^{-(2)}(\rho_2)\left(P1_m^{+(1)}(\rho_1)\right)^{-1} F1_m^z, \tag{14}$$

$$F^z = [\ F1^z \quad F2^z \quad F3^z\ ]^T. \tag{15}$$

The solution of the Equation (9) can be obtained analytically by using the substitution method to block matrices [5]. We do not cite the solution formula because of its awkwardness.

5. CONCLUSION

The offered convolution algorithm extension obtained for the case of arbitrary radiator orientation placed arbitrary near the multilayer coating allows replacing the initial coating by the equivalent one containing less layers when modeling the structure of the excited electromagnetic field. Herewith computational costs reduce significantly. Moreover, correlations describing tangential components of the field on the coating outer border can be obtained in the closed form. These correlations bind multilayer coating parameters and surface impedance tensor elements together.

ACKNOWLEDGMENT

We are grateful to Prof. Boris D. Manuilov and Prof. Valery P. Sizov for their useful suggestions regarding the improvement of material for this paper.

REFERENCES

1. Wait, J. R., "General solution for excitation by slotted aperture source in conducting cylinder with concentric layering," *IEEE Trans. in Microw. Theory and Techn.*, Vol. 35, No. 3, 321–325, 1987.
2. Zvezdina, M. Yu., O. S. Labunko, and S. N. Zabelkin, "Surface impedance evaluation algorithm for multilayer magneto dielectric cover of circular metallic cylinder," *An International Journal Electromagnetic Waves and Electronic Systems*, Vol. 12, No. 5, 16–21, 2007.
3. Brehovskih, L. M., *Waves in Layered Media*, Academy of Sciences URSS, 1957.
4. Vainstein, L. A., *Electromagnetic Waves*, M.: Radio and Svyaz', 1988.
5. Horn, R. A. and C. R. Johnson, *Matrix Analysis*, Cambridge University Press, 1986.

Nonstandard Refraction of Light from 1-D Quasi-periodic Surfaces

Zu-Han Gu[1] and Anting Wang[2]

[1]Surface Optics Corporation, 11555 Rancho Bernardo Road, San Diego, CA 92127, USA
[2]Department of Physics, University of Science & Technology of China, Hefei, Anhui 230026, China

Abstract— Not only do meta-materials have the properties of negative refraction, the planar designer surfaces have shown some of these properties as well [1]. Recently, we have undertaken an experimental study of nonstandard refraction of light from one-dimensional dielectric quasi-periodic surfaces. The mechanism behind this is the large local slope of the quasi-periodic surface that causes the nonstandard refraction.

1. INTRODUCTION

The negative index materials (NIM) have shown some unusual properties, such as an inverse Snell's law, which can be applied to the construction of a perfect lens for sub-wavelength imaging, a perfect corner cube, and many other applications [2, 3]. Not only meta-materials have the properties of negative refraction; a metal-dielectric-metal structure [4] and the planar designer surfaces [1] have also shown some of these properties.

Recently, we have undertaken an experimental study of nonstandard refraction of light from a one-dimensional dielectric quasi-periodic surface which is defined by the function $\zeta(x) = -\zeta_0 \cos[2\pi/a(x + bx^3)]$, in the finite interval $(-L/2.\ L/2)$, with $\zeta_0 = 1.0\,\mu\text{m}$, $a = 25.0\,\mu\text{m}$, $b = 0.0001\,\mu\text{m}^{-2}$, and $L = 300\,\mu\text{m}$. Such a surface was used to show enhanced backscattering from one-dimensional deterministic surfaces. [5] Since the quasi-periodic surfaces that we used have large local slopes, the nonstandard refraction of light is measured.

2. THE SCATTERING SYSTEM

We consider the transmission of light through a 1-D corrugated film. The scattering system consists of three regions (Figure 1), namely, a flat transparent glass substrate in the region $z > H$ (Region I), a dielectric film in the region $H > z > \zeta(x)$ (Region II), and air in the region $z < \zeta(x)$ (Region III). The flat transparent glass substrate, dielectric film, and air are characterized by real positive dielectric constants ε_1, ε_2 and ε_3, respectively. The surface profile function $\zeta(x)$, which defines the dielectric/air interface through the equation $z = \zeta(x)$, is assumed to be a differentiable single-valued function of x.

We assume that this system is illuminated from the region $z > H$ by an s-polarized monochromatic plane wave, whose plane of incidence is the x-z plane. The single nonzero component of the electric vector of the incident field is given by

$$\psi_{inc}(x, z) = \exp\left[ikx - i\alpha_1(k)z\right], \tag{1}$$

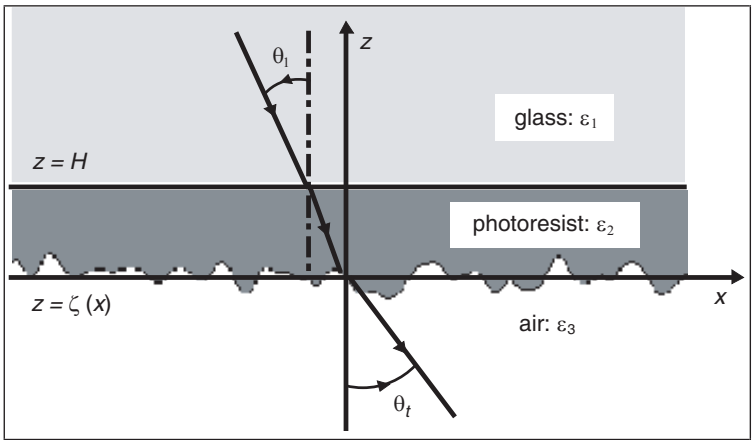

Figure 1: Schematic of the scattering problem considered.

with

$$k = (\omega/c)n_1 \sin\theta_1, \tag{2}$$

and

$$\alpha_1(k) = (\omega/c)n_1 \cos\theta_1, \tag{3}$$

where ω is the frequency of the incident field, c is the speed of light in vacuum, and the refractive index of the transparent glass substrate is $n_1 = \sqrt{\varepsilon_1}$.

The transmitted amplitude from Region II to Region III at the interface $z = \zeta(x)$ is [6–8]

$$T_0(q|k) = \frac{|\gamma(q|k)|\,\psi_0(k)}{\alpha_3(q)\,[|\gamma(q|k)| + |\beta(q|k)|]} \left\{ \frac{|\beta(q|k)|}{|\alpha_3(q) - \alpha_2(k)|} + \frac{\beta(q|k)}{\alpha_3(q) - \alpha_2(k)} \right\}, \tag{4}$$

where the functions $\psi_0(k)$, $\gamma(q|k)$, and $\beta(q|k)$ are defined as

$$\psi_0(k) = \frac{2\alpha_1(k)\exp[i\alpha_2(k)H]}{\alpha_1(k) + \alpha_2(k)} \tag{5}$$

$$\gamma(q|k) = qk + \alpha_3(q)\alpha_2(k) - \varepsilon_2\frac{\omega^2}{c^2}, \tag{6}$$

$$\beta(q|k) = \varepsilon_3\frac{\omega^2}{c^2} - qk - \alpha_3(q)\alpha_2(k). \tag{7}$$

We introduce the angle of transmission θ_t, measured anticlockwise from the $-z$ axis, by

$$q = (\omega/c)n_3 \sin\theta_t, \tag{8}$$

so that

$$\alpha_3(q) = (\omega/c)n_3 \cos\theta_t. \tag{9}$$

$\alpha_2(k)$ is the z component of the wave vector of the transmitted wave in Region II,

$$\alpha_2(k) = (\omega/c)\left[n_2^2 - n_1^2\sin^2\theta_1\right]^{1/2}. \tag{10}$$

The refractive indices of the dielectric film and air are $n_2 = \sqrt{\varepsilon_2}$ and $n_3 = \sqrt{\varepsilon_3}$, respectively.

We can write the transmitted field in the far field in the form

$$T(q|k) = T_0(q|k)\int_{-\infty}^{+\infty} dx \exp\left[-i(q-k)x\right]\exp\left\{i\left[(\alpha_3(q) - \alpha_2(k)\right]\zeta(x)\right\}, \tag{11}$$

and the far-field transmitted intensity distribution can express in the form

$$I(q|k) = \frac{c^2 n_3}{16\pi\omega}\left|T(q|k)\right|^2. \tag{12}$$

3. EXPERIMENTAL TECHNIQUES AND RESULTS

The sample that we used is a one-dimensional dielectric quasi-periodic surface that was fabricated in our lab. After glass plates are chemically cleaned, they are spin-coated for approximately 20–30 seconds with Shipley 1050 photoresist. The plates are then baked in an oven at 100°C for one hour. The photoresist plate is mounted on a pair of motorized orthogonal translation stages, and the grooves are etched in a raster scanning manner which is controlled by a PC computer. We use the same function $\zeta(x)$ and parameters shown in the introduction. Each minimum is 0.1 μm along the direction perpendicular to the groove and in steps of 1 μm along the groove direction. The illuminating source is an Argon ion laser with a wavelength of 0.457 μm. When the beam is well focused, the minimum size of the groove width can be reduced to the order of 2 μm. After exposure, the plates are processed with 351 Shipley developer for 2.5 minutes. The sample is then characterized using a Dektak 3030 stylus profilometer. The size of the sample that we made is about 4.5 mm by 4.5 mm, and consists of 15 identical 1-D quasi-periodic surfaces. The maximum value of the slope of the fabricated 1-D quasi-periodic surface is over 1.0, which is almost the same as the slope of the stylus tip.

The transmission experiments were conducted with a fully automated bi-directional reflectometer. It is configured to measure the angular dependence of light transmitted through the sample. Our illumination beam size is about 5 mm in diameter, which almost covers the entire sample. However, we cover the sample with metal taps and leave only a $200 \sim 300\,\mu$m slit open. We use a laser with a wavelength of $0.53\,\mu$m and permit in-plane measurements for any combination of angles in incidence and transmitting over the entire plane. We present the results for the s-polarized illumination.

Figure 2 shows the selected quasi-periodic surface region for measurement. The light is incident from vacuum with an incident angle θ_0 to the glass, which is the back surface of the sample, with a refracting angle θ_1, then passes through photoresist to the vacuum again. The transmitted beam in the air is measured with an angle of transmission θ_t.

The measurements for the s-polarized illuminations are shown in Figure 3. Here the far-filed in-plane transmission measurement was measured with the incident angle $\theta_0 = -20°$. Due to an ample amount of finite flat shoulders on the sample (see Figure 2), correspondingly, there is a large specular transmission peak at $\theta_t = -20°$ with a pair of side lope. Meanwhile, there is another peak at $\theta_t' = 20°$ which is the non-standard refraction from a 1-D dielectric quasi-periodic surface. We have also made measurements with the incident angles $\theta_0 = -4°$, $-6°$, and $-8°$. Figure 4 shows the relation for non-standard refraction with incident angle for a 1-D quasi-periodic surface at s-polarization.

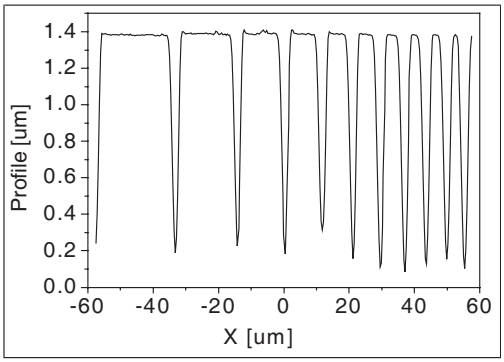

Figure 2: The quasi-periodic surface with $[-150\,\mu$m to $-35\,\mu$m] region.

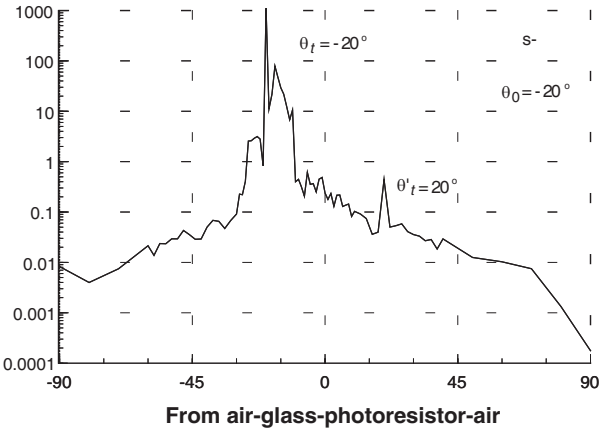

Figure 3: Transmission measurement for a 1-D quasi-periodic surface with an incident angle $\theta_0 = -20°$ for s-polarization.

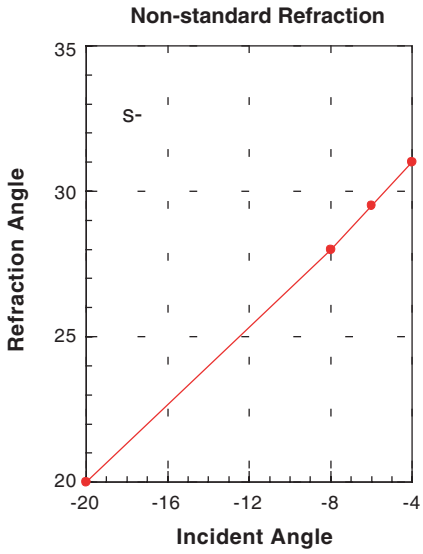

Figure 4: Non-standard refraction for 1-D quasi-periodic surface at s-polarization.

4. CONCLUSION

We report the observation of nonstandard refraction of light from one-dimensional dielectric quasi-periodic surfaces. The one-dimensional dielectric quasi-periodic surface is illuminated from the photoresist side, entering the sample from air through the glass plate [9, 10]. The nonstandard refraction of light is measured around the anti-specula direction for s-polarization; mainly it is due to local slopes at a dielectric-air interface.

To summarize, we have taken advantage of the quasi-periodic grating, there are not any order diffractions except the specular transmission, which is suitable to produce nonstandard refraction of light. The mechanism behind this is that the large local slope of the quasi-periodic surface causes the nonstandard refraction. The large difference between the dialectic constant of two contact mediums enhances the phenomenon as well.

ACKNOWLEDGMENT

The partial support from AFRL Grant FA9453-08-C-0230 is appreciated.

REFERENCES

1. Leskova, T. A., A. A. Maradudin, and I. Simonsen, "The design of random surfaces that produces nonstandard refraction of light," *Proc. of SPIE*, 7065–06, 2008.
2. Veselago, V. G., "The electrodynamics of substances with simultaneously negative values of ξ and μ," *Sov. Phys. Usp.*, Vol. 10, 509–514, 1968.
3. Pendry, J. B., "Negative refraction makes a perfect lens," *Phys. Rev. Lett.*, Vol. 85, 3966, 2000.
4. Shin, H. and S. Fan, "All-angle negative refraction for surface plasmon waves using a metal-dielectric-metal structure," *Phys. Rev. Lett.*, Vol. 96, 073907, 2006.
5. Josse, M., F. Pincemin, A. A. Maradudin, J. Q. Lu, and Z.-H. Gu, "Enhanced backscattering from one-dimensional deterministic quasi-periodic surfaces," *J. Opt. Soc. Am. A*, Vol. 13, No. 19, 1877–1883, 1996.
6. Maradudin, A. A., E. R. Méndez, and T. A. Leskova, *Designer Surfaces*, Elsevier Amsterdam, in press, 2008.
7. Gu, Z.-H. and A. Wang, "Experimental reconstruction for inverse scattering of onedimensional surfaces," *Proc. of SPIE*, Vol. 6672, 66720H, 2007.
8. Wang, A., T. Leskovo, A. Maradudin, and Z.-H. Gu, "Reconstruction of a 1-D surface from inverse transmission," *J. Opt. Soc. Am. A*, Vol. 25, No. 7, 1722–1727, July 2008.
9. Luna, R. E., E. R. Mendez, J. Q. Lu, and Z.-H. Gu, "Enhanced backscattering due to total internal reflection at a dielectric-vacuum interface," *Journal of Modern Optics*, Vol. 42, No. 2, 257–269, 1995.
10. Gu, Z.-H., J. Q. Lu, A. Martinez, E. R. Mendez, and A. A. Maradudin, "Enhanced backscattering from an one-dimensional rough dielectric grating on a glass substrate," *Optics Letters*, Vol. 19, No. 9, 604–606, May 1994.

Multiple Scatter of Vector Electromagnetic Waves from Random Surfaces with Infinite Slopes Using the Kirchhoff Approximation

N. C. Bruce
Centro de Ciencias Aplicadas y Desarrollo Tecnológico
Universidad Nacional Autónoma de México, México

Abstract— This paper presents double-scatter calculations of a new formulation of the 3D Kirchhoff approximation which allows calculation of the scattering of vector waves from perfectly conducting 2D rough surfaces containing structures with infinite slopes. This type of surface has applications, for example, in remote sensing and in testing or imaging of printed circuits. The results of some preliminary example calculations are presented.

1. INTRODUCTION

Surfaces with infinite surface slopes are of interest in many areas of research, for example printed circuits [1] or pattern surfaces used for growing nanostructures [2]. Numerical methods have been presented for calculating the light scattered from 1D surfaces with infinite slopes using modal methods [3], rigorous coupled-wave analysis [1] and integral equation methods [4]. These methods have problems for their generalization to scattering from 2D surfaces. Simpler geometrical optics methods (ray-tracing or specular point theory) have been presented for 2D surface scattering problems [5, 6], but they are limited in the range of surface structure size for accurate results and, of course, do not include diffraction effects. The Kirchhoff approximation [7] has been one of the most popular methods for calculating the scattering of light from rough surfaces for many years. However, the types of surface studied in this paper, with infinite slope, produce instabilities in the Kirchhoff approximation due to mean surface sampling problems and to the presence in the Kirchhoff integral of a term which is proportional to the slope. Recently a reformulation of the Kirchhoff method was presented for 1D rough surfaces which permits the multiple scatter calculation for infinite-slope surfaces and vector-electromagnetic single scattering in 2D rough surfaces [8]. In this paper we present the double scatter method for perfectly-conducting 2D rough surfaces with infinite slope.

2. THEORY

To calculate the vector-electromagnetic scattering in rough surfaces the Stratton-Chu equation is used [9]. For a perfectly conducting surface, the Kirchhoff approximation applied to the Stratton-Chu equation gives

$$\mathbf{E}_{sc}(\mathbf{r}) = -2\mathrm{i}k\eta \int_S \left(\mathbf{n} \times \mathbf{H}_{\mathrm{inc}}\left(r'\right)\right) \frac{\exp\left(-\mathrm{i}kr\right)}{4\pi r} \mathrm{d}S' \tag{1}$$

where $\mathbf{E}_{sc}(\mathbf{r})$ is the scattered electric field at position $\mathbf{r}$, k is the wave number, $\eta = (\mu/\varepsilon)^{1/2}$, $\mathbf{n}$ is the surface normal at position r' on the surface, and $\mathbf{H}_{\mathrm{inc}}(r')$ is the incident magnetic field on the surface S'. As in the case of 1D surface scattering from infinite-sloped surfaces, here the term which determines if the integral can be evaluated for infinite slopes is the combination $\mathbf{n}\mathrm{d}S'$. For a 2D surface, the normal can be written (see Figure 1)

$$\mathbf{n} = \frac{\mathbf{x} \times \mathbf{y}}{|\mathbf{x} \times \mathbf{y}|} = \frac{1}{\sin\theta}\left(-\sin\beta\,\cos\alpha,\, -\cos\beta\sin\alpha,\, \cos\beta\cos\alpha\right) \tag{2}$$

Using the definitions from Figure 1, the factor $\mathbf{n}\mathrm{d}S'$ can be written as

$$\mathbf{n}\mathrm{d}S' = \left(-\mathrm{d}y\,\mathrm{d}h_x,\, -\mathrm{d}x\mathrm{d}h_y,\, \mathrm{d}x\mathrm{d}y\right) \tag{3}$$

Substituting Equation (3) into Equation (1) gives three integrals and the surface slope will not appear explicitly in any of these terms. The integrations are over the combinations of variables $\mathrm{d}y\mathrm{d}h_x$, $\mathrm{d}x\mathrm{d}h_y$ and $\mathrm{d}x\mathrm{d}y$. If, for example, a surface segment has $\mathrm{d}x = 0$, i.e., a vertical wall parallel to the y-axis, only the first integral of variables $\mathrm{d}y\mathrm{d}h_x$ will contribute to the total scattered field

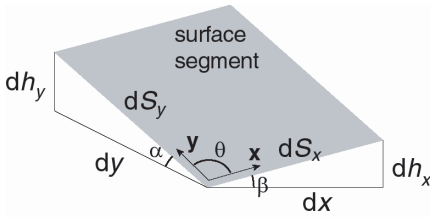

Figure 1: The geometry of a segment of a 2D surface.

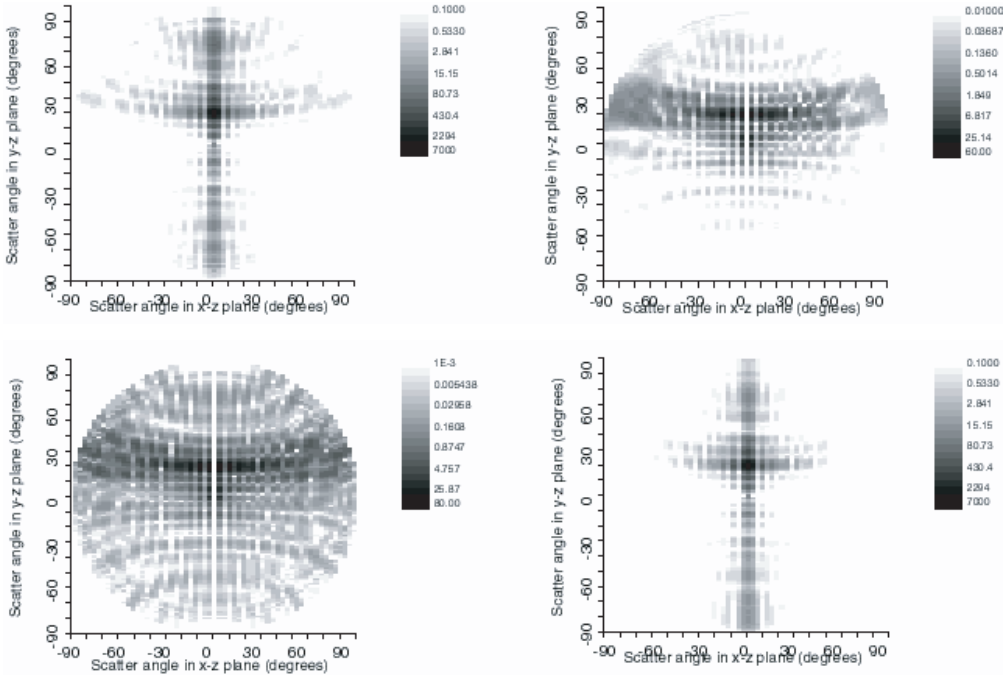

Figure 2: The single scattered intensities for a single groove in a perfectly conducting surface on a log scale of intensity. Incidence angle is 20°. Top left, polarization HH; top right, HV; bottom left, VH; bottom right, VV.

giving the correct contribution for this part of the surface. The combination of Equation (3) with Equation (1) gives the single scatter contribution to the total scattered field.

To calculate the double scatter contribution the scattered field from one point on the surface onto another point on the surface is required. Using Equation (1) this term can be written as

$$\mathbf{E}_{sc}^{(1)}(\mathbf{r}) = -2\mathrm{i}k\eta\left(\mathbf{n}_1 \times \mathbf{H}_{\mathrm{inc}}^{(1)}(r_1)\right)\frac{\exp(-\mathrm{i}kr_{12})}{4\pi r_{12}} \tag{4}$$

where the index 1 indicates scattering from the first surface point and r_{12} is the distance between the first and second surface scattering points. This scattered field, Equation (4), is then incident on the second surface scattering point

$$\mathbf{E}_{sc}^{(2)}(\mathbf{r}) = -2\mathrm{i}k\eta\left(\mathbf{n}_2 \times \mathbf{H}_{\mathrm{inc}}^{(2)}(r_2)\right)\frac{\exp(-\mathrm{i}kr_{2d})}{4\pi r_{2d}} \tag{5}$$

with the index 2 signifying the second surface scattering point and r_{2d} being the distance between the second surface point and the detector.

Substituting (4) in (5), assuming that the detector is in the far field, and integrating over all combinations of first and second points (except when the two points are the same), the total double scattered field is given by

$$\mathbf{E}_{sc}^{(2)}(\mathbf{r}) = -\frac{k^2}{4\pi^2}\frac{\exp(\mathrm{i}kr)}{r}\iint_S\left(\mathbf{n}_2\times\mathbf{k}_{12}\times\mathbf{n}_1\times\mathbf{k}_{inc}\times\mathbf{E}_{\mathrm{inc}}^{(1)}(r_1)\right)\exp(-\mathrm{i}\mathbf{k}_{sc}\cdot\mathbf{r}_2)\frac{\exp(-\mathrm{i}kr_{12})}{4\pi r_{12}}\mathrm{d}S_1\mathrm{d}S_2 \tag{6}$$

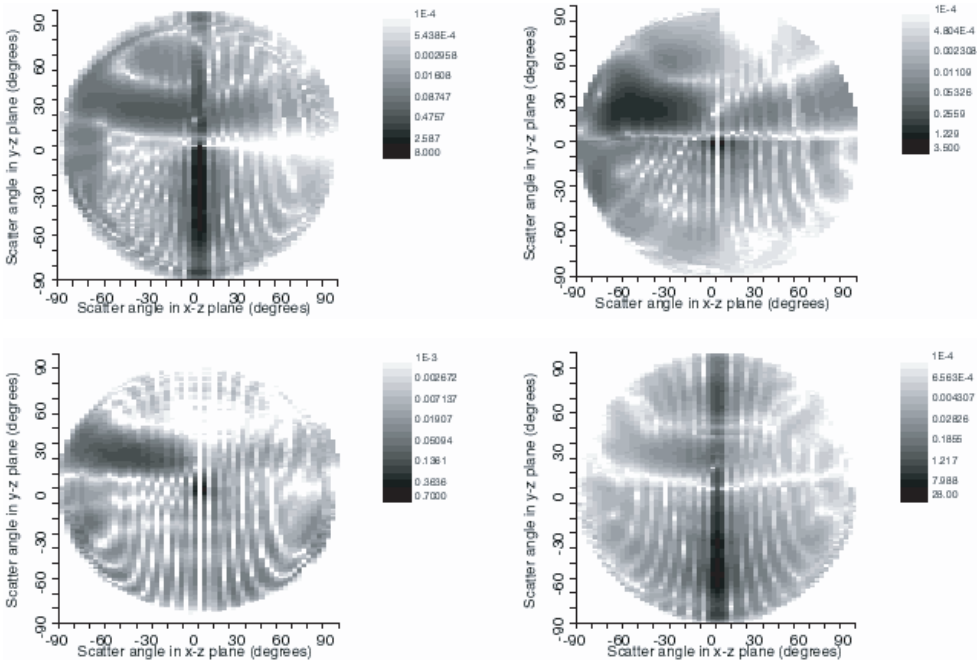

Figure 3: As Figure 2, but for the double scattered intensities.

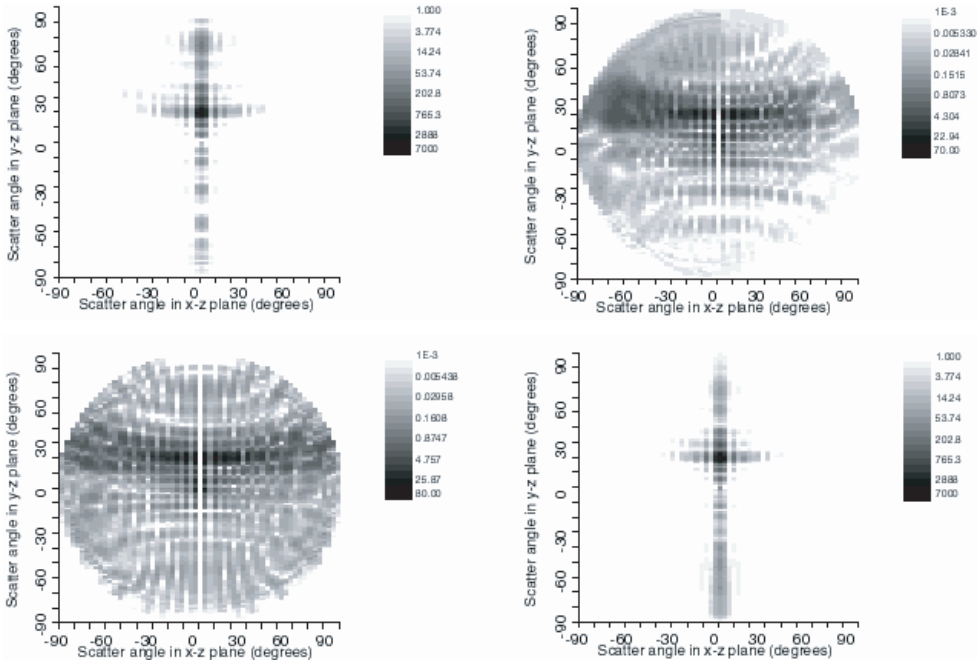

Figure 4: As Figure 2, but for the total (single + double) scattered intensities.

where r is the distance between the coordinate origin and the detector and $\mathbf{r}_2$ is the vector position of the second surface scattering point relative to the coordinate origin. Equation (6) is the expression used to calculate the double scattered field in this paper, with both surface normal vectors in the form given by Equation (3). Shadowing is included explicitly by raytracing to determine which points are illuminated and visible.

3. RESULTS

Here we present results of the numerical calculation of the single and double scattered intensities for a simple perfectly conducting surface: size $10\lambda \times 10\lambda$ with a single groove of width (in the x-direction) 4λ, depth 0.5λ and length (in the y-direction) 6λ. The incidence angle is 20° in the x-z plane.

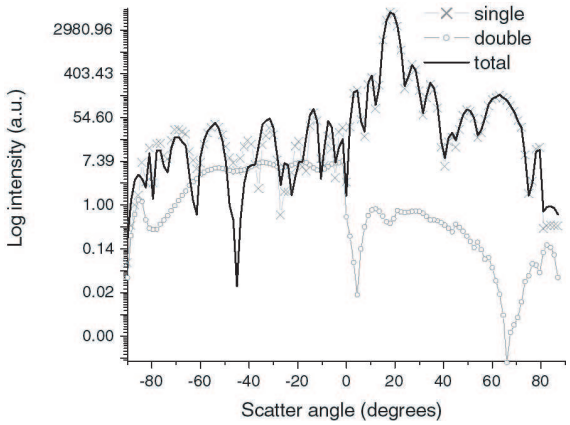

Figure 5: Cross-sections of the HH contributions for the single, double and total scatter from Figures 2, 3 and 4.

4. CONCLUSIONS

The application of the modified Kirchhoff method to scattering from perfectly conducting surfaces with infinite-sloped surfaces has been presented, as well as a simple example of the application of the method.

ACKNOWLEDGMENT

This research was supported by CONACYT, México through project 79814 and DGAPA, UNAM through project PAPIIT IN115209-3.

REFERENCES

1. Germer, T. A., "Effect of line and trench profile variation on specular and diffuse reflectance from a periodic structure," *J. Opt. Soc. Am. A*, Vol. 24, 696–701, 2007.
2. Rovira-Laparra, M., N. C. Bruce, O. G. Rodriguez-Herrera, J. G. Bañuelos-Muñeton, E. V. Basiuk, and J. M. Saniger-Blesa, "Characterisation of chemically etched Indium Phosphide surfaces with light scattering," *Waves in Random and Complex Media*, Vol. 17, 221–231, 2007.
3. Depine, R. A. and D. C. Skigin, "Scattering from metallic surfaces having a finite number of rectangular grooves," *J. Opt. Soc. Am. A*, Vol. 11, 2844–2850, 1994.
4. Mendoza-Suárez, A. and E. R. Méndez, "Light scattering by a reentrant fractal surface," *Applied Optics*, Vol. 36, 3521–3531, 1997.
5. Barrick, D. E., "Rough surface scattering based on the specular point theory," *IEEE Trans. Ant. Propag.*, Vol. 16, 449–454, 1968.
6. Tang, K., R. A. Dimenna, and R. O. Buckius, "Regions of validity of the geometric optics approximation for angular scattering from very rough surfaces," *Int. J. Heat Mass Transfer*, Vol. 40, 49–59, 1997.
7. Beckmann, P. and A. Spizzichino, *The Scattering of Electromagnetic Waves from Rough Surfaces*, Pergamon, 1963 (reprinted by Artech House, 1987).
8. Bruce, N. C., "Single-scatter vector-wave scattering from surfaces with infinite slope using the Kirchhoff approximation," *J. Opt. Soc. Am. A*, Vol. 25, 2011–2017, 2008.
9. Ogilvy, J. A., *Theory of Wave Scattering from Random Rough Surfaces*, IOP Publishing, 1991.

Optical Spectrum and Electromagnetic-Field Distribution at Double-Groove Metallic Surface Gratings

L. David Wellems[1], D. H. Huang[1], T. A. Leskova[2], and A. A. Maradudin[2]

[1]Air Force Research Laboratory, Space Vehicles Directorate
Kirtland Air Force Base, NM 87117, USA
[2]Department of Physics and Astronomy and Institute for Surface Science
University of California, Irvine, CA 92697, USA

Abstract— The Greens function model [8] for calculating the reflection and transmission of light at etched single-groove gratings on both sides of a thin silver film was extended to study the case of double-groove gratings. A splitting of surface-plasmon-polariton (SPP) modes was found due to electromagnetic (EM) coupling between the two grooves in the complex unit-cell of the grating. Spectral features corresponding to the split SPP branches as well as the minigap between them were found in this system. From the full spatial distributions of the total EM field, the high-surface-field regions, the coupling between two grooves in the same complex unit-cell and the coupling between two nearby grooves located at the upper and lower surfaces of the metal film can be identified.

1. INTRODUCTION

Surface plasmons in conductive materials with sub-wavelength structures are a rather interesting research subject, which emerged and attracted attention in recent years [1]. The extraordinarily high transmission of p-polarized light propagating through a two-dimensional periodic array of holes with subwavelength diameters, first reported by Ebbeson et al. [2–4], depends strongly on the lattice constant and metal-film thickness in the deep sub-wavelength regime [5]. For a thin metal film on a dielectric substrate, if both the upper and lower surfaces of the film are etched into a linear grating with aligned grooves on both surfaces, the coupling between the two surface-plasmon-polariton (SPP) modes localized at the two surfaces can be spatially modulated due to the variation of the film thickness [6, 7]. Meanwhile, the SPP mode for a planar surface becomes folded with a finite lattice constant and is split into many branches with a minigap either at the center or at the edge of the first Brillouin zone [8]. If a simple unit-cell (SUC) containing only a single groove is replaced by a double-groove complex unit-cell (CUC), each SPP branch will be further split into two branches with a new minigap controlled by an electromagnetic coupling [9] between the two grooves in the CUC. In the case of the CUC with different groove widths and filled dielectric materials, the circulation and weaving of light was found as a result of the excitation of phase resonance [10].

In this paper, we extend the previous spectral calculations [8] for a single-groove grating to include a comparison between results for single- and double-groove gratings. Both the transmissivity and reflectivity spectra are calculated for p polarization. Some new spectral features are found with a double-groove grating, and can be explained by the spatial distribution of the total EM field at these wavelengths.

The paper is organized as follows. In Section 2, we extend the previous model and formalism to include a double-groove grating. The conclusions drawn from these calculations are briefly summarized in Section 3.

2. MODEL AND THEORY

In order to make this paper stand alone, we repeat some of the key steps in deriving the spatial distribution of the EM field as well as the far-field transmissivity and reflectivity. Details of these derivations can be found in the paper by Baumeier, et al. [8].

The scattering system considered in this paper is divided into three regions in the z direction. The region-I for $z \geq \xi_1(x)$ is for air with a dielectric constant ϵ_a. The region-II for $-h + \xi_2(x) \leq z \leq \xi_1(x)$ is filled with a thin metal film with a thickness h and a frequency-dependent complex dielectric function $\epsilon_f(\omega)$ to include the loss effect, where $\hbar\omega$ is the incident photon energy. The region-III for $z \leq -h + \xi_2(x)$ corresponds to a substrate with a dielectric constant ϵ_s. Here, $\xi_1(x)$ and $\xi_2(x)$ are the profile functions for the patterned upper and lower surfaces of the metal film. In this paper, we will consider only the case of p-polarized incident light.

By using Green's second integral identity [11] in the xz-plane along with the boundary conditions, we get the following integral Equation (8) for the magnetic field $\mathcal{H}_y^{(\mathrm{I})}(x,\, z)$ within region-I for $z \geq \xi_1(x)$

$$\begin{aligned}\mathcal{H}_y^{(\mathrm{I})}(x,\, z) \;=\; & \mathcal{H}_y^{(\mathrm{inc})}(x,\, z) + \frac{1}{4\pi}\int_{-\infty}^{\infty} dx' \left[\frac{\partial}{\partial N_1'} G_a\left(x,\, z|x',\, z'\right)|_{z'=\xi_1(x')} \times \mathcal{H}_y^{(\mathrm{I})}\left(x',\, z'\right)|_{z'=\xi_1(x')}\right. \\ & \left. - G_a\left(x,\, z|x',\, z'\right)|_{z'=\xi_1(x')} \frac{\partial}{\partial N_1'}\mathcal{H}_y^{(\mathrm{I})}\left(x',\, z'\right)|_{z'=\xi_1(x')}\right], \end{aligned} \tag{1}$$

where $\mathcal{H}_y^{(\mathrm{inc})}(x,\, z) = \exp(ikx - i\beta z)$ (with $k = (\omega/c)\sqrt{\epsilon_a}\sin\theta_0$, $\beta = (\omega/c)\sqrt{\epsilon_a}\cos\theta_0$, where θ_0 is the angle of incidence) represents the incident magnetic-field component in p polarization. In a similar way, we can also obtain the integral Equation (8) for the magnetic field $\mathcal{H}_y^{(\mathrm{II})}(x,\, z)$ within region-II for $-h + \xi_2(x) \leq z \leq \xi_1(x)$

$$\begin{aligned}\mathcal{H}_y^{(\mathrm{II})}(x,\, z) \;=\; & -\frac{1}{4\pi}\int_{-\infty}^{\infty} dx' \left[\frac{\partial}{\partial N_1'} G_f\left(x,\, z|x',\, z'\right)|_{z'=\xi_1(x')} \times \mathcal{H}_y^{(\mathrm{I})}\left(x',\, z'\right)|_{z'=\xi_1(x')}\right. \\ & \left. - \frac{\epsilon_f(\omega)}{\epsilon_a} G_f\left(x,\, z|x',\, z'\right)|_{z'=\xi_1(x')} \frac{\partial}{\partial N_1'}\mathcal{H}_y^{(\mathrm{I})}\left(x',\, z'\right)|_{z'=\xi_1(x')}\right] \\ & + \frac{1}{4\pi}\int_{-\infty}^{\infty} dx' \left[\frac{\partial}{\partial N_2'} G_f\left(x,\, z|x',\, z'\right)|_{z'=-h+\xi_2(x')} \mathcal{H}_y^{(\mathrm{II})}\left(x',\, z'\right)|_{z'=-h+\xi_2(x')}\right. \\ & \left. - \frac{\epsilon_s}{\epsilon_f(\omega)} G_f\left(x,\, z|x',\, z'\right)|_{z'=-h+\xi_2(x')} \frac{\partial}{\partial N_2'}\mathcal{H}_y^{(\mathrm{II})}\left(x',\, z'\right)|_{z'=-h+\xi_2(x')}\right]. \end{aligned} \tag{2}$$

Finally, we obtain the integral Equation (8) for the magnetic field $\mathcal{H}_y^{(\mathrm{III})}(x,\, z)$ within region-III for $z \leq -h + \xi_2(x)$

$$\begin{aligned}\mathcal{H}_y^{(\mathrm{III})}(x,\, z) \;=\; & -\frac{1}{4\pi}\int_{-\infty}^{\infty} dx' \left[\frac{\partial}{\partial N_2'} G_s\left(x,\, z|x',\, z'\right)|_{z'=-h+\xi_2(x')} \mathcal{H}_y^{(\mathrm{II})}\left(x',\, z'\right)|_{z'=-h+\xi_2(x')}\right. \\ & \left. - \frac{\epsilon_s}{\epsilon_f(\omega)} G_s\left(x,\, z|x',\, z'\right)|_{z'=-h+\xi_2(x')} \frac{\partial}{\partial N_2'}\mathcal{H}_y^{(\mathrm{II})}\left(x',\, z'\right)|_{z'=-h+\xi_2(x')}\right]. \end{aligned} \tag{3}$$

In Equations (1)–(3), we have defined

$$\frac{\partial}{\partial N_{1,2}'} = -\frac{d\xi_{1,2}\left(x'\right)}{dx'}\frac{\partial}{\partial x'} + \frac{\partial}{\partial z'}. \tag{4}$$

In addition, the Green's functions in regions-I(a), region-II(f), and region-III(s) are respectively given by

$$G_{a,f,s}\left(x,\, z|x',\, z'\right) = i\pi Z_0^{(1)}\left[n_{a,f,s}\left(\frac{\omega}{c}\right)\sqrt{(x-x')^2 + (z-z')^2}\right], \tag{5}$$

where $n_{a,s} = \sqrt{\epsilon_{a,s}}$, $n_f(\omega) = \sqrt{\epsilon_f(\omega)}$ with $\mathrm{Re}[n_f(\omega)] > 0$ and $\mathrm{Im}[n_f(\omega)] > 0$. Moreover, $Z_0^{(1)}(\tilde{w})$ in Equation (5) is the zeroth-order Hankel function of the first-kind with a complex argument $\tilde{w}$.

The boundary conditions require both $\mathcal{H}_y(x,\, z)$ and $(1/\epsilon)\,\hat{\mathbf{n}}_0 \cdot \boldsymbol{\nabla}_{xz}\mathcal{H}_y(x,\, z)$ be continuous across the upper and lower surfaces at $z = \xi_1(x)$ and $z = \xi_2(x)$, where $\hat{\mathbf{n}}_0$ represents the unit vector along the normal direction of a surface-profile curve and $\boldsymbol{\nabla}_{xz} = (\partial/\partial x,\, 0,\, \partial/\partial z)$. Therefore, we obtain the following four equations from Equations (1)–(3)

$$\begin{aligned}\mathcal{H}_y^{(\mathrm{I})}(x,z)|_{z=\xi_1(x)} = & \mathcal{H}_y^{(\mathrm{inc})}(x,z)|_{z=\xi_1(x)} + \frac{1}{4\pi}\int_{-\infty}^{\infty} dx' \left[\frac{\partial}{\partial N_1'} G_a\left(x,z|x',\, z'\right)|_{z=\xi_1(x),\, z'=\xi_1(x')}\right. \\ & \left. \times \mathcal{H}_y^{(\mathrm{I})}(x',z')|_{z'=\xi_1(x')} - G_a\left(x,z|x',z'\right)|_{z=\xi_1(x),z'=\xi_1(x')} \frac{\partial}{\partial N_1'}\mathcal{H}_y^{(\mathrm{I})}(x',z')|_{z'=\xi_1(x')}\right], \end{aligned} \tag{6}$$

$$
\begin{aligned}
0 \;=\; & -\frac{1}{4\pi}\int_{-\infty}^{\infty} dx' \left[\frac{\partial}{\partial N_1'} G_f\left(x,\, z|x',\, z'\right)\,|_{z=\xi_1(x),\, z'=\xi_1(x')} \times \mathcal{H}_y^{(\mathrm{I})}\left(x',\, z'\right)\,|_{z'=\xi_1(x')}\right. \\
& \left. -\,\frac{\epsilon_f(\omega)}{\epsilon_a} G_f\left(x,\, z|x',\, z'\right)\,|_{z=\xi_1(x),\, z'=\xi_1(x')}\, \frac{\partial}{\partial N_1'}\mathcal{H}_y^{(\mathrm{I})}\left(x',\, z'\right)\,|_{z'=\xi_1(x')}\right] \\
& +\frac{1}{4\pi}\int_{-\infty}^{\infty} dx' \left[\frac{\partial}{\partial N_2'} G_f\left(x,\, z|x',\, z'\right)\,|_{z=\xi_1(x),\, z'=-h+\xi_2(x')}\, \mathcal{H}_y^{(\mathrm{II})}\left(x',\, z'\right)\,|_{z'=-h+\xi_2(x')}\right. \\
& \left. -\,\frac{\epsilon_s}{\epsilon_f(\omega)} G_f\left(x,\, z|x',\, z'\right)\,|_{z=\xi_1(x),\, z'=-h+\xi_2(x')}\, \frac{\partial}{\partial N_2'}\mathcal{H}_y^{(\mathrm{II})}\left(x',\, z'\right)\,|_{z'=-h+\xi_2(x')}\right], \qquad (7)
\end{aligned}
$$

$$
\begin{aligned}
\mathcal{H}_y^{(\mathrm{II})}(x,z)|_{z=-h+\xi_2(x)} = & -\frac{1}{4\pi}\int_{-\infty}^{\infty} dx' \left[\frac{\partial}{\partial N_1'} G_f\left(x,z|x',z'\right)|_{z=-h+\xi_2(x),z'=\xi_1(x')} \times \mathcal{H}_y^{(\mathrm{I})}\left(x',z'\right)|_{z'=\xi_1(x')}\right. \\
& \left. -\,\frac{\epsilon_f(\omega)}{\epsilon_a} G_f\left(x,\, z|x',\, z'\right)|_{z=-h+\xi_2(x),\, z'=\xi_1(x')}\, \frac{\partial}{\partial N_1'}\mathcal{H}_y^{(\mathrm{I})}\left(x',\, z'\right)|_{z'=\xi_1(x')}\right] \\
& +\frac{1}{4\pi}\int_{-\infty}^{\infty} dx' \left[\frac{\partial}{\partial N_2'} G_f\left(x,z|x',z'\right)|_{z=-h+\xi_2(x),z'=-h+\xi_2(x')}\right. \\
& \mathcal{H}_y^{(\mathrm{II})}\left(x',z'\right)|_{z'=-H+\xi_2(x')} - \frac{\epsilon_s}{\epsilon_f(\omega)} G_f\left(x,z|x',z'\right)|_{z=-h+\xi_2(x),z'=-h+\xi_2(x')} \\
& \left. \frac{\partial}{\partial N_2'}\mathcal{H}_y^{(\mathrm{II})}\left(x',z'\right)|_{z'=-h+\xi_2(x')}\right], \qquad (8)
\end{aligned}
$$

$$
\begin{aligned}
0 \;=\; & -\frac{1}{4\pi}\int_{-\infty}^{\infty} dx' \left[\frac{\partial}{\partial N_2'} G_s\left(x,z|x',z'\right)|_{z=-h+\xi_2(x),z'=-h+\xi_2(x')}\, \mathcal{H}_y^{(\mathrm{II})}\left(x',z'\right)|_{z'=-h+\xi_2(x')}\right. \\
& \left. -\,\frac{\epsilon_s}{\epsilon_f(\omega)} G_s\left(x,z|x',z'\right)|_{z=-h+\xi_2(x),z'=-h+\xi_2(x')}\, \frac{\partial}{\partial N_2'}\mathcal{H}_y^{(\mathrm{II})}\left(x',z'\right)|_{z'=-h+\xi_2(x')}\right]. \qquad (9)
\end{aligned}
$$

To simplify the notation, we denote the four unknowns in Equations (6)–(9) as

$$\mathcal{S}^{(1)}(x) \equiv \mathcal{H}_y^{(\mathrm{I})}(x,\, z)\,|_{z=\xi_1(x)}, \qquad (10)$$

$$\mathcal{S}^{(2)}(x) \equiv \mathcal{H}_y^{(\mathrm{II})}(x,\, z)\,|_{z=-h+\xi_2(x)}, \qquad (11)$$

$$\mathcal{L}^{(1)}(x) \equiv \frac{\partial}{\partial N_1}\mathcal{H}_y^{(\mathrm{I})}(x,\, z)\,|_{z=\xi_1(x)}, \qquad (12)$$

$$\mathcal{L}^{(2)}(x) \equiv \frac{\partial}{\partial N_2}\mathcal{H}_y^{(\mathrm{II})}(x,\, z)\,|_{z=-h+\xi_2(x)}\,. \qquad (13)$$

Since $G_a(x,\, z|x',\, z')$, $G_f(x,\, z|x',\, z')$, and $G_s(x,\, z|x',\, z')$ are all known analytically, Equations (6)–(9) constitute a set of self-consistent nonlocal equations with respect to $\mathcal{S}^{(1)}(x)$, $\mathcal{S}^{(2)}(x)$, $\mathcal{L}^{(1)}(x)$ and $\mathcal{L}^{(2)}(x)$, which can be solved by transforming them into a matrix Equation (8) in a finite range of x. Once the sources $\mathcal{S}^{(1)}(x)$, $\mathcal{S}^{(2)}(x)$, $\mathcal{L}^{(1)}(x)$ and $\mathcal{L}^{(2)}(x)$ in Equations (6)–(9) have been obtained, we can substitute them into Equations (1)–(3) to find the full spatial distribution of $\mathcal{H}_y(x,\, z)$ in all three regions including air, metal film and substrate.

Moreover, we can calculate the differential reflection coefficient [8] through the ratio of time-averaged fluxes of energy vertically crossing a xy-plane above $z = \xi_1(x)$

$$\frac{\partial R(\theta_s|\theta_0)}{\partial \theta_s} = \frac{c n_a}{8\pi\omega L}\frac{|r(\theta_s|\theta_0)|^2}{\cos\theta_0}, \qquad (14)$$

where θ_s is the scattering angle, L is the sample length in the x direction, and

$$
\begin{aligned}
r(\theta_s|\theta_0) \;=\; & \int_{-\infty}^{\infty} dx \exp\left\{\frac{-i\omega n_a}{c}\left[x\sin\theta_s + \xi_1(x)\cos\theta_s\right]\right\} \\
& \times\left\{\frac{i\omega n_a}{c}\left[\frac{d\xi_1(x)}{dx}\sin\theta_s - \cos\theta_s\right]\mathcal{S}^{(1)}(x) - \mathcal{L}^{(1)}(x)\right\}. \qquad (15)
\end{aligned}
$$

In a similar way, we can calculate the differential transmission coefficient [8] through the ratio of time-averaged fluxes of energy vertically crossing a xy-plane below $z = -h + \xi_2(x)$

$$\frac{\partial T(\theta_t|\theta_0)}{\partial \theta_t} = \frac{cn_a}{8\pi\omega L}\frac{|t(\theta_t|\theta_0)|^2}{\cos\theta_0}, \tag{16}$$

where θ_t is the transmission angle and

$$\begin{aligned} t(\theta_t|\theta_0) \;=\; & \int_{-\infty}^{\infty} dx \exp\left\{\frac{-i\omega n_s}{c}\left[x\sin\theta_t - \xi_2(x)\cos\theta_t\right]\right\} \\ & \times\left\{\frac{i\omega n_s}{c}\left[\frac{d\xi_2(x)}{dx}\sin\theta_t + \cos\theta_t\right]\mathcal{S}^{(2)}(x) - \frac{\epsilon_s}{\epsilon_f(\omega)}\mathcal{L}^{(2)}(x)\right\}. \end{aligned} \tag{17}$$

By using Equations (14) and (16), we can calculate the reflectivity $\mathcal{R}(\lambda)$ [the transmissivity $\mathcal{T}(\lambda)$] for normal incidence $\theta_0 = 0$ by integrating θ_s (θ_t) over a small interval around $\theta_s = 0$ ($\theta_t = 0$) in a symmetrical way [8].

For a double-groove grating, we assume the following surface profiles

$$\xi_1(x) = -d_1\sum_{j=-\infty}^{\infty}\exp\left[-\frac{(x-jb)^2}{a^2}\right] - d_2\sum_{j=-\infty}^{\infty}\exp\left[-\frac{(x-jb-s)^2}{a^2}\right] = -\xi_2(x), \tag{18}$$

where d_1 and d_2 are the depths for two Gaussian grooves, b is the period of the grating, a is the decay constant for the Gaussian groove, and $s < b/2$ is the separation between the two grooves in the CUC.

In our numerical calculations, we choose silver for the metal material, $\theta_0 = 0$, $h = 110\,\text{nm}$, $d_1 = 0.4h$, $b = 600\,\text{nm}$, $a = 0.1b$ (for a sharper groove), $L = 40\lambda$, $\epsilon_a = 1$, $\epsilon_s = 2.1025$, and $\epsilon_f(\omega)$ for silver is numerically input from the paper by Johnson and Christy [12].

3. CONCLUSION

By generalizing the Green's function formalism for a single-groove grating to one for a double-groove grating, we have found the splitting of a surface-plasmon-polariton mode into one symmetrical and one anti-symmetrical mode due to electromagnetic coupling between the two grooves in the same complex unit-cell. Additional peaks in the transmissivity can be found in this system as spectral features corresponding to the split surface-plasmon-polariton branches at individual surfaces of the metal film, which can be identified by the spatial distribution of the total electromagnetic field. From our studies, we have concluded that the split anti-symmetrical surface-plasmon-polariton mode due to the direct electromagnetic coupling in the same complex unit-cell, as well as the cross electromagnetic coupling in different complex unit-cells at both surfaces of the metal film, contribute new spectral features in the transmissivity.

ACKNOWLEDGMENT

Two of authors (TAL and AAM) would like to thank AFRL contract FA 9453-08-C-0230 for partial support. D. W. and D. H. would like to thank the Air Force Office of Scientific Research (AFOSR) for its support.

REFERENCES

1. Zayats, A. V., I. I. Smolynainov, and A. A. Maradudin, *Phys. Rep.*, Vol. 408, 131, 2005.
2. Ebbsen, T. W., H. J. Lezec, H. F. Ghaemi, T. Thio, and P. A. Wolff, *Nature*, Vol. 391, 667, 1998.
3. Ghaemi, H. F., T. Thio, D. E. Grupp, T. W. Ebbesen, and H. J. Lezec, *Phys. Rev. B*, Vol. 58, 6779, 1998.
4. Thio, T., H. F. Ghaemi, H. J. Lezec, P. A. Wolff, and T. W. Ebbesen, *J. Opt. Soc. Am. B*, Vol. 16, 1743, 1999.
5. Chang, J. C.-C., Z.-P. Yang, D. H. Huang, D. A. Cardimona, and S.-Y. Lin, *Opt.*, Vol. 34, 106, 2009.
6. Raether, H., *Surface Plasmons on Smooth and Rough Surfaces and on Gratings*, Springer-Verlag, Berlin, 1988.

7. Tan, W.-C., T. W. Preist, and R. J. Sambles, *Phys. Rev. B*, Vol. 62, 11134, 2000.
8. Baumeier, B., T. A. Leskova, and A. A. Maradudin, *J. Opt. A: Pure Appl. Opt.*, Vol. 8, S191, 2006.
9. Gumbs, G. and D. H. Huang, *Phys. Rev. B*, Vol. 75, 115314, 2007.
10. Crouse, D., E. Jaquay, and A. Maikal, *Phys. Rev. B*, Vol. 77, 195437, 2008.
11. Danese, A. E., *Advanced Calculus*, Vol. I, Allyn and Bacon, MA, Boston, 123, 1965.
12. Johnson, P. B. and R. W. Christy, *Phys. Rev. B*, Vol. 6, 4370, 1972.

Maximums of Backscattering from the Surface Edge above Mirror

A. M. Lebedev and A. I. Fedorenko
Institute for Theoretical and Applied Electromagnetics, Russian Academy of Sciences, Russia

Abstract— Besides the specular backscattering (BS) in normal direction, BS maximums from a given surface are observed when the direction of irradiation-observation (IO) is perpendicular to the surface edges. Here this finding is widened to include BS from the surface edges above mirror; the consideration is based on the concept of four rays. BS is quantitatively characterized via the backward radar cross section in sm, further RCS for short. Maximums of RCS are shown to be observed when the IO direction is perpendicular to real and mirrored edges, and also when the IO direction gets onto the diffracted ray cones, which result from the mirrored plane wave incidence on the edges, both real and mirrored. It causes 1) the increase of BS maximum from any horizontal edge and 2) the formation of three BS maximums per inclined edge.

1. INTRODUCTION

The BS of extended complex object can tentatively be divided into contributions cased by 1) shape and 2) local inhomogeneities on its surface. In turn, the edges often generate most of shape's BS contribution. For example, when the normals to the surfaces are redirected outside the meaningful angular range (the object is stealthy shaped). Hence the analysis of BS from the edges above the mirror is of major importance for prediction of radar signature of objects above the underlying surface.

Besides the specular BS in direction of normal to the surface, BS maximums from a given surface are observed when the IO direction is perpendicular to the surface edges. Indeed, the BS observer can only get on the diffracted ray cone in plane, perpendicular to the edge.

For the sake of illustration, the RCS spatial distributions $\sigma(\varphi, \alpha)$ of some metal triangle both in free space and above mirror were calculated, where φ and α are azimuth and elevation. The triangle was intentionally chosen as the simplest type of surface. The triangle with normal, inclined to horizon, can also be considered as the simplest object with stealth geometry.

The geometry of triangle is shown in Fig. 1. Calculations were conducted for the wavelength $\lambda_o = 3\,\text{cm}$. Thus, the horizontal base of triangle is updrawn $10 \cdot \lambda_o$, the base length is $15 \cdot \lambda_o$, normal to the triangle is oriented at $\varphi = 0°$, $\alpha = 10°$. Relatively moderate dimensions of triangle let us conduct all calculations with the moment method.

Spatial distribution $\sigma(\varphi, \alpha)$ of BS from triangle in free space for vertically polarized plane wave incidence is shown in Fig. 2, where the RCS values are up-limited at 1 sm for clearness. Foldings A_1NA_2 and C_1NC_2 correspond to BS in directions perpendicular to inclined edges, folding B_1NB_2 represents BS in directions perpendicular to the horizontal edge. All three foldings intersect at point N, corresponding to BS in normal direction.

Further we will analyse the changes in BS from the surface edge above mirror, basing on the known concept of four rays.

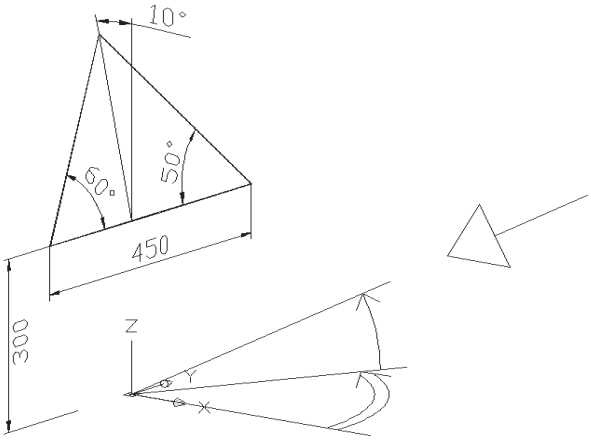

Figure 1: The geometry of triangle.

2. THE CONCEPT OF FOUR RAYS

According to the above mentioned concept, BS from the object above mirror is formed by four rays, as it is shown in Fig. 3. Formally removing the mirror, we have to continue the rays beyond the former points of reflection and to add the mirrored copy to the real object, see Fig. 3. Then real and mirrored plane waves impinge upon the doubled object. So BS from the object above mirror is the sum of, firstly, BS of real wave from the doubled object (cases 1 and 4 in Fig. 3) and, secondly, bistatic scattering of mirrored wave from the doubled object (cases 2 and 3 in Fig. 3).

3. MECHANISMS OF FORMATION OF BACKSCATTERING MAXIMUMS FROM THE EDGE ABOVE MIRROR

Maximums of BS from the edge above mirror are observed when the IO direction is **1)** perpendicular to real edge (case 1 in Fig. 3), **2)** perpendicular to mirrored edge (case 4 in Fig. 3), **3)** located on the diffracted ray cones, which result from the incidence of the mirrored wave on the edges, both

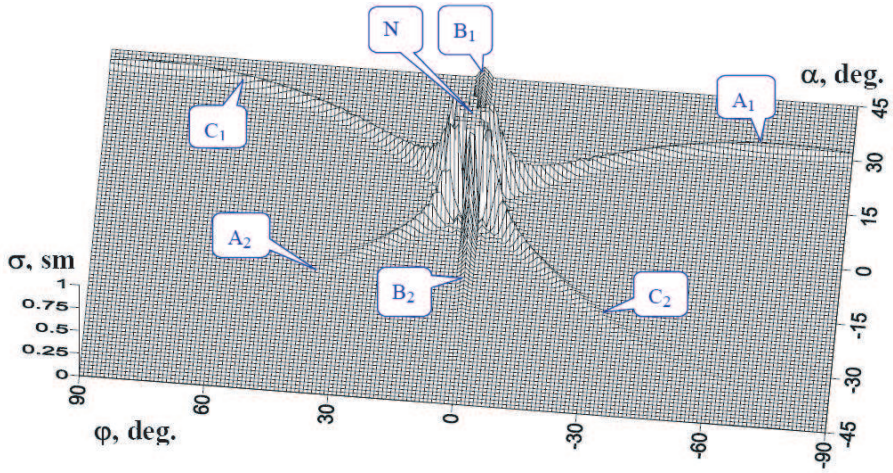

Figure 2: RCS of the triangle in free space.

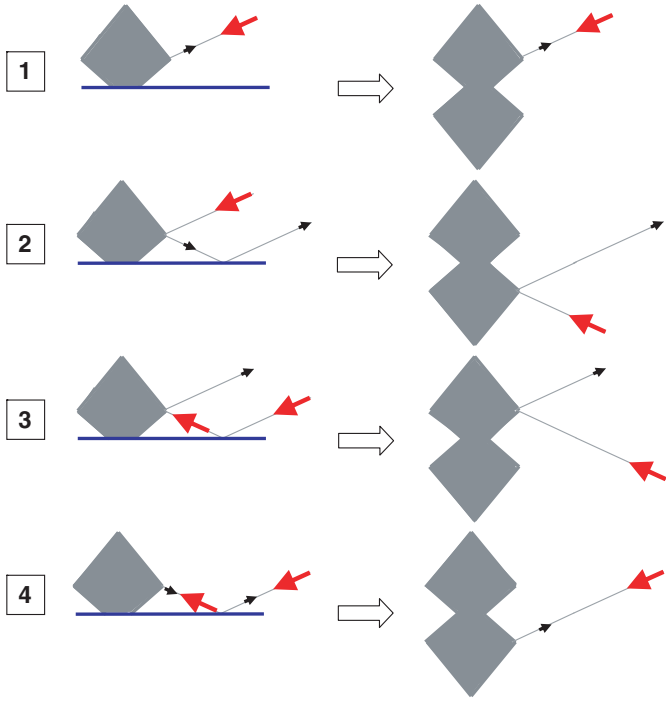

Figure 3: Four-ray backscattering from the object above the mirror.

real and mirrored (cases 2 and 3 in Fig. 3).

4. THE CONDITIONS OF BS MAXIMUMS FROM THE EDGE ABOVE MIRROR

Pair of angles $\{\varphi_e,\ \alpha_e\}$ specifies orientation of the edge, and angles $\{\varphi,\ \alpha\}$ define the IO direction. Then maximum of BS from the real edge is observed under the following condition

$$\varphi = \varphi_e \pm [90^\circ + \arcsin\ (\mathrm{tg}\alpha \cdot \mathrm{tg}\alpha_e)]. \tag{1}$$

Maximum of BS from the mirrored edge is observed under such condition

$$\varphi = \varphi_e \pm [90^\circ - \arcsin\ (\mathrm{tg}\alpha \cdot \mathrm{tg}\alpha_e)]. \tag{2}$$

Finally, maximum of BS corresponding to the IO direction occurrence on the cone of diffracted rays is observed under the condition

$$\varphi = \varphi_e \pm 90^\circ. \tag{3}$$

Under this condition, the IO direction simultaneously occurs on the diffracted ray cones from real and mirrored edges.

For horizontal edge and any IO elevation, and similarly for any edge in case of horizontal IO direction, all three mechanisms give maximums of BS at azimuth which differs 90° from the edge azimuth, as it follows from (1)–(3). The IO direction, when it is located on the diffracted ray cones, and the edge perpendicularly project onto the horizontal plane, see (3). In general case of inclined both incidence and the edge, the azimuths of maximums of BS from real and mirrored edges are equidistant from the azimuth $\varphi = \varphi_e \pm 90^\circ$, with the azimuth interval $\arcsin\ (\mathrm{tg}\alpha \cdot \mathrm{tg}\alpha_e)$, as it is immediately seen from (1)–(2). Even for minor IO direction elevation α, this azimuth interval can increase up to 90° if the edge is close to vertical $\alpha_e \to 90^\circ$.

5. BACKSCATTERING FROM THE TRIANGLE ABOVE THE MIRROR

The RCS distribution $\sigma\,(\varphi, \alpha)$ of the same metal triangle above mirror is presented in Fig. 4, again for the vertically polarized incident plane wave.

Here the foldings ANA_1, CNC_1 correspond to BS of the incident wave from the inclined edges of real triangle. Foldings AA_2 and CC_2 correspond to BS from the inclined edges of mirrored triangle. They represent the tails of foldings A_1NA_2 and C_1NC_2 in Fig. 2, cut by line of zero elevation $\alpha = 0$ and specularly "reflected" from it. The reason for foldings AA_3 and CC_3 is the occurrence of BS ray on the diffracted ray cone, which is produced by the mirrored wave incidence upon the inclined edges. Folding BNB_1 is the result of interference of all three sources of increased BS: BS from the perpendicular real edge, BS from the perpendicular mirrored edge and bistatic scattering of the mirrored plane wave from both real and mirrored edges, when the direction of observation belongs to the diffracted ray cones.

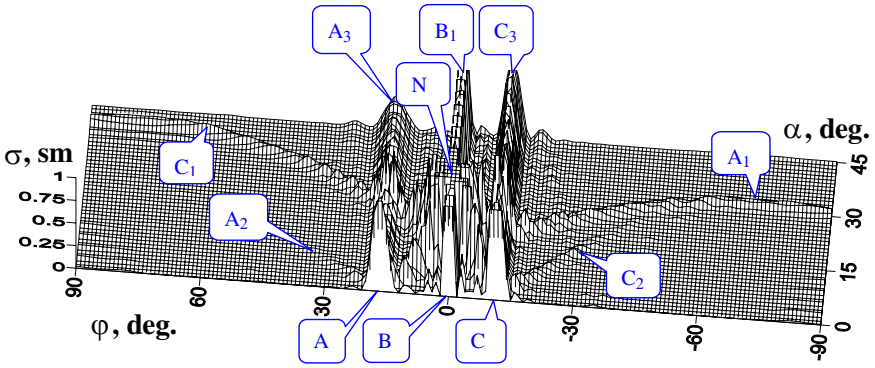

Figure 4: RCS of the triangle above mirror.

6. CONCLUSIONS

The existence of maximums of azimuthal backward RCS diagram, which correspond to the backscattering from the surface edge above mirror, is shown, and conditions, under which these maximums are observed, were found out. Maximums of backscattering are obtained when the direction of

irradiation-observation is perpendicular to real and mirrored edges, and also when the irradiation-observation direction gets onto the diffracted ray cones, resulting from the mirrored plane wave incidence on the edges, both real and mirrored. In comparison with the surface edge in free space, the only maximum of backscattering from the horizontal edge increases, and three backscattering maximums are observed for inclined incidence upon the inclined edge.

Some important questions were left beyond the scope of this publication. Describing the backscattering maximums formation, we told in fact about the envelope of the backward RCS spatial distribution. Actually this distribution has substantial cross-folding with deviation from the plane, perpendicular to the edge. Also the differences of backscattering of waves with different polarization from the edges above mirror require further thorough examination. The study of these questions will be the subject of further works.

The Second-order SPM Solution for Scattering from Multi-layer Dielectric Media with Slightly Rough Surface

Z. W. Lin[1,2], **X. J. Zhang**[1], **and G. Y. Fang**[1]

[1] Institute of Electronics, Chinese Academy of Sciences, China
[2] Graduate University of Chinese Academy of Sciences, China

Abstract— The second-order solution of the small perturbation method (SPM) for the scattering from arbitrary layered media with three-dimensional slightly rough surface is derived in this work. The second-order scattering fields and corresponding bistatic scattering coefficients for linear polarized waves are derived respectively. The results are validated against known solution for the case of a single rough surface. Numerical results illustrate the contribution of the second-order solution to the backscattering of the layered structure.

1. INTRODUCTION

The scattering from multi-layer dielectric media with rough interfaces has a number of applications such as environmental remote sensing, non-destructive detection of composite materials, thin films physics, etc. Several researches on this topic have been carried out in recent years. Fuks has investigated the scattering from multi-layer dielectric media with slightly rough surface [1]. Azadegan et al. have studied the scattering from homogeneous media with a slightly rough interface inside [2]. Franceschetti et al. have proved the consistency of the above results and illustrated the physical meaning of the analytical solution of the scattering from a layered structure with one rough interface [3].

All the works mentioned above focus on the derivation of the analytical solutions based on the first-order SPM. They all have explicit close-form expressions. However, the first-order SPM solution fails to characterize the cross-polarized backscattering coefficient which plays an important role in retrieve of surface and subsurface parameters (such as soil moisture and roughness etc.) from polarimetric synthetic aperture radar (PolSAR) data. For this purpose, we present the second-order solution of SPM for the scattering from arbitrary layered media with three-dimensional rough surface in this paper. We employ the method in [2] and exploit it to the second order to observe the cross-polarized component. As a result, the analytical expressions of the second-order scattering field and the corresponding bistatic scattering coefficients are derived. Since we suppose the height profile of the rough surface is a zero-mean Gaussian random process, the coupling between the first-order and the second-order solutions is ignored. The coupling between of the zeroth-order and the second-order solutions isn't taken into account either, because we only concern the backscattering case. Numerical samples are calculated to illustrate the contribution of the second-order solutions to the backscattering from the layered structure.

2. THE DERIVATION OF THE SECEOND-ORDER SPM SOLUTION

Figure 1 shows the two-dimensional slice of the proposed three-dimensional geometry. Each region is a homogeneous medium with a dielectric constant of ε_m, $m = 0, 1, \ldots, n$. The permeabilities of all regions are assumed equal to μ_0. The top and bottom regions are half spaces. The surface height profile is denoted by $z = f(x, y)$, where $f(x, y)$ is a zero-mean Gaussian random process with known statistical characteristics, namely the rms height h and correlation length l which are assumed to be small numbers compared to the incident wavelength so as to carry out the small perturbation approximation. The depth of the planar boundary between region m and region $m+1$ is denoted by d_m, $m = 1, 2, \ldots, n-1$.

The electric and magnetic fields in region m can be represented as superpositions of up-going and down-going waves in spectral domain [2]

$$\bar{E}_m = \int_{-\infty}^{+\infty} d\bar{k}_\perp \left[\left(f_{mh}^+ \hat{h}_m^+ + f_{mv}^+ \hat{v}_m^+ \right) e^{ik_{mz}z} + \left(f_{mh}^- \hat{h}_m^- + f_{mv}^- \hat{v}_m^- \right) e^{-ik_{mz}z} \right] e^{i\bar{k}_\perp \cdot \bar{r}_\perp} \tag{1}$$

$$\bar{H}_m = \frac{1}{\eta_m} \int_{-\infty}^{+\infty} d\bar{k}_\perp \left[\left(-f_{mh}^+ \hat{v}_m^+ + f_{mv}^+ \hat{h}_m^+ \right) e^{ik_{mz}z} + \left(-f_{mh}^- \hat{v}_m^- + f_{mv}^- \hat{h}_m^- \right) e^{-ik_{mz}z} \right] e^{i\bar{k}_\perp \cdot \bar{r}_\perp} \tag{2}$$

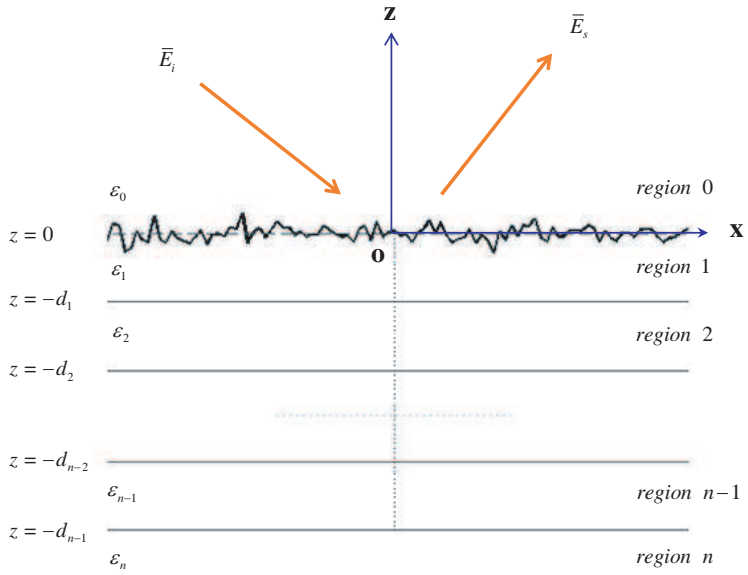

Figure 1: Two-dimensional geometry of a multi-layer dielectric media with a rough surface.

where $d\bar{k}_\perp = dk_x dk_y$, the superscripts "+" and "−" indicate up-going wave and down-going wave respectively, $f_{mh}^{\pm}$ and $f_{mv}^{\pm}$ denote the unknown amplitudes of H and V polarizations in region m respectively, $\hat{h}_m^{\pm}$ and $\hat{v}_m^{\pm}$ are the unit vectors of H and V polarizations in region m, η_m is the wave impedance of region m. Our purpose is to estimate $f_{0h}^{\pm}$ and $f_{0v}^{\pm}$ through the boundary conditions, because we only concern the scattering fields in region 0.

At the 1st planar interface, we have

$$f_{1h}^{+} = R_{h1} f_{1h}^{-} e^{2ik_{1z}d_1}, \quad f_{1v}^{+} = R_{v1} f_{1v}^{-} e^{2ik_{1z}d_1} \tag{3}$$

where $R_{h,v1}$ are the total reflection coefficient at the 1st planar interface [3]. According to the physical parameters of the layered structure, total reflection coefficients $R_{h,v1}$ can be calculated using the formula in [3]. Since the interface between region 0 and region 1 is a slightly rough surface, we can expand $f_{0h,v}^{\pm}$ and $f_{1h,v}^{\pm}$ into the perturbation series

$$f_{0h,v}^{\pm} = \sum_{j=0}^{+\infty} f_{0h,v}^{\pm(j)}, \quad f_{1h,v}^{\pm} = \sum_{j=0}^{+\infty} f_{1h,v}^{\pm(j)} \tag{4}$$

where the superscript j represents the order of the expansion coefficient and expand the exponential factor $e^{\pm ik_{0z}f(x,y)}$ into the Taylor series.

$$e^{\pm ik_{0z}f(x,y)} = \sum_{j=0}^{+\infty} \left[\pm ik_{0z} f\left(x,y\right)\right]^j / j\,! \tag{5}$$

We suppose the incident plane wave is $\bar{E}_i = \bar{E}_0 e^{i\bar{k}_i \cdot \bar{r}}$, where $\bar{k}_i$ is the wave number vector of the incident wave. From (1), we find $f_{0h}^{-} = \bar{E}_0 \cdot \hat{h}^{-} \delta(\bar{k}_\perp - \bar{k}_{\perp i})$, $f_{0v}^{-} = \bar{E}_0 \cdot \hat{v}^{-} \delta(\bar{k}_\perp - \bar{k}_{\perp i})$, where δ is the Dirac function. The unit normal vector of the rough surface is $\hat{n}_0 = (-f_x\hat{x} - f_y\hat{y} + \hat{z})/\sqrt{1 + f_x^2 + f_y^2}$, where $f_x = \partial f(x,y)/\partial x$ and $f_y = \partial f(x,y)/\partial y$.

By substituting (1) $\sim$ (5) into the boundary conditions

$$\hat{n}_0 \times \left(\bar{E}_0 - \bar{E}_1\right)\big|_{z=f(x,y)} = 0, \quad \hat{n}_0 \times \left(\bar{H}_0 - \bar{H}_1\right)\big|_{z=f(x,y)} = 0 \tag{6}$$

and balancing the equations up to the second order, we obtain three linear equations sets for the zeroth-, first- and second-order solutions of the perturbation series (4). The desired variables can be

found by solving the three equations sets. The complete expressions of the second-order solutions of $f^{+}_{0h,v}$ are a little bit long, and we only present the expression for the HH case here:

$$f^{+(2)}_{0hh}\left(\bar{k}_{\perp s},\bar{k}_{\perp i}\right)=\int d\bar{\kappa}_{\perp}F\left(\bar{k}_{\perp}-\bar{\kappa}_{\perp}\right)F\left(\bar{\kappa}_{\perp}-\bar{k}_{\perp i}\right)\tilde{f}^{+(2)}_{0hh}\left(\bar{k}_{\perp s},\bar{\kappa}_{\perp},\bar{k}_{\perp i}\right) \tag{7}$$

with

$$\tilde{f}^{+(2)}_{0hh}\left(\bar{k}_{\perp s},\bar{\kappa}_{\perp},\bar{k}_{\perp i}\right)=\tilde{f}^{+(2)}_{0hha}\left(\bar{k}_{\perp s},\bar{k}_{\perp i}\right)+\tilde{f}^{+(2)}_{0hhb}\left(\bar{k}_{\perp s},\bar{\kappa}_{\perp},\bar{k}_{\perp i}\right) \tag{8}$$

where

$$\begin{aligned}\tilde{f}^{+(2)}_{0hha}\left(\bar{k}_{\perp s},\bar{k}_{\perp i}\right) &= 1/4\left(k_1^2-k_0^2\right)\cos\left(\phi_s-\phi_i\right)\left[\left(1+R_{hi}\right)\left(1-R_{hs}\right)\right.\\ &\quad\left.+\left(1-R_{hi}\right)\left(1+R_{hs}\right)\cos\theta_i/\cos\theta_s\right]\end{aligned} \tag{9}$$

$$\begin{aligned}&\tilde{f}^{+(2)}_{0hhb}\left(\bar{k}_{\perp s},\bar{\kappa}_{\perp},\bar{k}_{\perp i}\right)\\ &=-1/4\left(1+R_{hs}\right)\left(1+R_{hi}\right)\left(k_1^2-k_0^2\right)^2\cos\left(\phi_s-\phi_\kappa\right)\cos\left(\phi_\kappa-\phi_i\right)\left[1+R_h\left(\bar{\kappa}_{\perp}\right)\right]/\left(k_0^2\cos\theta_s\cos\theta_\kappa\right)\\ &\quad+1/4\left(1+R_{hs}\right)\left(1+R_{hi}\right)\left(k_1^2-k_0^2\right)^2\sin\left(\phi_\kappa-\phi_i\right)\sin\left(\phi_s-\phi_\kappa\right)\left[1-R_v\left(\bar{\kappa}_{\perp}\right)\right]\cos\theta_\kappa/\left(k_0^2\cos\theta_s\right)\end{aligned} \tag{10}$$

The subscript i and s stand for the incident and the scattering waves respectively, the symbol κ stands for the integral variable, $F(\bar{k}_{\perp})$ is the Fourier transform of $f(x,y)$. Since the total reflection coefficient is used in (9) and (10), the total layer number of the structure can be arbitrary. It's easy to validate that the degraded forms of (9) and (10) for the simple case of single rough surface coincide with the result on [4].

We approximate (1) by employ the stationary phase method, thus the second-order scattering field in the far-field zone is

$$\bar{E}^{(2)}_{hh}=-\frac{e^{ik_0r}}{r}i2\pi k_0\cos\theta_s f^{+(2)}_{0hh}\hat{h}^{+}_{0}E_{0h} \tag{11}$$

The bistatic scattering coefficient of the second-order scattering field is [4]

$$\begin{aligned}\gamma^{(2)}_{hh}\left(\theta,\phi;\pi-\theta_i,\phi_i\right) &= 4\pi k_0^2\cos^2\theta/\cos\theta_i\cdot\int d\bar{\kappa}_{\perp}W\left(\bar{k}_{\perp}-\bar{\kappa}_{\perp}\right)W\left(\bar{\kappa}_{\perp}-\bar{k}_{\perp i}\right)\tilde{f}^{+(2)}_{ohh}\left(\bar{k}_{\perp},\bar{\kappa}_{\perp},\bar{k}_{\perp i}\right)\\ &\quad\cdot\left[\tilde{f}^{+(2)}_{ohh}\left(\bar{k}_{\perp},\bar{\kappa}_{\perp},\bar{k}_{\perp i}\right)+\tilde{f}^{+(2)}_{ohh}\left(\bar{k}_{\perp},\bar{k}_{\perp}-\bar{\kappa}_{\perp}+\bar{k}_{\perp i},\bar{k}_{\perp i}\right)\right]^{*}\end{aligned} \tag{12}$$

where $W(\bar{k}_{\perp})$ is the power spectral density of the rough surface and * denotes the operator of complex conjugation.

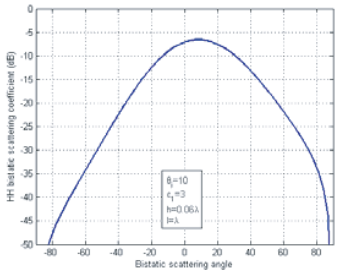

Figure 2: Reproducing the result on [5].

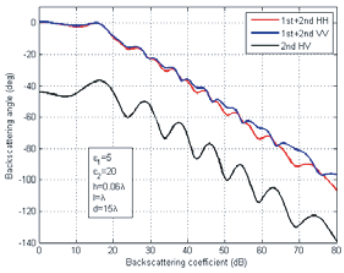

Figure 3: Backscattering from a two-layer structure.

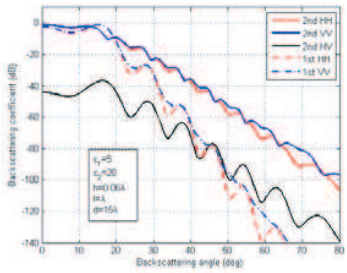

Figure 4: The contribution of the first-order and second-order solutions to the backscattering.

3. THE NUMERICAL RESULTS AND DISCUSSION

To validate the expression of the bistatic scattering coefficients, we reproduce the curve of the 2-2 term on Fig. 3 of [5]. The result is shown on Fig. 2. Fig. 3 shows the backscattering from a two-layer structure. The oscillatory behavior of the cross-polarized backscattering for the layered structure component is observed. Fig. 4 shows the contributions of the first-order and the second-order solutions respectively. It should be noted that the second-order solution not only contributes to the cross-polarized backscattering, but also enhances the co-polarized backscattering significantly.

4. CONCLUSION

The second-order solution of SPM for the scattering from a layered media with a three-dimensional rough surface is derived in this paper for the first time. The analytical solution is validated by comparing the degraded from with the known results. The contributions of the second-order solution to the co-polarized and cross-polarized backscattering are observed. The analytical expressions of the second-order scattering field and corresponding bistatic scattering coefficient result in integral forms which are less convenient for calculation than the first-order solution. However, the integral for variable κ is well behaved, numerical integration can be carried out without difficult. Our future works will focus on searching a proper physical explanation to the second-order solution and deriving the second-order solution of SPM for the scattering from layered media with rough interfaces.

ACKNOWLEDGMENT

This work is support by The National High Technology Research and Development Program ("863" Program) of China (Project No. 2009AA12Z132) and National Nature Science Foundation of China (Project No. 60890071).

REFERENCES

1. Fuks, I. M., "Wave diffraction by a rough boundary of an arbitrary plane-layered medium," *IEEE Transactions on Antenna and Propagation*, Vol. 49, No. 4, 630–639, April 2001.
2. Azadegan, R. and K. Sarabandi, "Analytical formulation of the scattering by a slightly rough dielectric boundary covered with a homogenous dielectric layer," *IEEE Antennas and Propagation Society International Symposium*, Vol. 3, 420–423, 2003.
3. Franceschetti, G., P. Imperatore, A. Iodice, et al., "Scattering from layered structures with one rough interface: A unified formulation of perturbative solutions," *IEEE Transaction on Geoscience and Remote Sensing*, Vol. 46, No. 6, 1634–1643, June 2008.
4. Tsang, L. and J. A. Kong, *Scattering of Elemagnetic Waves Advanced Topics*, Wiley, 2001.
5. Johnson, J. T., "Third-order small-perturbation method for scattering from dielectric rough surfaces," *J. Opt. Soc. Am. A*, Vol. 16, No. 11, 2720–2736, November 1999.

Propagation of Partially Coherent Light in Nonlinear Media

T. Hansson, D. Anderson, and M. Lisak
Department of Radio and Space Science, Chalmers University of Technology, Gothenburg, Sweden

Abstract— Dynamic self-similar solutions are derived describing the propagation of partially coherent solitons in media with saturable logarithmic nonlinearity. The analysis is made using both the Wigner and the coherent density formalisms and the solutions as well as the solution procedures of the different approaches are compared. Although the approaches involve different analysis, the solutions for the evolution of the physically relevant intensity distribution of the solitons are shown to be equivalent. Explicit analytical results are obtained for stationary solutions. An analysis of the interaction between two well separated partially coherent soliton stripes shows a behaviour qualitatively similar to that in a nonlinear Kerr medium.

1. INTRODUCTION

Propagation of partially coherent light in nonlinear media has attracted strong interest during the last ten years after the observation that solitons may also form from partially coherent light [1]. In fact, many of the classical phenomena associated with nonlinear coherent wave propagation, e.g., solitons, self-focusing, and modulational instability have been found to be present also for partially coherent light, although with new features that depend on the coherence properties of the light. A crucial requirement in the manifestation of these new phenomena is that the response time of the medium is long compared to the characteristic time of the statistical wave intensity fluctuations of the field. In such situations, the medium experiences only the statistical average of the wave intensity and consequently the nonlinear change of the refractive index also depends only on the statistical average of the wave intensity rather than on the instantaneous intensity as for ordinary solitons.

Several different formalisms have been developed for theoretical investigations of the propagation of partially coherent light in nonlinear media. Three of the most commonly used ones are based on the coherent density function [2], the mutual coherence function [3], and the Wigner function [4], respectively. Although the characteristic propagation equations appearing in these formalisms are very different in form, they provide equivalent descriptions of the propagation properties and depending on the problem under study, one or a combination of these methods may prove the most convenient [5, 6]. Due to the mathematical complexity of the propagation equations in all used methods of analysis (in some approaches being nonlinear integro-differential equations), very few explicit exact solutions have been found. A notable exception is media where the nonlinearity can be modelled in terms of a logarithmic nonlinearity, i.e., media where the nonlinear change in the refractive index, Δn, is given by $\Delta n \propto \ln\langle I\rangle$ where $\langle I\rangle$ denotes the statistical average of the instantaneous wave intensity, I. In this case explicit soliton solutions of Gaussian form have been found for the coherent case [7], and later for partially coherent waves using the coherent density approach [8] (although in the latter case only the stationary case was considered), as well as by means of the mutual coherence approach [9].

In the present work, we analyze partially coherent wave solutions in the case of the saturable logarithmic nonlinearity using both the Wigner and the coherent density function formalisms. In particular we discuss the properties of exact self-similar dynamic solutions of Gaussian form which also incorporate previously found stationary soliton solutions of varying degree of coherence as a special case. The discussion illustrates the different character of the approaches, e.g., whereas the Wigner function is a stationary function for the soliton solutions, the coherent density function exhibits significant oscillatory motion, in spite of the fact that the corresponding averaged light intensity profile remains constant during propagation.

An important issue in soliton dynamics is the properties of the mutual interaction between separated solitons, a problem that has been analyzed in detail for solitons of e.g., the Kerr type. A numerical study of this problem in the case of the logarithmic nonlinearity was made in [12] for partially coherent solitons. In the present work an analysis is first made of the interaction dynamics between two well separated coherent solitons in the case of the logarithmic nonlinearity. The analysis is based on the variational approach and closely follows the one given in Ref. [13]. The result gives a clear analytical picture of the different possible interaction scenarios and shows

that the interaction may be attractive as well as repulsive depending on the relative phase of the solitons and on the relative magnitude between amplitude and distance of separation (as in the Kerr case). Finally, the interaction between two partially coherent soliton stripes is analyzed using the coherent density formalism and it is found that the interaction behaves qualitatively as in the Kerr case [14], i.e., the partial coherence tends to decrease the strength of the interaction, but the possibility of attractive and repulsive behaviour persists although the character may change from attractive to repulsive and vice versa for decreasing coherence.

2. THE WIGNER APPROACH

Propagation of partially coherent light in a logarithmic saturable nonlinear medium is determined by the following normalized nonlinear Schrödinger equation [1, 8, 9], for the stochastic wave field $\psi(x,z)$

$$i\frac{\partial\psi}{\partial z}+\frac{1}{2}\frac{\partial^2\psi}{\partial x^2}+\ln\langle|\psi|^2\rangle\psi=0 \tag{1}$$

where z is the propagation variable. In the Wigner formalism of partial coherence, Eq. (1) is transformed to phase space by means of the Wigner transform

$$\rho(x,p,z)=\frac{1}{2\pi}\int_{-\infty}^{\infty}\langle\psi^*(x+\xi/2,z)\psi(x-\xi/2,z)\rangle e^{ip\xi}d\xi. \tag{2}$$

The Wigner distribution function $\rho(x,p,z)$ is a quasi probability distribution function that in the present problem can be shown to satisfy the following (Wigner-Moyal) evolution equation

$$\frac{\partial\rho}{\partial z}+p\frac{\partial\rho}{\partial x}+2\ln\langle|\psi|^2\rangle\sin\left(\frac{1}{2}\overleftarrow{\frac{\partial}{\partial x}}\overrightarrow{\frac{\partial}{\partial p}}\right)\rho=0;\qquad\langle|\psi|^2\rangle=\int_{-\infty}^{\infty}\rho(x,p,z)dp. \tag{3}$$

where the arrows in the Sine operator indicate the direction of the respective operations. This equation allows self-similar Gaussian solutions of the form

$$\rho(x,p,z)=A(z)e^{-a(z)x^2-b(z)p^2+c(z)xp};\qquad\langle|\Psi|^2\rangle=\sqrt{\frac{\pi}{b}}Ae^{-\frac{4ab-c^2}{4b}x^2}. \tag{4}$$

as can be shown by inserting this ansatz into Eq. (3), noting that the Sine operator truncates after its first term, and identifying coefficients for x and p. This yields the following evolution equations for the parameter functions

$$A'(z)=0;\quad a'(z)=-\frac{c}{2b}(4ab-c^2);\quad b'(z)=c;\quad c'(z)=2a-(4ab-c^2). \tag{5}$$

The solution of this system can be written in the form of three invariants and a single equation for the parameter b:

$$A=\text{constant};\quad 4ab-c^2=C_1=\text{constant};\quad a+\frac{C_1}{2}\ln b=C_2=\text{constant} \tag{6}$$

$$\left[b'(z)\right]^2=4C_2b-2C_1b\ln b-C_1. \tag{7}$$

Since the parameter combination $4ab-c^2$ is a constant of motion, the parameter b characterizes the width of the intensity distribution. An equivalent equation for the variation of the intensity width has been obtained using the mutual coherence function approach in [9]. The solution of Eq. (7) for the evolution of the parameter $b(z)$ in the non-stationary case, have not be found in explicit analytical form. However, the stationary case is easily analyzed since the stationary widths of the Wigner distribution in x and p are determined by the conditions $a'(z)=b'(z)=c'(z)=0$, which directly imply that $c=0$ and $b=1/2$. Assuming that the stochastic variation of the partially coherent wave has a Gaussian spectral distribution ($J(\theta)=1/\sqrt{2\pi\theta_0^2}\exp(-\theta^2/(2\theta_0^2))$ where the parameter θ_0 characterizes the width of the spectrum, i.e., the degree of partial coherence), the parameter b can easily be expressed in terms of a and θ_0, viz. $b=(a+2\theta_0^2)^{-1}$, c.f. [10], and the width of the stationary intensity distribution ($I(x)\propto\exp(-x^2/W)$) is determined by $\sqrt{W}=1/\sqrt{2(1-\theta_0^2)}$ in agreement with the corresponding results in [8] and [9]. In ordinary soliton theory,

amplitude and width are usually linked (inversely related) whereas for solitons in a logarithmic medium, the amplitude can take on any value and the width is unrelated to the amplitude. Instead the width is determined by the parameters of the medium and the degree of partial coherence and has a threshold behaviour in the sense that it becomes infinite for sufficiently large incoherence, i.e., solitons only exist as long as $\theta_0 < 1$, irrespective of amplitude.

3. THE COHERENT DENSITY FUNCTION APPROACH

For comparison the corresponding analysis is also carried out in terms of the coherent density function formalism. The evolution equation for the coherent density function $f(x,\theta,z)$ corresponding to the NLS equation can be taken as, c.f. Refs. [8, 11]

$$i\frac{\partial f}{\partial z} + \frac{1}{2}\frac{\partial^2 f}{\partial x^2} + \ln\left(I(x,z)\right) f = 0; \quad I(x,z) = \int_{-\infty}^{\infty} |f(x,\theta,z)|^2 d\theta. \tag{8}$$

together with the Gaussian initial condition $f(x,\theta,0) = A\sqrt{J(\theta)}\exp(-\frac{x^2}{2a_0^2} - i\theta x)$ where $J(\theta)$ is the normalized Gaussian spectrum used above.

The form of the solution of Eq. (8) is not obvious. However, it is clear that in order to allow for the proper dynamics, the phase must contain a second order polynomial in θ and x with coefficients that depend on the evolution variable z. It can be shown that the following ansatz is flexible enough to allow a solution

$$\begin{aligned} f(x,\theta,z) =& A(z)\sqrt{J(\theta)}\exp\left\{ -\frac{\left(x-\theta b(z)/\sqrt{2\theta_0^2}\right)^2}{2a^2(z)} + i\left[\delta(z) + \theta\frac{\mu(z)}{\sqrt{2\theta_0^2}}\left(x-\theta b(z)/\left(2\sqrt{2\theta_0^2}\right)\right)\right.\right. \\ &\left.\left. + \frac{\zeta(z)}{2a(z)}\left(x-\theta b(z)/\sqrt{2\theta_0^2}\right)^2\right]\right\}. \end{aligned} \tag{9}$$

The corresponding intensity variation is given by

$$I(x,z) = \frac{aA^2}{\sqrt{a^2+b^2}}\exp\left(-\frac{x^2}{a^2+b^2}\right). \tag{10}$$

Inserting this ansatz into Eq. (8), separating real and imaginary parts, and matching powers of x and θ, the following system of coupled nonlinear equations for the parameters is obtained:

$$A'(z) = -\frac{A\zeta}{2a}; \qquad \delta'(z) = -\frac{1}{2a^2} + \ln\left(\frac{aA^2}{\sqrt{a^2+b^2}}\right) \tag{11}$$

$$a'(z) = \zeta; \quad b'(z) = \mu; \quad \zeta'(z) = \frac{1}{a^3} - \frac{2a}{a^2+b^2}; \quad \mu'(z) = -\frac{2b}{a^2+b^2} \tag{12}$$

It is clear that the equation for the phase contribution $\delta(z)$ is unimportant for the soliton dynamics which is determined by the remaining five equations. From these equations it can be inferred that $aA^2 =$ constant and the last four equations can be reduced to the following second order system of coupled differential equations for the two parameters a and b that together determine the dynamics of the physically important intensity distribution:

$$a''(z) = \frac{1}{a^3} - \frac{2a}{a^2+b^2}; \qquad b''(z) = -\frac{2b}{a^2+b^2}. \tag{13}$$

From this system it is possible to derive a single nonlinear equation for the combination $W(z) \equiv a^2(z) + b^2(z)$ which characterizes the width of the intensity profile viz.

$$(W')^2 = 8HW - 8W\ln W - C. \tag{14}$$

where C is a constant of integration and H denotes the (constant) value of the Hamiltonian

$$H \equiv \frac{1}{2}(a')^2 + \frac{1}{2}(b')^2 + \frac{1}{2a^2} + \ln(a^2+b^2) = \text{constant}. \tag{15}$$

Comparing with the corresponding result in the Wigner case, Eq. (7), it is clear that the dynamic behaviour of the intensity widths in the two representations is identical.

The result in the stationary case can be obtained by matching the solution to the initial condition. In this case all initial values of the parameter functions vanish except for $a(0) = a_0$ and $\mu(0)/\sqrt{2\theta_0^2} = -1$. The condition $W = a^2 + b^2 =$ constant implies $W = a_0^2$ and requires $W'' = H - \ln W - 1 = 0$. The value of the Hamiltonian is obtained by noting that $a'(0) = \zeta(0) = 0$ and $b'(0) = \mu(0) = -\sqrt{2\theta_0^2}$, which implies

$$1 = H - \ln W = \frac{1}{2}\left(\dot{b}(0)\right)^2 + \frac{1}{2a_0^2} = \theta_0^2 + \frac{1}{2a_0^2} = \theta_0^2 + \frac{1}{2W} \tag{16}$$

and the stationary width is given by $\sqrt{W} = 1/\sqrt{2(1-\theta_0^2)}$ in full agreement with the result obtained by the Wigner analysis. It should be noted that even in the stationary case, the functions $a(z)$ and $b(z)$ are varying although the combination $a^2 + b^2$ remains constant.

4. SOLITON INTERACTION

An approximate analysis of the interaction between two well separated coherent solitons, $\psi_1(x,z)$ and $\psi_2(x,z)$ can be based on the system of two coupled NLS equations, c.f. [13]:

$$\begin{aligned} i\frac{\partial\psi_1}{\partial z} + \frac{1}{2}\frac{\partial^2\psi_1}{\partial x^2} + (\psi_1+\psi_2)\ln\left(|\psi_1|^2\right) = 0 \\ i\frac{\partial\psi_2}{\partial z} + \frac{1}{2}\frac{\partial^2\psi_2}{\partial x^2} + (\psi_1+\psi_2)\ln\left(|\psi_2|^2\right) = 0, \end{aligned} \tag{17}$$

In the present application the soliton interaction can be analyzed using the ansatz $\psi_n(x,z) = A_n(z)\exp[-(x-\xi_n(z))^2 + 2i\mu_n(z)(x-\xi_n(z)) + i\delta_n(z)]$, where $A_n(z), \xi_n(z), \mu_n(z)$ and $\delta_n(z)$ denote slowly varying functions of z representing amplitude, position, frequency and phase respectively. Following the same variational approach as used in [13], a single differential equation of Hamiltonian form describing the evolution of the relative distance $r(z) = \xi_1 - \xi_2$, is obtained viz.

$$\frac{1}{2}(r')^2 + 2\cos(\phi)\exp\left(-\frac{r^2}{2}\right)\left[r^2 + 5 - 2\ln(A^2)\right] \equiv \frac{1}{2}\left(\frac{dr}{dz}\right)^2 + \Pi(r;A,\phi) = H = \text{constant}. \tag{18}$$

The dynamics of the soliton interaction can be inferred from the properties of the potential function, $\Pi(r;A,\phi)$, in Eq. (18) as a function of separation, r, average amplitude, $A = (A_1 + A_2)/2$, and phase difference, $\phi = 4(\mu_1+\mu_2)r + \delta_2 - \delta_1$. Were the latter two quantities are constants of motion. A picture, qualitatively similar to that of the Kerr nonlinearity, emerges where both monotonously separating and oscillating behaviour are possible, depending on initial conditions. As for the Kerr case, the conditions for the different types depend on a combination of initial phase, amplitude, and relative distance.

An indication of the effect of partial coherence on soliton interaction can be inferred by generalizing the analysis in [14] of the interaction between two soliton stripes to the case of logarithmic nonlinear media. In this application the initial wave field is given as

$$\psi(x,y,z=0) = \psi_1(x)\int C(\theta)\exp(i\theta y)d\theta + \psi_2(x)\int C(\theta)\exp(i\theta y)d\theta \tag{19}$$

where $\psi_n(x)$ denote the (Gaussian shaped) solitons, the incoherence is restricted to the y direction, and $C(\theta)$ is a stationary stochastic process (common for both solitons) satisfying $\langle C^*(\theta_1)C(\theta_2)\rangle = J(\theta_1)\delta(\theta_1-\theta_2)$. Adapting the analysis in [14] to the logarithmic nonlinearity, one finds that the dynamic equation for the soliton separation is analogous to Eq. (18), except that the potential function now is given by

$$\Pi(r;A,J(\theta)) \equiv 2\int_{-\infty}^{\infty} J(\theta)\cos(\phi+\sigma(\theta))d\theta\exp\left(-\frac{r^2}{2}\right)\left[r^2+5-2\ln(A^2)\right] \tag{20}$$

where $\sigma(\theta)$ is the phase shift between the solitons, experimentally introduced by splitting a single beam into two beams and then passing one of them through a tilted glass plate. By analyzing the potential function given by Eq. (20), it is found that the effect of the partial coherence on the soliton dynamics in the logarithmic nonlinear medium is qualitatively the same as for the Kerr medium.

5. CONCLUSION

The present analysis has reconsidered the problem of the dynamics of partially coherent solitons in media with logarithmic nonlinearity using both the Wigner and coherent density function formalisms. Although the final results regarding the evolution of the intensity distribution of the solitons are equivalent, the Wigner approach (as well as the approach based on the mutual coherence function [9]) involves a more direct analysis than the coherent density approach in the sense that the Wigner approach is based on a smaller set of "natural" variables than the coherent density approach. In particular, the coherent density function approach requires a more comprehensive modelling of amplitude and phase characteristics of the coherent density function, which plays the role of an auxiliary function for which not all parameters have a physical interpretation. An illustration of this is the fact that even in the case of a stationary intensity profile, the coherent density function involves significant dynamics, although the physically relevant intensity profile remains constant. On the other hand, the coherent density function approach provides a more convenient frame work in other applications, e.g., for studying interaction between solitons in a logarithmic nonlinear medium c.f. [11, 14]. To illustrate this an analysis is made for the problem of interacting soliton stripes using the coherent density formalism. The result indicates that the interaction between the solitons is qualitatively similar to that in a Kerr medium. In particular, it is found that with decreasing coherence the interaction strength decreases and the character of the interaction may change between attractive and repulsive and vice versa.

REFERENCES

1. Mitchell, M., Z. Chen, M.-F. Shih, and M. Segev, "Self-trapping of partially spatially incoherent light," *Phys. Rev. Lett.*, Vol. 77, 490, 1996.
2. Christodoulides, D. N., T. H. Coskun, M. Mitchell, and M. Segev, "Theory of incoherent self-focusing in biased photorefractive media," *Phys. Rev. Lett.*, Vol. 78, 646, 1997.
3. Pasmanik, G. A., "Self-action of incoherent light beams," *Sov. Phys. JETP*, Vol. 39, 234, 1974.
4. Helczynski, L., D. Anderson, R. Fedele, B. Hall, and M. Lisak, "Propagation of partially incoherent light in nonlinear media via the Wigner transform," *IEEE J. STQE*, Vol. 8, 408, 2002.
5. Christodoulides, D. N., E. D. Eugenieva, T. H. Coskun, M. Segev, and M. Mitchell, "Equivalence of three approaches describing partially incoherent wave propagation in inertial nonlinear media," *Phys. Rev. E*, Vol. 63, 035601-1(R), 2001.
6. Lisak, M., L. Helzcynski, and D. Anderson, "Relation between different formalisms describing partially incoherent wave propagation in nonlinear optical media," *Optics Comm.*, Vol. 220, 321, 2003.
7. Snyder, A. W. and J. D. Mitchell, "Mighty morphing spatial solitons and bullets," *Optics Lett.*, Vol. 22, 16, 1997.
8. Christodoulides, D. N., T. H. Coskun, and R. I. Joseph, "Incoherent spatial solitons in saturable media," *Optics Lett.*, Vol. 22, 1080, 1997.
9. Krolikowski, W., D. Edmundson, and O. Bang, "Unified model for partially coherent solitons in logarithmically nonlinear media," *Phys. Rev. E*, Vol. 61, 3122, 2000.
10. Hansson, T., D. Anderson, M. Lisak, V. E. Semenov, and U. Österberg, "Propagation of partially coherent light beams with parabolic intensity distribution in noninstantaneous nonlinear Kerr media," *J. Opt. Soc. Am. B*, Vol. 25, 1780, 2008.
11. Semenov, V., M. Lisak, D. Anderson, T. Hansson, L. Helczynski-Wolf, and U. Österberg, "Mathematical basis for analysis of partially coherent wave propagation in nonlinear, noninstantaneous, Kerr media," *J. Phys. A*, Vol. 41, 335207, 2008.
12. Guo, R., C.-F. Huang, and S.-M. Liu, "Interactions of partially incoherent spatial solitons in logarithmic saturable nonlinear media," *J. Opt. A: Pure Appl. Opt.*, Vol. 8, 695, 2006.
13. Anderson, D. and M. Lisak, "Bandwidth limits due to mutual pulse interaction in optical soliton communication systems," *Optics Lett.*, Vol. 11, 174, 1986.
14. Anderson, D., L. Helczynski-Wolf, M. Lisak, and V. Semenov, "Interaction between two partially incoherent soliton stripes," *Optics Comm.*, Vol. 281, 3919, 2008.

Chirped Self-similar Spatial Solitary Waves

K. Senthilnathan[1], **Abdosllam M. Abobaker**[2], **and K. Nakkeeran**[3]

[1]Department of Physics, National Institute of Technology, Rourkela 769008, Orissa, India
[2]The Higher Institute of Electronics, Department of Computer Engineering
P. O. Box: 38645, Bani-Waild, Libya, Africa
[3]School of Engineering, Fraser Noble Building, King's College, University of Aberdeen
Aberdeen AB24 3UE, Scotland, UK

Abstract— We consider the evolution of nonlinear optical pulses in graded-index amplifiers exhibiting self-focusing or self-defocusing non-Kerr nonlinearities. The pulse propagation in such nonlinear media is governed by the generalized cubic-quintic nonlinear Schrödinger equation. Using the self-similar analysis, we analytically find the chirped bright soliton solutions in the anomalous and normal dispersion regimes. These chirped spatial solitary waves may find applications in future all optical networks.

1. INTRODUCTION

It is well known that soliton is a localized wave and is stable. It propagates over a long distance with neither attenuation nor change of shape in a nonlinear medium. In optical fibers, the resulting optical soliton is chirp free. In the recent past, chirped solitary pulses draw special attention owing to its potential applications in optical pulse compressors as well as amplifiers [1, 2]. Recently the dynamical evolution of the bright and dark chirped solitary pulses has been investigated by many techniques [1–6]. Self-similar analysis is one of the techniques with which self-similar chirped solitary pulses have been analyzed [1–3].

Self-similarity is a common phenomenon in nature. Common objects like tree branches, snowflakes, clouds, rivers, or shorelines, appear similar even at a wide range of magnification scales. An object is said to be self-similar if it looks roughly the same on any scale. Thus, self-similarity is defined as the property whereby an object or mathematical function preserves its structure when multiplied by a certain scale factor [7]. Self-similarity is more than a curiosity of nature.

By nature, during the evolution, self-similar chirped solitary pulse preserves the shape of the pulse profile whereas its amplitude and width scale with time or propagation distance [3]. The effective optical pulse compressor has also been discussed by using nonlinear non-uniform fiber Bragg grating [5]. The robust pedestal free pulse compressor has been investigated too under the influence of higher order nonlinearity called quintic nonlinearity [6]. The robustness of the proposed compressor has been tested in terms of stability of the temporal self-similar chirped solitary pulse.

When the pulse peak intensity is sufficiently large, the field-induced change of the refractive index is no longer described by the usual Kerr-type nonlinearity, i.e., $n(\omega, I) = n_0(\omega) + n_2 I$, where $n(\omega, I)$ is the refractive index of the medium, $n_0(\omega)$ is the linear refractive index of the medium, ω is the angular frequency, n_2 is the Kerr constant, and I is the intensity of the optical pulse. Higher order nonlinear effect such as the quintic nonlinearity will have to be taken into account and the refractive index will have to be modified as $n(\omega, I) = n_0(\omega) + n_2 I + n_4 I^2$, where n_4 is the quintic nonlinearity coefficient. If the optical intensity increases further due to compression, the medium will eventually become saturated. Formally the cubic-quintic nonlinearity can be obtained by expanding a saturable nonlinearity of the form $n(\omega, I) = n_0(\omega) + n_2 I/[1 + (n_4/n_2)I]$. The cubic-quintic nonlinearity can be obtained by doping a fiber or FBG with two appropriate semiconductor materials. For competing nonlinearities, one dopant should have a positive Kerr constant $n_2^{(1)} > 0$ and large saturation intensity $I_{\text{sat}}^{(1)}$ and other should have a negative Kerr constant $n_2^{(2)} < 0$ with nearly the same magnitude but much lower saturation intensity i.e., $I_{\text{sat}}^{(2)} \ll I_{\text{sat}}^{(1)}$. If the peak intensity approaches $1\,\text{GW/cm}^2$, then one can expand the expression for $n(\omega, I)$, truncate the series, and arrive at the cubic-quintic nonlinearity [1, 2]. In recent years, there are number of reports on the measurement of the cubic-quintic nonlinearity in these novel fibers [8–11]. Pulse propagation through the fibers with competing nonlinearities has received much attention since the competition between nonlinearities of different orders could result in strong stabilization of the pulse propagation [12]. Analytically, the generation of bright and dark solitons has been discussed under the cubic-quintic nonlinearity in optical fibers with constant dispersion [13, 14].

In addition to temporal chirped self-similar solitary pulses, recently the generation of spatial bright and dark chirped solitary waves has been investigated inside the planar, graded-index waveguide amplifiers with self-focusing and self-defocusing Kerr nonlinearities [3]. The main objective of the present work is to investigate whether the spatial self-similar solitary wave does exist in the presence of quintic nonlinearity.

2. THEORETICAL MODEL

The propagation of optical beam inside a planar, graded-index nonlinear waveguide amplifier under the influence of quintic nonlinearity is governed by following generalized cubic-quintic nonlinear Schrödinger (CQNLS) equation:

$$i\frac{\partial E}{\partial Z}+\frac{1}{2}\frac{\partial^2 E}{\partial X^2}-\frac{iG}{2}E+\frac{1}{2}X^2E+\gamma|E|^2E+\alpha|E|^4E=0. \tag{1}$$

Here all the physical parameters are in normalized form. The variable E is the envelope of the wave and G is the gain. γ and α represent the cubic and quintic nonlinearities, respectively. In order to solve the above CQNLS equation, we consider the following form of the self-similar wave

$$E=\frac{1}{W(Z)}\Psi\left[\frac{X-X_c(z)}{W(Z)}\right]\exp\left\{i\left[\Phi\left(X,Z\right)\right]\right\}, \tag{2}$$

where X_c is the position of the self-similar wave center.

The phase part of the self-similar wave is given by

$$\Phi(X,Z)=\frac{1}{2}CX^2+B(Z)X+\Theta(Z) \tag{3}$$

The parameter C measures the linear phase chirp of the self-similar solitary wave. Now, substituting the Eqs. (2) and (3) in Eq. (1), we get the following chirped spatial bright solitary wave under the influence of cubic-quintic nonlinearities

$$E=\frac{1}{W(z)}\left[\frac{\gamma}{4\beta}+\left[\frac{\alpha(Z)}{3\beta}+\frac{\gamma^2}{16\beta^2}\right]^{\frac{1}{2}}\cosh\left[\sqrt{8\beta}T\right]\right]^{-\frac{1}{2}}\exp[i\Phi], \tag{4}$$

where $T=\left[\frac{X-X_c(z)}{W(Z)}\right]$ and $\Phi(X,Z)=-\frac{1}{2}X^2+B_0e^ZX+\frac{(2\beta-B_0^2W_0^2)}{4W_0^2}e^{2Z}$.

The Eq. (4) represents the spatial bright chirped self-similar solitary wave which preserves the wave profile under the influence of cubic-quintic nonlinearity. However, its width and amplitude are scaled as above. In the absence of quintic nonlinearity $\alpha=0$, the resulting soliton solution is chirped and is self-similar that has already been reported in [3]. The localized solution discussed above is indeed not a soliton, strictly speaking, but rather a solitary wave, therefore it is crucial to assess the stability. The most important result in the stability theory of solitary waves is the so called Vakhitov-Kolokolov (VK) criterion for one-parameter families of solitary waves. From the VK criterion, it has been found that the above predicted spatial solitary wave is stable. The details of the calculation on the stability analysis will be presented in future publication.

3. RESULTS AND DISCUSSION

We have investigated analytically spatial soliton like self-similar wave in graded-index, nonlinear waveguide amplifiers under the influence of cubic-quintic nonlinearity. The stability of the above wave will be the crucial issue. The stability of the above wave will be analyzed by means of dint numerical techniques using split-step Fourier method. The potential application of the above predicted chirped spatial self-similar wave will be investigated and reported elsewhere. We expect to design a highly nonlinear pulse compressor which could either be more robust to variations in input pulse parameters if media with competing nonlinearities are used, or more efficient in producing the same compression ratio with small input pulse power if the two nonlinearities work together. Then, we shall also determine the true potential of the proposed pulse compressor.

REFERENCES

1. Kruglov, V. I., A. C. Peacock, and J. D. Harvey, "Exact self-similar solutions of the generalized nonlinear schrödinger equation with distributed coefficients," *Phys. Rev. Lett.*, Vol. 90, 113902, 2003.
2. Kruglov, V. I., A. C. Peacock, and J. D. Harvey, "Exact solutions of the generalized nonlinear Schrödinger equation with distributed coefficients," *Phys. Rev. E*, Vol. 71, 056619, 2005.
3. Ponomarenko, S. A. and G. P. Agrawal, "Do solitonlike self-similar waves exist in nonlinear optical media?," *Phys. Rev. Lett.*, Vol. 97, 013901, 2006.
4. Senthilnathan, K., K. Nakkeeran, K. W. Chow, Q. Li, and P. K. A. Wai, "Chirped optical solitons," *Advances in Nonlinear Waves and Symbolic Computation*, Nova, 2009.
5. Li, Q., K. Senthilnathan, K. Nakkeeran, and P. K. A. Wai, "Nearly chirp- and pedestal-free pulse compression in nonlinear fiber Bragg gratings," *J. Opt. Soc. Am. B*, Vol. 26, 432, 2009.
6. Senthilnathan, K., Q. Li, P. K. A. Wai, and K. Nakkeeran, "Robust pedestal-free pulse compression in cubic-quintic nonlinear media," *Phys. Rev. A*, Vol. 78, 033835, 2008.
7. Barenblatt, G. I., *Scaling, Self-similarity, and Intermediate Asymptotics*, Cambridge University Press, Cambridge, 1996.
8. Zhan, D. Z., D. Zhu, D. Wang, Y. Li, D. Li, Z. Lu, L. Zhao, and Y. Nie, "Third- and fifth-order optical nonlinearities in a new stilbazolium derivative," *J. Opt. Soc. Am. B*, Vol. 19, 369, 2002.
9. Boudebs, G., S. Cherukulappurath, H. Leblond, J. Troles, F. Smektala, and F. Sanchez, "Experimental and theoretical study of higher-order nonlinearities in chalcogenide glasses," *Opt. Commun.*, Vol. 219, 427, 2003.
10. Ogusu, K., J. Yamasaki, S. Maeda, M. Kitao, and M. Minakata, "Linear and nonlinear optical properties of Ag–As–Se chalcogenide glasses for all-optical switching," *Opt. Lett.*, Vol. 29, 265, 2004.
11. Sanchez, F., G. Boudebs, S. Cherukulappurath, H. Leblond, J. Troles, and F. Smektala, "Two- and three-photon nonlinear absorption in As_2Se_3 chalcogenide glass: Theory and experiment," *J. Nonlin. Opt. Phys. & Mat.*, Vol. 13, 7, 2004.
12. Kivshar, Y. S. and G. P. Agrawal, *Optical Solitons: From Fibers to Photonic Crystals*, Academic Press, San Diego, 2003.
13. Herrmann, J., "Bistable bright solitons in dispersive media with a linear and quadratic intensity-dependent refraction index change," *Opt. Comm.*, Vol. 87, 161, 1992.
14. Pushkarov, D. and S. Tanev, "Bright and dark solitary wave propagation and bistability in the anomalous dispersion region of optical waveguides with third- and fifth-order nonlinearities," *Opt. Comm.*, Vol. 124, 354, 1996.

Polarization Domain Wall Solitons in Elliptically Birefringent Optical Fibers

S. Wabnitz
Dipartimento di Elettronica per l'Automazione, Università degli Studi di Brescia
Via Branze 38, Brescia 25123, Italy

Abstract— We present analytical and numerical studies of the dynamics of polarization domains and domain wall solitons in optical fibers with elliptical birefringence. Applications to loss-free nonlinear polarizers and to cross-polarization modulation between signals in wavelength division multiplexed transmissions are discussed.

1. INTRODUCTION

First predicted by Zakharov and Mikhailov in 1987 [1], optical polarization domain walls were experimentally observed about ten years later by Pitois, Millot and Wabnitz with counter-propagating nanosecond pulses in nonlinear isotropic optical fibers [2, 3]. A polarization domain is a stable mutual arrangement of the polarization state of the two waves [1]. On the other hand, a domain wall is a kink soliton which represents a polarization switching between different domains composed of mutually orthogonal polarization states [1–3]. With perfectly isotropic fibers, in order to avoid any bending-induced birefringence, the experiments were limited by the short interaction length, which is typically of the order of one meter. Such short nonlinear interaction length prevents the observation of polarization domain walls with continuous wave (CW) beams.

We present the extension of the theory of polarization domain wall solitons to both counter and co-propagating beams of different frequency in highly birefringent (hibi), twisted and spun optical fibers [4]. In the counter-propagating case, we describe new analytical domain wall soliton solutions whose propagation velocity may be controlled, and even stopped, by simply varying the input relative intensity of the two beams [5]. These findings may open the way to a new class of low-power, nonlinear optical data storage and buffer devices based on the dynamic control of polarization encoded information in fiber loop memories. For co-propagating waves with different frequencies, mutual or cross-polarization modulation interactions may have a significant impact on polarization multiplexed wavelength-division-multiplexed (WDM) transmissions [6] and polarization-mode dispersion compensators [7]. Our analysis unveils the stable mutual polarization arrangements of WDM channels, reveals the existence of cross-polarization modulation supported domain wall solitons [8], and suggests novel polarization modulation schemes. An interesting application of our theory is the lossless polarization attraction [9, 10] of an initially depolarized probe beam into the same polarization state of either a co-propagating or a counter-propagating pump wave. Therefore we numerically investigated the feasibility of practical polarization domain-based lossless polarizers with sub-W level pumps and signals using km-long hibi fibers.

2. COUNTERPROPAGATING WAVES

Let us consider at first the counter-propagation of two waves with the same or different carrier frequency in a spun elliptically birefringent fiber. In a reference frame uniformly rotating along the fiber axis z with the spin rate τ, we may write the counter-propagating fields as $\mathbf{E}^{\pm}(Z,T) = E_x^{\pm}(Z,T)\mathbf{e}_x + E_y^{\pm}(Z,T)\mathbf{e}_y$, where $\mathbf{e}_{x,y}$ are the local linearly polarized fiber modes. In terms of elliptical eigen-polarizations (in the absence of nonlinearity) $\mathbf{e}_{1,2}$ of the fiber, we may write [4]

$$\mathbf{E}^{\pm}(Z,T) = A_1^{\pm}(Z,T)\exp\left(\pm i\beta_1 Z\right)\mathbf{e}_1 + A_2^{\pm}(Z,T)\exp\left(\pm i\beta_2 Z\right)\mathbf{e}_2 \tag{1}$$

where $\beta_{1,2}$ are the corresponding linear propagation constants, and the envelopes $A_{1,2}$ are slowly (with respect to the short linear beat length L_b of the high birefringence fiber) evolving in Z because of the nonlinear changes of the beam polarizations, that we may describe in terms of the Stokes vectors of the two beams as

$$\partial_\xi \mathbf{S}^+ = \mathbf{S}^+ \times \left(J_S\mathbf{S}^+ + J_X\mathbf{S}^-\right), \quad \partial_\eta \mathbf{S}^- = \mathbf{S}^- \times \left(J_S\mathbf{S}^- + J_X\mathbf{S}^+\right), \tag{2}$$

where the self-polarization rotation tensor $J_S = \mathrm{diag}(J_{S1}, J_{S2}, J_{S3}) = \mathrm{diag}(0, 0, \alpha)$, the cross-polarization rotation tensor $J_X = \mathrm{diag}(\beta, -\beta, \gamma)$, $\xi = (T + Z/V_g)/2$, $\eta = (T - Z/V_g)/2$, and V_g is

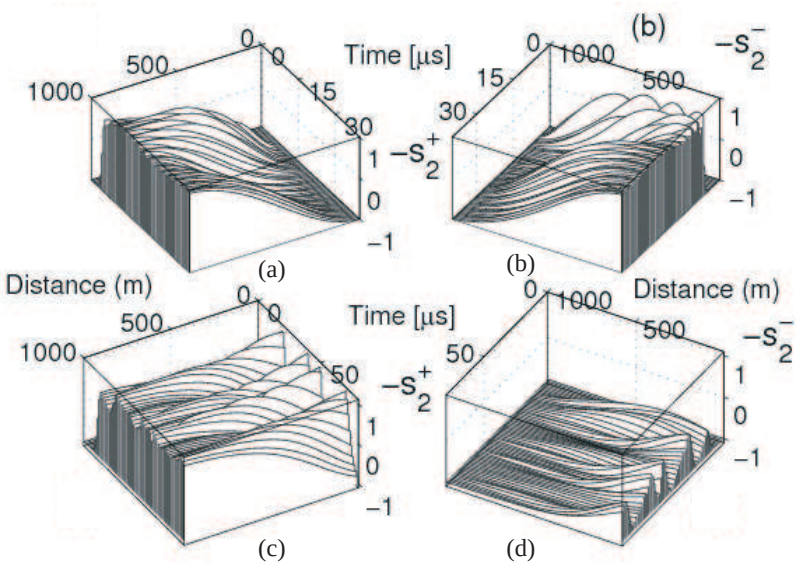

Figure 1: Space-time evolution of the s_2 stokes parameter of the counter-propagating waves, showing: (a), (b) polarization domain wall formation; (c), (d) damping (growth) of the initial polarization fluctuations of the forward (backward) wave.

the linear group velocity in the fiber. The parameters α, β, and γ depend upon the tensor response of the cubic nonlinearity, as well as the spin rate τ [4, 5]. In the special case of counter-propagating beams with equal power $P = P_+ = P_-$, one obtains the stationary (i.e., time-independent) polarization domain wall solution of Eq. (2)

$$\mathbf{s}^{\pm}(Z) = \pm \left(c_1 \operatorname{sec h}\left[\rho\left(Z - Z_0\right)\right],\ -\tanh\left[\rho\left(Z - Z_0\right)\right],\ c_3 \operatorname{sec h}\left[\rho\left(Z - Z_0\right)\right]\right) \tag{3}$$

where $\mathbf{s} = \mathbf{S}/P$ is the dimensionless Stokes vector, $c_1 = \sqrt{2/(3+\alpha')}$, $c_3 = \sqrt{(1+\alpha')/(3+\alpha')}$, $\rho = \sqrt{2(1+\alpha')}\beta/V_g$, $\alpha' = \alpha/\beta$, and z_0 is a position shift. In the case of unequal beam powers, and $\alpha = 0$, the solution (3) may be easily extended to a traveling-wave domain wall solution moving with the nonlinear group velocity

$$V_{nl} = V_g \left(P_+ - P_-\right) / \left(P_+ + P_-\right).$$

Polarization walls may be created in the fiber by imposing the proper boundary conditions [2, 3, 5]. Figures 1(a) and (b) show the evolution along $L = 1\,\mathrm{km}$ of linear hibi fiber of the s_2 Stokes parameter of the forward and backward beams with $P_+ = P_- = 500\,\mathrm{mW}$ and the same wavelength $\lambda = 1550\,\mathrm{nm}$. We set the fiber nonlinear index $n_2 = 3.2 \times 10^{-20}\,\mathrm{m}^2/\mathrm{W}$ and its effective area $A_{eff} = 10\,\mu\mathrm{m}^2$. The initial condition is the unstable arrangement consisting of two parallel linearly polarized waves oriented at 45° to the birefringence axes of the fiber.

Polarization attraction into the stable domains may be exploited to implement a nonlinear lossless polarizer [8]. This effect is illustrated in Figures 1(c) and (d) where we show the s_2 parameter of a forward signal with $P_+ = 250\,\mathrm{mW}$ and of a backward pump with $P_- = 500\,\mathrm{mW}$ in an elliptically birefringent fiber (with ellipticity angle $\theta = 35°$). Here we imposed a nearly 100% modulation of the forward s_2 at $Z = 0$ for $T > 0$. This creates stable antiparallel domains at $Z = L$. As a result, input polarization fluctuations of the forward beam are strongly damped at the fiber output, whereas backward beam polarization fluctuations are introduced at $Z = 0$ (see Figures 1(c) and (d)).

3. COPROPAGATING WAVES

A treatment similar to that of the previous section may be applied to describing the mutual nonlinear polarization changes of two optical waves at nearby frequencies ω_a and ω_b, that co-propagate in a spun birefringent optical fiber. In this case, one obtains for the Stokes vectors associated with the two waves the coupled equations

$$\partial_\xi \mathbf{S}^a = \mathbf{S}^a \times \left(J_S \mathbf{S}^a + J_X \mathbf{S}^b\right), \quad \partial_\eta \mathbf{S}^b = \mathbf{S}^b \times \left(J_S \mathbf{S}^b + J_X \mathbf{S}^a\right), \tag{4}$$

where $J_X = \mathrm{diag}(J_{x1}, J_{x2}, J_{x3}) = \mathrm{diag}(\delta, \delta, \rho)$, where δ and ρ depend upon the nonlinearity and the spin rate (note that a different J_X is obtained with respect to the case of counter-propagating beams). The characteristic coordinates read as $\xi = (Z + T/\Delta)/2$, $\eta = (Z - T/\Delta)/2$, with $\Delta = (1/V_a - 1/V_b)/2$, and $V_{a,b}$ are the group velocities of pulses at ω_a and ω_b. For an eigenmode ellipticity parameter $t = \tan(\theta/2) < \sqrt{3} - \sqrt{2}$, and equally intense waves of power P, the two vectors $\mathbf{s}^{a,b} = (\pm 1, 0, 0)$ represent unstable saddle points emanating separatrix trajectories (see the thick red curves in Figure 2, left) that represent the stationary (i.e., space-independent) kink solitons

$$\mathbf{s}^a(T) = (\mp \tanh\left[C\left(T - T_0\right)\right],\ \pm a/\cosh\left[C\left(T - T_0\right)\right],\ b/\cosh\left[C\left(T - T_0\right)\right]) \tag{5}$$

where $a = \sqrt{(J_{x3} - J_{x1} + J_{s3})\,/\,(J_{x3} + J_{x1} + J_{s3})}$, $b = \sqrt{2J_{x1}\,/\,(J_{x3} + J_{x1} + J_{s3})}$, $C = \sqrt{2J_{x1}(J_{x3} - J_{x1} + J_{s3})}P/\Delta$, and T_0 is an arbitrary time shift. Moreover we have set $\mathbf{s}^a \equiv \mathbf{S}^a/\mathbf{P} = (s_1^a, s_2^a, s_3^a) = (s_1^b, -s_2^b, s_3^b)$. The polarization domain wall (5) describes a switching of polarization between the two stable (with respect to spatio-temporal perturbations) parallel polarization arrangements $\mathbf{s}^{a,b} = (1, 0, 0)$ and $\mathbf{s}^{a,b} = (-1, 0, 0)$. On the other hand, Figure 2 (right) shows that, for $t > \sqrt{3} - \sqrt{2}$, the saddles coincide with the polarizations $\mathbf{s}^{a,b} = (0, 0, \pm 1)$, so that cross-polarization solitons similar to those in Eq. (5) can again be found [8].

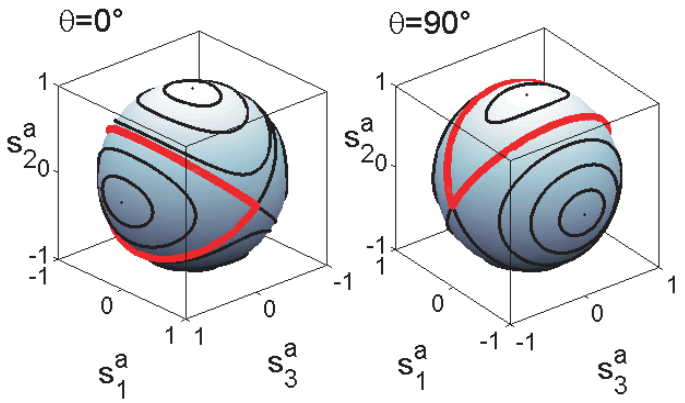

Figure 2: Trajectories of Stokes vector $\mathbf{s}^a$ on the Poincaré sphere representing space-independent solutions for the self and cross-polarization modulation in a linearly ($\theta = 0$) and circularly ($\theta = 90°$) birefringent fiber. Thick red curves represent polarization kink solitons.

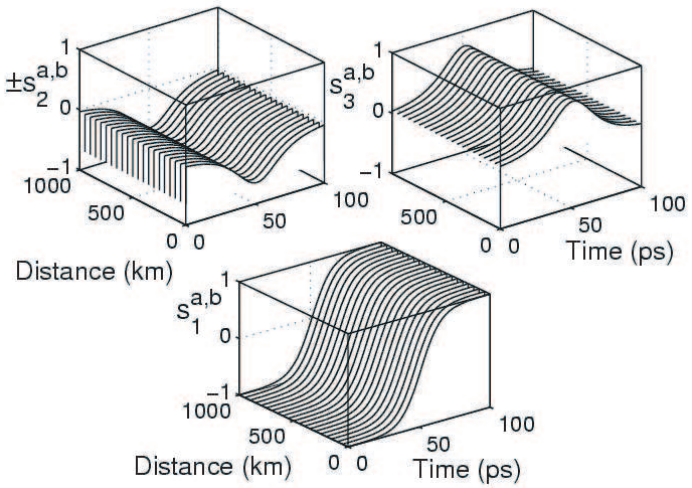

Figure 3: Stable numerical propagation of an input cross-polarization domain wall soliton over 1000 km of linearly birefringent fiber.

Figure 3 illustrates the results of the numerical integration of Eq. (4) with initial conditions given by the polarization domain wall soliton (5). We considered two 1 mW beams at $\lambda = 1550$ nm spaced by 50 GHz, co-propagating in a linearly hibi fiber ($\theta = 0$) with the GVD of $D = 1\,\mathrm{ps/(nm\ km)}$. As shown in Figure 3, full switching between two pairs of orthogonal polarization arrangements is obtained on a timescale of 60 ps. Figure 3 shows the propagation of the cross-polarization soliton (5) over 1000 km, and it confirms its spatio-temporal stability. Indeed, Figure 3 confirms that when the proper iniput polarization modulation is used, nonlinear cross-polarization modulation may compensate for the GVD induced temporal walk-off between the two wavelength channels.

The existence of stable domains of parallel mutual polarization arrangements for different wavelength channels in birefringent fibers may lead to the possibility of implementing nonlinear loss-free polarizers in a co-propagating configuration as well. A first proof of principle demonstration of such device was obtained by solving Eq. (4) with an initially randomly polarized in time, 1 mW CW probe wave, co-propagating in a short loop of linearly birefringent fiber along with a 50 GHz spaced, circularly polarized, 3 mW CW pump. After re-circulating for 50 ms, it was observed that the probe acquired the same polarization state of the pump [8].

4. CONCLUSION

In conclusion, we obtained stable polarization domain wall stationary as well as slow wave soliton solutions for the evolution of the state of polarization of counter-propagating waves in highly birefringent spun optical fibers. The sign and magnitude of the soliton propagation velocity may be controlled by varying the power of the two waves at their respective input ends. Additionally, we described the cross-polarization modulation mediated interaction between two WDM channels in optical fibers with elliptical birefringence. We obtained novel analytical domain wall soliton solutions that represent the locked temporal switching of the state of polarization of both beams. The possibility of implementing the loss-less nonlinear polarization attraction functionality in a co-propagating geometry was numerically predicted.

REFERENCES

1. Zakharov, V. E. and A. V. Mikhailov, "Polarization domains in nonlinear optics, *Pis'ma Zh. Eksp. Teor. Fiz.*, Vol. 45, No. 6, 279–282, 1987. [*JETP Lett.*, Vol. 45, No. 6, 349–352, 1987].
2. Pitois, S., G. Millot, and S. Wabnitz, "Polarization domain wall solitons with counterpropagating laser beams," *Phys. Rev. Lett.*, Vol. 81, No. 7, 1409–1412, 1998.
3. Pitois, S., G. Millot, and S. Wabnitz, "Nonlinear polarization dynamics of counterpropagating waves in an isotropic optical fiber: Theory and experiments," *J. Opt. Soc. Am. B*, Vol. 18, No. 4, 432–443, 2001.
4. Mikhailov, A. V. and S. Wabnitz, "Polarization dynamics of counterpropagating beams in optical fibers," *Opt. Lett.*, Vol. 15, No. 19, 1055–1057, 1990.
5. Wabnitz, S., "Chiral polarization solitons in elliptically birefringent spun optical fibers," *Opt. Lett.*, Vol. 34, No. 7, 908–910, 2009.
6. Mollenauer, L. F., J. P. Gordon, and F. Heismann, "Polarization scattering by soliton-soliton collisions," *Opt. Lett.*, Vol. 20, No. 20, 2060–2062, 1995.
7. Bononi, A., A. Vannucci, A. Orlandini, E. Corbel, S. Lanne, and S. Bigo, "Degree of polarization degradation due to cross-phase modulation and its impact on polarization-mode dispersion compensators," *J. Lightwave Technol.*, Vol. 21, No. 9, 1903–1913, 2003.
8. Wabnitz, S., "Cross-polarization modulation domain wall solitons for WDM signals in birefringent optical fibers," *Photonics Technol. Lett.*, Vol. 21, In press, 2009.
9. Pitois, S., A. Picozzi, G. Millot, H. R. Jauslin, and M. Haelterman, "Polarization and modal attractors in conservative counterpropagating four-wave interaction," *Europhys. Lett.*, Vol. 70, No. 1, 88–94, 2005.
10. Pitois, S., J. Fatome, and G. Millot, "Polarization attraction using counter-propagating waves in optical fiber at telecommunication wavelengths," *Opt. Express*, Vol. 16, No. 9, 6646–6651, 2008.

L-band Tunable High Repetition Rate Synchronized Fiber Laser

A. A. Sysoliatin[1], **M. Y. Salganskii**[1], **A. I. Konyukhov**[2], **L. A. Melnikov**[2], **and V. A. Stasyuk**[3]

[1]Fiber Optics Research Center, Russia
[2]Saratov State University, Russia
[3]Pritel, Inc., USA

Abstract— We experimentally demonstrate the possibility to build up the L-band tunable GHz repetition rate fiber laser via a dispersion flattened dispersion decreasing fiber. The dispersion decreasing fiber enhance effect of the Raman scattering on the pulse propagation. After propagation in 42 m-length fiber the 1550 nm input pulses obtain a large red-shifted spectral sideband. The spectral shift depends on the input pulse peak intensity. The band-pass filter applied for output radiation produces picosecond pulses at 1610 nm. The pulses are fully synchronized with clock source. Numerical simulations were made and show good agreement with the experimental results.

1. INTRODUCTION

A high repetition rate, widely tunable L-band source can be very attractive for modern optical networks. It is well known that the dense wavelength-division multiplexing is an efficient method for increasing the capacity of fiber transmission systems. As the number of channels increases, the required number of lasers becomes large if each channel has its own transmitter. Therefore, the spectral slicing of a single coherent broadband transmitter has attracted much attention, especially for Gbit/s systems with external modulators. A GHz repetition rate L-band source can be very important for high-capacity fiber transmission systems [1].

In particular, the dispersion decreasing fiber (DDF) waveguides with length varying anomalous dispersion are successfully applied to efficient compression of picosecond and subpicosecond pulses and generation of the smooth and stable against pump noise supercontinuum [2]. As theoretically shown, the propagation of a pulse in a waveguide with a length varying chromatic dispersion is formally equivalent to the propagation of the pulse in a fiber amplifier with a certain gain. This effect is physically based on the fact that nonlinear effects increase as compared to the dispersion effects in the process of propagation through the waveguide.

The design of dispersion varying fibers has been advanced through the development of novel technology for length-varying fiber drawing from standard preforms. It allows fibers with a necessary length dependence of the diameter to be fabricated. The dispersion deviation from the prearranged value is less than 0.5%. This technology has become possible thanks to the real time digital signal processing used for the control of the fiber drawing process.

The single mode fibers with dispersion varying along the length are attracting a considerable attention due to their value to control optical solitons in time and frequency domain. Improved pulse quality with minimal or no pedestal component can be achieved by the adiabatic compression technique using dispersion decreasing fibers. The DFDDF allows one to obtain an efficient spectral broadening that is stable in the presence of noise [3]. A tunable source can be based on the supercontinuum generation [3] and on the Raman conversion of the carrier frequency of the optical soliton [4]. Last method could be high efficient especially whether smooth tuning in some frequency range is required. Recently an efficient optical scheme has been proposed capable to generate 90 fs pulses at MHz pulse repetition rates, smoothly tuned in the telecommunication range using a high nonlinear dispersion decreasing fiber [5]. The smooth tuning is based on the Raman frequency conversion of ultrashort pulses. However, until now nobody was able to build up the L-band tunable GHz picosecond source well synchronized with basic clock.

We experimentally demonstrate the possibility to build up the L-band tunable GHz repetition rate fiber laser via a dispersion flattened dispersion decreasing fiber. High quality fully synchronized with clock source 0.9 ps pulses are generated.

2. EXPERIMENTS

Our experimental setup includes an actively mode-locked fiber laser operating at 5.37 GHz as a source of 2.6 ps pulses at central wavelength $\lambda_0 = 1552$ nm, high power fiber amplifier, DFDDF

(dispersion flattened dispersion decreasing fiber), filter at 1610 nm after the fiber (Fig. 1). To analyze the pulse propagation a spectrum analyzer, autocorrelator and power meter are used. The measurements have been carried out for different levels of EDFA pump current. The DFDDF fiber has convex dispersion function vs wavelength and linear dispersion function vs fiber length. In experiments 42 m-length fiber was used. Outer diameter of the fiber decreases from 148 μm to 125 μm. Group velocity dispersion (GVD) and effective area of fundamental mode are shown in Fig. 2. At 1552 nm the DFDDF's dispersion slopes are 0.01 ps km^{-1}nm^{-2}, 0.03 ps km^{-1}nm^{-2} and 0.04 ps km^{-1}nm^{-2} for outer diameters $d = 125$ μm, $d = 137$ μm and $d = 148$ μm correspondingly. The dispersion calculated for the fiber with constant diameter $d = 125$ μm agrees well with measurements (Fig. 2(a)).

Spectra obtained after propagation of 2.6 ps pulses in DFDDF are shown in Fig. 3. Due to the stimulated Raman scattering [4], a red-shifted sideband appears in the spectrum (Fig. 4(a)). Using commercially available WDM bandpass filter we produce 0.9 ps pulses at 1610 nm. These pulses

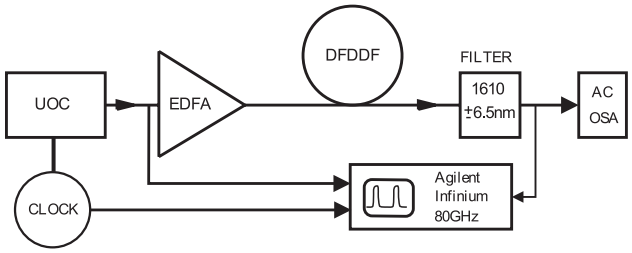

Figure 1: Experimental setup: Pritel UOC, picosecond pulse source; EDFA, Er-doped fiber amplifier; DFDDF, 42 m length of dispersion flattened dispersion decreasing fiber; AC, autocorrelator "Femtochrome"; OSA, optical spectrum analyzer "Ando AQ6317"; "Agilent Infinium", sampling scope with 80 GHz bandwidth; "FILTER", WDM filter "Koncent KOAD-020-A-1610-900L-NN".

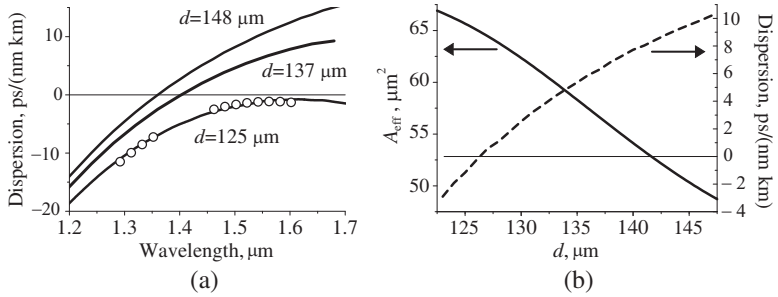

Figure 2: Dispersion properties of DFDDF. (a) Dispersion of three fibers with constant outer diameter. Curves show calculated dispersion. Open circles show measured dispersion, (b) dispersion and effective area (A_{eff}) of fundamental mode versus outer diameter of DDF.

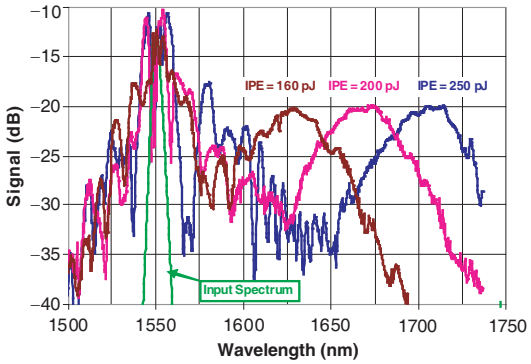

Figure 3: Optical spectra of the output of the DFDDF fiber at several input pulse energies (IPE). Input pulse repetition rate was 5.37 GHz.

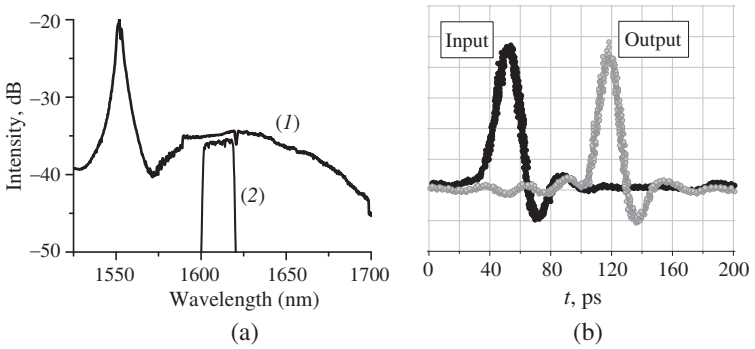

Figure 4: (a) Optical spectra of the output of the DFDDF fiber (1) and the radiation after the passing through the 1610 nm filter (2), (b) sampling scope trace of the pulse at DFDDF input (black color) and output signal of 1610 nm filter (gray color). Input pulse repetition rate was 5.37 GHz. Input pulse energy was 140 pJ.

are synchronized with the input (Fig. 4(b)). For a high pulse energies, a broadband continuum radiation was observed. However, it is essential that the input pulse energy should not exceed some critical value to obtain the high quality fully synchronized output pulses at 1610 nm after the filter.

3. SIMULATION

The numerical simulations which model pulse propagation in the DDF are based on the nonlinear Schrödinger equation:

$$\frac{\partial A}{\partial z} + \frac{\alpha}{2}A(z,t) = \sum_{m=2}^{7} \frac{i^{m+1}\beta_m(z)}{m!}\frac{\partial^m A}{\partial t^m} + i\left(P_{NL} + i\frac{2}{\omega_0}\frac{\partial P_{NL}}{\partial t}\right), \tag{1}$$

where z is the distance along fiber, t is the time, $A(z,t)$ is the complex pulse envelope, $\alpha = 0.08\,\mathrm{km}^{-1}$ is the linear absorption coefficient, which corresponds to 0.35 dB/km measured loss, ω_0 is the carrier frequency of the pulse. Functions $\beta_m(z)$ take into account longitudinal variation of the fiber dispersion. The approximation $\beta_m(z) = \sum_{i=-2}^{i=3} a_{mk} d(z)^k$ was used. Where $d(z)$ is the DDF outer diameter. Nonlinear polarization P_{NL} includes effects of Kerr nonlinearity and delayed Raman scattering.

$$P_{NL}(z,t) = \gamma(z)|A|^2 A + \gamma_R(z) Q A(z,t), \tag{2}$$

where $\gamma(z) = 2\pi\lambda_0^{-1} n_2 A_{\mathrm{eff}}(z)^{-1}$, $n_2 = 3.0 \times 10^{-20}\,\mathrm{m^2W^{-1}}$, $\gamma_R(z) = 0.3\gamma(z)$. The Raman delayed response $Q(z,t)$ is approximated by damping oscillations:

$$\left(\partial^2 Q/\partial t^2\right) + 2T_2^{-1}\left(\partial Q/\partial t\right) + \Omega^2 Q(z,t) = \Omega^2 |A(z,t)|^2, \tag{3}$$

where $T_2 = 32\,\mathrm{fs}$, $\Omega(2\pi)^{-1} = 13.1\,\mathrm{THz}$. The Equation (1) was solved using standard split-step Fourier algorithm [2].

Autocorrelation trace of input pulses was perfectly approximated by autocorrelation trace calculated for hyperbolic secant pulse: $A(0,t) = \sqrt{P_0}\,\mathrm{sech}(1.76\,tT_{\mathrm{FWHM}}^{-1})\exp(iCt^2/2)$, where P_0 is the pulse peak power, $T_{\mathrm{FWHM}} = 2.6\,\mathrm{ps}$ is intensity full-width at half maximum (FWHM) pulse duration. The chirp $C = 0.07\,\mathrm{ps}^{-2}$ was introduced to match spectral FWHM of initial pulses used in modelling and experiments.

Due to the decreasing of the absolute value of the dispersion the initial solitonic pulse is strongly compressed (Fig. 5(a)). As result the generation of Raman red-shifted radiation become efficient. Simulation shows that sideband at $\lambda > 1570\,\mathrm{nm}$ (Fig. 5(b)) appears after the propagation distance $z = 35\,\mathrm{m}$. Results demonstrate a good qualitative agreement between experimental and simulated characteristics of output pulses (Figs. 5(b) and 5(c)). The output pulse has narrow peak with broad pedestal (Fig. 5(a)). Due to this feature autocorrelation trace does not allow to estimate pulse width properly. However the calculated and measured autocorrelations demonstrate similar shapes (Fig. 5(c)). Filtering the spectrum (Fig. 5(b), top) numerically the single pulse was obtained. With the higher pulse energies a fine structure appears in the spectrum. The spectrum calculated after bandpass filter contains intensity oscillations, which destroys the formation of the single pulse after filter.

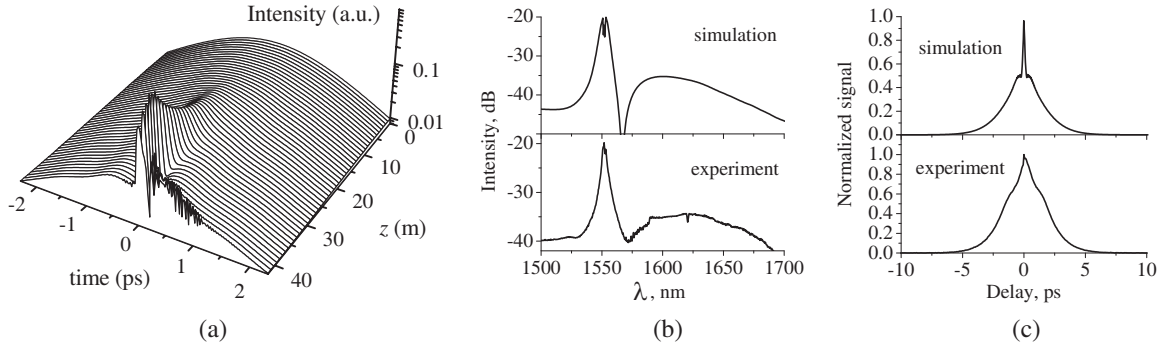

Figure 5: Simulation of the pulse compression and red-shifted sideband generation. (a) Pulse dynamics. Pulse spectra, (b) and autocorrelation curves, (c) after 42 m propagation in DFDDF. Input pulse energy is 140 nJ.

4. CONCLUSION

In conclusion, we have demonstrated what is, to the best of our knowledge, the first L-band tunable GHz repetition rate fiber laser. The novel efficient optical scheme allows to generate high quality 0.9 ps pulses at 1610 nm pulses, fully synchronized with basic clock at multi gigahertz pulse repetition rate.

ACKNOWLEDGMENT

The reported investigations were partially supported by the grant No. 09-02-00991-a of the Russian Fund of Basic Research. Authors are grateful to Prof. E. M. Dianov and Dr. K. V. Reddy for fruitful discussions and contribution to this work.

REFERENCES

1. Tamura, K., H. Kubota, and M. Nakazawa, "Fundamentals of stable continuum generation at high repetition rates," *IEEE J. of Quantum Electron.*, Vol. 36, 773–779, 2000.
2. Agrawal, G. P., *Nonlinear Fiber Optics*, 3rd Edition, Academic, San Diego, 2001.
3. Yu, C. X., H. A. Haus, E. P. Ippen, W. S. Wong, and A. Sysoliatin, "Gigahertz-repetition-rate mode-locked fiber laser for continuum generation," *Opt. Lett.*, Vol. 25, 1418–1420, 2000.
4. Dianov, E. M., A. Yu. Karasik, P. V. Mamyshev, et al., "Stimulated-Raman conversion of multisoliton pulses in quartz optical fibers," *JETP Lett.*, Vol. 41, 294–297, 1985.
5. Andrianov, A. V., S. V. Muraviev, A. V. Kim, and A. A. Sysoliatin, "DDF-based all-fiber optical source of femtosecond pulses smoothly tuned in the telecommunication range," *Laser Physics*, Vol. 17, 1296–1302, 2007.

Moving Solitons in a Cavity Soliton Laser

K. Mahmoud Aghdami[1], F. Prati[2], G. Tissoni[2], M. Brambilla[3], and L. A. Lugiato[2]

[1]Physics Department, Payame Noor University, Mini City, Tehran 19569, Iran
[2]INFM-CNR and CNISM, Dipartimento di Fisica e Matematica, Università dell'Insubria, Como, Italy
[3]INFM-CNR and CNISM, Dipartimento di Fisica Interateneo, Politecnico di Bari, Italy

Abstract— We show that in a cavity soliton laser based on a VCSEL with a saturable absorber the solitons can spontaneously move. A key parameter ruling the dynamical instability is the ratio of the carrier lifetimes in the amplifier and in the absorber. The direction of the spontaneous motion is arbitrary but it can be controlled by injecting a low-intensity guiding beam for a short interval of time. The final velocity of the moving soliton is determined by the parameters of the system.

1. INTRODUCTION

Cavity solitons (CSs) are bright intensity peaks over a dark homogeneous background. They typically arise in the coherent field transmitted by nonlinear optical resonators driven by a homogeneous holding beam, and are generated through diffraction-mediated light-matter interaction which leads to field self-localization within the cavity [1]. CSs have been experimentally demonstrated in broad area, driven vertical cavity surface emitting lasers (VCSELs) below and above threshold [2, 3]. A radical simplification could be achieved implementing the concept of Cavity Soliton Laser (CSL), i.e., a device generating CS without holding beam. Such a device, in addition to having maximum contrast between the CSs and the homogeneous background, would have tremendous advantages in terms of simplicity, robustness, and compactness, especially if realized in semiconductor-based microresonators.

The first theoretical prediction of dissipative optical localized structures (autosolitons) in a laser with a saturable absorber was proposed by Rosanov and co-workers [4] in the limit of fast materials, then it was extended to the case of finite relaxation times by the same group [5], and spontaneous motion of the localized structures was demonstrated [6].

Here, we consider a VCSEL with an absorbing medium integrated in the cavity, taking into account the finite relaxation rates of the material, the saturable dispersion associated with the linewidth enhancement factors [7], and the radiative recombination processes typical of semiconductors [8]. Different methods for switching on/off CSs and the dynamical behavior of the laser during the different switching processes have been investigated [9].

The first experimental demonstration of a semiconductor CSL has been achieved recently with an alternative scheme in which a frequency selective feedback element is placed in an external-cavity configuration for the VCSEL [10]. More recently, a saturable absorber based semiconductor CSL has been experimentally realized with two mutually coupled broad-area semiconductor resonators, where one is pumped above transparency and plays the role of the laser, while the other one plays the role of the saturable absorber [11].

In this paper, we investigate the mechanism giving rise to a dynamical instability leading to the spontaneous motion of cavity solitons. A key role is played by the ratio between nonradiative recombination lifetimes in the amplifier and in the absorber.

2. DYNAMICAL EQUATIONS

The dynamics of a laser with saturable absorber can be described by the following set of equations

$$\dot{F} = \left[(1-i\alpha)\,D + (1-i\beta)\,d - 1 + i\nabla_\perp^2\right] F \tag{1}$$

$$\dot{D} = b_1\left[\mu - D\left(1+|F|^2\right) - B\,D^2\right] \tag{2}$$

$$\dot{d} = b_2\left[-\gamma - d\left(1+s\,|F|^2\right) - B\,d^2\right] \tag{3}$$

where F is the slowly varying amplitude of the electric field, D and d are the population variables related to the carrier densities in the active and passive material, respectively. The parameters α and b_1 (β and b_2) are the linewidth enhancement factor and the ratio of the photon lifetime to

the carrier lifetime in the active (passive) material, μ is the pump parameter of the active material and γ is the absorption parameter of the passive material, s is the saturation parameter and B is the coefficient of radiative recombination. For more details on the definition of the parameters see [7, 8]. Time is scaled to the photon lifetime, and space to the diffraction length. Typically a time unit is $\sim 4\,\mathrm{ps}$ and a space unit $\sim 4\,\mu\mathrm{m}$. The parameters $s = 1$, $\gamma = 2$, $\alpha = 2$, $\beta = 1$, $b_1 = 0.01$, $B = 0.1$ are kept fixed throughout the paper. We use as free parameters the pump μ and the ratio $r = b_2/b_1 = \tau_1/\tau_2$ of the carrier lifetime in the active and in the passive medium.

The homogeneous stationary solution of Equations (1)–(3) consists in a lower branch corresponding to the non-lasing (off) state, that is stable up to the laser threshold μ_{thr}, and an upper branch which, for our choice of the parameters, is modulationally unstable everywhere in the positive slope part (solid line in Fig. 1) [8]. Numerical integration is performed for different values of the pump parameter μ via a split-step method on a 128×128 spatial grid (we use fast Fourier transform for integrating the diffraction term and Runge-Kutta for the rest).

In Fig. 1, we show the homogeneous stationary solution (solid line) and CS branch (dashed line), as a function of the pump parameter μ.

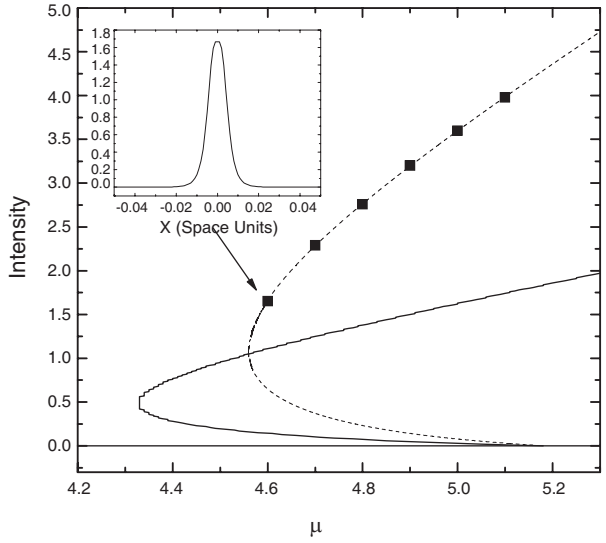

Figure 1: Intensity of homogeneous stationary solution and peak intensity of cavity soliton (CS) solution as a function of the pump parameter μ. Squares represent sample CSs whose dynamical properties will be considered later ($4.6 \leq \mu \leq 5.1$). Inset, bell shape intensity profile of the CS corresponding to $\mu = 4.6$.

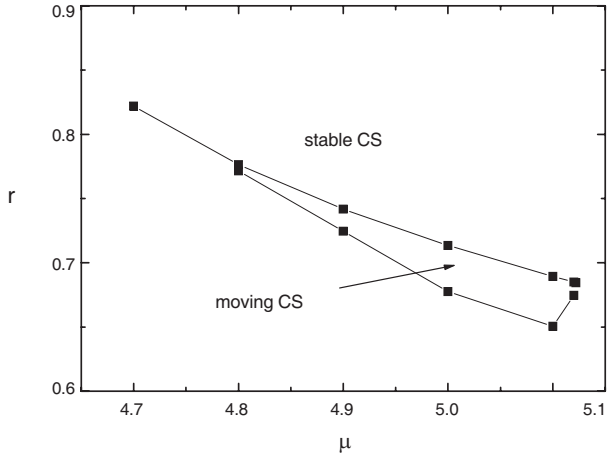

Figure 2: Stability domain of the stationary and moving CS in the plane of the parameters μ and r, obtained by numerical integration of the dynamical equations.

3. CS STABILITY AND MOTION

The linear stability analysis of the stationary CS solution can be performed via a Newton-Raphson method. The parameter $r = b_2/b_1 = \tau_1/\tau_2$ has a significant effect on CS stability, as it can be seen by looking at Fig. 2. If one considers the stable CS with $r \geq 0.72$ and $\mu = 5.0$, reduces r keeping μ fixed (crossing the instability boundary of Fig. 2 from above), the CS undergoes a dynamical instability, which is responsible for spontaneous moving of CS, as we can see when we numerically integrate the dynamical equations. As a matter of fact, starting the simulation from a stationary CS, after an initial motionless stage it begins to move along a line. The direction of motion is completely arbitrary and it is determined by noise. Fig. 3 (left) shows that, after a transient accelerated motion, the CS moves with a constant velocity that depends on r. As we further decrease r below the instability threshold the velocity of the CS increases and its peak intensity decreases, as shown in Fig. 3 (right).

For even smaller values of r, a further threshold is crossed and the moving CS is no longer stable. A fast displacement of CS requires fast transversal shift of the population deep (peak) in the amplifier (absorber) medium, and there is evidently a limit in what the system can tolerate. Depending on the values of r and μ, the system can either precipitate to the non-lasing solution or develop a turbulent behavior, similarly to what typically happens in the region above threshold $\mu > \mu_{th} = 5.18$ [7] The stability domain of the moving CS in the plane (r, μ) is shown in Fig. 2.

As briefly mentioned before, the direction of the CS motion is arbitrary, and it is determined by noise. This represents a strong limitation to the exploitability of this spontaneous CS motion for applications, such as a shift register or a delay line [12]. The problem could be solved if one could force the CS motion in a desired direction. This can be achieved by injecting a weak guiding beam in the vicinity of the CS for a short interval of time (hundreds of picoseconds, depending on the peak intensity and waist). The CS is immediately attracted towards the injected beam and will therefore start and perform its motion in the imposed direction, and even the initial "inertial" stage disappears. This method works for both guiding beams that have a frequency close to that of the laser field (semi-coherent injection [9]) and for guiding beams that have a very different frequency (incoherent injection [9]).

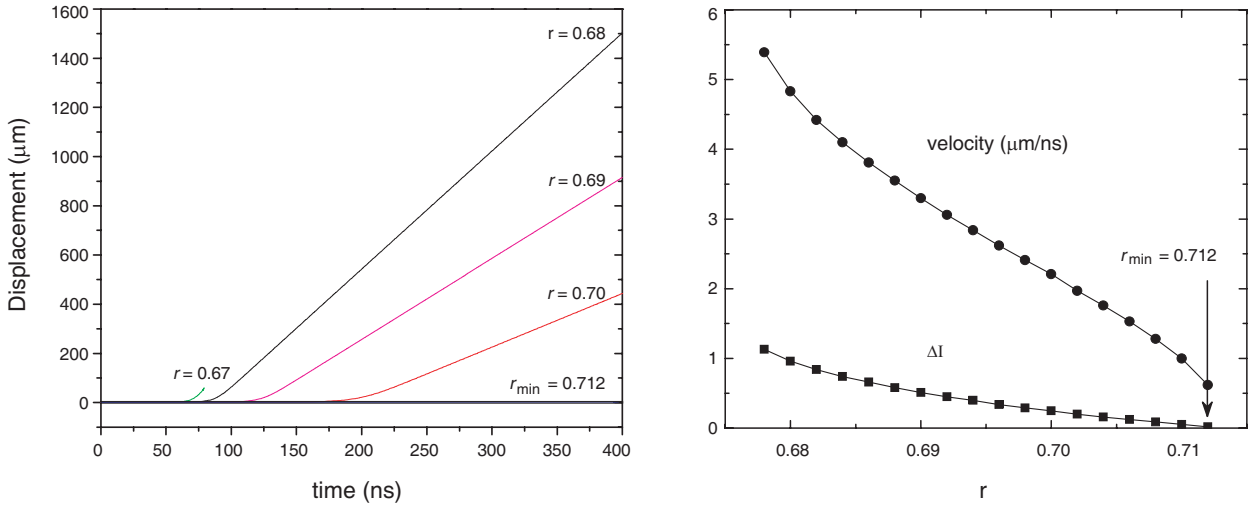

Figure 3: Left: Displacement of CS vs. time for different values of r. Right: Velocity of the moving CS and difference ΔI between the peak intensity of the stationary and of the moving CS as a function of the bifurcation parameter r. In both panels we consider the case $\mu = 5$.

4. CONCLUSION

We have shown that in a CSL scheme based on a VCSEL with a saturable absorber there are parametric conditions for which the CS can exist only if it moves in the transverse plane, with a velocity that depends on the parameters of the system. CS velocity is of the order of a few μm/ns. The possibility of handling the CS route by injecting a low-intensity guiding beam is one of the most remarkable properties.

REFERENCES

1. Lugiato, L. A., "Introduction to the feature section on cavity solitons: An overview," *IEEE J. Quantum Electron.*, Vol. 39, No. 2, 193–196, 2003.
2. Barland, S., et al., "Cavity solitons as pixels in semiconductor microcavities," *Nature*, Vol. 419, 699–702, 2002.
3. Hachair, X., et al., "Cavity solitons in a driven VCSEL above threshold," *Journal of Selected Topics in Quantum Electronics*, Vol. 12, 339–351, 2006.
4. Rozanov, N. N. and S. V. Fedorov, "Diffraction waves of switching and autosolitons in a saturable-absorber laser," *Opt. Spectrosc.*, Vol. 72, 1394, 1992.
5. Fedorov, S. V., A. G. Vladimirov, G. V. Khodova, and N. N. Rosanov, "Effect of frequency detunings and finite relaxation rates on laser localized structures," *Phys. Rev. E*, Vol. 61, 5814–5824, 2000.
6. Fedorov, S. V., N. N. Rozanov, and A. N. Shatsev, "Two-dimensional solitons in B-class lasers with saturable absorption," *Opt. Spectrosc.*, Vol. 102, 449–455, 2007.
7. Bache, M., et al., "Cavity soliton laser based on VCSEL with saturable absorber," *Appl. Phys. B*, Vol. 81, 913–920, 2005.
8. Prati, F., et al., "Effects of carrier radiative recombination on a VCSEL-based cavity soliton laser," *Appl. Phys. B: Lasers and Optics*, Vol. 88, 405–410, 2007.
9. Mahmoud Aghdami, K., et al., "Comparison of different switching techniques in a cavity soliton laser," *Eur. Phys. J. D.*, Vol. 47, 447–455, 2008.
10. Tanguy, Y., T. Ackemann, and W. J. Firth, "Realization of a semiconductor-based cavity soliton laser," *Phys. Rev. Lett.*, Vol. 100, 013907-4, 2008.
11. Genevet, P., S. Barland, M. Giudici, and J. R. Tredicce, "Cavity soliton laser based on mutually coupled semiconductor microresonators," *Phys. Rev. Lett.*, Vol. 101, 123905-4, 2008.
12. Pedaci, F., et al., "All-optical delay line using semiconductor cavity solitons," *Appl. Phys. Lett.*, Vol. 92, 011101, 2008.

Progress in Metal-insulator-metal Waveguide Lasers at Near-infrared Wavelengths

Milan J. H. Marell and Martin T. Hill
COBRA Research Institute, Technische Universiteit Eindhoven
Postbus 513, 5600 MB Eindhoven, The Netherlands

Abstract— Strong light confinement can be achieved in metallic cavities which can confine light to volumes with dimensions considerably smaller than the wavelength of light. It was commonly believed, however, that the high losses in metals are prohibitive for laser operation in metallic nano-cavities. Recently we have reported lasing in a metallic nano-cavity filled with an electrically pumped semiconductor. Importantly, the manufacturing approach employed for these devices permits even greater miniaturization of semiconductor lasers. Furthermore, the approach allows for complex device shapes and the guiding of light between devices. Of particular interest are the metal-insulator-metal (MIM) waveguides. These MIM waveguides can propagate a transverse magnetic (TM0) mode which permits true deep sub-wavelength guiding of light in two dimensions. The manufacturing process is adapted to produce a variant of MIM waveguides. The presentation will look at the modeling, fabrication and operation of these devices. An overview will also be given of latest results from devices.

Previously reported devices observed light that leaked out of the metallic nano cavity through the device base. This is not optimal as the lasing light travels transversally between the metal sidewalls of the pillar structure. Ideally, the transverse propagating mode needs to be coupled directly out to either a conventional dielectric waveguide or free space. We will discuss our progress in making metallic cavity nano lasers with coupling of the transverse propagating mode directly to free space, and present results from our latest attempts.

1. INTRODUCTION

So far all metallic waveguide lasers have been characterized by observing light leaking through the substrate of the chip [1]. This poses difficulties with respect to their integrability in photonic circuits. Ideally the propagating mode of such a device is coupled out directly to free space or a waveguide. There are various ways in which this can be done.

In order to sustain laser operation, only a fraction of the light can be extracted from the cavity. This can be realized by incorporating a Bragg reflector at the junction with the laser. However, recent experiments show that also a cleaved facet provides sufficient reflectivity.

2. FABRICATION

The side-emitting structures are fabricated on InP/InGaAsP/InP wafers, in which 8 InGaAs quantum wells are incorporated. The quantum wells are 4.1 nm thick and the total thickness of the film layer is 510 nm. The high index contrast between the InGaAs core and InP cladding layers provides vertical confinement.

The rectangular cross-section of the structures is defined by means of electron beam lithography and lift-off the width of the structures varies from 100 nm to 250 nm. After plasma etching with a CH_4/H_2 chemistry in an ICP system, the structures are covered with a 20 nm thick Si_3N_4 layer, which serves as electrical insulation. Finally the devices are encapsulated in metal and additional metal layers are deposited to form the top contact. A more detailed description of the manufacturing process is given in [1].

After fabrication the structures are cleaved in half, forming two devices with one open facet and one covered with metal, Figure 1.

3. CHARACTERIZATION

The first side-emitting metallic lasers have been characterized in a cryostat at a temperature of 80 K. At low temperatures semiconductor gain is higher, non-radiative recombination lower, and the metal can have lower optical losses. Hence, at lower temperatures the structures are more likely to lase. The results of CW current injection measurements are shown in Figures 1 and 2.

From Figure 3.1, it can be seen that the threshold current of the metallic lasers is less than 0.5 mA and the free spectral range is 4.47 nm. At $I = 1.5$ mA the side mode suppression ratio is

22.63 dB and the laser peak is approximately 26 dB above the spontaneous emission level. This is shown in Figures 2 and 3. The length of the waveguide was measured to be approximately 62 µm.

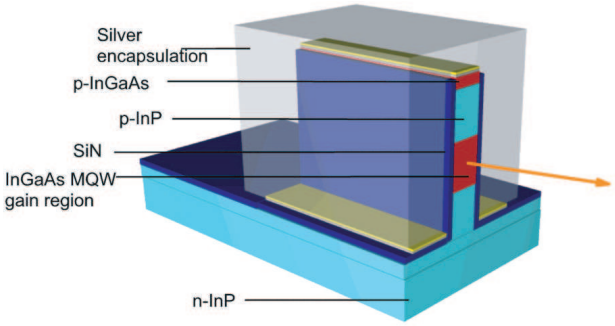

Figure 1: Schematic overview of a device after processing.

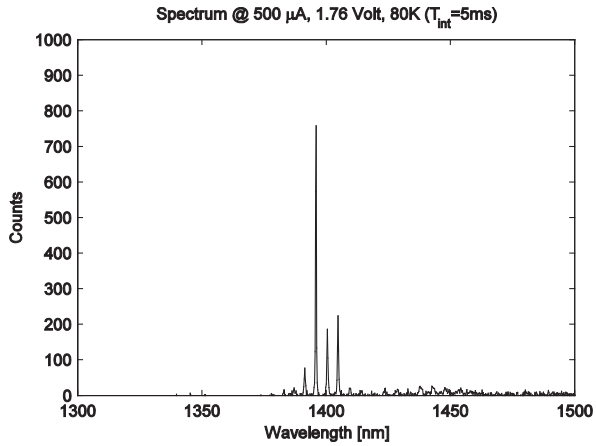

Figure 2: Power spectrum of the device just above threshold at an injection current of $I_{dev} = 0.5\,\mathrm{mA}$.

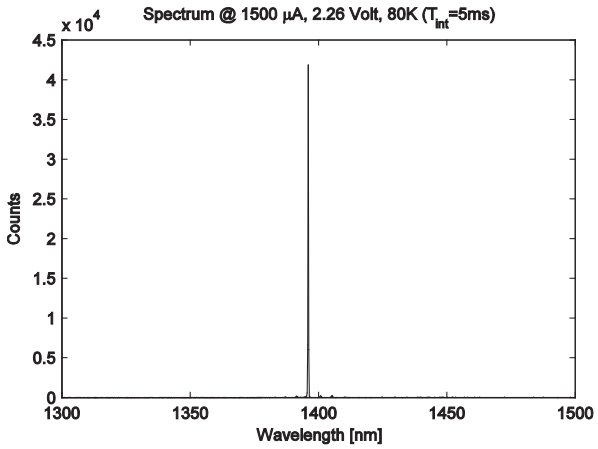

Figure 3: Power spectrum of the device well above the threshold ($I_{dev} = 1.5\,\mathrm{mA}$). One laser peak remains at a wavelength of 1396 nm.

Figure 4 shows the L-I curve of the measured device. The device does not exhibit a strong super linear L-I characteristic. This may be due to either strong coupling of spontaneous emission to the resonant modes, or possibly heating in the devices. The exact cause is under investigation.

CW Measurements have been performed for temperatures up to 200 K, the limiting factor being the current source. It is expected that lasing at room temperature is possible for pulsed current injection. These measurements, however, still need to be carried out.

4. FUTURE WORK

From the Figures 2 and 3, it can be seen that the lasing wavelength differs from the desired telecom wavelength range around 1550 nm. This can be explained by the gain material not being optimized for this purpose. In future devices a wavelength selective mirror (DBR) will be incorporated and better designed gain regions employed to achieve lasing at the desired wavelength.

FDTD Software is used to analyze the laser structures without gain. From these simulations facet reflectivities, propagation loss and optimal device dimensions can be estimated. In this section we will report briefly on the simulations we have done to determine the dimensions of the DBR reflector which we plan to use in future devices.

2D FDTD simulations have been performed. In the simulations the different materials are represented by their dielectric constant. The dielectric constant of silver is accounted for via a Lorentzian oscillator (Equation (1)), of which the parameters are chosen to match the complex

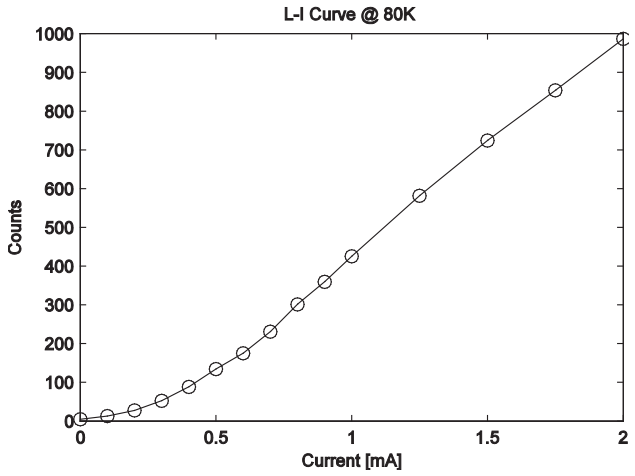

Figure 4: L-I curve of a metallic laser.

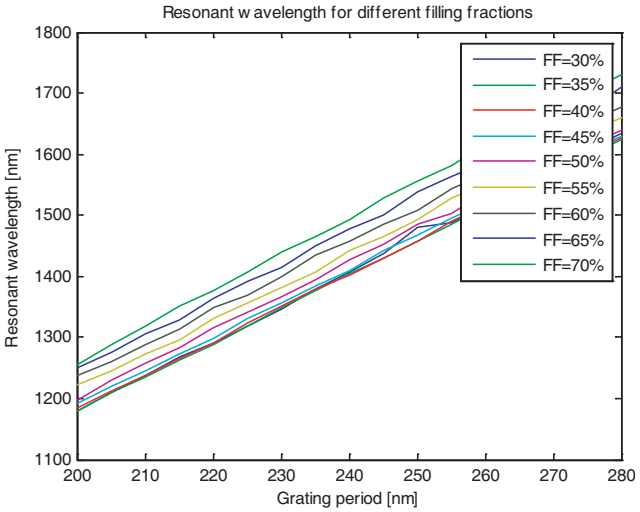

Figure 5: Results of 2D FDTD simulations of a unit cell of a metallic grating. The figure shows the resonant wavelength as a function of grating period and filling fraction (FF) defined as the fraction of outer width waveguide in a grating period.

refractive index data in the Johnson & Christy paper (2) in the wavelength range of 1 µm to 2 µm.

$$\varepsilon(\omega) = \varepsilon_\infty + \sum_n \frac{\Delta\varepsilon \cdot \omega_n^2}{\omega_n^2 - \omega^2 - i\gamma\omega} \tag{1}$$

The grating dimensions were determined by performing unit cell simulations of the structure. In these unit cell simulations inner width of the waveguide was 100 nm and the outer width of the waveguide 200 nm. The thickness of the Si_3N_4 layer was 20 nm throughout the simulations. Exclusion of the 3rd dimension in the simulations leads to a minor deviation in the resonant wavelength. More accurate 3D analysis can be performed as soon as feedback from fabrication and characterization is available.

5. CONCLUSIONS

We have shown that, despite high propagation loss in metallic waveguides, it is possible to fabricate side-emitting metallic lasers. The tested device has a side mode suppression ratio of ±23 dB and a free spectral range of 4.47 nm.

With around 0.3 mA, the threshold current of these lasers is considerably lower compared to conventional semiconductor lasers in this wavelength range. Currently the side-emitting metallic lasers operate at cryogenic temperatures < 200 K (CW), but room-temperature operation is expected for pulsed current injection.

The emission wavelength of 1396 nm is due to the material not being optimal for this purpose. Lasing at telecom wavelengths (i.e., 1550 nm) may be achieved by tuning the dimensions of the device and by incorporation of a wavelength dependent feedback mechanism, such as a distributed Bragg reflector.

REFERENCES

1. Hill, M. T., Y. S. Oei, B. Smalbrugge, et al., "Lasing in metallic-coated nanocavities," *Nature Photonics*, Vol. 1, No. 10, 589–594, October 2007.
2. Johnson, P. B. and R. W. Christy, "Optical constants of the noble metals," *Phys. Rev. B*, Vol. 6, No. 12, 4370–4379, 1972.

Slow-light Enhanced Nonlinear Optics in Silicon Photonic Crystal Waveguides

D. J. Moss[1], **B. Corcoran**[1], **C. Monat**[1], **C. Grillet**[1],
T. P. White[2], **L. O'Faolain**[2], **T. F. Krauss**[2], **and B. J. Eggleton**[1]

[1]IPOS, CUDOS, School of Physics, University of Sydney, New South Wales 2006, Australia
[2]School of Physics and Astronomy, University of St Andrews, St Andrews, Fife, KY16 9SS, UK

Abstract— We report slow-light enhanced nonlinear optics including third harmonic generation and self-phase modulation in dispersion engineered 2D silicon photonic crystal waveguides.

1. INTRODUCTION

There has been growing interest in slow light due to its potential application for optical delay lines and nonlinear optical signal processing [1]. The increase of the optical energy density due to spatial pulse compression in the slow light regime is regarded as a means for enhancing nonlinear phenomena such as Raman scattering, 2nd and 3rd harmonic generation or frequency conversion. However, apart from theoretical predictions this enhancement process has not been systematically demonstrated to date, partly due to the high dispersion that typically accompanies slow light, causing pulse distortion that compromises its benefit. Planar PhC waveguides, which combine a periodic lattice of air holes and a vertical step index waveguide, offer a unique platform to engineer the dispersion properties of light at the micrometer scale [2]. This architecture has proven to be effective and flexible to control both the speed of light and its associated dispersion in chip-scale devices. The last point is crucial for nonlinear optics as large dispersion is typically associated with slow light modes that tends to dramatically distort and stretch slow light pulses, compromising the pulse spatial compression related benefit of slow light [3]. Such a large dispersion has restricted the demonstration of nonlinear effects — such as stimulated Raman scattering or Self Phase Modulation (SPM) — in standard W_1 PhC waveguides to the fast light regime and using long ($\sim 1\,\mathrm{mm}$) waveguides. Very recently, several approaches have been successfully investigated to engineer the dispersion of slow light modes and to optimize the bandwidth-delay product in planar PhC waveguides [2, 4]. These efforts make it now possible to implement slow light in practical nonlinear functions. Combining optical confinement and dispersion engineering through the use of optimized 2D PhC waveguides is highly promising because I_ω is related to the peak power (P_ω) through

$$I_\omega \propto \frac{P_\omega}{A_\omega} \cdot \frac{n_g}{n} \tag{1}$$

where A_ω and n_g are the effective area and group index of the fundamental mode, respectively. Hence, by exploiting the extreme concentration of optical energy afforded by tight confinement of light within the high index, sub-μm scale ($A_\omega \sim 0.4\,\mu\mathrm{m}^2$) silicon PhC waveguides and spatial pulse compression in the slow light ($v_g = c/40$) regime, we significantly reduce the peak pump power required to observe nonlinear effects to the order of a few watts.

Here, we demonstrate slow light enhancement of nonlinear processes in engineered silicon PhC waveguides, including third harmonic generation (THG) and self phase modulation (SPM). Both the strong optical confinement within the waveguide and the slow light ($c/40$) mode supported by the PhC structure have enabled us to observe visible green light (at 520 nm) at low ($\sim$ several watts) peak pump powers at 1560 nm [5]. This is 5–6 orders of magnitude lower than previous free-space coupling experiments in porous silicon PhC geometries [6], and even 100x that of THG in quasi-phasematched KTP waveguides [7], and is a result of the increased optical energy density in our slow light PhC waveguide. We also report the experimental observation of slow light enhanced self-phase modulation (SPM) exhibited by picosecond-pulses propagating through silicon PhC waveguides as short as 80 μm [8]. Both of these are made possible due to engineering the PhC geometry to provide a series of waveguides with a controlled low group velocity ranging between $c/20$ and $c/50$ with a limited group velocity dispersion associated with the slow light regime over at least 5 nm bandwidth for all of the guides. The experimental results are supported by Split-Step-Fourier-Method (SSFM) modeling, including Two Photon Absorption (TPA) and free carrier (FC) effects in silicon, which gives further insight into the various contributions of these effects to both the output

pulse signature and the power transfer function. In particular, both experiment and simulation highlight the reinforcement of TPA and FC effects in the slow light regime.

2. EXPERIMENT

The structures were fabricated on a SOITEC silicon-on-insulator wafer comprising a 220 nm thick silicon layer on 2 µm of silica using e-beam lithography and Reactive Ion Etching. The total length of the waveguide structure is 0.9 mm; it comprises an 80 µm long suspended silicon PhC waveguide and two 0.4 mm long, 3 µm wide ridge access waveguides on both sides that are tapered down to 0.7 µm close to the PhC section. The PhC W_1 waveguide consists of a triangular lattice of air holes with a period a of $\sim$410 nm, and hole radii of $\sim 0.3a$, where one row of holes has been omitted along the ΓK direction. To enhance coupling from the access ridges into the slow light PhC waveguide, an intermediate region consisting of ten periods of PhC waveguide with a "stretched" lattice of period $\sim$440 nm was added at either end of the slow light PhC waveguide. The PhC waveguides were engineered to display slow group velocity with low dispersion over a substantial bandwidth ($>$ 5 nm) by appropriately shifting the two rows of holes adjacent to the W_1 PhC waveguide [2]. Figure 1(b) shows a typical measured group index dispersion of the fundamental mode of 3 engineered PhC waveguides with a group index (n_g) of varying from $c/20$ to $c/50$ over $>$ 7 nm at 1557 nm. Their parameters are summarized in [2, 8]. Figure 2 shows the band diagram of the waveguide studied for the THG experiments, both at the fundamental and third harmonic wavelengths, as well as the group index and loss versus wavelength. The device was probed using a polarization controlled, near transform-limited, figure-of-8 fibre laser, tunable over the C-band. The pulses (sech^2 shaped, $\sim$1.5 ps long, FWHM $\sim$2 nm, 4 MHz) were amplified through an EDFA and launched (TE polarized) into the waveguide, using lensed fibres with a 2.5 µm focal length. The coupling loss to the chip was obtained from modelling of the Self Phase Modulation experiments. When launching the pulses into the PhC waveguide, we observed green light emitted

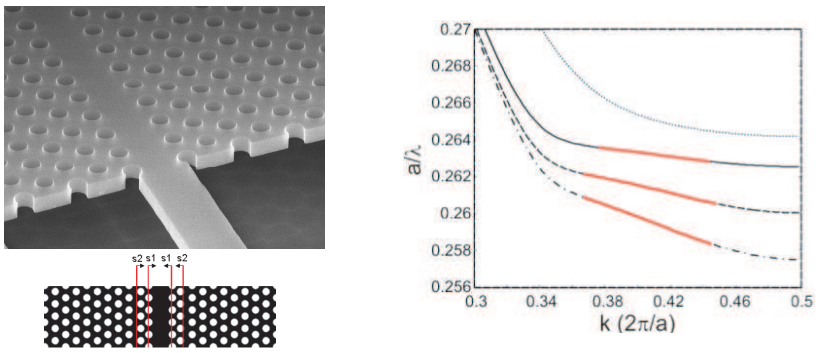

Figure 1: (a) (Left) SEM image of photonic crystal waveguide as well as (bottom) schematic showing strategy for engineering wide bandwidth low dispersion regions. (b) Right: dispersion diagram for different waveguides engineered to have high group indices.

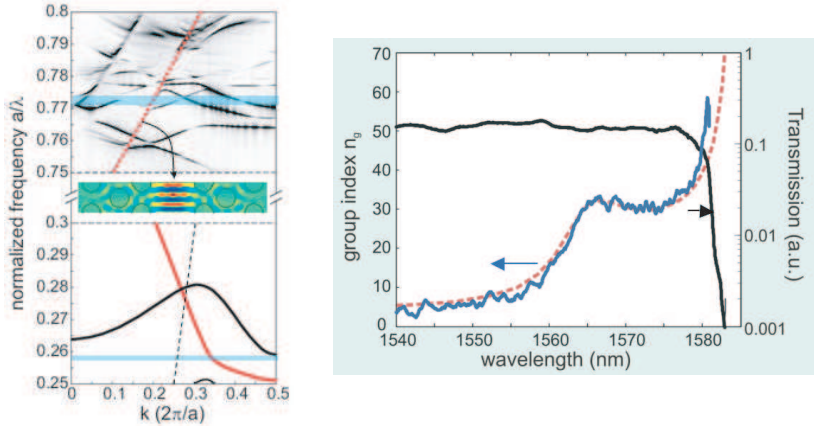

Figure 2: (a) Left: waveguide dispersion for fundamental (bottom) and third harmonic (top) wavelengths. (b) Right: group index and transmission versus wavelength.

from the surface of the chip by eye (Figure 3) emitted at an angle $\sim 10°$ from the vertical, in the backward direction. Imaging the emission onto a calibrated linear CCD camera (linearised, fixed gain, calibrated using a low RIN doubled Nd:YAG laser diode) with a 0.25 N.A. microscope objective revealed that it is localized above the PhC waveguide, and decays exponentially along its length (Figure 3). The total emitted green power at 520 nm ± 5 nm shows a cubic dependence on the coupled pump power up to $\sim 65\,\mu$W. At higher pump powers, a slight saturation occurs in the fundamental power transmission due to two-photon and subsequent free-carrier absorption. We observed a maximum THG output of ∼10 pW for 80 µW (10 W) average (peak) pump power. In order to minimize effects of propagation such as dispersion and nonlinear absorption, to determine the dependence of the THG efficiency solely on group velocity, we restricted our measurements of the THG to a within 5 µm of the PhC waveguide entrance, much smaller than the dispersion length associated with the GVD, even in the "fast light" regime. The self-phase modulation experiments were carried out by varying the input power and monitoring the output spectra on a spectrum analyzer (OSA).

3. RESULTS AND DISCUSSION

Figure 3 shows the observed THG from the waveguide as well as a schematic indicating the exit angle. Figure 4(a) shows the power dependence of the THG for as a function of input power for different wavelengths (corresponding to different group indices). The power dependence displays a clear enhancement for pump wavelengths near 1557 nm where the group velocity is lowest. Equation (1) predicts a cubic dependence on n_g of the THG power obtained at a fixed pump power. In order to minimize the nonlinear loss saturation effect discussed above at all wavelengths though, we chose instead to plot the input power density (P_ω/A_ω) required to produce a constant (and sufficiently low) THG output power (∼0.4 pW) as the wavelength (hence group index n_g) is varied. The results show very good agreement with a $1/n_g$ variation, as expected from $P_\omega/A_\omega \propto I_\omega/n_g$. Note both the trend and the variation in enhancement is well accounted for by using only the experimentally measured group velocity dispersion of Fig. 2. It is clear that a contribution from any other effect would cause a discrepancy with experiment — particularly if the wavelength variation were different to that of n_g and so these results demonstrate direct slow-light enhancement of this nonlinear process.

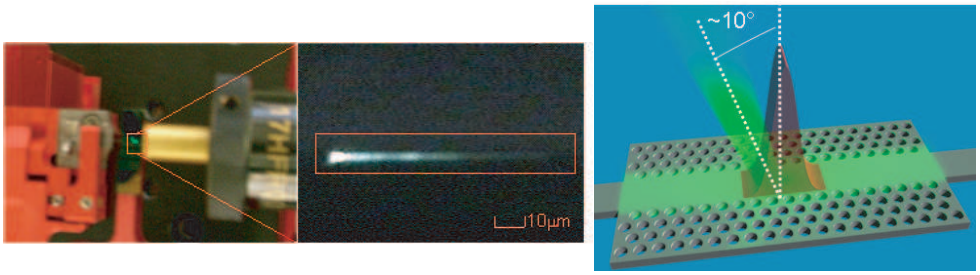

(a) (b)

Figure 3: (a) Left: Microscope image of third harmonic generation from sample and (b) Right: diagram showing green light emitted at 10°.

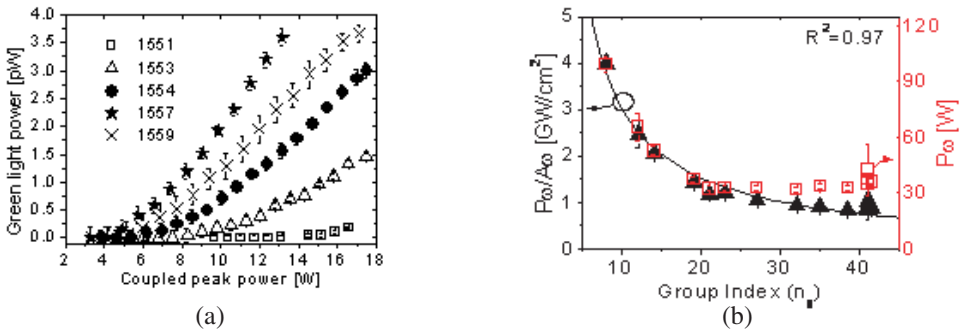

(a) (b)

Figure 4: (a) Left: Third harmonic power (top) versus coupled input power for different wavelengths and (right) THG efficiency versus n_g.

Our experiments were performed with $\sim 10\,\mathrm{W}$ peak pump powers, corresponding to a reduction of 5 to 6 orders of magnitude compared to previous reports of THG in silicon [6, 9, 10]. Even more significantly, this work represents a nearly 100-fold reduction in pump power relative to fully phase-matched THG in PPLN/KTP waveguides [7]. Although a comparable power density ($\sim \mathrm{GW/cm^2}$) has been achieved in ultra-high Q ($> 10^7$) cavities [11], the advantage of the PhC waveguide approach is that the full bandwidth of short optical pulses can be accommodated. We estimate our conversion efficiency η to be $\sim 10^{-7}$ (or 5×10^{-10} for 1 W of peak pump power), which represents an increase of 5 orders of magnitude over that reported in 3D polystyrene PhCs ($\eta \sim 10^{-15}$ for 1 W peak pump power as inferred from the quoted value of $\eta \sim 10^{-5}$ at $P_\omega = 10\,\mathrm{MW}$) [12]. This efficiency could be further improved, e.g., by decreasing the effective area ($\eta \propto 1/A_{eff}^3$) or the group velocity ($\eta \propto n_g^3$). A group velocity of $c/80$ can be reasonably well achieved with this PhC waveguide design — this would provide an order of magnitude improvement in η. Efficiency could also by improved at high pump powers by reducing the free-carrier lifetime through techniques such as ion implantation to reduce nonlinear loss of the pump.

Besides tight optical confinement and slow light, the 2D PhC geometry offers additional versatility to improve the third-harmonic generation and extraction efficiency. In periodic structures, the phase matching condition, $\Delta k = 0$, is relaxed to $\Delta k = \pm mG$, where mG can be any reciprocal lattice wave-vector, increasing the possibilities for phase matching. Perhaps more importantly in our case, since the absorption length at 3ω is extremely short ($3\,\mathrm{dB/\,\mu m}$ absorption loss at 520 nm in silicon), the PhC also provides a suitable platform for extracting light by coupling to surface radiating modes above the light-line. The directive nature of the emission ($\sim 10^\circ$) as well as the absence of green emission from the access waveguides, suggests that a component of the third-harmonic Bloch mode in the PhC lies above the light line, as illustrated by the band structure in Figure 2. This provides a mechanism for the THG to be extracted out-of-plane. However, because the 3ω Bloch mode also contains harmonic components well confined in the PhC slab below the light line, the measured pico-watt level of green emission is expected to be significantly lower than the total THG power generated in the PhC waveguide. The conversion efficiency reported above

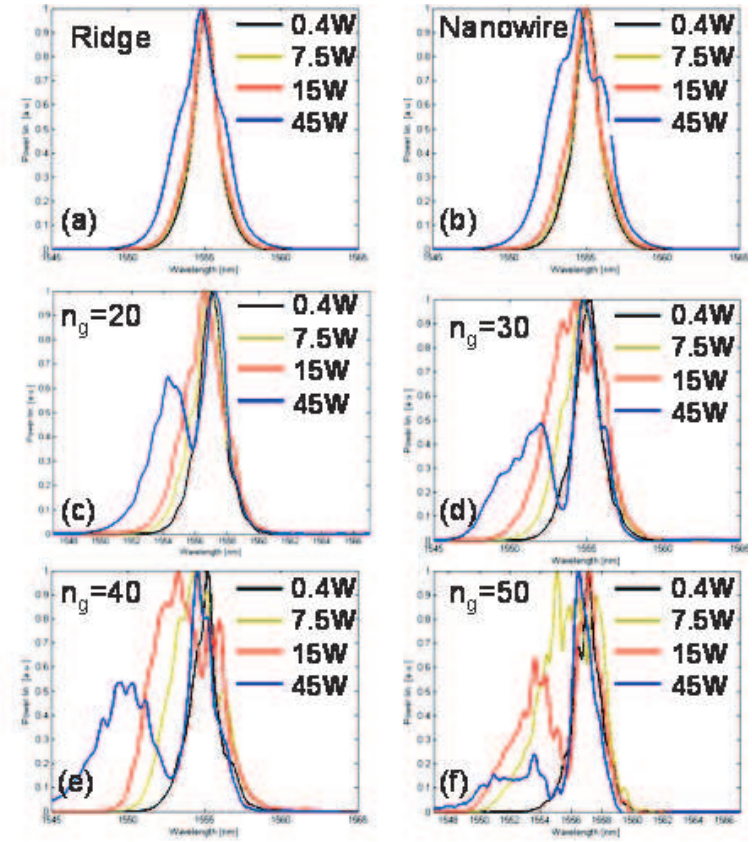

Figure 5: Output spectra of PhC waveguides for different input powers showing strong self phase modulation (SPM) enhanced by slow-light.

is therefore a conservative estimate.

For the SPM measurements, we first probed two reference structures. The first one is a 0.9 mm long, 3 µm wide ridge waveguide similar to the access ridges. The second one comprises an 80 µm long, 0.7 µm wide nanowire that is similar to the tapered ridges on both sides of the PhC section; on both sides of the nanowire, the access waveguide is tapered identically to the tapers coupling to the PhC guides therefore providing a reference fast waveguide with the same degree of optical confinement as the PhC waveguide. Figure 5 shows the spectra obtained while varying the input peak power between 2 W and 45 W. The actual peak power coupled inside the structures was $\sim 20\%$ of this. The 1.2-ps pulses were spectrally broadened due to SPM experienced in both reference waveguides. Note the slightly broader effect through the nanowire reference, as expected due to its higher optical confinement. Figure 5 also shows the spectra obtained when probing the 4 slow light waveguides with group velocities ranging between $c/20$ and $c/50$. These four sets of spectra exhibit SPM-induced spectral broadening when increasing power with a much larger effect than for either of the two reference structures. This clearly demonstrates the dominant contribution of the 80 µm slow PhC waveguides on the output spectral signatures observed in Figure 5. Most importantly, the observed spectral broadening through the slow light waveguides increases with the waveguide group index. Note that this slow light enhanced spectral broadening is more striking at lower coupled powers (7.5 W or 15 W for instance). In addition, the pulse spectra associated with the PhC waveguides become both asymmetric and strongly shifted towards blue when increasing input powers and the waveguide group index.

4. CONCLUSION

We demonstrate slow-light enhancement of nonlinear effects undergone by picosecond-pulses propagating through dispersion engineered 80 µm long silicon PhC waveguides with group velocities ranging between $c/20$ and $c/50$. The comparison of the respective output spectral signatures through fast and slow waveguides reveals significant enhancement in both SPM induced spectral broadening and optical third harmonic generation (THG).

ACKNOWLEDGMENT

The support of the Australian Research Council through its Federation Fellow, Centre of Excellence and Discovery Grant programs is gratefully acknowledged. We thank the School of Physics, University of Sydney, for its support through its Denison Foundation and the International Science Linkages program of the Department of Education, Science and Technology. The samples were fabricated in the framework of the EU-FP6 funded ePIXnet Nanostructuring Platform for Photonic Integration (www.nanophotonics.eu).

REFERENCES

1. Krauss, T. F., "Why do we need slow light?" *Nature Photonics*, Vol. 2, 448, 2008.
2. Li, J., T. P. White, L. O. Faolain, A. Gomez-Iglesias, and T. F. Krauss, "Systematic design of flat band slow light in photonic crystal waveguides," *Opt. Express*, Vol. 16, 6227–6232, 2008.
3. Baba, T., *Nature Photonics*, Vol. 2, 465–473, 2008.
4. Settle, M. D., et al., "Flatband slow light in photonic crystals featuring spatial pulse compression and terahertz bandwidth," *Opt. Express*, Vol. 15, 219–226, 2007.
5. Corcoran, B. C. M., C. Grillet, D. J. Moss, B. J. Eggleton, T. White, and T. Krauss, "Slow light enhanced visible optical third harmonic generation in 2D silicon photonic crystal waveguides," *Nature Photonics*, Vol. 3, No. 4, 1, 2009.
6. Martemyanov, M. G., et al., "Third-harmonic generation in silicon photonic crystals and microcavities," *Phys. Rev. B*, Vol. 70, 073311, 2004.
7. Rusu, M., et al., "Efficient generation of green and UV light in a single PP-KTP waveguide pumped by a compact all-fiber system," *Appl. Phys. Lett.*, Vol. 88, 121105, 2006.
8. Monat, C., B. Corcoran, M. Ebnali-Heidari, C. Grillet, B. J. Eggleton, T. P. White, L. O'Faolain, and T. F. Krauss, "Slow light enhancement of nonlinear effects in silicon engineered photonic crystal waveguide," *Optics Express*, Vo. 17, No. 4, 2944. 2009.
9. Moss, D. J., H. M. Van Driel, and J. E. Sipe, "Third harmonic generation as a structural diagnosis of ion-implanted amorphous and crystalline silicon," *Appl. Phys. Lett.*, Vol. 48, 1150–1152, 1986.
10. Moss, D. J., H. M. Van Driel, and J. E. Sipe, "Dispersion in the anisotropy for optical third harmonic generation in Si and Ge," *Opt. Lett.*, Vol. 14, 57–59, 1989.

11. Dolgova, T. V., A. I. Maidykovski, M. G. Martemyanov, A. A. Fedyanin, and O. A. Aktsipetrov, "Giant third-harmonic in porous silicon photonic crystals and microcavities," *JETP Lett.*, Vol. 75, 15–19, 2002.
12. Markowicz, P. P., et al., "Dramatic enhancement of third-harmonic generation in 3D photonic crystals," *Phys. Rev. Lett.*, Vol. 92, 083903, 2004.

Design of a Wideband Slot Bow-tie Antenna Excited by a Microstrip to CPW Transition for Applications in the Millimeter Wave Band

A. Colin[1] and P. Febvre[2]

[1]Instituto de Física de Cantabria (CSIC-UC), Av. Los Castros s/n, Santander 39005, Spain
[2]IMEP-LAHC, UMR 5130 CNRS, Campus Scientifique, University of Savoie
Le Bourget du Lac 73376, France

Abstract— We present a compact design of a slot bow-tie antenna excited by a microstrip to coplanar waveguide (CPW) transition, operating at the central frequency of 45 GHz in the millimeter wave range from 25 to 65 GHz. Simulation results have shown 85% bandwidth with VSWR < 2 for this antenna. Its small size and symmetric geometry facilitate the integration with microstrip circuits and the connection with active or passive elements. A comparison between normal and superconductive metallization in this design is also presented. This antenna can be used in array configurations for applications in wireless communications, or for astrophysical experiments based on the study of the Cosmic Microwave Background (CMB).

1. INTRODUCTION

Nowadays, studies of the Cosmic Microwave Background (CMB) require observational measurements at different frequency bands; for instance, the anomalous microwave emission is being studied as additional component of the diffuse galactic foregrounds. Previous studies have demonstrated some emission in the frequency range from 11 to 17 GHz [1]. That has also been recently measured at frequencies of ~ 31 GHz [2] although it can be observed up to 60 GHz but at lower emissivity levels. Some experiments for the CMB detection utilize conical horn antennas to receive the signal and are exposed to the environment temperature whereas the detectors system is cooled inside a cryostat at low temperature, thus giving a wide range of difficulties during the coupling of the setup. Planar array antennas could be useful to avoid some of these difficulties by selecting the correct design and materials, but that implies big challenges in the developments of new detection systems.

Bow-tie slot antennas are widely investigated for many applications where low profile, weigh, size, cost, and ease of installation are required. The bow-tie slot antennas usually present a wider bandwidth in comparison with the narrow bandwidths of the microstrip patch antennas, and have the advantage of a good impedance match and bi-directional radiation patterns. Commonly they are integrated in array systems operating in different bands, sometimes the setup is designed to use separate antennas for each band. With the emergence of new technologies, currently it turns to be possible and desirable to design a single antenna that operates in several bands as broad as possible for a same setup system. The characteristic input impedance of the feed line is one of the deciding factors which is directly associated to the antenna's bandwidth, therefore it must be carefully considered during its design. In this study the length and width of the transition stripline have been crucial for the final design, as well as the choice of the materials. The use of normal metal conductors will lead to increase losses caused by the skin depth of the order of magnitude of the film thickness. To avoid this issue, and since these arrays need to be cooled with the detectors, it is advisable to use superconducting materials.

In this paper we present the computed radiation characteristics for a single element bow-tie slot antenna printed on a commercial alumina substrate plated with gold (Au), which is excited by a microstrip to CPW transition. The feed lines have been computed and optimized using the commercial TXLINE-AWR package in order to keep the good microwave matching properties to the antenna. Then this antenna is compared with two identical antenna-geometries plated with niobium (Nb) at its corresponding normal and superconducting states. The antenna's performances were studied in both the unidirectional and bidirectional cases. To achieve the first one, we introduced a metallic reflector plane placed $\lambda_0/4$ below the substrate. All simulations were made under the environment of the HFSS-Ansoft software, which is based on the finite element method.

2. ANTENNA DESIGN

The antenna was designed as bow-tie slot centered on a rectangle ($25.4 \times 28\,\mathrm{mm}^2$) alumina substrate of 0.254 mm thickness with 3 µm electroplated gold, relative permittivity of 10, and loss tangent of

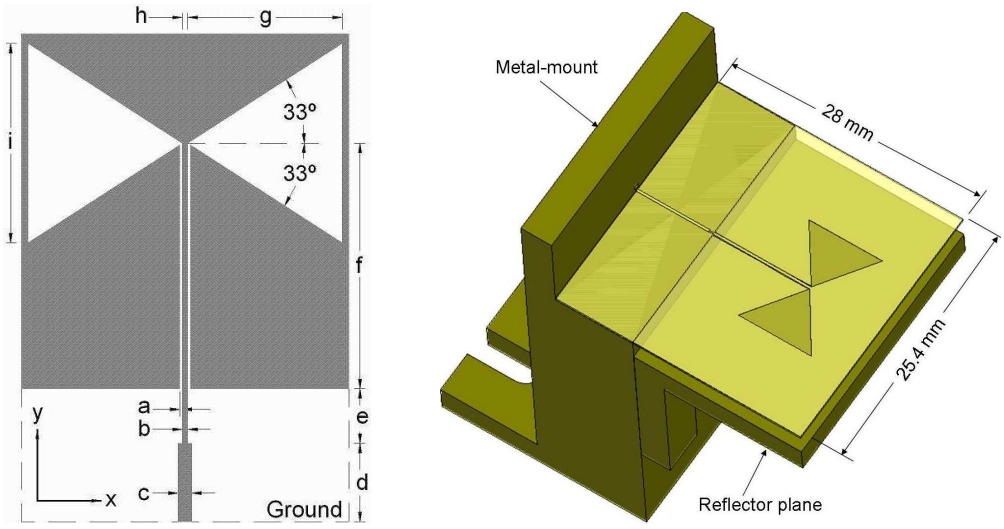

(a) (b)

Figure 1: (a) Antenna geometry (not to scale) and parameters: $a = 0.05,\ b = 0.1,\ c = 0.25,\ d = 7.5,\ e = 0.5,\ f = 10,\ g = 5.65,\ h = 0.1$, and $i = 7.3$ (all in mm). Alumina substrate: 0.254 mm thickness, 3 µm electroplated gold, $\varepsilon_r = 10$, and $\delta = 0.001$. (b) Experimental setup (not to scale) with a removable reflector plane..

0.001. The geometry and parameters of the antenna are shown in Fig. 1(a), where $a = 0.05,\ b = 0.1,\ c = 0.25,\ d = 7.5,\ e = 0.5,\ f = 10,\ g = 5.65,\ h = 0.1$, and $i = 7.3$. All dimensions are in mm. The bottom ground plane only covers the microstrip lines section (d and e dimensions). The widths of the microstrip line and gaps of the CPW were calculated to provide a characteristic impedance of approximately 50 Ohms, whose transition between them is made by means of a smaller and thinner stripline ($b \times e$ dimensions) of about 73 Ohms. Fig. 1(b) shows the experimental setup with a single element that can be attached to a metal mount with silver conductive epoxy (Epo-Tec H20E). The mount represents a metallic structure made of brass material in which a 50-Ohm hermetic seals with a coaxial jack/plug connector (Southwest Microwave, Inc.) could be integrated on its backside. A removable reflector plane is placed below the substrate in order to vary vertically its height. The centered pin-hole permits the connection between the pin-connector and the microstrip. The mount is designed to be used in direct contact with metal surfaces, as well as with the cold plate of cryostats when a low temperature experiment is required.

3. SIMULATED RESULTS

For our convenience, all numerical analysis were computed at the frequency $f_0 = 40$ GHz and the reflector plane placed at a distance of $\lambda_0/4$ below the substrate. In all cases we used an excitation wave port of 50 Ohms.

The computed return losses at the bidirectional and unidirectional cases for a single element bow-tie slot antenna metalized with Au are shown in Fig. 2 (left). According to these plots, the results show good agreement to each other and present various resonant frequencies over the entire range from 26 to 64 GHz providing around 85% bandwidth. During the design process we noticed the influence of various parameters on the antenna performance. For instance, when one of the dimensions of the transition-stripline is varied, a significant reduction of the total bandwidth and decrease of the input power transmission down to −5 dB have been observed. Fig. 2 (right), shows a comparison of the computed return losses for two identical geometries but metalized with Nb, more details will be given in Section 4.

The computed directivity radiation patterns in the x-z (H-plane) and the y-z (E-plane) at 40 GHz are shown in Fig. 3 (left). The patterns are normalized to a maximum and minimum of 0 and −40 dB respectively, with 10 dB/div. The antenna presents an average of −10 dB of cross polarization level and relatively high directivity with a narrow main lobe of around 20° in a beamwidth of 60° for both the E- and H-planes. In wireless communications one antenna can receive the signal from any direction with any polarization; hence this antenna could be utilized for this application. Whereas for the direct detection of specific electromagnetic signals, the antennas

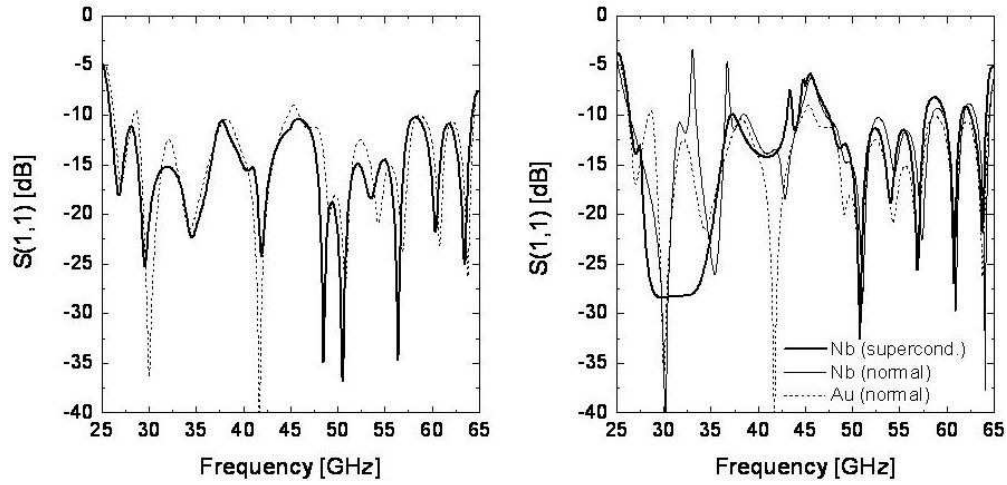

Figure 2: Left: Simulated return losses versus frequency with (dashed line) and without (solid line) reflector plane. Right: Comparison of the return losses between normal and superconducting states of *Nb*.

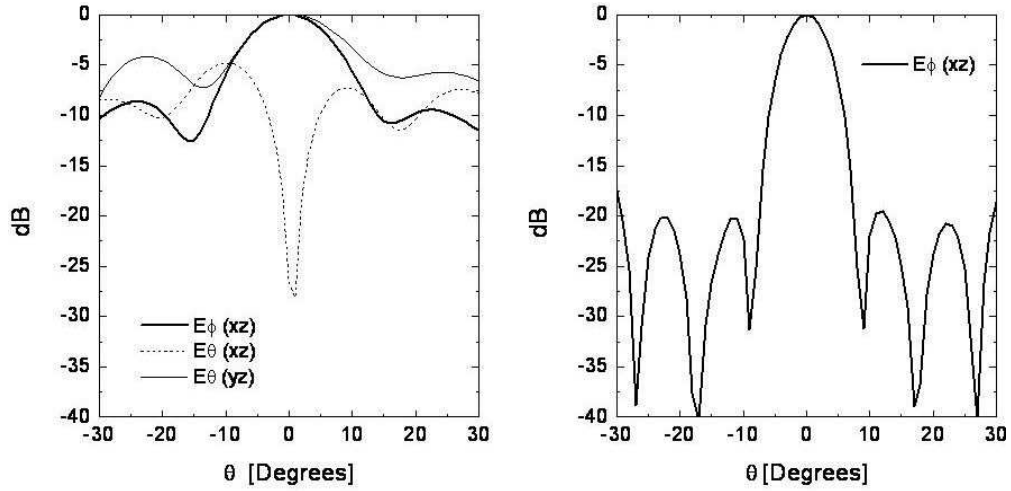

Figure 3: Simulated directivity radiation patterns using a reflector plane for a single element (left), and for a 4-element array separated by $5\lambda_0/3$ (12.5 mm) and aligned in the x-direction (right).

must be unidirectional and highly directives; to achieve this, the use of arrays can further improve the radiation patterns increasing the directivity level, as is shown in Fig. 3 (right), in which we simulated a configuration of four elements aligned in the x-direction separated by a distance of $5\lambda_0/3$ (12.5 mm) since it is the optimal free-space distance due to the antenna's geometry. For this case, the directivity level increases by a factor of about 2, thus providing side lobes at -20 dB approximately. In most cases the side lobes can be eliminated using low-pass optical filters for the desired frequency and hemispherical lenses to focus the entire signal to the receiving antenna which in turn could be connected and coupled to a detector. Therefore this antenna also provides a possibility to be used as an example, in astrophysical studies based in the CMB detection.

4. COMPARISON BETWEEN NORMAL AND SUPERCONDUCTING METALLIZATION

In order to know the superconducting behavior of this type of antenna, we simulated the full structure by replacing the *Au* by normal and superconductive *Nb*, but conserving the geometry and all the parameter dimensions. The simulations were made in two runs: the first one considers the metallization as normal metal but take into account the surface resistance in both electrodes, whereas the second one replaces the superconductive material by boundary surfaces with purely reactive surface impedance (a complete description for understanding this strategy is described in [3, 4], in which is taken into account the kinetic inductance inherent to the superconducting

state of *Nb* at 0.1 K). Although it is unusual to utilize thick films with superconductors, in these simulations we utilized them but only for comparative purposes. As we have seen in Fig. 2 (right), the comparison of the return losses show a very good matching for superconductive *Nb* but only in the frequency range from 26 to 43 GHz since the entire frequency band is divided into two parts. In contrast the normal state of *Nb* does not present good matching in the first part but in the second one, however we observed a very narrow bandwidh with a prominent resonant frequency centered around 30 GHz with a good matching.

The theoretical analysis was made following the methodology established in [4], and applied separately only to each section of the transmission feed line, as the microstrip line (MSL), the microstrip transition (MST) and the coplanar waveguide (CPW). In all cases we considered the London penetration depth as $\lambda_L = 85\,\text{nm}$ for bulk *Nb*. For convenience, we present only three of those equations given in [4] for the characteristic impedance (Z_0).

$$Z_{Wheeler}(w', h, \varepsilon_r) = 30\sqrt{\frac{2}{\varepsilon_r + 1}}\ln\left\{1+\left(\frac{4h}{w}\right)\left[\left(\frac{14+\frac{8}{\varepsilon_r}}{11}\right)\left(\frac{4h}{w}\right)+\sqrt{\left(\frac{14+\frac{8}{\varepsilon_r}}{11}\right)^2\left(\frac{4h}{w}\right)^2+\frac{1+\frac{1}{\varepsilon_r}}{2}\pi^2}\right]\right\} \quad (1)$$

$$Z_0 = Z_{vacuum}\sqrt{\frac{\mu_{eff}}{\varepsilon_{eff}}}\frac{h}{w_{eff}} \quad (2)$$

$$Z_0^t = Z_{vacuum}\sqrt{\frac{\mu_{eff}}{\varepsilon_{eff}^t}}\frac{1}{4g_1} \quad (3)$$

Equation (1), proposed in [5], was used to compute Z_0 as normal metals in the MSL and MST. For superconducting metals in the MSL and MST we used Eq. (2), here the analysis was made considering thin superconducting films of 250 nm thickness, with a silicon (SiO) lossless insulator of 200 nm thickness, and $\varepsilon_r = 5.7$. In this part of the analysis we found that by conserving the geometry dimensions of each line, the required Z_0, is reduced down to very low values associated to the very high aspect ratio of MSL. Finally Eq. (3) could be used in all cases for both the normal and superconducting states in the CPW. A summary of the simulated and computed results are shown in Table 1. Additionally the computed effective permittivity is also indicated.

Table 1: Comparison between analytical and 3D modeling results.

	Normal (Au) Thick film				**Normal (Nb) Thick film**				**Superconducting (Nb) Thin film**			
	TXLINE		**HFSS**		**Eqs. (1) & (3)**		**HFSS**		**Eqs. (2) & (3)**		**HFSS**	
	Z_0	ε_{eff}	Z_0	ε_{eff}	Z_0	ε_{eff}	Z_0	ε_{eff}	Z_0	ε_{eff}	Z_0	ε_{eff}
MSL	50.67	7.31	42.26	7.43	49.35	6.66	42.01	7.47	0.172	5.69	0.167	5.59
MST	73.24	6.71	63.27	6.83	72.11	6.31	63.49	6.82	0.425	5.51	0.38	5.22
CPW	51.10	5.16	50.18	5.30	49.70	5.06	50.89	5.36	0.169	4.28	0.153	2.81

5. CONCLUSIONS

Simulated and analytical results for bow-tie slot antennas plated with normal and superconducting metals have revealed feasibility and good expectation to be confirmed with the measurements of our prototypes.

Comparison between analytical formulas and HFSS simulations show a good agreement for superconducting structures which is promising to replace time-consuming simulations with simpler formulas whenever possible for the typical geometries.

REFERENCES

1. Watson, R. A., et al., "Detection of anomalous microwave emission in the Perseus molecular cloud with the COSMOSOMAS experiment," *Ap. J.*, Vol. 624, L89, 2005.
2. Dickinson, C., "Anomalous emission from HII regions," *CMB Component Separation and the Physics of Foregrounds*, Pasadena California, USA, July 14–18, 2008.

3. Rauly, D., A. Monfardini, A. Colin, and P. Febvre, "Design of two-band 150–220 GHz superconducting bolometric detection structure," *PIERS Online*, Vol. 4, No. 6, 671–675, 2008
4. Febvre, P., C. Boutez, S. George, and G. Beaudin, "Models of superconducting microstrip and coplanar elements for submillimeter applications," *Proc. of the Int. Conf. on Millimeter and Submillimeter Waves and Applications II*, Vol. SPIE 2558, 136–147, San Diego Convention Center, July 9–14, 1995.
5. Wheeler, H. A., "Transmission-line properties of a strip on a dielectric sheet on a plane," *IEEE Trans. Microwave Theory Tech.*, Vol. 25, 631–647, August 1977.

Numerical Reconstruction of the Refractive Index from the Reflection Data

O. V. Belai, L. L. Frumin, E. V. Podivilov, and D. A. Shapiro
Institute of Automation and Electrometry, Siberian Branch, Russian Academy of Sciences
1 Koptjug Ave, Novosibirsk 630090, Russia

Abstract— A new method of numerical reconstruction of the refractive index from the complex reflection coefficient is tested using the sinusoidal Bragg grating with deep modulation, the Rayleigh layer and the hyperbolic secant layer. The method demonstrates its high efficiency and accuracy.

1. INTRODUCTION

The inverse scattering problem (ISP) for one dimensional Helmholtz wave equation is of interest in optics, radiophysics, acoustics, geophysics. It is reduced to the reconstruction of the refractive index n as a function of coordinate x from the complex reflection coefficient. As a rule, only numerical solution is possible. The direct solution of ISP requires N^5 operations [1], where N is the number of discrete intervals. The layer peeling method requires N^2 operations [2], but it provides the first order approximation $O(1/N)$. Aiming at the accuracy ε we see that the layer peeling requires ε^{-2} operations. "Inner-bordering" method was proposed recently [3] ensuring N^{-2} approximation and N^2 operations, and then requires only ε^{-1} operations.

The aim of present paper is to test the method for errors with the help of several different types of spectra. We reconstruct the Bragg reflectors with deep modulation and transition layers between two media with different refractive index. We focus our attention on the errors of reconstruction. Section 2 is devoted to the Bremmer transformation of one-dimensional Helmholtz wave equation. We derive the set of first-order equations equivalent to the Helmholtz equation; the ISP for this set is solved in the next sections. Section 3 describes how the new method works for Bragg gratings. The direct scattering problem for these gratings was solved numerically which affected the accuracy of the input data to the inverse problem. To study the accuracy of the method on its own it is necessary to test it at exactly solvable cases. The corresponding formulas and numerical results are presented in Section 4.

2. BREMMER TRANSFORMATION

When the refractive index n depends on one coordinate x only, the Helmholtz equation has the form

$$E'' + k^2 n^2(x) E = 0, \quad k = \frac{\omega}{c}, \tag{1}$$

where E is a component of electric field, prime denotes the derivative with respect to coordinate x, k is the wavenumber, ω, c are the frequency and speed of light. Substitution

$$E(x) = \frac{1}{\sqrt{kn}} \left(A e^{iS} + B e^{-iS} \right), \quad E'(x) = i\sqrt{kn} \left(A e^{iS} - B e^{-iS} \right),$$

where $S = k \int n(x)\, dx$ is the phase, enables one to obtain the set of first order equations from (1)

$$A' = \frac{n'}{2n} B e^{-2iS}, \quad B' = \frac{n'}{2n} A e^{2iS}. \tag{2}$$

It is a particular case of Bremmer equations [4] for normal incidence. The set is completely equivalent to Eq. (1). The set describes the bulk reflection of waves from one-dimensional inhomogeneous medium. If the inhomogeneity is smooth and n' is small, both amplitudes A, B of forward and backward waves are almost constant.

Let us introduce a new coordinate, the optical path

$$\xi = \int_0^x n(x')\, dx'. \tag{3}$$

We integrate between 0 and x fixing the coordinate origin $\xi = 0$ at $x = 0$. Then the phase becomes linear function of ξ and the set reduces to

$$\frac{dA}{d\xi} = q(\xi)e^{-2ik\xi}B, \quad \frac{dB}{d\xi} = q(\xi)e^{2ik\xi}A, \tag{4}$$

where

$$q(\xi) = \frac{d\ln\sqrt{n}}{d\xi}. \tag{5}$$

The left direct scattering problem implies the absence of incident wave at the right end $x = L$ or $\xi = \Lambda$: $B(\Lambda) = 0$. This condition enables one to find the reflection and transmission coefficients r, d from Eq. (4) with known coupling function $q(\xi)$:

$$r = \frac{B(0)}{A(0)}, \quad d = \frac{A(\Lambda)}{A(0)}e^{ik\Lambda},$$

where

$$\Lambda = \int_0^L n(x)\,dx \tag{6}$$

is the complete optical path throughout the layer.

The ISP reduces to the reconstruction of function $q(\xi)$ from known frequency dependence of the reflection coefficient $r(k)$. If function $q(\xi)$ is known, then we can find the refractive index from Eq. (5) and the original coordinate from Eq. (3) by formulas of inversion:

$$n(\xi) = n(0)\exp\left[2\int_0^\xi q(\xi')\,d\xi'\right], \quad x = \int_0^\xi \frac{d\xi'}{n(\xi')}. \tag{7}$$

Zakharov and Shabat [5] reduced the ISP for a set of two linear differential equations to the pair of coupled integral equations, so called Gel'fand-Levitan-Marchenko (GLM) equations. The second-order numerical method for coupled GLM equations was proposed recently [6].

3. DEEP MODULATION

We treat a grating with deep sinusoidal modulation and Gaussian apodization function

$$n(x) = \overline{n} + \delta\exp\left[-\left(\frac{x - L/2}{Lw}\right)^2\right]\sin\kappa x, \quad 0 \leqslant x \leqslant L, \tag{8}$$

where L is the characteristic length of the grating, w is the dimensionless parameter, δ is the modulation depth. The grating consists of a small number of strips with relatively high Fresnel reflection from each.

Reflection spectrum $|r|^2$ is calculated for different values of the depth, Fig. 1. The lower solid line corresponding to relatively weak modulation $\delta = 0.1$ includes only one marked peak at the Bragg frequency given by condition $k\overline{n} = \kappa/2$. The reflectivity in its maximum is about 30%. Two upper curves demonstrate that deep modulation leads to additional peaks arising in the spectrum at higher harmonics $k\overline{n} = l\kappa/2, l = 2, 3, \ldots$. The results of ISP solution are shown in Fig. 2. The reconstructed profiles $n(x)$ are compared with initial ones. The plots are nearly coincide, and the accuracy of the reconstruction is of the order of 2×10^{-4}.

4. EXACT SOLUTIONS

The Rayleigh layer is a transition between half-spaces with constant refractive index n_1, n_2 having the hyperbolic dependence on coordinate [7]:

$$n(x) = \frac{n_1 n_2 l}{(n_1 - n_2)(x - x_0) + n_2 l}, \quad 0 \leqslant x - x_0 \leqslant l. \tag{9}$$

Here we count the coordinate x off from the left end of transition region x_0, l is the dimension of the layer. For its length in optical coordinates we get

$$\Lambda = \frac{n_1 n_2 L}{n_1 - n_2}\ln\frac{n_1}{n_2}.$$

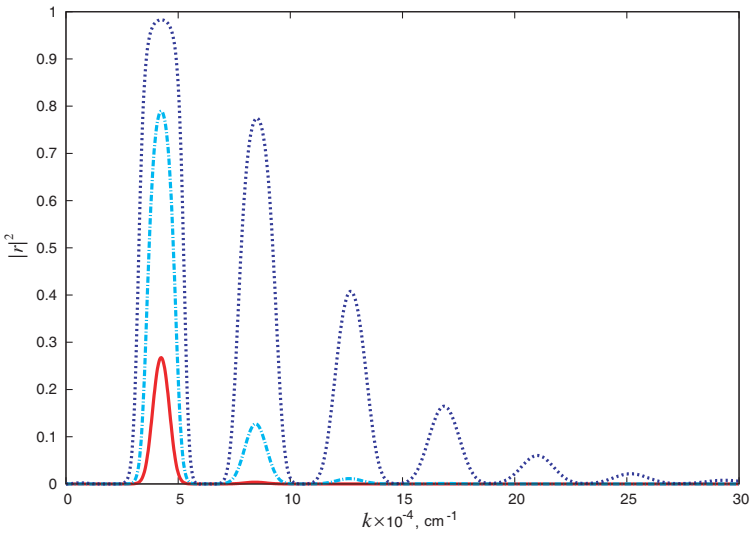

Figure 1: Reflection spectra of the sinusoidal grating at $L = 85\,\mu\text{m}$, $\lambda = 1.5\,\mu\text{m}$, $\overline{n} = 1.5$, $w = 0.008$ and modulation depth $\delta = 0.1$ (solid), 0.25 (dot-dash), 0.5 (dotted).

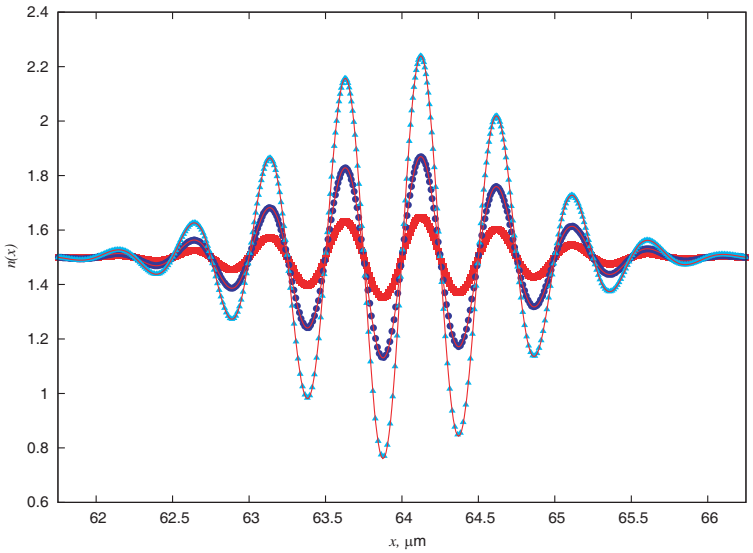

Figure 2: Refractive index n as a function of coordinate x: theoretical dependence (solid lines) and numerical solution with $N = 2^{13}$ at $\delta = 0.1$, (boxes), 0.25 (circles), 0.5 (triangles).

Going to the optical coordinate ξ according to (3) we see that $q = Q/\Lambda$ is constant at $0 \leqslant \xi \leqslant \Lambda$, where

$$Q = \frac{1}{2} \ln \frac{n_2}{n_1}. \tag{10}$$

Geometrical coordinate x is

$$x = \Lambda \frac{1 - e^{-2Q(\xi - \xi_0)/\Lambda}}{2Qn_1}. \tag{11}$$

The reflection coefficient of Rayleigh layer is

$$r(k) = \frac{(Q/\Lambda)\,\sinh \mu\Lambda}{\mu\,\cosh \mu\Lambda - ik\,\sinh \mu\Lambda}, \tag{12}$$

where $\mu = \sqrt{(Q/\Lambda)^2 - k^2}$. The reflection spectrum is shown in Fig. 3; the profile of the refractive index is shown in the left Fig. 4.

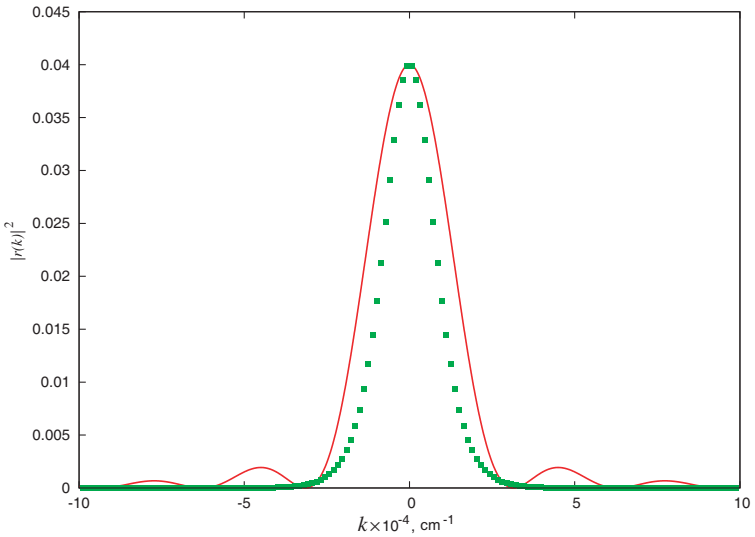

Figure 3: Reflection spectra of the Rayleigh layer (solid curve) and hyperbolic secant layer (squares) at $n_1 = 1$, $n_2 = 1.5$, $\Lambda = 1\,\mu$m.

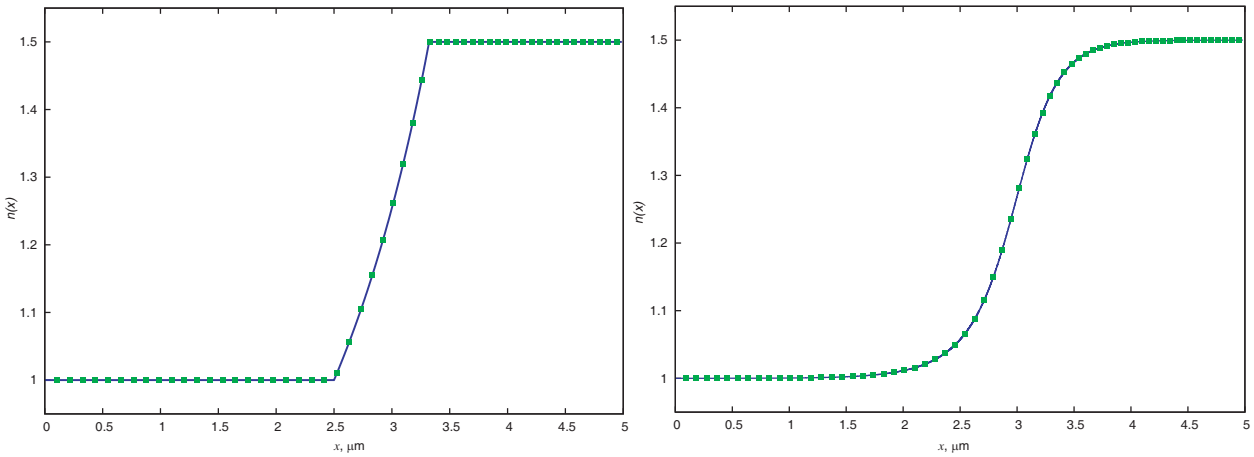

Figure 4: Rayleigh (left) and hyperbolic secant (right) layers at $\xi_0 = 3\,\mu$m, $n_1 = 1$, $n_2 = 1.5$: the analytic formula (squares) and numerically restored from the reflection coefficient (solid curve).

The second example of the solvable layer is the layer with

$$q(\xi) = \frac{Q/\Lambda}{\cosh(\pi(\xi - \xi_0)/\Lambda)}. \tag{13}$$

Here Q is a parameter, Λ is the effective length in optical coordinate. Correspondent refractive index is

$$n(\xi) = C \exp\left[2(Q/\pi)\ \arctan\exp(\pi(\xi - \xi_0)/\Lambda)\right], \tag{14}$$

where C is a constant. Parameter C is defined by limiting values n_1, n_2 of the refractive index $C = \sqrt{n_1 n_2}$, parameter Q is given by (10). Its reflection coefficient can be expressed in terms of the Euler gamma-functions

$$r(k) = \frac{Q}{\pi}\frac{\Gamma(d)\Gamma(f_-)\Gamma(f_+)}{\Gamma(d^*)\Gamma(g_-)\Gamma(g_+)}, \tag{15}$$

$$d = \frac{1}{2} + \frac{ik\Lambda}{\pi}, \quad f_\pm = \frac{1}{2} - \frac{ik\Lambda}{\pi} \pm \frac{iQ}{\pi}, \quad g_\pm = 1 \pm \frac{iQ}{\pi}.$$

The reflection spectrum of hyperbolic secant layer can be reduced to the elementary functions [8]

$$|r(k)|^2 = \frac{\cosh 2Q - 1}{\cosh 2Q + \cosh 2k\Lambda}. \tag{16}$$

The spectrum is shown in Fig. 3; the profile of the refractive index is shown in the right Fig. 4.

We test the inner-bordering method at the Rayleigh layer and at the hyperbolic secant layer. The results at $N = 2^{12}$ are shown in Fig. 4. The relative accuracy of numerical reconstruction of the second layer occurs to be 4×10^{-7}. The accuracy for Rayleigh layer is 2×10^{-2}, since it corresponds to square coupling coefficient providing wide spectrum, which is hard to treat numerically.

5. CONCLUSIONS

Comparing different curves in Fig. 1 we see that the deep modulation of the refractive index results in the Bragg peaks of high order in the spectrum. The couple mode equations take into account only the vicinity of the first order Bragg reflection. That is why the Helmholtz equation is necessary to treat the grating with deep modulation.

We also see that the hyperbolic secant and sinusoidal gratings are reconstructed far more accurate than the Rayleigh layer. This is due to jumps in refractive index derivative at the ends of the layer which lead to long oscillating tails in the reflection spectrum (Fig. 3).

The inner bordering method demonstrates its high accuracy and efficiency. It could be helpful for ISP in different fields: optics, radiophysics, acoustics.

ACKNOWLEDGMENT

This work is supported by the Civilian Research and Development Foundation grant RUP1-1505-NO-05, Program No. 27 by the Presidium of Russian Academy of Sciences, Russian Foundation of Basic Research grant 07-02-00552-a, the Government support program of the leading research schools (NSh-1527.2008.2) and interdisciplinary grant No 42 from the Siberian Branch of the Russian Academy of Sciences.

REFERENCES

1. Zhang, Y., J. A. Kong, and A. K. Jordan, "Numerical solution of the Gel'fand-Levitan-Marchenko integral equation for electromagnetic inverse scattering theory using matrix inversion," *Microwave and Optical Technology Letters*, Vol. 15, No. 5, 277–278, 1997.
2. Chen, Y. and V. Rokhlin, "On the inverse scattering problem for the Helmholtz equation in one dimension," *Inverse Probl.*, Vol. 8, No. 3, 365–391, 1992.
3. Belai, O. V., L. L. Frumin, E. V. Podivilov, and D. A. Shapiro, "Inverse scattering for the one-dimensional Helmholtz equation: Fast numerical method," *Opt. Lett.*, Vol. 33, No. 18, 2101–2103, 2008.
4. Bremmer, H., "The propagation of electromagnetic waves through a stratified medium and its W.K.B. approximation for oblique incidence," *Physica*, Vol. 15, No. 7, 593–608, 1949.
5. Zakharov, V. E. and A. B. Shabat, "Exact theory of two-dimensional self-focusing and one-dimensional self-modulation of waves in nonlinear media," *Zh. Eksp. Teor. Fiz.*, Vol. 61, No. 1, 118–134, 1971.
6. Belai, O. V., L. L. Frumin, E. V. Podivilov, and D. A. Shapiro, "Efficient numerical method of the fiber Bragg grating synthesis," *J. Opt. Soc. Am. B*, Vol. 24, No. 7, 1451–1457, 2007.
7. Rayleigh, L., "On the propagation of waves through a stratified medium, with special reference to the question of reflection," *Royal Society of London Proceedings Series A*, Vol. 86, 207–226, Feb. 1912.
8. Shapiro, D. A., "Family of exact solutions for reflection spectrum of Bragg grating," *Opt. Commun.*, Vol. 215, No. 4–6, 295–301, 2003.

Classical Theorems of Discrete Electrodynamics on Simplicial Complexes

J. M. Arnold
University of Glasgow, UK

Abstract— The question of the definition of an exact counterpart of Poynting's Theorem for the Maxwell equations on a simplicial complex or cell complex is considered. The cell complex approach is purely discrete and the discrete Maxwell equations in this framework are exact, rather than approximations to some order in a small mesh parameter of the continuum counterparts. The FDTD method is a direct example of Maxwell's equations on a cell complex with discrete time-stepping. An energy density is defined, along with a suitable candidate for a Poynting flux, and it is required that exact conservation hold over arbitrary closed surfaces in the complex.

1. INTRODUCTION

Maxwell's laws of classical electrodynamics have exact counterparts on a purely discrete space, reformulated as discrete Stokes' Theorems on simplicial complexes [1, 2]. The question naturally arises as to what other classical laws may be admitted by the discrete electrodynamical fields. Under certain time-discretisations there exist exact discrete versions of Poynting's Theorem, Green's Theorem, Kirchoff-Huyghens Theorems, plane wave superposition theorems, extinction theorems and other topological field theorems. These topological theorems constrain the numerical solutions of computational algorithms of discrete electrodynamics, particularly the FDTD method, on both structured and unstructured spatial meshes forming the simplicial complexes. Judicious application of constraint theorems potentially leads to significant reductions in the number of degrees of freedom necessary to compute in order that the algorithms produce topologically complete solutions.

The case of Poynting's Theorem for electrodynamics on a simplicial complex is considered. A discrete local quantity corresponding to total electric and magnetic field energy densities for the simplicial complex (a discrete 3-form W) is shown to lead to conserved global total energy ΣW in continuous time, but energy is not conserved in discrete time with simple Euler explicit time-stepping (the explicit FDTD method); this behaviour is well-known for explicit methods [3]. To obtain a conserved total energy, implicit time-stepping is required. To obtain a Poynting Theorem there is also required in addition to W a discrete 2-form S such that $\partial_t W = \mathrm{d}S$ in continuous time, and $W^{m+1} - W^m = \mathrm{d}S^m$ in discrete time, where m indicates the time-stepping variable and d is the discrete exterior derivative on r-forms on the simplicial complex. It is not obvious how to construct the compatible local energy density W and Poynting flux 2-form S, along with a suitable time discretisation. When dynamical sources drive the discrete fields, in the form of discrete charges on vertices and discrete current 2-forms, it is also necessary to have consistent energy transfers between the sources and the fields when the sources themselves may have internal dynamics, as considered for example in FDTD coupled to model quantum systems [4].

These aspects of energy density and energy flux for discrete electrodynamics on simplicial complexes are studied and presented in detail.

2. DISCRETE ELECTRODYNAMICS

We adopt the setting of a discretisation of 3-space by means of simplicial complexes. This consists of vertices (0-dimensional), edges (1-dimensional) whose end points are vertices, and faces (2-dimensional) whose boundaries are edges. Generally, faces are plane polygons, but we may restrict attention to those cases where the faces are triangles or rectangles. In the case of triangular faces, the simplicial complex segments the space into contiguous tetrahedra, each of which is a 3-simplex. Having defined the embedding of the simplicial complex in 3-space, we regard the vertices, edges, faces and simplices as fundamental coordinates for elements of the space. Vertices sample points of the space, edges sample vector fields, faces sample fluxes and volumes sample densities. We define discrete differential forms that live on each dimension of the simplicial complex, which are functions on each type of object. Thus, a scalar function (0-form) assigns a value to each vertex, a 1-form assigns a value to each edge, a 2-form assigns a value to each face, and a 3-form assigns a value to each volume. An operator, denoted by d, maps r-forms to $r+1$-forms, in a manner similar

to the ∇-operator of conventional vector calculus on a continuous space. The precise action of the d-operator on r-forms is given by a discrete Stokes' Theorem at each grade

$$\mathrm{d}\omega|_\sigma = \sum_{\partial\sigma} \omega \tag{1}$$

where ω is the value of an r-form on an r-chain, σ is an $r+1$-simplex and $\partial\sigma$ is the closed r-chain forming the boundary of σ. This formula resembles the the actions on a continuous space of the operators of gradient ($r=0$), curl ($r=1$), and divergence ($r=2$). A fundamental property of the d-operator is $\mathrm{d}(\mathrm{d}\omega) = \mathrm{d}^2\omega = 0$ for any r-form ω.

Complementary to the primary mesh as defined above, there exists a dual mesh. Vertices of the dual mesh lie at the circumcentres of the 3-simplices (volumes) of the primary mesh; dual edges join the dual vertices in pairs and intersect the faces of the primary mesh at their circumcentres; dual faces intersect primary edges at their circumcentres. Finally, we require the Hodge operator $*$ which maps r-forms on the primary mesh to $(n-r)$-forms on the dual mesh, and *vice versa*; here $n=3$.

It is convenient to have representations of r-forms and their values on r-chains in terms of vector spaces, with the d-operator, which is linear, having a matrix representation. Thus a 0-form ϕ is a vector whose elements are the values of ϕ assigned to each vertex of a complex, 1-form E is a vector whose elements are values of E on each edge with a local orientation, 2-form B is a vector whose elements are values of B on each facet with a local orientation, and similarly for forms on the dual cell complex.

In the vector space representation, the discrete Maxwell equations are

$$\mathrm{d}E = -\partial_t B, \qquad \mathrm{d}H = \partial_t D + J \tag{2}$$

$$\mathrm{d}D = \rho, \qquad \mathrm{d}B = 0, \quad \mathrm{d}J = -\partial_t \rho \tag{3}$$

$$D = \epsilon * E, \qquad B = \mu * H \tag{4}$$

Here the operator ∂_t is the derivative with respect to continuous time t; for this reason, these are called Maxwell's equations for discrete space and continuous time (DSCT). If the forms are sampled at time intervals $E^m = E|_{m\Delta_t}$, and ∂_t interpreted as a finite difference operator in the discrete-time, then we have discrete space discrete time (DSDT) Maxwell equations. An example of such an operator would be $\Delta_t\partial_t = \hat{Z} - 1$, where $\hat{Z}$ represents the forward time-shift operator $\hat{Z}f^m = f^{m+1}$.

In the discrete Maxwell equations the form-values E and B are related to the physical fields by scaling with the metric of the simplex on which they live; thus the physical electric field is $\mathcal{E} = E/h$ where h is the length of the edge on which the form E is evaluated, and $\mathcal{B} = B/s$ where s is the area of the face on which the 2-form B is evaluated.

The DSDT Maxwell equations represent a completely discrete dynamical system whose laws are formally identical to those of CSCT Maxwell equations. The DSDT system is essentially equivalent to the FDTD algorithm on an arbitrary unstructured spatial mesh. There is considerable choice available for the precise specification of the time-stepping discrete derivative ∂_t. The specification $\Delta_t\partial_t = \hat{Z} - 1$ leads to an explicit time-stepping algorithm, the specification $\Delta_t\partial_t = 2(\hat{Z}-1)(\hat{Z}+1)^{-1}$ is an implicit time-stepping algorithm. We show that there is no equivalent of Poynting's Theorem or the Poynting flux in explicit DSDT, but that implicit DSDT has both Poynting's Theorem and a properly defined Poynting flux.

3. DSCT POYNTING THEOREM

We begin with the discrete-space continuous-time (DSCT) case, as this gives a clear guide to the construction of conserved energy and Poynting flux. It is quite straightforward to demonstrate that there exists a global conserved quantity equivalent to the DSCT electromagnetic energy. It follows directly from the DSCT Maxwell Equation (2) in the source-free case ($J=0, \rho=0$) that

$$\frac{1}{2}\partial_t \left(E^T D + H^T B\right) = E^T \mathrm{d}H - H^T \mathrm{d}E = 0, \tag{5}$$

where T represents the transpose of the vector. The null value follows because as matrix operators the symmetry $\mathrm{d}^{n-k}_{\mathrm{dual}} = (-1)^k \mathrm{d}^{k-1\ T}_{\mathrm{primary}}$ holds, where the superscript represents the grade of form to

which the operator is applied, recalling that the vectors E and H represent 1-forms on the primary and dual meshes respectively. When sources are included,

$$\frac{1}{2}\partial_t(E^T D + H^T B) = E^T J. \tag{6}$$

These can be written more explicitly in terms of elements of vectors by

$$\frac{1}{2}\partial_t \left(\sum_{\text{edges}} E_k D_k + \sum_{\text{faces}} H_l B_l \right) = \sum_{\text{edges}} E_k J_k. \tag{7}$$

with the sums extending over an unbounded mesh, such that every primary cell face is common to two primary mesh cells. The left hand side of this identity is the rate of change of total energy in the fields, the right hand side is the rate of energy generation by the sources.

The previous identity confirms the conservation of total energy (over all infinite space) by the DSCT Maxwell system. Now we seek to refine this in the form of a Poynting Theorem, whereby the energy leaving a finite volume is related to the energy flux across the surface bounding the finite volume. To set up this construction in the discrete case, suppose that an entire infinite mesh is partitioned into two sets V_1 and V_2 by identifying a surface Σ separating the two sets. The surface itself consists of a set of vertices V_Σ, joined in pairs by edges that enclose simplicial (or polygonal) faces. We now define an energy density 3-form W by

$$W_j \;=\; \frac{1}{2}\left\{ \sum_{\text{edges}(j)} \alpha_k E_k D_k + \sum_{\text{faces}(j)} \frac{1}{2} H_l B_l \right\} \tag{8}$$

where the edges and faces in the sums are the boundary elements of a single primary cell indexed by j, and α_k is a weight factor for cells for which edge k is a common element ($\alpha_k = \frac{1}{4}$ for cubes). By summation over all such cells, we find that $W = \sum_j W_j$ is the total energy of the fields in the infinite mesh. By summation over the internal and external cells relative to the surface Σ there results two energies, the internal and external energy respectively, whose sum is the conserved total energy in the whole space. Now take each elemental volume in turn, and show that $\partial_t W_j = \mathrm{d}S|_j$, where S is some 2-form on the primary mesh. For a regular cubic cell complex, it turns out that

$$S_l \;=\; \frac{1}{2}\sum_{\text{edges}} E_k \bar{H}_k \tag{9}$$

where the edges are the boundary of face l in the cell j, and $\bar{H}_k = \sum_{l'} c_{l'} H_{l+l'}$ with $c_{l'} = \frac{1}{2}\sin\frac{1}{2}l'\pi$ is a weighted mean value of the H-forms around the dual 1-cycle surrounding the primary edge k. Eq. (9) is the equivalent for the discrete case of the cross product $\int_{\text{face } l} \mathbf{E}\times\mathbf{H}\cdot\mathrm{d}\mathbf{S}$. Since we now have a local conservation law $\partial_t W = \mathrm{d}S$ for every cell indexed by j, it follows that the individual cells can be summed over a finite volume V to obtain $\partial_t W_V = \sum_{\partial V} S$.

4. DSDT POYNTING THEOREM

When the time coordinate is discretised, the existence of even a global conserved quantity depends critically on the discretisation. Suppose first we have an explicit time stepping scheme, which would replace the source-free Maxwell Equation (2) with

$$-\Delta_t \mathrm{d}E^m = B^{m+1} - B^m, \qquad \Delta_t \mathrm{d}H^m = D^{m+1} - D^m. \tag{10}$$

Diagonalisation of the spatial part of the system (10) reduces it to

$$-\lambda\Phi_E^m = \Phi_H^{m+1} - \Phi_H^m, \qquad \lambda\Phi_H^m = \Phi_E^{m+1} - \Phi_E^m. \tag{11}$$

with a real eigenvalue λ. This discrete dynamical system does not conserve the energy quadratic form

$$W^m = \left\{ {\Phi_E^m}^T \Phi_E^m + {\Phi_H^m}^T \Phi_H^m \right\}, \tag{12}$$

so $W^{m+1} \neq W^m$. The situation is no better if interleaved time stepping is used

$$-\lambda\Phi_E^m = \Phi_H^{m+1} - \Phi_H^m, \qquad \lambda\Phi_H^{m+1} = \Phi_E^{m+1} - \Phi_E^m, \tag{13}$$

which also does not conserve the quadratic form W. However, if the implicit scheme

$$-\frac{1}{2}\lambda(\Phi_E^{m+1} + \Phi_E^m) = \Phi_H^{m+1} - \Phi_H^m, \qquad \frac{1}{2}\lambda(\Phi_H^{m+1} + \Phi_H^m) = \Phi_E^{m+1} - \Phi_E^m \tag{14}$$

is used, then $W^{m+1} = W^m$ for the total energy quadratic form. It follows that we require the implicit time stepping scheme

$$-\frac{1}{2}\Delta_t \mathrm{d}(E^{m+1} + E^m) = B^{m+1} - B^m, \qquad \frac{1}{2}\Delta_t \mathrm{d}(H^{m+1} + H^m) = D^{m+1} - D^m \tag{15}$$

in order to have conservation of the total energy W^m. There cannot be a local conservation law if there is no global conservation law, since the local energy density per unit cell is a positive quantity for every cell. It therefore follows that it only makes sense to search for a locally defined Poynting flux 2-form in the case of implicit time-stepping. The appropriate modification of the local Poynting flux at face l in the simplicial or cell complex then turns out to be

$$S_l^m \;=\; \frac{1}{2}\sum_{\text{edges}} \frac{1}{4}\left(E_k^{m+1} + E_k^m\right)\left(\bar{H}_k^{m+1} + \bar{H}_k^m\right). \tag{16}$$

5. CONCLUSION

The formulation of energy conservation laws and corresponding fluxes has been explored in the context of wholly discrete formulations of electrodynamics using the machinery of discrete exterior calculus. In this framework, the relations amongst discrete fields such as Stokes' Theorems, Green's Theorems, etc. are exact, not merely Taylor's Theorem approximations to continuous laws. Poynting's Theorem also has exact counterparts in the discrete case, for both continuous time (DSCT) and for time-stepping discretised by an implict algorithm (implicit DSDT).

It is of interest that the discrete Poynting flux S is topological in nature, and does not contain directly any metric data about the mesh. Metric data is implicit in the fluxes D and B *via* the discrete Maxwell equations since they are related to fields E and H through the Hodge star $*$ which is metric, but the metric data is not required in order to construct the Poynting flux. The implicit FDTD, which admits a Poynting Theorem, is known to be unconditionally stable for any time step Δ_t, whereas the explicit FDTD requires a Courant condition limiting the time step in order to be stable. The difference in stability is strongly related to the conservation of energy, since the existence of a conserved positive definite quadratic function of the fields is an absolute obstruction to the unconstrained growth of the field values as discrete time advances.

REFERENCES

1. Desbrun, M., E. Kanso, and Y. Tong, "Discrete differential forms for computational modelling," *Discrete Differential Geometry*, ed. A. I. Bobenko et al., Oberwolfach Seminars, Vol. 38, 287–323, *Birkhauser Verlag*, 2008.
2. Bossavit, A., *Computational Electromagnetism*, Academic Press, Boston, 1998.
3. Haiter, E., C. Lubich, and G. Wanner, *Geometric Numerical Integration*, Springer series in Computational Mathematics, Vol. 31, 2006.
4. Slavcheva, G., J. M. Arnold, and R. W. Ziolkowski, "Coupled Maxwell-pseudospin equations for investigation of self-induced transparency effects in a degenerate three-level quantum system in two dimensions: Finite-difference time-domain study," *Phys. Rev. A*, Vol. 66, 063418, 2002.

Maintenance of Current Limited Reactor Electromagnetic Compatibility and Safety

M. Sh. Misrikhanov[1], **N. B. Rubtsova**[2], **and A. Yu. Tokarskij**[1]

[1]Open JSC Federal Network Company Branch "Main Power Networks of the Center", Russia Federation
[2]RAMS Institute of Occupational Health, Moscow, Russian Federation

Abstract— By means of computer program "Reactor MF" magnetic field (MF) levels created by four three-phase current limited reactors RTOS-10-3150-0.25-UZ in 220 kV substation management control panel building are calculated. It is shown, that in halls of 10 kV closed switch-gear (10 kV CSG) where cases with automatics containing microprocessor devices are placed, MF intensity considerably above than maximum permissible value (MPV) on handicap immunity, and in located near reactor MF levels are more than occupational exposure hygienic norms. Combined electromagnetic screens (CEMS) application for decreasing of MF induced by current limited reactors levels efficiency is shown. CEMS allow reducing MF levels up to lower than corresponding norms both on noise immunity, and occupational exposure.

1. INTRODUCTION

Power frequency (PF) magnetic field (MF) occupational exposure hygienic standard (maximum permissible value MPV) in RF is accepted depending on work time. MPV are from 100 μT to 2000 μT for total (all body) exposure, and from 1 mT to 8 mT for local (extremities) exposure.

There are the norms of MF levels handicaps stability depending on rigidity degree under constant intensity — within the limits of from 1 A/m to 100 Am [2]. The equipment containing microprocessor has the fourth degree of rigidity, i.e., MF intensity in microprocessors locations should not exceed 30 A/m.

2. MAGNETIC FIELD, CREATED BY CURRENT LIMITED REACTORS IN 10 kV CLOSED SWITCH-GEAR

Let's examine the project of four current limited reactors (PTOC-10-3150-0.25-y3), and 10 kV closed switch-gear (CSG) located in technical building. The plan of reactors configuration in axes of coordinates XOY is shown in Figure 1. Technical cases containing microprocessors are located in CSG on the second floor. In Figure 2 the plan of cases position and calculative levels on axes OZ and OY in 10 kV CSG is shown.

Distribution of MF strength at concrete high levels calculated by means of computer program "Reactor MF" [3]. In Figure 3 distribution of MF intensity $H_{\max}$ (working value in greater semi-axis of ellipse), created by four three-phase reactors at +5.6 m high ($z = 5.6$ m, 2.0 m above 10 kV CSG floor) under 3150 A reactor rated current.

Maximal reactors MF exposure is to technical equipment located in nearest to reactors line of working cases in 10 kV CSG room. For second (distant from reactors) working cases line $H_{\max}$ doesn't achieve 30 A/m even under 3150 A current. Containing microprocessors automatic equipment is located in cases at 1.8 m from 10 kV CSG floor distance, i.e., at $z = 5.4$ m high. The schedule of MF strength distribution at $z = 5.4$ m for $y = 3.7$ m and change x from -24 m up to 33 m under 2850 A loading current overturned rather $x = 0$ m is shown in Figure 4. The schedule is combined with the plan of 10 kV CSG room.

In all cases at corresponding high MF strength is more than 30 A/m (maximal $H_{\max}$ value 54 A/m at $y = 3.7$ m and 44 A/m at $y = 4.1$ m), that can lead to failure of the microprocessors regulated by the fourth degree of rigidity on handicap stability.

For exception of microprocessors failure it is necessary or to remove reactors even on 0.5 m to the external wall of building, or to use microprocessors blocks, regulated on the fifth degree of rigidity [2] ($H_{\max} \leq 100$ A/m), or to install electromagnetic screens on reactors.

3. MAGNETIC FIELD CREATED BY CURRENT LIMITED REACTORS IN STAIRCASE

On 1572 mm distance from extreme reactor axis is the surface of staircase wall (Figures 1 and 5). In Figure 5 the area of MF calculation in technical building with 10 kV CSG staircase is shown.

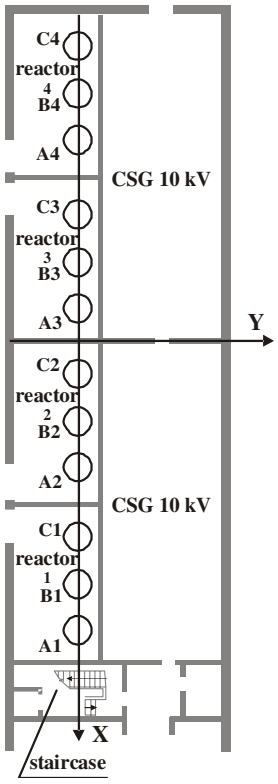

Figure 1: Plan of 4 reactors and XOY axes location in technical building and 10 kV CSG.

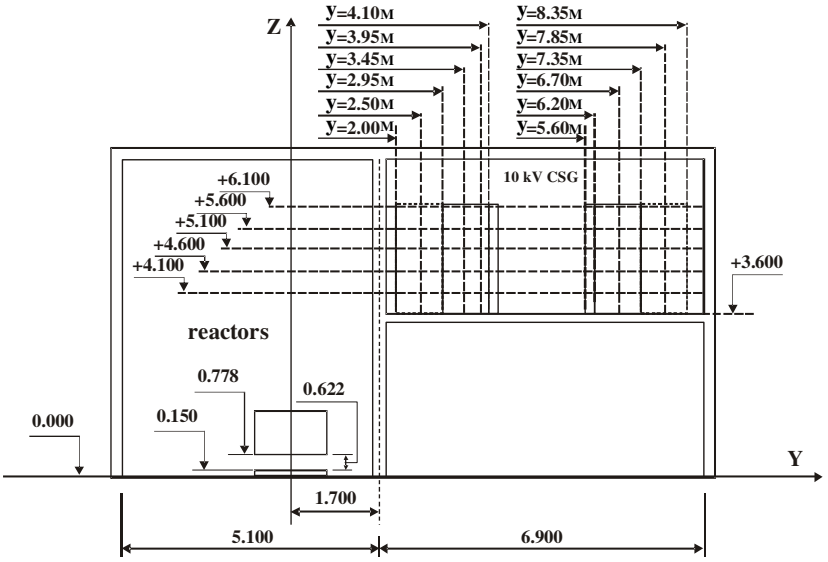

Figure 2: Current limited reactors PTOC-10-3150-0.25-y3 location, and discrete highs by OZ and OY axis in 10 kV CSG room.

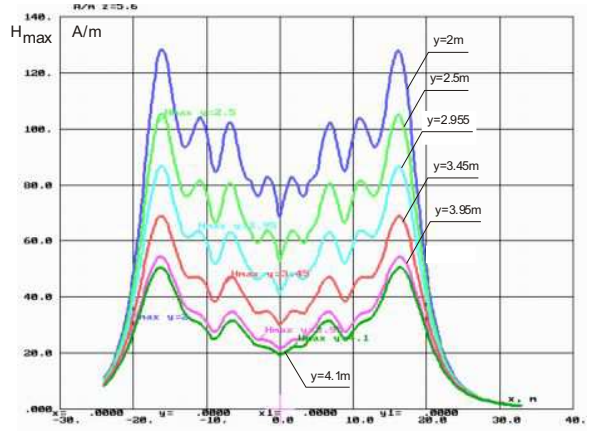

Figure 3: MF strength $H_{\max}$ distribution in 10 kV CSG room at +5.6 m high for $y = 2$ m, 2.5 m, 2.95 m, 3.45 m, 3.95 and 4.1 m.

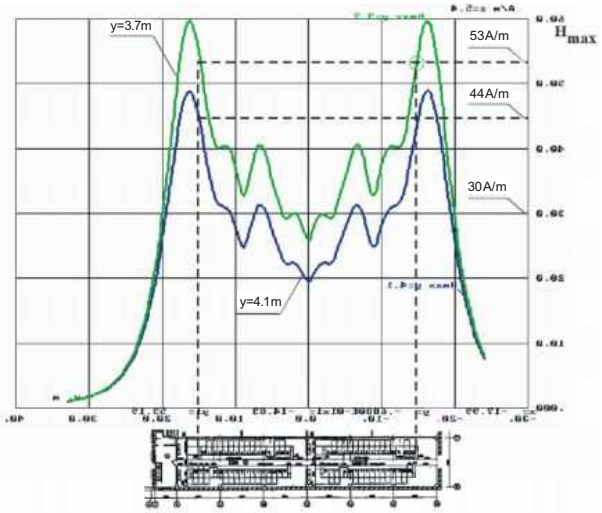

Figure 4: MF strength distribution at $z = 5.4$ m for $y = 3.7$ m and 4.1 m under x change from −24 m up to 33 m (correlated with 10 kV CSG room plan).

Calculation were carried out for line connecting reactors axes (at $y = 0$ m max have maximal value) at highs $x = 17.644$ m, 18.144 m, 18.644 m, 19.144 m and 19.644 m at z change from 0 m to 7 m. IP = 2850 A. In Figure 6 $H_{\max}$ distributions at certain highs.

MF level at the surface of staircase wall at 0.94 m and 1.58 m height is 1,954 A/m that (forbids staff stays in this hall see Figure 1). On 0.5 m distance from wall $H_{\max} = 860$ A/m, on 1 m distance — $H_{\max} = 450$ A/m, on 1.5 m distance — $H_{\max} = 260$ A/m, on 2 m distance — $H_{\max} = 170$ A/m.

For MF occupational exposure hazard effects elimination it is necessary or to remove staircase to opposite side of building or to shield the wall of reactor chamber by means of the ferromagnetic

screen (permalloy sheets, transformer iron, etc.) even up to MF levels at the staircase wall surface $H_{\max} \leq 1600$ A/m (with permissible time of occupational exposure less than 1 h per work day). In this case security personnel, cleaners, etc. should be included in group of personnel professionally connected with service and maintenance of PF electromagnetic fields sources with granting of special health services (preliminary and periodic physical examinations, correction and rehabilitation).

4. RESTRICTION OF MAGNETIC FIELD LEVEL BY MEANS OF COMBINED ELECTROMAGNETIC SCREENS

To decrease MF levels in 10 kV CSG room and in staircase hall is possible by installation of combined electromagnetic screens on reactors (CEMS) [4]. Let's examine one PTOC-10- 3150-0.25-y3 reactor (see Figure 7) with installed on the middle its winding single-row electromagnetic screen (EMS4b), containing 4 turns 0.8 m radius with 0.1 m step 0.1 m.

On 0.2 m distance from reactor winding end faces let's place two-layer electromagnetic screens (EMS 2×2), containing on two turns in a layer (0.95 m — internal turns radius), reeled up with step on layers of 0.1 m and on turns of 0.1 m. All EMS All EMS are made of copper rectangular wire 5 cm high and 4 cm width "by copper". All EMS connections in CEMS are coordination-parallel by trunks made of the same wire. Calculation of reactor, CEMS parameters, and MF levels carried out by means of computer program "Reactor MF" [5].

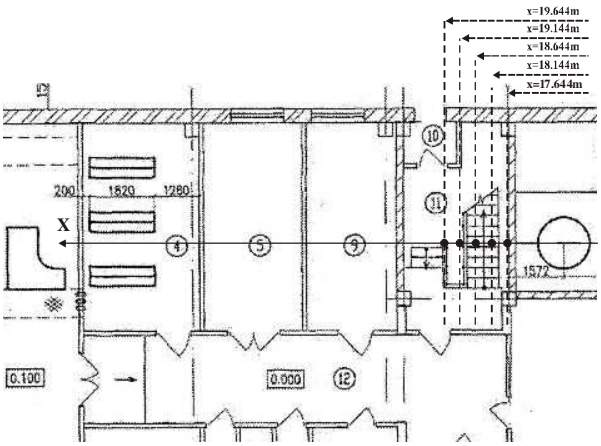

Figure 5: The area of MF calculation at staircase of technical building with 10 kV CSG.

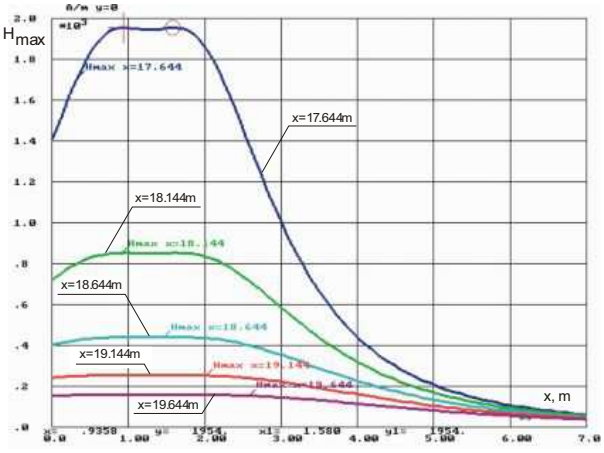

Figure 6: $H_{\max}$ levels distribution in staircase for different points $x = 17.644$ m, 18.144 m, 18.644 m, 19.144 m and 19.644 m. $I_P = 2850$ A.

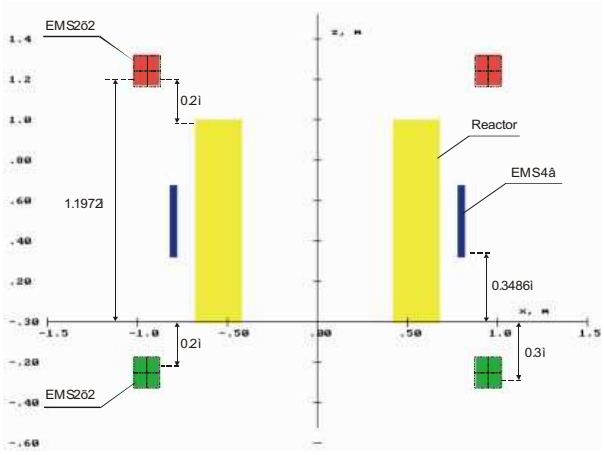

Figure 7: PTOC-10-3150-0.25-y3 reactor with combined electromagnetic screen.

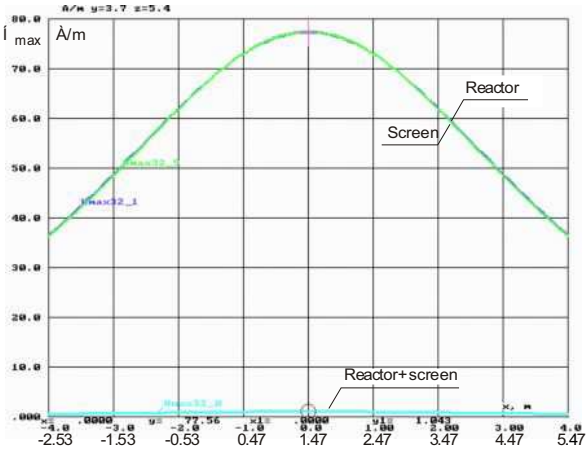

Figure 8: MF levels $H_{\max}$ distribution at $z = 5.4$ m high for $y = 3.7$ m.

Under 2850 A full reactor current in lateral EMS are induced $\dot{\mathrm{I}}_{\mathrm{EMS2times2}} = 2605\mathrm{e}^{-\mathrm{j}179^\circ}$ A currents, and in middle EMS – $\dot{\mathrm{I}}_{\mathrm{EMS4â}} = 5210\mathrm{e}^{-\mathrm{j}179^\circ}$ A currents.

Reactor winding inductive resistance is 0.270 Ohm, and in view of combined EMS influences under its coordination-parallel connection it decreases to 0.184 Ohm.

In Figure 8 distribution of MF intensity $H_{\max}$ at high $z = 5.4$ m (places of microprocessors in 10 kV CSG working cases location) for $y = 3.7$ m (nearest end face of microprocessor complex) are shown for creation by: reactor only (first reactor of third group — see Figure 1) — curve "Reactor"; placed on reactor CEMS — curve "Screen"; and reactor in complex with CEMS — curve "Reactor + screen". Curve "Reactor + screen" is shown separately in Figure 9.

Installation of CEMS on reactor has allowed decreasing MF intensity in microprocessor complexes location from 77.56 A/m up to 1.043 A/m.

Three-phase reactor neighbor windings currents MF and neighbor reactors windings currents MF in case of neighbor reactors windings are installed in sequence of type A1, B1, C1-A2, B2, C2- etc. (see Figure 1) due to phase currents shift on 120◦ compensate MF created by reactor winding. This solution allows to compensate MF and decrease $H_{\max}$ level from 78 A/m (see Figure 8) up to 30 A/m (see Figure 4, curve $y = 3.7$ m for $x = 1.47$ m), i.e., more than two times for this concrete case of reactors location. Thus, if identical design CEMS install on windings of all reactors, resulted MF level will decrease in comparison with one reactor with CEMS decrease even more than in 2 times and will be on examined place at $z = 5.4$ m at $y = 3.7$ m value 0.5 A/m about, it is less 1 A/m (limit value of MF intensity on handicap stability for first degree of rigidity 1 [2]).

Thus, equipment of current-limited reactors PTOC-10-3150-0.25-y3 by combined electromagnetic screens will allow using in examined 10 kV CSG rooms devices responding any degree of rigidity by handicap stability to power frequency MF. Calculate MF intensity created by reactors in staircase of technical building with 10 kV CSG.

In Figure 10 distribution of MF intensity created by reactor with combined EMS in staircase hall is shown: on wall surface $H_{\max} < 800$ A/m; on 0.5 m distance from wall surface $H_{\max} < 200$ A/m, and on 1 m distance from wall $H_{\max} < 60$ A/m Combined EMS installation has allowed to decrease MF levels at the staircase hall wall surface to $H_{\max} < 800$ A/m value.

Thus, installation of combined electromagnetic screen on current-limited reactor PTOC-10-3150-0.25-y3 gives the possibility to personnel stay in staircase hall not less than two hours per work day.

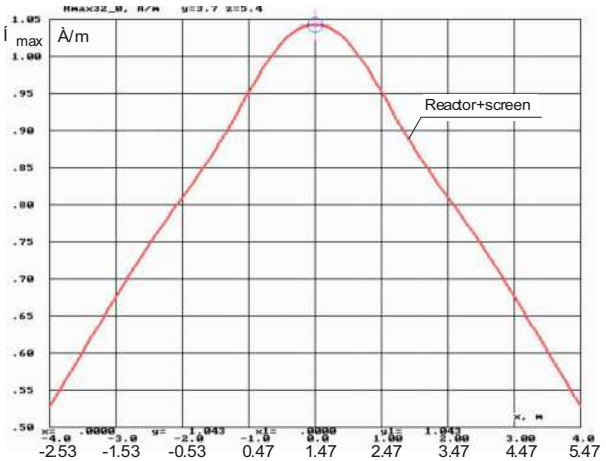

Figure 9: Curve "Reactor + screen" MF level $H_{\max}$ distribution at high $x = 5.4$ m for $y = 3.7$ m.

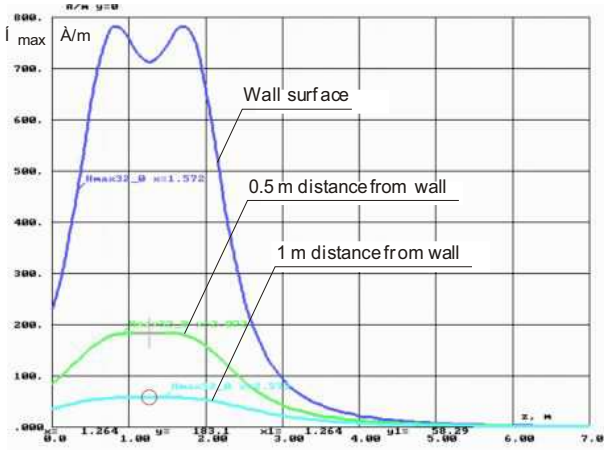

Figure 10: MF levels created by reactor currents in staircase hall on 0 m, 0.5 m and 1.0 m from wall surface.

REFERENCES

1. Sanitary Rules and Norms 2.2.4.1191-03, "Electromagnetic fields under occupational environments; which regulates conditions of PF electric and magnetic field occupational exposure," (in Russian).
2. Methodical instructions of electromagnetic environment and compatibility on power plants and substations definition, The standard of organization, M., Russian Open Society "Main Power Networks of Russia", MPI, 2004 (in Russian).

3. Misrikhanov, M. Sh., Yu. A. Jostson, N. B. Rubtsova, and A. Yu. Tokarskij, "Three-phase reactors without ferromagnetic core (Reactor MF)," *Computer Program*, No. 2006613743, Oct. 27, 2006 (in Russian).
4. Misrikhanov, M. Sh., N. B. Rubtsova, and A. Yu. Tokarskij, "Electromagnetic screen for reactor without ferromagnetic core," *Bull.*, No. 23, Patent RF No. 2304815, Aug. 20, 2007 (in Russian).
5. Misrikhanov, M. Sh., Yu. A. Jostson, N. B. Rubtsova, and A. Yu. Tokarskij, "Air reactor with electromagnetic screen (Reactor — EMS)," *Computer Program*, No. 2008610027, Jan. 09, 2008 (in Russian).

Method of Optimum Simple Iteration for the Solution of Large Complex Systems of the Linear Algebraic Equations Arising in Scattering Problems

Sergey P. Kulikov
Moscow State Institute of Radio Engineering, Electronics and Automation
78, Vernadsky av., Moscow 117454, Russia

Abstract— The method of successive approximation under condition of its fast convergence is the effective tool of the solution of the linear continuous operational equation of the second kind. The questions of optimization of convergence of the modified method on the basis of knowledge of complex area of an spectral set of the transition operator are investigated. The optimized method is applied to the numerical solution of electrodynamic scattering problems.

1. INTRODUCTION

The linear operational equation of the second kind is considered

$$x = T \cdot x + f \tag{1}$$

Here T — the linear continuous operator in Banah B-space, $x \in B$ — a required element, $f \in B$ — set elements of this space [1]. In specific case, there can be the linear continuous integral operator in infinite-dimensional space of a complex-unit functions on which it is certain. For example, it can be compact or singular (depending on dimension and a problem) the volume integral operator of scattering [2]. It also can be the finite-dimensional operator — the set square matrix of the size $n * n : T = \{t_{i,j}\},\ i, j = 1 \ldots n$, operating in n-dimensional complex space of vectors.

2. METHOD OF OPTIMUM SIMPLE ITERATION

It is known [1], that the usual method of stationary simple iteration for the solution (1)

$$x^{(m+1)} = T \cdot x^{(m)} + f, \quad m = 0, 1, 2, \ldots \tag{2}$$

converges for any $f \in B$ and any initial approach $x^{(0)} \in B$ if the spectral set (spectrum) $\sigma(T)$ of the transition operator T lays in a unit circle. In terms of spectral radius $\rho(T) = \sup|\sigma(T)|$, where ρ is the radius of the least circle with the center in the beginning of the coordinates, entirely containing a spectrum, a condition of convergence is $\rho(T) < 1$. This condition, as a rule, imposes rigid restrictions on convergence (2). A condition of an output from a converging computing process after achievement of the set accuracy ε of the solution is $|x^{(m+1)} - x^{(m)}| \le \varepsilon(1-\rho)/\rho$, where ρ is spectral radius of T.

We use the equivalent equation instead of (1) both (2) and the modified method of simple iteration (MMSI), having entered in the equation any complex parameter κ

$$x = \tilde{T}(\kappa) \cdot x + \varphi(\kappa); \quad x^{(m+1)} = \tilde{T}(\kappa) \cdot x^{(m)} + \varphi(\kappa), \quad m = 0, 1, 2, \ldots \tag{3}$$

Here the modified operator of transition (I — the unit operator) and the right part are

$$\tilde{T}(\kappa) = \frac{T - \kappa I}{1 - \kappa}, \quad \varphi(\kappa) = \frac{f}{1 - \kappa} \tag{4}$$

Let's show, that a choice of $\kappa\,(\kappa \neq 1)$ under enough wide conditions it is possible to achieve convergence (3) and, moreover, for many practically important cases of a localization of spectral area T construction of algorithm of search of optimum parameter in (4), minimizing radius of convergence of $\tilde{T}$ is possible.

The way of search of optimum parameter in (4) is known [2]. Let Ω_T is some circle completely including a convex envelope of a spectrum of T. Construction converging iterations (3) with the transition operator (4) is possible, if the point 1 on a complex plane does not belong to a convex envelope. The spectral set on a complex plane will be transformed under the same law, as operator

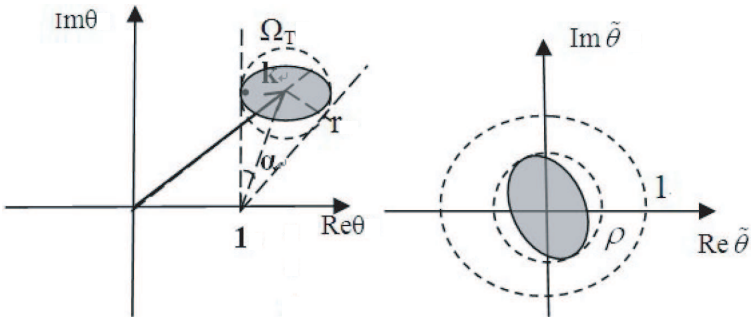

Figure 1.

T: $\tilde{\theta} = (\theta - k)/(1 - \kappa)$ (Figure 1). Thus the point 1 of complex plane θ passes into a point 1 of plane $\tilde{\theta}$, the center κ of a circle Ω_T passes into the center 0 of plane $\tilde{\theta}$, the circle of radius r passes into a circle $\Omega_{\tilde{T}}$ of radius $\rho = r/|1 - k| = \sin(\alpha)$. For optimum convergence it is necessary to find a circle $\Omega_T^{(0)}$ "visible" from a point 1 under the minimal corner $2 \cdot \alpha_0$, its center is optimum parameter κ_0, and the denominator of convergence is defined thus, as $\rho_0 = \sin(\alpha_0)$.

Let's note the important practical case, when a circle — a border of Ω_T — passes through a point 0. The point 0 at transformation (4) passes into a point $-\kappa/(1 - \kappa)$ which lays on border of a circle $\Omega_{\tilde{T}}$ and, thus, radius of convergence of modified series in this case

$$\rho = \left| \frac{\kappa}{1 - \kappa} \right| \tag{5}$$

3. OPTIMUM PARAMETER OF CONVERGENCE MOSI FOR SOME PRACTICALLY IMPORTANT CASES OF LOCALIZATION OF SPECTRUM AREA

Let the spectrum $\{\theta_\nu\}$ is localized on a beam which is starting with a point 1, and own numbers $\theta_{\min}$, $\theta_{\max}$ are known for which the minimal and maximal values on the module $|\theta_{\min} - 1|$ and $|\theta_{\max} - 1|$ (or the lower and upper borders of distance from a point 1 up to area of localization of a spectrum in case of continuous spectral set) are reached. Then for optimum parameter it is fair, obviously, simple formula (an optimum circle $\Omega_T^{(0)}$ — a circle, at which piece $[\theta_{\min}, \theta_{\max}]$ — diameter)

$$k_0 = \frac{\theta_{\min} + \theta_{\max}}{2} \tag{6}$$

Thus radius of convergence is $\rho = r/|1 - \kappa| = |(\theta_{\max} + \theta_{\min})/(2 - (\theta_{\max} + \theta_{\min}))|$.

In that specific case the Formula (6) is true in case of a real spectrum of the operator T if the operator $A = 1 - T$ is positively (negatively) certain. The Formula (6) also exact in case border of a complex circle of area of an arrangement of a spectrum also belongs to a spectrum. In these specified cases value of optimum parameter of convergence can be expressed analytically in the form of the Formula (6). There are practically important cases of localization of spectral set for which value of optimum parameter can be found algorithmically. These are cases when area of localization of a spectrum is the any complex piece, a triangle or a polygon.

In Figure 2, point 0 is the beginning of coordinates of a complex plane and a point A is a point 1 on a real axis. Piece BC is the area of localization of a transition operator spectrum. Point O_{ABC} is the center of the circle described around of triangle ABC. Through a medial perpendicular to piece BC we shall lead from point O_{ABC} beam $O_{ABC}x$, on which x is the distance from the beginning of a beam. A direction of a beam is aside a half plane which are not containing a point 1. Let the center of the circle ω_x, which are passing through a point B and a point C, lays on this beam on distance x from point O_{ABC} in point X, and this circle thus is "visible" from a point 1 under a corner 2ξ. AK is a tangent to this circle. $R = R(x)$ — its radius. If as parameter in (4) to accept complex value of point X the radius of convergence is equal $\rho = \sin(\xi) = R/AX$. Let's find function $\rho = \rho(x)$, its minimum and value in a minimum. It is obvious, that $\rho(0) = \rho(\infty) = 1$, and on other axis $0 < \rho(x) < 1$. Required function, using the theorem of cosiness and properties of the

central and entered corners in a circle with the center in point O_{ABC} and in point X

$$\rho(x) = R/AX = \sqrt{\frac{x^2 - 2rx\cos\alpha + r^2}{x^2 - 2rx\cos(\alpha + 2\gamma) + r^2}} \tag{7}$$

Here $\alpha = \angle BAC$, $\gamma = \angle BCA$ — the fixed corners set ΔABC, r is a radius of the circle described around ΔABC. The minimum of function (7) is equal $\rho(x_1) = \sqrt{(1-\cos(\alpha))/(1-\cos(\alpha+2\gamma))}$ and comes at $x_1 = r$. Thus, optimum parameter for convergence (3) in case of a spectrum-piece $\kappa = \overrightarrow{OX_1}$. Thus, the optimum parameter for convergence in case of a complex spectrum-piece is complex value of a point X_1 of crossing of circle O_{ABC} and a medial perpendicular to a piece, and it is necessary to choose from two values such, for which the "optimum" circle ω_1 does not contain a point 1.

In case when the localization area of a spectrum is a triangle, for example, ΔBCD on Figure 2, the algorithm of definition of optimum parameter is following. Let $\omega_i, i = 1, 2, 3$ — the "optimum" circles constructed for each piece from a triangle ΔBCD as it is described above. If the third top of a triangle belongs to any circle ω_i or its border the optimum parameter is found: $\kappa = \overrightarrow{OX_i}$. Otherwise (as it is presented on Figure 3) it is necessary to move from point X_i on the beam constructed for a given piece in the center described around of ΔBCD a circle — point X_0. The optimum parameter for convergence in this case $\kappa = \overrightarrow{OX_0}$, and speed of convergence is a little bit worse, than for any spectrum-piece from structure of a triangle. Let's name the circle found thus "optimum" for a triangle as its center is optimum parameter for convergence MMSI in case of localization of spectral set of the operator of transition on a complex triangle.

In case when the spectrum lays on a broken line consisting of several pieces or on a polygon algorithm of search of optimum parameter is following. The optimum circle of some characteristic triangle from structure of a polygon, which contains all area of localization of a spectrum, is defining. Value of its center is accepted to optimum parameter of convergence.

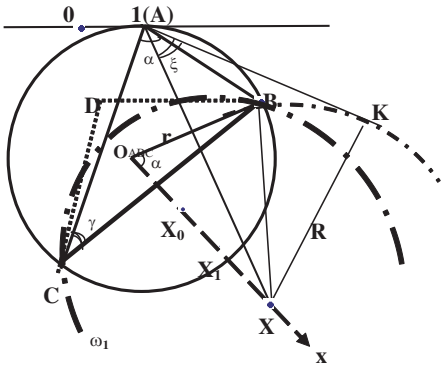

Figure 2.

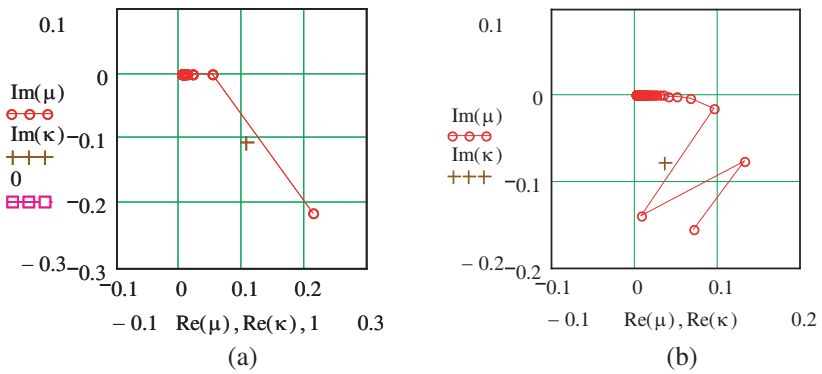

Figure 3. Spectral pictures in Rayleigh region.

4. NUMERICAL RESEARCHES

A stationary scalar problem of electromagnetic E-polarization wave scattering on transparent non-uniform in section the infinite cylinder is considered. This problem is described by 2D integral Fredholm equation of second kind for complex amplitude of the full electric field consisting of the sum of incident and scattering waves in the presence of dielectric [2].

$$E = TE + E^0, \quad E(p) = k_0^2 \iint\limits_S (\varepsilon(q) - 1)E(q)G(r)dq + E^0(p) \tag{8}$$

Here relative permittivity in the area of heterogeneity is a complex function of coordinates q, and ε_0, k_0 — accordingly permittivity and wave number of free space. $G(r) = -0.25iH_0^{(2)}(r)$ is Green's function of free space in a 2D case, Hunkel function of the second kind of the zero order, where $r = |p - q|$ — distance between a point of a source $q = (x', y')$ and a point of supervision $p = (x, y)$. The Equation (8) is already presented in the form of (1), convenient for application of a method of simple iteration. Spectrum of such compact integral operator is discrete with only one point of accumulation of own numbers in point 0.

In case of Rayleigh (low frequency) scattering, area of a spectrum is the small area near this accumulation point (Figures 3(a) and (b)).

On Figure 3(a), the spectrum in a problem of scattering on small in cross section the round cylinder with diameter $d = 0.1\lambda$, where λ is wavelength in a free space, and with constant relative permittivity $\varepsilon = 4$ is represented. On Figure 3(b) — the same, but on the cylinder, in which section thin, but resonant on other size a rectangular with the sizes accordingly 0.01λ and 1λ and $\varepsilon = 5$. In all cases in view of remoteness of a point 1 the optimum parameter is the center of the piece connecting the point 0 and the point μ_1, where μ_1 is the greatest on the module own number of a spectrum. So, in Rayleigh region (can only on one coordinate) optimum parameter $\kappa = \mu_1/2$ and radius of convergence MOSI, according to (5), $\rho = |\kappa/(1 - \kappa)| \approx |\mu_1|/2 \ll 1$. Value μ_1 can be effectively found, in view of isolation maximal on the module of own number, by means of an iterative power method.

On Figure 4, the dissymetric geometry of a resonant scattering problem (area of heterogeneity is of the order of a wavelength) of a flat electromagnetic wave of frequency of 900 MHz on the muscular cylinder with a diameter 0.25 meters with bone inclusion is resulted. Complex permittivity of biological structures in this range makes accordingly $\varepsilon_{\text{musc}} = 52 - 62i$ and $\varepsilon_{\text{bone}} = 13 - 4i$. Also on Figure 4, the picture of the specific absorption rate (SAR) is presented in case when the direction of the wave propagation is from non-uniform inclusion.

On Figure 5, the spectral picture of the given problem is presented. The behaviour of a spectrum near points 0 and 1 is allocated on Figure 5 separately. Number of points of a spectrum is $n = 192$ that corresponds to 2–3 units of a computing grid for a wavelength in the muscular environment.

The optimum parameter ("+" on Figure 5) is found as the center of the described circle around of the some characteristic triangle including a point 0. This triangle is formed by a point of accumulation of own numbers (a point 0), own number on a real axis to the left of a point 0 and one of own numbers near a point 1. Calculation of an absorption problem is lead with this optimum

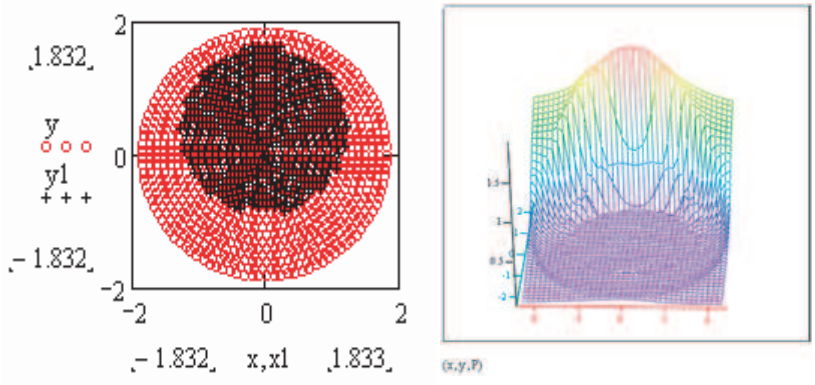

Figure 4. Geometry of a resonant scattering area and picture of SAR.

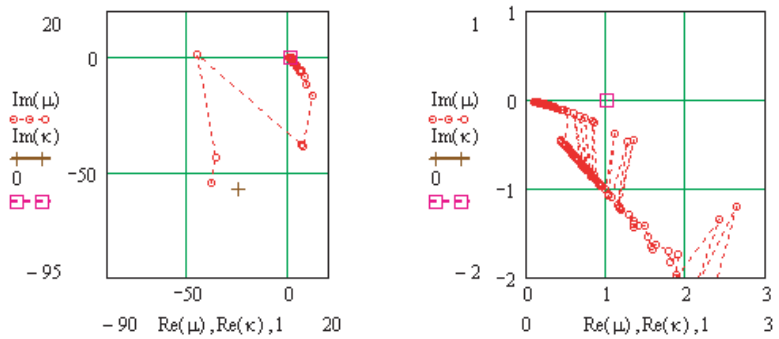

Figure 5. Spectral picture of resonant scattering on the non-uniform cylinder.

parameter at sufficient approximation to 7–8 units for a wavelength in the muscular medium. Thus the general number of complex unknowns is $n = 1728$ and it is already inaccessible to calculations on PC by means of direct methods. The solution with accuracy of $\varepsilon = 10^{-4}$ for electric field in medium is received for $m = 950$ iterations and has borrowed some minutes of machine time.

5. CONCLUSION

Algorithms of definition of optimum parameter and denominator of convergence MOSI on the basis of knowledge of localization of spectrum area of the transition operator in a method of usual simple iteration are developed. These algorithms are found in cases when the convex envelope of a spectrum has a figures configuration of the simple form, such as any complex piece, a circle, a triangle, a polygon. The opportunity of the numerical solution of the integral equation of scattering and large SLAE on the basis of a principle of anticipatory stability of a spectrum and optimum parameter is shown.

REFERENCES

1. Kantorovich, L. V. and G. P. Akilov, *Functional Analysis*, 744, Nauka, Moscow, 1977.
2. Samokhin, A. B., *Integral Equations and Iteration Methods in Electromagnetic Scattering,* 160, VSP, Utrecht, The Netherlands, 2001.

Numerical Solution of 2D and 3D Scattering Problems on a Dielectric Body by a Method of Optimum Simple Iteration

Sergey P. Kulikov
Moscow Institute of Radio Engineering, Electronics and Automation
78, Vernadsky av., Moscow 117454, Russia

Abstract— A numerical solution of volume integral equation of scattering by dielectric body in vector 2D and 3D cases in low-frequency and resonant region is under investigation. Examples of application of the method of optimal simple iteration (MOSI) are present. Efficient numerical technique is based on the spectral properties of the integral operator. The accuracy of the first approximation of the optimal series in vector 2D case and near-resonant region in comparison with so-called the Born approximation and with the solution of MOSI is under consideration.

1. INTRODUCTION

The vector stationary problem of scattering of electromagnetic wave by dielectric non-magnetic body in cases of H-polarization of the two-dimensional (2D) scattering and general three-dimensional (3D) vector case is under consideration. This task is described by a volume integral equation on the amplitude of electric field and its numerical solution studied by many authors [1–4].

$$\vec{E}(p) = \vec{E}^{(inc)}(p) + \nu\left(\varepsilon(p)-1\right)\vec{E}(p) + v.p.\int\limits_{Q}\left(\varepsilon(q)-1\right)\vec{E}(q)k_0^2G(r)dQ + \int\limits_{Q}\Big(\left(\varepsilon(q)-1\right)\vec{E}(q),\mathrm{grad}\Big)\,\mathrm{grad}G(r)dQ \tag{1}$$

Here, $\vec{E}^{(inc)}$ — Primary (incident) field in the absence of the body, $\vec{E} = \vec{E}^{(inc)} + \vec{E}^{(scat)}$ — Full, incident plus scattered field, $v.p.$ — The singular integral in the sense of principal value, the multiplier ν in non-integral member has a value $\nu = \frac{1}{3}$ in 3D case, and $\nu = \frac{1}{2}$ in 2D vector case, the Green's function in 3D case is $G(r) = \frac{\exp(-ik_0r)}{4\pi r}$, in 2D cases $G(r) = -0.25iH_0^{(2)}(r)$ — The Hankel function of the second kind of the zero order.

The integral operator of equation in these cases is a singular operator, and its spectrum has the continuous and the discrete components [5]. Consider the case when the permittivity is in the area Q set of piecewise constant complex values $\varepsilon_i, i = 1\ldots n$, for example, a one value $\varepsilon_1 \neq 1$. The continuous spectrum of the operator consists of the segments $[0, 1-\varepsilon_i], i = 1\ldots n$, in particular it is one segment $[0, 1-\varepsilon_1]$, regardless of the configuration and size of the area. The discrete spectrum is localized in the bottom complex half, as well as, perhaps, between the segments of continuous spectrum in the upper half and it has the points of accumulation on the continuous spectrum.

It is difficult to apply direct universal methods for solving linear algebraic systems arising after discretization of the integral Equation (IE) (1), because of the large amount of required computer resources. More acceptable for the numerical solution of IE are iterative methods [3, 4]. In this work, for this purpose is applicable method of optimal simple iteration (MOSI), the effectiveness of which is based on the spectral properties of the integral operator [6]. The Equation (1) is already represented in the form suitable for applying the usual method of successive approximations with the transition operator T

$$E = T\cdot E + E^{(inc)}, \quad E^{(m+1)} = T\cdot E^{(m)} + E^{(inc)}, \quad m = 0, 1, 2, \ldots \tag{2}$$

2. RAYLEIGH REGION CASE

On Figure 1(a), a spectrum of the transition operator in 2D vector Rayleigh case is presented. The size of a dielectric square cylinder in cross-section is $d = 0.075\lambda$, where λ — The wavelength, the value of permittivity is $\varepsilon = 2$. In this case, only a continuous spectrum in the form of an interval $[0, -1]$ is present, the discrete spectrum in the low frequency case is vanishing small. Thus [6], $\kappa = \frac{1-\varepsilon}{2} = -0.5$ — Optimal value of the convergence, as it coincides with the center of the "optimal" circle for such spectral segment.

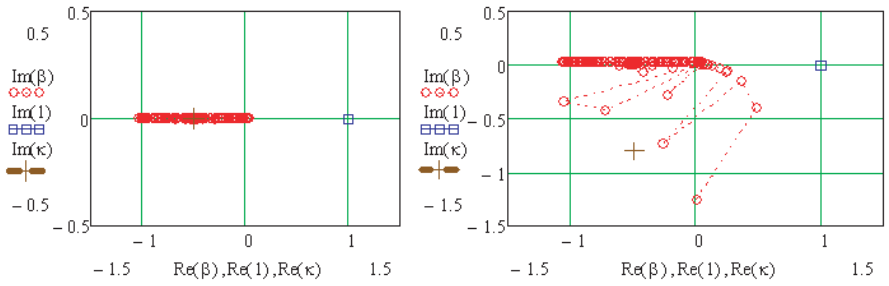

Figure 1.

On Figure 1(b), the same task, but in the resonance case $d = 0.75\lambda$ and the discrete spectrum is making a significant amendment to the optimal setting $\kappa = -0.5 - 0.8i$, is presented.

In the Rayleigh range, where the discrete spectrum is concentrated in a small little area near the continuous spectrum, in case of real $\varepsilon_i > 1$, $i = 1 \dots n$, $\varepsilon_{\max} = \max \varepsilon_i$, $i = 1 \dots n$ the optimum of κ is

$$\kappa = \frac{1 - \varepsilon_{\max}}{2} \tag{3}$$

For the case of a weak plasma, when the value of permittivity is on the interval $\varepsilon \in (0, 1)$, the value $\varepsilon_{\max}$ provides the maximum value $|1 - \varepsilon_{\max}|$. In all cases, when ε is real, radius of convergence of MOSI [6] is $\rho = |\frac{\kappa}{1-\kappa}| = |\frac{1-\varepsilon_{\max}}{1+\varepsilon_{\max}}|$. In a fast convergence MOSI with $\rho \leq \frac{1}{3}$ permittivity values are in range $\varepsilon_{\max} \in [\frac{1}{2}, 2]$. In the case of the fast convergence of the usual series (2), when $|\varepsilon - 1| \ll 1$, fairly good physical approximation gives the first member of a number of approximations (2), so-called the Born approximation.

$$\vec{E}^{(1)} = T\vec{E}^{(inc)} + E^{(inc)} \quad \text{or} \quad \vec{E}^{(1)} = (\varepsilon - 1)\hat{T}\vec{E}^{(inc)} + E^{(inc)} \tag{4}$$

Here T — is the transition operator (1), (2), the operator $\hat{T}$ — the same, but in the case $\varepsilon = \text{const}$, from which we made the multiplier $(\varepsilon - 1)$. For the first approximation of the optimal number of simple iterations, taking into account (3) and with the initial approximation $\vec{E}^{(0)} = \vec{E}^{(inc)}$, we get $\vec{E}^{(1)} = \frac{2}{1+\varepsilon_{\max}} T\vec{E}^{(0)} + \vec{E}^{(0)}$. In the case of a homogeneous scattering body with $\varepsilon = \text{const}$, we get the first approximation

$$\vec{E}^{(1)} = 2\frac{\varepsilon - 1}{\varepsilon + 1}\hat{T}\vec{E}^{(0)} + \vec{E}^{(0)} \tag{5}$$

The correction factor in (5) allows you to expand the applicability of approximation (4) from the interval $|\varepsilon - 1| \ll 1$ to the area $|\varepsilon - 1| \leq 1$ and more, including the case of complex values of ε. The significance of the optimal parameter (3) may be true in the near-resonant field and in the case when the size of one of the coordinates is in the Rayleigh or near-resonant region, while the second is in significantly resonant region and $|\varepsilon - 1| \leq 1$. Then the approximation (5) is also applicable with good accuracy, as well as significant in these cases, the discrete spectrum of the operator is typically in the "optimal" circle constructed without taking into account the discrete spectrum, but only on the basis of a priori knowledge of the continuous spectrum.

3. NEAR RESONANT AND RESONANT CASE

For example, consider 2D vector problem of diffraction of a plane wave H-polarization and frequency of 900 MHz for the dielectric plate with the permittivity $\varepsilon = 2$ of the thickness $d_y = 0.2\lambda$ (0.067 m) and length $d_x = 5\lambda$ (1,667 m), where $\lambda = 0.333$ m — wavelength in free space. Vector E is in x direction and the direction of wave vector is y.

On Figure 2(a), the spectral picture of the transition operator for this problem and an optimal setting that corresponds to the formula (3) are presented. On Figures 2(b) and 2(c), Scattering Pattern (SP) of wave in the far-zone ($\sigma(\psi)$) in the range of angles from the direction of the spread of the incident wave perpendicular to the plate (on axis y) $\psi - \pi/2 = 0$ to the reverse angle is shown. SP is calculated in 3D case as $\sigma(\psi) = \lim\limits_{R\to\infty} R^2 \frac{|\vec{E}^{(scat)}|^2}{|\vec{E}^{(inc)}|^2}$ and in 2D case as $\sigma(\psi) = \lim\limits_{R\to\infty} R\frac{|\vec{E}^{(scat)}|^2}{|\vec{E}^{(inc)}|^2}$

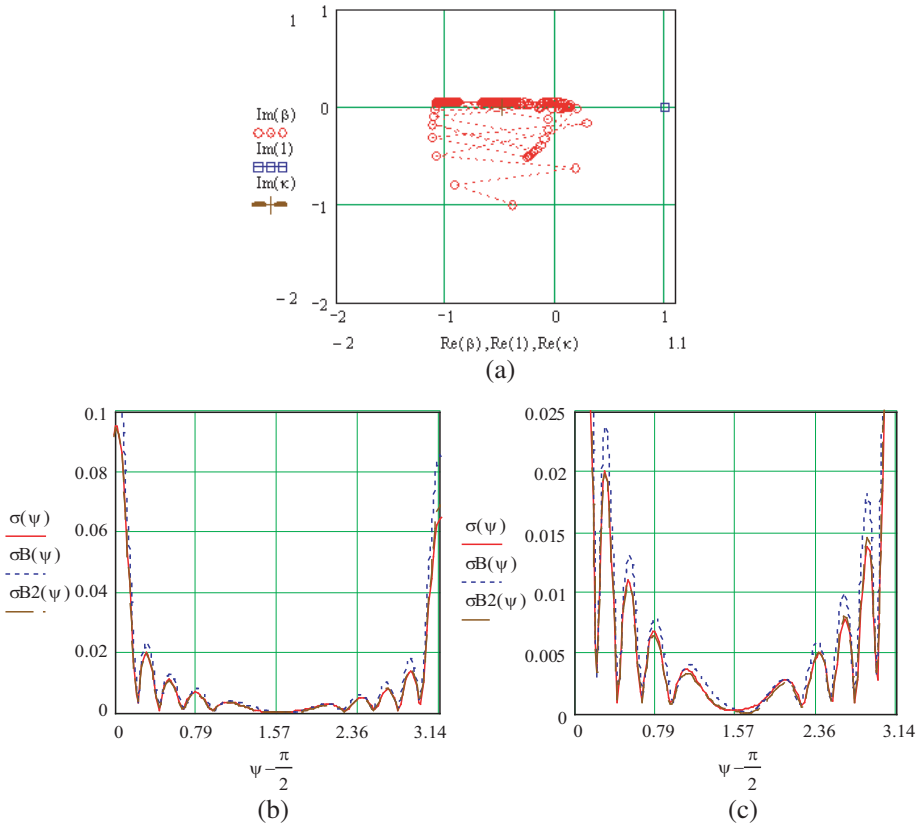

Figure 2.

and $\vec{E}^{(scat)} = T\vec{E}$. On Figure 2(c), SP is presented in more detail in its lower part. Here and in Figure 3 for better visibility of the value SP is respresented by $\sqrt{\sigma(\psi)}$. SP is shown in three different versions: First — calculation of SP $\sigma(\psi)$ is based on the value field in a dielectric body, which is obtained by IE and MOSI with an accuracy of 10^{-4} (discussed further in the examples the accuracy is the same) and with the number of optimal iterations $m = 10$, the second — SP $\sigma B(\psi)$ is obtained through the Born approximation (4), third — SP $\sigma B_2(\psi)$ is obtained using approximation (5). SP on approximation (5) $\sigma B_2(\psi)$ and calculated SP using IE and MOSI $\sigma B(\psi)$ coincide with a relative integral error $\delta B_2 = 0.13$ and the error $\sigma B(\psi)$ is $\delta B = 0.37$, that is almost 3 times more. The calculation carried out on the Cartesian grid in the $2 \times 50 = 100$ nodes.

The result can be used for engineering calculations of the antenna field, surrounded by homogeneous fairing. In the case of dielectric losses mistake of the Born approximation can be increased. At the same time, identifying the best option for $\kappa(\varepsilon)$ the method described [6] as the intersection of the circle passing through 0, 1, and $1-\varepsilon$ with mid-perpendicular to the segment of the spectrum $[0,\ 1-\varepsilon]$, we get a good engineering approximation

$$\vec{E}^{(1)} = \frac{1}{1-\kappa(\varepsilon)} T\vec{E}^{(0)} + \vec{E}^{(0)} \tag{6}$$

For example, consider a similar problem the previous case, but the dielectric losses are available $\varepsilon = 2 - 2i$. Spectral pattern with the optimal parameter and the diagram are presented in Figure 3. Discrete spectrum is visible, as well as a problem in one coordinate is resonant, but it fits in the optimal circle to the segment $[0,\ 1-\varepsilon]$. Solution using MOSI was obtained in 10 iterations and it corresponds to the first SP $\sigma(\psi)$. Curve $\sigma B_2(\psi)$ is a good tracking as the main and the revers lobe, and lateral lobes of SP too, in contrast to curve $\sigma B(\psi)$.

As can be seen from the spectral picture of Figure 3(a), a priori found to segment the optimal parameter is here in force, and the optimum circuit includes discrete spectrum. SP, on the basis of approximation (6) has a good graphic precision $\delta B_2 = 0.01$, while the usual approach no longer describes the field and the curve of the SP: $\delta B = 0.9$.

For the 3D problems features of the spectrum and the algorithms determine the optimal param-

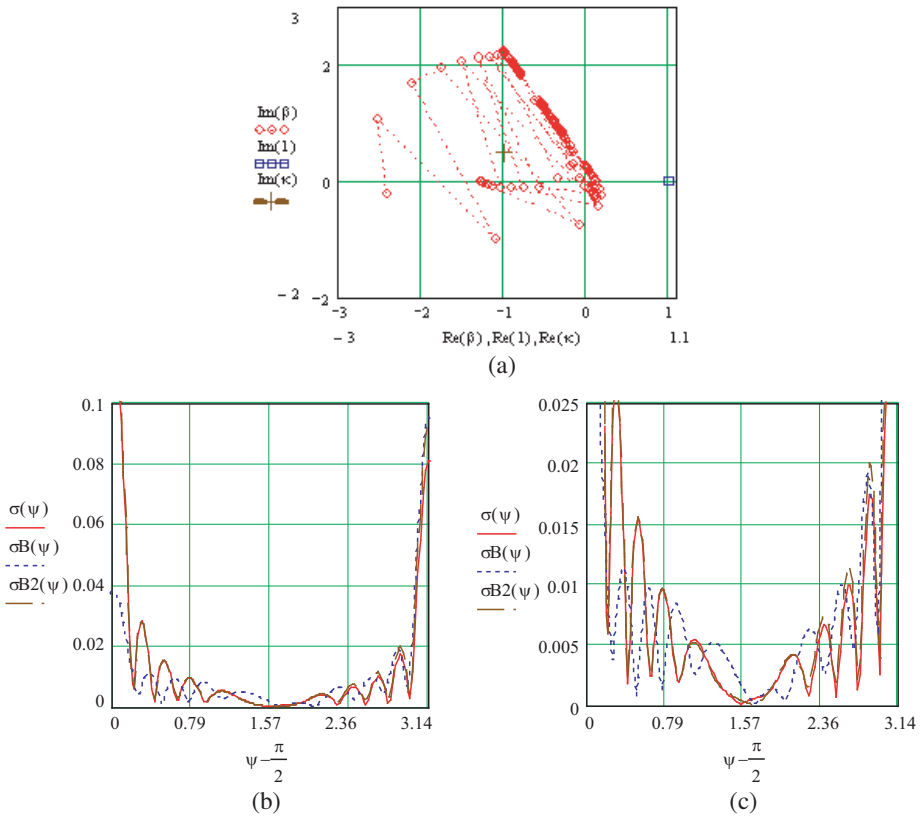

Figure 3.

eter MOPI are similar to those that were considered in the 2D vector case.

Thus, on Figure 4, the three-dimensional solution vector problem of scattering of plane waves in a cube with the side $k_0 d = 0.75\lambda$, where λ — the wavelength in free space and permittivity $\varepsilon = 4$ is present. The calculation of the spectrum and the optimal parameter value (Figure 4(a)) held in the weak approximation problem in computational grid with 3 node per a wavelength in the medium and the total number of grid nodes was $N = 6 \times 6 \times 6 = 216$. The real part of the optimal parameter is obtained from the continuous spectrum. SP (Figure 4(b)), which has not changed in the further improvement of the approximation obtained with the same optimal parameter and the total number of grid nodes $N = 9 \times 9 \times 9 = 729$. The size of the complex matrix of transition was $3 \times N = 2187$. The solution of this task is not available for the existing library of programs with direct algorithms for solutions of large SLAE.

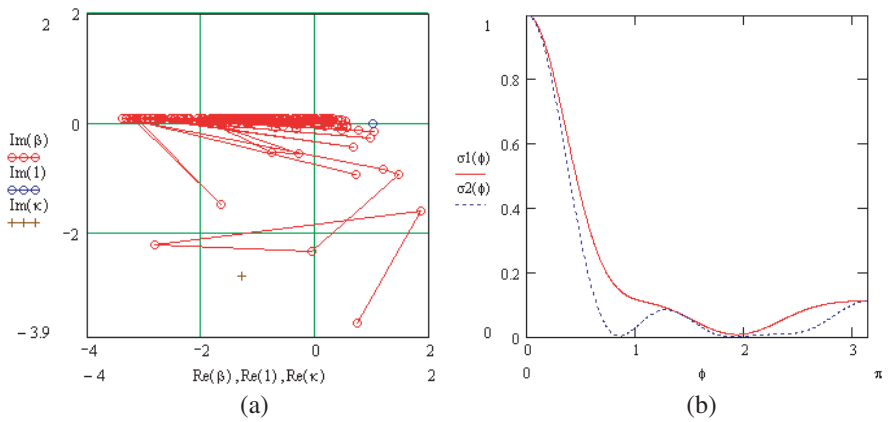

Figure 4.

4. CONCLUSION

Numerical solutions of the volume integral equations of scattering in 2D and 3D vector cases was based on the MOSI in this work. The spectral properties of the integral operator were numerically investigated in the low-frequency and resonant ranges, and on this basis, were provide recommendations on choosing the optimal parameter MOSI. It was shown that the approximation based on the first member of the optimal series of iterations allows to improve the efficiency of the use of the Born approximation.

REFERENCES

1. Livesay, D. E. and K. M. Chen, "Electromagnetic fields induced inside arbitrarily shaped biological bodies," *IEEE Trans. Microwave Theory Tech.*, Vol. 22, 1273–1280, 1974.
2. Lee, S. W., J. Boersma, C. L. Law, and G. A. Deschamps, "Singularity in Green's function and its numerical evaluation," *IEEE Trans. Anten. Propagat.*, Vol. 28, No. 3, 311–317, 1980.
3. Samokhin, A. B., *Integral Equations and Iteration Methods in Electromagnetic Scattering*, 160, VSP, Utrecht, The Netherlands, 2001.
4. Kleinman, R. E. and P. M. Van der Berg, "Iterative methods for radiowave problems," *The Review of Radio Science*, 57–74, Oxford University Press, 1993.
5. Budko, N. V. and A. B. Samokhin. "Spectrum of the volume integral operator of electromagnetic scattering," *SIAM J. Sci. Comput.*, Vol. 28, No. 2, 682–700, 2006.
6. Kulikov, S. P. and A. B. Samokhin, "Mathematical substantiations of library programs for solution SLAE by a method of optimum simple iteration," *Nauchny Vestnik MIREA*, Vol. 1, No. 2, 71–80, Moscow, 2007.

Design and Optimization of Wideband Multi Section Coupled-line Phase Shifters with Impedance Matching

Homayon Oraizi and Alireza Shamsafar
Department of Electrical Engineering
Iran University of Science and Technology, Tehran 1684613114, Iran

Abstract— A least squares based method is developed for the design and optimization of microstrip coupled line phase shifters. The multi-section coupled line theory is employed to calculate the phase shift in a frequency band. The algorithm also incorporates the load and source impedance matching. The minimization of error function determines the lengths, widths and spacings of strips. The performance of the optimized design perfectly agrees with the available commercial microwave simulation softwares.

1. INTRODUCTION

Phase shifters have many applications in the passive and active microwave circuits and the feed network of antennas. The Schiffman phase shifter has been the standard circuit for many years [1]. There are available some approximate design procedures for it. However, in this paper we propose a coupled-line phase shifter and present a design and optimization procedure for it, which is based on the method of least squares. This design method also incorporate source to load impedance matching. Consequently, combining the phase shifting and impedance matching functions in a microwave network configuration leads to the overall reduction of the microwave circuit and improvement of its frequency performance.

2. NUMERICAL IMPLEMENTATION

The coupled-line phase shifter consists of a microstrip multi-section line as the main path between the input and output ports (called ports 1 and 2, respectively) and a reference path as a microstrip line between ports 3 and 4. The phase shift is obtained as the phase difference between the two paths.

Consider the schematic diagram and equivalent circuit of a passive microstrip coupled-line phase shifter as shown on Figs. 1 and 2, respectively .The input and output ports are designated by 1 and 2, respectively. The reference and isolated ports are 4 and 3, respectively. The output phase shift is measured as the phase difference between S_{12} (phase of transmission coefficient from port 1 to port 2) and S_{14} (phase of transmission coefficient from port 1 to port 4) [2, 3].

$$\Delta\varphi = \angle S_{12} - \angle S_{14} \tag{1}$$

The even- and odd-mode analysis is used to determine the impedance matrix of the coupled-line

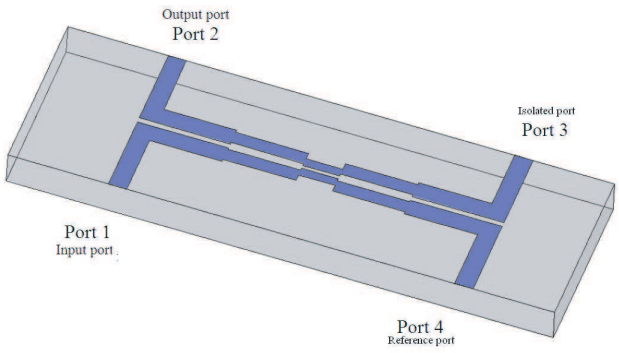

Figure 1: Layout of the proposed coupled-line phase shifter.

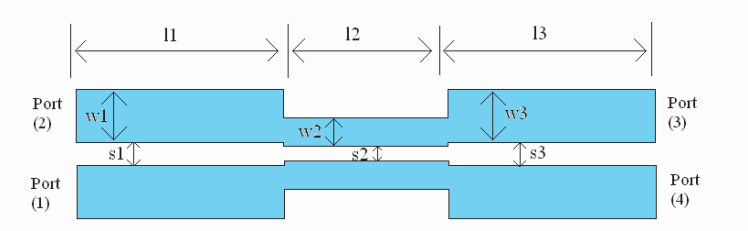

Figure 2: Dimensions of the configuration of the proposed coupled-line phase shifter.

phase shifter [4].

$$\begin{bmatrix} Z_{11} & Z_{12} \\ Z_{21} & Z_{22} \end{bmatrix} = \begin{bmatrix} \dfrac{(Z_{0e}\cot g\theta_e + Z_{0o}\cot g\theta_o)}{2} & \dfrac{(Z_{0e}\csc g\theta_e - Z_{0o}\csc g\theta_o)}{2} \\ \dfrac{(Z_{0e}\csc g\theta_e - Z_{0o}\csc g\theta_o)}{2} & \dfrac{(Z_{0e}\cot g\theta_e + Z_{0o}\cot g\theta_o)}{2} \end{bmatrix} \tag{2}$$

Then the $ABCD$ and scattering matrices are obtained [5, 6].

$$\begin{bmatrix} A & B \\ C & D \end{bmatrix} = \begin{bmatrix} \dfrac{Z_{11}}{Z_{21}} & \dfrac{Z_{11}Z_{22} - Z_{21}Z_{12}}{Z_{21}} \\ \dfrac{1}{Z_{21}} & \dfrac{Z_{22}}{Z_{21}} \end{bmatrix} \tag{3}$$

$$\begin{bmatrix} S_{11} & S_{12} \\ S_{21} & S_{22} \end{bmatrix} = \begin{bmatrix} \dfrac{AZ_L + B + CZ_LZ_S^* - DZ_S^*}{AZ_L + B + CZ_LZ_S + DZ_S} & \dfrac{2\sqrt{R_SR_L}}{AZ_L + B + CZ_LZ_S + DZ_S} \\ \dfrac{2\sqrt{R_SR_L}}{AZ_L + B + CZ_LZ_S + DZ_S} & \dfrac{AZ_L + B + CZ_LZ_S^* - DZ_S^*}{AZ_L + B + CZ_LZ_S + DZ_S} \end{bmatrix} \tag{4}$$

where Z_S and Z_L are the source and load impedances, respectively. The over all $ABCD$ matrix of the multi-section coupled-line phase shifter is obtained by the product of $ABCD$ matrices of each coupled-line section.

The phase shift is given by (1) and the reflection coefficient or the return loss is given by S_{11}.

Now, we construct an error function for the realization of specified phase shift ($\Delta\varphi$) and minimization of the reflection coefficient.

$$error = W_1 \sum_{f_k=4\,\mathrm{GHz}}^{10\,\mathrm{GHz}} |\Delta\varphi_{f_k} - 70|^2 + W_2 \sum_{f_k=4\,\mathrm{GHz}}^{10\,\mathrm{GHz}} |S_{11f_k}|^2 \tag{5}$$

where W_1 and W_2 are the weighting functions and the frequency bandwidth is divided into K discrete frequencies. The error is a function of lengths (l_i) and widths (w_i) of microstripes and gaps (g_i) between them. The dispersion relations due to Jansen and Kersching for the coupled-line are also used [5]. The minimization of error function is performed by the combination of genetic algorithm (GA) and conjugate gradient (CG) method. Consequently, the lengths, widths, and gaps of microstrip lines are determined.

3. DESIGN EXAMPLE

For an example, we design a three section coupled-line phase shifter for a phase difference of $\Delta\varphi = 70°$ over the frequency bandwidth 4–10 GHz. The substrate Roger Ro3210 is used, for which the dielectric constant of the substrate is $\varepsilon_r = 2.2$ and its thickness is $h = 0.4\,(\mathrm{mm})$.

The source and load impedances are selected as $R_s = 50\,\Omega$ and $R_L = 50\,\Omega$. The initial values of l_i, w_i and g_i are selected by the random generation in MATLAB under constraints. The constraints for w_i and g_i were specified as 0.1 h and 10 h, and the upper limit for the length of line sections was set at the wavelength of center frequency (λ).

The phase shift of the coupled-line phase shifter is drawn versus frequency in Fig. 3. The scattering parameters S_{11}, S_{12}, S_{13} and S_{14} are drawn in Fig. 4. The results of the MLS algorithm are verified by the HFSS and CST full-wave software. The dimensions of the optimized phase shifter configuration is given in Table 1.

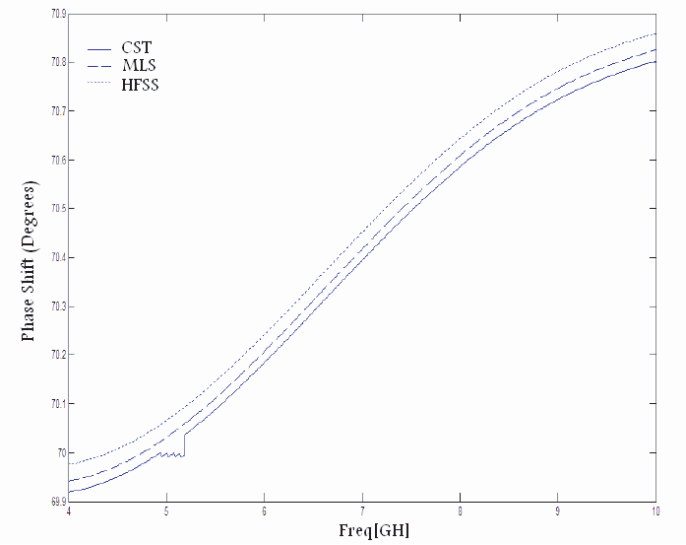

Figure 3: Phase shift vs frequency response of the coupled-line phase shifter.

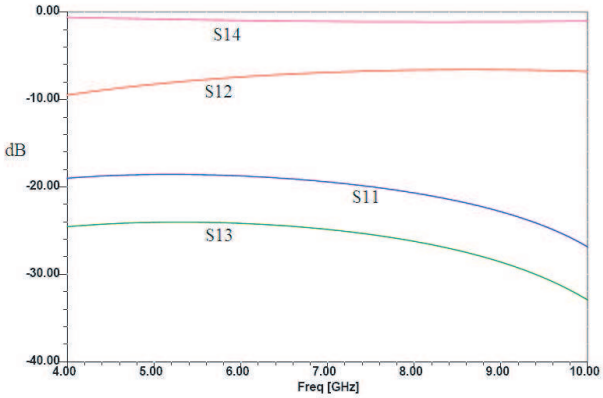

Figure 4: Scattering parameters of the proposed coupled-line phase shifter.

Table 1: Dimensions of the optimum design of coupled-line phase shifter.

After Optimization	l (optimum)	g (optimum)	w (optimum)
1	0.796 mm	0.0985 mm	0.145 mm
2	0.484 mm	0.0494 mm	0.0968 mm
3	0.796 mm	0.0985 mm	0.145 mm

4. CONCLUSIONS

The optimum design of coupled-line phase shifter based on the method of least squares is an improvement over the existing design methods, because it incorporates phase shift realization with impedance matching and considers dispersion relations and coupling parameters. The error function is minimized by the successive application of the Genetic Algorithm and the conjugate gradient method. The dimensions of the coupled-line phase shifter (lengths, widths and gaps of line sections) are determined. The performance of coupled-line phase shifters is favorably compared with those obtained by the available commercial softwares.

REFERENCES

1. Schiffman, B. M., "Multisction microwave phase shift network," *IEEE Trans. Microwave Theory Tech.*, Vol. 14, 209, Apr. 1966.

2. Free, C. E. and C. S. Aitchison, "Improved analysis and design of coupled-line phase shifters," *IEEE Trans. Microwave Theory Tech.*, 2126–2131, Sept. 1995.
3. Leong, Y. C. and S. Weinreb, "Novel technique of phase velocity equalization for microstrip coupled-line phase shifters," *IEEE MTT-S Intl. Microwave Symp. Digest*, 1453–1456, Boston, MA, 2000.
4. Pozar, D. M., *Microwave Engineering*, 2nd Edition, Wiley, New York, 1992.
5. Edwards, T. C., *Foundations for Microstrip Circuit Design*, 2nd Edition, Wiley, New York, 1992.
6. Frickey, D. A., "Conversions between S, Z, Y, h, $ABCD$, and T parameters which are valid for complex source and load impedances," *IEEE Trans. Microwave Theory Tech.*, Vol. 42, No. 2, Feb. 1994.
7. Ramos Quirarte, J. L. and J. P. Starski, "Novel schiffman phase shifters," *IEEE Trans. Microwave Theory Tech.*, Vol. 41, No. 1, Jan. 1993.

The Theory of R-functions and Wavelets in the Boundary Value Problems of Electrodynamics

V. F. Kravchenko[1] **and A. V. Yurin**[2]

[1]Kotel'nikov Institute of Radio Engineering and Electronics of RAS, Moscow, Russia
[2]Bauman Moscow State Technical University, Moscow, Russia

Abstract— The new approach to solving boundary value problems for partial differential equations is represented. It is based on Galerkin classic variation scheme which is converted with the help of R-functions and wavelets. As a result while matrix system compiling we obtain some calculating advantages: matrixes of the system are sparse, the calculation of matrix elements does not demand the integration and is carried out with the help of connection coefficients of the wavelet system. New fast computational algorithms based on fundamental wavelet properties for connection coefficients are also introduced in this work. The basic results were used for the solving of electrodynamics problems.

1. INTRODUCTION

Considering of a wide class of boundary value problems of different physical nature there occurs the necessity for solving partial differential equations in which the researched domain has a complex configuration. In such cases numerical methods are used: net (boundary-element (BEM), finite-element (FEM), finite-difference), variational and projective (Ritz, Galerkin, collocation, R-functions etc.) methods. Net methods have the great efficiency of algorithm, however they not precisely take into account the geometry of an object. In case of variational methods the construction of basic functions satisfying all the required conditions isn't always possible. Therefore they are used limitedly. The R-functions method is worth being especially examined [1, 3] as it obtains the geometrical flexibility and universality in relation to a way of functional minimization. The application of such approach demands significant computing expenses because of the structural formulas which are based on the constructed with the help of R-operations [1] domain functions $\omega_i(x, y)$ are used. They can have a complex structure, and the calculation of their integrals on non-standard form of area demands the application of the quadrature formulas of high accuracy. Owing to wavelet-bases it is possible to bypass the mentioned lacks [2, 4, 5] and to develop the adaptive computation scheme not using the operation of integration. Such approach is possible due to the introduction of a special connection coefficient (CC) reflecting the differential and integrated characteristics of basis. The basic tool for realization such new method is Galerkin schema [2–5] of solving partial differential equations.

2. PROBLEM DEFINITION

It is well known that Galerkin method is flexible enough to use the additional mathematical tool on purpose of increasing the efficiency of the algorithm as a whole. Therefore many various modifications are developed.

Let it is required to find in domain $\Omega \subset \mathbf{R}^2$ the solution u of the differential equation

$$Au = f \ (f \in H) \tag{1}$$

with boundary conditions $L_i u|_{\partial\Omega} = g_i, \ \ i = \overline{1, N}$ on parts $\partial\Omega_i$ of boundary $\partial\Omega$. Here, H is Hilbert space, A is a differential operator ($D(A)$, $R(A) \in H$), L_i are operators of boundary conditions, and f, g_i are known functions. The approximate solution (1) is searched in expanded form $u_n(x, y) = \sum\limits_{k=1}^{n} c_k \phi_k(x, y)$ where $\phi_k(x, y) \in D(A)$ is a sequence of basic functions, c_k are sought coefficients.

According to Galerkin method [2–4] c_k are found concerning the condition of the residual of the Equation (1) which should be orthogonal to functions $\{\phi_k\}$

$$(Au_n - f, \phi_k) = 0, \quad k = 1, \ldots, n. \tag{2}$$

The expression (2) is represented as a system of the algebraic equations concerning coefficients c_k. Then the following notation (2) in the matrix form concerning the vector $\mathbf{C}$ is true:

$$\mathbf{AC} = \mathbf{B} \tag{3}$$

where elements **A** and **B** are defined with the help of formulas: $a_{nk} = (A\phi_n, \phi_k)$, $b_{nk} = (f, \phi_k)$. The main difficulty is represented by the calculation of matrix system coefficients. The usage of wavelets as basic functions reduces the efforts required for calculation these elements. Basically it is caused by properties of localization, orthonormalized, vanishing moments, and algorithm FWT of Mullat [1, 2]. The use of these advantages allows to represent scalar products as a standard set of connection coefficients depending on a kind of wavelet-system and connecting derivative basic functions with the basic functions by themselves [2, 4, 5]. The primary difficulties which arise in choosing such basis are connected with the consideration of the object geometry and boundary conditions, as wavelets are orthonormal all over the space L_2. However the R-functions theory [1, 3] allows to overcome these difficulties.

3. CONNECTION COEFFICIENTS

Let it is given the wavelet-system $\varphi(x)$, $\psi(x) \in C^m$, $m \geq 1$ with filter $\{a_n\}$ and satisfying the scaling equations $\varphi(x) = \sum\limits_n a_n \varphi(2x - n)$, $\psi(x) = \sum\limits_n b_n \varphi(2x - n)$, $b_n = (-1)^{n+1} a_{-n-1}$. As the wavelet-decomposition of function $f(x)$ [1, 2] can be expressed only in the view of basis of scaling functions at fixed resolution J it is evident to use CC only on expressed $\varphi_{Jk}(x)$. In a general view such CC are entered as the following

$$\Gamma(k_1, k_2, \ldots, k_n, d_1, d_2, \ldots, d_n) = \Gamma_{k_1, k_2, \ldots, k_n}^{d_1, d_2, \ldots, d_n} = \int \prod_{i=1}^{n} \varphi_{Jk_i}^{d_i}(x) dx \tag{4}$$

where d_i is the order of differentiation $\varphi(x)$, k_i are shifts $\varphi(x)$. For CC calculation the systems of linear equations on basis of wavelet properties and multiresolution analysis (MRA) [2, 4, 5], are built. It does not demand the integration of high-oscillating functions which the wavelets do. Such approach for CC of the second order $\Gamma_l^{d_1, d_2} = \int \varphi^{d_1}(x) \varphi_l^{d_2} dx$ is submitted in [2, 4]. However for majority of practical applications greatly depends on CC with the bigger number of subintegral functions [4]. In the suggested algorithm the CC of the third and fourth orders are the basic ones:

$$\Gamma_{k,l,m}^{d_1,d_2,d_3} = \int \varphi_k^{d_1}(x) \varphi_l^{d_2}(x) \varphi_m^{d_3}(x) dx, \quad \Gamma_{l,m,k}^{d_1,d_2,d_3,d_4} = \int \varphi^{d_1}(x) \varphi_l^{d_2}(x) \varphi_m^{d_3}(x) \varphi_k^{d_4}(x) dx. \tag{5}$$

In case of wavelets with the compact or limited support ($\operatorname{supp}(\varphi(x)) = [N_1, N_2]$) the whole range of values of CC can be represented as a vector Γ. The elements of this vector are determined from the solution of the linear equation system [4]. Let us to perform the main theorems with the help of which the given system CC of the third order is obtained. The proof is given in [4].

Theorem 1. Let Γ be a vector with elements (5) then the equality is true

$$\mathbf{A}\Gamma = \Gamma / 2^{d-1}, \tag{6}$$

where $d = d_1 + d_2 + d_3$; $A_{l,m}^{q,r} = \sum\limits_p a_p a_{q-2l+p} a_{r-2m+p}$, $(l, m), (q, r) \in S$.

Here S is the range of values which can accept CC subscripts. System (6) is homogeneous. Its determinant is equal to zero [4]. Then (6) has many non-trivial solutions. In order to obtain the unique solution for the system it is necessary to redefine it by indispensable number of linear-independent inhomogeneous equations presented in the Theorem 2.

Theorem 2. Let P be a number of the vanishing moments $\psi(x)$, then if $d \leq P$ the relationships take place

$$\sum_m M_m^p \Gamma_{l,m}^{d_1,d_2,d_3} = \begin{cases} p! \Gamma_l^{d_1,d_2}, & p = d_3, \\ 0, & p < d_3, \end{cases} \qquad \sum_l M_l^p \Gamma_{l,m}^{d_1,d_2,d_3} = \begin{cases} p! \Gamma_m^{d_1,d_3}, & p = d_2, \\ 0, & p < d_2. \end{cases} \tag{7}$$

where M_r^s is r moment of function $\varphi_s(x)$. Substituting Equation (7) in (6) the linear system with the unique solution is received. For CC of the fourth order the similar theorems are available in [4].

4. WAVELETS AND STRUCTURE OF BOUNDARY VALUE PROBLEMS SOLUTION

The R-functions method of the solution of boundary value problems of the mathematical physics represents the constructive problem solving of the transformation of the geometrical information into analytical one without the approximation [3]. The construction of the solution is its basis

$$u = B\left(\Phi, \omega, \{\omega_i\}_{i=1}^N, \{g_i\}_{i=1}^N\right) \tag{8}$$

which at any choice of indefinite component Φ exactly satisfies to boundary conditions. Here, B is the operator depended on geometry Ω and $\partial\Omega_i$, and also on functions g_i and operators of boundary conditions L_i, but not depended on a kind of the operator A and function f; ω is a domain function having properties: $\omega(x,y) > 0$ inside Ω, $\omega(x,y) = 0$ on $\partial\Omega$ and $\omega(x,y) < 0$ outside of Ω; ω_i are functions satisfying conditions: $\omega_i(x,y) > 0$ in $\Omega_i \supset \Omega$, $\omega_i(x,y) = 0$ on $\partial\Omega_i$ and $\omega(x,y) < 0$ otherwise. Having solution structure (8) that considers the given boundary conditions it is necessary to choose an indefinite component Φ for of the best satisfaction of the equation, parts of boundary conditions, simplicity of numerical realization or other requirements which are demanded to the algorithm. In case of using wavelets as basis of Φ the following record is typical:

$$\Phi(x,y) = \sum_{p,q \in G_\Omega^j} c_{pq}\varphi_{jp}(x)\varphi_{jq}(y) \tag{9}$$

at a sufficiently small scale j. Here, G_Ω^j is an index set which corresponds to N possible pair values of indexes $(p,q) : G_\Omega^j = \{(p,q) \in \mathbb{Z} \times \mathbb{Z} : \mathrm{supp}(\varphi_{jp}(x)\varphi_{jq}(y)) \cap \Omega \neq 0\}$.

Let us represent the solution structures which were received with the help of fundamental wavelet properties and MRA [4] for the elliptic partial differential equations of the second order (Laplace, Poisson, Helmholtz).

1. Dirichlet boundary condition $(u|_{\partial\Omega} = g)$: $u^j(x,y) = \sum\limits_{p,q}\sum\limits_{n,m} c_{pq}^j \omega_{nm}^j \varphi_{jp}(x)\varphi_{jn}(x)\varphi_{jq}(y)\varphi_{jm}(y)$, $(p,q),(n,\,m) \in G_\Omega^j$.

2. Neumann boundary condition $(\partial u/\partial\mathbf{n}|_{\partial\Omega} = g)$: $u^j(x,y) = \sum\limits_{p,q} c_{pq}^j \varphi_{jp}(x)\varphi_{jq}(y)$
$- \sum\limits_{p,q}\sum\limits_{n,m}\sum\limits_{k,l} c_{pq}^j \omega_{nm}^j \omega_{kl}^j \varphi_{jn}(x)\varphi_{jm}(y)(\varphi'_{jp}(x)\varphi'_{jk}(x)\varphi_{jq}(y)\varphi_{jl}(y) - \varphi_{jp}(x)\varphi_{jk}(x)\varphi'_{jq}(y)\varphi'_{jl}(y))$, (p,q), (n,m), $(k,l) \in G_\Omega^j$. Let us examine the application of the given above method using the concrete physical examples.

5. THE ELECTRODYNAMIC ANALYSIS OF WAVEGUIDE COMPLEX CROSS-SECTION

One of the major tendencies in development of devices working in the microwave ranges consists in an attempt to compute and numerically to optimize the necessary physical characteristics, reducing experimental checks. Therefore the role of electrodynamics methods of calculation [3] increases. It is known that at designing the microwave devices waveguides of complex section (WCS) are used as the base structure element. The offered algorithm is used for the analysis of critical wavelengths of a homogeneous waveguide of the complex shape of cross-section Ω in case of E-waves. Walls of a waveguide are ideally conducting. To solve an eigenvalue problem it is necessary to represent a field through a vector potential [3] which satisfies to homogeneous Helmholtz equation with Dirichlet boundary condition on $\partial\Omega$ (Figure 1(a)).

$$\Delta u + \alpha u = 0 \quad \mathrm{B}\Omega(\Omega \in \mathbf{R}^2), \quad u|_{\partial\Omega} = 0. \tag{10}$$

Galerkin process leads to minimization of functional [3, 4] $J = -\int_\Omega \Delta u v dxdy / \int_\Omega uv dxdy = \alpha$. Solving the latter, an eigenvalue spectrum of E-wave for the examined structure is obtained.

As basic functions the wavelets at scale j are used. The solution of (10) is got on basis of the Dirichlet structure [3]. Domain function $\omega(x,y)$ has expansion $\omega^j(x,y) = \sum\limits_{n,m} \omega_{nm}^j \varphi_{jn}(x)\varphi_{jm}(y)$, $(n,m) \in G_\Omega^j$ on the chosen wavelet-basis with the resolution j. At $v = u_j$ the linear homogeneous system of the algebraic equations concerning coefficients c_{pq}^j but containing an unknown number α is obtained. This system has the non-trivial solution relatively c_{pq}^j under condition if $\det(\mathbf{A} - \alpha\mathbf{B}) = 0$ where $\mathbf{A}$, $\mathbf{B}$ are symmetric matrixes with elements

$$\begin{aligned} a_{pq}^{kl} &= 2^{2j} \sum_{n,m}\sum_{r,s} \omega_{nm}^j \omega_{rs}^j \left\{ \Pi_{k-p,n-p,r-p} \Gamma^{0,0,0,0}_{l-q,m-q,s-q} + \Gamma^{0,0,0,0}_{k-p,n-p,r-p} \Pi_{l-q,m-q,s-q} \right\}, \\ b_{pq}^{kl} &= \sum_{n,m} w_{nm}^j \Gamma^{0,0,0}_{k-p,n-p} \Gamma^{0,0,0}_{l-q,m-q}, (p,q),(k,l) \in G_\Omega^j. \end{aligned} \tag{11}$$

Here, Π is CC and is represented as $\Pi_{a,b,c} = -(2\Gamma^{0,1,0,1}_{a,b,c} + \Gamma^{0,0,0,2}_{a,b,c} + \Gamma^{0,2,0,0}_{a,b,c})$ and w^j_{nm} are expansion coefficients of $w(x,y) = \omega^2(x,y)$. Each number $\alpha^{(N)}_i$, $i = 1, \ldots, N$, is an approximation to an exact eigenvalue α_i of the Equation (10) given above.

Let us determine the critical wavelengths λ_i of four-ridged rectangular waveguide (Figure 1(a)) for the following parameters of section: $a/b = 1$, $c/a = h/b = 0.2$, $g/a = d/b = 0.6$. According to [1, 3] the R-operations for construction of the domain function $\omega(x,y)$ are used (Figure 2(b)).

$$\omega = \omega_1 \wedge (\omega_2 \wedge \omega_3), \quad \omega_1 = (x^2 - c^2) \vee (d^2 - y^2), \quad \omega_2 = (a^2 - x^2) \wedge (b^2 - x^2), \quad \omega_3 = (g^2 - x^2) \vee (y^2 - h^2). \quad (12)$$

The result of the first critical wavelength λ_1 computations and ratio error calculations of the corresponding eigenfunction (Figure 1(c)) in accordance to the results of FEM $\varepsilon = \|u_{FEM} - u_j\|_{L_2(\Omega)} / \|u_{FEM}\|_{L_2(\Omega)}$ for various wavelets is represented in Table 1.

The given data prove the efficiency of the developed algorithm. The best results are received on basis of Kravchenko $\{\widetilde{\text{fup}_2}(\omega)\}$ wavelet [4].

Table 1: The first critical wavelength λ_1 and error calculation of the eigenfunction.

	Daubechies 4	Coifman 4	Kravchenko $\{\widetilde{\text{up}}(\omega)\}$	Kravchenko $\left\{\widetilde{\text{fup}_2}(\omega)\right\}$	FEM, $N = 3472$
λ_1	2.2008	2.1916	2.1929	2.1907	2.1888
ε	$5.9 \cdot 10^{-2}$	$3.2 \cdot 10^{-2}$	$4.2 \cdot 10^{-2}$	$1.8 \cdot 10^{-2}$	-

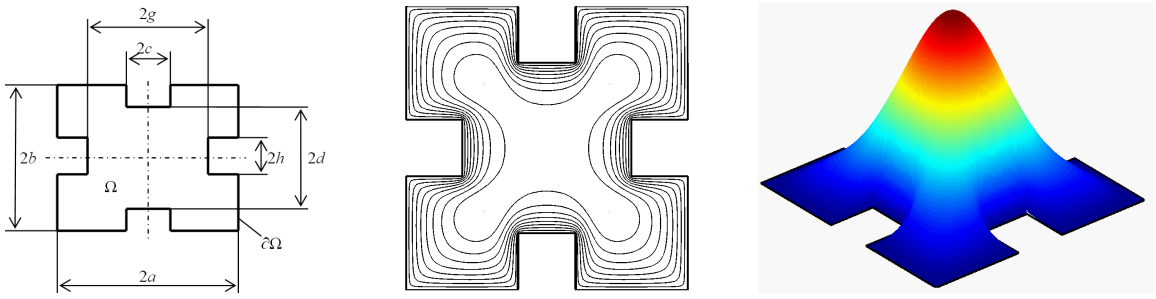

(a) (b) (c)

Figure 1: (a) Cross-section of WCS; (b) equiscalar line of $\omega(x,y)$; (c) E_{11}-wave of WCS.

6. CONCLUSION

The new method based on R-functions theory and wavelets with the application of Galerkin variational principle is proposed and proved. The main peculiarity of such approach is the construction of the flexible computing algorithm based on wavelet-approximation of analytical and geometrical components of a boundary value problem. The proposed method allows to use the parallel circuit of algorithm realization.

ACKNOWLEDGMENT

The investigations were supported by grant NSh-5708.2008.9 "The new methods in some problems of acoustooptics, radio physics and medicine on the basis of atomic functions, wavelets and fractals".

REFERENCES

1. Kravchenko, V. F. and V. L. Rvachov, *Boolean Algebra, Atomic Function and Wavelet in Physical Applications*, Fizmatlit, Moscow, 2006 (in Russian).
2. Resnikoff, H. L. and R. O. Wells, *Wavelet Analysis: The Scalable Structure of Information*, Springer, New York, 1998.
3. Kravchenko, V. F. and M. A. Basarab, *Boolean Algebra and Approximation Methods in Electrodynamics Boundary Value Problem*, Fizmatlit, Moscow, 2004 (in Russian).
4. Kravchenko, V. F. and A. V. Yurin, "Application of the R-functions theory and wavelets to the solution of elliptic type boundary value problems," *Electromagnetic Waves and Electronic Systems*, Vol. 14, No. 3, 4–39, 2009 (in Russian).

5. Kravchenko, V. F., O. S. Labun'ko, A. M. Lerer, and G. P. Sinyavsky, *Computing Methods in the Modern Radio Physics*, Edited by V. F. Kravchenko, Fizmatlit, Moscow, 2009 (in Russian).

Full Wave Hybrid Technique for CAD of Passive Waveguide Components with Complex Cross Section

M. B. Manuilov[1], **K. V. Kobrin**[1], **G. P. Sinyavsky**[1], **and O. S. Labunko**[2]

[1]Southern Federal University, Russia
[2]FGUP "Radiochastotny Centr YUFO", Russia

Abstract— A hybrid Galerkin Method/Mode Matching Technique/Generalized Scattering Matrix Method for CAD of waffle-iron filters, ridged and finned waveguide components is presented. The combined method is verified by available measurements as well as theoretical and experimental data of references. A number of low-pass waffle-iron filters have been designed for multi-band feeders of reflector antennas operating in S, C, X, Ku bands. New modifications of quasi-planar band-pass filters with improved performance have been designed for millimeter-wave communication applications.

1. INTRODUCTION

The passive components based on waveguides with complex cross section are widely used in many microwave and millimeter-wave applications. For example, waffle-iron filters are employed in both high-power and low-power applications as low-pass filters [1]. They were originally designed for high-power systems where it was desirable to suppress the harmonic frequencies generated by the transmitter. The general view of a typical waffle-iron filter section with rectangular teeth is schematically depicted in Fig. 1(a). In fact, this structure consists of cascaded multi-ridged waveguide subsections, which are coupled by rectangular waveguide subsections.

The main advantages of waffle-iron filters are both extended stop-band and pass-band and low insertion loss over a pass-band. Besides, waffle-iron filters attenuate all propagating waveguide modes whose frequency lies in the stop-band of filter. From this viewpoint the waffle-iron filters are very appropriate candidates for some satellite communication applications. For example, in reflector antennas of earth stations operating in S, C, X, Ku frequency bands multi-band feeders are used. Typically, diplexers included into multi-band waveguide feeder are implemented on the base of low-pass waffle-iron filters [2].

Ridged and all-metal finned waveguide structures find extensive applications in microwave and millimeter-wave filters, diplexers/multiplexers, transformers, polarizers etc. [3, 4]. In particular, evanescent-mode ridge waveguide filters (Fig. 1(b)) have well-known favorable electrical performances such as low insertion loss, wide stop-band and compact size. The finned version of the ridged waveguide components enables low-cost and easy-to-fabricate E-plane integrated circuits

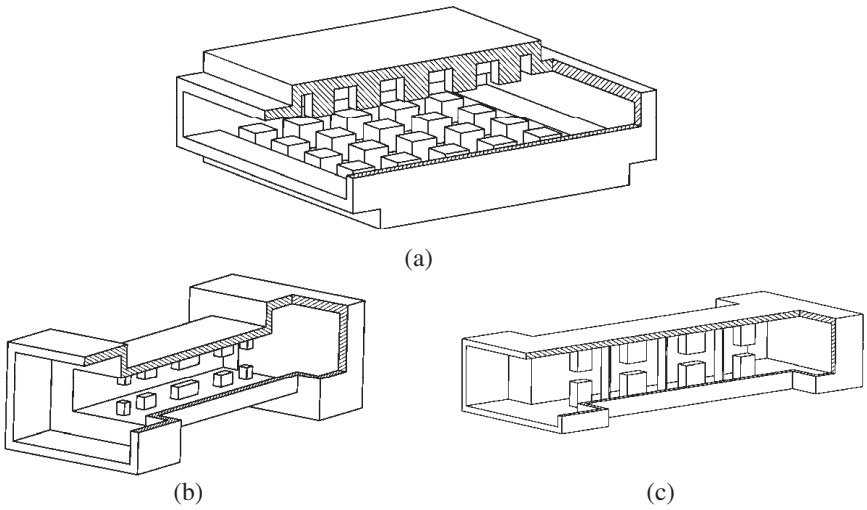

Figure 1: Waveguide filters: (a) waffle-iron filter, (b) quasi-planar ridged waveguide filter, (c) modified quasi-planar ridged waveguide filter with E-plane strips.

designs. On the other hand, there is a great potential of flexibility in ridge configuration according to different electrical and mechanical requirements.

Recently, electromagnetic CAD of waffle-iron filters, ridged and finned waveguide components is a point of a growing interest. Due to complexity of the problem the most advanced full wave CAD tools for waveguide components with complicated cross section are based on hybrid methods [5]. Undoubtedly, hybrid methods assure very high numerical efficiency, since they retain specific advantages of different EM methods and largely avoid their disadvantages. This paper presents a full wave approach to CAD of waffle-iron filters and ridge waveguide components including their analysis and numerical optimization.

2. THEORY

A fast and accurate EM analysis of waffle-iron filters and ridge waveguide filters (Fig. 1) is based on Galerkin Method/Mode Matching Technique/Generalized Scattering Matrix Method. Galerkin technique with taking into account field asymptotic at the edges was reported in [6, 7]. It is assumed that a waveguide structure under consideration (Fig. 1) consists of an arbitrary number of multi-ridged waveguide sections and stepped transitions connecting the filter with input and output waveguides. The solution is subdivided into the following steps: (i) decomposition of filter into elementary basic blocks, (ii) solving eigenvalue problems for multi-ridged waveguide sections, (iii) solving key scattering problems for basic discontinuities, (iv) direct combination of all S-matrices and evaluation of total S-matrix of filter.

Three discontinuities are considered as basic blocks of the structure: junction between rectangular and multi-ridged waveguide of the same size, double-plane step junction between two rectangular waveguides and waveguide bifurcation. The scattering problems for basic discontinuities are solved in terms of H- and E-modes. Therefore, two independent eigenvalue problems for both H- and E-modes of multi-ridged waveguide have been considered. For each of these modes, cut-off frequencies and field distributions are found.

The eigenvalue problem formulation for generalized multi-ridged waveguide is shown in Fig. 2. These problems for both H- and E-modes are reduced to the system of integral equations of the first kind for unknown electric field components on the common interfaces of regular regions in Fig. 2(a), ($z = t_i$, $i = 1, 2, \ldots, M-1$). For the solution of the integral equation system the Galerkin method is utilized. A key point of this approach is a special choice of basis functions [6, 7]. The unknown tangential electric field components on the common interfaces are expanded into series of Gegenbauer or Chebyshev polynomials with weight factor taking into account field asymptotic at the edges. Such a choice of basic functions accelerates the convergence of the method. The algebraization of the problems in accordance with Galerkin technique yields the final uniform system of linear algebraic equations. The cutoff frequencies of H- and E-modes are calculated as the zeros of the determinant of the matrix operator. Typically, it is enough to take into account 2 or 3 basis functions for convergence of the numerical solution.

We used Mode Matching Technique for analysis of junction between rectangular and multi-ridged waveguide and both Mode Matching Technique and Galerkin method for analysis of step waveguide junction and waveguide bifurcation. Eigenfunctions of multi-ridged waveguide were written in accordance with transverse resonance method [3]. Since Mode Matching Technique is well established method for waveguide problems, let's focus attention on the implementation of Galerkin technique.

The electromagnetic fields in rectangular waveguides are written as modal expansions in terms of H- and E-modes. Using orthogonality of waveguide modes we represent unknown amplitudes of scattered modes in terms of unknown tangential electric field on the aperture of the discontinuity.

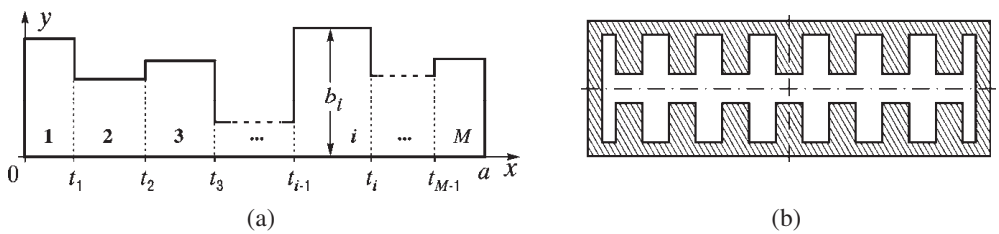

Figure 2: Eigenvalue problem formulation: (a) cross section of generalized multi-ridged waveguide; (b) cross section of waffle-iron filter.

Enforcing the continuity of the tangential magnetic field on the aperture and substituting relations for amplitudes of scattered waves into corresponding equations yield integro-differential equations for tangential electric field on the aperture.

For the algebraization of the integro-differential equations we used Gegenbauer or Chebyshev polynomials as basis functions. The weight factors of polynomials take into account field asymptotic at the edges in an explicit form. It leads to an extremely fast convergence of solution. In most cases, it is necessary to account only for 3 or 4 basis functions for each coordinate. As a result, the problems are reduced to the final systems of linear algebraic equation of minimal order. After solving these final systems the generalized scattering matrices of the corresponding discontinuities are calculated. The modal S-matrix of the filter is computed on the base of efficient combination procedure using only one matrix inversion.

3. RESULTS

For verification of the presented theory the obtained results have been compared with experimental and theoretical data of some references for waffle-iron filters [1] and quasi-planar ridged waveguide filters [3]. In all cases a good agreement is observed.

A number of waffle-iron filters for multi-band feeders of reflector antennas operating in S, C, X, Ku bands have been designed. The typical design specifications for low-pass waffle-iron filters are formulated as follows. The filter should have a pass-band and one or two separate stop-bands. One of the main requirements is a low insertion loss within the pass-band. So VSWR of the filter has to be minimized (VSWR < 1.05). Attenuation within stop-band should be usually greater than 30 dB.

In accordance with the analysis results, the initial dimensions of the filter are chosen to meet approximately pass-band and stop-band design specifications. The initial structures are taken consisting of identical equidistant multi-ridged subsections. The optimization is based on direct search method. The vector of arguments of the goal function includes longitudinal and transversal dimensions of the filter.

The design example of waffle-iron filter is plotted in Fig. 3. The blank rectangle corresponds to specified pass-band of the filter and the shaded rectangles show the stop-bands with required insertion loss. Calculated return loss within pass-band is about 40 dB and VSWR < 1.02. The total stop-band width by 30 dB value of attenuation is about 9.5 . . . 15.5 GHz. The filter in Fig. 3 was implemented as the cascade of four 5-ridge sections and its total length is about 35 mm.

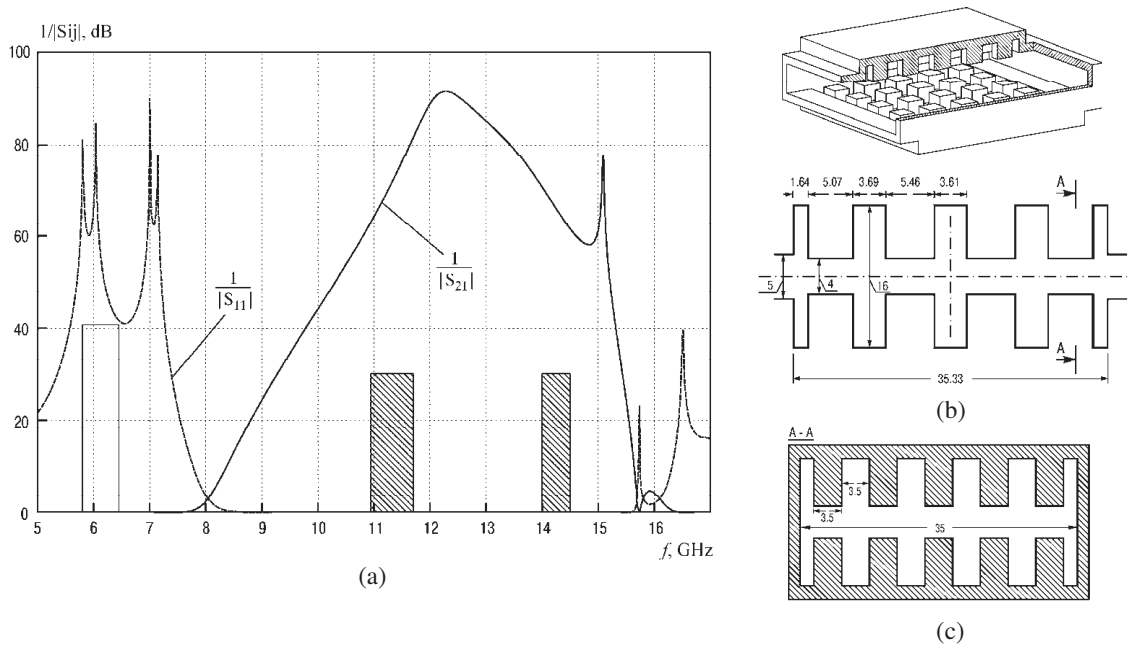

Figure 3: Frequency response (a) and configuration of longitudinal (b) and transversal (c) cross section of waffle-iron filter with 4 multi-ridged subsections (input waveguide 35×5 mm).

The modified evanescent-mode ridge waveguide filter (Fig. 1(c)) proposed in [4] has enlarged

height of the below-cut-off waveguide section. Moreover, additional inductive strips have been introduced between the ridged sections. This filter modification has more compact total size, wide spurious-free response and reduced ohmic loss. Fig. 4 shows frequency response of Ka-band four-resonator filter operating within pass-band 29–29.5 GHz. Return loss of the filter is better than 20 dB, upper stop-band limit is 48 GHz by $1/|S_{21}| = 50$ dB and the total length is approximately 22 mm.

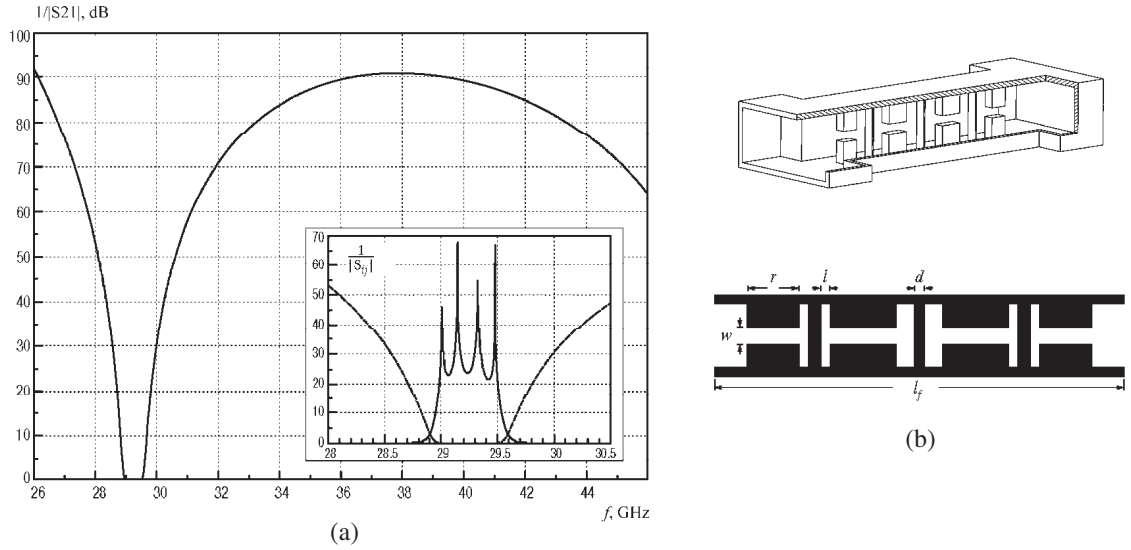

Figure 4: Frequency response (a) and configuration of Ka-band quasi-planar four-resonator waveguide filter (b). Dimensions in mm: input waveguide 7.2×3.4, evanescent waveguide 4.0×3.4, insert thickness 0.2, $r_i = 2.881$, 3.639; $d_i = 0.716$, 0.571; $l_i = 1.776$, 0.462, 0.968; $w = 0.88$; $l_f = 22.379$.

4. CONCLUSION

A hybrid full wave method for analysis and design of a wide class of ridged and finned waveguide components and waffle-iron filters is presented. The solution is based on Galerkin Method/Mode Matching Technique/Generalized Scattering Matrix Method. By implementation of Galerkin method for solving eigenvalue problems and key scattering problems the weighted Gegenbauer and Chebyshev polynomials were used as basis functions taking into account the field asymptotic at the edges. It leads to dramatically fast convergence and high accuracy of the solution. The obtained results are in good correspondece with available experimental and theoretical data of references.

A number of waffle-iron filters for multi-band feeders of reflector antennas operating in S, C, X, Ku bands has been designed. The potential of the new quasi-planar waveguide filter configuration has been studied. This filter configuration has improved pass-band selectivity and extended stop-band in comparison with the conventional ridge waveguide filters. Some modified quasi-planar pass-band filters with improved performance have been designed for Ka-band.

REFERENCES

1. Matthaei, G. L., L. Young, and E. M. T. Jones, *Microwave Filters, Impedance-Matching Networks, and Coupling Structures*, McGraw-Hill Book Co., New York, 1964.
2. Iida, M., R. Nuzuya, and A. Abe, "13 meter C/Ku dual frequency band earth station antenna," *NEC Res. & Develop.*, 98–112, 1990.
3. Bornemann, J. and F. Arndt, "Transverse resonance, standing wave, and resonator formulations of the ridge waveguide eigenvalue problem and its application to the design of E-plane finned waveguide filters," *IEEE Trans. Microwave Theory Tech.*, Vol. MTT-38, No. 8, 1104–1113, 1990.
4. Kirilenko, A., L. Rud, V. Tkachenko, and D. Kulic, "Evanescent-mode ridged waveguide bandpass filters with improved performance," *IEEE Trans. Microwave Theory Tech.*, Vol. MTT-50, No. 5, 1324–1328, 2002.
5. Arndt, F., J. Brandt, V. Catina, J. Ritter, I. Rullhusen, J. Dauelsberg, U. Hilgefort, and W. Wessel, "Fast CAD and optimization of waveguide components and aperture antennas by

hybrid MM/FE/MoM/FD Methods — state-of-the-art and recent advances," *IEEE Trans. Microwave Theory Tech.*, Vol. MTT-52, No. 1, 292–305, 2004.

6. Zargano, G., V. P. Lyapin, V. S. Mikhalevsky, Y. M. Sinelnikov, G. P. Sinyavsky, and I. M. Chekrygina, *Waveguides with Complicated Cross Sections*, Radio i Svyaz, Moscow, Russian, 1986.
7. Lyapin, V. P., M. B. Manuilov, and G. P. Sinyavsky, "Quasi-analytical method for analysis of multisection waveguide structures with step discontinuities," *Radio Science*, Vol. 31, No. 6, 1761–1772, 1996.

Diffraction of the Electromagnetic Pulses on Apertures in the Screen

E. V. Golovacheva, **A. M. Lerer**, **V. A. Lerer**,
P. V. Makhno, **and O. S. Labunko**
Southern Federal University, Rostov-on-Don, Russia

Abstract— Diffraction of the H- and E-polarized electromagnetic pulses (EMP) on infinitely long slit in perfectly conducting screen located on a boundary between two dielectric layers. This problem is of great importance because the diffraction on the slit is the classical problem in the theory of diffraction; and methods, applied to solve this problem, were also applied in the present work to solve the more complicated problem — diffraction of electro-magnetic pulse on the system of square apertures. Space-time integral equations (IEs) were obtained; methods of solving them, which consider the singularity at the edge and the logarithmic singularity of IE's kernel, were developed; the expression of the far field was obtained. The space-time integro-differential equation with logarithmic singularity of distribution of the magnetic field on the system of N narrow square holes in the screen was obtained and solved. The regularization of the equation was performed by isolation of analytically transformed static singular part. Transformed IEs we solved: by space coordinate using the collocation method, by time coordinate - using the method of step-by-step marching with spline-approximated time dependence.

1. INTRODUCTION

Picosecond electromagnetic pulses (EMP) have a wide range of applications in radiolocation and measurement equipment. Therefore equally with the problems of diffraction in frequency domain, solving problems of diffraction and excitation in time domain is of significant interest, and it can also be applied to increase the efficiency of calculation techniques in time domain. Calculation in the time domain followed by applying of Fourier transformation decreases several times the amount of time needed to calculate frequency characteristics. Another interesting and useful feature of such approach mentioned in [1]. It's well-known [2], that numerical solving of integral equation (IE) leads to so-called "mathematical" resonances on frequency dependencies, which are provided by numerical realization of solution. These resonance frequencies coincides with frequencies of inner oscillation of metallic body. Their appearance is the result of unavoidable inaccuracies in numerical solving of IE. Solving in the time domain allows to avoid this effect.

Traditional approach to solving the problem of EMP diffraction is based on solving this problem for monochromatic electromagnetic wave and further application of Fourier inversion. This approach was used, particularly, in [3, 4] to investigate the diffraction of EMP on objects, located in multilayer and inhomogeneous medias. Such way of solving is efficient for long EMPs, however, for picoseconds pulses there are some difficulties, conditioned by rapid increase of number of calculations. Therefore, though significant mathematical complexity, solving of Maxwell equations for microwave structures directly in time domain is challenging.

Let's consider the diffraction of EMP on the slits in perfectly conducting screen, located at the plane $y = 0$. Slits are infinite in direction z, the coordinate of the center and half-width of ν-th slit are — $\bar{x}_\nu$, l_ν, correspondingly. The angle of incidence ψ is counted from the perpendicular anticlockwise, the observation angle θ is also from the normal, but clockwise.

2. DIFFRACTION OF H-POLARIZE EMP

For the slit, located in perfectly conducting screen, the IE is:

$$\frac{1}{2\pi}\sum_{\nu=1}^{N}\int_0^{\pi}\int_{-\infty}^{t-u_{\mu\nu}}\frac{\dot{j}_\nu(\varphi',\tau)\,d\tau}{\sqrt{(t-\tau)^2-u_{\mu\nu}^2}}d\varphi' = Z_0 A\left(t-\left(l_\mu\sin\psi\cos\varphi+\bar{x}_\mu\right)/c\right)/2,\ 0\le\varphi\le\pi,\ \mu=1,2,\ldots,N \qquad (1)$$

where $u_{\mu\nu}(\varphi,\varphi') = \left|l_\mu\cos\varphi+\bar{x}_\mu-l_\nu\cos\varphi'-\bar{x}_\nu\right|/c$, c — the speed of light in the vacuum, $j_\nu(\varphi) = J_\nu(l_\nu\cos\varphi)/(Z_0 c)$, function J is expressed through transverse component of electric field strength on the slit $E_\nu(x') = J_\nu(x')/\sqrt{l_\nu^2-x'^2}$, the dot over j means partial derivative by time, $A(t)$ — incident EMP.

To solve IE (1) we shall use the method, close to that one, suggested in [5]. At $\varphi' \to \varphi$ integrand in IE (1) has the logarithmic singularity. Let's perform identical transformations to isolate this singularity:

$$\frac{1}{2\pi}\sum_{\nu=1}^{N}\int_0^{\pi}\left[\int_{-\infty}^{t-u_{\mu\nu}}\frac{\dot{j}_\nu(\varphi',\tau)\,d\tau}{\sqrt{(t-\tau)^2-u_{\mu\nu}^2}}+\delta_{\mu\nu}\dot{j}_\nu(\varphi,t)\ln\left(2\left|\cos\varphi-\cos\varphi'\right|\right)\right]d\varphi'+\dot{j}_\mu(\varphi,t)\,I$$
$$=\ A\left(t-(l_\mu\sin\psi\cos\varphi+\bar{x}_\mu)/c\right)/2,\quad 0\le\varphi\le\pi,\quad \mu=1,2,\ldots,N \tag{2}$$

where $\delta_{\mu\nu}$ — Kronecker symbol, $I=-\frac{1}{2\pi}\int_0^{\pi}\ln\left(2\left|\cos\varphi-\cos\varphi'\right|\right)d\varphi'=0$. Thus the singularity of operand in IE (1) at $\varphi'\to\varphi$ is terminated. Now we can use the collocation method to solve IE (2). Integration by φ' is substituted by square quadrature, which is the quadrature of highest accuracy for polynomials in trigonometric functions $\int_0^{\pi} f(\varphi)d\varphi \approx h\sum_{n=1}^{N_1} f(\varphi_n)$, $\varphi_n=(n-0.5)\,h$, $h=\pi/N_1$ and IE is satisfied in quadrature nodes φ_m. As a result we obtain the system of N IEs in unknown functions $\dot{j}_\nu(\varphi,t)$. These IEs are also solved by collocation method. To do that we shall satisfy them in grid nodes by variable $t=t_p$, $p=1,2,\ldots,P$. Values t_0, t_P are chosen to be such, that diffracted pulse at $t<t_0$ will be negligibly small, and at $t>t_P$ the process will sustain. While calculating the integral in τ we shall use the approximation by splines of s-th order $\sigma_q^{(s)}(t)$, and ${j_{np}}^{\nu}=h\dot{j}_\nu(\varphi_n,t_p)$ — are unknown coefficient: $h\dot{j}_\nu(\varphi_n,t)=\sum_{q=1}^{P} j_{nq}^{\nu}\sigma_q^{(s)}(t)$ at $\tau\in[t_0,t_p]$.

Then we obtain the system of P linear algebraic equations (SLAE) of n-th order for μ-th slit. Solving this SLAE we obtain unknown values for each slit.

Let's determine the far field. The diffracted pulse is determined by following expression:

$$H(x,y,t)=\frac{1}{2\pi}\sum_{\nu=1}^{N}\int_0^{\pi}\int_{-\infty}^{t-u_\nu}\frac{\dot{j}_\nu(\varphi',\tau)\,d\tau}{\sqrt{(t-\tau)^2-u_\nu^2}}d\varphi', \tag{3}$$

where $u_\nu=r_\nu/c$, $r_\nu=\sqrt{(x-l_\nu\cos\varphi'-\bar{x}_\nu)^2+y^2}$. Let's take into account, that At the point $x=R\sin\theta$, $y=R\cos\theta$ at the far field we can put $r_\nu\approx R-(l_\nu\cos\varphi'+\bar{x}_\nu)\sin\theta$. Let's introduce the time $\bar{t}=t-R/c$. Let's substitute $\chi_\nu=(l_\nu\cos\varphi'+\bar{x}_\nu)\sin\theta/c$. Let's transform the expression (3) at $R/c\gg T$ (T — the length of the pulse):

$$H(R,\theta,t)\approx\frac{1}{2\pi\,(2R/c)^{1/2}}\sum_{\nu=1}^{N}\int_0^{\pi}\int_{-\infty}^{\bar{t}+\chi_\nu}\frac{\dot{j}_\nu(\varphi',\tau)\,d\tau}{\sqrt{(\bar{t}+\chi_\nu-\tau)}}d\tau'. \tag{4}$$

Thus, assigned boundary problem is solved: the IE in space-time representation is obtained; the method of it's solving is developed; the expression for the far field is obtained.

3. DIFFRACTION OF E-POLARIZED EMP

For simplicity let's consider one slit in the screen, located in a vacuum. In this case the integro-differential equation is reduced to solving the integral equation:

$$\frac{1}{2\pi}\int_0^{\pi}\int_{-\infty}^{t-u}\frac{\dot{j}(\phi',\tau)\,d\tau}{\sqrt{(t-\tau)^2-u^2}}d\phi' \ =\ C\left(t-\frac{l+l\cos\phi}{c}\right)+D\left(t-\frac{l-l\cos\phi}{c}\right)$$
$$+cA\left(t-l\sin\psi\cos\phi/c\right)/(2\cos\psi),\ \ 0\le\phi\le\pi, \tag{5}$$

where $C(t)$, $D(t)$ — unknown functions, $j(\phi,t)=(l\sin\phi)^2\,J(l\cos\phi,t)$, $E(x,t)=J(x,t)\sqrt{l^2-x^2}$, $E(x,t)$ — longitudinal component of electric field strength on the slit.

The solution of (5) is analogous to the solution of (1). After isolation of singular part of the kernel we obtain:

$$\frac{1}{2\pi}\int\limits_0^{\pi}\left[\int\limits_{-\infty}^{t-u}\frac{\dot{j}\left(\phi',\tau\right)d\tau}{\sqrt{(t-\tau)^2-u^2}}+\dot{j}\left(\phi,t\right)\ln\left|\cos\phi-\cos\phi'\right|\right]d\phi'+\dot{j}\left(\phi,t\right)I$$
$$=\ C\left(t-\frac{l+l\cos\phi}{c}\right)+D\left(t-\frac{l-l\cos\phi}{c}\right)+cA\left(t-l\sin\psi\cos\phi/c\right)/(2\cos\psi),\ 0\le\phi\le\pi. \quad (6)$$

Equation (6) differs from (2) only by functions $C\left(t-\frac{l+l\cos\phi}{c}\right)+D\left(t-\frac{l-l\cos\phi}{c}\right)$ in the right part. To approximate them we shall use splines $C(t)=\sum\limits_{q=1}^{p}C_q\sigma_q^{(1)}(t)$, $D(t)=\sum\limits_{q=1}^{p}D_q\sigma_q^{(1)}(t)$. Then we repeat the transformations, listed at solving of (2). The main difference is due to appearance of new unknown coefficients C_q, D_q. Therefore we shall satisfy (6) not only at quadrature nodes ϕ_m $(m=1,\ldots,N)$, but and on the endings of the slit $x=\pm l$ $(\phi=0,\pi)$. Then we obtain SLAE, which has in comparison to SLAE for E-polarized EMP additional terms in the right part and two additional equations.

4. NUMERICAL RESULTS

Let's consider incident EMP to be Gaussian unipolar $A(t)=\exp\left[-\left(t/T\right)^2\right]$. Let's introduce parameter $\chi=cT/l$, which is the ratio of the distance $c2T$, passed by EMP in the time of it's length $2\,T$, to the width of the slit $2l$. If $\chi\gg1$, the EMP is long, $\chi\approx1$ — short, $\chi\ll1$ — ultrashort. To validate the results the boundary problem is solved by two methods: in space-time domain and in frequency-space domain with consequent application of Fourier transformation. Results, obtained by two different methods, are completely coincide, proving the accuracy of developed methods, algorithms and software. At all figures $F\left(\theta\right)$ is the scattering pattern, normalized on it's maximum at $-\infty<t<\infty$. $\tau=\bar{t}/T$ — normalized time, the width of the slits $2l=4\,\text{mm}$. The investigation of internal convergence shows, that for long and short EMPs the curves are indistinguishable. To calculate with the accuracy less than 1% of internal convergence $N=5$–10 at $\chi\ge1$ and $N=10$–30 at $\chi\ll1$ is quite enough. The time of calculation of one curve is less than a second on a modern PC (Core 2 or analogous).

At changing the distance between slits at different angles of incidence we can see that decrease of the distance between slits the distance between maximums decreases, except the case of normal incidence and angle of observation.

Parameters of dielectric, as we can see from Fig. 2, influence in the same way on the shape of EMP: at oblique incidence and $\varepsilon_1>\varepsilon_2$ the distance between maximums increases, because of the decrease of the speed of wave's propagation in the dielectric.

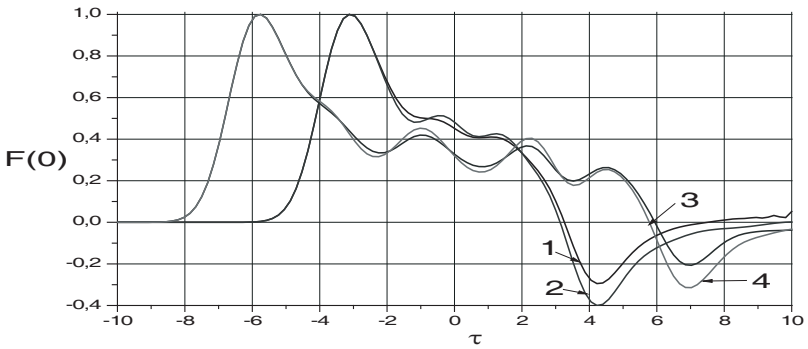

Figure 1: Diffraction of H-polarized EMP on two slits with the distance between them 4 mm, located at the boundary. $\psi=30^0$, $\theta=0$. $\chi=0.3$. Curve 1 — $\varepsilon_1=1$, $\varepsilon_2=1$, 2 — $\varepsilon_1=1$, $\varepsilon_2=3$, 3 — $\varepsilon_1=3$, $\varepsilon_2=1$, 4 — $\varepsilon_1=3$, $\varepsilon_2=2$.

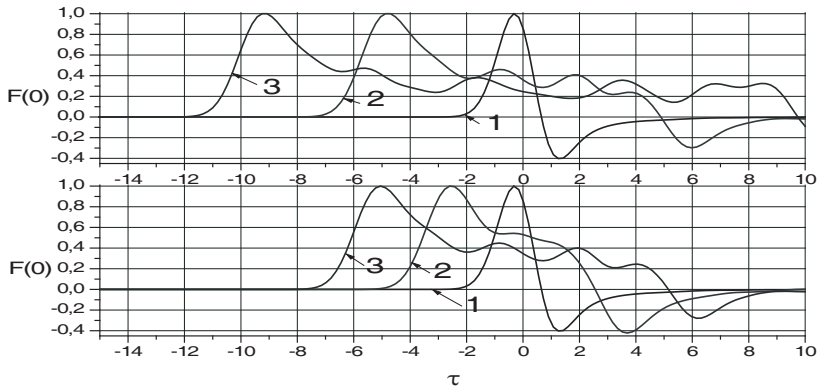

Figure 2: Change of the shape of H-polarized EMP at different dielectric parameters. The observation angle is $\theta = 0$, distance between slits is 4 mm. $\chi = 0.3$. ???? (a) $\varepsilon_1 = 1$, $\varepsilon_2 = 3$, (b) $\varepsilon_1 = 3$, $\varepsilon_2 = 1$. Curves1–3 corresponds to $\psi : 0; 25°; 50°$.

5. CONCLUSIONS

Boundary problems of diffraction of EMP on N-slits and apertures in the perfectly conducting screen are reduced to Space-Time (ST) IE of the 1-st kind with logarithmic singularity of the kernel.

Isolation and analytical transformation of the singular part of ST IE and further application of collocation method reduces the solution of space-time IEs to solving of the system of linear algebraic equations, the order of which is usually not exceeds 20.In approximation of solution by time we can use splines, or Lagrange-polynomials, however, splines lead to simpler systems. Numerical calculations of one and two slits shown, that at normal angle of incidence and at angle of observation $\theta = 0$ the shape of the EMP is almost independent on dielectric constant of layers. At oblique incidence EMPs expands. Especially it's noticeable at $\varepsilon_1 > \varepsilon_2$ and angle of incidence, larger than critical.

The comparison of time of calculation of pulse characteristics using ST IEs an frequency-space IEs with consequent translation to time domain was performed. It shown significant advantage of ST IEs, especially for ultrashort pulses and multi-slit systems.

REFERENCES

1. Lerer, A. M., "Radiofizika I elektronika," *RE*, Vol. 51, No. 7, 843–846, 2006.
2. Mitra, P., *Numerical Methods in Electrodynamics*, Mir, Moscow, 1977.
3. Vitebskiy, S., *IEEE Trans. V. AP*, Vol. 44. No. 2. 143–151, Feb. 1996.
4. Yarmahov, I. G., "Radiofizika I elektronika," *RE*, Vol. 49, No. 4, 411–420, 2004.
5. Lerer, A. M., "Radiofizika I elektronika," *RE*, Vol. 46, No. 3, 313–319, 2001.

Mathematical Model of the Phased Open Ended Waveguides Array Antenna with Multilayered Grids from Cylindrical Conductors before the Aperture

Andrey A. Prilutskiy
Scientific Research Institute of Long Distance Radio Communication, Russia

Abstract— The decision of an electrodynamics problem of radiation of waves from infinite periodic array antenna, generated of the open ends of flat wave guides in case of TE-waves with multilayer grids from cylindrical conductors before the aperture is offered. The problem is reduced to system of the integral equations which dares concerning unknown fields in the aperture of wave guides and currents on conductors. In a wideband of frequencies, the numerical analysis of influence of multilayer grids parameters on electrodynamics characteristics of phased array antenna carried out at scanning.

1. INTRODUCTION

It is known, that owing to an mutual coupling between elements of array antenna from the open ends of waveguides at beam steering, there is a mismatch of entrance resistance of the aperture to a power supply circuit, that at the big corners of a deviation to lead to considerable falling of strengthening of array antenna [1]. Radius this effect it can is possible introduction of elements which provide compensation of change of entrance resistance of the aperture at scanning [2–4]. The simple jack is sub array from the passive cylindrical wires, established before the aperture array antenna [3, 4]. In the given work, the electrodynamics analysis of radiation of the TE-waves from an infinite periodic array of flat wave guides is resulted, before aperture which the multilayered grid of cylindrical wires in parallel the E-plane of waveguides is established. The step sub array from wires coincides with period wave guides array. The multilayer grid of wires can structurally settle down in dielectric layers, forming the artificial medium. The geometry of one period PAR is shown on Fig. 1.

Wave guides are in regular intervals raised by waves of type H_{10} with progressive attack of a phase. Under the influence of the waves falling on having opened a lattice, the waveguides aperture are raised and radiate electromagnetic waves as back in wave guides, and in free space, raising passive wires. The electromagnetic field in free space is defined by electric field $e(y)$ to the aperture

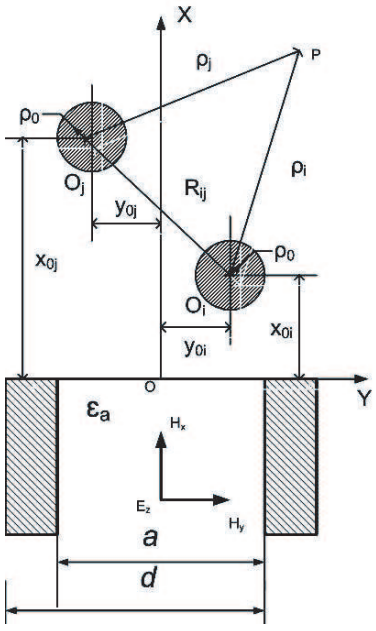

Figure 1.

of a wave guide and electric currents I_{0i} on cylindrical conductors. The system of the equations for field definition in the aperture of wave guide $e(y)$ and amplitudes of currents I_{0i} turns out from boundary conditions for tangential a component of full electric field on wires:

$$E_z^{(e)} + \sum_i E_z^{(i)} = 0\big|_{\rho=\rho_0}^{x=h_i}; \tag{1}$$

And conditions of continuity tangential a component of a full magnetic field in aperture wave guides:

$$H_y^{(i)} - H_y^{(e)} - \sum_i H_y^{(i)} = 0|x = 0. \tag{2}$$

Field in wave guides we will present in the form of decomposition abreast on system of own functions of wave guide $\{f_m(y)\}$, and decomposition factors we will express through a field in the aperture of a wave guide from ΓY $E_z^{(i)} = e(y)$:

$$\begin{cases} H_y^{(i)} = -\dfrac{2\gamma_1^{(i)}}{z_s} f_1(y) e^{-ik\gamma_m^{(i)} x} + \dfrac{1}{z_s} \displaystyle\sum_{m=1}^{\infty} \tilde{e}_m^{(i)} \gamma_m^{(i)} f_m(y) e^{ik\gamma_m^{(i)} x}; \\ E_z^{(i)} = f_1(y) e^{-ik\gamma_m^{(i)} x} + \Gamma_1 f_1(y) e^{ik\gamma_m^{(i)} x} + \displaystyle\sum_{m=2}^{\infty} \tilde{e}_m^{(i)} f_m(y) e^{ik\gamma_m^{(i)} x}; \\ \Gamma_1 = \tilde{e}_1^{(i)} - 1; \end{cases} \tag{3}$$

where:

$$f_m(y) = \sin\frac{m\pi}{a}\left(y + \frac{a}{2}\right),\ \gamma_m^{(i)} = \sqrt{\varepsilon - \left(\frac{m\lambda}{2a}\right)^2},\ J_m\left(\gamma_m^{(i)}\right) \le 0,\ \tilde{e}_m^{(i)} = \frac{2}{a}\left(e(y), f_m(y)\right),\ \Gamma_1$$

reflection coefficient of the basic mode H_{10}.

Field array of the open ends of flat wave guides in free space we will present in the form of decomposition abreast on spatial harmonics (to harmonics the Flocke):

$$\begin{cases} E_z^{(e)} = \displaystyle\sum_{m=-\infty}^{\infty} \tilde{e}_m^{(e)} \varphi_m(y) e^{-ik\alpha_m^{(e)} x}; \\ H_y^{(e)} = \dfrac{1}{z_0} \displaystyle\sum_{m=-\infty}^{\infty} \tilde{e}_m^{(e)} \alpha_m^{(e)} \varphi_m(y) e^{-ik\alpha_m^{(e)} x}; \end{cases} \tag{4}$$

where:

$$\varphi_m(y) = e^{-ikv_m y},\ v_m = \sin\theta + \frac{m\lambda}{d},\ J_m\left(\alpha_m^{(e)}\right) \le 0;\ \alpha_m^{(e)\,2} + v_m^2 = 1,\ \tilde{e}_m^{(e)} = \frac{1}{d}\left(e(y), \varphi_m(y)\right).$$

Electric field $E_z^{(i)}$ of currents of the sub array from the cylindrical wires raised by falling field array from the open ends of waveguides we will present in the form of superposition of own waves of cylindrical wires:

$$E_z^{(si)} = -\frac{I_{zi}}{4} k z_0 \sum_{m=-\infty}^{m=\infty} e^{-ikv_0 md} \sum_{n=-\infty}^{n=\infty} H_n^{(2)}\left(k\sqrt{(x-h_i)^2 + (md-y)^2}\right) e^{-in(\varphi - \psi_m)}$$

Using the theorem of addition for cylindrical functions and a condition, that the radius of conductors is small $\rho_0 \ll \lambda, d$, we will receive expression for field $E_z^{(si)}$:

$$E_z^{(si)} = -\frac{I_{zi}}{4} k z_0 \left\{ H_0^{(2)}(k\rho) + 2\sum_{m=1}^{\infty} H_0^{(2)}(kmd) J_0(k\rho) \cos kmv_0 d \right\} \tag{5}$$

Expression (5) describes a field of i-th of some cylindrical wires in the local system of co-ordinates combined with the central wire an index $m = 0$. For electric field representation sub array wires of

i-th number in coordinate system sub array j-th number we will take advantage of carrying over of polar system of coordinates and the theorem for cylindrical functions. The field sub array in coordinates local sub array j-th number will look like i-th number:

$$E_z^{(si,j)} = -\frac{I_{zi}}{4} k z_0 \left\{ H_0^{(2)}(kR_{ij}) J_0(k\rho_j) + 2\sum_{m=1}^{\infty} H_0^{(2)}(kmd) J_0(k\rho_j) J_0(kR_{ij}) \cos kmv_0 d \right\}. \quad (6)$$

Let's define an unknown field in the aperture of wave guide $e_z(y)$ and amplitudes of currents I_{zi} on the multilayered grids conductors within one period array. We will substitute components of an electromagnetic field (3)–(5) in boundary conditions (1), (2), preliminary having transformed a field of a array of the open ends of wave guides in local cylindrical system of coordinates for satisfaction boundary conditions (1) and having transformed a magnetic field of i-th sub array cylindrical wires in decarts system of coordinates of central wave guide array of wave guides. As a result we will receive system of the linear operational equations, the first equation of system is integral equation concerning an unknown field in the aperture and amplitudes of currents on wires. The system of the equations looks like:

$$\iint_{-\frac{a}{2}}^{\frac{a}{2}} e(y') \Big(K^{(i)}(y,y') + K^{(e)}(y,y') \Big) dy dy' + \sum_i \frac{I_{zi}}{2d} \sum_{m=-\infty}^{m=\infty} \varphi_m(y) e^{-ikv_m y_{oi}} e^{-ik\sqrt{1-v_m^2} h_i} = \frac{2\gamma_{10}^{(i)}}{z_s} f_0(y);$$

$$\sum_{m=-\infty}^{m=\infty} \tilde{e}_m^{(e)} J_0(kv_m\rho_0) J_0(k\alpha_m\rho_0) \alpha_m^{(e)} e^{-ikv_m y_{oi}} e^{-ik\alpha_m h_i}$$

$$-\frac{I_{zi}}{4} k z_0 \left\{ H_0^{(2)}(k\rho_0) + 2\sum_{m=1}^{\infty} H_0^{(2)}(kmd) J_0(k\rho_0) \cos kmv_0 d \right\}$$

$$+\sum_j -\frac{I_{zi}}{4} k z_0 \left\{ H_0^{(2)}(kR_{ij}) J_0(k\rho_0) + 2\sum_{m=1}^{\infty} H_0^{(2)}(kmd) J_0(k\rho_0) J_0(kR_{ij}) \cos kmv_0 d \right\} = 0;$$

where integral equation kernels:

$$K^{(i)}(y,y') = \frac{2}{z_s a} \sum_{m=1}^{\infty} \gamma_m^{(i)} e(y') f_m(y') f_m(y);$$

$$K^{(e)}(y,y') = \frac{1}{z_0 d} \sum_{m=-\infty}^{\infty} \alpha_m^{(e)} e(y') \varphi_m^*(y') \varphi_m(y).$$

The system of the operational equations dares moment method (MoM). At application of this method the problem decision is reduced to the decision of algebraically equations systems. Characteristics of radiation array-reflection coefficient on the basic mode of a wave, the pattern of array element are completely defined by electric field in aperture and currents on wires.

Let's result results of numerical research of influence of geometrical parameters of a double layers grid of conductors on characteristics open-ended waveguides array antenna at scanning for

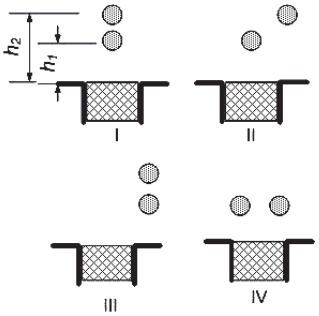

Figure 2.

four characteristic variants of placing of wires (Fig. 2). Geometry of array antenna: $a = 0.475\lambda$, $d = 0.5\lambda$, $\varepsilon_a = 2.0$.

On Figs. 3–6, characteristics of the coordination of an element of array antenna depending on height h_1 for four variants of placing of cylindrical wires before the aperture are resulted at $h_2 = 0.35\lambda$ for the phasing angles. The optimum coordination at radiation on a normal is reached for $h_1 = 0.32 - 0.35\lambda$ in all configurations. Thus, for the chosen geometry array the optimum coordination at radiation on a normal is reached, when two sub array from cylindrical wires take places almost at identical height, forming a grid with the doubled step.

On Fig. 7, curves of reflection coefficient are resulted at scanning by beam array for $\lambda = 1.0$ and $\lambda = 1.2$. The curve 1 on Fig. 7 corresponds array with the compensation grid of wires, a curve 2 — Waveguides array.

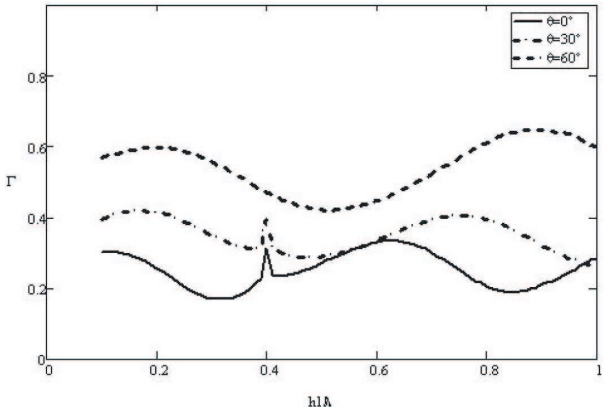

Figure 3. Reflection coefficient for Variant I.

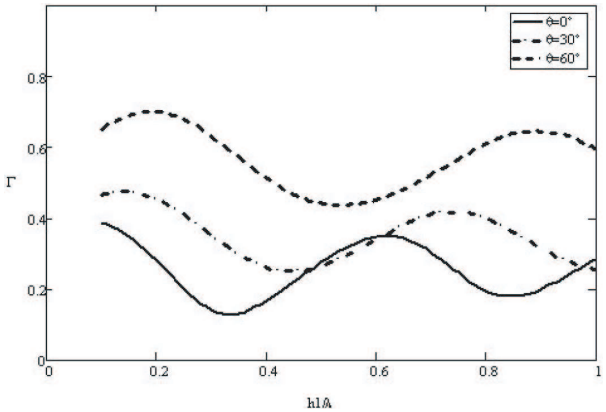

Figure 4. Reflection coefficient for Variant II.

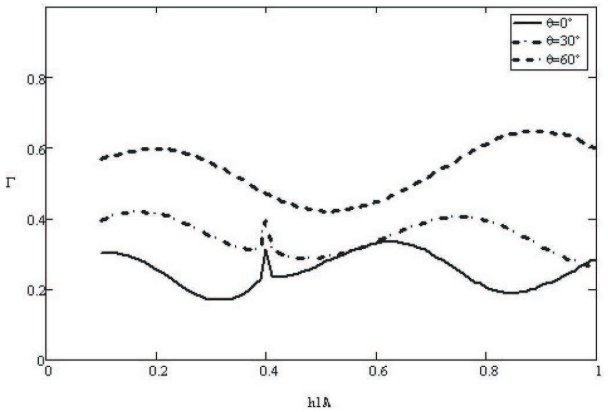

Figure 5. Reflection coefficient for Variant III.

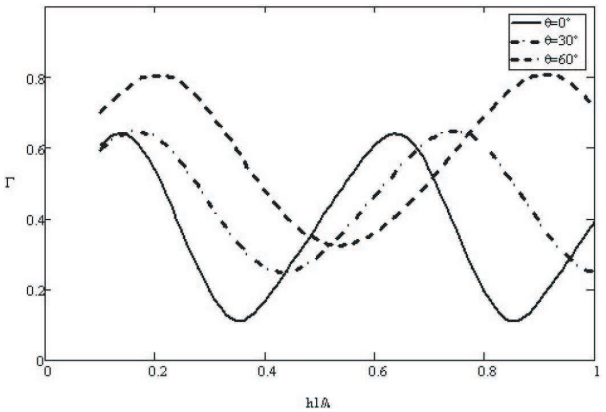

Figure 6. Reflection coefficient for Variant IV.

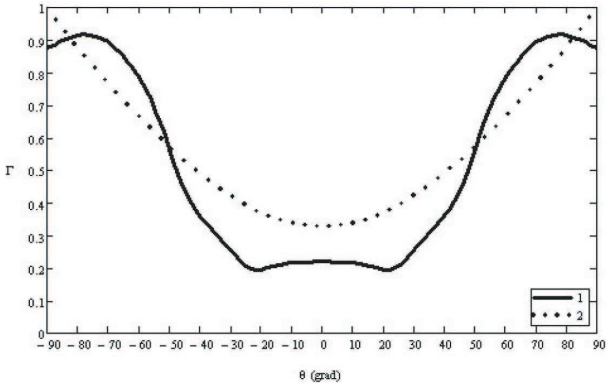

(a)

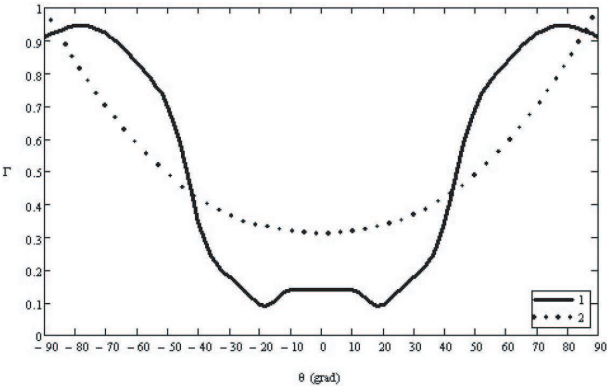

(b)

Figure 7. Reflection coefficient at scanning: $h_1 = 0.4\lambda$, $h_2 = 0.45\lambda$. (a) $\lambda = 1.0$, (b) $\lambda = 1.2$.

2. CONCLUSION

1. Use of the multilayer's grids established before aperture, expands possibilities of coordination array in sector of corners and a frequency band. The scanning sector $\pm 45^{\circ}$ and a frequency band of 32% is reached at a maximum level of reflection coefficient 0.4.
2. Expedient is to use spending grids as a part of Radom for giving of mechanical durability by it and as an element of fine tuning of parameters of Phased array antenna, at installation Radom in a near field of the aerial.

REFERENCES

1. Meyluks, R. J., *AP IEEE*, Vol. 70, No. 3, 5–62, 1978.
2. Skobelev, S. P., "Radiation from an array of plane waveguides with slot coupling elements," *Radiotekhnika i Elektronika*, Vol. 32, No. 5, 1117–1120, 1987.
3. Henderson, L. W., *IEEE AP-S Int. Symp. Dig.*, Vol. 1, No. 4, 3–6, June 8–13, 1986.
4. Evstropov, G. A. and A. A. Prilutskiy, *Radio Physics*, News of High Schools, No. 2, 34, 1989.

Phase Behaviour of a Two-Layered Circular Ferrite-Dielectric Waveguide with Azimuthal Magnetization

Georgi Nikolov Georgiev[1] **and Mariana Nikolova Georgieva-Grosse**[2]

[1]Faculty of Mathematics and Informatics, University of Veliko Tirnovo
"St. St. Cyril and Methodius", BG-5000 Veliko Tirnovo, Bulgaria
[2]Meterstrasse 4, D-70839 Gerlingen, Germany

Abstract— The phase behaviour of the circular waveguide with a dielectric cylinder and azimuthally magnetized ferrite toroid for normal TE_{0n} modes, is explored by complex confluent hypergeometric and real Bessel functions. For both directions of magnetization the waves are supported in restricted frequency bands. If the dielectric filling thickness varies, the differential phase shift provided changes sign.

1. INTRODUCTION

The ability to produce differential phase shift (to operate as nonreciprocal phase shifter), the existence of magnetically controlled cutoff, of a backward-wave region for frequencies, lower than the cutoff one and of envelope curves, restricting the areas of wave transmission in case of negative magnetization from the side of higher frequencies, are the main features of the circular waveguide, entirely filled with azimuthally magnetized ferrite that supports normal TE_{0n} modes [1–10]. The investigation of some multilayered ferrite-dielectric geometries has shown that they could provide an increased value of the differential phase shift [11–15]. Its computation and the study of the phase performance of these structures as a whole, however, turned out to be a difficult task [11–16].

Here, the phase characteristics of a two-layered configuration of the above type whose inner region contains dielectric and the outer one — ferrite, are examined, using results of the solution of propagation problem for normal TE_{0n} modes in this set-up [14, 15]. To simplify the study, the discussion is confined to the TE_{01} mode solely. It is assumed also that the relative permittivities of both media are equal, the relative size of the region, occupied by dielectric is small, compared to the one of the transmission line and the lower part of frequency band in which the wave could be sustained, is considered only.

2. FORMULATION OF THE PROBLEM

The propagation of normal TE_{0n} modes is explored in an infinitely long, perfectly conducting circular waveguide of radius r_0, comprising a coaxial dielectric cylinder of radius r_1. The structure's remainder is filled by a latching ferrite toroid, magnetized azimuthally to remanence with the help of an infinitely thin central wire. It is described by a Polder permeability tensor of off-diagonal element $\alpha = \gamma M_r/\omega$, γ — gyromagnetic ratio, M_r — ferrite remanent magnetization, ω — angular frequency of the wave and a scalar permittivity $\varepsilon = \varepsilon_0\varepsilon_r$. The dielectric has a scalar permittivity and permeability $\varepsilon^d = \varepsilon_0\varepsilon_d$ and $\mu^d = \mu_0\mu_d$, resp. It is accepted that $\varepsilon_r = \varepsilon_d$.

3. PHASE CHARACTERISTICS

The normalized phase characteristics $\bar{\beta}(\bar{r}_0)$ of the geometry, corresponding to normal TE_{01} mode, are plotted in Figs. 1(a), (b) and Figs. 2(a), (b) with solid and dashed lines for $\alpha_+ > 0$ and $\alpha_- < 0$, assuming the dielectric cylinder to waveguide radius ratio $\rho = 0.1, 0.2, 0.3$ and 0.4, resp. as parameter, ($\bar{\beta} = \beta/(\beta_0\sqrt{\varepsilon_r})$, $\bar{r}_0 = \beta_0 r_0\sqrt{\varepsilon_r}$, $\rho = \bar{r}_1/\bar{r}_0$, $\bar{r}_1 = \beta_0 r_1\sqrt{\varepsilon_r}$, $\beta_0 = \omega\sqrt{\varepsilon_0\mu_0}$, β — phase constant of the wave). They are reckoned, harnessing the procedure, developed for the ferrite case [2] with the values of roots $\eta^{(c)}_{k\pm,n}(\varepsilon_d, \varepsilon_r, \rho, \alpha_\pm)$ of the characteristic equation of the two-layered set-up, derived by real Bessel and complex confluent hypergeometric functions in which $c = 3$, $n = 1$ [14, 15, 17]. (The subscripts "+" and "−" relate to positive and negative magnetization.) The solid and dashed curves for the same $|\alpha|$ ($|\alpha| < 1$) form a pair. The characteristics for both signs of α, belonging to it which originate in the cutoff frequency points $\bar{r}_{0cr} = [\eta^{(c)}_{0,1}/2]/(1-\alpha^2)^{1/2}$ at the horizontal axis, end at the dotted En_{1+} — and En_{1-} — envelopes. (An exception makes the curve for $\alpha = 0$ solely which describes the dielectric case.) This is due to the appearance of the $L_\pm(c, \varepsilon_d, \varepsilon_r, \rho, \alpha_\pm, n)$ numbers, linked with the roots $\eta^{(c)}_{k_\pm,n}(\varepsilon_d, \varepsilon_r, \rho, \alpha_\pm)$ of characteristic

Table 1: Values of the $L_{\pm}(c, \varepsilon_d, \varepsilon_r, \rho, \alpha_{\pm}, n)$ numbers for $c = 3$, $n = 1$, $\rho = 0.4$, $\varepsilon_d = \varepsilon_r$ as a function of $|\alpha|$.

$\lvert\alpha\rvert$	0.01	0.02	0.03	0.04	0.05	0.06	0.07	0.08	0.09	0.10
L_-	7.34189	7.34099	7.33951	7.33742	7.33474	7.33146	7.32758	7.32311	7.31803	7.31234
L_+	4.72548	4.72468	4.72335	4.72150	4.71911	4.71618	4.71273	4.70874	4.70422	4.69916
$\lvert\alpha\rvert$	0.11	0.12	0.13	0.14	0.15	0.16	0.17	0.18	0.19	0.20
L_-	7.30605	7.29916	7.29165	7.28353	7.27479	7.26543	7.25545	7.24484	7.23360	7.22173
L_+	4.69356	4.68743	4.68075	4.67354	4.66578	4.65747	4.64862	4.63923	4.62928	4.61877
$\lvert\alpha\rvert$	0.21	0.22	0.23	0.24	0.25	0.26	0.27	0.28	0.29	0.30
L_-	7.20921	7.19605	7.18224	7.16778	7.15265	7.13686	7.12039	7.10324	7.08540	7.06687
L_+	4.60771	4.59609	4.58391	4.57117	4.55785	4.54397	4.52951	4.51447	4.49885	4.48264
$\lvert\alpha\rvert$	0.31	0.32	0.33	0.34	0.35	0.36	0.37	0.38	0.39	0.40
L_-	7.04763	7.02768	7.00701	6.98560	6.96346	6.94056	6.91691	6.89248	6.86726	6.84125
L_+	4.46584	4.44845	4.43045	4.41185	4.39265	4.37282	4.35237	4.33130	4.30959	4.28725
$\lvert\alpha\rvert$	0.41	0.42	0.43	0.44	0.45	0.46	0.47	0.48	0.49	0.50
L_-	6.81442	6.78677	6.75827	6.72892	6.69870	6.66759	6.63556	6.60261	6.56872	6.53385
L_+	4.26426	4.24061	4.21631	4.19133	4.16568	4.13935	4.11233	4.08460	4.05617	4.02701
$\lvert\alpha\rvert$	0.51	0.52	0.53	0.54	0.55	0.56	0.57	0.58	0.59	0.60
L_-	6.49798	6.46110	6.42318	6.38419	6.34410	6.30288	6.26049	6.21691	6.17210	6.12601
L_+	3.99712	3.96650	3.93512	3.90298	3.87006	3.83635	3.80184	3.76652	3.73037	3.69337
$\lvert\alpha\rvert$	0.61	0.62	0.63	0.64	0.65	0.66	0.67	0.68	0.69	0.70
L_-	6.07860	6.02984	5.97966	5.92802	5.87486	5.82013	5.76375	5.70565	5.64576	5.58399
L_+	3.65552	3.61678	3.57715	3.53661	3.49513	3.45271	3.40931	3.36491	3.31949	3.27302
$\lvert\alpha\rvert$	0.71	0.72	0.73	0.74	0.75	0.76	0.77	0.78	0.79	0.80
L_-	5.52026	5.45446	5.38648	5.31620	5.24350	5.16821	5.09019	5.00924	4.92516	4.83772
L_+	3.22549	3.17685	3.12709	3.07616	3.02403	2.97068	2.91605	2.86012	2.80283	2.74414
$\lvert\alpha\rvert$	0.81	0.82	0.83	0.84	0.85	0.86	0.87	0.88	0.89	0.90
L_-	4.74666	4.65167	4.55242	4.44850	4.33946	4.22475	4.10372	3.97559	3.83941	3.69400
L_+	2.68400	2.62235	2.55913	2.49428	2.42773	2.35939	2.28919	2.21702	2.14276	2.06628
$\lvert\alpha\rvert$	0.91	0.92	0.93	0.94	0.95	0.96	0.97	0.98	0.99	1.00
L_-	3.53788	3.36913	3.18519	2.98256	2.75615	2.49821	2.19567	1.82312	1.31540	
L_+	1.98743	1.90599	1.82170	1.73417	1.64279	1.54638	1.44224	1.32156	1.13173	

equation [14]. Some of their values are listed in Table 1. Thus, unlike the ferrite configuration [2–5], the propagation may take place in restricted frequency bands both for $\alpha_- < 0$ and $\alpha_+ > 0$.

In case of small ρ, e.g., $\rho = 0.1$ and 0.2, (cf. Figs. 1(a) and (b)), in the mass of pairs the characteristics for negative lie above those for positive magnetization. For the relevant normalized phase constants $\bar{\beta}_-$ and $\bar{\beta}_+$, corresponding to specific normalized guide radius $\bar{r}_0$ and $|\alpha|$, it holds $\bar{\beta}_- > \bar{\beta}_+$ and the structure provides positive differential phase shift $\Delta\bar{\beta} = \bar{\beta}_- - \bar{\beta}_+$. There are values of $\bar{r}_0$, however, at which the solid cross the dashed curves for the same $|\alpha|$, and for larger $\bar{r}_0$ the first are situated above the second ones. At the crossing points no differential phase shift is obtained and to the right of them (for higher frequencies) $\Delta\bar{\beta}$ becomes negative. For large $|\alpha|$ the characteristics from the relevant pair for positive are entirely above those for negative magnetization and $\Delta\bar{\beta} < 0$ (cf. the pairs of curves for $|\alpha| = 0.8$, 0.9 and 0.95 in Fig. 1(b)). To the left of cutoff there exists a backward-wave region where $\bar{\beta}_-$ is a double-valued function of $\bar{r}_0$. If ρ grows, for example $\rho = 0.3$ and 0.4, (see Figs. 2(a) and (b)), the phase performance alters to a great extent. Now in the majority of pairs the curves for positive are situated above the ones for negative magnetization (i.e., $\bar{\beta}_- < \bar{\beta}_+$ and $\Delta\bar{\beta} < 0$). This tendency is especially strongly pronounced in Fig. 2(b). If $|\alpha|$ gets large, for instance $|\alpha| = 0.95$, the curves for $\alpha_+ > 0$ lie wholly to the left of cutoff and a vast

backward-wave region is observed. Here $\bar{\beta}_+$ could be one or double-valued function of $\bar{r}_0$. Moreover, for all ρ values of $|\alpha|$ may be found, for which a magnetically controlled cutoff exists. Besides, with the increase of ρ the cutoff frequencies and the envelopes are shifted towards the lower frequencies.

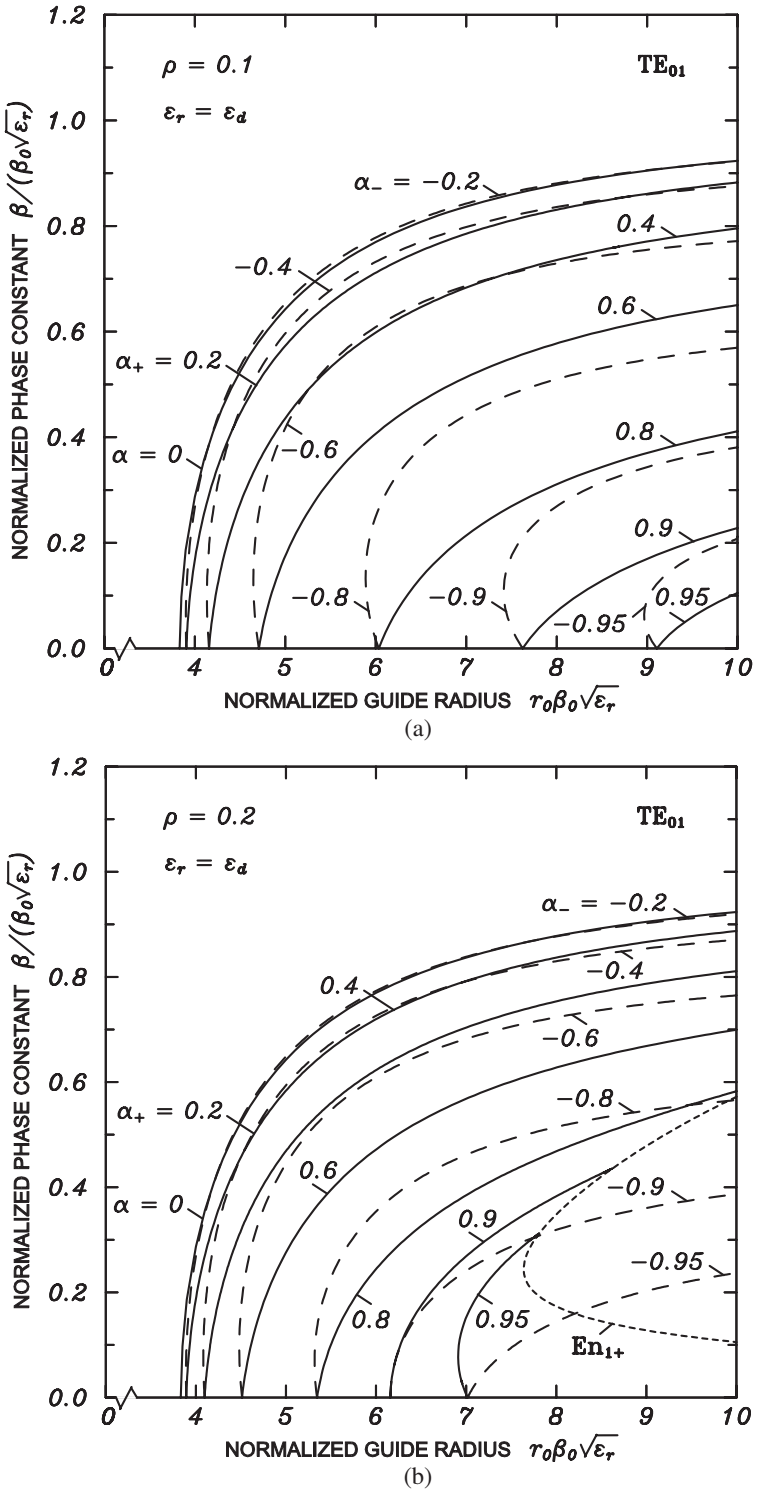

Figure 1: Phase curves $\bar{\beta}(\bar{r}_0)$ of the two-layered circular ferrite-dielectric waveguide for normal TE_{01} mode with α as parameter, assuming $\varepsilon_d = \varepsilon_r$ in case (a) $\rho = 0.1$; (b) $\rho = 0.2$.

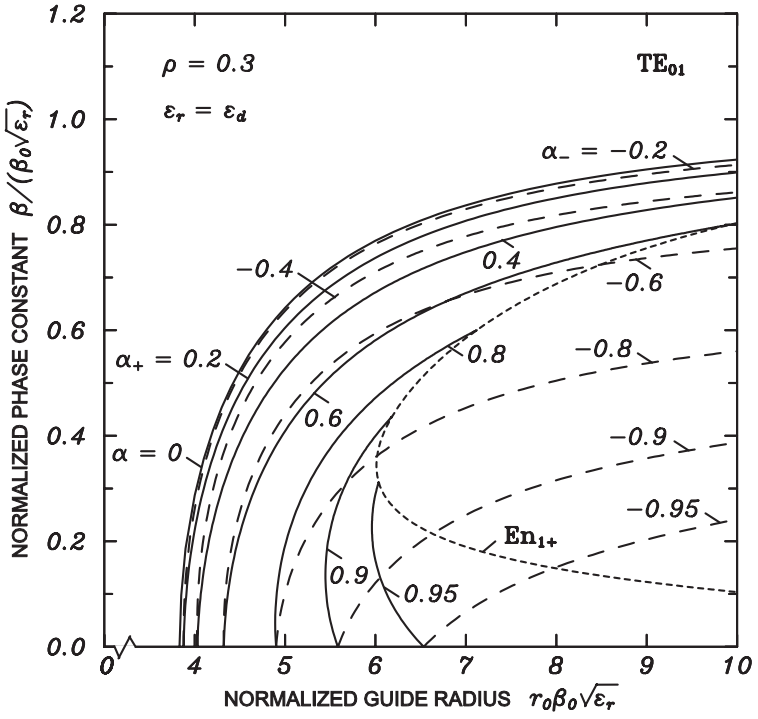

(a)

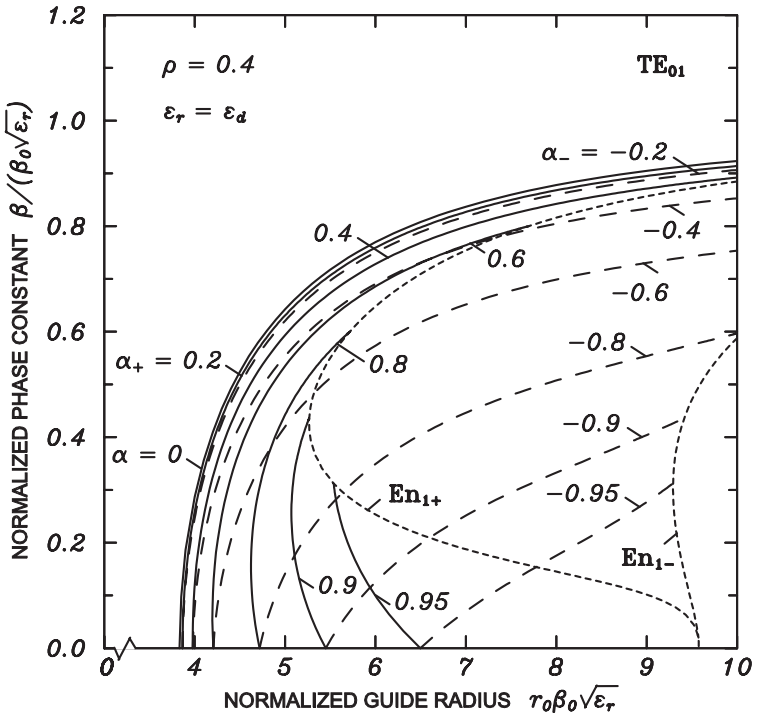

(b)

Figure 2: Phase curves $\bar{\beta}(\bar{r}_0)$ of the two-layered circular ferrite-dielectric waveguide for normal TE_{01} mode with α as parameter, assuming $\varepsilon_d = \varepsilon_r$ in case (a) $\rho = 0.3$; (b) $\rho = 0.4$.

4. CONCLUSION

The replacement of the inner part of the circular ferrite waveguide of azimuthal magnetization, propagating normal TE_{0n} modes by a dielectric cylinder complicates considerably its phase portrait. Envelope curves appear at which the phase characteristics for both signs of magnetization terminate. The dimensions of the area of wave propagation, of the frequency band in which differential phase shift is produced, as well its sign, are substantially influenced by the magnitude of dielectric insert.

ACKNOWLEDGMENT

We express our gratitude to our mother Trifonka Romanova Popnikolova for her self-denial, patience and for the tremendous efforts she exerts to support all our undertakings.

REFERENCES

1. Georgiev, G. N. and M. N. Georgieva-Grosse, "Formulae for differential phase shift computation in an azimuthally magnetized circular ferrite waveguide," in *Proc. Millenn. Conf. Antennas Propagat. AP-2000*, 1002, in CDROM, Davos, Switzerland, April 9–14, 2000.
2. Georgiev, G. N. and M. N. Georgieva-Grosse, "A new property of the complex Kummer function and its application to waveguide propagation," *IEEE Antennas Wireless Propagat. Lett.*, Vol. 2, 306–309, 2003.
3. Georgiev, G. N. and M. N. Georgieva-Grosse, "Some applications of the L numbers," in *Proc. Int. Conf. Antenna Technol. ICAT 2005*, 83–87, ISRO, Ahmedabad, India, February 23–24, 2005.
4. Georgiev, G. N. and M. N. Georgieva-Grosse, "Some new simple methods for differential phase shift computation in the circular waveguide with azimuthally magnetized ferrite," in *Proc. 28th ESA Antenna Worksh. Space Antenna Syst. Technol.*, Pt. 2, 1159–1166, ESA/ESTEC, Noordwijk, The Netherlands, May 31–June 3, 2005.
5. Georgiev, G. N. and M. N. Georgieva-Grosse, "The Kummer confluent hypergeometric function and some of its applications in the theory of azimuthally magnetized circular ferrite waveguides," *J. Telecomm. Information Technol.*, Vol. 6, No. 3, 112–128, 2005.
6. Georgiev, G. N. and M. N. Georgieva-Grosse, "An approximate method for analysis of azimuthally magnetized circular ferrite waveguide phase shifter," in *Proc. 1st Europ. Conf. Antennas Propagat. EuCAP 2006*, in CDROM, Nice, France, November 6–10, 2006.
7. Georgiev, G. N. and M. N. Georgieva-Grosse, "The $L(c, n)$ numbers and their application in the theory of waveguides," in *Proc. Int. Conf. Days Diffr. DD'08*, 44–56, St. Petersburg, Russia, June 3–6, 2008.
8. Georgiev, G. N. and M. N. Georgieva-Grosse, "A theorem for the properties of some classes of numbers, connected with the zeros of complex Kummer function and its application in the theory of circular ferrite waveguides with azimuthal magnetization," in *Proc. XXIX URSI General Assembly*, in CDROM, D05.4(182), Chicago, IL, USA, August 7–16, 2008.
9. Georgieva-Grosse, M. N. and G. N. Georgiev, "The A, B, C numbers and their application in the theory of waveguides," in *Proc. 26th Progr. in Electromagn. Res. Symp.*, Moscow, Russia, August 18–21, 2009 (in print).
10. Georgiev, G. N. and M. N. Georgieva-Grosse, "Some classes of real numbers and their application in the theory of circular waveguide with azimuthally magnetized ferrite," in *Proc. Int. Sci. Conf. Adv. Lightweight Structures Refl. Antennas*, Tbilisi, Georgia, October 14–16, 2009 (in print).
11. Clarricoats, P. J. B. and A. D. Olver, "Propagation in anisotropic radially stratified circular waveguides," *Electron. Lett.*, Vol. 2, No. 1, 37–38, 1966.
12. Georgiev, G. N. and M. N. Georgieva-Grosse, "Some new properties of the circular waveguides with azimuthally magnetized ferrite," in *Proc. 25th ESA Antenna Worksh. Satell. Antenna Technol.*, 601–608, ESA/ESTEC, Noordwijk, The Netherlands, September 18–20, 2002.
13. Georgiev, G. N. and M. N. Georgieva-Grosse, "Several hypotheses in the confluent hypergeometric functions based theory of the azimuthally magnetized circular ferrite waveguides," in *Proc. East-West Worksh. Adv. Techn. Electromagn.*, 197–204, Warsaw, Poland, May 20–21, 2004.
14. Georgiev, G. N. and M. N. Georgieva-Grosse, "Propagation in an azimuthally magnetized circular ferrite-dielectric waveguide," in *Proc. 3rd Europ. Conf. Antennas Propagat. EuCAP 2009*, 345–349, in CDROM, Berlin, Germany, March 23–27, 2009.
15. Georgiev, G. N. and M. N. Georgieva-Grosse, "An application of the complex Tricomi function," in *Proc. Eleventh Int. Conf. Electromagn. Adv. Applicat. ICEAA'09*, Turin, Italy, September 14–18, 2009 (in print).
16. Dib, N. and A. Omar, "Dispersion analysis of multilayer cylindrical transmission lines containing magnetized ferrite substrates," *IEEE Trans. Microwave Theory Tech.*, Vol. 50, No. 7, 1730–1736, 2002.
17. Tricomi, F. G., *Funzioni Ipergeometriche Confluenti*, Edizioni Cremonese, Rome, Italy, 1954.

Theorem for the L (c, ρ, n) Numbers

Georgi Nikolov Georgiev[1] **and Mariana Nikolova Georgieva-Grosse**[2]

[1]Faculty of Mathematics and Informatics, University of Veliko Tirnovo
"St. St. Cyril and Methodius", BG-5000 Veliko Tirnovo, Bulgaria
[2]Meterstrasse 4, D-70839 Gerlingen, Germany

Abstract— The theorem for existence and for the main features of the $L(c, \rho, n)$ numbers (c, ρ — real, $0 < \rho < 1$, $n = 1, 2, 3, \ldots$), is formulated by three lemmas and proved numerically. Lemma 1 reveals the existence of quantities and determines them in case $c \neq l$, ($l = 0, -1, -2, -3, \ldots$) as the common limits of some couples of infinite sequences of positive real numbers, devised with the help of the positive purely imaginary zeros of a function, involving complex Kummer and Tricomi confluent hypergeometric ones of specially chosen parameters. Lemma 2 defines the same for $c = l$ (when the Kummer function has no sense) through the relation $L(c, \rho, n) = L(2 - l, \rho, n)$. Lemma 3 states that for any allowable c, ρ, and n it is true: $L(c, \rho, n) = L(2 - c, \rho, n)$ and $L(1 + h, \rho, n) = L(1 - h, \rho, n)$, ($h = \pm(1 - c)$). The theory of waveguides is pointed out as a field of application of the numbers considered.

1. INTRODUCTION

L numbers are named the common limits of some infinite sequences of real numbers, coherent with definite zeros of certain functions, taking in confluent hypergeometric function(s) (CHFs) [1] of expressly picked out parameters and eventually cylindrical ones, as well [2–5]. They sprung up in the built in terms of the functions referred to theory of azimuthally magnetized circular ferrite waveguides, propagating normal or slow TE_{0n} modes (structures apt for the design of various microwave components, e.g., of nonreciprocal phase shifters for the normal TE_{01} mode) [2–5].

The main contribution of this study is the numerical proof of the existence of finite limits (called $L(c, \rho, n)$ numbers) of the infinite sequences of real numbers $K_-(c, \rho, n, k_-) = |k_-|\, \chi^{(c)}_{k_-, n}(\rho)$ and $M_-(c, \rho, n, k_-) = |a_-|\, \chi^{(c)}_{k_-, n}(\rho)$ in case $k_- \to -\infty$, ($\chi^{(c)}_{k, n}(\rho)$ — nth positive purely imaginary zero of the function $F(a, c; x, \rho) = \Phi(a, c; x)\Psi(a, c; \rho x) - \Phi(a, c; \rho x)\Psi(a, c; x)$ in x, $\Phi(a, c; x)$ and $\Psi(a, c; x)$ — Kummer and Tricomi CHFs, resp. [1], $a = c/2 - jk$, c — any real number, except $c = l$, $l = 0, -1, -2, -3, \ldots$, k — real, $-\infty < k < +\infty$, $x = jz$, z and ρ — real, positive, $0 < \rho < 1$, $n = 1, 2, 3 \ldots$). This fact makes up the essence of the formulated Theorem for the $L(c, \rho, n)$ numbers which examines also the case $c = l$ and the symmetry relations for quantities. The possibility to use the latter is discussed, too.

Table 1(a): Zeros $\chi^{(c)}_{k_-, n}(\rho)$ of $F(a, c; x, \rho)$ and numbers $K_-(c, \rho, n, k_-)$ and $M_-(c, \rho, n, k_-)$ for large negative k_- in case $c = 1, 2, 3$ and 4, $n = 1$ and $\rho = 0.1$.

c / k_-	χ_-	K_-	M_-	χ_-	K_-	M_-	χ_-	K_-	M_-	χ_-	K_-	M_-
	1			2			3			4		
–10	0.50860	**5.**08600	**5.**09235	0.57243	**5.7**2433	**5.7**5288	0.75829	**7.5**8292	**7.6**6775	1.05112	**10.**51119	**10.**71936
–20	0.25538	**5.10**762	**5.10**922	0.28760	**5.7**5204	**5.7**5922	0.38166	**7.63**311	**7.65**454	0.53061	**10.61**215	**10.66**508
–30	0.17039	**5.11**167	**5.11**238	0.19191	**5.7**5723	**5.76**043	0.25475	**7.64**254	**7.65**209	0.35438	**10.63**126	**10.65**485
–40	0.12783	**5.11**309	**5.11**349	0.14398	**5.7**5905	**5.76**085	0.19115	**7.64**585	**7.65**123	0.26595	**10.63**798	**10.65**126
–50	0.10227	**5.11**375	**5.114**00	0.11520	**5.7**5989	**5.761**04	0.15295	**7.64**739	**7.650**83	0.21282	**10.64**109	**10.64**960
–60	0.08524	**5.114**10	**5.114**28	0.09601	**5.76**035	**5.761**15	0.12747	**7.64**822	**7.650**61	0.17738	**10.64**279	**10.64**870
–70	0.07306	**5.114**32	**5.114**45	0.08229	**5.76**063	**5.761**21	0.10927	**7.64**873	**7.650**48	0.15205	**10.64**381	**10.64**815
–80	0.06393	**5.114**46	**5.114**56	0.07201	**5.76**081	**5.761**26	0.09561	**7.64**905	**7.650**40	0.13306	**10.64**447	**10.64**780
–90	0.05683	**5.114**55	**5.114**63	0.06401	**5.76**093	**5.761**28	0.08499	**7.64**928	**7.650**34	0.11828	**10.64**493	**10.64**755
–100	0.05115	**5.114**62	**5.114**69	0.05761	**5.761**02	**5.761**30	0.07649	**7.64**944	**7.650**30	0.10645	**10.64**525	**10.64**738

2. THEOREM FOR EXISTENCE AND FOR THE MAIN PROPERTIES OF THE $L(c, \rho, n)$ NUMBERS

Theorem 1: The statement of the theorem is expressed by the following three Lemmas:

Lemma 1: *If $\chi^{(c)}_{k,n}(\rho)$ is the nth positive purely imaginary zero of the function $F(a, c; x, \rho) = \Phi(a, c; x)\Psi(a, c; \rho x) - \Phi(a, c; \rho x)\Psi(a, c; x)$ in x ($n = 1, 2, 3 \ldots$) in which $\Phi(a, c; x)$ and $\Psi(a, c; x)$ are the Kummer and Tricomi CHFs with $a = c/2 - jk$ — complex, $c = 2Rea$ — restricted positive or negative real number, different from zero or negative integer ($c \neq l$, $l = 0, -1, -2, -3, \ldots$), k — real, $-\infty < k < +\infty$, $x = jz$ — positive purely imaginary, z, ρ — real, positive, $0 < \rho < 1$, and if $K_{\pm}(c, \rho, n, k_{\pm}) = |k_{\pm}|\chi^{(c)}_{k_{\pm},n}(\rho)$ and $M_{\pm}(c, \rho, n, k_{\pm}) = |a_{\pm}|\chi^{(c)}_{k_{\pm},n}(\rho)$, then the infinite sequences*

Table 1(b): Zeros $\chi^{(c)}_{k_-,n}(\rho)$ of $F(a, c; x, \rho)$ and numbers $K_-(c, \rho, n, k_-)$ and $M_-(c, \rho, n, k_-)$ for large negative k_- in case $c = 1, 2, 3$ and 4, $n = 1$ and $\rho = 0.2$.

k_- \ c	χ_-	K_-	M_-	χ_-	K_-	M_-	χ_-	K_-	M_-	χ_-	K_-	M_-
	1			2			3			4		
–10	0.78654	**7**.86537	**7**.87520	0.83610	**8**.36098	**8**.40268	0.98334	**9.8**3336	**9.9**4337	1.22404	**12**.24042	**12.4**8283
–20	0.39635	**7.9**2691	**7.9**2939	0.42154	**8.4**3072	**8.4**4125	0.49653	**9.9**3065	**9.9**5854	0.61966	**12**.39323	**12.4**5505
–30	0.26462	**7.9**3852	**7.9**3962	0.28146	**8.4**4389	**8.4**4858	0.33164	**9.9**4908	**9.96**151	0.41408	**12.4**2236	**12.44**994
–40	0.19856	**7.94**260	**7.94**322	0.21121	**8.4**4851	**8.45**115	0.24889	**9.9**5557	**9.96**256	0.31082	**12.4**3262	**12.44**815
–50	0.15889	**7.94**449	**7.94**489	0.16901	**8.45**066	**8.45**235	0.19917	**9.9**5857	**9.963**05	0.24875	**12.4**3738	**12.44**733
–60	0.13243	**7.94**552	**7.94**579	0.14086	**8.45**183	**8.45**300	0.16600	**9.96**021	**9.963**32	0.20733	**12.4**3997	**12.44**688
–70	0.11352	**7.94**614	**7.94**634	0.12075	**8.45**253	**8.45**339	0.14230	**9.96**120	**9.963**48	0.17774	**12.44**153	**12.44**661
–80	0.09933	**7.94**654	**7.94**669	0.10566	**8.45**299	**8.45**365	0.12452	**9.96**184	**9.963**59	0.15553	**12.44**255	**12.44**644
–90	0.08830	**7.94**681	**7.94**694	0.09393	**8.45**330	**8.45**382	0.11069	**9.96**228	**9.963**66	0.13826	**12.44**324	**12.44**632
–100	0.07947	**7.947**01	**7.947**11	0.08454	**8.45**352	**8.45**395	0.09963	**9.96**259	**9.963**71	0.12444	**12.44**374	**12.44**623

Table 2: Zeros $\chi^{(c)}_{k_-,n}(\rho)$ of $F(a, c; x, \rho)$ and numbers $K_-(c, \rho, n, k_-)$ and $M_-(c, \rho, n, k_-)$ for large negative k_- in case $c = -8.0791324685$, 0.4157906328, 1.5842093672, 10.0791324685; $n = 1$ and $\rho = 0.1$, 0.2.

k_- \ c	χ_-	K_-	M_-	χ_-	K_-	M_-	χ_-	K_-	M_-	χ_-	K_-	M_-
	–8.0791324685			0.4157906328			1.5842093672			10.0791324685		
	$\rho = 0.1$											
–10	4.23305	**4**2.33045	**45**.65376	0.53050	**5.3**0496	**5.3**0611	0.53050	**5.3**0496	**5.3**2158	4.23305	**4**2.33045	**47**.40202
–20	2.21997	**4**4.39930	**45**.29589	0.26643	**5.3**2858	**5.3**2887	0.26643	**5.3**2858	**5.33**276	2.21997	**4**4.39930	**45**.78714
–30	1.49424	**4**4.82707	**45**.23163	0.17777	**5.33**300	**5.33**313	0.17777	**5.33**300	**5.33**486	1.49424	**4**4.82707	**45**.45516
–40	1.12451	**4**4.98059	**45**.20938	0.13336	**5.33**455	**5.33**462	0.13336	**5.33**455	**5.33**560	1.12451	**4**4.98059	**45**.33618
–50	0.90105	**45**.05234	**45.1**9913	0.10671	**5.33**527	**5.33**532	0.10671	**5.33**527	**5.33**594	0.90105	**45**.05234	**45**.28060
–60	0.75153	**45**.09150	**45.1**9358	0.08893	**5.33**566	**5.33**569	0.08893	**5.33**566	**5.336**13	0.75153	**45**.09150	**45**.25028
–70	0.64450	**45.1**1518	**45.1**9024	0.07623	**5.33**590	**5.33**592	0.07623	**5.33**590	**5.336**24	0.64450	**45.1**1518	**45**.23194
–80	0.56413	**45.1**3057	**45.1**8807	0.06670	**5.336**05	**5.336**07	0.06670	**5.336**05	**5.336**31	0.56413	**45.1**3057	**45**.22003
–90	0.50157	**45.1**4114	**45.1**8658	0.05929	**5.336**15	**5.336**17	0.05929	**5.336**15	**5.336**36	0.50157	**45.1**4114	**45**.21185
–100	0.45149	**45.1**4870	**45.1**8552	0.05336	**5.336**23	**5.336**24	0.05336	**5.336**23	**5.336**40	0.45149	**45.1**4870	**45**.20599
	$\rho = 0.2$											
–10	4.23867	**4**2.38670	**45**.71443	0.80348	**8**.03480	**8**.03653	0.80348	**8**.03480	**8**.05996	4.23867	**4**2.38670	**47**.46501
–20	2.22340	**4**4.46801	**45**.36598	0.40495	**8**.09908	**8**.09952	0.40495	**8**.09908	**8.1**0543	2.22340	**4**4.46801	**45**.85799
–30	1.49662	**4**4.89867	**45**.30387	0.27037	**8.1**1121	**8.1**1140	0.27037	**8.1**1121	**8.1**1403	1.49662	**4**4.89867	**45**.52776
–40	1.12633	**45**.05326	**45.2**8242	0.20289	**8.1**1547	**8.1**1558	0.20289	**8.1**1547	**8.1**1706	1.12633	**45**.05326	**45**.40942
–50	0.90251	**45**.12551	**45.2**7255	0.16235	**8.1**1745	**8.1**1752	0.16235	**8.1**1745	**8.1**1846	0.90251	**45**.12551	**45**.35415
–60	0.75275	**45**.16495	**45.2**6720	0.13531	**8.1**1852	**8.1**1857	0.13531	**8.1**1852	**8.1**1923	0.75275	**45**.16495	**45**.32399
–70	0.64555	**45**.18880	**45.2**6398	0.11599	**8.1**1917	**8.1**1920	0.11599	**8.1**1917	**8.1**1969	0.64555	**45**.18880	**45**.30576
–80	0.56505	**45.2**0430	**45.2**6189	0.10149	**8.1**1959	**8.1**1962	0.10149	**8.1**1959	**8.1**1999	0.56505	**45.2**0430	**45.2**9390
–90	0.50239	**45.2**1494	**45.2**6046	0.09022	**8.1**1988	**8.1**1990	0.09022	**8.1**1988	**8.120**19	0.50239	**45.2**1494	**45.2**8577
–100	0.45223	**45.2**2256	**45.25**944	0.08120	**8.120**08	**8.120**10	0.08120	**8.120**08	**8.120**34	0.45223	**45.2**2256	**45.2**7995

Table 3: $L(c, \rho, n)$ and $L(2-c, \rho, n)$ numbers with $c = l - \varepsilon$ and $c = l + \varepsilon$ in case $l = 0, -1, \ldots, -5$, $\varepsilon = 1.10^{-i}$, $i = 1, 2, \ldots, 5$, $n = 1$, $\rho = 0.1$ and 0.2.

$L(c, \rho, n)$							$L(2-c, \rho, n)$					
ε \ l	−5	−4	−3	−2	−1	0	0	−1	−2	−3	−4	−5
$\rho = 0.1$												
$L(l-\varepsilon, \rho, n)$							$L(2-(l-\varepsilon), \rho, n)$					
1.10^{-1}	**25**.27733	**19.8**1008	15.01887	**11**.00057	**7.9**0261	**5.8**9602	**5.8**9602	**7.9**0261	**11**.00057	15.01887	**19.8**1007	**25**.27732
1.10^{-2}	**24.7**5917	**19.3**5012	**14.6**2370	**10.6**8155	**7.6**7484	**5.7**7428	**5.7**7428	**7.6**7484	**10.6**8155	**14.6**2371	**19.3**5011	**24.7**5918
1.10^{-3}	**24.70**763	**19.3**0442	**14.58**453	**10.6**5006	**7.65**256	**5.76**266	**5.76**266	**7.65**256	**10.6**5006	**14.58**454	**19.3**0442	**24.70**764
1.10^{-4}	**24.70**248	**19.299**86	**14.580**62	**10.646**92	**7.650**33	**5.761**50	**5.761**50	**7.650**33	**10.646**92	**14.580**63	**19.299**85	**24.70**249
1.10^{-5}	**24.70196**	**19.299**40	**14.580**22	**10.646**60	**7.650**11	**5.761**39	**5.761**39	**7.650**11	**10.646**60	**14.580**24	**19.2993**9	**24.70198**
$L(2-l, \rho, n)$												
	24.70192	**19.29934**	**14.58019**	**10.64657**	**7.65009**	**5.76137**	**5.76137**	**7.65009**	**10.64657**	**14.58019**	**19.29934**	**24.70192**
$L(l+\varepsilon, \rho, n)$							$L(2-(l+\varepsilon), \rho, n)$					
1.10^{-5}	**24.70**188	**19.2993**0	**14.5801**6	**10.6465**3	**7.6500**6	**5.7613**6	**5.7613**6	**7.6500**6	**10.6465**3	**14.5801**5	**19.299**29	**24.701**86
1.10^{-4}	**24.701**36	**19.29**884	**14.5**7976	**10.646**22	**7.6**4984	**5.761**24	**5.761**24	**7.6**4984	**10.646**22	**14.5**7976	**19.29**883	**24.701**35
1.10^{-3}	**24.**69621	**19.29**428	**14.5**7585	**10.64**308	**7.6**4762	**5.76**009	**5.76**009	**7.6**4762	**10.64**308	**14.5**7585	**19.29**427	**24.**69620
1.10^{-2}	**24.**64474	**19.2**4865	**14.5**3676	**10.6**1168	**7.6**2544	**5.7**4859	**5.7**4859	**7.6**2544	**10.6**1168	**14.5**3675	**19.2**4864	**24.**64473
1.10^{-1}	**24.**13279	18.79541	**14.**14933	**10.**30192	**7.**40867	**5.**63922	**5.**63922	**7.**40867	**10.**30192	**14.**14933	18.79540	**24.**13278
$\rho = 0.2$												
$L(l-\varepsilon, \rho, n)$							$L(2-(l-\varepsilon), \rho, n)$					
1.10^{-1}	**25.**74953	**20.**59821	16.24217	**12.**83147	10.16895	**8.**56060	**8.**56060	10.16895	**12.**83147	16.24217	**20.**59821	**25.**74952
1.10^{-2}	**25.2**5497	**20.1**7264	**15.8**9133	**12.4**7534	**9.9**8393	**8.4**6460	**8.4**6460	**9.9**8393	**12.4**7534	**15.8**9134	**20.1**7264	**25.2**5498
1.10^{-3}	**25.20**584	**20.1**3044	**15.85**662	**12.44**871	**9.96**586	**8.45**544	**8.45**544	**9.96**586	**12.44**871	**15.85**664	**20.1**3044	**25.20**586
1.10^{-4}	**25.200**93	**20.12**623	**15.85**316	**12.44**605	**9.96**406	**8.454**53	**8.454**53	**9.96**406	**12.44**605	**15.85**318	**20.12**622	**25.200**95
1.10^{-5}	**25.2004**4	**20.125**80	**15.852**81	**12.4457**9	**9.9638**8	**8.4544**4	**8.4544**4	**9.9638**8	**12.4457**8	**15.852**83	**20.125**79	**25.2004**5
$L(2-l, \rho, n)$												
	25.20040	**20.12575**	**15.85279**	**12.44576**	**9.96386**	**8.45443**	**8.45443**	**9.96386**	**12.44576**	**15.85279**	**20.12575**	**25.20040**
$L(l+\varepsilon, \rho, n)$							$L(2-(l+\varepsilon), \rho, n)$					
1.10^{-5}	**25.200**36	**20.1257**1	**15.8527**5	**12.4457**3	**9.9638**4	**8.4544**2	**8.4544**2	**9.9638**4	**12.4457**3	**15.8527**5	**20.1257**0	**25.200**34
1.10^{-4}	**25.**19987	**20.125**29	**15.852**41	**12.445**46	**9.963**66	**8.454**33	**8.454**33	**9.963**66	**12.445**46	**15.852**41	**20.125**29	**25.**19986
1.10^{-3}	**25.**19496	**20.12**107	**15.8**4894	**12.44**280	**9.96**186	**8.45**342	**8.45**342	**9.96**186	**12.44**280	**15.8**4894	**20.12**107	**25.**19495
1.10^{-2}	**25.**14591	**20.**07895	**15.8**1433	**12.4**1627	**9.9**4389	**8.4**4437	**8.4**4437	**9.9**4389	**12.4**1627	**15.8**1433	**20.**07895	**25.**14590
1.10^{-1}	**24.**65868	19.66132	**15.**47208	**12.**15504	**9.**76851	**8.**35831	**8.**35831	**9.**76851	**12.**15504	**15.**47208	19.66132	24.65867

of positive real numbers $\{\chi^{(c)}_{k_-,n}(\rho)\}$, $\{K_-(c, n, \rho, k_-)\}$ *and* $\{M_-(c, n, \rho, k_-)\}$ *are convergent for* $k_- \to -\infty$ (c, n — *fixed*). *The limit of the first sequence is zero and the limit of the second and third ones is the same. It equals the finite positive real number* L *where* $L = L(c, \rho, n)$. *It holds:*

$$\lim_{k_- \to -\infty} K_-(c, \rho, n, k_-) = \lim_{k_- \to -\infty} M_-(c, \rho, n, k_-) = L(c, \rho, n). \tag{1}$$

Lemma 2: *If* $L(l-\varepsilon, \rho, n)$ *and* $L(l+\varepsilon, \rho, n)$ *are finite positive real numbers in the sense of Lemma 1 in which* $l = 0, -1, -2, -3, \ldots$ *is zero or negative integer,* ε *is a positive real number, less than unity,* $(0 < \varepsilon < 1)$ *and* $n = 1, 2, 3 \ldots$, *then the infinite sequences of positive real numbers* $\{L(l-\varepsilon, \rho, n)\}$ *and* $\{L(l+\varepsilon, \rho, n)\}$ *are convergent for* $\varepsilon \to 0$ *and possess a common limit. The sequence* $\{L(l-\varepsilon, \rho, n)\}(\{L(l+\varepsilon, \rho, n)\})$ *tends to it from the left (right). The limit mentioned is accepted as a value of the* $L(c, \rho, n)$ *number in case* $c = l$ (c — *zero or negative integer). Thus, it is assumed that:*

$$L(c, \rho, n) = \lim_{\varepsilon \to 0} L(l-\varepsilon, \rho, n) = \lim_{\varepsilon \to 0} L(l+\varepsilon, \rho, n). \tag{2}$$

Lemma 3: *Under the conditions of Lemmas 1 and 2, it is true: i) In case* $c \neq l$, *it holds:* $L(c, \rho, n) = L(2-c, \rho, n)$; *ii) The requirement* $c = l$ *yields:* $L(l, \rho, n) = L(2-l, \rho, n)$; *iii) If* $c = 1 \pm h$, $h \neq l$, $(c \neq 0, \pm1, \pm2, \pm3, \ldots)$, *it is valid:* $L(1+h, \rho, n) = L(1-h, \rho, n)$; *iv) When* $c = 1 \pm l$, $(c = 0, \pm1, \pm2, \pm3, \ldots)$, *it is fulfilled:* $L(1+l, \rho, n) = L(1-l, \rho, n)$.

Numerical proof: The proof of Lemma 1 is illustrated in Tables 1(a), (b) and 2, and of Lemmas 2 and 3 — in Table 3 for c — positive integers and arbitrary real numbers save for $c = l$, $n = 1$, and $\rho = 0.1$ and 0.2 (cf. the digits marked by bold face type). Table 2 shows that $\chi^{(c)}_{k_-,n}(\rho) = \chi^{(2-c)}_{k_-,n}(\rho)$, $K_-(c, \rho, n, k_-) = K_-(2-c, \rho, n, k_-)$ and $M_-(c, \rho, n, k_-) = M_-(2-c, \rho, n, k_-)$, as well. The effect of ρ and c on $L(c, \rho, n)$ in case $n = 1$ is presented in Table 4 and Figs. 1 and 2.

Table 4: Values of $L(c, \rho, n)$ as a function of c for $\rho = 0.1$ and 0.2 in case $n = 1$.

c	L	c	L	c	L	c	L	c	L	c	L	c	L	c	L
$\rho = 0.1$															
−4.0		−3.0		−2.0		−1.0		0.0		1.0	5.11490	2.0	5.76137	3.0	7.65009
−3.9	18.79541	−2.9	14.14933	−1.9	10.30192	−0.9	7.40867	0.1	5.63922	1.1	5.12141	2.1	5.89602	3.1	7.90261
−3.8	18.29834	−2.8	13.72641	−1.8	9.96680	−0.8	7.17853	0.2	5.52966	1.2	5.14093	2.2	6.04306	3.2	8.16608
−3.7	17.80823	−2.7	13.31157	−1.7	9.64138	−0.7	6.95982	0.3	5.43277	1.3	5.17344	2.3	6.20238	3.3	8.44031
−3.6	17.32516	−2.6	12.90495	−1.6	9.32584	−0.6	6.75271	0.4	5.34865	1.4	5.21893	2.4	6.37384	3.4	8.72513
−3.5	16.84922	−2.5	12.50670	−1.5	9.02037	−0.5	6.55733	0.5	5.27735	1.5	5.27735	2.5	6.55733	3.5	9.02037
−3.4	16.38052	−2.4	12.11698	−1.4	8.72513	−0.4	6.37384	0.6	5.21893	1.6	5.34865	2.6	6.75271	3.6	9.32584
−3.3	15.91915	−2.3	11.73594	−1.3	8.44031	−0.3	6.20238	0.7	5.17344	1.7	5.43277	2.7	6.95982	3.7	9.64138
−3.2	15.46523	−2.2	11.36375	−1.2	8.16608	−0.2	6.04306	0.8	5.14093	1.8	5.52966	2.8	7.17853	3.8	9.96680
−3.1	15.01887	−2.1	11.00057	−1.1	7.90261	−0.1	5.89602	0.9	5.12141	1.9	5.63922	2.9	7.40867	3.9	10.30192
−3.0		−2.0		−1.0		0.0		1.0	5.11490	2.0	5.76137	3.0	7.65009	4.0	10.64657
$\rho = 0.2$															
−4.0		−3.0		−2.0		−1.0		0.0		1.0	7.94781	2.0	8.45443	3.0	9.96386
−3.9	19.66132	−2.9	15.47208	−1.9	12.15504	−0.9	9.76851	0.1	8.35831	1.1	7.95289	2.1	8.56060	3.1	10.16895
−3.8	19.20496	−2.8	15.10010	−1.8	11.87364	−0.8	9.58294	0.2	8.27225	1.2	7.96811	2.2	8.67679	3.2	10.38374
−3.7	18.75675	−2.7	14.73690	−1.7	11.60161	−0.7	9.40718	0.3	8.19627	1.3	7.99348	2.3	8.80298	3.3	10.60818
−3.6	18.31675	−2.6	14.38256	−1.6	11.33900	−0.6	9.24127	0.4	8.13040	1.4	8.02899	2.4	8.93914	3.4	10.84224
−3.5	17.88502	−2.5	14.03713	−1.5	11.08586	−0.5	9.08525	0.5	8.07463	1.5	8.07463	2.5	9.08525	3.5	11.08586
−3.4	17.46163	−2.4	13.70067	−1.4	10.84224	−0.4	8.93914	0.6	8.02899	1.6	8.13040	2.6	9.24127	3.6	11.33900
−3.3	17.04665	−2.3	13.37325	−1.3	10.60818	−0.3	8.80298	0.7	7.99348	1.7	8.19627	2.7	9.40718	3.7	11.60161
−3.2	16.64014	−2.2	13.05491	−1.2	10.38374	−0.2	8.67679	0.8	7.96811	1.8	8.27225	2.8	9.58294	3.8	11.87364
−3.1	16.24217	−2.1	12.83147	−1.1	10.16895	−0.1	8.56060	0.9	7.95289	1.9	8.35831	2.9	9.76851	3.9	12.15504
−3.0		−2.0		−1.0		0.0		1.0	7.94781	2.0	8.45443	3.0	9.96386	4.0	12.44576

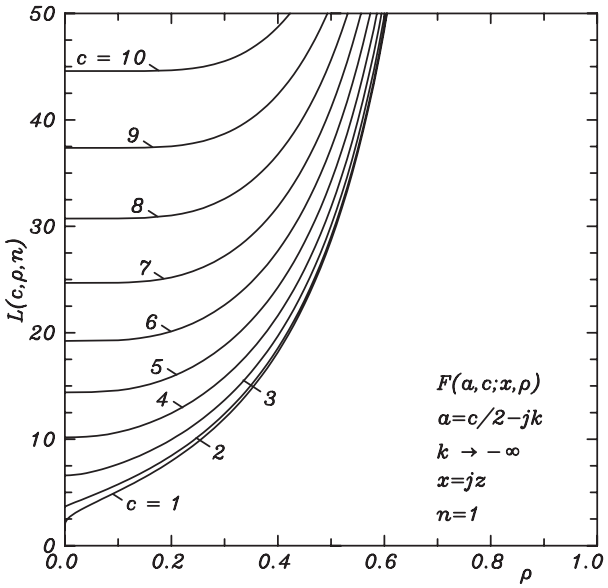

Figure 1: $L(c, \rho, n)$ numbers vs. ρ with c as parameter for $n = 1$.

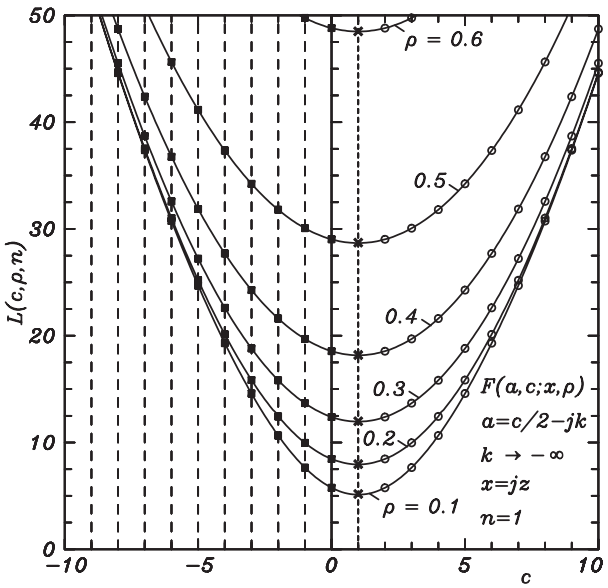

Figure 2: $L(c, \rho, n)$ numbers vs. c with ρ as parameter for $n = 1$.

3. APPLICATION

The zeros of $F(a,\, c;\, x,\, \rho)$ determine the eigenvalue spectrum $\bar{\beta}_2 = \chi^{(c)}_{k,n}(\rho)/(2\bar{r}_0)$ of the coaxial waveguide of outer and inner conductor radii r_0 and r_1, resp., filled with azimuthally magnetized ferrite of off-diagonal element of the Polder permeability tensor $\alpha = \gamma M_r/\omega$, ($\gamma$ — gyromagnetic ratio, M_r — remanent magnetization, ω — angular frequency of the wave) and scalar permittivity $\varepsilon = \varepsilon_0\varepsilon_r$ for normal TE_{0n} modes of phase constant β, if it holds $c = 3$, $k = \alpha\bar{\beta}/(2\bar{\beta}_2)$, $\bar{\beta}_2 = (1 - \alpha^2 - \bar{\beta}^2)^{1/2}$, $x = x_0$, $x_0 = jz_0$, $z_0 = 2\bar{\beta}_2\bar{r}_0$, $\rho = \bar{r}_1/\bar{r}_0$, $\bar{\beta} = \beta/(\beta_0\sqrt{\varepsilon_r})$, $\bar{\beta}_2 = \beta_2/(\beta_0\sqrt{\varepsilon_r})$, $\bar{r}_0 = \beta_0 r_0\sqrt{\varepsilon_r}$, $\bar{r}_1 = \beta_0 r_1\sqrt{\varepsilon_r}$, $\beta_0 = \omega\sqrt{\varepsilon_0\mu_0}$, ($\beta_2$ — radial wave number) [2]. There is an En_{1-} — envelope curve in the $\bar{\beta}(\bar{r}_0)$ — phase diagram of TE_{01} mode of equation $\bar{\beta}_{en-} = \bar{\beta}_{en-}(\bar{r}_{0en-})$, written in parametric form as: $\bar{r}_{0en-} = L(3,\, \rho,\, 1)/[|\alpha_{en-}|(1 - \alpha^2_{en-})^{1/2}]$, $\bar{\beta}_{en-} = (1 - \alpha^2_{en-})^{1/2}$, with α_{en-} as parameter, restricting from the side of higher frequencies the characteristics for negative magnetization [2]. If $\Delta\bar{\beta} = \bar{\beta}_- - \bar{\beta}_+$ is the normalized differential phase shift produced for specific ρ, $\bar{r}_0$ and $|\alpha|$, then $\lambda = \Delta\bar{\beta}\bar{r}_0/|\alpha|$ is called characteristic parameter of the structure. (Throughout the paper the subscripts "+", "−" and "$en-$" distinguish the quantities, relevant to positive ($\alpha > 0$, $k > 0$) and negative ($\alpha < 0$, $k < 0$) magnetization, resp. to the envelope.) Harnessing for both signs of the varying k the procedure for finding the $\bar{\beta}(\bar{r}_0)$ — curves [2], with the zeros $\chi^{(c)}_{k,n}(\rho)$ allows to compute $\Delta\bar{\beta}$ (λ) for any set ρ, $\bar{r}_0$ and $|\alpha|$ of parameters of the coaxial geometry. The numerical analysis shows that if ρ is fixed, λ is slightly influenced by both $\bar{r}_0$ and $|\alpha|$, e.g., assuming $\rho = 0.1$, in case $\bar{r}_0 = 4$, $|\alpha| = 0.1$, $\lambda = 1.932288$, whereas provided $\bar{r}_0 = 10$, $|\alpha| = 0.5$, $\lambda = 1.940370$. Neglecting this dependence, it is suggested to specify λ at the couple of points ($\bar{r}_{0en-}$, $\bar{\beta}_{en-}$) and ($\bar{r}_{0en-}$, $\bar{\beta}_{en+}$) of the same parameter $|\alpha_{en-}|$, the first of which lies at the En_{1-} — line and the second — at the relevant $\bar{\beta}(\bar{r}_0)$ — curve for positive magnetization [2], by the formula $\lambda_{en-} = L(3, \rho, 1)[1 - \bar{\beta}_+/(1 - \alpha^2_{en-})^{1/2}]/|\alpha^2_{en-}|$ and to use this value everywhere, where the structure exhibits properties of phase shifter. (For example, in case $\rho = 0.1$, taking $\lambda_{en-} = 1.9430$ for $\bar{r}_{0en-} = 76.8864$, $|\alpha_{en-}| = 0.1$ and employing it for $\bar{r}_0 = 5$, $|\alpha| = 0.1$, yields by the term $\Delta\bar{\beta} = \lambda|\alpha|/\bar{r}_0$ $\Delta\bar{\beta}_{\mathrm{approx},en-} = 0.0389$. The exact computations for the same $\bar{r}_0$ and $|\alpha|$ give $\lambda_{\mathrm{exact}} = 1.9323$ and $\Delta\bar{\beta}_{\mathrm{exact}} = 0.0386$.) Obviously, the absolute error of the calculations $\delta\Delta\bar{\beta} = |\Delta\bar{\beta}_{\mathrm{exact}} - \Delta\bar{\beta}_{\mathrm{approx},en-}| = 0.0003$ could be ignored.

4. CONCLUSION

The positive real numbers $L(c,\, \rho,\, n)$ are defined for c — arbitrary real, ρ — real, positive, less than unity and n — natural number as limits of certain sequences of real numbers. In case $c \neq l$, $l = 0, -1, -2, -3, \ldots$, the terms of the latter are composed through definite zeros of a formed by complex CHFs of suitably selected parameters function, whereas if $c = l$ (for which the Kummer CHF does not exist), as such serve the quantities $L(l \pm \varepsilon,\, \rho,\, n)$ with $\varepsilon \to 0$. Besides, a symmetry of the numbers toward the point $c = 1$ is found. The employment of quantity $L(3,\, \rho,\, 1)$ is also commented.

ACKNOWLEDGMENT

We express our gratitude to our mother Trifonka Romanova Popnikolova for her self-denial, patience and for the tremendous efforts she exerts to support all our undertakings.

REFERENCES

1. Tricomi, F. G., *Funzioni Ipergeometriche Confluenti*, Edizioni Cremonese, Rome, Italy, 1954.
2. Georgiev G. N. and M. N. Georgieva-Grosse, "A new property of the complex Kummer function and its application to waveguide propagation," *IEEE Antennas Wireless Propagat. Lett.*, Vol. 2, 306–309, 2003.
3. Georgiev G. N. and M. N. Georgieva-Grosse, "The $L(c,\, n)$ numbers and their application in the theory of waveguides," in *Proc. Int. Conf. Days Diffr. DD'08*, 44–56, St.Peterburg, Russia, June 3–6, 2008.
4. Georgiev G. N. and M. N. Georgieva-Grosse, "A property of the $L(c,\, \rho,\, n)$ numbers and its application to waveguide propagation," in *Proc. XXIX URSI General Assembly*, in CDROM, BK.6(120), Chicago, IL, USA, August 7–16, 2008.
5. Georgiev G. N. and M. N. Georgieva-Grosse, "Propagation in an azimuthally magnetized circular ferrite-dielectric waveguide," in *Proc. 3rd Europ. Conf. Antennas Propagat. EuCAP 2009*, 345–349, in CDROM, Berlin, Germany, March 23–27, 2009.

Comparative Analysis of Approaches for High Frequency Electromagnetic Simulation

D. S. Butyugin, V. P. Il'in, and A. V. Petukhov
Institute of Computational Mathematics and Mathematical Geophysics, SBRAS
Novosibirsk, Russia

Abstract— The efficiency of various numerical approaches are compared for solving 3D electromagnetic boundary value problems (BVPs) in frequency domain. The differential and variational statements in terms of electric field as well as in terms of vector and scalar potentials, with different types of boundary conditions (perfect electrical and magnetic conductor, absorption surfaces, wave ports) are approximated at the non-structured grids by finite volume method (FVM) or finite element methods (FEM). FVM is applied for barycentric Voronoi cells, with computing the local balance matrices and assembling the global matrix of the system of linear algebraic equations (SLAE). In FEM, the scalar and vector basis functions are implemented at the tetrahedral elements. The solutions of obtained non-symmetric indefinite SLAEs are made by different preconditioned iterative processes in Krylov subspaces. The Eisenstat modification of incomplete factorization and various preconditioning matrices are combined with semi-conjugate residual (SCR), BiCGStab and other Krylov algorithms. The results of numerical experiments for the representative set of the model problems are presented and demonstrate performance of the proposed algorithms. Computational technologies include parallelization and using the program tools of Mathematical Kernel Library of Intel (MKL).

1. INTRODUCTION

The goal of this paper includes the comparative analysis of the different approaches for numerical solution of the 3D mixed boundary value problems for the system of time-harmonic Maxwell equation, see [1, 2] for example:

$$\begin{array}{ll} \nabla\times\vec{E}=-i\omega\dot{\mu}\vec{H}, & \nabla\times\vec{H}=i\omega\dot{\varepsilon}\vec{E}+\vec{J}, \\ \nabla\cdot(\varepsilon_r\vec{E})=\rho/\varepsilon_0, & \nabla\cdot(\mu_r\vec{H})=0. \end{array} \tag{1}$$

Here $\varepsilon_r, \dot{\varepsilon}, \varepsilon_0, \mu_r, \dot{\mu}$ are physical parameters of the media, ω is frequency, $\rho, \vec{J}$ are charge and current densities, $\vec{E}$ and $\vec{H}$ are the vector electric and magnetic fields.

For $\rho = 0$ the above system is transformed to complex "electrical" Helmholtz equation

$$\nabla\times\left(\frac{1}{\mu_r}\nabla\times\vec{E}\right)-\varkappa\vec{E}=-ik_0Z_0\vec{J}, \tag{2}$$

where $\varkappa = k_0^2\dot{\varepsilon}_r$, $k_0=\omega\sqrt{\varepsilon_0\mu_0}$, $Z_0=\sqrt{\mu_0/\varepsilon_0}$, $\dot{\varepsilon}_r=\dot{\varepsilon}/\varepsilon_0$.

The solution of (1) or (2) is defined in open domain Ω with boundary $\Gamma=\bigcup\limits_i\Gamma_i$, under various types of boundary conditions at the perfect electric or magnetic conductor Γ_1, Γ_2 respectively, wave port Γ_3, and absorbtion surface Γ_4:

$$\begin{array}{lll} \Gamma_1: & \vec{n}\times\vec{E}=0, & \Gamma_2: \quad \vec{n}\times\vec{H}=0, \\ \Gamma_3: & \vec{E}_\tau=\vec{E}_0, & \Gamma_4: \quad \vec{E}_\tau=Z_0\left(\vec{H}\times\vec{n}\right). \end{array} \tag{3}$$

Here τ is tangent vector component at the surface with the external normal $\vec{n}$. If we introduce scalar and vector potentials $\vec{B}=\mu_r\vec{H}=\frac{i}{\omega}\nabla\times\vec{A}, \quad \vec{E}=\vec{A}+\nabla V$, the equation (2) can be rewritten in the following:

$$\nabla\times\left(\frac{1}{\mu_r}\nabla\times\vec{A}\right)-k_0^2\dot{\varepsilon}_r\left(\vec{A}+\nabla V\right)=-ik_0Z_0\vec{J}. \tag{4}$$

For the problems with piece-wise smooth material properties, the well-known conjugation conditions are given on the internal boundaries additionally.

The classical statements (2), (5) can be reformulated in variational forms, see [3, 4]:

$$\int\limits_{\Omega} \frac{1}{\mu_r}(\nabla\times\vec{E})\cdot(\nabla\times\vec{\Psi})d\Omega - \int\limits_{S}\Big(\frac{1}{\mu_r}(\nabla\times\vec{E})\times\vec{n}\Big)\cdot\vec{\Psi}dS - \int\limits_{\Omega}\varkappa(\vec{E}\cdot\vec{\Psi})d\Omega$$
$$= \int\limits_{\Omega}(\vec{F}\cdot\vec{\Psi})d\Omega, \quad \forall\vec{\Psi}\in\mathbb{H}_0^{\rm rot}, \tag{5}$$

$$\int\limits_{\Omega} \frac{1}{\mu_r}\Big(\nabla\times\vec{A}\Big)\cdot\Big(\nabla\times\vec{\Psi}\Big)d\Omega - \int\limits_{S}\Big(\frac{1}{\mu_r}\Big(\nabla\times\vec{A}\Big)\times\vec{n}\Big)\cdot\vec{\Psi}dS - \int\limits_{\Omega}\varkappa\Big(\vec{A}\cdot\vec{\Psi}\Big)d\Omega - \int\limits_{\Omega}\varkappa\Big(\nabla V\cdot\vec{\Psi}\Big)d\Omega$$
$$= \int\limits_{\Omega}\Big(\vec{F}\cdot\vec{\Psi}\Big)d\Omega, \quad \forall\vec{\Psi}\in\mathbb{H}_0^{\rm rot}, \tag{6}$$

where $\vec{\Psi}$ are some vector probe functions, $\vec{E}\in H^{rot}, V\in H_0^1(\Omega)$.

The approximations of the above BVPs by FVM or FEM were implemented and investigated in the numerous papers, see [3–6] and literature citied there. Also, in these and other articles much attention is payed to the special algorithms for iterative solution of complex non-Hermitian SLAEs which arise in discretization of original problems.

This paper is organized as follows. In point 2 we describe shortly the approximative FVM and FEM to be applied on the non-structural tetrahedral grids as well as algebraic preconditioned iterative methods in the Krylov subspaces which are used for solution of large sparse SLAEs with non-symmetric indefinite matrices for real variables. In the last section the results of numerical experiments for the representative set of the model problems demonstrate the convergence of different grid solutions and the efficiency of algebraic solvers for the various physical parameters and meshsteps.

2. APPROXIMATIONS AND ITERATIVE ALGORITHMS

We construct the discretization of the considered 3D BVPs on the adaptive non-structured grids with tetrahedral elements, i.e., the vertices and edges of the boundary Γ are the mesh nodes and mesh edges also.

Let $\vec{r}_j, j=1,2,3,4$, be the verteces of some tetrahedron T, and let $u(e), v(e)$ be the beginning and the end points of some edge e in T. In each tetrahedron we introduce the linear basis functions $\mathcal{L}_i$ and vector functions $\vec{W}_e$:

$$\mathcal{L}_i(\vec{r}_j)=\delta_{i,j}, \quad \vec{W}_e=\mathcal{L}_{v(e)}\nabla\mathcal{L}_{u(e)}-\mathcal{L}_{u(e)}\nabla\mathcal{L}_{v(e)}. \tag{7}$$

The unknown vector and the scalar functions are presented in the form

$$\vec{E}=\sum u_i^E\vec{W}_i, \quad \vec{A}=\sum u_i^A\vec{W}_i, \quad V=\sum u_i^V\mathcal{L}_i \tag{8}$$

where the coefficients u_i^E, for example, are sought from the resulting finite dimensional approximation of (5):

$$\sum_i u_i^E\Big[\int\limits_{\Omega}\frac{1}{\mu_r}\Big(\nabla\times\vec{\Psi}_i\Big)\cdot\Big(\nabla\times\vec{\Psi}_j\Big)d\Omega - \int\limits_{S}\Big(\frac{1}{\mu_r}\Big(\nabla\times\vec{\Psi}_i\Big)\times\vec{n}\Big)\cdot\vec{\Psi}_j dS - \int\limits_{\Omega}\varkappa\Big(\vec{\Psi}_i\cdot\vec{\Psi}_j\Big)d\Omega\Big]$$
$$= \int\limits_{\Omega}\Big(\vec{F}\cdot\vec{\Psi}_j\Big)d\Omega, \tag{9}$$

The similar relations for each j-th grid edge can be written for $\vec{A}-V$ variational statement (7).

The relations (8), (9) define SLAE

$$A^E u^E = f^E, \quad A^E=\{A_{i,j}^E\}, \quad u^E=\{u_i^E\}, \quad f^E=\{f_i^E\}, \tag{10}$$

which dimension N_e equals to the number of mesh edges. The entries of matrix $A_{i,j}^E=S_{i,j}-M_{i,j}$ and vector entries f_i^E are defined via integrals on the finite elements, see [4]:

For the potential statement SLAE can be written in the following form, see [7]:

$$A^{AV}u \equiv \begin{bmatrix} I \\ G^T \end{bmatrix} \cdot \left[A^E\right] \cdot \begin{bmatrix} I & G \end{bmatrix} \cdot \begin{bmatrix} u^A \\ u^V \end{bmatrix} = \begin{bmatrix} I \\ G^T \end{bmatrix} \cdot \left[f^E\right] \equiv f^{AV}, \tag{11}$$

where identity matrix I and subvector u^A have order N_e, the dimension of subvector u^V equals to the number of nodes N_n, and $G = \{g_{i,j}\} \in R^{N_e,N_n}$ is incident "edge-node" matrix: $g_{i,j} = -1$ or 1 if j is node number of the beginning or end vertex of the i-th mesh edge respectively, and $g_{i,j} = 0$ otherwise.

The finite volume approximation of complex Helmholtz equation

$$-\Delta E + \mu_r \varkappa E = 0, \tag{12}$$

which is derived for the uniform media by means of relation rot rot $= -\Delta +$ grad div is made using barycentric Voronoi cells on the same non-structured tetrahedral grid, see [6]. In the case of piece-wise constant material properties, the conjugation conditions on the internal boundaries are satisfied automatically in FVM approach.

The iterative solution of SLAE $Au = f, \quad A = D - L - U$, where $D, -L$ and $-U$ are diagonal, low and upper triangular parts of A, is made by preconditioned Krylov methods. In particular, we use preconditiong matrix

$$B = (G + L)G^{-1}(G + U), \quad G = \frac{1}{\theta}D, \tag{13}$$

where θ is iterative relaxation parameter, and B can be presented in the factorized form, see [7]:

$$B = L_B U_B, \quad L_B = (G - L)G^{-1/2}, \quad U_B = G^{-1/2}(G - U). \tag{14}$$

Then the efficient Eisenstat modification of two side preconditioning can be realized as follows:

$$\bar{A}\bar{u} = L_B^{-1} A U_B^{-1} U_B u = L_n^{-1} f \equiv \bar{f}, \quad \bar{u} = U_B u. \tag{15}$$

The advantage of such approach consists in the fast multiplication of some vector by matrix $\bar{A}$.

The iterative solution of preconditioned SLAE (15) is made by various Krylov methods: conjugate gradient (CG, for symmetric case), biconjugate gradient (BiCG), biconjugate gradient stabilized (BiCGStab) and semi-conjugate residual (SCR), see [7]. Let us remark that the complex SLAEs were transformed to real non-symmetric form.

3. NUMERICAL EXPERIMENTS

The efficiency of the described algorithms is demonstrated by the results of numerical experiments for three test problems (wave guides) with known exact solutions. The computational domain Ω is parallelepiped $0 < x < 72, \quad 0 < y < 34, \quad 0 < z < 200$. The surface z=200 is wave port with boundary condition $\overrightarrow{E} = \overrightarrow{e_y} \sin(\frac{\pi x}{72})$, and the rest boundary surfaces are perfect electric conductors. The frequency is $\omega = 6\pi$ GHz.

Test 1 includes uniform real parameters $\varepsilon_r = \mu_r = 1$. In the Test 2 the values $\varepsilon_r = 5$ for $0 < z < 100$ and $\varepsilon_r = 1$ for $100 < z < 200$ ($\mu_r = 1$ everywhere in Ω). The third test corresponds to complex parameters $\varepsilon_r = 1 - 0.1i$, $\mu_r = 1$.

The computations were made under double precision real arithmetics on the uniform grids with the number of parallelepipeds $N_p = 16^3, 32^3, 64^3$ which were divided into 6 tetrahedron. The stopping criterion was choosen for the iterative residual norm $\|r\| \leqslant \|f\| \cdot 10^{-7}$. The implementation of the iterative solvers was made for conventional compressed sparse row matrix format, see [8]. The tests have been performed using server with four Intel Itanium 2 processor and 64 GB of memory.

Table 1 demonstrates the maximum error ΔE for three test problems, obtained by FVM and FEM on the different grids. In FEM approximations, the accuracy is the same for $\vec{E}$ and A-V statement.

Table 2 demonstrates the number of iterations for preconditioned BiCGStab algorithm which are required for solving three test problems at different grids for FVM and FEM approximations. In FEM approach, the A-V formulations (11) was solved. For "electric" SLAE (10) the numbers of iterations are considerably bigger.

In Table 3 we present the computational resources which are necessary for solving Test 3 by iterative SCR method (for A-V variables in FEM statement (6), (11)) and direct PARDISO solver

from MKL [8]. Here N means the order of the SLAEs for different grids, T_1 and T_4 are execution times in seconds for one- and four-threads parallel implementations under OpenMP system, and MemGB is the required volume of memory in gigabyte. For 64^3 grid, the PARDISO solver fails because of memory deficit. Let us remark, that in the last experiments the implementation of SCR solver was done by using SPARS BLAS computational tools from MKL. This technology helps to save code execution time about 50%.

Table 1: The errors of numerical solution.

N_p	Test 1		Test 2		Test 3	
	FEM	FVM	FEM	FVM	FEM	FVM
16^3	$7.1 \cdot 10^{-1}$	$1.6 \cdot 10^{0}$	$2.6 \cdot 10^{-1}$	$1.0 \cdot 10^{0}$	$6.7 \cdot 10^{-1}$	$1.7 \cdot 10^{-1}$
32^3	$2.7 \cdot 10^{-1}$	$2.8 \cdot 10^{-1}$	$1.4 \cdot 10^{-1}$	$5.5 \cdot 10^{-1}$	$3.1 \cdot 10^{-1}$	$4.1 \cdot 10^{-2}$
64^3	$1.1 \cdot 10^{-1}$	$6.4 \cdot 10^{-2}$	—	$7.9 \cdot 10^{-2}$	$1.6 \cdot 10^{-1}$	$1.0 \cdot 10^{-2}$

Table 2: Number of iterations for different approaches.

N_p	Test 1		Test 2		Test 3	
	FEM	FVM	FEM	FVM	FEM	FVM
16^3	173	53	1169	225	242	112
32^3	402	96	2240	356	509	216
64^3	—	154	—	531	1544	395

Table 3: Test 3: computational resources for different solvers.

Grid	N	SCR				Pardiso		
		n	T_1, sec	T_4, sec	$MemGB$	T_1, sec	T_4, sec	$MemGB$
16^3	59582	216	15.4	13.4	0.28	15.6	6.7	0.44
32^3	50009	411	664	495	3.73	865	302	5.78
64^3	4096766	988	—	17844	47.6	—	—	> 64

4. CONCLUSION

The comparative analysis of the presented results and many others numerical experiments allows to make the following conclusions:

- the FVM and FEM approaches provide approximately the same accuracy for considered test problems, including complex and piece-wise constant material properties, but the order of convergence for $h \to 0$ is the first one for FEM and the second one for FVM;
- in FVM case the algebraic properties of SLAE are better considerably which helps to obtain faster iterative solution;
- direct solver PARDISO is really competitive for relatively small SLAEs, but it fails for the very large orders;
- the variational A-V statement has the considerable advantage compared to FVM for $\vec{E}$ formulation, because of better algebraic properties of SLAE.

REFERENCES

1. Monk, P., *Finite Element Methods for Maxwell's Equations*, Oxford University Press, New York, 2003.
2. Soloveichik, Y. G., M. E. Rojak, and M. G. Persova, "Finite element method for solution of scalar and vector problems," *Novosibirsk*, NSTU Publ., 2007 (in Russian).
3. Il'in, V. P. and A. V. Petukhov, "On numerical solution of the complex Helmholtz equation," *Rus. J. Num. Anal. and Math. Modell.*, Vol. 22, No. 1, 19–37, 2007.

4. Dyczii-Eslinger, R., G. Peng, and J.-F. Lee, "A fast vector-potential method using tangentially continuous vector finite elements," *IEEE Trans. on Microwave Theory and Tech.*, Vol. 46, No. 6, 863–867, 1998.
5. Greif, C. and D. Schotzau, "Preconditioners for the discretized time-harmonic Maxwell equations in mixed form," *Numer. Linear. Alg. Applic.*, Vol. 14, 281–297, 2007.
6. Petukhov, A. V., "Solution of 3D complex Helmholtz equation by barycentric finite volume method," *Autometria*, No. 2, 112–123, 2007 (in Russian).
7. Il'in, V. P., "Finite element methods and technologies," *Novosibirsk*, NCC Publ., 2007 (in Russian).
8. http://www.mvs.icc.ru/documentation/mkl.

Experimental Characterisation of Radiowave Signal Propagation for Indoor UWB Wireless Communications

T. H. Loh and L. R. Arnaut
National Physical Laboratory, United Kingdom

Abstract— A methodology is presented for experimental characterisation of ultra wideband (UWB) signal propagation in an indoor propagation environment for wireless communication networks. Time-harmonic S-parameters measurement is reported of radiowave propagation and scattering inside a typical indoor office environment between 500 MHz and 3000 MHz (which covers, in particular, the GSM and ISM bands), measured across a scanned sample volume. The main objective of these indoor radiowave propagation measurements is to determine the effect of location and multipath on radiowave propagation with different propagation channels. A 1×1 Single-input-single-output (SISO) and 2×1 multiple-input-single-output (MISO) channels measurements were methodically carried out to simplify the propagation channels considered. A data acquisition system, based upon a vector network analyzer and multichannel antenna array is described, together with its use to collect channel measurement matrices.

1. INTRODUCTION

Over the past two decades the market for short-range wireless office information networks such as the IEEE 802.11a/b/g/n wireless local area network (WLAN), IEEE 802.15.1 Bluetooth, and IEEE 802.15.4 ZigBee, has grown rapidly in response to consumer demand. This has been exploited and has encouraged, in recent years, extensive research activities in the application of UWB systems as a solution for the high-capacity requirements of short-range indoor wireless applications and the application of multiple-input-multiple-output (MIMO) channels for these wireless systems, due to their rich scattering nature that provides improved spectral efficiencies and increased network capacity. Due to the complexity of scattering and diffraction characteristics of localised objects, frequency dispersion of UWB communications, and the variety of types of propagation environments, large efforts have been expended on their characterisation, both theoretically and experimentally ([1–4]), yet much work remains to be done. To achieve the capacity increase envisaged for future mobile radio systems, it is necessary to exploit the entire spatial-temporal characteristics of the propagation channel. Accurate characterisation of the indoor environment propagation model for the propagation channel relies on extensive precision measurement methods and data collection, which will take into account all electromagnetic aspects on a firm physical basis and be rooted in accurate yet sufficiently simple models to be of practical use.

An extensive and systematic measurement campaign on the effect of location and multipath effects on radiowave propagation for UWB signals was conducted inside an office environment at the U.K. National Physical Laboratory (NPL). SISO and MISO continuous-wave (CW) indoor transmission was measured and sampled, respectively, across a scanned volume inside the room and across a scanned area at a fix height. Furthermore, since the CW fields measured inside the office consist of direct and indirect multipath fields and the scattered field analysis enables quantification of the room effect on the propagation characteristics, the SISO measurement setup in the office was carefully replicated inside a fully anechoic room (FAR) at NPL, with identical input power and measurement setup. Measurement in a FAR provides a fair approximation to the direct path field of the propagation inside the office; the differences in the corresponding complex S-parameter values between the office and the FAR give the multipath field component for each scanned position and frequency.

2. EXPERIMENTAL DETAIL

The measurements were performed inside an unoccupied office, with a size of $5.895\,\mathrm{m} \times 4.427\,\mathrm{m}$ and a height of 2.685 m, located on the first floor in a two-storey building with offices and laboratories. As depicted in Fig. 1(b), the empty office was equipped with typical office furniture, such as swivel chairs, surround desk and metallic under-desk drawer units. Apart from the glass wall between the office and the building interior corridor the office is surrounded by plasterboard walls adjoining other offices. There is a double-glazed window between the office and the building exterior. The floor defines the reference height $Z_0 = 0$ and is concrete and carpeted. The ceiling is suspended

with a 0.6 m square grid of thin metal ribs. To enhance the multipath scattering effects, during the measurement, all the measurement instruments are considered as part of the room by locating inside the room. The measurement system consists of a standard desktop computer, a Rohde & Schwarz ZVB8 four-port vector network analyzer (VNA), three Schwarzbeck SBA9113 wideband omnidirectional biconical broadband antennas, a two-axis positioner and computer controlled DIGIPLAN stepping motor drives control module.

All the measurements are conducted in the frequency domain across the frequency band from 500 MHz to 3000 MHz, in steps of 12.5 MHz, with the aid of the VNA, which provides a synthesized microwave source, and delivered to and received from the biconical antennas through coaxial cables. The VNA settings were: source power +13 dBm, frequency band sweep time 1 second and RF resolution bandwidth 1 kHz. For SISO measurements two identical vertically polarized biconical antennas were used to form a 1×1 propagation channel where VNA Port 1 and Port 2 were the transmitting and receiving terminals respectively; for MISO measurements three identical biconical antennas were used to form a 2×1 propagation channel, where VNA Ports 1 and 3 were the transmitting and receiving terminals respectively. It is noted that for MISO measurements the receiving antenna was vertically polarized whereas the two transmitting antennas were either both vertically or horizontally polarized or a combination of both. Full two- (SISO) and three-port (MISO) calibrations were performed to take the losses of coaxial cables into account.

For both SISO and MISO measurements, the receiving antenna was fixed at the corner of the office while the transmitting antennas were mounted on a fiberglass tube at a fixed but manually adjustable height. They were moved horizontally during the experiments with a uniform 5 cm × 5 cm grid within an area of 75 cm × 75 cm, by using a planar computer-automated XY-scanning system placed on the floor at the middle of the room. For SISO measurements, 25 different heights were performed between 0.5 m and 1.7 m with a 5 cm increment, which yields 6400 spatial sample points per frequency. By contrast, for MISO measurements only one height at 1.3 m was considered, which yields 256 spatial sample points per frequency for each polarisation combination of two vertically

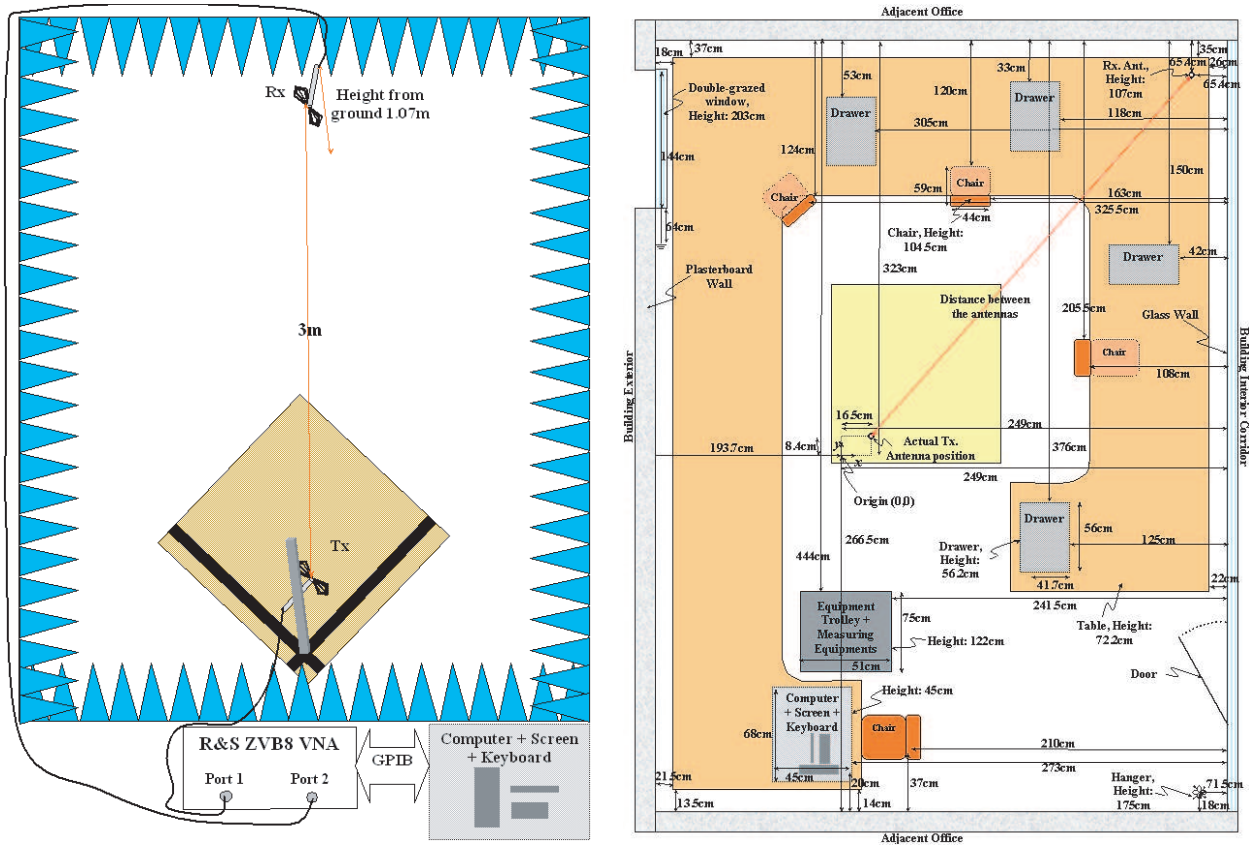

(a) (b)

Figure 1: The measurement setup and layout for: (a) the fully anechoic range, and (b) the indoor office.

oriented transmitting antennas where Antenna 1 and 2 are located at 1.3 m and 1.45 m, respectively. The objective of these experiments was to determine the effect of location and multipath effects on radiowave propagation. The XY-scanning system was formed by two single-axis stepping motors mounted together, which creates a virtual antenna array by moving the antenna across the user specific pre-programmed locations. The complex S-parameters from the VNA were stored on the computer. To avoid the variations of the channel during the acquisition time, measurements were exclusively performed early in the morning and late at night so the surrounding environment was kept stationary by preventing movements close to the antennas caused by personnel passing by, and minimize external interference by electronic equipment in adjacent office spaces. The FAR in NPL has a dimension of $9\,\mathrm{m} \times 6\,\mathrm{m} \times 6\,\mathrm{m}$. This room is fully lined with ferrite tiles, fully covered with 1 m hybrid pyramidal foam absorber, except for a central corridor on the floor that was covered with Riken 10 cm ferrite pyramids. Fig. 1(a) shows the FAR measurement setup for SISO measurements.

3. EXPERIMENTAL RESULTS

The measured SISO CW field obtained from the office indoor propagation measurement contains both direct path and multipath reflected field, hence the multipath field can be obtained by subtracting coherently, for each scanned position at each frequency point, the corresponding measured S-parameter of the FAR from the office:

$$S_{ij}^{\mathrm{Multipath}}(f,\Omega) = S_{ij}^{\mathrm{Office}}(f,\Omega) - S_{ij}^{\mathrm{FAR}}(f,\Omega), \quad (i,j=1,2) \tag{1}$$

where f, $\Omega = (x,y,z)$, i and j represent the frequency, spatial coordinates, VNA receiving port and driving port respectively. It is noted that Equation (1) assumes that $S_{ij}^{\mathrm{FAR}} = S_{ij}^{\mathrm{Direct\ Path}}$ and $S_{ij}^{\mathrm{Office}} = S_{ij}^{\mathrm{Direct\ Path+Multipath}}$. As the absorber in the FAR is imperfect there will be standing wave, which could course error of S_{ij} up to $\pm 2\,\mathrm{dB}$. Figs. 2(a) and (b) show the magnitude of measured S_{21} for all measurement points in the office and in the FAR, respectively. Figs. 3(a) and (b) show, respectively, the corresponding multipath field obtained after subtraction using Equation (1) and the comparison between the experimental cumulative distribution function (CDF) of $|S_{12}^{\mathrm{Multipath}}(f,\Omega)|^2$ at 3 GHz for a subset of all measurement points and the statistical model.

The statistical model used here is a gamma distribution Γ, for the scattered transmitted power P, whose probability density function and CDF are given as [4]

$$f_P\left(p;\frac{M}{2},\theta\right) = \frac{p^{\frac{M}{2}-1}e^{-\frac{P}{\theta}}}{\theta^{\frac{M}{2}}\Gamma\left(\frac{M}{2}\right)} \quad \text{and} \quad F_P\left(p;\frac{M}{2},\theta\right) = \frac{\gamma\left(\frac{M}{2},\frac{p}{\theta}\right)}{\Gamma\left(\frac{M}{2}\right)} \tag{2}$$

respectively, with incomplete gamma function, γ, and ensemble average given by $\langle P\rangle = \theta M/2$, in which θ is a scale parameter, and M is a free distribution parameter. In Fig. 3(b), Γ for selected values of M are shown and χ_2^2 denotes the chi-squared distribution with 2 degrees of freedom. It was shown that the best fit was obtained for $M = 2$. Figs. 4(a) and (b) show the comparison between

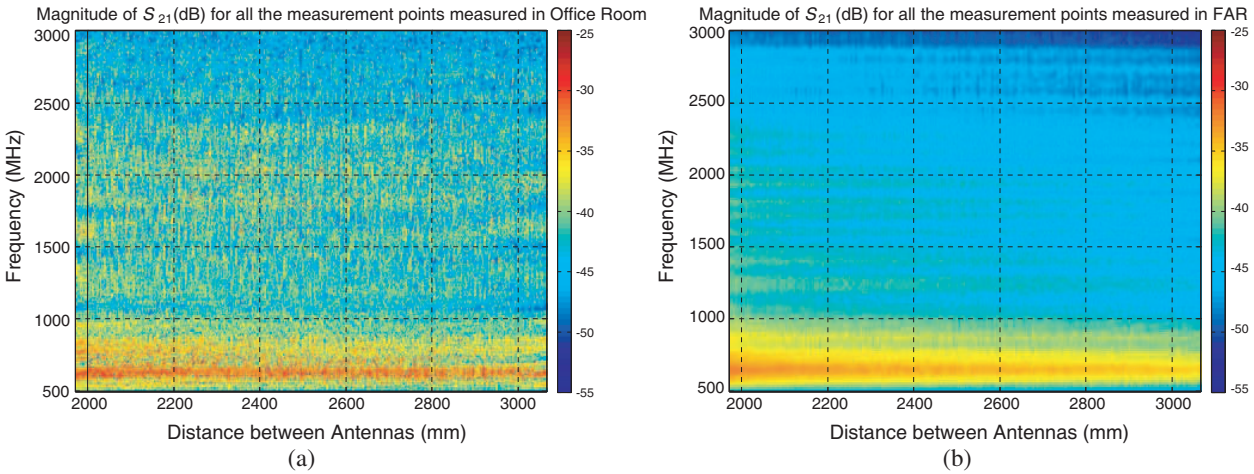

Figure 2: The magnitude of S_{21} for SISO propagation channel measured in (a) office and (b) FAR.

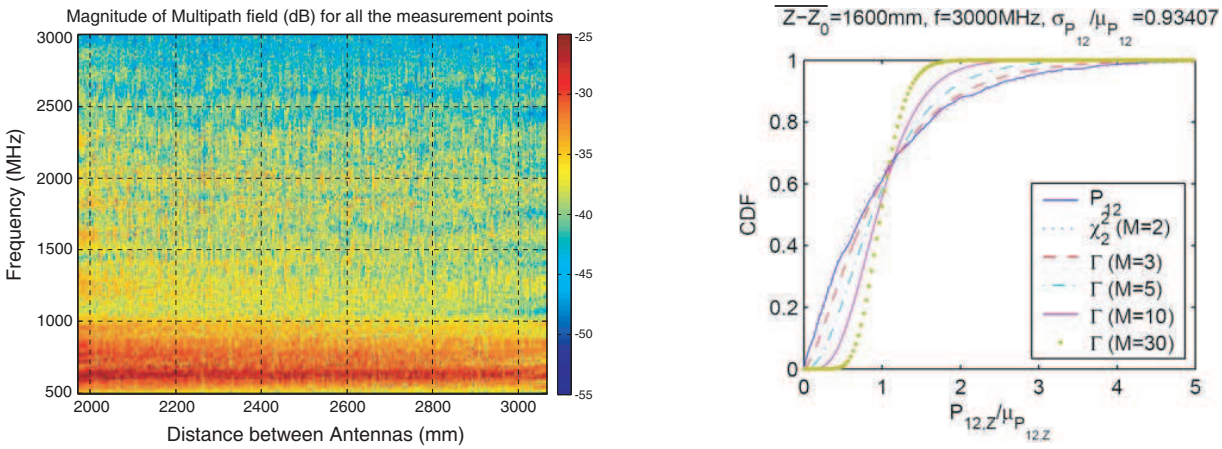

Figure 3: (a) The scattered field of the office; (b) cumulative distribution function of $|S_{12}^{\text{Multipath}}(f,\Omega)|^2$ at $f = 3\,\text{GHz}$ for $Z - Z_0 = 1.5 \ldots 1.7\,\text{m}$ with $0.05\,\text{m}$ increment (i.e., 5 consecutive planes with $256 \times 5 = 1280$ total number of points).

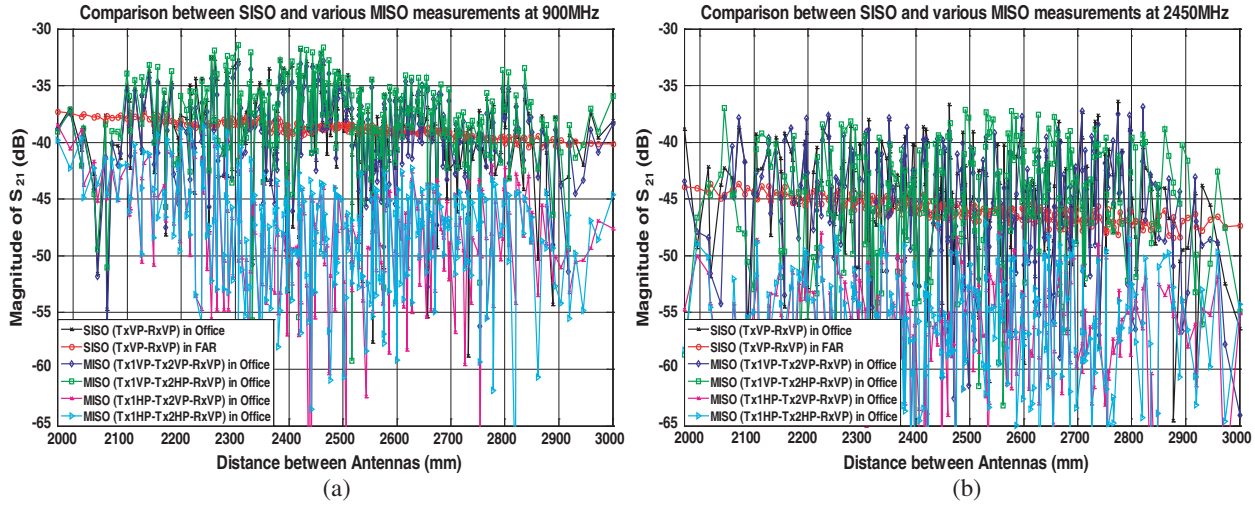

Figure 4: Comparison between the magnitude of S21 for various SISO and MISO propagation channel measurements at: (a) 900 MHz (GSM band), (b) 2450 MHz (ISM band).

the magnitude of the measured S_{21} for various SISO and MISO propagation channel respectively at GSM and ISM band. From the results, it is observed that there is some increase in signal level across most of the scanned points due to the multipath effects as a result of the introduction of an extra antenna where the polarisation combination of the transmitting antennas plays an important role.

4. CONCLUSION

We have presented a methodological approach to assess the UWB signal-propagation-channel in an indoor office environment using an additional set of carefully replicated SISO measurements, in a FAR, that separate the direct-path and the multi-path signals. This approach simplifies the analysis and reduces the measurement uncertainties. A fixed receiving antenna was used and detailed measurements of the propagation characteristics within the office environment for SISO (volume scan) and MISO (area scan at a fixed height) were conducted over 0.5 GHz to 3 GHz. Results presented for the two analysis scenarios show, as expected, that there is significant spatial dependence of the quality of a channel link due to multi-path interference and the measured scattering distributions near the middle of the office can be fairly closely approximated by a gamma distribution with $M = 2$, demonstrating that the S_{21} have a circular Gauss normal distribution. These data can be made available on request for further analysis. The addition of a second antenna (MISO

case) can improve the channel link in the GSM and ISM bands where the polarisation combination of the transmitting antennas plays an important role and their influence is suggested to be the future work. The results are useful in the study and mitigation of signal outages and bit error rates in indoor environments for the deployment of short-range wireless office information and sensor networks.

ACKNOWLEDGMENT

This work was supported by the 2006–2009 Physical programme of the National Measurement System Policy Unit of the UK Department for Innovation, Universities and Skills (DIUS) under Project 109962.

REFERENCES

1. Andersen, J. B., J. O. Nielsen, G. F. Pederson, G. Bauch, and M. Herdin, "Room electromagnetics," *IEEE Antennas Propag. Mag.*, Vol. 49, No. 2, 27–33, 2007.
2. Cramer, R. J.-M., R. A. Scholtz, and M. Z. Win, "Evaluation of an ultra-wide-band propagation channel," *IEEE Trans. on Antennas Propag.*, Vol. 50, No. 5, 561–570, 2002.
3. Cassioli, D., M. Z. Win, and A. F. Molisch, "The ultra-wide bandwidth indoor channel: From statistical model to simulations," *IEEE J. Selec. Areas Comm.*, Vol. 20, No. 6, 1247–1257, 2002.
4. Arnaut, L. R., T. H. Loh, and B. O. Peters, "Statistical experimental characterisation of indoor radio wave propagation in an office environment," *COST 2100 Report TD (08) 403*, Wroclaw, Poland, 2008.

Performance of Wireless Communication System with Ultrawideband Chaotic Signals in the Multipath Channel

L. V. Kuzmin[1], **S. O. Starkov**[2], **and A. V. Kletzov**[3]

[1]Institute of Radio Engineering and Electronics of the RAS, Russia
[2]Obninsk State Technical University for Nuclear Power Engineering, Russia
[3]Moscow Institute of Physics and Technology (State University), Russia

Abstract— Performance of wireless communication scheme with ultrawideband chaotic signals in the multipath channel is evaluated. We consider channel models based on multipath channel models elaborated by IEEE 802.15 working group for high bitrate (IEEE 802.15.3a channel model) and low bitrate (IEEE 802.15.4a channel model) ultrawideband wireless communication systems. Pathloss and waveform of chaotic radio pulses propagating over multipath channel are experimentally measured as characteristics determining the achievable distance range between transmitter and receiver and achievable bitrates in the presence of additive Gaussian noise.

1. INTRODUCTION

Chaotic signals as information carrier for communication systems are widely studied theoretically and experimentally since 1990 when a special type of chaotic synchronization was introduced [1], where chaotic synchronous response was studied as a possible method for information transmission. Further investigations showed that chaotic synchronization has low immunity to the channel distortions [2] as a result, performance of such systems is significantly worse than performance of traditional communication systems.

Essential practical profit was achieved when the direct chaotic communication scheme (DCCS) was introduced and experimentally approved [2, 3]. DCCS means that chaotic signal is generated and modulated in microwave band without intermediate heterodyning. Such a scheme belongs to wideband or ultrawideband (UWB) communication systems, in which chaotic radio pulses are used as information symbols. It was shown that performance of DCCS in AWGN channel is comparable (a little bit worse) with the performance of communication systems based on orthogonal signals. DCCS scheme allow to design high-bitrate systems [2, 3] as well as low-bitrate ones [4]. This is so due to possibility to design effective sources of chaotic signals of microwave band [5–7].

Recently the DCCS performance was numericaly evaluated in multipath channels [8, 9], in which achievable bitrates in the presence of significantly dominating multipath interference were estimated. The subject of this work is to experimentally analyze the influence of multipath propagation on chaotic radio pulses and evaluate DCCS performance in the presence of additive Gaussian noise.

2. DCCS STRUCTURE AND CHANNEL MODEL

The structure of DCCS physical layer [2] is depicted in Fig. 1. Basically DCCS modulator implements "On-Off" keying (OOK) modulation scheme: chaotic radio pulse of length τ_p is emitted to transmit symbol "1" and is not emitted to transmit symbol "0". Between chaotic radio pulses a guard interval of length τ_g is inserted to prevent intersymbol interference. DCCS also allows to use pulse position modulation or combination of these methods.

Realistic channel models make possible to adequately evaluate wireless system performance and allow to compare it with systems of other type. Channel model considered here for numerical evaluation of DCCS performance is based on the UWB channel models adopted by working groups developing high bitrate [10] and low bitrate [11] wireless channel model for UWB communication systems:

$$y(t) = h(t) \otimes s(t) + n(t) \tag{1}$$

where $s(t)$ — signal emitted by transmitter to an air; $h(t)$ — channel impulse-response; $\otimes$ means convolution; $n(t)$ — additive Gaussian noise; $y(t)$ — signal at the receiver input.

Channel impulse-response $h(t)$ corresponds to $h^{(i)}(t)$ channel realization for some relative position of transmitter and receiver, some geometrical size of accommodations and some indoor layouts

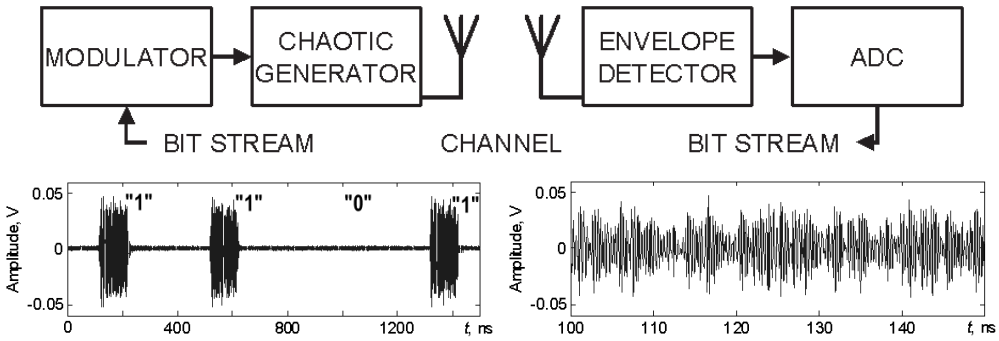

Figure 1: The structure of DCCS physical layer (top), chaotic radiopulses encoding symbols "1 1 0 1" (left) and chaotic signal waveform within the pulses (right).

described by the models [10, 11]:

$$h^{(i)}(t) = X^{(i)} \sum_{l=0}^{L} \sum_{k=0}^{K} \alpha_{k,l}^{(i)} \delta \left(t - T_l^{(i)} - \tau_{k,l}^{(i)} \right) \tag{2}$$

where i-th channel realization of response function $h^i(t)$ to δ-pulse is formed as a sum of statistically distributed amplitudes $\alpha_{k,l}^{(i)}$ of paths; $\{T_l^i\}$ is the delay of the lth cluster, $\{\tau_{k,l}^i\}$ is the delay of the kth multipath component relative to the lth cluster arrival time (T_l^i). The value $\{X_i\}$ represents the log-normal shadowing, and i refers to the ith realization. See [10, 11] for details regarding model's parameters and distributions of time intervals $(T_l - T_{l-1})$ and $(\tau_{k,l} - \tau_{(k-1),l})$ between the cluster and the path arrival delays respectively.

Channel model [10] for high bitrate systems (wireless piconets where bitrate is varied from 110 Mbps to 480 Mbps) describes four situations: CM1 is LOS channel, range up to 4 m between transmitter and receiver; CM2 is NLOS, up to 4 m; CM3 is NLOS, 4 m to 10 m and CM4 is NLOS, 4 m to 10 m.

For low bitrate wireless communication systems (wireless personal area networks, e.g., sensor networks), channel models [11] describe nine different multipath environments: residential (CM1, 2), office (CM3, 4), outdoor (metropolitan suburban CM5, 6), industrial (CM7, 8), farm (CM9) and near human body. Model with odd numbers describe LOS situation, even — NLOS.

Multipath propagation leads to intersymbol (interpulse) interference, so if the guard interval length τ_g between pulses is less than the length of impulse channel response, the receiver gathers not only the energy of the current pulse but also a fraction of energy of the previous pulse.

For UWB signal correlation time Δt_c is inversely proportional to the signal bandwidth Δf, i.e., $\Delta t_c = 1/\Delta f$. So, chaotic signal (Fig. 1 (at the right)) generated by transistor oscillator [6] with autocorrelation function depicted in the Fig. 2 has correlation time $\Delta t_c = 1$ ns, which means that paths coming into receiver with delays longer than the correlation time are summed noncoherently and play a role of interference with respect to the next pulse. It allows us to introduce the signal to interference ratio SIR for the current pulse as follows:

$$SIR = 10 \lg \left(\frac{P_S(d)}{P_N + P_M(R)} \right) \tag{3}$$

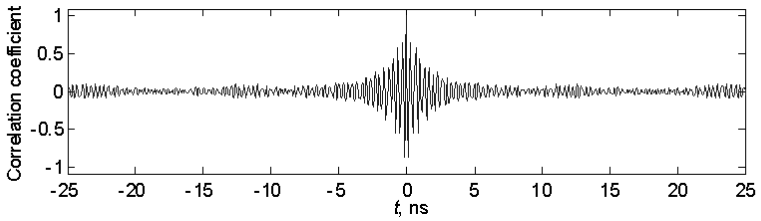

Figure 2: Autocorrelation function of the chaotic signal in the Fig. 2.

where P_S is signal power of the direct path at the receiver; P_N is additive Gaussian noise power; $P_M(R)$ is the power of multipath interference from previous pulse for the bitrate $R = 1/(\tau_p + \tau_g)$.

3. EXPERIMENTAL ESTIMATION OF CHAOTIC RADIO PULSE PROPAGATION

In order to experimentally demonstrate the multipath tails of chaotic radio pulses limiting bitrates (and to estimate the SIR value), to obtain experimental proof of nocoherent summation of paths, to analyze variability of chaotic pulse envelope at the receiver output for different propagation conditions and for different distances between transmitter and receiver, we carried out the following experiment.

The scheme of experimental setup is depicted in Fig. 3. It consists of a transmitter of chaotic radio pulses, logarithmic UWB receiver and oscilloscope to record signal waveforms (Fig. 3, bottom) for further computer analysis. Chaotic pulse length is $\tau_p = 100$ ns. Guard interval between pulses is $\tau_g = 300$ ns.

Experiments were carried out in office conditions: in a corridor (height 4 m, length 40 m, width 3 m) and in a conference hall (length 20 m, height 4 m, width 16 m). The distance d between transmitter and receiver was varied from 1 to 20 m in the corridor and from 1 to 14 m in the conference hall. Transmitter and receiver were located at the one meter height above floor in the corridor and at the two meters in the conference hall.

Experimental results are depicted in the Fig. 4, where the averaged envelopes of chaotic radio pulses for different distances d between transmitter and receiverat are shown at the left for the corridor and for the conference hall at the right.

The pathloss P_L was calculated with the use of averaged envelopes of chaotic radio pulses. Amplitude of the pulse envelope are proportional to the pulse power, so the ratio of the given envelope amplitude to the amplitude of the envelope corresponding to the $d = 1$ m (upper curves) is the pathloss for the given channel.

Calculated pathloss P_L is depicted in the Fig. 5, where the pathloss in the corridor and in the conference hall are shown at the left and at the right respectively. Experimental pathloss estimates are rather good approximated by theoretical pathloss low $P_L(d) = -10n \lg(d/d_0)$, where $d_0 = 1$ m and $n = 1.75$ for the corridor and $n = 1.3$ for the conference hall. Obtained pathloss exponent values are close to the corresponding values estimated for LOS channels of IEEE 802.15.4a model [11].

Averaged envelope waveform remains the same at all distances between transmitter and receiver, which indicates good averaging of the power of paths coming to receiver. It permits to conclude that dependence of BER as a function of the guard interval τ_g, i.e., bitrate, will remain the same for different distances between transmitter and receiver. It also should be noted that pathloss function

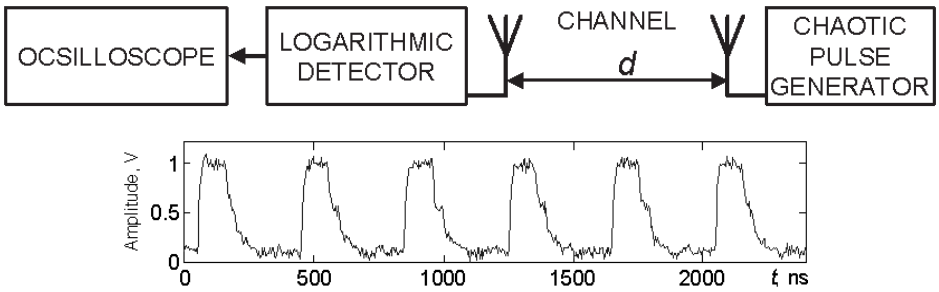

Figure 3: The scheme of experimental setup (top) and the envelope of chaotic pulses at the logarithmic detector output (bottom).

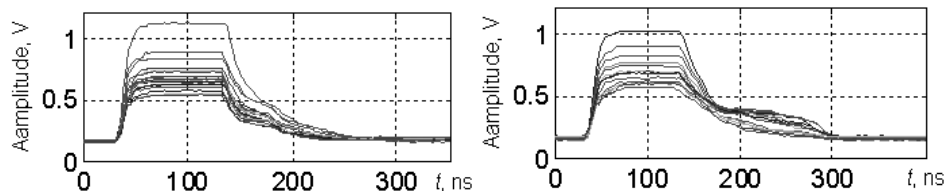

Figure 4: Averaged envelopes in the corridor (left) and in the conference hall (right): upper curve corresponds to the minimum distance $d = 1$ m, lower one corresponds to the maximum d.

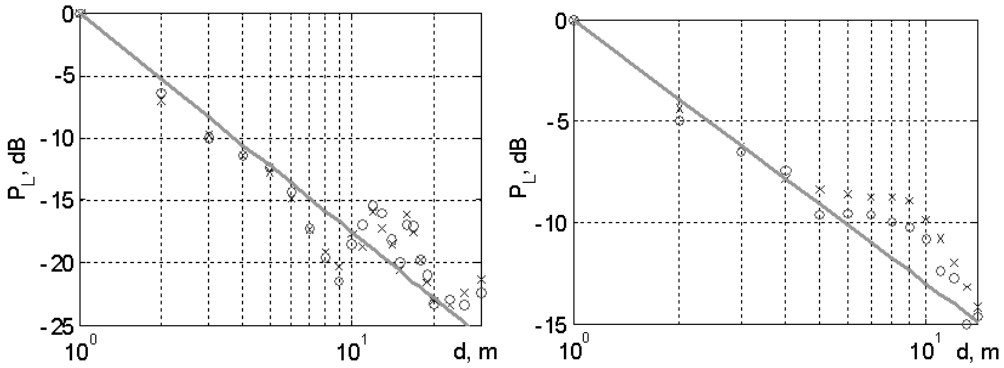

Figure 5: Pathloss P_L in the corridor (left) and in the conference hall (right).

shows no signs of small-scale fading-caused notches.

4. DCCS PERFORMANCE

Performance characteristic, we are finally interested in, is the BER as function of bitrate for given E_b/N_0 ratio and the BER as function of E_b/N_0 for the given bitrate, i.e., for given τ_p, τ_g and for signal bandwidth Δf. Experimental estimation of chaotic radio pulse propagation permits to make prediction regarding DCCS performance for the real channels.

Noncoherent receiver gathers energy within the pulse length τ_p and decides what symbol it receives: "0" or "1". It is assumed that the symbol synchronization is established between transmitter and receiver. Due to noncoherent summation of paths the pulse power can be estimated as a sum of the paths power within time interval τ_p, i.e., $P_R = \sum_{l=0}^{L_p} \sum_{k=0}^{K_p} \alpha_{k,l}^{(i)}$, where L_p and K_p is the number of clusters and paths respectively coming in receiver within time interval τ_p. L_p and K_p are determined by the multipath channel environment: the smaller channel dispersion, the larger pulse energy coming in receiver within time interval τ_p. So, in order to achieve maximum pulse power P_R, pulse length τ_p has to be matched with the channel impulse-response time. Under assumption that the channel impulse-response energy is normalized to unity, i.e., $\sum_{l=0}^{L} \sum_{k=0}^{K} \alpha_{k,l}^{(i)} = 1$ the P_R is the estimate of the energy loss due to signal dispersion. Numerical evaluations of this ratio are depicted in the Fig. 6 for IEEE 802.15.3a and IEEE 802.15.4a channel models.

As can be seen from Fig. 6 pulse energy loss rapidly decrease with increasing pulse length. Namely for pulse length $\tau_p = 10$ ns, for all channel types the energy loss is no more than 4 dB. For LOS channel of IEEE 802.15.3a model it is about 0 dB. The use of pulse length $\tau_p = 100$ ns permits to decrease energy loss to 0 dB for all channel types.

If the guard interval between chaotic pulses τ_g essentially exceeds the length of channel impulse response, multipath interference has no effect on BER because $P_M \ll P_N$. In this case the additive Gaussian noise plays a dominant role at the receiver and DCCS performance is the same as in AWGN channel [2] taking into account that the pulse energy E_p should be corrected according to the loss due to multipath dispersion (see Fig. 6). This is a typical situation for low bitrate wireless networks where the characteristic bitrates are about several Mbps.

Taking into account this energy loss estimate we can calculate link margin for multipath channels in the same style as by calculation of AWGN link margin, with corresponding pathloss exponents

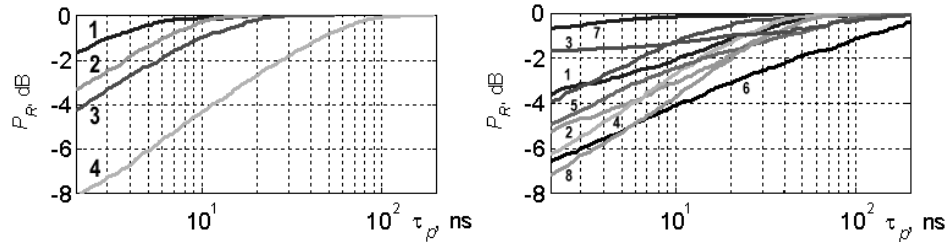

Figure 6: Loss of chaotic pulse energy due to multipath dispersion.

accounted for.

The second typical situation is that the power of multipath interference is much higher than the noise power. In this case the BER is governed by the power of multipath interference ($P_M \gg P_N$). This situation takes place in wireless piconets where transceivers are close to each other (i.e., $E_b \gg N_0$), the guard interval τ_g is comparable with the channel impulse-response length and achievable bitrates is about 30 Mbps [9] for the BER $= 10^{-4}$. The use of special receiving algorithms allows to achieve bitrates up to 100 Mbps [8].

5. CONCLUSIONS

Performance estimation shows that the proposed direct chaotic communication scheme is immune to signal propagation conditions in different channel environments, in particular in the channel with strong multipath conditions (NLOS with no dominating path that could be used to coherently receive the signal). In spite of its simple structure, simulations with realistic channel models show that DCCS is suitable for wireless local networks where multimedia data is transferred between network nodes, as well as for wireless sensor networks operating in complex propagation environment with low bitrates.

ACKNOWLEDGMENT

Authors acknowledge support from Russian Fund for Basic Research, grant No. 09-02-00983-a.

REFERENCES

1. Pecora, L. M. and T. L. Carroll, "Synchronization in Chaotic systems," *Phys. Rev. Lett.*, Vol. 64, No. 8, 821–824, 1990.
2. Dmitriev, A. S., B. E. Kyarginskii, A. I. Panas, and S. O. Starkov, "Plain scheme of chaotic-carrier data communications at microwave frequencies," *J. Communications Technology and Electronics*, Vol. 46, No. 2, 224, 2001.
3. Dmitriev, A. S., B. Y. Kyarginsky, A. I. Panas, et al., "Experiments on ultra wideband direct chaotic information transmission in microwave band," *Int. J. Bifurcation and Chaos*, Vol. 13, No. 6, 1495, 2003.
4. Dmitriev, A. S., E. V. Efremova, A. V. Kletsov, et al., "UWB wireless communications and sensor networks," 2008.
5. Andreyev, Y. V., A. S. Dmitriev, E. V. Efremova, et al., "Qualitative theory of dynamical systems, chaos and contemporary communications," *Int. J. Bifurcation and Chaos*, Vol. 15, No. 11, 3639–3651, 2005.
6. Dmitriev, A. S., E. V. Efremova, N. A. Maksimov, and E. V. Grigor'ev, "Generator of microwave Chaotic oscillations based on a self-oscillating system with 2.5 degrees of freedom," *J. Communications Technology and Electronics*, Vol. 52, No. 10, 1137, 2007.
7. Dmitriev, A., E. Efremova, L. Kuzmin, and N. Atanov, "Forming pulses in non-autonomous chaotic oscillator," *Int. J. Bifurcation and Chaos*, Vol. 17, No. 10, 1–6, 2007.
8. Kuzmin, L. V., V. A. Morozov, S. O. Starkov, and B. A. Khadzhi, "Analysis of the interference immunity during reception of ultrawideband chaotic signals in an indoor multipath propagation environment," *J. Communications Technology and Electronics*, Vol. 51, No. 11, 1283, 2006.
9. Kuz'min, L. V. and V. A. Morozov, "Statistical characteristics of an ensemble of ultrawideband communications channels under the conditions of multipath signal propagation in rooms," *J. Communications Technology and Electronics*, Vol. 54, No. 3, 313–322, 2009.
10. Channel Modeling Sub-committee Report Final. November 2002. IEEE P802.15 Working Group for Wireless Personal Area Networks (WPANs). http://grouper.ieee.org/groups/802/15/pub/2002/Nov02/02490r0P802-15_SG3a-Channel-Mo-deling-Subcommittee-Report-Final.zip.
11. Channel Modeling Sub-committee Report Final./IEEE P802.15.4a Working Group for Wireless Personal Area Networks (WPANs), Dec. 2004. http://grouper.ieee.org/groups/802/15/pub/0-4/15-04-0662-02-004a-channel-model-final-report-r1.pdf.

Experimental Generation of Chaotic Oscillations in Microwave Band by Phase-locked Loop

A. S. Dmitriev, **A. V. Kletsov**, **and L. V. Kuzmin**
Institute of Radio Engineering and Electronics of the RAS, Russia

Abstract— The problem of generation of ultrawideband phase-chaotic signal in microwave band by the phase-locked loop is considered. Mathematical simulation of the third order phase-locked loop taking into account realistic characteristics of the phase detector, frequency dividers and voltage controlled oscillator is carried out. Simulations allow to estimate parameter's values of the experimental phase-locked loop testbed to be operated in chaotic mode. Based on the obtained numerical results and standard electronic elements the phase-locked loop testbed generating UWB phase-chaotic signal with even power spectrum in 700–1300 MHz band was developed and experimentally tested.

1. INTRODUCTION

One of prospective types of ultrawideband (UWB) signals that are going to be widely used in a number of applications [1–3] are chaotic signals. Chaotic signal is used in direct chaotic communication scheme suggested in IRE of RAS [4–6] in which chaotic radio pulses are used as a data carrying signal. The direct chaotic wireless data transmission scheme was included in the IEEE 802.15.4a standard on a UWB local wireless communications as optional [7] solution for physical layer of homogeneous wireless networks.

In order to obtain chaotic oscillations transistor chaos generators [8, 9] based on the oscillating systems with small number of degrees of freedom are typically used in the direct chaotic communication scheme. During last years design techniques of such generators are well developed and they are used in compact transceivers [10].

Transistor chaotic sources generate so name amplitude chaos, i.e., chaotic signal with irregular envelope. However for some applications, it is more preferable to use not amplitude, but the phase chaos, i.e., signals with remains almost constant envelope and the chaotically varied phase.

The phase-locked loop (PLL) operating in a chaotic mode can be used for phase-chaotic generation, i.e., when chaotic signal $X(t)$ with chaotically varied phase $\varphi(t)$ and constant envelope is generated by PLL. Waveform of shuch signal is described by the relation:

$$X(t) = A\sin(\omega_0 t + \varphi(t)) \tag{1}$$

where $\varphi(t) = 2\pi\alpha \int_{t_0}^{t} y(p)dp$, α is the VCO sensitivity, $y(t)$ is the signal which is fed to the voltage controlled oscilator (VCO) input from loop filter of PLL; A is the amplitude of phase-chaotic signal, ω_0 is the natural frequency of voltage controlled oscillator, t is time.

The subject of this work is to experimentally find chaotic modes in the PLL with structure which is similar to the PLL structure used in the microwave electronic devices. In order to do this we firstly consider the mathematical model taking into account specific properties of such PLLs and based on this model we determine parameters of PLL testbed.

2. MATHEMATICAL MODEL

The considered structure of PLL is represented in the Fig. 1. It consists of VCO, master oscillator (MO), phase detector (PD), loop filter (LF), two frequency dividers (FD) and amplifier (AA) with variable gain.

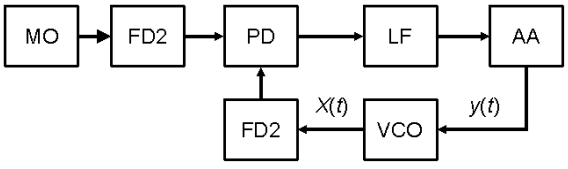

Figure 1: The structure of considered PLL.

PLL chaotic dynamic was in details studied for sinusoidal nonlinear characteristic of PD: $F(\varphi) = \sin(\varphi)$ [11–13]. Here we consider characteristic of PD in the following form:

$$F(\varphi) = \begin{cases} \frac{2}{\pi}(\varphi - \frac{\pi}{2}), & 0 < \varphi < \pi \\ 0, & \pi < \varphi < 2\pi \end{cases} \tag{2}$$

It corresponds to the realistic characteristic of PD [14, 15] used in the modern communication systems.

Dimensionless mathematical model of PLL with second order loop filter is described by the third order ordinary differential equation:

$$\mu\varphi + \varepsilon\dddot{\varphi} + \ddot{\varphi} = \gamma - F(\varphi), \tag{3}$$

where γ, μ, ε are PLL parameters, which are as follows [14]

$$\mu = \left(\frac{\Omega_h}{m}\right)^2 LC, \quad \varepsilon = \frac{\Omega_h}{n} RC, \quad \gamma = \frac{n}{\Omega_h}\left(\frac{\omega_{mo}}{m} - \frac{\omega_0}{n}\right), \tag{4}$$

where Ω_h is the frequency holding range; R, L, C are the resistance, inductance and capacity respectively, consisting of the second order low-pass filter (LPF); m and n are division factors of frequency dividers FD1 and FD2 respectively; ω_{mo} is the frequency of the MO.

3. SIMULATIONS

Simulation's goal was to estimate parameter's values where chaotic modes exist in the sufficiently wide values range. In order to achieve this we consider the PLL with low-pass filter having Q-factor ($Q = \sqrt{\mu}/\varepsilon$) equals to 10 due to the fact that increasing the Q-factor value from 1 to 10 allowed to significantly extent chaotic zones for all values of parameter γ [14, 15].

Finally it allows to extend the areas of system parameters values where chaotic oscillation modes could appear without essential complication of PLL system.

Bifurcation analysis was carried out for the parameter γ because as can be seen from (4) this is only one parameter, which can be easily varied in the experiment by means of changing m and n.

The analysis showed that oscillatory chaos exists for small values of γ (Fig. 2(a)), wide zones of oscillatory-rotatory chaos for $\gamma \in (0.15, 0.65)$ appears (Fig. 2(b)) and rotatory chaos for $\gamma \sim 0.7$ takes place (Fig. 2(c)).

According to these results and taking into account the relation of dimensionless parameters (4) with parameters of PLL testbed to be developed we estimated that variation of division factor m in the range $14 \ldots 19$ permits to obtain the oscillatory-rotatory mode in experiment. This mode is most preferable from the point of view of statistical and spectral properties of chaotic signal $X(t)$ [16].

The power spectrum density of the signal at the VCO output $X(t)$ for oscillatory-rotatory mode we are finally interested in is depicted in the Fig. 3.

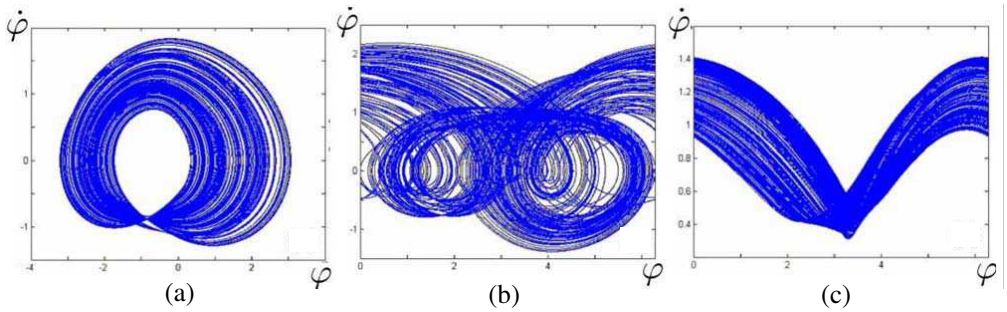

Figure 2: Phase portraits in the plane $(\varphi, \dot{\varphi})$ for $\mu = 3$, $\varepsilon = 0.35$: (a) oscillatory mode, $\gamma = 0.03$; (b) oscillatory-rotatory mode, $\gamma = 0.3$; (c) rotary mode, $\gamma = 0.704$.

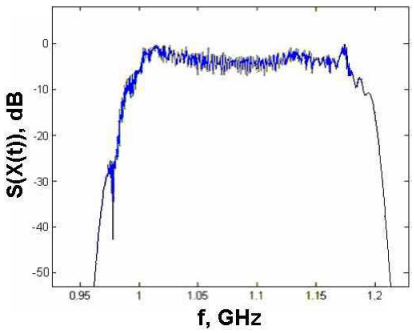

Figure 3: Typical power spectrum of VCO output signal $X(t)$ for $\mu = 10.6$, $\gamma = 0.6$ and $\varepsilon = 0.35$.

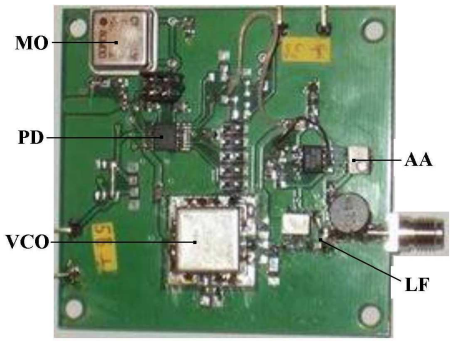

Figure 4: Testbed layout.

4. PLL TESTBED

The testbed layout is shown in the Fig. 4. It consists of VCO, PD integrated circuit, MO, the amplifier with variable gain and the second order low-pass filter. All elements are closed in a loop according to the scheme in the Fig. 1.

VCO operates in the 800–1300 MHz frequency band.

The MO frequency is 80 MHz.

PD integrated circuit includes frequency dividers of MO and VCO signals. VCO frequency divider consists of two independently tunable frequency dividers. The division factor of the first one can be set to the 64 or 128. The division factor of the second one can be set in the range from 3 up to 2047. The MO frequency divider permits to vary its division factor n in the range from 3 up to 16383.

Amplifier gain can be changed from 0.7 up to 2.

5. EXPERIMENTAL RESULTS

The experiments goal was to find chaotic oscillation modes in PLL testbed. In order to do this it was necessary to change the PLL parameters and there were only two tunable parameters could be easily changed: frequency division factors of master and voltage-controlled oscillators. In the experiments the frequency division factor n of MO was varied in the range from 11 up to 19, where

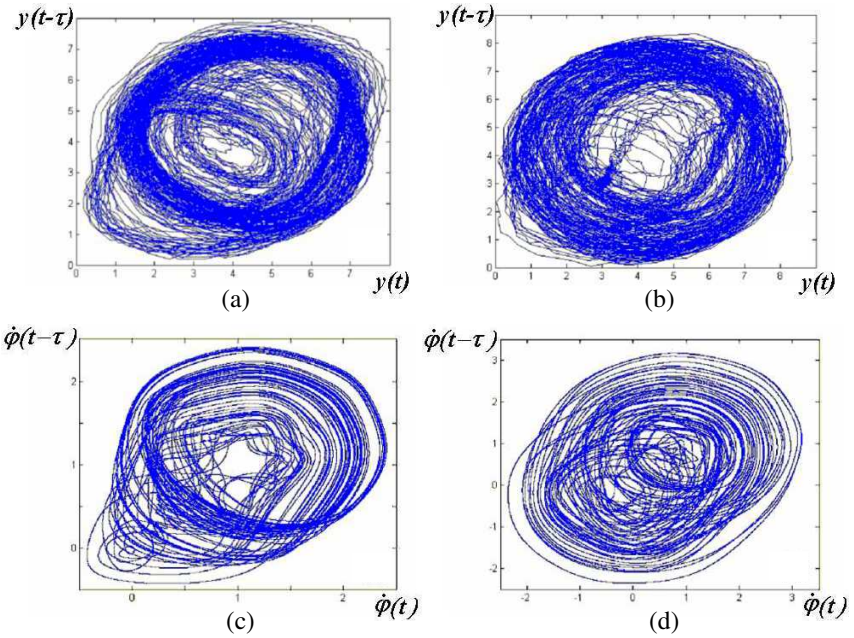

Figure 5: Phase portraits in the plane $(y(t), y(t-\tau))$ (experiment) and in the plane $(\dot{\varphi}(t), \dot{\varphi}(t-\tau))$ (simulation) for (a), (c) $m = 12$, (b), (d) $m = 16$ and $\tau = 250$ ns.

chaotic modes may appear according to the simulation results.

Appearance of chaotic oscillations was determined by means of observation of $y(t)$ waveform, which was recorded by oscilloscope for further computer analysis and for comparison with the simulation results. Also spectrum of VCO signal $X(t)$ was observed.

In order to identify oscillation modes in the simulations and in the experiment, the phase portraits in the plan $(y(t), y(t-\tau))$ and $(\dot{\varphi}(t), \dot{\varphi}(t-\tau))$ were compared. Unlike numerical simulations, where it is possible to calculate the first derivative of the $\varphi(t)$ numerically, it is not possible to do it in the experiments, so we had to be find experimental analogue of the phase portrait in the $(\varphi(t), \dot{\varphi}(t))$ plain. Delay τ equals about 1/4 of quasiperiod of $y(t)$.

Phase portraits for $y(t)$ and power spectrum of the VCO signal $X(t)$ are shown in the Fig. 5 and Fig. 6, respectively. Comparison of the experimental phase portraits (Figs. 5(a), 5(b)) with the simulated phase portraits (Figs. 5(c), 5(d)) confirms the qualitative conformity of dynamics of the experimental testbed and mathematical model. It allows to conclude that oscillatory-rotatory chaos was observed in the experiment.

It can be seen that power spectrum density of the VCO signal $X(t)$ is sufficiently even within its spectrum frequency band. Due to possibility to control frequency of VCO signal $X(t)$ by means of electricity signal the spectrum bandwidth and center frequency of chaotic signal also can be controlled in order to generate chaotic signal at the necessary band. In this case it is important to keep the dimensionless parameter's values (3) to be constant that will guaranty the existence of oscillatory-rotary mode.

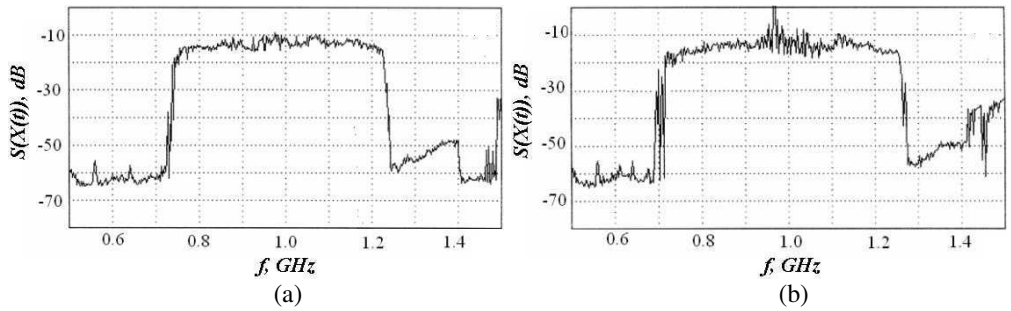

Figure 6: The power spectrum of the VCO output signal $X(t)$ in the experiment for (a) $m = 12$ and (b) $m = 16$.

6. CONCLUSIONS

Theoretical and experimental results outlined in this paper show the possibility to generate phase-chaotic signal by PLL in microwave band. The power spectrum of phase-chaotic signal covers bandwidth from 650 up to 1250 MHz and its envelope is constant.

Thus, it is theoretically proved and experimentally confirmed that chaotic generator based on PLL allows to obtain chaotic signal with properties, which are optimal for some applications, where direct chaotic communication system can be used.

ACKNOWLEDGMENT

Authors acknowledge support from Russian Fund for Basic Research, grant No. 09-02-00983-a.

REFERENCES

1. Win, M. Z. and R. A. Scholtz, "Impulse Radio: How it works," *IEEE Comm. Lett.*, Vol. 2, No 2, 36, 1998.
2. Fontana, R. J., A. Ameti, E. Richley, et al., "Recent advances in ultra wideband communications systems," *Proc. IEEE Conference on Ultra Wideband Systems and Technology*, 129, Baltimore, USA, May 2002.
3. Texas Instruments, et al., "Multi-band OFDM physical layer proposal. IEEE 802.15.3a working group submission," Jul. 2003, http://www.ieee802.org/15/pub/2003/Jul03/03268r2P802-15_TG3a-Multi-band-CFP-Document.pdf.
4. Dmitriev, A. S., B. E. Kyarginskii, A. I. Panas, and S. O. Starkov, "Plain scheme of chaotic-carrier data communications at microwave frequencies," *J. Communications Technology and Electronics*, Vol. 46, No. 2, 224, 2001.

5. Dmitriev, A. S., B. E. Kyarginskii, and A. I. Panas, "Experiments on ultrawideband direct chaotic data transmission in the microwave band," *J. Communications Technology and Electronics*, Vol. 47, No. 10, 1219, 2002.
6. Dmitriev, A. S., B. Ye. Kyarginsky, A. I. Panas, et al., 'Experiments on ultra wideband direct chaotic information transmission in microwave band," *Int. J. Bifurcation and Chaos*, Vol. 13, No. 6, 1495, 2003.
7. 802.15.4a-2007, IEEE Standard for Information Technology — Telecommunications and information exchange between systems — Local and metropolitan area networks — specific requirement Part 15.4: Wireless Medium Access Control (MAC) and Physical Layer (PHY) Specifications for Low-Rate Wireless Personal Area Networks (WPANs), C. 181. http://ieeexplore.ieee.org/servlet/opac?punumber=4299494.
8. Atanov, N. V., A. S. Dmitriev, E. V. Efremova, and N. A. Maksimov, "Formation of chaotic radio pulses in the generator with external periodic influence," *Pisma v ZTF*, Vol. 32, No. 15, 1–6, 2006.
9. Dmitriev, A. S., E. V. Efremova, N. A. Maksimov, and E. V. Grigor'ev, "Generator of microwave chaotic oscillations based on a self-oscillating system with 2.5 degrees of freedom," *J. Communications Technology and Electronics*, Vol. 52, No. 10, 1137, 2007.
10. Dmitriev, A. S., A. V. Kletsov, A. M. Laktushkin, et al., "Ultrawideband wireless communications based on dynamic chaos," *J. Communications Technology and Electronics*, Vol. 51. No. 10, 1126, 2006.
11. Endo, T. and L. O. Chua, "Chaos from phase-locked loops," *IEEE Trans. V. CAS*, Vol. 35, No. 8, 87, 1988.
12. Kolumban, G. and B. Vizvari, "Nonlinear dynamics and chaotic behaviour of the analog phase-locked loop," *Proc. NDES'95*, 99–102, Dublin, Ireland, 1995.
13. Korsinova, M. V., V. V. Matrosov, and V. D. Shalfeev, "Communications using cascade coupled phase-locked loop chaos," *Int. J. Bifurcation and Chaos*, Vol. 9, No. 5, 963–973, 1999.
14. Dmitriev, A. S., A. V. Kletsov, and L. V. Kuzmin, "RF chaotic oscillations in phase-locked loop," *Uspehi Sovremennoy Radioelektroniki*, No. 1, 46, 2008 (in Russian).
15. Dmitriev, A. S., A. V. Kletsov, and L. V. Kuzmin, "Generation of ultrawideband phase-chaotic signals in microwave band," *J. Communications Technology and Electronics*, Vol. 54, No. 6, 2009.
16. Dmitriev, A. S. and M. E.S hirokov, "Choice of generator for a direct chaotic communications system," *J. Communications Technology and Electronics*, Vol. 49, No. 7, 790, 2004.

Multi-band Chaotic Oscillator with Phase-locked Loop

K. G. Mishagin[1,3], **V. V. Matrosov**[1], **L. V. Kuzmin**[2], **and A. V. Kletsov**[2]

[1]University of Nizhny Novgorod, Russia
[2]Institute of Radioengineering and Electronics of RAS, Russia
[3]JSC "Vremya-Ch", Nizhny Novgorod, Russia

Abstract— The use of phase locked loops (PLLs) gives the opportunity to develop wideband chaotic oscillator with manipulated spectrum (electronic switching of frequency bands, electronic control of spectrum width). This paper contains results on numerical study of mathematical model of PLL and results of modeling with the use of specialized electronic design software. Considered models take into account peculiarities of modern components of phase locked loops (pulse phase discriminators, frequency dividers). Analysis of these models approves the possibility of control of spectrum width and possibility of electronic shifting of spectrum of chaotic phase-modulated signals in wide frequency range. Shift of the frequency range is obtained by means of changing coefficients of frequency dividers in phase locked loop. Additional control of the loop gain allows keeping the same dynamic properties of chaotic frequency modulation during spectrum shifting. As an example we have modeled generator of phase chaos with spectrum width about 500 MHz and ability of spectrum steering in the range 3–5 GHz.

1. INTRODUCTION

At present, research activity in the field of communications using chaotic signals switches from theoretical studies to the area of real engineering developments, which have perspectives of commercial application. It is worth mentioning that direct chaotic communication system, which was developed in IRE RAS [1–3], is included in the international standard for information technology 802.15.4a-2007, specifications for low-rate wireless personal area networks, as an optional solution for physical layer [4]. The majority of developed chaotic oscillator schemes for chaos communications, and also for direct chaotic communication system, produce chaotic signals with amplitude, varying irregularly in time. However for simple receiving system, which contains amplitude detector, it is preferable to use wideband signals with fixed amplitude and chaotically varying phase. In a number of theoretical [5–8] and experimental works [8–12], the possibility of applying phase locked loops to produce oscillations with chaotic phase was shown. The results presented in these works tell us that voltage controlled oscillator (VCO) with phase locked loop can produce wideband and ultra-wideband oscillations with homogeneous spectrum in different frequency ranges, including UHF range [12]. In this work, we show that PLL allows generating wideband phase-modulated oscillations with steerable spectrum. Steering range can be greater than the spectrum width for several times, therefore it is possible to realize in one device electronic switching of wideband UHF oscillations between non-overlapping frequency bands. We have accomplished modeling of PLL taking into account peculiarities of modern widespread microchips. Results confirm that chaotic wideband oscillations can be produced in wide domains of system parameters and spectrum of such oscillations can be controlled easily.

Let us consider standard PLL scheme, presented in Fig. 1, which contains voltage controlled oscillator, phase discriminator (comparator), loop filter, two frequency dividers, and additional amplifier in the control loop. Before describing the mathematical model (Section 3), we discuss some peculiarities of modern phase detectors in Section 2.

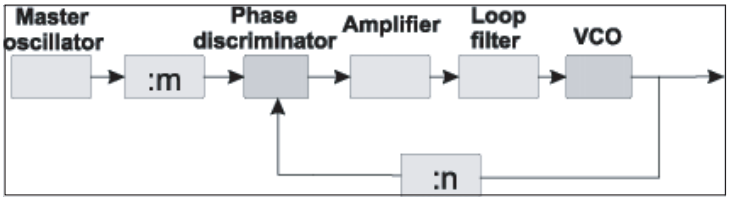

Figure 1: Functional diagram of PLL.

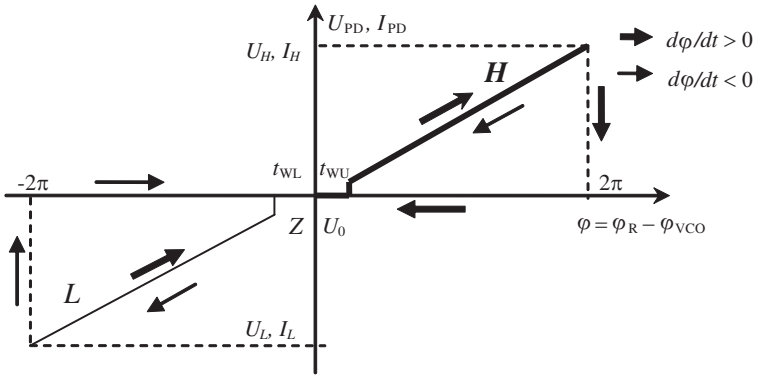

Figure 2: Proportional phase-frequency detector characteristic — Dependence of averaged output voltage ($U_{\rm PD}$) or current ($I_{\rm PD}$) on phase difference φ between input signals.

2. PHASE DISCRIMINATOR MODEL

The simplest phase detector (PD), used in modern PLLs, is an XOR gate. The average value of this square wave is the DC component that sets the VCO frequency. The square-wave changes duty-cycle in proportion to the phase difference resulting, after the filter, in the VCO control voltage. Its characteristics are very similar to the analog mixer for capture range, lock time, and low-pass filter requirements. Its model characteristic [9] is 2π-periodical and close to sine-characteristic of analog mixer. That is why nonlinear dynamics (including chaotic regimes) of PLL with XOR phase detector is much similar to dynamics of classical PLL model, which assumes sinusoidal model characteristic of PD.

Another widespread type of PD is proportional phase-frequency detector (PPFD), which employs a charge pump that supplies charge amounts in proportion to the phase error detected (Fig. 2). Some have dead bands (Z in Fig. 2), which are areas where small changes in phase difference produce no correction to the VCO. If the inputs are slightly mismatched, either the up (H-level) or down (L-level) pulse will contain slightly more charge than the other and the PLL will be able to correct the offset.

Model characteristic of PPFD substantially differs from characteristic of analog mixer that is why we present it in Fig. 2. It has linear part (excluding dead-zone) on the interval $[-2\pi, 2\pi]$, but it is not 4π-periodical. Lock-in range of PLL with PPFD equals to the holding range in contrast to PLL with analog mixer or XOR PD demonstrating hysteresis phenomenon on the boundary of synchronization regime.

Results of modeling presented below were obtained for both characteristics: XOR and PPFD. For modeling of PPFD in electronic design software, we considered parameters of PPFD close to parameters of MB15E03SL. Moreover, for simplicity we assumed that only one output of PPFD (for up-pulses or for down-pulses) is used in PLL-scheme, i.e., only one part of PPFD characteristic (Fig. 2) takes place.

3. PLL MODEL

Experiments in UHF range [12] confirm that PLL with low-pass RLC-filter in the control loop allows producing wideband oscillations with chaotic phase and homogeneous spectrum. Let us consider mathematical model of PLL with frequency dividers (Fig. 1) and second-order low-pass loop-filter [5, 10, 11]:

$$\mu\frac{d^3\varphi}{d\tau^3} + \varepsilon\frac{d^2\varphi}{d\tau^2} + \frac{d\varphi}{d\tau} + F(\varphi) = \gamma, \tag{1}$$

$$\varepsilon = \frac{\Omega}{n}RC, \quad \mu = \left(\frac{\Omega}{n}\right)^2 LC, \quad \gamma = \frac{n}{\Omega}\left(\frac{\omega_0}{n} - \frac{\omega_{\rm REF}}{m}\right), \quad \varphi = \frac{\theta_{\rm VCO}}{n} - \frac{\theta_{\rm REF}}{m}, \quad \tau = t\frac{\Omega}{n}. \tag{2}$$

In Equations (1)–(2): n — Frequency divider coefficient for VCO oscillations, m – Frequency divider coefficient for reference oscillations, R, L, C — Filter parameters (resistance, inductance, capacitance), ω_0 — Natural frequency of VCO, $\omega_{\rm REF}$ — Frequency of the reference signal, $\theta_{\rm VCO}$ and $\theta_{\rm REF}$ — Phases of VCO and reference oscillations. Parameter Ω is the half of frequency holding

rage:

$$\Omega = \pi SG(U_H - U_L) \tag{3}$$

Here S — Frequency tuning sensitivity of VCO, U_H and U_L — Maximum and minimum voltages on the output of phase discriminator, G — Gain of amplifier in the control loop of PLL (Fig. 1).

PLLs may feature various chaotic regimes in which the phase difference between response and master signals is either limited (quasi-synchronous chaotic regimes) or exhibits unlimited growth or decay (chaotic beats). It is known [8–12], that chaotic attractors which combine oscillatory and rotatory motions of phase difference (see Fig. 3) correspond to the oscillations with more wide and homogeneous spectrum than attractors corresponding to quasi-synchronous regimes or regimes of beats with pure rotatory dynamics of phase difference.

Chaotic regime presented in Fig. 3 exists in wide regions of parameters of model (1) which were studied for μ, $\varepsilon > 1$ [5, 8]. The presence of divider coefficient n in the model leads to small ε and μ, close or even smaller than 1. It occurs because n can be large enough in case of big ratio of VCO frequency to the reference frequency. For small ε and μ dynamics of (1) looks more complicated, nevertheless chaotic oscillations can be excited if $\mu \gg \varepsilon$. This qualitative condition means high Q-factor of the loop filter: $Q = (\mu)^{1/2}/\varepsilon$.

4. RESULTS OF MODELING

Here the topical result of electronic steering of the spectrum of wideband chaotic oscillations is presented. Modeling was carried out in specialized electronic design software and by numerical analysis of (1). In modeling PPFD phase, discriminator is used. We divide frequency range 3–5 GHz into four bands: 3–3.5 GHz, 3.5–4 GHz, 4–4.5 GHz, 4.5–5 GHz. To make electronic switching between bands we have to change natural frequency of VCO together with divider coefficient n for minimizing frequency difference between input signals at the input of phase discriminator. In this case, parameters ε and μ depending on n substantially changes. It can cause changing of dynamic properties of chaotic oscillations or even hitting in regular regime. To prevent changing of selected

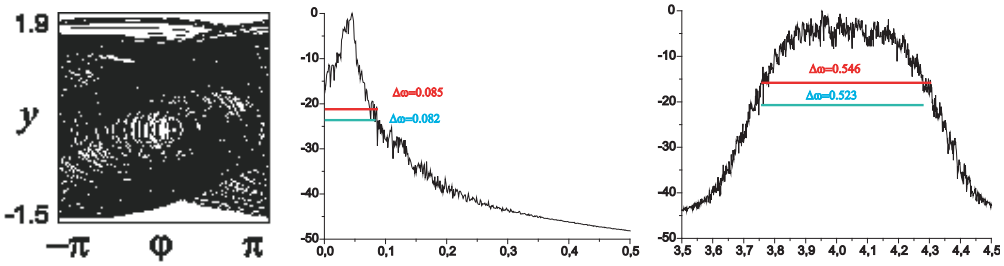

Figure 3: Phase portrait, $y = d\varphi/\tau$ (left), spectrum of oscillations at the input of VCO (center), spectrum of modulated oscillations at the output of VCO (right). Results for model (1) with XOR phase discriminator.

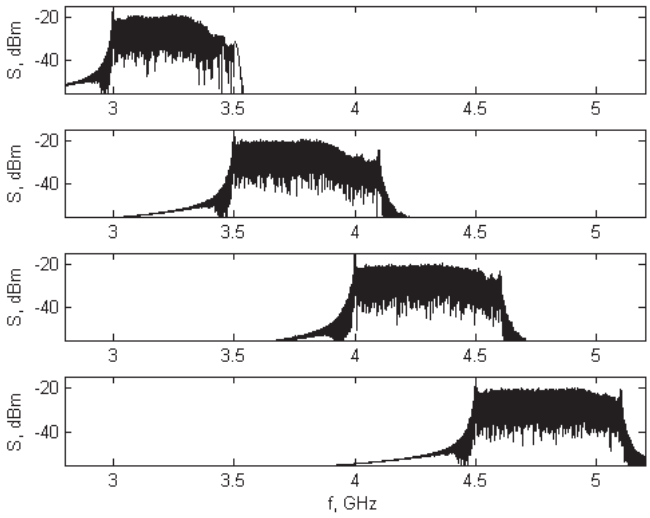

Figure 4: Electronic steering of chaotic spectrum in PLL.

chaotic regime it is necessary to keep constant all parameters in (1). It is possible if in addition to keeping $\omega_0/n = \text{const}$, we guarantee that $\Omega/n = \text{const}$. To fulfill the second condition, control of loop amplifier gain G is required (see Eq. (3)).

In modeling parameters, ω_0, n and G were been changing to switch frequency bands and to keep constant dimensionless parameters: $\varepsilon \approx 0.117$, $\mu \approx 1.52$, $\gamma \approx -1.58$ (variation of parameters is few percents of its values). Results of modeling (Fig. 4) demonstrate possibility of electronic switching of wideband chaotic oscillations between different frequency bands. Note, that manipulation of gain parameter G leads to change of spectrum width, because it effects on amplitude of modulation in the control loop of PLL.

5. CONCLUSION

Electronic manipulation of the spectrum of wideband oscillations with chaotic phase, realized in one device — PLL, looks perspective to be applied in modern wireless communications. For instance, it can be used for additional frequency division multiplexing. PLL is widespread, robust system which can be easily implemented, it makes chaotic generator based on PLL simple and feasible.

Before applying oscillations with chaotic phase produced by PLL to direct chaotic systems we have to answer the key question about the speed of chaotic modulation, because it limits the maximum rate of information transmission. Mathematical model (1) does not include any delay or inertance of control element of PLL, so in modeling it is possible to achieve maximum frequency modulation with the rate comparable to the frequency of pulses (or oscillations) at the output of the phase discriminator. To study the inertance of VCO, we considered a simple VCO scheme based on transistor BFP405. We have found that rough retuning of VCO frequency from 6 to 7 GHz takes less than $\tau^* = 3$ ns. Therefore we can estimate the maximum rate of frequency modulation as 300 MHz (note that for smaller frequency deviation and for smooth retuning, maximum modulation rate can be much greater). If the length of chaotic pulses is ten times longer than τ^*, then the transmission rate will be approximately 30 Mbps.

ACKNOWLEDGMENT

We thank Professor A. S. Dmitriev and Professor V. D. Shalfeev for stimulating and valuable discussions. Authors acknowledge support from RFBR, grants No. 07-02-01404, 09-02-00983-a.

REFERENCES

1. Dmitriev, A. S., B. Y. Kyarginsky, A. I. Panas, et al., "Experiments on ultra wideband direct chaotic information transmission in microwave band," *Int. J. Bifurcation and Chaos*, Vol. 13, No. 6, 1495, 2003.
2. Dmitriev A. S., K. V. Zakharchenko, and D. Y. Puzikov, "Introduction to the theory of direct chaotic communications," *Journal of Communications Technology & Electronics*, Vol. 48, No. 3, 293–302, 2003.
3. Dmitriev, A. S., A. V. Kletsov, A. M. Laktyushkin, A. I. Panas, and S. O. Starkov, "Ultrawideband wireless communications based on dynamic chaos," *Journal of Communications Technology & Electronics*, Vol. 51, No. 10, 1126–1140, 2006.
4. 802.15.4a-2007, *IEEE Standard for Information Technology — Telecommunications and Information Exchange between Systems — Local and Metropolitan Area Networks — Specific Requirement Part 15.4: Wireless Medium Access Control (MAC) and Physical Layer (PHY) Specifications for Low-Rate*, Wireless Personal Area Networks (WPANs), 181, 2007, http://ieeexplore.ieee.org/servlet/opac?punumber=4299494.
5. Matrosov, V. V., "Regular and chaotic oscillations of phase systems," *Technical Phys. Letters*, Vol. 22, No. 23, 4–8, 1996.
6. Korsinova, M. V., V. V. Matrosov, and V. D. Shalfeev, *Int. J. Bifurcation and Chaos*, Vol. 9, No. 5, 963, 1999.
7. Shalfeev, V. D. and V. V. Matrosov, *Chaos in Circuits and Systems*, Ed. by G. Chen and T. Ueta, World Scientific Publishing Company, Singapore, 2002.
8. Matrosov, V. V., "Self-modulation regimes of a phase-locked loop with the second-order filter," *Radiophysics and Quantum Electronics*, Vol. 49, No. 4, 322–332, 2006.
9. Kolumban, G. and B. Vizvari, "Nonlinear dynamics and chaotic behavior of the analog phase-locked loop," *Proceedings of NDES'95*, 99, Dublin, Ireland, 1995.

10. Mishagin, K. G., V. V. Matrosov, V. D. Shalfeev, and V. V. Shokhnin, "Generation of chaotic oscillations in the experimental scheme of two cascade-coupled phase systems," *Journal of Communications Technology & Electronics*, Vol. 52, No. 10, 1064–2269, 2007.
11. Dmitriev, A. S., A. V. Kletsov, and L. V. Kuzmin, "Generation of RF chaos with PLL circuit," *Uspekhi Sovremennoy Radioelektroniki*, No. 1, 46, 2008 (in Russian).
12. Dmitriev, A. S., A. V. Kletsov, and L. V. Kuzmin, "Generation of ultrawideband phase-chaotic signals in microwave band," *Journal of Communications Technology & Electronics*, No. 6, 2009.

3–5 GHz Ultra-wideband Omnidirectional Printed Circuit Antenna

Ant. V. Uvarov[1], **N. P. Chybinskiy**[1], **and Andr. V. Uvarov**[1, 2]

[1]Moscow Institute of Physics and Technology (State University), Moscow, Russia
[2]Kotel'nikov Institute of Radio Engineering and Electronics of Russian Academy of Sciences, Russia

Abstract— A compact printed ring-sector microstrip monopole antenna is proposed for 3–5 GHz frequency band. A technique of translation antenna design for different substrate materials is presented. A comparison with conventional quarter-wavelength dipole antenna is also considered and described.

1. INTRODUCTION

Evolution of miniature ultra-wideband transceivers based on different type of signals (for example, direct chaotic communication systems [1]) for wireless communication networks has led to the integration of antennas on the same substrate with a transceiver microwave module. The standard approach means separate development of both microwave printed circuit board (PCB) topology and antenna topology, e.g., die mounting on the PCB surface. Integration of printed circuit antenna on the same substrate with the microwave electronics module lets to achieve new levels of compactness, to get rid of unnecessary processes (surface assembling non-standard size antenna installation) and to investigate further interaction between antenna and electronics. The article describes developed ultra-wideband omnidirectional printed circuit antenna with small dimensions and simple (well-reproduced in standard manufacturing processes of two-layer printed circuit board technology) topology. The initial analysis has examined the various electrodynamics configurations of antennas, such as either dipole antenna or monopole polygon antenna with different forms of the radiating surface.

2. PRINTED RING SEGMENT MONOPOLE ANTENNA

Recently printed monopole antennas are becoming more and more disseminate [2–4]. The original monopole antennas represent a monopole located above a metal screen. It has been shown in [2] that for disk monopole currents flow mainly in the area of projection of the disc in the plane of the screen. This fact suggests the possibility of developing monopole with very thin screen, namely, the screen reduced to a thickness of a metal plating of the printed circuit board. Printed monopole antenna may have different shapes of the radiating surface, such as triangular, square or even hexagonal, but more popular are circular and ellipsoidal due to wider bandwidth [2–4].

The majority of papers describe print monopole antennas with frequency band width of 3 : 1 and greater. As shown in [2] widebandness of a monopole antenna is a result of existence weak resonances fine grid distribution, due to standing wave currents modes. Wideband matching is achieved by setting the proper antenna impedance at the resonant frequencies close to the feed line impedance. In this case, the maximum wavelength of the antenna operating range (and accordingly, the lower limit of frequency range) is determined by the first resonance frequency corresponding to the length of the perimeter of the antenna equaled to the wavelength. So for monopole disc antenna with diameter d the antenna linear size to the highest wavelength ratio can be evaluated as:

$$\frac{d}{\lambda_{\max}} = \frac{1}{\pi\sqrt{\varepsilon_{eff}}}, \tag{1}$$

where ε_{eff} — effective dielectric permittivity of material surrounding the antenna (could be assumed as mean of vacuum and substrate dielectric constants). The numerical valuation for the most common FR4 substrate gives: $d/\lambda_{\max} = 0.2$. However, if you do not need ultra wide band, the size of the radiating surface can be reduced in times!

The compact ring sector printed monopole antenna (see Fig. 1) has been developed for the frequency range of 3–5 GHz for UWB direct chaotic transceiver for wireless sensor networks [5]. The linear size of the antenna (outer diameter of the ring sector) is approximately $0.1{\cdot}\lambda_{\max}$, two times less than for a standard ultra wideband monopole. We could reduce antenna area in four times because of matching the impedance of feed line with the impedance of monopole at the non-resonant frequency. Fee for small size of antenna reduced the width of frequency band to 50%.

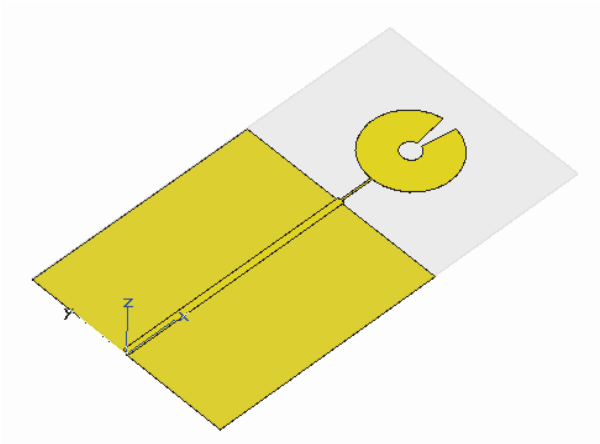

Figure 1: Configuration of the printed ring segment monopole antenna on the 0.254 mm thickness Rogers RT-5870 substrate ($\varepsilon = 2.33$). The outer diameter of ring is 10 mm, the inner diameter is 2 mm, the gap width between monopole and edge of ground plane is 3.4 mm and the angle of cutted ring sector if 17 deg. 50 Ohm-microstrip line is used as a feed line and thin (0.2 mm width) strip is utilized to excite the monopole.

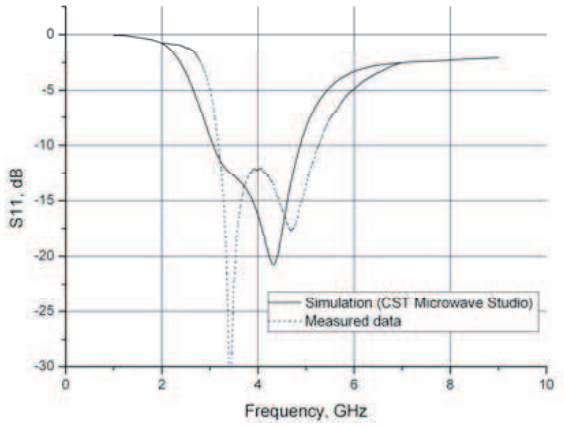

Figure 2: Comparison of calculated VSWR with measured one of printed ring segment monopole antenna.

The developed antenna is made in the shape of a ring sector: center hole and triangular notch are produced to remove the area with the lowest current density. As shown in Fig. 2, we have reached VSWR less than 2 : 1 throw the 3–5 GHz frequency band. Full-wave electromagnetic simulator CST Microwave Studio [6] was used to analyze the structure. As shown in Fig. 2 experimental results with good accuracy confirmed the calculated data. The antenna design represents a platform of ring sector over the metal screen. The monopole and screen are located in different layers of the printed circuit board, made on a Rogers RT-5870 substrate with the permittivity $\varepsilon = 2.33$ and thickness 0.254 mm. 50 Ohm-microstrip line is used as a feed line and thin (0.2 mm width) strip is utilized to excite the monopole. The gap between the screen and monopole determines the impedance and thus the antenna tuning. The gap was chosen to achieve VSWR better than 2 : 1 in the desired frequency band (3–5 GHz). The calculated beam pattern of monopole antenna in various cross sections shown in Fig. 3. In the E-plane (yz-section) beam pattern looks like a typical beam pattern for monopole antenna, in H-plane beam pattern is almost isotropic.

Beam pattern of proposed antenna depends basically on the shape of a monopole radiating surface. Antenna impedance is determined by the gap between the monopole and the screen, so antenna can be easily optimized for a different types or thicknesses of the substrate by recalculating the width of the gap. A correlation between gap width monopole antenna tuned to 4 GHz central frequency and substrate material permittivity for different thicknesses represented on Fig. 4.

Despite the fact that the linear size of the radiating surface of the monopole antenna is succeeded to be reduced two times in comparison with a standard size of classical dipole antenna. The effective value of minimum required size of antenna will be at least twice as much as linear size of monopole

radiating surface, as far as it highly depends on the width of the screen. Thus, the effective width of the antenna will not be determined by the size of emitting area, but by the width of the screen, which will be at least $0.2\lambda_{\max}$. As a result, the size of the antenna will be almost equal to the length of a standard quarter-wavelength dipole (described in the next section).

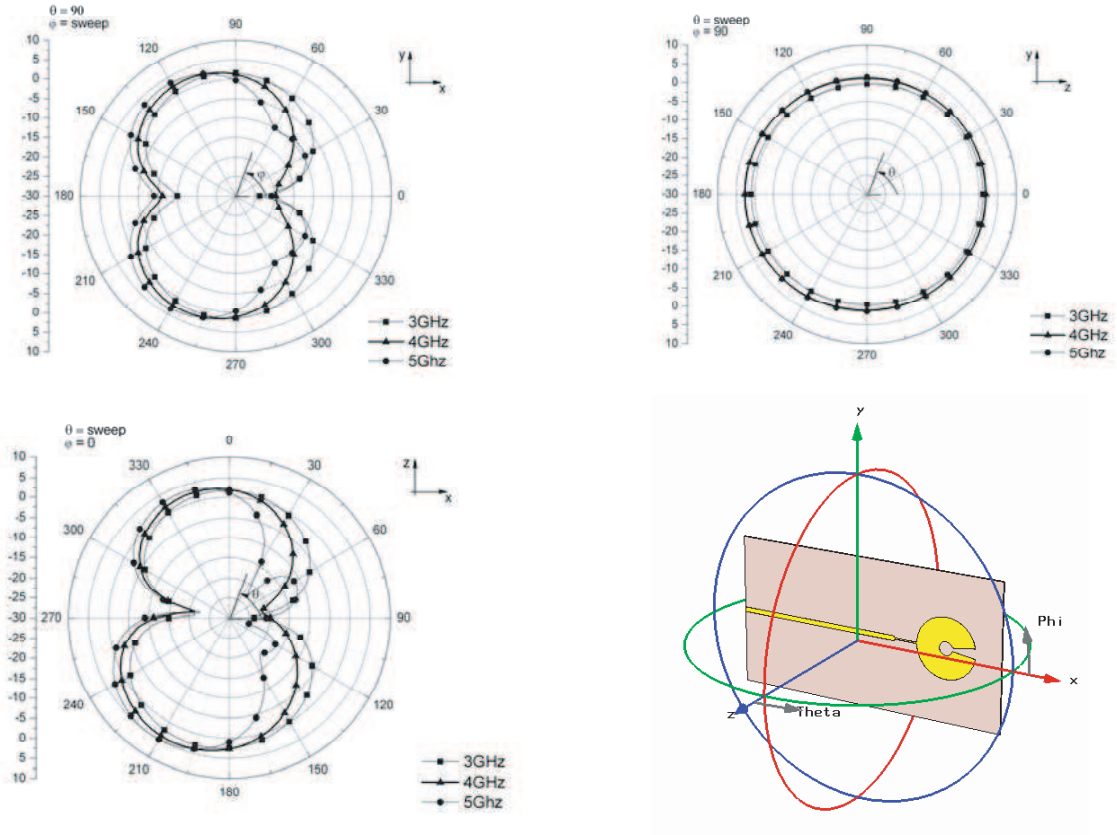

Figure 3: Beam pattern of ring-sector printed monopole antenna for main polarization.

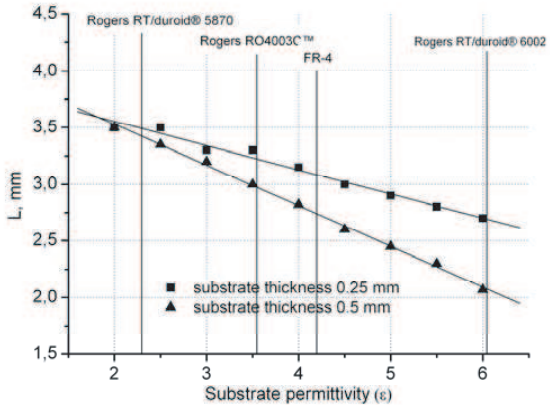

Figure 4: Optimized for tuning on 4 GHz central frequency gap width between monopole and the screen edge over typical substrate permittivity range.

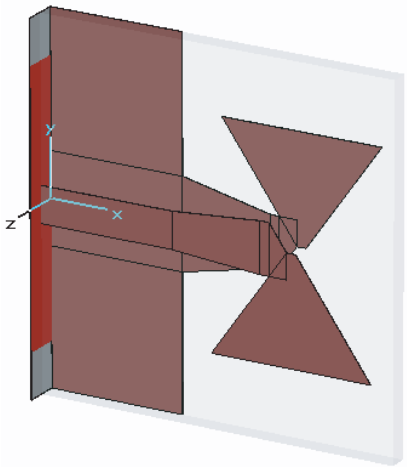

Figure 5: Configuration of 6–8 GHz band quarter-wavelength bow-tie dipole antenna printed on the 1mm-thikness FR-4 substrate.

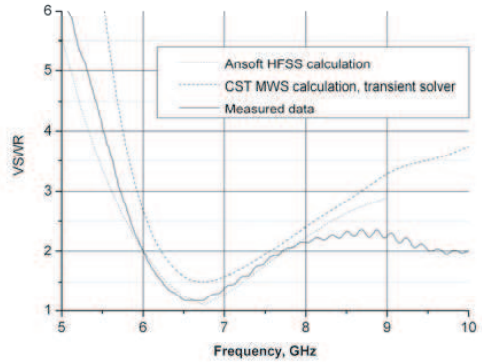

Figure 6: Comparison of calculated VSWR with measured one for printed bow-tie dipole antenna.

3. COMPARISON WITH PRINTED QUOTER-WAVELENGTH BOW-TIE DIPOLE ANTENNA

Also, we have developed and tested prototype dipole bow-tie antenna for 6–8 GHz band. The frequency choice was made due to the current needs; to compare with monopole antenna the results of dipole can be scaled at the center frequency of 4 GHz. Relative bandwidth can be increased through a more precise tuning of the system. Dipole antenna (see Fig. 5) consists of a microstrip feed line, bow-tie dipole and transforming line (transition from microstrip to the plane-parallel line). The antenna was designed for the FR-4 substrate with $\varepsilon = 4.2$ and a thickness of 1 mm. At a given frequency range VSWR has been achieved better than 2 : 1 (Fig. 6). Results of comparison of tow printed antennas are presented in Table 1.

Table 1: Comparison of main parameters of proposed printed monopole and quarter-wavelength bow-tie dipole.

	Ring sector monopole antenna	Quarter-wavelength bow-tie dipole antenna
Frequency band	3–5 GHz	6–8 GHz
Bandwidth	50%	30%
VSWR (throw the band)	2 : 1	2 : 1
Directivity	4 dBi	5.7 dBi
Substrate material	Rogers RT-5870 ($\varepsilon = 2.33$)	FR-4 ($\varepsilon = 4.2$)
Linear geometric size: length × width (in wavelength at center frequency)	$(0.18{\cdot}\lambda) \times (0.28{\cdot}\lambda)$	$(0.26{\cdot}\lambda) \times (0.28{\cdot}\lambda)$

4. CONCLUSIONS

Two basic approaches for ultra wide band miniature omnidirectional printed antennas were considered. We optimized antennas for each frequency band (3–5 GHz and 6–8 GHz) since current prototypes of the receiving-transmitting modules with direct chaotic modulation is not required bandwidth of more than 50%. Therefore antenna actually acts as a band-pass filter and cut industrial noises and noise outside the specified frequency band. We developed two compact UWB antennas with approximately the same geometrical size (see Table 1). An advantage of proposed monopole antenna over quarter-wavelength dipole is approximately two times wider bandwidth for 30%-smaller required PCB area. Designed monopole antenna could be easily translated to another

production technology (namely, the substrate material) by means of antenna tuning involves changing of a table known (for each substrate materials) parameter - the gap between monopole and the screen edge.

ACKNOWLEDGMENT

Authors thank Alexander S. Dmitriev for encouragement and many fruitful discussions.

REFERENCES

1. Dmitriev, A. S., B. Y. Kyarginsky, A. I. Panas, and S. O. Starkov, "Experiments on ultra wideband direct chaotic information transmission in microwave band," *Int. J. Bifurcation & Chaos*, Vol. 13, No. 6, 1495–1507, 2003.
2. Liang, J., "Antenna study and design for ultra wideband communication applications," Ph.D. thesis, Department of Electronic Engineering Queen Mary, University of London, United Kingdom, July 2006.
3. Kobayashi, H., T. Sasamori, T. Tobana, and K. Abe, "A study on miniaturization of printed disc monopole antenna for UWB applications using notched ground plane," *IEICE Trans. Commun.*, Vol. E90–B, No. 9, 2239–2245, 2007.
4. Azenui, N. C. and H. Y. D. Yang, "A printed crescent patch antenna for ultrawideband applications," *IEEE Antennas and Wireless Propagation Letters*, Vol. 6, 113–116, 2007.
5. Dmitriev, A. S., A. Laktushkin, Y. Andereyev, A. Kletsov, L. Kuzmin, and V. Sinyakin, "UWB direct chaotic transceiver for wireless sensor networks," *ICECS-2008*, Malta, August 31–September 3, 2008.
6. CST MWS software, On-line available: http://www.cst.com.